

**SUBSTORMS** VIII

Proceedings of the 8<sup>th</sup> International  
Conference on Substorms

Edited by Mikko Syrjäsuo and Eric Donovan

**Copyright © Institute for Space Research, University of Calgary**

The papers in this book comprise the proceedings of the Eighth International Conference on Substorms.

**ISBN 0-88953-312-1**

**ISBN 978-0-88953-312-7**

The cover art by Emma Spanswick is a composite of the photographs by Jouni Jussila (auroras) and Mikko Syrjäsuo (Rundle Mountain in Banff)

# Preface

In March 2006, roughly 140 substorm researchers from around the world descended on Banff Canada for the Eighth International Conference on Substorms (ICS VIII). The meeting was held at The Banff Centre which provided a beautiful venue for the event. Two satellite meetings were held on the preceding weekend. These were a storm-substorm relationship workshop, and the Second International Riometer Workshop. Both drew around 20 attendees, many of whom stayed for ICS VIII.

In the time leading up to ICS VIII, it was clear that while we are in an exciting period of substorm research, there is frustration in the space physics community related to this topic. On the one hand, recent observational, theoretical, and simulation work has uncovered fascinating new facets of the substorm problem. For observational examples, we now have direct and unambiguous observations of mid-tail reconnection from Geotail and Cluster, and we are developing a clear picture of the global evolution of the magnetosphere during the substorm, its role in the storm, and interesting new global substorm related phenomena such as sawtooth events. On the theoretical and simulation side, great progress has been made in the use of simulations ranging from global MHD right down to kinetic scales to explore the many instabilities and waves that we know are at work during the substorm. New work on natural complexity is challenging our long held reductionist views. Substorm studies are at least as interesting and rich as it has ever been.

Still, as a sub-discipline we continue to struggle with age-old questions. This is the source of the angst. The fundamental problem relates to paucity of data and temporal resolution insufficient to differentiate between competing theories. At this ICS, we somehow managed to avoid debates that are fundamentally unresolvable, but still consider the dominant paradigms. Maybe the specter of THEMIS and our ever-increasing ability to deliver truly synoptic observations was offering light at the end of that long tunnel. Whatever the reason, by the end of ICS VIII there was unquestionably energy for the subject and we had, as a community, decided that there will be at least three more ICS meetings (Graz, Napa Valley, Braunschweig in 2008, 2010, and 2012, respectively). We also agreed that we should evolve the nature of these conferences and possibly even the theme itself.

This conference proceeding contains 61 papers. As for all other ICS publications, these papers have not been refereed. Many authors took this opportunity to say things more strongly than they could in a refereed venue, and so some of the ideas here may be ahead of their time, overstated, or even both. That is the spirit of an unrefereed forum.

The ICS VIII Scientific Program Committee is grateful to all of the attendees for contributing to this successful meeting and to both the Canadian Space Agency and the University of Calgary for their financial support. There was an excellent international turnout, and dozens of students. The presentations were well thought out, and the attendees contributed to lively discussions in and around the meeting room.

See you in Graz in 2008!

Eric Donovan,  
on behalf of the ICS VIII Scientific Organizing Committee



# Contents

Onset of substorm expansion phase: theory predictions and results of experimental observations .....	1
<i>E.E. Antonova</i>	
Formation of the thin current sheets in substorms and its relation to the magnetic reconnection .....	7
<i>Y. Asano, R. Nakamura, A. Runov, W. Baumjohann, T. Takada, I. Shinohara, A. Balogh, B. Klecker and H. Rème</i>	
The dependence of magnetospheric topology and convection (including night-side reconnection) on the average magnetic flux transfer rate .....	13
<i>G. Atkinson</i>	
On the role of entropy conservation and entropy loss governing substorm phases .....	19
<i>J. Birn, M. Hesse and K. Schindler</i>	
Depletion of electrons in a multiple substorm event on November 15th, 2001 .....	25
<i>C.R. Bryant, J.S. Murphree, E. Donovan and S.B. Mende</i>	
Spatio-temporal dynamics of substorms during intense geospace storms .....	31
<i>J. Chen, A.S. Sharma and X. Shao</i>	
Interpretation of automated forward modeling parameters for sawtooth events and substorms .....	37
<i>M. Connors, R.L. McPherron and C.R. Clauer</i>	
Forced current sheets in a flapping magnetotail .....	43
<i>C.M. Cully, R.E. Ergun, E. Lucek, A. Eriksson, D.N. Baker and C. Mouikis</i>	
Nonlinear stability of the near-earth plasma sheet during substorms .....	49
<i>P. Dobias, J.A. Wanliss and J.C. Samson</i>	
The azimuthal evolution of the substorm expansive phase onset aurora .....	55
<i>E. Donovan, S. Mende, B. Jackel, M. Syrjäsuo, M. Meurant, I. Voronkov, H. Frey, V. Angelopoulos and M. Connors</i>	

On the role of non-Maxwellian forms of distribution functions in the process of acceleration of auroral particles .....	61
<i>N.O. Ermakova E.E. Antonova</i>	
Observations of tail dynamics using ground and space based instruments during a period of multiple substorm events .....	65
<i>C. Forsyth, M. Lester, S.E. Milan, A. Grocott, H.U. Frey, E. Lucek, H. Reme and J. Watermann</i>	
Substorm onsets as observed by IMAGE-FUV .....	71
<i>H.U. Frey and S.B. Mende</i>	
Polar spacecraft observations near 9 RE: rapid multiple dipolarizations and their interpretation .....	77
<i>Y.S. Ge, C.T. Russell, T.-S. Hsu and R.L. McPherron</i>	
SuperDARN observations of ionospheric convection during magnetospheric substorms .....	81
<i>A. Grocott and T.K. Yeoman</i>	
Are we on the right approach to solve the substorm problem? .....	87
<i>W.J. Heikkila</i>	
Physics modeling of storms and substorms with solar wind data .....	93
<i>W. Horton, M.L. Mays and E. Spencer</i>	
Kinetic instabilities in substorm dynamics .....	99
<i>W. Horton, J.-H. Kim, E. Spencer and C. Crabtree</i>	
The statistical characteristics of IMF triggered substorms .....	105
<i>T.-S. Hsu and R.L. McPherron</i>	
Low-latitude geomagnetic disturbances caused by solar wind pressure impulses and storm-time periodic substorms during southward interplanetary magnetic field .....	111
<i>C.-S. Huang and K. Yumoto</i>	

Monitoring the dayside and nightside reconnection rates during various auroral events using IMAGE-FUV and SuperDARN data .....	117
<i>B. Hubert, M. Palmroth, S.E. Milan, A. Grocott, P. Janhunen, K. Kauristie, S.W.H. Cowley, T.I. Pulkkinen and J.-C. Gérard</i>	
Energy flux of electron precipitation as monitored by an all-sky camera .....	123
<i>K. Kauristie, N. Partamies, S. Mäkinen, R. Kuula and A. Strømme</i>	
Solar wind and interplanetary magnetic field features before magnetic storm onset .....	127
<i>O. Khabarova, V. Pilipenko, M.J. Engebretson and E. Rudenichik</i>	
Cluster observations of plasma sheet activity during the September 14-28, 2003 corotating high speed stream event .....	133
<i>A. Korth, E. Echer, F.L. Guarnieri, M. Fränz, R. Friedel, W.D. Gonzalez, C.G. Mouikis and H. Rème</i>	
EISCAT radar and optical studies of black aurora: a signature of magnetospheric turbulence? .....	139
<i>M. J. Kosch, B. Gustavsson, E.M. Blixt, T. Pedersen, A. Senior, A.J. Kavanagh and J. Semeter</i>	
Small scale Cluster observations of current sheet disruptions during substorm .....	143
<i>O. Le Contel, F. Sahraoui, A. Roux, D. Fontaine, P. Robert, J.-A. Sauvaud, C. Owen and A. Fazakerley</i>	
Convection vortices in pre- and post-midnight sector during magnetospheric substorms .....	149
<i>J. Liang, G. Sofko and H. Frey</i>	
An avalanche model of magnetospheric substorms based on cross-scale coupling in the central plasma sheet .....	153
<i>W. Liu, P. Charbonneau, E. Donovan and J. Manuel</i>	
The active plasma sheet: definition of 'events' and statistical analysis .....	159
<i>P. Louarn, C. Jacquy, E. Budnik, V. Génot and the CDPP, FGM, CIS and STAFF teams</i>	
Relation of substorm disturbances triggered by abrupt solar-wind changes to physics of plasma sheet transport .....	165
<i>L.R. Lyons, D.-Y. Lee, C.-P. Wang and S.B. Mende</i>	

Challenges of multi-spacecraft missions to end the substorm controversy .....	171
<i>R.L. McPherron and T.-S. Hsu</i>	
SuperDARN and IMAGE WIC observations during intervals of steady magnetospheric convection .....	175
<i>K.A. McWilliams, J.B. Pfeifer, R.L. McPherron and H.U. Frey</i>	
EL — a possible indicator to monitor the magnetic field stretching at global scale during substorm expansive phase: case study .....	181
<i>M. Meurant, C. Blockx, E. Spanswick, E.F. Donovan, B. Hubert, J.-C. Gérard, T.S. Trondsen and M. Connors</i>	
Magnetic flux transport in the Dungey cycle: the role of substorms in flux closure .....	187
<i>S.E. Milan, G. Provan and B. Hubert</i>	
Pi2 pulsation periodicity and variations in magnetotail flows .....	191
<i>K.R. Murphy, A. Kale, I.J. Rae, I.R. Mann and Z.C. Dent</i>	
Fast flow, dipolarization, and substorm evolution: Cluster/Double Star multipoint observations .....	197
<i>R. Nakamura, T. Takada, W. Baumjohann, M. Volwerk, T.L. Zhang, Y. Asano, A. Runov, Z. Vörös, E. Lucek, C. Carr, B. Klecker, H. Rème and O. Amm</i>	
Simultaneous observations of ions of ionospheric origin over the ionosphere and in the plasma sheet at storm-time substorms .....	203
<i>M. Nosé, T. Kunori, Y. Ono, S. Taguchi, K. Hosokawa, T.E. Moore, M.R. Collier, S.P. Christon and R.W. McEntire</i>	
Automated detection of Pi2 pulsations to monitor substorm signatures: its application to real-time data and archived data .....	209
<i>M. Nosé, T. Iyemori, M. Takeda, T. Kamei, F. Honary, S.R. Marple, J. Matzka, T. Ookawa, K. Takahashi and G. Cifuentes-Nava</i>	
Conjugate imaging of substorms .....	215
<i>N. Østgaard, S.B. Mende, H.U. Frey, J.B. Sigwarth, A. Aasnes and J.M. Weygand</i>	
Time history effects at the magnetopause: hysteresis in power input and its implications to substorm processes .....	219
<i>M. Palmroth, T.I. Pulkkinen, T.V. Laitinen, H.E.J. Koskinen and P. Janhunen</i>	

Observing the MLT and L-shell dependence of ground magnetic signatures of the ionospheric Alfvén resonator <i>A. Parent, I.R. Mann and K. Shiokawa</i>	225
Strong stretching in dusk sector: stormtime activations and sawtooth events compared <i>N. Partamies, T.I. Pulkkinen, E.F. Donovan, H.J. Singer, E.I. Tanskanen, R.L. McPherron, M.G. Henderson and G.D. Reeves</i>	231
An attempt to locate substorm onsets using Pi1 signatures <i>V.A. Pilipenko, I.I. Tchebotareva, M.J. Engebretson, J.L. Posch and A. Rodger</i>	237
Effects of pressure gradients and convection on the inner plasma sheet stability <i>V. Prosofin, I. Voronkov and E. Donovan</i>	241
Thin current sheets as part of the substorm process <i>T.I. Pulkkinen, C.C. Goodrich, J.G. Lyon and H.J. Singer</i>	247
Pi2 pulsations: field line resonances or a driven response? <i>I.J. Rae, I.R. Mann, D.K. Milling, Z.C. Dent and A. Kale</i>	253
Auroral oval boundary observations by Meteor 3M satellite <i>M.O. Riazantseva, E.E. Antonova, B.V. Marjin, V.V. Hoteenkova, I.L. Ovchinnikov, M.A. Saveliev, V.M. Feigin and M.V. Stepanova</i>	259
Substorm theories and Cluster multi-point measurements <i>A. Roux, O. Le Contel, D. Fontaine, P. Robert, P. Louarn, J.A. Sauvaud and A.N. Fazakerley</i>	263
Cluster observations during pseudo-breakups and substorms <i>A. Runov, I.O. Voronkov, Y. Asano, R. Nakamura, W. Baumjohann, M. Volwerk, T. Takada, Z. Voros, T.L. Zhang, A. Vaivads, S. Haaland, H. Rème and A. Balogh</i>	269
Magnetic reconnection and current disruption in the inner magnetosphere — a case study <i>V. Sergeev, M. Kubyshkina, W. Baumjohann, R. Nakamura, A. Runov, Z. Voros, T. Zhang, K. Glassmeier, J.-A. Sauvaud, P. Daly, V. Angelopoulos, H. Frey and H. Singer</i>	275

Multilayered structure of thin current sheets: multiscale "Matreshka" model .....	279
<i>A.S. Sharma, L.M. Zelenyi, H.V. Malova, V. Yu. Popov and D.C. Delcourt</i>	
Decrease in Bz prior to the dipolarization in the near-Earth plasma sheet .....	285
<i>K. Shiokawa, Y. Miyashita, I. Shinohara and A. Matsuoka</i>	
Ground and satellite observations of substorm onset arcs .....	291
<i>K. Shiokawa, K. Yago, K. Yumoto, K. Hayashi, D.G. Baishev, S.I. Solov'yev, F.J. Rich and S.B. Mende</i>	
Auroral secondary ions in the inner magnetosphere .....	297
<i>G. Sofko, M. Watanabe, R. Schwab and C. Huang</i>	
The macroscale evolution of the substorm injection .....	303
<i>E. Spanswick, E. Donovan, R. Friedel and D. Danskin</i>	
Automatic classification of auroral images in substorm studies .....	309
<i>M.T. Syrjäsoo, E.F. Donovan, X. Qin and Y.-H. Yang</i>	
Impossibility of calculating magnetic field change from current disruption .....	315
<i>V.M. Vasyliūnas</i>	
Features of magnetosphere-ionosphere coupling during breakups and substorm onsets inferred from multi-instrument alignment .....	319
<i>I. Voronkov, A. Runov, A. Koustov, K. Kabin, M. Meurant, E. Donovan, C. Bryant and E. Spanswick</i>	
Scaling properties of high latitude magnetic field data during different magnetospheric conditions .....	325
<i>J.A. Wanliss and D.O. Cersosimo</i>	
IMAGE analysis and modelling of substorm onsets .....	331
<i>J.A. Wanliss and G. Rostoker</i>	
Five plus four equals nine: combining the THEMIS and Cluster missions .....	337
<i>J.A. Wild and M.A. Hapgood</i>	

# Onset of substorm expansion phase: theory predictions and results of experimental observations

E. E. Antonova

**Abstract:** The problem of substorm expansion phase onset continues to be one of the most actual problems of the physics of magnetospheric substorm. It is deeply connected to the problems of the plasma transport in the magnetosphere, stability of magnetospheric magnetic and plasma configurations. The most popular mechanisms of substorm expansion phase onset are based on the analysis of the stability of magnetospheric currents and distribution of plasma pressure. The results of observations of substorm expansion phase onset are summarized and compared with predictions of different theories. It is shown that the existence of high level of plasma sheet turbulence produces the limitation on the action of possible mechanisms of substorm expansion phase onset. Configurations of magnetospheric current systems developed during substorm growth and expansion phases are discussed.

*Key words:* substorm expansion phase onset, magnetospheric plasma pressure, magnetospheric turbulence.

## 1. Introduction

It is possible to identify three periods of the study of substorm expansion phase onset. Akasofu [1] showed that the most equatorial arc brightening takes place during the substorm expansion phase onset. Posteriorly the substorm auroral disturbance moved to the pole. The inner plasma sheet boundary was observed in [42] not so far from the geostationary orbit. Injections of energetic particles near the inner edge of the plasma sheet are known as one of the fundamental signatures of magnetospheric substorms from the beginning of 70-th [27]. The existence of dispersionless injections demonstrated the action of acceleration processes near the geostationary orbit. Therefore the substorm expansion phase onset as the result of the development of the inner magnetospheric instability became the dominant point of view at this first period.

Second period is related to the analysis of geomagnetic tail dynamics. It was shown that the change of the topology of magnetic field lines (reconnection processes) and plasmoid formation occur nearly simultaneously with the substorm expansion phase onset. The concept of tail current instability as a source of substorm expansion phase onset [17] became the dominant one for more than two decades. Great number of brilliant theoretical investigations have been done to describe the tail reconnection process. Nevertheless the tail current instability hypothesis have met a number of difficulties even at the first stages of its development. It was clear that the stability of tail current depends on the value of  $B_z$  component of magnetic field, where  $B_z$  is given in GSM coordinate system. Theoretical studies showed that the decrease of  $B_z$  leads to the instability development. However it also was known that  $B_z$  decreases with the increase of geocentric distance. Therefore it was very difficult to explain why the first auroral arc

brightening occur near the equatorial plasma sheet boundary. As a consequence, it was proposed [36] that the auroral initial brightening is caused by the braking of earthward high-speed flow (bursty bulk flow — BBF) having as a source the tail reconnection processes. Nevertheless, it also was clear from the beginning of the BBF studies, that they take place even under very quite geomagnetic conditions (see [33]) and that they occur much more frequently than substorms. This means that the probability to observe BBF in the plasma sheet 1–5 min before the substorm expansion phase onset is very high. One-to-one correspondence between flow bursts in the plasma sheet and equatorward-moving auroral structures (auroral streamers) was found later [35]. Another difficulty was connected to the high level of turbulence observed at the auroral field lines and in the plasma sheet [3] as all reconnection models suggest the existence of laminar plasma flows outside the reconnection regions.

Third period began with AMPTE/CCE registration of substorm expansion phase onset at the geocentric distances less than  $9 R_E$  [39] and continues till now. These investigations lead to the appearance of tail current disruption hypothesis (see the review [24]) and disrupted current closing in the ionosphere.

In this paper we try to summarize the latest findings concerning the role of plasma sheet turbulence for substorm dynamics, analyze the substorm expansion phase onset and select a number of effects which can be quite important for the solution of substorm problem. We try to show that the analysis of plasma pressure redistribution can help to clarify some modern findings connected to the physics of substorm. We also try to select the key problems which may be interesting to solve during the realization of future auroral satellite missions.

## 2. Magnetospheric turbulence and localization of substorm expansion phase onset

Numerous observations showed (see [9]) the existence of high level of plasma sheet turbulence. These results are quite

Received 15 May 2006.

E. E. Antonova, Skobeltsyn Institute of Nuclear Physics Moscow State University, Moscow, 119992, Russia; Space Research Institute of RAS, Moscow, Russia

natural, taking into account that the magnetic field of the Earth represents an obstacle for the solar wind flow. Plasma sheet appears due to solar wind flow around magnetic field of the Earth at very large values of Reynolds number ( $> 10^{10}$ ) forming a turbulent wake. It is necessary to mention also that solar wind can also be considered as turbulent medium [40]. Power low spectra obtained for fluctuations of solar wind parameters, indexes for magnetospheric activity [41] and scale-free statistical distributions of nighttime auroral emission regions [20] demonstrate this feature of magnetospheric dynamics quite clearly.

The localization of substorm onset at the geocentric distances less than  $9 R_E$  is now supported by many observations (see reviews [2, 12, 24, 25, 28, 32]). Realization of THEMIS program will probably finally identify this exact position. However the reason of such localization is not clear till now. Antonova [9] argues that the localization of substorm expansion phase onset near the equatorial boundary of auroral oval can be explained taking into account the existence of plasma sheet turbulence. It is a common point of view that the substorm expansion phase onset is the result of the development of some kind of instability. However, only a region stable before an onset can become unstable. Comparatively stable plasma distribution exists in the inner magnetospheric region. Therefore the transition region from dipole to tailward stretched field lines (not very far from the geostationary orbit) is selected as the most probable one.

The existence of plasma sheet turbulence requires the reanalysis of the process of plasma transport. The diffusion-like terms appear in transport equations in the simplest one-fluid analysis (see [3, 5]). The continuity equation has the form

$$\frac{\partial \rho}{\partial t} + \frac{\partial}{\partial \mathbf{r}} \left( \rho \mathbf{V} - D \frac{\partial \rho}{\partial \mathbf{r}} \right) = 0 \quad (1)$$

where  $\rho$  is plasma density,  $\mathbf{V}$  is the regular velocity,  $D$  is the effective quasisdiffusion coefficient. Correlation time of plasma sheet velocity fluctuations is  $\sim 2$  min and the correlation time of magnetic field fluctuations is  $\sim 10$  min [10]. Therefore it is possible to consider that Amperes force in the momentum equation is nearly constant and consider the velocity fluctuations only. Then taking into account results of [19] the momentum equation has the form

$$\frac{\partial \rho V_i}{\partial t} + \frac{\partial}{\partial r_j} \left[ \left( \rho V_j - D \frac{\partial \rho}{\partial r_j} \right) V_i \right] = - \frac{\partial p}{\partial r_i} - \frac{\partial \pi_{ij}}{\partial r_i} + [\mathbf{jB}]_i \quad (2)$$

where  $p$  is the plasma pressure,  $\pi_{ij}$  is the viscous tensor,  $\mathbf{j}$  and  $\mathbf{B}$  are the current density and magnetic field respectively. The observed nonequipotentiality of magnetic field lines and turbulent character of plasma flow leads to the nonconservation of the number of particles in a magnetic flux tube. The solution of the problem of plasma transport in such a case becomes very complicated. The complexity of the problem is increased due to nonisotropic character of plasma sheet turbulence (existence of particle beams). Developed models of plasma transport by dawn-dusk electric field inside the magnetosphere can be used when the value of regular flux becomes much larger than the value of turbulent flux.

### 3. Mechanisms of substorm onset

Many mechanisms have been developed for the explanation of main features of isolated substorm onset (see reviews [12, 24]). It is possible to select four main classes of these instabilities:

- 1) instabilities of transverse tail current;
- 2) instabilities of plasma pressure gradients;
- 3) instabilities of shear velocity distributions;
- 4) instabilities of field-aligned currents.

Instabilities which are not related to kinetic effects have definite preferences, because electromagnetic fluctuations are constantly observed at the auroral field lines.

Every suggested theory must explain such well known experimental results as auroral brightening, transverse current disruption, magnetic field dipolarization, dispersionless particle injections, fast plasma flows, generation of Pi2 and Pi1B geomagnetic micropulsations. Some new results have been obtained during the last years, which must be included in substorm onset picture. First of all it is shown that only nearly equatorial arc has a brightening without any auroral activity to the north [16, 26]. Arcs poleward of the arc that breaks up appear to be unaffected by substorm onset until expansion-phase auroral activity moves poleward to the location of such arcs. The azimuthal extent of the initial brightening was determined in [14]. It is found that the projection of the initial dispersionless injection into the ionosphere are similar to the brightening arc. It is found also [22] that Pi2 bursts can often lag behind the brightening of the onset arc. Enhanced plasma flows were observed using SuperDarn data in a spatially confined region near the auroral oval for a period of  $\sim 5$  minutes prior to the brightening [11]. Comprehensive ground (optical, riometer and magnetometer) data and FAST satellite field and particle high resolution observations [15] demonstrate the substorm onset at the geocentric distances  $\sim 8 R_E$ . The arc flux tube stays in the region of considerable plasma pressure gradient where the pressure values are close to 12 nPa. The arc was located just  $0.4^\circ$  poleward of the proton isotropic (b2i) boundary (which roughly gives the value of  $\sim 40$  nT for the equatorial magnetic field) and close to the peak of the diffuse electron precipitation. The results [15] are in a rather good agreements with AMPTE/CCE measurements [23] in which the value of plasma pressure in the region of substorm expansion phase onset was  $\sim 1$  nPa. Onset arc in the work [15] is localized in the upward field-aligned current region. Three cases of onset arc observations are analyzed in [37]. The brightening arcs are also located in the upward field-aligned current region.

The latest findings and early mentioned difficulties of tail reconnection theories lead to the real restrictions of possible scenario of substorm expansive phase onset. It is clear that local instability is developed in the region mapped into the equatorial boundary of discrete auroral precipitations. This instability produces auroral brightening, launches Pi1B and Pi2 micropulsations. The development of processes must create the change in magnetospheric transverse currents. The latest process produces magnetic field dipolarization and corresponding particle injections. The development of instability must also lead to the changes in tail current configuration, appearance of reconnection events and corresponding fast plasma flows. The brightening of the arc before the beginning of Pi2 burst and the existence of fast plasma flow before brightening can mean the

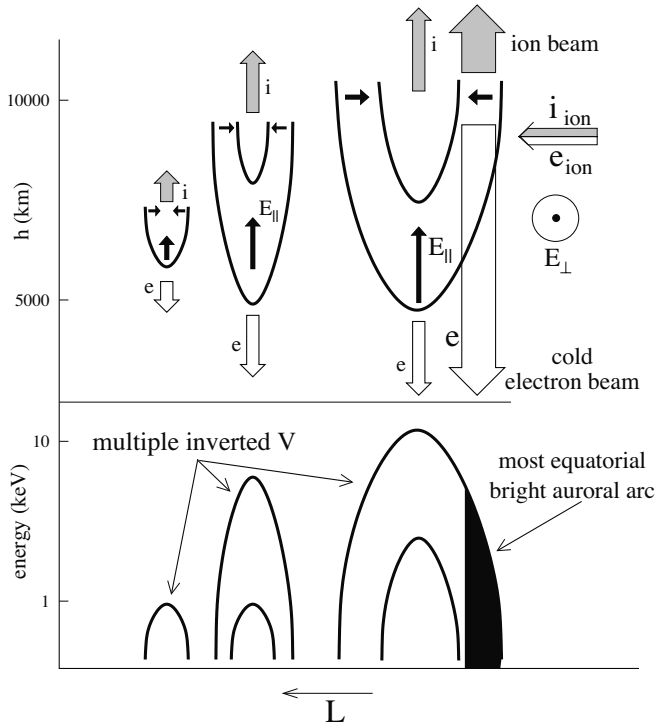


**Fig. 1.** Sketch illustrating the scheme of onset arc brightening.

development of some kind of electrostatic instability. Electrostatic instabilities generally have greater increments than electromagnetic ones because they do not require the distortion of magnetic field. These findings are in agreement with the predictions of [4, 38].

The analysis of multiple inverted V structures during substorm growth phase demonstrate the existence of latitudinal asymmetry [38]. The most equatorial inverted V is the most powerful one. This means that the upward field-aligned current is distributed inhomogeneously during substorm growth phase across current band and the most intense field-aligned current is concentrated at the equatorial boundary of the band.

Particle acceleration inside an inverted V structure is connected with the existence of field-aligned potential drop. The existence of such field-aligned potential drop means magnetosphere-ionosphere decoupling. Ionospheric damping of magnetospheric disturbances is decreased in such regions. Penetration of cold ionospheric plasma inside the region of field-aligned potential drop creates the powerful directed to the ionosphere anisotropic electron beam and ion beam directed to the magnetosphere at the boundary of inverted V [38]. Energy of electrons in such a beam are smaller than field-aligned potential drop and the electron flux in it can be 1–2 orders of magnitude larger than the flux of accelerated magnetospheric electrons. Therefore the auroral arc brightening or the formation of new very bright arc can be the result of discussed process. The analysis of Fig. 3 of [15] and Fig. 5 of [37] supports the possibility of such process development.

Observed fast plasma flows before the substorm expansion phase onset in the conditions of stable magnetic field can be the result of the development of some kind of electrostatic in-

stability. One of such instabilities is connected to the existence of azimuthal plasma pressure gradients. It can be named modified interchange instability. The main features of such instability development in the region of upward field-aligned current are discussed in [4, 38]. Azimuthal plasma pressure gradients are identified as a source of large-scale Region 1 and Region 2 field-aligned currents of Iijima and Potemra. Therefore the growth of field-aligned currents during substorm growth phase is connected to the increase of azimuthal plasma pressure gradients. The loss of the stability of azimuthal plasma pressure gradient leads to the appearance of localized electric fields. Fig. 1 schematically shows the suggested scenario of auroral arc brightening. Accelerated in the preexisted field-aligned potential drop electrons and ions of ionospheric origin create thin sheet of field-aligned current which leads to launching of Alfvén waves (Pi1B and Pi2 micropulsations) and the destabilization of magnetic configuration.

#### 4. Substorm onset and transverse current configuration

The configuration of magnetospheric currents before the substorm expansion phase onset is not clear till now. Theories of tail magnetic field reconnection and current disruption suggest that the substorm expansion phase onset takes place at the tail current lines. Near Earth tail current in accordance with these theories is increased during substorm growth phase. Decrease of tail current and magnetic field line dipolarization takes place when tail current is decreased. Tail current lines are closed by magnetopause currents. But it is possible to argue that current lines in the region of substorm expansion phase onset do not cross the magnetopause.

The appearance of drift echo is one of the constantly observed features of magnetospheric substorm. The drift echo in accordance with [18] can be observed till geocentric distances 12–13  $R_E$ . Therefore the trajectories of the part of substorm injected particles are closed inside the magnetosphere. However trajectories of particles may not coincide with current lines. The configuration of current lines is clear in the case of magnetostatic equilibrium when plasma pressure is nearly isotropic and plasma bulk velocity is much smaller than Alfvén and sound velocity. Then

$$[\mathbf{j}\mathbf{B}] = \nabla p. \quad (3)$$

The relation (3) shows that plasma pressure is constant at current lines. Therefore plasma pressure can be considered as a marker of current lines. According to [23] plasma pressure is nearly isotropic in the region of substorm expansion phase onset and is  $\sim 1$  nPa. This value is typical for regions inside the magnetosphere in accordance with AMPTE/CCE investigations [13]. The value of plasma pressure at current lines closed by the magnetopause currents is limited by the condition of magnetopause stress balance on the tail flanks (see [7]). Traditionally modeled magnetospheric current configuration includes magnetopause current, tail current, ring current and field-aligned currents. Ring current is ordinarily concentrated at geocentric distances  $\sim 5 R_E$ . Nevertheless, plasma population similar to the plasma sheet is observed at daytime to the equator from cusp and low latitude boundary layer (see

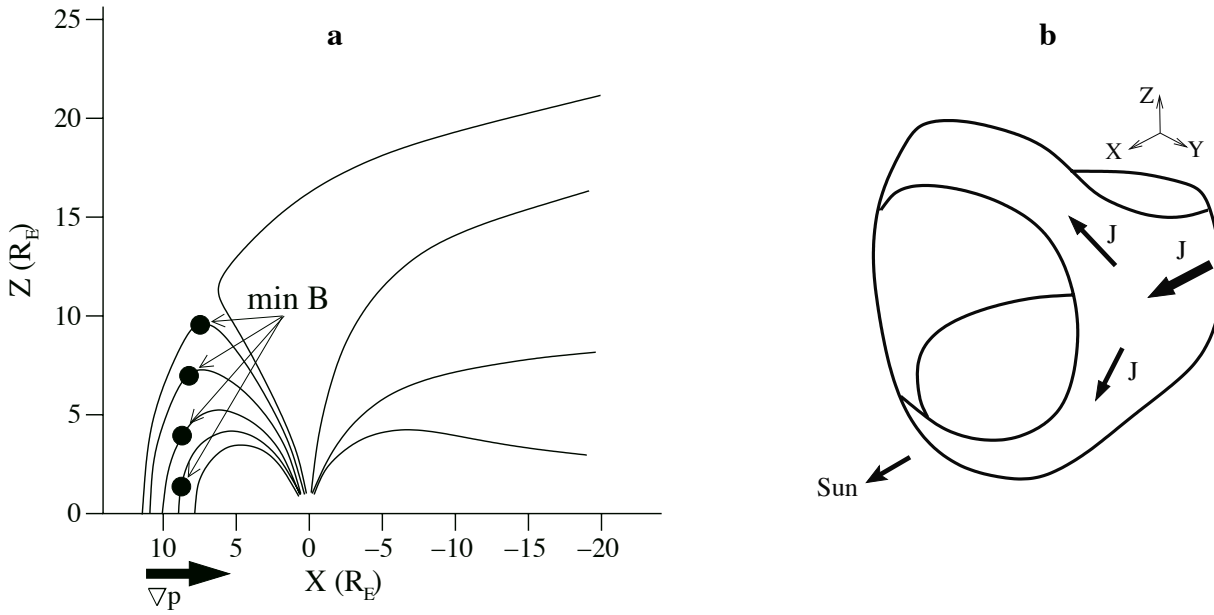


**Fig. 2.** The positions of magnetic field minima on daytime magnetic field lines (a) and sketch illustrating the configuration of cut ring current (CRC).

[30]). Pictures of plasma pressure distribution in the equatorial plane [13] show the existence of near to ring structures of plasma pressure. Therefore directed to the Earth radial daytime plasma pressure gradients are nearly the same as nighttime plasma pressure gradients. But daytime values of magnetic field near the equator are much larger than near noon. Therefore calculated in [13] values of transverse current are much smaller at noon than at midnight. However, the position of the magnetic field minimum for the daytime fieldlines are situated far from the equatorial plane (see Fig. 2a). This means that daytime transverse currents connected to directed to the Earth plasma pressure gradient are concentrated far from the equatorial plane. It is suggested (see [6]) that ordinary ring current has the high latitude continuation (see Fig. 2b) cut ring current (CRC). Current lines of this system close inside the magnetosphere, and are concentrated in the equatorial plane near midnight and at high latitudes near noon. It is possible to see using plasma pressure as a marker of current line that substorm expansion phase onset is localized at CRC current lines.

CRC is not unique large scale inner magnetosphere current system missed during the magnetic field modeling. The increase of the plasma pressure during magnetospheric substorm near the geostationary orbit is supported by many experimental observations. Two possible cases of such increase are analyzed in Fig. 3. Fig 3a correspond to pressure increase without change in the direction of plasma pressure gradient, Fig. 3b corresponds to the appearance of antiearthward directed plasma pressure gradient. However the eastward transverse current must appear in both cases. Case on Fig. 3a corresponds to the creation of effective eastward current (due to decrease of westward current), Fig. 3b corresponds the appearance of real high latitude eastward current. Eastward current increase the value of the magnetic field to the Earth and increase this value to the tail. It was shown in [8] that the appearance of eastward current can lead to the decrease of  $B_z$  component of

near tail magnetic field till the formation of neutral line. Therefore the observed tail reconnection during substorm can have the forced character and can be connected to the increase of plasma pressure at the quasidipole magnetic field lines.

Another important aspect of eastward current formation is the possibility of appearance of over-dipolarization after the beginning of substorm expansion phase. It was stressed in [2] that when the eastward current becomes stronger than the cross-tail current the over-dipolarization of magnetic field lines occurs ( $B_z$  component of magnetic field at the equator from the region of increased pressure becomes larger than in the case of dipole field). The case of over-dipolarization corresponds to plasma pressure distribution shown on Fig. 3b.

One of the main features of the magnetospheric substorm is the magnetic field line stretching before the substorm expansion phase onset. Such stretching is ordinarily prescribed to the formation of a thin and intensified cross-tail current sheet in the near-Earth plasma sheet region ( $\sim 6-13 R_E$ ) [34]. But such interpretation encounters with a number of difficulties. Tail current is closed by magnetopause currents. Therefore the increase of tail current can not have the local character. Nevertheless many observations show the local longitudinal character of field line stretching and dipolarization. This means that currents which produce magnetic field stretching and dipolarization have local character and are closed inside the magnetosphere. The configuration of local currents producing the field line stretching is not clear till now. Analysis of Fig. 1 helps to select the process which leads to field line stretching during substorm growth phase and appearance of thin current sheets. Multiple inverted V structures are the sources of upward directed beams of ionospheric ions. Ions in such beams have energy  $\sim 10$  keV after field-aligned acceleration. Ionospheric ion beam leads to the increase of plasma pressure at the top of field line. Such increase can produce local field line stretching. Azimuthal scale of the inverted V region is much smaller than

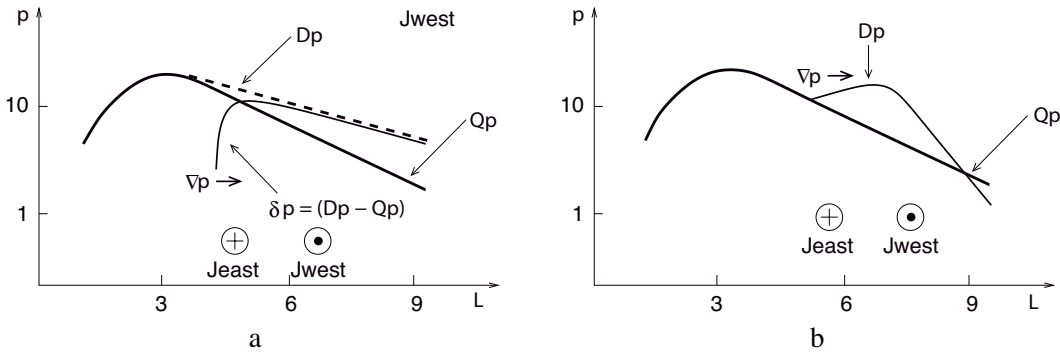


**Fig. 3.** Two possible cases of pressure increase and transverse current formation during substorm.

azimuthal scale of tail current. Therefore produced field-line stretching is longitudinally limited. Time scale of the process is  $\sim 30$  min. It is necessary to mention also that ionospheric ion beam can be considered as a source of the anisotropy of ion distribution. Such anisotropy is the necessary condition for the creation of super thin transverse current sheets in the kinetic models [21, 43]. Therefore it may be interesting to investigate more carefully the distribution of plasma and its anisotropy in the region of substorm onset.

Ion beam (see Fig. 1) formed in the process of onset arc formation is 1–2 orders of magnitude more powerful than ion beam connected to the inverted V structure. Its development in the process of first auroral arc brightening can help to explain explosive growth phase of roughly 30 sec period just before the beginning of dipolarization (Ohtani effect [31]).

## 5. Conclusions and discussion

More than forty years of study of substorm dynamics does not lead to the agreement about the cause and location of the substorm onset. Realization of THEMIS program will greatly increase the understanding of the substorm process. But THEMIS mission is designed mainly to solve the problem of onset location. The additional efforts will require for the understanding the mechanisms of substorm dynamics. The conducted analysis shows that the latest auroral substorm findings can be used as important tests of suggested substorm theories. We try to show that the development of the system of multiple inverted V with the most powerful inverted V at the equatorial boundary of the upward field-aligned current band can be considered as a mechanism of change in the magnetospheric plasma distribution and magnetic configuration and that the formation of onset auroral arc is the key process of substorm onset. It contains powerful upward field-aligned current and produces impulse injection of accelerated ionospheric ions into the magnetosphere. At the same time it creates the magnetic field distortion and launches irregular Alfvénic waves (P1B and P2 micropulsations). The injected ion beam leads to superstretching of magnetic field lines. Such magnetic configuration becomes unstable. The developed instability leads to field line dipolarization and powerful particle acceleration. But all these suggestions need the experimental verification.

Very important aspect of the problem also is the configuration of magnetospheric currents connected with substorm on-

set. We summarize the arguments showing that these currents are closed inside the magnetosphere and have local character.

## Acknowledgments

The research was supported by RFBR grant 05-05-64394-a and INTAS grant 03-51-3738.

## References

1. Akasofu, S.-I., The development of the auroral substorm, *Planet. Space Sci.*, 12(4), 273–282, 1964.
2. Akasofu, S.-I., Several controversial issues on substorm, *Space Science Reviews*, 113(1), 140, 2004.
3. Antonova, E. E., Nonadiabatic diffusion and equalization of concentration and temperature in the plasma layer of the magnetosphere of the Earth, *Geomagnetism and Aeronomia (Engl. Transl.)*, 25(4), 517–520, 1985.
4. Antonova, E. E., The development of initial substorm expansion phase disturbance due to generation of localized electric fields in the region of maximum upward field-aligned current, *Advances in Space Research*, 13(4), 261–264, 1993.
5. Antonova, E. E., and Ovchinnikov, I. L., Magnetostatically equilibrated plasma sheet with developed medium scale turbulence: Structure and implications for substorm dynamics, *Journal of Geophysical Research*, 104(A8), 17,289–17,297, 1999.
6. Antonova, E. E., and Ganushkina, N. Yu., Inner magnetospheric currents and their role in the magnetosphere dynamics, *Physics and Chemistry of the Earth(C)*, 25(1–2), 23–26, 2000.
7. Antonova, E. E., Radial gradients of plasma pressure in the magnetosphere of the Earth and the value of Dst variation, *Geomagnetism and Aeronomy*, 41(2), 148–156, 2001.
8. Antonova, E. E., and Ovchinnikov, I. L., Reconnection in the conditions of developed turbulence, *Advances in Space Research*, 29(7), 1063–1068, 2002.
9. Antonova, E. E., Magnetostatic equilibrium and turbulent transport in Earth's magnetosphere: A review of experimental observation data and theoretical approach. *International Journal of Geomagnetism and Aeronomy*, 3(2), 117–130, 2002.
10. Borovsky, J. E., Thomsen, M. F., and Elphic, R. C., The driving of the plasma sheet by the solar wind, *Journal of Geophysical Research*, 103(A8), 17,617–17,639, 1998.
11. Bristow, W. A., Sotko, G. J., Stenbaek-Nielsen, H. C., Wei, S., Lummerzheim, D., and Otto, A. Detailed analysis of substorm observations using SuperDarn, UVI, ground-based magnetometers, and all-sky images, *Journal of Geophysical Research*, 108(A3), doi:10.1029/2002JA009242, 2003.

12. Cheng, C. Z., Physics of substorm growth phase, onset, and dipolarization, *Space Science Reviews*, 113(1), 207–270, 2004.
13. DeMichelis, P., Daglis, I. A. and Consolini, G., An average image of proton plasma pressure and of current systems in the equatorial plane derived from AMPTE/CCE-CHEM measurements, *Journal of Geophysical Research*, 104(A12), 28,615–28,624, 1999.
14. Donovan, E., Jackel, B., Spanswick, E., Mende, S. and Angelopoulos, V., Azimuthal extent of substorm expansive phase onset, *ICS8 Abstracts*, Banff Centre, March 27–31, 2006, 14, 2006.
15. Dubyagin, S. V., Sergeev, V. A., Carlson, C. W., Marple, S. R., Pulkkinen, T. I. and Yahnin, A. G., Evidence of near-Earth breakup location, *Geophysical Research Letters*, 30(6), doi:10.1029/2002GL016569, 2003.
16. Frank, L. A., and Sigwarth, J. B., Findings concerning the position of substorm onsets with auroral images from the Polar spacecraft, *Journal of Geophysical Research*, 105(A6), 12,747–12,761, 2000.
17. Hones, E. W., Transient phenomena in the magnetotail and their relation to substorms, *Space Science Reviews*, 23(3), 393–410, 1979.
18. Hori, T., Ohtani, S., Lui, A. T. Y., McEntire, R. W., Maezawa, K., Sato, Y., and Mukai, T., A substorm associated drift echo of energetic protons observed by Geotail: Radial density gradient structure, *Geophysical Research Letters*, 30(6), doi:10.1029/20002GL016137, 2003.
19. Klimontovich, Yu. L., Turbulent motion and the structure of chaos. The new approach to the statistical theory of open systems, Kluwer Academic Publishers, Dordrecht, 317 pp., 1990.
20. Kozelov, B. V., and Uritsky, V. M., Scale-free statistics of spatiotemporal auroral emissions obtained from groundbased optical observations, in *ICS-7 Proceedings*, Levy, Finland, 22–26 March 2004, Finnish Meteorological Institute, edited by N. Ganushkina and T. Pulkkinen, Helsinki, 160–163, 2004.
21. Kropotkin, A. P., Malova, H. V., and Sitnov, M. I., Self-consistent structure of a thin anisotropic current sheet, *Journal of Geophysical Research*, 102(A10), 22,099–22,032, 1997.
22. Liou, K., Meng, C.-I., Lui, A. T. Y., Newell, P. T., Brittnacher, M., Parks, G., Reeves, G. D., Anderson, R. R., Yumoto, Y., On relative timing in substorm onset signatures, *Journal of Geophysical Research*, 104(A10), 22,807–22,817, 1999.
23. Lui, A. T. Y., Current disruption in the Earth's magnetosphere: Observations and models, *Journal of Geophysical Research*, 101(A6), 13,067–13,088, 1996.
24. Lui, A. T. Y., Potential plasma instabilities for substorm expansion onsets, *Space Science Reviews*, 113(1), 127–206, 2004.
25. Lyons, R. L., Determination of relative timing of near Earth substorm onset and tail reconnection, in *Proceedings of the 5th International conference on Substorms*, St. Petersburg, Russia, 16–20 May 2000, *Eur. Space Agency Spec. Publ.*, ESA SP-443, 255–262, 2000.
26. Lyons, L. R., Voronkov, I. O., Donovan E. F., Zesta, E., Relation of substorm breakup arc to other growth-phase auroral arcs, *Journal of Geophysical Research*, 107(A11), doi:10.1029/2002JA009, 2002.
27. McIlwain, C. E., Substorm injection boundaries, in *Magnetospheric physics*, ed. by B. M. McCormac, D. Reidel, Hingham, Mass, 143–154, 1974.
28. Meng, C.-I., and Liou K., Substorm timing and timescales: A new aspect, *Space Science Rev.*, 113(1), 41–75, 2004.
29. Millino, A., Orsini, S., and Daglis, I. A., Empirical model of proton flux in the equatorial inner magnetosphere: Development, *Journal of Geophysical Research*, 101(A11), 25,713–25,729, 2001.
30. Newell, P. T., and Meng, C.-I., Mapping the dayside ionosphere to the magnetosphere according to particle precipitation characteristics, *Geophys. Res. Lett.*, 19(6), 609–612, 1992.
31. Ohtani, S., Takahashi, K., Zanetti, L. J., Potemra, T. A., and McEntire, R. W., Initial signatures of magnetic field and energetic particle fluxes at tail reconfiguration: Explosive growth phase, *Journal of Geophysical Research*, 97(A12), 19,311–19,324, 1992.
32. Ohtani, S.-I., Flowbursts in the plasma sheet and auroral substorm onset: Observational constraints on connection between midtail and near-Earth substorm processes, *Space Science Reviews*, 113(1), 77–96, 2004.
33. Rostoker, G., Why we have not yet solved the substorm problem, *Sixth International Conference on Substorms, University of Washington, Seattle March 25–29, 2002*, 1–8, 2002.
34. Sergeev, V. A., Tanskanen, P., Mursula, K., Korth, A. and Elphic, R. C., Current sheet thickness in the near-Earth plasma sheet during substorm growth phase, *Journal of Geophysical Research*, 95(A4), 3819–3828, 1990.
35. Sergeev, V. A., Liou, K., Meng, C.-I., Newell, P. T., Brittnacher, M., Parks, G., and Reeves, G. D., Development of auroral streamers in association with impulsive injections to the inner magnetotail, *Geophys. Res. Lett.*, 26, 417–420, 1999.
36. Shiokawa, K., Baumjohan, W., Haerendel, G., Paschmann, G., Fennell, J. F., Friis-Christensen, E., Luhr, U., Reeves, G. D., Russell, C. T., Sutcliffe, P. R., Takahashi, K., High-speed ion flow, substorm current wedge, and multiple Pi 2 pulsations, *Journal of Geophysical Research*, 103(A3), 4491–4508, 1998.
37. Shiokawa, K., Yago, K., Yumoto, K., Baishev, D. G., Solov'yev, S. I., Rich, F. J., and S. B. Mende, Ground and satellite observations of substorm onset arcs, *Journal of Geophysical Research*, 110(A12), doi:10.1029/2005JA011281, 2005.
38. Stepanova, M. V., Antonova, E. E., Bosqued, J. M., Kovrazhkin, R. A. and Aubel, K. R., Asymmetry of auroral electron precipitations and its relationship to the substorm expansion phase onset, *Journal of Geophysical Research*, 107(A7), doi:10.1029/2001JA003503, 2002.
39. Takahashi, K. L., Zanetti, L. J., Lopez, R. E., McEntire, R. W., Potemra, T. A., Yumoto, K., Disruption of the magnetotail current sheet observed by AMPTE/CCE, *Geophysical Research Letters*, 14(10), 1019–1022, 1987.
40. Tu, C.-Y., and Marsch, E., MHD structures, waves and turbulence in the solar wind: Observations and theories, *Space Science Reviews*, 73(1/2), 1–210, 1995.
41. Uritsky, V. M., and Pudovkin, M. I., Low frequency 1/f-like fluctuations of the AE-index as a possible manifestation of self-organized criticality in the magnetosphere, *Annales Geophysicae*, 16(12), 1580–1588, 1998.
42. Vasyliunas, V. M., The interrelationship of magnetospheric processes, in *Earth's Magnetospheric Processes*, edited by B.M. McCormac, Higham, Mass., Holland, 29–38, 1972.
43. Zelenyi, L. M., Delcourt, D. C., Malova, H. V., Sharma, A. S., “Aging” of the magnetotail thin current sheets, *Geophysical Research Letters*, 29(12), doi:10.1029/2001GL013789, 2002.

# Formation of the thin current sheets in substorms and its relation to the magnetic reconnection

Y. Asano, R. Nakamura, A. Runov, W. Baumjohann, T. Takada, I. Shinohara, A. Balogh, B. Klecker, and H. Rème

**Abstract:** The dynamical structure of current sheets during the growth phase of substorms is examined using Cluster multi-satellite observations. We present an event in which the current sheet temporarily becomes a non-Harris current sheet, namely, a bifurcated current sheet, and then a sheet with an over-intense current in the center in the last stage of the growth phase. Temporal variation of the current sheet thickness caused by a compressional wave with a time period of several minutes is also observed. It seems associated with the local activity in a different local time sector. Sausage-mode oscillation of the current sheet which is observed in the expansion phase or associated with fast plasma flows, is not found during the growth phase.

*Key words:* substorm, magnetotail, current sheet.

## 1. Introduction

Formation of thin current sheets with a vertical scale of an ion inertial length is considered to be one of the most important processes in substorm onset mechanisms. In particular, it is believed to be closely related to the occurrence of the magnetic reconnection in the magnetotail. Gradual thinning of the current sheet in the growth phase has been reported repeatedly [10, 11, 18, 17]. However, these previous observations of the thin current sheet before the substorm onset was limited in the region  $X_{gsm} > -15R_E$ .

On the other hand, the initial location of the X line formation is revealed to be in the region  $-30 R_E < X_{gsm} < -20 R_E$  from the past observations [12, 13, 6]. Only a part of the near-Earth current sheet becomes thin comparable to the ion inertial length [1]. On average it is only down to several thousands km. This is usually interpreted as the spatial localization of the “real” thin current sheet formation.

However, recent observations have revealed that the current sheet structures frequently deviate from the normal Harris-type current sheet, namely, over-intense current in the center or bifurcated current sheets [2]. An embedded thin intense current in the center is found to be extended to the tail region  $X_{gsm} = -30 R_E$  [14]. Such a type of current sheet may be important in the evolution of instabilities which lead to the X line formation, yet the direct observation of such type of the thin current sheet by the single satellite was difficult.

Furthermore, the current sheet in the growth phase frequently shows flapping motions [24] or kink-like-mode oscillation [19,

16]. Temporal variation of the current sheet structure might be also important in triggering magnetic reconnection. Especially, since the existence of the sausage-mode oscillation temporarily creates a intense current in the center or bifurcated structure. Although such type of the variation has been reported only in the substorm expansion phase or associated with fast flows [9], this may be another important mechanism if it exists in the growth phase.

In this paper, we report two examples of the current sheet dynamical structure in the substorm growth phase, with a temporal oscillation of the current sheet and with a current sheet structure different from the Harris-type structure. We also discuss the possibility of these structure relating to the formation of the magnetic neutral line.

## 2. Observation

We use magnetic field data obtained by the fluxgate magnetometer (FGM) experiment [3] with the time resolution of 4 seconds, and proton moments obtained by the Composition and Distribution Function Analyser (CODIF) or ion bulk velocity by the Hot Ion Analyzer (HIA) of the Cluster Ion Spectrometry (CIS) instrument [15] with the time resolution of 4 - 12 seconds (depends on the interval and the instrument). Presented current density is calculated using curlometer-technique with the magnetic field obtained from four satellites with the time resolution of 4 seconds.

### 2.1. Oscillation

The first example is observed in September 3, 2004 slightly on the dawn side of the magnetotail. Fig.1(a) shows the summary plot of the Cluster observation from 0200 to 0240 UT. From top to bottom, three components of the magnetic field, proton density and temperature, current density, and  $x$ -component of the ion velocity are plotted, respectively. Panel (b) shows the relative location of the satellites in the  $xz$ -,  $yz$ -, and  $xy$ -planes. Separation among the satellites is about 1500 km, CL3 (dotted line) is in the southern-most location, while the CL1 (solid line) is in the northern-most location. Substorm onsets are identified from the ground magnetograms at 0212

Received 31 May 2006.

**Y. Asano.** Tokyo Institute of Technology (JSPS Research Fellow), Meguro, Japan.

**R. Nakamura, A. Runov, W. Baumjohann, and T. Takada.** Space Research Institute, Austrian Academy of Sciences, Graz, Austria.

**I. Shinohara.** Institute of Space and Astronautical Science, Japan Aerospace Exploration Agency, Sagami-hara, Japan.

**A. Balogh.** Imperial College, London, UK.

**B. Klecker.** Max-Planck-Institut für extraterrestrische Physik, Garching, Germany.

**H. Rème.** CNRS/CERS, Toulouse, France.

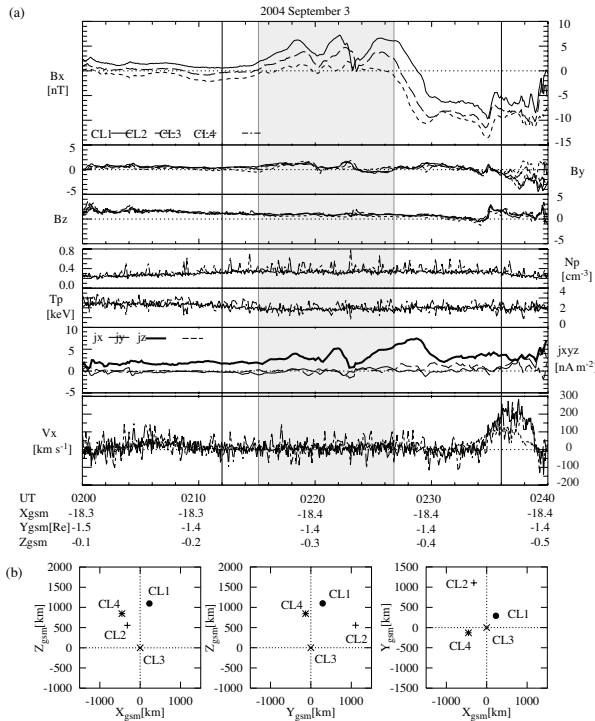


**Fig. 1.** (a) Summary plot of September 03, 2004 event. (b) Relative location of the four satellites at 0230 UT. See detail in the text.

UT and 0236 UT (not shown), indicated by vertical lines in the panel (a). Evolution of the negative / positive bays in the ground magnetograms and auroral breakup (not shown) at 0212 UT onset shows that substorm activities are observed only on the pre-midnight sector, there was no activity on the dawn side. Associated with the next onset at 0236 UT, the evolution of the negative and positive bays as well as auroral expansion extends to the post-midnight region, where the satellites are located and the Earthward fast flow is observed.

Before the first onset at 0212 UT, Cluster observes almost constant cross-tail current density  $j_y \sim 3 \text{ nA m}^{-2}$  without any distinct variation or disturbance of the magnetic field or any fast plasm flow.  $B_z$  shows slight decrease, indicating the formation of the stretched magnetic field configuration in the magnetotail.  $B_y$  remains  $\sim$  zero, namely,  $j_y$  remains to be a cross-tail perpendicular current in the neutral sheet. Associated with the first onset, periodic variation of the current sheet ( $B_x$ ) initiates. While the southern-most spacecraft CL3 stays in the neutral sheet,  $B_x$  from other satellites changes between 0 and several nT. It can be seen that associated with the peak of  $B_x$  at CL1 (0218 UT and 0222 UT),  $B_x$  at CL3 has the smallest value, indicating the existence of the out-of-phase oscillation in the neutral sheet. Hence, the calculated cross-tail current density  $j_y$  in the neutral sheet changes temporarily from 0 to 8  $\text{nA m}^{-2}$ . This variation does not accompany any  $B_y$  or  $B_z$  variation, which suggests that the oscillation is purely compressional.

Fig.2 (a,b) shows the Fourier power spectra of the oscillation by CL1 (northern hemisphere) and CL3 (neutral sheet). While both satellites show the oscillation with the time period

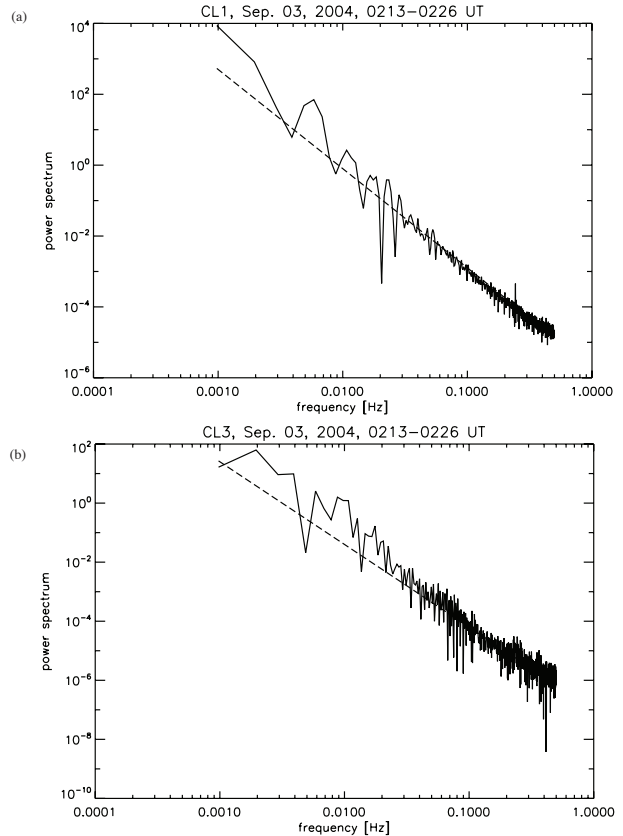


**Fig. 2.** Wave power spectra between 0213 UT and 0226 UT obtained by CL1 (a) and CL3 (b).

of 2-4 min ( $f = 0.004 - 0.008 \text{ Hz}$ ) which comes from the in-phase (kink-mode) oscillation, CL3 in the neutral sheet also shows the oscillation of up to 0.02 Hz ( $T = 50 \text{ sec}$ ) in the compressional variation. Note that the kink-like mode oscillation is found to propagate toward the dusk side of the magnetotail with the velocity of about  $50 \text{ km s}^{-1}$ , namely, toward the local onset active region, with the timing analysis of  $B_x$  during the interval. Thus, the current sheet can temporarily change its thickness before the local onset of the substorm activities at 0236 UT.

## 2.2. Temporal atypical structure

Here, we show another example of the current sheet in the growth phase. This event is observed in August 24, 2003. At 1830 UT, the satellites are located slightly on the dawn side of the magnetotail. Fig.3 (a) shows the summary plot of the Cluster observation at 1820-1845 UT in the same format as the Fig.1(a). Fig.3(b) shows the relative location of the four satellites in the  $xz$ -,  $yz$ -, and  $xy$ -planes. The separation among the satellites is about 200 km, which is smaller than the ion inertial scale ( $\sim 350 \text{ km}$  with  $n_i = 0.4 \text{ cm}^{-3}$ ). The CL4 satellite is located at the southern-most position. Pi2 onset of the substorm is identified from Yinchuan magnetogram at 1836 UT, indicated by a vertical line in the panel (a), which is followed by a clear positive bay (not shown). Proton velocity  $V_x$  shows a weak tailward flow with negative  $B_z$  just before (1834 UT) and after (1837 UT) the onset, then the clear fast tailward flow is

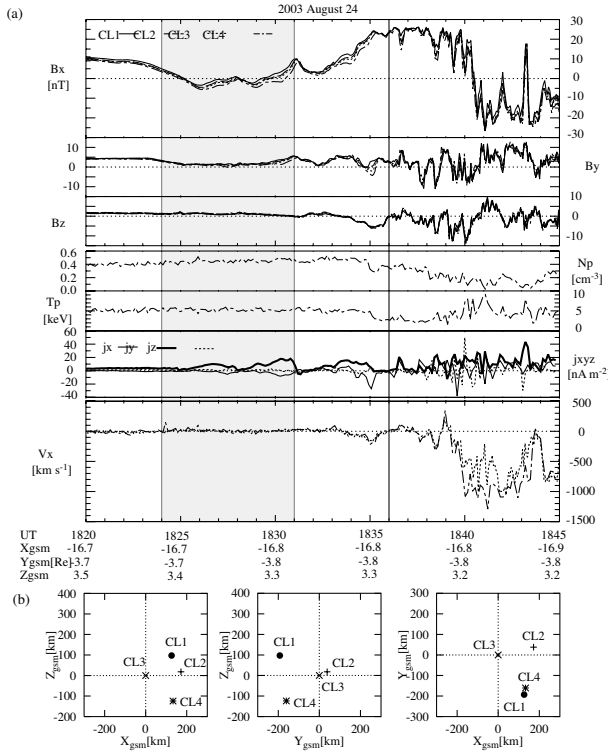


**Fig. 3.** (a) Summary plot of August 24, 2003 event and (b) the relative locations of the satellites at 1830 UT.

observed at 1840 UT. Before the onset until 1835 UT, all satellites are located inside the plasma sheet, and repeatedly cross the neutral sheet ( $B_x = 0$ ) during the interval in a gray-hatched area. This vertical motion of the current sheet is with the time period of about 1-2 min ( $f = 0.008$  Hz) as is also obtained by the power spectrum obtained from the satellite observation (not shown). Other components of the magnetic field are generally small,  $B_y$  is about 1.5 nT,  $B_z$  decreases from 1 nT to zero.

During the first crossing at 1825 UT from the northern hemisphere to the southern hemisphere, we can easily find that the cross-tail current density  $j_y$  is the smallest ( $\sim 0$  nA m<sup>-2</sup>) when the satellites are at the neutral sheet. This means that the structure of the current sheet is bifurcated during the interval. During the second crossing of the neutral sheet (1827-1828 UT),  $j_y$  changes from 6 nA m<sup>-2</sup> to 9 nA m<sup>-2</sup>, then quickly reduces to  $-1$  nA m<sup>-2</sup>, inside the region where  $|B_x|$  of the barycentric magnetic field is smaller than 2 nT. In the third interval from the southern hemisphere to the northern hemisphere, CL4 stays just on the south side of the plasma sheet from 1829 to 1830 UT ( $B_x = -2$  nT),  $B_x$  of CL1 in the northern-most location becomes larger in the northern hemisphere, indicating the increase of the current density in the neutral sheet.  $j_y$  changes from 6 nA m<sup>-2</sup> up to 19 nA m<sup>-2</sup> at the end of the interval. The half thickness of the Harris-type current sheet with its peak value 19 nA m<sup>-2</sup> and lobe magnetic field  $B_L = 25$  nT, is about 1000 km. The result suggests that the current is concentrated in the center of the plasma sheet in this interval. Fig.4 shows the variation of  $j_y$  against  $B_x$  of barycentric magnetic field among the satellites. A thick solid line shows the time sequence of the observation from 1824 UT to 1826 UT, a thin

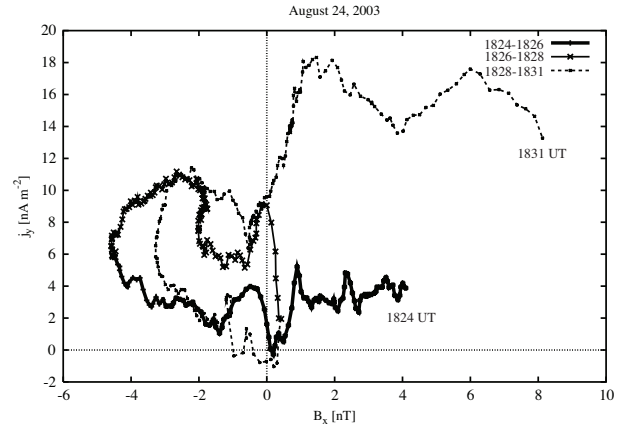


**Fig. 4.**  $j_y$  is plotted against  $B_x$  of the barycentric magnetic field.

solid line is from 1826 UT to 1828 UT, and a thin dashed line is the evolution from 1828 UT to 1831 UT. We can see that the first crossing shows the minimum current density in the center, during the second crossing, current density quickly decreases from 9 nA m<sup>-2</sup> to  $-1$  nA m<sup>-2</sup>, and the third crossing shows the intense current in the center.

From the result of these three crossings, we find that the structure of the current sheet changes from the bifurcated to the over-intense structure within a few minutes just before the onset of a substorm onset.

### 3. Discussion

In the above section, we showed that the current sheet can be dynamically changed in the growth phase of substorms. Fig.5

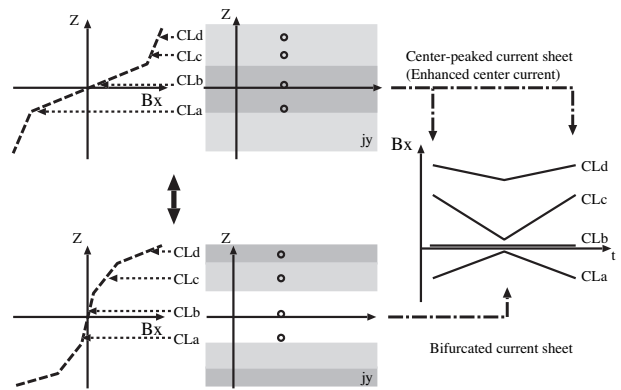


**Fig. 5.** Schematic picture of the variation of the current sheet structure from center-peaked current sheet and bifurcated current sheet, and associated observations by four satellites.

is the schematic picture of the variation of the current sheet structure between center-peaked current sheet and the bifurcated current sheets, and associated observations of the magnetic field ( $B_x$ ) by four satellites is shown in the right panel. There is a report of the sausage-mode oscillation of the current sheet in the substorm expansion phase [9] in which they discussed that the oscillation can be described in the frame of the

magnetotail eigen-mode oscillation with the time frequency of 0.03-0.06 Hz and 0.15 Hz. There also exists a compressional wave in the neutral sheet [4, 5, 25]. These studies revealed that the wave is closely related to the existence of fast plasma flows. Note that such kind of oscillation in the growth phase without any fast flow has not been reported. We surveyed from the four-years' Cluster observations of the neutral sheet associated with the substorm growth phase, but the presented 2004 September 3 event is an only clear event which shows the oscillation in the growth phase. Although formation of the thin current sheet frequently prevents us from observing the neutral sheet in the growth phase, and not so many events are suitable for the analysis of the current sheet, the result indicates that the sausage-mode oscillation or the compressional wave is rare in the growth phase.

Theoretically, while the possibility of evolution of the sausage-mode instability is discussed [7], however, the sausage-mode instability is found to be not favorable in the substorm growth phase [26]. Considering their conclusion and our observational result, it seems difficult that the sausage-mode oscillation enhances in the substorm growth phase, although our result cannot fully deny the possibility. Furthermore, our example is associated with the breakup at different local time, and there is the possibility that the oscillation is caused by this remote activity, propagating to the satellite location associated with the local disturbances such as fast plasma flows. The possibility that the perturbation generated at the other area can also be the source of another onset of the reconnection is discussed in the solar flare [20].

The other possibility that the variation of the current sheet structure changed from the Harris-type current sheet to the bifurcated or the over-intense current in the center and its relation to the formation of an X line is, on the other hand, suggested in several theoretical studies. Formation of the current sheet different from the Harris-type structure is classically discussed [8] considering the pressure anisotropy, which has been further generalized [21]. It is also discussed that the instabilities in the non-Harris current sheet leads to the substorm onset mechanisms, considering drift-kink instability and lower-hybrid drift instability [22]. Using three-dimensional full particle simulation, the quick triggering of the magnetic reconnection in the ion-scale thin current sheet from the intense current in the center [23]. Considering these results, our result that the current sheet temporarily becomes thin in the center and forms the intense current in the late stage of the growth phase, can satisfy the condition which enhanced some kinds of instabilities leading to the magnetic reconnection, and seems to be one of the candidate which is related to the trigger process of the magnetic reconnection. Further analysis of the temporal variation of the current sheet structure is expected in the future study.

#### 4. Summary

Cluster observations of the magnetotail current sheet in the substorm growth phase show that in the course of the gradual current sheet thinning, the current sheet temporarily changes its structure to the bifurcated structure and the structure with the over-intense current in the center. The current sheet also shows temporal variation of current sheet thickness in the center, with the time frequency of  $\sim 0.01$ -0.02 Hz. The compres-

sional-mode oscillation is possibly associated with the local substorm activity at different local time. Such compressional variation are observed associated with the kink-like-mode variation of the current sheet.

#### Acknowledgements

This work is supported by the INTAS 03-51-3738 grant. We thank H. U. Eichelberger for the help with the FGM data. Data from ground magnetograms are provided by WDC for Geomagnetism, Kyoto.

#### References

- Asano Y., T. Mukai, M. Hoshino, Y. Saito, H. Hayakawa, and T. Nagai, Statistical study of thin current sheet evolution around substorm onset, *J. Geophys. Res.*, *109*, A05213, doi:10.1029/2004JA010413, 2004.
- Asano Y., R. Nakamura, W. Baumjohann, A. Runov, Z. Vörös, M. Volwerk, T. L. Zhang, A. Balogh, B. Klecker, and H. Rème, How typical are atypical current sheets?, *Geophys. Res. Lett.*, *32*, L031081, doi:10.1029/2004GL021834, 2005.
- Balogh A., C. M. Carr, M. H. Acuña, M. W. Dunlop, T. J. Beek, P. Brown, K.-H. Fornacon, E. Georgescu, K.-H. Glassmeier, J. Harris, G. Musmann, T. Oddy, and K. Schwingenschuh, The Cluster magnetic field investigation: Overview of inflight performance and initial results, *Ann. Geophys.*, *19*, 1207-1217, 2001.
- Bauer T. M., W. Baumjohann, R. A. Treumann, N. Sckopke, and H. Lühr, Low-frequency waves in the near-Earth plasma sheet, *J. Geophys. Res.*, *100*, 9605-9617, 1995a.
- Bauer T. M., W. Baumjohann, and R. A. Treumann, Neutral sheet oscillations at substorm onset, *J. Geophys. Res.*, *100*, 23,737-23,743, 1995b.
- Baumjohann W., M. Hesse, S. Kokubun, T. Mukai, T. Nagai, and A. A. Petrukovich, Substorm dipolarization and recovery, *J. Geophys. Res.*, *104*, 24,995-25,000, 1999.
- Büchner J. and J.-P. Kuska, Sausage mode instability of thin current sheets as a cause of magnetospheric substorms, *Ann. Geophys.*, *17*, 604-612, 1999.
- Cowley S. W. H., The effect of pressure anisotropy on the equilibrium structure of magnetic current sheets, *Planet. Space Sci.*, *26*, 1037, 1978.
- Fruit G., P. Louarn, E. Budnik, J. A. Sauvaud, C. Jacquy, D. Le Quéau, H. Rème, E. Lucek, A. Balogh, and N. Cornilleau-Wehrin, On the propagation of low-frequency fluctuations in the plasma sheet: 2. Characterization of the MHD eigenmodes and physical implications, *J. Geophys. Res.*, *109*, A03217, doi:10.1029/2003JA010229, 2004.
- Kaufmann R. L., Substorm currents - Growth phase and onset, *J. Geophys. Res.*, *92*, 7471-7486, 1987.
- Mitchell D. G., D. J. Williams, C. Y. Huang, L. A. Frank, and C. T. Russell, Current carriers in the near-Earth cross-tail current sheet during substorm growth phase, *Geophys. Res. Lett.*, *17*, 583, 1990.
- Nagai T., M. Fujimoto, Y. Saito, S. Machida, T. Terasawa, R. Nakamura, T. Yamamoto, T. Mukai, A. Nishida, and S. Kokubun, Structure and dynamics of magnetic reconnection for substorm onsets with Geotail observations, *J. Geophys. Res.*, *103*, 4419, 1998.

13. Nagai T., M. Fujimoto, R. Nakamura, W. Baumjohann, A. Ieda, I. Shinohara, S. Machida, Y. Saito, and T. Mukai, Solar wind control of the radial distance of the magnetic reconnection site in the magnetotail, *J. Geophys. Res.*, *110*, A09208, doi:10.1029/2005JA011207, 2005.
14. Pulkkinen T. I., D. N. Baker, L. L. Cogger, L. A. Frank, J. B. Sigwarth, S. Kokubun, T. Mukai, H. J. Singer, J. A. Slavin, and L. Zelenyi, Spatial extent and dynamics of a thin current sheet during the substorm growth phase on December 10, 1996, *J. Geophys. Res.*, *104*, 28475, 1999.
15. Rème H., C. Aostin, J. M. Bosqued, I. Danduras, B. Lavraud, J.-A. Sauvaud, A. Barthe, J. Bouyssou, Th. Camus, O. Coeur-Joly and others, First multispacecraft ion measurements in and near the Earth's magnetosphere with the identical Cluster ion spectrometry CIS experiment, *Ann. Geophys.*, *19*, 1303-1354, 2001.
16. Runov A., V. A. Sergeev, W. Baumjohann, R. Nakamura, S. Apatenkov, Y. Asano, M. Volwerk, Z. Vörös, T. L. Zhang, A. Petrukovich, A. Balogh, J.-A. Sauvaud, B. Klecker, and H. Rème. Electric current and magnetic field geometry in flapping magnetotail current sheets, *Ann. Geophys.*, *23*, 1391-1403, 2005.
17. Sanny J., R. L. McPherron, C. T. Russell, D. N. Baker, T. I. Pulkkinen, and A. Nishida, Growth-phase thinning of the near-Earth current sheet during the CDAW 6 substorm, *J. Geophys. Res.*, *99*, 5805, 1994.
18. Sergeev V. A., D. G. Mitchell, C. T. Russell, and D. J. Williams, Structure of the tail plasma/current sheet at  $\sim 11R_E$  and its changes in the course of a substorm, *J. Geophys. Res.*, *98*, 17345, 1993.
19. Sergeev V. A., A. Runov, W. Baumjohann, R. Nakamura, T. L. Zhang, A. Balogh, P. Louarn, J.-A. Sauvaud, and H. Rème, Orientation and propagation of current sheet oscillations, *Geophys. Res. Lett.*, *31*, L05807, doi:10.1029/2003GL019346, 2004.
20. Shibata K., and S. Tanuma, Plasmoid-induced-reconnection and fractal reconnection, *Earth Planets Space*, *53*, 473-482, 2001.
21. Sitnov, M. I., P. N. Guzdar, and M. Swisdak, A model of the bifurcated current sheet, *Geophys. Res., Lett.*, *30*(13), 1712, doi:10.1029/2003GL017218, 2003.
22. Sitnov, M. I., A. T. Y. Lui, P. N. Guzdar, and P. H. Yoon, Current-driven instabilities in forced current sheets, *J. Geophys. Res.*, *109*(A3), A03205, doi:10.1029/2003JA010123, 2004.
23. Tanaka K. G., I. Shinohara, and M. Fujimoto, Quick magnetic reconnection triggering in an ion-scale current sheet: Transition from Type-I to Type-II, *Geophys. Res. Lett.*, *32*, L17106, doi:10.1029/2005GL023718, 2005.
24. Toichi T., and T. Miyazaki, Flapping motions of the tail plasma sheet induced by the interplanetary magnetic field variations, *Planet. Space Sci.*, *24*, 147, 1976.
25. Volwerk M., W. Baumjohann, K.-H. Glassmeier, R. Nakamura, T. L. Zhang, A. Runov, Z. Vörös, B. Klecker, R. A. Treumann, Y. Bogdanova, H.-U. Eichelberger, A. Balogh, and H. Rème, Compressional waves in the Earth's neutral sheet, *Ann. Geophys.*, *22*, 303-315, 2004.
26. Yoon P. H. and A. T. Y. Lui, On the drift-sausage mode in one-dimensional current sheet, *J. Geophys. Res.*, *106*, 1939-1947, 2001.



# The dependence of magnetospheric topology and convection (including night-side reconnection) on the average magnetic flux transfer rate

G. Atkinson

**Abstract:** The average transfer rate of magnetic flux into the tail is determined, to a good approximation, by dayside reconnection. The topology and behavior of the magnetosphere adjusts to maintain the same average return transfer rate from the tail to the dayside, despite "obstructions" resulting from energetic plasma in the system and the conductivity of the ionosphere. It follows that there is an average topology and behavior corresponding to each constant dayside reconnection rate. We may expect that evolution toward a new average topology is important in triggered substorms and growth phases. We focus on earthward flux transfer through the plasma sheet, initially for a constant dayside reconnection rate. It is hard to see how it maintains the appropriate average value, unless it is controlled by a collaboration of both the lobe (upstream) and the near-earth (downstream) boundaries. The same is true for reconnection in the tail since it determines flux transfer rates. It is proposed that lobe pressure provides a stressed plasma sheet in which the onset of reconnection is most likely if there is a strong earthward  $E \times B$  convection on the earthward side of a possible X-line site. For the nearest-earth neutral line, this corresponds to a strong earthward  $E \times B$  component in the dipole-like region. For MHD models, this occurs at midnight. For models with energetic ions, it occurs at the Harang discontinuity, for the following reasons. The upward current at the Harang suggests that energetic ions are drifting westward off flux tubes in the Harang, resulting in an energy difference between the west and east sides. This difference in ion energy would be expected to produce an  $E \times B$  convection cell with an earthward component in and east of the Harang and an outward component west of it. Thus reconnection onset is most probable in the tail at the local time of the Harang. However, reconnection provides positive feedback by adding energy to the earthward  $E \times B$  convection. Instability would be expected (essentially driven by energy from both reconnection and the interchange/ballooning motion). This explains non-triggered substorms. Turning to time-dependent dayside reconnection, we suggest that triggered substorms are essentially the same as non-triggered, except that there is more energy input to the convection cell by the ions. The reduction in dayside reconnection requires additional outward  $E \times B$  convection of energetic "shielding" ions west of the Harang. Conversely, an increase in dayside reconnection requires inward convection of the shielding ions, and hence a reduction of the Harang convection. It is expected that reconnection onsets would be suppressed during growth phases.

*Key words:* substorms, reconnection, Harang.

## 1. Convection: fundamentals and some general considerations

We can define the rate of transfer of magnetic flux through any line as  $\int E \cdot dl$ . Conservation of the earth's magnetic flux then requires that the average transfer rates through the parts of the magnetosphere must be equal. The average value is imposed, to a good approximation, by the rate of transfer into the tail resulting from dayside reconnection.

The return transfer from the tail to the dayside must maintain the same average, despite the obstructing effects of energetic plasma and the conducting ionosphere. The obstructing effects include (Fig. 1): (1) compression of the plasma during earthward convection in the tail (in fact energy must be removed from tail-like flux tubes to resolve the pressure catastrophe: [3]); (2) "shielding" of convection from the inner magnetosphere by energetic plasma in the earthward edge of the plasma sheet; (3) Ohmic dissipation in the ionosphere as flux is transferred from the nightside to the dayside in the dipole-like

region (shielding plays a role by limiting the width of the convection channel requiring stronger electric fields for the same flux transfer rate). The topology of the magnetosphere must be consistent with closure of the currents, shown in Fig. 2, associated with the above obstructing effects. The currents include: (1) ionospheric current across the polar cap and dayside closing approximately one quarter of the region 1 Birke-land currents; (2) ionospheric closure of the remaining region 1 currents to region 2 currents, which then closes by near-earth plasma-sheet current across midnight from dawn to dusk; (3) cross-tail current. Observations and simulations (e.g. [5]) indicate that these currents increase with average dayside reconnection rate. Ionospheric currents increase (expected from Ohm's law), the plasma sheet approaches the earth with stronger near-earth currents, and the average amount of tail flux increases implying stronger cross-tail current.

Since dayside reconnection is an independent input parameter, it is useful to consider "average" magnetospheres (topologies, currents, convection patterns) corresponding to each dayside reconnection rate. This average would be approached if reconnection remained constant for a sufficiently long time. (We do not assume the average is a steady-state, as it is for MHD models [5].) Changes in dayside reconnection would be

Received 9 May 2006.

G. Atkinson, Department of Physics and Astronomy, University of British Columbia, Vancouver, B.C.V6T1Z1; atkinson@chem.ubc.ca

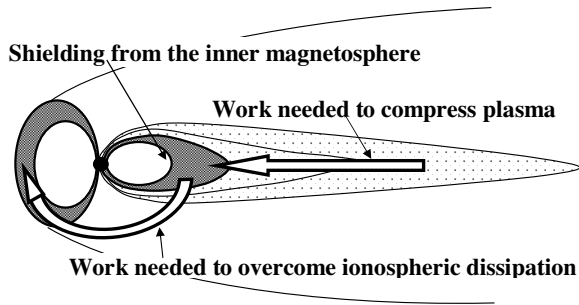


**Fig. 1.** Obstructions to the return flux transfer: (1) Work is required to compress plasma for earthward convection in the plasma sheet; (2) Convection of plasma into the inner magnetosphere is prevented by shielding; (3) Convection to the dayside is given by  $V=WE$ . The width of the channel,  $W$ , is decreased by shielding, requiring stronger  $E$  and increased dissipation.

expected to initiate evolution toward a new average topology with different amounts of flux in the tail and the nightside magnetosphere, and increases or decreases in the radial distance to the earthward edge of the plasma sheet. Some properties of triggered substorms and growth phases will be explained by these changes. In this paper we consider a model in which an

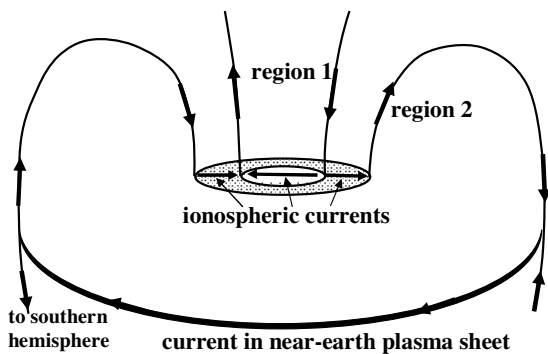


**Fig. 2.** A simplified illustration of currents associated with shielding and ionospheric closure, viewed from midnight above the equatorial plane. Other currents of obstructions include electrojets and cross-tail.

$E \times B$  convection pattern near the Harang discontinuity, driven by energy from the energetic "shielding" ions in the near-earth plasma sheet, provides boundary conditions which favour reconnection onset and non-triggered substorms. Triggered substorms are then essentially the same as non-triggered, but there is additional energy input to the convection pattern from the near-earth plasma sheet ions because their convection includes an additional outward component as the topology responds to a decrease in dayside reconnection. We therefore discuss the behavior for a constant dayside reconnection rate in some detail before considering how time-dependent dayside reconnection

modifies the constant reconnection case. It is noted that the existence of non-triggered substorms has been questioned [8].

## 2. Magnetic flux transfer through the plasma sheet

It is useful to consider magnetic flux transfer from the tail lobes to the dayside as the two steps shown by the arrows in Fig. 1: from the lobes into the nightside dipole-like magnetosphere, and from the nightside to the dayside in the dipole-like magnetosphere. The first step is of greatest interest because of its relationship to substorms. We shall consider the second step only to the extent that it provides a boundary condition for the first. The properties governing step 1 of the flux transfer are illustrated in Fig. 3. The pressure catastrophe dictates that en-

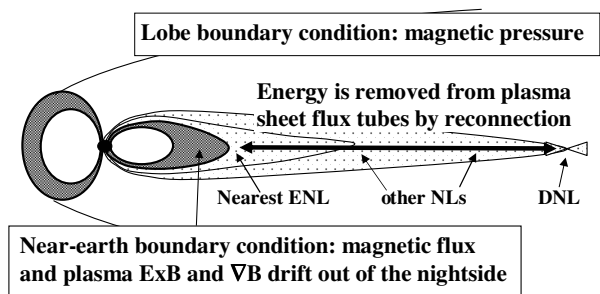


**Fig. 3.** Lobe and near-earth boundary conditions on magnetic flux transfer through the plasma sheet. In between the boundaries, energy is removed to overcome the pressure catastrophe. The nearest earth neutral line must produce flux tubes that can convect to the dayside at the appropriate average rate.

ergy must be removed from tail-like plasma sheet flux tubes to allow magnetic flux transfer into the nightside dipole-like region. It has long been believed that this occurs by reconnection, with energy travelling down the tail in the form of plasmoids. Recent observations [10] indicate that there are probably multiple, multiscale, reconnections throughout the plasma sheet, possibly involving self-organized criticality resulting in a behavior similar to avalanches on a sand pile [6].

Magnetic flux transfer in the tail has to proceed at the appropriate average rate. By analogy with similar systems, this requires that both the upstream boundary (the lobes) and the downstream boundary (the nightside dipole-like region) participate in controlling flux transfer and hence also reconnection. The analogies include compressible fluid-flow, in which flow through any part of the system depends on the pressures at the upstream and downstream boundaries; and even more relevant, transfer of sand by avalanches in the sand-pile analogue mentioned above. Avalanches can be triggered by adding sand to the top of the pile or removing it from the bottom since the slope of the surface depends on both boundary conditions.

A simple description of the role of the lobes in controlling flux transfer in the tail-like plasma sheet is that the transfer of magnetic flux into the tail increases the lobe pressure until,

consistent with the pressure catastrophe [3], the plasma sheet becomes thin enough and sufficiently tail-like that the onset of reconnection at a neutral line can result in a decrease in magnetic energy. (In a thick plasma sheet, the downtail flow accompanying reconnection stretches closed field lines and increases the magnetic energy.) However, it is difficult to see how reconnection at the nearest earth neutral line produces flux which can convect to the dayside at the appropriate average rate, unless the near-earth boundary is also involved. A modification of this process is described below.

It has been argued that the outflow boundary conditions control reconnection in a tail-like configuration [1]. Both up-tail and down-tail magnetic flux transfer must be possible in a reference frame attached to the X line during reconnection. This suggests that, other factors being equal, reconnection onset is most probable at locations where  $dv/dx$  is a maximum before reconnection onset, where  $v$  is the component of  $E \times B$  convection in the earthward direction. This condition is satisfied in two well-known and well-studied situations. First, for dayside reconnection, hydrodynamics indicates that the maximum divergence of the flow component parallel to the magnetopause is at the subsolar point, and hence reconnection would be expected to be at the subsolar point. Second, the condition is implicit in the onset described in the previous paragraph since  $dv/dx > 0$  is required to produce a more tail-like configuration with a reduced normal component of B.

We are now in a position to discuss control of reconnection onset by earthward convection. As discussed above, increases in lobe pressure cause plasma sheet thinning, increased tail-likeness, and eventually reconnection. However, the nearer-earth boundary condition can increase or decrease  $v$  and hence  $dv/dx$ . Compare the situation in which earthward flow is completely blocked with one where there is a fast earthward flow. For the blocked case, the X line must move downtail faster and the tailward outflow speed must be greater, with the result that more work goes into stretching closed field lines. Hence reconnection onset is more likely if earthward outflow exists. Thus, earthward convection at the nearer-earth boundary can change  $dv/dx$  and control reconnection onset.

The above applies to both mid-tail and near-earth reconnection. Mid-tail reconnection can be controlled by nearer-earth flows, allowing avalanche-like behavior, as discussed later. At the nearest-earth neutral line, the uptail boundary is provided by the dipole-like region. Thus  $dv/dx$  would be a maximum and reconnection onset most likely at local times where the earthward component of  $E \times B$  drift is a maximum in the outer dipole-like region. In an MHD magnetosphere, this occurs near midnight where convection is toward lower L values and then around dawn and dusk. We argue later that the inclusion of the curvature and gradient drifts of energetic ions places the maximum earthward component of  $E \times B$  drift near the Harang discontinuity, and hence reconnection is most likely on tail-like field lines at the same local time as the Harang.

In summary of this section, observations indicate that multiple reconnection events, distributed throughout the plasma sheet, remove energy from flux tubes and result in earthward magnetic flux transfer. The boundary conditions are provided by the tail lobes and the nightside dipole-like region. Both boundaries must play a role in maintaining the appropriate average flux transfer rate. Reconnection is most likely to be ini-

tiated where  $dv/dx$  is a maximum, which for a nearest-earth neutral line is in the near-earth tail at the local time where the earthward component of  $E \times B$  is a maximum in the dipole-like region. The maximum is at midnight for MHD models. Radar observations indicate an  $E \times B$  component toward lower latitudes in and east of the Harang discontinuity [7]. Hence reconnection in the near-earth tail is expected and observed at the same local time as the Harang. Control of mid-tail reconnection by nearer-earth flows may lead to avalanche-like behaviour.

### 3. The near-earth boundary condition

For a population of monoenergetic ions, upward currents occur at particle boundaries where there is an increase in density and energy in going from east to west through the boundary [11], and magnetic flux transfer ( $E \times B$  drift) is from west to east through the boundary. In simplest terms, ions are curvature and gradient drifting off magnetic flux tubes (defined as moving with the  $E \times B$  drift). Similar behavior has been discussed for a more-general distribution, [9]. Since there is upward current at the Harang discontinuity, we associate it with a westward increase in number density and ion energy, and with eastward magnetic flux transfer in a reference frame moving with the Harang.

However, radar observations of the Harang ([7]) appear to indicate that the  $E \times B$  flux transfer is in the opposite direction. The conflict can be removed in a time-dependent model of the Harang. Fig. 4 illustrates a model for times of no flux transfer into the dipole-like region (no reconnection). Properties include: 1) the Harang drifts westward with a velocity determined by the ions; 2) magnetic flux transfer is from west to east through the Harang because the ions drift westward in the  $E \times B = 0$  frame, and 3) the total ion energy decreases on magnetic flux tubes while they are being transferred through the Harang from west to east.

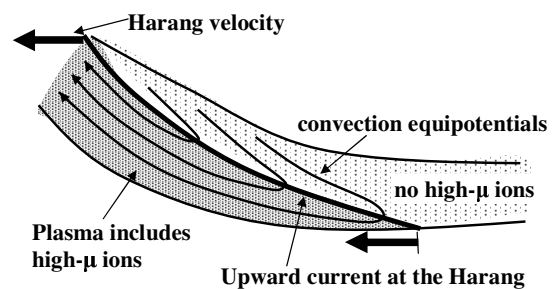


**Fig. 4.** Time-dependent model of the Harang: Upward current at the Harang closes to a drift current of high- $\mu$  ions in the magnetosphere. The Harang moves westward with the drifting ions with a velocity faster than the westward component of  $E \times B$  drift. The decrease in energy (shielding) on flux tubes causes the convection pattern with a component toward lower L in and east of the Harang and toward higher L west of the Harang.

There is an important consequence of the above properties. The decrease in ion energy as flux tubes  $E \times B$  drift through

the Harang results in flux tubes with decreased ion energy (decreased shielding) on the east side. The resulting imbalance in radial stresses drives an  $E \times B$  convection cell with a component toward lower L values in and east of the Harang, where the total ion energy is reduced, and a component toward higher L values west of the Harang where the ion-energy content of flux tubes is higher. Energy input to the convection cell comes from the difference between energy lost by outward-convecting ions and the energy gained by inward-convecting ions. The current system and convection are illustrated in Figs. 4 and 5 for times of no reconnection. Observational support for the above be-

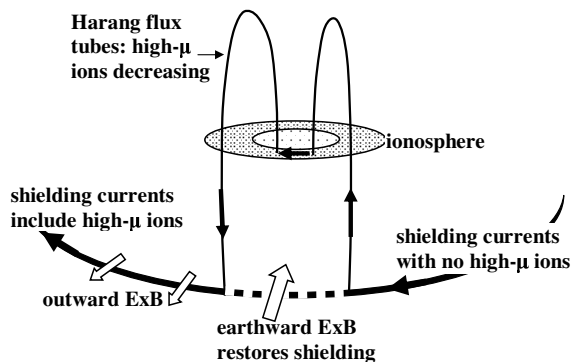


**Fig. 5.** The Harang-driven convection and its current system: The Harang moves westward as high- $\mu$  ions drift off flux tubes, causing an earthward  $E \times B$  component until shielding is restored by the lower- $\mu$  ions and electrons. There is an outward  $E \times B$  component west of the Harang which closes the convection streamlines (equipotentials). The system is a weak current wedge when there is no reconnection.

havior of the Harang is provided in a case study [7]. A Harang with a westward velocity of 1 km/sec was observed. The measured westward component of  $E \times B$  drift was approximately half the Harang velocity, consistent with eastward magnetic flux transfer. The convection pattern shows the appropriate equatorward and poleward components of Fig. 4. The superposition of the Harang-driven cell on a large-scale two-celled convection offers an explanation of the observed eastward protrusion of the duskside convection cell near midnight.

#### 4. Control of reconnection by Harang-driven convection

Figs. 4 and 5 illustrate the Harang-driven convection and current system in the magnetosphere at quiet times. The ion energy on flux tubes (shielding) is reduced as the Harang moves westward in the  $E \times B = 0$  frame, resulting in an inward  $E \times B$  drift component until the shielding is restored by energy increase of the remaining ions and electrons (which have lower values of the adiabatic invariants). The currents associated with the ion drifts are diverted to the ionosphere at local times where shielding is reduced. The inward  $E \times B$  convection of dipole-like flux at local times of reduced shielding is closed by outward convection at local times of high shielding; that is west of the Harang.

It is now straightforward to relate the Harang-driven  $E \times B$  convection to reconnection. The  $E \times B$  drift to lower L values on dipole-like field lines at the Harang provides the conditions discussed earlier ( $dv/dx$  at maximum) that favor the onset of reconnection on tail-like field lines outside the dipole-like region. Thus, when near-earth reconnection is initiated, it would be expected to be at the local time of the Harang discontinuity.

However, reconnection produces stress changes that enhance the inflow at the Harang. This provides positive feedback, amplifying the Harang-driven convection shown in Figs. 4 and 5. The resulting instability is either an interchange or a ballooning instability with energy supplied by both magnetic field changes due to reconnection, and by the radial convection component of ions. The above offers an explanation of non-triggered expansions.

Now we can return to time variations of dayside reconnection and triggered substorms. A decrease in dayside reconnection requires increased  $E \times B$  drift of the ions (west of the Harang) away from the earth, since shielding must decrease. This provides more energy input by ions to the Harang-driven convection cell of Figs. 4 and 5; that is more energy than for the non-triggered case. This results in a corresponding increase in the probability of reconnection onset at the Harang in the inflowing part of the convection cell. It offers an explanation of triggered expansions, and explains why the energy involved is greater for triggered substorms ([4]. It is consistent with a suggestion in [2] that the energy for triggered substorms comes from the convection of the shielding ions to higher L values.

Finally, there are a few additional properties of the model that should be noted: (1) The instability may involve east-west scales which are smaller than the Harang, since energy is available for a Harang-type convection cell wherever there is a westward increase in total ion energy. According to our earlier discussions there is a westward increase of total ion energy over most of the Harang. (2) An increase in the dayside reconnection rate is expected to produce electric fields that convect the shielding ions closer to the earth. The inward convection opposes the Harang-driven convection cell and would cause suppression of reconnection onset in the growth phase of substorms. (3) Since the Harang cell moves westward with the drifting ions, reconnection, after onset, would be likely to follow the motion as the expansion develops, consistent with westward travelling surges. (4) Fig. 5 illustrates that the sum of the ion currents and the westward electrojet should be constant over several hours of local time around midnight. At times when the westward electrojet current is comparable to the integrated region 2 current (one or two mega-amps), there is very little shielding in the magnetosphere. This suggests that the large increase in the conductivity of the ionosphere in substorms plays an important role in slowing down the earthward component of  $E \times B$ , and delaying the restoration of shielding.

#### 5. Summary

Dayside reconnection transfers magnetic flux into the tail, and determines the average transfer rate, which must be the same through all parts of the magnetosphere. The return transfer to the dayside is obstructed by the plasma and the ionosphere. The topology of the magnetosphere adjusts to close the currents of these obstructions. It is useful to compare average

topologies corresponding to different constant dayside reconnection rates. The average amount of magnetic flux in the tail and on the nightside increases with dayside reconnection rate, and the earthward edge of the plasma sheet moves closer to the earth. Growth phases and triggered substorms both involve topology change in response to increases or decreases in dayside reconnection rate. We focussed on magnetic flux transfer through the plasma sheet since this is related to substorms. Energy must be removed from flux tubes to resolve the pressure catastrophe. Observations indicate that multiple reconnections remove energy from flux tubes, reducing the energy content until they can convect to the dayside at the appropriate average rate. The appropriate average can be maintained only if both tail-lobe and near-earth boundary conditions play a role in controlling reconnection and flux transfer. It is proposed that reconnection onset is most probable at locations where and times when  $dv/dx$ , the uptail gradient of the earthward component of flow, is a maximum before onset. In the plasma sheet,  $dv/dx$  can be increased by a strong  $E \times B$  earthward component at the earthward boundary of a region where other factors favor reconnection. This allows an avalanche-like process in the mid-tail with reconnection controlled by nearer-earth flows (which may themselves be the result of nearer-earth reconnection). At the nearest-earth reconnection site, the boundary condition is provided by the earthward component of  $E \times B$  in the dipole-like region. In MHD models, this is a maximum at midnight. In the presence of energetic ion drifts, it is at the Harang discontinuity. A time-dependent model of the Harang discontinuity is presented in which it is the eastern limit of westward drifting highest- $\mu$  ions. The drift of high- $\mu$  ions off flux tubes at the Harang creates an east-west distribution of energy that is not in equilibrium. This causes a convection component toward lower latitudes at and east of the Harang and to higher latitudes at points west. These  $E \times B$  components favor reconnection onset on tail-like field lines at the local time of the Harang. However, reconnection changes magnetic stresses so as to create a positive feed-back to the convection cell. The result is an interchange/ballooning instability with energy provided by both ion-drift and reconnection. This explains non-triggered substorms. Decreases in dayside reconnection require additional outward  $E \times B$  drift of the shielding plasma west of the Harang. This enhances the Harang-driven convection and provides a boundary condition that is even more favorable for reconnection onset. Conversely, increases in dayside reconnection require inward  $E \times B$  drift, which suppresses Harang-driven convection and reconnection during growth phases.

## References

1. Axford, W.I., Reconnection, substorms and solar flares solar flares, in *Physics and Chemistry of the Earth (C)*, Vol. 24, No.1-3, 147 1999.
2. Atkinson, G., A magnetosphere wags the tail model of substorms, in *Magnetospheric Substorms, Geophysical Monograph 64. American Geophysical Union* 191, 1991.
3. Erickson, G. M., and Wolf, R. A., Is steady-state possible in the earth's magnetosphere?, *Geophysical Research Letters*, 6, 897, 1980.
4. Hsu, T. S., and McPherron, R. L., Average characteristics of triggered and nontriggered substorms, *Journal of Geophysical Research*, 109, A07208, doi:10.1029/20003JA009933 2004
5. Kabin, K., Rankin, R., Rostoker, G., Marchand, R., I. J., Ridley, A. J., Gombosi, T. I., Clauer, C. R., and DeZeeuw, D. L., Open-closed field line boundary position: A parametric study using an MHD model, *Journal of Geophysical Research*, 109, 2004.A05222, doi: 10.1029/2003JA010168. 2004.
6. Klimas, A. J., Uritsky, V. M., Vassiliadis, D., and Baker, D. N., Reconnection and scale-free avalanching in a driven current-sheet model, *Journal of Geophysical Research*, 109, A02218, doi: 10.1029/2003JA010036. 2004.
7. Kunkel, T., Baumjohann, W., Untiedt, J., and Greenwald, R. A., Electric fields and currents at the Harang discontinuity: a case study, *Journal of Geophysics*, 59, 73, 1986.
8. Lyons, L. R., Liu, S., Ruohoniemi, J. M., Solov'yev, S. I., and Samson, J. C., Observations of dayside convection reduction leading to substorm onset, *Journal of Geophysical Research*, 108, 1119, doi:10.1029/2002JA009670 2003a.
9. Lyons, L. R., Wang, C. P., and Nagai, T., Substorm onset by plasma sheet divergence, *Journal of Geophysical Research*, 108, 1427, doi:10.1029/2003JA010178 2003b.
10. Uritsky, V. M., Klimas, A. J., Vassiliadis, D., Chua, D., and Parks, G., Scale-free statistics of spatiotemporal auroral emissions as depicted by POLAR UVI images: dynamic magnetosphere is an avalanching system, *Journal of Geophysical Research*, 107, A12, doi:10.1029/2001JA000281 2002
11. Vasyliunas, V. M., The interrelationship of magnetospheric processes, in *Earth's Magnetospheric Processes*, edited by B. M. McCormac, D. Reidel, Hingham, Mass. 1972.



# On the role of entropy conservation and entropy loss governing substorm phases

J. Birn, M. Hesse, and K. Schindler

**Abstract:** MHD theory and simulations have shed light on the role of entropy conservation and loss during the course of a substorm. Entropy conservation appears to be a crucial element leading to the formation of thin embedded current sheets in the late substorm growth phase, causing the onset of an instability or a catastrophe (loss of equilibrium). Entropy loss (in the form of plasmoids) is essential in the earthward transport of flux tubes (bubbles, bursty bulk flows). Entropy loss may also change the tail stability properties and render ballooning modes unstable and thus contribute to cross-tail variability. We illustrate these effects through results from theory and simulations. We also verify that the entropy conservation as used in MHD remains a valid concept in particle simulations.

*Key words:* Entropy, Substorms.

## 1. Introduction

The large-scale dynamic evolution of the magnetosphere, including the substorm growth phase and the substorm expansion phase, is usually modeled by the one-fluid magnetohydrodynamic (MHD) equations. Major assumptions used in the derivation of the MHD equations from the more general framework of collisional or collisionless Vlasov/Boltzmann equations are (a) the neglect of the electric field in the plasma rest frame (ideal MHD),

$$\mathbf{E} + \mathbf{v} \times \mathbf{B} = 0 \quad (1)$$

(b) the assumption of isotropic plasma pressure  $p$ , and (c) the neglect of heat flux or, more narrowly, the divergence of the heat flux tensor. Here heat flux represents the third order moment of the particle distribution function, representing thermal energy transport in the plasma rest frame. This leads to the adiabatic, i.e., entropy conserving, law of state, which may be written as

$$\frac{d}{dt} \frac{p}{\rho^\gamma} = 0 \quad (2)$$

where  $d/dt \equiv \partial/\partial t + \mathbf{v} \cdot \nabla$  is the time derivative in a comoving frame. Here  $\gamma = 5/3$  is appropriate for an isotropic plasma distribution function (taken in the plasma rest frame), which also implies the absence of heat flux.

Although the details of substorm onset in the magnetotail are still a matter of debate, there is no doubt that magnetic reconnection, and plasmoid formation and ejection, play a crucial role in the expansive phase of substorms. This requires a local violation of the ideal MHD constraint (1) associated with a dissipative electric field

$$\mathbf{E}' = \mathbf{E} + \mathbf{v} \times \mathbf{B} \neq 0 \quad (3)$$

In MHD simulations this is usually accomplished by some ad-hoc model of resistivity (or by numerical diffusion). In collisionless models appropriate for the magnetotail, resistivity from binary collisions does not play any role. Many of the investigations of magnetic reconnection in the magnetotail therefore have focused on the break-down of (1) and the properties of the dissipative electric field resulting particularly from electron inertia effects [14, 9, 11, 8, 13].

However, the entropy conservation (2) and its break-down also have important implications for the evolution of the magnetotail, the accessibility of certain states, and the stability of the tail. This is the topic of the present paper. In Sec. 2 we present results from quasi-static theory and MHD simulations that demonstrate the potential role of entropy conservation in the growth phase of substorms in governing thin current sheet formation and the loss of equilibrium. As discussed in Sec. 3, the subsequent loss of entropy by the severance of a plasmoid results in a ballooning unstable configuration. The entropy loss enables depleted flux tubes to penetrate close to the earth, while ballooning instability may provide cross-tail structure and filamentation. These results rely on the entropy conservation (2), which is imposed in the MHD model. However, as demonstrated in Sec. 4 from a comparison between an MHD simulation and a full particle simulation, the integral of entropy on moving flux tubes is well conserved in particle simulations as well, providing credence to the results of the MHD simulations.

## 2. Substorm growth phase: Thin current sheet formation, loss of equilibrium

In this section we discuss the possible role of entropy conservation during the substorm growth phase. Recently Birn and Schindler [3] investigated the quasi-static response of the magnetotail to a deformation of the magnetopause boundary, affecting particularly the inner tail. Using two-dimensional magnetohydrostatic (MHS) equilibrium theory, together with flux, entropy, and topology conservation (equivalent to ideal MHD for slow, quasi-static, evolution), they demonstrated that a finite boundary deformation of magnetotail equilibria can lead to strong local current density enhancement, that is, the form-

Received 18 June 2006.

**J. Birn.** Los Alamos National Laboratory, Los Alamos, New Mexico, USA

**M. Hesse.** NASA/Goddard Space Flight Center, Greenbelt, Maryland, USA

**K. Schindler.** Institut für Theoretische Physik, Ruhr-Universität Bochum, Bochum, Germany

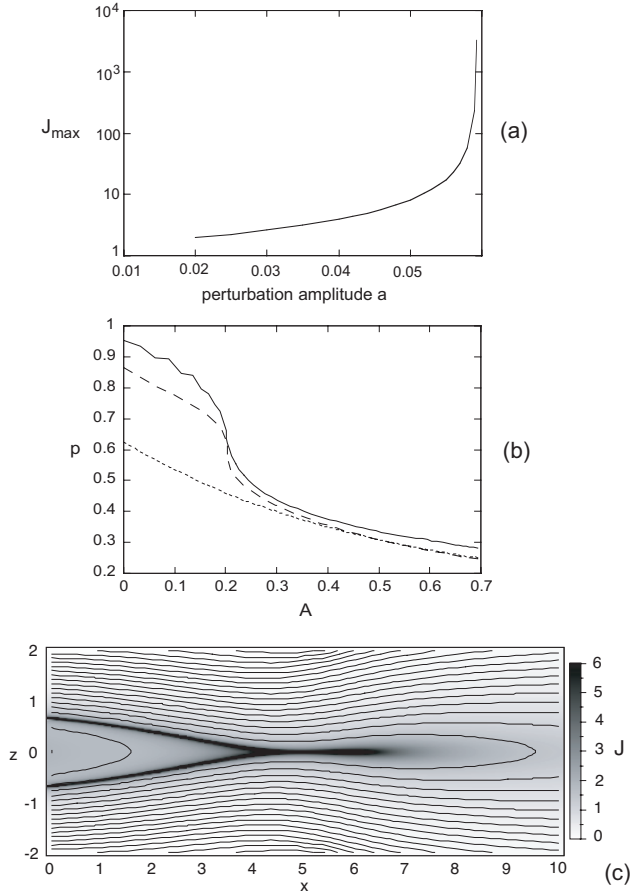


**Fig. 1.** (a) Maximum current density as function of the amplitude of the boundary indentation; (b) pressure as function of the flux variable  $A$  for the unperturbed state (dotted line), the theoretical limit obtained from quasi-static theory (dashed), and from an MHD simulation (solid line). Modified after [4]; (c) magnetic field configuration near the critical limit, consisting of a thin embedded current sheet (gray scale) that bifurcates toward the Earth (left).

ation of a thin current sheet. Equilibrium configurations that satisfy the constraints cease to exist when the boundary deformation exceeds a critical value.

Figure 1 illustrates this result. Panel (a) shows the maximum current density in the tail as a function of the amplitude of the boundary indentation  $a$ , which diverges at a finite value of  $a$ . Panel (b) shows the pressure  $P$  as a function of the magnetic flux variable  $A$ , where the magnetic field is given by  $\mathbf{B} = \nabla A \times \hat{\mathbf{y}}$ . The dotted line corresponds to the unperturbed state and the dashed line to the critical state, where  $J = dP/dA$  becomes locally infinite. The solid line represents the result of an MHD simulation, where the critical state is obtained by a slow temporal evolution resulting from a temporal inflow through the boundary, which causes a similar deformation as in the quasi-static model [4]. Panel (c) illustrates the configuration near the critical state, showing an enlarged inner portion of the tail. A thin sheet with strongly enhanced current density (gray scale) becomes embedded in the plasma sheet. This sheet bifurcates into two sheets toward the Earth (to the left in Fig. 1).

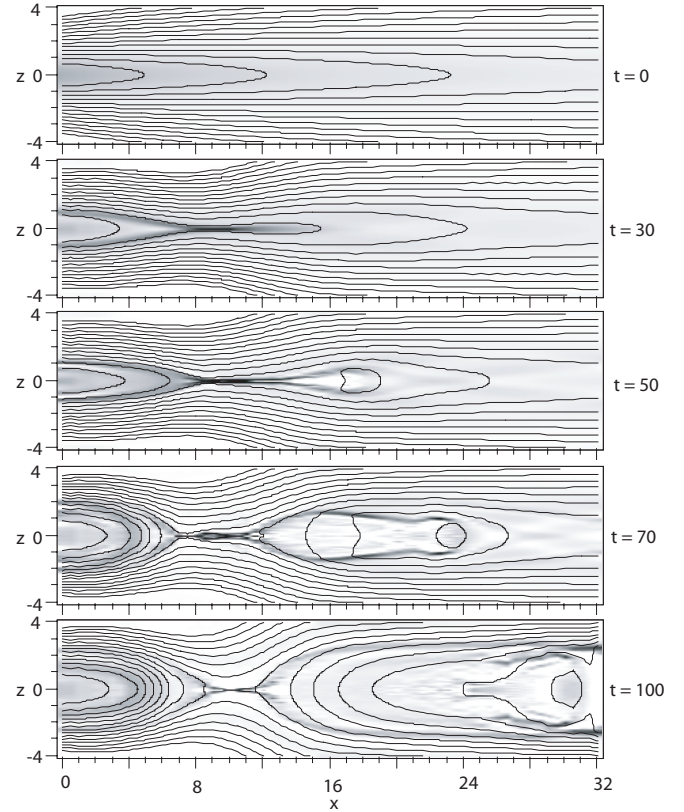


**Fig. 2.** MHD simulation of thin current sheet formation and plasmoid ejection in the tail, resulting from boundary deformation in the near tail. The gray scale indicates the current density.

### 3. Expansion phase: Role of reconnection, propagation of bubbles

The results of Sec. 2 showed the strong coupling between boundary perturbations, resulting from the impact of the solar wind, and current density intensification within a thin sheet forming within the plasma sheet. It is plausible that this leads to the onset of instability or the loss of equilibrium, regardless of the dissipation mechanism. In the presence of dissipation the strong current density enhancement is expected to cause reconnection. We simulated this by imposing finite, uniform, resistivity. As demonstrated by Fig. 2, this indeed leads to reconnection in the near tail and the formation and ejection of a plasmoid. Similar results can also be obtained from full particle simulations, where dissipation results from electron inertia causing nongyrotropy of the electron pressure tensor [7].

The plasmoid formation has a further consequence for closed field lines, connected with earth at both ends. Because parts of these field lines are severed, the remaining closed section becomes shorter and its total entropy content reduced. This is demonstrated in Fig. 3, showing the integrated quantity  $S(A)$  defined by

$$S = \int p^{1/\gamma} dV = \int p^{1/\gamma} \frac{ds}{B} \quad (4)$$

where  $A$  is again the flux variable in the two-dimensional magnetic field, integrated at various times along field lines crossing the near-Earth boundary  $x = 0$ .  $A$  is normalized to 0 at

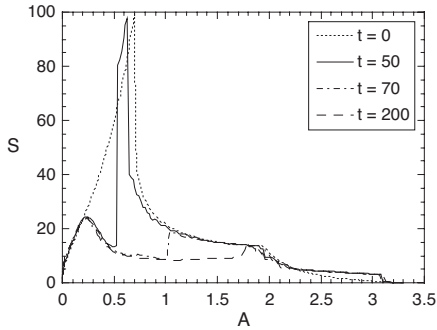


**Fig. 3.** Entropy function for the MHD simulation of Fig. 2 at various times indicated in the legend.

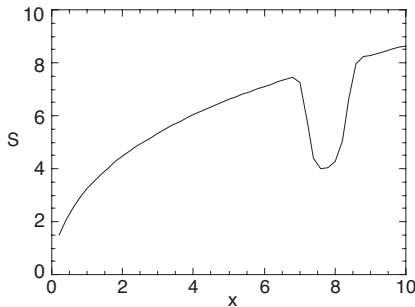


**Fig. 4.** Entropy function for a depleted flux tube (bubble).

$x = 0, z = 0$  and increases outward. The sharp decrease of the initial  $S(A)$  (dotted line) near  $A = 0.7$  marks the transition from closed to open field lines, which cross the far boundary  $x = 32$ , rather than the equatorial plane  $z = 0$ . In the absence of dissipation, that is, for vanishing resistivity, this function should be conserved. As a result of reconnection, however,  $S(A)$  becomes reduced for field lines that are affected by reconnection. The sharp increase of  $S(A)$  (near  $A = 0.5$  for  $t = 50$ ) marks the location of reconnection; it moves to higher  $A$  values, and from closed to open field lines, as time proceeds. Below this value the functions  $S(A)$  show a deep minimum but remain essentially identical for the part that has undergone reconnection, that is, left of the steep jump. This shows that there is little further dissipation.

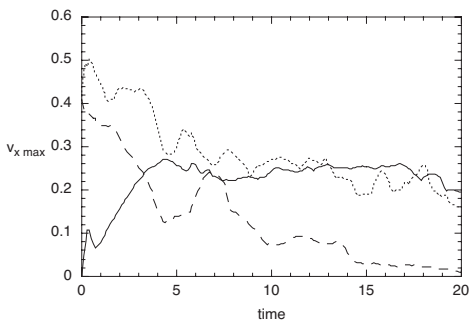


**Fig. 5.** Maximum earthward flow speed as function of time for bubbles with  $y_m = 0.2$  and (a) pressure reduction but no initial velocity (solid line), (b) pressure reduction and initial velocity (dotted line), (c) no pressure reduction but finite initial velocity (dashed line). After [1].

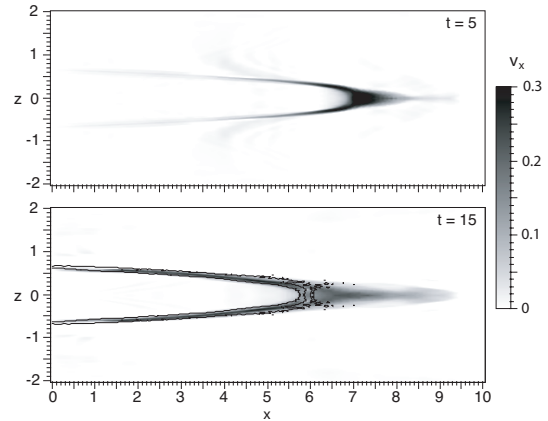


**Fig. 6.** Evolution of an entropy-depleted flux tube (bubble). The gray scale shows the earthward flow speed and the contours the boundary of the region of reduced entropy density in the  $x, z$  plane.)

As shown by [12], the nonmonotonic variation of the entropy function, resulting from the plasmoid loss, also changes the stability properties of the configuration and, specifically, the depleted flux tubes, which are often denoted a plasma “bubble” [10, 6]. The non-monotonic variation of the entropy leads to ballooning or interchange instability. Using three-dimensional magnetohydrodynamic simulations, Birn et al. [1] investigated the propagation of low-entropy bubbles in the magnetotail. To distinguish the role of the entropy depletion versus acceleration by reconnection, they studied the evolution of a closed magnetic flux tube with artificially reduced pressure (and thus entropy density). The initial entropy variation is shown in Fig. 4 and is qualitatively the same as in Fig. 3, resulting from reconnection. Birn et al. found that the depletion was crucial in permitting the earthward propagation of the bubble, reaching speeds of the order of 200–400 km/s, depending on the initial amount of depletion and the cross-tail extent of a bubble. Fig. 5 illustrates this result by a comparison of three simulations, one starting with a depleted flux tube (solid line), one with additional added initial earthward momentum (dotted line), and one with initial momentum but without depletion (dashed line). Obviously, simple acceleration without depletion does not lead to significant earthward propagation, whereas the two depleted flux tubes, after some initial phase, show similar evolution and propagation toward Earth. This result can be considered as the consequence of interchange instability, originally postulated by [10].

The instability of the depleted flux tube configuration against ballooning also leads to structuring of the depleted region in the cross-tail direction. This is demonstrated by Figs. 6 and 7, which show the earthward flow speed (gray scale) associated with the bubble at two different times in the  $x, z$  plane and the  $x, y$  plane, respectively. The top section shows the earthward propagation, confined within the depleted flux tube. The plots in the equatorial plane (bottom two panels), however, demonstrate that the bubble, which originally consists of a single connected flux tube, breaks apart into several pieces of flux tubes. This is the result of ballooning modes with a wave structure in the cross-tail direction.

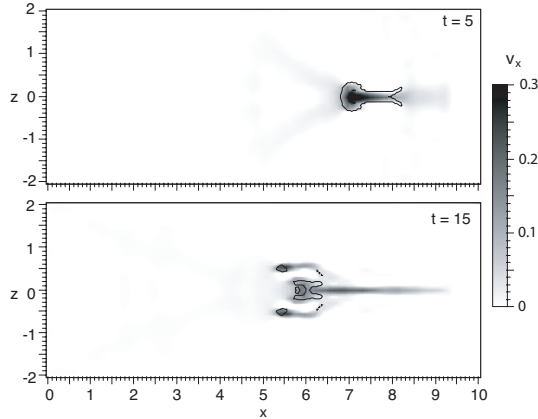


**Fig. 7.** Evolution of an entropy-depleted flux tube (bubble). The gray scale shows the earthward flow speed and the contours the boundary of the region of reduced entropy density in the  $x, y$  plane.)

#### 4. Validity: Comparison between MHD and kinetic simulations

The results discussed in sections 2 and 3 are based on the entropy conservation (2), which is imposed in the MHD model. In a full kinetic model, this approximation may break down through the development of anisotropy and effects of heat conduction, in addition to reconnection. We have therefore investigated the conservation of entropy in a comparison of a particle simulation of magnetic reconnection with an MHD simulation [2]. This study was motivated by a recent comparative study of forced magnetic reconnection with various particle and fluid codes, named the “Newton challenge.” In these simulations, the formation of a thin current sheet and magnetic reconnection are initiated in a plane Harris-type current sheet by temporally limited, spatially varying, inflow of magnetic flux (from top and bottom in Fig. 8). All simulations resulted in surprisingly similar final configurations [5] with a concentration of the current in rings around the center of the magnetic islands, as illustrated in Fig. 8. This suggested that entropy conservation operated similarly in fluid and particle codes despite the fact that kinetic approaches include anisotropy, a different dissipation mechanism, and different waves not included in MHD.

Specifically we investigated again the integral entropy measure  $S(A)$ , defined by Eq. (4), using a gauge in which  $A$  is frozen in the plasma outside the reconnection region. In the absence of dissipation and for vanishing heat flux (or, more generally, vanishing divergence of heat flux)  $S(A)$  should be a conserved function. This function was evaluated for both a PIC simulation and an MHD simulation with localized resistivity given by

$$\eta = \eta_1 / \cosh^2 s \quad s^2 = (x/d_x)^2 + (z/d_z)^2 \quad (5)$$

choosing  $d_x = d_z = 1$  and  $\eta_1 = 0.01$ . Magnetic flux values  $A$  were derived from integrating  $B_x = -\partial A / \partial z$  along the boundary  $x = 16$ . We note that, without dissipation, the flux values at the corners of the simulation box and, for symmetry reasons, at  $x = \pm 16, z = 0$  should be conserved. We normalized  $A$  to vanish at  $x = \pm 16, z = 0$ , that is, at the o-type magnetic neutral points in the center of the evolving magnetic islands, where the plasma stays at rest.

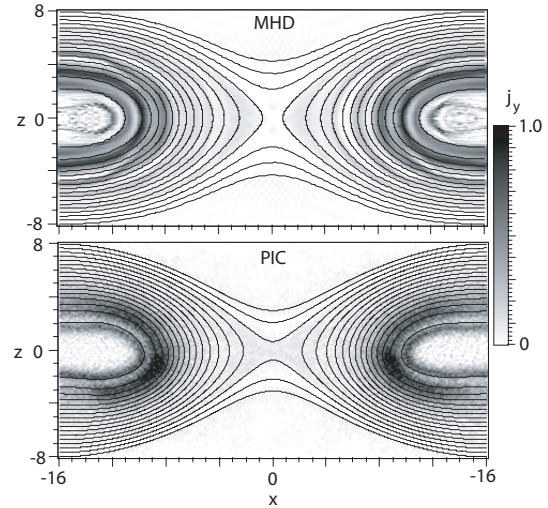


**Fig. 8.** Late magnetic field configuration and current density (gray scale) for an MHD (top) and a PIC simulation (bottom) of the Newton challenge problem [5, 2]. The outermost field lines are the ones that originally formed the boundaries  $z = \pm 8$ . To show the deformation more clearly, field lines outside of these are omitted.

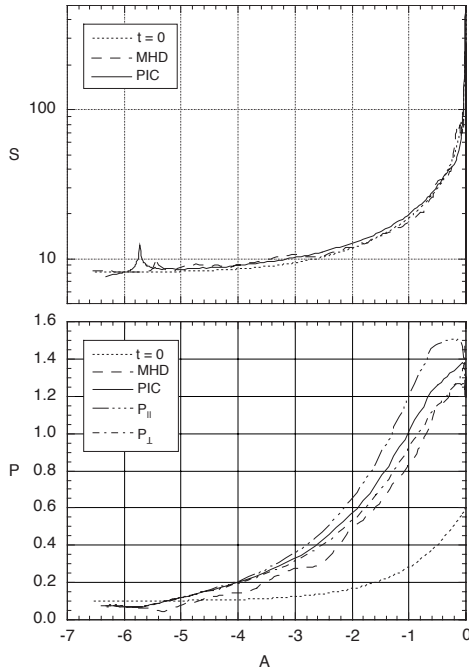
With this gauge, the flux values should be frozen in the plasma fluid within the ideal MHD regime, that is, prior to and after reconnection. However, it makes sense also to compare the entropy before and after reconnection, because of the symmetry of the configuration and the fact that the entropy measure defined by (4) is an additive quantity. Thus we can compare the entropy measure  $S$  of a section of a field line that extends from the  $z$  axis to the boundary before reconnection with the corresponding field line that extends from the  $x$  axis to the boundary after reconnection.

Figure 9 (top) shows the entropy function (4) obtained in this way as function of the magnetic flux variable for both MHD and PIC simulations at the late stages of the simulations together with the initial distribution (dotted line). The bottom part of Figure 9 shows the corresponding pressure variations, also averaged over the field lines. For the PIC simulation the pressure  $p$  is defined by the trace of the full pressure tensor, given by

$$p = \frac{1}{3}p_{\parallel} + \frac{2}{3}p_{\perp} \quad (6)$$

For an indication of the anisotropy in the PIC simulation, the parallel and perpendicular components of the pressure tensor are shown as well as functions of  $A$ , again averaged over field lines.

The entropy functions in Figure 9 (top) show remarkable agreement with each other and with the initial distribution, despite the fact that most field lines at the late times have undergone reconnection. This demonstrates that the Joule dissipation at the reconnection site leads only to a minimal increase in the total entropy on a field line. In contrast, the pressure functions  $P(A)$  have change drastically from the initial distribution but agree closely between MHD and PIC simulations. The small difference is largely due to the fact that the PIC simulation has evolved slightly more than the MHD simulation. The



**Fig. 9.** Entropy (top) and pressure (bottom) as functions of the magnetic flux variable  $A$  for MHD (dashed line) and PIC simulations (solid line) of the Newton challenge problem [5]. Also shown are the parallel and perpendicular pressure components for the PIC simulation.

PIC simulation shows some anisotropy, particularly at values of  $A$  close to 0, which corresponds to the center of the magnetic islands.

The (approximate) entropy conservation through the reconnection process is a particular property that results from the symmetry of the Newton challenge problem with the x-point located at the center of the symmetrical box. This has the consequence that at the reconnection site a field line is split into two halves, which are then reconnected with symmetrical two halves, so that, in the absence of significant dissipation, the total entropy remains the same. In more general configurations without symmetry, such as the tail configuration of Fig. 2, only the sum of the entropies of the affected field lines would be conserved. That is, the entropy loss from a shortened reconnected field line corresponds to the entropy of the severed part contained within the plasmoid.

## 5. Summary and Discussion

We have discussed how entropy conservation and the loss of entropy might affect various substorm phases, including the growth phase, onset, and the expansion phase, in the magnetotail. Results from quasi-static theory and MHD simulations demonstrated how entropy conservation, together with flux and topology conservation in the growth phase of substorms governs thin current sheet formation and the loss of equilibrium. The strong current density intensification, which occurs when the critical state is approached, suggests the onset of instability or a catastrophe, that is, loss of equilibrium, regardless of the dissipation mechanism. This eventually leads to the onset of

reconnection and plasmoid formation and ejection.

The subsequent loss of entropy by the severance of a plasmoid results in a ballooning or interchange unstable configuration. The loss of entropy is essential in enabling depleted closed flux tubes (bubbles) to penetrate to the inner magnetosphere closer to Earth, as suggested by [10]. Ballooning instability may also be responsible for providing cross-tail structure and filamentation of bubbles, which may be closely associated with localized fast flow bursts in the tail.

These results rely on the entropy conservation (2), which is imposed in the MHD model. However, as demonstrated by the comparison between an MHD simulation and a full particle simulation, the integral of entropy on moving flux tubes is well conserved in particle simulations as in MHD simulations, providing credence to the results of the MHD simulations. The (approximate) conservation of entropy, even through the reconnection process, is a consequence of the strong localization of Joule dissipation (given by  $\mathbf{j} \cdot \mathbf{E}'$ , where  $\mathbf{E}' = \mathbf{E} + \mathbf{v} \times \mathbf{B}$ ) and of the lack of significant heat flux across the field.

*Acknowledgments.* This work was performed under the auspices of the US Department of Energy, supported by a grant from NASA Goddard Space Flight Center, and by NASA's Sun-Earth Connection Theory and Living With a Star Programs.

## References

1. Birn, J., Hesse, M., and Schindler, K., On the propagation of bubbles in the geomagnetic tail, *Ann. Geophys.*, 22, 1773, 2004.
2. Birn, J., Hesse, M., and Schindler, K., Entropy conservation in simulations of magnetic reconnection, *Phys. Plasmas*, 2006, submitted.
3. Birn, J. and Schindler, K., Thin current sheets in the magnetotail and the loss of equilibrium, *J. Geophys. Res.*, 107, SMP18, doi:10.1029/2001JA0291, 2002.
4. Birn, J., Schindler, K., and Hesse, M., Formation of thin current sheets in the magnetotail: Effects of propagating boundary deformations, *J. Geophys. Res.*, 108, 1337, doi:10.1029/2002JA009641, 2003.
5. Birn, J., *et al.*, Forced magnetic reconnection, *Geophys. Res. Lett.*, 32, L06105, doi:10.1029/2004GL022058, 2005.
6. Chen, C. and Wolf, R., Interpretation of high-speed flows in the plasma sheet, *J. Geophys. Res.*, 98, 21409, 1993.
7. Hesse, M. and Schindler, K., The onset of magnetic reconnection in the magnetotail, *Earth Planets Space*, 53, 645, 2001.
8. Hesse, M. and Winske, D., Electron dissipation in collisionless magnetic reconnection, *J. Geophys. Res.*, 103, 26479, 1998.
9. Lyons, L. R. and Pridmore-Brown, D. C., Force balance near an X-line in a collisionless plasma, *J. Geophys. Res.*, 95, 20903, 1990.
10. Pontius, D. and Wolf, R. A., Transient flux tubes in the terrestrial magnetosphere, *Geophys. Res. Lett.*, 17, 49, 1990.
11. Pritchett, P. L., Effect of electron dynamics on collisionless reconnection in two-dimensional magnetotail equilibria, *J. Geophys. Res.*, 99, 5935, 1994.
12. Schindler, K. and Birn, MHD stability of magnetotail equilibria including a background pressure, *J. Geophys. Res.*, 109, A10208, doi:10.1029/2004JA010537, 2004.

13. Shay, M. A. and Drake, J. F., The role of electron dissipation on the rate of collisionless magnetic reconnection, *Geophys. Res. Lett.*, 25, 3759, 1998.
14. Vasyliūnas, V. M., Theoretical models of magnetic field line merging, 1, *Rev. Geophys. Space Phys.*, 13, 303–336, 1975.

# Depletion of electrons in a multiple substorm event on November 15th, 2001

C. R. Bryant, J. S. Murphree, E. Donovan, and S. B. Mende

## Abstract:

Using the IMAGE FUV instrumentation it is possible to determine the power of auroral events. Proton power can be calculated using the SI12 instrument and the power of the LBH spectrum can be calculated using the WIC camera. The resulting power spectrums can be compared, examining the relationship of the precipitating particles. Data will be presented from a multiple substorm event from November 15, 2001.

The multiple substorm event consists of two events that have no apparent IMF trigger during a strong southward IMF (-10 nT). These events are then followed by two substorm events that have external triggers (that being northward turnings). The peaks of the events starting at 1738 UT and 1815 UT have ratios of the SI-12/LBH power of roughly 45%, indicating that the aurora is primarily due to precipitating electrons. The breakup at 1900 UT has a peak of SI-12/LBH power of 170%. Clearly the protons make up much more of the particle precipitation into the auroral oval as the WIC images show weak intensities likely related to secondary electrons from the proton precipitation. The recovery phase after this final substorm is quick for the LBH power but the proton power shows that the decay is longer, perhaps even with another event occurring at 2140 UT with only a proton power signature.

Loss cone for the electrons means they are favoured to precipitate into the oval but are depleted in the later substorm and protons make up the majority of the precipitating particles. Particle measurements will be used in conjunction with images from IMAGE FUV instruments to help determine the relationship between the protons and electrons in this multiple substorm event scenario.

*Key words:* substorms, IMAGE FUV, multiple events.

## 1. Introduction

November 15th, 2001 provides an interesting example of a multiple substorm event. In this example, observations reveal an extended growth phase with a strongly southward IMF, a non-IMF triggered pseudo-breakup and breakup, and two breakups triggered by northward turnings. The recovery phase of each part of the event is interesting as many of the features remain when the next breakup occurs in another portion of the oval.

The far ultraviolet instruments on board the IMAGE satellite are the primary vehicle for the selection of the dataset used in this paper. In particular, the wideband imaging camera (WIC) and a spectral imager (SI-12) are used. The WIC instrument operates in the Lyman-Birge-Hopfield (LBH) band from 140 - 190 nm where the prominent excitation mechanism is electron impact excitation for the LBH band [7]. Due to O<sub>2</sub> absorption in part of the LBH band there are significant losses as well as dayglow associated with solar radiation on the dayside. As well, there is also contamination from precipitating protons which are efficient at creating secondary electrons contaminating the pure electron signal [9, 3]

The SI-12 imager measures Doppler shifted Lyman- $\alpha$  emission at 121.567 nm produced by energetic protons cascading into the atmosphere. Geocoronal emissions due to solar radi-

ation at 121.6 nm is a concern but is filtered out to produce only photons associated with proton aurora. Due to limitations of the instrument, however, only protons with energies of at least several keV will be detected [8].

Other than IMAGE FUV, ACE solar wind and interplanetary magnetic field measurements are also used in describing the events. The ACE data is Weimer-mapped from the ACE location near the L1 point back to the bow shock at 12 MLT. This means that the displayed ACE data is much closer to the time that the magnetosphere would actually react to the solar wind and magnetic field.

Using the MLT images for the WIC and SI-12 cameras, it is possible to estimate the power [2]. In this paper, the auroral substorm power is estimated by contouring the hemisphere with a minimum value that was calculated from multiple images of quiet time. Once this minimum level is defined, the contour is run in order to calculate the area [1] of the auroral intensity above the quiet level. Therefore a power level of zero represents a quiet oval.

The auroral substorm power, like other indices such as AE [10], can be used to determine onset/expansion and beginning of the recovery phase. The power dramatically increases at onset. At the beginning of the recovery phase, the power reaches a maximum. As the recovery phase continues, the power continues to decrease until it reaches zero which would indicate the end of the recovery phase.

## 2. Observations

Looking at the two hours prior to the event, Weimer-propagated ACE data in the figure 1 reveals that there would likely be two

Received 25 May 2006.

C. R. Bryant, J. S. Murphree, and E. Donovan. Institute for Space Research, University of Calgary, Calgary, AB, CAN  
S. B. Mende. Space Science Laboratory, University of California, Berkeley, CA, USA

substorms due to northward turnings following the strongly southward  $B_z$  period. The growth phase for these two substorms appears to start with a sudden drop of  $B_z$  from 5 nT to -7 nT at 1642 UT. It is followed 5 minutes later by a downward shift of  $B_y$ .  $B_z$  is strongly southward for about 90 minutes before the first northward turning and the first of two externally triggered events.

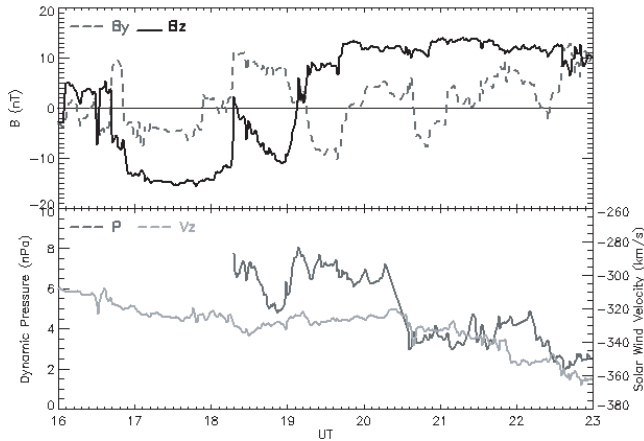


**Fig. 1.** Weimer-mapped ACE data from 16-23 UT on November 15, 2001. The top panel shows the  $B_z$  and  $B_y$  components of the solar wind while the lower panel shows the dynamic pressure and the  $V_z$  component of the solar wind. (Data is courtesy of Dr. J. Weygand at IGPP, UCLA.)

The growth phase is also evident in figure 2. One expects the poleward edge of the auroral oval to move equatorward during the loading process as the tail is stretched out. Examining the four keograms, the WIC and SI-12 keograms at 3.0 MLT clearly show equatorward movement of the poleward boundary until the first breakup at 1737 UT. The keograms at 23.0 MLT also show equatorward movement but show a potential pseudo-breakup near 1636 UT and then show expansion both equatorward and poleward at the first clear pseudo-breakup at 1720 UT.

The substorms externally triggered by the two separate northward turnings are at 1815 UT and 1900 UT. The first northward turning, from -13 nT to 2 nT, occurs simultaneously with a duskward shift in  $B_y$  as seen in figure 1. In figure 2 it is clearly seen that there are increases in intensity at 1815 in both local times. The 1900 UT substorm is not nearly as clear in the MLT images although there is an increase in the intensity of the SI-12 keograms. In figure 3, there is a very clear rise in power starting at 1815 UT. A similar increase is also seen in the SI-12 power. Figure 4 ratio of SI-12 to WIC power is less than 100% during this substorm.

After spiking at 2 nT at 1815 UT,  $B_z$  begins to fall off to -10 nT loading energy into the system again over the next 45 minutes. The second northward turning beginning at 1900 UT has a gradual rise in  $B_z$  from -10 nT to 8 nT that lasts nearly 8 minutes. At the same time,  $B_y$  again moves downward. In this case, the keograms in figure 2 barely show any intensity increase and it appears later than 1900 UT. Most of the intensity increase is also in the post-midnight sector. Similarly, figure 3 shows the SI-12 power increasing at 1900 UT while the

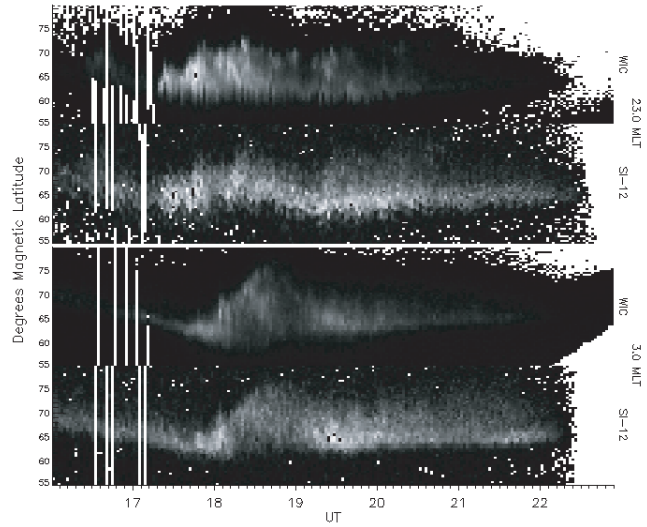


**Fig. 2.** Keograms for WIC and SI-12 from 16 UT to 23 UT. The top two keograms are taken at 23.0 MLT which is the local time of the pseudo-breakup and close to the first breakup. The bottom two keograms are from 3.0 MLT in order to illustrate the proton aurora later in the sequence of events.

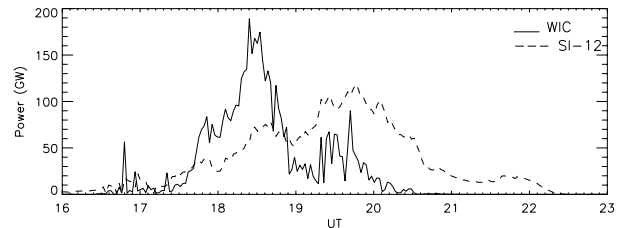


**Fig. 3.** WIC (LBH) and SI-12 (proton) total auroral substorm power between 16 UT and 23 UT. The solid line is the WIC power and the dashed line is the SI-12 power.

WIC power remains fairly consistent until its rise near 1920 UT. The rise at 1920 UT is also related to secondary electron contamination from the proton precipitation. Figure 4 shows that the ratio of WIC to SI-12 power is near one before 1900 UT. The SI-12 power climbs steadily to nearly five times the WIC power by 1920 UT.

In figure 1,  $B_z$  becomes steadily northward at 1940 UT. The recovery phase happens during periods of prolonged northward IMF after a northward turning. Further, examining the keograms in figure 2, it is seen that the WIC camera shows decreasing intensities at both 23.0 MLT and 3.0 MLT. The 23.0 MLT also shows a weak double oval formation. Both of these are characteristics of the recovery phase. Figure 3 also shows decreases in power starting around 1940 UT. This is in agreement as the power is related to the intensity of the auroral oval.

### 2.1. Pseudo-Breakup - 1720 UT

The pseudo-breakup occurs during the strongly southward IMF and appears to not be IMF triggered. This is being defined as a pseudo-breakup as there is limited poleward and latitudinal expansion.

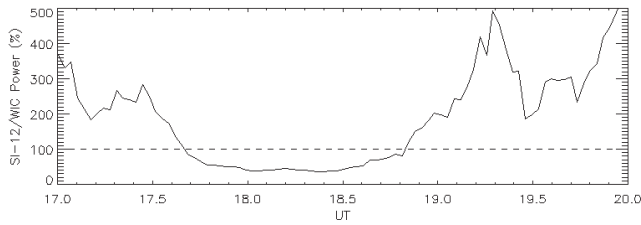


**Fig. 4.** Power ratio from 17 to 20 UT. The ratio is given as a percentage of power of the SI-12 instrument to the WIC instrument.

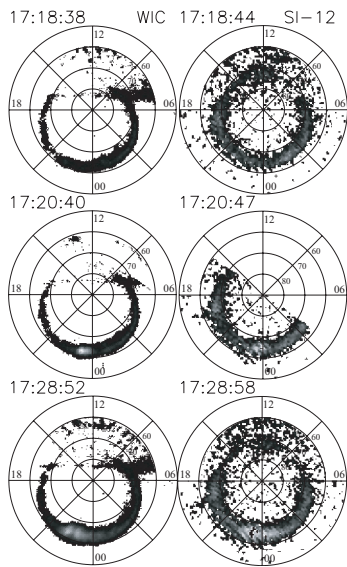


**Fig. 5.** 1720 UT pseudo-breakup. This is a series of MLT images from the IMAGE WIC and SI-12 cameras. Each row represents one UT time and the left column is WIC and the right column is SI-12.

In figure 5, 1718 UT (the top row) shows the auroral oval to be reasonably quiet. Weak activity does exist and it appears in the same region on both the SI-12 and WIC images. At 1720 UT, a breakup is evident at 23.0 MLT. Both WIC and SI-12 images clearly show a sharp increase in activity. This is confirmed in figure 2 in the 23.0 MLT keograms which also show a sharp boundary in intensity at 1720 UT. Over the next few images (not shown) activity increases and a small auroral bulge forms. At 1728 UT, the pseudo-breakup is already in recovery phase in the WIC image though some activity remains in the SI-12 image. This is confirmed in the 23.0 MLT keograms again as there is a significant decrease in intensity.

## 2.2. Substorm One - 1737 UT

This substorm occurs during the strongly southward IMF and appears not to be IMF triggered. Although a duskward shift (increase) in  $B_y$  occurs at this time and it has been noted that  $B_y$  maybe a possible trigger [6]. Solar wind pressure pulses have also been noted to trigger substorms [5] however there is not a complete dataset over that time period in order to determine if the breakup was caused by a change in solar wind dynamic pressure.

At 1735 UT (the top row), in figure 6a, the oval shows weak activity in the WIC image although there is more intense activity in the SI-12 image, mostly in the post-midnight sector. The images at 1737 UT clearly show a breakup at 22.5 MLT in the WIC images and an increase in the intensity of the activity in the pre-midnight sector in the SI-12 image. This means that breakup occurred between 1735 and 1737 as the IMAGE satellite has a two minute cadence. This conclusion is supported by the keograms in figure 2 which also show a significant intensity increase in both the SI-12 and WIC keograms at 23.0 MLT. The keograms at 3.0 MLT also show that the equatorward motion associated with the growth phase has stopped. Figure 3 also clearly shows a dramatic increase in WIC power at this time. The power continues to grow throughout the expansion phase. This is consistent with figure 4 which shows the ratio of SI-12 to WIC power is decreasing throughout the expansion phase.

At 1751 UT, the substorm has reached the beginning of the recovery phase. The oval has begun to decrease latitudinally and in intensity. This intensity decrease can be seen in the keograms at 23.0 MLT. The local maximum power in the SI-12 and WIC occurs at this time. In the final row of images in figure 6a at 1807 UT, the activity has continued to move into the morning sector. Some recovery phase phenomena (double oval formation and increase in the morning sector activity) are visible. The power has decreased from its maximum at 1751 UT for both WIC and SI-12 which is also an indicator of recovery. The WIC power remains larger than the SI-12 power during this period indicating that both WIC and SI-12 power are dropping simultaneously.

## 2.3. Substorm Two - 1815 UT

This substorm is triggered by a sudden northward turning at 1815 UT following a prolonged (90 minute) strongly southward IMF. Once it peaks, however, the IMF decreases again for 40 minutes down to  $-10$  nT.  $B_y$  remains duskward over this time. There is a decrease in the dynamic pressure during the decreasing IMF after onset. As there appears to be no sustained northward IMF, the recovery phase should likely be shortened or non-existent.

In figure 6b, the first row at 1814 UT shows a moderate amount of activity, most of which is still left from the previous substorm seen in figure 6a. There is recovery phenomena seen such as a large latitudinal extent on the morning side, north-south structures, and a double oval. The proton aurora, though not as wide also shows moderate activity in three sectors. Figure 3 shows that there is still significant auroral substorm power.

In the second row, there is obviously a major increase in intensity. The major increase is around 21 MLT with a bifurcation from 21 MLT to 00 MLT as discrete aurora move poleward and the diffuse aurora, still present from the previous substorm moves equatorward during the expansion phase. Proton aurora also brightens, but further east than the WIC image, with the greatest intensity increases near 22.5 MLT. During this time, both WIC and SI-12 power is increasing. The keograms confirm the onset near 1815 UT. The SI-12 keogram at 23.0 MLT is especially good as the SI-12 intensity increases are closest. The 3.0 MLT keograms show tremendous poleward expansion of the oval.

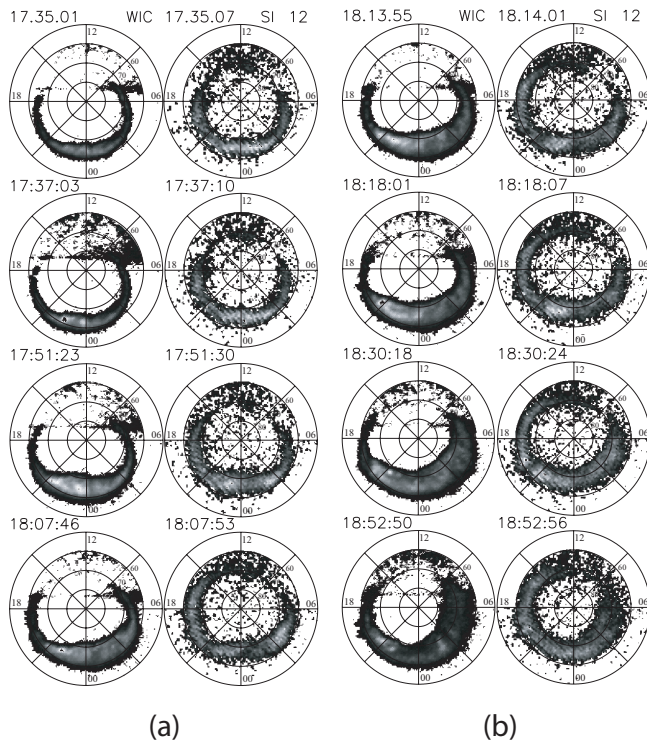


**Fig. 6.** This is a series of MLT images from the IMAGE WIC and SI-12 cameras. Each row represents one UT time and the left column is WIC and the right column is SI-12. The images in figure (a) represent the first substorm at 1737 UT and figure (b) represents the substorm at 1815 UT.

At 1830 UT, there is a marked decrease in the intensity of the oval as the beginning of the recovery phase of this second substorm starts. A double oval has formed and the morning sector has continued to expand from the recovery phase of the first substorm, now covering over  $15^\circ$  MLAT. Many north-south structures exist from midnight into the morning side as a result of previous recovery phase still continuing. The WIC power curve reaches its maximum at this point, while the SI-12 power curve reaches its maximum a few minutes later. The end of expansion is also evident in the keograms as both the WIC and SI-12 keograms at 23.0 MLT stop poleward motion and the entire oval begins to move equatorward. In the case of the WIC keogram, the intensity also drops off rapidly and a double oval is evident by 1851 UT. The morning side continues to expand latitudinally.

By 1852 UT, the oval appears to be in full recovery phase. The SI-12 image, is also less intense but still has much more activity than the WIC image. This is fully supported by the 23.0 MLT keograms in figure 2. The double oval in the WIC keogram is an indicator of the recovery phase. The WIC power drops off rapidly to a consistent value near 20 GW while the SI-12 power has barely changed at all. Based on the WIC data, the substorm is in full recovery though that is not evident from the SI-12 data. This is clearly shown in figure 4.

#### 2.4. Event - 1900 UT

After the decrease to  $-10$  nT, there is a slow northward turning to 7 nT. At the same time there is an increase in the dynamic

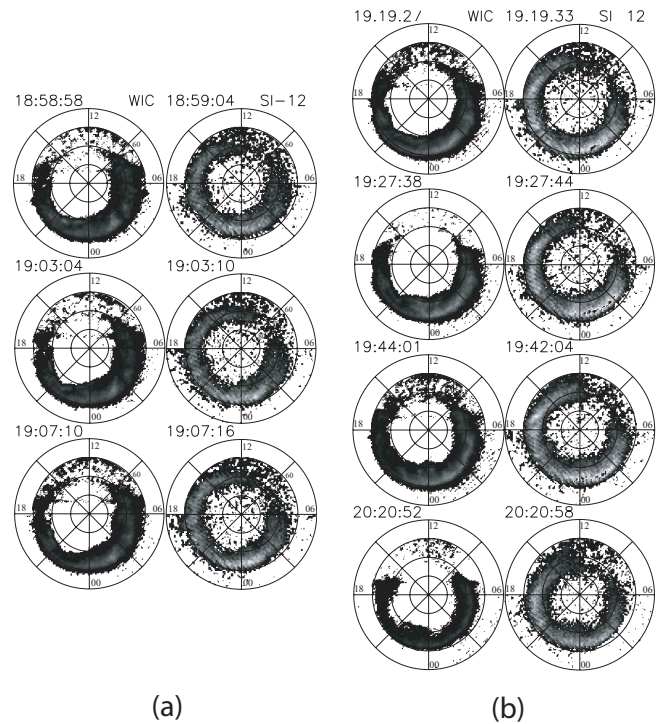


**Fig. 7.** This is a series of MLT images from the IMAGE WIC and SI-12 cameras. Each row represents one UT time and the left column is WIC and the right column is SI-12. The 1900 UT event is outlined in this set of images. Figures in (a) show the strengthening SI-12 intensities while the WIC intensities remain weak. Figures in (b) show the progression through expansion to recovery 'phases' of the event.

pressure. Based on this solar wind evidence, there is another event, substorm or not, starting at 1900 UT. The SI-12 power also illustrates an event that begins at 1900 UT where as WIC power does not increase until twenty minutes later and never increases above the power of the SI-12.

In figure 7a, at 1859 UT (the first row), the WIC image shows a double oval and weak intensities. The morning sector has expanded over  $15^\circ$ . The SI-12 image, on the other hand, has strong activity near midnight that stretches well into the dusk sector. Four minutes later, the WIC image has continued to decrease in intensity. The SI-12 continues to increase in intensity, expanding further east and latitudinally as if breakup had taken place and the oval was in an expansion phase. Four minutes after that, at 1907 UT, the WIC image continues to show recovery. A slight increase in intensity near 02 MLT is due to proton contamination, secondary electrons are being measured by the WIC imager.

At 1919 UT in figure 7b the SI-12 image intensity has increased dramatically, with a peak near 01 MLT but activity spreading from noon all the way to morning. The WIC image shows activity corresponding to the SI-12 image due to secondary electrons. The SI-12 power locally peaks and stays above 90 GW until 20 UT when it begins to fall off. There are three peaks in the SI-12 power during this time. The WIC power is lower than the SI-12 and is related to secondary electrons. The keograms all show the event happens near 1920 UT based on

intensity increases.

At 1927 UT and 1944 UT the SI-12 images remain active while the WIC images remain weakly active due to secondary electrons. There are north-south features near midnight that are unseen in the SI-12 images. The keograms for these times show the SI-12 is in the expansion phase, the latitudinal expansion still occurring. In the final images, at 2020 UT, the WIC image is nearly retreated into a quiet state. The SI-12 intensity has also decreased significantly. The multi-substorm event is now in full recovery in both WIC and SI-12. The recovery phase started near 1945 UT based on figure 3. The WIC power reaches a quiet state much more quickly than the SI-12 proton power which does not reach a quiet state for about 90 minutes more. This is illustrated in figure 4. After reaching a peak of five times the power, the power ratio drops off as more secondary electrons are measured by the WIC camera. Once the SI-12 power begins to decrease, the secondary electron production decreases rapidly and the WIC power drops to zero. The ratio climbs rapidly during this point and the time is cut off at 20 UT as the ratio becomes infinite shortly thereafter.

### 3. Discussion and Conclusions

Detailed observations have been presented for a multiple substorm event that clearly show a reduction and depletion of the LBH electron signature after prolonged substorm activity. Several breakups have been presented to occur during this period including both non-IMF and IMF triggered examples. The power measured by the SI-12 and WIC instruments was also presented to illustrate the differences in the observed signals. It is important to note that the calculated power is related to the intensity of the magnetic local time images.

The event occurring at 1900 UT onwards is a strong proton event fitting the the substorm description of growth, onset, expansion and recovery phases. The lack of a primary electron signature in the LBH band is interesting. However, the precipitating protons evoke a secondary electron response in the LBH range measured by WIC. Figures 3 and 4 clearly illustrate this point.

In figure 3, the SI-12 power is smaller than the WIC power starting after the onset of the first substorm. This is also clear in figure 4. The LBH signal is strong until also 1900 UT while in the recovery phase of the second substorm. During the recovery phase, the proton signature measured by SI-12 remains high and becomes greater than the WIC power near 1852 UT. The WIC camera continues to display recovery phase characteristics event as the protons bring to enter into another active cycle. Figure 3 shows that the power of the SI-12 is higher than WIC power. The WIC power displayed is contaminated by secondary electrons elevating the power artificially. Once the power calculated from SI-12 observations begins to decrease (beginnings of the recovery phase), the WIC power drops extremely rapidly as the secondary electron contamination is removed. Figure 4 shows the ratio getting closer to one until such time as the recovery phase begins and the ratio increases rapidly. As the WIC power reaches zero the power calculated from SI-12 remains above zero for two more hours. This leaves us with the question: Is this proton event actually a substorm with a depleted electron signature?

Several possible explanations may account for some or all of the depletion of the electrons in the LBH. Perhaps the plasma source region has been reduced in electrons of the proper energies to produce an LBH signal. Since the bounce period for electrons is 1000 times shorter, the electrons deplete faster. This sets up a parallel electric current due to charge separation. It may be possible to measure this current during this time and observe the magnitude of the current. This would provide insight into the behaviour of the electrons in the source region. Mapping the footprint back into the tail and examining where the source region is and potentially what L-shell it is on during the entire multiple-substorm event could provide insight on the type of source region involved.

Based on the ACE data and the keograms, it could be that the electron loss cone may not have a chance to completely refill between substorms leaving a fuller proton loss cone later in the event. Considering  $B_z$ , if the electron loss cone starts to fill, at 1642 UT, the first optical signature of precipitation starts at 1720 UT with the pseudo break and then the non-IMF triggered substorm. During this time, the magnetosphere should continue to be loaded. At 1815 UT, the second substorm occurs. After onset, it appears to continue to load based on  $B_z$ . However, if the precipitation has emptied the loss cone significantly by this point, the short time period between the second substorm and the final event may not allow enough loading before  $B_z$  remains northward.

The energy of particle precipitation is dissipated in several ways including heat and light. Due to the prolonged precipitation, the atmosphere is being heated. This heating causes the scale height of the atmosphere to increase. Since electrons penetrate deeper into the atmosphere than protons due to their smaller collision frequency.  $O_2$  is a major absorber in the LBH range, therefore with the increase of  $O_2$  at higher altitudes more of the LBH photons are absorbed.

What has been useful in this event is the determination of the beginning of the recovery phase based the power of IMAGE-FUV. Pulkkinen's paper [10] used the AE to determine the possible start of the recovery phase. While the AE is taken at a higher frequency than the IMAGE data, due to lack of magnetometers the AE can no longer be calculated with accuracy. The use of auroral substorm or hemispheric power of the global images may provide a very good indicator of the start of the recovery phase.

Future work may include looking for other examples of prolonged events where the proton power calculated from the SI-12 is greater than the WIC power. If several more of these events can be identified, what ramifications does this have on interpreting substorms? Identification of other data sets that may maybe used in defining ionospheric and auroral behaviour will be important. FAST and DMSP may provide particle measurements in the near Earth environment. Also, gathering data from downtail sources such as Geotail and Cluster may give hints to the magnetospheric topology that leads to such optical auroral observations as this.

### 4. Acknowledgements

The authors would like to thank Benoit Hubert for valuable discussions and James Weygand for the Weimer-mapped ACE

data. This research is supported by a grant from the Natural Science and Engineering Research Council of Canada.

## References

1. Carbary, J. F., Liou, K., Lui, A. T. Y., Newell, P. T. and C.-I. Meng, Blob analysis of auroral substorm dynamics, *Journal of Geophysical Research*, 105, 16083–16091, 2000.
2. Frey, H. U., Mende, S. B., Immel, T. I., Gerard, J.-C., Hubert, B., Habraken, S., Spann, J., Gladstone, G. R., Bisikalo, D. V., and Shematovich, V. I., Summary of Quantitative Interpretation of IMAGE Far Ultraviolet Auroral Data, *Space Science Reviews*, 109, 255–283, 2003.
3. Hubert, B., Gerard, J.-C., Bisikalo, D. V., Shematovich, V. I., and Soloman, S. C., The role of proton precipitation in the excitation of the auroral FUV emissions, *Journal of Geophysical Research*, 106, 15.1–15.1221475–21494, 2001 2002.
4. Hubert, B., Gerard, J.-C., Evans, D. S., Meurant, M., Mende, S. B., Frey, H. U., Immel, T. J., Total electron and proton energy input during auroral substorms: remote sensing with IMAGE-FUV, *Journal of Geophysical Research*, 107, 15.1–15.12, 2002.
5. Lyons, L. R., A new theory for magnetic substorms, *Journal of Geophysical Research*, 100, 19069–19081, 1995.
6. Lyons, L. R., Blanchard, G. T., Samson, J. C., R. P. Lepping, T. Yamamoto, and T. Moretto, Coordinated observations demonstrating external substorm triggering, *Journal of Geophysical Research*, 102, 27039–27051, 1997.
7. Mende, S. B. et al., Far ultraviolet imaging from the IMAGE spacecraft: 2. Wideband Imaging Camera, *Space Science Reviews*, 91, 271–286, 2000.
8. Mende, S. B. et al., Far ultraviolet imaging from the IMAGE spacecraft: 3. Spectral Imaging of Lyman-alpha and OI 135.6 nm, *Space Science Reviews*, 91, 287–318, 2000.
9. Mende, S. B., Frey, H. U., Immel, T. J., Gerard, J.-C., Hubert, B., Fuselier, S. A., Global Imaging of Proton and Electron Aurorae in the Far Ultraviolet, *Space Science Reviews*, 109, 211–254, 2003.
10. Pulkkinen, T. I., Baker, D. N., Toivanen, P. K., Pellinen, R. J., Friedel, R. H. W., and Korth, A., Magnetospheric field and current distributions during the substorm recovery phase, *Journal of Geophysical Research*, 99, 10955–10966, 1994.

# Spatio-temporal dynamics of substorms during intense geospace storms

J. Chen, A. S. Sharma, and X. Shao

**Abstract:** The nonlinear dynamical models of the coupled solar wind-magnetosphere system derived from observational data are used to yield efficient forecasts of the magnetospheric conditions. A correlated database of solar wind and magnetospheric time series data for the last solar cycle near its peak (year 2001) is compiled and used to model the magnetospheric dynamics under strong driving. The dynamical models of the magnetosphere during superstorms developed with this database are used to forecast the geospace storms of October-November 2003 and April 2002, and yields improved forecasts of the intense storms. A new technique which consider the contributions of the nearest neighbors weighted by factors inversely proportional to the distances in the reconstructed phase space yields better predictions, especially during the strongly driven periods. Also the time series data of the distributed observations are used to develop spatio-temporal dynamics of the magnetosphere using phase space reconstruction techniques. This nonlinear model is used to study the spatial structure of geomagnetic disturbances during intense geospace storms. The ground magnetometer data are from the two chains of stations: CANOPUS (13) and IMAGE (26). This new data set, with 1-minute resolution, is used to study the spatio-temporal structure, including the coupling between the high and mid-latitude regions. From the point of view of space weather the predictions of the spatial structure are crucial, as it is important to identify the regions of strong disturbances during intense geospace storms

*Key words:* Substorms, Nonlinear Dynamics, Prediction, Space Weather.

## 1. Introduction

The solar wind-magnetosphere coupling is enhanced when the interplanetary magnetic field (IMF) turns southward, leading to geospace storms and substorms. The magnetosphere is a highly dynamic system under these conditions. The Earth's magnetosphere is a non-autonomous dynamical system, driven by the solar wind. Studies of the magnetospheric dynamics using models derived from the correlated database of the solar wind - magnetosphere system have enhanced our understanding of the complex behavior of the magnetosphere. The advantage of this approach is the ability to yield the dynamics, inherent in observational data, independent of modeling assumptions. There has been considerable progress in the modeling and forecasting of the solar wind-magnetosphere coupling as an input-output system by linear and nonlinear approaches.

The linear prediction filter technique was used to obtain the response time of the magnetosphere from the  $AL - VB_s$  database [3][hereafter referred to as the BBMH dataset]. This database spans the period from November 1973 to December 1974 and has 2.5 min resolution. The response functions from this analysis have been used to interpret how the magnetospheric response to the solar wind driver with changes in the activity level, indicating nonlinearity. These response functions exhibited two time scales, corresponding to the directly driven and loading-unloading processes. The modeling of magnetospheric substorms as a low dimensional system using the time series data of the electrojet indices,  $AL$  or  $AE$ , to reconstruct its dynamics has shown its low dimensionality and the nonlinear nature of the magnetosphere [6] [7] [8] [17]. The reconstruc-

ted phase space show clear evidence that the dynamical system follows a pattern in the reconstructed phase space [9] [10]. This implies that the dynamics of the magnetosphere is predictable and this recognition has stimulated the study of forecasting substorms [18] and storms [14]. Vassiliadis [18] used the local-linear technique on the BBMH dataset, with the solar wind convective electric field  $VB_s$  as the input and the  $AL$  index as the output, and obtained good predictions. These predictions gave strong evidence that nonlinear models can be used to develop accurate and reliable forecasting tools for space weather. Recent studies using time series data have shown that the coherence on the global magnetospheric scale can be obtained by averaging over the dynamical scales. A model for the global features can be obtained by a mean field technique of averaging outputs corresponding to similar states of the system in the reconstructed phase space [12] [13]. With such a mean-field model, accurate iterative long-term predictions can be obtained, as the model parameters need not be changed during the prediction.

Recently, some dynamical models incorporating the spatial structure have been studied beyond the global indices. The successful standard nonlinear dynamic approach using the  $AL - VB_s$  coupling has been generalized to consider the dynamical evolution of spatial structure of magnetic perturbation. Valdivia [15] [16] studied and modeled the evolution of the spatial structure of the middle and high latitude current structure by a set of mid- and high-latitude ground magnetometers distributed at different longitudes around the Earth, providing the representation of the effect of the currents at the ground. A 2D dynamical solar wind driven model for the evolution of the spatial structure of the mid-high latitude magnetic field perturbations was generated from IMAGE chain of magnetometers. The prediction model gives some new and interesting results.

During April 2002 and October-November 2003, nearly 2 years after the last solar maximum, three extremely big G5

Received 27 June 2006.

J. Chen, A. S. Sharma, and X. Shao. Department of Astronomy, University of Maryland, College Park, Maryland, USA.

geospace storms occurred, an extreme geomagnetic storm on the NOAA space weather scale that runs from G1 to G5. These three G5 extreme geomagnetic storms were driven by the solar wind with the southward IMF of  $-58.3$  nT,  $-32.03$  nT and  $-53.02$  nT, measured by ACE, and these led to the  $AL$  index values of  $-2778$  nT,  $-1851$  nT and  $-2499$  nT, respectively. These three intense geospace storms provide interesting opportunities for the study of nonlinear phase space reconstruction under extreme conditions. In order to model and predict such intense storms, a correlated database of the solar wind and magnetospheric variables of the year 2001, which is close to the peak period of 11-year solar cycle, was compiled [4].

To study the spatial structure as observed by the latitudinal chain of magnetometers, CANOPUS and IMAGE, the ground magnetometer measurements from 26 stations of IMAGE array and 13 stations of CANOPUS array for year 2002 with resolution of 1 minutes are compiled. The correlated solar wind input is  $VB_s$ , as in the earlier studies.

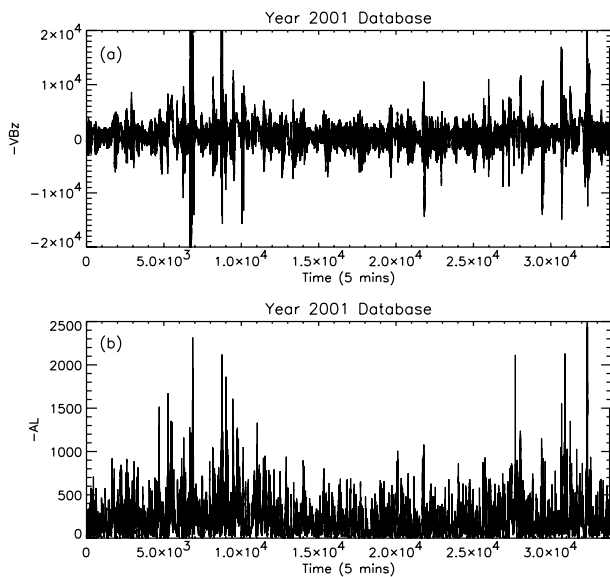


**Fig. 1.** The correlated solar wind induced electric field  $VB_z$  (panel a) and the auroral electrojet index  $AL$  (panel b) for 81 intense storm intervals during year 2001. The geomagnetic activity in these intervals during the peak of the last solar cycle is very high and correspond to strong driving by the solar wind.

## 2. Correlated Database of Solar Wind-Magnetosphere Coupling under Strong Driving

During the period of maximum solar activity, the magnetosphere is strongly driven and the year 2001 near the last solar maximum is chosen for compiling a database for such an epoch. This database contains solar wind flow speed  $V$ , the north-south component of the IMF  $B_z$  and the  $AL$  index for the 11 months of 2001 (January to November). The solar wind data for 2001 were compiled for a set of data intervals, each defined as any continuous data longer than 12 hours with no more than half-hour data gap. The dataset contains 81 intervals with periods 12 hours to 3 days long. During January-November 2001,

there were 81 such data intervals containing 33931 data points at 5-min resolution, satisfying the above conditions. The correlated solar wind induced electric field  $VB_z$  and the auroral electrojet index  $AL$  for 81 intense storm intervals during year 2001 are shown on Figure 1. During this period of strong solar activity, intense substorms and storms were triggered with higher frequency. If we define a strong geomagnetic storm as having  $Dst$  less than  $-100$  nT, we find that there are 12 such storms in 2001 compared with 4 such storms in 1995 and 1 in 1996. Thus the 2001 database is appropriate for studying the properties of geomagnetic activity during a solar maximum. The selected 81 events are separated into 3 activity levels by the average values of  $VB_s$ : medium ( $\langle VB_s \rangle \leq 1500$  nT km/s), high ( $1500$  nT km/s  $\leq \langle VB_s \rangle \leq 2500$  nT km/s), and super ( $\langle VB_s \rangle \geq 2500$  nT km/s). To model a specific event, we choose the corresponding activity level to which it belongs and use it as a reference database.

During 2002-2003 there were three intense storms, occurring in April 2002, October 2003, and November 2003. The solar wind data from ACE through CDAWEB and the corresponding geomagnetic field index  $AL$  were compiled for these storms.

The magnetic perturbations from the 39 magnetometers of IMAGE and CANOPUS of year 2002 are used to visualize and predict the spatial evolution of the current systems. This database contain solar wind key parameters from ACE and magnetic perturbation from ground magnetometers with 1 minute resolution. We have both the magnetic perturbation  $H_x$ , geographic north, and  $H_y$ , geographic east, of the individual magnetometer. A valuebase, defined as the average value of the 15 quietest days in the whole year 2002, is subtracted from each component at each magnetometer.

We partition the dataset by mapping the magnetometer measurements in the universal time and the magnetic latitude to a 2D grid of magnetic local time and magnetic latitude  $\lambda$  [16]. Such mapping is possible because the perturbation is measured at the different location in the magnetosphere as the Earth rotates.

## 3. Nonlinear Dynamical Modeling Using Correlated Data

### 3.1. Input-Output Modeling of the Magnetosphere

The magnetosphere has been shown to exhibit the features of a nonlinear dynamical system, and its global features have been modeled by a few variables [2]. This remarkable property arises from the inherent property of phase space contraction in dissipative nonlinear systems. A dynamical input-output model can be constructed based on local-linear filters, which represent the relationship between the input  $I(t)$  and the output  $O(t)$  of the system.

The time delay embedding technique is an appropriate method for the reconstruction of the phase space and for obtaining its characteristic properties [5] [11]. In this technique, a  $m$  component phase vector  $X_i$  is constructed from this time series  $x(t)$  as:

$$X_i = \{x_1(t_i), x_2(t_i), \dots, x_m(t_i)\}, \quad (1)$$

where  $x_k(t_i) = x(t_i - (k - 1)T)$  and  $T$  is a time delay. If the embedding procedure is properly performed, the dynamical attractor underlying the observed time series will be completely unfolded, and the constructed states have one to one correspondence with the states in the original phase space. Appropriate values of the time delay  $T$  and the embedding dimension  $m$  can be obtained by using techniques such as the average mutual information and the correlation integral [1].

In an input-output model of the solar wind-magnetosphere system during substorms, the solar wind convective electric field  $VB_s$  is commonly used as the input and the geomagnetic activity index  $AL$  or  $AE$  as the output. Thus the input-output vector in the  $2m$  dimensional embedding space can be constructed as

$$X_i = (I_1(t_i), \dots, I_{M_I}(t_i), O_1(t_i), \dots, O_{M_O}(t_i)), \quad (2)$$

where  $M_I = M_O = m$ . The  $2m$ -dimensional state vector  $X_i$  at  $t = t_1, t_2, \dots, t_N$ , can now be used to construct a trajectory matrix for the dynamics of the system as:

$$X = \begin{bmatrix} I_1(t_1) & \cdots & I_m(t_1) & O_1(t_1) & \cdots & O_m(t_1) \\ x_1(t_2) & \cdots & I_m(t_2) & O_1(t_2) & \cdots & O_m(t_2) \\ \vdots & \ddots & \vdots & \vdots & \ddots & \vdots \\ I_1(t_N) & \cdots & I_m(t_N) & O_1(t_N) & \cdots & O_m(t_N) \end{bmatrix} \quad (3)$$

where  $N$  is the number of vectors. This  $N \times 2m$  matrix contains all the dynamical features of the system contained in the data and yields its evolution in the reconstructed phase space.

### 3.2. Local-Linear and Weighted Mean Field Filters

The reconstructed phase space obtained from time series data has one-to-one correspondence with the states in the original phase space, thus making the prediction of the dynamical system possible. The main idea of this method is the use of the trajectories in the neighborhood of the state at time  $t$  to predict its location at the next time step. Knowing how the neighboring trajectories evolve, the location of the current state  $x(t)$  at next time step  $t + T$  can be predicted. The procedure is locally linear but is essentially nonlinear as the features of the neighboring trajectories are taken into account by considering a small neighborhood.

Given the current state, the states similar to it in the training set are selected as the first step. The similarity of the current state with any other state in the known data, which is referred to as the training set, is quantified by the Euclidean distance between them in the embedding space. The states within a specified distance of the current state are referred to as the nearest neighbors ( $NN$ ). The prediction using the mean field approach have been used with the correlated BBMH database of solar wind and geomagnetic activity time series [12] [13].

$$O_{n+1} = \frac{1}{NN} \sum_{k=1}^{NN} X_k \quad (4)$$

In the mean field model, all the states in the specified neighborhood, the  $NN$  nearest neighbors, were used to obtain the center of mass by a simple averaging procedure. It is however the prediction can be improved if the states close to the current state contribute more than those farther away. Based

on this recognition, a new filter based on the mean field filter is proposed to improve the accuracy and efficiency of predictions. This weighted filter takes into account the distance of the nearest neighbors, a set of weight factors  $g$  which depend inversely on the distances of each nearest neighbor from the mass center is introduced as

$$g_k = \frac{1}{d_k^2} / \sum_{i=1}^{NN} \frac{1}{d_i^2} \quad (5)$$

where  $d_i$  is the Euclidean distance of the  $i$ th nearest neighbor from the center of mass. The predicted output that includes this weighting of the neighbors is

$$O_{n+1} = \frac{1}{NN} \sum_{k=1}^{NN} X_k \bullet g_k, \quad (6)$$

The prediction accuracy is quantified by normalized mean square error (NMSE):

$$\eta = \frac{1}{\sigma_o} \sqrt{\frac{1}{N} \sum_{i=1}^N (O_i - O_i^*)^2}, \quad (7)$$

where  $O_i$  and  $O_i^*$  are the observed and predicted data, respectively, and  $\sigma_o$  is the standard deviation of  $O_i$ .

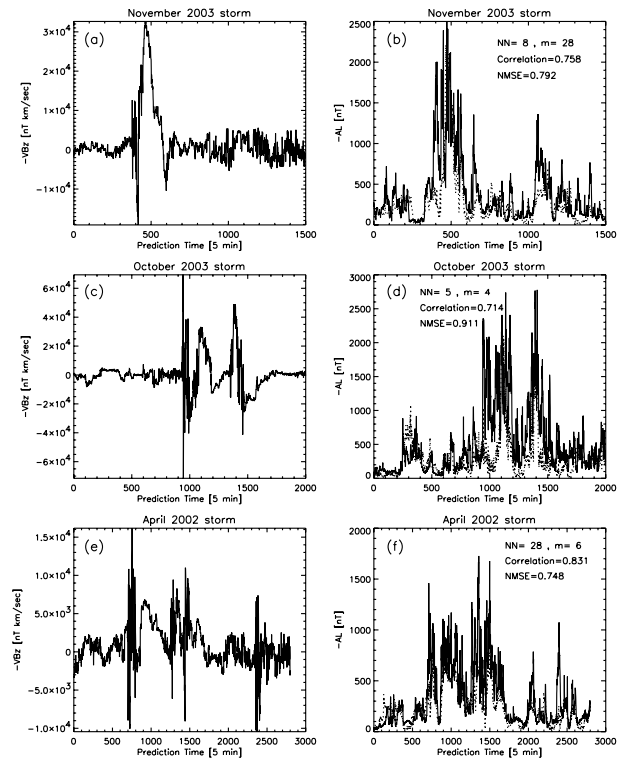


**Fig. 2.** The weighted mean-field predictions for storms: (a-b): November 19-26, 2003, (c-d): October 26-November 03, 2003, and (e-f): April 15-24, 2002. The left panel is  $VB_z$ , and the right panel is the real  $AL$  (solid line) and predicted  $AL$  (dotted line).

## 4. Modeling and Prediction during Superstorms

### 4.1. October-November 2003 and April 2002 Superstorms

The weighted mean field filter is used to model the solar wind-magnetosphere coupling during the superstorms of October-November 2003 and April 2002. In order to obtain the optimal nonlinear weighted mean field filter for superstorms, the following steps are adopted. First, the activity level of the solar wind driving is computed by averaging the southward component of  $VB_z$ . Then both the input ( $VB_z$ ) and output ( $AL$ ) of the time interval corresponding to the same activity level of the magnetospheric activity from the 2001 database are selected as the training set. For these three superstorms, the super level ( $\langle VB_s \rangle \geq 2500$  nT km/s) of the 2001 database is selected. Second, using all of the selected data interval of input ( $VB_z$ ) and its corresponding ( $AL$ ) as a training set, the index  $AL$  is predicted for the superstorms using the weighted mean filter discussed above. The normalized mean square error (NMSE) is used to determine the optimal parameters for the prediction by comparing the predicted and actual  $AL$ . In this model, the time resolution (5 min) of the training set is chosen as the time delay  $T$ , and the other three free parameters are used to minimize the NMSE. The first two parameters are the embedding dimensions  $M_I$  and  $M_O$ , and as in the previous studies, we take  $m = M_I = M_O$ , which determines the vector length in the phase space to be  $2m$ . The third parameter is the number of nearest neighbors  $NN$ . A wide range of values of these parameters are used in the model to obtain the optimal predictions and these are shown in Figure 2. The solar wind convective electric field ( $-VB_z$ ) for these events are shown on Figure 2a, 2c and 2e. There is a sudden enhancement of the solar wind convective electric field in the early part of these events and this drives the geospace storms. The predicted and real  $AL$  are plotted in the panels (b), (d) and (f) of Figure 2. The solid lines represent the real  $AL$  and the dotted lines represent the predicted  $AL$ . Iterative predictions of the November 2003 storm were carried out for 7500 minutes (125 hours) with a minimum NMSE of 0.792 and the maximum correlation coefficient of 0.758. Also for the predictions of the October 2003 and April 2002 storms, yielded a minimum NMSE of 0.911 and 0.748, a maximum correlation coefficient of 0.714 and 0.831, respectively. In these figures the model output closely reproduces the large-scale variations of  $AL$  and captures some of the most abrupt changes. Also preceding the  $AL$  minima, there are sharp jumps, corresponding to the abrupt enhancements of the northward IMF. However, the southward IMF is the main driver of the geomagnetic storms, and it is not clear how well the model captures the effects of positive IMF enhancements.

In the earlier studies using the BBMH dataset [12] [13] [18], a major part of the dataset was used as the training set and the predictions were made for the remainder of the dataset. Consequently there were many similar states in the phase space. However for the two superstorms of 2003, it is hard to find so many similar big substorms in the available databases, such as that of year 2001. The nearest neighbor searches in these cases yields only a few states close to the superstorms. If we use a large number of nearest neighbors and a simple arithmetic averaging, the output of the model is smoothed over these and

cannot capture the peak of the substorms. In such cases the weight factor  $g$  plays an important role and the averaging procedure yields improved predictions.

### 4.2. Comparison of Predictions using Bargatze [3] and Year 2001 databases

In order to compare the predictions using different databases as the training set, the storms of November 2003 are predicted using the BBMH database. To highlight the differences clearly, the periods of quiet and low activity before and after the main phase of the storms are neglected. The results of the storm of November 2003 are shown in Figure 3(a). It is clear that the peaks of  $AL$  cannot be predicted, mainly due to the absence of similar strong substorms in the BBMH database. The overall predictions have an NMSE of 0.847 and a correlation coefficient of 0.772. The predictions of for the same period using the year 2001 database and the combined database of year 2001 and BBMH are shown on Figure 3(b) and 3(c), respectively. A comparison of these predictions, Figure 3(a)-(c), shows the substantial improvement with the inclusion of the year 2001 database, either as the complete training set or as a part of a bigger training set. This is clearly due to the presence of many events in the year 2001 database similar to those in the November 2003 storm. In order to compare the predictability for different segments of the database, the November 2003 event was separated into smaller segments of 250 min or 50 data points each. The comparisons of the NMSE for the different segments are shown in Figure 3(d). It is clear that the NMSE for the data segments with large values of  $AL$  in the 2001 dataset are much smaller than those of the similar segments in the BBMH dataset.

The predictions and the NMSE for the storm of April 2002, a weaker storm compared to the November 2003 storm, are shown in Figure 4(a)-(c). The predictions are found to be almost the same when the three databases, viz. BBMH, year 2001, and the two combined, are used as the training sets. Also the NMSE values for 250 min intervals are shown in Figure 4 (d), and that NMSE have similar values in most of the segments.

In the case of the April 2002 storm, all the NMSE values obtained using different databases are similar, indicating that the BBMH and the 2001 databases yield similar predictions. However the 2001 database is a better choice for the October-November 2003 storms, as the comparisons in Figures 3 and 4 indicate. The remaining quieter periods of the October-November 2003 and the whole of April 2002 storms can be predicted very well using both the BBMH and Year 2001 databases as the training sets.

The analysis of the storms with different intensities and using different databases indicates that the geomagnetic response during the solar minimum and solar maximum periods have similar predictability. The 2001 and BBMH databases can thus be considered to complement each other. The combination of these two databases under different solar activities provides a comprehensive database for improved modeling and prediction of magnetospheric activity under a wide range of solar wind conditions.

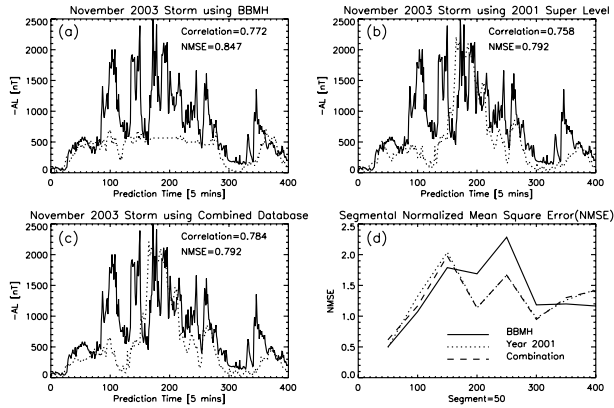


**Fig. 3.** The weighted mean field predictions on November 2003 storm using the BBMH, Year 2001 and combined databases. The solid line is real  $AL$  data, dotted line is predicted results. (a) BBMH database (b) Year 2001 database (c) Combined database (d) NMSE for 250-minute segments, the solid line represent BBMH database, dotted line represent Year 2001 database, dashed line represent combined database.

### 4.3. Spatial Structure of the High Latitude Magnetic Perturbations

The latitudinal chain of the magnetometers samples the spatial structure as the Earth rotates. So a full 2D dynamical model, driven by solar wind, of the spatial structure of the magnetic perturbations can be constructed. From such a 2D model, with a proper simultaneous solar wind selection, the localized solar wind-magnetic perturbation model can be established, and the prediction of locally region, instead of global indices, can be estimated.

The ground magnetic perturbations from 26 IMAGE and 13 CANOPUS are used to construct the 2D mapping during the April 2002 storm time. All of the station measurements are partitioned in a 2D grid that contains 24 hourly bins in magnetic local time and 26 or 13 bins, corresponding to the ground stations in IMAGE or CANOPUS array. Because of the simultaneous measurement of each magnetometer with same local time and different latitude, the high latitude magnetic perturbation can be seen on the average mapping both in magnetic latitude and local time as:

$$\langle H(\lambda, \xi) \rangle = \frac{1}{N} \sum_{i=1}^N H(\lambda, t_i) \quad (8)$$

for  $H_x$  and  $H_y$  as shown at Figure 5 and Figure 6. Because the  $H_x$  and  $H_y$  are related to the east-west and south-north components of the current system. The Fig 5(a) and Fig 6(a) show a clear pattern of the westward and eastward currents during April 17-21, 2002, corresponding to the negative  $H_x$  in the midnight sectors and positive  $H_y$  in the noon sectors.

The basic structures of the high latitude magnetic perturbation are shown on these 2D averaged locally measurements. We are interested in the study this spatial dynamical system by considering the proper spatially dependent time delay between the onset solar wind and response of the magnetosphere response on different location.

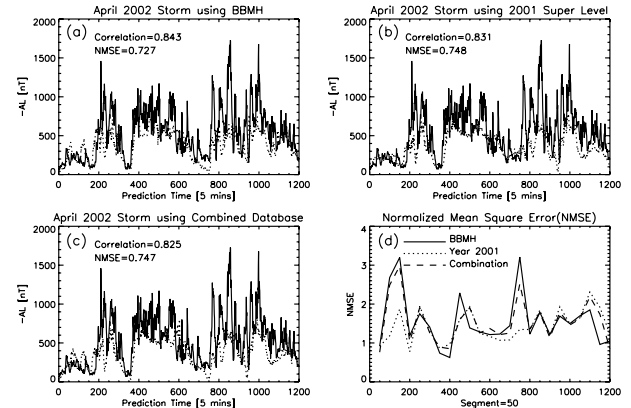


**Fig. 4.** The weighted mean field predictions on April 2002 storm using the BBMH, Year 2001 and Combined databases. The solid line is real  $AL$  data, dotted line is predicted results. (a) BBMH database (b) Year 2001 database (c) Combined database (d) NMSE for 250-minute segments, solid line represent BBMH database, dotted line represent Year 2001 database, dashed line represent combined database.

## 5. Conclusion

The modeling of magnetospheric response to strong driving by the solar wind is important not only for a better understanding of the solar wind - magnetosphere coupling and but also for developing our capability to forecast extreme conditions. During the last solar maximum there were many intense geospace storms and the existing models had limited success in forecasting these accurately. In order to develop better models and improve forecasting capability, a correlated database of the solar wind and the magnetospheric response is compiled for the year 2001 during the peak of the last solar cycle. In this database, the solar wind variable is the induced electric field and the magnetospheric response is the auroral electrojet index  $AL$ . This database is particularly well-suited for modeling using the phase space reconstruction techniques. The mean field approach to the modeling of the global magnetospheric dynamics [12] [13] is used to develop nonlinear dynamical models of the magnetospheric response from the year 2001 database. These predictions are then compared with the models based on the Bargatze [3] database, corresponding to a solar minimum period (1973 - 1974). The predictions for the big storms of October and November 2003 and April 2002 yields improved forecasts, especially for the intense storms.

The mean field approach has the advantage of yielding iterative predictions without having to fix model parameters, in particular the number of nearest neighbors  $NN$  and the dimension of the embedding space  $m$  [12] [13]. However during intense storms the number of similar events is usually small and this limits the ability to predict big events. In order to improve the predictability in such situations the mean field approach is modified by assigning weights to each of the nearest neighbors. These weights are inversely proportional to the square of the distance and leads to improvements in the predictions. The forecasting capability of the model is quantified in terms of a normalized mean square error (NMSE) computed from the predicted and actual  $AL$  values.

The two dimensional high latitude magnetic field perturb-

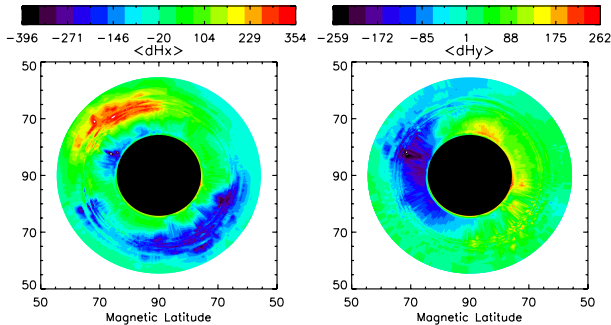


**Fig. 5.** The average value of  $H_x$  and  $H_y$  components measured by IMAGE in both magnetic latitude and local time over April 17-21, 2002.

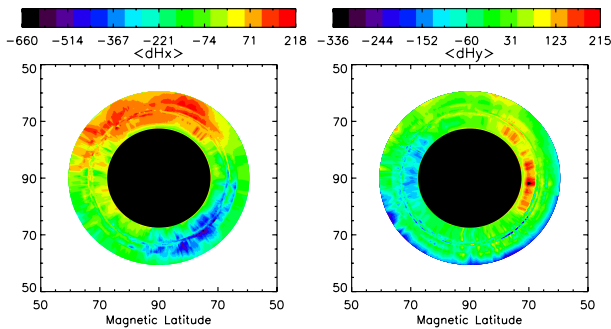


**Fig. 6.** The average value of  $H_x$  and  $H_y$  components measured by CANOPUS in both magnetic latitude and local time over April 17-21, 2002.

ations show the current structure of the magnetosphere. The solar wind driven model for these spatial variations can be derived from measurements of ground magnetometer chains after consider the proper time delay between the solar wind onset and proper magnetosphere response locations. With this model, we can study the spatial evolution of the current system as observed by multiple ground stations, and use it as a space weather forecasting tool.

**Acknowledgments:** We thank R. M. Skoug for the solar wind SWEPAM data and G. Lu for the  $AL$  data, and both for many fruitful discussions. We thank IMAGE and CANOPUS providing the data of ground magnetometers. The research is supported by NSF grants ATM-0318629 and DMS-0417800.

## References

1. Abarbanel, H. D., R. Brown, J. J. Sidorowich and L. S. Tsimring(1993), The analysis of observed chaotic data in physical systems, *Rev. Mod. Phys.*, *65*, 1331.
2. Baker, D. N., A. J. Klimas, R. L. McPherron and J. Buchner, The evolution from weak to strong geomagnetic activity: An interpretation in terms of deterministic chaos, *Geophys. Res. Lett.*, *17*, 41,1990
3. Bargatze, L. F., D. N. Baker, R. L. McPherron and E. W. Hones, Magnetospheric Impulse Response for Many Levels of Geomagnetic Activity, *J. Geophys. Res.*, *90*, 6387, 1985
4. Chen, J., A. S. Sharma, Modeling and prediction of the magnetospheric dynamics during intense geospace storms. *J. Geophys. Res.*, *111*, A04209,2006. doi: 10.1029/2005JA011359.
5. Gershenfeld, N. A. and A. S. Weigend, The future of time series: Learning and understanding: in *Time Series Prediction: Forecasting the future and Understanding the Past*, Santa Fe Inst. Stud. In the Sci. of Complexity, vol. XV, edited by A. S. Weigend and N. A. Gershenfeld, pp. 1-70, Addison-Wesley, Reading, Mass., 1993
6. Shan, L. H., P. Hansen, C. K. Goertz and R. A. Smith, Chaotic appearance of the AE index, *Geophys. Res. Lett.*, *18*,147,1991a
7. Shan, L. H., C. K. Goertz and R. A. Smith, On the embedding-dimension analysis of AE and AL time series, *Geophys. Res. Lett.*, *18*, 1647, 1991b
8. Sharma, A. S., D. Vassiliadis and K. Papadopoulos, Reconstruction of low-dimensional magnetospheric dynamics by singular spectrum analysis, *Geophys. Res. Lett.*, *20*, 335, 1993.
9. Sharma, A. S., Assessing the magnetosphere's nonlinear behavior: Its dimensional is low, its predictability is high, *Rev. Geophys. Supple.*, *33*, 645, 1995
10. Sharma, A. S., Nonlinear Dynamical Studies of Global Magnetospheric Dynamics, in *Nonlinear Wave and Chaos in Space Plasmas*, edited by T. Hada and H. Matsumoto, pp.359-389, chap.11, Terra Sci., Tokyo. 1997
11. Strogatz, S. H., *Nonlinear Dynamics and Chaos. With Applications to Physics, Biology, Chemistry, and Engineering*, Westview, Cambridge, Mass. 2000
12. Ukhorskiy, A. Y., M. I. Sitnov, A. S. Sharma and K. Papadopoulos, Global and multiscale aspects of magnetospheric dynamics in local-linear filters, *J. Geophys. Res.*, *107*, (A11), 1369, 2002, doi:10.1029/2001JA009160.
13. Ukhorskiy, A. Y., M. I. Sitnov, A. S. Sharma and K. Papadopoulos, Global and multi-scale features of solar wind - magnetosphere coupling: From modeling to forecasting, *Geophys. Res. Lett.*, *31*, L08802, 2004 doi:10.1029/2003GL018932
14. Valdivia, J. A., A. S. Sharma and K. Papadopoulos, Prediction of magnetic storms by nonlinear models, *Geophys. Res. Lett.*, *23*, 21, 2899, 1996
15. Valdivia, J. A., Vassiliadis, D., A. Klimas, A. S. Sharma and K. Papadopoulos, Spatiotemporal activity of magnetic storms. *J. Geophys. Res.*, *104*, 12,239, 1999a
16. Valdivia, J. A., D. Vassiliadis, A. Klimas and A. S. Sharma, Modeling the spatial structure of the high latitude magnetic perturbations and the related current systems. *Physics of Plasma*, Vol.6, No.11 pp.4185-4193, 1999b
17. Vassiliadis, D. V., A. S. Sharma, T. E. Eastman, and K. Papadopoulos, Low Dimensional chaos in magnetospheric activity from AE time series, *Geophys. Res. Lett.*, *17*, 1841, 1990
18. Vassiliadis, D. V., A. J. Klimas, D. N. Baker and D. A. Roberts, A description of the solar wind-magnetosphere coupling based on nonlinear filters, *J. Geophys. Res.*, *100*, 3495,1995.

# Interpretation of automated forward modeling parameters for sawtooth events and substorms

M. Connors, R. L. McPherron, and C. R. Clauer

**Abstract:** Automated Forward Modeling (AFM) is an inversion technique based on magnetic data alone, which can indicate physical parameters associated with electrojets. From perturbations along a meridian, the total electric current crossing the meridian may be determined, as well as the latitudes between which it flowed. The technique is based on nonlinear optimization of the parameters of a forward model. It is possible to compare model output to the original input to ensure that the routine has functioned well and that output parameters are reliable and presumably have physical meaning. Characteristic behaviors of substorms are readily seen in modeling output: the current strengthens rapidly and considerably at an expansive phase onset, following a growth phase during which the electrojet borders move equatorward, usually with some strengthening of current. At onset the poleward border is often seen to move poleward rapidly. Poleward border activity may be noted then and also at other times. After an onset, the recovery phase is often marked by a retreat of the equatorward border, indicating the well-known shrinkage of the auroral oval then. These complete cycles of activity are absent in sawtooth events. Our output parameters can be diagnostic of onsets and useful in determining their location and role in sawtooth events. These have many of the characteristics of expansive phase onsets, but maximum poleward expansion of the poleward border is followed by equatorward movement reminiscent of a growth phase. Since this is correlated with the interplanetary magnetic field remaining southward, the difference from common expansive phase phenomenology may simply be the lack of a recovery phase.

*Key words:* Sawtooth Events, Substorms, Inversion Techniques.

## 1. Introduction

The complete cycles of growth phase, expansive phase, and recovery typical of substorms are absent in sawtooth events. They show many of the characteristics of growth and expansive phases, but maximum poleward expansion of the poleward border is often immediately followed by equatorward movement reminiscent of a growth phase. We do not directly consider interplanetary magnetic field in this work, but it has been noted that sawtooth behavior is often correlated with a persistent IMF southward condition. The difference between sawtooth behavior and common expansive phase phenomenology may simply be the lack of a recovery phase due to continued forcing. Our work in modeling sawtooth events suggests many similarities to substorms. The most notable difference is that the currents across the active meridian (usually near midnight) are rather intense compared to those of typical substorms.

## 2. Automated Forward Modeling (AFM)

Interpretation of ground magnetic data is difficult, even if the data come from the same magnetic meridian. Examples of magnetic data from many locations are common in the literature, or one may examine the solid lines in Fig. 5 or Fig. 7. In those figures the X (northward) and Z (downward) com-

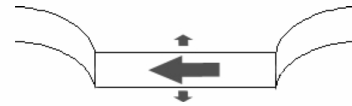


**Fig. 1.** By varying the current (large horizontal arrow) and latitudinal boundaries (small vertical arrows) an optimal match of model results and data can be made and these physical parameters determined. Field-aligned currents may be included (as shown at ends of ionospheric current flow region).

ponents of the magnetic field are shown from the six stations on the Canadian Churchill meridian most relevant to studying auroral zone currents. Automated Forward Modeling proposes a forward model of current systems which could give rise to the magnetic perturbations observed. The parameters in that model are varied in such a way that the deviation between the observed magnetic fields and those predicted by the model are reduced. In the ideal case, the parameters can be chosen to correspond to simple physical parameters associated with the current system. A forward model can be made using the Biot-Savart law in combination with Earth induction, by specifying where currents flow in space and the ionosphere [6] [7]. Adjustment of the parameters specifying the current system can be done until the match to the input data is optimal. In principle, arbitrarily complex current systems may be described in three dimensions in near-Earth space and their parameters determined. In practice, available magnetic data is sparse and well-determined solutions can be difficult to obtain.

The optimum situation can be found when data from me-

Received 20 May 2006.

**M. Connors.** Centre for Science, Athabasca University, Athabasca AB, Canada T9S 3A3

**R. L. McPherron.** Institute for Geophysics and Planetary Physics, University of California, Los Angeles, USA

**C. R. Clauer.** Space Physics Research Laboratory, University of Michigan, Ann Arbor, Michigan, USA

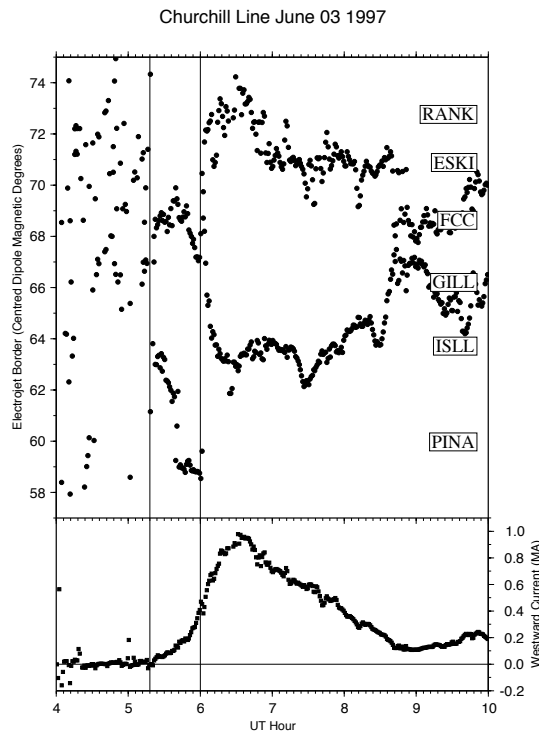


**Fig. 2.** Growth phase and onset of a substorm on June 3 1997. Upper panel shows the electrojet north and south boundaries as it traversed the Churchill meridian. Bottom panel shows total current across the meridian. The growth phase is clear. Subsequent substorm onset is somewhat unusual in being well poleward of the region of growth phase currents. However in general this event is illustrative of the strength of a typical substorm.

ridian chains is available, since in many cases a simple model involving an electrojet flowing across the meridian chain is physically realistic, and in this case there is a good ratio of data available to parameters to be determined. From meridian chain data a forward modeling procedure can give the current across the meridian and the latitudes between which it flowed. In this way the many data points specifying the magnetic perturbations along a meridian can be reduced to three simple parameters, which have an easily understood physical significance. For efficient processing of large amounts of magnetic data, the matching process can be automated. In the Automated Forward Modeling (AFM) procedure this is done using the Levenberg-Marquardt algorithm [9]. A schematic of the variables involved and the way in which they are varied is shown in Fig. 1. Detailed descriptions of the AFM procedure are given elsewhere [4] [5].

### 3. Substorms

AFM has been applied on the CANOPUS Churchill meridian ( $336^\circ$  mag.; station latitudes shown on graph) to invert the whole year of 1997. We do not show the input data, but output initially chosen as to show growth, expansion, and some degree of recovery is shown in Fig. 2. This event from June 3 1997 does show some atypical features deserving followup,

but a strong growth phase is visible from 5.3 UT to 6.0 UT (between vertical bars). The onset at 6.0 is mainly marked by a poleward leap of the current, which subsequently strengthens over about one half hour to 1 MA. This is at the upper end of what is typical of a substorm: currents usually are below 1 MA, and the latitudinal range expands rapidly to over  $10^\circ$ , with rapid poleward motion of the poleward border just after onset. The overall time scale for substorm-associated enhanced currents is of order one hour.

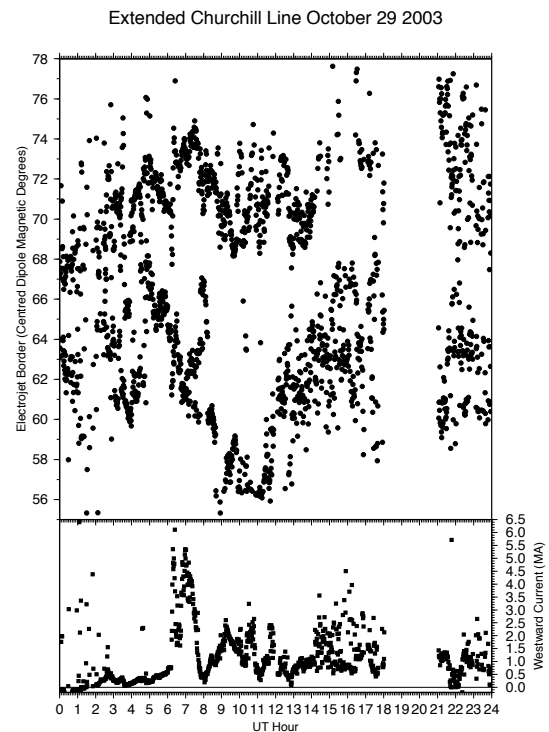


**Fig. 3.** Superstorm activity on October 29 2003. Upper panel shows the electrojet north and south boundaries as it traversed the extended Churchill meridian. Bottom panel shows total current across the meridian.

### 4. Superstorm Onset

The "Hallowe'en storm" of October 2003 featured currents on Oct 29, 2003, which can be regarded as being at the upper limit of those associated with substorm activity. The electrojets extended to rather low latitude, so that data had to be used from an extended Churchill line featuring Cambridge MN (X only), Boulder, and Tucson. Accurate modeling down to  $40^\circ$  magnetic latitude was done as shown in Fig. 3. A recognizable growth phase took place starting at about 5 UT. This is seen through the steady equatorward motion of the electrojet boundaries (upper panel) by about 3 degrees until about 6:15 UT. At that time, following a possible large impulsive current, the current rose steadily and the electrojet poleward border moved rapidly poleward. By 7 UT, the electrojet was about  $15^\circ$  wide with nearly 6 MA of current. Other aspects of the onset are like those of substorms, so this may be regarded as a very large

substorm onset. This large current may be used for comparison with that during sawtooth events.

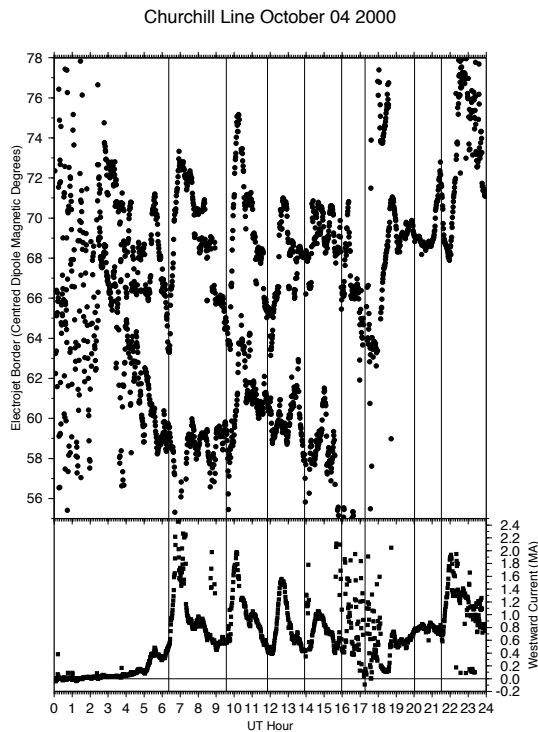


**Fig. 4.** Sawtooth event of October 4 2000. Upper panel shows the electrojet north and south boundaries as it traversed the Churchill meridian. Bottom panel shows total current across the meridian. Vertical lines are onset times deduced from Pi 2 pulsations.

## 5. Sawtooth Events

The typical signature of sawtooth events as seen in ground magnetic signatures is recurrent X bays initiated rapidly, like substorms.

### 5.1. October 4, 2000 Sawtooth Event

Fig. 5 shows sawtooth bays as the lower trace in each panel for the sawtooth event of October 4, 2000. The bays are present in various sizes at the different stations in this data from the Churchill meridian. Although the sawtooth nature is evident, examination of the data does not make it very clear what actually took place in terms of physical parameters. From satellite observations of energetic particle injections or ground observations of Pi 2 pulsations, onset times were determined for this event. Those times are indicated by vertical lines. Fig. 4 shows the results of AFM inversion of the data presented in Fig. 5. At times between 3 and 16 UT the scatter in the inversion results is minimal and they can be considered reliable. The onset times determined by other methods are again indicated; at these times the current strengthens rapidly and the poleward border moves rapidly poleward, features typical of substorm onset. Preceding each such onset during the period of reliable

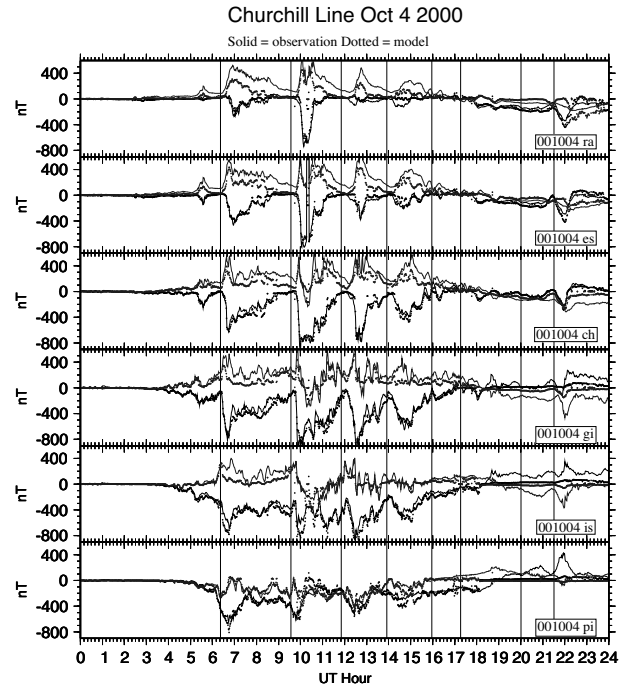


**Fig. 5.** Sawtooth event of October 4 2000. Comparison of observed (solid) and model, with X black and Z gray (X generally the lower trace, Z generally upper). Vertical lines are onset times deduced from Pi 2 pulsations.

inversion, there is a growth phase with steady equatorward motion of the electrojet borders. Rise times for current are similar to those for substorms, and the repetition period is usually similar to that for the rise and decline of substorm total current. However, the total current across a meridian is generally larger for sawtooth events than for substorms, in this case up to 2.5 MA. It may be noted that even during the growth phase analogs, currents were at levels of approximately 0.5 MA, that is, stronger than in many typical substorm expansive phases.

Further examination of Fig. 5 shows the degree to which the AFM modeling has succeeded in representing the data from the six magnetic stations by three simple parameters. The X (generally lower) component data is shown by a solid line, while the X resulting from the model is shown by discrete points. At times from 0 UT to 18 UT the two agree very well. Some care has to be taken in interpreting this agreement when the perturbations are near zero. At such times the geometric parameters may not be well determined simply since there is basically no current upon which to base an inversion. Generally, as indicated above, when this happens there will be large scatter in the electrojet border parameters. However, between 3 and 16 UT both the match to X data and the lack of scatter suggest an excellent model fit. The Z component is also plotted (generally the upper trace). Here the fit is generally very good but not quite as excellent as that for X. This is attributed to the more rapid variation in Z when a station is near a current source in the ionosphere. Z can reflect structure in the electrojet which is not present in the simple model and thus is harder to match than is X.

### 5.2. February 18, 1999 Sawtooth Event

Much as with the previous pair of figures, Fig. 6 and Fig. 7 present modeling results and comparison to data, in this case for the sawtooth event of February 18, 1999. This event was recently discussed in detail using magnetic and other sources of data [3] [8]. Once more it is generally clear when the results were valid, and the match to data was good for a large part of the UT day and of the event. The substorm-like pattern of expansive phase current intensification and poleward motion of the poleward border is clear, and in most cases a clear growth phase is seen. Expansive phase analog currents of up to about 3.5 MA were present, and the growth phase portions had currents averaging 1 MA, stronger than those of most substorm expansive phases. Once more the comparison of data and model output is very good, suggesting that the physical parameters derived are realistic.

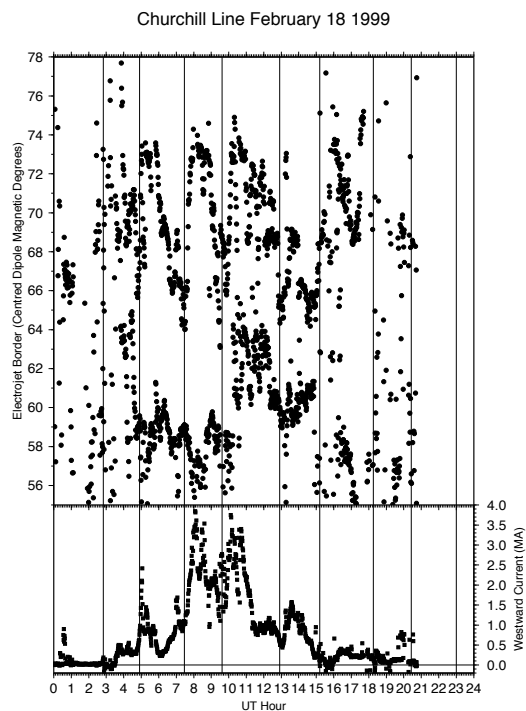


**Fig. 6.** Sawtooth event of February 18, 1999. Upper panel shows the electrojet north and south boundaries as it traversed the Churchill meridian. Bottom panel shows total current across the meridian. Vertical lines are onset times deduced from Pi 2 pulsations.

### 5.3. November 8, 2004: Sawtooth Event with Optical Data

Ground optical data was not available for the events described above. For an event on November 8, 2004, however, two meridian scanning photometers in the Churchill meridian were operative under clear skies. These instruments are located at the southern end of the chain at Pinawa and near the middle of the auroral zone at Gillam. The instrument further north at Rankin Inlet was not returning data on this date. The relative locations of these stations may be seen in the right hand part

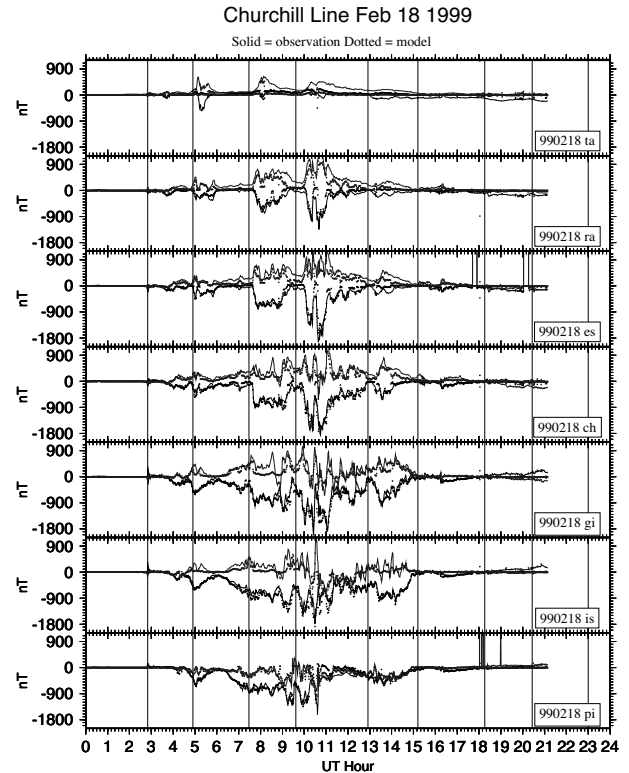


**Fig. 7.** Sawtooth event of February 18, 1999. Comparison of observed (solid) and model, with X black and Z gray (X generally the lower trace, Z generally upper). Vertical lines are onset times deduced from Pi 2 pulsations.

of Fig. 2, and their dipole magnetic coordinates read from the latitude scale. The meridian scan data from Pinawa and Gillam may be stacked timewise (each scan lasts 2 minutes) and placed one station above the other to cover approximately 1000 km along the meridian. Such keogram data is shown in Fig. 8 for comparison with magnetic inversion results. The latter must be regarded as preliminary since only Canadian data was used. Since the electrojets clearly extended rather far south, well beyond the  $60^\circ$  dipole magnetic latitude of Pinawa, there was no good constraint at the southern border. In this sense the predominance of low latitude activity suggested by Fig. 8 is deceptive: so much so that one of the optical plots has been used to cover some of the inversion results for latitudinal borders since they are not highly significant. Nevertheless, the total currents shown correlate very well with the optical intensifications. Between 5 and 6 UT, the electrojet had extended very far north and this is borne out by the optical data. At this time the indication of 6 MA across the meridian is likely quite accurate. At other times, the overestimation of the electrojet width leads to an overestimation of the current. However, the maximal current in this event approaches very closely that of the Halloween superstorm. In both cases part of the reason for the large total current was the width of the electrojet, allowing current to be carried over approximately a  $20^\circ$  band of latitude. This is supported in this sawtooth example by the optical data showing bright aurora extending past the horizons of both meridian scanning photometers.

## 6. Conclusions

Very wide electrojets and large currents are a consistent feature of the sawtooth events studied, as indicated by modeling giving good agreement with station data across the Churchill meridian, and in the last case supported by optical data. Independent studies of related parameters have recently shown that the degree of dipolarization observed at geosynchronous orbit is larger for sawtooth events than for substorms in a statistically significant way [1]. Further, cross polar cap potential is larger [2]. These results are also consistent with our finding of very large currents across the modeling meridian. Our studies use local magnetic perturbations in the auroral zone (extended equatorward as needed and possible) and largely correspond to the effects of Hall currents in the local ionosphere. Studies including low-latitude perturbations conclude that the three-dimensional current system in a sawtooth event is likely similar to the of the three-dimensional substorm current wedge (SCW) usually associated with substorm onsets [8] but with a larger longitudinal extent than is typical of such onsets [8] [3]. We note that AFM can be used in to model SCW systems in a natural way, and could in principle answer some of the questions about the low-latitude perturbations, such as unusual D/H perturbation ratios, which arose from these recent studies.

## 7. Acknowledgements

Magnetic data from the Canopus/CARISMA project, funded by the Canadian Space Agency, has been used. Some USGS data has been used when lower latitudes were modelled. The work has been supported by NSERC and the Canada Research Chairs programme.

## References

1. X. Cai, M. G. Henderson, and C. R. Clauer, A statistical study of magnetic dipolarization for sawtooth events and isolated substorms at geosynchronous orbit with GOES data, submitted to *Annales Geophysicae*, 2006.
2. X. Cai, C. R. Clauer, and A. J. Ridley, Statistical analysis of ionospheric potential patterns for isolated substorms and sawtooth events, submitted to *Annales Geophysicae*, 2006.
3. C. R. Clauer, X. Cai, D. Welling, A. DeJong, and M. G. Henderson, Characterizing the 18 April 2002 Storm-time Sawtooth Events using Ground Magnetic Data, *J. Geophys. Res.*, *111*, A04S90, 2006.
4. M. Connors, Auroral Current Systems Studied Using Automated Forward Modelling Ph.D. Thesis, Department of Physics, University of Alberta, 410 pp., 1998.
5. M. Connors and G. Rostoker, A Substorm Sequence Studied with Automated Forward Modeling, in Sixth International Conference on Substorms (ISBN 0-9711740-3-2), R. Winglee, ed., University of Washington Press, Seattle, 490-495, 2002.
6. J. L. Kisabeth and G. Rostoker, Modeling of the three-dimensional current systems associated with magnetospheric substorms, *Geophys. J. R. astr. Soc.* *49*, 655-683, 1977.
7. J. L. Kisabeth, On Calculating Magnetic and Vector Potential Fields due to Large-Scale Magnetospheric Current Systems and Induced Currents in an Infinitely Conducting Earth, in Quantitative Modeling of Magnetospheric Processes, edited by W. P.

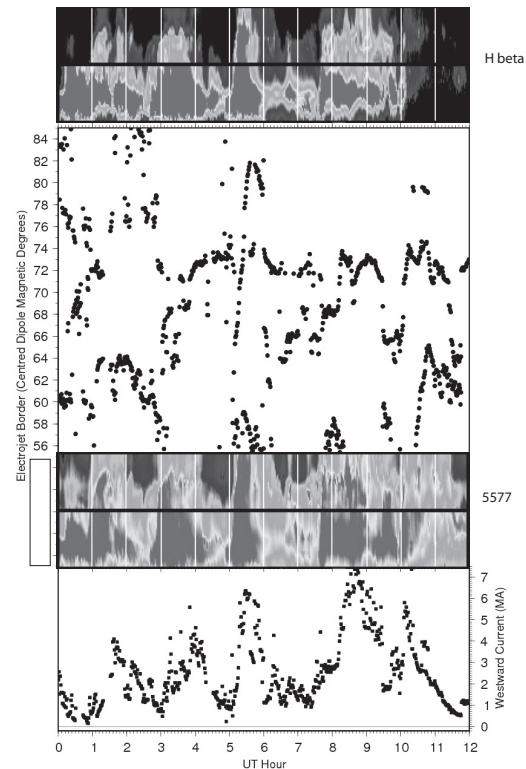


**Fig. 8.** Sawtooth event of November 8, 2004. Upper middle panel shows the electrojet north and south boundaries as it traversed the Churchill meridian. Bottom panel shows total current across the meridian. Meridian scanning photometer from Pinawa and Gillam superposed, 557.7 nm green line in lower middle, H beta emission at top. The color scale maximizes at red, which is 15 kR for 557.7, 70 R for H beta.

Olson, American Geophysical Union, Washington, pp. 473-498, 1979.

8. K. Kitamura, H. Kawano, S. Ohtani, A. Yoshikawa, and K. Yumoto (2005), Local-time distribution of low and middle latitude ground magnetic disturbances at sawtooth injections of April 1819, 2002, *J. Geophys. Res.*, *110*, A07208, 2005.
9. W. H. Press, S. A. Teukolsky, W. T. Vetterling, and B. P. Flannery, *Numerical Recipes in C*, Second Edition, Cambridge University Press, Cambridge, 1992.



# Forced current sheets in a flapping magnetotail

C. M. Cully, R. E. Ergun, E. Lucek, A. Eriksson, D. N. Baker, and C. Mouikis

**Abstract:** In the late growth phase, a thin current sheet often forms in the magnetotail, with a scale size comparable to the thermal ion gyroradius. This thin current sheet is typically embedded within a much thicker plasma sheet, and often precedes substorm onset. In that sense, it is the initial condition for reconnection or current disruption. A number of models have been developed to explain the equilibrium kinetic solution of such a current sheet. One popular model is the forced current sheet. In this one-dimensional solution, the current is supported by the pressure anisotropy seen in a rapidly translating deHoffmann-Teller frame. In this paper, we search for forced current sheets in the Cluster data from 2001 (at  $\sim 19 R_E$  apogee). First, we develop a forced current sheet model using typical parameters for the magnetotail, including flapping motion. Using this model, we identify the observational characteristics of forced current sheets, concentrating on the DC electric field. We then search for these features in the Cluster data from 2001. Despite searching through more than 100 encounters with stable current sheets, we were unable to find a suitable example. We conclude that the relative velocity between the satellites and the deHoffmann-Teller frame is low, except in extremely dynamic situations. Consequently, forced current sheet models with anisotropy supplied by the deHoffmann-Teller translation are not widely applicable to the stable magnetotail at  $\sim 19 R_E$ .

*Key words:* Substorms, magnetotail structure, forced current sheets.

## 1. Introduction

In the past decades, increasingly sophisticated kinetic simulations have been brought to bear on the fundamental processes driving substorms. The impact of these codes has been substantial; for example, the “GEM reconnection challenge” [2] has shaped the way many authors view reconnection. Nonetheless, the utility of these simulations depends on finding the correct initial and boundary conditions.

Some simulations are relatively insensitive to the initial conditions. For example, the GEM challenge imposes a rather extreme perturbation at the boundary, which forces the reconnection to develop in a manner relatively insensitive to the initial conditions. The reasoning is that these simulations focus on the basic plasma physics, and the development from initial conditions is not of interest.

The magnetosphere probably doesn’t supply such radical boundary conditions, and the processes that occur within are thus more influenced by initial conditions. Several authors have noted that the magnetotail exhibits hysteresis [15,26], which is a dramatic example of sensitivity to initial conditions. We feel that it is important to understand the stable equilibrium of the magnetotail.

Most simulations use a Harris model [10] for the initial condition. While simple and attractive, the Harris model is one dimensional and does not include the observed normal component of the magnetic field ( $B_z$ ). Some authors simply add a constant normal component to construct a field geometry more

consistent with observations. However, the magnetic tension force in the resulting configuration is unbalanced, resulting in a non-equilibrium state.

More complicated equilibrium solutions do exist. One major class of equilibrium solutions assumes an isotropic distribution, and allows the plasma parameters to vary across field lines [13, 18, 21, 22]. In this paper, we will not focus on these 2-dimensional models.

A second major class of solutions assumes anisotropic distributions ( $P_{\parallel} > P_{\perp}$ ) at the model boundaries [6–8, 12, 25, 28]. Known as forced current sheet models, this class of solutions is entirely one-dimensional. In this paper, we try to better understand the applicability of forced current sheets at Cluster apogee ( $\sim 19 R_E$ ).

Our first task is to extend some of the numerical simulations of forced current sheets [6]. One of the key discoveries of the Cluster mission is extensive spatial structure in the  $\pm y$  direction, often seen as even-parity (kink-type) oscillations [20, 23]. Indeed, since this flapping is what usually causes the satellites to pass through the current sheet, the vast majority of observations occur during intervals of flapping. Consequently, the particular extension we are interested in is this: what happens to a forced current sheet if wave structure develops in the current-carrying ( $\pm y$ ) direction?

After developing the model, we are in a position to assess how much forcing is required to drive these models in realistic circumstances (i.e. how large of an electric field). We then use this knowledge to search for an example of a forced current sheet in the Cluster data from 2001.

The first section of this paper is a review of the basics of forced current sheet models. The second section extends the models to situations with kink-type structure in the  $y$  direction, and quantifies how much forcing is required. After a brief comparison of the required forcing to previously-published average conditions, we then describe a search for these conditions using Cluster data from 2001. The results of the search are negative: we were unable to find an example of a forced current sheet.

Received 5 June 2006.

**C. M. Cully, R. E. Ergun, and D. N. Baker.** Laboratory for Atmospheric and Space Physics, University of Colorado, Boulder, USA.

**E. Lucek.** Space and Atmospheric Physics Group, Imperial College, London, UK.

**A. Eriksson.** Swedish Institute of Space Physics, Uppsala, Sweden.

**C. Mouikis.** Department of Physics, University of New Hampshire, USA.

## 2. Forced Current Sheets

Forced current sheets are sheet configurations in which the magnetic field is supported by an anisotropic plasma pressure. There is an extensive literature that discusses these models, from early work in the 1970's [12, 19] to recent work published in the past few months [31].

Consider a current sheet in the  $\hat{y}$  direction, with the sheet normal to  $\hat{z}$ , as sketched in Figure 1. The resulting magnetic field reverses sign at  $z = 0$ , and there is an additional constant normal component  $B_z$  (assumed positive). The sheet is connected at large values of  $z$  (both positive and negative) to a reservoir of particles. Because of the normal component  $B_z$ , particles may flow along the field lines and interact with the sheet, either crossing it to flow into the reservoir on the other side, or reflecting back to the initial reservoir.

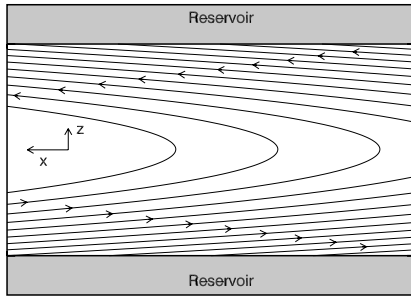


**Fig. 1.** Magnetic field configuration and coordinate system.  $\hat{y}$  is out of the page.

The essential idea for a forced current sheet is that particles in the reservoirs have a larger parallel pressure than perpendicular pressure. Their parallel velocities are initially to the right in Figure 1, and are bent back to the left by their interaction with the sheet. They consequently exert a reaction force on the sheet in the negative  $\hat{x}$  direction. Equilibrium is achieved when this force exactly balances the magnetic tension force.

The pressure anisotropy in the reservoir is generally assumed to arise from one of two conditions. Either the parallel temperature is larger than the perpendicular temperature, or the distribution flows along the field line with some parallel velocity. A combination of these two conditions is also possible. Early formulations tended to focus on the first possibility, while more recent works [6, 25, 28] focus on the second possibility: large parallel flow. The term “forced current sheet” was coined by Burkhardt et al., and applies principally to this second condition [6].

Parallel flow might at first seem to be an unlikely candidate to support a quiet-time current sheet, since satellite observations seldom show the near-Alfvénic flows required. However, the relevant frame in which to assess the pressures is the deHoffmann-Teller frame. If the normal magnetic field  $B_z$  is small, then a small convection field  $E_y$  can cause the deHoffmann-Teller frame to translate very rapidly in the  $\hat{x}$  direction. For example, a convection electric field  $E_y=1$  mV/m combined with a constant normal field  $B_z=2$  nT creates a deHoffmann-Teller frame moving at 500 km/s. Near the particle reservoirs at the edges, this motion is very nearly parallel to  $\vec{B}$ .

The maximum current that can be generated from an anisotropic distribution is given by the marginal firehose criterion [12, 19]:

$$\frac{B^2}{\mu_0} = P_{\parallel} - P_{\perp} \quad (1)$$

where both the magnetic field  $B$  and the pressures  $P_{\parallel}$  and  $P_{\perp}$  are taken at the boundary, far from the sheet. The pressures are functions of both the conditions at the reservoir (which determines the incoming half of the distribution function) and the current sheet itself (which determines the outgoing half).

In the case where the excess parallel pressure is supplied by a parallel drift  $V_D$  at the boundary, and in the limit of zero pitch angle scattering by the sheet, the marginal firehose condition reduces simply to  $V_D = V_A$ , the Alfvén speed far from the sheet. In the other limit, that of perfect isotropization by the sheet, a larger speed is required:  $V_D = \sqrt{3}V_A$  [6].

The drift speed  $V_D$  is related to the deHoffmann-Teller speed  $V_{HT}$  by the relation  $V_D = V_{HT} \cos(\theta)$ , where  $\theta$  is the (small) inclination angle of the asymptotic field  $\theta = \tan^{-1}(B_z/B_x)$  with  $B_x$  and  $B_z$  evaluated at the boundary. The drift is strictly parallel to  $\vec{B}$  in the deHoffmann-Teller frame, as required by the condition that the electric field vanish.

The marginal firehose condition is, however, only an upper bound on the possible current. Numerical simulation [6] has shown that this maximum current is attained for sufficiently thin sheets. “Sufficiently thin” in this case can be assessed using the parameter

$$\kappa = \sqrt{\frac{R_{\min}}{\rho_{\max}}} \quad (2)$$

where  $R_{\min}$  is the minimum radius of curvature of the field line and  $\rho_{\max}$  is the maximum Larmor radius of a thermal-energy ion [4]. In order to reach the marginal firehose limit,  $\kappa$  must be less than about 0.2 [6]. In this regime, the sheet is sufficiently thin that the ions execute Speiser-type orbits [29].

For values of  $\kappa$  between roughly 0.2 and 0.7, a forced current sheet still develops, but with a smaller magnetic field (closer to the lower limit  $V_D = \sqrt{3}V_A$ ). No solutions have been found for values of  $\kappa$  above 0.7. This condition marks the onset of deterministic chaos in the particle trajectories [4]. It has been proposed [6] that no equilibrium solution exists in this chaotic range  $\kappa \approx 1$ , and that a sheet that approaches this condition may suffer a catastrophic loss of equilibrium.

Assuming a small value of  $\kappa$  ( $\lesssim 0.2$ ), the quasi-adiabatic invariant

$$I_z = \frac{1}{2\pi} \oint m v_z dz \quad (3)$$

is approximately conserved [24]. An elegant analytical model [25] can be created by explicitly conserving this quantity. This extends the applicability of the forced current sheet models into the regime  $V_D \lesssim V_T$  (with  $V_T$  the thermal velocity). This regime is difficult to access with numerical studies due to poor signal-to-noise ratio. With the assumption  $\kappa \ll 1$ , the marginal firehose condition gives the appropriate field magnitude (not just an upper bound).

### 3. Numerical Investigation

The numerical model we chose is an iterative self-consistent method fundamentally similar to the one used by Burkhart et al. [5, 6]. The method treats the full motion of the ions, but treats the electrons as a charge-neutralizing fluid using a simple Boltzmann approximation. Ions are initially traced through trial electric and magnetic fields, with the resulting velocity and density moments calculated on a grid. New fields are then computed using these moments, and the particles are traced through these new fields. This process is repeated until the fields converge from one iteration to the next (or diverge – see below).

The simulation box in our study is a 256 by 256 element rectangular domain in the  $y$ - $z$  plane. We initialize ions at the top and bottom edges of the domain according to a drifting Maxwellian distribution. The drift is parallel to the magnetic field, as required in the deHoffmann-Teller frame. Particles are then traced in three dimensions through the simulation box using the non-relativistic Lorentz force equation. We use a fourth-order adaptive-stepsize Runge-Kutta integrator, and 20000 to 100000 particles per iteration.

The magnetic field on the first iteration is given by an initial guess as a hyperbolic tangent with an asymptotic field strength given by the marginal firehose condition and a constant normal component  $B_{z0}$ . On subsequent iterations, we find the magnetic field by

$$\vec{B} = \nabla \times \vec{A} + B_{z0} \hat{z} \quad (4)$$

$$\nabla^2 \vec{A} = -\mu_0 n(y, z) \vec{v}(y, z) \quad (5)$$

$$(6)$$

where  $B_{z0}$  is a constant and all other symbols have their usual meanings. Velocities and densities are computed directly from the particle distributions at each grid point. Velocities in the  $x$  direction are small, and we do not include them in the calculation of the magnetic field.

The electric field is initially set to zero. On subsequent iterations, we calculate it by

$$\vec{E} = -\nabla\phi + \vec{E}_{\text{external}} \quad (7)$$

$$\frac{e\phi(y, z)}{kT_e} = \ln\left(\frac{n(y, z)}{n_0}\right) \quad (8)$$

$$(9)$$

where  $T_e$  is the electron temperature and  $n_0$  is the average density at the top boundary. The results are relatively independent of the electron temperature, as noted previously [6].

Convergence for this method typically takes only a few iterations. It indicates the existence of a time-stationary solution, but does not guarantee stability. Some of the distribution functions encountered both in this work and in the other forced current sheet literature are clearly unstable to a variety of instabilities. Assessing this is, however, outside the scope of this article.

Divergence typically occurs for one of two reasons. First, when the drift speed is small relative to the thermal speed ( $V_D \lesssim V_T$ ), numerical noise becomes a problem. This can be remedied by simply adding more particles, and has no physical

relevance. Second, the method diverges when the  $\kappa$  parameter (equation 2) is larger than  $\sim 0.7$ . As discussed above, it seems likely that no stationary solution can exist in this chaotic range, in which case the method diverges for physically meaningful reasons [6].

We report here on two simulation runs. In the first run, we used a flat sheet with no electric field  $E_y$ , a normal component of the magnetic field  $B_{z0} = 2$  nT and a density  $n_0$  of  $0.3 \text{ cm}^{-3}$ . The thermal speed of the incoming distribution was 600 km/s (i.e. 1.9 keV), and we varied the (parallel) drift speed up to 2000 km/s. The asymptotic magnetic field far from the resulting current sheet is shown as the filled circles in Figure 2.

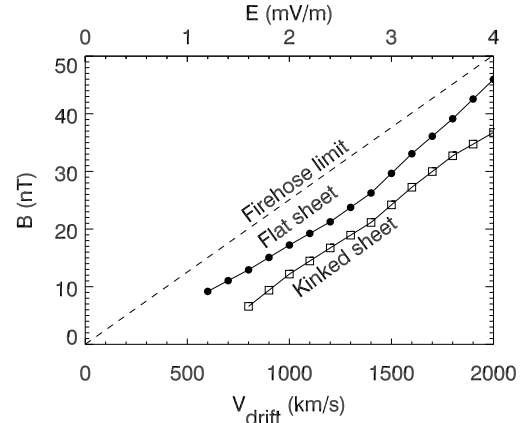


**Fig. 2.** Maximum magnetic field as a function of drift velocity  $V_D$ , for a flat sheet and a sheet with a kink-type wave. Equivalent electric fields in the 2 nT normal magnetic field are shown on the upper abscissa.

Setting the electric field to zero puts the simulations in the deHoffmann-Teller frame. An equivalent simulation was also performed in the drifting frame, with the drift velocity set to zero and the external electric field varied. The results of the two techniques are consistent.

At larger values of the drift velocity  $V_D$ , the magnetic field asymptotes to the marginal firehose limit. However, at more realistic values of  $V_D$ , the finite temperatures of both the ions and the electrons ( $T_e=400$  eV) cause the sheet to thicken. The wider sheet increases the value of  $\kappa$  enough that increased pitch angle scattering occurs, and the magnetic field is closer to the strong-scattering limit of  $1/\sqrt{3}$  times the marginal firehose limit.

The second set of simulations used the same parameters, except that we introduced an even parity (kink-type) wave structure into the sheet. The waves were supported by an electric field

$$E_y = -\omega a B_x \cos(ky) \quad (10)$$

with  $\omega$ ,  $a$  and  $k$  the wave frequency, amplitude and wavenumber respectively. This is the induced electric field

$$\nabla \times \vec{E} = -\frac{\partial B}{\partial t} \quad (11)$$

caused by a changing magnetic field

$$B_x(y, z, t) = B_x(z') \quad (12)$$

$$z' = a \sin(ky - \omega t) \quad (13)$$

in the rest frame. The introduced wave had a period of 60 seconds, an amplitude of 500 km and a wavelength of 7500 km. We implicitly assume here that a stable, non-growing kink-type mode exists. While observationally reasonable (see section 5), we cannot verify this stability with the current model.

This induced field is not curl-free, and cannot be transformed away. That is, no deHoffmann-Teller frame exists under these conditions. This isn't a problem in the simulations, since the physics is independent of the frame, and the simulation frame can be switched easily. However, since the method is time-independent, there is one restriction on the frame: it must be co-moving in  $\hat{y}$  with the wave. In the frame moving at  $\vec{c}_{\text{frame}} = (\omega/k)\hat{y}$ , an additional electric field  $\vec{E}' = \vec{c}_{\text{frame}} \times \vec{B}$  arises from the Galilean transformation. Since the solution in this co-moving frame is time-independent, the numerical method is applicable without the need to extend to the time domain.

The numerical technique converges for roughly the same range of parameters as the flat sheet. Although the familiar caveats apply regarding the stability of the solution, this means that we have found an equilibrium solution with a kink-type wave present. Figure 3 is a pair of contour plots of the converged solution for  $V_D=2000$  km/s. Shown are the density and velocity. The sheet is roughly 700 km across, with a strong density peak near the centre. Lower drift speeds result in a broader sheet (up to twice as thick) with a less-pronounced density maximum. The velocity enhancement is somewhat wider than the density enhancement. The direction of the velocity vectors closely follows the kink motion.

The asymptotic magnetic field for this simulation run is plotted using open squares in Figure 2. For the same drift speed, the structured current sheet does not support as much current. The reason for this behaviour seems to be that the kinked sheet randomizes the trajectories more than the flat sheet. This widens out the sheet (by about a factor of 2) and reduces the total current.

The goal of these numerical studies is to estimate the minimum electric field required to support a forced current sheet under realistic conditions. Referring to Figure 2, it's clear that for a typical 25 nT asymptotic field, the electric field must be at least 2 mV/m in a sheet with a density of  $0.3 \text{ cm}^{-3}$ .

#### 4. Comparison to published averages

In the satellite frame, the anisotropy required for a forced current sheet could manifest itself in three different ways. A large anisotropy in the ion distribution is one fairly obvious signature. Observationally, however, the required anisotropies are rarely observed [17, 22]. Typical observed anisotropies in the current sheet are substantially less than 10% [14]. Assuming a typical pressure of 0.2 nPa at  $20 R_E$  [14], a 10% anisotropy results in a maximum field strength of only 5 nT (using the marginal firehose condition). While certainly possible in extremely dense sheets, or under conditions of unusually large anisotropy, it seems unlikely that the temperature anisotropy could frequently support forced current sheets.

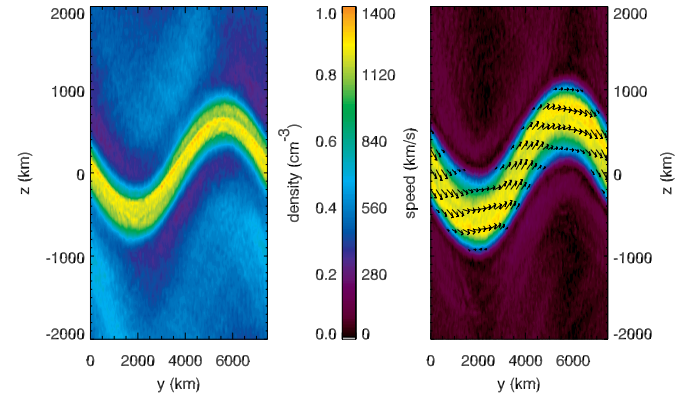


**Fig. 3.** Density (left) and speed (right) for a forced current sheet with a kink-type wave. Selected velocity vectors have been plotted in the right hand panel.

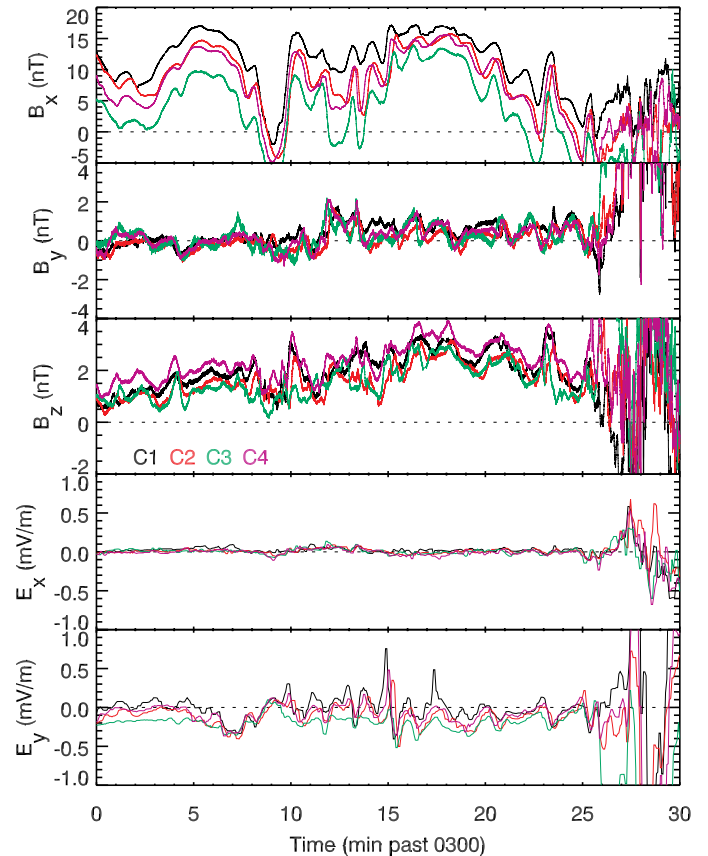


**Fig. 4.** Cluster magnetic and electric field data from 2001 October 11. Colour coding is black, red, green, magenta for Cluster satellites 1 through 4 respectively (see panel 3).

A second possibility is that the anisotropy could manifest itself as a bulk flow in the spacecraft frame. With typical bulk flows less than 50 km/s [14], this translates to no more than a few nT.

The final possibility is that the deHoffmann-Teller frame is translating rapidly with respect to the spacecraft frame. Typical electric fields are roughly 0.2 mV/m [30], which when coupled

with a normal magnetic field of some 2 nT results in a 100 km/s drift. Again using typical parameters, this yields only a  $\pm 5$  nT asymptotic magnetic field.

From the statistical observations, it seems fair to conclude that the average magnetotail is not described by a forced current sheet model. On the other hand, thin current sheets are not “statistically average” events. Indeed, large anisotropies have occasionally been observed prior to substorm onset [16]. Consequently, we decided to re-examine the observations to search for forced current sheets.

## 5. Case study

Figure 4 shows Cluster observations of a stable current sheet encounter on October 11<sup>th</sup> 2001, immediately prior to a substorm. The top three panels display the magnetic field from the FGM fluxgate magnetometer [1] in a coordinate system chosen to match the simulation coordinates. The current sheet normal  $\hat{z}$  was found at each data point as the gradient [11] in the magnetic field strength. The coordinate system for Figure 4 uses the average  $\hat{z}$  direction, and  $\hat{x}$  was found by rotating about this axis to maximize the field in  $x$  and minimize the field in  $y$ .

Between 0310 UT and 0320 UT, there are strong waves that rotate the sheet normal  $\hat{z}$  by roughly 60 degrees. The mode is largely even parity (kink-type), as evidenced by the fact that the oscillations at C3 remain in phase even when  $B_x$  is negative (i.e. the satellite is on the opposite side of the sheet). Timing analysis on the oscillations gives a phase velocity of  $\sim 120$  km/s in the  $\hat{y}$  direction. With the 60 second period, this gives a wavelength of 7200 km. Using this wavelength, the 60 degree rotation of  $\hat{z}$  implies an amplitude of 500 km.

The amplitude can be independently verified by noting the satellite separation in  $z$ . Cluster 3 is lowest in  $z$ , followed by C4, then C2, and C1 is highest. The relative  $z$  separations are 893 km, 1061 km and 1986 km respectively. Since the top of the C3 trace barely overlaps with the C2 and C4 traces, which in turn barely overlap with the C1 trace, the amplitude must be roughly half the separation distance, or  $\sim 500$  km. The embedded sheet thickness can also be estimated in this manner as something like 2500 km.

At 0325 UT, the current sheet begins to rapidly break up. On the ground, there is evidence of a pseudobreakup at this time; the main substorm follows after that. For this study, however, we’re interested more in the interval before this happens.

The bottom two panels show the electric field from the Cluster EFW double-probe electric field instrument [9] in the same rotated coordinate system. Cluster EFW only measures in two dimensions: roughly  $\hat{x}$  and  $\hat{y}$ . To project to this system, we have assumed zero electric field along the unmeasured axis. An offset has also been subtracted from the sunward direction ( $\sim \hat{x}$ ).

As a check on the assumption that the unmeasured component is roughly zero, we tried determining it using the constraint  $\vec{E} \cdot \vec{B} = 0$ . This yielded similar results, except when  $\vec{B}$  was near the spin plane (in which case this second method has a well known divide-by-zero failure).

There is a clear oscillation in  $E_y$ . It has the same period as the magnetic kink-mode oscillations, but is 90 degrees out of phase. Applying equation 10, the induced electric field in the  $y$  direction should be  $\sim 0.2$  mV/m for kink-mode oscillations

with the characteristics found above, and should be 90 degrees out of phase. Consequently, we interpret these oscillations as resulting from the same even-parity perturbation to the sheet.

In summary, kink-type waves are clearly seen, and the electric field measurements resolve the  $\sim 0.2$  mV/m fields from this motion. What is notably lacking, however, is any evidence of a strong DC electric field. The field is much less than the  $> 2$  mV/m that would be required for this to be a forced current sheet. There is also little anisotropy in the particle measurements (not shown). This is clearly not an example of a forced current sheet.

## 6. Event search

We tried to find an example of a stable forced current sheet driven by DC electric fields in the 2001 Cluster data. Based on the results shown in Figure 2, the required electric field is

$$E_y \gtrsim (2\text{mV/m}) \sqrt{\frac{0.3\text{cm}^{-3}}{n}} \left( \frac{B_z}{2\text{nT}} \right). \quad (14)$$

In order to include as many events as possible, we looked for stable sheets that had  $E_y$  greater than half this value. Despite looking at more than 100 stable current sheets, no events were found.

There were certainly intervals in the Cluster data when  $E_y$  exceeded this threshold. However, these were invariably in extremely dynamic, unstable current sheets. The portion of the event shown in Figure 4 after 0325 UT is an example.

## 7. Conclusions

We used an iterative self-consistent method to find a stationary solution for a forced current sheet with a kink-type wave. This is the first report of this type of solution. The solution is similar in many ways to the solution for a flat forced current sheet, except that the sheet is considerably thicker. This thicker sheet translates into a reduced efficiency for converting the pressure anisotropy into an organized current.

We estimated the electric field required to establish a forced current sheet with equal parallel and perpendicular pressures in the satellite frame. The result was quite large: at least 2 mV/m in typical sheets.

We then searched the Cluster data for 2001 for an example of a stable forced current sheet supported by a DC electric field, either with or without kink-type structure. Our failure to find an example means that the relative velocity between the satellite frame and the deHoffmann-Teller frame is low, except in extremely dynamic situations. We conclude that forced current sheet models (with anisotropy supplied by the deHoffmann-Teller translation) are not widely applicable to the stable magnetotail at  $\sim 19 R_E$ .

This does not mean that these models are never applicable. However, it does restrict their domain. First, they could be useful in very dynamic situations with large DC electric fields. This is an important class of phenomena including reconnection outflow regions and bursty bulk flows. Second, periods of unusually large pressure anisotropy do exist. A follow-on study searching for such events would be worthwhile.

## 8. Acknowledgments

We thank Melvyn Goldstein for PEACE data and useful discussions. The FGM data were accessed through the Cluster Active Archive. This work was supported by THEMIS (Time History of Events and Macroscale Interactions during Substorms).

## References

- Balogh, A., Carr, C.M., Acuña, M.H., Dunlop, M.W., Beek, T.J., Brown, P., Fornacon, K.-H., Georgescu, E., Glassmeier, K.-H., Harris, J., Musmann, G., Oddy, T., and Schwingenschuh, K., The Cluster Magnetic Field Investigation: overview of in-flight performance and initial results, *Ann. Geophysicae*, *19*, 1207-1217, 2001.
- Birn, J., Drake, J.F., Shay, M.A., Rogers, B.N., Denton, R.E., Hesse, M., Kuznetsova, M., Ma, Z.W., Bhattacharjee, A., Otto, A., and Pritchett, P.L., Geospace Environmental Modeling (GEM) magnetic reconnection challenge, *J. Geophys. Res.*, *106*, 3715-19, 2001.
- Birn, J., Galsgaard, K., Hesse, M., Hoshino, M., Huba, J., Lapenta, G., Pritchett, P.L., Schindler, K., Yin, L., Büchner, J., Neukirch, T., and Priest, E.R., Forced magnetic reconnection, *Geophys. Res. Lett.*, *32*, L06105, 2005.
- Büchner, J., and Zelenyi, L., Regular and chaotic charged particle motion in magnetotail-like field reversals 1. Basic theory of trapped motion, *J. Geophys. Res.*, *94*, 11,821-11,842, 1989.
- Burkhart, G.R., Drake, J.F., and Chen, J., The structure of the dissipation region during magnetic reconnection in collisionless plasma, *J. Geophys. Res.*, *96*, 11,539-53, 1991.
- Burkhart, G.R., Drake, J.F., Dusenbery, P.B., and Speiser, T.W., A particle model for magnetotail neutral sheet equilibria, *J. Geophys. Res.*, *97*, 13,799-815, 1992.
- Eastwood, J.W., Consistency of fields and particle motion in the Speiser model of the current sheet, *Planet. Space Sci.*, *20*, 1555, 1972.
- Eastwood, J.W., The warm current sheet model, and its implications on the temporal behaviour of the geomagnetic tail, *Planet. Space Sci.*, *22*, 1641, 1974.
- Gustafsson, G., Boström, R., Holback, B., Holmgren, G., Lundgren, A., Stasiewicz, K., Åhlén, L., Mozer, F.S., Pankow, D., Harvey, P., Berg, P., Ulrich, R., Pedersen, A., Schmidt, R., Butler, A., Fransen, A.W.C., Klinge, D., Thomsen, M., Fälthammar, C.-G., Lindqvist, P.-A., Christenson, S., Holtet, J., Lybekk, B., Sten, T.A., Tanskanen, P., Lappalainen, K., and Wygant, J., The electric field and wave experiment for the Cluster mission, *Space Science Reviews*, *79*, n 1-2, 137-56, 1997.
- Harris, E.G., On a plasma sheet separating regions of oppositely directed magnetic fields, *Nuevo Cimento*, *23*, 115, 1962.
- Harvey, C.C., Spatial gradients and the volumetric tensor, in *Analysis Methods for Multispacecraft Data*, edited by G. Paschmann and P.W. Daly, 307-322, ISSI, Bern, 1998.
- Hill, T.W., Magnetic merging in a collisionless plasma, *J. Geophys. Res.*, *80*, 4689, 1975.
- Kan, J.R., On the structure of the magnetotail current sheet, *J. Geophys. Res.*, *78*, 3773, 1973.
- Kaufmann, R.L., Paterson, W.R., Frank, L.A., Relationships between the ion flow speed, magnetic flux transport rate, and other plasma sheet parameters, *J. Geophys. Res.*, *110*, A09216, 2005.
- Klimas, A.J., Uritsky, V.M., Vassiliadis, D., Baker, D.N., Reconnection and scale-free avalanching in a driven current-sheet model, *J. Geophys. Res.*, *109*, A02218, 2004.
- LeContel, O., Perraut, S., Roux, A., Pellat, R., and Korth, A., Substorms in the inner plasma sheet, *Adv. Space Res.*, *25*, 2395-2406, 2000.
- Nötzel, A., Schindler, K., and Birn, J., On the cause of the approximate pressure isotropy in the quiet near-Earth plasma sheet, *J. Geophys. Res.*, *90*, 8293-300, 1985.
- Pritchett, P.L., and Coroniti, F.V., Formation of thin current sheets during plasma sheet convection, *J. Geophys. Res.*, *100*, 23,551-65, 1995.
- Rich, F.J., Vasyliunas, V.M., and Wolf, R.A., On the balance of stresses in the plasma sheet, *J. Geophys. Res.*, *77*, 4670, 1972.
- Runov, A., Nakamura, R., Baumjohann, W., Zhang, T.L., Volwerk, M., and Eichelberger, H.-U., Cluster observation of a bifurcated current sheet, *Geophys. Res. Lett.*, *30*, 1036, 2003.
- Schindler, K., Pfirsch, D., and Wobig, H., Stability of two-dimensional collision-free plasmas, *Plasma Phys.*, *15*, 1165, 1973.
- Schindler, K., and Birn, J., Models of two-dimensional embedded thin current sheets from Vlasov theory, *J. Geophys. Res.*, *107*, 1193, 2002.
- Sergeev, V., Runov, A., Baumjohann, W., Nakamura, R., Zhang, T.L., Volwerk, M., Balogh, A., Rème, H., Sauvaud, J.A., André, M., and Klecker, B., Current sheet flapping motion and structure observed by Cluster, *Geophys. Res. Lett.*, *30*, 1327, 2003.
- Sonnerup, B.U.O., Adiabatic particle orbits in a magnetic null sheet, *J. Geophys. Res.*, *76*, 8211, 1971.
- Sitnov, M.I., Zelenyi, L.M., Malova, H.V., and Sharma, A.S., Thin current sheet embedded within a thicker plasma sheet: self-consistent kinetic theory, *J. Geophys. Res.*, *105*, 13029-43, 2000.
- Sitnov, M.I., Sharma, A.S., Papadopoulos, K., and Vassiliadis, D., Modeling substorm dynamics of the magnetosphere: From self-organization and self-organized criticality to nonequilibrium phase transitions, *Physical Review E - Statistical, Nonlinear, and Soft Matter Physics*, *65*, 016116, 2001.
- Sitnov, M.I., Guzdar, P.N., and Swisdak, M., A model of the bifurcated current sheet, *Geophys. Res. Lett.*, *30*, 1712, 2003.
- Sitnov, M.I., Lui, A.T.Y., Guzdar, P.N., and Yoon, P.H., Current-driven instabilities in forced current sheets, *J. Geophys. Res.*, *109*, A03205, 2004.
- Speiser, T.W., Particle trajectories in model current sheets, 1, Analytical solutions, *J. Geophys. Res.*, *70*, 4219, 1965.
- Wang, C.-P., Lyons, L.R., Weygand, J.M., Nagai, T., and McEntire, R.W., Equatorial distributions of the plasma sheet ions, their electric and magnetic drifts, and magnetic fields under different interplanetary magnetic field  $B_z$  conditions, *J. Geophys. Res.*, *111*, A04215, 2006.
- Zelenyi, L.M., Malova, H.V., Popov, V.Y., Delcourt, D.C., Ganushkina, N.Y., and Sharma, A.S., "Matreshka" model of multilayered current sheet, *Geophys. Res. Lett.*, *33*, L05105, 2006.

# Nonlinear stability of the near-earth plasma sheet during substorms

P. Dobias, J. A. Wanliss, and J. C. Samson

**Abstract:** We analyze a nonlinear stability of the near-Earth plasma sheet via a Grad-Shafranov equilibrium constrained by CANOPUS data. Using a stability analysis based on comparison of various orders in a Taylor expansion of the potential energy density, we demonstrate that an occurrence of field line resonances followed by a development of a Kelvin-Helmholtz instability at about 10 Re causes the near-Earth plasma sheet to become unstable minutes before the onset.

*Key words:* Substorms, Kelvin-Helmholtz, Ballooning.

## 1. Introduction

In the present work we address a nonlinear stability of the near-Earth plasma sheet during the substorm onset assuming a presence of the Kelvin-Helmholtz (KH) instability. [12] outline a possible sequence of events that take place during the substorm expansion phase. This sequence assumes the initiation of the expansion phase near Earth. While there are other opinions we believe that the near-Earth initiation provides the simplest explanation for the observed sequence of events [8].

We use a stability analysis approach suggested by [9], improved further by [4]. This stability method can be summarized as follows. A plasma equilibrium is modeled using the Grad-Shafranov equation constrained by CANOPUS observations [4] to ensure that our tested configurations are relevant for the substorm event being analyzed. We are not modeling a transition between equilibrium states, rather, we calculate each configuration as a separate equilibrium based on observations. In the second step we define plasma plasma perturbation in the form of a displacement connecting Lagrangian and Eulerian description  $\hat{x}(\mathbf{x}, t) = \mathbf{x} + \boldsymbol{\xi}(\mathbf{x}, t)$ . All other perturbed quantities are expressed in terms of the displacement. Then this plasma displacement is used to calculate expansion terms in the potential energy density. Comparison of the terms yields the stability properties of the system [9]. If the second order term is dominant, the system is well described by linear approximation. If the third order is dominant, the system is explosively unstable [9, 7]. The dominant fourth order term means that the system is nonlinearly stable [7]. This method allows us to estimate a possible maximum growth of the instability before it is saturated by nonlinear effects [5].

The above method is then used to analyze the nonlinear stability of the near-Earth plasma sheet during the February 9, 1995 substorm. We extend previous work of [6] by considering a possible development of Kelvin-Helmholtz instabilities due to a strong velocity shear caused by field line resonances [14]. We analyze changes of the stability properties of the plasma sheet due to the presence of a vortex, and also dis-

cuss a possible influence of the stability on the further development of this vortex. Our stability analysis is based on the ideal MHD, and it does not include influences of various other factors such as diffusion, Larmor radius effects, or azimuthal pressure gradient.

## 2. Equilibrium Magnetospheric Model

For the stability analysis we use a Grad-Shafranov equilibrium in the form [12]

$$\psi(r, \theta) = 2\pi \frac{M \sin^2 \theta}{r} \left[ 1 + \frac{1 - \alpha}{2} \left( \frac{r}{R_X} \right)^3 + \frac{\alpha}{4} \left( \frac{r}{R_X} \right)^5 \right]. \quad (1)$$

The radius  $r$ , polar angle  $\theta$ , and azimuthal angle  $\phi$  are spherical coordinates.  $M$  is the dipolar moment, and  $\alpha$  and  $R_X$  are parameters characterizing pressure gradient and position of the X line. The solution (1) is a reasonable approximation as far as the position of the x-line, but breaks down at large distances. Its advantage is that it allows a relatively simple correlation with experimental observations via adjustment of the two parameters  $\alpha$  and  $R_X$  using a position of the proton isotropy boundary and the position of the red emissions obtained from CANOPUS ground based observations [16, 17].

We use the distribution of auroral luminosity, from meridian scanning photometer data, to gain information about the nature and location of various plasma boundaries in the magnetotail. As shown previously by [16] and [17] meridian scanning photometers are excellent tools for investigating precipitation of charged particles in the auroral ionosphere and can quite easily be used to constrain magnetospheric magnetic field models.

The idea that we exploit in this paper relies on nonconservation of the first adiabatic invariant when magnetic field variations occur on the scale of a particle gyroradius. A measure of nonconservation is determined by the square root of the ratio of the magnetic field line radius of curvature to the particle gyroradius [2]. Theoretical effort by [18] suggests that the transition between the taillike and dipolelike field configurations occurs where the above ratio equals 3. In addition to the need for a magnetic field model, one can only find these locations if the energy of the precipitating particles is known. In the present work, the energies of the precipitating particles are determined directly from the equilibrium magnetotail model and are not a free parameter.

Received 11 May 2006.

**P. Dobias.** DRDC CORA, Ottawa, ON, K1A 0A2, Canada.

**J. A. Wanliss.** ERAU, Daytona Beach 32114, USA.

**J. C. Samson.** Univ. of Alberta, Edmonton, Alberta, T6G 2J1, Canada.

A new constraint is obtained from the model in that one of the model parameters is directly related to the location of the last closed magnetic field line. This boundary can also be obtained from ground-based photometer data [1]. They demonstrated that the poleward border of 630.0 nm optical emissions is very close to the transition between open and closed field lines in the dusk-midnight sector. In this present paper we follow the same methodology to determine the ionospheric location of the last closed magnetic field line.

Once an event has been selected for analysis, we calculate the equatorward edge of the 486.1 nm proton aurora, and the poleward edge of the 630.0 nm electron aurora as described above. The two free parameters in the magnetic field model are varied via the Levenburg-Marquardt nonlinear optimization method to minimize the sum of the square of the error between the model boundaries and the boundaries obtained from the photometer data.

We analyze the stability of the near-Earth plasma sheet during the February 9, 1995 event. The substorm onset occurred approximately at 4:37 UT, with the first weak disturbances appearing between 4:30 and 4:35 UT [6]. We performed stability tests for three times around the onset. The first stability test was performed at 4:30 UT, just before any significant disturbances started occurring. The second test was performed for the 4:35 UT configuration, at the time just prior to onset. The last test we have performed corresponded to the beginning of the recovery phase at 4:40 UT. The last test was performed to investigate changes of energy balance that the onset might have caused. Plasma pressure and magnetic field calculated in the equatorial plane are shown in Figures 1 and 2. The pressure gradient increases and the region of maximum pressure is moving earthward. The value of plasma  $\beta$  at 10 Re is 14 for the 4:30UT, later it increases to 40 for 4:35 UT, and then drops to 10 for 4:40 UT configuration. The magnetic field lines are being stretched, this is marked by a drop of magnetic field in the near-Earth region.

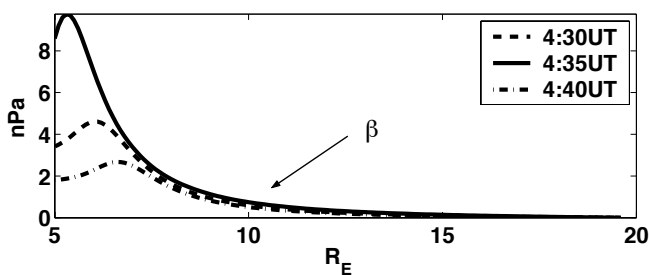


Fig. 1. Plasma pressure in the equatorial plane for 4:30, 4:35 and 4:40 UT configurations.

### 3. Plasma Displacement for K-H Instability

To perform the stability analysis we needed to choose is the specific form of plasma displacement. Here we extend the work of [6] where the authors assumed the plasma displacement corresponding to field line resonances, and have conclusively shown that approximately 2 minutes prior to onset the plasma sheet becomes nonlinearly unstable. [14] showed that a presence of the  $180^\circ$ -phase shift in the velocity will lead to

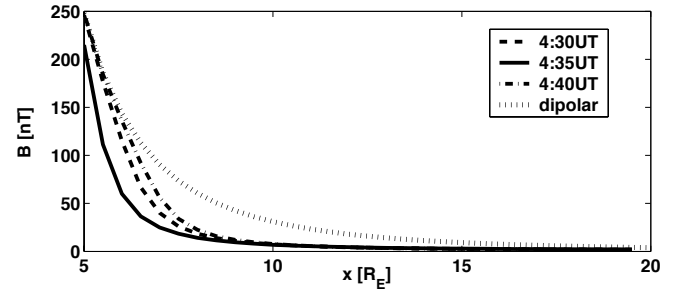


Fig. 2. Magnetic field in the equatorial plane for 4:30, 4:35 and 4:40 UT configurations. Dotted line shows dipolar field for the reference.

a development of the Kelvin-Helmholtz instability, that can be further coupled to a ballooning modes. Therefore in this paper we study the influence of the development of K-H instability on the overall stability of the near-earth plasma sheet.

We assume azimuthal symmetry for our analysis, and performed the stability analysis around  $10 R_E$ , in the region where FLRs are likely to occur [12]. This location further corresponds to a possible location of the processes responsible for forming the breakup arc [13]. The development of the K-H instability along the azimuthal position of the resonance will have a two fold effect on the dynamics of the displacement. First, it will increase the gradient of the plasma displacement due to development of a vortex structure. The second effect of the wrapping is the limitation of the growth of the magnitude of the displacement. If the K-H instability is coupled to a ballooning type instability the growth can continue as the shear flow-ballooning instability [14].

We use a fluid approximation to model development of the K-H instability. This is justified by the fact that our analysis is restricted to the equatorial plane where the magnetic field is perpendicular to the velocity field and thus there is no wrapping of magnetic field lines present. To model the K-H instability into its nonlinear stage we use a semi-analytical approach first presented by [10]. It is based on approximating the surface of discontinuity by a series of elementary vortices. Figure 3 shows development of the surface of discontinuity including the direction of velocity vectors. The distance in  $x$  and  $y$  directions is normalized in terms of wavelength  $\lambda$  of the instability. The wrapping of the surface of discontinuity is clearly visible at the later stages of the development. The magnitude of the displacement is approximately  $0.2\lambda$ . The ambient velocity is scaled as  $\pm 1$ .

Once we calculate temporal development of the K-H vortex, we are ready to model coupling between FLR's and the K-H instability. For simplicity, we can assume that the resonance introduces the velocity shear  $\pm |u_{\phi FLR}|$  along the azimuthal direction. Since we are dealing with the dynamics close to the midnight plane, we can approximate the plasma sheet by a box model, with positive  $x$  in the tailward direction and  $y$  in the azimuthal direction. Then the surface of discontinuity is in the  $y$ -direction at the position of resonance,  $x_r$ . The necessary radial perturbation is introduced by the resonance itself.

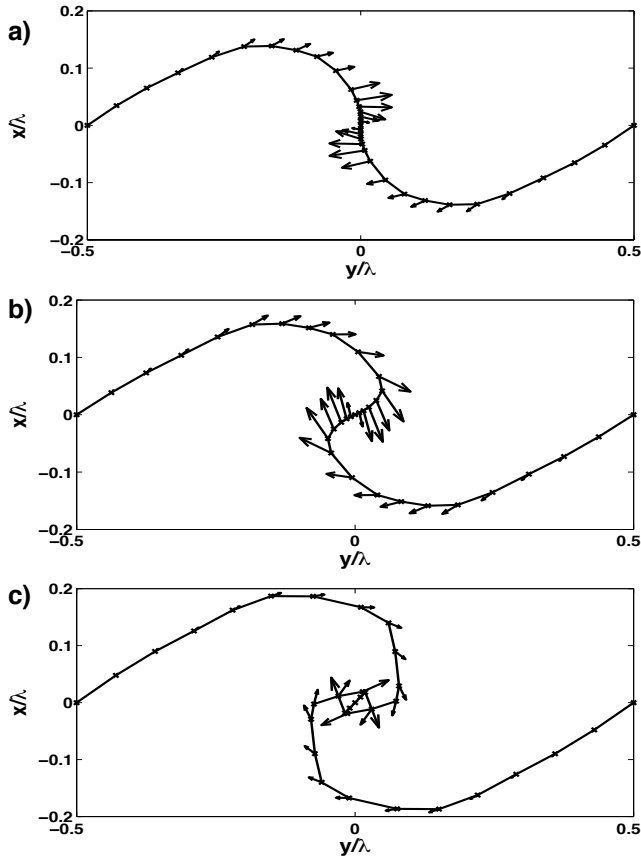


**Fig. 3.** Development of the Kelvin-Helmholtz instability in the equatorial plane.

#### 4. Results of Stability Analysis

We assumed that K-H instability developed as a consequence to the preexisting FLR around  $10 R_E$ . We started with the magnitude of the resonance at  $0.75 R_E$ . The magnitude of the displacement defines the magnitude of the velocity shear. Then we assumed that there is a perturbation in the radial direction that will initiate vortex development (Fig. 3). For the stability analysis we have chosen stages a, c, and d of the vortex. Then we repeated tests with the initial magnitude of the FLR at  $1 R_E$ . Presence of the K-H instability leads to broadening of the disturbed region, propagating the perturbation further away from the resonance site. The initial setting (magnitude of resonance  $0.75 R_E$ ) ensures that the initial energy density is in the linear regime. Just as in the case of a pure FLR type of displacement, for the 4:30 UT configuration the dominance of the second order was followed directly by the dominance of the fourth order term as the vortex development progresses. It means that any instability growth will be saturated due to nonlinear effects. For the initial magnitude of the displacement at  $1 R_E$  we obtained similar results, with the difference that the fourth order term was dominant from the onset of the K-H instability.

For the 4:35 UT configuration starting with the initial magnitude of the FLR's at  $0.75 R_E$  ensures the initial energy density to be in the linear regime (dominant second order term). However, even for the initial stages of the K-H instability, the third order term is much more important than for the pure

resonance-type displacement. Further development of the vortex leads to a strong dominance of the third order term. This means that the presence of the vortex further destabilizes the near-Earth plasma sheet. For the initial magnitude of the resonance of  $1 R_E$ , even the initial stages of the vortex development lead to a dominant third order term in the energy density. We obtained the strongest dominance of the third order term for stage (c) (Fig. 3) of the vortex development. Further wrapping of the vortex leads to dominance by the fourth order term which means that it provides a stabilizing effect on the system.

The results of the analysis of the 4:40 UT configuration were analogical to the results at later growth phase. The initially dominant second order term for early stages of the vortex development are followed by the dominance of the fourth order term. This confirms that at this stage the excess energy was already released and the system is back in the lower energy state.

Figure 4 shows results for the magnitude of the resonance set at  $0.75 R_E$  for the most unstable stage of the vortex (Fig. 3c) for all four configurations. The cross-section is taken through the region of maximum gradient in the velocity. Parts (a) and (c), corresponding to 4:30 UT and 4:40 UT configurations respectively, show stable behavior (dominant 4th order term). Part (b), corresponding to 4:35 UT configuration is explosively unstable. For this configuration, the third order term is dominant. Thus, around 4:35 UT, just minutes prior the onset, the near Earth plasma sheet became explosively unstable, while during growth phase and the recovery phase the near-Earth plasma sheet was nonlinearly stable.

Since the K-H instability does not extract potential energy, and only redistributes the kinetic energy, the presence of the K-H instability alone is not able to explain the energy reconfiguration in the near-Earth plasma sheet. Note in Fig. 3, that the presence of vortex wrapping leads to a saturation of the magnitude of the displacement. [14] proposed that a coupling between K-H and ballooning modes could lead to a growth of the vortex and thus to reconfiguration of the energy in the region.

To test the effect of this scenario on the change in the stability properties, we have assumed an increase in the size of the vortex, and calculated the energy density for such configurations. Fig. 5 shows energy density terms for a vortex that grows to twice its original size. Parts a) and b) corresponds to vortex sizes of  $1 R_E$  and  $2 R_E$ . As the vortex grows, the fourth order term in energy becomes dominant, suggesting nonlinear saturation of the instability. This result agrees with the scenario of reconfiguration of energy due to K-H ballooning coupling and is consistent with the computational model of the shear-flow ballooning instabilities and observations of auroral arcs in [14] and [15].

To summarize, the development of the K-H instability from the velocity shear due to field line resonance provided similar stability properties for various stages of the Feb. 9, 1995 sub-storm as did the field line resonance alone. This suggests that these general stability results are not dependent on the type of the displacement, and any realistic displacement yields to the explosively unstable near-Earth plasma sheet minutes prior to the onset while it remained stable during the most of the growth phase.

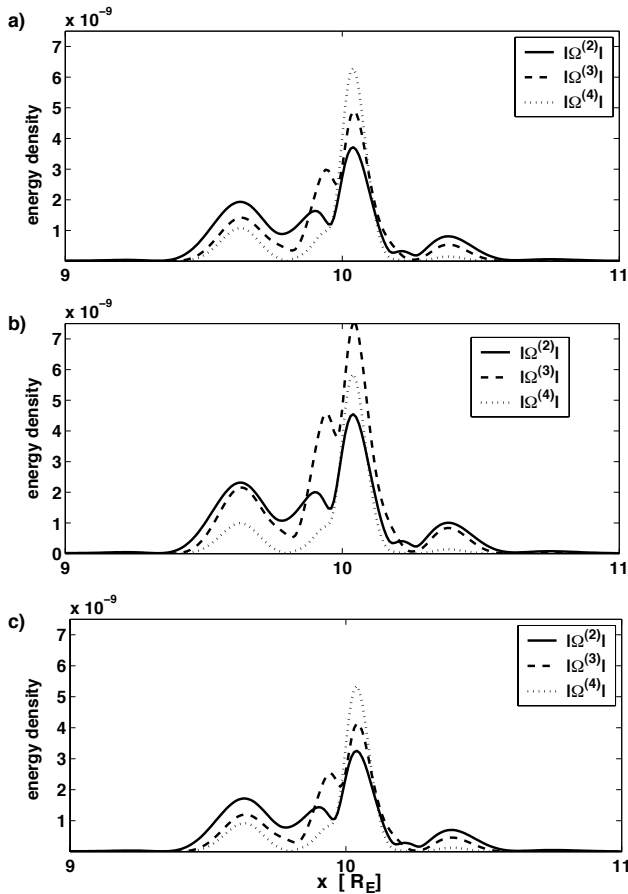


Fig. 4. Potential energy density in the case of a Kelvin-Helmholtz instability in the equatorial plane. The magnitude of the initial FLR was 0.75 Re.

## 5. Conclusions

We improved previous stability analysis by including a possibility of the development of a Kelvin-Helmholtz vortex in the system and analyzing its influence on the stability of the system. Our results suggest that during the stable state of a substorm the presence of the K-H vortex does not influence the general stability of the system. Since there is no available free energy, such a vortex must be saturated. In the case of unstable configuration during the onset, the presence of the K-H instability can cause a faster initiation of the explosive instability due to enhanced gradients in plasma displacement. However, we need to note that the K-H instability can be initiated in the presence of any shear in velocity and does not have to be tied to the presence of FLRs. On the other hand, if there is resonance present, it is likely that the K-H instability will appear. We can conclude that for the studied event, the transition between stable and unstable configurations corresponds to the time of onset no matter what the displacement is. The K-H instability alone cannot extract potential energy from the system. It only transforms different forms of kinetic energy. Therefore, we have also investigated what happens if the vortex grows due to coupling with ballooning modes. It appears that the growth of the vortex might eventually lead to reconfiguration of the energy and the saturation of the instability.

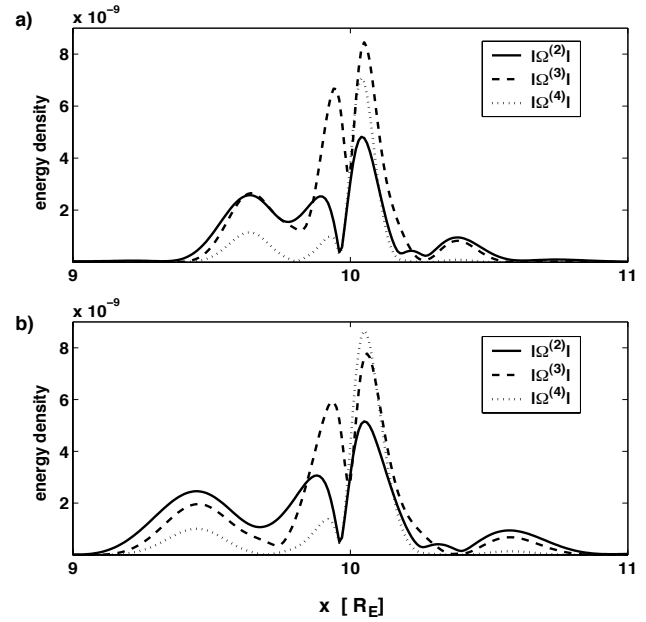


Fig. 5. Potential energy density for the 4:35 UT configuration for the K-H ballooning type of the displacement.

## 6. Acknowledgments

This research was funded by the Natural Sciences and Engineering Research Council of Canada (NSERC). CANOPUS is an array funded by the Canadian Space Agency (CSA).

## References

1. Blanchard, G. T., L. R. Lyons, J. C. Samson, and F. J. Rich, Locating the polar cap boundary from observations of 6300 Å emission, *J. Geophys. Res.*, 100, 7855, 1995.
2. Büchner, J., and L. M. Zelenyi, Chaotization of the electron motion as the cause of an internal magnetotail instability and the substorm onset, *J. Geophys. Res.*, 92, 13,456, 1987.
3. Chandrasekhar, S., *Hydrodynamic and hydromagnetic stability*, Oxford Press, 1961
4. Dobias, P., and J. C. Samson, Nonlinear instabilities in magnetized plasmas: A geometrical treatment, *Can. J. Phys.*, 82, 593, 2004.
5. Dobias, P., I. O. Voronkov, and J. C. Samson, On nonlinear plasma instabilities during the expansive phase onset, *Phys. Plasmas*, 11, 2046, 2004a.
6. Dobias, P., J. A. Wanliss, I. O. Voronkov, and J. C. Samson, On the stability of the near-Earth magnetotail at growth phase, in: *Proceedings of the 7th International Conference on Substorms*, pg. 152, 2004b.
7. Fong, B. H., S. C. Cowley, O. A. Hurricane, Metastability of magnetically confined plasmas, *Phys. Rev. Lett.*, 82, 4651, 1999.
8. Lyons, L. R., I. O. Voronkov, E. F. Donovan, and E. Zesta, Relation of substorm breakup arc to other growth phase auroral arcs, *J. Geophys. Res.*, 107, 1390, 2002.
9. Pfirsch, D., and R. N. Sudan, Nonlinear ideal magnetohydrodynamic instabilities, *Phys. Fluids*, 7, 2052, 1993.
10. Rosenhead, L, Formation of vortices from a surface of discontinuity, *Proc. Roy. Soc. A*, 134, 170, 1931.

11. Samson, J. C., L. L. Cogger, and Q. Pao, Observations of field line resonances, auroral arcs, and auroral vortex structures, *J. Geophys. Res.*, 101, 17373, 1996.
12. Samson, J. C., and P. Dobias, Explosive instabilities and substorm intensification in the near-Earth magnetotail, in: *Multiscale Coupling of Sun-Earth Processes*, edited by A.T.Y. Lui, Y. Kamide, and G. Consolini, 2004.
13. Samson, J. C., R. Rankin, and V. T. Tikhonchuk, Optical signatures of auroral arcs produced by field line resonances; comparison with satellite observations and modeling, *Annales Geophysicae*, 21, 933, 2003.
14. Voronkov, I., R. Rankin, P. Frytz, V. T. Tikhonchuk, and J.C. Samson, Coupling of shear flow and pressure gradient instabilities, *J. Geophys. Res.*, 102, 9639, 1997.
15. Voronkov, I., E. F. Donovan, B. J. Jackel, and J. C. Samson, Large-scale vortex dynamics in the evening and midnight auroral zone: Observations and simulations, *J. Geophys. Res.*, 105, 18,505, 2000.
16. Wanliss, J. A., J. C. Samson, and E. Friedrich, On the use of photometer data to map dynamics of the magnetotail current sheet during substorm growth phase, *J. Geophys. Res.*, 105, 27,673, 2000.
17. Wanliss, J. A., R. Rankin, J. C. Samson, and V. T. Tikhonchuk, Field line resonances in a stretched magnetotail: CANOPUS optical and magnetometer observations, *J. Geophys. Res.*, 107, 10.1029, 2002.
18. Zelenyi, L., A. Galeev, and C. F. Kennel, Ion precipitation from the inner plasma sheet due to stochastic diffusion, *J. Geophys. Res.*, 95, 3,871, 1990.



# The azimuthal evolution of the substorm expansive phase onset aurora

E. Donovan, S. Mende, B. Jackel, M. Syrjäsoo, M. Meurant, I. Voronkov, H. U. Frey, V. Angelopoulos, and M. Connors

**Abstract:** We use data from two white light All-Sky Imagers, deployed as part of the THEMIS Ground-Based Observatory program, to explore the azimuthal evolution of the breakup aurora during a pseudobreakup that occurred on November 28, 2005. We find that this breakup occurred on a pre-existing auroral arc. It began with a brightening that formed on an extended region along the arc, and consisted of eastward propagating beads with a wavelength of  $\sim 100$  km. During the five minutes following the breakup, a second pre-existing arc that was poleward of the first remained undisturbed. The initial azimuthally extended region of enhanced brightness along the arc did not expand further for at least two minutes, after which it expanded rapidly along the arc. From these observations, we conclude that the breakup in this event corresponds to Current Disruption in the inner magnetosphere caused by an instability that creates azimuthally propagating waves and that is not triggered by a fast Earthward flow.

## 1. Introduction

Identifying the macroscale instability responsible for substorm expansive phase onset is an important goal in space physics. Bringing closure to this question has been the motivation for numerous, theoretical, simulation, and observational event and statistical studies over the years. We now understand that both reconnection in the mid-tail and current disruption in the inner magnetosphere occur as integral parts of the substorm, but their interrelationship and in particular whether one starts and then sets in motion a sequence of events that leads to the other is not currently understood [2, 7, 8]. Careful examination of coordinated *in situ* and ground observations have provided perhaps the best insights in this direction (see e.g., [13, 9]), however it has become clear that although the expansive phase onset unfolds very rapidly, the data with which we are able to address these questions is fundamentally limited in its spatio-temporal coverage and resolution.

In general, substorm event studies are predicated on the idea that the correct combination of solar wind, *in situ*, and remote sensing of the ionospheric electrodynamics from the ground and space would be able to provide sufficient information to rule out some proposed onset mechanisms and provide constraints for models and simulations used to explore mechanisms that are still viable. For example, the typical substorm *breakup arc* is embedded in the bright proton aurora which maps to the transition between tail-like and dipolar field lines [12, 3, 4], most often in the region between geosynchronous orbit and  $L \simeq 10$  Re. We also understand that the breakup, substorm current wedge, current disruption, dipolarization, and injection are all manifestations of the same inner Central Plasma Sheet (CPS) disturbance (see, for example, [9]). The ground-based auroral and magnetic field data in particular point to

a disturbance that begins in the inner CPS and evolves azimuthally and meridionally, the latter reflecting radial evolution in the magnetosphere [5], consistent with the Current Disruption (CD) paradigm. However, attempts to create a synoptic picture of the evolution of the expansive phase from analysis of combined *in situ* and ionospheric remote sensing data has led to a more ambiguous picture, leading to at least three sets of inconsistent conclusions: 1) expansive phase began in the inner CPS after which it progressed tailward (consistent with the CD paradigm); 2) expansive phase began in the mid-tail with reconnection, fast Earthward flows, and subsequent inner CPS effects (i.e., consistent with the Near-Earth Neutral Line or “NENL” paradigm); 3) that the mid-tail and inner CPS expansive phase processes might evolve largely independently of one another [9, 11, 13, 10, 17].

Bringing closure the question of how and where expansive phase onset is initiated in the magnetotail is the primary scientific motivation for the upcoming NASA Time History of Events and Macroscale Interactions in Substorms (THEMIS) MIDEX mission. THEMIS represents the first true constellation-class geospace mission, and will involve five satellites on equatorial orbits. The orbits will have 1, 2 and 4 day periods, corresponding to  $\sim 10$ , 20, and 30 Re apogee distances, respectively. The outer two satellites will be at or near apogee for more than ten hours every four days. The inner three will together provide coverage of the  $\sim 10$  Re region for those same ten hours. Throughout the mission, the apogee conjunctions will be over central Canada, on a meridional line bracketed by GOES East and West. During the winter months, apogee will be in the magnetotail, where the seven THEMIS and GOES satellites will bracket the NENL and CD regions. Although the THEMIS constellation will provide numerous and unprecedented opportunities to study the radial evolution of the expansive phase in the magnetotail, the satellites by themselves would not be able to bring closure to the question at hand. While it is true that the expansive phase evolution is most often couched in radial terms (as outlined in the previous two paragraphs), the disturbance also evolves azimuthally. Thus, although data from the satellites might indicate a clear ordering of events, it might also be that the process started away from the apogee

Received 9 July 2006.

**E. Donovan, B. Jackel, M. Syrjäsoo, M. Meurant, and I. Voronkov.** Department of Physics and Astronomy, University of Calgary  
**S. Mende, H. U. Frey, and V. Angelopoulos.** Space Physics Laboratory, University of California, Berkeley  
**M. Connors.** Athabasca University, Athabasca, Alberta, Canada

meridian and later swept over it.

The THEMIS program has a ground-based component which is specifically designed to deal with the azimuthal uncertainties that would be present if all that was available were satellites on a more or less radial line through the CPS. The apogee meridian was chosen to be over central Canada to take advantage of the fact that a large fraction of the auroral oval is over land in northern Canada and that ground-based space science instrumentation is already operating in that sector (e.g., instruments operated by Canadian GeoSpace Monitoring, SuperDARN, the University of Alaska Geophysics Institute, MACCS, and other programs). In addition, a continent-wide array of fluxgate magnetometers and white light auroral imagers is being deployed specifically as part of THEMIS. In Figure 1, we show the locations and fields of view (FOVs) of the 20 All-Sky Imagers (ASIs) that make up the THEMIS ASI array.

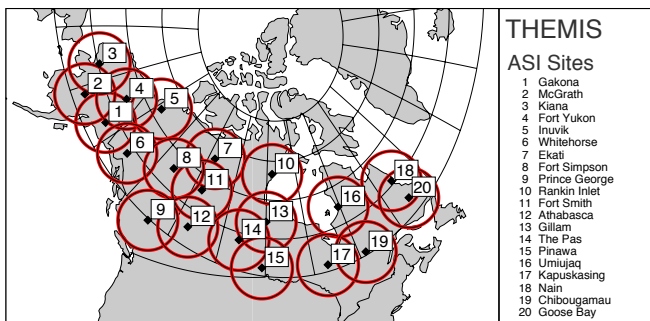


**Fig. 1.** Fields of view of white light ASIs that will be operating as part of the THEMIS Ground-Based Observatory network. The fields of view assume 110 km emissions 10 degrees above the horizon. The black contours indicate constant magnetic latitude and longitude (Altitude Adjusted Corrected Geomagnetic Coordinates or “AACGM” Epoch 2000 - [1]). The magnetic latitude contours are for  $60^\circ$  through  $80^\circ$  in  $5^\circ$  increments. The magnetic longitude contours are separated by one hour of magnetic local time.

The THEMIS ASIs will take one image every three seconds. Imaging will be synchronized across the array with Global Positioning System (GPS) timing. While the ASIs and magnetometers will provide essential contextual information in support of THEMIS meeting its objectives, these new instruments will also bring something truly new to substorm studies. For example, existing arrays of ground-based optical instruments have provided numerous instances of simultaneous observations across all relevant latitudes. The Finnish MIRACLE ASI, Canadian NORSTAR ASI, and CANOPUS Meridian Scanning Photometer arrays are but three examples of this (see e.g., [5]). The azimuthal evolution of the expansive phase aurora has been extensively studied using global auroral imagers on satellites, but the temporal and spatial resolution afforded by those instruments have not been sufficient to explore the details of the expansive phase onset (see e.g., [6]). Since we know that, at the time of the auroral breakup, the auroral features can evolve azimuthally (i.e., east-west) beyond the FOV of a single imager (see [16]) in several tens of seconds, being able to track the evolution of the expansive phase aurora across several hours Magnetic Local Time (MLT) with three second temporal res-

olution will be an important step forward in constraining substorm theories.

One of the great advantages to being involved in the ground-based component of a mission like THEMIS is that we have data before the satellites are launched. Deployment and operation of the imagers started in 2004, and the array will be completely in place by the fall of 2006. By the end of the northern hemisphere 2005-2006 winter, there were 13 ASIs operating in Canada and Alaska. Summary keograms and thumbnail images can be seen on the “GAIA” auroral virtual observatory (<http://gaia-vxo.org>).

In this paper, we present data from a small substorm that occurred over the Alaska-Canada border region. The initial auroral breakup was in the FOV of one ASI and quickly spread east into that of an adjacent imager. We have two objectives in this paper. First, we want to highlight some of the new capabilities that the THEMIS ASI array will bring to the THEMIS program and substorm studies in general. Second, we want to explore the azimuthal evolution of the breakup aurora on a time scale of tens of seconds, and comment on what the auroral data indicates in terms of the substorm onset mechanism. We point out in advance that we are presenting data from only one event. Further, as the auroral expansion lasts only  $\sim 10$  minutes, and as it does not appear to lead to lobe flux reconnection, this event is a pseudobreakup (see [17] and references therein for what we mean by “pseudobreakup”).

## 2. The Event

The event that we focus on occurred between 10:00 and 10:30 UT on November 28, 2005. In the several hours leading up to the event, the solar wind speed and dynamic pressure were relatively steady, and consistently below 400 km/s and 4 nPa, respectively. As well, during the time leading up to the event the Interplanetary Magnetic Field was consistently southward. In short, the IMF and solar wind plasma observations do not indicate any trigger for the event. At  $\sim 10:10$  UT, a  $\sim 200$  nT negative H-bay was observed in western Canada and Alaska (see below). The event does not have any noticeable signature in the geosynchronous GOES East or GOES West magnetic field data. In Figure 2, we show FUV auroral images from the IMAGE WIC instrument for this event. The auroral breakup is evident in the 23:00-24:00 MLT sector, starting first at roughly  $\sim 10:14$  UT, and ending by  $\sim 10:20$  UT.

On that night, there were relatively clear skies over two of the THEMIS ASIs under the region where the auroral breakup shown in Figure 2 occurred. These were the Fort Yukon (Alaska, USA) and Whitehorse (Yukon, Canada) ASIs, the FOVs of which are shown in the expanded map in Figure 3. In Figure 4, we show a sequence of auroral images at 12 second intervals (top) from the Fort Yukon ASI, and the X-component magnetic field data from the Fort Yukon magnetometer (bottom). Looking first at the ASI images, we see the onset arc was in the south of the imager FOV, located at roughly  $64^\circ$  magnetic latitude (see Figure 3). The image sequence begins at 10:12 UT, at which time the substorm brightening was already visible in the south. As well, there was a quasi-stable auroral arc just slightly north of overhead in the imager. Over the next  $\sim 5$  minutes, the brightening evolved into a vortex which grew poleward and azimuthally. It was only after  $\sim 10:17$  UT (i.e., more than 5

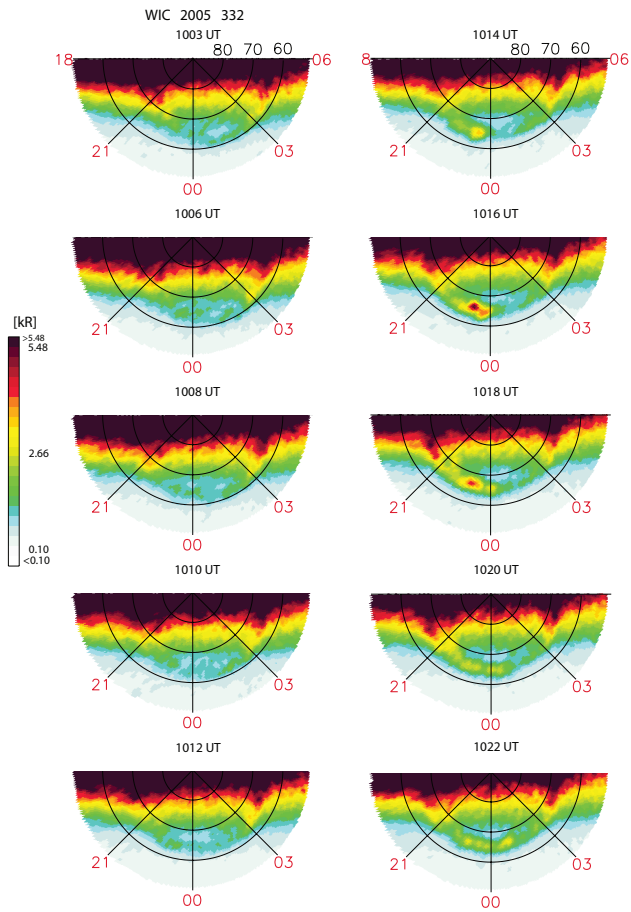


**Fig. 2.** IMAGE WIC FUV auroral images obtained in the southern hemisphere have been mapped into geomagnetic coordinates and subsequently into the northern hemisphere to produce this figure.

minutes after the initial brightening) that the more poleward arc was noticeably disturbed. The image sequence spans the time period bracketed by the two dashed lines in the lower panel, and hence the time during which there is an enhanced westward electrojet and corresponding negative H-bay.

In Figure 5, we focus in on the step-by-step development of the auroral breakup from 10:11:12 until 10:12:54 UT. As the arc that brightened was in the southern part of the FOV of the Fort Yukon ASI, we restrict our attention to partial images, which comprise the left-hand column of the figure. The image at 10:11:12 UT is the first image in which there is unmistakable evidence of the onset. Note that this is more than a minute before the negative H-Bay is noticeable in the Fort Yukon magnetometer data, and a full three minutes prior to the pseudobreak being clearly evident in the IMAGE WIC data. In the right-hand panel of Figure 5, we show differences between successive images (see figure caption), which highlight the wave disturbance more clearly than do the raw images. The differ-

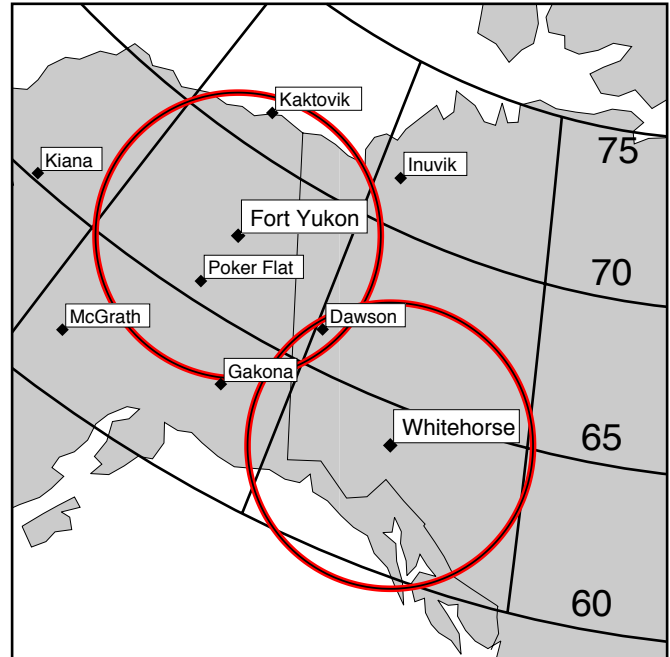


**Fig. 3.** Fields of view of the two THEMIS ASIs that obtained the white light images used in this study. These two imagers are located at Fort Yukon in Alaska and Whitehorse in Yukon Canada. The black contours indicate constant magnetic latitude and longitude (AACGM Epoch 2000). The magnetic latitude contours correspond to  $60^\circ$  through  $75^\circ$  in  $5^\circ$  increments. The magnetic longitude contours are separated by one hour of magnetic local time.

ence image sequence shows a bead-like structure that emerges on the pre-existing breakup arc. Over the nearly two minutes spanned by the image sequence, the beads brightened, and propagated eastward (note that examination of the three second data shows that there is no problem with aliasing). The wavelength and azimuthal propagation speeds of the beads were estimated at  $\sim 100$  km, and  $\sim 5$  km/s, respectively (presuming 110 km altitude emissions).

Referring to Figure 3, the arc visible to the south of Fort Yukon must have extended into the poleward part of the Whitehorse FOV. In Figure 6, we show a time sequence of partial images from Fort Yukon and Whitehorse side by side. Before 10:12:00 UT, the brightening was restricted to the Fort Yukon FOV, although it did expand rapidly in the azimuthal direction, involving the entire arc within the FOV in less than 30 seconds. By 10:12:24, the brightening was clearly visible on the arc at the western edge of the Whitehorse FOV. For the next 90 seconds, the eastern edge of the disturbance remained fixed. That is, the brightening extended azimuthally along the arc until it appeared just inside the Whitehorse field of view, at which time the azimuthal growth stalled for 90 seconds or more. By 10:14:24, the brightening was spreading rapidly eastward along the pre-existing arc. The speed of this expansion was  $\sim 0.5$  km/s.

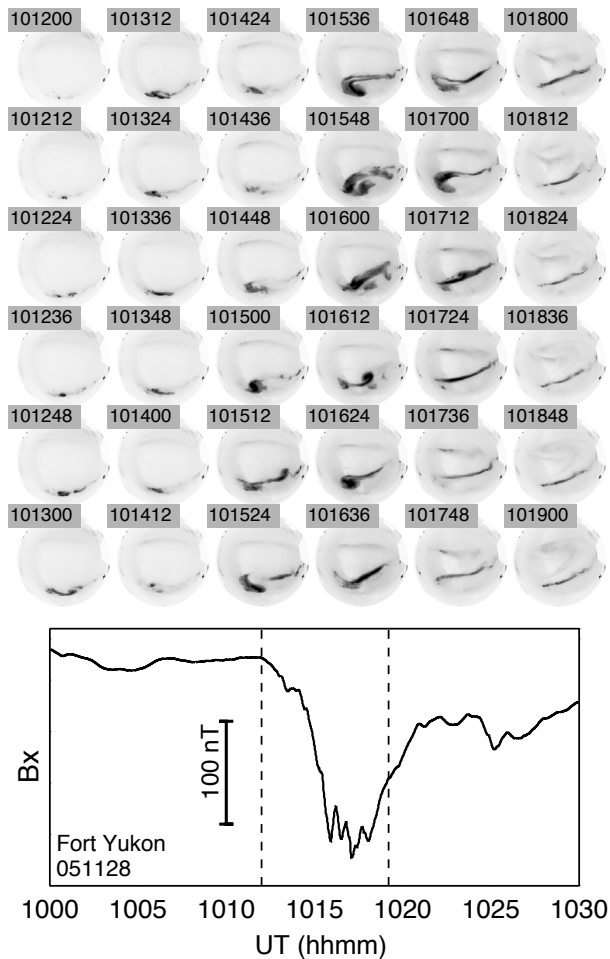


**Fig. 4.** The negative H-bay associated with the pseudobreakup is clearly evident in the Fort Yukon magnetometer data. Images are from the Fort Yukon THEMIS ASI, separated by 12 seconds, and spanning the time range indicated by the two vertical dashed lines. UT for each image shown is indicated in the grey boxes and is given in hhmmss format.

### 3. Summary

This event was a pseudobreakup that does not appear to have been triggered by changes in the interplanetary medium. The event unfolded in just over ten minutes. Seen in ASI data, the event began with a brightening that spread rapidly along the pre-existing arc. While this azimuthal expansion was occurring, there was a well-defined wave form in the brightness along the arc that grew in intensity and also propagated rapidly eastward. The azimuthal expansion stalled for 90 seconds or more, and then proceeded further with the brightening extending across the entire FOV of the Whitehorse ASI over the next two minutes. While this expansion phase was unfolding, there was a pre-existing arc poleward of the breakup arc that remained undisturbed until at least five minutes after the initial brightening.

As discussed in the Introduction, there is intense debate over what macroscale instability leads to the expansive phase onset. While the data that we present here in this paper is only for

one event, and utilizes data from only two of the soon to be 20 THEMIS white light ASIs, it brings forward some interesting points. First of all, the pre-existing arc that brightened was equatorward of another pre-existing arc. That arc remained undisturbed for at least five minutes while the expansive phase is clearly unfolding. Although we do not have proton auroral data available for this event, the onset arc was at only  $64^\circ$  magnetic latitude, and so in this event was likely embedded in the bright proton aurora (see the relevant discussion in the introduction). Further, the auroral brightening occurred at the same time as the negative H-Bay, and so it is compelling to associate it with CD in the inner CPS. Thus, if the CD was initiated by the braking of a fast flow that was in turn launched by mid-tail reconnection, then all of the dynamics leading up to the CD created no auroral signatures that were detectable by the THEMIS ASIs, and had no detectable effect on the second, poleward arc. Thus, subject to the caveats discussed below, these observations are (in our opinion) more consistent with the CD rather than the NENL model.

The azimuthal propagation of the beads that formed during the first few minutes of the brightening point to the growth of a wave in the CPS magnetically conjugate to the arc. Although this is only one event, the azimuthal structuring and propagation were very clear, and occurred during the first 1.5 minutes of the brightening, and commensurate with the formation of the negative H-bay. It is thus compelling to associate these waves with an instability that leads to a decrease in the cross-tail current. In a recent study, [11] used Cluster observations to show the presence of eastward propagating waves during the initial several minutes of expansive phase onset, and argued that these waves were a manifestation of ballooning mode instability. Those authors went on to argue that the azimuthal structuring would lead to filamentation of the perpendicular current in the current sheet, and via  $\nabla \cdot \vec{J} = 0$  would generate periodic and eastward propagating filaments of parallel current. This could account for the bead-like structuring of the breakup arc shown in Figure 5.

The initial brightening occurred in the FOV of the Fort Yukon ASI. The brightening rapidly expanded azimuthally until it was in the FOV of the Whitehorse ASI (we have no images from west of Fort Yukon so we do not know how far expansion went beyond the western edge of the FOV of the imager). At that time, the azimuthal expansion stalled, only to pick up again several minutes later. Our interpretation of this is that the instability that gave rise to the eastward propagating structures discussed in the previous paragraph formed virtually instantaneously (i.e., in less than 30 seconds) in an azimuthally extended but radially localized region in the CPS. Again, in our view, this region in which the initial instability formed was magnetically conjugate to the part of the arc that initially brightened. It is interesting to note that a separate study found that the radial and azimuthal extent of the initial dispersionless injection region is azimuthally extended and radially limited in much the same way [15]. Further, that study also found that, on average, the initial dispersionless injection region forms outside of geosynchronous distance, most likely 8-10 Re from the Earth.

These results are obviously preliminary, and are subject to several important caveats. First, we have no idea what an auroral arc corresponds to in the magnetosphere. This is a tremendously troubling issue given our field's reliance on the

evolution of discrete aurora in studying the expansive phase onset. Second, in this particular case, we do not have some fundamentally important complementary observations that would allow us to place the two arcs in the Fort Yukon FOV in a better magnetospheric context. On the one hand, if we had good complementary proton auroral observations, then we would be able to place the breakup arc relative to the ionospheric footprint of the transition between dipolar and tail-like field lines (which is where we believe that arc maps to). On the other hand, if we had good 630 nm auroral “redline” observations, we would know where the open-closed boundary was relative to the poleward arc. This latter point would allow us to assess how strongly the lack of disturbance of that arc supports the notion that formation of a NENL and subsequent fast flows cannot have preceded this auroral breakup. Subject to these caveats, we assert that the data presented here supports the following conclusions for this event:

1. the breakup corresponded to CD in the inner CPS.
2. the CD was not triggered by fast Earthward flows.
3. the breakup was initiated by an instability that produced azimuthally propagating waves.
4. the initial instability formed in a radially localized but azimuthally extended region in the CPS.
5. our results are consistent with the CD rather than the NENL substorm model.

As we come into the THEMIS era, it is clear the the THEMIS ASI array will provide synoptic white light images with unprecedented spatial and temporal resolution. Future work along the lines of this study will involve the building up of a repertoire of events, comparing wavelengths and propagation with those predicted for magnetospheric waves and instabilities, and attempts to better constrain the mapping between the magnetosphere and ionosphere. Finally, we point out that we need to develop an understanding of what auroral arcs correspond to in the magnetosphere.

## Acknowledgements

Operational support for the THEMIS All-Sky Imager array is provided by NASA and the Canadian Space Agency. The Fort Yukon magnetometer is operated by the Alaska Geophysics Institute. The IMAGE WIC data was mapped to the northern hemisphere using a technique developed by Nikolai Ostgaard. We used NASA CDAWeb to survey complementary data referred to but not included in the paper.

## References

1. Baker, K. B., and S. Wing, A new magnetic coordinate system for conjugate studies at high latitudes, *J. Geophys. Res.*, *94*, 9139-9143, 1989.
2. Baker, D. N., T. I. Pulkkinen, V. Angelopoulos, W. Baumjohann, and R. L. McPherron, Neutral line model of substorms: Past results and present view, *J. Geophys. Res.*, *101*, 12975-13010, 1996.
3. Deehr, C. S., Ground-based optical observations of hydrogen emissions in the auroral substorm, *Proceedings of the Second International Conference on Substorms*, 229-XXXX, 1994.
4. Deehr, C., and D. Lummerzheim, Ground-based optical observations of hydrogen emission in the auroral substorm, *J. Geophys. Res.*, *106*, 33-44, 2001.
5. Friedrich, E., J. Samson, I. Voronkov, and G. Rostoker, Dynamics of the substorm expansive phase, *J. Geophys. Res.*, *106*, 13145-13164, 2001.
6. Liou, K., C.-I. Meng, A. T. Y. Lui, and P. T. Newell, On the relative timing of substorm onset signatures, *J. Geophys. Res.*, *104*, 22807-22819, 1999.
7. Lui, A. T. Y., Extended consideration of a synthesis model for magnetospheric substorms, in *Magnetospheric Substorms, Geophys. Monogr. Ser., Volume 64, Edited by J. R. Kan, T. A. Potemra, S. Kokobun, and T. Iijima*, pp 43-, AGU, Washington, DC, 1991.
8. Lui, A. T. Y., Current disruption in the Earth's magnetosphere: Observations and models, *J. Geophys. Res.*, *101*, 13067-13088, 1996.
9. Ohtani, S.-I., S. Kokobun, and C. Russell, Radial expansion of the tail current disruption during substorms: A new approach to the substorm onset region, *J. Geophys. Res.*, *96*, 3129-3136, 1991.
10. Ohtani, S.-I., F. Creutzberg, T. Mukai, H. Singer, A. T. Y. Lui, M. Nakamura, P. Prikryl, K. Yumoto, and G. Rostoker, Substorm onset timing: The DEcember 31, 1995, event, *J. Geophys. Res.*, *104*, 22713-22727, 1999.
11. A. Roux, O. Le Contel, D. Fintaine, P. Robert, P. Louarn, J. A. Sauvaud, and A. N. Fazakerley, Substorm theories and Cluster multi-point measurements, this issue.
12. Samson, J. C., L. R. Lyons, P. T. Newel, F. Creutzberg, and B. Xu, Proton aurora and substorm intensifications, *Geophys. Res. Lett.*, *19*, 2167-2170, 1992.
13. Shiokawa, K., W. Baumjohann, G. Harendel, G. Paschmann, J. F. Fennel, E. Friis-Christensen, H. Luhr, G. D. Reeves, C. T. Russell, P. R. Sutcliffe, and K. Takahashi, High-speed ion flow, substorm current wedge, and multiple Pi 2 pulsations, *J. Geophys. Res.*, *103*, 4491, 1998.
14. Spanswick, E., E. Donovan, R. Friedel, and A. Korth, Ground-based identification of dispersionless electron injections, submitted to *Geophys. Res. Lett.*, 2006.
15. Spanswick, E., E. Donovan, R. Friedel, and D. Danskin, The macroscale evolution of the substorm injection, this issue.
16. Voronkov, I., E. Donovan, J. Samson, and B. Jackel, Large-scale vortex dynamics in the evening and midnight auroral zone: Observations and simulations, *J. Geophys. Res.*, *105*, 18505-18518, 2000.
17. Voronkov, I., E. Donovan, and J. Samson, Observations of the phases of the substorm, *J. Geophys. Res.*, *108*, doi: 10.1029/2002JA009314, 2003.

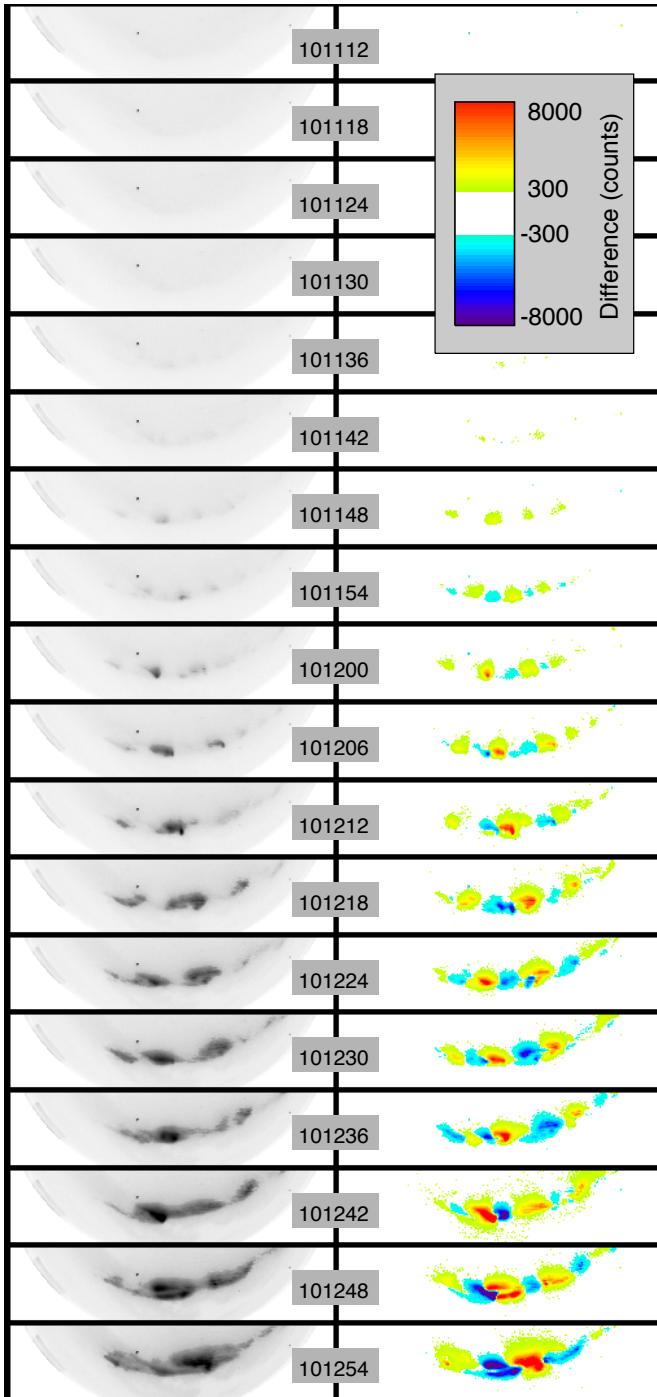


**Fig. 5.** The left column consists of partial Fort Yukon white light ASI images (roughly the bottom quarter of the image in each case) separated in time by 6 seconds with time increasing down on the plot. The time corresponding to each image is indicated in hhhmss format. The images go from 10:11:12 UT through 10:12:54 UT, and so span 1 minute and 42 seconds (as an aside, we note that the THEMIS ASIs will operate at a cadence of one image every three seconds). The right hand column consists of differences between successive images in false color. We have mapped a range of differences around zero to white so as to suppress the effects of CCD readout noise.

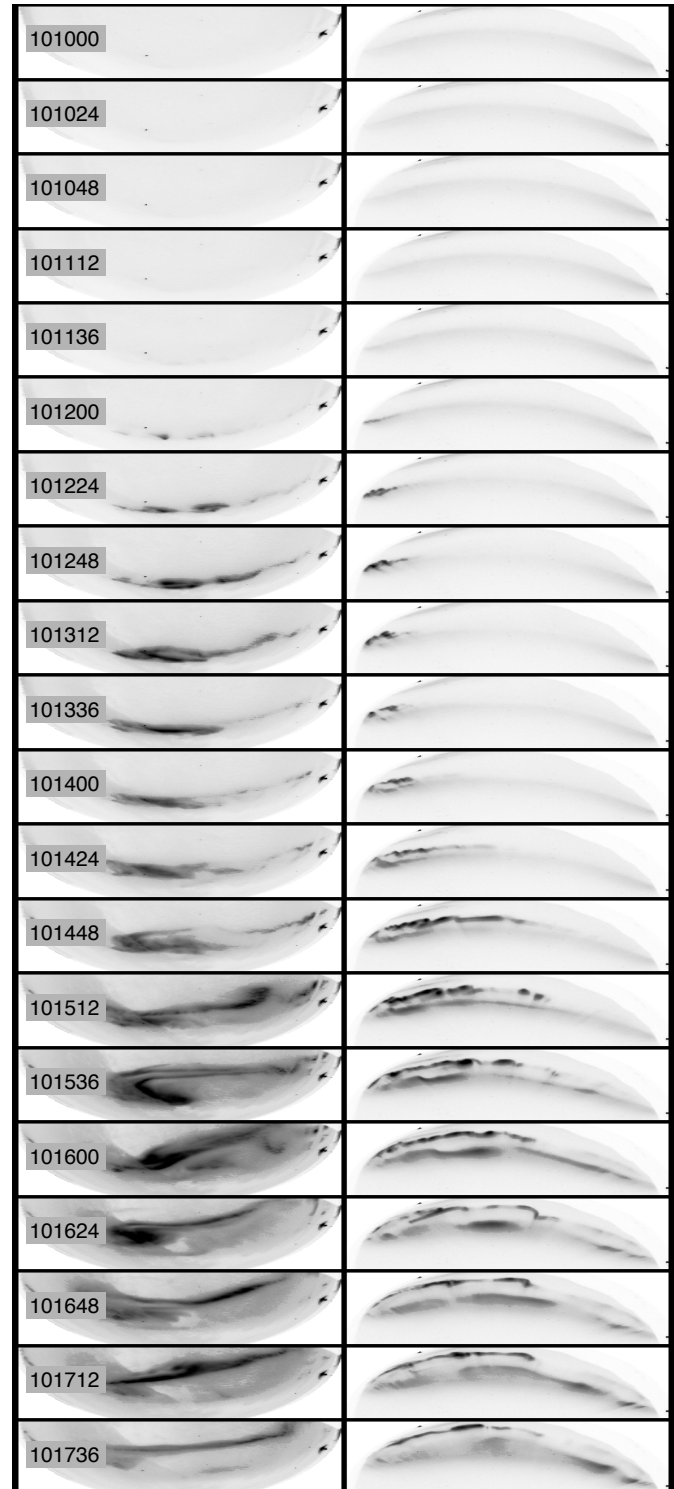


**Fig. 6.** The onset and subsequent expansion can be seen in the images collected by both the Fort Yukon and Whitehorse imagers (see Figure 3). The onset arc is in the southern part of the Fort Yukon field of view and the northern part of the Whitehorse field of view. In this figure, we show subsequent (time increasing downwards) partial images from the Fort Yukon (left) and Whitehorse (right) ASIs. The Fort Yukon partial images are roughly the bottom third of the field of view. The whitehorse images are roughly the top one third of the field of view.

# On the role of non-Maxwellian forms of distribution functions in the process of acceleration of auroral particles

N. O. Ermakova and E. E. Antonova

**Abstract:** Most theories of auroral particle acceleration are based on the suggestion of Maxwellian form of distribution function of accelerated particles. At the same time in most cases experimentally measured distribution functions are better described by kappa distribution. The formation of kappa distributions is connected with the action of relaxation processes in the turbulent magnetosphere in the conditions of the absence of collisions. Field-aligned acceleration of ionospheric ions leads to the appearance of particle population with plato-type distribution functions. The trapping of particles inside the region of acceleration also leads to the appearance of non-Maxwellian distributions. The model of auroral particle acceleration is developed taking into account the processes of modifications of distribution functions. The existence of conjugate regions of acceleration in the north and south hemispheres is suggested. It is shown that the kinetic treatment and the formation of non-Maxwellian distributions with reduced number of low energy particles gives the possibility to reanalyze the criteria of the formation of field-aligned jumps of electrostatic potential.

*Key words:* auroral acceleration, double layers, kappa distribution.

## 1. Introduction

Results of numerous observation at the auroral field lines demonstrate the existence of field-aligned potential drops (see the review [1]). However the processes of field-aligned potential drops formation are not clear till now. The most popular model is the model of the formation of double layers. Many theoretical studies of the processes of auroral particle acceleration were made under an assumption that the particle distribution functions have a Maxwellian form. Nevertheless, the collisionless character of magnetospheric plasma suggests the possibility of the existence of non-Maxwellian distribution functions.

Plasma sheet particle spectra can be approximated by a kappa distribution [2, 3]. The kappa distribution has the form

$$f(E) = \frac{n}{\pi^{3/2} \varepsilon_0^{3/2} k^{3/2}} \frac{\Gamma(k+1)}{\Gamma(k-1/2)} \cdot \left[ 1 + \frac{\varepsilon}{k\varepsilon_0} \right]^{-k-1}, \quad (1)$$

where  $\varepsilon$  is the particle energy,  $\varepsilon_0$  is the energy corresponding to the core thermal speed of the distribution,  $k$  is a parameter determining the high-energy power law index,  $n$  is the particle density,  $\Gamma$  is the gamma function. The kappa-function resembles a Maxwellian distribution at low energies, making a smooth transition into a power law tail at much higher energies. If the parameter  $k \rightarrow \infty$  Maxwellian distribution is formed

$$f(E) = \frac{n}{\varepsilon_0^{3/2} \pi^{3/2}} \exp \left\{ -\frac{\varepsilon}{\varepsilon_0} \right\}. \quad (2)$$

Hotter, more Maxwellian distributions may be identified as older in the sense of having undergone more velocity space diffusion.

The use of kappa distributions instead of Maxwellian distribution lead to the modifications of the theory of auroral particle acceleration. In this paper we consider the modifications of this theory by introducing the kappa distribution functions for population of hot magnetospheric electrons and ions.

## 2. Kappa distributions and classical double layer

The model of classical double layer considers the motion of cold current-carrying electrons and ions, together with warm electrons and ions, which are reflected by the double layer potential. The current-carrying electrons and ions are accelerated in opposite directions and gain energy from the double layer potential. The density of plasma in a double layer is much less, than outside of a double layer. Intensity of an electric field inside a layer is much larger then the intensity of a field in surrounding plasma. Occurrence of strong field-aligned fields in a double layer is caused by destruction of quasineutrality. The Poisson equation describes the distribution of potential  $\Phi$  inside the double layer (Gaussian system of units is traditionally used)

$$\nabla^2 \Phi = -4\pi e(n^i - n^e), \quad (3)$$

where  $n^i$ ,  $n^e$  are the ion and electron densities,  $e$  is the electron charge. In the one-dimensional double-layer all parameters depend only on one coordinate  $z$  along the magnetic field  $\mathbf{B}$  and  $d^2\Phi/dz^2 = 0.5(\Phi')^2/d\Phi$ ,  $\Phi' = d\Phi/dz$ . The equation (3) has the form

$$\frac{d}{d\Phi}(\Phi')^2 = -8\pi e [n^i(\Phi) - n^e(\Phi)] \quad (4)$$

Received 15 May 2006.

**N. O. Ermakova.** Skobeltsyn Institute of Nuclear Physics Moscow State University, Moscow, 119992, Russia

**E. E. Antonova.** Skobeltsyn Institute of Nuclear Physics Moscow State University, Moscow, 119992, Russia; Space Research Institute of RAS, Moscow, Russia

Necessary conditions for the formation of double layer with the potential drop  $\Phi_k$  have the form

$$\begin{aligned} n^e &> n^i & \text{if } \Phi \rightarrow 0 \\ n^i &> n^e & \text{if } \Phi \rightarrow \Phi_k \end{aligned} \quad (5)$$

The condition of quasineutrality outside the layer has the form

$$n^e(\Phi)_{\Phi=0} = n^i(\Phi)_{\Phi=0}, \quad n^e(\Phi)_{\Phi=\Phi_k} = n^i(\Phi)_{\Phi=\Phi_k}, \quad (6)$$

and the condition of electric field vanishing outside the layer

$$\int_0^{\Phi_k} [n^e(\Phi) - n^i(\Phi)] d\Phi = 0 \quad (7)$$

The distribution of charges and electric field inside the layer are determined by the analysis of particle motion inside the layer in the conditions of fixed distribution functions on the boundary of the layer. We shall consider laminar changes of potential (neglect the processes of distribution function relaxations inside the layer) and suggest the conservation of particle energy and magnetic moment.

Classical one-dimensional Langmuir double-layer suggests the existence of two cold and two hot populations of ions and electrons. If  $j_i$  is a beam of cold ions and  $j_e$  is a beam of cold electrons electron and ion concentrations are

$$\begin{aligned} n^{ec} &= j_e / [V_{0e}^2 + 2e\Phi/m_e]^{1/2}, \\ n^{ic} &= j_i / [V_{0i}^2 + 2e(\Phi_k - \Phi)/m_i]^{1/2} \end{aligned} \quad (8)$$

where  $V_{0e}$  and  $V_{0i}$  are electron and ion velocities before the acceleration,  $m_e$  and  $m_i$  are the electron and ion masses. It is considered that  $\Phi = 0$  on the cathode part of the layer,  $\Phi = \Phi_k$  on the anode part of the layer. If hot ions have Maxwell distribution function with temperature  $T_i$  and hot electrons with temperature  $T_e$

$$\begin{aligned} n^{ih} &= n_0^{ih} \exp[-e\Phi/T_i], \\ n^{eh} &= n_0^{eh} \exp[-e(\Phi_k - \Phi)/T_e]. \end{aligned} \quad (9)$$

The condition (5) then leads to the Bohm-Block criterion for cold beams (see [4])

$$\begin{aligned} m_e V_{0e}^2 &> T_i, \\ m_i V_{0i}^2 &> T_e. \end{aligned} \quad (10)$$

Using of kappa distribution function leads to the modification of the criterion (10). For kappa distribution of hot ions with parameters  $\varepsilon_0^{ih}$ ,  $k^{ih}$  and hot electrons with parameters  $\varepsilon_0^{eh}$ ,  $k^{eh}$

$$\begin{aligned} n^{ih} &= n_0^{ih} \left(1 + \frac{e\Phi}{k^{ih}\varepsilon_0^{ih}}\right)^{-k^{ih}+1/2}, \\ n^{eh} &= n_0^{eh} \left(1 + \frac{e(\Phi_k - \Phi)}{k^{eh}\varepsilon_0^{eh}}\right)^{-k^{eh}+1/2}, \end{aligned} \quad (11)$$

and relations (10) are changed to

$$\begin{aligned} m_e V_{0e}^2 &> \varepsilon_0^{ih} \left(1 - \frac{1}{k^{ih}}\right), \\ m_i V_{0i}^2 &> \varepsilon_0^{eh} \left(1 - \frac{1}{k^{eh}}\right). \end{aligned} \quad (12)$$

The comparison of relations (11) and (12) shows that the existence of non-Maxwellian tails of distribution functions leads to increase of ion and electron beam energies necessary for the formation of classical double layer. This limitation is stronger for more young distribution functions with smaller  $k$ .

The condition of the existence of stationary strong double layer has the form (Langmuir criterion):

$$j_e/j_i = \sqrt{m_i/m_e} \quad (13)$$

where  $j_e$ ,  $j_i$  are the electron and ion particle fluxes,  $m_e$ ,  $m_i$  are the electron and ion masses. This condition is strongly modified if we take into account the existence of trapped populations of particles and kappa-form of distribution functions.

### 3. Kappa distribution and kinetic double layer

The collisionless character of magnetospheric particle motion leads to the development of kinetic theory of double layer formation (see [5]). The existence of double layers in the conjugate hemispheres and the possibility of the existence of non-Maxwellian population of hot ions produced by depredated ion beams accelerated by field-aligned potential drops from both hemispheres are taken into account in [6]. A water bag distribution function have been selected for this ion population, trapped in the equatorial plane. The contribution of the population of secondary electrons trapped between field-aligned potential drop and the ionosphere was analyzed in [7]. It was shown that the existence of trapped populations of electrons and ions gives the possibility to overcome the limitations given by Bohm-Block criterion.

We consider the model of electron and ion acceleration for the case of the existence of 3 ion populations and 3 electron populations: cold ionospheric electrons, hot magnetospheric ions described by kappa distribution, trapped near the equatorial plane ions of ionospheric origin accelerated in the field-aligned potential drop with the value  $\Phi_k$ , cold electrons of ionospheric origin, hot electrons of magnetospheric origin described by kappa distribution, warm secondary electrons of magnetospheric origin trapped between the magnetic and electrostatic mirrors. The acceleration takes place in the region where  $B = B_c$ . All particles which can move up to ionospheric altitudes where  $B = B_k$  are absorbed. However the contribution of particles lost in the ionosphere is comparatively small if the acceleration takes place at great geocentric distances (as it is ordinarily observed). Therefore we shall neglect such particles in the first approximation and consider the potential jump leading to great changes of particle concentrations. We shall also consider that the criterion (5) is satisfied due to the existence of trapped populations of ions and electrons.

The condition (6) leads to the expression

$$\begin{aligned} n_0^{em} + n^{ei} \Big|_{\Phi=0} &= n_0^{im} + n_t^{ii} + n^{ii} \Big|_{\Phi=0} \\ n_0^{ei} + n^{em} \Big|_{\Phi=\Phi_k} &+ n_t^{em} = n_0^{ii} + n^{im} \Big|_{\Phi=\Phi_k} \end{aligned} \quad (14)$$

where the first upper indexes correspond to type of particle ( $e$  is for electrons,  $i$  is for ions), the second upper index corresponds to the type of population ( $i$  is for the ionospheric population,

$m$  is for the magnetospheric population), symbol  $t$  shows the trapped particle population.

Taking into account the conservation of energy  $\varepsilon$  and magnetic moment  $\mu$  in the process of acceleration, we shall use the electron and ion distribution functions in the form (1). Then

$$f d\mathbf{v} = \frac{n_0^m}{2} \frac{\Gamma(k^m + 1)}{\Gamma(k^m - 1/2)} \frac{B}{(\varepsilon_0^m)^{3/2} \pi^{1/2} (k^m)^{3/2}} \times \left[ 1 + \frac{\varepsilon}{k^m \varepsilon_0^m} \right]^{-k^m - 1} \frac{d\varepsilon d\mu}{(\varepsilon - e\Phi - B\mu)^{1/2}} \quad (15)$$

where  $k^m = k^{im}$  and  $\varepsilon_0^m = \varepsilon_0^{im}$  for hot magnetospheric ion population,  $k^m = k^{em}$  and  $\varepsilon_0^m = \varepsilon_0^{em}$  for hot magnetospheric electron population,  $e$  is the charge of particle.

The calculation of ion density inside the acceleration region leads to the expression

$$n^{im} = n_0^{im} \left( 1 + \frac{e\Phi}{k^{im} \varepsilon_0^{im}} \right)^{-k^{im} + 1/2} \quad (16)$$

Ion distribution is isotropic. Expression (16) gives  $n^{im}|_{\Phi=\Phi_k}$  if  $\Phi = \Phi_k$ .

The calculation of the density of hot magnetospheric electrons inside the double-layer leads to the expression

$$n^{em} = n_0^{em} \left\{ \left( 1 - \frac{e\Phi}{k^{em} \varepsilon_0^{em}} \right)^{-k^{em} + 1/2} - \frac{4}{3\pi^{1/2}} \frac{\Gamma(k^{em} - 1/2)}{\Gamma(k^{em} - 1)} \times \left( 1 - \frac{e\Phi}{k^{em} \varepsilon_0^{em}} \right)^{-k^{em} - 1} \left( \frac{e\Phi}{k^{em} \varepsilon_0^{em}} \right)^{3/2} \times {}_2F_1 \left( k^{em} + 1, \frac{3}{2}, \frac{5}{2}, \frac{e\Phi}{k^{em} \varepsilon_0^{em} - e\Phi} \right) - \frac{1}{k^{em}} \sqrt{\frac{e\Phi}{k^{em} \varepsilon_0^{em}}} \right\} \quad (17)$$

where we use the expression

$$\int_0^u \frac{x^{\mu-1} dx}{(1 + \beta x)^\nu} = \frac{u^\mu}{\mu} {}_2F_1(\nu, \mu, 1 + \mu, -\beta u).$$

Expression (17) gives  $n^{em}|_{\Phi=\Phi_k}$  if  $\Phi = \Phi_k$ .

Temperature of ionospheric ions is an order of magnitude lower than the multiplied on the electron charge field aligned potential drop. Therefore it is possible to neglect the term in the expression (14). We have for cold beam of ionospheric ions

$$n^{ii}|_{\Phi=0} = n^{ii}(\Phi_k, B_c) \left( \frac{m_i (V_0^{ii})^2}{2e\Phi_k} \right)^{1/2}, \quad (18)$$

where  $V_0^{ii}$  is the beam velocity.

Condition (7) gives

$$n_0^{em} k^{em} \varepsilon_0^{em} \left\{ \left( \frac{1}{k^{em} - 3/2} \left( 1 - \frac{e\Phi_k}{k^{em} \varepsilon_0^{em}} \right)^{-k^{em} + 3/2} - 1 \right) - \left( \frac{e\Phi_k}{k^{em} \varepsilon_0^{em}} \right)^{5/2} \times \frac{8}{15\pi^{1/2}} \left( 1 - \frac{e\Phi_k}{k^{em} \varepsilon_0^{em}} \right)^{-k^{em} - 1} \times {}_2F_1 \left( k^{em} + 1, \frac{5}{2}, \frac{7}{2}, \frac{e\Phi_k}{e\Phi_k - k^{em} \varepsilon_0^{em}} \right) - \frac{4}{3\pi^{1/2}} \frac{\Gamma(k^{em} - 1)}{\Gamma(k^{em} - 1/2)} \frac{1}{k^{em}} \left( \frac{e\Phi_k}{k^{em} \varepsilon_0^{em}} \right)^{5/2} \right\} + n_0^{ei} \frac{k^{ei} \varepsilon_0^{ei}}{3/2 - k^{ei}} \left\{ \left( 1 + \frac{e\Phi_k}{k^{ei} \varepsilon_0^{ei}} \right)^{-k^{ei} + 3/2} - 1 \right\} + \int_0^{e\Phi_k} n_t^{em}(\Phi, B_c) e d\Phi = n_0^{ii} (2e\Phi_k m_i)^{1/2} V_0^{ii} + \frac{n_0^{im} k^{im} \varepsilon_0^{im}}{k^{im} - 3/2} \times \left\{ \left( 1 + \frac{e\Phi_k}{k^{im} \varepsilon_0^{im}} \right)^{-k^{im} + 3/2} - 1 \right\} + \int_0^{e\Phi_k} n_t^{ii}(\Phi, B_c) e d\Phi \quad (19)$$

Analyzing (19) and comparing it with (13) it is possible to see that the condition of the existence of stationary strong double layer is greatly changed in the case of the double layer in the magnetic trap. It is interesting to mention that the appearance of such kind of structures leads to great jumps of plasma density.

## 4. Conclusions and discussion

The problem of the acceleration of auroral electrons by field-aligned potential drops is considered as a part of the problem of auroral particle acceleration and therefore as a part of the problem of magnetospheric substorm. The most popular model of such acceleration is the model of the formation of double layers [4–25]. But this problem in the majority of cases is analyzed in the suggestion of Maxwellian form of distribution functions. At the same time kappa distributions are formed in the collisionless magnetospheric plasma. Taktakishvili *et al.* [26] have shown that the results of INTERBALL/Tail probe observations of kappa distribution functions in the geomagnetic tail are well described by the process of acceleration by the inductive electric fields. This finding is supported by the results of [27]. Milovanov and Zelenyi [28] associate the origin of kappa distributions with the macroscopic ordering of the system. They prove that the canonical distribution corresponding to the Tsallis definition of entropy coincides with the kappa distribution. In accordance with [29] hotter, more Maxwellian distributions may be identified as older in the sense of having undergone more velocity space diffusion. Therefore it is quite interesting to reanalyze the conclusions of double-layer theories in the case of kappa distribution. We show that the real modifications appear as in the case of classical double layers as in the case of double layer in the magnetic trap. The later mainly leads to

drops of particle densities. The condition of the existence of stationary double layer is obtained in both cases. The obtained relations can be used in the analysis of the results of auroral particle observations during substorms.

## Acknowledgments

The research was supported by RFBR grant 05-05-64394-a and INTAS grant 03-51-3738.

## References

1. Paschmann, G., Haaland, S., and Treumann, R., Auroral plasma physics, *Space Sci. Rev.*, 103(1–4), 1–485, 2002.
2. Sarris, E. T., Krimigis, S. M., Lui, A. T. Y., Ackerson, K. L., Frank, L. A., and Williams, D. J., Relationship between energetic particles and plasmas in the distant plasma sheet, *Geophys. Res. Lett.*, 8(3), 349–352, 1981.
3. Christon, S. P., Williams, D. J., Mitchell, D. G. *et al.*, Spectral characteristics of plasma sheet ion and electron population during undisturbed geomagnetic conditions, *J. Geophys. Res.*, 94(10), 13,409–13,424, 1989.
4. Kan, J. R., Towards a unified theory of discrete auroras, *Space Sci. Rev.*, 31(1), 71–117, 1982.
5. Antonova, E. E., and Tverskoy, B. A., Nature of electron precipitation band of the inverted V type and of Harang discontinuity in the evening sector of the auroral ionosphere, *Geomagnetism and Aeronomy (English translation)*, 15(1), 85–90, 1975.
6. Antonova, E. E., Large-scale double layers, *Geomagnetism and Aeronomy (English translation)*, 19(5), 586–589, 1979.
7. Kan, J. R., and Lee, L. C., On the auroral double layer criterion, *J. Geophys. Res.*, 85(A2), 788–790, 1980.
8. Alfvén, H., and Carlqvist, P., Currents in the solar atmosphere and a theory of solar flares, *Solar Physics*, 1(2), 200–228, 1967.
9. Block, L. P., Potential double layers in the ionosphere, *Cosmic Electrodynamics*, 3(3), 352–376, 1972.
10. Carlqvist, P., On the formation of double layers in plasma, *Cosmic Electrodynamics*, 3(3), 377–388, 1972.
11. Carlqvist, P., On the physics of relativistic double layers, *Astrophysics and Space Science*, 87, 21–39, 1982.
12. Kan, J. R., Energization of auroral electrons by electrostatic shock waves, *J. Geophys. Res.*, 80(16), 2089–2095, 1975.
13. Kan, J. R., Lee, L. C., and Akasofu, S. I., Two-dimensional potential double-layers and discrete aurora, *J. Geophys. Res.*, 84(A8), 4305–4315, 1979.
14. Swift, D. W., A mechanism for energizing electrons in the magnetosphere, *J. Geophys. Res.*, 70(13), 3061–3073, 1965.
15. Swift, D. W., On the formation of auroral arcs and acceleration of auroral electrons, *J. Geophys. Res.*, 80(16), 2096–2108, 1975.
16. Swift, D. W., Steinback-Nielsen, H. C., and Hallinan, T. Y., An equipotential model for auroral arcs 1, *J. Geophys. Res.*, 81(22), 3931–3934, 1976.
17. Swift, D. W., An equipotential model for auroral arcs 2. Numerical solutions, *J. Geophys. Res.*, 81(22), 3955–3943, 1976.
18. Goertz, C. K., and Joyce, G., Numerical simulation of the plasma double layers, *Astrophys. Space Sci.*, 32(1), 165–173, 1975.
19. Hubbard, R. F., and Joyce, G., Simulation of auroral double layers, *J. Geophys. Res.*, 84(A8), 4297–4304, 1979.
20. Singh, N., and Thiemann, H., Some features of inverted V events as seen from simulated double layers, *Geophys. Res. Lett.*, 75(10), 737–740, 1980.
21. Sato, T., and Okuda, H., Ion-acoustic double layers, *Phys. Rev. Lett.*, 44(11), 740–743, 1980.
22. Sato, T., and Okuda, H., Numerical simulations on ion acoustic double layers, *J. Geophys. Res.*, 86(A5), 3357–3368, 1981.
23. Singh, N., and Schunk, R. W., Dynamical features of moving double layers, *J. Geophys. Res.*, 87(A5), 3561–3586, 1982.
24. Borovsky, J. E., Joyce, G., Numerically simulated two-dimensional auroral double layers, *J. Geophys. Res.*, 88(A4), 3116–3126, 1983.
25. Bespalov, P. A., and Mizonova, V. G., Charged particle acceleration by electrostatic turbulent structures in regions with field-aligned electric current in the auroral magnetosphere, *Phys. Chem. Earth*, 26(1–3), 113–119, 2001.
26. Taktakishvili, A. L., Zelenyi, L. M., Lutsenko, V. N., Kudela, K., On the spectra of energetic particles in the tail of the magnetosphere of the Earth, *Kosm. Issl.*, 36(2), 282–291, 1998.
27. Pisarenko, N. F., Budnik, E. Yu., Ermolaev, Yu. I., Kirpichev, I. P., Lutsenko, V. N., Morozova, E. I., Antonova, E. E., The ion differential spectra in outer boundary of the ring current: November 17, 1995 case study, *J. Atmosf. and Solar-terrestrial Phys.*, 64(5–6), 573–583, 2002.
28. Milovanov, A. V., and Zelenyi, L. M., Functional background of the Tsallis entropy: coarse-grained systems and kappa distribution functions, *Nonlinear Processes in Geophysics*, 7(2), 211–221, 2000.
29. Collier, M. R., Evolution of kappa distributions under velocity space diffusion: A model for the observed relationship between their spectral parameters, *J. Geophys. Res.*, 104(A12), 28,559–28,564, 1999.

# Observations of tail dynamics using ground and space based instruments during a period of multiple substorm events

C. Forsyth, M. Lester, S.E. Milan, A. Grocott, H.U. Frey, E. Lucek, H. Reme, and J. Watermann

**Abstract:** We present initial observations from an ongoing investigation into the dynamics of the magnetotail during a period of multiple substorms. The investigation coordinates data from ground and space-based instruments including the Cluster and IMAGE spacecraft, SuperDARN and ground magnetometers during the period 00:00UT to 05:00UT on 25th August, 2003. The first substorm expansion phase, which is preceded by two pseudo-breakups at 00:38UT and 00:57UT, takes place between 01:11UT and 01:50UT during which time IMAGE WIC(FUV) data for the Southern auroral oval shows enhanced auroral activity almost solely in the post-midnight sector and the occurrence of auroral streamers within the auroral bulge. SuperDARN map potential analysis shows a flow diversion with a northern hemisphere footprint that is conjugate to a southern hemisphere auroral streamer. During this time, Cluster CIS and FGM instruments detect the passage of under-populated flux tubes, or plasma bubbles, and a field rotation event, discussed as a flux rope. These observations agree with current predictions on the relationship between streamers and under-populated flux tubes in the tail from the Chen and Wolf model.

*Key words:* Substorms, Cluster, Magnetotail Dynamics, Auroral Streamers, Under-populated flux tubes.

## 1. Introduction

Magnetotail dynamics and their auroral and ionospheric manifestations have been the subject of much debate since Akasofu [1] published his seminal paper on auroral substorms. Now, with space based instrumentation, such as that onboard the Cluster and IMAGE satellites, and ground based instrument networks, such as SuperDARN and various magnetometer arrays, we can relate auroral and ionospheric signatures to the dynamic morphology of the magnetotail.

During the interval between 00:00UT and 05:00UT on the 25th August, 2003, the Cluster spacecraft were near apogee, downtail, in the post-midnight sector of the southern plasma sheet, the IMAGE spacecraft was monitoring the Southern auroral zone and the magnetometers of the IMAGE, Greenland and CANOPUS chains and radars of SuperDARN were passing through the night sector. During this interval, multiple substorm onsets and auroral enhancements were detected by these instruments. One of these onsets showed North-South auroral forms, or streamers [12], in the IMAGE WIC(FUV) and Greenland magnetometer data and under-populated flux tubes, or plasma bubbles, in the Cluster CIS and FGM data. Another

was preceded by a quasi-periodic  $B_x$  component in the Cluster FGM data.

## 2. Observations

### 2.1. Interval Overview

#### 2.1.1. IMAGE WIC(FUV)

During the interval, IMAGE WIC(FUV) [7, 8] monitored the Southern auroral zone, with the optimum field of view (i.e. time before auroral oval was at the edge of the field of view) being before 03:00UT. Three substorms were identified based on the following criteria; duration ( $>10$ min), poleward expansion ( $>10^\circ$  magnetic latitude), extension ( $>2$ hrs magnetic local time). These substorms began at 01:17UT, 02:29UT and 04:17UT. Three further events (enhancements) were observed, although we do not classify these as substorms since one or more of the criteria were not met. These enhancements began at 00:38UT, 00:57UT and 01:50UT.

#### 2.1.2. Cluster

The Cluster spacecraft were located near apogee in the Southern post-midnight sector throughout the interval, during which time the Fluxgate Magnetometer (FGM, [3]) (Fig. 1) measured two large ( $>10$ nT) decreases in the field strength, which was dominated by the  $B_x$  component throughout the interval. The first of these decreases begins at 01:15UT and lasts until 02:00UT and coincides with the first substorm expansion phase seen in the IMAGE WIC(FUV) data. During this event, the field strength becomes very close to 0nT at 01:27UT. The second major field decrease starts at 03:50, with the  $B_x$  component appearing to be quasi-periodic until 04:25UT. During this substorm the field drops by approximately 10nT to a level below that predicted by the Tsyganenko T96 field model.

Received 12 May 2006.

**C. Forsyth, M. Lester, S.E. Milan, and A. Grocott.** Dept. Physics & Astronomy, University of Leicester, Leicester, UK

**H.U. Frey.** Space Sciences Laboratory, University of California, Berkeley, California, USA

**E. Lucek.** University of London, Imperial College of Science, Technology & Medicine, Blackett Lab., London, UK

**H. Reme.** Centre d'Etude Spatiale Des Rayonnements, Toulouse, France

**J. Watermann.** Atmosphere Space Research Division, Danish Meteorological Institute, Copenhagen, Denmark

The Cluster Ion Spectrometer (CIS, [10]) showed drops in ion density (not shown) between 00:45UT-01:15UT and 02:45UT-04:00UT indicating that Cluster moved from the plasma sheet boundary layer (PBSL) [4] into the tail lobes. Preceding and following Cluster passing into the lobes, there is a slight increase in the plasma density above the level seen in the PBSL, indicating that Cluster briefly passed into the central plasma sheet.

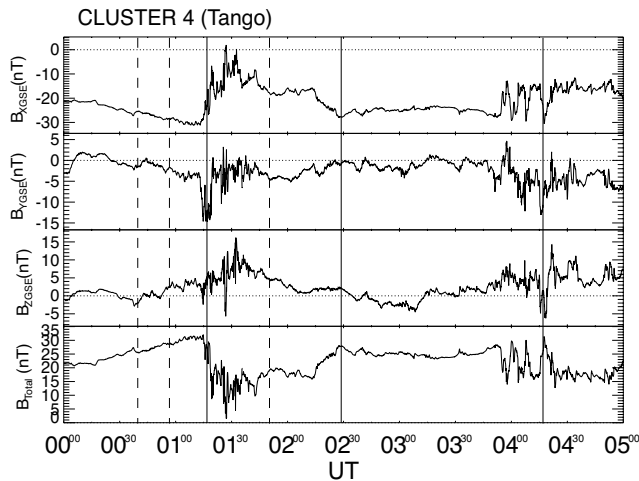


**Fig. 1.** Cluster FGM data from 25th August, 2003 (00:00UT-05:00UT). The  $B_x$ ,  $B_y$ ,  $B_z$  components in GSM coordinates and  $B_{Total}$  component are shown from Cluster 4 (Tango). Dashed lines indicate enhancements from the WIC(FUV) data and solid lines represent expansion phase onset from the same data.

### 2.1.3. Ground Magnetometers

The magnetometers of the CANOPUS [13], IMAGE [16] and Greenland (e.g. [9]) chains pass through the night sector during the 5hr interval. The  $B_x$  (northward) components of the magnetometers give an indication of substorm related electrojet activity over the various chains at different times. The Sodankyla (SOD) station of the IMAGE chain shows a magnetic bay of 400nT (Fig. 2) occurring in conjunction with the first substorm expansion phase onset as seen in the IMAGE WIC(FUV) data. The Scoresbysund (SCO) station in the Greenland East chain shows three negative bays in the field of 500nT, 100nT and 500nT respectively that begin in conjunction with the respective substorms. The Narsarsuaq (NAQ) station of the Greenland West chain measures negative bays of 200nT, and 150nT in association with the first enhancement and the first substorm respectively. The Gillam (GILL) station of the CANOPUS chain shows a 400nT negative bay in conjunction with the second substorm and a 300nT negative bay starting 75mins before the last substorm.

## 2.2. Substorm 1: Post-midnight sector substorm

### 2.2.1. Ground Magnetometers

Previous work [2] has demonstrated that the passage of auroral streamers over ground magnetometer arrays relates to specific magnetic signatures; a minimum in  $B_z$  and a

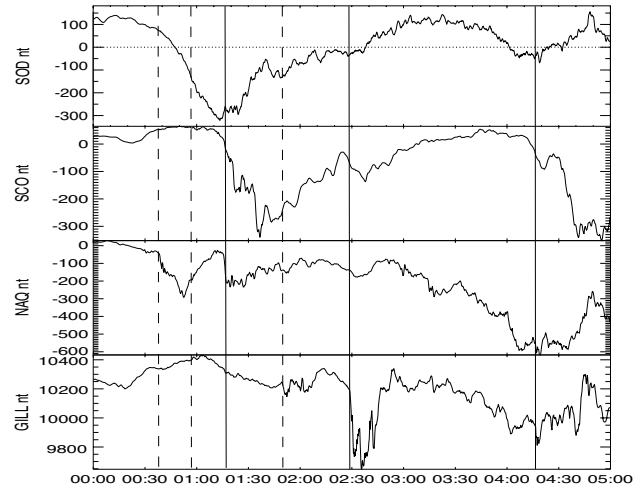


**Fig. 2.** Ground magnetometer data from 25th August, 2003 (00:00UT-05:00UT). The  $B_x$  (northward) component is shown from Sodankyla (IMAGE), Scoresbysund (Greenland East), Narsarsuaq (Greenland West) and Gillam (CANOPUS). Dashed lines indicate enhancements from the WIC(FUV) data and solid lines represent expansion phase onset from the same data.

sawtooth-like feature in  $B_y$ . Assuming that auroral disturbances in the southern hemisphere map to similar locations in the northern hemisphere, we find that the Ammassalik (AMK) and Narsarsuaq (NAQ) stations were closest to the auroral bulge formed during the substorm and in the vicinity of the auroral streamers.

The  $B_x$  (northward) components recorded by the Greenland magnetometer stations Ammassalik and Narsarsuaq (Fig. 3) show the first substorm expansion phase onset begins at 01:15UT, as indicated by the formation of a negative bay. The  $B_y$  component at both stations shows an increase followed shortly after by a drop to below 0nT. The interval between the maxima is 4-5mins, with a similar time for the interval between the minima. We note that the field feature at AMK has a form that is more like a sawtooth than the field at NAQ. The  $B_z$  (radially inwards) components show minima that coincide with the peaks in the  $B_y$  components at each station, however the Narsarsuaq station shows a further drop in the field that is coincident with the minima in the  $B_y$  component.

### 2.2.2. Cluster

At Cluster, the total field (Fig. 4 panel 6) begins to drop from 30nT at 01:15UT, dominated by the drop in the  $B_x$  component (Fig. 4 panel 3). The field remains in decline until 01:27UT, at which point the field begins to increase towards the Tsyganenko [15] model field level, indicated by the dashed line. Between 01:24UT and 01:26.30UT the  $B_z$  component (Fig. 4 panel 5) increases by 5nT and the  $B_x$  component shows deviation away from its decline by 10nT, with both components showing a brief spike back to the expected level at 01:26UT. Between 01:26.30UT and 01:27.30UT all of the field components changed direction and the angle of the field in the XZ plane (Fig. 4 panel 7) rotated through over 180° before rapidly returning to its previous direction.

The Cluster Ion Spectrometer CODIF instrument on Cluster 4 shows that the density (Fig. 4 panel 2) throughout varies

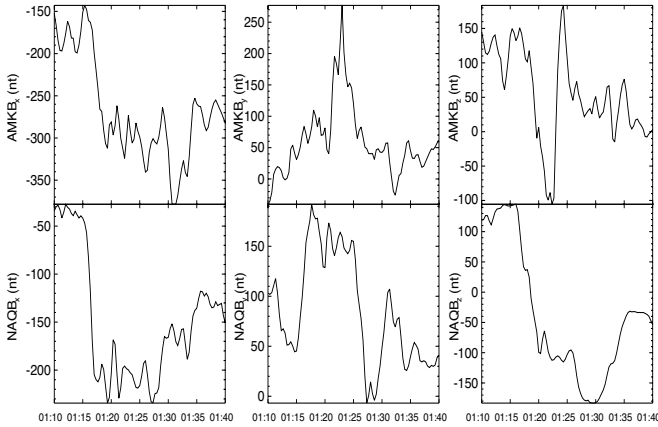


**Fig. 3.** Ground magnetometer data from 25th August, 2003 (01:10UT-01:40UT). The  $B_x$  (northward),  $B_y$  (westward) and  $B_z$  (radially inward) component are shown from Ammassalik (top line) and Narsarsuaq (bottom line) of the Greenland East and West chains respectively.

about  $0.25\text{cm}^{-3}$ . There are drops in the density to approximately  $0.1\text{cm}^{-3}$  that coincide with the increases in the  $B_z$  components as seen in the FGM data. There are also decreases, lasting approximately 1min, at 01:16UT and 01:17UT down to  $0.1\text{cm}^{-3}$  and  $0.01\text{cm}^{-3}$ . This indicates that Cluster was in the plasma sheet throughout the substorm although there were times when Cluster was in an area of much lower plasma density.

### 2.2.3. SuperDARN

A map potential analysis [11] of the line of sight velocities measured by the northern hemisphere SuperDARN radars provides the global ionospheric flows during the substorm (Fig. 5). From 01:18UT to 01:30UT, there is a diversion of the flow in the 01MLT sector that moves downwards and approximately coincides with the auroral form as seen in the southern hemisphere. This may indicate a flow signature of the auroral streamer for the northern hemisphere. Radar scatter for the southern hemisphere was very weak, hence the map potential flows are dominated by the model flows and consequently are not used further.

### 2.2.4. IMAGE WIC(FUV)

At 01:18UT, IMAGE WIC(FUV) images show that an auroral bulge had formed and extended through 5hrs of magnetic local time and had a width of approximately  $10^\circ$  of magnetic latitude at its widest point. Prior to this, the auroral bulge had expanded from an active auroral oval, although its intensity had been constant. At this time, IMAGE WIC(FUV) shows that the bulge intensity increased considerably, indicating substorm expansion phase onset. The bulge then expanded polewards, reaching a maximum poleward excursion at 01:42UT, when the majority of the poleward edge of the bulge had reached  $-87^\circ$  (magnetic latitude).

From 01:20UT (Fig. 6), there are structured areas of enhanced intensity within the auroral bulge. These enhancements stretch across approximately  $7^\circ$  of magnetic latitude of the auroral bulge and lie approximately along the lines of magnetic longitude. One structure began in the 23MLT sector, moved to

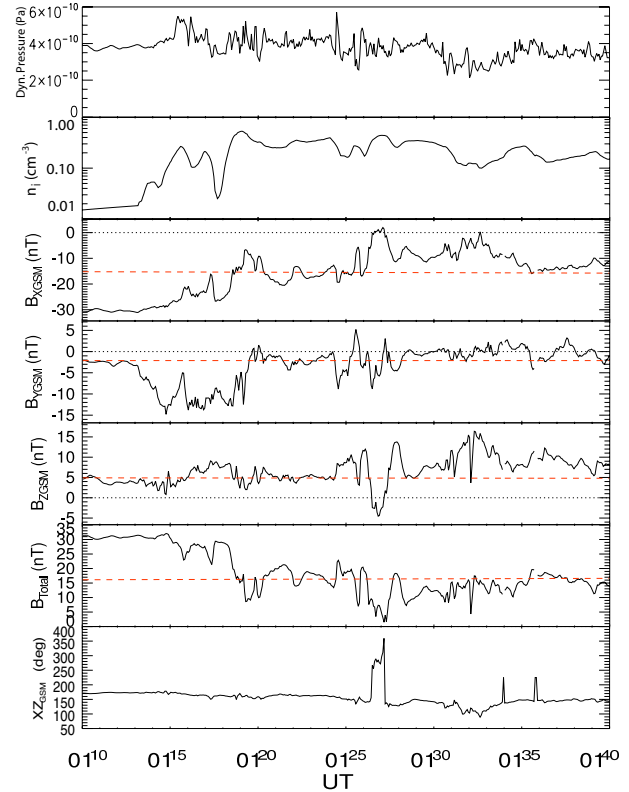


**Fig. 4.** Cluster CIS and FGM data from 25th August, 2003 (01:10UT-01:40UT) from Cluster 4 (Tango). The dynamic pressure is shown (panel 1), along with total ion density measured by the CIS instrument and the  $B_x$ ,  $B_y$ ,  $B_z$  components in GSM coordinates and  $B_{Total}$  component measured by the FGM instrument. The dashed line indicates the Tsyganenko [15] model field level

the midnight meridian at 01:22UT and then propagated westwards until it was absorbed into the background auroral oval on the 23MLT meridian. A second structure began near the 01MLT meridian and moved mostly downwards throughout the interval, although its termination cannot be determined accurately due to its proximity to the field of view of the spacecraft.

## 3. Discussion

We have shown data from a period of three substorm events, as identified by the IMAGE WIC(FUV) instrument, two of which are seen by Cluster and all of which are seen in various ground magnetometer chains. We shall now comment on the ionospheric and tail signatures from the first event.

Auroral images of the southern auroral oval from the IMAGE WIC(FUV) show that during the substorm expansion phase there was significant structure within the auroral bulge. These structures have a north-south form and can be interpreted as being auroral streamers. Their presence in the north cannot be directly observed due to the positions of the various auroral imaging spacecraft and all-sky camera data being limited by the northern hemisphere summer. Using the SuperDARN radars of the northern hemisphere and comparing this

to the IMAGE WIC(FUV) data, we are able to infer flow signatures that indicate that auroral streamers are present in the northern hemisphere and move dawnwards over the Greenland magnetometer chain during the substorm.

Intervals of lower ion density, stronger magnetic fields and constant plasma pressure in the magnetotail are the signatures of an under-populated flux tubes ([14] and references therein). During the substorm expansion phase, the plasma ion pressure is dominated by the ion density and hence the drops in plasma density represent drops in plasma pressure. At 01:25 there is a significant drop in plasma density and a corresponding increase in  $B_z$  at Cluster. The plasma pressure (Fig. 4 panel 1) shows little variation during this time. This indicates that Cluster detected an under-populated flux tube, or plasma bubble. Furthermore, comparing the FGM data from the four Cluster spacecraft seems to indicate that the bubble is travelling in a dawnwards direction.

The ground magnetic signature of auroral streamers has been described [2] as a sawtooth-like  $B_y$  component and a minimum in the  $B_z$  component coinciding with the maximum in  $B_y$ . The signatures seen in the ground magnetometers are similar to this description, although not as well defined. However, coupling this with the southern hemisphere auroral data, which shows definite structures in the southern auroral bulge, it is reasonable to conclude that there were similar north-south auroral forms in the northern hemisphere.

The Tsyganenko T96 model indicates that the footprint of Cluster 4 is in the vicinity of AMK during the interval, and comparison of the ground magnetometer data and Cluster FGM and CIS data shows that there is a 4min delay between the start of the signature at AMK and the detection of the under-populated flux tube at Cluster. The Tsyganenko model-based Cluster footprint moves by up to 15min MLT in a random motion between the successive images from the IMAGE WIC(FUV) instrument, indicating that during the substorm period the footprint location is variable, but also that there are limitations to the model during such periods. As the footprint of Cluster is always east of AMK during this interval, and the Cluster FGM data shows that the plasma bubble is moving eastwards, it is not unreasonable to suggest that the ground and space signatures are from one and the same feature, i.e. that the auroral streamer is closely associated with the plasma bubble. Chen and Wolf [5] predicted that under-populated flux tubes would cause a localised current wedge and Amm et al. [2] showed that under a westward moving streamer, the predicted current system from this localised current wedge matched the observed currents.

The rotational field feature seen in the FGM data at 01:26.30UT is associated with the low field event. Comparing the field angle and the field magnitude (Fig. 4) indicates that the field strength is much lower during this rotation and appears to show no gradual change between the low and high field states. This suggests that the rotation is due to some magnetic structure, possibly a plasmoid or flux rope, which moves over the spacecraft. A comparison of magnetic field data at 4s-resolution from the individual Cluster spacecraft indicates that the structure passes partially over the constellation in an Earthwards direction, then changes direction and moves tailwards.

## 4. Conclusion

Data from IMAGE WIC(FUV), SuperDARN and the Ammassalik magnetometer indicate the dawnward propagation of an auroral streamer during the substorm expansion phase between 01:15UT and 01:45UT on the 25th August, 2003. Using the Tsyganenko T96 model, the footprint of Cluster 4 (Tango) is mapped to the ionosphere in the vicinity, but dawnwards, of Ammassalik. In the Cluster FGM and CIS data, the signature of a dawnward moving under-populated flux tube can be seen shortly after the streamer's passage in the ionospheric data. These observations match the prediction of Amm et al. [2] that the current system within the auroral streamers, and hence the streamers themselves, are the ionospheric manifestation of under-populated flux tubes.

Data from Cluster indicates that shortly after the passage of the under-populated flux tube there is a further structure observed and that this structure has a low magnetic field that rotates through  $>180^\circ$  as the structure passes over the spacecraft. Analysis of the 4s-resolution FGM data shows that the structure is initially moving Earthwards, then moves tailwards. We suggest that this structure is a plasmoid or flux rope, but that the whole of the structure is not seen by Cluster. We also suggest that this structure is independent of the under-populated flux tube, given that this structure is seen to pass Cluster both Earthwards and tailwards, whereas the under-populated flux tube is seen only to move Earthwards.

*Acknowledgements* The authors thank the Canadian Space Agency for supplying the CANOPUS magnetometer data, the PIs for the SuperDARN radars for data from leading to the presented data, the Finnish Meteorological Institute and those institutes that maintain the IMAGE magnetometer array for supplying the IMAGE magnetometer data, and to CDAWEB for providing IMAGE WIC(FUV) data. The authors acknowledge and thank O.Amm for useful discussions on the data presented. C. Forsyth is funded by PPARC grant PPA/S/S/2005/04156. M.Lester, S.E.Milan and A.Grocott are funded by PPARC grant PPA/G/0/2003/00013.

## References

1. Akasofu, S., The development of the auroral substorm *Planetary and Space Science*, 12, 273-282, 1964
2. Amm, O., Pajunpaa, A., Brandstrom, U., Spatial distribution of conductances and currents associated with a north-south auroral form during a multiple substorm period, *Annales Geophysicae*, 17, 1385-1396, 1999.
3. Balogh, A., Dunlop, M. W., Cowley, S. W. H., Southwood, D. J., Thomlinson, J. G., Glassmeier, K. -H., Musmann, G., Lühr, H., Buchert, S., Acuña, M. H., Fairfield D. H., Slavin, J. A., Riedler, W., Schwingenschuh, K., and Kivelson, M. G., The Cluster magnetic fields investigation *Space Science Review*, 79, 65-91, 1997.
4. Baumjohann, W., Paschmann, G., Scokopke, N., Cattell, C. A., and Carlson, C. W., Average ion moments in the plasma sheet boundary layer *Journal of Geophysical Research*, 93, 11507-11520, 1988.
5. Chen, C. X., Wolf, R. A., Interpretation of High-Speed Flows in the Plasma Sheet *Journal of Geophysical Research*, 98, 21409-21419, 1993.

6. Greenwald, R. A., Baker, K. B., Dudeney, J. R., Pinnock, M., Jones, T. B., Thomas, E. C., Villain, J. -P., Cerisier, J. -C., Senior, C., Hanuise, C., Hunsucker, R. D., Sofko, G., Koehler, J., Nielson, E., Pellinen, R., Walker, A. M. D., Sato, N., and Yamagishi, H., DARN/SuperDARN: A global view of the dynamics of high-latitude convection *Space Science Review*, 71, 761-796, 1995.
7. Mende, S. B., Heeterds,H., Frey H. U., Lampton, M., Geller, S. P., Habraken, S., Renotte, E., Jamar, C., Rochus, P., Spann, J., Fuselier, S. A., Gerard, J., -C., Gladstone, R., Murphree, S., and Cogger, L., Far ultraviolet imaging from the IMAGE spacecraft 1. System design *Space Science Review*, 91, 243-270, 2000a.
8. Mende, S. B., Heeterds,H., Frey H. U., Lampton, M., Geller, S. P., Abiad, R., Siegmund, O. H. W., Tremsin, A. S., Spann, J., Dougani, H., Fuselier, S. A., Magoncelli, A. L., Bumala, M. B., Murphree, S., and Tronsden, T., Far ultraviolet imaging from the IMAGE spacecraft 2. Wideband FUV imaging *Space Science Review*, 91, 271-285, 2000b.
9. Popov, V. A., Papitashvili, V. O., and Watermann, J. F., Modeling of equivalent ionospheric currents from meridian magnetometer chain data *Earth Planets Space*,53, 129-137, 2001.
10. Rème, H., Bosqued, J. -M., Sauvaud, J. A., Cros, A., Dandouras, J., Aoustin, C., Bouyssou, J., Camus, Th., Cuvilo, J., Martz, C., M'Edale, J. L., Perrier, H., Romefort, D., Rouzard, J., d'Uston, C., Möbius, E., Crocker, K., Granoff, M., Kistler, L. M., Poppecki, M., Hovestadt, D., Klecker, B., Paschmann, G., Scholer, M., Carlson, C. W, Curtis, D. W., Lin, R. P., McFadden, J. P., Formisano, V., Amata, E., Bavassamp-Cattaneo, M. -B., Baldetti, P., Belluci, G., Bruno, R., Chionchio, G., Di Lellis, A., Shelley. E. G., Ghielmetti, A. G., Lennatsson, W., Korth, A., Rosenbauer, H., Lundin, R., Olsen, S., Parks, G. K., McCarthy, M., and Balsiger, H., The Cluster Ion Spectrometry (CIS) Experiment *Space Science Review*, 79, 303- 350, 1997.
11. Ruohoniemi, J.M. and Baker, K.B., Large-scale imaging of high-latitude convection with Super Dual Auroral Radar Network HF radar observations *Journal of Geophysical Research*, 103, 20797-20811, 1998.
12. Rostoker, G., Lui, A. T. Y., Anger, C. D., and Murphree, J. S., North-South structure in the midnight sector auroras as viewed by the Viking imager *Geophysical Research Letters*, 14, 407, 1987
13. Rostoker, G., Samson, J. C., Creutzberg, F., Hughes, T. J., McDiarmid, D. R., McNamara, A. G., Vallance Jones, A., Wallis, D. D., and Cogger, L. L., CANOPUS - A ground based instrument array for remote sensing the high latitude ionosphere during the ISTP/GGS program *Space Science Review*, 71, 743, 1995.
14. Sergeev, V., Angelopoulos, V., Gosling, J. T., Cattell, C. A., and Russell, C. T., Detection of localized, plasma depleted flux tubes or bubbles in the midtail plasm sheet, *Journal of Geophysical Research*, 101, 10817-10826, 1996.
15. Tsyganenko, N. A. and Stern, D. P., Modelling the global magnetic field of the large-scale Birkeland current systems *Journal of Geophysical Research*, 101, 27187-27198, 1996.
16. Viljanen, A. and Häkkinen, L., IMAGE magnetometer network. In: Satellite-Ground Coordination Sourcebook (eds. Lockwood, M., Wild, M. N., and Opgenoorth, H. J.) ESA Publications SP-1198, 111-117, 1997.

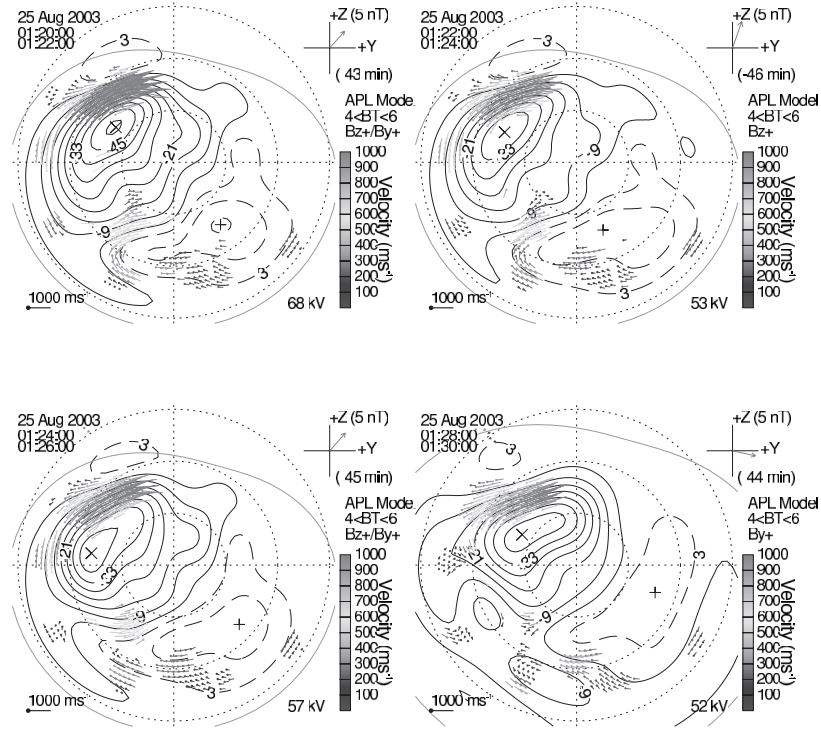


**Fig. 5.** SuperDARN map potential models from 25th August, 2003 (01:10UT-01:40UT). Flows in the post-midnight sector appear to divert around a feature that moves downwards. This coincides with the auroral streamer in the southern hemisphere IMAGE WIC(FUV) data.

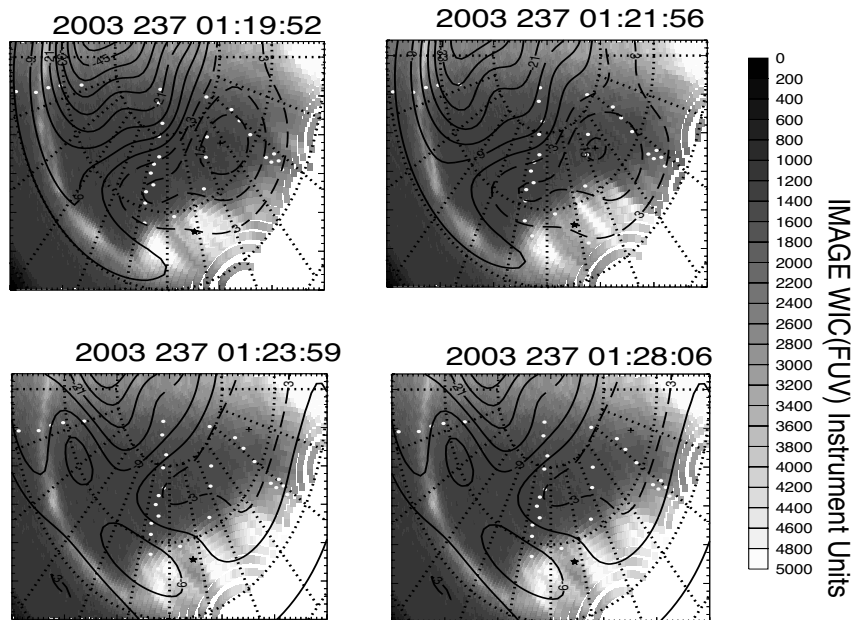


**Fig. 6.** IMAGE WIC(FUV) data mapped to magnetic coordinates. Timestamps above each image indicate the time of the IMAGE WIC(FUV) image. Contours from the SuperDARN map potential model are also shown. The black star represents the footprint of Cluster 4 using the Tsyganenko model [15]. The filled circles represent the locations ground magnetometers discussed.

# Substorm onsets as observed by IMAGE-FUV

H. U. Frey and S. B. Mende

**Abstract:** The FUV instrument observed more than 4000 substorm onsets during the 5.5 years of the IMAGE mission. About 2/3 were observed during the first 3 years in the northern hemisphere, while 1/3 were observed towards the end of the mission in the southern hemisphere. The locations of individual substorms are influenced by the external solar wind conditions, primarily the  $B_y$  and  $B_z$  components of the IMF. However, when averaged over all seasons and several years, the average substorm onset locations are the same in both hemispheres with respect to magnetic latitude and local time. This result signifies that the source region of substorms and the final onset location in the ionosphere, are primarily determined by the internal properties of the magnetosphere, and only secondarily influenced by external conditions.

*Key words:* Substorms, onset location, hemispheres.

## 1. Introduction

Substorms are one of the most outstanding signatures of the coupling between the magnetosphere and the ionosphere. They suddenly release hundreds of GW of power in the magnetotail, create intense plasma flows in the plasma sheet, build up strong field-aligned currents, excite almost all kinds of electromagnetic waves, and cause strong energetic particle precipitation that create bright and dynamic auroras in the ionosphere. Their temporal development is reasonably well described by the traditional picture of growth, onset, expansion, and recovery phases [1, 16]. What is still the topic of intense discussion are the exact temporal development of the single phases, the locations of phenomena in the magnetosphere, and the conjugacy of the auroral breakup. Two substorm theories propose different onset locations and sequences of events. The Current Disruption Model puts the onset location near Earth ( $< 8R_e$ ) with a current disruption that is quickly followed by the auroral breakup [14, 2]. The Near-Earth Neutral Line Model [9] places the substorm initiation at  $\approx 15 - 25R_e$  and the auroral breakup occurs later than in the Current Disruption Model when the fast flows break near the earth [22].

The first extensive study of seasonal and interplanetary magnetic field (IMF) effects on substorm onsets used 648 Polar UVI northern hemisphere observations in 1996-1997 shortly after the minimum of the past solar cycle [11]. The authors found systematic changes of lower onset latitude for  $B_x > 0$  or  $B_z < 0$  and increased latitudes for  $B_x < 0$  or  $B_z > 0$ , respectively. The onset longitude depends on season and IMF  $B_y$ . In summer, substorms tend to occur in the early evening, whereas in winter they tend to occur near midnight with an average difference of  $\approx 1$  hour of MLT. Onset locations also shift toward earlier local times for  $B_y > 0$  and toward midnight for  $B_y < 0$ . The authors also concluded that substorm onsets should not be conjugate.

This conclusion was confirmed in 2001 and 2002, when the Imager for Magnetopause-to-Aurora Global Exploration (IMAGE) satellite had its apogee in the Northern Hemisphere and the Polar spacecraft, owing to the apsidal precession of its or-

bit, reached higher altitudes in the Southern Hemisphere [19]. The two spacecraft offered a unique opportunity to study the aurora in the conjugate hemispheres simultaneously. Five substorm onsets were compared in the two hemispheres, which had asymmetric locations. The longitudinal displacement in one hemisphere compared with the other can be as much as 1.5 hours of local time. For southward IMF the hemispherical asymmetry in local time is strongly correlated with the IMF clock angle. These findings were interpreted as the magnetic tensions force acting on open magnetic field lines before re-connecting in the magnetotail. A similar asymmetry of substorms was found with SuperDARN radars [20]. Systematic asymmetries in the interhemispheric signatures of the auroral westward flow channels probably arose because the magnetic flux tubes were distorted at L shells passing close to the substorm dipolarisation region.

The FUV imager on the IMAGE spacecraft observed the northern hemisphere aurora between 2000 and 2002. Small subsets of its images were used to compare the behavior of the proton and electron aurora during the substorm expansion. The analysis of 78 winter substorms did not find any significant difference in the spatial distribution of the proton and electron onsets [6]. However, they found a strong anti-correlation between the onset latitude and the one-hour averaged solar wind dynamic pressure before the onset. The analysis of 91 substorms established that there are differences in the expansion of the electron and proton precipitation after onset [18]. The investigation of the high-latitude ionospheric flow during 67 substorms demonstrated the increase of the dawn-to-dusk transpolar voltage during the first minutes after substorm onset [21].

A much more extensive investigation determined all substorm onsets that were observed in the northern hemisphere by IMAGE-FUV between May 2000 and December 31, 2002 [5]. A total of 2437 substorms were found and their average onset location was 2300 hours MLT and  $66.4^\circ$  magnetic latitude. These values agreed reasonably well with previous reports though such investigations used smaller numbers of substorms and/or were limited to certain seasons [3, 7, 11, 6]. The published list of substorm onsets has so far been used in one published paper that investigated the location of auroral breakups in response to solar illumination and solar coupling parameters [24]. It was found that solar illumination and the related ionospheric conductivity have significant effects on the most

Received 10 May 2006.

H. U. Frey and S. B. Mende. University of California, Space Sciences Laboratory, Berkeley, CA 94720, USA.

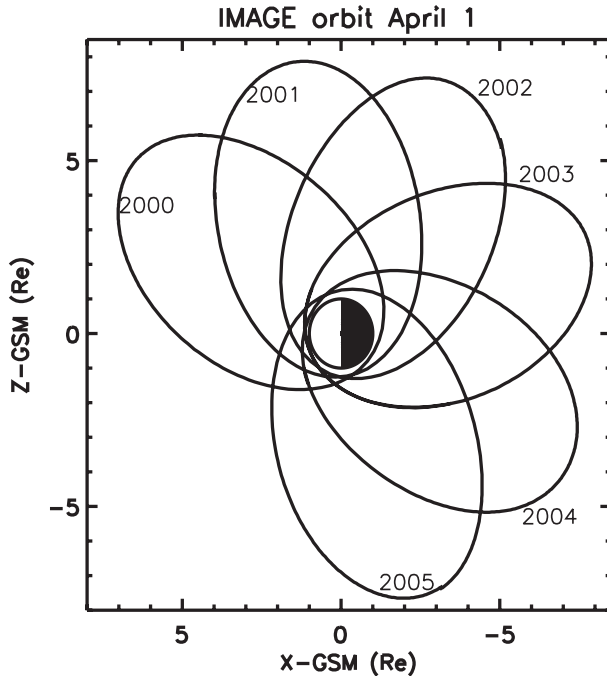


**Fig. 1.** Change of the IMAGE orbit from launch in 2000 until 2005. The orbit is shown for April 1st each year when the orbital plane was located in the GSM x-z-plane.

probable substorm onset latitude and local time. In sunlight, substorm onsets occur 1 hour earlier in local time and 1.5 more poleward than in darkness. The solar wind input, represented by the merging electric field, integrated over 1 hour prior to the substorm, correlates well with the latitude of the breakup. Most poleward latitudes of the onsets were found during very quiet times. Field-aligned and Hall currents observed concurrently with the onset are consistent with the signature of a westward traveling surge evolving out of the Harang discontinuity. The observations suggest that the ionospheric conductivity has an influence on the location of the precipitating energetic electrons, which cause the auroral break-up signature.

For the present report all FUV-images from January 1, 2003 to the end of the IMAGE science mission on December 18, 2005 were analyzed to identify substorm onsets in time and location. The strong orbit precession of IMAGE had moved the apogee across the equator and a large portion of the onsets was observed in the southern hemisphere. That allows for a comparison between the hemispheres. Furthermore, observations between May 2000 and December 2002 cover the peak of the past solar cycle while the present study interval occurred during the declining phase. As in the first publication, the full data set is published electronically and provides a list to the scientific community that can be used for further research.

## 2. Instrumentation

The IMAGE satellite is in a highly elliptical polar orbit of 1000 x 45600-km altitude with a 14:14 hours orbital period and had the apogee over the North Pole in 2001. The strong precession of  $\approx 45^\circ$  per year moved its apogee across the equator in 2003 and down over the South Pole in 2005 (Figure 1).

The Far Ultra-Violet imager (FUV) consists of three imaging sub-instruments and observes the aurora for 5-10 seconds during every 2 minutes spin period [17]. As in the previous report we used the Wideband Imaging Camera (WIC) and the Spectrographic Imager channel (SI-13), and we neglect the proton contribution to the substorm onset aurora [18].

WIC offers the best spatial resolution with a pixel size from apogee of 50 km while the pixel size of SI-13 is 100 km from apogee. During closer proximity the spatial resolution improves but the field of view becomes too small to cover the whole Earth. FUV is turned off during the passage through the radiation belt. That operation scheme limits the observation time to 8-10 hours during each orbit. From apogee around the equator the conditions for auroral observations are unfavorable as aurora appears close to the Earth's limb and the location determination becomes unreliable. That limited the useful time for aurora observations to just a few hours per orbit in 2003/2004.

FUV is mounted on the spinning IMAGE satellite. The pointing within the spin plane is regularly corrected with bright UV stars that cross through the field of view [4]. However the final pointing error in the spin plane can be up to 4 pixels while the one perpendicular to the spin plane can be up to 2 pixels. That amounts to the larger uncertainties for the determination in local time in summer and winter, and in latitude in spring and fall.

## 3. FUV observations

As in the first study we searched through the FUV data and determined the time and location of substorm onsets. The prime data source were the WIC images because of their better spatial resolution. Some additional SI-13 images were used whenever the WIC high voltage was not turned on or they offered a better view. Substorms were identified if they fulfilled the following criteria:

- A clear local brightening of the aurora has to occur.
- The aurora has to expand to the poleward boundary of the auroral oval and spread azimuthally in local time for at least 20 Minutes.
- A substorm onset was only accepted as a separate event if at least 30 Minutes had passed after the previous onset.

Within the image of the initial auroral brightening the center of the substorm auroral bulge was first determined visually. Then a computer program determined the brightest pixel close to this location and calculated its geographic and geomagnetic locations. The full data set is available electronically at <http://sprg.ssl.berkeley.edu/image/> and other scientists are invited to use the data for their research. The list is given in the same format as in [5]. It contains the date and time of each substorm onset, which FUV instrument was used for the identification (WIC or SI-13), the spacecraft geocentric distance, and the brightness (instrument counts) and location (x/y pixel, geographic and geomagnetic) of the brightest pixel within the onset surge. The list can easily be searched for specific criteria like onsets at high magnetic latitude, late local time, onsets within a certain distance to a particular ground station, or onsets with a small distance to the IMAGE spacecraft promising better spatial resolution.

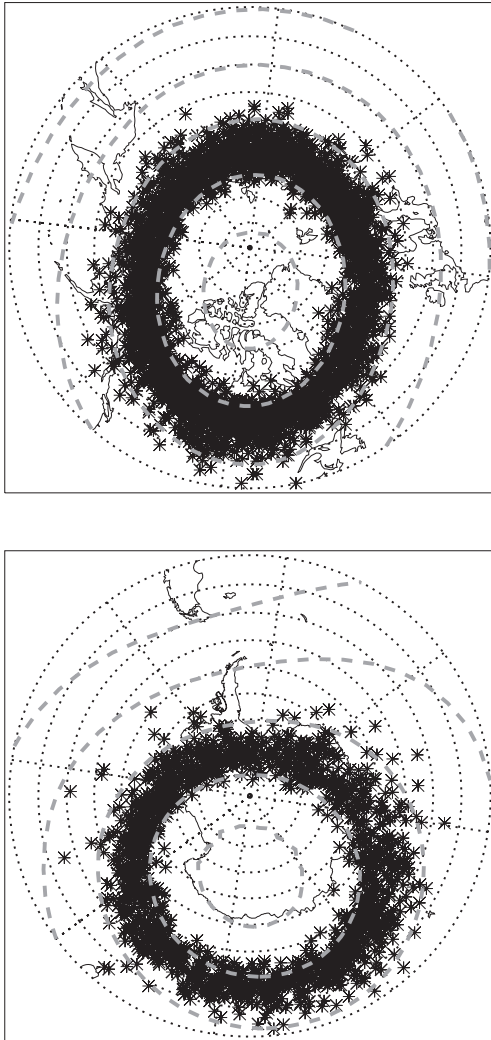


**Fig. 2.** Maps of the northern (top) and southern (bottom) polar regions with the substorm onset locations in geographic coordinates regardless of the local time of onset. A geomagnetic grid is given as dashed gray lines.

#### 4. Discussion

All onset locations irrespective of their local time are given in Figure 2 separated in the northern and southern hemispheres, respectively. Please note that these plots do not represent the auroral ovals, which are asymmetric between local noon and midnight and move over time in latitude for a fixed longitude (see e.g. [8]). These plots should rather be considered as representations of the auroral zone, statistical maps of the probability for onset observations at a specific geographic location, and maybe as guides to tourists, where to go if you want to see a substorm onset at that particular town/hotel.

The averaged results for the substorm onsets confirm results of earlier studies (Table 1). What is remarkable is the almost perfect reproduction of the locations from the first study with an average MLT of  $2250 \pm 0127$  hours (previously  $2300 \pm 0121$ ) and latitude of  $66.4^\circ \pm 2.96^\circ$  (previously  $66.4^\circ \pm 2.86^\circ$ ) (Figure 3). The match of both parameters is somewhat surprising as other studies found dependences of onset latitudes and local

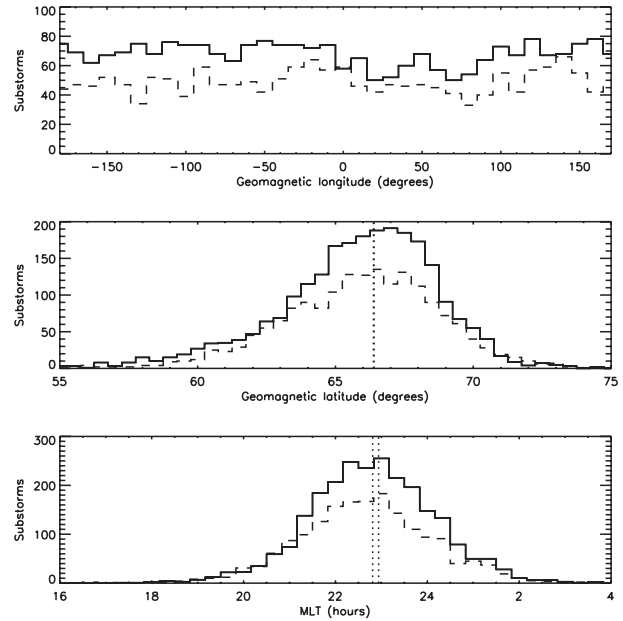


**Fig. 3.** Histograms of the distribution of substorm onsets in geomagnetic longitude (top), latitude (middle) and local time (bottom) from 2003-2005 (dashed lines) and 2000-2002 (solid lines). The median values are marked in the two bottom panels.

times on the signs of all three IMF components and seasons (see introduction). Especially with respect to the onset latitude, it is not unreasonable to expect some difference between the two data sets as the first one was collected during the peak of the solar cycle and the present one during the declining phase [23]. There are differences between the solar wind properties in the course of the solar cycle. During solar minimum high speed streams are more common [10] and the number of interplanetary coronal mass ejections tracks approximately the sunspot number [12]. That could well influence for instance the onset latitude if these solar cycle changes were for instance accompanied by more negative  $B_z$  during solar maximum.

In order to investigate this possibility we analyzed all solar wind plasma and magnetic field measurements by ACE and determined their average properties. Figure 4 summarizes the average IMF conditions for the two time periods from May 2000

**Table 1.** Median and mean (in parentheses) values of auroral substorm onsets from several statistical studies (from [5]). A large portion of the present onsets was observed in the southern hemisphere and the absolute values of the magnetic latitude were used in the row labeled IMAGE'03.

Satellite	#	MLT (hours)	MLAT (Degrees)	Ref.
DE-1	68	2250 (22.8)	65° (?)	[3]
Viking	133	2305 (22.8)	66.7° (65.8°)	[7]
Polar	648	2230 (22.7)	67° (66.6°)	[11]
IMAGE (winter)	78	2324	65.6°	[6]
IMAGE'00	2437	2300 (23.0)	66.4° (66.1°)	[5]
IMAGE'03 all	1755	2250 (22.8)	66.4° (66.1°)	
IMAGE north	2760	2300 (23.0)	66.3° (66.0°)	
IMAGE south	1432	2245 (22.8)	-66.5° (-66.3°)	

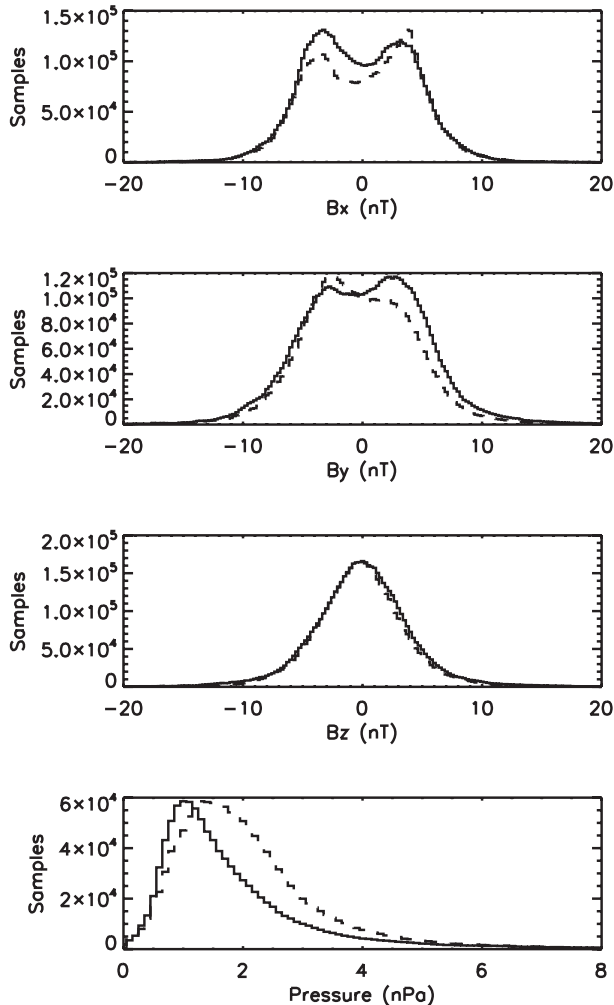


**Fig. 4.** Histograms of the average IMF conditions as measured by ACE during the two study intervals 2000-2002 (solid lines) and 2003-2005 (dashed lines). Different numbers of measurements were scaled to the maximum of both distributions for easier comparison.

to December 31, 2002 and from January 1, 2003 to December 2005. Accounting for the different numbers of samples in each period we normalized all the distributions to the maximum value in each of the histograms. Table 2 summarizes the median values for the solar wind plasma and magnetic field during these years.

It turns out that the average solar wind properties are not that different between the two time periods. The distributions of GSM- $B_z$ , which could influence the onset latitude, are exactly the same. The distributions of GSM- $B_x$  and  $B_y$  are somewhat different.  $B_x$  was more negative in 2000-2002 (2.63 Mio. measurements less than 0.0 nT compared to 2.47 Mio. measurements greater than 0.0 nT) than it was in 2003-2005 (2.49 Mio. less than 0.0 nT and 2.77 Mio. greater than 0.0 nT). According to the results in [11] that could have influence on the onset latitude, which we however did not find. The IMF  $B_y$  was also slightly different during the two periods. It was more positive in 2000-2002 with 2.68 Mio. measurements with values greater than 0.0 nT compared to 2.42 Mio. measurements

greater than 0.0 nT. This situation was reversed in 2003-2005 when  $B_y$  was more negative with 2.80 Mio. measurements less than 0.0 nT and 2.47 Mio. measurements greater than 0.0 nT. In a general sense (see [11]) that should have caused earlier onset local times in 2000-2002 and later onset local times in 2003-2005, what we find neither.

Table 2 also lists the average solar wind plasma conditions during each year of the two periods. However, we only plot the distribution of the solar wind dynamic pressure in Figure 4 as this is the only parameter that was identified as influencing the inset latitude [6]. The two distributions are very different with much larger pressure in 2003-2005 than in 2000-2002. It appears that with a large enough number of events and averages over all seasons, previously established general trends of solar wind influences on the onset locations are suppressed and the magnetosphere creates substorm onsets at constant locations.

## 5. Summary

The data of the new 1755 substorm onset locations between January 1, 2003 and December 18, 2005 confirm previous findings of average distributions in geomagnetic latitude and local time. The surprising result is the almost perfect match of averaged onset locations that were observed by IMAGE-FUV between 2000 and 2002. The solar wind properties in these two periods at the solar maximum and during the declining phase of the solar cycle were slightly different ( $B_x$  and  $B_y$ ) but these differences were not big enough to change the averaged onset locations substantially. It appears that the average onset locations are more controlled by internal magnetospheric processes than that they are driven by the solar wind.

The prime purpose of this report is to publish the list of FUV substorm observations the same way as it was done in the first investigation. Files summarizing all substorm onsets used for this study are available electronically at the website <http://sprg.ssl.berkeley.edu/image/>. Other researchers are invited to look at those time periods with their data and different instrumentation. The database can easily be searched for specific criteria like onsets at high magnetic latitude, late local time, onsets within a certain distance to a particular ground station, or those with a small distance to the IMAGE spacecraft giving better spatial resolution.

During almost all of the reported substorm onsets there exist also images of the proton aurora taken by the SI-12 channel on IMAGE. Previous analysis of small subsets of FUV images did not find any significant difference in the spatial distribution of the proton and electron onsets [6], but differences in the expansion of the electron and proton precipitation dominated auroras

**Table 2.** Median values of solar wind plasma and magnetic field properties in the years 2000-2005.

Year	$B_x$ (nT)	$B_y$ (nT)	$B_z$ (nT)	Density ( $\text{cm}^{-3}$ )	Speed (km/s)	Temp. (K)
2000	0.23	0.27	-0.09	4.7	435	68000
2001	-0.17	0.20	0.07	4.5	421	71000
2002	-0.65	0.68	0.10	4.8	439	92000
2003	0.34	-0.41	-0.09	4.1	539	139000
2004	0.79	-0.40	-0.12	4.7	452	92000
2005	-0.05	-0.43	0.01	3.8	501	107000

[18]. Such investigation has not been performed for this study and more statistically significant results could be obtained with a further analysis of the present data set.

**Acknowledgments:** The IMF and solar wind data were obtained from the ACE Magnetic Field instrument (PI: N. Ness, Bartol Research Institute) and the ACE Solar Wind Experiment (PI: D. J. McComas, Southwest Research Institute). This investigation was supported through subcontract number 03-757 at the University of California at Berkeley under NASA grant NAG5-12762 to the University of New Hampshire.

## References

1. Akasofu, S.-I., The development of the auroral substorm, *Planet. Space Sci.*, *12*, 273, 1964.
2. Birn, J., M. Hesse, G. Haerendel, W. Baumjohann, K. Shiokawa, Flow braking and the substorm current wedge, *J. Geophys. Res.*, *104*, 19895, 1999.
3. Craven, J.D. and L.A. Frank, Diagnosis of auroral dynamics using global auroral imaging with emphasis on large-scale evolution, in *Auroral Physics*, ed. C.-I. Meng, M.J. Rycroft, and L.A. Frank, pp. 273-297, Cambridge Univ. Press, New York, 1991.
4. Frey, H.U., S. B. Mende, T.J. Immel, J.-C. Gérard, B. Hubert, S. Habraken, J. Spann, G.R. Gladstone, D.V. Bisikalo, V.I. Shematovich, Summary of quantitative interpretation of IMAGE far ultraviolet auroral data, *Space Science Reviews*, *109*, 255, 2003.
5. Frey, H.U., S.B. Mende, V. Angelopoulos, E.F. Donovan, Substorm onset observations by IMAGE-FUV, *J. Geophys. Res.*, *109*, A10304, doi:10.1029/2004JA010607, 2004.
6. Gérard, J.-C., B. Hubert, A. Grard, M. Meurant, S.B. Mende, Solar wind control of auroral substorm onset locations observed with the IMAGE-FUV imagers, *J. Geophys. Res.*, *109*, A03208, doi:10.1029/2003JA010129, 2004.
7. Henderson, M.G. and J.S. Murphree, Comparison of Viking onset locations with the predictions of the thermal catastrophe model, *J. Geophys. Res.*, *100*, 1857, 1995.
8. Holzworth, R.H. and C.-I. Meng, Mathematical representation of the auroral oval, *Geophys. Res. Lett.*, *2*, 377, 1975.
9. Hones, E.W., Plasma flows in the magnetotail and its implications for substorm theories, in *Dynamics of the Magnetosphere*, ed. S.-I. Akasofu, pp. 545-562, D. Reidel, Norwell, Mass., 1979.
10. Huttunen, K.E.J., R. Schwenn, V. Bothmer, H.E.J. Koskinen, Properties and geoeffectiveness of magnetic clouds in the rising, maximum and early declining phases of solar cycle 23, *Ann Geophys.*, *23*, 625, 2005.
11. Liou, K., P.T. Newell, D.G. Sibeck, C.-I. Meng, M. Brittner, and G. Parks, Observation of IMF and seasonal effects in the location of auroral substorm onset, *J. Geophys. Res.*, *106*, 5799, 2001.
12. Liu, Y., J.D. Richardson, and J.W. Belcher, A statistical study of the properties of interplanetary coronal mass ejections from 0.3 to 5.4 AU, *Planet. Space Sci.*, *53*, 3, 2005.
13. Lui A.T.Y., A. Mankofsky, C.-L. Chang, K. Papadopoulos, C.S. Wu, A current disruption mechanism in the neutral sheet: a possible trigger for substorm expansions, *Geophys. Res. Lett.*, *17*, 745, 1990.
14. Lui, A.T.Y., C.-L. Chang, A. Mankofsky, H.-K. Wong, and D. Winske, A cross-field current instability for substorm expansion, *J. Geophys. Res.*, *96*, 11389, 1991.
15. Lyons, L.R., Substorms: Fundamental observational features, distinction from other disturbances, and external triggering, *J. Geophys. Res.*, *101*, 13011, 1996.
16. McPherron, R.L., Substorm related changes in the geomagnetic tail: the growth phase, *Planet. Space Sci.*, *20*, 1521, 1972.
17. Mende, S. B. et al., Far ultraviolet imaging from the IMAGE spacecraft, *Space Sci. Rev.*, *91*, 287, 2000.
18. Mende, S.B., H.U. Frey, B.J. Morosny, and T.J. Immel, Statistical behavior of proton and electron auroras during substorms, *J. Geophys. Res.*, *108*, 1339, doi:10.1029/2002JA009751, 2003.
19. Østgaard, N., S.B. Mende, H.U. Frey, T.J. Immel, L.A. Frank, J.B. Sigwarth, T.J. Stubbs, Interplanetary magnetic field control of the location of substorm onset and auroral features in the conjugate hemispheres, *J. Geophys. Res.*, *109*, A07204, doi:10.1029/2003JA010370, 2004.
20. Parkinson, M.L., M. Pinnock, J.A. Wild, M. Lester, T.K. Yeoman, S.E. Milan, H. Ye, J.C. Devlin, H.U. Frey, and T. Kikuchi, Interhemispheric asymmetries in the occurrence of magnetically conjugate sub-auroral polarization streams, *Ann. Geophys.*, *23*, 1371-1390, 2005.
21. Provan, G., M. Lester, S. Mende, and S. Milan, Statistical study of high-latitude plasma flow during magnetospheric substorms, *Ann. Geophys.*, *22*, 3607, 2004.
22. Shiokawa, K. G. Haerendel, W. Baumjohann, Azimuthal pressure gradient as driving force of substorm currents, *Geophys. Res. Lett.*, *25*, 959, 1998.
23. Tanskanen E., T.I. Pulkkinen, H.E.J. Koskinen, J.A. Slavin, Substorm energy budget during low and high solar activity: 1997 and 1999 compared, *J. Geophys. Res.*, *107*, 15-1-11, 2002.
24. Wang, H., H. Lühr, S.Y. Ma, P. Ritter, Statistical study of the substorm onset: its dependence on solar wind parameters and solar illumination, *Ann. Geophys.*, *23*, 2069, 2005.



# Polar spacecraft observations near 9 RE: rapid multiple dipolarizations and their interpretation

Y. S. Ge, C. T. Russell, T.-S. Hsu, and R. L. McPherron

**Abstract:** The Polar spacecraft has probed the near-Earth tail region at 9 RE with its orbit in the meridian plane and apogee near the magnetic equator. The onboard magnetometer frequently recorded dipolarizations of the magnetic field during the crossing of the current sheet, including rapid multiple dipolarizations. The interval between two rapid dipolarizations is about 30 minutes, which is close to the time interval of multiple Pi 2 pulsations in a substorm. On several occasions, three or more dipolarizations occur within 2 hours, but most occurrences involve have two rapid dipolarizations. The normal component of the magnetic field to the current sheet rises in a stepwise manner in some events. In others it recovers to the previous level before the next dipolarization. Rapid multiple dipolarizations may occur in a single substorm. We interpret these dipolarizations in terms of the initial onset of reconnection in the near-Earth plasma sheet, followed by more rapid reconnection when lobe plasma reaches the x-point and reconnection on open field lines releases the plasmoid.

*Key words:* Substorms, Dipolarization, Reconnection.

## 1. Introduction

Multiple onsets are a common feature of substorms observed on the ground. If these occur before the main breakup, they are called pseudobreakups [2, 5]. After onset they are referred to as intensifications. *Koskinen et al.* [2] and *Nakamura et al.* [5] showed that pseudobreakups have almost all of the features of a substorm onset, but the disturbance seems to "quench" rather than proceed to full expansion phase development. Pseudobreakup features are found to subside quickly and be tightly localized [5]. However, the physics behind pseudobreakups has not been clearly understood. Dipolarization of the tail magnetic field which is often used to study the onset of magnetospheric substorms is an important feature at onsets. In near-Earth tail region beyond the geosynchronous orbit, the dipolarization is believed caused by the pile-up of magnetic flux transported from tail by reconnection processes [9]. The investigation of multiple dipolarizations in near-Earth region at multiple onsets can help us to understand what leads to the different evolutions of pseudo-onsets and major onsets.

In the Near-Earth Neutral Line (NENL) model of substorms, near-Earth reconnection takes place in two stages, i.e., on closed field lines and then on open lobe field lines. Recently, *Russell* [8] re-emphasized their behavior while presenting a substorm triggering model to understand how northward turnings of the IMF can lead to substorm expansion onsets. In this model, the two stages of reconnection are modulated by the conditions of IMF and a pseudo-onset should take place before the major one. This model is also consistent with the observational conclusion of *Mishin et al.*, [3, 4] that substorms have two distinct forms of onset. Though many studies of pseudo-onset using ground observations have been made, the investigations on their signatures in space have rarely been performed. The in

situ observations can be more revealing because some ground signatures of pseudo-onset are very weak or localized. In this work, we use the Polar spacecraft studying the multiple onsets seen in near-Earth tail region where is believed the earthward transported flux starts to pile up.

## 2. Near-Earth Tail Magnetic Field

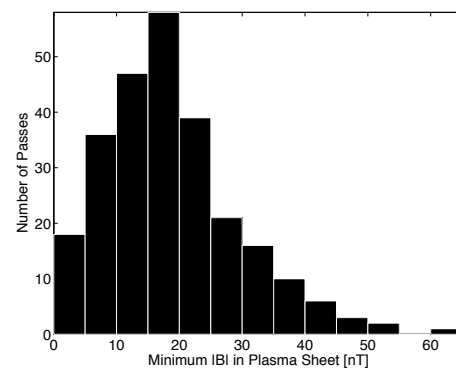


**Fig. 1.** Minimum magnetic field each orbit (2001-2003) when Polar was at apogee and within 2 hours LT of midnight.

The Polar spacecraft with an orbit of 9 RE apogee spent significant time at near-Earth tail region during the Falls of 2001, 2002, and 2003. Near 9 RE the tail magnetic field is usually quiet and somewhat weakened around the current sheet where  $B_x$  reverses. Sometimes the magnetic field is highly disturbed and a strong tail current reduces the magnitude to a low value. The survey using 6-second magnetic field data [7] has been performed on each orbit in the three years when Polar's apogee was within 2 hours local time of midnight. The distribution of minimum field strength during each crossing of the current sheet is shown in Figure 1. The median value is 20 nT, which is much less than the contribution of the dipole field of the Earth at 9 RE on the magnetic equator, about 40 nT.

Received 13 June 2006.

Y. S. Ge, C. T. Russell, T.-S. Hsu, and R. L. McPherron. Institute of Geophysics and Planetary Physics, University of California Los Angeles, CA 90095-1567, USA.

Weakened by the strengthened cross-tail current, sometimes the field strength can be as low as 5 nT or less. In weak fields in this region, many interesting disturbances are seen by the magnetic field measurements, e.g., the mirror mode instability (see details in the paper 'Mirror Mode Waves Detected by Polar in Near-Midnight Tail', *Ge et al.*, in preparation).

An anti-correlation is observed (Figure 2 (a) and (b)) between the solar wind density and the dynamic pressure with the near-tail magnetic field using one minute resolution propagated ACE data from the advection technique of [10]. It indicates that larger solar pressures (mainly caused by larger densities) compress the tail field more, enhancing the tail current and producing lower fields near 9 RE. Similarly the correlation with the convected southward IMF in Figure 2(c) shows that the more IMF flux (left half side shows southward IMF flux) is moved to the magnetotail, the lower is the near-Earth tail magnetic field. More details can be found in [1].

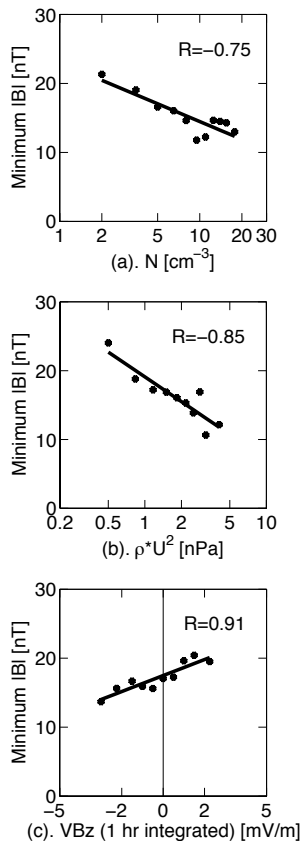


**Fig. 2.** Relation between median tail magnetic field at the current sheet crossing (reversal in Bx) and solar wind parameters: (a). Solar wind number density; (b). Solar wind dynamic pressure; (c). Convected IMF flux. Values shown are medians in overlapping (by half) bins. R is the correlation coefficient of the medians.

### 3. Multiple Dipolarizations

The magnetosphere can be reconfigured in shorter time than the duration of a typical substorm. Figure 3 shows a typical multiple dipolarization event recorded by the Polar spacecraft

in near tail. The Polar spacecraft crossed the current sheet at 1120 UT on October 16, 2001. Three sudden increases of Bz component are seen from 1140 UT to 1230 UT. All these increases are accompanied by sudden decreases of Bx component, which indicates that the magnetic field changes from tail-like to more dipolar field. The immediate decrease in the Bx component and in the magnetic field strength and the fluctuations of magnetic field also indicate that plasma sheet expanded and Polar reentered hot plasma region. Every dipolarization has a sharp front and a following gradual decrease of Bz component, corresponding to a explosive release of tail field energy and a slow recovery phase respectively. But the Bz component does not return to the level before the dipolarization. This process is repeated for three times within one hour during this interval. The second event also involves a stretching of tail field which is indicated by the rapid increase of Bx component before the dipolarization. A quite weak dipolarization occurs at 12:46 UT.

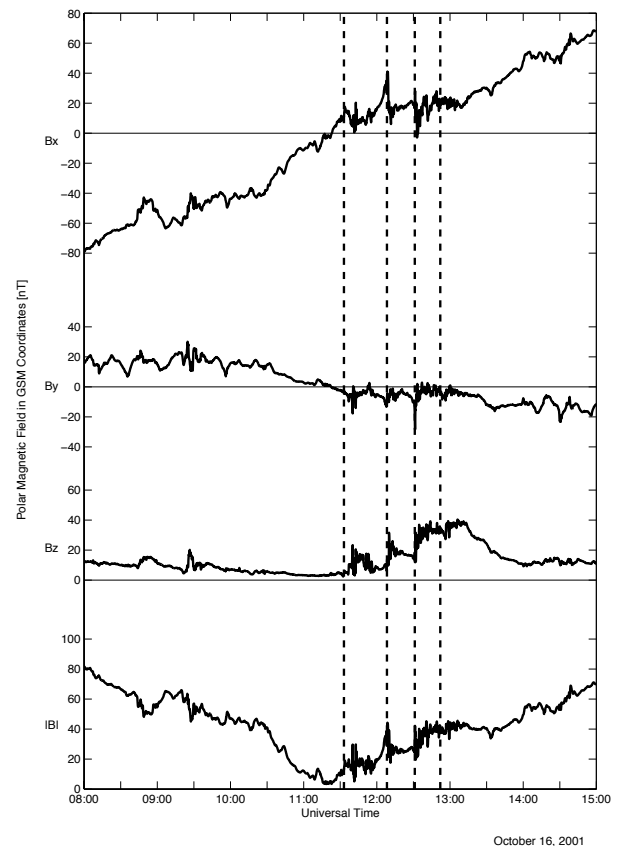


**Fig. 3.** Time series of magnetic field on a multiple dipolarization event, October 16, 2001 (6s resolution). Dash lines show the dipolarizations seen by Polar.

Figure 4 shows the AL index and the power of ground Pi2 pulsations during this event. The Pi2 power is averaged over all stations that recorded Pi2 onsets in MEASURE ground magnetometer chain. Multiple ground Pi2 onsets appear corresponding to the dipolarizations except for the first one. Considering that the MEASURE chain is located at dawn at this universal time, this suggests that the first onset does not generate a global

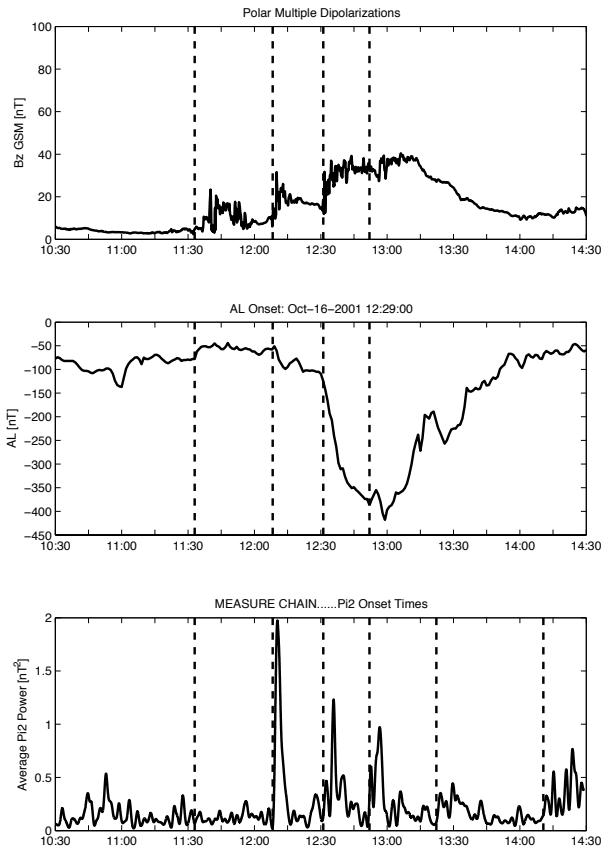


**Fig. 4.** Top panel: Polar MFE Bz in GSM; Middle panel: Quick-look AL index; Bottom panel: Averaged ground Pi2 power over MEASURE chain

Pi2 pulsation. At the second dipolarization, AL starts to drop and ground stations record the strongest Pi2 onset, which suggests that this onset can be the major onset of the substorm. There are also multiple Pi2 onsets corresponding to the following dipolarizations seen by Polar, even to the minor one at 12:46 UT. However, the determination of a major onset here should be made with care. Solely from the AL index, a major onset would be selected corresponding to the third dipolarization seen on Polar. Since there is limited station coverage for AL near midnight at this Universal Time (12:31), the major onset is uncertain here. Although the ground signatures for multiple onsets are very variable and some are too weak to be detected, in situ observations by Polar record the disturbances more clearly. The change of magnetic field in the dipolarization for the pseudo-onset (11:32 UT) is comparable to that in the major onset. Another multiple onsets event (details can be found in a paper in preparation by *Ge et al.*) shows Pi2 onsets as well as AL index onsets for every dipolarization when the ground station is close to midnight. Furthermore, good optical observations, i.e., all-sky image, in that event are very helpful in the determination of major onsets.

The IMF condition for the event is examined using the propagated ACE data which is shown in Figure 5. We can see from this figure that the dipolarizations occur when IMF is southward. The first and second dipolarizations occur when the south-

ward component of IMF begins to increase, and the third event corresponds to a northward turning of the IMF.

#### 4. Summary and Discussions

In substorms, multiple onsets are quite common features. Using the Polar spacecraft magnetic field observations, we can more readily record every onset of a substorm when the spacecraft is in the near-Earth tail region. The multiple dipolarizations appear typically separated by 30 minutes which is close to the median time separation of two consecutive Pi2 onsets on the ground (*Hsu and McPherron*, submitted recently) and is also consistent with the results of earlier work done by [6]. Pi2 pulsations generated at multiple onsets can be different. The pseudo-onset appears to generate Pi2 pulsations that are quite confined in local time. Determination of the substorm major onset only from ground Pi2 and AL index should be performed very carefully when the aurora image or observations in space are not available.

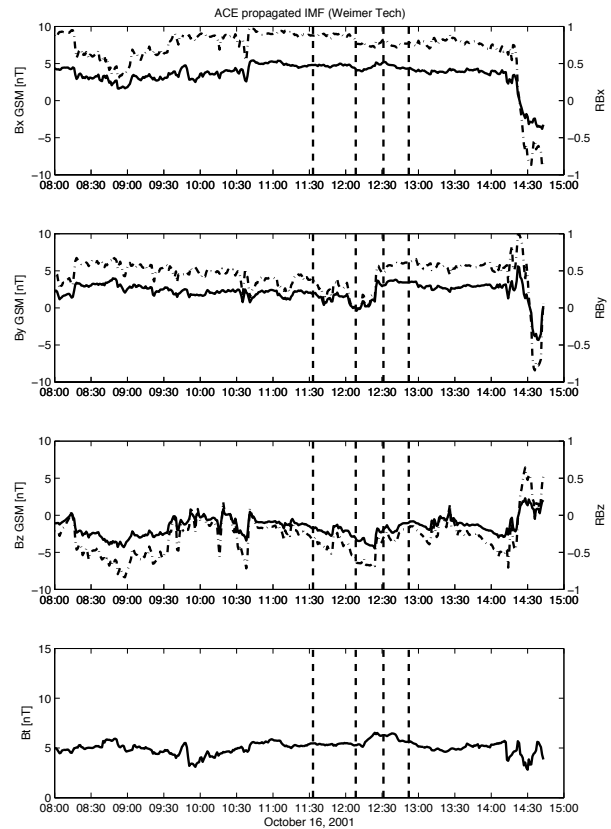


**Fig. 5.** Propagated ACE IMF data using Weimer Technique: Three components in GSM coordinates and the field magnitude (solid lines); Cosine of angles of three components (solid-dot lines)

The localization of Pi2 at the pseudo-onset is not hard to understand. Since the aurora does not expand significantly in the pseudo-breakup [5], the disturbance on polar cap region cannot be strong enough to generate a global pulsation. In the model suggested by [8] and also in other NENL models (e.g., [3, 4]),

the pseudo-onset very possibly corresponds to the reconnection beginning on the closed field lines of the plasma sheet. The reconnection rate is limited until lobe open field lines start to reconnect. Once reconnection reaches the tail lobe, information on the substorm can propagate quickly and globally. The more subtle effects of the pseudo-onsets are more difficult to be detected remotely making in situ observations more important in this situation.

So far, we still do not have an unambiguous answer to why the magnetosphere changes its configuration on this time scale (around 30 minutes) during a substorm. Perhaps it is the time for reconnection to move through the plasma sheet to the lobes. The incoming THEMIS mission should provide the observations needed to shed light on this question.

## Acknowledgements

The authors wish to thank Dan Weimer and James Weygand for providing time-propagated solar wind data. This work was supported by the National Aeronautics and Space Administration under grant NNG05GC87G.

## References

1. Ge, Y. S. and C. T. Russell (2006), Polar survey of magnetic field in near tail: Reconnection rare inside 9 RE, *Geophys. Res. Lett.*, 33, L02101, doi:10.1029/2005GL024574.
2. Koskinen, H. E. J., R. E. Lopez, R. J. Pellinen, T. I. Pulkkinen, D. N. Baker, and T. B. Singer (1993), Pseudobreakup and substorm growth phase in the ionosphere and magnetosphere, *J. Geophys. Res.*, 98, 5801-5813.
3. Mishin, V. N., C. T. Russell, T. I. Sifudinova, and A. D. Bazarzhapov (2000), Study of weak substorms observed during December 8, 1990, Geospace Environment Modeling Campaign: Timing of different types of substorm onsets, *J. Geophys. Res.* 105, 23,263-23,276.
4. Mishin, V. N., T. I. Sifudinova, A. D. Bazarzhapov, C. T. Russell, W. Baumjohann, R. Nakamura, and M. Kubyshkina (2001), Two distinct substorm onset, *J. Geophys. Res.* 106, 13,105-13,118.
5. Nakamura, R., D. N. Baker, T. Yamamoto, R. D. Belian, E. A. Bering III, J. R. Benbrook, and J. R. Theall (1994), Particle and field signatures during pseudobreakup and major expansion onset, *J. Geophys. Res.*, 99, 207-221.
6. Rostoker, G. (1968), Macrostructure of Geomagnetic Bays, *J. Geophys. Res.*, 73, 4217-4229.
7. Russell, C. T., R. C. Snare, J. D. Means, D. Pierce, D. Dearborn, M. Larson, G. Barr and G. Le (1995), The GGS/Polar magnetic fields investigation, *Space Sci. Rev.*, 71, 563 - 582.
8. Russell, C. T. (2000), How northward turnings of the IMF can lead to substorm expansion onsets, *Geophys. Res. Lett.*, 27, 3257-3259.
9. Shiokawa, K., W. Baumjohann, and G. Haerendel (1997), Braking of high-speed flows in the near-Earth tail, *Geophys. Res. Lett.*, 24, 1179-1182.
10. Weimer, D.R., D.M. Ober, N.C. Maynard, M.R. Collier, D.J. McComas, N.F. Ness, C.W. Smith, and J. Watermann (2003), Predicting interplanetary magnetic field (IMF) propagation delay times using the minimum variance technique, *J. Geophys. Res.*, 108(A1), 1026, doi:10.1029/2002JA009405.

# SuperDARN observations of ionospheric convection during magnetospheric substorms

A. Grocott and T. K. Yeoman

**Abstract:** The coupled nature of the magnetosphere-ionosphere system makes measurements of ionospheric convection, such as those provided by the SuperDARN HF radars, extremely useful in diagnosing magnetospheric dynamics. Flux Transfer Events (FTEs) at the dayside magnetopause, for example, are well-resolved in ionospheric flow data as Pulsed Ionospheric Flows (PIFs). Similarly, Bursty Bulk Flows (BBFs) associated with the earthward transport of flux in the tail have a discernable flow signature in the nightside ionosphere. The large-scale convection associated with magnetospheric substorms is also readily identifiable in ionosphere flow data. During the growth phase, for example, the expansion of the polar cap due to enhanced open flux production is evidenced in the equatorward motion of radar backscatter. On the nightside, fast equatorward flows emanating from the polar cap after substorm onset, followed by a poleward contraction of the flow reversal boundary, provide evidence for tail reconnection and the closure of open flux. The complex electrodynamics associated with substorms, however, ensures immense variety in the nature of the flow signatures which are observed. Some studies, for example, have reported a reduction in the nightside flows at the time of substorm onset, possibly resulting from enhancements in auroral conductivity associated with substorm energetic particle precipitation which imposes a limit on the size of the local electric field. Enhanced electric field phenomena such as Substorm-Associated Radar Auroral Surges (SARAS) and Auroral Westward Flow Channels (AWFC) provide additional constraints on the global substorm picture. This paper provides an overview of these and other important convection signatures associated with substorms and briefly discuss how future developments of SuperDARN can further enhance our understanding of substorm physics.

*Key words:* SuperDARN, Convection.

## 1. Introduction

Magnetospheric substorms are a major contributing factor to large-scale magnetosphere-ionosphere dynamics and give rise to some of the most significant auroral and magnetospheric disturbances that occur in the terrestrial system. As a consequence they have been extensively studied over the past 40 years and many aspects of their large-scale behaviour are now very well understood. Early studies of substorm current systems identified two distinct patterns of ionospheric currents [5]. The first of these, referred to as DP-2 (disturbance polar of the second type), corresponds to the twin-vortex current pattern driven by magnetospheric convection, and the resulting eastward and westward convection electrojets in the dawn and dusk auroral zones. This current system is associated with a substorm growth phase in which energy extracted from the solar wind is stored in the magnetosphere [33]. During this interval an enhancement in magnetospheric and ionospheric convection, being driven by reconnection at the dayside magnetopause, causes an increase in the size of the polar cap and a growth in the convection electrojets. The second pattern, DP-1, corresponds to the ionospheric portion of the substorm current wedge and takes the form of an enhanced westward current in the midnight sector auroral zone called the substorm electrojet [1]. This current system is governed by enhancements in conductivity rather than in the electric field [27] and as such it is not representative

of the flow. HF radars, however, make direct measurements of the ionospheric convection and are therefore able to observe the electric field during all phases of a substorm. This paper presents a review of HF radar studies which have contributed to our current understanding of substorm physics.

## 2. SuperDARN

The Super Dual Auroral Radar Network (SuperDARN) is an international array of HF coherent radars spanning the auroral regions of both the northern and southern hemispheres [16]. At the present time, the northern hemisphere network consists of ten radars and the southern hemisphere network consists of seven. In standard operating mode, SuperDARN scans through 16 beams of azimuthal separation  $3.24^\circ$ , producing the full fields-of-view shown in Fig. 1 (the grey field-of-view is that of the first mid-latitude StormDARN radar, discussed below). Each radar dwells for 3 or 7 seconds on each beam, along which line-of-sight measurements of the convection velocity are obtained, with a full scan therefore taking either 1 or 2 minutes. Large-scale maps of the high-latitude convection can be derived from these measurements using the 'Map Potential' model [42]. In this model the line-of-sight velocities are mapped onto a polar grid and used to determine a solution for the electrostatic potential which is expressed in spherical harmonics. The equipotentials of the solution then represent the plasma streamlines of the modelled convection pattern. Information from a statistical model [41], parameterised by concurrent IMF conditions, is used to stabilise the solution where no measurements are available.

Received 15 May 2006.

**A. Grocott and T. K. Yeoman.** Department of Physics and Astronomy, University of Leicester, University Road, Leicester, LE1 7RH, U.K.

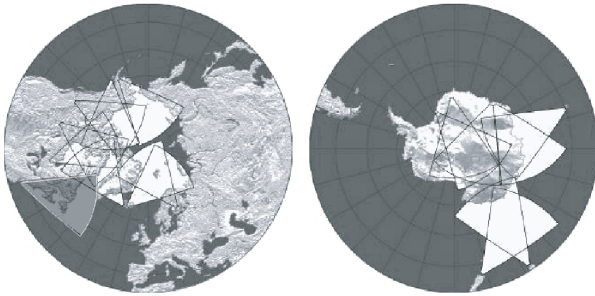


**Fig. 1.** Fields-of-view of the northern (left) and southern (right) hemisphere SuperDARN HF radars

### 3. Growth Phase Convection

Whilst there are various phenomena associated with growth phase intervals, the primary effect leading to an expansion phase onset is the addition of open flux to the magnetotail lobes via reconnection at the dayside magnetopause. Flow is then excited as this newly reconnected flux is distributed around the polar cap, which consequently expands equatorward. Shown in Fig. 2 is a latitude-time-velocity plot of SuperDARN data, grey-scaled to velocity either towards (positive) or away (negative) from the radar's location (from [28]). The vertical line indicates the time of substorm onset, prior to which the radar scatter can be seen to have moved to lower latitudes as the polar cap expanded. Observations such as these are common during substorm growth phases, and fairly straightforward to interpret. As can be seen, however, after substorm onset the nature of the scatter changes - in places it actually disappears - and in general interpretation of the data becomes a lot more complicated, and to a certain degree, more interesting.

### 4. Expansion Phase Observations

Although there is still much to be learned about the complex nature of substorm electrodynamics, the basic flow features associated with the expansion phase were revealed by one of the earliest studies using HF radars [35]. These features are illustrated in the example of Fig. 3, which shows the local convection pattern derived from SuperDARN data during the evolution of a substorm [48]. The top panel shows the pre-onset conditions, which consist of a nominal twin-cell convection pattern. Then, just after onset (2nd panel) a suppression of the flow becomes evident at the location of the substorm bulge, with faster flows being diverted around the sides. About 10 minutes into the expansion phase (3rd panel) the twin-vortex pattern reappears as the falling conductivity 'frees up' flux which can be convected away.

As was mentioned earlier, in addition to the suppression of flow, there is sometimes a loss of data altogether during the substorm expansion phase. This was investigated by a number of studies and was found to be due to absorption of the HF radio signal by the enhanced electron densities in the precipitation region [34]. Whilst observing the expansion phase using HF radars can therefore prove problematic, there are often large areas of radar scatter still present in the vicinity of the substorm disturbed region which can reveal much about the electrodynamics. In the example presented in Fig. 4, a number

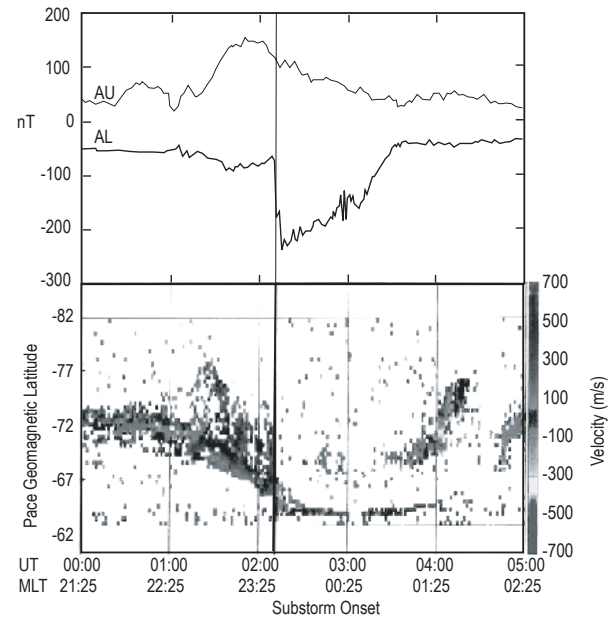


**Fig. 2.** Line-of-sight SuperDARN radar data illustrating the equatorward motion of backscatter during the substorm growth phase, from [28]

of substorm cycles are shown (onsets marked with the vertical dashed lines) where there are continuous data over much of the interval [47]. Between 2130 and 2200 UT there was evidence of an ongoing growth phase, with scatter continuing to expand equatorward. After this time, between 2200 and 2230 UT, a clear poleward motion of the scatter is evident, implying a contraction of the polar cap, presumably due to the removal of open flux by tail reconnection.

#### 4.1. Large-scale Convection

The ability to combine observations from a large number of radars makes SuperDARN ideally suited to investigating large-scale convection. Following earlier work on boundary motions and flows [40, 44, 13] it was supposed that significant large-scale twin-vortex flows should be excited during substorms, corresponding in essence to the DP-2 current systems associated with dayside-driven convection cited above [6]. Observations have been reported of surges of transpolar flow into the midnight sector associated with a substorm intensification, which it was suggested were due to bursts of reconnection in the tail [12]. Analyses of SuperDARN flow data obtained during isolated substorms have also been presented, that found evidence for the excitation of twin-vortex flow cells centred in the nightside ionosphere, which enhance the transpolar voltage by  $\sim 40$  kV compared with pre-onset values [17, 18]. This is illustrated in Fig. 5, which shows maps of the northern hemisphere high-latitude convection before (top panel) and after (bottom panel) the onset of a substorm. The excitation of flow (e.g. longer vectors on the bottom map) and enhanced voltage are clearly evident. Following this work, a statistical study of substorm flows was conducted which also revealed enhancements across the polar cap and in the low-latitude return flow region during the expansion phase [39]. A systematic increase in the transpolar voltage from  $\sim 40$  kV 2 minutes before on-

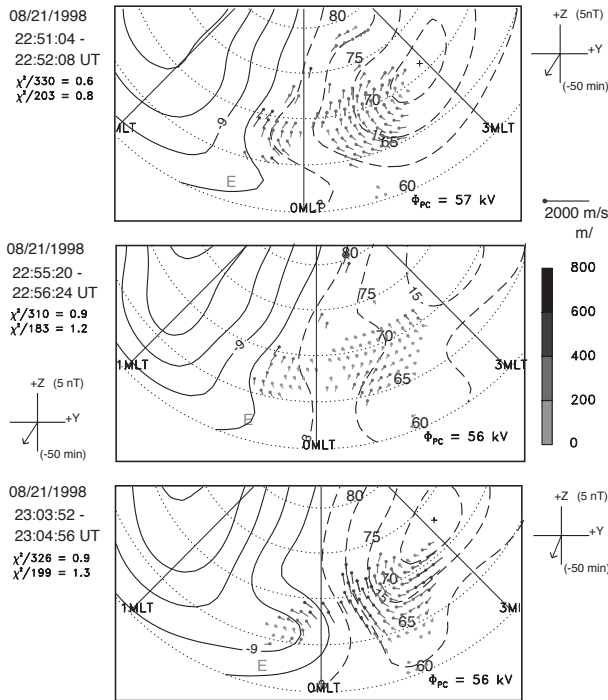


**Fig. 3.** SuperDARN convection maps showing the development of substorm flows, from [48]

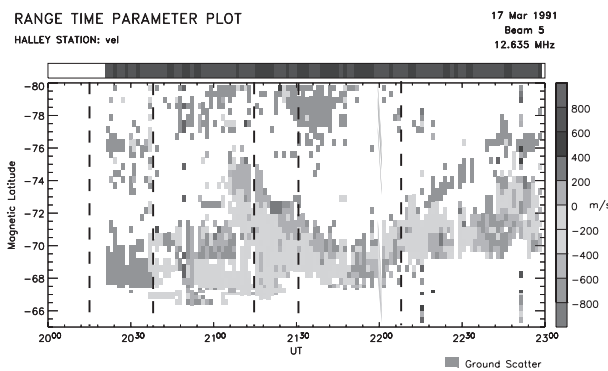


**Fig. 4.** SuperDARN line-of-sight velocity data showing the development of the ionospheric flows during a number of substorm cycles, from [47]

set to  $\sim 75$  kV 12 minutes after was also found, and this was attributed to the removal of open flux from the polar cap by nightside reconnection.

Other studies of the ionospheric response to substorms have suggested that convection enhancements occur simultaneously across the ionosphere, with an imposed electric field affecting the global current systems. For example, measurements of the electric field response some  $90^\circ$  of longitude away from the onset region have revealed enhancements coincident with onset [36]. In contrast to this, observations of a global reduction in ionospheric convection at the time of substorm onset have also been reported [32]. This reduction occurred in concert with a northward turning of the IMF, however, which is something often found to precede a substorm onset and will itself cause a reduction in the solar wind driven flows. If no direct evi-

dence of substorm driven flows is observed by SuperDARN on the nightside, then the level of global convection will indeed appear to be reduced. Recent studies of the dayside convection response to substorms, which occurred during steady IMF conditions such that changes in the level of solar wind driven convection are not apparent, have indeed revealed enhancements in the convection, beginning about 10-15 minutes after the time of substorm onset observed by ground magnetometers [25].

Finally, recent work has discussed the possibility of two distinct flow systems in the substorm convection pattern [29, 26]. The first is a post-midnight anticlockwise convection vortex (PoACV) at higher latitudes and the second is an azimuthally extended clockwise vortex at lower latitudes. These are explained in terms of a combination of the nightside reconnection driven twin-vortex flows and those resulting from field line slippage processes associated with dipolarisation [30].

#### 4.2. Mesoscale Convection Features

Whilst it is thus becoming clear that large-scale electric fields play a significant role in the electrodynamics of the substorm expansion phase, it is also apparent that mesoscale phenomena are integral to the substorm process. For example, azimuthally-localised impulsive events have been observed in which auroras are first intensified at the poleward boundary of the nightside auroral zone, and then expand equator-

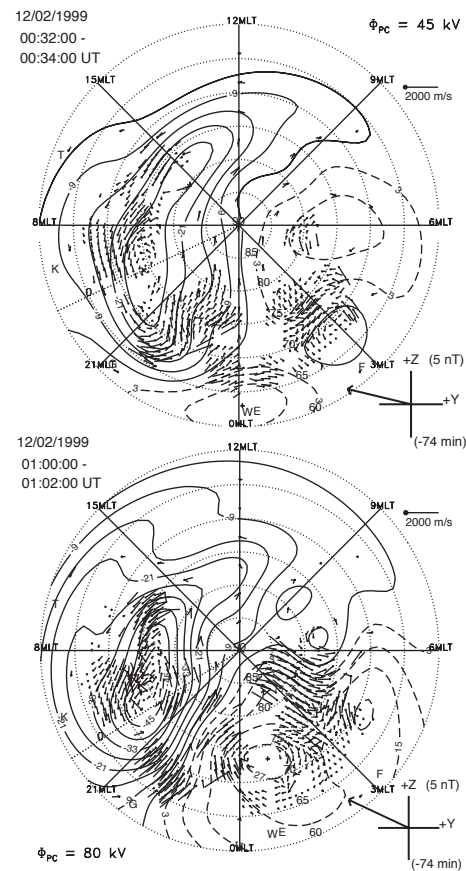


**Fig. 5.** SuperDARN convection maps showing the pre-onset flows (top) and expansion phase flows (bottom) during an isolated substorm, from [18]

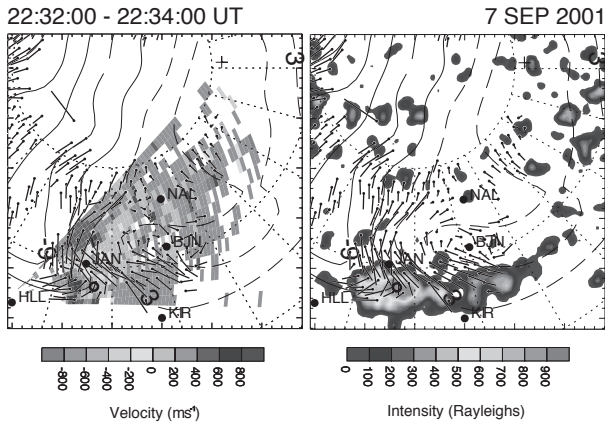


**Fig. 6.** SuperDARN line-of-sight radar data and IMAGE FUV auroral data of the ionospheric signature of a Bursty Bulk Flow, from [20]

ward, reaching to near the equatorward boundary of the oval emissions after  $\sim 5$  min [23]. These events, termed ‘poleward boundary intensifications’ (PBIs) [31], have been found to occur in all phases of the substorm cycle, including during long intervals of magnetic quiet, though they appear to be more frequent during substorm expansion phases. They are associated with azimuthally-localised ‘bursty bulk flows’ (BBFs) in the near-Earth plasma sheet [3, 4] and the excitation of flow in the ionosphere [9, 46, 20, 21]. These features are strongly suggestive of the occurrence of localised impulsive reconnection in the tail [7, 8]. Pseudobreakups, occurring during substorm growth phase, have also been associated with BBFs [20] and have been shown to accompany significant enhancements in the nightside flux closure rate [24].

The ionospheric counterpart of a BBF which occurred during a pseudobreakup in the course of a substorm growth phase, about 10 min after a southward turning of the IMF and  $\sim 50$ -60 min before a major expansion phase onset, was recently studied in some detail [20]. This was the first study showing both the ionospheric flow pattern and the auroral activation associated with the simultaneous observation of a flow burst in the magnetosphere. Ionospheric observations during the flow event observed by the CUTLASS radars (the eastern most pair of SuperDARN) and the FUV auroral imager on the IMAGE spacecraft are shown in Fig. 6. A small, negative excursion in the X component of the magnetic field with an amplitude of 10 nT and some Pi2 activity, were observed at ground stations close to the footprint of Cluster during the BBF (not shown). Clear signatures associated with the BBF are observed in the ionospheric flow obtained by CUTLASS, as well as in the auroral precipitation pattern in the IMAGE UV data.

An extended study of the ionospheric signatures of BBFs and their relationship to the substorm cycle is currently being undertaken (e.g. [21]) and some examples are shown in Fig. 7. The top example shows the signature of a BBF observed during the recovery phase of a substorm. As can be seen in the figure, this BBF occurred in association with a poleward boundary intensification and was accompanied by an enhancement in the auroral zone flows. The middle panel shows the flow signature of a BBF which occurred during an interval of northward IMF. Here, the flow pattern developed into an azimuthal configura-

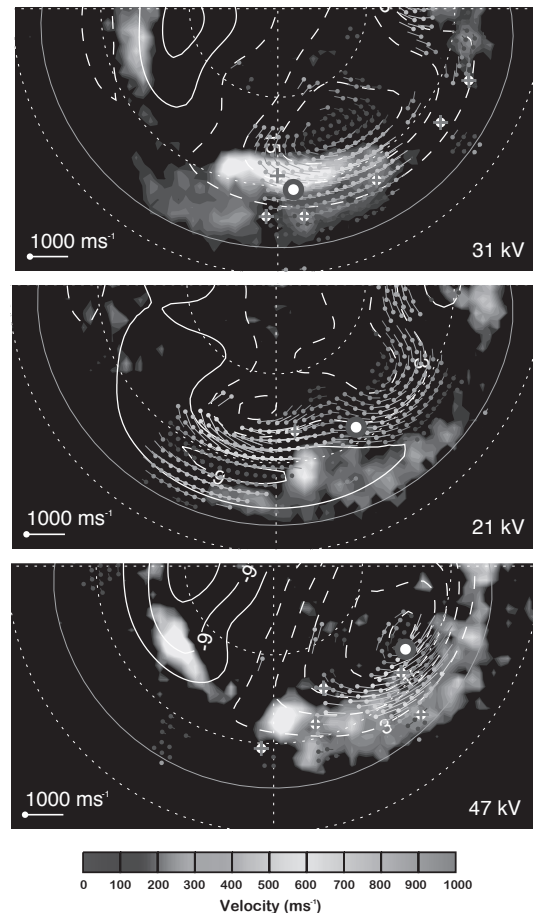


**Fig. 7.** SuperDARN convection maps with superimposed IMAGE FUV auroral data showing the ionospheric signature of a selection of Bursty Bulk Flows.

tion, which has been previously related to tail reconnection under the continued influence of IMF By [19, 22]. In the bottom panel, the flows associated with a BBF that occurred during a small ( $\sim 100$  nT) substorm are shown and appear to take the form of enhanced return flow in the dawn convection cell. Observations such as these require further investigation if we are to fully understand the role of BBFs in magnetospheric flux transport.

Another series of substorm related phenomena believed to drive magnetospheric circulation are the polarisation jets (PJs) [15], or sub-auroral ion drifts (SAIDs) [45]. PJ/SAIDs are fast ( $1 - 4 \text{ km s}^{-1}$ ) narrow ( $1 - 2^\circ$ ) channels of westward plasma flow which occur just equatorward of the equatorward edge of the auroral oval in the evening sector. Related phenomena identified in radar data include substorm-associated radar auroral surges (SARAS) [14, 43] and auroral westward flow channels (AWFCs) [37, 38]. AWFCs, however, have been observed to appear any time between substorm onset and recovery [38] whereas PJ/SAIDs identified in satellite data appear during recovery [2]. The term ‘sub-auroral polarisation stream’ (SAPS) is used to encompass all of these phenomena [10], which includes broader ( $3 - 5^\circ$ ), weaker ( $100 - 400 \text{ m s}^{-1}$ ), background

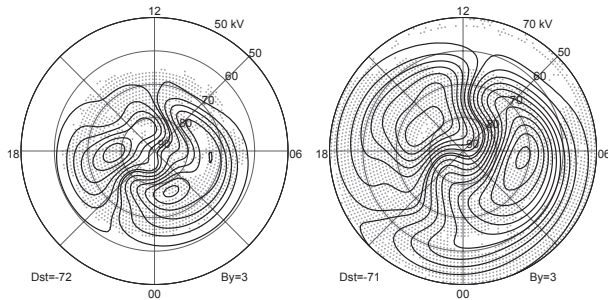


**Fig. 8.** An illustration of the effect on the SuperDARN convection patterns of including data from the mid-latitude radar on Wallops Island. The shaded areas indicate gridded radar measurements (courtesy, Jo Baker).

flows which persist beyond midnight into the predawn sector. These sub-auroral electric fields play critical roles in energising and transporting ring current ions as well as convecting thermal plasma in the inner magnetosphere and mid- to low-latitude ionosphere [11].

## 5. StormDARN

Finally, it is worth briefly mentioning the future of SuperDARN, called StormDARN, which consists of a series of mid-latitude radars, ultimately extending SuperDARN coverage down to about  $40^\circ$  north. One such radar is already in operation (shown in grey on Fig. 1) on Wallops Island. Data from this radar have been used to produce the illustration shown in Fig. 8, which reveals the effect on the convection pattern of adding in lower-latitude data. It is clear that during active times, when substorms generally occur, these new radars will be essential if we are to fully observe the substorm disturbed region.

## 6. Summary

There is little doubt that HF radar observations, such as those provided by SuperDARN discussed above, have revealed much about substorms and substorm-related phenomena. What is still yet to be achieved, however, is an overall synthesis of these observations which is essential if we are to fully understand the role of substorms in coupled magnetospheric-ionospheric dynamics. Clearly, the multi-instrument, multi-scale approach afforded to us by current Cluster-SuperDARN studies and by the advent of Themis, KuaFu, and StormDARN, is our passport to a more complete understanding of substorm physics.

**Acknowledgements:** A. Grocott's attendance at this conference was supported by a Royal Society Conference Grant.

## References

1. Akasofu, S.-I., Chapman, S., and Meng, C.-I.: The polar electrojet, *J. Atmos. Terr. Phys.*, *27*, 1275–1305, 1965.
2. Anderson, P.C., Hanson, W.B., Heelis, R.A., Craven, J.D., Baker, D.N., and Frank, L.A.: A proposed production model of rapid

subauroral ion drifts and their relationship to substorm evolution, *J. Geophys. Res.*, *98*, 6069–6078, 1993.

3. Angelopoulos, V., Baumjohann, W., Kennel, C.F., Coroniti, F.V., Kivelson, M.G., Pellat, R., Walker, R.J., Lühr, H., and Paschmann, G.: Bursty bulk flows in the central plasma sheet, *J. Geophys. Res.*, *97*, 4027–4039, 1992.
4. Baumjohann, W., Paschmann, G., and Lühr, H.: Characteristics of high-speed flows in the plasma sheet, *J. Geophys. Res.*, *95*, 3801–3809, 1990.
5. Clauer, C.R., and Kamide, Y.: DP-1 and DP-2 current systems for the March 22, 1979 substorms, *J. Geophys. Res.*, *90*, 1343–1354, 1985.
6. Cowley, S.W.H., and Lockwood, M.: Excitation and decay of solar wind-driven flows in the magnetosphere-ionosphere system, *Ann. Geophysicae*, *10*, 103–115, 1992.
7. Cowley, S.W.H., Excitation of flow in the Earth's magnetosphere-ionosphere system: observations by incoherent-scatter radar, in *Polar Cap Boundary Phenomena* edited by A. Egeland, J. Moen, and M. Lockwood, Kluwer Academic Publ., Dordrecht, p. 127, 1998.
8. Cowley, S.W.H., Khan, H., and Stockton-Chalk, A.: Plasma flow in the coupled magnetosphere-ionosphere system and its relationship to the substorm cycle, in *Substorms-4* edited by S. Kokobun and Y. Kamide, Terra Sci. Publ. Co., Tokyo, p. 623–628, 1998.
9. de la Beaujardière, O., Lyons, L.R., Ruohoniemi, J.M., Friis-Christensen, E., Danielsen, C., Rich, F.J., and Newell, P.T.: Quiet-time intensifications along the poleward boundary near midnight, *J. Geophys. Res.*, *99*, 287–298, 1994.
10. Foster, J.C. and Burke, W.J.: SAPS, A new categorization for subauroral electric fields, *EOS*, Transactions, American Geophysical Union, *83*(36), 393–394, 2002.
11. Foster, J.C. and Vo, H.B.: Average characteristics and activity dependence of the subauroral polarisation stream, *J. Geophys. Res.*, *107*, 1475, doi:10.1029/2002JA009409, 2002.
12. Fox, N.J., Cowley, S.W.H., Davda, V.N., Enno, G., Friis-Christensen, E., Greenwald, R.A., Hairston, M.R., Kivelson, M.G., Lester, M., Lockwood, M., Lühr, H., Milling, D.K., Murphree, J.S., Pinnock, M., and Reeves, G.D.: A multipoint study of a substorm occurring on 7 December 1992 and its theoretical implications, *Ann. Geophysicae*, *17*, 1369–1384, 1999.
13. Freeman, M.P., and Southwood, D.J.: The effect of magnetospheric erosion on mid- and high-latitude ionospheric flows, *Planet. Space Sci.*, *36*, 509–522, 1988.
14. Freeman, M.P., Southwood, D.J., Lester, M., Yeoman, T.K., and Reeves, G.D.: Substorm-associated radar auroral surges, *J. Geophys. Res.*, *97*, 12173–12185, 1992.
15. Galperin, Y.I., Ponomarev, V.N., and Zosimova, A.G.: Direct measurements of ion drift velocity in the upper ionosphere during a magnetic storm, 2. Results of measurements during the November 3, 1967, magnetic storm, *Cosmic Res (Russian)*, *11*, 283–292, 1973.
16. Greenwald, R.A., Baker, K.B., Dudeney, J.R., Pinnock, M., Jones, T.B., Thomas, E.C., Villain, J.-P., Cerisier, J.-C., Senior, C., Hanuise, C., Hunsucker, R.D., Sofko, G., Koehler, J., Nielsen, E., Pellinen, R., Walker, A.D.M., Sato, N., and Yamagishi, H.: DARN/SuperDARN: A global view of the dynamics of high-latitude convection, *Space Sci. Rev.*, *71*, 761–796, 1995.

17. Grocott, A., Cowley, S.W.H., and Davies, J.A.: Comparison of ionospheric electric currents and plasma convection patterns observed during substorms, in *Proc. Fifth Internat. Conf. on Substorms*, ESA SP-443, ESA, Noordwijk, The Netherlands, pp. 295–298, 2000.
18. Grocott, A., Cowley, S.W.H., Sigwarth, J.B., Watermann, J.F., and Yeoman, T.K.: Excitation of twin-vortex flow in the night-side high-latitude ionosphere during an isolated substorm, *Ann. Geophysicae*, *20*, 1577–1601, 2002.
19. Grocott, A., Cowley, S.W.H., and Sigwarth, J.B.: Ionospheric flows and magnetic disturbance during extended intervals of northward but BY-dominated IMF, *Ann. Geophysicae*, *21*, 509–538, 2003.
20. Grocott, A., Yeoman, T.K., Nakamura, R., Cowley, S.W.H., Rème, H., and Klecker, B.: Multi-instrument observations of the ionospheric counterpart to a bursty bulk flow in the near-Earth plasma sheet, *Ann. Geophysicae*, *22*, 1061–1075, 2004.
21. Grocott, A., Yeoman, T.K., Cowley, S.W.H., Rème, H.: Multi-instrument observations of bursty bulk flows and their ionospheric counterpart, in *Proc. Seventh Internat. Conf. on Substorms*, UDK-52-854, FMI, Helsinki, Finland, 103–106, 2004.
22. Grocott, A., Yeoman, T.K., Milan, S.E., and Cowley, S.W.H.: Interhemispheric observations of the ionospheric signature of tail reconnection during IMF-northward non-substorm intervals, *Ann. Geophysicae*, *23*, 1763–1770, 2005.
23. Henderson, M.G., Reeves, G.D., and Murphree, J.S.: Are north-south aligned auroral structures an ionospheric manifestation of bursty bulk flows?, *Geophys. Res. Lett.*, *25*, 3737–3740, 1998.
24. Hubert, B., Milan, S.E., Grocott, A., Blockx, C., Cowley, S.W.H., and Gérard, J.-C.: Dayside and nightside reconnection rates inferred from IMAGE-FUV and SuperDARN data, *J. Geophys. Res.*, *111*, doi:10.1029/2005JA011140, 2006.
25. Jayachandran, P.T., MacDougall, J.W., Donovan, E.F., Ruohoniemi, J.M., Liou, K., Moorcroft, D.R., and St. Maurice, J.-P.: Substorm associated changes in the high-latitude ionospheric convection, *Geophys. Res. Lett.*, *30*, doi:10.1029/2003GL017497, 2003.
26. Kamide, Y., Richmond, A.D., Emery, B.A., Hutchins, C.F., Ahn, B.H., de la Beaujardière, O., Foster, J.C., Heelis, R.A., Kroehl, H.W., Rich, F.J., and Slavin, J.A.: Ground-based studies of ionospheric convection associated with substorm expansion, *J. Geophys. Res.*, *99*, 19451–19466, 1994.
27. Lester, M.: HF coherent scatter radar observations of ionospheric convection during magnetospheric substorms, *Adv. Polar Upper Atmos. Res.*, *14*, 179–201, 2000.
28. Lewis, R.V., Freeman, M.P., Roger, A.S., Reeves, G.D., and Milling, D.K.: The electric field response to the growth and expansion phase onset of a small isolated substorm, *Ann. Geophysicae*, *15*, 289–299, 1997.
29. Liang, J., Sofko, G.J., and Frey, H.U.: Postmidnight convection dynamics during substorm expansion phase, *J. Geophys. Res.*, *111*, doi:10.1029/2005JA011483, 2006.
30. Lui, A.T.Y., and Kamide, Y.: A fresh perspective of the substorm current system and its dynamo, *Geophys. Res. Lett.*, *30*, 1958, doi:10.1029/2003GL017835, 2003.
31. Lyons, L.R., Nagai, T., Blanchard, G.T., Samson, J.C., Yamamoto, T., Mukai, T., Nishida, A., and Kokubun, S.: Association between Geotail plasma flows and auroral poleward boundary intensifications observed by CANOPUS photometers, *J. Geophys. Res.*, *104*, 4485–4500, 1999.
32. Lyons, L.R., Ruohoniemi, J.M., and Lu, G.: Substorm-associated changes in large-scale convection during the November 24, 1996, Geospace Environment Modelling event, *J. Geophys. Res.*, *106*, 397–405, 2001.
33. McPherron, R.L.: Growth phase of magnetospheric substorms, *J. Geophys. Res.*, *75*, 5592–5599, 1970.
34. Milan, S.E., Davies, J.A., and Lester, M.: Coherent HF radar backscatter characteristics associated with auroral forms identified by incoherent radar techniques: a comparison of CUTLASS and EISCAT observations, *J. Geophys. Res.*, *104*, 22 591–22 604, 1999.
35. Morelli, J.P., Bunting, R.J., Cowley, S.W.H., Farrugia, C.J., Freeman, M.P., Friis-Christensen, E., Jones, G.O.L., Lester, M., Lewis, R.V., Lühr, H., Orr, D., Pinnock, M., Reeves, G.D., Williams, P.J.S., and Yeoman, T.K.: Radar observations of auroral zone flows during a multiple-onset substorm, *Ann. Geophysicae*, *13*, 1144–1163, 1995.
36. Opgenoorth, H.J., and Pellinen, R.J.: The reaction of the global convection electrojets to the onset and expansion of the substorm current wedge, in *Substorms-4* edited by S. Kokobun and Y. Kamide, Terra Sci. Publ. Co., Tokyo, pp. 663–668, 1998.
37. Parkinson, M.L., Pinnock, M., Dyson, P.L., Ye, H., Devlin, J.C., and Hairston, M.R.: On the lifetime and extent of an auroral westward flow channel observed during a magnetospheric substorm, *Ann. Geophys.*, *21*, 893–913, 2003.
38. Parkinson, M.L., Dyson, P.L., and Pinnock, M.: On the occurrence of auroral westward flow channels and substorm phase, *Adv. Space Res.*, doi:10.1016/j.asr.2005.08.028, 2005.
39. Provan, G., Lester, M., Mende, S.B., Milan, S.E.: Statistical study of high-latitude plasma flow during magnetospheric substorms, *Ann. Geophysicae*, *22*, 3607–3624, 2004.
40. Russell, C.T.: The configuration of the magnetosphere, in *Critical Problems of Magnetospheric Physics*, edited by R. Dyer, pp. 1–16, Nat. Acad. of Sci., Washington, D.C., 1972.
41. Ruohoniemi, J.M., and Greenwald, R.A.: Statistical patterns of high-latitude convection obtained from Goose Bay HF radar observations, *J. Geophys. Res.*, *101*, 21743–21763, 1996.
42. Ruohoniemi, J.M., and Baker, K.B.: Large-scale imaging of high-latitude convection with Super Dual Auroral Radar Network HF radar observations, *J. Geophys. Res.*, *103*, 20797–20811, 1998.
43. Shand, B.A., Lester, M., Yeoman, T.K.: Substorm associated radar auroral surges: a statistical study and possible generation model, *Ann. Geophysicae*, *16*, 441–449, 1998.
44. Siscoe, G.L., and Huang, T.S.: Polar cap inflation and deflation, *J. Geophys. Res.*, *90*, 543–547, 1985.
45. Spiro, R.W., Heelis, R.A., and Hanson, W.B.: Rapid subauroral ion drifts observed by Atmospheric Explorer C, *Geophys. Res. Lett.*, *6*, 660–663, 1979.
46. Yeoman, T.K., and Lühr, H.: CUTLASS/IMAGE observations of high-latitude convection features during substorms, *Ann. Geophysicae*, *15*, 692–702, 1997.
47. Yeoman, T.K., and Pinnock, M.: The high latitude convection response to an interval of substorm activity, *Ann. Geophysicae*, *14*, 518–532, 1996.
48. Yeoman, T.K., Davies, J.A., Wade, N.M., Provan, G., and Milan, S.E.: Combined CUTLASS, EISCAT and ESR observations of ionospheric plasma flows at the onset of an isolated substorm, *Ann. Geophysicae*, *18*, 1073–1087, 2000.

# Are we on the right approach to solve the substorm problem?

W. J. Heikkila

**Abstract:** It is time to have a serious appraisal on the correct approach to solve the substorm problem, bearing in mind as to what happened with continental drift some four decades ago. We must deal in 3-D, not 2-D (the basis of the reconnection model). We must ascertain the source of energy,  $\mathbf{E} \cdot \mathbf{J} < 0$ , for the dissipation associated with reconnection. We must close all currents to treat cause vs effect, i.e.  $\mathbf{E} \cdot \mathbf{J} < 0$  vs  $\mathbf{E} \cdot \mathbf{J} > 0$ . We need to face some harsh realities.

*Key words:* magnetic reconnection, viscous interaction, substorms.

## 1. Introduction

After five decades of observations and theoretical research the mechanisms for the interaction of the solar wind with the magnetosphere are far from being resolved. Two mechanisms have been proposed long ago in 1961, magnetic reconnection by Dungey [10], and viscous interaction by Axford and Hines [1]. The process of magnetic reconnection was sketched in the  $x, z$  noon-midnight meridian plane, while viscous interaction uses the  $x, y$  equatorial plane, both in 2-D. Importance of three dimensions is beyond doubt; still, the difficulty in conveying that idea on 2-D paper seemed to be overwhelming. I first discuss magnetic reconnection on the dayside since the conditions there are easier to resolve, then the substorm problem.

## 2. Magnetic reconnection (MR)

An X-line, or reconnection line, appears on the dayside [10]; this is clearly the case for a southward IMF in view of topological considerations. The magnetic field direction in the equatorial plane near noon meridian has to go from southward (IMF) to northward (Earth's dipole) in a continuous fashion, so that somewhere it must go through zero. There is an X-line in the magnetotail as well [10]. In fact, there should be an X-ring around the entire magnetosphere in 3-D; the X-lines are the intersection of this ring with the meridian plane. The conditions are modified for any other choice of the IMF but the physics is clearer for the southward case. The analysis in the  $x, z$  noon-midnight meridian plane has been widely used in research on magnetic reconnection, both dayside and nightside, even in the presentation of substorm data.

### 2.1. Reconnection is defined in 2-D

Figure 1 shows a hatched box around the X-line with the assumed spatially constant electric field; curl  $\mathbf{E}$  is zero by definition as an initial condition. The plasma moves toward the X-line from both sides by  $\mathbf{E} \times \mathbf{B}$  drift. The only possible outflow is toward open magnetic field lines (one foot in the IMF, the other in the ionosphere). The magnetic field lines from the X-line indicate the separatrix surfaces, S1 going to the IMF, S2 to the geomagnetic field.

to the geomagnetic field. One definition of reconnection that is commonly used was well stated by Sonnerup [34] as:

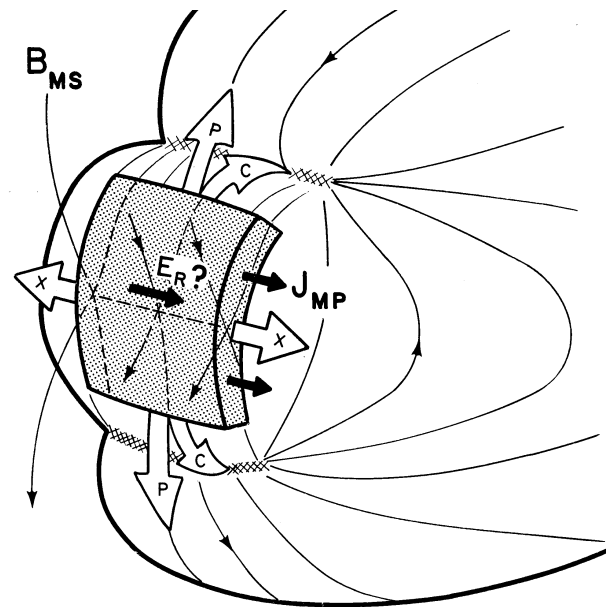


**Fig. 1.** Plasma moving toward the X-line at the magnetopause from both sides with the assumed spatially constant electric field; curl  $\mathbf{E}$  is zero as an initial condition. The only possible outflow is toward open magnetic field lines. The magnetic field lines from the X-line indicate the separatrix surfaces, S1 going to the IMF, S2 to the geomagnetic field.

“any plasma process with a non-zero component along the X-line separating magnetic fields from two different sources. . . . No plasma physics has been introduced into the above discussion but it is the presence of a highly conducting plasma that assures that the condition  $\mathbf{E} \cdot \mathbf{B} = 0$  is satisfied everywhere except at the separator.”

The above definition was viewed as being quite general and broad, non-restrictive. This in spite of the requirement “the condition  $\mathbf{E} \cdot \mathbf{B} = 0$  is satisfied everywhere except at the separator”, this implying that essential plasma physics must be used

Received 15 May 2006.

W. J. Heikkila, University of Texas at Dallas, P. O. Box 830688, Richardson, TX, USA : heikkila@utdallas.edu

in the explanation (see Section 4.3.4). In contrast to the outflow with MR on open magnetic field lines, the low latitude boundary layer extends to closed field lines.

MR has led to considerable research for over the past four decades. Birn et al. [3, p.3718] summarized the results of a coordinated study in the Geospace Environmental Modeling (GEM) program. "The key conclusion of this project is that the Hall effect is the critical factor which must be included to model collisionless magnetic reconnection." These authors continue with an important stipulation:

"The conclusions of this study pertain *explicitly* to the 2-D system. There is mounting evidence that the narrow layers which develop during reconnection in the 2-D model are strongly unstable to a variety of modes in the full 3-D system."

## 2.2. Anomalous resistivity

The constant electric field did pose a significant problem, that of maintaining an electric field when the Lorentz force vanishes at the X-line. An anomalous resistivity seemed to be a requirement in the so-called diffusion region [31]. This is still unresolved, prompting an article by Coroniti, *Turbulent Dissipation: Reality or Myth* [8]. In spite of this warning, the reconnection model continues to be in 2-D. The manner in which the electric field is handled in the theoretical work is commonly stated as follows [30]:

"We divide the problem into two parts. One part concerns the specification of the electric field inside the diffusion region. The process which gives rise to this electric field should be studied with the aid of kinetic theory. This topic is poorly understood at present and seems to depend on the particular situation being considered. We therefore prescribe the reconnection electric field as an input parameter, i.e., a given function along the reconnection line, which is directed along the y axis. This allows us to investigate the large-scale consequences of an arbitrary functional behavior of the reconnection rate, which forms the second part of the problem. Strictly speaking, of course, we should solve these two parts self-consistently."

## 2.3. Source of energy dissipated by MR

In reconnection theory only the dissipation is considered, an electrical load with  $\mathbf{E} \cdot \mathbf{J} > 0$  (current parallel to the electric field). In 2-D it is not possible to discuss the source of this energy, to search for another region in space where  $\mathbf{E} \cdot \mathbf{J} < 0$  in the same current circuit. It is very important to develop a model of a substorm in 3-D for this reason alone. This has been echoed by Siebert and Siscoe [32]:

"The result has the profound consequence that if there is a segment of a closed current tube in which energy is being dissipated (for example, in magnetic reconnection), and thus  $\mathbf{J} \cdot \mathbf{E}$  is positive, there must exist another segment of the [current] tube in which  $\mathbf{J} \cdot \mathbf{E}$  is negative so as to exactly compensate for the dissipation segment in the closed line integral of I."

In the case of the Dungey model of the magnetosphere there is a dynamo with  $\mathbf{E} \cdot \mathbf{J} < 0$  over the lobe magnetopause (the current being in the dusk-dawn direction with the assumed dawn-dusk electric field); this could, in principle, deliver energy in the steady state by the magnetopause current to the reconnection region with  $\mathbf{E} \cdot \mathbf{J} > 0$  (both dayside reconnection but also nightside reconnection within the magnetotail). Thus the source of energy for dayside reconnection is not upstream, as suggested by steady state reconnection defined in two dimensions, with the inflow of magnetic energy to power dayside reconnection, but it is instead a dynamo over the lobes. However, there are questions for the reality of this location of the dynamo, e.g., the northward direction of the magnetic field (see Figure 3), travel time for the energy, and several more.

## 2.4. Definition of Magnetic Reconnection

The definition of reconnection [34] seems to be quite general; however, it is *fatally deficient* in that it does not address the essential quantity:  $\text{curl } \mathbf{E}$ . This does not mean that the state of interconnection between the geomagnetic field and the interplanetary magnetic field can not change, but it does mean that the advocated process is not relevant to such changes. Only the following term is concerned with magnetic energy:

$$\iiint_{vol} \frac{\mathbf{B}}{\mu_0} \cdot \frac{\partial \mathbf{B}}{\partial t} d\tau = \frac{d}{dt} \iiint_{vol} \frac{B^2}{2\mu_0} d\tau \quad (1)$$

The wrong term was used, and still is, in Poynting's theorem for the reconnection problem [17]. By this simple, yet fundamental, argument it can be concluded that magnetic reconnection, as presently understood, and practiced, is unphysical.

## 2.5. Interconnection of magnetic fields

The above volume integral has been used in [17] for analysis of plasma transfer events (PTE, considered in the next section). True reconnection is accomplished only by the electromotive force through which energy can be interchanged with stored magnetic energy. By Faraday's law

$$\nabla \times \mathbf{E} = -\partial \mathbf{B} / \partial t \quad (2)$$

we see that  $\text{curl } \mathbf{E}$  is vital to deal with changes in the magnetic field. Such a curl is not included as an initial condition in Figure 1 because the electric field is assumed to be spatially constant, thus no curl. This is obvious in the integral form:

$$\epsilon = \oint \mathbf{E} \cdot d\mathbf{l} = -d\Phi^M / dt \quad (3)$$

where  $\epsilon$  is the electromotive force ( $\Phi^M$  is the magnetic flux through the contour). The sense of the electric field is different on the two sides of the magnetopause [16]; a finite value for the line integral over any closed path that includes the magnetopause means a finite electromotive force. Energy can be extracted from the magnetic field; the induction electric field acts as intermediary.

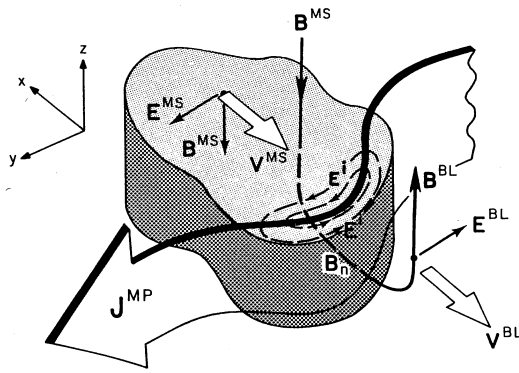


**Fig. 2.** A localized plasma cloud impacting the magnetopause current sheet. With its assumed excess momentum it distorts the current, a localized meander, causing an induction electric field as indicated, everywhere opposed to the current perturbation by Lenz's law. The plasma response depends on the conductivity; in a collisionless plasma the Pedersen conductivity vanishes, but the field-aligned conductivity is very high, denoting a dependence on the interplanetary magnetic field (IMF).

### 3. Viscous interaction (VI)

I accept the view that the existence of the boundary layer inside the magnetopause (LLBL) is crucial to the physics of the magnetosphere [7, 11, 15, 22, 23]. The boundary layer flow is so massive that it can generate its own electric field by a polarization current for continued anti-sunward flow. At great distances (some  $100 R_E$  downstream from the earth) the dawn and dusk boundary layers become joined together, and the magnetotail from there is essentially just boundary layer plasma, on closed magnetic field lines, all traveling tailward with no return flow [33, 37] (see Figure 4).

It is a dynamo with  $\mathbf{E} \cdot \mathbf{J} < 0$ , energy going from the plasma to the electromagnetic field. This is the viscous interaction that Axford and Hines [1] had sought. When they proposed their process they had little idea as to the responsible mechanism for the effective viscosity [private communication by Hines, 1985]. The LLBL had not been discovered.

#### 3.1. Faraday's law and electromotive force (emf)

Figure 2 shows a cloud of magnetosheath plasma impacting the magnetopause current. It is assumed that the magnetic flux tube extends in the  $z$ -direction; nevertheless, the figure is essentially three dimensional:  $x - z$  to show the magnetic topology, and  $x - y$  to show curl  $\mathbf{E}$  with finite dimension in the  $y$ -direction. The induced electric field shown follows from elementary electromagnetic theory; the assumed motion of the magnetopause, an earthward meander of the magnetopause current, will create an induction electric field, with a finite curl [17].

#### 3.2. The total electric field

The electric field shown in Figure 2 is only the induction electric field. It is likely that the local plasma can modify this field, for example by charge separation to create an electrostatic field if the normal component of the magnetic field is

finite. Briefly, the plasma response depends on the local conductivity, or rather, the tensor conductivity in the gyromagnetic medium. A collisionless plasma has a Pedersen conductivity that is very low. On the other hand, the direct conductivity along the magnetic field is very high. Thus we expect that the actual electric field at the magnetopause depends on having a finite  $B_n$  at the magnetopause. The electric field has two sources:

$$\mathbf{E} = -\nabla\phi - \partial\mathbf{A}/\partial t \quad (4)$$

The electrostatic field is conservative, while the induction is solenoidal. A localized induction electric field is forced upon the plasma, not an electrostatic field. It is entirely local, opposed to the current perturbation by Lenz's law.

#### 3.2.1. Motion of the magnetopause with $B_n = 0$

We need to consider 2 cases regarding  $B_n$ . If  $B_n = 0$  the plasma cannot respond by charge separation, and no electrostatic field is created. The magnetosheath flow is tangential to the magnetopause as observed in [25] with low shear.

#### 3.2.2. Response of the plasma: $B_n$ is finite

The plasma response changes dramatically with an open magnetosphere. If there is a normal component of the magnetic field through the current sheet  $\mathbf{E}^{ind}$  can polarize the plasma along  $B_n$  causing an electrostatic field tangential to the MP. We see that this  $\mathbf{E}^{es}$  will drive the SW plasma into the current sheet, in the reconnection frame [25].

On the other side, since both  $\mathbf{B}$  and  $\mathbf{E}$  reverse, the electric drift  $\mathbf{E} \times \mathbf{B}$  will be also earthward. Plasma transfer is created.

### 3.3. Plasma transfer event (PTE)

There is no question about the reality of a plasma transfer event (PTE); observations come from a variety of sources beginning with the rocket results of Carlson and Torbert [6] (see the reviews in [17, 21, 23, 38]).

In summary, there are two complementary processes: polarization electric field, which does not depend on the movement of the magnetopause itself, and induction electric field due to magnetopause erosion, which does. Lemaire and Roth [21] used electric energy of the plasma, i.e. plasma in motion, in a process they called impulsive penetration (IP), based on the pioneering work by Schmidt [28, 29]. I used a different process, that of tapping magnetic energy with the induction electric field in a complete current circuit [17].

A finite  $B_n$  is crucial to the PTE. This process was seen by C3 of the Cluster mission [19].

#### 3.4. Low latitude boundary layer (LLBL)

The LLBL is earthward of separatrix S2, on closed field lines [11, 12, 13]. This layer *completely insulates* the plasma mantle on open field lines from the plasma sheet. Plasma flow must still be tailward; it is strong flow of a hefty plasma, ( $n \sim 1 - 5 \text{ cm}^{-3}$  [37], delivering ion/electrons of about  $\sim 10^{27}/\text{s}$ ). Since this is mostly  $\mathbf{E} \times \mathbf{B}$  flow it is necessary to maintain an electric field on closed field lines; this is accomplished by a polarization current (preceding section). The polarization current has to move charges against the field, so that it must be a dynamo with  $\mathbf{E} \cdot \mathbf{J} < 0$ .

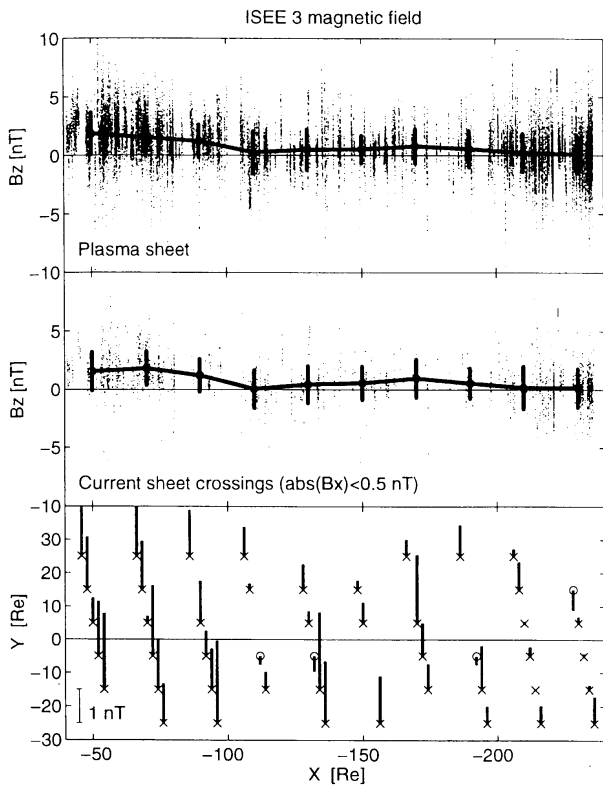


**Fig. 3.** Top: Plasma sheet  $B_z$  as a function of  $X$  in the anti-sunward direction. The averages ( $20R_E$  bins) and variances are shown with heavy lines. Middle: Plasma sheet  $B_z$  at current sheet crossings ( $|B_x| < 0.5$  nT). The averages and variances are shown. Bottom: A quasi-three-dimensional view of the  $B_z$  at the plasma sheet. The vertical bars indicate the average  $B_z$ , the scale is given in the lower left hand corner [26].

## 4. The substorm problem

A magnetospheric substorm is a transient process of energy storage, release, and dissipation. For the past 40 years many substorm models have been put forward but none can completely explain the various phenomena of substorms. According to Vasyliunas, “Explaining the sudden onset of the expansion phase of magnetospheric substorms has proved to be one of the most intractable problems in magnetospheric physics to date” [36]. Baker et al. noted: “... fundamental issues remain to be resolved. Why, for example, is the magnetosphere stable most of the time, and why do substorms occur just when they do? What allows the violation of the frozen-flux constraint necessary for an efficient energy release by reconnection in the course of substorms?” [2].

### 4.1. The setting

Several spacecraft have explored the magnetotail as far as  $220 R_E$ ; [26] have used ISEE-3 to evaluate the z-component  $B_z$  as shown by Figure 3. They found that it was positive (northward) in the average values, using all the data in the top panel, but also in the current sheet. It did not reverse as it should have according to the Dungey model.

## 4.2. The far tail is a dynamo

It was found that at  $180 R_E$  the plasma flow was tailward, implying an electric field that was from dusk to dawn [33, 37]. Since the current was dawn-dusk in view of the extreme tail-like shape, the conclusion is that  $\mathbf{E} \cdot \mathbf{J} < 0$  (see Figure 4).

### 4.2.1. Exit at the distant magnetopause

All that plasma must exit the closed field line region that is apparent in Figure 3 beyond several  $100 R_E$  to the right in Figure 4 [14]. Perhaps the process is similar to a PTE event on the dayside.

### 4.2.2. The dip in $B_z$ at $120 R_E$

Something strange happens just beyond  $100 R_E$ ; it appears to be where the plasma sheet boundary (PSBL) is located. The dip in  $B_z$  at  $120 R_E$  could be caused by a cross-tail current separating the plasma sheet (with earthward flow) with the LLBL (with tailward flow).

## 4.3. Substorms begin near midnight

A substorm is initiated by a growth phase which feeds particles and energy into the plasma sheet. The plasma supplies this energy by a dynamo in the LLBL where  $\mathbf{E} \cdot \mathbf{J} < 0$ : the plasma particles release energy to the electromagnetic field. In contrast to this is a region where  $\mathbf{E} \cdot \mathbf{J} > 0$ : here the particles are accelerated and energy is dissipated, as in auroral arcs, in auroral electrojets, in the hypothesized ‘reconnection’ region.

### 4.3.1. Trigger phase

This important activity is localized in the plasma sheet at first during a trigger phase, reaching into the distant boundary layer somewhat later. In fact, we have known for a long time that a breakup usually starts on an equatorward arc; therefore, we must look in the inner plasma sheet ( $10 - 20 R_E$ ) for the trigger mechanism.

We have proposed [18] that the appropriate instability to trigger a substorm is a tailward meander in the equatorial plane of the strong current filament that develops during the growth phase. From this single assumption follows the entire sequence of events for a substorm.

### 4.3.2. Motion becomes chaotic

The particle acceleration mechanism in the plasma sheet is curvature drift with a dawn-dusk electric field, leading to the production of auroral arcs. Eventually the curvature becomes so high that the ions cannot negotiate the sharp turn at the field-reversal region, locally, at a certain time [9]. The particle motion becomes chaotic, causing a local outward meander of the cross-tail current.

### 4.3.3. Electromotive instability

An induction electric field is produced  $\mathbf{E}^{ind} = -\partial\mathbf{A}/\partial t$ , by Lenz’s law. An outward meander with  $B_z > 0$  causes  $\mathbf{E} \times \mathbf{B}$  flow everywhere out from the disturbance; this reaction is a macroscopic instability which we designate the *electromotive instability*.

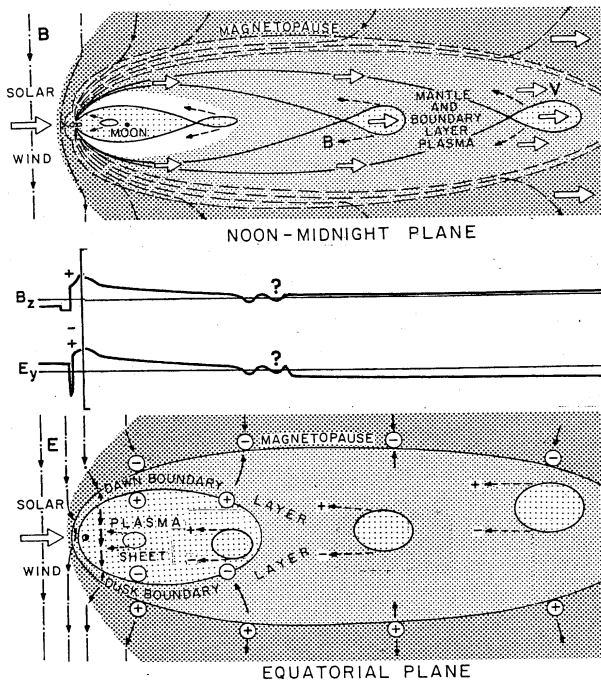


**Fig. 4.** Two views of the magnetosphere, noon-midnight median (top) and equatorial (bottom). The low latitude boundary layer is a dipole layer with negative and positive charges for a southward IMF. The dawn and dusk layers come together at 100 to 150  $R_E$ . Middle: the profiles of the magnetic field  $B_z$  and the electric field  $E_y$  are based on spacecraft data. During substorms plasmoids may be created near the Earth, propagating tailwards. Within the plasma sheet they proceed against the normal earthward flow, but they coast with the tailward flow farther out.

**4.3.4. The response of the plasma**

The response of the plasma to the sudden formation of an induction electric field  $\mathbf{E}^{ind} = -\partial\mathbf{A}/\partial t$  is through charge separation and a scalar potential,  $\mathbf{E}^{es} = -\nabla\phi$ . Both types of electric fields have components parallel to  $\mathbf{B}$  in a realistic magnetic field. For MHD theory to hold the net  $\mathbf{E}_{\parallel}$  must be small:

$$\mathbf{E}_{\parallel} = \mathbf{E}_{\parallel}^{es} + \mathbf{E}_{\parallel}^{ind} \sim 0 \tag{5}$$

This usually seems to happen because MHD often does hold, but not always. The requirement “the condition  $\mathbf{E} \cdot \mathbf{B} = 0$  is satisfied everywhere except at the separator” (section 2.1) does imply some essential plasma physics.

**4.3.5. Formation of field-aligned currents**

Part of the response is the formation of field-aligned currents producing the well-known substorm current diversion. This is a direct result of a strong  $\mathbf{E}_{\parallel}^{ind}$  (the cause) needed to overcome the mirror force of the current carriers; this enables charge separation to produce an opposing electrostatic field  $\mathbf{E}_{\parallel}^{es}$  (the effect). Satellite data confirm the reality of a strong  $\mathbf{E}_{\parallel}$  in the plasma sheet by counter-streaming of electrons and ions [20], and by the inverse ion time dispersion, up to several 100 keV [27].

**4.3.6. Free energy of the stressed magnetotail**

However, with zero curl, the electrostatic field  $\mathbf{E}^{es}$  cannot modify the emf  $\varepsilon = \oint \mathbf{E} \cdot d\mathbf{l} = -d\Phi^M/dt$  of the inductive electric field  $\mathbf{E}^{ind}$ ; the charge separation that produces a reduction in the parallel component  $\mathbf{E}_{\parallel}$  must enhance the transverse component  $\mathbf{E}_{\perp}$ . The enhanced transverse component will lead to strong flows perpendicular to the magnetic field depending on the solenoidal electric field (e.g. bursty bulk flows).

**4.3.7. Plasmoid may be created**

On the tailward side of the developing plasmoid the dusk-dawn electric field with  $\mathbf{E} \cdot \mathbf{J} < 0$  will cause tailward motion of the plasma; a plasmoid may be created. It will move in the direction of least magnetic pressure, tailward. A dynamo is a necessity since the plasmoid has to proceed against the earthward flow within the plasma sheet. This may require that field aligned currents reach into the polar caps, observed to exist as far as  $80^\circ$ . Once it gets into the LLBL beyond 100  $R_E$  it can coast along with little resistance.

**4.3.8. Electric field near the emerging X-line**

It is likely that an emerging X-line will develop; this will depend on the strength of the dynamo. On the earthward side the enhanced dawn-dusk induction electric field with  $\mathbf{E} \cdot \mathbf{J} > 0$  will cause injection into the inner plasma sheet, repeatedly observed at moderate energies up to 50 keV.

**4.3.9. Acceleration to high energies**

This same electric field near the emerging X-line will accelerate particles non-adiabatically to moderate energies. With high magnetic moments in a weak magnetic field, electrons (ions) can benefit from gradient and curvature drift to attain high energies (by the ratio of the magnetic field magnitude) in seconds (minutes) [4, 24].

**5. Problems to be resolved**

There is always a strong inclination for a body of professionals to oppose an unorthodox view. In the case of continental drift Sir Edward Bullard [5] summarized his own view:

“Clearly it is more prudent to keep quiet, to be a moderate defender of orthodoxy, or to maintain that all is doubtful, sit on the fence, and wait in statesmanlike ambiguity for more data (my own line till 1959).”

as quoted by David Stern [35]. Here we must recognize some essential points as follows.

- 5.1. The far tail is a dynamo with  $\mathbf{E} \cdot \mathbf{J} < 0$
- 5.2. Plasma must exit at the distant magnetopause
- 5.3. Consequences of the current between PS and LLBL
- 5.4. Cause(s) of the trigger phase
- 5.5. Limited response of the plasma,  $\mathbf{E}^{ind} = -\partial\mathbf{A}/\partial t$  vs  $\mathbf{E}^{es} = -\nabla\phi$
- 5.6. Plasmoid and flux ropes are created
- 5.7. Sources of electric field near the emerging X-line
- 5.8. Acceleration to high energies, still unresolved

## References

1. Axford, W. I., and C. O. Hines, A unifying theory of high-latitude geophysical phenomena and geomagnetic storms, *Can. J. Phys.*, **39**, 1433, 1961.
2. Baker, D. N., Pulkkinen, T. I., Büchner, and Klimas, A. J., *J. Geophys. Res.*, **104**, 14601, 1999.
3. Birn, J., J. F. Drake, M. A. Shay, B. N. Rogers, R. E. Denton, M. Hesse, M. Kuznetsova, Z. W. Ma, A. Battacherjee, A. Otto, and P. L. Prichett, Geospace Environmental Modeling (GEM) Magnetic Reconnection Challenge, *J. Geophys. Res.*, **106**, 3715, 2001.
4. Bulanov, S. V. and Sasorov, P. V., *Astron. J.*, **52**, 763, 1975 (in Russian).
5. Bullard, E., The Emergence of Plate Tectonics: A Personal View, *Annual Review of Earth and Planetary Sciences*, **3**, 1-30 (quotation p.5), 1975.
6. Carlson, C. W., and R. B. Torbert, Solar Wind Ion Injections in the Morning Auroral Oval, *J. Geophys. Res.*, **85**, 2903, 1980.
7. Cole, K. D., On solar wind generation of polar geomagnetic disturbances, *Geophys. J. Royal Astro. Soc.*, **6**, 103, 1961.
8. Coroniti, F., Space plasma turbulent dissipation: reality or myth?, *Space Sci. Rev.*, **42**, 399, 1985.
9. Delcourt, D. and Belmont, G., in AGU Monograph 105, *New Perspectives on the Earth's Magnetotail*, eds. Nishida, A., Baker, D. N., and Cowley, S. W. H., 193, 1998.
10. Dungey, J. W., Interplanetary magnetic field and the auroral zones, *Phys. Rev. Lett.*, **6**, 47, 1961.
11. Eastman, T. E., E. W. Hones, Jr., S. J. Bame, and J. R. Asbridge, The magnetospheric boundary layer: Site of plasma, momentum, and energy transfer from the magnetosheath into the magnetosphere, *Geophys. Res. Lett.*, **3**, 685, 1976.
12. Eastman, T. E., and E. W. Hones, Jr., Characteristics of the Magnetospheric Boundary Layer and Magnetopause Layer as Observed by Imp 6, *J. Geophys. Res.*, **84**, 2019, 1979.
13. Fujimoto, M. T. Terasawa, T. Mukai, Y. Saito, T. Yamamoto, and S. Kokubun, Plasma entry from the flanks of the near-Earth magnetotail: Geotail observations, *J. Geophys. Res.*, **103**, 4391, 1998.
14. Heikkila, W. J., Exit of boundary layer plasma from the distant magnetotail, *Geophys. Res. Lett.*, **10**, 218, 1983.
15. Heikkila, W. J., Magnetospheric Topology of Fields and Currents, AGU Monograph Volume 28, *Magnetospheric Currents*, ed. T. Potemra, 208, 1984.
16. Heikkila, W. J., Interpretation of recent AMPTE data at the magnetopause, *J. Geophys. Res.*, **102**, 2115, 1997.
17. Heikkila, W. J., Cause and effect at the magnetopause, *Space Sci. Rev.*, **83**, 373, 1998.
18. Heikkila, W. J., T. Chen, Z. X. Liu, Z. Y. Pu, R. J. Pellinen, and T. I. Pulkkinen, Near Earth Current Meander (NECM) Model of Substorms, *Space Sci. Rev.*, **95**, 399, 2001.
19. Heikkila, Canu, Dandouras, Keith, and Khotyaintsev, Plasma transfer event seen by Cluster, Polar Cusp and Magnetopause in ESTEC SP-598, *Cluster and Double Star Symposium, 5th Anniversary of Cluster in Space*, 2006.
20. Kirsch, E., Krimigis, S. M., Sarris, E. T., Lepping, R. P., and Armstrong, T. P., Evidence for an electric field in the magnetotail from observations of oppositely directed anisotropies of energetic ions and electrons, *Geophys. Res. Lett.*, **4**, 137, 1977.
21. Lemaire, J. and M. Roth, Non-steady-state solar wind-magnetosphere interaction, *Space Sci. Rev.*, **57**, 59, 1991.
22. Lundin, R. and D. Evans, Boundary layer plasmas as a source for high-latitude, early afternoon, auroral arcs, *Planet. Space Sci.*, **33**, 1389, 1985.
23. Lundin, R., On the Magnetospheric Boundary Layer and Solar Wind Energy Transfer into the Magnetosphere, *Space Sci. Rev.*, **48**, 263, 1988.
24. Pellinen, R. J. and W. J. Heikkila, W. J., Energization of Charged Particles to High Energies by an Induced Substorm Electric Field Within the Magnetotail, *J. Geophys. Res.*, **83**, 1544, 1978.
25. Phan, T.-D. and G. Paschmann, The low-latitude dayside magnetopause and boundary layer for high magnetic shear: 1. Structure and motion, *J. Geophys. Res.*, **101**, 7801, 1996.
26. Pulkkinen, T. I., D. N. Baker, C. J. Owen, and J. A. Slavin, A model for the distant tail field: ISEE-3 revisited, *J. Geomag. Geoelectr.*, **48**, 455, 1996.
27. Sarafopoulos, D. V. and Sarris, E. T., Inverse velocity dispersion of energetic particle bursts inside the plasma sheet, *Planet. Space Sci.*, **36**, 1181, 1988.
28. Schmidt, G., Plasma motion across magnetic fields, *Phys. Fluids*, **3**, 961, 1960.
29. Schmidt, G., *Physics of High Temperature Plasmas*, Academic, San Diego, Calif., 1979.
30. Semenov, Vladimir S. et al., Time-dependent localized reconnection of skewed magnetic fields, *J. Geophys. Res.*, **97**, 4251, 1992.
31. Sibeck D. G., et al., Plasma transfer processes at the magnetopause, *Space Sci. Rev.*, **88**, 1999; also as Volume 6 of *Space Science Series* of ISSI, Kluwer Academic Publishers, Page 207-283, 1999.
32. Siebert, K. D. and G. L. Siscoe, Dynamic circuits for magnetopause reconnection, *J. Geophys. Res.*, **107**, 2002.
33. Slavin et al., An ISEE-3 Study of Average and Substorm Conditions in the Distant Magnetotail, *J. Geophys. Res.*, **90**, 10875, 1985.
34. Sonnerup, B. U. Ö., Magnetic field reconnection in cosmic plasma, in M. R. Kundu and G. D. Holman (eds.), *Unstable current systems and plasma instabilities in astrophysics*, D. Reidel, Dordrecht, the Netherlands, 1985.
35. Stern, D., Why was Wegener Rejected?, *Forum article in EOS*, April 7, 1998.
36. Vasyliunas, V. M., Abstract, *ICS-5*, Lake Hamana, Japan, 1998.
37. Yamamoto, T. et al., Dense plasmas in the distant magnetotail observed by GEOTAIL, *Geophys. Res. Lett.*, **21**, 2879, 1994.
38. Woch, J. and R. Lundin, Signatures of transient boundary layer processes observed with Viking, *J. Geophys. Res.*, **97**, 1431, 1992.

# Physics modeling of storms and substorms with solar wind data

W. Horton, M. L. Mays, and E. Spencer

**Abstract:** Analytic solar wind signals are constructed using data from the ACE satellite for the 3-6 October 2000 and 15-24 April 2002 geomagnetic storm events which included interplanetary shocks and magnetic clouds. The response of the WINDMI model, an eight dimensional model of the solar wind driven magnetosphere-ionosphere system, to the analytic signals was examined for these events. The role of the shocks are examined by using analytic signals in which the shock feature in the density, solar wind velocity, and magnetic field magnitude are tested individually. During the 3-6 October 2000 event, the shock near the end of the 42 hr magnetic cloud is shown to be largely responsible for the very large region 1 field aligned current surges associated with the  $-AL > 1300\text{nT}$  peaks at the end of the main phase of the storm. Real-time WINDMI is being tried as a prediction tool and we briefly describe the first results in the new mode. Real-time data from ACE is used and provides a prediction for the  $AL$  and  $Dst$  about 1-2 hours before the data is available for these indices. We show WINDMI real-time predictions that were captured for a recent storm in 14-15 April 2006.

*Key words:* Substorms, Modeling.

## 1. Introduction

Interplanetary coronal mass ejections (ICMEs) are the interplanetary counterparts of coronal mass ejections (CMEs) at the Sun and are observed as enhanced magnetic structures in the solar wind lasting on the order of a day [7]. Magnetic clouds (MCs) are a subclass of ICMEs with above-average strength magnetic fields which rotate smoothly through a large angle in a low beta plasma [1]. Earth-directed Halo ICMEs often trigger geomagnetic storms such as the storms of 3-6 October 2000 and 15-24 April 2002. Interplanetary (IP) shocks and their resulting geomagnetic activity are usually caused by Halo CMEs [6-8]. Solar wind velocity and magnetic field strength variation across interplanetary shocks are correlated with the  $Dst$  index [3]. In addition multiple interplanetary magnetic structures are more geoeffective than single interplanetary magnetic structures [4].

In order to understand the effect of IP shocks and MCs on geomagnetic activity, we use the WINDMI model which takes driving voltage derived from Advanced Composition Explorer (ACE) satellite data as input and outputs a predicted westward auroral electrojet index ( $AL$ ) and equatorial disturbance storm time index ( $Dst$ ). We construct analytic solar wind signals from ACE data for the 3-6 October 2000 event and derive an analytic input driving voltage. The role of the shocks are examined by removing the shock features individually from each analytic parameter: density, solar wind velocity, and magnetic field magnitude, then examining the change in the WINDMI output of  $AL$  and  $Dst$ .

The WINDMI model is described in section 2. The analysis of the shock events in the 3-6 October 2000 storm presented in section 2.1 and the 15-24 April 2002 storm in section 2.2. The new real-time WINDMI model is discussed in section 3.

Received 15 May 2006.

W. Horton, M. L. Mays, and E. Spencer. Institute for Fusion Studies, University of Texas at Austin, Austin, Texas, USA.

## 2. WINDMI Model Description

The WINDMI model solves eight coupled ODE's for current, velocity, and pressure in the solar wind driven magnetosphere-ionosphere system. The model is explained in detail in [9] and [10]. WINDMI has ring current energization from substorm injections and therefore outputs a predicted westward auroral electrojet index ( $AL$ ) and equatorial disturbance storm time index ( $Dst$ ).

Complete measurements of solar wind proton density, solar wind velocity and the Interplanetary Magnetic Field (IMF) in GSM coordinates for the two geomagnetic storm periods are available from the Advance Composition Explorer (ACE) satellite. We use these quantities to derive the input dynamo driving voltage for the WINDMI model. The dynamo driving voltage  $V_{sw}(t)$  was calculated from the analytic data using a formula given by Siscoe *et al.* [19], [18], and [17] for the coupling of the solar wind to the magnetopause using the solar wind dynamic pressure  $P_{sw}$  to determine the standoff distance. The formula for  $V_{sw}$  is given by,

$$V_{sw}(kV) = 30.0(kV) + 57.6E_{sw}(mV/m)P_{sw}^{-1/6}(nPa) \quad (1)$$

where  $E_{sw} = v_{sw}(B_y^2 + B_z^2)^{1/2} \sin(\frac{\theta}{2})$  is the solar wind electric field with respect to the magnetosphere and the dynamic solar wind pressure  $P_{sw} = n_{sw}m_p v_{sw}^2$ . Here  $m_p$  is the mass of a proton. The IMF clock angle  $\theta$  is given by  $\tan^{-1}(B_y/B_z)$ . The solar wind flow velocity  $v_{sw}$  is taken to be approximately the  $v_x(t)$  component in GSM coordinates as measured by the solar wind monitor ACE.

The  $AL$  index is derived from measurement of the horizontal component of the Earth's magnetic field at stations located along the auroral arc in the Northern hemisphere. The  $AL$  index is compiled every minute over a 24 hour period in a day and is obtained by selecting the smallest values measured among 12 stations located along the Auroral zone, all of them above  $50^\circ$  latitude. The minimum values are taken to be the strongest activity of the westward auroral electrojet and here

it is compared to  $I_1$  of the WINDMI model, the field aligned current (Region 1 FAC) that closes the electric current  $\mathbf{j}$  in the nightside magnetosphere through the nightside auroral ionosphere. A scaling factor is allowed in the calculation of the prediction  $AL$  index from the model's  $I_1(t)$  current. The method for determining this scaling factor is given in *Spencer et al., 2006* [20].

The  $Dst$  indices are obtained from the measurement of the Earth's magnetic field from observatories that are sufficiently distant from the auroral and equatorial electrojets and located at approximately  $\pm 20^\circ$  latitude, while being evenly distributed in longitude. The  $Dst$  index is compared to the output from the WINDMI model through the ring current energy  $W_{rc}$  using the Dessler-Parker-Schopke relation [12].

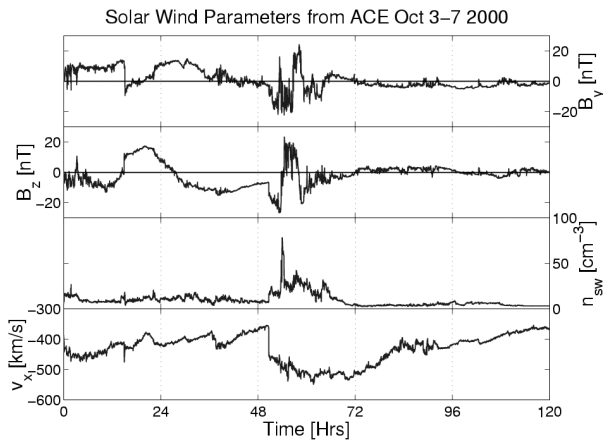


**Fig. 1.** ACE satellite measurement of the solar wind velocity  $v_x$ , proton density  $n_{sw}$ , IMF  $B_z$  and  $B_y$  components for October 3-7 2000, in GSM coordinates. The satellite was located at approximately  $X = 224, Y = -29, Z = -5$  Earth radii in GSM coordinates during this period. The data shows a magnetic cloud from 3 October at 10:18 UT through 5 October at 05:34 UT and an IP shock at 02:40 UT on 5 October. On 3 and 4 October the  $AL$  index shows the occurrence of sawtooth oscillations, during the growth phase of the storm.

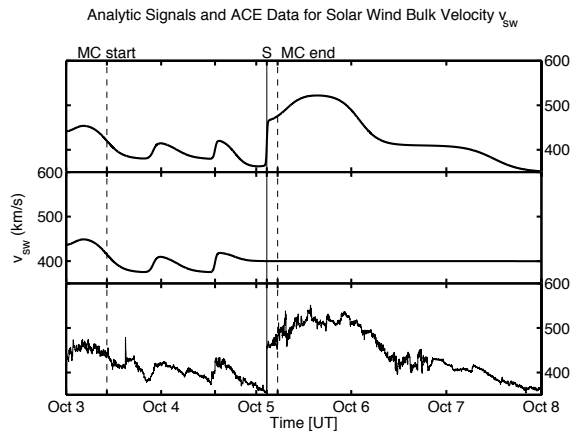


**Fig. 2.** Analytic input signal for  $v_{sw}$ , solar wind bulk velocity.

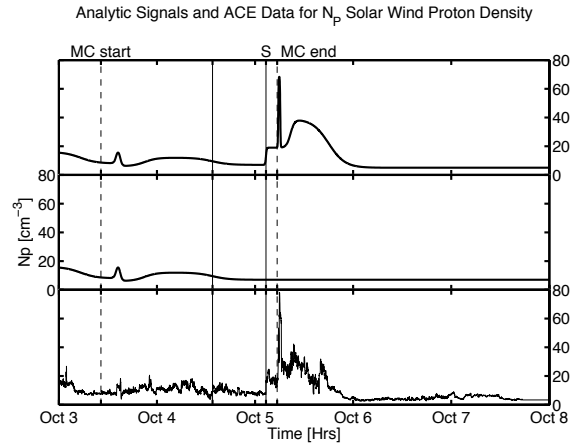


**Fig. 3.** Analytic input signals for the proton density  $N_p$ .

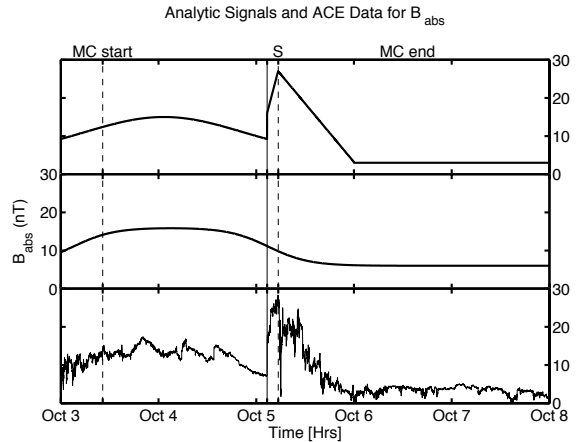
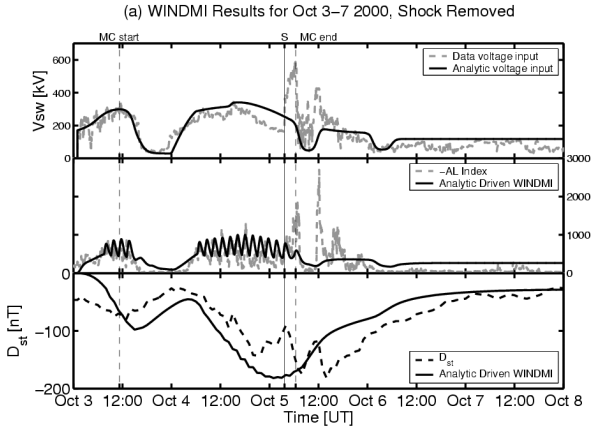


**Fig. 4.** Analytic input signals for the magnetic field magnitude  $B_{\perp}$ . The signals for all of the input fields for WINDMI from ACE solar wind data are shown in the above three figures. Top graphs: Analytic input signals for WINDMI. Middle Graphs: Analytic signals with removed shock features. Bottom graphs: Corresponding 3-6 October 2000 ACE data. MC shows where the magnetic cloud starts and stops. S denotes the location of the shock.

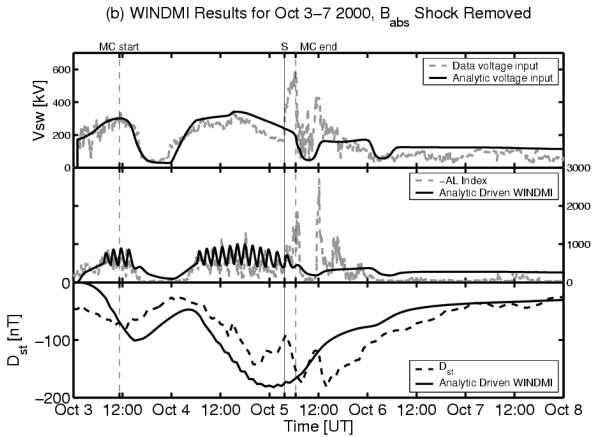
### 2.1. 3-6 October 2000

Figure 1 shows ACE observations for this storm. This event included a fast forward shock advancing into a preceding magnetic cloud [21]. ACE data shows a magnetic cloud from 3 October at 10:18 UT through 5 October at 05:34 UT lasting about 42 hours. The signature of the magnetic cloud can be seen from the plots of IMF  $B_y$  and  $B_z$  in Figure 1 as sinusoid-like waveforms, the IMF clock angle changes linearly through an angle of  $180^\circ$  through this period. The fast forward shock occurs at 02:40 UT on 5 October with a calculated shock speed of 534 km/s and compression ratio of 2.3. There are jumps in the velocity from 364 km/s to 460 km/s, the proton density from  $7 \text{ cm}^{-3}$  to  $16 \text{ cm}^{-3}$ , and perpendicular magnetic field from 7 nT to 16 nT across the shock front.

The  $AL$  data shows a first large spike with a peak of  $-1938$  nT occurring at 0651 UT on 5 October 2000. A second, larger spike of approximately  $-2790$  nT in the  $AL$  index occurs at



**Fig. 5.** WINDMI results: (a) The shock is removed from all analytic input signals.



**Fig. 6.** WINDMI results: (b) The shock is removed from  $B_{\perp}$  only.

1210 UT on 5 October 2000 initiated by a strong southward IMF excursion detected at ACE about an hour earlier. The  $Dst$  minimum of -180 nT is reached on 5 October slightly after the strong southward IMF surge.

Detailed analysis of the ACE data driven WINDMI results is given in [20] and [11]. These data driven results for the  $Dst$  and  $AL$  are compared to the analytic signal driven WINDMI results. The analytic signals based on the ACE data were constructed using hyperbolic tangent, gaussian, and linear functions. To study the role of the shock, the shock feature is removed from the solar wind parameters individually. In order to remove the shock feature from the analytic signals it was assumed that the parameter values would remain the values upstream of the shock. To compute an analytic driving voltage, signals for solar wind velocity  $v_{sw}$ , proton density  $N_p$ , magnetic field  $B_z$ ,  $B_{\perp}$ , and clock angle  $\theta$  were created. In Figures 2-4 the analytic solar wind parameters of solar wind velocity, proton density, and magnetic field are shown with and without the shock along with the corresponding ACE data.

The solar wind driving voltage was calculated using Equation 1 with our analytic signals with and without the shock feature. Using this input solar wind driving voltage the WINDMI model output was compared with and without the shock. In

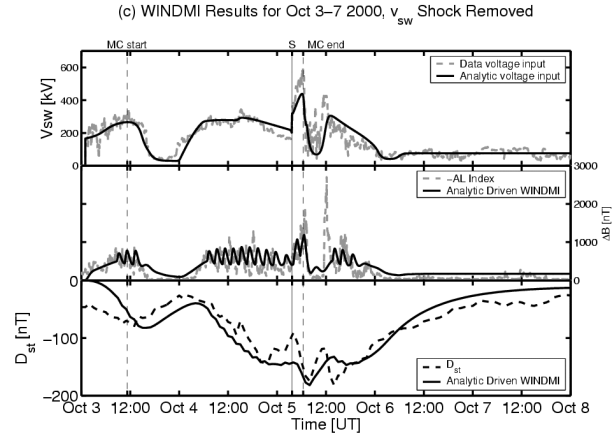


**Fig. 7.** WINDMI results: (c) The shock is removed from  $V_{sw}$  only.

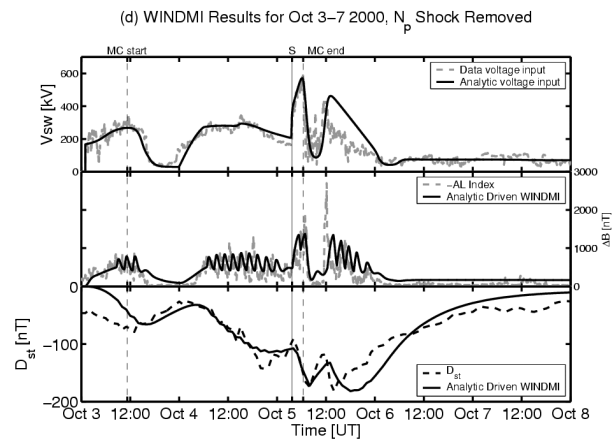


**Fig. 8.** WINDMI results for the  $AL$  (middle panel) and  $Dst$  (bottom panel) when (d) the shock is removed from  $N_p$  only when computing the solar wind driving voltage  $V_{sw}$  (top panel).

Figure 2 the shock feature is dropped from the solar wind velocity  $v_{sw}$  at ACE, the second  $AL$  peak (5 Oct 1200 UT) is lost due to the decreased solar wind driving voltage. In Figure 2 the shock is dropped from  $N_p$  we see an increase in both  $AL$  peaks (5 Oct 0700 and 1200 UT) due to an increased solar wind driving voltage. In Figure 2 the jump in  $B_{\perp}$  is dropped both  $AL$  peaks (5 Oct 0700 and 1200 UT) decrease by 40% and 70% respectively, due to significantly decreased driving voltage. When the shock is dropped from all three parameters the result shown in Figure 2 is identical to removing the shock from  $B_{\perp}$  only. These results show that the first large  $AL$  spike with a peak of -1938 nT occurring at 0720 UT 5 October 2000 was triggered by the shock front, and most strongly by the jump in  $B_{\perp}$ .

## 2.2. 15-24 April 2002

We have begun a similar analytic signal analysis for this storm period. ACE data during this period shows three fast forward shock events which are associated with halo CMEs observed in SOHO/LASCO. The first shock event occurred during the main phase of the storm and was observed by ACE

at 1020 UT on 17 Apr moving at a calculated shock speed of 480 km/s and is associated with a halo CME observed by SOHO/LASCO at 0350 UT moving at 720 km/s [16]. This CME is observed by ACE as a MC beginning at the start of 18 Apr and continuing until approximately 0200 UT 19 Apr. The next shock event occurred during the main phase of the storm at 0801 UT on 19 Apr moving at a calculated speed of 650 km/s and is associated with a halo CME leaving the Sun at 0826 on 17 Apr moving at 1240 km/s [2]. This MC possibly produced the complex structure observed by ACE from 20-21 Apr. The third shock event occurred during the recovery phase at 0413 UT on 23 Apr moving at a calculated speed of 680 km/s and is associated with a non-geoeffective [22] halo CME leaving the Sun at 0127 UT on 21 Apr at a speed of 2393 km/s.

The shock analysis of this storm with the WINDMI model is ongoing but gives results consistent with those given in Section 2.1 for October. The jump in  $B_{\perp}$  is the dominant source for the spikes in the AL index.

### 3. Real-time WINDMI

Real time measurements of the solar wind bulk velocity ( $V$  bulk), proton number density ( $N_p$ ), and the interplanetary magnetic field ( $B_x$ ,  $B_y$ ,  $B_z$  in GSM) are available from the Advanced Composition Explorer (ACE) satellite. These quantities are used to derive an input solar wind driving voltage for the WINDMI model. The rectified driving voltage is calculated in realtime using  $V_{sw} = v_{sw} B_s^{IMF} L_y^{eff}$  where  $v_{sw}$  is the x-directed component of the solar wind velocity in GSM coordinates,  $B_s^{IMF}$  is the southward IMF component and  $L_y^{eff}$  is an effective cross-tail width over which the dynamo voltage is produced.

The WINDMI real time prediction of the  $AL$  and  $Dst$  indices is updated every 10 minutes for 2 day periods. Every 10 minutes the ACE data is automatically downloaded, formatted, and missing data points are replaced by the data point just before. From this data the solar wind driving voltage is calculated from both the rectified method and the Siscoe formula given in Equation 1. Currently the model is taking the rectified voltage as input, but this can be switched to the Siscoe driver at any time for comparison. Using this input, the WINDMI model runs every 10 minutes for the last 48 hour period with nominal parameters (parameters which have not been optimized for a particular storm) and outputs the  $AL$  and  $Dst$  prediction. The output is shown as a series of plots on the website<sup>1</sup>, which show real time ACE data, the calculated driving voltage, the WINDMI  $AL$  and  $Dst$ , and real time  $AL$  and  $Dst$  data. There is also an email alert system set up which sends a notification when  $Dst$  activity is predicted below -50 nT or  $AL$  activity above 500 nT.

WINDMI predictions are compared to near realtime quicklook  $Dst$  data available the World Data Center for Geomagnetism, Kyoto University (also downloaded automatically every 10 minutes). WINDMI predicts the  $Dst$  index about two hours before the near realtime data is available from WDC Kyoto. WDC Kyoto also provides real time quicklook AE index data in the form of daily plots. WINDMI predicts the  $AL$  index about one hour before the data is available from WDC Kyoto.

<sup>1</sup><http://orion.ph.utexas.edu/~windmi/realtime/>

#### 3.1. First Results: 14-15 April 2006

The first example of captured substorms by the real-time WINDMI model was on 14-15 April 2006. There were two storms on 5 April and 9 April leading up to 14 April, both with  $Dst$  minima around -100 nT. In Figure 9 the downloaded ACE real time solar wind data for this period is shown, including the calculated driving voltages. During this period the  $Dst$  reached a minimum of -122 nT at ~0900 UT on 14 April and the  $AL$  index showed several large peaks from -1000 to -1500 nT. ACE data shows a magnetic cloud at the beginning of 14 April until about 1200 UT and from 14 - 15 April the solar wind bulk velocity was on the order of 600 km/s.

In Figure 10 the resulting  $AL$  and  $Dst$  predictions are shown in the bottom two panels. The WDC Kyoto real time  $Dst$  index is also plotted on the WINDMI  $Dst$  prediction plot. During most of the initial phase of the storm, from 14 April 0000 - 0700 UT, the  $Dst$  prediction underestimates the data by 30 - 70 nT. By the end of the initial phase the prediction is within 30 nT of the data. During the main phase between 0700 - 1500 UT 14 April, the prediction overestimates the  $Dst$  by about 20 nT and is about two hours behind. The prediction follows the  $Dst$  by 20 - 30 nT throughout the recovery phase.

The WDC Kyoto real time AE index is shown in Figure 11 in which the  $AL$  index shows a series of large peaks of about -1000 nT at 0600 UT, -1500 nT from 1000 - 1200 UT, and -1000 nT from 1700 - 2000 UT on 14 April. The  $AL$  continues to oscillate until the end of 15 April up to -500 nT. The  $AL$  prediction captures some global oscillatory behavior and the peaks of -1000 nT and -1500 nT on 14 April and more peaks up to -500 nT on 15 April.

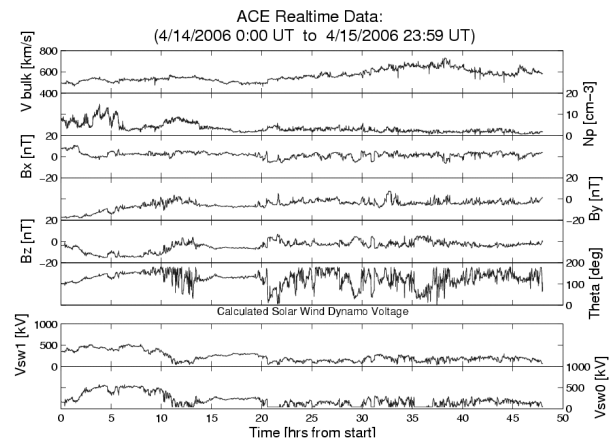


**Fig. 9.** Real-time solar wind parameters from ACE: Solar wind bulk velocity, proton density,  $B_x$ ,  $B_y$ ,  $B_z$ , and clock angle theta. Bottom panels show the solar wind driving voltage calculated by the Siscoe method ( $V_{sw1}$ ) and rectified method ( $V_{sw0}$ ).

#### 3.2. Northward Turning Trigger

The northward turning trigger rules as discussed in [15] do not work for the October 2000 and April 2002 data. More complete rules have recently been proposed by Lyons at the ICS-8 conference. They have classified global auroral responses into a few fundamental response types, described as dynamic pressure, substorm, and null events [14]. When the IMF is not

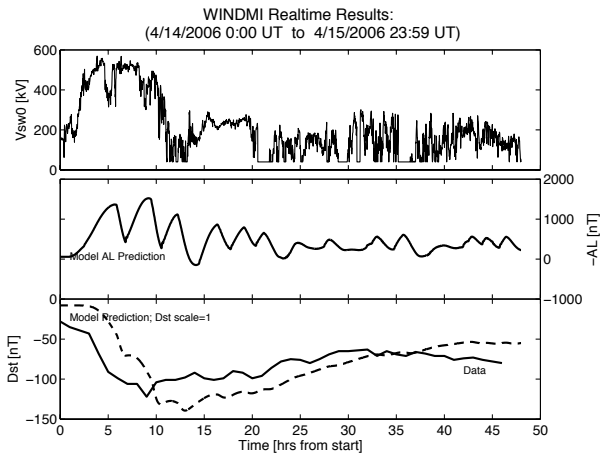


**Fig. 10.** Real-time WINDMI model predictions of  $AL$  (middle) and  $Dst$  (bottom) using the rectified driving volage (top) calculated in real-time as input. The  $Dst$  prediction is shown with a dotted line and follows the qualitative features of the data shown as with a solid line.

strongly southward but remains negative for about 30 minutes, and is followed by IMF changes leading to convection electric field reduction, typical substorms are observed. If it is instead followed by solar wind dynamic pressure enhancements, the magnetosphere is compressed which leads to global auroral enhancement without substorm bulge-region aurora or current wedge formation. When the IMF is strongly southward for a prolonged time and IMF changes lead to convection electric field reduction, this results in a typical substorm disturbance. For steady, strongly southward IMF conditions, the enhancement in the solar wind dynamic pressure causes compressive auroral brightening away from the bulge region and Harang-region substorm brightening. Null events are described as simultaneous IMF and dynamic pressure changes, which lead to a decrease in both  $E_y$  and  $B_{trans}$  in the inner plasma sheet, which prevents the occurrence of a substorm [14].

**3.3. Future Work**

The real-time WINDMI model can be broadened in two steps. The first step is to add the generalized northward turning trigger set of rules. An alarm would be sent with the type of condition violated and record the data for that 12 hour period. For future analysis, the second phase is building terms into the dynamical equations that represent the physical processes suggested by the northward turning models. In particular the weakening of the ratio of transitional fields  $B_{trans}$  in the -6.6 to -10  $R_E$  region and the strengthening of the convection electric field pressure in the central plasma sheet.

WINDMI and real-time WINDMI will be more useful when THEMIS (Time History of Events and their Macroscopic Interactions during Substorms) operates in real-time. THEMIS consists of five identical probes with orbits near the equatorial magnetotail to provide prolonged tail-aligned, crosstail and cross-sheet measurements. There will be in-situ particle and field measurements in addition to ground magnetometer network measurements of auroral onset [5].

Real-time WINDMI can be improved by including optim-

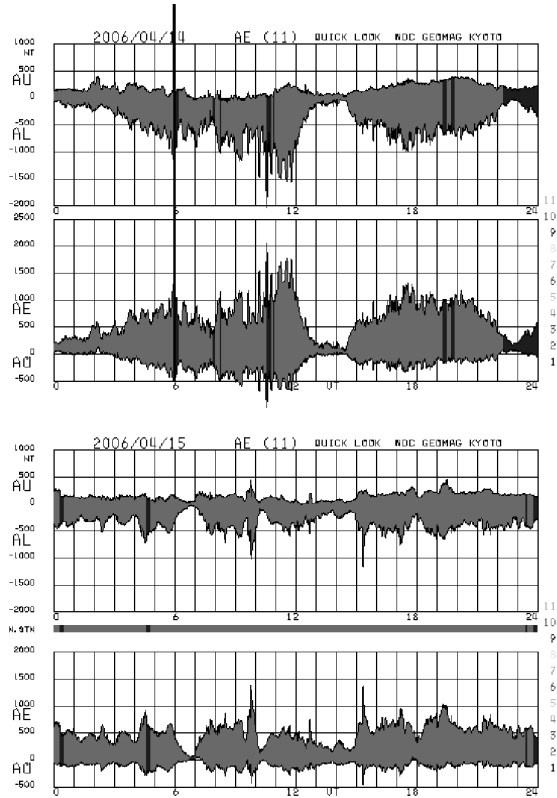


**Fig. 11.**  $AL$  data from WDC Kyoto for comparison. WINDMI  $AL$  prediction shown in Figure 10 captures the global features found in the data including the -1000 nT and -1500 nT peaks on 14 April.

ization of model parameters using a genetic algorithm, which has already been implemented for WINDMI [20]. The real-time version would update the optimized parameters every few hours based on the current parameters and recent magnetosphere conditions. Initial conditions can also be better determined by using the Local Ensemble Kalman Filter (LEKF) data assimilation scheme used in numerical weather models [13].

**4. Summary**

The effect of the IP shock events during the 3-6 October 2000 and 15-24 April 2002 geomagnetic storms on the  $AL$  and  $Dst$  indices were examined by the construction of analytic solar wind signals. WINDMI results from the analytic inputs show that the shock events impacted the  $AL$  index values but changed the  $Dst$  very little. In particular the first large  $AL$  spike during the October storm was triggered by the shock front, and particularly by the jump in  $B_{\perp}$ .

The real-time WINDMI model collects ACE data every 10 minutes and outputs a prediction for the  $AL$  and  $Dst$  indices. The  $AL$  prediction is available one hour before any  $AL$  data is available, and for the  $Dst$  prediction this is two hours. Recently the real-time model captured a storm including substorms on 14-15 April 2006.

## Acknowledgements

This work was partially supported by NSF grant ATM-0539099. The solar wind plasma and magnetic field data were obtained from ACE at NASA's CDAWeb site and the ACE Real Time Solar Wind site. The SOHO LASCO CME Catalog is generated and maintained by NASA and The Catholic University of America in cooperation with the Naval Research Laboratory. The geomagnetic indices used were obtained from the WDC for Geomagnetism, Kyoto.

## References

1. L. Burlaga, E. Sittler, F. Mariani, and R. Schwenn, Magnetic loop behind an interplanetary shock - Voyager, Helios, and IMP 8 observations, *Journal of Geophysical Research*, 86, 6673–6684, 1981.
2. H. V. Cane, and I. G. Richardson, Interplanetary coronal mass ejections in the near-Earth solar wind during 1996-2002, *Journal of Geophysical Research*, 108, 6, 2003.
3. E. Echer, M. V. Alves, and W. D. Gonzalez, Geoeffectiveness of interplanetary shocks during solar minimum (1995-1996) and solar maximum (2000), *Solar Physics*, 221, 361–380, 2004.
4. E. Echer, and W. D. Gonzalez, Geoeffectiveness of interplanetary shocks, magnetic clouds, sector boundary crossings and their combined occurrence, *Geophysical Research Letters*, 31, 9808, 2004.
5. H. U. Frey, S. B. Mende, V. Angelopoulos, and E. F. Donovan, Substorm onset observations by IMAGE-FUV, *Journal of Geophysical Research*, 109(A18), 10304, 2004.
6. W. D. Gonzalez, and B. T. Tsurutani, Criteria of interplanetary parameters causing intense magnetic storms ( $D_{st} < -100$  nT), *Planetary and Space Sciences*, 35, 1101–1109, 1987.
7. J. T. Gosling, Coronal mass ejections and magnetic flux ropes in interplanetary space, *Washington DC American Geophysical Union Geophysical Monograph Series*, 58, 343–364, 1990.
8. J. T. Gosling, S. J. Bame, D. J. McComas, and J. L. Phillips, Coronal mass ejections and large geomagnetic storms, *Geophysical Research Letters*, 17, 901–904, 1990.
9. W. Horton, and I. Doxas, A low-dimensional energyconserving state space model for substorm dynamics, *Journal of Geophysical Research*, 101(A12), 223-227, 1996.
10. W. Horton, and I. Doxas, A low-dimensional dynamical model for the solar wind driven geotail-ionosphere system, *Journal of Geophysical Research*, 103(A3), 4561-4572, 1998.
11. W. Horton, E. Spencer, I. Doxas, and J. Kozyra, Analysis of the October 3-7 2000 GEM Storm with the WINDMI Model, *Geophysical Research Letters*, 31, L22102, 2005.
12. Introduction to Space Physics, edited by M.G. Kivelson and C.T. Russell, Cambridge Univ. Press, 1995.
13. D. Kuhl, I. Szunyogh, E. J. Kostelich, D. J. Patil, G. Gyarmati, M. Oczkowski, B. R. Hunt, E. Kalnay, E. Ott, and J. A. Yorke, Assessing Predictability with a Local Ensemble Kalman Filter, *Journal of the Atmospheric Sciences*, submitted, 2006.
14. L. R. Lyons, D.-Y. Lee, C.-P. Wang, and S. B. Mende, Global auroral responses to abrupt solar wind changes: Dynamic pressure, substorm, and null events, *Journal of Geophysical Research*, 110(A9), 8208, 2005.
15. G. T. Blanchard, L. R. Lyons, and J. Spann, Predictions of substorms following northward turnings of the interplanetary magnetic field, *Journal of Geophysical Research*, 105(A1), 375-384, 2000.
16. P. K. Manoharan, N. Gopalswamy, S. Yashiro, A. Lara, G. Michalek, and R. A. Howard, Influence of coronal mass ejection interaction on propagation of interplanetary shocks, *Journal of Geophysical Research*, 109(A18), 6109, 2004.
17. D. M. Ober, N. C. Maynard, and W. J. Burke, Testing the Hill model of transpolar potential saturation, *Journal of Geophysical Research*, 108, 1467, 2003.
18. G. L. Siscoe, N. U. Crooker, and K. D. Siebert, Transpolar potential saturation: roles of region-1 current system and solar wind ram pressure, *Journal of Geophysical Research*, 107(A10), 1321, 2002.
19. G. L. Siscoe, G. M. Erickson, B. U. O. Sonnerup, N. C. Maynard, J. A. Schoendorf, K. D. Siebert, D. R. Weimer, W. W. White, and G. R. Wilson, Hill model of transpolar potential saturation: comparisons with MHD simulations, *Journal of Geophysical Research*, 107(A6), 1075, 2002.
20. E. Spencer, W. Horton, M. L. Mays, I. Doxas, and J. Kozyra, Analysis of the October 3-7 2000 and April 15-24 2002 Geomagnetic Storms with an Optimized Nonlinear Dynamical Model, *Journal of Geophysical Research*, submitted, 2006.
21. Y. M. Wang, P. Z. Ye, S. Wang, and X. H. Xue, An interplanetary cause of large geomagnetic storms: Fast forward shock overtaking preceding magnetic cloud, *Geophysical Research Letters*, 30(13), 2003.
22. X. P. Zhao, and Y. Liu, Source Regions and Storm Effectiveness of Earth-Directed Halo CMEs Between 14 and 24 April 2002, *AGU Fall Meeting Abstracts*, 2003.

# Kinetic instabilities in substorm dynamics

W. Horton, J.-H. Kim, E. Spencer, and C. Crabtree

**Abstract:** A brief survey is given of the kinetic theory of plasma instabilities that are potentially important in substorm dynamics. Instabilities associated with the release of the pressure gradients in the dipole-to-near geotail transition region are key candidates to explain the initial release of stored energy with the simultaneous onset of auroral brightening. Instabilities driven by the plasma sheet current gradient in the region beyond 15-20  $R_E$  are responsible for release of lobe magnetic energy and the initiation of high speed Earthward flowing streams. Generally, either instability could occur first or both essentially simultaneous according to local plasma gradients and the  $B$ -field.

*Key words:* Kinetic instability, Substorms, magnetic reconnection.

## 1. Introduction

Space science has been remarkably successful in identifying the large number of plasma instabilities that occur in the magnetosphere and ionosphere. The one central problem where the identification of the key instabilities is still controversial is the substorm dynamics. Recent advances in multiple spacecraft missions and the IMAGE space craft have defined the issues in substorm dynamics much more sharply. At the same time the kinetic theory of the key substorm instabilities has advanced dramatically. Here we review the advances made in the kinetic theory of instabilities thought to dominate the substorm problem.

There are four classes of kinetic instabilities invoked to explain the substorm growth and expansion phases. They are (1) the pressure gradient driven ballooning interchange modes with shear Alfvén wave polarization of  $\delta B_{\perp}$  and a smaller  $\delta B_{\parallel}$ , (2) the drift compressional ballooning mode driven by the ion temperature gradient with a dominantly  $\delta B_{\parallel}$  polarization and small  $\delta B_{\perp}$  and electrostatic field part, (3) the large set of collisionless tearing modes driven by the gradient of the plasma current density  $\partial j/\partial\psi = j'/B$  in contrast to the density and temperature gradients, (4) the cross field current driven instabilities (CCI) that require no spatial gradients but have large  $v_d = j_{\perp}/en \geq v_i$  where  $v_i = (T_i/m_i)^{1/2}$ . There is a large class of current driven instabilities that are well known in the plasma literature. There is a recent review article of [18] covering the CCI instabilities. Needless to say, they can be a key player in substorm dynamics and often can appear as the nonlinear development to small space scales of the first three types of instabilities.

Technically, the tearing mode instabilities are the most difficult plasma instabilities to calculate and have been actively debated for decades. The tearing mode is ubiquitous in the laboratory tokamak plasma. While the toroidal geometry plays some role in the mode tearing many features are in common with the geomagnetic tail. The large plasma current  $\mu_0 j(\psi) \rightarrow j(\psi)$  (hereafter) is confined to the core with a peaking  $dj/d\psi$  that increases with time or with core heating of the electrons. Here

$\psi$  is the flux function from the magnetic field produced by the plasma current, and the external coil driven toroidal field  $B_T$  drops out of the tearing mode stability problem except for determining the location of the  $k_{\parallel} = 0$  surfaces. The situation is the same with the  $B_y$  field component in the geomagnetic tail. The standard tearing mode theory is given in [3] and involves the solution of the zero frequency shear Alfvén mode equation around the field reversing current layer of width  $L_z$ . Here we use the GSM coordinates of the geomagnetic tail. The solution of the field structure gives the logarithmic derivative of the perturbed flux function  $\delta\psi$  with  $\Delta' = (d\delta\psi/dz)/\delta\psi$  at the tearing layer. The value of  $\Delta'$  is negative for stable modes, crosses zero for unstable modes and goes to infinity as the plasma becomes ideal MHD unstable from the pressure gradient exceeding the critical  $dp/d\psi$  of the ballooning modes. These features are seen in the magnetic field and core soft x-ray spectrometers of tokamaks as in [4]. The lowest magnetic mode  $m/n=1/1$  shows the sawteeth crashes at intervals of about 100 Alfvén periods and the 3/2 mode is stable but repeatedly kicked or seeded by the pulses from the 1/1 mode. Finally, as the core plasma pressure rises high enough the 3/2 mode catches on and grows to form a large magnetic island.

Qualitatively, the description of this evolution of the stability of the tearing mode is seen from the formula for  $\Delta' = -2k_z \cot(k_z L_z)$  where  $k_z = (dj/d\psi - k_x^2)^{1/2}$ . As the current density gradient increases so that  $k_z L_z \rightarrow \pi$  the  $\Delta'$  goes to infinity and the island width is observed to grow to the size that is comparable to the scale  $L_z$  of the current layer width. In kinetic theory of collisionless tearing modes it is not necessary to introduce the  $\Delta'$  of the external solutions when the whole region of the tearing mode function is treated globally. As we will see, the lack of a full global treatment of the tearing mode led to a long term misconception about the mode being more stable than it is known from recent kinetic theory calculations and simulations.

In this article, we first describe the state of the kinetic ballooning mode instability and the drift compressional mode instability in Sec. 2. In Sec. 3 we describe the current understanding of the collisionless tearing modes which is a complex field. There are basically two scales of the tearing mode instability, that of the ion tearing mode and that of the electron mode. Both modes have been seen in high resolution simulations which are again too wide a topic to summarize here. The ion tearing mode is considerably more unstable than was presented by [16] as is acknowledged in [24]. The electron tearing mode is

Received 5 June 2005.

**W. Horton, J.-H. Kim, and E. Spencer.** Institute for Fusion Studies, The University of Texas at Austin  
**C. Crabtree.** Laboratory for Nuclear Science, MIT

easier to simulate and discuss since the ions play only the role of quasineutrality here. We give an electron tearing mode simulation with the electron Hall terms of the skin depth and the ion inertial scale length that shows a 60% conversion of stored magnetic energy into electron particle energies in a period of 50 Alfvén times which is sufficiently fast and strong to be a dominant energy release mechanism in the growth phase of a substorm.

## 2. Kinetic Ballooning Interchange Instabilities

The kinetic theory of the drift ballooning interchange modes require bounce averaged response to both the electron and ion perturbed distribution function  $\delta f_e(\epsilon, \mu, \mathbf{x}, t)$  and  $\delta f_i(\epsilon, \mu, \mathbf{x}, t)$  where  $\mu$  is the magnetic moment  $\mu = v_\perp^2/2B$  and  $\epsilon$  the kinetic energy per unit mass  $\epsilon = v^2/2$ .

The ballooning interchange maximum growth rate is approximately  $\gamma_{max} = 0.1v_i/(L_p R_c)^{1/2}$  where  $L_p$  is the ion pressure gradient scale length defined by  $1/L_p = \partial \ln p_i / \partial x$  and  $R_c$  is the minimum radius of curvature which is given by  $\kappa(x, z = 0) = B'_x/B_n = 1/R_c$ . This growth computed as a function of distance down the geomagnetic tail reaches a maximum in the region  $x = -6$  to  $-10 R_E$  where the Earthward pressure gradient is steepest.

In the plasma sheet the local magnetic field is given by  $\mathbf{B} = B_x(z)\hat{\mathbf{x}} + B_n\hat{\mathbf{z}}$  where  $|z| \leq L_z$ . At the edge of the central plasma sheet  $|z| = L_z$  the field is  $\mathbf{B} = B_{x0}\hat{\mathbf{x}} + B_n\hat{\mathbf{z}}$ . In the CPS the local B-field magnitude varies as  $B = (B_n^2 + B_x^2 z^2)^{1/2}$  with a large mirror ratio  $R_m = B_{x0}/B_n \geq 10$  where  $B_{x0} = B_x(z = L_z) = B'_x L_z$  is the lobe magnetic field. Pressure balance across the central plasma sheet gives  $B_{x0}^2/2\mu_0 = p_0 \approx n_0 T_i$ . Thus there is a very high ratio of local plasma pressure-to-magnetic field energy density at the equatorial plane  $\beta = 2\mu_0 p_0/B_n^2 = (B_{x0}^2/B_n^2) \geq 100$ . Owing to the high mirror ratio  $R_m$ , ions and electrons with pitch-angles greater than  $\alpha \approx 15^\circ$  mirror in the CPS and the ballooning eigenfunctions are confined to the CPS.

[8] solved the integral equation for the ballooning drift-Alfvén eigenmodes and show that these modes first go unstable in the transitional region  $X = -6$  to  $-10 R_E$  where the  $\nabla p_i/p R_c$  is maximized and  $\beta < 10$ . Closer to the Earth the large value of  $k_\parallel^2 v_A^2$  from the short connection length  $\pi/k_\parallel$  stabilizes the interchange modes. Deep into the geomagnetic tail for  $X \leq -10 R_E$  the plasma compressional energy in the interchange motion overcomes the destabilization from the interchange energy released. Similar results are given in [6].

Kinetic theory predicts that as the Earthward pressure gradient increases the first mode to go unstable is the ballooning interchange mode in the region that maps to the auroral brightening zone. This pressure-gradient instability releases a pressure pulse  $\delta p > 0$  with  $\delta B_z < 0$  that propagates tailward and typically sets off magnetic reconnection in the tail at  $X = -20$  to  $-25 R_E$ . This regime is called the inside-out model of substorm.

[7] considered the finite-gyroradius effects on drift compressional modes. Drift-Compressional modes (DCM) are similar to Drift-Mirror modes (DM) in that they are dominated by the compressional part  $\delta B_\parallel$  of the polarization. However DCM have as their source of free energy spatial inhomogeneities

whereas DM rely on temperature anisotropy to drive the mode unstable. Crabtree and Chen used the ratio of the electron temperature to the ion temperature as a small parameter to decouple the electrostatic component from the compressional component. They also considered frequencies below the shear Alfvén frequency which eliminates the coupling between the compressional component and the shear component of the perturbed magnetic field. With these orderings the following integral eigenvalue problem was derived

$$k_\perp^2 \rho_i^2 \delta B_\parallel + \beta_i \left\langle \epsilon \lambda \left[ \frac{\omega - \omega_{*ti}}{\omega - \bar{\omega}_{Di}} \right] \overline{(\delta B_\parallel \sqrt{B} J_1)} \sqrt{B} J_1 \right\rangle = 0. \quad (1)$$

where the angle brackets refer to velocity space integrations and the overline refers to bounce-averaging along the field line  $\bar{F} = 1/\tau \int_{-s_t}^{s_t} F ds/v_\parallel(\epsilon, \mu, s)$ ,  $s_t$  is the turning point in the mirror field. Also  $\omega_{*ti}$  is the ion diamagnetic drift frequency containing the ion pressure gradient,  $\bar{\omega}_{Di}$  is the grad-B/curvature drift frequency averaged over the bounce motion and  $\eta_i$  is  $\eta_i = \partial \ln T_i / \partial \ln n_i$  is the ion temperature gradient relative to the ion density gradient, and  $J_1$  is the finite-gyroradius Bessel

This equation was solved numerically and analytically. Maximal growth rates were found to occur when  $k_\perp \rho_i \sim O(1)$ , with  $\gamma_{max} \sim v_i(\eta_i - 2/3)/R_c$  and for  $\eta_i \sim -1$ . The radial mode width may also be estimated as  $\sqrt{\rho_i}$ . [11] studied the kinetic generalization of the standard MHD ballooning equation studied by [15] and others. From a quadratic form in the drift-kinetic approximation a reduced kinetically correct quadratic form was derived that accounted for the strong coupling between the shear Alfvén wave with the interchange dynamics given by,

$$\begin{aligned} & \int d\psi dy \int \frac{ds}{B} \left[ -\frac{\omega^2}{v_A^2} |\xi^\psi|^2 + \frac{1}{\mu_0} \left| \frac{\partial \xi^\psi}{\partial s} \right|^2 + \frac{1}{\mu_0} |Q_L^{(0)}|^2 \right. \\ & - \frac{2\mu_0 p' \kappa \cdot \nabla \psi}{B^2} |\xi^\psi|^2 \\ & - 4\pi \sum_a \int d^3 v \frac{\partial F_a}{\partial \epsilon} \left( \frac{\omega - \omega_{*a}}{\omega} \right) \left| \mu Q_L^{(1)} \right|^2 \\ & \left. + i\pi(4\pi) \sum_a \int d^3 v \frac{\partial F_a}{\partial \epsilon} (\omega - \omega_{*a}) \delta(\omega - \omega_{Da}) \left| \mu Q_L^{(1)} \right|^2 \right] \\ & = 0. \end{aligned} \quad (2)$$

Here  $\xi^\psi$  is the contravariant component of the displacement ( $\xi^\psi = -ik_y \chi$ ) of the perturbed flux tube that is the kinetic theory generalization of the MHD displacement field  $X(s)$ . Here  $Q_L^{(0)}$  and  $Q_L^{(1)}$  are functions of  $\xi^\psi$  so that Eq. (2) contains only one field variable, as in MHD theory. This kinetic theory is given in [30].

## 3. Magnetic Reconnection Instabilities

The reversed magnetic field  $\pm B_{x0}$  in the geotail is a large reservoir of energy available energy to drive plasma flows and to increase the thermal energies. These tearing modes are of two types :

- microscale electron tearing modes on the scale of  $c/\omega_{pe} \sim 10$  km and
- the macroscale tearing modes on the scale of  $c/\omega_{pi} \sim \rho_i \sim 400$  km.

There must be and can be hundreds of the  $c/\omega_{pe}$ -scale tearing mode sites to release the required magnetic energy to explain substorms. The ion tearing mode sites will be of the order of a few. The electron modes grow very fast on the time scale of seconds whereas the ion tearing modes require minutes.

### 3.1. Ion Scale Tearing Modes

Tearing models occurring on the ion gyroradius scale are difficult to analyze theoretically due to fast bounce motion of electrons with period  $\tau = \int_{-s_t}^{s_t} ds/v_{\parallel}(\epsilon, \mu, s)$  that yields an integral response for the perturbed plasma density  $\delta n$  and current  $\delta j$  in the ion tearing dynamics. The ion tearing mode growth rate  $\gamma_k^i$  is given by

$$\gamma_k^i = k_x v_i \left( \frac{c^2}{\omega_{pi}^2} \right) \frac{\Delta'_k}{L_z} = \omega_{cxo} \left( \frac{\rho_i}{L_z} \right)^3, \quad (3)$$

where  $\omega_{cxo} = eB_x/m_i = 2$  rad/s for  $B_x = 20$  nT lobe field. When the current sheet thickness exceeds  $L_z = 3\rho_i$ , the growth rate is too slow to play a role in the substorm dynamics.

Using the quasineutrality condition [28]

$$\frac{e\phi_1}{T_i} n_0 + \tilde{n}_1 = 0 \quad (4)$$

and integrating over velocity space the trapped and transient contribution to the total perturbed electron distribution yields the perturbed electron density

$$\tilde{n}_1 = (\ll n_e \gg - n_e) \frac{e\phi_1}{T_e} + \frac{\delta n_e}{\delta A} A_1 \quad (5)$$

where the vector potential contribution term  $(\delta n_e/\delta A)\delta A_1$  is given in detail in [29].

The key point is to include the contribution of the perturbed density over the long flux tube where the small pitch angle electrons make long excursions toward the ionosphere. Previous simulations in [5] and [25] may not have included sufficiently long flux tubes to capture this physics.

### 3.2. Electron Scale Tearing Modes

The latest developments on the electron-scale magnetic reconnection (MR) modes are given in [1] and [23]. The impulsive reconnection model of Bhattacharjee has the field-line-breaking mechanism of electron inertial given by finite  $d_e = c/\omega_{pe}$ . Therefore, it is necessary to use the generalized Ohm's Law

$$\mathbf{E} + \mathbf{v} \times \mathbf{B} = \frac{c^2 \mu_0}{\omega_{pe}^2} \frac{d\mathbf{J}}{dt} - \frac{\nabla p_e}{ne} + \frac{\mathbf{J} \times \mathbf{B}}{ne} + \eta \mathbf{J} \quad (6)$$

where  $\mathbf{E}$  is the electric field,  $\mathbf{B}$  is the magnetic field,  $\mathbf{v}$  is the plasma flow velocity,  $c$  is the speed of light,  $\mathbf{J}$  is the current density,  $p_e$  is the electron pressure,  $\omega_{pe}$  is the electron plasma

frequency,  $n$  is the electron density,  $e$  is the magnitude of the electron charge.

In the simulations shown here we take the limit of zero plasma resistivity  $\eta$  and check energy conservation to five digits. With high order time integrators it is possible to run for finite times with zero resistivity. The dynamics exhibits a long exponential growth time ending with a nonlinear, faster than linear exponential growth pulse that saturates into a coherent nonlinear structure. Typically 50-60% of the initial magnetic energy is redistributed into the sum of the parallel and perpendicular flow energies and the electron thermal pressure by the reconnection pulse.

The simplest electron tearing mode dynamics occurs when plasma flow is almost incompressible. This occurs when there is a guide field  $B_y$ . The small flow compression comes from the polarization drift of the ions and is given by  $\partial U/\partial t$  where  $U = \nabla_{\perp}^2 \phi$  with  $\mathbf{E} = -\nabla \phi$  and  $\mathbf{B} = \hat{\mathbf{y}} \times \nabla \psi + B_y \hat{\mathbf{y}}$ . The vorticity  $U$  grows to feed plasma into the reconnection layer. The compressional Alfvén wave propagates drops out of the dynamics in this regime owing to its higher frequency and different polarization. The plasma is described in an electron-Hall fluid limit by the following two field equations

$$\frac{\partial F}{\partial t} + [\phi, F] = \rho_s^2 [U, \psi] \quad (7)$$

$$\frac{\partial U}{\partial t} + [\phi, U] = [J, \psi] \quad (8)$$

where  $J = -\nabla_{\perp}^2 \psi$ ,  $F = \psi + d_e^2 J$ ,  $U = \nabla_{\perp}^2 \phi$ , and the Poisson bracket is defined by  $[\phi, F] = \hat{\mathbf{y}} \cdot \nabla \phi \times \nabla F$ . All quantities are dimensionless (this will be fixed with the proper dimensions). The distance is normalized by the system size  $L_z$  and time is normalized by Alfvén time scale  $\tau_A = L_z/v_A$  where the Alfvén velocity  $v_A = \sqrt{B^2/2\mu_0\rho}$ . Also two dimensionless parameters  $d_e$  and  $\rho_s$  are the electron skin depth  $d_e = (c/\omega_{pe})/L_z$  and the ion sound gyro radius  $\rho_s = (c_s/\omega_{ci})/L_z$ .

The computation has been done with

$$\psi = \sum_{n,m} \psi_{m,n}(t) \exp(inz + im\epsilon x) \quad (9)$$

$$\phi = \sum_{n,m} \phi_{m,n}(t) \exp(inz + im\epsilon x) \quad (10)$$

where  $n, m$  are integers,  $\epsilon = L_z/L_x$  is an aspect ratio of the system. The initial profile are the unstable current sheet  $\psi_{1,0}$  with small perturbations  $\psi_{4,1}$  and  $\phi_{4,1}$ , that is,

$$\psi(0) = \cos z + \delta\psi \cos(4z) \cos(\epsilon x)$$

$$\phi(0) = \delta\phi \sin(4z) \sin(\epsilon x).$$

The electron model conserves the total energy of electrons and the magnetic field. The energy formula and the conservation law are given by

$$\begin{aligned} \frac{dE_{tot}}{dt} &= \frac{d}{dt} (E_B + E_{\parallel} + E_{E \times B} + E_p) \\ &= \frac{1}{2} \frac{d}{dt} \int dx dz [(\nabla \psi)^2 + d_e^2 (\nabla^2 \psi)^2 \\ &\quad + (\nabla \phi)^2 + \rho_s^2 (\nabla^2 \phi)^2] = 0 \end{aligned} \quad (11)$$

where  $E_B$  is magnetic energy,  $E_{\parallel}$  is electron parallel flow energy,  $E_{E \times B}$  is the electron perpendicular flow energy and  $E_p$

is the electron thermal energy. As shown in Fig. (1), there are four transfers between the different energy components. The magnetic energy  $E_B$  and the electron parallel flow energy  $E_{\parallel}$  are transferred back and forth to the thermal energy  $E_p$  by thermal interaction  $\langle v_{e\parallel} \nabla_{\parallel} p_e \rangle$ . And the energies,  $E_B$  and  $E_{\parallel}$ , are transferred back and forth to the perpendicular flow energy  $E_{E \times B}$  by the electric interaction  $\langle j_{\parallel} \nabla_{\parallel} \phi \rangle$ .

The energy change relevant to the  $\phi, U, \psi$  and  $J$  are shown in Fig. (2). During the process, almost 60% of the magnetic energy is released and About 30% of the released energy is transferred to the ion thermal energy. The simulation box is  $20\pi c/\omega_{pe} \times 40\pi c/\omega_{pe}$  and the unit of energy is  $E_0 = B_0^2 L_z^2 / 2\mu_0$  which for 10 nT reversed field over a  $L_z = 10 c/\omega_{pe} = 100\text{km}$  is  $2.5 \times 10^6 \text{ J/R}_E$ . In the upper panel, we see the released magnetic energy  $\Delta E_B$  of  $12 E_0$  and the increase of the parallel flow kinetic energy in the electrons is  $5 E_0$ . In the bottom panel the perpendicular flow energy increases first to  $8, E_0$  and then drops to  $2 E_0$  while the electron thermal energy continually increases to  $5 E_0$ . Energy is conserved by the 12 units of released magnetic energy going to  $5+2+5$  units of parallel flow, perpendicular flow and thermal plasma energies. In terms of fractional changes this is approximately a 60% decrease of magnetic energy transformed into 10%  $E \times B$  flow, 25% parallel flow and 25% electron thermal energy. The space and time scales are  $10 c/\omega_{pe}$  and  $60 L_z/v_A$ . In the central plasma sheet these scales are typically 100 km and 1 min.

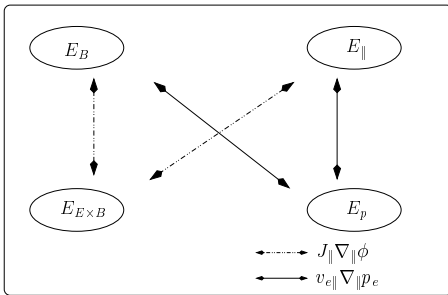


**Fig. 1.** Diagram of the energy transfer among magnetic energy  $E_B$ , perpendicular kinetic energy  $E_{E \times B}$ , parallel kinetic energy  $E_{\parallel}$  and electron thermal energy  $E_p$ .

### 3.3. Global Driven Reconnection Model

The solutions described above are for local instability of the current sheet with the growth rate driven by the gradient of the current density  $dj_y/d\psi$ . The wave functions are localized at the current sheet dropping off to negligible values in the lobe plasma. There is another type of global driven reconnection solution that is obtained by changing the exterior boundary conditions. In the global solution the boundary conditions are changed to be those given on the upper and lower magnetopause with mixed values of  $\delta\psi$  and  $d\delta\psi/dz$  at  $z = \pm H$ . These are called driven reconnection solutions and are used in [9] and [10]. These global solutions are those that are created in the driven reconnection simulations of [26] and [2].

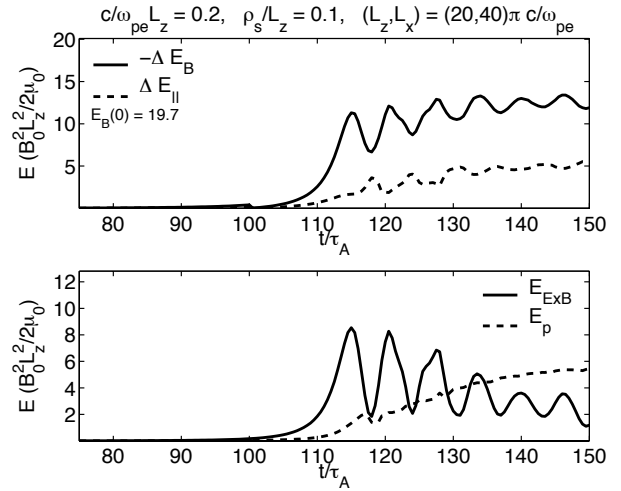


**Fig. 2.** Plot of energy evolution in time for  $d_e = 0.2, \rho_s = 0.1$  with initial mode  $(k_z, k_x) = 2\pi(4, 0.5)/L_z$ . Almost 60% of magnetic energy is released.

### 4. Crossfield Current Drive Instabilities

In the driven reconnection simulations, and other plasma sheet instabilities including the firehose instability driven by the bursty bulk flows ([13, 14] and [12]), the gradient of the magnetic field is locally very large and the associated drift velocity  $v_d = j/en_e \geq v_i = \sqrt{T_i/m_i}$  locally. This condition when satisfied over a region of sufficient volume gives rise to the crossfield current driven instabilities called CCI. Lui and his collaborators [19, 20, 21] have worked out many details of the CCI instabilities and have shown them to be capable of producing a turbulent resistivity that increases the local electric field in proportional to the level of these fluctuations. [17] gives a review of these instabilities and their effects on the currents in the plasma connected to the regions of auroral brightenings. The Geotail space data in this region of  $10-13 R_E$  shows strong magnetic field fluctuations as shown for five substorms in detail in [27].

### 5. Conclusion

Thus we see there are three classes of kinetic instabilities that can be associated with substorm expansion phases. The most widely used instabilities are the pressure gradient driven ballooning interchange mode in the near Earth transitional region between the dipole field and the inner edge of the central plasma sheet. Transient conditions of either sharply increasing or decreasing convection electric field from the interplanetary magnetic and electric field create the steep Earthward pressure gradient to trigger this strong instability with growth periods of the order of minutes. The growth rate divided by the local proton cyclotron frequency is of order the proton gyroradius divided by the geometric mean of the plasma pressure scale length  $L_p$  and the local radius of magnetic curvature.

In the midtail region, which is stable to the ballooning interchange mode owing to the high local plasma pressure, the first instability to be excited is the ion scale tearing mode. The ion tearing mode occurs when the current gradient scale length  $L_z$

is sufficiently short estimated here as three ion gyroradii in the lobe field  $B_{x0}$  and  $B_n/B_{x0} \leq 0.1$ . The mode produces a large magnetic island but grows slowly with the growth rate divided by the lobe cyclotron frequency proportional to the third power of  $\rho_i/L_z$ , that is  $\gamma_{max}/\omega_{ci} \sim (\rho_i/L_z)^3$ .

When local current filaments of size less than the proton gyroradius are present then the electron scale tearing mode is driven unstable. The electron tearing mode grows very rapidly with time scales of seconds but the magnetic islands are small scaling with the electron collisionless skin depth  $d_e$  which is tens of kilometers.

We show a simulation for these small scale tearing modes that gives a conversion of 60% of the magnetic energy into electron thermal energy and electron parallel and perpendicular flow energies. There would be a high mode density  $d^3k$  of the electron tearing modes, and they are not restricted to the symmetry plane of the geomagnetic tail but can occur locally wherever the local gradient of the current density  $dj_y/dz$  is sufficiently strong. On the dayside magnetopause [22] shows evidence for a high density of electron reconnection sites.

Finally, the current density itself, without a gradient, can produce a high frequency kinetic instabilities that produce turbulent scattering of the electrons that create an anomalous resistivity. There is a wide variety of these instabilities that go under the name of CCI (crossfield current instabilities) as reviewed by [18]. It seems likely that all three types of instabilities are active in various types and stages of the substorm dynamics.

With the THEMIS mission and then the MMS mission we may expect to learn which type of instability is dominant in various types of substorms and responsible for which effects such as conversion of magnetic energy to various forms of ion and electron energies.

## Acknowledgements

This work is supported by the NSF Grant ATM-0539099.

## References

- Bhattacharjee, A., K. Germaschewski, and C. S. Ng, Current singularities : Drivers of impulsive reconnection, *Phys. Plasmas*, *12*, 042,305, 2005.
- Biskamp, D., Magnetic reconnection via current sheets, *Phys. Fluids*, *25*(5), 1520–1531, 1986.
- Biskamp, D., *Magnetic Reconnection in Plasmas*, chap. 4, pp. 82 – 95, Cambridge University Press, 2000.
- Brennan, D. P., et al., A mechanism for tearing onset near ideal stability boundaries, *Phys. Plasmas*, *10*(5), 1643–1652, 2003.
- Brittnacher, M., K. B. Quest, and H. Karimabadi, A new approach to the linear theory of single-species tearing in two-dimensional quasi-neutral sheets, *J. Geophys. Res.*, *100*(A3), 3551–3562, 1995.
- Cheng, C. Z., and A. Lui, Kinetic ballooning instability for substorm onset and current disruption observed by ampte/cce, *Geophys. Res. Lett.*, *25*(21), 4091, 1998.
- Crabtree, C., and L. Chen, Finite gyroradius theory of drift compressional modes, *Geophys. Res. Lett.*, *31*(L1), 7804, 2004.
- Crabtree, C., W. Horton, H. V. Wong, and J. W. V. Dam, Bounce-averaged stability of compressional modes in geotail flux tubes, *J. Geophys. Res.*, *108*, 1084, 2003.
- Hahm, T., and R. Kulsrud, Forced magnetic reconnection, *Phys. Fluids*, *28*(8), 2412–2418, 1985.
- Horton, W., and T. Tajima, Linear theory of driven reconnection, *J. Geophys. Res.*, *93*(A4), 2741–2748, 1988.
- Horton, W., H. V. Wong, J. W. V. Dam, and C. Crabtree, Stability properties of high-pressure geotail flux tubes, *J. Geophys. Res.*, *106*(A9), 18,803–18,822, 2001.
- Horton, W., B.-Y. Xu, H. Wong, and J. V. Dam, Nonlinear dynamics of the firehose instability in a magnetic dipole geotail, *J. Geophys. Res.*, *109*(A0), 9216, 2004.
- Ji, S., and R. Wolf, Double-adiabatic-MHD theory for motion of a thin magnetic filament and possible implications for bursty bulk flows, *J. Geophys. Res.*, *108*(A5), 1191, 2003.
- Ji, S., and R. Wolf, Firehose instability near substorm expansion phase onset?, *Geophys. Res. Lett.*, *30*(24), 2242, 2003.
- Lee, D.-Y., and R. A. Wolf, Is the earth's magnetotail balloon unstable, *J. Geophys. Res.*, *97*(A12), 19,251–19,257, 1992.
- Lembege, B., and R. Pellat, Stability of a thick two-dimensional quasineutral sheet, *Phys. Fluids*, *25*(11), 1995–2004, 1982.
- Lui, A., Current disruption in the earth's magnetosphere : Observation and models, *J. Geophys. Res.*, *101*(A6), 13,067–13,088, 1996.
- Lui, A., Potential plasma instabilities for substorm expansion onsets, *Space Sc. Reviews*, *113*(1), 127–206, 2004.
- Lui, A., L. Frank, K. Ackerson, C. I. Meng, and S.-I. Akasofu, Systemic study of plasma flow during plasma sheet thinnings, *J. Geophys. Res.*, *82*, 4815–4825, 1977.
- Lui, A., C. Chang, A. Mankofsky, H. Wong, and D. Winske, A cross-field current instability for substorm expansions, *J. Geophys. Res.*, *96*(A7), 11,389–11,401, 1991.
- Lui, A., et al., Current disruptions in the near-earth neutral sheet region, *J. Geophys. Res.*, *97*(A2), 1461–1480, 1992.
- Mozer, F., Criteria for and statistics of electron diffusion regions associated with subsolar magnetic field reconnection, *J. Geophys. Res.*, *110*(A1), 2222, 2005.
- Ottaviani, M., and F. Porcelli, Fast nonlinear magnetic reconnection, *Phys. Plasmas*, *2*(11), 4104–4117, 1995.
- Pellat, R., O. A. Hurricane, and J. Luciani, New mechanism for three-dimensional current dissipation/reconnection in astrophysical plasmas, *Phys. Rev. Lett.*, *77*(21), 4353, 1996.
- Pritchett, P., and F. Coroniti, The role of the drift kink mode in destabilizing thin current sheets, *J. Geomagn. Geoelectr.*, *48*, 833, 1996.
- Sato, T., and T. Hayashi, Externally driven magnetic reconnection and a powerful magnetic energy converter, *Phys. Fluids*, *22*(6), 1189–1202, 1979.
- Sigsbee, K., C. A. Cattell, D. Fairfield, K. Tsuruda, and S. Kokubun, Geotail observation of low-frequency waves and high-speed earthward flows during substorm onsets in the near magnetotail from 10 to 13  $r_e$ , *J. Geophys. Res.*, *107*(A7), 1141, 2002.
- Sitnov, M. I., H. V. Malova, and A. S. Sharma, Role of the temperature ratio in the linear stability of the quasi-neutral sheet tearing mode, *Geophys. Res. Lett.*, *25*(3), 269–272, 1998.
- Sitnov, M. I., A. S. Sharma, P. N. Guzdar, and P. H. Yoon, Reconnection onset in the tail of earth's magnetosphere, *J. Geophys. Res.*, *107*(A9), 1256, 2002.

30. Wong, H. V., W. Horton, J. V. Dam, and C. Crabtree, Low frequency stability of geotail plasma, *Phys. Plasmas*, 8(5), 2415–2424, 2001.

# The statistical characteristics of IMF triggered substorms

T.-S. Hsu and R.L. McPherron

**Abstract:** To understand the magnetospheric substorm it is necessary to determine whether substorm onset is always externally triggered by the interplanetary magnetic field (IMF) or whether substorm onset sometimes occurs spontaneously as a result of internal processes. One of the proposed mechanisms for substorm onsets requires that every substorm be triggered by a northward turning of the interplanetary magnetic field (IMF) [8, 9, 10]. A statistical study performed by [7] has demonstrated that the association between IMF triggers and substorm onsets is a real physical phenomenon. However, this result was recently challenged. It is suggested that the high confidence level in the association between IMF triggers and substorm may be due to the condition of substorm growth phase. In essence, the argument is that “after 20 minutes of southward IMF, there ought to be a very high probability of a northward turning of the IMF”. In this study, we examine the probability of association after 20 minutes of southward IMF and found that the probability of northward turning is not as high as expected.

*Key words:* Substorms, IMF triggering.

## 1. Introduction

Twenty-five years ago [1] used superposed epoch analysis to demonstrate that a maximum in the tail lobe field is associated with the onset of the expansion phase of a magnetospheric substorm as measured by midlatitude positive bays. Quite by accident they also found that this maximum, and hence the substorm onset, is also associated with an apparent northward turning of the interplanetary magnetic field (IMF). [1] pointed out that a similar statistical association could be seen in an earlier study of isolated substorms [4]. In a subsequent study [2] demonstrated that this same association was present in time series of IMF Bz and traces of auroral zone magnetometers. Sudden decreases in the horizontal component of the magnetic field occurring at the time of a brightening of the aurora appeared to be associated with northward turnings of the IMF. They concluded that the change in the orientation of the IMF was somehow “triggering” the onset of the magnetospheric substorm.

These results did not receive much attention until [14] and [15] published several particularly clear examples of apparent triggering. [3] and [17] also suggested that the explosive phase of isolated substorms could begin under the influence of a change in the IMF Bz component. Shortly thereafter [16] used the technique of generalized superposed epoch analysis to again demonstrate a statistical association between substorm onset as defined by ground magnetograms from former U.S.S.R. stations and northward turnings of the z component of the IMF. Most researchers at this time dismissed this apparent relation as simply coincidence. The Bz component of the IMF is constantly changing from positive to negative. Substorm expansions occur frequently when the IMF has been southward for about an hour. This is close to what is thought to be the typ-

ical time that the IMF remains southward so it is inevitable that some onsets will appear to occur about the time of a northward turning. To counter this view [13] performed a statistical examination of all substorms occurring in a six-month interval. They found that nearly half of all substorms could be associated with northward turnings of the IMF.

These results were again ignored until [8] proposed a substorm model ultimately requiring that all substorm expansions are triggered by northward turnings of the IMF or changes in IMF By. This view was so extreme that it immediately drew criticism from numerous researchers. [6] and [13] had published several examples of substorm onsets that occurred when there was no apparent change in IMF Bz. [9] dismissed these examples as either not being substorms or as having been triggered by changes in the IMF By component. However, [5] immediately published examples that were unambiguously substorms (as determined by synchronous particle injection), yet there were no changes in any component of the IMF. The conclusion appeared to be that triggering of substorm expansion by the IMF is not necessary. Many researchers continued to believe that those events that appeared to be triggered were simply a matter of coincidence.

In an attempt to examine the probability of association between IMF triggers and substorm onsets, [7] used a point process technique to examine the chance association between IMF triggers and substorm onsets. They found that the association between IMF triggers and substorm onsets is a real physical phenomenon. However, this result was recently challenged. They suggested that the high confidence level in the association between IMF triggers and substorm may be due to the condition of substorm growth phase. In essence, the argument is that “after 20 minutes of southward IMF, there ought to be a very high probability of a northward turning of the IMF”. In this study, we examine the probability of occurrence of IMF triggers after 20 minutes.

Received 22 June 2006.

**T.-S. Hsu and R.L. McPherron.** Institute of Geophysics and Planetary Physics, University of California, Los Angeles, 90095-1567, e-mail: thsu@igpp.ucla.edu/rmcpherron@igpp.ucla.edu

## 2. Probability of Northward IMF Turning from Southward IMF

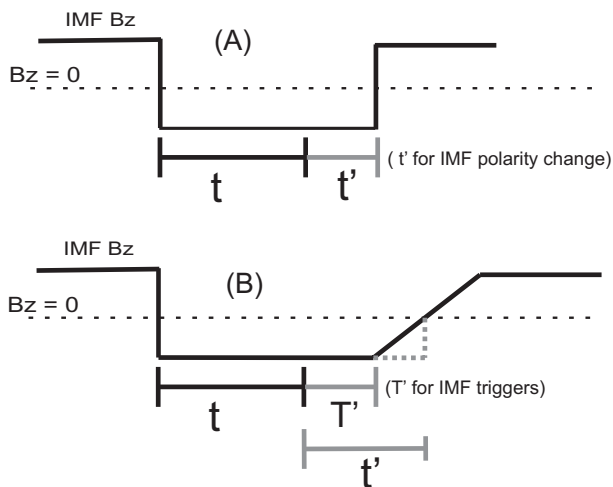


**Fig. 1.** Schematic explanation of IMF northward turning, where  $t'$  is the IMF polarity change time and  $T'$  is the IMF triggers time after some waiting time  $t$ . Panel (A) is an schematic example of a south to north IMF can be a IMF trigger. Panel (B) is a more general case for IMF triggers. In this schematic example, it is obvious that some additional time  $t'-T'$  has been calculated in the previous analysis [7].

In the statistical study done by [7], they found that the probability of their chance association between two point processes appears to be extremely low. However, it might be suggested that the high probability of association is a consequence of the natural tendency of the IMF to turn northward after an interval of southward IMF. If it were the case that all intervals of southward IMF were exactly one hour long, and all substorm growth phases were as well, then every onset would be correlated with a northward turning. Such a circumstance is unlikely to occur because of the power law spectrum of the IMF, and because the duration of the growth phase of substorms varies over a range of 20-200 minutes, with 55 minutes most typical [e.g. [12]]. None-the-less we are led to consider the question “what is the probability for a northward turning of the IMF after some extended interval of southward IMF?” If the probability of an IMF polarity change after some specified interval of southward IMF Bz is extremely high, then the association between IMF Bz northward turnings and substorm onsets may still be coincidental rather than physical. In our case our trigger criteria requires that the IMF have been southward for at least 20 of the 30 preceding minutes.

[7] used a procedure developed by [18] to examine the probability of IMF polarity change after a certain amount of time. In essence, the question is whether “the longer there has been southward IMF, the shorter the expected time till a northward turning”? A detailed theoretical argument can be found in [7]. The argument is focused on a determination of the sign of  $\frac{d\langle t' \rangle}{dt}$  in which  $t'$  is an additional time we must wait until the northward turning IMF Bz, given the time  $t$  since the southward turning (Figure 1).

It should be pointed out that [7] only estimated the probability of IMF polarity change in their paper, i.e., from southward IMF to northward IMF. In Figure 1, we have plotted two schematic examples for the analysis. The panel (A) is an example which has a sharp change of IMF sign. Panel (B) is a more general case for IMF triggers. In the previous analysis, the waiting time is  $t'$  [7]. If we use a more general case for the IMF triggers (Figure 1, panel B) and assume the waiting time is  $T'$ , we can see that there is an additional  $t'-T'$  waiting time for the polarity change (panel B). Figure 2 shows an example of automatic identified IMF triggers by [11] criteria. It is clear that case (a) and (c) are more general examples of IMF triggers while the case (b) is a classic change in sign of the IMF. Nevertheless, both cases satisfy the criteria [11] and should be considered in the same group.

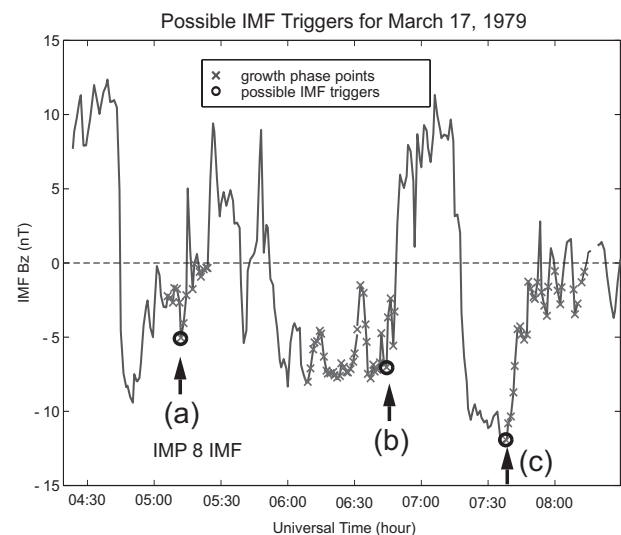


**Fig. 2.** An example of automatic identified IMF triggers by [11] criteria. IMF triggers (a) and (c) are a more general example of IMF triggers while trigger (b) is more likely the sharp change of IMF sign. In this figure, x means point satisfies the growth phase criteria and O is the selected IMF triggers.

The estimation the probability distribution between southward and northward turnings of IMF Bz is obtained by using six continuous months of 5-minute resolution ISEE-3 data (January to June 1979) [7]. The duration of southward IMF Bz intervals was calculated and used to construct the probability distribution. In Figure 3, this complementary cumulative probability distribution is plotted for IMF polarity change and IMF triggers. Using a least square fit we find that this distribution,  $P_{>}$  can be represented as  $P_{>} = 1.4e^{(-\sqrt{t}/33.1)}$  for IMF polarity change (Bs to Bn) and  $P_{>} = 1.7e^{(-\sqrt{t}/23.5)}$  for IMF triggers, in which  $t$  is the time duration of the southward IMF Bz. It should be noticed that  $P_{>}(t)$  is actually  $f'(t)$ , the cumulative integral of  $p(u)$  [7]. In essence, this distribution is a Weibull distribution with an exponent less than 1 [ see also Chapter 6 in *Sornette*, 2000; [18]], a stretched exponential distribution. A particular characteristic of this distribution is that “the longer we have waited since the last event, the longer the time to the next event”. This has been demonstrated in the [7]

which is shown briefly here.

Given that  $f'(t) = ce^{-\sqrt{t/\tau}}$ , we have  
 $f(t) = -2c\tau[\sqrt{t/\tau}e^{-\sqrt{t/\tau}} + e^{-\sqrt{t/\tau}}]$  and  
 $f''(t) = \frac{-c}{2\sqrt{t\tau}}e^{-\sqrt{t/\tau}}$  in which we have set  $c = 1.4$ ,  $\tau = 33.1$  (IMF Bs to Bn, polarity change) and  $c = 1.7$ ,  $\tau = 23.5$  (IMF triggers) for simplicity. After substituting these formulas into equation (20) of [7], we have

$$f(t)f'(t) - [f'(t)]^2 = \frac{c^2 e^{-2\sqrt{t/\tau}}}{\sqrt{t/\tau}} \quad (1)$$

It is apparent that this equation has  $\frac{d\langle t' \rangle}{dt} > 0$  for finite  $t$ . If  $t \rightarrow \infty$ ,  $\frac{d\langle t' \rangle}{dt} \rightarrow 0$ . However, this would imply that IMF Bz can remain southward forever, a nearly impossible situation for IMF Bz. Thus, this result suggests that the hypothesis Q, “the longer it has been since the last southward turning of IMF, the shorter the time expected till the northward turning” is not correct. Instead, the opposite hypothesis that, “the longer it has been since the last southward turning of IMF Bz, the longer the time expected till the northward turning” is true. While the previous estimation of [7] has only estimated the Bs to Bn (polarity change, Figure 2 (A)), it is shown here that the consideration of more general IMF trigger cases (Figure 2 does not significantly change the probability distribution. This implies that the probability of a northward turning of IMF Bz (either for polarity change or IMF triggers) after our “pre-selected” southward IMF Bz period of 20 minutes used in determining a trigger may not be “extremely” high as has been suggested.

Comparison of Bs2Bn and Northward Turning Probability Distribution ISEE-3 1979

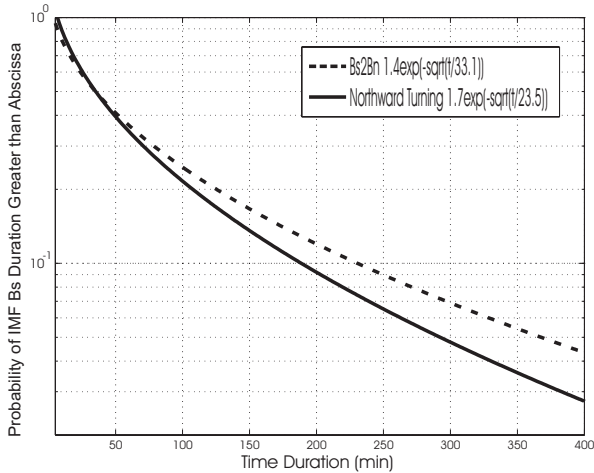


**Fig. 3.** Probability of southward IMF duration for Bs to Bn (polarity change, dashed line) and IMF triggers (solid line).

A study done by [14] examining the duration of intervals of IMF polarity obtained a similar result. Their study found that 65.7% of the IMF Bz data do not change their polarity in a one-hour time interval. This is consistent with our finding, i.e., the polarity change from southward IMF to northward IMF occurred in a time frame much longer the 20 minutes used in our trigger selection.

From the complementary cumulative probability distribution, we can estimate the probability that a northward turning will have occurred within some specified time after the southward turning by using the cumulative probability distribution. Now the problem is to find the northward turning probability  $P_{north}$  at  $t'$  after a time  $t$ . In Figure 3 we have the cumulative probability that the duration of southward IMF Bz exceeds a time  $T$ . Thus the probability that Bz will have turned northward within an additional time  $t'$  can be estimated by the difference in cumulative probabilities at  $t$  and  $t+t'$ , which is  $P_{>}(t \geq T) - P_{>}(t \geq T + t')$ . Thus,

$$\begin{aligned} P_{north}(t') &= \frac{P_{>}(t \geq T) - P_{>}(t \geq T + t')}{P_{>}(t \geq T)} \\ &= 1 - \frac{e^{-\sqrt{(T+t')/\tau}}}{e^{-\sqrt{T/\tau}}} \end{aligned} \quad (2)$$

Which is normalized because  $P_{north} = 0$  at  $t' = 0$  and  $P_{north} = 1$  as  $t' \rightarrow \infty$ .

In our case, we can set  $T = 20$  minutes because this is the growth phase requirement in the “IMF trigger” selection procedure [11]. The result presented in Figure 4 shows that the probability of a northward turning within the first 10 minutes after 20 minutes of southward IMF is about 15% (for polarity change) and 18% for IMF triggers. It is thus not correct to say that there is an extremely high probability of a northward turning within our  $\pm 10$ -minute association window if the field has been southward for 20 minutes. Based on this result, it does not seem likely that the occurrence of northward IMF after 20 minutes of southward IMF is highly probable in the next 10~20 minutes. On the contrary, there is only a 50% (polarity change) and 54% (IMF triggers) of chance occurred 50 minutes beyond the end of our trigger selection window.

The preceding argument can be extended to estimate the number of substorm onsets that will appear to be associated with a trigger as a result of our selection criterion that the IMF must have been southward for longer than 20 minutes before the northward turning. If we assume that all of the substorms in our list had a growth phase with duration 60 minutes, i.e. that the time of the substorm onset was actually 60 minutes after the southward turning. We can estimate the probability of a northward turning (polarity changes or IMF triggers) within a 20-minute interval centered at 60 minutes. Let  $T = T_0 - h$  and  $t = 2h$  in Equation 2 so that we obtain

$$P_{north}(T_0 \pm h) = 1 - \frac{e^{-\sqrt{(T_0+h)/\tau}}}{e^{-\sqrt{(T_0-h)/\tau}}} \quad (3)$$

For the chosen values this reduces to  $P_{north} = 0.2019$  (polarity change) and 0.2345 (IMF triggers). If the typical growth phase were either 30 min or 90 min the corresponding probabilities would be 0.2756 and 0.1679 for polarity change and 0.3176 and 0.1957 for IMF triggers. Note that the probability of a chance association decreases with increasing duration of the growth phase because of the likelihood that the IMF has already turned northward at an earlier time. Since the most probable duration of substorms in our list was 55 minutes (data not shown) it is apparent that the probability of a chance association will be about 20% (for polarity change) and 23% (for

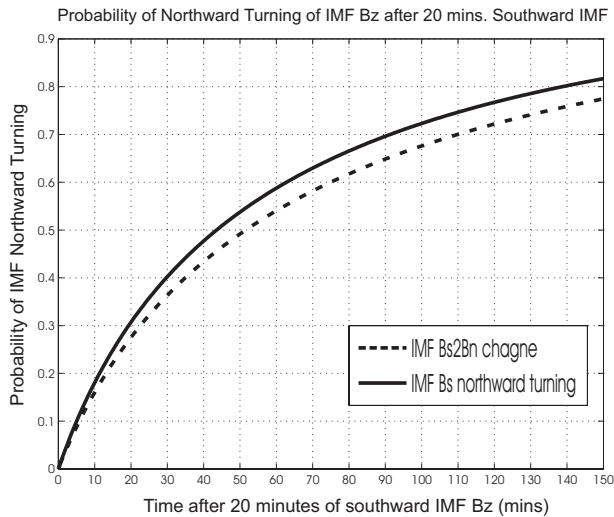


**Fig. 4.** The estimated probability for a northward IMF polarity change and IMF triggers as a function of time after a 20 minutes interval of southward IMF Bz is plotted. The probability of northward IMF polarity change increases very slowly with the time  $t'$  beyond the end of the IMF trigger criterion. The probability of a northward IMF polarity change soon after the end of the 20-minute interval is very low. The same thing applies to IMF triggers probability.

IMF triggers). If we multiply the 145 observed substorm onsets by this fraction we obtain 29 events (for polarity change) and 32 events (for IMF triggers) that were possibly a result of chance. This number should be compared to the observation of 15 chance associations at times far from the expected arrival at the Earth of the IMF trigger [7]. The number of associations is clearly larger than what we would expect if the two events were independent, but is still much smaller than the 52 associations actually observed at zero lag from [7]. The difference divided by the standard deviation is  $(52-29)/4.5$  or 5.11 standard deviations from the background level for polarity change. Similarly, it is  $(52-32)/4.5=4.44$  standard deviation above the background level for IMF triggers. For a normal distribution the probability of obtaining this difference by chance is about  $1.6 \times 10^{-7}$  (for polarity change) and  $4.5 \times 10^{-6}$  (for IMF triggers). This number is somewhat larger than the earlier estimate from [7] for independent processes, but still represents an exceedingly unlikely coincidence. Even so, an important result from this estimation is that the previous estimation of IMF probability [7] after some certain time ( $\sim 20$ -30 minutes) is confirmed even when we consider a more general IMF trigger criteria. It is thus very unlikely that the IMF triggered substorm is a chance association.

A more accurate estimate of the associations resulting from our growth phase criterion would require knowledge of the actual duration of every substorm growth phase in our list of substorms. This list could then be used to weight the probabilities of chance association for different durations. If this distribution were skewed it could either increase or decrease our estimate somewhat. Unfortunately this information was not retained in our survey of the data because our null hypothesis viewed the two processes as completely independent. However, since most substorms have about an hour-long growth phase we are

confident that our estimate is reasonably correct, and that our primary conclusion remains unchanged.

## Acknowledgement

We would like to acknowledge support for this work from NSF grant ATM 02-08501, from NASA grant NNG-04GA93G, and from a LANL grant #12224001054H. We also would like to thank Yasong Ge for the help of Latex file preparation.

## References

1. Caan, M. N., R. L. McPherron, and C. T. Russell (1975), Substorm and interplanetary magnetic field effects on the geomagnetic tail lobes, *Journal of Geophysical Research*, 80, (1), 191-194.
2. Caan, M. N., R. L. McPherron, and C. T. Russell (1977), Characteristics of the association between the interplanetary magnetic field and substorms, *Journal of Geophysical Research*, 82, (29), 4837-4842.
3. Dmitrieva, N. P., and V. A. Sergeev (1983), The Spontaneous and induced Onset of the Explosive Phase of a Magnetospheric Substorm and the Duration Its Preliminary Phase, *Geomagnetism and Aeronomy*, 23, (3), 380-383.
4. Foster, J. C., D. H. Fairfield, K. W. Ogilvie, and T. J. Rosenberg (1971), Relationship of interplanetary parameters and occurrence of magnetospheric substorms, *Journal of Geophysical Research*, 76, (28), 6971.
5. Henderson, M. G., G. D. Reeves, R. D. Belian, and J. S. Murphree (1996), Observation of magnetospheric substorms occurring with no apparent solar wind/IMF trigger, *Journal of Geophysical Research*, 101, (A5), 10773-10791.
6. Horwitz, J. L. (1985), The substorm as an internal magnetospheric instability: substorms and their characteristic time scales during intervals of steady interplanetary magnetic field, *Journal of Geophysical Research*, 90, (A5), 4164-4170.
7. Hsu, T.-S., and R. L. McPherron (2002), An Evaluation of the Statistical Significance of the Association between Northward Turnings of the IMF and Substorm Expansion Onsets, *Journal of Geophysical Research*, 107, (A11), 1398, doi:1310.1029/2000JA000125.
8. Lyons, L. R. (1995), A new theory for magnetospheric substorms, *Journal of Geophysical Research*, 100, (A10), 19069-19081.
9. Lyons, L. R. (1996a), Evidence suggests external triggering of substorms, *Eos*, 77, (9), 88-89.
10. Lyons, L. R. (1996b), Substorms: fundamental observation features, distinction from other disturbances and external triggering, *Journal of Geophysical Research*, 101, (A6), 13011-13026.
11. Lyons, L. R., G. T. Blanchard, J. C. Samson, R. P. Lepping, T. Yamamoto, and T. Moretto (1997), Coordinated observations demonstrating external substorm triggering, *Journal of Geophysical Research*, 102, (A12), 27039-27051.
12. McPherron, R. L. (1991), Physical Processes Producing Magnetospheric Substorms and Magnetic Storms, in *Geomagnetism*, edited by J. Jacobs, pp. 593-739, Academic Press, London.
13. McPherron, R. L., T. Terasawa, and A. Nishida (1986), Solar wind triggering of substorm expansion onset, *Journal of Geomagnetism and Geoelectricity*, 38, (11), 1089-1108.

14. Rostoker, G. (1983), Triggering of expansion phase intensifications of magnetospheric substorms by northward turning of the interplanetary magnetic field, *Journal of Geophysical Research*, 88, 6981.
15. Rostoker, G., W. Baumjohann, and C. T. Russell (1983), A case study of the response of the magnetosphere to changes in the interplanetary medium, *Journal of Geophysics*, 53, 170-181.
16. Samson, J. C., and K. L. Yeung (1986), Some generalizations on the method of superposed epoch analysis, *Planetary and Space Science*, 34, (11), 1133-1142.
17. Sergeev, V. A., N. P. Dmitrieva, and E. S. Barkova (1986), Triggering of substorm expansion by the IMF directional discontinuities: time delay analysis, *Planetary and Space Science*, 34, (11), 1109-1118.
18. Sornette, D., and L. Knopoff (1997), The paradox of the expected time until the next earthquake, *Bulletin of the Seismological Society of America*, 87, (4), 789-798.



# Low-latitude geomagnetic disturbances caused by solar wind pressure impulses and storm-time periodic substorms during southward interplanetary magnetic field

C.-S. Huang and K. Yumoto

**Abstract:** The interplanetary magnetic field (IMF) may be continuously southward for many hours during magnetic storms. The geomagnetic field at middle and low latitudes often shows periodic ( $\sim 3$  hour) increases in association with the storm-time sawtooth-like oscillations of energetic plasma particle flux at geosynchronous orbit. Recent studies have demonstrated that the sawtooth oscillations represent flux injections of substorms. However, there is a significant controversy as to whether the periodic geomagnetic disturbances are caused by magnetospheric substorms or by solar wind pressure enhancements. In order to find a solution to this controversy, we perform a statistical study of the low-latitude geomagnetic response to solar wind pressure enhancements during southward IMF. Our result shows that the change of the geomagnetic field is proportional to the change of the square root of the solar wind pressure, and an empirical formula is derived. We may use this quantitative relationship to estimate the possible effect of the solar wind pressure on the geomagnetic field. This method is useful for identification and interpretation of magnetospheric-ionospheric disturbances related to storm-time periodic substorms during a prolonged interval of southward IMF. We apply the empirical formula to two storm cases in which periodic substorms occur. It is found that the periodic increases of the geomagnetic field are related to the substorm onsets but not to solar wind pressure variations.

*Key words:* Geomagnetic field, Periodic substorms, Sawtooth oscillations, Magnetic storms, Solar wind pressure..

## 1. Introduction

The solar wind dynamic pressure has important influence on the Earth's magnetosphere. When the dayside magnetosphere is compressed by an enhancement of the solar wind pressure, the magnetopause current is intensified, which results in an increase of the geomagnetic field in the dayside magnetosphere and on the ground. Observations of geomagnetic field variations measured by ground magnetometers during northward interplanetary magnetic field (IMF) were reported by [13, 14, 15, 16, 17]. Beside solar wind pressure enhancements, IMF southward turnings and magnetospheric substorms can also cause geomagnetic deviations at middle and low latitudes [19, 8, 18, 6].

The IMF can be continuously southward for many hours during magnetic storms. The magnetosphere becomes very dynamic, and a series of substorms can occur. The term, "periodic substorms", has been used to describe a specific type of substorms that last for many cycles, show well-defined waveforms, and have nearly constant periods. It is suggested by [3, 4, 5] that magnetospheric substorms have an intrinsic cycle time of  $\sim 3$  hours; this periodicity is determined by the magnetosphere, rather than by the solar wind. A prominent feature of energetic plasma particle flux variations during periodic substorms measured at geosynchronous orbit is the sawtooth-

like shape with periodic repetitions of sudden flux increases followed by gradual flux decreases, so the storm-time periodic substorms are also termed sawtooth events [1, 2]. The sudden increases of the flux represent the plasma particle flux injections from the magnetotail to the inner magnetosphere at substorm onsets.

The low-latitude geomagnetic field often shows an increase on both the dayside and nightside after each onset during periodic substorms. It is shown by [6, 7] that the increases of the geomagnetic field are caused by three processes: magnetotail current disruption, magnetospheric dipolarization, and ionospheric electric field; all these processes are related to the onsets of substorms. On the other hand, it was argued by [9, 10] that the variations of the geomagnetic field were the signatures of solar wind pressure enhancements and that sawtooth oscillations were directly driven by series of solar wind pressure enhancements.

The solar wind always has some fluctuations, although the amplitude of the fluctuations may be large or small. In order to identify whether a specific variation in the geomagnetic field is caused by a variation in the solar wind pressure, we need a quantitative measure to determine how large the contribution of the solar wind pressure can be. This is important because it is related to the identification and interpretation of magnetospheric-ionospheric disturbances during storm-time substorms with continuous southward IMF. In this paper, we present the statistical result of low-latitude geomagnetic response to solar wind pressure enhancements during southward IMF and use the derived empirical formula to identify the generation mechanism of periodic geomagnetic disturbances during magnetic storms.

Received 15 May 2006.

**C.-S. Huang.** Haystack Observatory, Massachusetts Institute of Technology, Westford, Massachusetts, USA.

**K. Yumoto.** Space Environment Research Center, Kyushu University, Fukuoka, Japan

## 2. Observations

We first present the observations of geomagnetic changes in response to solar wind pressure enhancements during southward IMF in two cases. Figure 1a shows, from top to bottom, the IMF  $B_z$  component and solar wind pressure measured by the ACE satellite and the deviations of the geomagnetic field northward ( $H$ ) component. The vertical dotted line indicates the solar wind pressure impulse and the sudden increase of the geomagnetic field. ACE was located at  $X_{GSM} = 250 R_E$  during the period of interest. We use the solar wind velocity and satellite position to calculate the propagation delay and then match the solar wind pressure impulse with the corresponding increase of the geomagnetic field. Accordingly, the ACE data are shifted by 53 min in Figure 1a. For all cases, including those used in the statistics, we use the same method to determine the solar wind propagation delay from the satellite position to the magnetosphere. The measurements of the geomagnetic field are made with the ground magnetometers of the Solar-Terrestrial Energy Program (STEP) 210 (degree) magnetic meridian chain around geographic longitudes 110-140° [21]. We choose five magnetometers, spanning from magnetic latitude 36° (in northern hemisphere) to -36° (in southern hemisphere), for each event to calculate the geomagnetic response to the solar wind pressure impulse. It is obvious that the increase of the geomagnetic field is well correlated with the solar wind pressure impulse. The IMF  $B_z$  remains southward across the solar wind pressure impulse, but its magnitude has some changes. It is not certain whether the change in the magnitude of the IMF  $B_z$  has any significant effects on the geomagnetic field. We assume that the sudden increase of the geomagnetic field is attributed solely to the solar wind pressure enhancement.

Local time of the STEP magnetometers is about UT plus 9 hours. The case in Figure 1a occurred on the dayside. We present another case in Figure 1b that occurred on the nightside. The response of the nightside geomagnetic field to a solar wind pressure enhancement is similar to that on the dayside.

A quantitative relationship between the solar wind pressure enhancement and low-latitude geomagnetic response was studied previously. The following formula without distinguishing the IMF orientation was derived by [20]:

$$\Delta H = k(\sqrt{P_{sw2}} - \sqrt{P_{sw1}}), \quad (1)$$

where  $\Delta H$  is the change of the geomagnetic field,  $k$  is a constant, and  $P_{sw1}$  and  $P_{sw2}$  are the solar wind pressure values before and after the pressure enhancement, respectively. The study of [20] included 13 cases. A coefficient of  $k = 18.4$  from 14 cases during northward IMF was derived by [15]. In addition,  $k = 7.26$  was used in the calculations of the corrected  $Dst$  index [11].

We are interested in the geomagnetic disturbances during southward IMF, and the events are selected through the following procedure. First, we search the STEP magnetometer data by vision to find the cases in which the low-latitude geomagnetic field shows a sudden increase, such as those shown in Figure 1. Second, we check the solar wind pressure and IMF data measured by the ACE and/or Wind satellites. The solar wind must have a sharp pressure impulse with a consistent

propagation delay from the satellite position to the magnetosphere. The IMF  $B_z$  must be continuously negative for at least 1 hour prior to the solar wind pressure impulse and remain southward across the pressure impulse, in order to make sure that the magnetosphere is in a state that is controlled by southward IMF. We searched the geomagnetic data over seven years (1998-2005) and found 43 events that satisfy the above criteria.

The statistical result is shown in Figure 2. Figure 2a includes all events. The horizontal axis represents the change of the square root of the solar wind pressure across the impulse, and the vertical axis represents the increase of the geomagnetic field  $H$  component in response to the solar wind pressure impulse. As said above, five magnetometer stations are chosen, so there are five data points for each event. Figure 2 shows the result over a latitudinal range between 36° and -36° but not at a single latitude.

We have performed the least square fitting of the data, which are given by the dashed lines in Figure 2. In Figure 2a for all events, the data fitting can be expressed by the following formula

$$\Delta H = 21.67 \times (\sqrt{P_{sw2}} - \sqrt{P_{sw1}}) - 2.74, \quad (2)$$

where  $\Delta H$  is measured with nT, and  $P_{sw}$  is measured with nPa. The solid line in Figure 2a is plotted from Eq. (2), so it overlaps the dashed line (data fitting). Note that our result is derived exclusively from southward IMF, which is different from [15] for northward IMF.

There is an offset of -2.74 nT on the right-hand side of Eq. (2). Several potential processes may cause the offset. First, the statistics includes 43 events, and the limited number of events may be unable to guarantee an accurate empirical formula. Second, we neglected possible effects of the change in the magnitude of the IMF  $B_z$  when we calculated the net increase of the geomagnetic field, which may bring some uncertainty to the result. Third, the offset means that the increase of the geomagnetic field will be zero if the increase of the square root of the solar wind pressure is  $0.126 \text{ (nPa)}^{-1/2}$ ; this amount may represent the minimum solar wind pressure increase required to cause observable changes in the geomagnetic field. We will further study this issue in the future.

Figures 2b and 2c show the events that are detected when the magnetometers are on the dayside and on the nightside, respectively. The dashed line represents the least square fitting for each category, and the solid line is from Eq. (2). The data fitting line in Figure 2c for the nightside events is very close to the solid line. However, the data fitting line in Figure 2b for the dayside events does not coincide very well with Eq. (2) because of the data scatter in fewer cases.

The statistical result, Eq. (2), can be used as an estimate of the possible contribution of the solar wind pressure to the generation of geomagnetic disturbances. We examine such a case that occurred on 18 April 2002 during a prolonged interval of continuous southward IMF. Figures 3a and 3b present the shifted IMF  $B_z$  and solar wind pressure data measured by the ACE satellite. The IMF is continuously southward for the whole day. The solar wind pressure shows an enhancement at 0030 UT and a second, smaller one around 0300 UT. The solar wind pressure becomes small ( $\sim 1$  nPa) after 0500 UT. Figures 3c and 3d display the energetic electron flux measured by the LANL 1991-080 and 1990-095 geosynchronous satellites.

The sawtooth like variations of the electron fluxes have been analyzed in detail by [4, 2] and identified as the signature of periodic substorms with a period of  $\sim 3$  hours. The vertical dotted lines indicate the sudden increases in the electron fluxes at the substorm onsets.

Figure 3e shows the geomagnetic deviations measured by the STEP magnetometers. Only the measurements from five magnetometers are plotted over a latitudinal range between  $36^\circ$  and  $-36^\circ$  magnetic latitudes. There are more magnetometers within this range and beyond this range, and all magnetometer measurements have similar characteristics. The most interesting feature in Figure 3e is that the geomagnetic field shows an increase after each onset of the periodic substorms. The only exception is a decrease after 0530 UT and then an increase after 0600 UT. Note that the periodic increases of the geomagnetic field occur over an interval of 24 hours. Half of the geomagnetic increases occur on the dayside, and half on the nightside.

We examine whether the periodic increases of the geomagnetic field can be caused by corresponding variations in the solar wind pressure. Eq. (2) provides a method to estimate the effect of the solar wind pressure. However, it is difficult to determine the background solar wind pressure. In stead, we take  $P_{sw1} = 0$  and  $P_{sw2} = P_{sw}$ , so Eq. (2) is reduced to

$$\Delta H = 21.67 \times \sqrt{P_{sw}} - 2.74, \quad (3)$$

where  $P_{sw}$  is the total solar wind pressure. It is obvious that Eq. (3) overestimates the contribution of the solar wind pressure. We plot in Figure 3f the possible effect of the solar wind pressure predicted by Eq. (3) with the measured pressure as input.

We are now able to identify which increases of the geomagnetic field are related to the solar wind pressure and which are not. At 0030 UT, an increase of the geomagnetic field is measured by the magnetometers (Figure 3e) and predicted by the empirical formula (Figure 3f), so this increase may be the geomagnetic response to the solar wind pressure enhancement. At 0240 UT, the predicted geomagnetic increase is smaller than the measured value, implying that the contribution from substorms is important for this one. After 0500 UT, the possible geomagnetic disturbances caused by the solar wind pressure are very small. However, the measured geomagnetic field shows large periodic increases in coincidence with the substorm onsets. The comparison between the measurements and prediction indicates that the periodic increases of the geomagnetic field are related to the substorms but not to the solar wind pressure.

Another example of the difference between the solar wind pressure and substorm effects is shown in Figure 4. This case occurred on 6 November 2000. Figure 4 shows the IMF  $B_z$ , solar wind pressure, energetic electron flux measured by the LANL 1994-084 and 1989-046 geosynchronous satellites, geomagnetic field deviations measured by the STEP magnetometers, and the possible effect of the solar wind pressure predicted by the empirical formula. There are some fluctuations in the IMF  $B_z$ . The solar wind pressure shows three enhancements of 2.2 nPa at 0949 UT, 20 nPa at 1757 UT, and 12 nPa at 1838 UT, respectively, as indicated by the vertical dashed lines. The solar wind pressure is relatively stable at other times.

Figure 4c and 4d show the energetic electron flux at geosynchronous orbit. The sudden increase of the flux, as indicated

by the vertical dotted lines, is a typical signature of magnetospheric substorm onsets [4, 5, 12]. The solar wind pressure does not have any noticeable variations at the times of the substorm onsets. The geomagnetic field in Figure 4e shows an increase after each substorm onset, as well as after each solar wind pressure impulse. However, the increases of the geomagnetic field after the substorm onsets with stable solar wind pressure are comparable to, or even larger than those caused by the significant enhancements of the solar wind pressure at 1757 and 1838 UT.

As discussed above, Eq. (2) provides an estimate of the solar wind pressure effect on the geomagnetic field, which is depicted in Figure 4f. The geomagnetic field has a gradual decrease from 1000 to 2200 UT, which is related to the storm-time drift. What we are interested is the sudden increases of the geomagnetic field after the substorm onsets or after the solar wind pressure impulses. The measured increases of the geomagnetic field at 1757 and 1838 UT coincide reasonably with the value predicted by Eq. (2), indicating that they are caused by the solar wind pressure impulses. The increase of the geomagnetic field at 0949 UT is also consistent with the effect of the solar wind pressure. However, the increases of the geomagnetic field at 1051, 1300, and 1554 UT are obviously related to the substorm onsets, as indicated by the vertical dotted lines, and the contribution from the solar wind pressure is negligible at these times.

### 3. Discussion and Conclusions

As mentioned in Introduction, there is a controversy as to what causes storm-time geomagnetic disturbances during continuous southward IMF. It was argued by [10] that all geomagnetic field variations were caused by solar wind pressure enhancements and that the sawtooth oscillations were driven directly by the solar wind pressure but not related to magnetospheric substorms. However, the different effects of the solar wind pressure and magnetospheric substorms were not appropriately separated in the study of [10]. In contrast, the characteristics of the magnetospheric substorms and relevant ionospheric disturbances are carefully examined by [7, 2], and the authors conclude that the sawtooth oscillations are indeed caused by periodic substorms. Our statistics deals with the effects of the solar wind pressure on the low-latitude geomagnetic field during southward IMF. The result shows that the increases of the geomagnetic field are caused by the periodic substorms but not by solar wind pressure enhancements.

The changes of the low-latitude geomagnetic field caused by solar wind pressure enhancements during southward IMF can be estimated by Eq. (2). If multiple processes, such as solar wind pressure enhancements and magnetospheric substorms, occur nearly simultaneously, we may use Eq. (2) to find which process is responsible for the generation of low-latitude geomagnetic disturbances. This method is particularly useful in identification and interpretation of the magnetospheric and ionospheric disturbances related to storm-time periodic substorms with continuous southward IMF.

**Acknowledgements.** The work at MIT Haystack Observatory was supported by the National Science Foundation under grant ATM 0435125. Solar-Terrestrial Environment Laboratory, Nagoya University supports construction of the STEP

magnetometer database. We thank Geoff Reeves of Los Alamos National Laboratory for providing the electron flux data and acknowledge the CDAWeb for providing access to the ACE and Wind solar wind data.

## References

1. Henderson, M. G., The May 2-3, 1986 CDAW-9C interval: A sawtooth event, *Geophys. Res. Lett.*, *31*, L11804, doi:10.1029/2004GL019941, 2004.
2. Henderson, M. G., G. D. Reeves, R. Skoug, M. T. Thomsen, M. H. Denton, S. B. Mende, T. J. Immel, P. C. Brandt, and H. J. Singer, Magnetospheric and auroral activity during the 18 April 2002 sawtooth event, *J. Geophys. Res.*, *111*, A01S90, doi:10.1029/2005JA011111, 2006.
3. Huang, C. S., Evidence of periodic (2-3 hour) near-tail magnetic reconnection and plasmoid formation: Geotail observations, *Geophys. Res. Lett.*, *29*(24), 2189, doi:10.1029/2002GL016162, 2002.
4. Huang, C. S., J. C. Foster, G. D. Reeves, G. Le, H. U. Frey, C. J. Pollock, and J.-M. Jahn, Periodic magnetospheric substorms: Multiple space-based and ground-based instrumental observations, *J. Geophys. Res.*, *108*(A11), 1411, doi:10.1029/2003JA009992, 2003a.
5. Huang, C. S., G. D. Reeves, J. E. Borovsky, R. M. Skoug, Z. Y. Pu, and G. Le, Periodic magnetospheric substorms and their relationship with solar wind variations, *J. Geophys. Res.*, *108*(A6), 1255, doi:10.1029/2002JA009704, 2003b.
6. Huang, C. S., J. C. Foster, L. P. Goncharenko, G. D. Reeves, J. L. Chau, K. Yumoto, and K. Kitamura, Variations of low-latitude geomagnetic fields and *Dst* index caused by magnetospheric substorms, *J. Geophys. Res.*, *109*, A05219, doi:10.1029/2003JA010334, 2004.
7. Huang, C. S., G. D. Reeves, G. Le, and K. Yumoto, Are sawtooth oscillations of energetic plasma particle fluxes caused by periodic substorms or driven by solar wind pressure enhancements?, *J. Geophys. Res.*, *110*, A07207, doi:10.1029/2005JA011018, 2005.
8. Kikuchi, T., H. Luhr, K. Schlegel, H. Tachihara, M. Shinohara, and T. I. Kitamura, Penetration of auroral electric fields to the equator during a substorm, *J. Geophys. Res.*, *105*, 23,251, 2000.
9. Lee, D.-Y., and L. R. Lyons, Geosynchronous magnetic field response to solar wind dynamic pressure pulse, *J. Geophys. Res.*, *109*, A04201, doi:10.1029/2003JA010076, 2004.
10. Lee, D.-Y., L. R. Lyons, and K. Yumoto, Sawtooth oscillations directly driven by solar wind dynamic pressure enhancements, *J. Geophys. Res.*, *109*, A04202, doi:10.1029/2003JA010246, 2004.
11. O'Brien, T. P., and R. L. McPherron, An empirical phase space analysis of ring current dynamics: Solar wind control of injection and decay, *J. Geophys. Res.*, *105*, 7707, 2000.
12. Reeves, G. D., et al., IMAGE, POLAR, and geosynchronous observations of substorm and ring current ion injection, in *Disturbances in Geospace: The Storm-Substorm Relationship*, *Geophys. Monogr. Ser.*, vol. 142, Edited by A. S. Sharma, Y. Kamide, and G. S. Lakhina, pp. 91-101, AGU, Washington, D. C., 2003.
13. Russell, C. T., and M. Ginskey, Sudden impulses at low latitudes: Transient response, *Geophys. Res. Lett.*, *20*, 1015, 1993.
14. Russell, C. T., and M. Ginskey, Sudden impulses at subauroral latitudes: Response for northward interplanetary magnetic field, *J. Geophys. Res.*, *100*, 23,695, 1995.
15. Russell, C. T., M. Ginskey, and S. M. Petrinec, Sudden impulses at low-latitude stations: Steady state response for northward interplanetary magnetic field, *J. Geophys. Res.*, *99*, 253, 1994a.
16. Russell, C. T., M. Ginskey, and S. M. Petrinec, Sudden impulses at low-latitude stations: Steady state response for southward interplanetary magnetic field, *J. Geophys. Res.*, *99*, 13,403, 1994b.
17. Russell, C. T., M. Ginskey, S. M. Petrinec, and G. Le, The effect of solar wind dynamic pressure changes on low and mid-latitude magnetic records, *Geophys. Res. Lett.*, *19*, 1227, 1992.
18. Sastri, J. H., J. V. S. V. Rao, D. R. K. Rao, and B. M. Pathan, Daytime equatorial geomagnetic *H* component response to the growth phase and expansion phase onset of isolated substorms: Case studies and their implications, *J. Geophys. Res.*, *106*, 29,925, 2001.
19. Sibeck, D. G., K. Takahashi, K. Yumoto, and G. D. Reeves, Concerning the origin of signatures in dayside equatorial ground magnetometers, *J. Geophys. Res.*, *103*, 6763, 1998.
20. Siscoe, G. L., V. Formisano, and A. J. Lazarus, Relation between geomagnetic sudden impulses and solar wind pressure changes - An experimental investigation, *J. Geophys. Res.*, *73*, 4869, 1968.
21. Yumoto, K., and the CPMN Group, Characteristics of Pi 2 magnetic pulsations observed at the CPMN stations: A review of the STEP results, *Earth Planets Space*, *53*, 981, 2001.

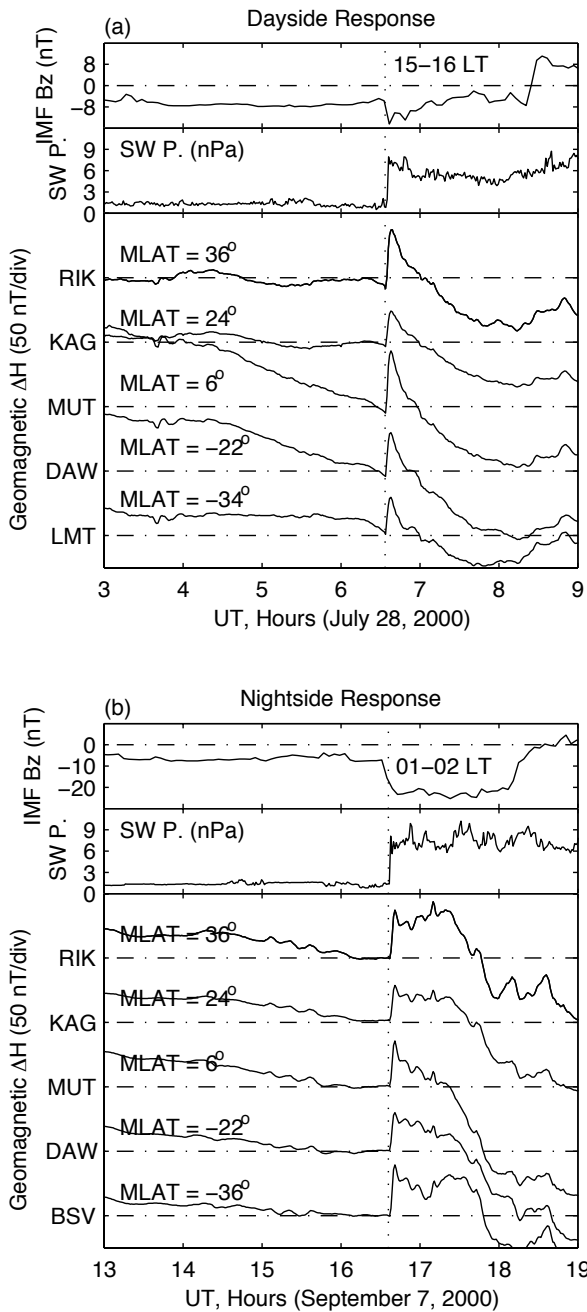


**Fig. 1.** Sudden increases of the geomagnetic field northward ( $H$ ) component at low latitudes in response to a solar wind pressure impulse during southward interplanetary magnetic field (IMF). Shown from top to bottom are the IMF  $B_z$  component, solar wind pressure, and geomagnetic  $H$  deviations. The event in Figure 1a occurred during daytime on 28 July 2000. The event in Figure 1b occurred at night on 7 September 2000. The magnetometer stations are Rikubetsu (RIK), Kagoshima (KAG), Muntinlupa (MUT), Darwin (DAW), Learmonth (LMT), and Birdsville (BSV). Magnetic latitude (MLAT) for each station is given in the figure.

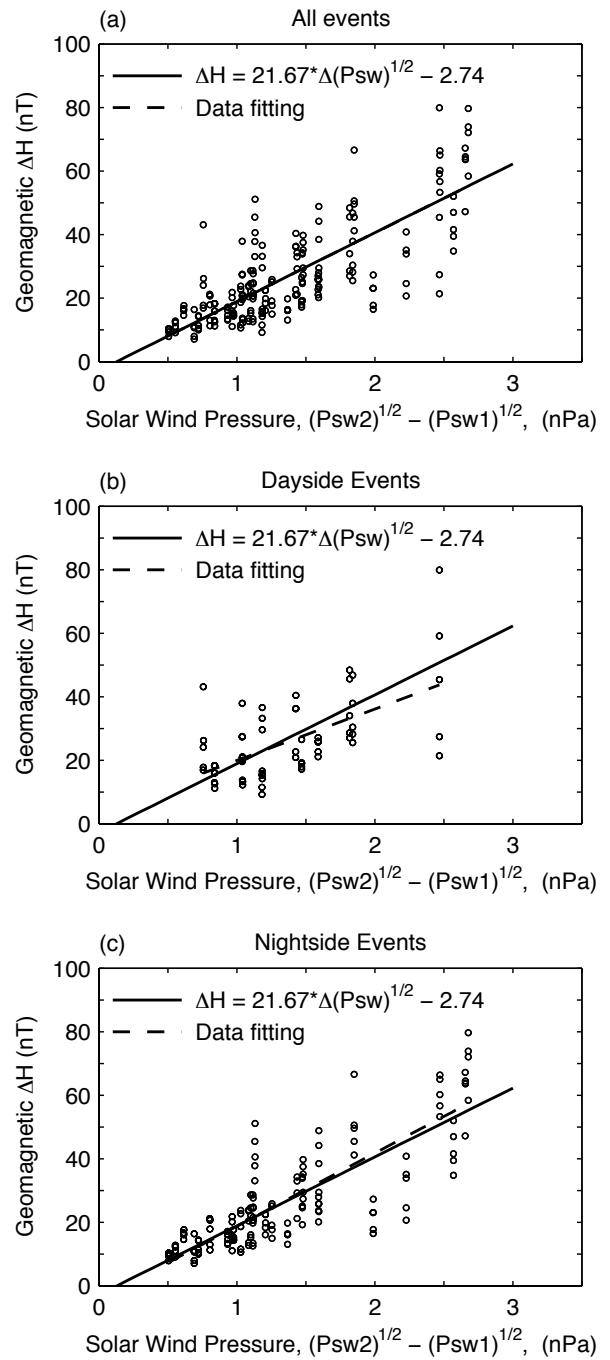


**Fig. 2.** Statistical results of the sudden increases of the low-latitude geomagnetic field  $H$  component caused by solar wind pressure impulses during southward IMF for (a) all events, (b) dayside events, and (c) nightside events, respectively. The dashed line represents the least square fitting of the data. The solid line represents Eq. (2).

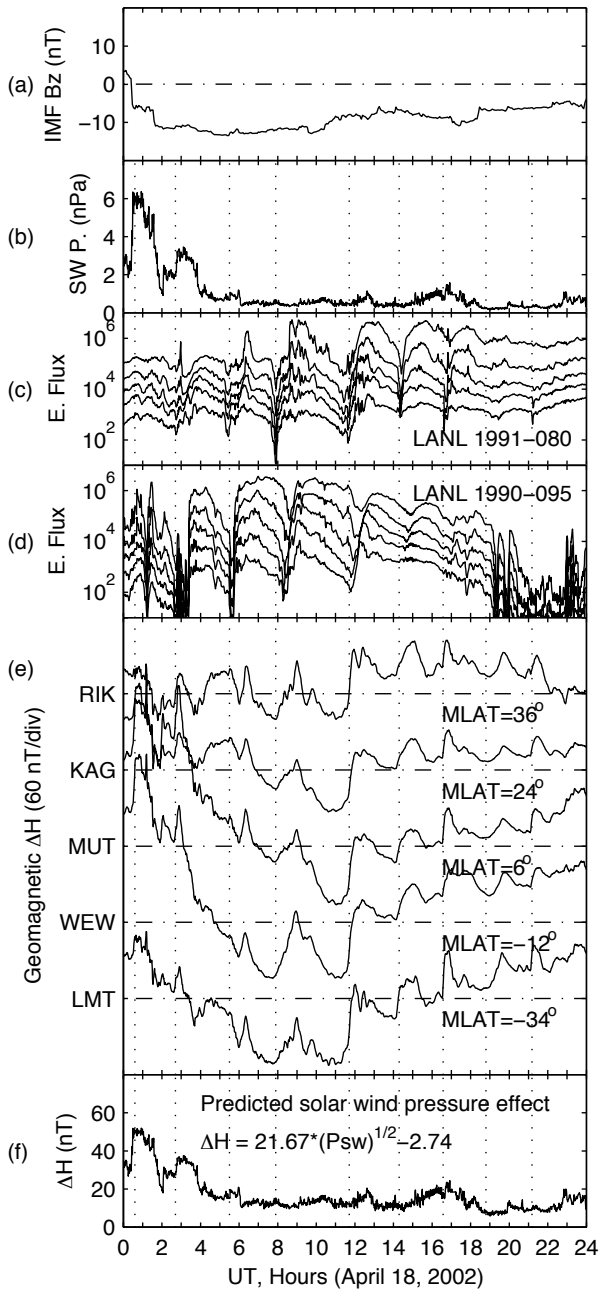


**Fig. 3.** Effects of storm-time periodic substorms on the geomagnetic field during southward IMF on 18 April 2002. From top to bottom are (a) IMF  $B_z$ , (b) solar wind pressure, (c)-(d) energetic electron fluxes at geosynchronous orbit, (e) measured low-latitude geomagnetic  $H$  deviations, and (f) possible geomagnetic  $H$  deviations caused by the solar wind pressure. The vertical dotted lines indicate substorm onsets.

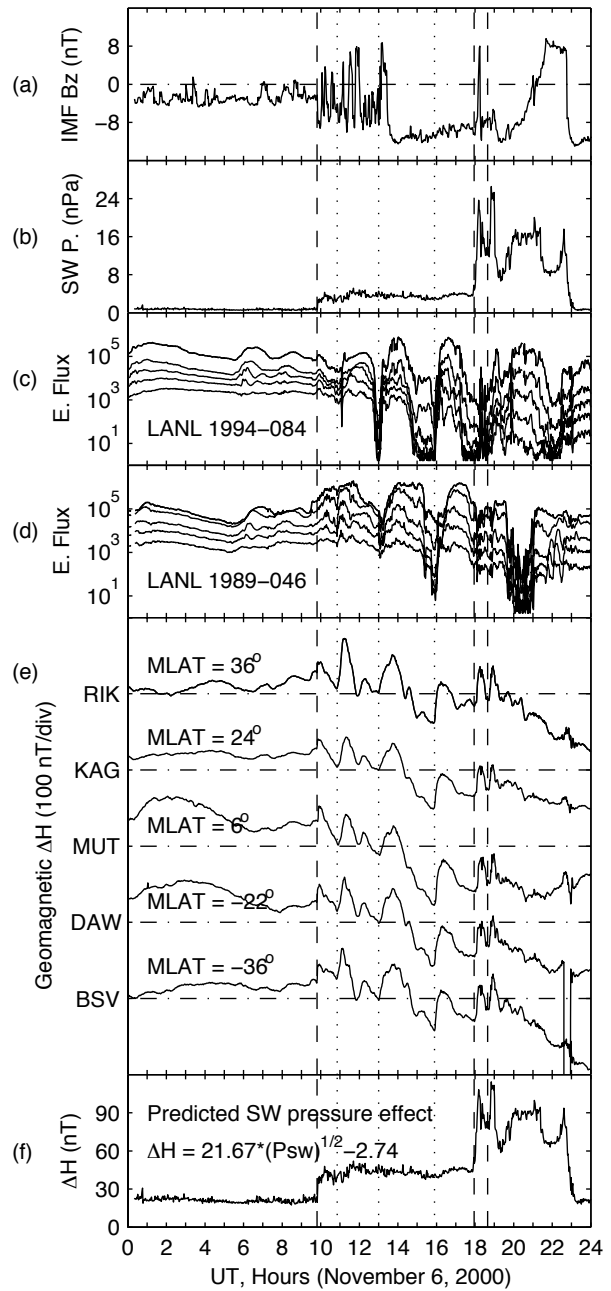


**Fig. 4.** Same as Figure 3 but for 6 November 2000.

# Monitoring the dayside and nightside reconnection rates during various auroral events using IMAGE-FUV and SuperDARN data

B. Hubert, M. Palmroth, S.E. Milan, A. Grocott, P. Janhunen, K. Kauristie, S.W.H. Cowley, T.I. Pulkkinen, and J.-C. Gérard

**Abstract:** The Imager for Magnetopause to Aurora Global Exploration (IMAGE) spacecraft was launched in 2000 with several imaging instruments onboard. The Far UltraViolet (FUV) experiment was devoted to the imaging of the N2 LBH (Wideband Imaging Camera - WIC-), OI 135.6 nm (Spectrographic Imager -SI13-) and Doppler-shifted Lyman-alpha auroral emission (SI12). The Doppler-shifted Lyman-alpha emission is solely due to proton precipitation and is not contaminated by dayglow, allowing to monitor the auroral oval at dayside as well as at nightside. Remote sensing of the polar aurora can be advantageously completed by ground based data of the Super Dual Auroral Radar Network (SuperDARN) that monitors the ionospheric convection flow pattern in the polar region. In the present study, the SI12 images are used to determine the open/closed (o/c) field line boundary, and monitor its movement. The SuperDARN data are used to compute the electric field of the polar cap at the location of the o/c boundary. The total electric field is then computed along the boundary accounting for its movement applying Faraday's law, so that the dayside and nightside reconnection voltages can be retrieved. This procedure is applied to monitor the dayside and nightside reconnection voltages during several events. The phases of the substorm cycle can be identified: the growth phase characterised by intense dayside flux opening and occasionally pseudobreakups, the onset which is immediately followed by a maximum intensity of the flux closure rate, and the recovery phase during which the flux closure voltage slowly returns to undisturbed values, with occasional poleward boundary intensifications which appear along with a slight intensification of the closure voltage. The transient response to an interplanetary shock is also monitored and reveals a sharp intensification of the closure rate, despite a low open flux value for the studied case. A case of auroral streamer event has also been studied, presenting a remarkably large flux closure rate. This feature is related with a bursty enhancement of the ionospheric convection. Bursty bulk flow events can thus be associated as well with enhanced flux closure. The tool that we developed can also be used to study the relations between the topology of the magnetotail and the flux closure rate as well as to set up proxies relating the solar wind conditions with the dayside reconnection voltage. The monitoring of dayside and nightside reconnection rates can thus be considered as an investigation tool for nearly all types of auroral features.

*Key words:* Reconnection, Substorm, Shock.

## 1. Introduction

The solar wind plasma outflow from the Sun carries the interplanetary magnetic field. Interaction between the solar wind plasma and the Earth magnetosphere on the dayside of the planet causes the production of open magnetic flux. Opened field lines, that map from the polar cap into the solar wind, are carried antisunward by the solar wind flow and are stretched into a long magnetic tail, in which the field lines eventually reconnect and return to the Earth [6]. The auroral substorm cycle classically consists of a growth phase, a substorm onset, an expansion phase and finally a recovery phase [1, 11]. During the growth phase, the interplanetary magnetic field (IMF) carried by the solar wind is usually oriented southward so that

it efficiently reconnects with the geomagnetic field, producing new open flux. This phase ends in a substorm onset characterized by a sudden localized brightening of the polar aurora near midnight, which announces the expansion phase during which accumulated openflux is closed by intense magnetic reconnection in the magnetotail [14] (and references therein). The system then returns to a quiet state during the recovery phase.

We have developed a method combining space-based measurements of the proton aurora and ground-based measurements of the ionospheric flow to compute the global rates at which flux is opened and closed in the Earth's magnetosphere [8]. These rates are expressed as voltages, with 1 V being equivalent to 1 Wb s<sup>-1</sup> from Faraday's law. The images of the proton aurora are from the Spectrographic Imager at 121.8 nm (SI12) instrument of the Far UltraViolet (FUV) experiment onboard the Imager for Magnetopause to Aurora Global Exploration (IMAGE) satellite [12]. They allow us to estimate the location of the boundary between open and closed field lines, as well as its latitudinal motion [8]. The ionospheric flow velocity  $\vec{v}_i$  is measured with the Super Dual Auroral Radar Network (SuperDARN) radar system and is used to retrieve the ionospheric electric field  $\vec{E}_i$  given by  $\vec{E}_i = -\vec{v}_i \times \vec{B}$  where  $\vec{B}$  is the Earth's

Received 16 May 2006.

**B. Hubert and J.-C. Gérard.** Laboratory for Planetary and Atmospheric Physics, University of Liège, Liège, Belgium.

**M. Palmroth, P. Janhunen, K. Kauristie, and T.I. Pulkkinen.** Finnish Meteorological Institute, Helsinki, Finland

**S.E. Milan, A. Grocott, and S.W.H. Cowley.** Radio and Space Plasma Physics Group, University of Leicester, Leicester, UK

magnetic field [15]. The electric field in the reference frame of the open-closed field boundary can then be obtained, and integrated along the boundary to compute the voltages associated with flux opening and closure [4] (and references therein). This method is applied to the study of the substorm cycle [8] and of interplanetary shocks [9]. The IMAGE-FUV instrument captures an image of the planet every 2 min, though the filtering process that is applied in our method to denoise our results and allow time derivative computation reduces the time resolution to 12 min, thus slightly smearing rapidly varying signals.

## 2. Reconnection voltages during the substorm cycle

### 2.1. Open-close boundary identification with SI12

We summarize here the results extensively discussed in [8]. The location of the open-close field line boundary is estimated using the polar boundary of the proton aurora observed with the SI12 instrument of the IMAGE-FUV experiment. The method is calibrated using a comparison between the open-close boundary deduced from in situ measurement of the precipitating particles from the DMSP satellites. This comparison shows that the polar boundary of the proton aurora that we determine with SI12 images is on average 0.55 equatorward of that deduced from DMSP observations. This shift is thus accounted for in the open-close field line boundary location that we determine. Note that particles can diffuse across the separatrix as they travel between the tail and the ionosphere. This is a source of uncertainty that affects both methods used in the calibration. This process would actually affect any method based on auroral observations in the vicinity of the boundary. The detailed structure of the cusp is not accounted for. This approximation only affects the opening voltage through the contribution associated with the motion of the boundary, which is not dominant in the cusp sector [8].

Images of the proton aurora are preferred for the absence of significant dayglow contamination. This allows the determination of the boundary over the whole oval at any time of the year and for any diameter of the polar cap. The boundary is fitted with Fourier series, which allows an easy computation of its velocity using several consecutive snapshots of the proton aurora. The motional component of the electric field can thus be retrieved and combined with the ionospheric electric field deduced from SuperDARN radar data to retrieve the total reconnection electric field, as explained in the introduction.

### 2.2. Flux closure during substorm intervals

Fig. 1 shows the location of the open-close boundary estimated with SI12 images of the proton aurora on 29 December 2000. Pseudobreakups are observed at 0241, 0320 and 0341 UT. An expansion phase onset takes place at 0359 UT, and poleward boundary intensifications (PBI's) are seen between 0650 and 1000 UT, with a maximum brightness around 0800 UT. Although these PBI's do not clearly appear in the proton aurora, they better show up in images of the electron aurora obtained with the Wide band Imaging Camera (WIC) of the IMAGE-FUV experiment.

The open flux and reconnection voltages that we deduce from the SI12 and SuperDARN observations during this interval are presented in Fig. 2. The open flux increases between

0230 and 0400 UT, an interval during which the IMF was northward (Fig. 3). During this growth phase, the magnetosphere accumulates open flux up to 0.78 GWb. Magnetic flux closure is seen to intensify at the time of the pseudobreakups, but the time resolution of the method does not allow to discriminate between a progressive or a transient intensification.

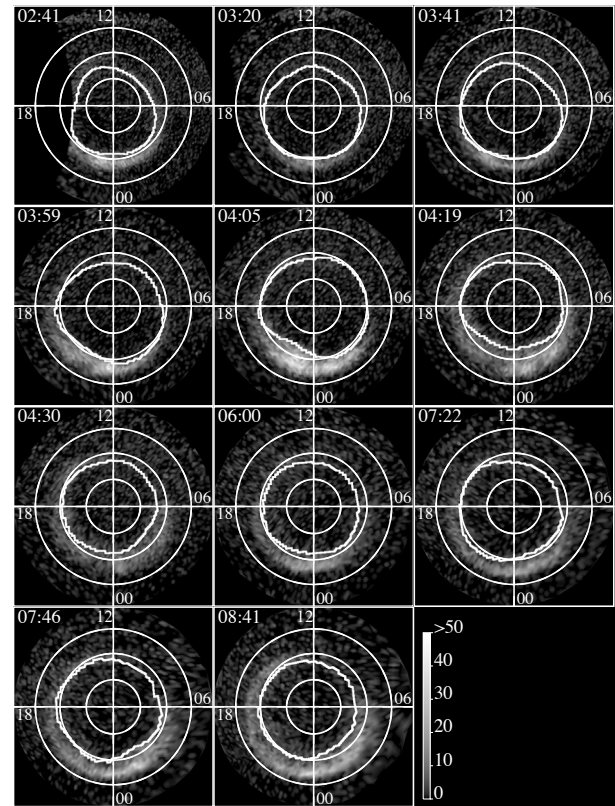


**Fig. 1.** Sample of polar views of the proton aurora obtained with IMAGE-FUV SI12 between 0235 and 1120 UT on 29 December 2000. The fitted open/closed field line boundary is overlaid in white. The colour scale is expressed in SI12 counts.

The closure voltage reaches its maximum intensity shortly after substorm onset (140 kV), which is in favour of the near earth neutral line paradigm. These trends have been found in other substorms as well, although exceptions exist, for complicated events having multiple onsets, for example. At the time of the PBI's, during the recovery phase, the closure voltage intensifies as well, suggesting a relation between PBI's and magnetic flux closure. The quiet times closure voltage is found to be 30 kV.

### 2.3. Flux opening during substorm intervals

As already outlined above, intense production of open magnetic flux has been observed during the substorm growth phase between 0230 and 0400 UT on 9 December 2000. Dayside reconnection is favoured during intervals of southward IMF, and proxies based on the solar wind properties can be set up to estimate the electric field responsible for magnetic reconnection along the dayside neutral line, where magnetospheric and interplanetary field lines merge. This electric field must

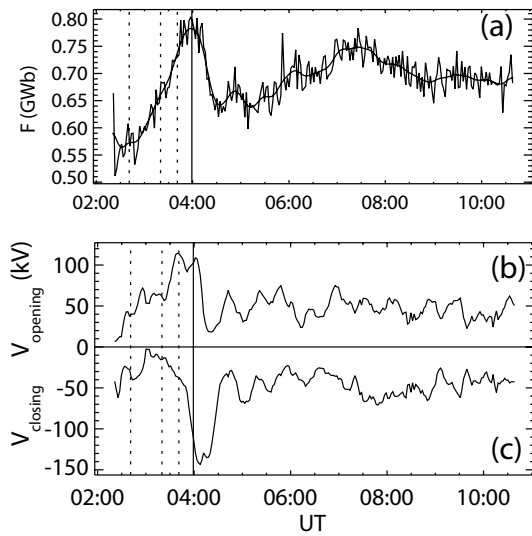


**Fig. 2.** Open magnetic flux (a), flux opening voltage (b) and flux closure voltage (c) derived from SI12 and SuperDARN data on 9 December 2000.

then be multiplied by an effective length in order to retrieve the reconnection voltage inferred from the solar wind properties. Conversely, the ratio of the opening voltage that we deduce and the solar wind electric field gives an estimate of the effective length of the reconnection site. This length is typically of a few Earth radii. Fig. 4 presents the effective length obtained comparing the opening voltage of Fig. 2 and the proxy for the reconnection electric field proposed by [16], i.e.  $E = v_{sw} B_T \sin^4(\theta/2)$  where  $v_{sw}$  is the solar wind velocity,  $B_T$  is the transverse magnetic field and  $\theta$  is the clock angle.

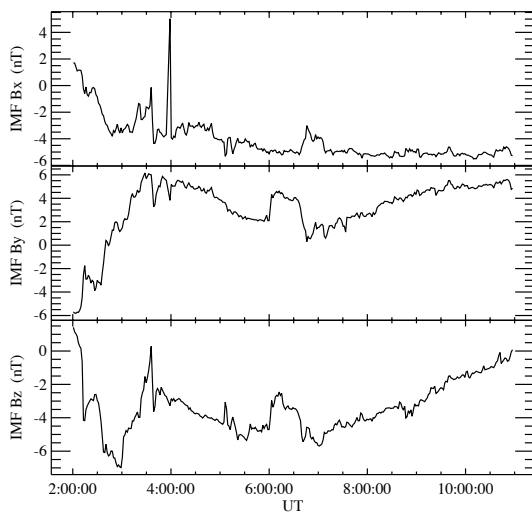


**Fig. 3.** Interplanetary magnetic field components measured by the WIND satellite on 9 December 2000.

The computed effective length of the merging site is of reasonable order of magnitude, and relatively stable versus time

in the present case, during which the IMF was nearly always southward as indicated by the shading. However, during other intervals presenting a northward IMF, the computed effective length can be off by several orders of magnitude. This suggests that proxies of the reconnection field are valid during southward IMF, i.e. when reconnection is large, whereas they should be considered with caution during northward IMF intervals.

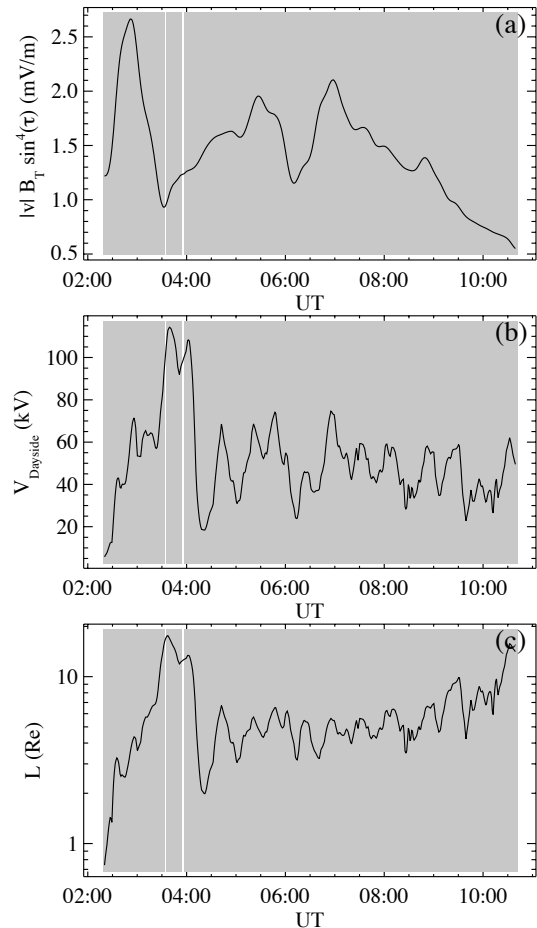


**Fig. 4.** Proxy for the reconnection electric field at the dayside merging site, based on solar wind properties (a), flux opening voltage obtained from SI12 and SuperDARN observations (b), and effective reconnection length deduced from curves a and b on 9 December 2000. Shadings indicate southward IMF.

### 3. Shock-induced flux closure

We summarize here the results presented in [9]. It is well known that, among other disturbances, interplanetary shocks can trigger flux closure and the development of an expansion phase [5] (and references therein), [13, 14]. Flux closure induced by the interaction of IP shocks and the magnetosphere is presented and analyzed in the light of an MHD simulation of the space environment with GUMICS-4.

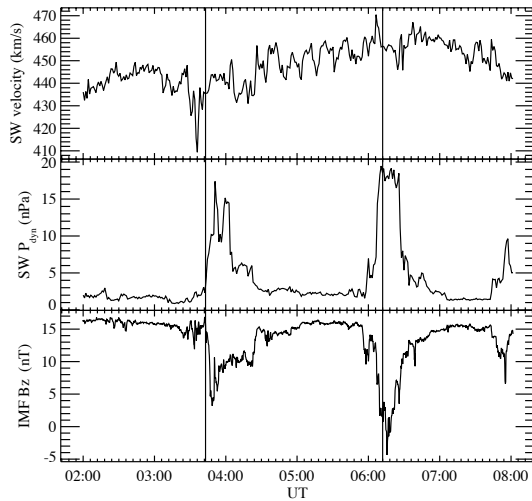


**Fig. 5.** Solar wind properties measured with the ACE spacecraft on 8 November 2000. The vertical solid lines indicate the ramp of the solar wind pressure pulse.

### 3.1. Observational analysis

On 8 November 2000 between 0300 and 0700 UT, two interplanetary shocks (Fig. 5) impinged on the Earth during a prolonged interval of northward IMF. The magnetosphere did not accumulate large amounts of open flux during that interval and no substorm expansion phase could develop at all. The open flux and reconnection voltages deduced from SI12 and SuperDARN observations are shown in Fig. 6. A transpolar arc was observed between 0400 and 0530 UT that disturbed our algorithms and impaired their reliability, although the presence of a transpolar arc is not of crucial importance in this study because these structures evolve only slowly whereas we are studying transient phenomena. Both shocks triggered a day-side subauroral proton flash (DSPF) when they reached the dayside magnetosphere [7]. The flux closure rate intensified shortly after the interaction of each shock and the magnetosphere, reaching up to 130 kV despite the low value of the open flux and the absence of substorm expansion activity. The flux closure, confirmed by the dipolarization detected with the GOES-8 satellite, is clearly induced by the interaction of both solar wind high pressure fronts and the magnetosphere. A simulation of the space environment representing the interaction between an IP shock and the magnetosphere during a northward IMF interval was conducted to clarify the mechanism responsible for the flux closure.

### 3.2. MHD simulation

The GUMICS-4 model was used to solve the equations of ideal MHD in the case of an IP shock impinging on the Earth magnetosphere during an interval of northward IMF. Magnetic reconnection is not explicitly included in GUMICS-4 [10], but a phenomenon of numerical diffusion mimics resistive processes, so that magnetic flux is nevertheless closed in the modelled magnetotail. The computed plasma flow and density maps can be used to analyze how the compression of the tail leads to flux closure. As the IP shock sweeps along the magnetotail, it compresses the magnetospheric plasma. The compression extends all the way down to the central plasmashet, where a

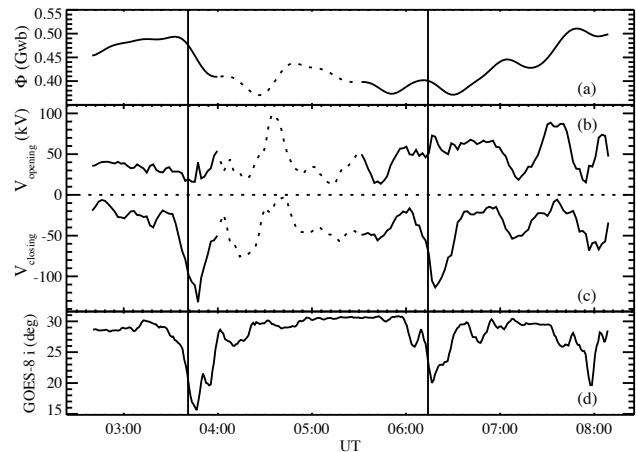


**Fig. 6.** Open magnetic flux of the magnetosphere (a), flux opening rate at the dayside (b) and flux closure rate in the magnetotail (c), 8 November 2000, deduced from combined ground-based and global remote sensing observations. Inclination angle of the magnetic field deduced from measurements of the GOES-8 satellite at geosynchronous altitude (d). Vertical lines indicate the arrival time of the main ramp of each interplanetary shock at the Earth magnetopause. A transpolar arc was observed between 0400 and 0530 UT that disturbed our algorithms and impaired their reliability (dotted lines in panels a, b and c).

thinning of the plasma sheet takes place, leading to the formation of an X line where magnetic flux is closed, and to the formation of a plasmode expelled downtail. A detailed analysis of the computed magnetic field reveals that the flux closure is due to the compression of the tail.

## 4. Flux closure during an auroral streamer event

An auroral streamer is a north-south aligned bright arc. It has an upward (downward) field-aligned current on its dusk (dawn) side, and it is surrounded by two vortices. It has been shown that the magnetic field lines threading auroral streamers map to the magnetotail into plasma bubbles forming bursty bulk flows (BBF). It has also been shown that the magnetic field of these plasma bubbles is dipolarized [3, 2]. A preliminary study has been undertaken on a streamer event observed on 7 December 2000 around 2200 UT that shows that intense flux closure takes place at the time of the observed streamer, especially along magnetic field lines threading the polar edge of the streamer.

## 5. Summary

A method that combines FUV imaging of the proton aurora and radar observations of the ionospheric convection has been developed to estimate the open flux threading the polar cap as well as the flux opening and closure voltages. Application of that method to substorm intervals reveals that 1. magnetic flux closure can intensify prior to substorm onset, producing pseudobreakups. 2. The flux closure voltage generally reaches a maximum value shortly after onset. 3. The closure voltage

progressively returns to the quiet times value of 30 kV during the recovery phase. 4. PBI's sometimes occurring during the recovery phase are associated with an intensification of the closure rate. 5. Proxies used to estimate the reconnection electric field responsible for field line merging between the solar wind and the magnetosphere are valid during southward IMF intervals, but should only be used with caution when the IMF is northward. An application to an interval presenting the interaction of IP shocks in the absence of substorm expansion, analyzed in the light of an MHD simulation, showed how the compression of the tail leads to the formation of a neutral line in the plasmashet. This process causes magnetic flux to be closed at a rate that can reach 130 kV, despite the absence of substorm expansion activity.

## References

1. Akasofu, S. I., The development of the auroral substorm, *Planet. Space Sci.*, *12*, 273, 1964.
2. Amm, O. and K. Kauristie, Ionospheric signatures of bursty bulk flows, *Surv. Geophys.*, *23*, 1, 2002.
3. Angelopoulos, V., W. Baumjohann, C. F. Kennel, F. V. Coroniti, M. G. Kivelson, R. Pellat, R. J. Walker, H. Lhr, and G. Paschmann, Bursty bulk flows in the inner central plasmashet, *J. Geophys. Res.*, *97*, 4027, 1992.
4. Blanchard, G. T., C. L. Ellington, L. R. Lyons, and F. J. Rich, Incoherent scatter radar identification of the dayside magnetic separatrix and measurement of magnetic reconnection, *J. Geophys. Res.*, *106*, 8185, 2001.
5. Boudouridis, A., E. Zesta, L. R. Lyons, P. C. Anderson, D. Lummerzheim, Enhanced solar wind geoeffectiveness after a sudden increase in dynamic pressure during southward IMF orientation, *J. Geophys. Res.*, *110*, doi: 10.1029/2004JA010704, 2005.
6. Dungey, J. W., Interplanetary field and the auroral zones, *Phys. Res. Lett.*, *6*, 47, 1961.
7. Hubert, B., J.-C. Gérard, S. A. Fuselier, S. B. Mende, Observation of dayside subauroral proton flashes with the IMAGE-FUV imagers, *Geophys. Res. Lett.*, *30*, 10.1029/2002GL016464, 2003.
8. Hubert, B., S. E. Milan, A. Grocott, C. Blockx, S. W. H. Cowley, and J.-C. Gérard, Dayside and nightside reconnection rates inferred from IMAGE FUV and Super Dual Auroral Radar Network data, *J. Geophys. Res.*, *111*, A03217, doi:10.1029/2005JA011140, 2006a.
9. Hubert B., M. Palmroth, T.V. Laitinen, P. Janhunen, S.E. Milan, A. Grocott, S.W.H. Cowley, T. Pulkkinen, and J.-C. Grard, Compression of the Earth's magnetotail by interplanetary shocks directly drives transient magnetic flux closure, *Geophys. Res. Lett.*, in press, 2006b.
10. Janhunen P., A positive conservative method for magnetohydrodynamics based on HLL and Roe methods, *J. Comp. Phys.*, *160*, 649-661, 2000.
11. McPherron, R. L., Growth phase of magnetospheric substorms, *J. Geophys. Res.*, *75*, 5592, 1970.
12. Mende, S.B., H. Heeterks, H.U. Frey, J.M. Stock, M. Lampton, S. Geller, R. Abiad, O. Siegmund, S. Habraken, E. Renotte, C. Jamar, P. Rochus, J.C. Gérard, R. Sigler, and H. Lauche, Far ultraviolet imaging from the IMAGE spacecraft : 3. Spectral imaging of Lyman alpha and OI 135.6 nm, *Space Sci. Rev.*, *91*, 287, 2000.
13. Meurant, M., J.-C. Gérard, B. Hubert, V. Coumans, C. Blockx, N. stgaard, S. B. Mende, Dynamics of global scale electron and proton precipitation induced by a solar wind pressure pulse, *Geophys. Res. Lett.*, *30*, 2032 10.1029/2003GL018017, 2003.
14. Milan, S. E., S. W. H. Cowley, M. Lester, D. M. Wright, J. A. Slavin, M. Fillingim, C. W. Carlson, and H. J. Singer, Response of the magnetotail to changes in the open flux content of the magnetosphere, *J. Geophys. Res.*, *109*, doi: 10.1029/2003JA010350, 2004.
15. Ruohoniemi, J. M., and K.B. Baker, Large scale imaging of high latitude convection with Super Dual Auroral Radar Network HF radar observations, *J. Geophys. Res.*, *103*, 20797, 1998.
16. Wygant, J. R., R. B. Torbert, and F. S. Mozer, Comparison of S3-3 polar cap potential drops with the interplanetary magnetic field and models of the magnetopause reconnection, *J. Geophys. Res.*, *88*, 5727, 1983.



# Energy flux of electron precipitation as monitored by an all-sky camera

K. Kauristie, N. Partamies, S. Mäkinen, R. Kuula, and A. Strømme

**Abstract:** We use the inversion method of [4] to estimate the energy flux of electron precipitation from the emission rates recorded by our All-Sky Camera in Kilpisjärvi (KIL). The beam of the incoherent scatter radar EISCAT is in the central field of view of the camera which enables comparisons of the ASC and radar based precipitation flux estimates. Our data set of 533 pairs of simultaneous flux estimates show a correlation of  $r = 0.72$  between the two data sets. In global scale the energy flux of auroral precipitation is known to have a linear correlation with the AE-index. We find a similar relationship between the energy flux as integrated over the KIL ASC field-of-view and the local auroral electrojet index defined from the IMAGE magnetometer chain (IE-index). The linear relationship holds especially when the epsilon parameter of solar wind input stays below 0.2 TW (as 10 min averages) and then one can see 10-20% of the global auroral precipitation energy flux with one ASC located in the midnight sector.

*Key words:* auroral precipitation, all-sky cameras, substorms.

## 1. Introduction

The inversion method by [4] (hereafter ASCinv) can be used to estimate the energy flux of electron precipitation from the basis of multiwavelength All-Sky Camera (ASC) observations. The method makes the inversion from ASC data to volume emission rates and to the corresponding energy flux as a single step. The energy range of the method is 0.1–8 keV. The coupling between the energy deposition of the electron precipitation and the auroral emission is modelled with the empirical formulas of [9, 10] and [11]. [8] evaluate the performance of ASCinv by comparing its output with flux estimates as deduced from DMSP and EISCAT data. The study demonstrates that in favourable conditions (stable arc near the ASC zenith) ASCinv estimates of electron energy flux agree within 10% relative error with the DMSP flux measurements. Using the modifications suggested by [12] in the emission physics yields better consistency between the two data sets. With EISCAT based flux estimates (deduced with the SPECTRUM method of [6]) the correlation is less obvious: smaller than 50% relative errors were found only in 36% of the analysed cases. The differences between the energy range and time resolution of ASCinv and SPECTRUM at least partly explain the inconsistencies in the flux estimates. The analysis of [8] also revealed that ASCinv reproduces more reliably the energy flux values than the number flux values.

In this paper we continue the comparison study of EISCAT and ASC based electron flux estimates. While [8] selected for their analysis individual images with stable auroras in the EISCAT beam location, we use here events of longer duration (and thus not always auroras in the EISCAT measurement point) to search some general trends in the flux estimate inconsistencies.

Probing the performance of ASCinv in different conditions is an intermediate step to reach our final goal which is the routine usage of ASC-data for monitoring mesoscale energy dissipation due to auroral precipitation similarly as local AE-indices are used to monitor Joule heating rates. The latter part of this paper we study mesoscale energy dissipation with ASC-recordings during 17 substorm periods and discuss the relation between local and global energy consumption rates.

## 2. ASC-EISCAT comparisons

The events for the EISCAT-ASC comparison study were selected carefully in order to avoid periods with clouds or too bright auroras which saturate the camera. Auroral brightnesses around 2-7 kR appeared to be suitable for our analysis. The point in the ASC image comparable with the EISCAT observation depends naturally on the altitude of the auroras. The altitude could be estimated for each time separately e.g. by investigating the EISCAT electron density profiles. In this study, however, we used the constant beam location of 69.4 N and 19.2 E, which corresponds to the altitude of 110 km. Using a constant location for all the events may cause additional scatter especially in the cases where the assumed altitude is slightly erroneous and there are sharp gradients in the precipitation around the EISCAT beam location. In these cases EISCAT measurements may come from a dark region while ASC recordings come from bright region (or vice versa).

The electron precipitation which typically causes 557.7 nm auroras has average energies around 2–20 keV and thus it increases electron densities at altitudes 95–130 km [10]. In Fig. 1 we test how accurately the KIL ASC and EISCAT observations follow this principle. The data have been recorded during five 1–2 hour long periods of moderate substorm activity. The plotted parameters are the ASCinv energy flux from KIL ASC data and the electron content along the EISCAT field line as integrated over 95–130 km altitudes. The electron content show increasing trend with increasing energy fluxes like it should, but the scatter of the data points is large especially at the high flux values. The linear fit between the points is TEC

Received 17 May 2006.

**K. Kauristie and S. Mäkinen.** Finnish Meteorological Institute, Space Research, P.O.Box 503, FIN-00101 Helsinki, Finland.

**N. Partamies.** Institute for Space Research, University of Calgary, Alberta, Canada.

**R. Kuula.** University of Oulu, Finland

**A. Strømme.** EISCAT Association, Sweden

$\times 10^{-16} = 166.40(\text{Wm})^{-1} \times \text{Eflux} + 1.01 \text{ m}^{-3}$  with  $r = 0.66$ .

Precipitation causing visual auroras increases especially the ionospheric Hall conductances. Thus in the auroral regions the ratio of Hall to Pedersen conductance (hereafter the  $\alpha$ -parameter) is enhanced and in substorm auroras it can vary in the range 1–5 [2]. Fig. 2 shows the dependency of the  $\alpha$ -values by EISCAT on the energy flux values by ASCinv. In the flux range from 3–10  $\text{mW/m}^2$  the majority of data points show roughly a linear relationship with the  $\alpha$ -values increasing from 0.5 to 2.3. This picture is obscured somewhat by a secondary branch of points which show high  $\alpha$ -values for minimal flux values. These  $\alpha$ -values, however, are less significant as they have been measured in dark conditions where both Hall and Pedersen conductances have been small (c.f. the group of points with  $\text{TECU} < 1$  in Fig. 1).

The relationship between the energy flux estimates by EISCAT computed with the SPECTRUM program [6] and the flux values by ASCinv are shown in Fig. 3. This data set suggests that EISCAT-based flux values tend to be slightly larger than the ASCinv based flux values. The linear fit best describing this relationship is  $\text{Eflux}_{\text{EISCAT}} = 1.35 \times \text{Eflux}_{\text{ASCinv}} - 0.70 \text{ mW/m}^2$  with  $r = 0.72$ . Obviously the data set should be expanded with more events having energy flux values above 15  $\text{mW/m}^2$  to get further confirmation for this result.

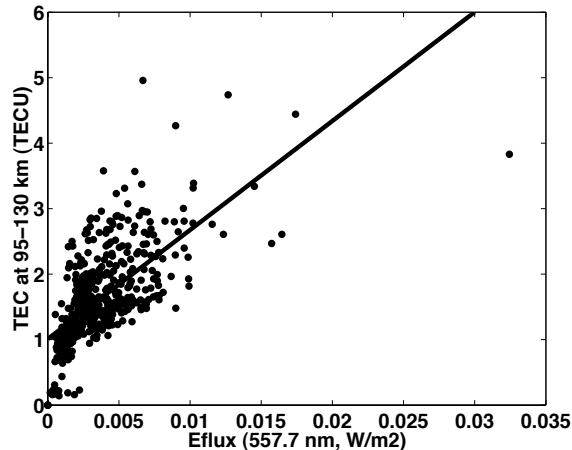


**Fig. 1.** Energy flux as deduced from ASC data versus the electron content along the EISCAT field line and integrated over 95–130 km altitudes ( $\text{TECU} = 10^{16} \text{ m}^{-3}$ ). The number of data points is 486 and  $r = 0.66$  for the linear fit.

### 3. Precipitation power over ASC field-of-view

In order to study the auroral precipitation power in meso-scales we integrate the energy flux values by ASCinv over the field-of view of the KIL ASC which is a circle of  $\sim 300 \text{ km}$  radius. The original size of an ASC image is  $512 \times 512$  pixels which corresponds to a spatial resolution in the range from about one km (near the zenith) to tens of km (near horizon). We use in the integration  $8 \times 8$  superpixels, i.e. a grid of  $64 \times 64$  points and again the situations of intensity saturation are avoided (i.e. we handle only luminosities between 2–7 kR).

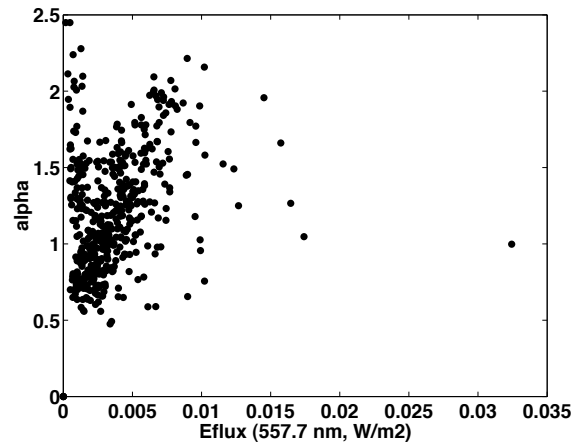


**Fig. 2.** Energy flux as deduced from ASC data versus the Hall to Pedersen conductance ratio ( $\alpha$ ). The number of data points is 486.

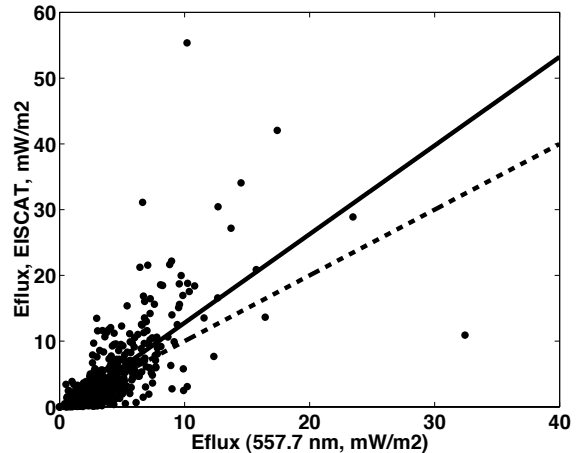


**Fig. 3.** Energy flux as deduced from ASC data versus the flux values computed from EISCAT data with the SPECTRUM-programme. Dashed line shows the one-to-one correspondence. Solid line shows the best linear fit with  $r = 0.72$ . The number of data points is 533.

Our data set consists of 17 1–2 hour periods of substorm activity with one minute time resolution which corresponds to 2290 ASC-fov-power values.

#### 3.1. MLT distribution

Fig. 4 shows the distributions of ASC-fov-power values in the different MLT-sectors. In the evening and midnight sectors the distributions have the peak at the values 1–2 GW and the occurrences of the higher power values show an exponential decay. In the morning sector the distribution has in addition to the main peak at 1–2 GW another maximum at 4–6 GW. The morning sector distribution is consistent with the previous findings by [7] of enhanced energy dissipation in the morning sector during substorms.

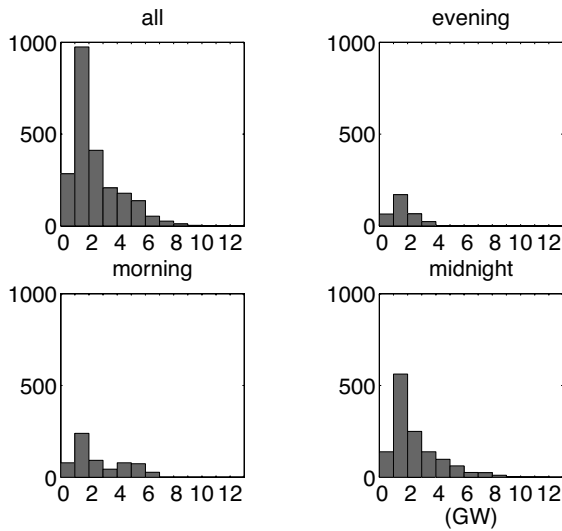


**Fig. 4.** Distributions of the ASC-fov-power values in the different MLT sectors: Evening sector 17.5–21.5 MLT, morning sector 3.5–8.5 MLT, and midnight sector 21.5–3.5 MLT.

### 3.2. Connection with the electrojet activity

ASC-fov-power can be anticipated to correlate with electrojet activity only during moderate activity when the oval is at the latitudes of KIL (MLAT  $\sim 66$ ) and the ASC field-of-view monitors a significant portion of the auroral oval. We characterize the global activity level with the solar wind energy input as estimated with the Akasofu  $\epsilon$ -parameter [3].  $\epsilon$  is computed from the data of the ACE satellite and shifted in time according to the propagation time from the satellite to the nominal magnetopause distance ( $10 R_E$ ). In comparisons with the nightside activity it is also reasonable to smoothen out the rapid time variations from the  $\epsilon$ -parameter. Instead of pure  $\epsilon$ -values we use the energy values achieved by the time integration of  $\epsilon$  over the 10-min period preceding each ASC-fov-power observation.

As a measure of electrojet activity we use the IE-index which is derived with the AE-index method from the recordings of the Fennoscandian IMAGE magnetometer chain. When the IMAGE magnetometer chain monitors the MLT-sectors 00–04 the IE-index can be considered as a representative estimate of the global AE-activity [5]. KIL ASC-fov-power values appeared to have the best correlation with IE-values when the solar wind input energy 10-min values stay below 100 TJ (corresponds roughly to 10-min average of  $\epsilon \sim 0.2$  TW). Under this condition we can write  $E_{\text{flux}} = 0.0071 \text{ (GW/nT)} \times \text{IE} + 0.6 \text{ GW}$  (with  $r = 0.68$ , c.f. Fig. 5).

### 3.3. Example event

Our example event is a substorm which took place on Oct 20–21 2004 during 23:00–02:00 UT. The solar energy input, IE-index, and KIL ASC-fov-power recorded during this substorm are shown in Fig. 6. The  $\epsilon$ -values varied around 0.3–0.4 TW during the hour preceding the substorm onset which was associated with IMF  $B_Z$  northward turning and consequent  $\epsilon$  drop to zero. After a break of  $\sim 45$  the energy input from the solar wind rose up again and  $\epsilon$  values increased back to level

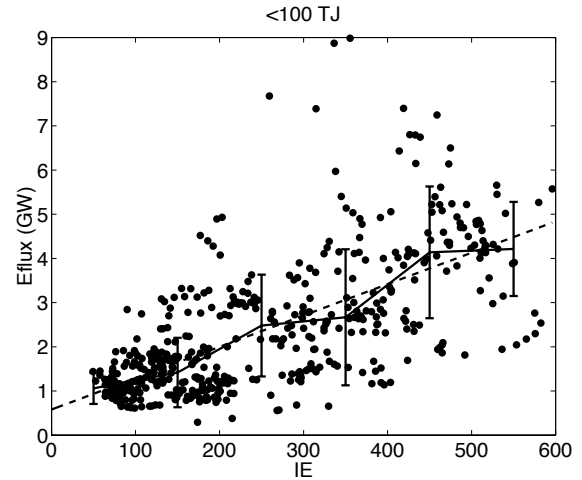


**Fig. 5.** Dependency between the IE-index and KIL ASC-fov-power when  $\int^{10\text{-min}} \epsilon dt < 100$  TJ. Dashed line shows the linear fit with  $r = 0.68$ . Solid line and the errorbars show the ASC-fov-power median and standard deviation values in bins 0–100 nT, 100–200 nT, 200–300 nT, 300–400 nT, 400–500 nT and 500–600 nT.

0.4–0.5 TW (corresponding to 10-min power values of 100–200 TJ) where it stayed until the recovery of the substorm. According to the AE quicklook plots in the Kyoto WDC website the IE-index represented the global electrojet activity quite well: The duration of the event is roughly the same in both indices and the peak in IE is only  $\leq 50$  nT smaller than that of AE.

The KIL ASC-fov-power was largest at  $\sim 23:50$  UT, i.e. about 15 minutes after the start of onset in the IE-index. The peak value was 5.1 GW while the few values recorded before the breakup were around 0.3 GW and after the expansion phase (i.e. after 00:15 UT) the values remained at the level of 1 GW for 1.5 hours. During the period 23:38–00:15 UT of bright auroras (c.f. Fig. 7 for example images) the energy dissipation in the ionosphere due to electron precipitation was 5.1 TJ and during the recovery phase period 00:15–01:45 UT of dimmer auroras the dissipation was 6.4 TJ.

## 4. Summary and conclusions

We have investigated the electron precipitation energy flux values as deduced from ASC data with the method of [4]. Our data set of five 1–2 hour periods of substorm activity with simultaneous ASC and EISCAT observations shows a relatively good correlation ( $r = 0.72$ ) between the ASC-based and EISCAT-based energy flux estimates.

We have also studied the variations of the electron precipitation power in the area of one ASC field-of-view (circle with  $\sim 300$  km radius, luminosity range 2–7 kR). In the data set of 17 1–2 hour periods of moderate substorm activity the most typical power values varied between 1–2 GW. Larger values, 5–6 GW, were recorded during the auroral breakups, as can be anticipated, but also during the morning sector auroras.

The ASC-fov-power values of our KIL camera (MLAT  $\sim 66$ ) correlate with the global electrojet activity if auroras are mon-

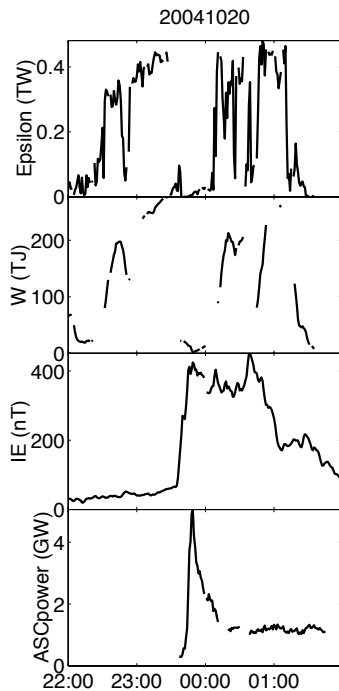


**Fig. 6.** Energy and power values recorded during the substorm on Oct 20–21 2004. From top to bottom: Solar wind  $\epsilon$ , energy values achieved by intergating  $\epsilon$  over the preceding 10 minutes, IE-index from the IMAGE magnetometer chain and KIL ASC-fov-power values.

itored in the MLT-sector 00–04 and if the solar wind input is moderate (10-min  $\epsilon$  average  $\leq 0.2$  TW). If we under these conditions use the estimate of [1] for the dependency of global precipitation power on AE-index ( $E_{flux}(GW) = 0.06 * AE$  (nT)) together with the corresponding formula for local activity achieved in this study we come to the conclusion that one ASC can see 10–20% of the global precipitation energy in the AE-range of 100–600 nT.

## References

1. Ahn, B.-H., Akasofu, S.-I. and Kamide Y., The Joule heat production rate and the particle energy injection rate as a function of the geomagnetic indices AE and AL, *J. Geophys. Res.*, **88**, 6275–6287, 1983.
2. Aikio, A. T. and Kaila, K. U., A substorm observed by EISCAT and other ground-based instruments - evidence for near-Earth initiation, *J. Atmos. Terr. Phys.*, **58**, 5–21, 1996.
3. Akasofu, S.-I., Energy coupling between the solar wind and the magnetosphere, *Space Sci. Rev.*, **28**, 121, 1981.
4. Janhunen, P., Reconstruction of electron precipitation characteristics from a set of multi-wavelength digital all-sky auroral images, *J. Geophys. Res.*, **106**, 18505–18516, 2001.
5. Kauristie, K., Pulkkinen, T. I., Pellinen, R. J. and Opgenoorth, H. J., What can we tell about global auroral-electrojet activity from a single meridional magnetometer chain?, *Ann. Geophys.* **14**, 1177–1185, 1988.
6. Kirkwood, S., SPECTRUM - a computer algorithm to derive the flux-energy spectrum of precipitating particles from EISCAT

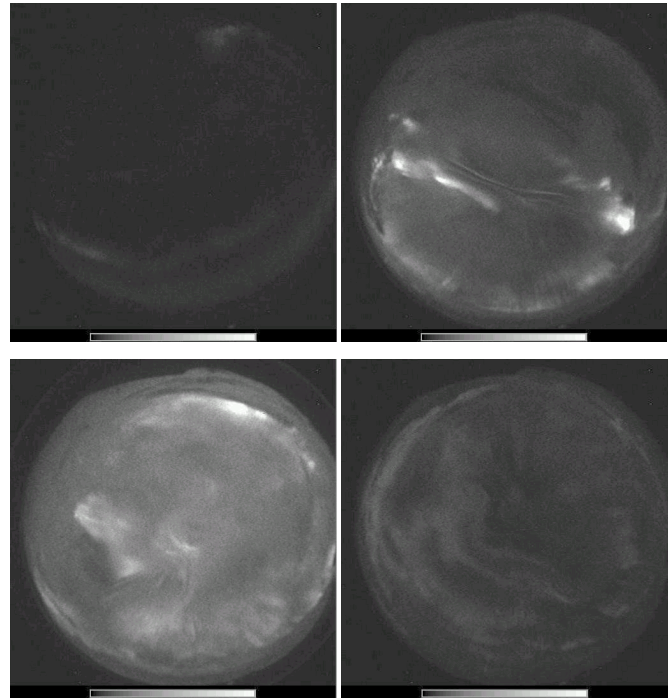


**Fig. 7.** KIL ASC images (557.7 nm) acquired during the substorm on Oct 20–21 2004. From top left to bottom right: 23:38 UT (growth), 23:45 UT (breakup), 23:48 UT (expansion) and 00:55 UT (recovery).

electron density profiles, *IRF Tech. Rep.*, 034, Swedish Institute of Space Physics, 1988.

7. Opgenoorth, H. J., Persson, M. A. L., Pulkkinen, T. I. and Pellinen, R. J., Recovery phase of magnetospheric substorms and its association with morning sector aurora, *J. Geophys. Res.*, **99**, 4115–4129, 1994.
8. Partamies, N., Janhunen, P., Kauristie, K., Mäkinen, S. and Sergienko, T., Testing an inversion method for estimating electron energy fluxes from all-sky camera images, *Ann. Geophys.*, **22**, 1961–1971, 2004.
9. Rees, M. H., Auroral ionization and excitation by incident energetic electrons, *Planet. Space Sci.*, **11**, 1209–1218, 1963.
10. Rees, M. H., *Physics and Chemistry of the Upper Atmosphere*, Cambridge University Press, New York, 1989.
11. Rees, M. H. and Luckey, D., Auroral electron energy derived from ratio of spectroscopic emissions, 1. Model computations, *J. Geophys. Res.*, **79**, 5181–5186, 1974.
12. Sergienko, T. and Ivanov, V. E., A new approach to calculate the excitation of atmospheric gases by auroral electron impact, *Ann. Geophys.*, **11**, 717–727, 1993.

# Solar wind and interplanetary magnetic field features before magnetic storm onset

O. Khabarova, V. Pilipenko, M.J. Engebretson, and E. Rudenichik

**Abstract:** The presented results, concerning the features of the solar wind plasma structure as observed by spacecraft upstream of Earth, could be used for development of middle-term forecasts of magnetic storms. We have analyzed 1-hour data for 1995-2005 and a whole year of 1-min data during solar minimum (1995) and during solar maximum (2000) with 48 and 60 storms, respectively. The long-term statistical correlations between the solar wind/IMF parameters are found to vary during the solar cycle, and this fact should be taken into account for the prognostic aims. During solar maximum the yearly correlation of  $V$  with ground geomagnetic indices drops, and the correlation of  $N$  with these indices becomes significant during solar minimum only. Elevated solar wind density enhances statistically the IMF magnitude, but not the IMF  $B_z$  component. A remarkably high correlation exists between the low-frequency solar wind plasma turbulence with time scales 4-32 min and the IMF magnitude. It was shown that solar wind dynamic pressure variations are mainly determined not by speed, but density. The density changes play a significant geoeffective role. In many cases magnetic storms with  $-30 \text{ nT} < Dst < -100 \text{ nT}$  are the result of sharp increases in solar wind density with consequent negative  $B_z$  at the background of low and steady solar wind velocity. Besides, about 2 days before  $\sim 80\%$  of magnetic storm commencements a weak increase of density is observed. This increase of the solar wind density is irregular and accompanied by fluctuations with time scales  $\sim 2 - 120$  min, on the average, 2 days prior to storm commencements. The possible mechanisms of these pre-storm solar wind/IMF variations have not been firmly established yet. Thus, variations of the solar wind plasma are a largely underestimated factor in magnetic storm triggering and could be effectively used for space weather forecasting.

*Key words:* magnetic storms, solar wind, geomagnetic storm forecasting.

## 1. Introduction

Magnetic storm forecasting is one of the most important problems of solar-terrestrial physics and the keystone of space weather science. As in seismology, forecasting methods can be roughly classified into short-term (about 1 hour in advance using spacecraft measurements at the L1 point), middle-term (from several hours to several days), and long-term (solar cycles). The short-term forecasts are rather exact, up to  $\sim 90\%$ , but their alert time ( $\Delta T < 1\text{h}$ ) is too small for usage of this information in practical aims. The quality of medium-term forecasting remains rather modest: during solar maximum the successful forecasting rate is  $\sim 75\%$  (see, for example, the Lund Space Weather Center and Naval Research Laboratory webpages). However, the actual forecast quality is lower, because most of the medium-term forecasting methods are oriented toward the prediction of probability of severe storms only, and, drops to  $\sim 30\%$  during solar minimum [1]. There are several unsolved problems, leading to our inability to produce the desired level of middle-term prognosis of geomagnetic storms.

Direct monitoring of solar eruptive processes cannot solve the problem of middle-term magnetic storm forecasting, because it is very uncertain whether an ejecta would reach the Earth and how a solar plasma stream would evolve upon the propagation.

One of the main reasons is that most of the techniques used for magnetic storm forecasting are oriented toward the prediction of severe magnetic storms, with  $Dst < -100 \text{ nT}$ . It is commonly assumed that the majority of severe magnetic storms ( $\sim 80\%$ ) are caused by the arrival of magnetic clouds (MCs) from coronal mass ejections (CMEs) and, to a much lesser extent, by corotating interaction regions (CIRs) [2, 3]. As a result, the space weather community is overwhelmingly oriented to the study of CMEs with a strong southward interplanetary magnetic field (IMF), so the following paradigm has been formed: "The main controlling factors of geomagnetic activity are the solar wind speed  $V$  and the north-south IMF component  $B_z$ ".

However, the number of strong storms is less than 10% of the total storm number [2]. Meanwhile, less intense storms should not be disregarded because of their seemingly low geoeffectiveness. There are many examples indicating that moderate storms ( $Dst \sim -50\text{nT}$ ) often produce much higher increases of relativistic electron fluxes near the geosynchronous orbit than intense storms ( $Dst < -100 \text{ nT}$ ) do [4, 5].

Most of the medium-term forecasting methods are oriented towards the prediction of the probability of CME arrival. Meanwhile, according to recent investigations, the existing estimates of the geoeffectiveness of real CMEs are close to estimates of the geoeffectiveness of solar flares (30-40%) [6]. At the same time, for a random distribution of solar processes and magnetic storms the formally calculated coefficient of correlation can be 30-40%. This value is comparable with the forecast success rate  $\sim 30\%$  during the solar minimum [1].

Commonly, the geoeffectiveness of the solar wind is overwhelmingly characterized by the combinations of the velocity  $V$  and the IMF  $B_z$  component: the interplanetary dawn-dusk

Received 8 June 2006.

**O. Khabarova and V. Pilipenko.** Space Research Institute, Moscow

**M.J. Engebretson.** Augsburg College, MN

**E. Rudenichik.** Institute of Terrestrial Magnetism, Troitsk, Russia

electric field  $E_{EW} = V * B_z$  or total electric field  $E_T = V * B$ . Implicitly, the paradigm of determining the role of CMEs and  $E_{EW}$  has been expanded to all the processes of solar wind-magnetosphere interaction. Sometimes, e.g. [2], a magnetic storm is even defined as "an interval of time when a sufficiently intense and long-lasting interplanetary convection electric field leads ... to an intensified ring current strong enough to exceed some key threshold of the quantifying storm time  $Dst$  index". This definition assumes that all other factors of the solar wind and IMF play no role in the storm production, and the only physical mechanism influencing the magnetosphere is reconnection. Such solar wind/IMF parameters like plasma density  $N$ , level of turbulence, etc., commonly have not been taken into account and examined for their geoeffectiveness. In particular, density was considered as a minor factor, just increasing the storm intensity or enhancing negative  $B_z$  at the leading edge of a magnetic cloud [7].

Meanwhile, statistical analysis shows that upon a decrease of magnetic storm intensity, the solar wind velocity has ever diminishing influence on  $Dst$  disturbance. Only 23% of mild storms with  $-50\text{nT} < Dst < -30\text{nT}$  are related to high-velocity streams [2]. At the same time, there are indications of the geoeffectiveness of other solar wind/IMF parameters, especially the solar wind plasma density which might enhance the effect of southward IMF and production of the ring current [8, 9]. Introduction into a forecasting algorithm of solar wind dynamic pressure improved the quality of short-term storm prediction, especially for the most intense storms [10].

It would be an intriguing possibility to find an alternative approach to medium-term forecasting, in which solar wind/IMF features might be used as a prognostic factor. It is worthwhile to pay more attention to the solar wind plasma density, a still underestimated factor of storm stimulation as compared with the recognized storm-makers - velocity and IMF  $B_z$  [11]. This paper is mostly focused on the study of features of the solar wind and IMF dynamics before magnetic storm onset, with special emphasis on solar wind density and its fluctuations.

## 2. Data, techniques, and features of magnetic storms under study

To characterize the solar wind changes and magnetospheric disturbances we have used speed  $V$ , proton concentration (density)  $N$ ; and IMF from Wind and ACE spacecraft, as well as SYM-H and  $Dst$  indices. We have analyzed statistically the interval 1995-2005 on the basis of hourly OMNI data and have tested in detail an entire year of 1-min Wind spacecraft data during solar minimum (1995) and solar maximum (2000).

To estimate the power of the solar wind density fluctuations we have used the database of hourly ULF indices [5] - the spectral power of IMF and  $N$  fluctuations integrated over the 2-7 mHz frequency band. Additionally, we have applied the wavelet technique to estimate the integrated power  $W_N$  of density fluctuations with various time scales (commonly, from 4 to 32-64-128 min) with 1-min cadence.

In order to have the possibility to analyze statistically pre-storm intervals we must know how to identify magnetic storm onsets. For automatic detection of storm onset we have applied the following algorithm. We have calculated a 30-minute moving gradient of the SYM-H index,  $\nabla_{30min} |\text{SYM-H}|$ , where the

gradient has been estimated as the tangent of the inclination of the autoregression straight line for 30 points. A storm onset was reported when the absolute value of this gradient had exceeded a certain threshold value (0.3) before geomagnetic indices ( $Kp$ ,  $Dst$ ) indicated disturbed conditions at least 2 hours after this moment. This algorithm reliably detected an SSC moment as well as an onset of magnetic storm growth phase without SSC. In contrast to the technique proposed here, the usage of hourly  $Dst$  and 3-hour  $Kp$  indices enables one to detect the storm main phase onset, but not the onset of the growth phase. With application of this technique, 48 and 60 storms with  $Dst < -30$  nT were detected during 1995 and 2000, respectively.

A histogram of magnetic storm occurrence with respect to its intensity is shown in Fig.1 for two phases of solar activity cycle: minimum, 1995-1996, and maximum, 2000-2001. According to the IAGA SSC catalogue, all the storm events have been classified as storms with SSC (dark columns) and without it (gray columns). The distribution of intensity of magnetic storms with identified origins (whenever it was possible) is also shown in Fig.1: CIR-related storms (marked by diagonal lines), and MC-related storms (white columns). During both the solar minimum and maximum years, the geoeffectiveness of CIRs and MCs in the production of medium and severe magnetic storms was nearly equal, which is in a good correspondence with [6], but in contrast to the commonly accepted point of view about the prevailing geoeffectiveness of MCs. The number of storms caused by CIRs is about 1.7 times larger than the number of storms caused by MCs both during solar minimum and maximum. Overall storm statistics show that such

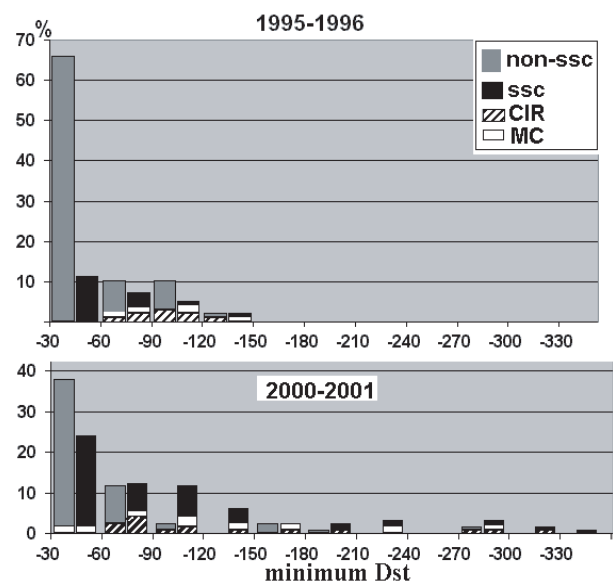


**Fig. 1.** Histograms of magnetic storm occurrence (in %) in respect to their intensity (as measured by the  $Dst$  index) for solar minimum (1995-96) and solar maximum (2000-01) for various categories of magnetic storms: with SSC (black), without SSC (gray), CIR-produced (diagonal lines), and MC-produced (white).

events as CIRs and MCs are rather rare, so most storms are produced either by recurrent streams without evident CIR, or

by streams of mixed origin [13]. Therefore, it would be useful for prognostic aims to classify the geoeffectiveness of the solar streams not by their affiliation with CIRs or MCs, but by simple physical characteristics: velocity, density, magnetic field, and the intensity of the magnetospheric disturbances produced.

### 3. Relationships between basic solar wind and geomagnetic activity parameters

For a long time it was supposed that the solar wind dynamic pressure  $D = NV^2$  is the dominant geoeffective factor influencing storm development. Though since that time the paradigm in storm studies has changed, variations of the dynamic pressure are still one of the key space weather parameters, influencing, for example, the size and shape of the magnetosphere. Then, a question arises: which of the components - density or velocity - are most significant for pressure variations? Are the mechanisms of the magnetospheric response to the variations of  $N$  and  $V$  different or the same?

It might seem that velocity is geoeffective [14] because it provides a second power contribution ( $\propto V^2$ ) to the dynamic pressure variations. However, analysis of solar wind data has shown that the possible geoeffectiveness of solar wind dynamic pressure is determined mainly by changes of density, but not velocity. The correlation coefficient between plasma density and dynamic pressure is  $R \simeq 0.8$ , which is about 10 times more than that between the speed and dynamic pressure (for 1-min cadence data for 1995 and 2000). Therefore, we examine in greater detail the statistical properties of the solar wind density, because variations of  $N$  may be significant for storm dynamics and space weather purposes.

For space weather forecasting purposes it is important to know whether the relationships between different interplanetary parameters and their geoeffectiveness are stable from year to year and independent of solar activity level. We have found that statistical relationships between the solar wind and IMF parameters have turned out to differ, sometimes significantly, at various solar cycle phases (Fig. 2). The following results of correlative analysis should be highlighted:

During solar maximum the correlation between  $V$  and  $Dst$  dropped to  $R \simeq 0.3$  (Fig. 2a). The correlation between  $N$  and  $Dst$  is significant ( $R \simeq 0.4 - 0.5$ ) during solar minimum only. Correlation between  $Bz$  and  $Dst$  is stable and statistically significant, but low,  $R \simeq 0.2 - 0.4$  (Fig. 2b).

The correlation between  $N$  and  $Bz$  is practically absent (Fig. 2b). Thus, the popular hypothesis about an increase of southward IMF by an enhanced  $N$  [7] has not been supported by our statistical results. Meanwhile the correlation of  $N$  with IMF magnitude  $|B|$  is much higher. Thus, the solar wind density indeed can drag and compress the IMF lines, but  $N$  equally enhances IMF of any direction, not only southward.

A remarkably high correlation between the low-frequency solar wind plasma turbulence, as characterized by the wavelet power  $W_N$  of density fluctuations with time scales 4-32 min and IMF magnitude  $|B|$  is observed:  $R \simeq 0.40 - 0.55$  (Fig. 2c). Thus, the high magnitudes of IMF are commonly accompanied by an elevated level of solar wind plasma turbulence. A surprisingly high correlation is observed between the wavelet power  $W_N$  and  $Kp$  (Fig. 2c). We also checked the

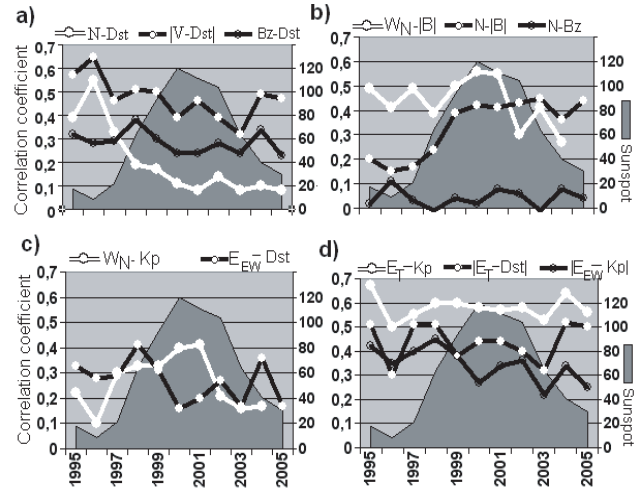


**Fig. 2.** The yearly variations of pair correlation coefficients between various solar wind/IMF parameters and geomagnetic indices for the solar cycle period 1995-2005.

geoeffectiveness of various solar wind / IMF parameters. The correlation between the most famous storm-makers, the interplanetary electric fields  $E_{EW}$  and  $E_T$ , and the  $Dst$  and  $Kp$  indices is shown in Fig. 2d. The highest and most stable correlation coefficient is observed between  $E_T$  and  $Kp$ , in good correspondence with [12]. Our analysis also shows, rather surprisingly, that  $E_{EW} - Kp$  and  $E_{EW} - Dst$  correlations are not so high (Fig. 2d), comparable with the  $Bz - Dst$  correlation (Fig. 2a).

These facts may indicate that intrinsic properties of the solar wind and IMF, as well as their magnetospheric response, vary during a solar cycle. Therefore, storm prediction algorithms must adapt to these variations, otherwise they would be not equally effective during various phases of solar cycle.

### 4. Magnetic storm driving by the solar wind density and IMF

There is a common view that magnetic storms are produced by extended intervals (more than  $\sim 3$  hours) of southward  $Bz < 0$ , whereas  $V$  determines the storm intensity, because the main driver is supposed to be the interplanetary electric field  $E_{EW}$ . However, this rule works for severe storms only, and in reality just a moderate southward IMF, even with high  $V$ , is not sufficient to produce a storm. For example, between 04/30 and 05/02, 1999 (Fig. 3a) there were many intervals with  $Bz \simeq -2$  nT with duration of a few hours under high  $V \simeq 600 - 650$  km/s and low  $N$ , but they have not produced any significant disturbance ( $Dst > -30$  nT). At the same time, mild and moderate magnetic storms can be produced by moderately negative  $Bz$  without significant growth of  $V$ , but after substantial and steep  $N$  growth (see examples in Fig. 3b-d).

In total, 84 storms ( $\sim 80\%$ ) with  $Dst < -30$  nT, during both solar minimum (1995) and maximum (2000), were preceded by a rapid solar wind density increase, whereas the velocity growth occurred after storm development. The delay between a rapid rise in density and a velocity peak is commonly about 1 day, therefore a storm is in its recovery phase

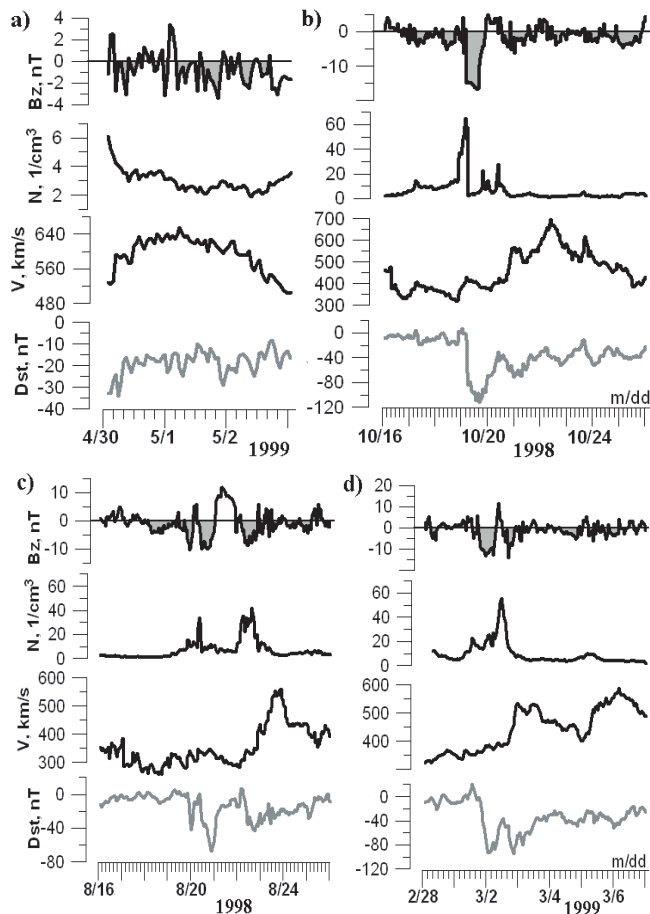


**Fig. 3.** Variations of the IMF  $B_z$  component, solar wind density  $N$  and velocity  $V$  (taken from OMNI), and the  $Dst$  index during space weather events on (a) 04/30-05/02, 1999; (b) 10/16-10/26, 1998; (c) 08/16-08/26, 1998; and (d) 02/28-03/07, 1999.

during the arrival of the high-speed-stream. So, the usually cited conditions of the storm production "long-term occurrence of southward IMF and high velocity" are not both equally necessary. For example, Fig. 3c shows the event when two subsequent storms have been stimulated with some delays by rapid increases of  $N$  at the background of low  $V$ . However, in another event (Fig. 3d) the first storm is triggered by the  $N$  increase, whereas the second storm is related to the increase of  $V$ .

Probably, in events like these the loading-unloading mechanism supplies energy into the magnetosphere, maybe even during periods preceding storm onset. This energy is eventually released as a magnetic storm only after strong "shaking" of the magnetosphere by the high pressure solar wind pulses.

## 5. Behavior of solar wind parameters prior storm onset

Case-study analysis shows that the solar wind behavior before a magnetic storm persistently demonstrates important features. Besides the rapid increase of the plasma density, provoking magnetic storm beginning, a more gradual increase of  $N$  occurs for a few hours or even days before the main density

growth. The increase of  $N$  is not steady, but is accompanied by irregular fluctuations. These features can be used as a storm precursor.

Typical features of the solar wind before magnetic storm onset are illustrated by the 03/21-03/29, 1995 event (Fig. 4a). The increase of  $N$  is accompanied by an elevated level of density fluctuations with time scale 4-32 min, as revealed by the wavelet power, and strong changes in the 6-h running gradient of density. This case describes a typical situation, when a magnetic storm has precursors in the solar wind: a weak and irregular increase of density before the main jump of  $N$ . The

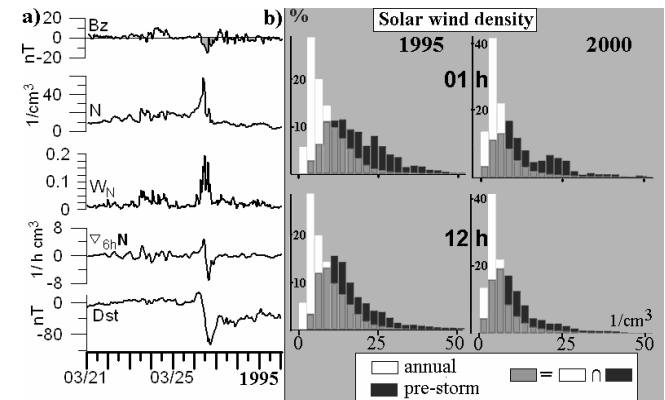


**Fig. 4.** (a) Variations of IMF  $B_z$  component, solar wind density  $N$ , wavelet power of density fluctuations  $W_N$ , six-hour running gradient of  $N$ , and the  $Dst$  index during the magnetic storm of 03/21-03/29, 1995. (b) Histograms of statistical distributions of  $N$  for the whole year and for the periods 1 hour and 12 hours before storm onsets for 1995 (left-hand panels) and 2000 (right-hand panels).

observations of case studies such as the above are confirmed by the following statistical analysis. We have compared two distributions of various interplanetary parameters from 1-min Wind data: overall yearly distribution (white bars) and distribution during time intervals before magnetic storm onsets (dark bars). The comparison of these distributions has shown that:

The pre-storm density values are increased in comparison with the annual distribution (Fig. 4b) both for the year of maximum (1995, left-hand panel) and minimum (2000, right-hand panel) of solar activity. This increase is observed at time intervals 1 hour (upper panels) and 12 hours (bottom panels) before storm onset. The effect becomes weaker for the time interval 24 hours and entirely disappears at the 2 day interval (not shown). The solar wind velocity, on the other hand, demonstrates a tendency to decrease slightly before storm onsets, both during solar minimum and maximum. Density fluctuations in the ULF range are enhanced before onset, as revealed by the shift of the distribution of the  $T_N$  index to higher values, both during solar minimum and maximum (Fig. 5). This enhancement becomes less evident for the 2 day interval. The tendency of increase of background solar wind density and its variability before magnetic storms can be seen from histograms of the distribution of running 6-hour gradients of  $N$  for the entire year and periods before storms (Fig. 6). Before storms the magnitude of the density gradient increases both during

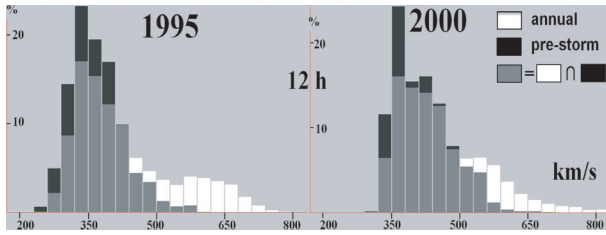


**Fig. 5.** Comparison of histograms of annual distributions and pre-storm distributions of the solar wind velocity during solar minimum (1995) and maximum (2000) for 12 hours time intervals before storm commencement.

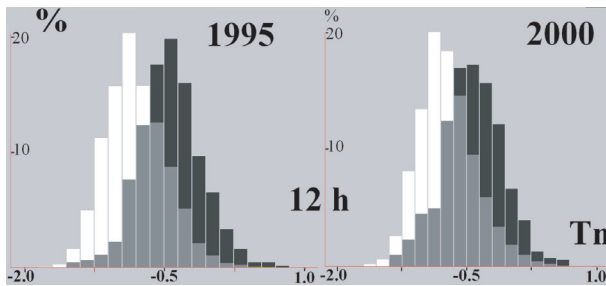


**Fig. 6.** Comparison of histograms of annual distributions and pre-storm distributions for fluctuations of the solar wind density, as characterized by the ULF power index  $T_N$ , during solar min (1995) and max (2000) for 12 hours time intervals before storm commencement.

solar minimum and maximum. The power of solar wind long-period density fluctuations  $W_N$  increases  $\sim 12$  hours before storm onset, especially during solar maximum (1995) (Fig. 7). The same distribution for the 2-day time interval (not shown) demonstrates a substantial decrease of the effect. Thus, the solar wind density becomes more turbulent and irregular about 1 day before the main growth of  $N$ .

## 6. Discussion

The main problems of medium-term magnetic storm forecasting are a consequence of the shift of scientific interest to prognosis of severe magnetic storms only and toward estimation of the probability of the registration of CMEs near Earth. The most proper path toward their solution may be to search for additional prognostic factors in the solar wind. Recent work shows that variations of the solar wind plasma and IMF are a largely underestimated factor in magnetic storm triggering and could be effectively used for space weather forecasting analysis.

These studies show that the solar wind density plays a more significant geoeffective role than was previously assumed. A sharp density increase and consequent negative  $B_z$  can produce weak, moderate and even strong magnetic storms without any significant changes of the solar wind velocity. The triggering role of density is not revealed clearly with standard statistical analysis because a delay time between the rapid jump of  $N$  and  $Dst$  minimum varies substantially from storm to storm. Probably, the density increase may stimulate the release of en-

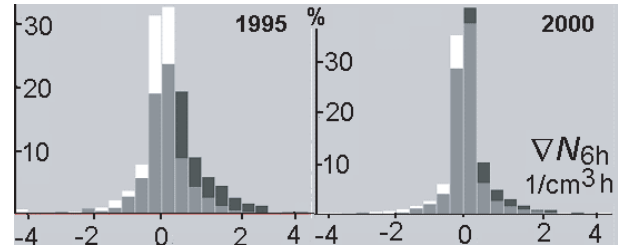


**Fig. 7.** Comparison of histograms of annual distributions and pre-storm distributions (12 hours before storm commencements) of hourly values of the 6-hour gradient of  $N$  for the solar minimum (1995) and maximum (2000).

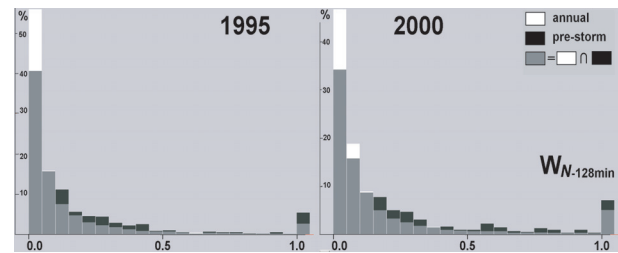


**Fig. 8.** Comparison of the statistical distributions of the wavelet power  $W_N$  of plasma density fluctuations with time scales 4-128 min for the whole year and for the period 12 hours before storm onsets for 1995 (left-hand panels) and 2000 (right-hand panels).

ergy accumulated in the magnetosphere, whereas  $V$  pumps instantly solar wind/IMF energy into the magnetosphere under favorable IMF orientation.

Case studies and analysis of statistical distributions have revealed some new features of the solar wind/IMF behavior several hours to days before storms. A weak irregular increase of density is observed before a storm commencement, starting, on average,  $\sim 2$  days before the main geoeffective density growth. The power of low-frequency solar wind density fluctuations (with time scales from  $\sim 2$  min to  $\sim 100$  min), as estimated by the wavelet power and ULF wave index, starts to grow, on average,  $\sim 1$  day prior to storm commencement.

Possible mechanisms of pre-storm irregular growth of the solar wind density have not been established. One possible mechanism may be related to the stream instability of solar wind plasma, resulting in the excitation of MHD waves.

Also, studies of the solar wind have revealed plasma density enhancements near the heliospheric current sheet (HCS) and high-speed corotating streams adjacent to the HCS plasma sheet [15]. Thus, a high plasma density and low velocity may be an indicator that a spacecraft and Earth are approaching the HCS region owing to the presence of naturally occurring high densities near the HCS and also to stream-stream compressive effects. The southward IMF orientation, which eventually causes moderate storms, may be related to the corotating stream interaction with the HCS and its plasma sheet.

Finally, fluctuations in active regions on the Sun, anticipating development of CMEs or solar flares, may modulate the solar wind. An investigation of the relationship between long-period pulsations of CM radio emission and solar proton flares showed an occurrence of a relationship between them. This

phenomenon has been suggested for use in solar ejection forecasting [17]. Recently, indications of solar wind modulation by various modes of solar oscillations have also been found [16].

Though possible mechanisms of these phenomena have not been reliably identified yet, observed features of the solar wind plasma structure before magnetic storms may be classified as medium-term precursors, and thus could be used for forecasting purposes.

## 7. Conclusion

None of the methods proposed so far for magnetic storm and substorm forecasting provides sufficient accuracy and proper timing. Therefore, the space weather community should try to implement the cybernetic principle - "to build a reliable system from non-reliable components," and combine various forecasting tools. This study has shown that solar wind density plays a more significant geoeffective role than is usually considered. It was found that sharp density increases and consequent negative  $Bz$  excursions can produce weak, moderate and even strong magnetic storms without any significant changes in solar wind velocity.

The statistical correlations for the period 1995-2005 indicate that intrinsic properties of the solar wind and IMF, as well as their magnetospheric response, vary during a solar cycle. During solar maximum the geoeffectiveness of  $V$  drops, and geoeffectiveness of  $N$  is significant during solar minimum only. Throughout the solar cycle the geoeffectiveness of interplanetary electric field,  $E_{EW}$  and  $E_{EW}$ , has turned out to be not very high, just slightly higher than that of  $Bz$ . The correlation between  $N$  and  $Bz$  is low, but the correlation of  $N$  with  $|B|$  is much higher. A remarkably high correlation between the low-frequency solar wind plasma turbulence with time scales 4-32 min and IMF magnitude  $|B|$  occurs.

Case studies and analysis of statistical distributions have revealed some new features of the solar wind/IMF behavior several hours to days before storms. A weak turbulent increase of density is observed before a magnetic storm commencement, starting, on average, 2 days before the geoeffective density growth. The power of low-frequency solar wind density fluctuations (with time scales from  $\sim 2$  min to  $\sim 100$  min), as estimated with the wavelet technique and ULF wave power index, starts to grow, on the average,  $\sim 1$  day prior to storm commencement. An elevated level of solar wind/IMF turbulence in the Pc5 band before storm onsets may induce enhanced ULF magnetic activity on the ground.

These features of the solar wind plasma structure before magnetic storms may be classified as medium-term precursors of magnetic storms, and thus could be used for forecasting purposes. We suggest that variations of the solar wind plasma are a largely underestimated factor in magnetic storm triggering and could be effectively used for space weather forecasting.

**Acknowledgements.** This study is supported by grant 03-51-5359 from INTAS (OVK, VAP) and by National Science Foundation grant ATM-0305483 to Augsburg College (MJE). The short-term and middle-term space weather forecasting web-pages are supported by DMI, IKI, and by SEC, IPG, IZMIRAN, correspondingly. Database of hourly ULF indices, more examples of density-triggered storms, and the space weather event

list can be found on an anonymous FTP site [space.augsburg.edu/maccs/](http://space.augsburg.edu/maccs/).

## References

1. Eiselevich, V.G., and V.G. Fainshtein, An investigation of the relationship between the magnetic storm Dst-index and different types of solar wind streams, *Ann. Geophysicae*, *11*, 678-684, 1993.
2. Gonzales, W.D., et al., What is a geomagnetic storm? *J. Geophys. Res.*, *99*, 5771-5792, 1994.
3. Crooker, N.U., Solar and heliospheric geoeffective disturbances. *J. Atmosph. Solar-Terr. Phys.*, *62*, 1071-1085, 2000.
4. O'Brien, T.P., et al., Which magnetic storms produce relativistic electrons at geosynchronous orbit? *J. Geophys. Res.*, *106*, 15533-15544, 2001.
5. Kozyreva, O.V., et al., In search of a new ULF wave index: Comparison of Pc5 power with dynamics of geostationary relativistic electrons, *Planet. Space Sci.*, *54*, 2006 (in press).
6. Yermolaev, Yu.I., et al., Statistical studies of geomagnetic storm dependencies on solar and interplanetary events: a review, *Planet. Space Sci.*, *53*, 189-196, 2005.
7. Gosling, J.T., et al., Geomagnetic activity associated with Earth passage of interplanetary shock disturbances and coronal mass ejections, *J. Geophys. Res.* *96*, 7831, 1991.
8. Smith, J.P. et al., Solar wind density as a driver for the ring current in mild storms, *Geophys. Res. Lett.* *26*, 1797, 1999.
9. Daglis, I.A., et al., Intense space storms: Critical issues and open disputes, *J. Geophys. Res.*, *108*, 1208, doi:10.1029/2002JA009722, 2003.
10. Temerin, M. and X. Li, A new model for the prediction of Dst on the basis of the solar wind, *J. Geophys. Res.*, *107*, 1472, doi:10.1029/2001JA007532, 2002.
11. Khabarova, O.V., and E.A. Rudenchik, New method of magnetic storm middle-term forecast on the base of solar wind data analysis, *Proc. of 10-th International Conference "Contemporary Problems of Solar-Terrestrial Influences"*, 49-52, Bulgaria, Sofia, 2003.
12. Papitashvili, V.O., N.E. Papitashvili, and J.H. King, Solar cycle effects in planetary geomagnetic activity: Analysis of 36-year long OMNI dataset, *Geophys. Res. Lett.*, *27*, 2797-2800, 2000.
13. Ivanov, K.G., Solar sources of the interplanetary plasma streams in the Earth's orbit, *Geomagn. Aeronomy*, *36*, 158-163, 1996.
14. Petrukovich, A.A., and S.I. Klimov, The use of solar wind measurements for analysis and forecast of geomagnetic activity, *Cosmic Research*, *38*, 463-468, 2000.
15. Gonzalez, W.D., et al., Interplanetary origin of geomagnetic storms, *Space Sci. Reviews*, *88*, 529-562, 1999.
16. Thomson, D.J., et al., Coherence of charged particle oscillations in the heliosphere ( $f \sim \mu\text{Hz}$ ): Implications for a solar modulation source, *J. Geophys. Res.*, *106*, 29341-29354, 2001.
17. Bystrov, M.V., M.M. Kobrin, and S.D. Snegirev, Quasi-periodic oscillations of the terrestrial geomagnetic field with periods 20-200 min and their relationships to similar pulsations of Sun's radioemission before proton flares, *Geomagn. Aeronomy*, *19*, 306, 1979.

# Cluster observations of plasma sheet activity during the September 14-28, 2003 corotating high speed stream event

A. Korth, E. Echer, F. L. Guarnieri, M. Fränz, R. Friedel, W. D. Gonzalez, C. G. Mouikis, and H. Rème

## Abstract:

In recent years there has been renewed discussion on the nature of recurrent substorm activity in the magnetosphere and their causative drivers. There is an active debate on periodic substorm versus sawtooth events, and triggered versus non-triggered substorms. We perform here a cross-wavelet analysis between the solar wind drivers and the plasmashet at  $\sim 20 R_E$  and geosynchronous responses during the September 2003 high speed stream event, using ACE, Cluster and LANL geosynchronous data. We show that the magnetospheric response with a periodicity of 2-4 hours is well correlated with the Alfvén wave structure embedded in the fast streams. This indicates that the recurrent activity observed here is directly driven in contrast to the periodic sawtooth events which occur under conditions of steady driving.

*Key words:* substorms, plasma sheet, geosynchronous orbit.

## 1. Introduction

The question of what external or internal events cause or trigger recurring periodic substorms has been one of the fundamental issues of substorm research, and one on which there is as yet no consensus.

Individual substorm occurrence has been linked to northward turnings of the interplanetary magnetic field (IMF) at the end of intervals of southward IMF [10, 3]. While random or isolated substorms form the largest class of events, periodic substorms are often observed with inter-substorm times of around 3 hours [4].

Periodic activity, such as during sawtooth events, has been directly correlated with corresponding solar wind dynamic pressure enhancements [9]. Others suggest that sawtooth events can be viewed as a magnetospheric mode similar to Steady Magnetospheric Convection intervals (SMCs) except that for sawtooth events, the flow of energy from the solar wind into the magnetosphere becomes too large to dissipate without the periodic occurrence of substorms. They further suggest that the quasi-periodicity arises because the magnetosphere may only become susceptible to external or internal triggering after it has been driven beyond a stability threshold. This can account for the existence of more potential external triggers (in the interplanetary magnetic field or solar wind) than teeth, namely that the magnetosphere may be selectively responsive to such a structure [7].

During the descending and minimum phases of solar cycles,

CMEs become less frequent and another type of solar structure occur more often: coronal holes. Coronal holes are open magnetic field regions, from where high speed solar wind streams emanate [15, 16, 17, 6]. High speed streams have velocities much higher than the typical velocities observed in the solar wind, forming an interface region between the slow and fast streams. At large heliocentric distances (typically larger than 1 AU), these stream interface/interaction regions are bounded by a pair of shocks [18].

Since coronal holes are long lived structures, they can persist for more than one solar rotation, and the high speed streams originated from the same region reappear at intervals of approximately 27 days [18]. This reappearance leads to the term "recurrent stream". The spiral-like structure formed by these streams, distorted due to the solar rotation, and its interaction regions with slower streams, is known as Corotating Interaction Region (CIR).

For this study, an important aspect of these fast streams is that they are embedded with Alfvén waves [2]. These Alfvén waves are believed to be remnants of heating processes in the solar corona [8]. In the interplanetary data, these waves appear as large amplitude oscillations in magnetic field components with periods from a few minutes to a few hours, well correlated with the oscillations of the velocity components in the same direction [2, 21].

When these structures reach the Earth, they can lead to the development of a geomagnetic storm, due to the compressed plasma region in front of the high speed stream, the increase in the velocity, and the presence of Alfvén waves. Relativistic electron energization and flux enhancements occur in association with high-speed solar wind streams and the Alfvén waves embedded in them [11]. These Alfvén waves, with intermittent negative IMF  $B_z$  and large IMF  $y$ -component  $|B_y|$ , may lead to significantly enhanced magnetospheric convection and thus substorm activity. We intend to show in this paper that the periodic substorm activity observed during the September 2003 high speed stream event is directly correlated with the

Received 2 June 2005.

**A. Korth and M. Fränz.** MPI für Sonnensystemforschung, Katlenburg-Lindau, Germany.

**E. Echer, F. L. Guarnieri, and W. D. Gonzalez.** INPE, Sao Jose dos Campos, Brazil

**R. Friedel.** LANL, Los Alamos, NM, USA

**C. G. Mouikis.** UNH, Durham, NH, USA

**H. Rème.** CESR, Toulouse, France

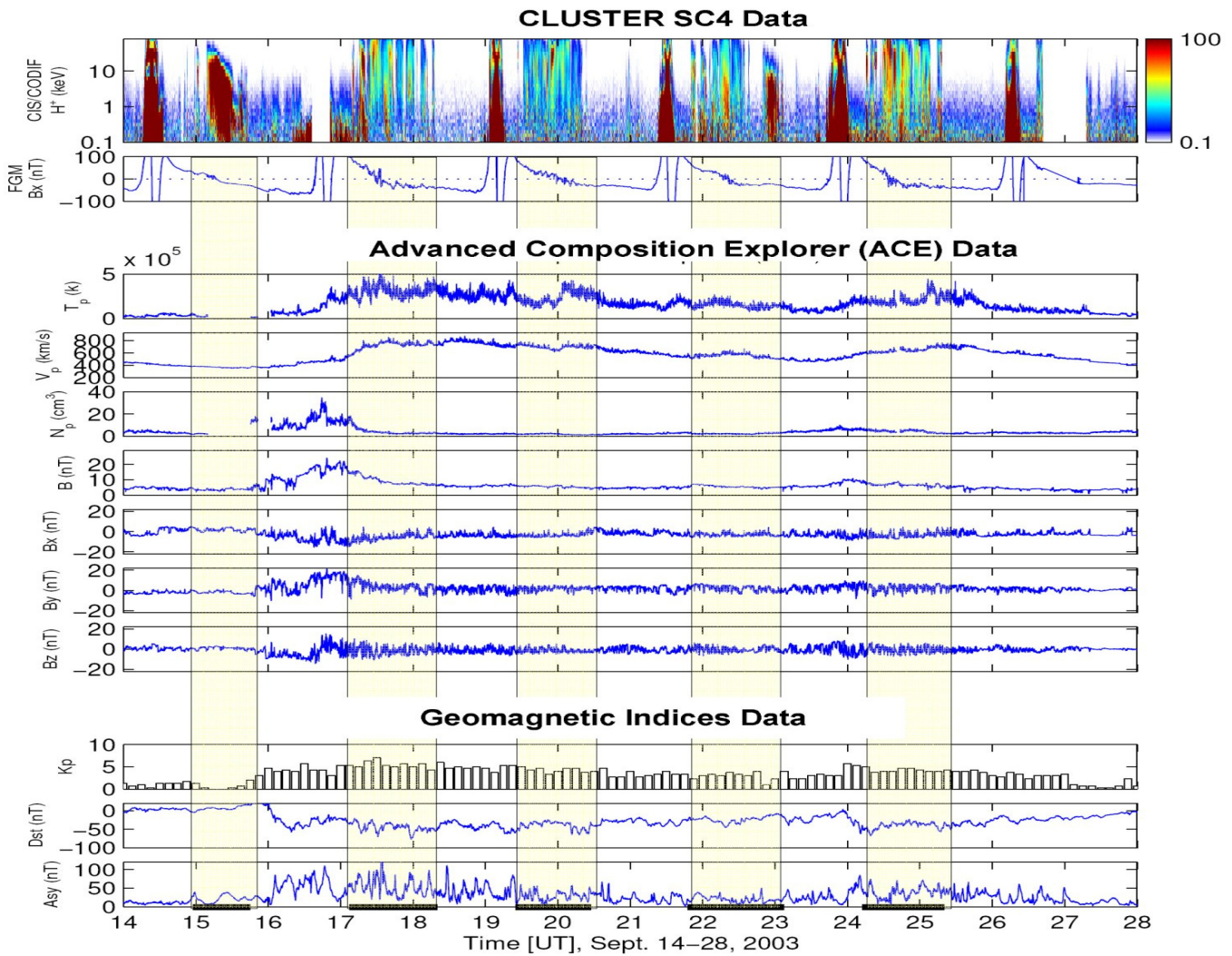


**Fig. 1.** Overview of the plasma sheet, the solar wind, and geomagnetic conditions for the September 14–28, 2003 period.

Alfvén wave periodicity observed in the solar wind.

## 2. Observations

This study uses particle and magnetic field measurements from Cluster SC4 [5], velocity, density and magnetic field measurements from the Advanced Composition Explorer (ACE) [19], and Los Alamos geosynchronous orbit data [14] during the September 14–28, 2003 corotating high speed stream event. The four Cluster satellites are in highly elliptical orbits, with apogee at  $19.8 R_E$  and perigee of  $4.0 R_E$ . In the September period the Cluster tetrahedron shows small distances of 2000 km between the satellites, so that only data from one spacecraft are used in the magnetospheric plasma sheet. The four Cluster spacecraft crossed the tail from north to south in the midnight sector between 23:00 and 24:00 LT.

We use particle data from the Cluster Ion Spectrometry (CIS) plasma instrument [13], the Cluster energetic particle spectrometer RAPID (Research with Adaptive Particle Imaging Detectors) [22], and the Flux Gate Magnetometer FGM [1]. The

CIS data shown in this paper are from the COMposition and DIstribution Function (CODIF) analyzer, which is one of the sensors of the CIS instrument. CODIF measures the 3-dimensional distribution functions of the major ion species in the energy per charge range 0.03–40 keV/e. The RAPID spectrometer performs species identification with a time-of-flight measurement in the energy range from 50 to 1500 keV for protons and 30 to 300 keV for electrons.

## 3. Results

In Figure 1 we present an overview of the magnetotail plasma sheet, solar wind, and geomagnetic conditions for the September 14–28 period. In the first two panels the CIS/CODIF  $H^+$  energy spectrogram and the  $B_x$ -component of the magnetic field in GSE coordinates are shown for Cluster SC4. The yellow high-lighted areas indicate time periods when Cluster SC4 crosses the plasma sheet in the magnetotail. Thick black horizontal bars are given in addition on the time axis for these crossings. The positive  $B_x$ -component of the magnetic field is

directed towards the Sun and the negative towards the tail of the magnetosphere. Therefore it is an excellent indicator to show the magnetic equatorial crossings near perigee (large field) and apogee (small field). The proton spectrogram in the first panel shows during the first tail traversal (first high-lighted time interval) a cold plasma sheet. The plasma sheet is hotter after the arrival of the fast solar wind in the second and third highlighted period.

In the next panels solar wind plasma parameters and the interplanetary magnetic field are shown from the ACE spacecraft. In particular the density ( $N_p$ ), the velocity ( $V_p$ ), and the total magnetic field ( $B_t$ ) with its components in GSE coordinates are given. The bottom panels show the  $K_p$ , Sym, and Asy geomagnetic activity indices. The Sym index is a 1-min version of the  $D_{st}$  index, and the Asy index indicates the level of asymmetries in the ring current.

The solar wind behavior was dominated by the presence of a large coronal hole which was just left of central meridian in the beginning of the period. The signature of the interaction region and the high speed stream is observed from September 15, 2003 to September 28, 2003. The first signs of it were noted as a slight increase in the solar wind velocity (from  $355$  to  $380$  km·s<sup>-1</sup>) and a large density enhancement in the solar wind recorded by ACE on Sept 15, between 18:20 UT and midnight due to the compression of the solar wind in front of the high speed stream. Later a slow but steady increase of the solar wind speed was noted peaking at  $800$  km·s<sup>-1</sup> around noon on September 18. The interplanetary magnetic field  $B_z$  was mostly southward-directed during the beginning of the event with its minimum at  $-15$  nT on September 16 in the afternoon. Later from September 17, large amplitude Alfvén waves were observed in all three magnetic field components with amplitudes of plus/minus  $10$  nT especially in the  $B_z$ -component, which is responsive not to reconnection on the front side of the Earth and the energy input into the magnetosphere. The Alfvén waves continued during the passage of the interaction region until September 27, 2003.

The average speed and density of the slow solar wind, measured in the first yellow highlighted area were approximately  $365$  km·s<sup>-1</sup> and  $2.3$  protons·cm<sup>-3</sup>. The He<sup>++</sup>/H<sup>+</sup> ratio (not shown in the figure) was  $\sim 0.1$  and the total magnetic field was approximately  $4$  nT. In the interaction region the observed densities were  $30$  protons·cm<sup>-3</sup> and the total magnetic field  $20$  nT. In the second yellow highlighted period - the beginning of the first high speed stream - the average solar wind was approximately  $720$  km·s<sup>-1</sup> and the density was  $4$  protons·cm<sup>-3</sup>. A sharp decrease in the density to  $2$  protons·cm<sup>-3</sup> were observed. The average total magnetic field showed the same behavior as the density, with a sharp decrease to approximately  $5$  nT. In the next two yellow highlighted periods (3 and 4) a decrease in the solar wind speed and density is seen and the magnetic field remained on the same level of  $\sim 5$  nT. In the last highlighted period the solar wind speed, the density, and the total magnetic field increased again resulting from the interaction of a second high speed stream with the first one. During this period an increase in the He<sup>++</sup> abundance was observed.

The geomagnetic field was initially at quiet levels ( $K_p < 3$ ) but switched to a major storm regime on September 16 and even severe storm regime ( $K_p = 7$ ) on September 17. The geomagnetic conditions persisted until September 27. During the

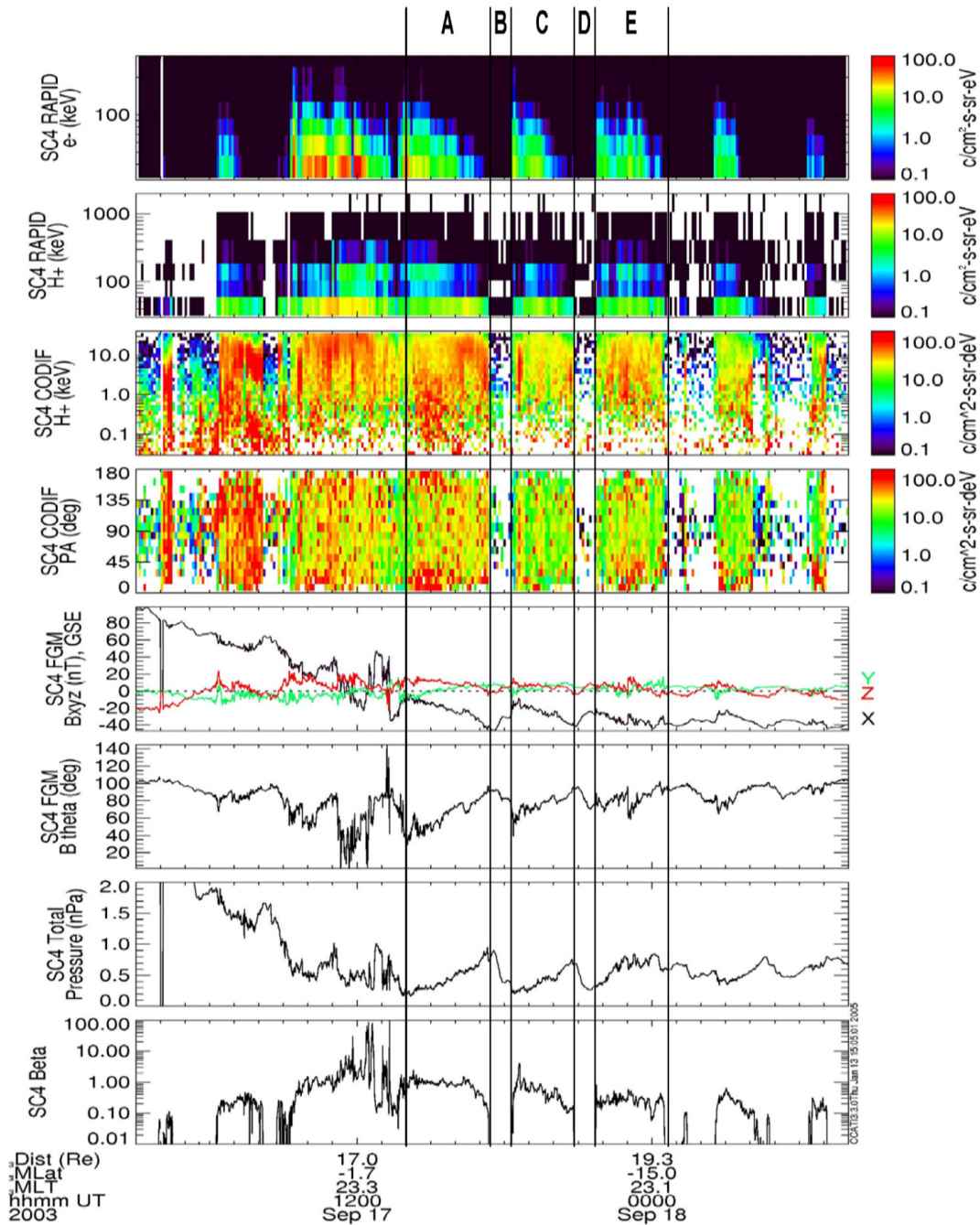
first yellow highlighted period the average  $K_p$  index was approximately  $1$ -, the average  $D_{st}$  index was slightly positive ( $6.7$  nT) and the average Asy index was  $\sim 21$  nT. The  $D_{st}$  and the Asy index reached their peak values of  $-50$  nT and  $+100$  nT, respectively, during the passage of the interaction region, indicating the occurrence of a moderate magnetic storm. During the passage of the high speed stream the geomagnetic indices indicated a constant level of activity, decreasing during the 4th highlighted period and increasing again in the 5th highlighted period, when a second interaction region arrived.

Figure 2 shows the Cluster plasma sheet crossing during disturbed conditions on September 17 and 18, 2003, the second highlighted period at the beginning of the first high speed stream. From top to bottom we plotted an electron spectrogram in the energy range from  $30$ - $300$  keV, and a proton spectrogram in the energy range from  $50$  to  $1500$  keV from the Cluster SC4 RAPID instrument, and a CIS proton spectrogram with its pitch angle distribution in the energy range from  $0.03$  to  $40$  keV/e. Further we present magnetic field data from Cluster in GSE coordinates, the theta angle (angle between the z-axis and the xy-plane, +z-axis north), the total (magnetic plus kinetic) pressure in nPa, and the plasma Beta parameter. The  $B_x$ -component of the magnetic field indicates where Cluster SC4 crosses the magnetic equator. The theta angle points out how much the magnetic field is stretched.  $\beta = 1$  implies that the spacecraft is in the plasma sheet, and  $\beta < 1$  means that it is in the plasma sheet boundary layer or even in the lobes.

We observe a hot and disturbed plasma sheet. The spacecraft during its traversal moves in and out of the plasma sheet. In the time intervals A, C, and E the spacecraft is inside the plasma sheet and in the intervals B and D outside of the plasma sheet in the lobes. Inside the plasma sheet we observe electrons up to  $300$  keV and protons up to  $1000$  keV. The spacecraft crosses the magnetic equator three times between  $11:00$  and  $14:00$  UT ( $B_x = 0$ ). Due to an intermittently large negative IMF  $B_z$  there is a continuous energy input into the magnetosphere and into the magnetotail. This can be observed in the total pressure (kinetic and magnetic) which increases and decreases three times on September 17, 2003 in the time interval from  $14:00$  to  $24:00$  UT. During the pressure increase, the magnetic field stretches, and during the decrease the field dipolarizes which can also be observed in the theta angle of B in panel 6. These pressure changes are comparable to a loading and unloading process also called the growth and recovery phase of a substorm. During the growth phase, the total pressure increases from  $0.2$  to  $1$  nPa, the tail magnetic field stretches and the spacecraft moves out of the plasma sheet into the tail lobe. In the lobe the total pressure is similar to the magnetic pressure while the kinetic pressure is almost zero. At the end of the growth phase the tail field dipolarizes or thickens and the spacecraft is back in the plasma sheet.

During quiet solar wind conditions on September 14 and 15, 2003 (not shown) we find a cold plasma sheet with an energy of less than  $40$  keV and an isotropic H<sup>+</sup> pitch angle distribution. We find a few counts in the electron and proton energy channels at higher energies above  $30$  keV. The total pressure is very low at  $0.2$  nPa.

In order to investigate the coupling power from the solar wind into the magnetotail, we have calculated the cross-wavelet power between ACE  $B_z$  and Cluster  $B_x$  data. We used the Mor-

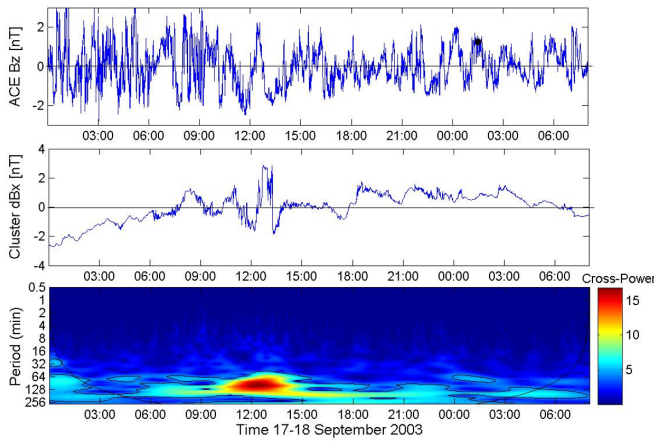


**Fig. 2.** Cluster plasma sheet crossing during a high speed stream and large IMF  $B_z$  amplitudes of more than  $\pm 10$  nT on September 17 and 18, 2003. From top to bottom: energy spectrograms of electrons and protons from RAPID, energy and pitch angle spectrograms of protons from CIS, x-y,z-components and theta from FGM, total (kinetic and magnetic) pressure, and beta.

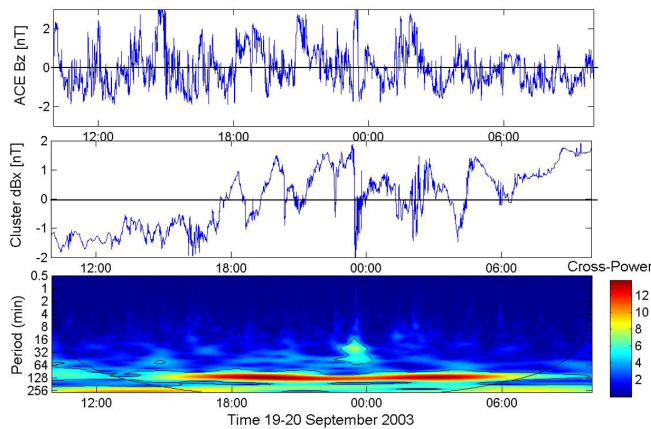
let wavelet analysis [20, 12], because it is the most adequate to detect variations in the periodicities of geophysical signals in a continuous way along time scales. The Morlet Wavelet is a plane wave modulated by a gaussian. The cross-wavelet power indicates the scales of higher covariance between two time series. This analysis gives the correlation between two time series as a function of the period of the signal and its time evolution with a 95% confidence level contour.

Figure 3a and 3b show each from top to bottom, the in-

terplanetary magnetic field  $B_z$ -component measured by ACE, shifted by 35 minutes taking into account a solar wind velocity of  $800 \text{ km s}^{-1}$ , the sunward  $B_x$ -component in the magnetotail observed by Cluster, and the cross-wavelet power spectrum between them. Figure 3a shows data from the second plasma sheet crossing and Figure 3b from the third (see Figure 1). We have used 16 second averages for the interplanetary and the magnetospheric field components. The Cluster  $B_x$ -component was filtered with a polynomial fit (3rd order)



(a)

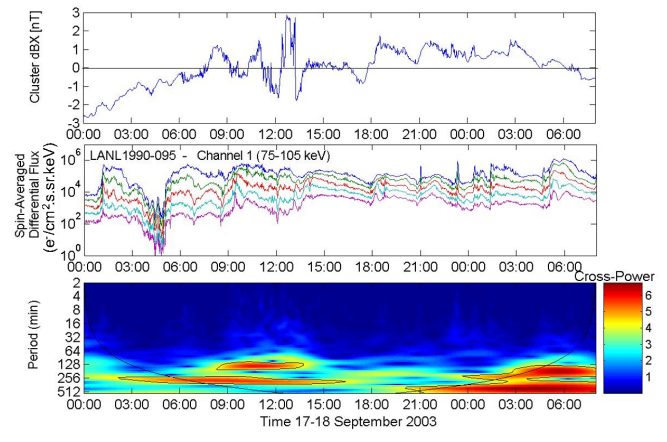


(b)

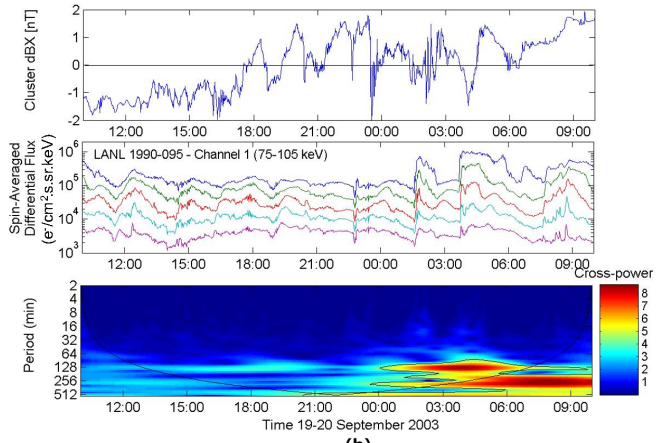
**Fig. 3.** Figure 3a: Cross-wavelet analysis of ACE interplanetary  $B_z$  component and of Cluster  $dB_x$  for September 17 (03:00 UT) to 18 (08:00 UT), 2003. Figure 3b: Same as Figure 3a, but for September 19 (10:00 UT) to September 20 (10:00 UT), 2003.

to remove the longest variations. The cross-wavelet spectrum in the third panel covers the period range from 1 minute to  $\sim 4$  hours. We observe enhanced power around 2-3 hours for the second plasma sheet crossing on September 17/18, 2003, and enhanced power of about 2 hours during the third crossing on September 19/20, 2003 period. For the crossing on September 17/18 the power is more concentrated around 12:00 UT, because of the strong fluctuations in  $B_z$  and  $B_x$ . During the September 19/20 crossing, a strong cross-power is seen around 2 hours during most of the interval. In this event we can see the presence of quasi-periodical fluctuations in the Cluster  $B_x$  data, of the same time. In ACE we see strong fluctuations around this time, but with presence of high frequency oscillations.

As seen from Figure 2 the fluctuations in the  $B_x$ -component are proportional to the pressure change which is again a measure of the amount of substorms. In comparing the  $B_x$ -component with substorms closer to Earth at geosynchronous orbit the cross-power was calculated between the Cluster  $B_x$ -component and the electron flux at geosynchronous orbit. Figure 4a and b show the cross-wavelet power of the Cluster  $dB_x$  and the LANL 1990-095 spacecraft electron flux data. Chan-



(a)



(b)

**Fig. 4.** Figure 4a: Cross-wavelet power between Cluster  $dB_x$  and the first (75 - 105 keV) of five electron channels from spacecraft LANL 1990-095, for September 17 (00:00 UT) to September 18 (08:00 UT), 2003. Figure 4b: Same as Figure 4a, but for September 19 (10:00 UT) to September 20 (10:00 UT), 2003.

nels 0 to 4 ( $\sim 50$  to 315 keV) are shown. The cross-wavelet power was calculated between Cluster  $dB_x$  and channel 1 (75-105 keV). For September 17/18 a significant cross-power is observed around 2 hours during a short time ( $\sim 09:00-13:00$  UT) and an extended cross-power around 3-4 hours for most of the interval. Figure 4b shows for September 19/20 a cross-power at 2 hours which is significantly enhanced after  $\sim 00:00$  UT of September 20.

#### 4. Conclusions

We have shown here that the September 2003 fast solar wind streams and their embedded large amplitude Alfvén waves have a direct influence on the recurrent substorm activity observed. In linking the recurrent 2-4 hour substorm activity directly to the periodicities in the solar wind Alfvén waves we not only confirm the results of Borovsky et al. [4], but show that the causative driver in the solar wind are prolonged periods of intermittently large negative IMF  $B_z$  that can lead to heating of the plasma sheet and to substorm activity.

We have demonstrated the direct link between the interplan-

etary magnetic field (IMF)  $B_z$  and the sunward magnetic  $B_x$ -component measured with Cluster in the plasma sheet, and the subsequent injection signatures seen at geosynchronous orbit.

In the wavelet spectrum enhanced power is observed between 2-4 hours which means that a loading/unloading process takes place every 2-4 hours.  $B_x$  is the largest magnetic field component in the plasma sheet ( $B_y$  and  $B_z$  are about zero) and therefore it is proportional to the pressure. The change in pressure is related to substorms. In comparing this period with substorms at geosynchronous orbit, the wavelet spectra show enhanced power also in the 2-4 hour period. The triggering of this kind of substorms seems to be pressure driven and direct, in contrast to the sawtooth events described by Henderson et al. [7] where the magnetosphere is under SMC-like conditions where triggering may be controlled more by internal stability thresholds than distinct external triggers.

Further work remains to be done to establish the timing (phase) relationship between the correlations (Solar wind to plasma sheet, plasma sheet to geosynchronous), which we did not attempt here.

## Acknowledgements

The authors would like to thank the ACE SWEPAM and MAG teams for making solar wind plasma and magnetic field data available. We thank the Kyoto World Data Center for Geomagnetism for the Dst and AE indices. E. Echer and F. L. Guarnieri thank FAPESP for their post-doctoral fellowships (04/11115-4 and 04/14784-4) and their financial supports (05/03501-4).

## References

- Balogh, A., Carr, C. M., Acuna, M. H., Dunlop, M. W., Beek, T. J., Brown, P., Fornacon, K. H., Georgescu, E., Glassmeier, K.-H., Harris, J., Musmann, G., Oddy, T., and Schwingenschuh, K., The Cluster Magnetic Field Investigation: overview of in-flight performance and initial results, *Ann. Geophys.*, 19, 1207–1217, 2001.
- Belcher, J. W. and Davis Jr., L., Large Amplitude Alfvén waves in the interplanetary medium, 2, *J. Geophys. Res.*, 76, 3534, 1971.
- Blanchard, G. T., Lyons, L. R., and Spann, J., Predictions of substorms following northward turnings of the interplanetary magnetic field, *J. Geophys. Res.*, 105, 375–84, 2000.
- Borovsky, J. E., Nemzek, R. J., and Belian, R. D., The occurrence rate of magnetospheric substorm onsets: Random and period substorms, *J. Geophys. Res.*, 98, 3897, 1993.
- Escoubet, C. P., Fehringer, M., and Goldstein, M., The Cluster mission, *Ann. Geophys.*, 19, 1197–1200, 2001.
- Harvey, K., Suess, S., Aschwanden, M., Guhathakurta, M., Harvey, J., Hathaway, D., LaBonte, B., Sheeley, N., and Tsurutani, B. T., A NASA workshop on coronal holes near solar maximum and over the solar cycle, Washington: NASA, 2000.
- Henderson M. G., Reeves, G. D., Skoug, R., Thomsen, M. T., Denton, M. H., Mende, S. B., Immel, T. J., Brandt, P. C., and Singer, H. J., Magnetospheric and auroral activity during the 18 April 2002 sawtooth event, *J. Geophys. Res.*, 111, A01S90, doi:10.1029/2005JA011111, 2005.
- Hollweg, J. V., Some physical processes in the solar wind, *Rev. Geophys. Space Phys.*, 16, 689, 1978.
- Lee, D. Y., Lyons, L. R., and Yumoto, K., Sawtooth oscillations directly driven by solar wind dynamic pressure enhancements, *J. Geophys. Res.*, 109, A04202, 2004.
- Lyons, L. R., Blanchard, G. T., Samson, J. C., Lepping, R. P., Yamamoto, T., and Moretto, T., Coordinated observations demonstrating external substorm triggering, *J. Geophys. Res.*, 102, 27039–51, 1997.
- Lyons, L. R., Lee, D.-Y., Thorne, R. M., Horne, R. B., and Smith, A. J., Solar wind-magnetosphere coupling leading to relativistic electron energization during high-speed streams, *J. Geophys. Res.*, 110, A11202, doi: 10.1029/2005JA011254, 2005.
- Percival, D. B. and Walden, A. T., Wavelet Methods for Time Series Analysis, Cambridge University Press, 2000.
- Rème, H., et al., First multispacecraft ion measurements in and near the Earth's magnetosphere with the identical Cluster Ion Spectrometry (CIS) experiment, *Ann. Geophys.*, 19, 1303–1354, 2001.
- Reeves, G. D., Belian, R. D., Cayton, T. C., Henderson, M. G., Christensen, R. A., McLachlan, P. S., and Ingraham, J. C., Using Los Alamos geosynchronous energetic particle data in support of other missions. In Satellite-Ground Based Coordination Source Book, edited by M.N. Wild M. Lockwood, and H.J. Opgenoorth, pages 263–272. ESA Publications, ESTEC, Noordwijk, The Netherlands, June 1997.
- Sheeley, N. R., Harvey Jr., J. W., and Feldman, W. C., Coronal holes, solar wind streams, and recurrent geomagnetic disturbances, 1973–1976, *Solar Physics*, 49, 271, 1976.
- Sheeley, N. R., Harvey Jr., J. W., and Feldman, W. C., Coronal holes, solar wind streams, and geomagnetic activities during new sunspot cycle, *Solar physics*, 59, 159, 1978.
- Sheeley, N. R. and Harvey Jr., J. W., Coronal holes, solar wind streams, and geomagnetic disturbances during 1978 and 1979, *Solar Physics*, 70, 237, 1981.
- Smith, E. J. and Wolf, J. H., Observations of interaction regions and corotating shocks between one and five AU: Pioneers 10 and 11, *Geophys. Res. Lett.*, 3, 137, 1976.
- Stone, E. C., Frandsen, A. M., Mewaldt, R. A., Christian, E. R., Margolies, D., Ormes, J. F., and Snow, F., The advance composition explorer, *Space Science Rev.*, 86, 1–22, 1998.
- Torrence, C. and Compto, G. P., A Practical Guide to Wavelet Analysis, *Bulletin of the American Meteorological Society*, 79, 61–78, 1998.
- Tsurutani, B. T., Gonzalez, W. D., Gonzalez, A. L. C., Tang, F., Arballo, J. K., and Okada, M., Interplanetary origin of geomagnetic activity in the declining phase of the solar cycle, *Geophys. Res.*, 100, 21717–21733, 1995.
- Wilken, B., et al., First results from the RAPID imaging energetic particle spectrometer on board Cluster, *Ann. Geophys.*, 19, 1355–1366, 2001.

# EISCAT radar and optical studies of black aurora: a signature of magnetospheric turbulence?

M.J. Kosch, B. Gustavsson, E.M. Blixt, T. Pedersen, A. Senior, A.J. Kavanagh, and J. Semeter

**Abstract:** Black auroras are recognised as spatially well-defined regions within a uniform diffuse auroral background where the optical emission is significantly reduced, or possibly totally absent. Black auroras typically appear post-magnetic midnight and during the substorm recovery phase, but not exclusively so. Their horizontal size is typically 1x5 km, elongated in the east-west direction, and they move predominantly in an eastward direction with a speed of 1-4 km/s. There is no accepted theory for the phenomenon of black aurora, although they seem associated with substorms. We report on the first incoherent scatter radar observations of black aurora by EISCAT, coupled to white-light TV recordings of the phenomenon. From a 2002 observation, we show that non-sheared black auroras are most probably not associated with field-aligned currents. From 2002 and 2003 observations, we show that the apparent motion of the black aurora is most probably controlled by the drift of particles in the magnetosphere and not ExB drift in the ionosphere. The drift speed is therefore dependent on the energy of the precipitating particles forming the diffuse background. From 2005 bi-static observations, we attempt to confirm this by relating the height and propagation speed of the black aurora to precipitating particle energy within the surrounding background diffuse aurora. Hence, the mechanism for black aurora is most probably active within the magnetosphere and substorm associated plasma turbulence within the magnetosphere may account for the optical morphology of the black aurora, in particular the lack of pitch angle diffusion into the loss cone.

*Key words:* Black aurora.

## 1. Introduction

Black auroras, first reported by [1], are regions devoid of optical emissions, occurring within the normal aurora, where an observer may reasonably expect aurora to be normally present, i.e. not just a black sky. They are a fairly common phenomenon, which has been under-reported in the literature. Their morphology has been studied from the ground by [2, 3, 4] and their main features have been summarised by [5]: Black auroras are mostly east-west aligned arc segments or patches, with a typical size of 0.5-1.5 x 2.5-5 (up to 20) km. They normally occur post-substorm, typically in a diffuse aurora background, and drift eastward post-magnetic midnight with a typical velocity of 0.5-1.5 (up to 4) km/s. They may exhibit shear or vortices. Although the mechanism is unknown, satellite observations suggest they occur in regions of downward field-aligned current. In many respects, the black aurora is analogous to the negative of normal aurora [2]. Hence, just like normal aurora, the different morphologies of the black aurora (e.g. sheared forms showing vorticity versus un-sheared forms having smooth boundaries) may be due to different mechanisms.

Received 16 May 2006.

**M.J. Kosch, A. Senior, and A.J. Kavanagh.** Dept. of Communication Systems, Lancaster University, Lancaster, UK

**B. Gustavsson and E.M. Blixt.** Dept. of Physics, University of Tromsø, Tromsø, Norway

**T. Pedersen.** Space Vehicles Directorate, Air Force Research Laboratory, Hanscom AFB, Massachusetts, USA

**J. Semeter.** Dept. of Electrical and Computer Engineering, Boston University, Boston, Massachusetts, USA

## 2. Satellite Observations

Although no optical observations were available to confirm the presence of black auroras, [6, 7, 8] found small regions (down to  $\approx 1-2$  km) of excess positive space charge in FREJA satellite data at auroral latitudes in the altitude range between 800 and 1700 km. These observations they associated with intense diverging electric fields (up to  $\approx 1-2$  V/m), downward field-aligned currents, depletion of the thermal background plasma, dropouts of precipitating electrons, and strong wave activity. They speculated that the satellite observations were associated with east-west aligned black aurora vortex streets. [7, 8] found that the black aurora is the optical and electro-dynamical counterpart to small-scale auroral forms.

In joint aircraft-based optical and FAST satellite observations, [9] found that the black vortex streets consisted of spatial regions where the pitch angle diffusion was strongly suppressed for  $> 2$  keV electrons, causing precipitation dropouts of the higher energy particles. They estimated the altitude of the aurora immediately adjacent to the black aurora to be 115 km.

## 3. Radar Observations

The first combined radar-optical observations were performed by [10] from Skibotn, Norway. They found that the drift velocity of un-sheared black arc segments had no relationship to the ionospheric E-region ExB plasma drift as inferred by the Scandinavian Twin Auroral Radar Experiment (STARE), although both drifts had the same general direction, i.e. eastward.

The un-sheared black aurora, embedded in a diffuse background, was studied by [11, 12] using the European Incoherent Scatter facility (EISCAT), located near Tromsø, Norway, in

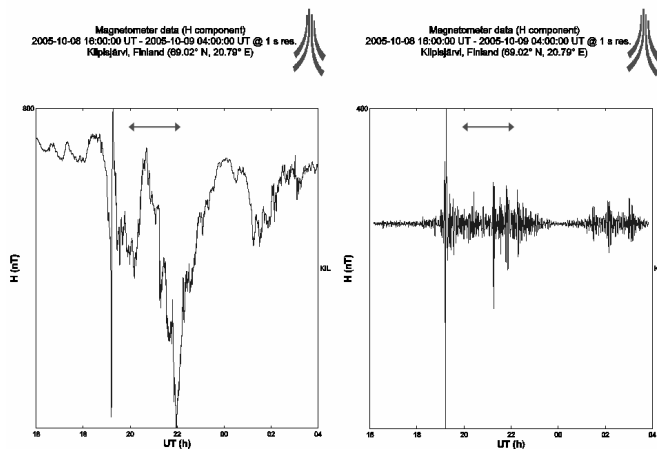


**Fig. 1.** SAMNET magnetometer data (left panel) showing the period when black auroras were observed (arrows). These data have been filtered to highlight Pi2 pulsations (right panel), indicating substorm onset prior to the onset of the black auroras.

conjunction with the ODIN night-vision TV camera. No evidence for ionospheric plasma depletion within the black aurora was found [11]. The first ever westward traveling black aurora was reported [12]. The black aurora drift speed had no relationship to the ionospheric F-region plasma drift [12]. However, significantly, the black aurora drift velocity was related to the characteristic energy of the precipitating particles within the adjacent diffuse aurora, as inferred from the EISCAT data [12, 13] (ignoring the single westward observation). This result suggests that the black aurora are the result of a magnetospheric mechanism, as the eastward gradient-curvature drift velocity of magnetospheric electrons is energy-dependent.

#### 4. New Results

In order to further address the relationship between the drift speed of the un-sheared black aurora and the precipitating particle energy in the adjacent diffuse aurora, bi-static optical observations in conjunction with the EISCAT radar were undertaken. The concept was to check whether the black aurora drift speed related to the height, and therefore the precipitating particle energy, of the diffuse background aurora. Here we report on the initial results.

On 8 October 2005, the DASI TV imager was located at the EISCAT radar site, recording in white-light with a  $\approx 30^\circ$  field of view and pointing into the magnetic zenith. The ODIN TV imager was located 27 km away, also recording in white-light with a similar field of view and pointing into the common volume. The EISCAT UHF radar was performing a 7-position scan for an unrelated purpose, pointing into the magnetic zenith once every 5 minutes. Black auroras were observed in the interval 20–22 UT. Fig. 1 shows the unfiltered (left panel) and filtered (right panel) SAMNET magnetometer data for this event from Kilpisjärvi, Finland. It is clear that the black aurora not only occurred during a negative bay (left panel), but the Pi2 activity (right panel) indicates a substorm onset  $\approx 40$  minutes

prior, which is consistent with the black aurora appearing in substorm recovery phase.

Fig. 2 (top row of panels) shows optical data from DASI, clearly showing evidence of un-sheared black auroras. The blue dot indicates the EISCAT UHF radar pointing direction along the magnetic field direction. Fig. 2 (middle row of panels) shows the electron density profile from EISCAT. The red dot indicates the mean altitude of the surrounding diffuse aurora, inferred from bi-static triangulation of the black aurora. The altitude is in the range  $\approx 110$ – $115$  km, consistent with [9]. Fig. 2 (bottom row of panels) shows the precipitating particle energy spectrum, inferred from the EISCAT data [13]. There is a peak in the spectrum around 3–6 keV, which is consistent with the inferred altitude.

Fig. 3 shows an example of the bi-static tomographic inversion from 22:24:19 UT. The retrieval of the volume emission rates was a simplified version of [14] where we use the DASI images for the column emission rate and then search for the best fit between images from both DASI and ODIN. The top panels show the raw white light data, with red intensity contours overlaid, for DASI (left) and ODIN (right). The black aurora arc is seen diagonally bottom-left to top-right in the DASI image and in the bottom left quadrant of the ODIN image. The bottom panels show, in false colour, horizontal (left) and vertical (right) cuts through the diffuse aurora layer, which include the black aurora. Again, the black aurora is clearly seen diagonally top-left to bottom-right in the horizontal cut and in the bottom left quadrant of the vertical cut.

#### 5. Conclusion

The evidence to date suggests that sheared black auroras (vortex streets) are associated with space charge, downward field-aligned currents and thermal plasma depletion, whereas the un-sheared black auroras (arc segments) are not. Since black auroras always seem to occur post-substorm, are clearly regions devoid of particle precipitation, and their drift velocity appears to be energy-dependent, it is proposed that the black auroras are “images” of small-scale flux tubes of stably trapped particles within the magnetosphere [15], which occur as a result of substorm activity. The mechanism remains unknown.

The un-sheared black auroras often give the impression of turbulence, similar to smoke rising from a fire. This analogy suggests an association between the black auroras and post-substorm plasma turbulence, which may be due to the intermingling of hot electron fluxes with the cold background plasma population.

In addition, the radar observations described for un-sheared black aurora arc segments, compared to the satellite observations described for observed or inferred black vortex streets, suggests that the black aurora has at least two different mechanisms associated with it.

#### References

1. Parson, N. R. and Thomas, I. L., Spatially forbidden regions in the aurora, *Canadian Journal of Physics*, 51, 1377–1378, 1973.
2. Trondsen, T. S. and Cogger, L. L., High-resolution television observations of black aurora, *Journal of Geophysical Research*, 102, 363–378, 1997.

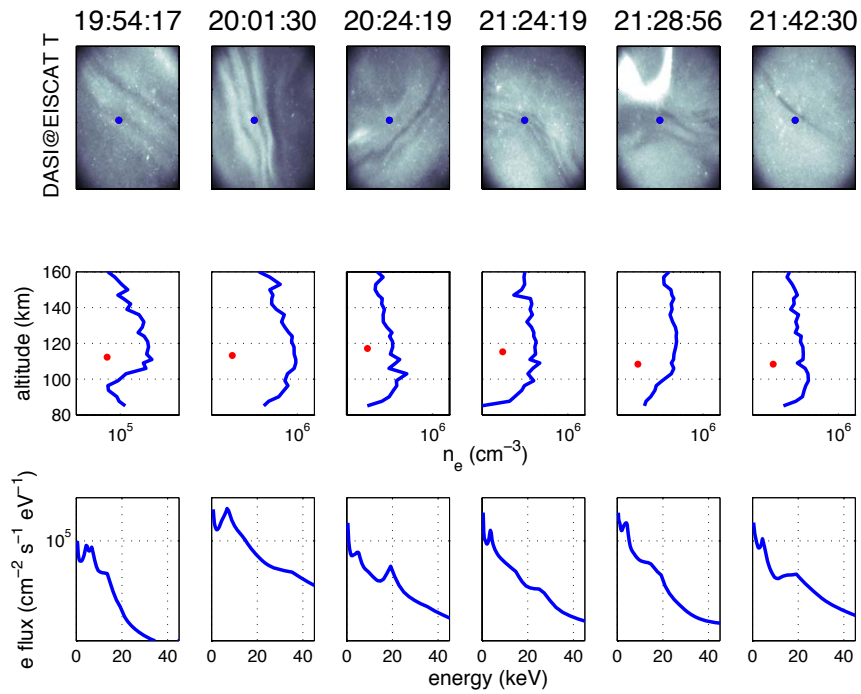


**Fig. 2.** Data from the 8 October 2005 campaign taken at Tromsø, Norway. The top row of panels show white-light optical data from DASI with a  $\approx 30^\circ$  field of view, clearly showing evidence of black auroras. The blue dot indicates the EISCAT UHF radar pointing direction along the magnetic field direction. The middle row of panels show the electron density profile from EISCAT. The red dot indicates the mean altitude of the black aurora, inferred from bi-static triangulation. The bottom row of panels show the precipitating particle energy spectrum, inferred from the EISCAT data.

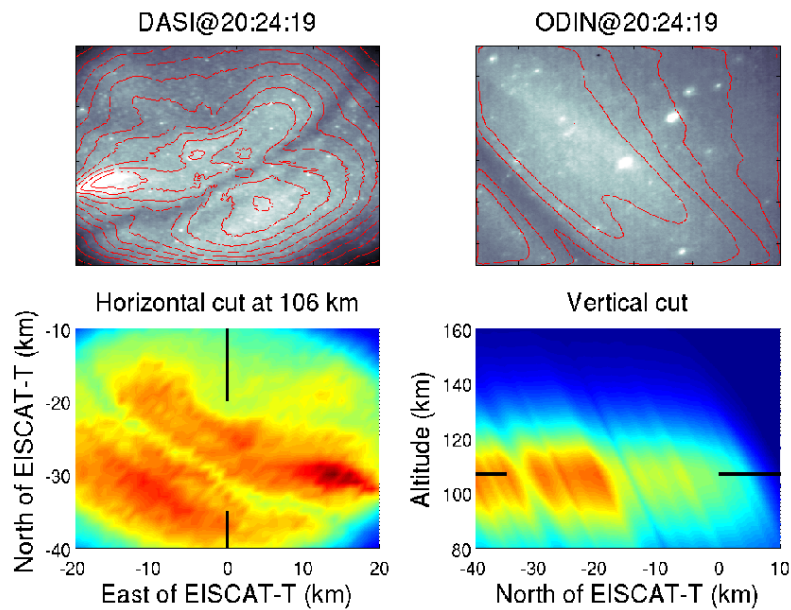


**Fig. 3.** Bi-static white-light recordings of the black aurora on 8 October 2005 (top panels) with intensity contours (red lines). The same black auroral “arc” is seen in both images. False-colour horizontal and vertical cuts through the tomographic reconstruction of the black aurora (bottom panels).

3. Kimball, J. and Hallinan, T. J., Observations of black auroral patches and of their relationship to other types of aurora, *Journal of Geophysical Research*, *103*, 14671–14682, 1998.
4. Kimball, J. and Hallinan, T. J., A morphological study of black vortex streets, *Journal of Geophysical Research*, *103*, 14683–14695, 1998.
5. Kosch, M. J., Scourfield, M. J. W., and Nielsen, E., A self-consistent explanation for a plasma flow vortex associated with the brightening of an auroral arc, *Journal of Geophysical Research*, *103*, 29383–29391, 1998.
6. Marklund, G., Blomberg, L., Fälthammar, C.-G., and Lindqvist, P.-A., On intense diverging electric fields associated with black aurora, *Geophysical Research Letters*, *21*, 1859–1862, 1994.
7. Marklund, G., Auroral phenomena related to intense electric fields observed by the Freja satellite, *Plasma Physics and Controlled Fusion*, *39*, 195–226, 1997.
8. Marklund, G., Karlsson, T., and Clemmons, J., On low-altitude particle acceleration and intense electric fields and their relationship to black aurora, *Journal of Geophysical Research*, *102*, 17509–17522, 1997.
9. Peticolas, L. M., Hallinan, T. J., Stenbaek-Nielsen, H. C., Bonnell, J. W., and Carlson, C. W., A study of black aurora from aircraft-based optical observations and plasma measurements on FAST, *Journal of Geophysical Research*, *107*, doi: 10.1029/2001JA900157, 2002.
10. Schoute-Vanneck, H., Scourfield, M. W. J., and Nielsen, E., Drifting black aurora?, *Journal of Geophysical Research*, *95*, 241–246, 1990.
11. Blixt, E. M. and Kosch, M. J., Coordinated optical and EISCAT observations of black aurora, *Geophysics Research Letters*, *31*, L06813, doi:10.1029/2003GL019244, 2004.
12. Blixt, E. M., Kosch, M. J., and Semeter, J., Observations of black aurora and their drift relative to the plasma, *Annales Geophysicae*, *23*, 1611–1621, 2005.
13. Semeter, J., and Kamalabadi, F., Determination of primary electron spectra from incoherent scatter radar measurements of the auroral E region, *Radio Science*, *40*, RS2006, doi: 10.1029/2004RS003042, 2005.
14. Yabu, T., Aso, T., Hashimoto, T., Abe, M., and Ejiri, M., An upgraded method for reconstructing 3-dimensional structure of aurora from stereo images, *Nankyoku Shiryo (Antarctic Record)*, *37*, 231–251, 1993, Publisher National Institute of Polar Research, Tokyo, Japan.
15. Roederer, J. G., Dynamics of geomagnetically trapped radiation, *Physics and Chemistry in Space*, Springer-Verlag, Berlin, 1970.

# Small scale Cluster observations of current sheet disruptions during substorm

O. Le Contel, F. Sahraoui, A. Roux, D. Fontaine, P. Robert, J.-A. Sauvaud, C. Owen, and A. Fazakerley

**Abstract:** We present a substorm event and show that the pre-existing thin current sheet with a thickness of the order of the proton Larmor radius and current carried by electron (in the spacecraft frame) thickens under the effect of electromagnetic fluctuations at three scales: (1) low-frequency drift waves ( $\simeq 20$  mHz), (2) proton cyclotron / electron bounce waves (0.2 – 10 Hz), (3) whistler waves (40 – 180 Hz). We focus on the latter type and show that they are associated with small scale current structure ( $c/\omega_{pe} < l < c/\omega_{pi} \simeq \rho_i$ ).

*Key words:* current sheet thickening, proton cyclotron/ electron bounce resonance, whistler waves.

## 1. Introduction

Schematically two categories of substorm models can be distinguished depending on the onset location [19] : (i) the near-earth neutral line models where an X-line at  $X \sim -23R_E$  produces earthward and tailward flows; the pileup of these earthward flows accounting for the tailward propagating front of the dipolarization. (ii) current disruption models where a micro-instability interrupts the cross-tail current which is diverted toward the ionosphere first between  $6 - 15R_E$ .

Analytically, these two categories are also clearly distinct [30]. The formation of a near-earth neutral line is understood as resulting from a tearing instability characterized by a wave vector  $k_x \gg k_y$  along the magnetotail therefore perpendicular to the equilibrium cross-tail current  $J_y$  (e.g. [38]). On the other hand, the current disruption models rely upon instabilities with a wave vector  $k_y \gg k_x$  along the cross-tail current and producing parallel and perpendicular current signatures modulated in the  $y$  direction.

These two categories of models have induced two types of data analysis. Indeed in the former case the time-variation of the magnetic field are interpreted as a signature of a steady structure, the so-called "Hall current system" with its characterized quadrupolar  $B_y$  signatures (e.g. [32]), moving across the spacecraft (s/c) whereas in the latter case magnetic structures are interpreted as signatures of azimuthally moving unstable waves passing by the s/c (e.g. [31, 6]).

The mechanism of energy dissipation characterized by its temporal and spatial scales can be considered as a way to distinguish between these different models. Indeed in a weakly collisional or collisionless plasma, the identification of the processes which lead to the energy dissipation is a longstanding issue. Again in the former class, often called collisionless mag-

netic reconnection models, it is suggested that the energy dissipation occurs at different scales for ions and electrons. It is shown that ions are decoupled from the magnetic field by Hall terms (in the generalized Ohms law) at a scale corresponding to their inertial length  $c/\omega_{pi}$ . This scale being larger than the electron scale, the reconnection rate is found to increase compared with classical resistive MHD rate, where ions and electrons are not considered separately. In the region in between ion and electron inertial lengths, the electrons are still magnetized whereas ion dynamics can be neglected; the dynamics is expected to be controlled by whistler waves (e.g. [22, 4]). In the latter class, the energy dissipation can occur at many scales from the largest corresponding to the scale of the length of the magnetic field line via field line or bounce resonance (e.g. [39]) to the smallest via the ion and electron Larmor radius scales (e.g. [8, 9]). All these processes can be present simultaneously. The present data analysis belongs to the latter category. We present a substorm event observed by Cluster and interpret the observations as a tailward propagating thickening of the current sheet as described by [24] resulting from different kind of unstable waves at different scales.

## 2. Observations

### 2.1. Global view

During the summer 2003, the average Cluster inter-satellite distance was about 200 km. Such a small distance allows accurate computations of the current density using the curlometer technique (e.g. [29]) even for very thin current sheets or relatively long wavelength waves ( $\lambda > 200$  km). We investigate a substorm event observed on August 17th 2003. Around 1650 UT Cluster was located at  $[-16.8, -5.55, 3.33] R_E$  GSM. Most instruments were in burst mode. Magnetic field data are provided by the FGM instrument at 14.87 ms time resolution [3]. Ion and electron particles data come from CIS [28] (only CODIF on C4 is available) and PEACE [14] respectively. The time resolution for the moment calculation is 4 s for both particles instruments but the burst mode allows us to display electron spectrograms with time resolution of 125 ms. High-frequency fluctuations of magnetic and electric fields are provided by STAFF [7] and EFW [11] instruments. Their time resolution is 2.22 ms (450 sample/s). Data from different satellite

Received 24 May 2005.

**O. Le Contel, F. Sahraoui, A. Roux, D. Fontaine, and P. Robert.** Centre d'étude des Environnements Terrestre et Planétaires (CETP), 10-12, avenue de l'Europe, F-78140 Vélizy, France.  
**J.-A. Sauvaud.** Centre d'Etude Spatial des Rayonnements (CESR), 9 avenue du colonel Roche, F-31028 Toulouse cedex 4, France.  
**C. Owen and A. Fazakerley.** Mullard Space Science Laboratory (MSSL), University College London, Dorking RH5 6NT, United Kingdom.

are displayed using the following color code: black for C1, red for C2, green for C3 and blue for C4. According to the

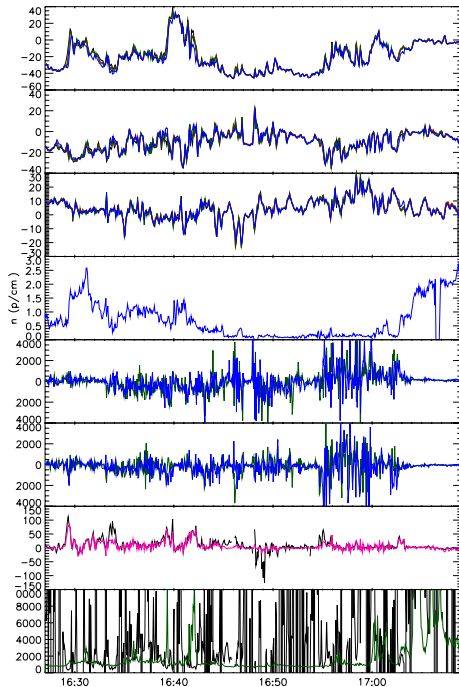


**Fig. 1.** All data are plotted in GSM coordinates:  $B_x$ ,  $B_y$ ,  $B_z$  components of the magnetic field, ion density,  $V_x$  and  $V_y$  components of the electron (thin line) and ion (thick line) velocities,  $J_y$  component of the electrical current density computed from curlB (pink line) and equatorial value of the  $J_y$  current density estimated from a Harris model (black line), half-thickness of the current sheet estimated from a Harris model (see text for details).

Kyoto quick look AE monitor (not shown), the magnetic activity was high as the AE reaches 1000 nT around 1700 UT indicating that we are probably observing a large substorm. Fig. 1, first panel, shows that from 1627 UT to 1709 UT, while the spacecraft cross the magnetic equator several times, the current sheet thickens as the GSM  $B_x$  component of the magnetic field varies from  $-40$  nT to  $0$  nT. During this thickening three-dimensional electromagnetic waves are present at low-frequencies ( $\approx 20$  mHz) as shown by the first three panels. The study of the low-frequency waves corresponding to the range of the so-called ballooning mode is out of the scope of the present paper but is carried out by [18]. On panel 4 the ion density profile corresponds to the expected variations as the s/c move from the central plasma sheet ( $n_i \approx 1.5$  p $\cdot$ cm $^{-3}$ ) to the boundary ( $n_i < 0.1$  p $\cdot$ cm $^{-3}$ ). The  $V_x$  component of the electron velocity is larger than that of ions but shows the same variations from tailward, at the beginning of the interval, to earthward at the end (panel 5). The  $V_y$  component of the electron velocity is also larger than that of ions but is almost always downward (negative) whereas ion  $V_y$  is duskward (positive) except at the end of the interval where the electron and ion  $V_y$  have large positive as well as negative values (panel 6). On panel 7 the  $J_y$  current density computed using the curlometer technique (pink) is displayed as well as an estimate

of the equatorial current density (black) from a Harris sheet model [12]. In order to compute the Harris current density we fitted the  $B_x$  component of the magnetic field measured by C1 and C3 with an instantaneous Harris sheet model defined by  $B_x(t) = B_L(t) \tanh((z(t) - z_0(t))/H(t))$  where  $z_0$  and  $H$  represent the centre and the half-thickness of the current sheet, respectively.  $B_L$  is obtained either from direct measurements in the lobe region (if the s/c happen to be located in the lobes) or by assuming the equilibrium of the vertical pressure within the plasma sheet. Both computations lead to similar results during the interval. We find that  $J_y$  can increase up to  $80$  nA/m $^2$  and corresponds to the current carried by electron in the s/c frame ( $J_{y,e} = -en_0V_{y,e} \approx -e * 0.5(\text{p}\cdot\text{cm}^{-3}) * (-1000 \text{ km/s}) \approx 75 \text{ nA/m}^2$ ). The fit with a Harris sheet has also been used to estimate the half-thickness of the CS ( $H$ ) displayed on the last panel of Fig. 1. As soon as the s/c are located inside the CS, the fit works and gives a half-thickness which is around  $1000$  km or less. The green curve corresponds to the local ion Larmor radius computed at the location of C3. At the beginning of the interval, when all s/c are located far from the equator ( $B_x \approx -40$  nT) it corresponds to the ion Larmor radius computed in the asymptotic magnetic field of the Harris sheet model. During this period  $H \approx \rho_i$  (as well as  $c/\omega_{pi}$ ) and the observed CS structure agrees with the CS equilibrium models described by [34] in such a regime. Thus Cluster is observing a thin current sheet with large amplitude low-frequency electromagnetic fluctuations. The ion dynamics is very likely stochastic and the current is carried by electrons (in s/c frame see also [1]).

## 2.2. Ion scale observations

Now, we focus on a smaller time period (1659-1701 UT) corresponding to a fast thickening of the CS and a variation of  $B_x$  from  $-30$  nT to  $-10$  nT (Fig. 2). However, one should remark that even for these two-minutes time interval, the four s/c measure almost the same magnetic field, indicating that the spatial scale of the current sheet is larger than the average inter-satellite distance (200 km). Indeed for this time interval the estimated half-thickness from a Harris model is greater than  $1000$  km. Thus, the spatial scale of the CS is of the same order or larger than the proton Larmor radius, computed at the edge of the CS. However, the validity of the calculation of ion velocity in such a thin current sheet has been questioned by [41]. Between 1659:40 and 1700 UT, we observe a strong decrease of  $|B_x|$  associated with large electric field fluctuations as well as quasi-dc electric field around  $20$  mV/m, and a large increase of the  $V_x$  component of the ion velocity (up to  $1000$  km/s), while the ion density remains constant. The same observations are obtained for electrons velocities up to  $4000$  km/s for C4 and to  $3000$  km/s for C3 (not shown) which confirms the ion moment calculation. Simultaneously, the current density obtained from curlB displays large amplitude oscillations on  $J_x \approx \pm 20$  nA/m $^2$  as well as on  $J_y \approx$  from  $\pm 10$  to  $\pm 30$  nA/m $^2$ . Thus, ion acceleration seems to be associated with large amplitude current density fluctuations. One can remark that these correlations were also observed just a few seconds before and after, when all s/c were located at the edge of the current sheet (1659:10 UT- 1659:25 UT and 1700:10-1700:25 UT), although with smaller amplitudes of the electric and magnetic fields and current density fluctuations. In order

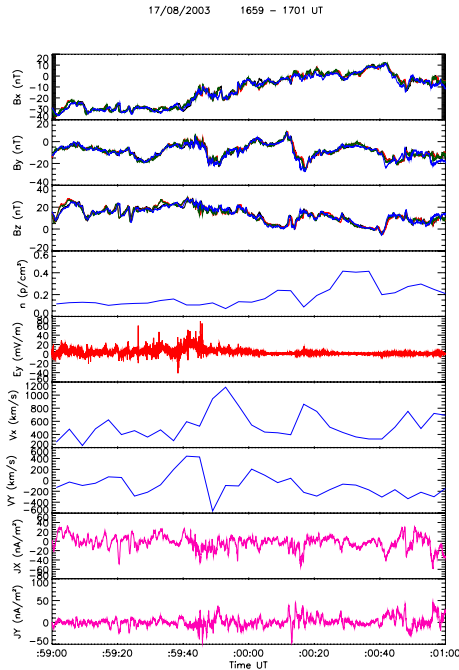


**Fig. 2.** All data are plotted in GSM coordinates excepted the electric field in SR2 frame:  $B_x$ ,  $B_y$ ,  $B_z$  components of the magnetic field, ion density,  $E_y$  component of the electric field,  $V_x$  and  $V_y$  components of ion velocity,  $J_x$  and  $J_y$  components of the electrical current density computed from curlB.

to better characterize the current density fluctuations we have performed a spectrogram of the current density waveform obtained from FGM data, via the curlometer technique. Fig. 3 displays the three components of current density fluctuations in the (4 s average) magnetic field aligned (MFA) frame. The largest amplitude is found to correspond to the current density parallel to  $\mathbf{B}$  ( $J_z$ ) while the largest amplitude of the average magnetic field fluctuations is found to be in the perpendicular direction (not shown). Frequency range of these fluctuations corresponds to the proton cyclotron frequency ( $f_{ci} \simeq 0.2 - 0.4$  Hz for  $B_0 \simeq 15 - 30$  nT) as well as the electron bounce frequency  $f_{be} \simeq v_e/L \simeq 0.15$  Hz for  $L = 20 R_E$  and  $E_e = 1$  keV). We obtain the same results using the current density waveform computed from STAFF-SC data (not shown). These spectrograms show a clear signature of parallel current density fluctuations associated with a fast thickening of the CS which suggests a micro-instability as a source of these fluctuations, and that this instability is involved in this magnetic field re-configuration.

### 2.3. Electron scale observations

Data gathering in burst mode on STAFF-SC allows us to analyse the magnetic wave form up to 180 Hz. Fig. 4 (left panel) displays the average Fourier spectrum computed from the sum of all 4.55 s duration (2048 points at 450 s/s) Fourier spectrum performed from 1627 to 1709 UT. Data have been moved in a (4 s average) MFA frame. We find that the spectrum is isotropic below 40 Hz and strongly anisotropic  $\delta B_R \gg \delta B_{\parallel}, \delta B_L$  ( $R$  in red and  $L$  in green meaning classical right and left hand components when  $\mathbf{k} \cdot \mathbf{B} > 0$ ) from 40 Hz to

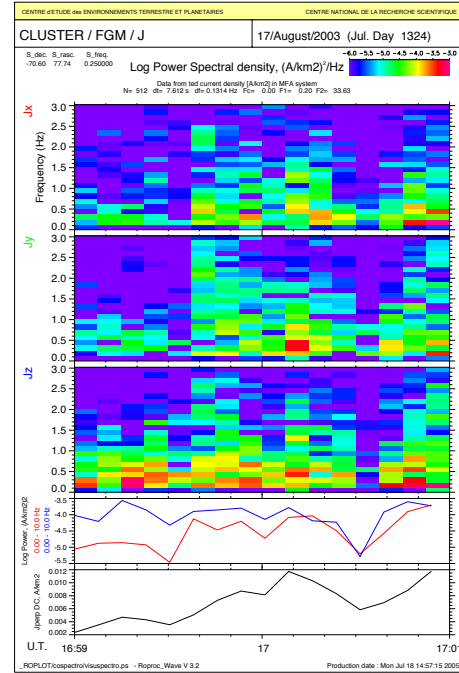


**Fig. 3.** Spectrograms of current density fluctuations computed from FGM data in a magnetic field aligned frame ( $J_z$  corresponding to  $J_{\parallel}$ ). The time resolution of the spectrogram is 7.612 s and the frequency resolution is 0.1314 Hz. The lower cut-off frequency has been fixed at 0.2 Hz to be consistent with the magnetic field aligned frame mapping.

180 Hz. Looking at the spectrogram on Fig. 4 (right panel) for the same time period, we observe that the anisotropic part of the spectra is caused by very intense short lasting emissions in the range below the electron cyclotron frequency, observed during the whole period. A wave polarization analysis, assuming that at each frequency corresponds a unique wave vector ( $\mathbf{k} \cdot \delta \mathbf{B} = 0$ ), shows that these short time emissions have a right-hand circular polarization and parallel wave vector (not shown). However, only a  $\mathbf{k}$ -filtering analysis such as the one carried out by [33] in the magnetosheath region will fully determine the wave vector of these intense waves and will permit to estimate a possible Doppler shift effect. Indeed, assuming a plasma velocity of 1000 km/s with a wavelength of  $c/\omega_{pe} \simeq 10$  km gives a Doppler shift about 100 Hz. Now, we focus on one of the most intense short duration emission observed between 1657:00 and 1657:30 UT. We can see on Fig. 5 panels 2 and 4 that Cluster detects a current structure with a spatial scale comparable to or smaller than the intersatellite distance of 200 km, as  $B_y$  and  $B$  amplitudes are strongly different on C4 than on the others s/c. Therefore this current structure has a scale smaller than the proton Larmor radius or proton inertial length which are about 1000 km. Associated with this small scale current structure and minimum of the modulus of  $\mathbf{B}$ , we observe on C2 (red) an electromagnetic wavepacket with a huge magnetic amplitude of  $\pm 1$  nT whereas the electric field amplitude is about  $\pm 2$  mV/m (panels 5 and 6). Note that this wavepacket is also detected on C1 and C3 (not shown) but not on C4 (blue). Therefore the wavepacket seems to be very localized within the current structure. Furthermore one can remark

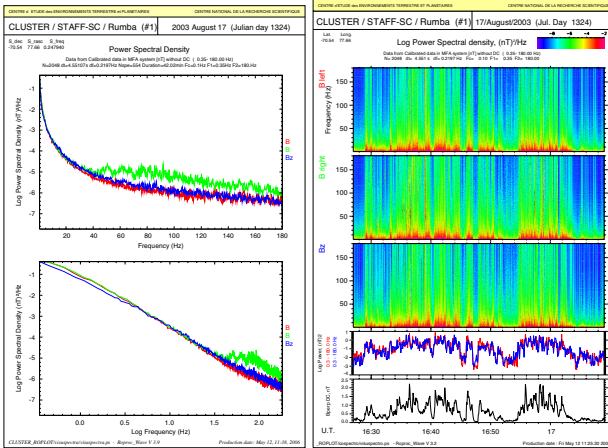


**Fig. 4.** Fourier spectra (left picture) and spectrograms (right picture) of magnetic fluctuations from STAFF-SC data in a MFA frame ( $\delta B_z$  corresponding to  $\delta B_{\parallel}$ ). The time resolution of the spectrogram is 4.55 s and the frequency resolution is 0.22 Hz. The lower cut-off frequency has been fixed at 0.35 Hz to get rid of any spin modulation effect (see text for more details).

that intense quasi-electrostatic structures are detected before and after this electromagnetic wavepacket. On panels 7 and 8, electron and ion moments are plotted but clearly the magnetic field varies strongly on the 4 s time resolution of particle measurements. Thus there is a large uncertainty in the calculation of particle moments ( $V_{xi} \approx 1000$  km/s and  $V_{yi} \approx -500$  km/s,  $V_{xe} \approx \pm 2000$  km/s and  $V_{ye} \approx 2000$  km/s). These moments can also fluctuate over a time scale shorter than 4 s. For the same reasons, the comparison between the current density, computed from curlB, and from particles (panels 9 and 10) can just be done qualitatively. One can remark that during most of the time interval the ion current density (thick blue line) is directed antiparallel to curlB, which implies that the electron should be the current carriers in the *s/c* frame. In average the trend of the electron currents ( $J_x$  and  $J_y$ ) agree quite well with curlB calculations. Finally, the current density measurements (from curlB) show that the magnetic wave packet is associated with intense currents up to  $60 \text{ nA/m}^2$  ( $J_x$ ) and to  $80 \text{ nA/m}^2$  ( $J_z$  not shown). These intense currents seem to be parallel as well as perpendicular to the magnetic field (pink dotted line). Therefore a modeling of these intense whistler waves requires a stability analysis of a three-dimensional CS equilibrium. Finally, the high-time resolution electron fluxes show a strong anisotropy and enhanced fluxes (first and second panels from the bottom) in association with the large amplitude magnetic field fluctuations, while Cluster is still located in the plasma sheet. At this stage, we speculate that this anisotropy corresponds to larger fluxes parallel to  $\mathbf{B}$  than perpendicular. Fluxes as a function of electron pitch angle will be showed in a next paper in order to confirm this point. Nevertheless, these observations are sufficient to indicate that the electron dynamics seems to be strongly related to the whistler wave activity, as expected in the electron MHD regime.

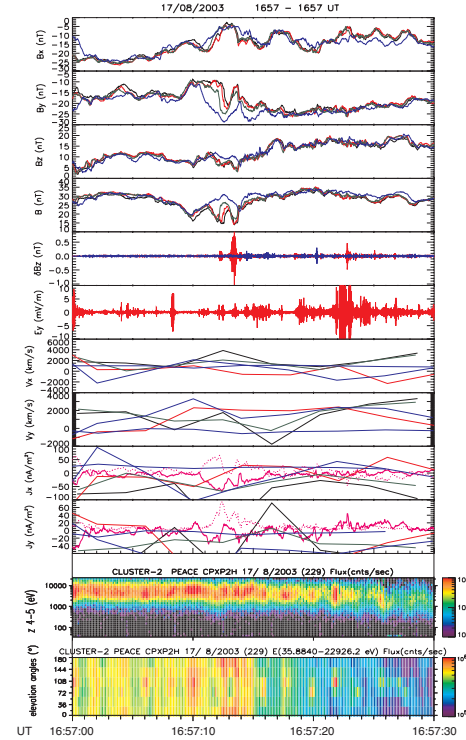


**Fig. 5.** All data are plotted in GSM coordinates excepted the electric and magnetic field fluctuations in SR2 frame:  $B_x$ ,  $B_y$ ,  $B_z$ ,  $B$  components of the magnetic field,  $\delta B_z$ ,  $\delta E_y$  components of the electric and magnetic fields from 30 Hz to 180 Hz,  $V_x$  and  $V_y$  components of electron (thin colored line) and ion (thick colored line) velocities,  $J_x$  and  $J_y$  components of the electrical current density computed from curlB (pink line) and from electron (thin colored line) and ion (thick colored line) moments. The pink dotted line in  $J_x$  panel corresponds to the parallel current density while the pink dotted line in  $J_y$  panel corresponds to the perpendicular current. Two last panels are the high-time resolution (125 ms) electron fluxes: (i) for different energy ranges (from 35.8 eV - 22.9 keV) for one angular sector and (ii) integrated in energy for different angular sectors respectively.

### 3. Discussion

In addition to low-frequency ballooning modes which are regularly observed during substorm expansion phase [31, 10, 37, 18], as well as on present data, we have shown that intense waves ( $f \approx f_{H+} \approx f_{be} \approx 0.2$  Hz) are detected together with a fast thickening of the CS. The association of these waves with dipolarisation and fast flows was reported also all through the tail [27, 36, 26, 37]. It was suggested by [16] that the level of emission of the waves may control the plasma transport in the magnetotail and that this mechanism can be efficient all through the tail using GEOS-2, Geotail and Cluster data [17]. It was shown by [25] that the waves can be generated by a parallel current instability as soon as the drift velocity between protons and electrons is close to the proton thermal velocity. However, the fact that the proton cyclotron frequency is very close to the electron bounce frequency implies that any consistent theoretical calculations should take into account the effect of the bounce motion of electrons on the

growth rate of the instability. Such a study considering the parallel current driven instability is currently on progress. Furthermore, while classical wave polarization analysis fail to characterize these waves, we have shown, using the current density measurements, that these waves corresponds to intense parallel current density fluctuations and perpendicular magnetic field fluctuations. These results should be taken into account in the future as constraints for testing any instabilities as a source of these emissions. At smaller scale and higher frequencies, we have identified intense short duration ( $< 4$  s) whistler emissions ( $f < f_{ce} \simeq 400$  Hz for  $B_0 = 15$  nT) during the oscillations of the thin current sheet. The classical dispersion relation of whistler (helicon) waves [13], assuming  $\omega \ll \omega_{ce}$  gives:  $\omega/(k_{\parallel}v_A) = (\omega/\omega_{ci})^{1/2} \simeq 14$  at  $f = 40$  Hz and agrees with the phase velocity obtained from the ratio of  $\delta E(\omega)/\delta B(\omega) \simeq 20000$  km/s. These intense whistler waves are observed in association with small scale ( $l \simeq 200$  km  $< \rho_i \simeq c/\omega_{pi}$ ) current structures. These kind of waves belongs to the regime of electron magnetohydrodynamics described theoretically by [5, 15]. It was shown in a laboratory experiment by [40] that a pulse of current at the whistler time scale propagates through the plasma by a whistler waves and suggest by analogy to “Alfvén wing” to speak about “whistler wing”. Therefore two different questions can be addressed for understanding the existence of such intense whistler waves: (1) what is the origin of such small scale current structures with  $c/\omega_{pe} < l < c/\omega_{pi}$ ? (2) what produces such pulses of current at the whistler time scale? In the former case we can suggest that proton cyclotron/electron bounce waves may generate such small scale current structures which can in turn generate whistler waves. In the latter case, we suggest that the short duration pulse of current could be generated by a fast reconnection process as described by [5, 2]. To summarize we can distinguish two scenarii (1) top/bottom: at the scale of the current sheet, the CS eigen modes correspond to low-frequency waves like ballooning. The parallel and perpendicular current fluctuations associated with ballooning modes can cause parallel [25] or perpendicular [21] current driven instabilities at  $\omega \simeq \omega_{ci}, \omega_{be}$ . Then these instabilities create small scale current structure which can generate intense whistler waves. On the other hand a bottom/top scenario corresponding to an inverse cascade, as suggested by [20]. However, in the present case the process would start by a fast reconnection at  $\omega_{ci} < \omega < \omega_{ce}$  and at small scale  $c/\omega_{pe} < l < c/\omega_{pi}$ . The corresponding fluctuations could provide a kind of anomalous resistivity for lower frequency instabilities with larger spatial scale. Note that the whistler waves are also expected by collisionless magnetic reconnection models in the ion diffusion region ( $\leq c/\omega_{pi}$ ). However, hybrid simulation results showed the formation of a standing whistler wave close to the separatrix (e.g. [35]). Given our observations of numerous short-duration emissions of whistler wave in association with small scale current structure, Cluster would have to remain close to the separatrix during the whole period which seems unlikely. Finally, the full characterization of such small scale structures will not be possible due to the time resolution of the particle measurement. Furthermore, even smaller scale structures  $c/\omega_{pe}$ , the so-called “electron diffusion region” are already detected in the subsolar region [23] and are also expected in the magnetotail. Such studies are the principal objectives of the future Magnetospheric

Multi-Scale (MMS) mission that includes optimized high-time resolution of particles as well as field measurements, three-dimensional electric field and small inter-satellite distances. On the other hand, the spatial distribution of such small scale structures and their role on the global dynamics of the magnetosphere will be addressed by the Time History of Event and Macroscale Interactions during Substorms (THEMIS) mission.

## 4. Conclusion

We have presented a substorm event and have shown that the pre-existing thin current sheet with a thickness of the order of the proton Larmor radius and current carried by electron (in the *s/c* frame) thickens under the effect of electromagnetic fluctuations at three scales. While the low-frequency ( $\simeq 20$  mHz) scale has not been discussed in detail, we have shown that fluctuations at the proton cyclotron / electron bounce frequency (0.2 – 10 Hz) correspond to signatures of parallel current density fluctuations. They are detected in association with a fast thickening of the CS and accelerated particles suggesting a micro-instability as a source of these fluctuations as well as a trigger for the CS thickening, and the subsequent fast flow. At higher frequencies, we have identified short duration bursts ( $< 4$  s) of whistler waves (right-hand circular polarization with  $\mathbf{k} \cdot \mathbf{B}_0 \simeq 0$ ) associated with small scale current structures ( $l < \rho_i \simeq c/\omega_{pi}$ ) during the whole substorm period. Focusing on a particularly intense burst of whistler waves we have shown that these bursts are also associated with enhanced electron fluxes with a strong anisotropy. More investigations are needed to understand the origin of these whistler waves and their coupling with the other scales.

## References

- Asano, Y., Mukai, T., Hoshino, M., Saito, Y., Hayakawa, H., and Nagai, T., Current sheet structure around the near-earth neutral line observed by geotail, *J. Geophys. Res.*, 109, doi: 10.1029/2003JA010114, 2004.
- Attico, N., Califano, F., and Pegoraro, F., Kinetic regimes of high frequency magnetic reconnection in a neutral sheet configuration, *Phys. Plasmas*, 9, 458–464, 2002.
- Balogh, A., *et al.*, The Cluster magnetic field investigation, *Space Science Reviews*, 79, 65–91, 1997.
- Biskamp, D., Schwarz, E., and Drake, J. F., Two-fluid theory of collisionless magnetic reconnection, *Phys. Plasmas*, 4(4), 1002–1009, 1997.
- Bulanov, S. V., Pegoraro, F., and Sakharov, A. S., Magnetic reconnection in electron dynamics, *Phys. Fluids B*, 4, 2499–2508, 1992.
- Cheng, C. Z. and Lui, A. T. Y., Kinetic ballooning instability for substorm onset and current disruption observed by AMPTE/CCE, *Geophys. Res. Lett.*, 25, 4091, 1998.
- Cornilleau-Wehrin, N., *et al.*, The CLUSTER spatio-temporal analysis of field fluctuations (STAFF) experiment, *Space Science Reviews*, 79, 107–136, 1997.
- Daughton, W., Nonlinear dynamics of thin current sheets, *Phys. Plasmas*, 9(9), 3668–3678, 2002.
- Daughton, W., Electromagnetic properties of the lower-hybrid drift instability in a thin current sheet, *Phys. Plasmas*, 10(8), 3103–3119, 2003.

10. Erickson, G. M., Maynard, N. C., Burke, W. J., Wilson, G. R., and Heinemann, M. A., Electromagnetics of substorm onsets in the near-geosynchronous plasma sheet, *J. Geophys. Res.*, 105, 25265–25290, 2000.
11. Gustafsson, G., *et al.*, The electric field and wave experiment for the cluster mission, *Space Science Reviews*, 79, 137, 1997.
12. Harris, E. G., On a plasma sheath separating regions of oppositely directed magnetic field, *Il Nuovo Cimento*, XXIII, 115, 1962.
13. Heliwell, R. A., *Whistlers and Related Ionospheric Phenomena*, Stanford University Press, Stanford, CA, 1965.
14. Johnstone, A., *et al.*, PEACE: A plasma electron and current experiment, *Space Science Reviews*, 79, 351–398, 1997.
15. Kingsep, A. S., Chukbar, K. V., and Yankov, V. V., Electron magnetohydrodynamics, in *Reviews of Plasma Physics*, volume 16, edited by B. Kadomtsev, 243, Consultants Bureau, New York, 1990.
16. Le Contel, O., Roux, A., Perraut, S., Pellat, R., Holter, Ø., Pedersen, A., and Korth, A., Possible control of plasma transport in the near-earth plasma sheet via current-driven Alfvén waves ( $f_{H+}$ ) during substorm growth phase and relation to breakup, *J. Geophys. Res.*, 106, 10817–10827, 2001.
17. Le Contel, O., *et al.*, Role of the parallel current instability during substorms: Theory and observations, in *Sixth International Conference on Substorms (ICS-6)*, March 25-29, 2002, edited by R. Winglee, 326–333, University of Washington, Seattle, 2002.
18. Louarn, P., Fruit, G., Budnik, E., Sauvaud, J.-A., Jacquey, C., Lucek, E., the CDPP, CIS, and teams, F., Low frequency fluctuations of the plasma sheet - cluster observations and models, in *Eighth International Conference on Substorms (ICS-8)*, March 27-31, 2006, edited by E. Donovan, University of Calgary, Canada, 2006, this issue.
19. Lui, A. T. Y., Current controversies in magnetospheric physics, *Rev. Geophys.*, 39(4), 535–563, 2001.
20. Lui, A. T. Y., Relating plasma instabilities in the magnetotail to observables, in *Eighth International Conference on Substorms (ICS-8)*, March 27-31, 2006, edited by E. Donovan, University of Calgary, Canada, 2006, this issue.
21. Lui, A. T. Y., Chang, C.-L., Mankofsky, A., Wong, H.-K., and Winske, D., A cross-field current instability for substorm expansions, *J. Geophys. Res.*, 96, 11389–11401, 1991.
22. Mandt, M. E., Denton, R. E., and Drake, J. F., Transition to whistler mediated magnetic reconnection, *Geophys. Res. Lett.*, 21(1), 73–77, 1994.
23. Mozer, F. S., Bale, S. B., McFadden, J. P., and Torbert, R. B., New features of electron diffusion regions observed at sub-solar magnetic field reconnection sites, *Geophys. Res. Lett.*, 32, L24102, doi:10.1029/2005GL024092, 2005.
24. Perraut, S., Le Contel, O., Roux, A., Parks, G., Hoshino, M., Mukai, T., and Nagai, T., Substorm expansion phase: Observations from Geotail, Polar and IMAGE network, *J. Geophys. Res.*, 108, 1159, doi:10.1029/2002JA009376, 2003.
25. Perraut, S., Le Contel, O., Roux, A., and Pedersen, A., Current-driven electromagnetic ion cyclotron instability at substorm onset, *J. Geophys. Res.*, 105, 21097–21107, 2000.
26. Perraut, S., Le Contel, O., Roux, A., Pellat, R., Korth, A., Holter, Ø., and Pedersen, A., Disruption of parallel current at substorm breakup, *Geophys. Res. Lett.*, 4041–4044, 2000.
27. Perraut, S., Morane, A., Roux, A., Pedersen, A., Schmidt, R., Korth, A., Kremser, G., Aparicio, B., and Pellinen, R., Characterization of small scale turbulence observed at substorm onsets: Relationship with parallel acceleration of particles, *Adv. Space Res.*, 13(4), 217, 1993.
28. Rème, H., *et al.*, The CLUSTER Ion Spectrometry Experiment, *Space Science Reviews*, 79, 303, 1997.
29. Robert, P., Dunlop, M., Roux, A., and Chanteur, G., Accuracy of current density determination, in *Analysis Methods for Multi-Spacecraft Data*, edited by G. Paschman and P. Daly, ISSI Scientific Report SR-001, chapter 16, 395–418, European Space Agency, 1998.
30. Roux, A., Le Contel, O., Fontaine, D., Louarn, P., Sauvaud, J.-A., and Fazakerley, A. N., Role of instabilities at substorms, in *Eighth International Conference on Substorms (ICS-8)*, March 27-31, 2006, edited by E. Donovan, University of Calgary, Canada, 2006, this issue.
31. Roux, A., Perraut, S., Robert, P., Morane, A., Pedersen, A., Korth, A., Kremser, G., Aparicio, B., Rodgers, D., and Pellinen, R., Plasma sheet instability related to the westward traveling surge, *J. Geophys. Res.*, 96, 17697, 1991.
32. Runov, A., *et al.*, Current sheet structure near magnetic x-line observed by cluster, *Geophys. Res. Lett.*, 30(11), 1579, doi:10.1029/2002GL016730, 2003.
33. Sahraoui, F., *et al.*, Ulf wave identification in the magnetosheath: the k-filtering technique applied to cluster II data, *J. Geophys. Res.*, 108, 1335, doi:10.1029/2002JA009587, 2003.
34. Schindler, K. and Birn, J., Models of two-dimensional embedded thin current sheets from Vlasov theory, *J. Geophys. Res.*, 107, 1193, doi:10.1029/2001JA000304, 2002.
35. Shay, M. A., Drake, J. F., Denton, R. E., and Biskamp, D., Structure of the dissipation region during collisionless magnetic reconnection, *J. Geophys. Res.*, 103, 9165–9176, 1998.
36. Shinohara, I., Nagai, T., Fujimoto, M., Terasawa, T., Mikai, T., Tsuruda, K., and Yamamoto, T., Low-frequency electromagnetic turbulence observed near the substorm onset site, *J. Geophys. Res.*, 103, 20365, 1998.
37. Sigsbee, K., Cattell, C. A., Fairfield, D., Tsuruda, K., and Kokubun, S., Geotail observations of low-frequency waves and high-speed earthward flows during substorm onsets in the near magnetotail from 10 to 13  $R_E$ , *J. Geophys. Res.*, 107, 1141, doi:10.1029/2001JA000166, 2002.
38. Sitnov, M. I., Malova, H. V., and Sharma, A. S., Role of the temperature ratio in the linear stability of the quasi-neutral sheet tearing mode, *Geophys. Res. Lett.*, 25, 269–272, 1998.
39. Tikhonchuk, V. T. and Rankin, R., Electron kinetic effects in standing shear alfvén waves in the dipolar magnetosphere, *Phys. Plasmas*, 7(6), 2630–2645, 2000.
40. Urrutia, J. M. and Stenzel, R. L., Transport of current by whistler waves, *Phys. Rev. Lett.*, 62(3), 272–275, 1989.
41. Wilber, M., *et al.*, Cluster observations of velocity space-restricted ion distributions near the plasma sheet, *Geophys. Res. Lett.*, 31, L24802, doi:10.1029/2004GL020265, 2004.

# Convection vortices in pre- and post-midnight sector during magnetospheric substorms

J. Liang, G. Sofko, and H. Frey

**Abstract:** In this study the nightside ionospheric plasma convection pattern during two substorm events is investigated from global SuperDARN observations. We find that, a postmidnight anticlockwise convection vortex (PoACV) usually emerges at latitudes higher than the auroral brightening region after the substorm expansion phase onset. Meanwhile, an east-to-west flow reversal region wrapping around the intensified auroras extends into the postmidnight sector. A premidnight clockwise vortex is gradually attenuated or even absent, during the substorm expansion. The substorm current system inferred from the relative positions of the PoACV and the auroral brightening region is in general northeast-southwest aligned, implying a mixture of a meridional current system (MCS) and a zonal system associated with the substorm current wedge (SCW).

*Key words:* Substorm expansion phase, plasma convection, meridional current system.

## 1. Introduction

High-latitude ionospheric plasma convection flows usually undergo dramatic changes and display fundamentally different features during successive stages of a magnetospheric substorm. By using the AMIE algorithm, [8] (referred to as KY94 hereafter) proposed that a new pair of convection vortices appears in the nightside during a substorm expansion phase (EP) in addition to the pre-existing global 2-cell pattern. The new pair of vortices consists of a higher-latitude anticlockwise vortex located mainly in the postmidnight sector, and a lower-latitude clockwise vortex extending from the premidnight to the postmidnight sector. [9] suggested that these vortices are signatures of the unloading component of the auroral electrojet associated with substorm expansion, as opposed to the solar wind directly driven component. One of the most important features of the KY94 model is that the current pattern associated with the two new vortices is characterized by a meridional current system (MCS) as opposed to the more azimuthally-aligned (zonal) system usually related to the substorm current wedge (SCW) geometry [14]. [1] suggested that the substorm current system was dominated by the MCS form. [13] proposed a non-MHD mechanism driving the MCS. For a small substorm event, [11] found that an enhancement of nightside convection and the appearance of a small postmidnight anticlockwise vortex immediately after the first pseudobreakup were signatures of the tail unloading process. In this paper we will present two events to illustrate the dynamic change of ionospheric convection pattern around the midnight sector associated during the substorm EP. In particular, we investigate the different evolution of convection vortices in the pre- and post-midnight sectors after the substorm onset. Possible generation mechanisms of the convection vortices and the associated current system will be discussed. sent two events to illustrate

the dynamic change of ionospheric convection pattern around the midnight sector associated during the substorm EP. In particular, we investigate the different evolution of convection vortices in the pre- and post-midnight sectors after the substorm onset. Possible generation mechanisms of the convection vortices and the associated current system will be discussed.

## 2. Observations

We will use the global potential map procedure [15] to obtain the SuperDARN convection maps. Global optical auroral observations are taken from the IMAGE FUV/WIC imager [5].

### 2.1. February 22, 2001 event

The first interval considered is from 0830-0842 UT on February 22, 2001. The auroral breakup observed by the IMAGE FUV camera was at 0833 UT. This onset time was supported by ground-based magnetometer and also geosynchronous observations (see [12]). A series of the ionospheric plasma convection maps based on SuperDARN radar measurements taken from 0830 UT to 0842 UT are presented in Figure 1. From 0830 to 0832 UT, an interval which marked the end of the substorm growth phase, the large-scale convection pattern in the morning sector was a single convection cell centered at 4.2 MLT. In the postmidnight sector from 0-3 MLT, the flows were dominantly equatorward. At lower latitudes ( $< 70$  MLAT) the flows was in general southeastward and rather weak in magnitude. The postmidnight convection pattern changed substantially from 0832 to 0834 UT, during which time the substorm auroral breakup region was seen in the evening sector around 20.5-22 MLT. Note that the postmidnight flows at this stage started to show evidence of zonal shear; the flows were dominantly westward above 72 MLAT but almost purely eastward at lower latitude. The zonal flow shear continued to develop after the onset, and the eastward auroral flows at about 70 MLAT were considerably enhanced as seen from the next two frames from 0834 to 0838 UT. Finally, at 0838-0840 UT, about 6 minutes after the EP onset, a well-defined anticlockwise convection vortex formed. It is centered at 1.2 MLT and 72.5 MLAT in the postmidnight sector, while the preexisting

Received 16 May 2006.

**J. Liang.** Canadian Space Agency, St-Hubert, Quebec, Canada.

**G. Sofko.** ISAS, Univ. of Saskatchewan, Saskatoon, Canada.

**H. Frey.** Space Sciences Laboratory, University of California, Berkeley, US.

dawn cell is still visible in the early morning sector. At the same time, in the vicinity of the region of brightest auroral emissions at 22.5 MLT, the flows were diverted around the zone of intensified aurora, eastward at higher latitudes and westward at lower latitudes, forming an intruding part of the original dusk cell. This intruding flow reversal region was found to extend into the postmidnight sector. Despite the small number of data points at lower auroral latitudes, there is still evidence that an east-to-west flow reversal at least at about 67 MLAT and 1.2 MLT. Unlike the evening sector, the flow reversal region in the postmidnight sector did not correspond to intense auroral intensification, probably because conditions were unfavorable for the onset of the magnetospheric-ionospheric feedback instability which would have led to auroral brightening [2]. It is important to notice that, the intruding flow reversal region shown in Figure 5e could be equivalently viewed as the lower unloading cell in KY94 model (see Figure 1) that is attached to a background dusk cell seen in previous frames. Thus the overall convection pattern in Figure 5e is consistent with the two unloading cells postulated by KY94. Those convection features persisted during the interval 0840-0842 UT. In this event the focus of the PoACV was 2-3 higher in latitude than and 2.5-3 h MLT to the east of the brightest auroral region around 22.5 MLT (There was also bright aurora around 20 MLT in the dusk sector). During the whole event, there is no evidence of the existence of a premidnight clockwise vortex other than the persisting dusk cell.

### 2.2. December 15, 2001 event

The event was studied in [10] for other research purpose. The substorm EP onset time was determined from the IMAGE FUV/WIC observation, ground magnetometer and LANL geosynchronous observation as 0915 UT. Figure 2 gives a series global convection maps for this event. A well-defined clockwise vortex centered at 750 MLAT, 22 MLT can be identified as early as 0858-0900 UT, 16 minutes prior to the substorm EP onset. Such premidnight clockwise vortex persisted till the end of the growth phase (0912-0914 UT). At 0914-0916 UT, the interval marking the substorm auroral breakup, the premidnight clockwise vortex was significantly enhanced. So far there was not any clear signature of a PoACV, and the convection in postmidnight sector was overall weak in magnitude. At the interval 0918-0920 UT, 4 minutes after the onset, a clear identifiable PoACV centered at 730 MLAT, 2.8 MLT appeared, while the preexisting premidnight vortex clearly attenuated. At 0922-0924 UT, though there was an enhancement of westward flows near the equatorward edge of brightened auroras, which is identified as sub-auroral polarization stream (SAPS) by [10], the flow magnitude directly associated with the premidnight clockwise vortex significantly decreased compared to the onset frame 0914-0916 UT. At 0924-0926 UT, such premidnight vortex became deformed and no longer clearly identifiable. Similar to the first event, there was continuous eastward flow enhancements at the equatorward part of the PoACV in the postmidnight sector, and we notice that, an east-to-west flow reversal, as an intruding part of the dusk convection cell, extend progressively toward postmidnight after substorm onset. At 0924-0926 UT, evidences of such east-to-west flow reversal can be seen as far as 640 MLAT, 4 MLT.

### 3. Discussion

We have studied in detail the evolution of convection vortices in the nightside ionosphere during the substorm EP for two events. In both events we have seen that a postmidnight anticlockwise convection vortex emerge a few minutes after the substorm onset. The foci of the anticlockwise vortices were located at higher latitudes than, and east of, the brightest auroral region. The anticlockwise cell (upward vorticity) implies downward FACs, while the bright optical aurora is usually associated with the precipitating electrons and thus upward FACs. The inferred substorm closure current system showed northeast-to-southwest alignment, and therefore can be resolved into a meridional component and a zonal component, with the latter corresponding to the traditional SCW configuration. Another consistent feature is an east-to west flow reversal region at lower latitudes. It represents a transition from the westward electrojet (eastward flows) in the auroral region to the SAPS-like westward flows near and/or south of the equatorward border of the auroral oval [4][10]. This flow reversal region progressively expands into the postmidnight sector during the substorm EP, which is consistent with the observations that SAPS may extend well into the postmidnight sector during strongly magnetically disturbed periods [7][4]. One of the consequences of this postmidnight intrusion of the flow reversal region is that it becomes closer in longitude to the PoACV located at higher latitude. For example, at 0838-0840 UT in the first event, the east-to-west flow reversal region was visible up to 1.2 MLT, which is roughly the same longitude as the focus of the PoACV. Although the most intense upward FACs in this event are undoubtedly located in the brightest auroral region in the evening sector well to the west of the PoACV, a smaller portion of upward FACs also occurred in the flow reversal region at 67 MLAT in the postmidnight sector. This portion would form a primarily MCS geometry with the PoACV at higher latitude. This result again reveals the coexistence of the meridional and zonal components of the substorm current system. In the first event (and also in all events in [11][12]), there was no signature of a premidnight clockwise vortex other than the dusk cell during the whole event interval. In the second event, however, a premidnight clockwise vortex was present the late growth phase. This premidnight vortex was significantly intensified right at the EP onset frame, but tended to attenuate and deform afterwards. Together with the postmidnight anticlockwise vortex that appeared 4 minutes after the substorm EP onset, the pair of vortices consists the twin-vortex convection system generated by nightside reconnection [3]. The foci of the twin-vortex flows are located at each end of the nightside merging gap. [6] performed an event study to demonstrate the excitation of nightside twin-vortex flow during a substorm EP; the focus of the postmidnight vortex was at 73 MLAT and 1 MLT, which is quite comparable to our results. The sudden enhancement of the premidnight clockwise vortex right at the substorm onset time seems to be consistent with the reconnection-driven scenario. However, the observational fact that such premidnight vortex gradually attenuated and deformed after the substorm onset is not easily explained by the above nightside reconnection-driven mechanism. Also, the strong enhancement of eastward flows at the equatorward part of the PoACV implies the presence of other dynamics associated with the substorm EP process. We believe the en-

hanced eastward flows at auroral latitudes are likely directly related to the substorm-associated process in the central plasma sheet and the dynamo of MCS. The underlying mechanism is not fully understood. [13] proposed a non-MHD mechanism for the earthward magnetospheric electric field which drives the eastward plasma convection and the MCS. [1] suggested a MHD dynamo for the MCS. No matter the actual process driving the MCS, the combination of such process and the nightside reconnection may explain the observed convection feature during substorm EP. If one compares the vorticities expected from the reconnection-driven process and from the MCS configuration (Figure 3a), it is clear that, in the premidnight sector the high-latitude vortices generated by the above two mechanisms have different rotational senses and tend to cancel each other, leading to an attenuation or even absence of the premidnight vortex, while in the postmidnight sector they have the same rotational sense and reinforce each other to form a strong PoACV. The remnant part of the evening reconnection cell concatenates with the lower-latitude MCS cell to form a unified flow region with clockwise convection reversal (Figure 3b).

## References

1. Akasofu, S.-I., A source of auroral electrons and the magnetospheric substorm current systems, *Journal of Geophysical Research*, *108*, 8086, doi:10.1029/2002JA009547, 2003.
2. Atkinson, G., Auroral arcs: Result of the Interaction of a Dynamic Magnetosphere with the Ionosphere, *Journal of Geophysical Research*, *75*, 4746-4755, 1970.
3. Cowley, S. W. H. and M. Lockwood, Excitation and decay of solar wind-driven flows in the magnetosphere-ionosphere system, *Annales Geophysicae*, *10*, 103115, 1992.
4. Foster, J. C., and H. B. Vo, Average characteristics and activity dependence of the subauroral polarization stream, *Journal of Geophysical Research*, *107*, doi: 10.1029/ 2002JA009409, 2002.
5. Frey, H. U., S. B. Mende, V. Angelo-poulos, and E. F. Donovan, Substorm onset observations by IMAGE-FUV, *Journal of Geophysical Research*, *109*, A10304, doi:10.1029/2004JA010607, 2004.
6. Grocott, A., S. W. H. Cowley, J. B. Sigwarth, J. F. Watermann, and T. K. Yeoman, Excitation of twin-vortex flow in the nightside high-latitude ionosphere during an isolated substorm, *Annales Geophysicae*, *20*, 1577-1601, 2002.
7. Huang, C.-S., J. C. Foster, and J. M. Holt, Westward plasma drift in the midlatitude ionospheric F region in the midnight-dawn sector, *Journal of Geophysical Research*, *106*, 30349-30362, 2001.
8. Kamide, Y., A. D. Richmond, B. A. Emery, C. F. Hutchins, B.-H. Ahn, O. de la Beaujardiere, J. C. Foster, R. A. Heelis, H. W. Kroehl, F. J. Rich, and J. A. Slavin, Ground-based studies of ionospheric convection associated with substorm expansion, *Journal of Geophysical Research*, *99*, 19451-19466, 1994.
9. Kamide, Y., and S. Kokubun, Two-component auroral electrojet:Importance for substorm studies, *Journal of Geophysical Research*, *101*, 13027-13046, 1996.
10. Koustov, A. V., R. A. Drayton, R. A. Makarevich, K. A. McWilliams, J.-P. St-Maurice, T. Kikuchi, and H. U. Frey, Observations of high-velocity SAPS-like flows with the King Salmon Super-DARN radar, *Annales Geophysicae*, *24*, in press, 2006.
11. Liang, J., G. J. Sofko, E. F. Donovan, M. Watanabe, and R. A. Greenwald, Convection dynamics and driving mechanism of a small substorm during dominantly IMF By+, Bz+ conditions, *Geophysical Research Letters*, *31*, L08803, doi:10.1029/2003GL018878, 2004.
12. Liang, J., G. J. Sofko, and H. U. Frey, Postmidnight convection dynamics during substorm expansion phase, *Journal of Geophysical Research*, *111*, A04205, doi:10.1029/2005JA011483, 2006.
13. Lui, A. T. Y., and Y. Kamide, A fresh perspective of the substorm current system and its dynamo, *Geophysical Research Letters*, *31*, 1958,doi:10.1029/2003GL017835, 2003.
14. McPherron, R. L., C. T. Russell, and M. Aubry, Satellite studies of magnetospheric substorms on August 15, 1978, 9, Phenomenological model for substorms, *Journal of Geophysical Research*, *78*, 3131-3149, 1973.
15. Ruohoniemi, J. M., and K. B. Baker, Large-scale imaging of high-latitude convection with Super Dual Auroral Radar Network HF radar observations, *Journal of Geophysical Research*, *103*, 20797-20811, 1998.



# An avalanche model of magnetospheric substorms based on cross-scale coupling in the central plasma sheet

W. Liu, P. Charbonneau, E. Donovan, and J. Manuel

**Abstract:** Recent observational evidence has indicated that auroral and ionospheric signatures of substorms exhibit robust scale-free distributions over several decades of size measures. The suggestion that the substorm is a self-organized critical (SOC) phenomenon has hence gained considerable currency. Whereas the SOC concept offers an interesting and potentially fruitful approach in substorm study, it is important that any SOC-based substorm model be based on physics believed to operate in the magnetosphere and also consistent with established substorm phenomenology. In this paper we construct a cellular automaton model of the central plasma sheet; we further propose that substorms are energy avalanches self-organizing in the central plasma sheet so represented. The model has the following key ingredients: global energy transport according to the known physics of large-scale convection, destabilization of an energy-carrying unit (a flux tube) by known plasma instabilities operating in the central plasma sheet (ballooning and/or current-driven), and a physically motivated redistribution rule for the energy released from an unstable site. We make the argument that the behavior of the model is controlled by the boundary condition imposed on the system, and conjecture how different substorm initiation theories can be accommodated and tested in the present theoretical framework.

*Key words:* Complexity, SOC, Cross-Scale Coupling.

## 1. Introduction

Chang [6] speculated the applicability of self-organized criticality to magnetospheric physics. Recent observational evidence has established that the magnetosphere exhibits a range of scale-free distributions suggestive of SOC [9, 23, 32, 33, 10]. It is generally suggested that SOC is a state of dynamical systems significantly removed from a minimum-energy equilibrium; sometimes, the system is referred to as being metastable. Intermittently, global, avalanching instabilities occur in what is called a systemwide discharge. Although the extension of SOC from abstract mathematical models to a multiscale, multispecies magnetized plasma is not trivial, the concept offers a new perspective to look at magnetospheric dynamics, particularly those aspects associated with the onset of magnetospheric substorms.

Bargatze et al. [3] showed that the magnetosphere is a nonlinear system, as its response function to the solar wind depends on the level of activity. Vassiliadis et al. [34] developed a mathematical model of nonlinear filters to explain the observed behavior. Complementary to time-series analysis, intermittencies in the spatiotemporal domain such as the bursty-bulk flows have been interpreted as another manifestation of a magnetosphere in SOC. A related, but not identical observation is due to Borovsky et al. [5] who showed that the current sheet exists in a permanent state of turbulence without a well-ordered velocity.

Although there is no widely accepted definition of SOC in relation to the magnetosphere, many believe that it is different from a mere turbulent state in that a SOC state is capable of a system-wide discharge or avalanche. Chapman et al. [7] constructed a sandpile model to elucidate such behaviors, but the model itself is quite abstract, and its relevance to the actual magnetospheric physics is metaphorical.

One avenue to further advance the SOC model is to couple its universalist perspective with details of magnetospheric physics, that is, to construct magnetospheric models wherein dynamics are globally connected on all scales. Klimas et al. [15, 16] adapted the reduced MHD theory of Lu [20] to the magnetotail and found that an anomalous resistivity following a hysteretic cycle can reproduce a number of intermittent phenomena observed in the magnetosphere, including the power-law distributions suggested by empirical studies.

Although the comparison between the hysteretic MHD and SOC-inspired data analyses has been encouraging, there remains some doubt whether scale-free distributions observed in POLAR auroral images and of geomagnetic indices such as AE can be directly attributed to the hysteretic MHD. Statistically, magnetic reconnection occurs tailward of 20 Re in the magnetotail [25], whereas the auroral substorm expansion typically maps to a distance of 10 Re or less [28]. Bursty bulk flows have been invoked to link the near-Earth neutral line (NENL) to aurora intensification [30], but this proposal is unsettled and controversial. Many researchers support a point of view that posits a different causal relationship.

In this paper we give the essential outline of a model describing multiscale energy transport and release in the central plasma sheet Earthward of 15 Re. Our survey of the literature indicates a near-consensus that releasing excessive energy and mass stored in this region is an essential aspect of substorm expansion. Substorm phenomenology from the beginning has

Received 6 June 2006.

**W. Liu and J. Manuel.** Space Science Branch, Canadian Space Agency.

**P. Charbonneau.** Département de Physique, Université de Montréal  
**E. Donovan.** Department of Physics and Astronomy, University of Calgary

shown that the expansion starts from an equatorward auroral arc and progresses in ways mimicking an avalanche [1]. The current controversy is centered on the question of substorm trigger. Our objective in this paper is to construct a model of energy transport and release, taking into account of the basic physics while taking care to instill into the model a propensity for avalanche. The model admits, in principle, different triggers of energy release and does not have a built-in preference to any. We shall argue that most proposed substorm triggers can set off an avalanche in the confine of the model; which triggering mechanism is dominant depends on how the balance of energy inflow and outflow through this region is affected by boundary conditions in the magnetotail, dayside magnetopause, and ionosphere. In this sense, the proposed model can be used to test various substorm triggering theories in the context of global solar wind-magnetosphere interaction.

## 2. Physics of Energy Transport and Release in the Central Plasma Sheet

It is generally agreed that the substorm is a result of coupling among processes on the global, meso, and microscopic scales. However, relatively few attempts have been made to address quantitatively the cross-scale coupling problem. Part of the problem has to do with the limitation of the prevalent MHD theory; the rest may be attributed to mental inertia - an established point of view takes years to form and a lifetime to abandon. Yet, it has become clear to many that, in order to advance the substorm research, the traditional methodology of correlation, be them event- or statistically based, must be complemented by a mathematically more sophisticated view and methodology so that deeper relationships can be probed and revealed. It is further necessary that borrowed concepts such as SOC not become an end in itself but be a device to help develop higher-level physical models. Our objective in this paper is to couple certain known aspects of magnetospheric physics with several attractive aspects of SOC, in an attempt to form a new perspective of substorm physics.

### 2.1. Global Physics

Our model region spans the part of the equatorial plane that coincides with the central plasma sheet active in the substorm. The plane is divided into a two-dimensional grid, shown in Fig. 1; each grid point represents a magnetic flux tube that crosses the equatorial plane at that point.

The global physics of our model concerns the energy transport through the grid and is described quantitatively by the Rice Convection Model. The energy inflow into the grid is controlled by the outer boundary condition (B1). Energy outflow from the grid, on the other hand, is determined by three factors: A) return flow to the dayside magnetosphere (B2); B) Poynting flux into the ionosphere (B3), and C) Particle injection into the ring current (B4). The balance between B1, B2, B3, and B4 determines the state of the central plasma sheet. Since the magnetosphere is perpetually interacting with the solar wind, none of the boundary conditions is nil at any given time. The claim that the central plasma sheet is in a SOC state implies that the energy sources and sinks controlling the boundaries keep the energy distribution on the grid always near the "boiling point".

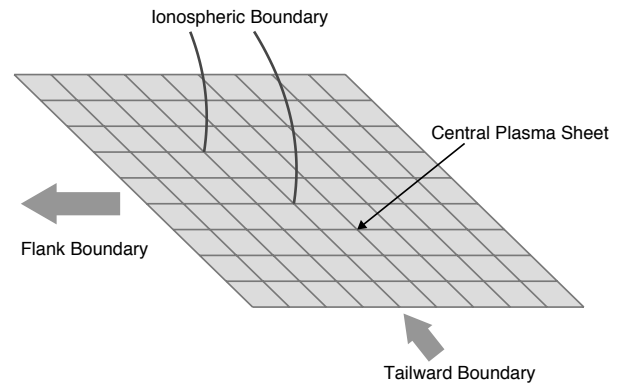


**Fig. 1.** A 2D cellular automaton to model energy avalanches in the central plasma sheet.

While the studies cited in the introduction give some evidence that this might indeed be the case, the proof is not yet conclusive. The model proposed here provides a theoretical means to verify this assertion.

The model depicted in Figure 1 is rich in potential behaviors. Taking the very simplistic view that each of the 4 boundary conditions can have only two modes of variation, up ( $\uparrow$ ) and down ( $\downarrow$ ), one can see that energy accumulation on the grid will exhibit 16 different modes, more than the number of distinct substorm triggering theories!

The latest development of RCM is described by Lemon et al. [17]. In essence, the plasma energy distribution, expressed in terms of the plasma pressure, can be calculated at each grid point, subject to the boundary conditions. An array  $p(i, j, t)$ , as an output of the RCM, gives the internal energy accumulation as a function of time, at the grid point  $(i, j)$ . During the growth phase, convection intensifies, and we can compute in detail how  $p(i, j, t)$  increases with time.

### 2.2. Micro-scale physics

During periods of the growth phase of the substorm (corresponding to an  $\uparrow$  state of B1 in Figure 1), energy increases over the entire grid. Recalling that each grid point represents a flux tube, the energy increases generally leads to a tailward stretching of the flux tube. Because the central plasma sheet is an open system (i.e.,  $Bn \neq 0$ ), this increase of internal energy does not provoke an immediate relaxation to a lower-energy state. As a Gedanken experiment, let us assume only  $B1 \neq 0$  in Figure 1, i.e., energy is accumulated on the grid without sinks. An instability (or substorm) is foreordained in this case. With respect to an individual flux tube, the above situation corresponds to an indefinite stretching, which leads to an indefinite increase of two parameters, the plasma  $\beta$  and the current density  $j$  volume-averaged over the flux tube. Eventually one or both quantities will exceed the threshold of local instability. The  $\beta$ -critical instability belongs to the family of ballooning modes [12, 27, 19] and is generally MHD in character. The  $j$ -critical instability belongs to the family of current-driven modes [21, 22] and is generally non-MHD in character.

Let the threshold values for the above two local criticalities be  $\beta_h$  and  $j_h$ , respectively. Whether  $\beta_h$  or  $j_h$  dominates de-

depends on the detail of the stretching and which instabilities is excited first. It is quite possible that one of the two will dominate some regions on the grid, while the other will dominate the rest; this aspect will be studied in future simulations. An important aspect of plasma instability is its hysteretic nature, a point emphasized by Klimas et al. [15, 16] in regard to the formation of SOC. The hysteresis consists in the high thresholds of onset ( $\beta_h$  and  $j_h$ ) and the lower thresholds of settlement ( $\beta_l$  and  $j_l$ ). A rudimentary example is a mass resting on an inclined plane. Initially, the mass stays stationary even though the plane is raised. This lasts until a high threshold height  $H_h$  at which the static friction is equal to the pull of gravity along the plane. Once the mass starts moving, it will settle on a low threshold  $H_l = 0$ , releasing the potential energy into heat and kinetic energy.

In the present case, the high threshold values can be determined by a detailed analysis of the unstable mode in question. For example, Liu [19] showed that the ballooning mode will become unstable when the threshold  $\beta_h = k_{\parallel}^2 / (\kappa_p \kappa_c)$  is crossed, where  $k_{\parallel}$  is the parallel wavenumber of the perturbation, and  $\kappa_p$  and  $\kappa_c$  are the pressure scale factor and field line curvature, respectively. Similar thresholds can be established for current-driven instabilities. The lower thresholds, on the other hand, are subject to some indeterminacy because they are not instability criteria but some “typical” relaxed states a flux tube is wont to settle in. There are different ways to handle this problem. In the case where the high threshold is much greater than the low threshold, setting the latter to zero is often acceptable. Alternatively, we can adopt a scheme where the system always strives to return to its original state, i.e.,  $\beta_l(i, j) = \beta(i, j, t = 0)$ . We will investigate other possible ways in later studies, but the essential point at present is that, once destabilized a flux tube will release a finite amount of energy proportionate to the difference of the high and low thresholds ( $\beta_h - \beta_l$  or  $j_h - j_l$ ).

### 2.3. Mesoscale Physics

The above discussion established that energy transport on the global scale can drive individual flux tubes to instability and release part of the potential energy stored therein. This has the classical direction of a cascade where inputs from the large-scale end drive small-scale activities. There is also a possibility of a backward propagation, namely, small-scale release causes an avalanche of collapses and a systemwide discharge. This is our main motivation in this paper.

Suppose that, through a local destabilization of a flux tube, a certain quantity of energy  $\propto \Delta\beta = \beta_h - \beta_l$  is released. This energy is propagated in space and perturbs neighboring flux tubes. An essential factor governing the behavior of the cellular automaton in Figure 1 is how the released energy is distributed over the grid.

Without loss of generality, assume that  $\kappa\Delta\beta$  of the released energy goes into the Alfvén mode, which carries the energy to the ionosphere and creates little disturbance to the neighbors. The rest,  $(1 - \kappa)\Delta\beta$ , is in the cross-field propagating compressive mode, and changes the state of neighboring flux tubes; we call this latter release the effective energy. The partition of energy among the shear and compressional mode can be done randomly in each individual case, with a statistical

mean  $\langle \kappa \rangle$ , which can be a global parameter controlling the avalanche.

Since the central plasma sheet is an inhomogeneous medium, a fast-mode wave will experience any combination of reflection, mode-conversion, and absorption. There are two possible ways to write the redistributive rule of the effective energy. In a system that is globally smooth and locally uniform (i.e., one-scale global distribution), the effective energy propagates as classical MHD fast modes. There is a long series of theoretical works dedicated to this subject [8, 31, 11, 18]. The general conclusion from this body of works is that the effective energy will either be spent or escape the system after a distance  $R$  comparable to the scale length of global distributions. In this scenario, the cellular automaton in Figure 1 would be maximally connected. In the alternative possibility that the central plasma sheet is globally smooth and locally granulated (i.e., two-scale distribution, which is consistent with the observation of Borovsky et al. [5]), the effective energy is likely to be dissipated before the fast mode has a chance to travel far. In this case, the cellular automaton would be minimally connected. We believe that the second scenario is more realistic, both because of the extreme implausibility for the central plasma sheet not to have any localized graininess and of the logic of the cellular automaton model: the very fact that a flux tube is treated as an energy storing unit means that two flux tubes are considered different.

## 3. Relationship With Existing Substorm Theories

We stress that our model is not a microscopic substorm triggering theory per se. Rather, it represents a different perspective to view the substorm as a global systemic behavior facilitated by two-way cross-scale coupling. In the forward direction, the enhanced global transport leads to localized release of energy by way of small-scale instabilities. In the backward direction, the localized releases can, under certain conditions, self-organize into an avalanche and trigger a systemwide discharge, namely substorm.

A salient point to emphasize, precedent to any specific computation, is that for fixed energy redistribution rules and global transport physics, the behavior of substorm onset is controlled by the four boundary conditions indicated in Figure 1. In fact, we believe most substorm triggering theories are consistent with at least one way to change the boundary conditions. In this sense, the present model can be used as a quantitative test to arbitrate which possible trigger has the lowest onset threshold, hence becoming *the* trigger, for a given condition. Here we discuss some of the most discussed onset scenarios and substorm features to establish a context for future numerical studies.

### 3.1. “Internally Driven” Onset: $|B1| > |B2| + |B3| + |B4|$

This corresponds roughly to the situation where the IMF persists in the southward direction, and the energy inflow from the tail exceeds the combined outflow for a sufficiently long time so that the overall energy distribution on the grid is driven to the critical avalanche point. The term “internally driven” suggests that the onset is independent of a reconnection-related trigger and that the onset is owing to an instability (either  $\beta$ - or

$j$ -critical) internal to the region of energy storage. The likely path to this instability is that a localized region of the central plasma sheet goes unstable, and the instability avalanches in space, as the effective energy releases set off a chain reaction.

### 3.2. BBF Onset: |B1| = Output of Hysteretic MHD Module

While we believe that the hysteretic MHD model of Klimas et al. [15, 16] is not spatially conjugate to dominant auroral substorm features, it is possible, however, to connect the model to SOC-like behavior in auroral substorms by way of bursty bulk flows as described by Shiokawa et al. [30]. Effectively, it is asserted that bursty-bulk flows from intermittent and spatially localized reconnections in the midtail inject large quantities of mass and flux to the central plasma sheet; the slowdown of the BBFs results in a reduction of cross-tail current. In our present model, we can use the output of the hysteretic MHD, which exhibits intermittent behavior reminiscent of BBF, as B1. As the BBFs interact with the internal grid points (flux tubes), an avalanche may result.

### 3.3. Northward IMF Trigger: $\partial|B2|/\partial t < 0$

Lyons et al. [24] argued that a northward trending of the IMF precedes many substorms, and suggested that the substorm is essentially a solar-wind triggered event. This possibility can be incorporated into the present model. As the IMF turns northward, the return flow to the dayside is temporarily suppressed. During this interval, the net energy accumulation on the grid increases, and an avalanche again may result.

### 3.4. Ionospheric Trigger: $\partial|B3|/\partial t < 0$

Some authors (see eg., [14]) suggested that the ionosphere can play a role in triggering a substorm. The basic idea is that during periods of enhanced magnetospheric convection, the increase in the ionospheric conductance can result in a positive feedback, which has the sense to disrupt the near-Earth current sheet. In our present model, an increase in ionospheric conductivity will temporarily reduce the Joule heating rate for a given magnetospheric current (i.e.,  $\propto J^2/\Sigma$ ). Choking off the ionospheric channel of outflow will lead to an enhanced energy accumulation on the grid.

### 3.5. SMC and Sawtooth events: $\langle B1 \rangle = \langle B2 + B3 + B4 \rangle$

Steady magnetospheric convection (SMC) [29] refers to a period of prolonged southward IMF (several hours) during which no substorm expansion is observed. Rather, the convection is more intense and moves to more equatorward latitudes. The sawtooth events corresponds roughly to the same solar wind condition, but the magnetosphere is marked by a periodic oscillation of injected particle fluxes (see eg. [13]). Many associate sawtooth events with quasi-periodic recurrence of substorms. Since the solar wind driver is the same for the two classes, it is not illogical to suppose that they are two solutions of the same problem, under different boundary conditions. We propose that SMC and sawtooth events correspond to a condition where the energy inflow and outflow on the grid are balanced

in a time-averaged sense. The phasing among the four conditions, however, determines whether the solution on the grid is steady-state or quasiperiodic.

The above discussion is not exhaustive, only to underscore our principal argument that the route to substorm is not a one-lane highway, but a manifold of possibilities. The chief controlling factor is the boundary conditions governing energy inflow and outflow out of the expansion onset region, the central plasma sheet. Some of the phenomena such as pseudo-breakup, poleward boundary intensification, and the boundary-layer model [26] can all be incorporated as part of the model, with proper adjustment of the boundary conditions.

We remind the reader that some of our descriptions of the path to avalanche is different from the view originally associated with a particular boundary-condition trigger. For example, the ionospheric trigger theory of Kan et al. [14] involves more than just choking off energy outflow to the ionosphere. A more accurate characterization is a redistribution of energy flow pattern so that the ionosphere actually sends an inflowing flux (reflected Alfvén waves) to trigger the substorm in the central plasma sheet.

## 4. Summary

We have developed a model whereby energy transport and release in the central plasma sheet can be studied as a cellular automaton problem. We have focused on the conceptual aspect of the development, leaving a number of details and the numerical implementation to the future. We believe that the conceptual underpinning of the model represents a potentially new and fruitful approach to substorm research and warrants a report in this proceeding, notwithstanding a certain lack of details.

We believe that recent evidence and theoretical argument for self-organized criticality in the magnetosphere are not merely an importation of faddish terms from another field but reveal a deep order in what is now commonly accepted as a very nonlinear magnetosphere; the substorm problem, as a “going concern”, can be most profitably studied by treating the magnetosphere holistically. According to this dictum, our model is guided by the following principles:

1. The substorm problem must be studied by treating the entire region implicated in the process as a whole;
2. We subscribe to the view that most of the energy release during a substorm takes place in the central plasma sheet, and that, based on statistical evidence, reconnection is not directly involved in tapping the free energy stored in this region;
3. Partly in response to the recent evidence suggestive of a magnetosphere in SOC, we develop the model with a view to a potential for avalanche behavior;
4. We believe, despite the opinion which the elephant may hold of the blind man, the latter has gotten a part of the elephant that is real. In other words, a “higher-level” substorm theory should ideally be “backward-adaptable” to accommodate more elemental theories, unless there are good reasons not to include some.

The conceptual model developed in this paper has the following principal features:

1. Magnetic flux tubes in the central plasma sheet are treated as the unit of energy storage, and a cellular automaton comprised of the equator-crossing points of the flux tubes form the basis of our model;
2. The model is driven by known magnetospheric physics on the global, meso, and microscale;
3. Energy deposit on each grid point (flux tube) is determined quantitatively by the Rice Convection Model or an equivalent computational model;
4. Each flux tube has an energy-containing threshold above which a localized energy release takes place;
5. The local release is hysteretic, whereby the flux tube settles on to an energy state lower than the threshold; the threshold physics depends on the nature of the instability incorporated; both MHD (ballooning-type) and non-MHD (current-driven type) can be included;
6. Grid points near a local release are coupled through a redistributive rule, whose exact form depends on the assumption of propagation physics of waves in the magnetosphere. We favor a minimally-connected grid, on the assumption that the central plasma sheet is grainy on a local scale, but will consider redistributive rules with longer-range connections;
7. The behavior of the cellular automaton is determined by four boundary conditions: a) the energy inflow into the grid from the tailward boundary; b) the energy outflow through the flanks to the dayside magnetosphere; c) the energy outflow into the ionosphere; and d) the energy outflow through the inner edge of the plasma sheet into the ring current; we believe that the balance of energy flows at the boundary determines whether or how a substorm as a global avalanche will occur, and which substorm trigger mechanism prevails.

We discussed some examples how the model can be triggered to produce substorms by boundary condition changes. It appears that the model is general enough to accommodate different trigger theories proposed in the past and, more importantly, provide a quantitative means to test under which condition(s) each can set off energy avalanches in the central plasma sheet.

As a moral of sort, self-organized criticality offers a new perspective to studying magnetospheric physics in a rather profound way: The magnetosphere is an open system subject to changing energy fluxes across its boundary. In contrast to the classical energy principle analysis appropriate for closed systems, the substorm problem is controlled by the balance of energy flows into and out of the system, not free energy measured against a global minimum. Although this point may sound obvious, it is not universally realized; SOC and sandpile models provide an initial glimpse to how a changed perspective can lead to new insights and a drastic departure from established expectations.

## Acknowledgements

The authors thank V. Uritsky, A. T. Y. Lui, and A. Crouch for illuminating discussions. This work was supported by the Canadian Space Agency and Natural Sciences and Engineering Research Council of Canada.

## References

1. Akasofu, S.-I., The development of the auroral substorm, *Planet. Space Sci.*, *12*, 273, 1964.
2. Angelopoulos, V., W. Baumjohann, C. F. Kennel, F. V. Coroniti, M. G. Kivelson, R. Pellat, R. J. Walker, H. Luhr, and G. Paschmann, Bursty bulk flows in the inner central plasma sheet, *J. Geophys. Res.*, *97*, 4027, 1992.
3. Bargatze, L. F., D. N. Baker, R. L. McPherron, and E. W. Hones, Jr., Magnetospheric impulse-response for many levels of geomagnetic activity, *J. Geophys. Res.*, *90*, 6387, 1985.
4. Baumjohann, W., G. Paschmann, and H. Luhr, Characteristics of high-speed ion flows in the plasma sheet, *J. Geophys. Res.*, *95*, 3801, 1990.
5. Borovsky, J. E., R. C. Elphic, H. O. Funsten, and M. F. Thomsen, The Earth's plasma sheet as a laboratory for flow turbulence in high-beta MHD, *J. Plasma Phys.*, *57*, 1-34, 1997.
6. Chang, T., Low-dimensional behavior and symmetry-breaking of stochastic systems near criticality: Can these effects be observed in space and in the laboratory, *IEEE Trans. Plasma Sci.*, *20*, 691, 1992.
7. Chapman, S. C., N. W. Watkins, R. O. Dendy, P. Herlander, and G. Rowlands, A simple avalanche model as an analogue for magnetospheric activity, *Geophys. Res. Lett.*, *25*, 2397, 1998.
8. Chen, L., and A. Hasegawa, A theory of long-period magnetic pulsations, 1: Steady-state excitation of field-line resonances, *J. Geophys. Res.*, *79*, 1024, 1974.
9. Consolini, G., Sandpile cellular automata and magnetospheric dynamics, in *Cosmic Physics in the Year 2000*, edited by S. AIELLO et al., p. 123, Soc. Ital. Di Fis, Bologna, Italy, 1997.
10. Freeman, M. P., and N. W. Watkins, The heavens in a pile of sand, *Science*, *298*, 979, 2002.
11. Goertz, C. K., and R. A. Smith, The thermal catastrophe model of substorms, *J. Geophys. Res.*, *94*, 6581, 1989.
12. Hameiri, E., P. Laurent, and M. Mond, The ballooning instability in space plasmas, *J. Geophys. Res.*, *96*, 1513, 1991.
13. Henderson, M. G., The May 2-3, 1986 CDAW-9C interval, A sawtooth event, *Geophys. Res. Lett.*, *31*, L11804, doi:10.1029/2004GL019941, 2004.
14. Kan, J. R., L. Zhu, and S.-I. Akasofu, A theory of substorms, Onset and subsidence, *J. Geophys. Res.*, *93*, 5624, 1988.
15. Klimas, A. J., J. A. Valdivia, D. Vassiliadis, D. N. Baker, M. Hesse, and J. Takalo, Self-organized criticality in the substorm phenomenon and its relation to localized reconnection in the magnetospheric plasma sheet, *J. Geophys. Res.*, *105*, 18765, 2000.
16. Klimas, A. J., V. M. Uritsky, D. Vassiliadis, and D. N. Baker, Reconnection and scale-free avalanching in a driven current sheet model, *J. Geophys. Res.*, *109*, A02218, doi:10.1029/2003JA010036, 2004.
17. Lemon, C., R. A. Wolf, T. W. Hill, S. Sazykin, R. W. Spiro, F. R. Toffoletto, J. Birn, and M. Hesse, Magnetic storm ring current injection modeled with Rice Convection Model and a

- self-consistent magnetic field, *Geophys. Res. Lett.*, *31*, L21801, doi:10.1029/2004GL020914, 2004.
18. Liu, W. W., B. L. Xu, J. C. Samson, and G. Rostoker, Theory and observation of auroral substorms: A magnetohydrodynamic approach, *J. Geophys. Res.*, *100*, 79, 1995.
  19. Liu, W. W., Physics of the explosive growth phase: Ballooning instability revisited, *J. Geophys. Res.*, *102*, 4927, 1997.
  20. Lu, E. T., Avalanche in continuum driven dissipative systems, *Phys. Rev. Lett.*, *74*, 2511, 1995.
  21. Lui, A. T. Y., A. Mankovsky, C. L. Chang, K. Papadopoulos, and C. S. Wu, A current disruption mechanism in the neutral sheet - a possible trigger for substorm expansion, *Geophys. Res. Lett.*, *17*, 745, 1990.
  22. Lui, A. T. Y., T. Chang, and P. H. Yoon, Preliminary nonlocal analysis of cross-field current instability for substorm expansion onset, *J. Geophys. Res.*, *100*, 19147, 1995.
  23. Lui, A. T. Y., S. C. Chapman, K. Liou, P. T. Newell, C. I. Meng, M. Brittacher, and G. K. Parks, Is the dynamic magnetosphere an avalanching system, *Geophys. Res. Lett.*, *27*, 911, 2000.
  24. Lyons, L. T., G. T. Blanchard, J. C. Samson, R. P. Lepping, T. Yamamoto, and T. Moretto, Coordinated observation demonstrating external substorm triggering, *J. Geophys. Res.*, *102*, 27039, 1997.
  25. Nagai, T., M. Fujimoto, Y. Saito, S. Machida, T. Terasawa, R. Nakamura, T. Yamamoto, T. Mukai, A. Nishida, and S. Kokubun, Structure and dynamics of magnetic reconnection for substorm onsets with Geotail observations, *J. Geophys. Res.*, *103*, 4419, 1998.
  26. Rostoker, G. and T. Eastman, A boundary layer model for magnetospheric substorms, *J. Geophys. Res.*, *92*, 12187, 1987.
  27. Roux, A., S. Perrault, P. Robert, A. Morane, A. Pedersen, A. Korth, G. Kremser, B. Aparicio, and R. Pellinen, Plasma sheet instability related to the westward traveling surge, *J. Geophys. Res.*, *96*, 17697, 1991.
  28. Samson, J. C., Samson, L. R. Lyons, P. T. Newell, F. Creutzberg, and B. Xu, Proton aurora and substorm intensifications, *Geophys. Res. Lett.*, *19*, 2167, 1992.
  29. Sergeev, V. A., On the state of the magnetosphere during prolonged southward oriented IMF, *Phys. Solarterr.*, *5*, 39, 1977.
  30. Shiokawa, K., W. Baumjohann, G. Harendel, G. Paschmann, J. F. Fennel, E. Friis-Christensen, H. Luhr, G. D. Reeves, C. T. Russell, P. R. Sutcliffe, and K. Takahashi, High-speed ion flow, substorm current wedge, and multiple Pi 2 pulsations, *J. Geophys. Res.*, *103*, 4491, 1998.
  31. Southwood, D. J., Some features of field-line resonances in the magnetosphere, *Planet. Space Sci.*, *22*, 483, 1974.
  32. Uritsky, V. M., A. J. Klimas, and D. Vassiliadis, Comparative study of dynamical critical scaling in the auroral electrojet index versus solar wind fluctuations, *Geophys. Res. Lett.*, *28*, 3809, 2001.
  33. Uritsky, V. M. A. J. Klimas, D. Vassiliadis, D. Chua, and G. Parks, Scale-free statistics of spatiotemporal auroral emissions as depicted by POLAR UVI images: Dynamic magnetosphere is an avalanching system, *J. Geophys. Res.*, *107*, 1426, doi:10.1029/2001JA000281, 2002.
  34. Vassiliadis, D. A. J. Klimas, D. N. Baker, and D. A. Roberts, A description of the solar-wind magnetosphere coupling based on nonlinear filters, *J. Geophys. Res.*, *100*, 3495, 1995.

# The active plasma sheet: definition of 'events' and statistical analysis

P. Louarn, C. Jacquey, E. Budnik, and V. Génot, the CDPP, FGM, CIS and STAFF teams

**Abstract:** A statistical analysis of the plasma sheet activity is performed from CLUSTER observations (years 2001 to 2004). Different types of 'events' are defined by using the plasma flow velocity (V-events), the low frequency magnetic fluctuations (B-events), and the spectral density of higher frequency waves (HF-events). They are selected by an automatic procedure from 2 criteria: a lower threshold for the fluctuations and a minimal duration for each events. The V-events correspond to the usual 'BBF'. The three types of 'events' form an homogenous set, their number (20 to 50 for each Cluster 'tail' season, depending on the selection criteria) and their total duration (5-10% of the time spent by CLUSTER in the sheet) being comparable. 'Events' of different types are positively correlated with percentages of common detection reaching 50%. They are also organized in bunches that characterize local active states in the plasma sheet. However, these active states do not present a one-to-one relationship with substorms or auroral activations. Analysing how the number of 'events' varies with the selection criteria, it is concluded that the B-events saturate at 2-4 nT and have a rather long duration (more than 1-2 minutes) when HF-events are more likely bursty and intense since their number significantly increases for duration smaller than 1 minute. In average, B-events and HF-events begin before V-events. We cannot conclude on a cause-to-effect relationship between 'events', nevertheless, the study shows that the three types of 'events' are likely related to the same basic physical phenomena. They could be fundamental elements of the plasma sheet turbulence.

## 1. Introduction

A significant feature of the Earth's plasma sheet is the presence of large fluctuations in the magnetic field, in the flow velocity and, in the spectral density of high frequency waves, with timescales ranging from seconds to minutes. This defines a 'turbulence' that characterizes the 'active' plasma sheet. Its description and the analysis of its relationships with heating and acceleration processes are of paramount importance for understanding the magnetospheric activity in general, and more specifically the magnetospheric 'substorms' and their consequences.

The investigation of the plasma sheet turbulence is a vast program. One may concentrate on the analysis of field fluctuations, as it was done using the Geotail and AMPTE/IRM spacecraft by ([11], [8], [7], [4], [5]) and, more recently CLUSTER ([15], [12], [10], [16]). The main objective of these studies is to compare models of the turbulence (intermittency or multi-fractals) and various generation mechanisms of the fluctuations with the observations. Fluctuations in the flow velocity - the bursty bulk flows (BBF) - are other manifestations of 'activity'. They have been studied into details given their possible associations with sporadic magnetic dissipations and their role in the plasma convection (for example: [3], [1], [14]).

These studies demonstrate that the plasma sheet 'activity' is a multi-form phenomena. As seen locally by a spacecraft, the plasma sheet is not in a permanent 'turbulent' state for hours. 'Calm' and 'active' periods alternate, the durations of active periods ranging from a few minutes to a few 10 minutes. Furthermore, as discussed in the present paper, active periods are often a succession of 'events' lasting a few 10 s or minutes

during which the fluctuations of a given parameter are particularly large. If the active periods corresponds to global energy releases in the plasma sheet then the 'events' would be the fundamental elements that organize the energetic processes. In many respects, BBF's are archetypical 'events' defined from the flow velocity. The notion of 'events' can also be extended to other physical quantities (magnetic fluctuations, high frequency waves, temperature, pressure...) which will modify the definition of 'activity'. It is then interesting to study the 'activity' resulting from the choice of different kinds of 'events', to make the statistical analysis of their occurrence and, to investigate their possible relationships. Surprisingly, this was rarely made in a systematic way.

For the present investigation, we define 'events' from 4 parameters: (1) the flow velocity (which corresponds to BBF), (2) the amplitude of the low frequency magnetic fluctuations, (3) the spectral density of 'high frequency' waves (1-10 Hz) and, (4) the thickness of the sheet. This corresponds to 4 different classes of 'events'. We then make statistics on the resulting sets of 'events': How often are they observed? What is their cumulative duration? What does it mean in terms of proportion of time spent by spacecraft in the plasma sheet? The study of their correlations is also interesting. Do they occur together? Are there classes of 'events' that statistically occur before other, so that a cause-to-effect relationship could be established between them? In particular, we will investigate the relationship between BBF's and 'events' defined from magnetic fluctuations and waves.

The selection of 'events' is hard from the simple visual inspection of the data. The visual method introduces subjectivity and restricts the analysis to a limited number of criteria for the selection. To solve this methodological difficulty, we use the facilities given by the CDPP (Centre de Données de la Physique des Plasmas, a plasma physics data centre result-

Received 26 June 2006.

P. Louarn, C. Jacquey, E. Budnik, and V. Génot, the CDPP, FGM, CIS and STAFF teams. CNRS/CESR, Toulouse, France

ing from a French national program) to investigate CLUSTER data. We consider a large data set corresponding to CLUSTER 'tail' seasons, from 2001 to 2004. Each of them lasts  $\sim 3$  months and corresponds to orbits with apogee in the magnetotail. We further choose crossings at  $-10 \text{ Re} < Y_{gsm} < 10 \text{ Re}$ . The measurements are performed by 3 different instruments (FGM [2], CIS [13] and STAFF [6]) on the 4 CLUSTER spacecraft.

## 2. Data and Methods

To illustrate the selection of 'events', the measurements performed during a long crossing of the plasma sheet, with a succession of 'active' and 'calm' periods are presented in Figure 1 (14-15th September 2001, from 2245 UT to 0630 UT). We show the  $B_x$  magnetic field measured by the 4 spacecraft (panel 1, from the top), the  $V_x$  component of the plasma flow measured by SC1 and 3 (panel 3) and, the spectral density of the magnetic fluctuations in the range 1-10 Hz (panel 5). GSM coordinates are used. From the 4 spacecraft measurements, we compute the magnetic field gradient. We then deduce the typical thickness of the sheet as the ratio between the magnetic field in the lobe - assuming pressure balance - and the magnetic gradient.

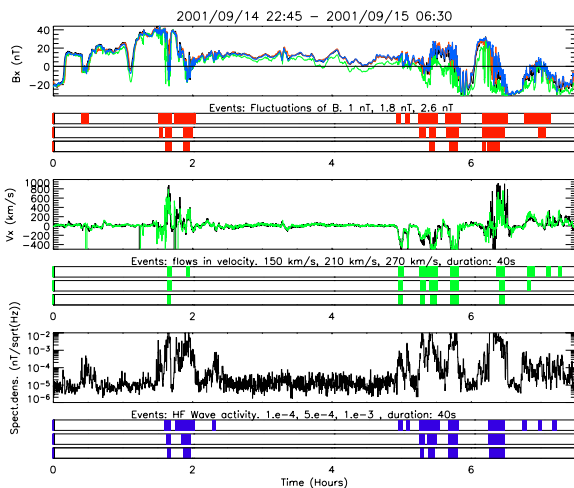


**Fig. 1.** Example of plasma sheet crossing and selection of events. From top to bottom (panel 1 to 6),  $B_x$  magnetic component and selected B-events,  $V_x$  flow and selected V-events, high frequency spectral density and HF-events.

Multiple signs of 'activity' are observed in Figure 1: (1) large magnetic fluctuations with periods ranging from a few seconds to several minutes, (2) flows with positive and negative  $V_x$  larger than 100 km/s and, (3) time intervals corresponding to large spectral density of waves. These manifestations of 'activity' are also associated with variations of the total pressure, of the thickness, and the current of the sheet (not shown here). The observation of this strong activity is not surprising since two substorms or auroral activations have occurred during this time period, at 2353 UT on day 14/09 ( $t = 1:10$ , in the

Figure) and 0412 UT on day 15/09 ( $t = 5:30$ ) ([9], from IMAGE data). The last case is related to the most active time period.

Using colour bars, we also indicate the selected 'events'. From the amplitude of the low frequency magnetic fluctuations we define 'B-events' (red bars in panel 2), from the plasma flows we define 'V-events' (green bars in panel 4), and from the wave spectral density 'HF-events' (blue bars in panel 6). An 'event' can be defined by two parameters. It corresponds to a time interval of minimal duration ( $T_a$ ) during which a given parameter - indicated by the subscript 'a' - is larger than a threshold ( $S_a$ ). For example, by considering  $S_v = 100 \text{ km/s}$  and  $T_v = 60 \text{ s}$ , we can select 'V-events' as time intervals longer than 60 s during which the flow velocity is permanently larger than 100 km/s. The definition of 'B-events' is more complex. As seen in Figure 1, discrete and variable frequencies seem to dominate the low frequency magnetic fluctuations for given time intervals. This type of signal is better analysed by a wavelet than a Fourier transform. We thus perform a wavelet analysis of the magnetic field and then take into account 3 parameters for defining 'B-events': a threshold for the amplitude of the fluctuations ( $S_b$ ), a minimal duration for the 'events' ( $T_b$ ) and an upper value for the periods of the fluctuations ( $P_b$ ). A 'B-events' is thus a time intervals of minimal duration  $T_b$  during which wavelet-like fluctuations with periods smaller than  $P_b$  reach amplitude larger than  $S_b$ . We choose  $P_b = 30 \text{ s}$  for the present study. Of course, this choice must be consistent with the minimal duration of the B-events:  $P_b$  must be smaller than  $T_b$ . Given their respective frequency ranges and the polarisation, B-events rather correspond to MHD compressional fluctuations when HF-events take into account fluctuations close to the ion gyrofrequency. They are thus related to different types of plasma/wave interactions.

The 'events' shown in Figure 1 have been selected with  $T_a = 40 \text{ s}$ . We use different thresholds: 1.0, 1.8 and 2.6 nT for the magnetic fluctuations, 150, 210 and 270 km/s for the flows, 0.1, 0.5 and 1  $\text{pT}/\text{Hz}^{1/2}$  for the spectral density. The selection is made by considering the maximum values seen by any of the 4 spacecraft. For 'V-events', we also impose that the magnetic/total pressure ratio is smaller than 0.5. 'V-events' actually correspond to flows in the central plasma sheet and are equivalent to BBF's.

A detailed analysis of Figure 1 reveals that the procedure adequately selects 'events' from the different data sets. Given the apparent simplicity of the variations of the wave spectral density and of the flow velocity, the identification of 'HF-events' and 'V-events' seem straightforward, the latter clearly corresponding to BBF's. Conversely, the selection of 'B-events' would be impossible from a simple visual inspection. It is interesting to note how accurate is the procedure based on the wavelet analysis. A careful inspection of the period 5:00-6:30 shows that 'B-events' actually correspond to precise time intervals during which, intuitively, the dominant component of the fluctuations has changed in amplitude or period so that fluctuations with periods smaller than 30 s become large.

The procedure of selection leads to comparable sets of 'events'. This concerns the number of events, their individual as well as their total duration. This important point will be more discussed in next sections. It is not as natural as it could look like and indicate that the different type of 'events' are likely related to the same basic physical phenomena.

### 3. Application to complete 'tail' season

Figure 2 is a general view of 'events' selected during several crossings of the plasma sheet. We consider here the 2002 tail season. The crossings are organized by frames corresponding to 10 hours of observations. For reason of readability, seven over more than thirty recorded crossings are shown. The colour code is the same as in Figure 1 (red: 'B-events', green: 'V-events', blue: 'HF-events'). The minimal duration of events is 40s and the thresholds are: 1.5 nT, 150 km/s and 0.6 pT/Hz<sup>1/2</sup>. The yellow bars indicate the periods during which at least one of the spacecraft measures a thermal/total pressure ratio larger than 0.5, which means that it is located in the internal part of the plasma sheet. By overlying the yellow bar by a dark blue one, we further indicate the periods of 'thin' plasma sheet, with a half thickness smaller than 0.45 Re. We choose examples of 'active' plasma sheet (21/08, 28/08, 18/09), cases with sparse detections of events (13/08, 18/08), and examples of 'calm' plasma sheet (25/08, 13/09).

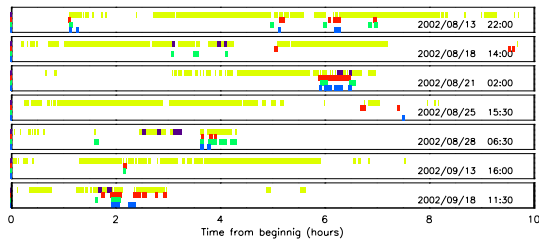


**Fig. 2.** Global view of selected events during 7 crossing of the plasma sheet. Yellow: presence of CLUSTER in the internal sheet, Red: B-events, Green: V-events and, Blue: HF-events.

As seen in Figure 2, the 'events' generally occur in bunches and present a rather clear positive correlation. This defines periods of 'activity' with typical duration of a few 10 minutes. Nevertheless, none of the periods of 'activity' shown here corresponds to a substorm onset listed by [9]. According to this list, auroral activations or substorms do occur at the days presented in the Figure, in particular on 21/08 or 18/09, by not while CLUSTER was in the plasma sheet. However, when CLUSTER is in the plasma sheet during a recorded substorm, we check that 'events' are actually detected. It is the case of the day 15/09/2001 shown in Figure 1, precisely when a strong activity is observed. Let us also note that there is no clear relationship between the observation of a thin plasma sheet and 'events'. On day 21/08, a thin plasma sheet is observed during the activity, on 18/09 and 28/08, a thin plasma sheet is observed well before the activity.

Table 1 summarizes the statistical study of the different types of 'events' selected during the 2001-2004 'tail' seasons as Cluster was at  $-10 \text{ Re} < Y_{gsm} < 10 \text{ Re}$ . They are selected using the same thresholds as for Figure 2. The cumulated duration for each type of 'events' is indicated in hours. We also indicate the number of selected events ('e' in parenthesis). We define common events (B/V, B/HF and V/HF), see next section. The cumulated duration of the common events and the corresponding

**Table 1.** Statistics of events performed from 2001 to 2004.

'sheet' corresponds to magnetic/total pressure ratio smaller than 0.5, and 'thickness' to an observed sheet thinner than 0.45 Re. 'B', 'V', 'HF'... corresponds to the type of 'events'.

	2001	2002	2003	2004
sheet	59.93	59.5	40.72	36.7
thickness	3.45	1.02	1.06	0.71
V	3.34 (38e)	2.9 (35e)	1.72 (21e)	0.84 (13e)
HF	2.95 (37e)	2 (26e)	1.96 (30e)	2.62 (21e)
B	6.41 (57e)	3.27 (40e)	1.74 (18e)	1.54 (18e)
B/V	1.74 (26%)	0.7 (21%)	0.59 (34%)	0.59 (38%)
B/HF	2.3 (35%)	1.1 (34%)	0.55 (31%)	0.63 (41%)
V/HF	1.15 (18%)	0.7 (21%)	0.78 (45%)	0.5 (32%)

proportion with respect to the total duration (% in parenthesis) are given.

The total time spent by CLUSTER in the plasma sheet is  $\sim 60$  hours in 2001 and 2002 and  $\sim 40$  hours in 2003 and 2004. We interpret this difference by the fact that the spacecraft are closer each to the others in 2003 and 2004 which decreases the probability to have at least one of them in the sheet. In average, events are detected during  $\sim 3-5\%$  of the total time spent in the plasma sheet, meaning a cumulated duration of  $\sim 1.5-3$  hours. The number of events varies from 13 (V-events in 2004) to 57 (B-events in 2001). One may consider that B-events are particularly frequent in 2001 and, conversely V-events are rare in 2004. In general, the plasma sheet seems to become less and less active from 2001 to 2004. Note also that the total time spent in a thin current sheet is more than three times longer during 2001 than during the other years. This certainly has to be related to a decrease of the solar activity from 2001.

The common time between different types of events (B/V, B/HF, V/HF) varies from 0.5 to 2 hours, which represent 20 to 35% of the total duration of the events. There are some exceptions (45% for V/HF events in 2003) that will deserve a more careful examination. All these percentages are larger than what would be expected from a random occurrence of the events. This confirms that events of different types generally do not occur independently and are thus likely related to the same underlying physical process.

### 4. Parametric study of the occurrence of 'events'

The use of an automatic procedure for the selection of 'events' has also the advantage to make easy modifications of their definition and their selection parameters. The contour plots shown in Figure 3 present the total duration of the events as a function of the thresholds ( $S_a$ ) and of the minimal duration of each events ( $T_a$ ). In addition of B,V and HF events, we consider 'thickness-events' corresponding to time intervals during which the plasma sheet is thinner than a given threshold. The values of the parameters of selection are chosen in such a way that the total duration of the events varies in the same range, from nearly 0 for severe constraints to typically 5-6 hours.

These plots help to understand how the different events are organized. Considering B-events, one may note that the contour levels are almost perpendicular to the axis representing

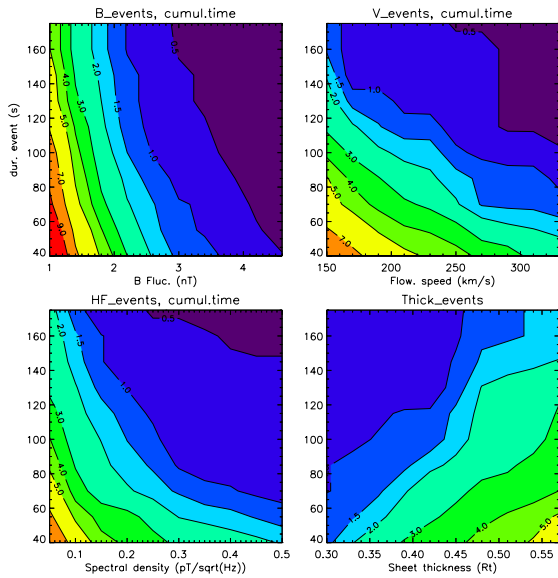


**Fig. 3.** Parametric study of the total duration of the events. Only 2001 events are considered. Both the minimal duration and the threshold vary.

the amplitude of fluctuations. The important parameter for the selection of B-events is thus the amplitude and not the minimal duration of the events. This means that B-events are rather organized in long time intervals with typical duration of a few minutes. The possible existence of a saturation effect is not excluded: when the thresholds is increased from 1.5 nT to 4 nT, the total duration of B-events decreases by almost one order of magnitude and becomes smaller than 0.5 hour. This demonstrates that the amplitude of the fluctuations with periods smaller than 30s hardly reaches 10-20% of the magnetic field in the lobes. HF-events show an interesting contrasted organisation. For events longer than  $\sim 100$  s, the amplitude is again the most efficient criteria of selection. Conversely, when short events are taken into account ( $T < 80$ s), the minimal duration becomes a strong criteria of selection. The total duration of HF-events decreases by a factor of  $\sim 3$  from  $T=40$  s to  $T=80$  s. HF-events thus tend to be organized in short intense bursts. V-events are equally well organized by their minimal duration or the threshold of velocity. Finally, let us note that the minimum duration is a rather efficient discriminating criteria for the selection of 'thickness-events'. This would mean that the thickness of the sheet significantly varies on short time intervals, with typical duration of 40-80 s. A more detailed analysis is needed to understand the causes and the consequences of this variability.

## 5. Association between events and possible cause-to-effect relationships

After studying separately the different types of 'events', we now analyse their relationships. Three plots presenting the percentage of common B/V, B/HF and V/HF events are shown in Figure 4. To obtain these percentages, we consider the time intervals corresponding to events of a given type (B-events, for example) and we calculate how often events of another type (V-events or HF-events) are detected during the same time intervals. The results is then normalized to the total number of events.

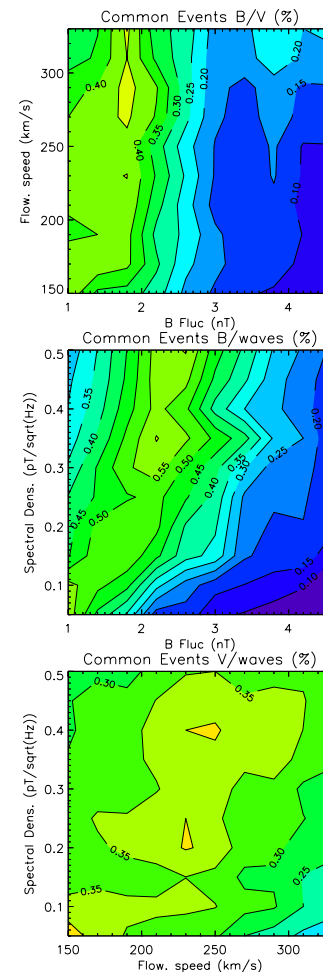


**Fig. 4.** Analysis of the commonality between the different types of events. It is expressed as the number of common events, normalized to the total number of events. Plot 1 to 3 from top to bottom

Considering B/V-events, the best correlation ( $\sim 50\%$ ) is obtained for fluctuations with amplitude 2 nT and flows above 250 km/s. The correlation between large fluctuations and slow flows (below 250 km/s) is negligible. However, this correlation seems to increase when larger flow velocities are considered (velocity larger than 300 km/s). It will be interesting to check if the correlation further increases when extreme V and B-events are considered. We note that B-events and HF-events

are closely related: as the amplitude of the MHD fluctuations increases, the maximum correlation is obtained for larger spectral density of the high frequency waves. In some way, there is thus a relationship between the level of compressible MHD fluctuations (B-events) and the turbulence at kinetic scale (HF-events). The V/Wave correlation present a maximum for flow speeds in the 200-250 km/s range. One notes that the maximum correlation is obtained for higher spectral density as the flow speed increases. The sharp local maximum that appears on the plots are not significant.

In terms of possible cause-to-effect relationship, we conclude from plot 1 that, if we make the hypothesis that flows trigger magnetic fluctuations, then flows below 300 km/s cannot trigger magnetic fluctuation larger than 2-3 nT. In reverse, if magnetic fluctuations generate flows, then there is no clear relationship between the amplitude of the fluctuations and the velocity of the flows below 250 km/s. Large fluctuations (above 3 nT) could nevertheless generate high speed flows (above 250 km/s). Concerning V/HF wave relationship (plot 3), a positive cause-to-effect may exist: high speed flows could generate a stronger turbulence or, in reverse, large turbulence could more efficiently trigger high speed flows. The good correlation between B and HF-events is likely linked to some continuity in the turbulent spectra, from the low to the high frequencies.

To get a better view of possible cause-to-effect relationships between events, we produce more precise plots that take into account the relative time of detection of the events (Figure 5). To make plot 1, we consider common V/B events. We then identify B-events that start before V-events and calculate the time intervals that separates the start of both events. We add all these time intervals (black line). We do the same for B-events finishing after V-events, and calculated the period that separate the end of the V-events and the end of the B-events (blue line). The plots thus corresponds to the total advanced time of B over V-events (black) and the total retarded time of B over V-events (blue). The same is done for V and HF events in plot 2. The continuous, dotted and dashed lines correspond to increasing thresholds for the selection of events.

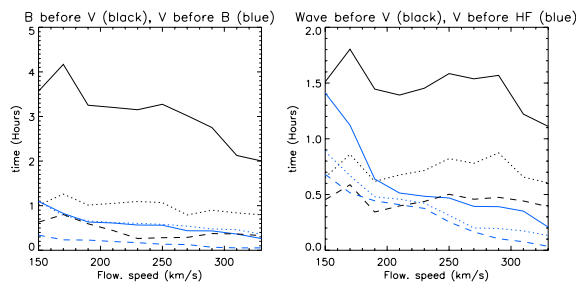


**Fig. 5.** advanced (black) and retarded (blue) time between B/V-events (plot 1), and HF/V-events (plot 2).

The proportion of B-events and HF-events that start before a V-events is generally much larger than the reverse, by a factor 3. This is especially true for low amplitude fluctuations (continuous line), the difference being less pronounced as the amplitude of the wave increases. This indicates that, in average, low and high frequency fluctuations are seen before the flows. They also do not persist for a long time after the flows. A

simple interpretation would be that V-events, HF-events, and B-events are triggered by the same process, the higher velocity of propagation of the magnetic fluctuations (sound or Alfvén speed) allowing to detect B-events or HF-events before V-events. It is nevertheless not excluded that the fluctuations could also have a positive role in the formation of flows: a burst of magnetic turbulence could change the dynamics of the plasma sheet and trigger plasma flows. A more detailed analysis is needed to firmly conclude on these fundamental questions.

## 6. Conclusion

The prime purpose of this report is to publish a first extended study of the plasma sheet activity from CLUSTER measurements. We perform a statistical analysis of different kinds of 'events' that characterize the plasma sheet activity. They are defined from the flow velocity (V-events, equivalent to BBF), the amplitude of low frequency magnetic fluctuation (B-events), the spectral density of high frequency waves (HF-events) and the thickness of the sheet (thickness-events). We use automatic procedures for the selection of 'events' based on the facilities given by the CDPP.

Depending on quantitative criteria, an 'active' plasma sheet is observed some  $\sim 5-10\%$  of the total time spent by spacecraft in the sheet. We obtain comparable proportions using B-events, V-events and HF-events. If 'activity' is generally identified as a substorm develops when CLUSTER is in the sheet, many examples of active periods are reported without any recorded auroral intensifications or substorms. There is thus certainly not a one-to-one relationship between the development of local active processes and auroral phenomena. We also show that the three types of events present a positive correlation, as large as 50%. This is a strong indication that V, B and HF events are basically related to the same phenomena.

There are different interpretations of the phenomena. One is simply that a localised dissipation process (a reconnection, for example) generates flows and fluctuations. They then propagate independently from the same location and are detected almost simultaneously given the large propagation speeds. However, in such a case, the 'events' cannot be considered as physically related phenomena, they would simply result from a common process. The second interpretation is that a cause-to-effect relationship links the events. For example, magnetic fluctuations generate flows that, in reverse, trigger fluctuations in a large frequency domain. This would create a self-consistent non-linear system that organize the local dissipation. The observed correlation would then be an essential ingredient of turbulence in collisionless plasmas. More detailed analysis are required to answer this dilemma.

## References

1. Angelopoulos, V., Kennel, C. F., Coroniti, F.V., Pellat, R., Kivelson, M. G., Walker, R. J., Russell, C. T., Baumjohann, W., Feldman, W. C., Gosling, J. T., Statistical characteristics of bursty flow events, *J. Geophys. Res.*, 99, 21257, 1994.
2. Balog, A. et al, The Cluster magnetic field investigation: Overview of inflight performance and initial results, *Ann. Geophys. Res.*, 19, 1207, 2001.

3. Baumjohann, W., Paschmann, G., Luhr, H., Characteristics of high speed flows in the plasma sheet, *J. Geophys. Res.*, *95*, 3801, 1990.
4. Borovsky, J. E., Helpic, R. C., Funsten, H. O., Thomsen, M. F., The Earth's plasma sheet as a laboratory for flow turbulence in high beta MHD, *J. Plasma Phys.*, *57*, 1, 1997.
5. Borovsky, J. E., Funsten, H. O., MHD turbulence in the Earth's plasma sheet: Dynamics, dissipation, and driving, *J. Geophys. Res.*, *108*, 1284, doi:10.1029/2002JA009625, 2003.
6. Cornilleau-Wherlin, N. et al., First result obtained by the Cluster STAFF experiment, *Ann. Geophys. Res.*, *21*, 437-456, 2003.
7. Ohtani, M., Higuchi, A., Lui, T. Y., Takahashi, Magnetic fluctuations associated with tail current disruption: Fractal analysis, *J. Geophys. Res.*, *100*, 19, 1995.
8. Bauer, P. M., Baumjohann, W., Treumann, R. A., Sckopke, N., Luhr, H., Low-frequency waves in the near-Earth plasma sheet, *J. Geophys. Res.*, *100*, 9605, 1995.
9. Frey, H. U., Mende, S. B., Angelopoulos, V., Donovan, E. F., Substorm onset observations by IMAGE-FUV, *J. Geophys. Res.*, *109*, 10304, doi:10.1029/2004JA010607, 2004.
10. Fruit, G., Louarn, P., Budnik, E., Sauvaud, J. A., Le Quéau, D., Rème, H., Lucek, E., Balogh, A., On the propagation of low frequency fluctuations in the plasma sheet: 2. Characterisation of the MHD eigenmodes and physical implications, *J. Geophys. Res.*, *109*, 3217, 2004.
11. Hoshino, S. T. and 11 co-authors, A statistical study of compressional waves in the tail current sheet, *J. Geophys. Res.*, *108*, 1429, doi:10.1029/2003JA010404, 2003.
12. Louarn, P., Fruit, G., Budnik, E., Sauvaud, J. A., Le Quéau, D., Rème, H., Lucek, E., Balogh, A., On the propagation of low frequency fluctuations in the plasma sheet: 1. CLUSTER observations and MHD analysis, *J. Geophys. Res.*, *109*, 3216, 2004.
13. Rème, H. et al, First multispacecraft ion measurements in and near the Earth's magnetosphere with the identical Cluster Ion spectrometry (CIS) experiment, *Ann. Geophys. Res.*, *19*, 1303, 2001.
14. Schodel, R., Baumjohann, W., Nakamura, R., Sergeev, V., Mukai, T., Rapid flux transport in the central plasma sheet, *J. Geophys. Res.*, *106*, 301, 2001.
15. Volwerk, M. and 11 co-authors, A statistical study of compressional waves in the tail current sheet, *J. Geophys. Res.*, *108*, 1429, doi:10.1029/2003JA010404, 2003.
16. Voros, Z. and 10 co-authors, Magnetic turbulence in the plasmasheet, *J. Geophys. Res.*, *109*, A11215, doi:10.1029/2004JA010155, 2004.

# Relation of substorm disturbances triggered by abrupt solar-wind changes to physics of plasma sheet transport

L. R. Lyons, D.-Y. Lee, C.-P. Wang, and S. B. Mende

**Abstract:** Substorm onset occurs within the near-Earth plasma sheet in the region that maps to the Harang electric field reversal observed within the ionosphere. IMF changes that are expected to reduce the convection electric field after  $\gtrsim 25$  min of negative IMF  $B_z$  are well known to cause substorms. Solar wind dynamic pressure  $P_{dyn}$  enhancements following prolonged strongly southward IMF ( $B_z \lesssim -8$  nT) also cause substorms. However, an interplay of effects from a simultaneous IMF and  $P_{dyn}$  change can prevent the occurrence of a substorm, leading to what we refer to as null events. We show that the combination of inward convection and energy-dependent magnetic drift in the finite-width plasma sheet offers an explanation for the IMF and pressure triggered substorms, for their onset within the Harang reversal region, and for the null events. These same aspects of the plasma sheet transport also offer an explanation for the growth-phase development of the Harang reversal, for steady-magnetospheric convection events, and for pseudo-substorms.

*Key words:* Substorms, Harang discontinuity, Dynamic pressure, Plasma sheet.

## 1. Introduction

Abrupt changes in the interplanetary magnetic field (IMF) and solar wind lead to large-scale disturbances of the magnetosphere-ionosphere system and in particular to substorms. Furthermore, auroral observations have been used to show that substorm onset occurs within a region of converging electric fields known as the Harang discontinuity [1, 6, 8, 18, 19]. Note that the Harang discontinuity is a region where the north-south component of electric fields reverses direction, and is not actually a discontinuity. For this reason, it is referred to here as the “Harang reversal.” Observations of ionospheric flows have shown that the Harang reversal enhances during the substorm growth phase and decreases dramatically at onset, implying that the evolution of the Harang reversal is “related to the cause of substorm expansion onsets” [3].

Here we first describe how disturbance features depend on the type of interplanetary change and identify which changes lead to substorms and which do not. We then describe our proposal for how basic plasma sheet transport leads to the growth phase development of the Harang reversal, causes substorm onset within the Harang reversal, explains why some changes cause substorm onset and others do not, and offers a feasible explanation for steady magnetospheric convection intervals (SMCs, also known as convection bays) and pseudo-substorms (also known as pseudo-breakups).

## 2. Disturbance Features

It is well known that IMF changes that lead to a convection reduction after a  $\gtrsim 25$  min period of negative  $B_z$  lead to the onset of substorms. Global auroral images from the Wideband Imaging Camera (WIC) on board the IMAGE spacecraft are shown in the top row of Fig. 1 for a substorm triggered by an IMF northward turning following a  $\sim 30$  min period of IMF  $B_z \sim -2$  to  $-4$  nT on 9 December 2000 (color images and other data for this and other events discussed here are shown in [16]). These images illustrate what typically is observed for substorms triggered by an IMF change under constant solar wind dynamic pressure,  $P_{dyn}$ .

The images show that brightening within the equatorward portion of the oval was first visible at 1914 UT at  $\sim 00$  to 01 MLT. Such brightening indicates the onset of a substorm expansion. Based on the previous studies referred to in the introduction, this brightening occurs within the region of the Harang reversal. The region of enhanced expansion-phase aurora then spreads azimuthally and poleward over the next 4–6 min, forming a typical aurora bulge and reaching a maximum azimuthal coverage of  $\sim 5$  hr of MLT. This expansion-phase bulge indicates that current-wedge formation occurred within the inner plasma sheet. Consistent with this, the geosynchronous energetic particle data for this event show the clear dispersion-less flux enhancements near midnight that result from current wedge formation.

WIC images from 26 July 2000 illustrating the typical auroral response to an increase in  $P_{dyn}$  under steady IMF are shown in the second row of Fig. 1. An enhancement of auroral emissions is observed over a wide range of MLT, both on the dayside and nightside. This enhancement is first clearly seen in the 1857:09 UT image and was as close to simultaneous with the  $P_{dyn}$  impact as can be determined with the 2-min time resolution of WIC. Also note that, unlike for substorms, there is no evidence for bulge formation. Such a global auroral enhancement, without the bulge formation associated with current wedge formation, is the response to the  $P_{dyn}$  driven com-

Received 12 May 2006.

**L. R. Lyons and C.-P. Wang.** Department of Atmospheric and Oceanic Sciences, University of California, Los Angeles, California, USA.

**D.-Y. Lee.** Department of Astronomy and Space Science, College of Natural Sciences and Institute for Basic Science Research, Chungbuk National University, Chungbuk, South Korea.

**S. B. Mende.** Space Sciences Laboratory, University of California, Berkeley, California, USA.

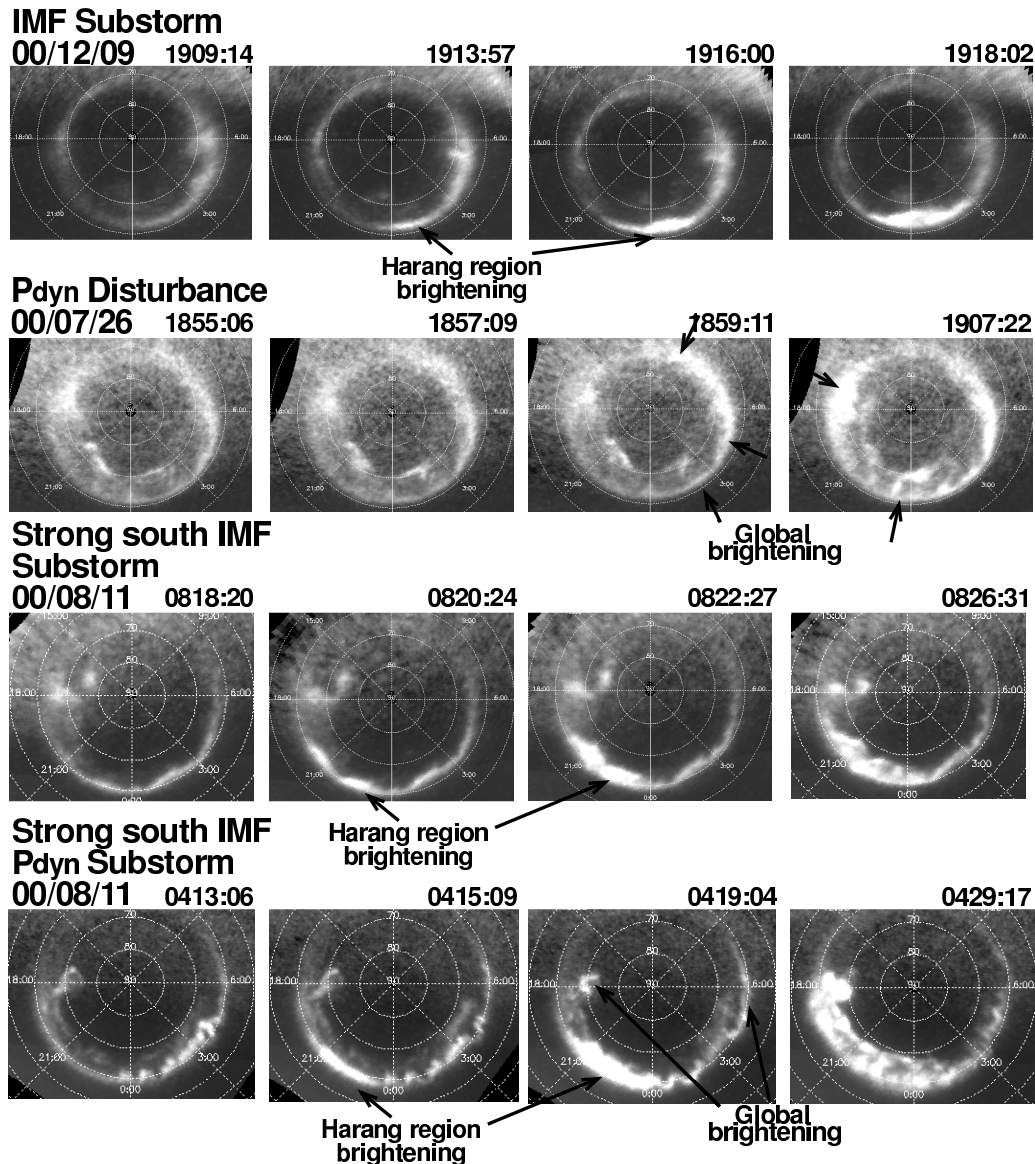


**Fig. 1.** Selected global auroral images from WIC for four different types of events as identified.

pressional heating of plasma sheet electrons, which undergo strong pitch-angle scattering losses to the atmosphere. Direct evidence for a lack of current wedge formation during this type of event has also been found using geosynchronous observations [10]. We attribute most of the global auroral enhancement to enhancement of the diffuse aurora, though some discrete auroral features will also be enhanced due to the increase in the global field-aligned current system that has been observed in response to an increase in  $P_{dyn}$ .

We next address several disturbances that occurred during the 00–12 UT period on 11 August 2000 when the IMF was generally strongly southward at about  $-10$  nT. This period illustrates two important surprises [16]. The IMF and solar wind dynamic pressure for this period from two spacecraft are shown in Fig. 2 as mapped to just in front of the bow shock using the [23] mapping technique.

WIC images for an IMF triggered substorm that followed

$\sim 40$  min of IMF  $B_z \sim -10$  nT are shown in the third row of Fig. 1. This is the second of the two events labeled  $S_{Bz}$  in Fig. 2. The auroral brightening within the expected region of the Harang reversal is first evident in the 0820:24 UT image. The only significant difference from the images for typical substorms is that the region of enhanced expansion-phase aurora after onset spreads azimuthally to a maximum azimuthal coverage of  $\sim 6$ –7 hr of MLT, which is somewhat broader than for the typical substorms. A similar IMF substorm, also labeled  $S_{Bz}$  in Fig. 2, occurred at  $\sim 0640$  UT.

WIC images for a disturbance triggered by an enhancement in  $P_{dyn}$  are shown in the bottom row of Fig. 1, which illustrate the first of our major surprises. Dayside imaging was not particularly good for this event because of sunlight and limitations in the algorithm for subtracting dayglow from the images. However, some auroral brightening can be seen just to the dayside of the dawn-dusk meridian in the 0415:09 and 0419:04 UT

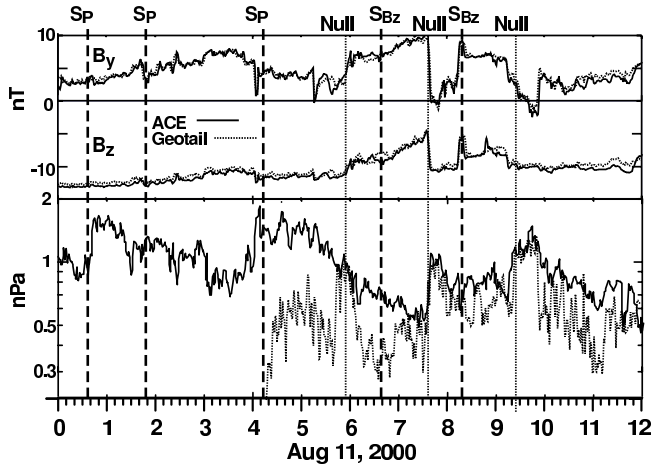


**Fig. 2.** [23]-mapped IMF  $B_y$ ,  $B_z$  and  $P_{dyn}$  from ACE and Geotail, and for 0–12 UT on 11 August 2000. Vertical dashed lines identify events discussed in the text.

images. This is as expected from the magnetospheric compression caused by the pressure enhancement. However, simultaneously, there is a Harang region auroral brightening, which is initially seen at 21–23 MLT in the 0415:09 UT image and then expands azimuthally. The Harang region brightening looks essentially the same as the auroral bulge for northward turning substorms. This suggests that the pressure enhancement led to formation of a substorm current wedge as well as to magnetospheric compression.

The WIC observations thus show evidence for both compressive and substorm auroral enhancements for this  $P_{dyn}$  increase event which occurred following prolonged strongly southward IMF. Furthermore, as the bulge-region aurora expands azimuthally, it seems to merge with the compressive auroral enhancement, particularly on the dusk side. This leads to an unusually broad region of enhanced auroral emissions covering 10–14 hrs of MLT by 0421:17 to 0425:22 UT. Also, clear evidence for current wedge formation within the nightside near-Earth plasma sheet, and for its occurring together with global magnetospheric compression, is seen in the geosynchronous particle data for this event [10]. This event is identified as  $S_P$  in Fig. 2, and there were two other similar events during the time interval shown that are identified in Fig. 2 and were considered along with other such events by [16].

The above events were all selected because they are quite ideal in that there was either an IMF northward turning with approximately steady  $P_{dyn}$  or an increase in  $P_{dyn}$  with approximately steady IMF  $B_z$ . However, it is far more common for a solar wind change to simultaneously affect both  $B_z$  and  $P_{dyn}$ . If increases in solar wind dynamic pressure and northward turnings of the IMF can cause nightside substorm disturbances, it makes sense that effects of changes in these quantities should interact if both occur simultaneously. For example, it would seem that an IMF northward turning accompanied by an increase in  $P_{dyn}$  might lead to a stronger disturbance than would an equal change in only one of the quantities. This idea has not yet been evaluated.

However, the second significant surprise is that we have been able to determine that there indeed is important interaction between effects of IMF  $B_z$  changes and  $P_{dyn}$  changes under

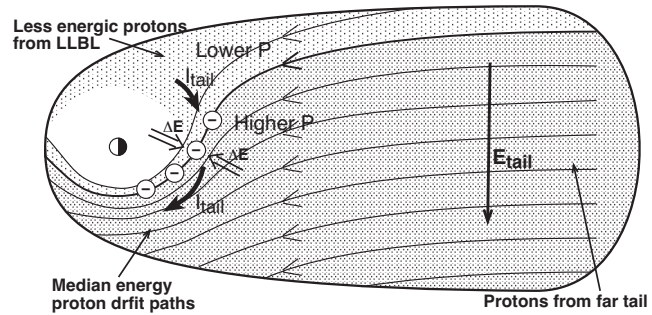


**Fig. 3.** Illustration in the equatorial plane of physics of formation of the Harang reversal. Shaded regions identify the location of the plasma sheet. (based on [5]).

strongly southward IMF conditions when  $P_{dyn}$  decreases (increases) with a simultaneous northward (further southward) turning of the IMF.

Three such events occurred on 11 August 2000 and are identified in Fig. 2 as “Null”. The first had an IMF northward turning from  $B_z < -10$  nT and a simultaneous decrease in  $P_{dyn}$ . The other two events had a further southward IMF turning and an increase in  $P_{dyn}$ . The impacts of the  $P_{dyn}$  changes for these events were clearly seen in the low-latitude H observations. Based on the results from other events, we would expect that the IMF northward turning for the first event and the  $P_{dyn}$  increases for the second two events would, by themselves, have caused a significant, large-scale auroral disturbance. However, the WIC images for these events (see [16]) clearly show that such a disturbance did not occur for these events.

These results for the 11 August 2000 events suggest that the effects of a decrease (increase) in  $P_{dyn}$  and a simultaneous northward (further southward) turning of the IMF can nullify each other, so that a large-scale disturbance, and in particular a substorm response, does not occur.

### 3. Harang Reversal Physics

In order to understand how particle transport associated with the Harang reversal offers an explanation for the types of interplanetary changes discussed above that do, and do not, trigger substorms, it is necessary to first consider the formation of the Harang reversal during the substorm growth phase. This is illustrated in Fig. 3 and can be understood in terms of the equatorial continuity equation for flux tubes

$$\begin{aligned} \frac{\partial}{\partial t}(n\mathcal{V}) + (\mathbf{V}_E \cdot \nabla)(n\mathcal{V}) &= -\frac{\hat{\mathbf{B}}_e \cdot \nabla P \times \nabla \mathcal{V}}{qB_e} \\ &= -\frac{2}{qB_i} j_{\parallel,i} \end{aligned} \quad (1)$$

Here  $\mathbf{V}_E$  is the electric drift velocity,  $n$  is the plasma density,  $\mathcal{V}$  is flux tube volume,  $q$  is the electronic charge,  $j_{\parallel,i}$  is the upward field-aligned current density mapped to the ionosphere, and  $B_e$  and  $B_i$  are the equatorial and ionospheric field strength, respectively. The top portion of (1) is a re-written form of the plasma sheet continuity equation obtained by [7] by integrating the single species mass conservation equation over the volume of a flux tube.

The second term on the left-hand-side of (1) represents a source term to the inner plasma sheet due to inward convection. This leads to an increase in inner plasmasheet flux tube particle content  $n\mathcal{V}$  and plasma pressure after an increase in convection speed. However, as protons drift earthward, the increasing magnetic drift deflects them toward the dusk side as illustrated in Fig. 3. Thus the highest plasma pressure occurs on the dusk side of the inner plasma sheet. Because of the finite width of the tail, higher energy protons from the distant tail do not have access to the dawn side plasma sheet, where such particles must originate from the dawn side low-latitude boundary layer (LLBL). The LLBL source for high-energy protons is far smaller than is the source from the deep tail, and protons reaching the dawn side have moved a smaller distance across the tail, and thus gain less energy from the cross tail electric field than do the particles that reach the dusk side. As a result, pressure at the same radial distance on the dawn side will be less than on the dusk side, giving a significant dawn-to-dusk gradient in pressure within the inner plasma sheet.

Since the magnetic drift speed is proportional to pressure, this azimuthal pressure gradient gives a divergence of proton flux, which is also a divergence of cross tail current. This must be balanced by upward field-aligned current from the ionosphere as given by the well-known relation between  $\nabla P \times \nabla \mathcal{V}$  and  $j_{\parallel,i}$  in (1). However, current continuity must also be maintained in the ionosphere. This requires the formation of electric fields  $\Delta \mathbf{E}$  in the ionosphere that give Pedersen currents that converge towards the region of upward field-aligned currents. These converging electric fields add to the convection electric field to give the reversal of the north-south electric fields that forms the Harang reversal. They also map along field lines to the equatorial plasma sheet as indicated by the  $\Delta \mathbf{E}$  vectors in Fig. 3.

Equation (1) thus allows us to view the local change in  $n\mathcal{V}$  as a balance between a source due to earthward convection, given by  $\mathbf{V}_E \cdot \nabla(n\mathcal{V})$ , and a loss due to divergence driven by magnetic drift. This balance provides a framework for understanding the evolution of the plasma sheet during the substorm growth phase and near the onset of the substorm expansion phase as described by [15]. During periods of weak convection, plasma pressure and  $n\mathcal{V}$  are low throughout the inner plasma sheet and both the source and loss terms in (1) are low. An increase in the strength of convection will increase the particle source due to earthward convection, leading to the increase in plasma pressure and  $n\mathcal{V}$  that gives rise to the substorm growth phase. This will slowly increase the loss term in (1) and simultaneously lead to the growth-phase intensification of the Harang reversal. This increase will continue until either a steady state is reached between sources and losses or the convection strength is reduced so that the source term becomes smaller than the loss term.

#### 4. Steady Magnetospheric Convection Events

Note that a balance between source and loss terms can be reached and allows for a stable plasma sheet configuration without substorms during periods of enhanced convection [21, 22], as occurs during steady magnetospheric convection events (SMCs). This occurs without the pressure inconsistency of [4] because the loss term in (1) is the same divergence that gives a

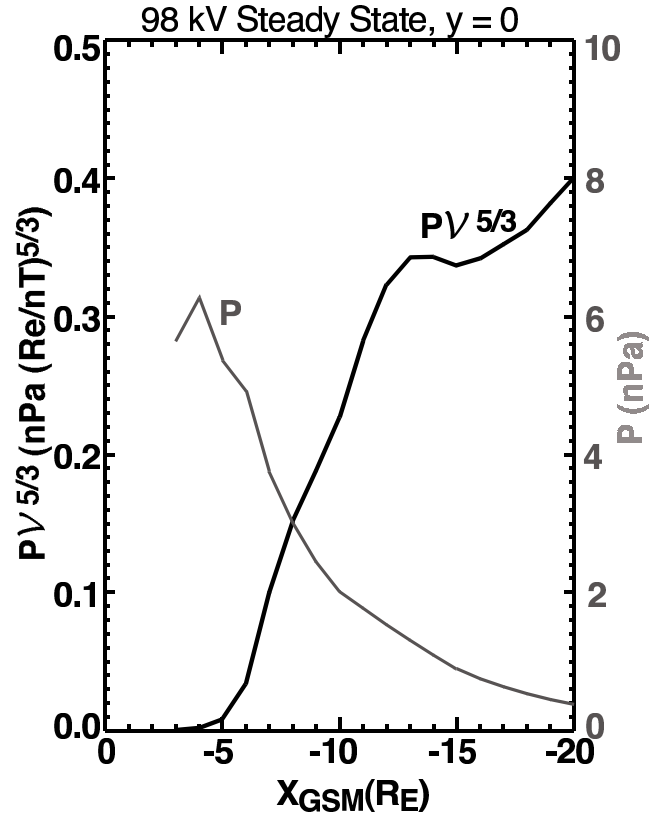


Fig. 4. Equatorial proton pressure and  $P\mathcal{V}^{5/3}$  at midnight MLT from the model of [22].

divergence in the heat flux vector [7], causing a reduction in entropy and thus  $P\mathcal{V}^{5/3}$  along drift paths. This reduction is seen in the model results of [21, 22] where the energy-dependent particle drift is included, as shown in Fig. 4 at the equator along the midnight meridian. The pressure balance inconsistency is based on conservation of  $P\mathcal{V}^{5/3}$  as particles electric field drift earthward on the nightside, whereas the model results show that the energy dependent magnetic drift cause  $P\mathcal{V}^{5/3}$  to decrease substantially along the midnight meridian. This gives plasma pressures at geosynchronous orbit, for example, that are more than a factor of four lower than would be if  $P\mathcal{V}^{5/3}$  were conserved along the midnight meridian.

#### 5. IMF and $P_{dyn}$ and Substorms

A reduction in the source term relative to the loss term in (1) will lead to a loss rate that exceeds the source rate and give  $(\partial/\partial t)(n\mathcal{V}) < 0$ . This will lead to a reduction in  $n\mathcal{V}$ ,  $P$ , and cross tail current as is necessary for current wedge formation and the onset of the expansion phase of substorms. This process is discussed in [15] and [13], where it is also addressed how this substorm process leads to a non-linear enhancement in the rate of current wedge formation and thus to the rapid development of the substorm expansion phase. The source term in (1) is proportional to  $\mathbf{V}_E$ , which equals  $E/B_e$ , where  $E$  is the electric field within the equatorial plasma sheet. On the other hand the loss term in (1) is proportional to  $P\mathcal{V}/B_e$ , which

varies as  $B_e^0$  to  $B_e^{-1/3}$  [15], and is thus nearly independent of  $E$  and  $B_e$ . Therefore a significant reduction in  $V_E$  within the plasma sheet should lead to substorm onset, which can occur from a decrease in  $E$  or an increase in  $B_e$ . IMF changes modify  $E$ , and the magnetopause current changes resulting from  $P_{dyn}$  changes modify  $B_e$ , thus offering a plausible explanation for why substorm onset can be caused by either an IMF change that reduces  $E$  or a  $P_{dyn}$  increase. Note that the same particle divergence gives rise to both the Harang reversal during the substorm growth phase and the reduction in  $nV$  when the strength of convection is reduced. Thus, following a reduction in convection, the maximum rates of reduction of  $nV$  should occur within the region of the equatorial mapping of the Harang reversal, explaining why substorm onset is observed within the Harang region.

Typical increases in  $B$  on the nightside in responses to increases in  $P_{dyn}$  are  $\sim 10$  nT at synchronous orbit (e.g., [9]). Such an increase most often is not significant compared to  $B_e$  in the inner plasma sheet (which, from the Earth's dipole field alone, is  $\sim 100$  nT at geosynchronous orbit). However, modeling has shown that  $B_e$  can become below 10 nT within the  $r \sim 7-10 R_E$  region of the inner plasma sheet following prolonged periods of enhanced convection [20, 22], and  $B_e$  values below 10 nT have been observed within this region of the plasma sheet prior to substorm onset [11, 14]. Thus, an increase in  $P_{dyn}$  can cause a significant increase in  $B_e$  if it occurs following a period of strongly southward IMF, when  $B_e$  is substantially reduced within the inner plasma sheet. However, it is unlikely to do so under other situations. This is particularly important because increases in  $P_{dyn}$  have been observed to cause an increase in the strength of convection [2, 12], so that a large relative increase in  $B_e$  is necessary for an increase in  $P_{dyn}$  to reduce  $E/B_e$  and thus cause current wedge formation.

## 6. Null Events and Pseudo-Substorms

The above arguments also offer an explanation for the null events, since it is a decrease in  $V_E$  that leads to current wedge formation. An IMF change leading to a reduction in  $E$  (such as a northward turning) that occurs simultaneously with a decrease in  $P_{dyn}$  can cause a simultaneous decrease in  $E$  and  $B_e$ , which could leave  $V_E$  unchanged or increased within the inner plasma sheet. Similarly, an increase in  $P_{dyn}$  and a simultaneous IMF change that leads to an increase in  $E$  (such as a further southward turning) could leave  $V_E$  unchanged or increased. In both cases, there would not be a decrease in  $V_E$ , so that current wedge formation would not be expected to occur.

This nullification phenomenon also suggests a plausible explanation for pseudo-substorms where substorms initiate in a manner that is indistinguishable from a full substorm, but the expansion phase is terminated before full development (which is often defined as before expansion-phase auroral activity expands poleward to the polar-cap boundary). If an IMF or  $P_{dyn}$  trigger occurs and is soon followed (in  $\lesssim 10$  min) by an IMF or  $P_{dyn}$  change in the other direction (a nullifying change), then at first the source term in (1) would be reduced and substorm onset would proceed as it does following any other trigger. But then the source term would be increased, thus terminating the loss of particles necessary for further current wedge develop-

ment and thus ending the expansion phase development. Examples where this appears to have occurred are shown by [17].

## 7. Conclusions

We thus conclude that the physics of the particle transport that leads to the Harang electric field reversal offers a potential explanation for the IMF and  $P_{dyn}$  changes that do and do not cause substorm onset, as well as for SMCs and pseudo-storms as follows:

**SMCs:** The finite tail width together with the energy dependent magnetic drift gives particle & energy flux divergence that prevents excess build up of pressures. This allows for a stable balance within the inner plasma sheet between the source from inward convection and the loss from azimuthal magnetic drift.

**IMF & strong south IMF  $P_{dyn}$  substorms:** An IMF change or increase in  $P_{dyn}$  decreases the inner plasma sheet source from inward convection. It is necessary for  $B_e$  to be considerably lower than average for a  $P_{dyn}$  increase to trigger a substorm, so that such triggering only occurs after a period of strongly southward IMF.

**Null events:** Competing effects of an IMF or  $P_{dyn}$  trigger and a simultaneous nullifying IMF or  $P_{dyn}$  change lead to an approximately unchanged or increased source term.

**Pseudo-substorms:** A nullifying IMF or  $P_{dyn}$  change enhances the inner plasma sheet source term after onset, terminating substorm development before it becomes fully developed.

## Acknowledgements

This research was supported in part at UCLA by NSF grant OPP-0136139 and NASA grant NNG05GF29G. The work at Chungbuk National University was supported by the Korea Research Foundation grant funded by the Korean Government (MOEHRD) (KRF-2005-041-C00207).

## References

1. Baumjohann, W., R. J. Pellinen, H. J. Opgenoorth, and E. Nielsen, Joint two-dimensional observations of ground magnetic and ionospheric electric fields associated with auroral zone currents: Current systems associated with local auroral break-ups, *Planetary and Space Science*, 29, 431–447, 1981.
2. Boudouridis, A., E. Zesta, L. R. Lyons, P. C. Anderson, and D. Lummerzheim, Magnetospheric reconnection driven by solar wind pressure fronts, *Annales Geophysicae*, 22, 1367–1378, 2004.
3. Bristow, W. A., A. Otto and D. Lummerzheim, Substorm convection patterns observed by the Super Dual Auroral Radar Network, *Journal of Geophysical Research*, 106, 24,593–24,609, 2001.
4. Erickson, G. M., and R. A. Wolf, Is steady state convection possible in the Earth's magnetosphere?, *Geophysical Research Letters*, 6, 897, 1980.

5. Erickson, G. M., R. W. Spiro, and R. A. Wolf, The physics of the Harang discontinuity, *Journal of Geophysical Research*, *96*, 1633, 1991.
6. Gjerloev, J. W., R. A. Hoffman, E. Tanskanen, M. Friel, L. A. Frank, and J. B. Sigwarth, Auroral electrojet configuration during substorm growth phase, *Geophysical Research Letters*, *30*(18), 1927, doi: 10.1029/2003GL017851, 2003.
7. Heinemann, M., Role of collisionless heat flux in magnetospheric convection, *Journal of Geophysical Research*, *104*, 28,397–28,410, 1999.
8. Hughes, J. M., and W. A. Bristow, SuperDARN observations of the Harang discontinuity during steady magnetospheric convection, *Journal of Geophysical Research*, *108*(A5), 1185, doi:10.1029/2002JA009681, 2003.
9. Lee, D.-Y., and L. R. Lyons, Geosynchronous magnetic field response to solar wind dynamic pressure pulse, *Journal of Geophysical Research*, *109*, A04201, doi: 10.1029/2003JA010076, 2004.
10. Lee D.-Y., L. R. Lyons, G. D. Reeves, Comparison of geosynchronous energetic particle flux responses to solar wind dynamic pressure enhancements and substorms, *Journal of Geophysical Research*, *110*, A09213, doi:10.1029/2005JA011091, 2005.
11. Lui, A. T. Y. et al., A case study of magnetotail current disruption and diversion, *Geophysical Research Letters*, *15*, 721, 1988.
12. Lukianova R., Magnetospheric response to sudden changes in solar wind dynamic pressure inferred from polar cap index, *Journal of Geophysical Research*, *108*(A12), 1428, doi:10.1029/2002JA009790, 2003.
13. Lyons, L. R., and C.-P. Wang, Fundamental aspects of substorm onset, in *Substorms-7: Proceedings of the Seventh International Conference on Substorms*, p. 186, Finish Meteorological Institute, Finland, 2004.
14. Lyons, L. R., C.-P. Wang, T. Nagai, T. Mukai, Y. Saito, and J. C. Samson, Substorm inner plasma sheet particle reduction, *Journal of Geophysical Research*, *108*(A12), 1426, doi: 10.1029/2003JA010177, 2003a.
15. Lyons, L. R., C.-P. Wang, and T. Nagai, Substorm onset by plasma sheet divergence, *Journal of Geophysical Research*, *108*(A12), 1427, doi:10.1029/2003JA010178, 2003b.
16. Lyons, L. R., D.-Y. Lee, C.-P. Wang, and S. B. Mende, Global auroral responses to abrupt solar wind changes: Dynamic pressure, substorm, and null events, *Journal of Geophysical Research*, *110*, A08208, doi:10.1029/2005JA011089, 2005.
17. Lyons, L. R., D.-Y. Lee, S. Zou, C.-P. Wang, J. Weygand and S. B. Mende, External triggering and the large-scale nature of sawtooth event injections, *Journal of Geophysical Research*, submitted, 2006.
18. Nielson, E., Ionosphere-magnetosphere mapping of dynamic auroral structures during substorms, in *Auroral Physics*, p. 409, eds. C.-I. Meng, M. J. Rycroft, Cambridge University Press, Cambridge, UK, 1991.
19. Nielsen, E., and R. A. Greenwald, Variations in ionospheric currents and electric fields in association with absorption spikes during the substorm expansion phase, *Journal of Geophysical Research*, *83*, 5645, 1978.
20. Sergeev, V. A., T. I. Pulkkinen, R. J. Pellinen, and N. A. Tsyganenko, Hybrid state of the tail magnetic configuration during steady convection events, *Journal of Geophysical Research*, *99*, 23,571–23,582, 1994.
21. Wang, C.-P., L. R. Lyons, M. W. Chen, R. A. Wolf, and F. R. Toffoletto, Modeling the inner plasma sheet protons and magnetic field under enhanced convection, *Journal of Geophysical Research*, *108*, 10.1029/2001JA009620, 2003.
22. Wang, C.-P., L. R. Lyons, M. W. Chen, and F. R. Toffoletto, Modeling the transition of the inner plasma sheet from weak to enhanced convection, *Journal of Geophysical Research*, *109*, A12202, doi:10.1029/2004JA010591, 2004.
23. Weimer, D. R., D. M. Ober, N. C. Maynard, M. R. Collier, D. J. McComas, N. F. Ness, C. W. Smith, and J. Watermann, Predicting interplanetary magnetic field (IMF) propagation delay times using the minimum variance technique, *Journal of Geophysical Research*, *108*, 10.1029/2002JA009405, 2003.

# Challenges of multi-spacecraft missions to end the substorm controversy

R. L. McPherron and T.-S. Hsu

**Abstract:** Magnetospheric substorms are one of the most important phenomena that occur in the Earth's magnetosphere. Substorms are caused by magnetic reconnection between the interplanetary magnetic field and the Earth's dipole field. Reconnection on the dayside is usually followed within an hour by reconnection in the tail. Isolated substorms consist of three phases: growth, expansion, and recovery. The process causing the onset of the expansion phase is not known. One model postulates it is reconnection that occurs first at 22 Re down the tail. Pile up of reconnection flows in the inner magnetosphere then causes the onset of the expansion phase. The other model postulates that some other process first disrupts the tail current in the inner magnetosphere and this creates the onset. This process launches a rarefaction wave down the tail that minutes later initiates reconnection. It has not been possible to identify the process causing onset because there are insufficient spacecraft and ground observations to determine the time of onset and direction of propagation. The Themis mission consisting of five spacecraft and numerous ground stations is designed to solve this problem. However, there are questions concerning whether a sufficient number of "perfect substorms" will be observed by Themis in its two-year lifetime. In this paper we estimate the probability of observing the "perfect substorm" and determine how many such events are likely to be seen. Depending on the assumptions we make we obtain between one and ten such substorms.

*Key words:* Magnetospheric Substorm, Expansion Onset, Themis Mission.

## 1. Introduction

The magnetospheric substorm is a sequence of processes in the Earth's magnetosphere during which energy is extracted from the solar wind and deposited in the magnetosphere and the ionosphere. Substorms are caused by the process of magnetic reconnection which allows two magnetic fields separated by a current sheet to connect to each other. In the Earth's magnetic field this happens when the interplanetary magnetic field (IMF) turns southward antiparallel to the Earth's dipole field at the sub-solar point of the magnetopause. Dipole field lines that were previously closed are opened and connected to the IMF. The solar wind carries these field lines over the poles and adds them to the lobes of the magnetic tail. Eventually these open field lines reconnect at the center of the tail and return to the dayside. If nightside reconnection did not occur all dayside magnetic flux would eventually be removed.

An isolated substorm driven by a short interval of southward IMF consists of three phases [8]: growth, expansion, and recovery. The onset of the expansion phase is signaled by the sudden brightening of the aurora around midnight near the equatorward boundary of the auroral oval. Within 1-2 minutes of this brightening, onset signatures consistent with magnetic reconnection are seen in the tail. The question that has not been answered is whether reconnection is the cause of the auroral brightening or a consequence.

Presently there are two main theories for the cause of substorm expansion onset. The first called the near-Earth neutral line model [1] postulates that thinning of the plasma sheet dur-

ing the growth phase creates conditions allowing tail reconnection. Jets of plasma produced by reconnection flow parallel to the tail axis, one jet is Earthward carrying northward magnetic field, and the other is tailward carrying southward magnetic field. Within minutes after reconnection begins the Earthward jet piles-up in the inner magnetosphere creating the substorm current wedge that diverts tail current into the ionosphere as well as other effects characteristic of the expansion phase [14]. The alternative view is that some other process originates in the inner region and disrupts the tail current causing the current wedge characteristic of the substorm expansion phase [5]. This current disruption process generates a rarefaction wave that propagates down the tail initiating magnetic reconnection some minutes after expansion onset [6, 15].

Despite many years of study it has not been possible to resolve this controversy. There are several reasons for this as noted by [12]. First, the time for information to propagate between the two suggested regions of onset by either fast flows or waves is of order 2-3 minutes. Second, the cadence of modern measurements is too slow and of the same order as the time delays caused by propagation. Third, there are not a sufficient number of spacecraft in the tail at any time to unambiguously determine the direction or speed of propagation. As a consequence the proponents of the two main models remained fixed in their convictions and the controversy is unresolved.

## 2. The Themis Mission

To resolve the substorm controversy Dr. Vassilis Angelopoulos successfully proposed a NASA Midex mission that will place five identical spacecraft in orbit to monitor substorms. The spacecraft will be moved into three different orbits with 1-, 2-, and 4-day periods. The distance of apogee for these orbits will be  $\sim 30$ ,  $\sim 20$ , and  $\sim 10$  Re. Since the reconnection

Received 22 June 2006.

**R. L. McPherron and T.-S. Hsu.** Inst. Geophys. Planet. Phys. And Dept. Earth Space Sciences, Univ. of Calif., Los Angeles, 90095-1567 USA

site in the tail is most often initiated at  $\sim 22$  Re and the current disruption region is located near 12 Re this arrangement should bracket the region of space containing the two proposed onset mechanisms. In addition one spacecraft will be located in between the two sites to provide information about the direction of propagation of disturbances. This mission is named Themis ( $\Theta\epsilon\mu\iota\varsigma$ ) after the Greek god of justice who weighs the evidence and decides the truth of a hypothesis. In this case the name is also an abbreviation for Time History of Events and Macroscale Interactions during Substorms.

In addition to spacecraft the NASA mission includes ground support from ten magnetometers located in high schools and community colleges in the northern part of the United States. Even more support is provided by Dr. Eric Donovan of the University of Calgary whose team will deploy 16 imagers across Canada. Combined with imagers in Alaska the THEMIS array has 20 ground-based observatories (GBOs). Each GBO includes a white light all sky camera and a host of support equipment such as a computer, GPS antenna, and a satellite dish.

### 3. A Search for the Perfect Substorm

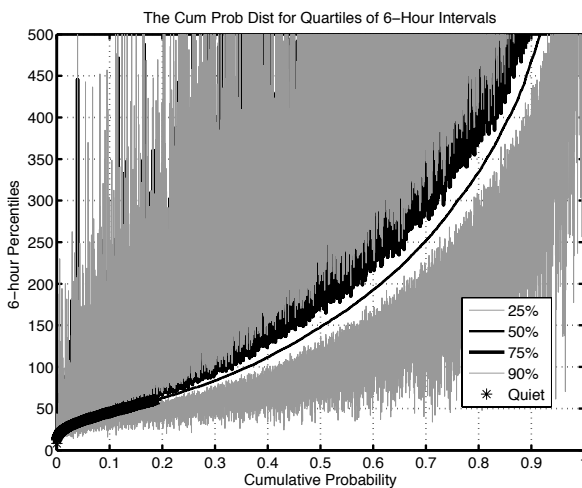


**Fig. 1.** Ten year's of cumulative distributions of 6-hour intervals of the AE index sorted by median value of each cdf. About 20% of all intervals are very quiet.

The primary objective of the Themis mission is to determine where the substorm expansion is initiated. This will be accomplished by placing the five Themis spacecraft in orbits such that all spacecraft are at apogee in the same meridian every four days. As the Earth travels around the Sun this meridian passes from dawn to dusk across the nightside allowing the spacecraft to simultaneously observe different regions of the magnetotail. Many substorms will be observed in the 3-4 months that the meridian is close to midnight. Some of these substorms will be so complex that it will not be possible to determine where or when the expansion began so it is important to identify "perfect substorms". By definition a perfect substorm is characterized by observations that unambiguously determine the location of

onset. In the following paragraphs we attempt to make an estimate of how many such events are likely to be encountered each year.

For a substorm to occur it is essential that there be geomagnetic activity in progress. We can estimate the probability of some type of activity using 10 years of the AE index. Assuming that the spacecraft are optimally aligned for six hour intervals every four days we have calculated cumulative probability distribution functions (cdfs) of AE for successive 6-hour intervals. These cdfs were sorted in ascending order based on the median of each distribution. We identify any interval with a median below 60 nT and a ninth decile below 200 as geomagnetically quiet times. The results are summarized in Figure 1. They show that magnetic activity defined in this way occurs at least 83% of the time. Thus the probability that Themis will encounter geomagnetic activity on any pass is  $P_{ac} = 0.85$ .

It has recently become evident that there are other forms of geomagnetic activity besides substorms. Steady magnetospheric convection (SMC) [13] is by definition a disturbed interval without substorms. The occurrence of SMC were studied statistically using the AE indices [7, 9] finding 2400 events in 10 years. The average duration of these events was about 2 hours corresponding to a total of 4800 hours of SMC in 10 years. This is an overall occurrence rate of  $\sim 5\%$ , or  $\sim 7\%$  of disturbed intervals. It has been suggested that this is an underestimate of SMC occurrence because this work did not include highly disturbed intervals that may be SMC.

It is clear, however, that substorms occur much more frequently than SMC. The waiting time distribution between onsets were determined by [2]. The upper panel of Figure 2 shows this probability distribution function (pdf). The mode of the pdf is 3 hours and the average time between onsets is 5.75 hours. With this separation we would expect about 15,234 substorms in ten years. If each substorm is about 4 hours long then substorms are present about 70% of the time. As a fraction of disturbed intervals this is about 84%. If instead we integrate this distribution to obtain the cdf shown in the lower panel we find that the probability of observing an onset in a 6-hour interval is also 85%. Thus we take the probability of observing a substorm during disturbed times to be  $P_{sub} = 0.85$ .

One of the problems in substorm studies is the relatively high probability that the substorm onset will be preceded by a pseudo breakup. When a pseudo breakup occurs it is possible to question the association of phenomena in the tail with phenomena elsewhere, for example an Earthward flow preceding the main onset might be considered a consequence of the earlier pseudo breakup. To be classified as a perfect substorm the main onset should not be preceded by a pseudo breakup.

Both pseudo breakups and expansion onsets are associated with bursts of Pi 2 pulsations [10, 11]. Because of this we can use the occurrence of Pi 2 pulsations to assess the probability that the main expansion onset is preceded by a pseudo breakup. The results of such a study are shown in Figure 3. According to this graph about 58% of all substorms have the main onset associated with the first Pi 2 pulsation burst. Thus  $P_{nopb} = 0.58$ .

Another important consideration is the distribution of substorm occurrence in local time. Since substorm onsets do not occur on the dayside the probability of observing a substorm at sometime in the year is clearly less than  $\frac{1}{2}$ . Most substorm

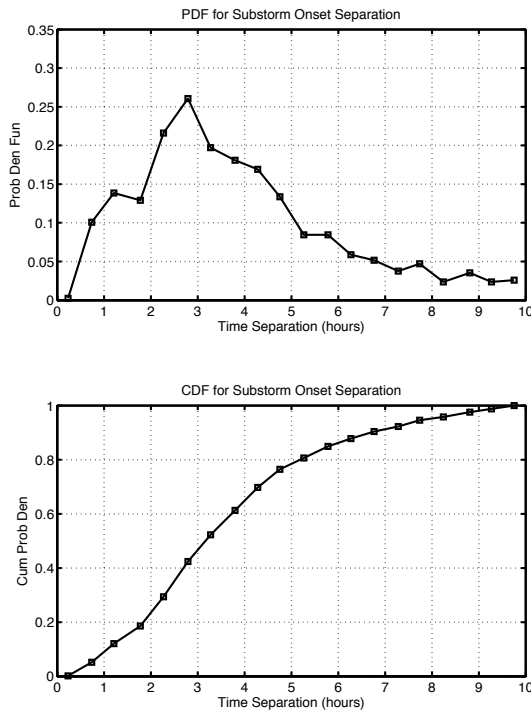


**Fig. 2.** Top panel shows the probability distribution for the waiting time between successive substorm expansion onsets obtained by [2]. The bottom panel presents the cumulative probability distribution obtained by integrating data in the top panel. There is an 85% chance that a substorm expansion will occur within a 6-hour interval.

onsets tend to occur just before midnight so the probability of observing an onset at other local times is much reduced relative to that at midnight. The local time pattern of substorm onset determined from Image satellite auroral images by [4] is presented in Figure 4. The distribution is peaked at 23 hours magnetic local time (mlt) and is zero throughout the dayside. The median of the distribution occurs at 22.4 mlt. There is less than 10% chance that a substorm will be seen before 21 mlt or after 24:30. We can roughly approximate this distribution by a uniform distribution of width four hours. In this case there is zero probability of observing an onset outside this interval so that the probability that Themis will observe a substorm onset at some mlt is  $P_{sloc} \approx (4/24) = 0.166$ .

The probability of observing a substorm at conjunction is the ratio of the time in conjunction to the time between conjunctions or  $P_{conj} = 6/96 = 0.0625$ . The requirement of conjunction significantly reduces the probability of observing a substorm.

Thus far we have tacitly assumed that all flows are in a meridian plane. Numerical simulations suggest that this is not the case. Observations also show that there can be significant east-west components of the flow velocity. As a crude approximation we assume that there is only one chance in 3 that the flow will be near the meridian plane of conjunction. If it is not in this plane then one or more of the spacecraft will not observe the flow and we do not obtain a perfect set of observations.

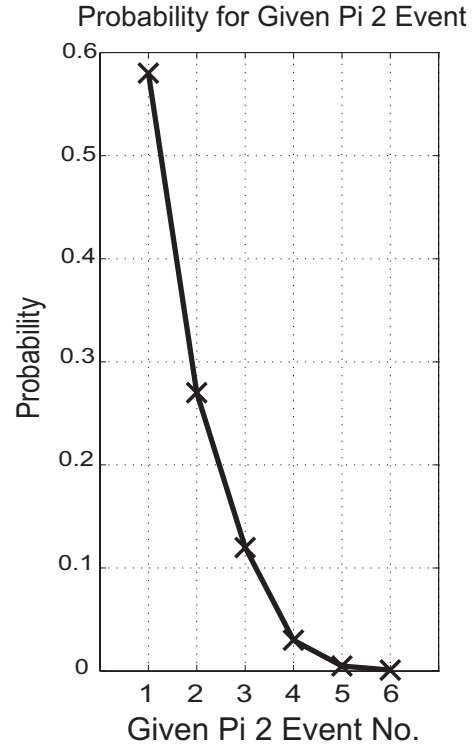


**Fig. 3.** The probability that a given Pi 2 during a substorm will correspond to the main onset of the expansion phase is plotted versus the sequence number of the Pi 2 in a single substorm.

Thus we take  $P_{flow} \approx 0.333$ .

The Themis mission will use ground observations with all sky cameras and magnetometers to locate the magnetic local time and magnetic latitude of expansion onset. A magnetic field model will then be used to map this to the equatorial plane to determine whether the spacecraft are aligned in the same meridian as the onset. As shown by [3] it is likely that field-aligned currents will distort the mapping from that given by the model. As a consequence there is some possibility that a substorm supposedly in the conjunction meridian is actually located in another meridian. It is also possible that a substorm observed to be in a different meridian actually maps to the conjunction meridian. We do not know how to estimate the effect of distortion of mapping on the probability of good observations. For the sake of argument we arbitrarily assume that the mapping is correct 75% of the time, or that  $P_{map} \approx 0.75$ .

Determination of the onset meridian depends primarily on all sky camera observations of the aurora. If the weather is bad then it may not be possible to do this well, although it is often possible to see a change in auroral luminosity through thin layers of clouds. Magnetic modeling of ground magnetic perturbations provides an alternative method for locating the meridian of onset and Themis will have one of the densest collections of stations in existence to do this modeling. Finally, it should be recognized that not all equipment will be operational all the time. How the loss of one or more ground stations affects the probability of observing a perfect substorm is difficult to estimate. Collectively all of these factors will reduce the probability of observing the perfect substorm. We arbitrarily set the net probability of these factors to 90% so that  $P_{oper}$

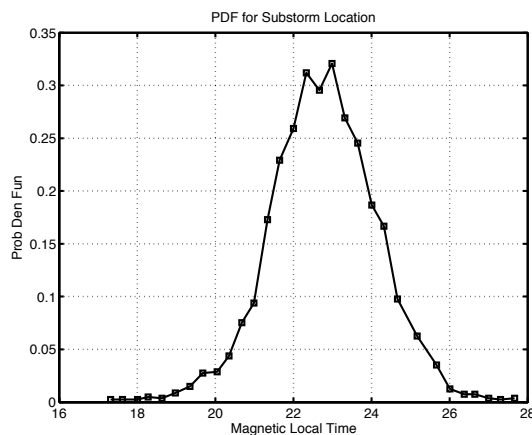


**Fig. 4.** Probability of observing a substorm at a particular magnetic local time [4].

$\approx 0.9$ .

To estimate the total effect of all of the factors discussed above we assume they are independent. Then the total probability of a perfect substorm is the product of the individual probabilities. We thus have

$$PP = (P_{act}) * (P_{sub}) * (P_{conj}) * (P_{sloc}) * (P_{nopb}) * (P_{flow}) * (P_{map}) * (P_{oper})$$

Substituting values estimated gives

$$PP = (0.83) * (0.85) * (0.0625) * (0.166) * (0.58) * (0.333) * (0.75) * (0.9) = 9.54 \times 10^{-4}$$

In one year we expect about 1525 substorms will occur. Multiplying by the aggregate probability we obtain a total of only 1.45 perfect substorms likely to be observed by Themis!

#### 4. Discussion

Our estimate of the expected number of perfect substorms likely to be observed by the Themis mission is very small, only one per year. However, note that most of these factors are poorly known and it is easy to obtain more optimistic results. For example if we take into account the dwell of the spacecraft at apogee we can double the number of hours of conjunction to 12 hours. Also, our estimates of the probability of aligned flows and mapping problems may be too pessimistic and we can increase these probabilities. It may not be necessary to reject all substorms preceded by a pseudo breakup increasing this factor. Making less pessimistic assumptions we get 9.7 very good substorms.

If pessimism is justified we can be certain that data obtained during only one substorm will not convince the proponents of either of the two substorm models. On the other hand ten "perfect substorms" all displaying the same behavior should be sufficient to convince most researchers that one of the models is correct. However, it seems more likely that Themis will provide an unprecedented collection of new data that rather than solve all the problems of substorm physics it is more likely

that Themis will reveal additional details concerning the complexity of substorms.

#### Acknowledgments

The author would like to acknowledge support for this work from an NSF Space Weather Grant ATM 02-08501, from a Los Alamos IGPP Grant #1224001054, and from the CISM project funded at the University of Colorado in Boulder by the STC Program of NSF under Agreement Number ATM-0120950. The author also thanks Dr. James Weygand for providing the data used to generate Figure 4 and YaSong Ge for his help in converting this manuscript to LaTeX. The AE indices were obtained from WDC-C2 in Kyoto, Japan.

#### References

1. Baker, D. N., et al. (1996), Neutral line model of substorms: past results and present view, *J. Geophys. Res.*, 101, 12975-13010.
2. Borovsky, J. E., et al. (1993), The occurrence rate of magnetospheric-substorm onsets: random and periodic substorms, *J. Geophys. Res.*, 98, 3807-3813.
3. Donovan, E. F. (1993), Modeling the magnetic effects of field-aligned currents, *J. Geophys. Res.*, 98, 13529-13543.
4. Frey, H. U., et al. (2004), Substorm onset observations by IMAGE-FUV, *J. Geophys. Res.*, 109, 6.
5. Lui, A. T. Y. (1996), Current disruption in the earth's magnetosphere: Observations and models, *J. Geophys. Res.*, 101, 13,067-013,088.
6. Lui, A. T. Y., et al. (1988), A case study of magnetotail current sheet disruption and diversion, *Geophys. Res. Lett.*, 15, 721-724.
7. McPherron, R. L., et al. (2005), Solar Wind Drivers For Steady Magnetospheric Convection, in *Multiscale Coupling of Sun-Earth Processes*, edited by A. T. Y. Lui, et al., pp. 113-124, Elsevier, Amsterdam.
8. McPherron, R. L., et al. (1973), Satellite studies of magnetospheric substorms on August 15, 1978, 9. Phenomenological model for substorms, *J. Geophys. Res.*, 78, 3131-3149.
9. O'Brien, T. P., et al. (2002), Steady magnetospheric convection: statistical signatures in the solar wind and AE, *Geophys. Res. Lett.*, 29, 10.1029/2001GI014641.
10. Olson, J. V. (1999), Pi 2 pulsations and substorm onsets: a review, *J. Geophys. Res.*, 104, 17499-17520.
11. Saito, T., et al. (1976), Magnetic pulsation Pi2 as a sensitive indicator of magnetospheric substorm, *Planetary and Space Science*, 25, 1025-1029.
12. Samson, J. C. (1998), Nonlinear, hybrid, magnetohydrodynamic instabilities associated with substorm intensifications near the Earth, in *International Conference on Substorms (ICS-4)*, edited by S. Kokubun and Y. Kamide, pp. 505-509, Terra Scientific Publishing Company and Kluwer Academic Publishers, Tokyo and Dordrecht.
13. Sergeev, V. A., et al. (1996), Steady magnetospheric convection: a review of recent results, *Space Sci. Revs.*, 75, 551-604.
14. Shiokawa, K., et al. (1997), Braking of high-speed flows in the near-Earth tail, *Geophys. Res. Lett.*, 24, 1179-1182.
15. Takahashi, K., et al. (1987), Disruption of the magnetotail current sheet observed by AMPTE/CCE, *Geophys. Res. Lett.*, 14, 1019-1022.

# SuperDARN and IMAGE WIC observations during intervals of steady magnetospheric convection

K.A. McWilliams, J.B. Pfeifer, R.L. McPherron, and H.U. Frey

**Abstract:** If steady magnetospheric convection (SMC) occurs when the magnetosphere is in a relatively steady state of flux transfer, i.e., dayside and nightside reconnection is balanced, then signatures of magnetic reconnection that are common to the dayside magnetosphere may be observable on the nightside also. Magnetic reconnection on the dayside produces relatively clear data signatures, such as reconnection-associated field-aligned currents (FACs), the reconnection electric field and associated convection, and energy-dispersion of precipitating ions. The processes involved produce these clear signatures, because the dayside magnetosphere is less distorted and there exists more direct connection to the solar wind driver than the nightside magnetosphere. The more global scale convection and current patterns, such as the Region 1 and 2 FACs, develop when the dayside magnetosphere is controlled by a moderately steady solar wind driver for a longer period. We present examples of energy-dispersed ions in the substorm sector during an interval of SMC, and we also discuss inferred FAC patterns based on the combined auroral images and convection patterns.

*Key words:* steady magnetospheric convection, magnetosphere, field-aligned currents.

## 1. Introduction

In any physical system the characteristics of the stability of that system is of fundamental importance to understanding the system's behaviour. The Earth's magnetosphere is an open system that is driven by its interaction with the solar wind. The dynamics of the magnetosphere is therefore a function of the upstream driver. The solar wind is not a steady, continuous stream of plasma from the Sun, so the magnetosphere finds itself in a highly variable space plasma environment. The variability of the upstream driver results in variability of convection in the magnetosphere, which is further complicated by internal processes intrinsic to the magnetosphere itself that also affect its dynamics. The result is a complex interaction between internal and external processes.

Steady magnetospheric convection (SMC) [10] events are intervals of enhanced convection without any classical substorm signatures (see [12] and references therein). When the magnetosphere is driven to this relatively steady state, there is, effectively, a balance between the creation of open flux on the dayside and the closure of flux on the nightside. Magnetospheric convection maps down to ionospheric altitudes, where the plasma drift can be measured by SuperDARN [3]. Global ionospheric convection maps are created by assimilating data from all available SuperDARN radars, and these can be used to quantify convection in the magnetosphere. Currents in the magnetosphere and ionosphere induce ground magnetic perturbations, which are detected by networks of ground magnetometers. Magnetic activity indices, such as the auroral electrojet (AE) index, quantify the activity of the magnetosphere, and they are also one of the substorm indicators.

## 2. SMC selection: Statistics

One of the more commonly used set of criteria for systematically selecting SMC intervals was presented by [11], and this scheme included: requirements of the orientation of the upstream IMF, enhanced convection determined using the AE and AL indices, and no ground or in situ magnetotail substorm signatures.

The criteria of [11] require extensive data collection and analysis, which was not easily automated, so we have chosen to use the more recent and entirely ground-based definition of SMC of [1], which is based solely on the behaviour of the AE and AL indices. In the present study, SMC was deemed to have occurred when the AE and AL indices satisfied the following criteria for a minimum of three hours: (a) AE index values larger than 200 nT to ensure active conditions, and (b) the AL index did not decrease at a rate faster than 25 nT per minute to ensure no substorm onset. These criteria effectively select the longer intervals of [1].

The number of events, as a function of months, for years between 1990 and 2001 are presented in Fig. 1. The total number of SMC intervals in a year ranged from about 10 to 50. The number of SMC events appears to depend on both the solar cycle and the season. More events were detected near solar maximum, as would be expected because of the more active solar and geomagnetic conditions at these times. More events were detected during the northern summer months. This appears to be the result of the way that the AE and AL indices are derived, as discussed by [6], rather than a geophysical process. The AE and AL indices are determined using solely northern hemisphere auroral region magnetometers, which respond to changes in the northern auroral electrojet currents. The magnitude of these currents depends strongly on the conductivity of the ionosphere, which is affected in a large part by the amount of sunlight impinging on the upper atmosphere. During the northern summer months the conductivity in the northern ionosphere is higher than during the northern winter months. The higher conductivity produces larger currents and therefore larger AE values during the summer months. If there

Received 25 May 2005.

**K.A. McWilliams and J.B. Pfeifer.** Dept. of Physics & Engineering Physics, University of Saskatchewan, Saskatoon, Canada

**R.L. McPherron.** Institute for Geophysics and Planetary Physics, University of California, Los Angeles, CA, USA

**H.U. Frey.** Space Sciences Laboratory, University of California, Berkeley, CA, USA

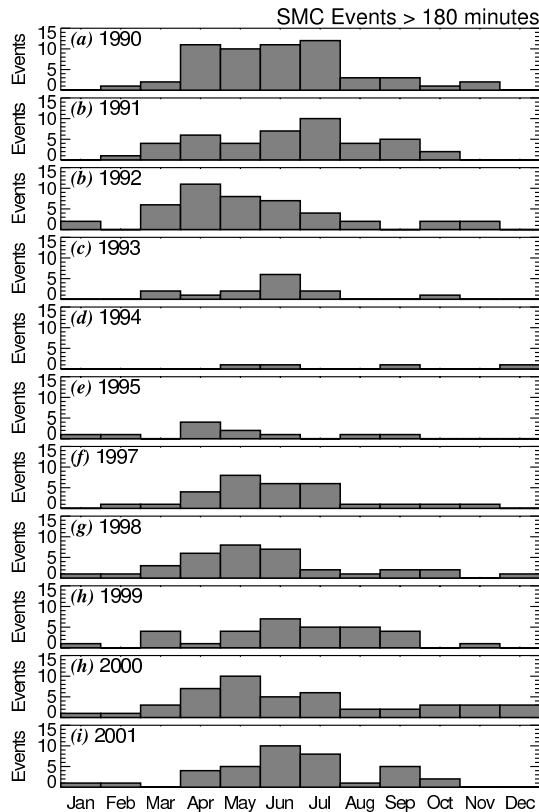


**Fig. 1.** The number of SMC intervals selected for each month during selected years between 1990 and 2001, inclusive.

were an analogous AE index in the southern hemisphere we would expect to observe the opposite bias, with more events in the winter months.

For the solar maximum years presented in Fig. 1, lowering the minimum AE threshold from 200 nT to 80 nT resulted in roughly 10-12 events detected during the winter months. Varying the AE threshold between 80 and 200 nT during the year could reduce the northern summer bias.

### 3. SuperDARN global convection during SMC

SuperDARN global convection maps were produced for the 1999 and 2001 SMC events. (Note that for 2001 there are no AE/AL data in November and December, so the apparent lack of events is not a geophysical effect.) The northern hemisphere convection maps were produced every two minutes, using all available data. The polar cap potential difference  $\Phi_{PC}$  is directly related to the strength of the ionospheric convection, so we have used  $\Phi_{PC}$  averaged over the SMC interval to quantify the magnetospheric convection for that interval. The mean  $\Phi_{PC}$  values for each SMC event are presented in Fig. 2, plus or minus one standard deviation. The greyscale indicates the number of data points in the SuperDARN convection maps, and this value is obtained by averaging the number of points in a two-minute map over the entire SMC interval. The yearly mean of  $\Phi_{PC}$  is nearly 60 kV for both 1999 and 2001, but the mean voltage appears to be lower in the summer than in the winter. This is consistent with the seasonal dependence of SMC occur-

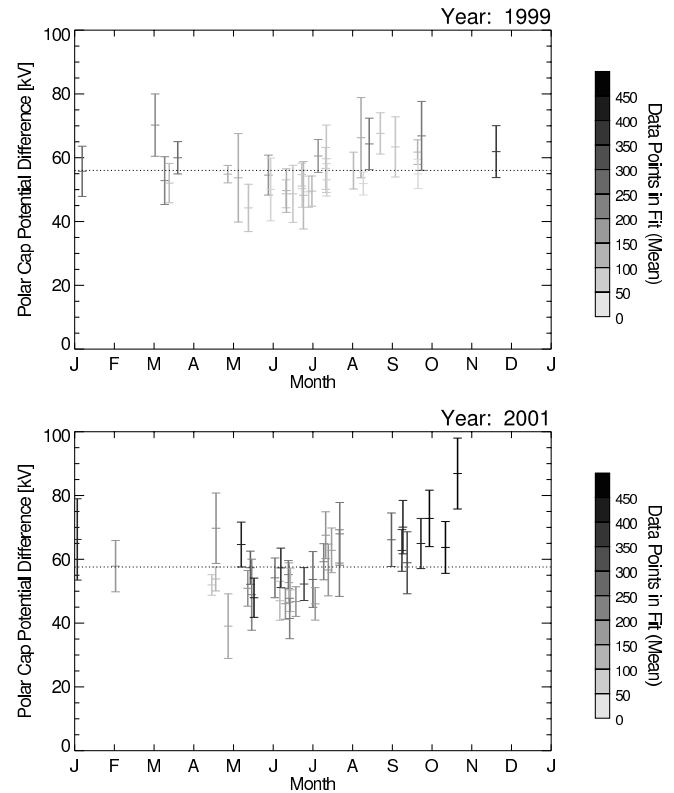


**Fig. 2.** The mean polar cap potential difference  $\Phi_{PC}$ , plus or minus one standard deviation, for all SMC intervals in 1999 and 2001. The greyscale indicates the mean number of SuperDARN velocity data points used to produce each map during each SMC interval.

rence rate. During the northern winter months, when the conductivity is reduced, stronger convection (and therefore higher transpolar voltage) is required to produce larger currents to achieve the  $AE > 200$  nT threshold.

It is interesting to note that during all SMC intervals when global SuperDARN convection patterns were calculated, the number of SuperDARN data points was relatively large. Some maps included more than one thousand data points. This increases confidence in the fitting techniques used to determine the equipotential contours. We have yet to determine if this excellent data coverage is characteristic of SMC intervals, and we intend to investigate this in more detail.

### 4. Case study: 2001/01/03, 02:57-06:46 UT

This case study, which occurred between 02:57 and 06:46 UT on 3 January 2001, was the first of the SMC events found in 2001. At the SMC onset the AL index drops weakly in a manner that is similar to a weak substorm, but the AL value decreases at a rate less than 25 nT per minute, and so it satisfies the SMC selection criteria. In contrast to a more typical substorm, the AE index remains high for nearly 4 hours. This SMC interval has the appearance of a weak substorm with a prolonged recovery phase. SuperDARN convection patterns were available for the duration of the event, and IMAGE WIC images [8] were available from prior to the onset until about

05:30 UT.

#### 4.1. IMF conditions

The IMF data for this case study are presented in Fig. 3. A simple ballistic time delay from ACE was calculated to be 73 minutes, using a speed of  $350 \text{ km s}^{-1}$  and a distance of  $240 R_E$ . The lagged SMC interval is plotted as vertical dashed lines. The IMF was relatively steady and moderate during this SMC interval, but the high solar wind concentration of nearly  $40 \text{ cm}^{-3}$  shortly before onset and  $\sim 20 \text{ cm}^{-3}$  during the first half of the SMC interval suggests this SMC occurred during a magnetic cloud event. The values of the other solar wind parameters were less unusual. The IMF  $B_z$  component rotates from  $-10 \text{ nT}$  to  $+5 \text{ nT}$ , as expected for a magnetic cloud.

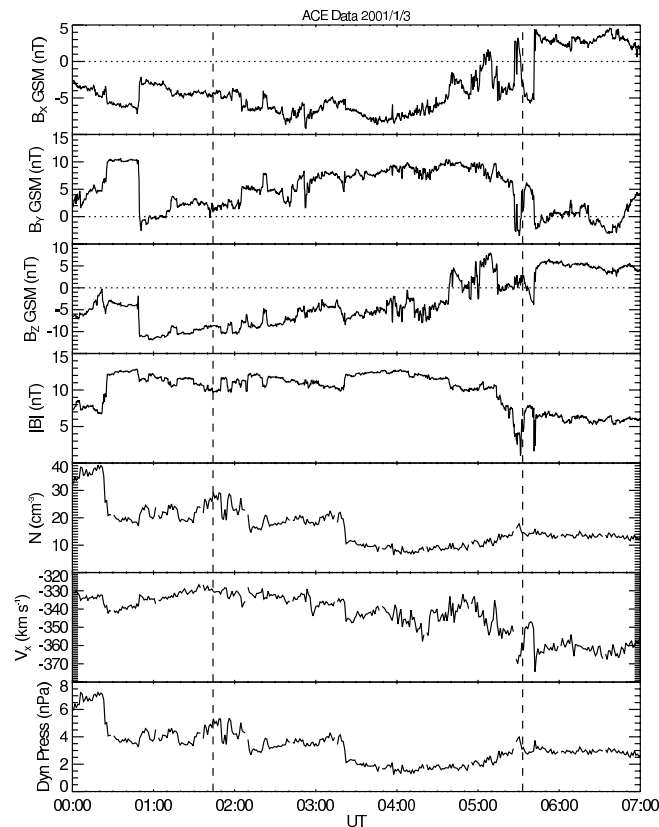


**Fig. 3.** The IMF and solar wind data measured from 00–07 UT on 03 January 2001.

#### 4.2. Dayside convection driver

Energy dispersed cusp ions (not shown) were observed by several of the DMSP satellites throughout the duration of this SMC interval. This provides strong evidence of continual open flux loading on the dayside throughout the entire interval. Cusp ions were measured over a very large range of magnetic local times on the dayside,  $\sim 7$  hours of MLT, indicating that merging on the dayside was occurring over vast portions of the frontside magnetopause prior to and during the SMC event. The very extensive dayside reconnection footprint provides evidence of substantial opening of flux on the dayside, which continually replenishes the open flux in the polar cap that is lost to

reconnection on the nightside, thereby maintaining a relatively steady amount of open flux in the polar cap.

#### 4.3. Nightside convection and aurora

Several examples of combined convection and aurora plots from this event are presented in Fig. 4. These data were measured (a) near the onset of SMC, (b) approximately one hour after the SMC onset, and (c) 3.5 hours after SMC onset, when the double oval had fully developed. These particular images were selected because they coincided with DMSP passes near local midnight. The corresponding DMSP particle spectrograms are presented in Fig. 5.

The flow out of the polar cap shortly after the SMC onset occurred between 21 and 23 MLT in the region of bright aurora, as shown in Fig. 4(a). The flow had a zonal component towards earlier local times. The DMSP F15 spacecraft traversed the midnight auroral zone in the southern hemisphere, and the conjugate footprint in the northern hemisphere crossed the eastern end of the bright aurora near midnight. DMSP F15 encountered auroral precipitation between 03:18 and 03:22 UT. Energy dispersed ions were first encountered near the poleward edge of the bright aurora (see Fig. 5(a)). The low-energy cutoff exhibits an energy dispersion with lower cutoff energies observed at lower latitudes. This energy dispersion was observed over several degrees of magnetic latitude, over distances at least as large as the latitudinal width of the auroral oval.

Nearly an hour after the start of the SMC interval (Fig. 4(b)), the double oval is not yet fully developed, but there exists a marked difference in luminosity between the poleward and equatorward regions of the auroral oval, with the poleward portion being significantly brighter. The bright poleward aurora occurred near the premidnight convection reversal boundary, as expected for a region of downward FAC and therefore diverging electric field. DMSP F12, whose magnetically conjugate trajectory is presented in Fig. 4(b), began to measure ion flux near the poleward edge of the bright northern aurora (Fig. 5(b)), but the more obvious energy dispersion did not begin until roughly 03:52 UT. The minimum ion cutoff energy decreased with decreasing magnetic latitude, as before.

The double oval, a common feature of SMC and of the substorm recovery phase (e.g., see [4]), is now fully developed, as evident in Fig. 4(c). The auroral images at this time suffer from significant distortion in the postmidnight sector, because of the oblique viewing angle of IMAGE WIC. DMSP F12 performed a skimming orbit of the auroral region (in the southern hemisphere), so it is difficult to determine with great precision where the ion energy dispersion began in Fig. 5(c). There was a strong flux of ions that coincided with the equatorward oval, and the energy dispersion becomes evident from near the poleward edge of the equatorward oval. The region of convection out of the polar cap has shifted slightly toward midnight. It is important to note that the IMF orientation has begun to change around this time.

## 5. Discussion

Smaller scale (of the order of  $\sim 100 \text{ km}$  or less) energy dispersion features in the precipitating particles in the substorm sector have been examined (e.g., [5]), but we are considering

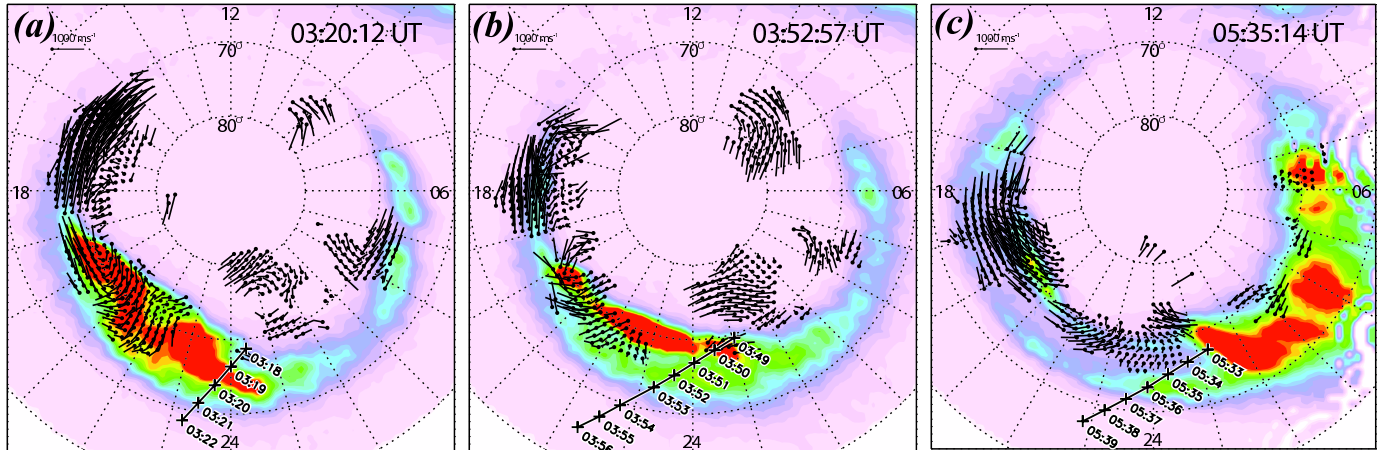


**Fig. 4.** The (a) 03:20:12 UT, (b) 03:52:57, and (c) 05:35:14 UT IMAGE WIC auroral image, overlaid with the corresponding two-minute SuperDARN convection velocities. DMSp trajectories in the substorm sector are indicated with the black line, with crosses denoting specific times along the trajectory, as listed.

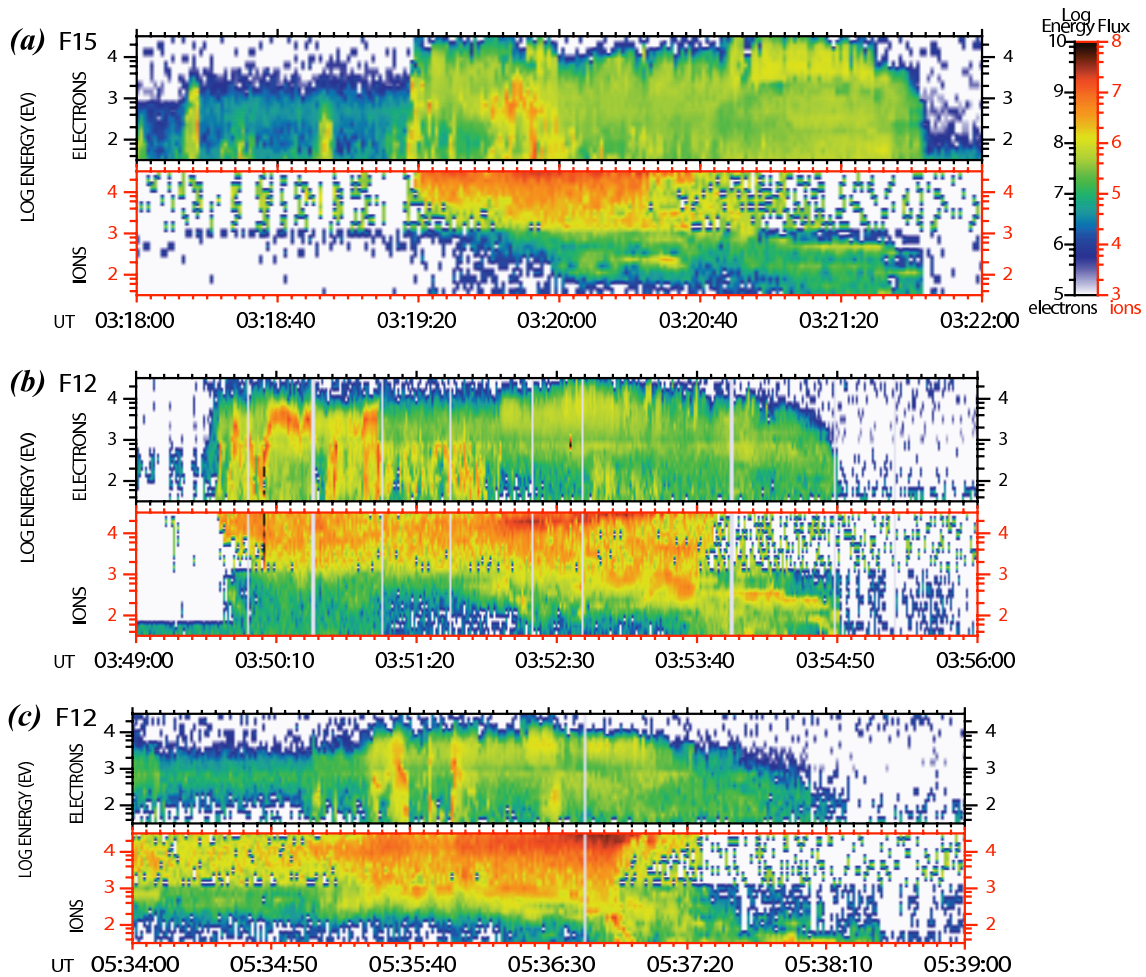


**Fig. 5.** The DMSP electron and ion particle spectrograms from the nightside passes, which correspond to the panels in Fig. 4. The location of the spacecraft are indicated in Fig. 4.

here the global magnetosphere response during SMC and we are concentrating on energy-dispersed ions that extended over several degrees of magnetic latitude. These large-scale ion energy features have been presented in previous studies, but they have not been noted. For example [9] presented FAST particle observations during substorm aurora, and the particles exhibited a clear energy dispersion with a low-energy cutoff. The highest cutoff energies were observed near the poleward edge of the auroral oval, and the cutoff energy decreased as the spacecraft moved equatorward. These observations are very consistent with our SMC nightside ions, and we propose a simple nightside velocity filter effect picture, analogous and consistent with dayside models, that could explain the large-scale signatures that we observed during SMC.

Models of dayside convection and FACs, and their dependence on IMF  $B_y$ , were presented by [2]. We have adapted their dayside convection and FAC diagram to the nightside, assuming that the magnetosphere could reach some equilibrium convection state, which is what we believe SMC approaches. The top panel in Fig. 6 most closely approximates our observations in the 03 January 2001 case study. In general, the SuperDARN convection pattern revealed flows out of the polar cap that were tilted towards earlier local times during most of the SMC interval. The fitted convection patterns did not exhibit such a pronounced Harang Discontinuity as this simplified model, and this may or may not be due to data coverage and quality in the fitted equipotential contours in the dawn convection cell. The configuration of the tail magnetic field is also highly complex, which will lead to deviations from this simple picture of the footprint of magnetospheric convection.

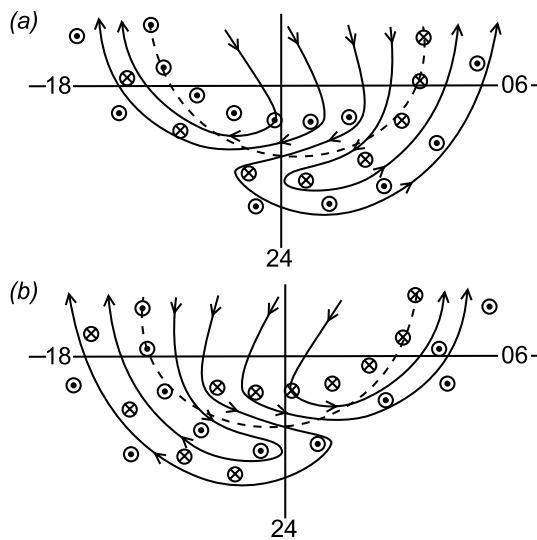


**Fig. 6.** A proposed pattern of nightside convection and FACs during SMC. The dashed line indicates the approximate expected location of the polar cap boundary.

The direction of the FACs in Fig. 6 are predicted primarily based on the proposed convection pattern. The vorticity of the plasma convection is an indicator of the general direction of FAC flow [13]. In the northern hemisphere, downward vorticity (including both vortical and shear flow) corresponds to upward FAC, and vice versa. The recorded development of the double

oval is consistent the top panel in Fig. 6. It is important to note that the very clear double oval, with two large and distinct bands of aurora, was observed at local times earlier than  $\sim 02$  MLT. When compared with Fig. 6(a), one can see that there are two upward FAC bands that flank a downward FAC band. This is only a very simple comparison for an idealized situation. In reality, the bright aurora also indicates regions of enhanced conductivity and conductivity gradients, which modify and refine the estimated FAC distributions.

The dashed line in Fig. 6 represents the open-closed field line boundary, and this is also consistent with DMSP particle spectrograms. The most energetic energy-dispersed ions appeared in the vicinity of the poleward FAC band, near the polar cap boundary, and the ions exhibited decreasing energy with decreasing latitude, as expected. One would expect that the most recently reconnected flux tubes would have precipitating ions with the highest minimum energy, with ever decreasing minimum energies observed as the flux tubes convect out of the polar cap.

### 5.1. Preferred Dayside Merging Site

Why might one expect convection to be directed towards the premidnight sector? One must consider the accumulation of open flux in the magnetotail, as controlled by the IMF orientation. In the event presented, when there were both auroral images and convection maps, the magnitudes of the three IMF components were comparable (see Fig. 3), with  $B_z < 0$ ,  $B_y > 0$ , and  $B_x < 0$ .

Preferred magnetopause merging sites for positive IMF  $B_y$  are expected at high latitudes – a prenoon southern hemisphere region and a postnoon northern hemisphere region. The presence of a strongly negative IMF  $B_x$  would tend to favour the southern prenoon site, which is the case shown in Fig. 7. Fig. 7 is an idealized artistic rendering of the frontside magnetopause, adapted from [14]. An IMF line (“1”) with negative  $B_z$  and

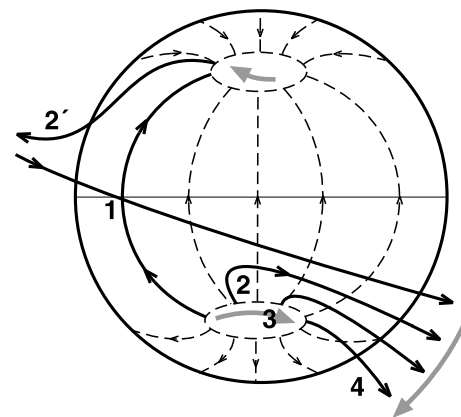


**Fig. 7.** Evolution of magnetic field lines following reconnection at a southern prenoon high-latitude site. Figure modified from the original version of [14]. The numbers indicate the temporal evolution of the flux tube following reconnection, with the primed numbers mapping to the northern hemisphere and the unprimed numbers mapping to the southern hemisphere.

positive  $B_y$  approaches the geomagnetic field. Following reconnection the flux tubes convect away from the reconnection

site, and the subsequent positions of the flux tube are denoted by the numbers, with the “primed” flux tubes mapping into the northern ionosphere and the “unprimed” flux tubes mapping to the southern.

This gives rise to southern hemisphere prenoon flux tubes convecting towards the postnoon magnetotail in the southern hemisphere and the prenoon magnetotail in the northern hemisphere, under the influence of the positive IMF  $B_y$  component. This asymmetric accumulation of open flux in magnetotail would be expected to give rise to asymmetric convection patterns in the ionosphere. The accumulation of more flux in the northern postmidnight tail would lead to the convection in the northern hemisphere towards earlier local times following reconnection. We would expect the opposite to be true for the southern hemisphere, and preliminary analysis of the southern hemisphere SuperDARN data (not shown) support this hypothesis, with convection out of the southern polar cap directed towards later local times.

## 6. Summary and conclusions

The particle, aurora and convection observations were all consistent with the model of ionospheric convection and FACs presented in Fig. 6(a). Because SMC intervals are believed to approach as steady a state as one might expect of magnetospheric convection, we believe that SMC intervals are ideal to deduce properties of the magnetospheric state towards which the magnetosphere tends regardless of whether it is driven in a steady or irregular manner.

We identified SMC intervals with a minimum duration of three hours using the criteria of [1]. The occurrence statistics displayed a seasonal and solar cycle dependence, such that more active and more sunlight times had more SMC intervals. The strength of the ionospheric convection, quantified using  $\Phi_{PC}$ , also displayed a seasonal dependence consistent with the SMC occurrence rates, such that stronger convection was required during the dark northern winter to achieve the same auroral electrojet currents as in the sunlit northern summer months.

SuperDARN had very good data coverage in the pre-midnight and midnight sector during our case study of 03 January 2001. The flow out of the polar cap was observed in the pre-midnight sector for the majority of the interval, and the flow was directed towards earlier local times coming out of the polar cap. This is believed to be consistent with the asymmetric accumulation of open flux in the tail lobes as a result of day-side occurring at a prenoon, high-latitude southern hemisphere merging site.

The IMAGE WIC images showed the development of a double auroral oval during the SMC case study. This is consistent with two bands of upward FAC poleward and equatorward of a band of downward FAC. The vorticity of the SuperDARN convection patterns, which is an estimator of FAC direction, was consistent with the regions of bright aurora.

Several DMSP passes through the midnight sector showed clear energy dispersion of precipitating ions, consistent with the velocity filter effect on recently reconnected field lines.

## References

- O'Brien, T.P., Thompson, S.M., and McPherron, R.L., Steady magnetospheric convection: Statistical signatures in the solar wind and AE, *Geophys. Res. Lett.*, 29:7, 10.1029/2001GL014641, 2002.
- Cowley, S.W.H., and Lockwood, M., Excitation and decay of solar wind-driven flows in the magnetosphere-ionosphere system, *Ann. Geophys.*, 10, 103–115, 1992.
- Greenwald, R.A., et al., DARN/SuperDARN: A global view of high-latitude convection, *Space Sci. Rev.*, 71, 763–796, 1995.
- Henderson, M.G., Reeves, G.D., Skoug, R., Thomsen, M.F., Denton, M.H., Mende, S.B., Immel, T.J., Brandt, P.C., and Singer, H.J., Magnetospheric and auroral activity during the 18 April 2002 sawtooth event, *J. Geophys. Res.*, 111:A01S90, doi:10.1029/2005JA011111, 2006.
- Lockwood, M., Identifying the open-closed field line boundary, in *Polar Cap Boundary Phenomena*, edited by J. Moen et al., pp. 73–90, Kluwer Academic Publishers, Netherlands, 1998.
- McPherron, R.L., O'Brien, T.P., and Thompson, S.M., Solar wind drivers for steady magnetospheric convection, in *Multiscale Coupling of Sun-Earth Processes*, edited by A.T.Y. Lui, Y. Kamide, and G. Consolini, pp. 113–124, Elsevier, Amsterdam, 2005.
- Ruohoniemi, J.M., Baker, K.B., Large-scale imaging of high latitude convection with Super Dual Auroral Radar Network HF radar observations, *J. Geophys. Res.*, 103, 20797–20811, 1998.
- Mende, S.B., et al., Far ultraviolet imaging from the IMAGE spacecraft. 3. Spectral imaging of Lyman- $\alpha$  and OI 135.6nm, *Space Sci. Rev.*, 91:1-2, 287–318, doi:10.1023/A:1005292301251, 2000.
- Mende, S.B., Frey, H.U., Carlson, C.W., and McFadden, J., IMAGE and FAST observations of substorm recovery phase, *Geophys. Res. Lett.*, 29:12, 10.1029/2001GL013027, 2002.
- Pytte, T., McPherron, R.L., Hones, J.E.W., and West, J.H.I., Multiple-satellite studies of magnetospheric substorms, III. Distinction between polar substorms and convection-driven negative bays, *J. Geophys. Res.*, 83:A2, 663–679, 1978.
- Sergeev, V.A., and Lennartsson, W., Plasma sheet at  $X \sim -20 R_E$  during steady magnetospheric convection, *Planet. Sp. Sci.*, 36:4, 353–370, 1988.
- Sergeev, V.A., Pellinen, R.J., and Pulkkinen, T.I., Steady magnetospheric convection: A review of recent results, *Space Sci. Rev.* 75, 551–604, 1996.
- Sofko, G.J., Greenwald, R.A., and Bristow, W.A., Direct determination of large-scale magnetospheric field-aligned currents with SuperDARN, *Geophys. Res. Lett.*, 22, 2041–2044, 1995.
- Wild, J.A., et al., Coordinated interhemispheric SuperDARN radar observations of the ionospheric response to flux transfer events observed by the Cluster spacecraft at the high-latitude magnetopause, *Ann. Geophys.*, 21, 1807–1826, 2003.

# EL — a possible indicator to monitor the magnetic field stretching at global scale during substorm expansive phase: case study

M. Meurant, C. Blockx, E. Spanswick, E.F. Donovan, B. Hubert, J.-C. Gérard, T.S. Trondsen, and M. Connors

**Abstract:** The Ion Isotropy Boundary (IB) is known to correlate well with the magnetic field inclination at geosynchronous orbit around 00 MLT and therefore provides a way to monitor the magnetotail stretching. Several ways to identify IB have been developed in the literature. Based on *in situ* spacecraft data, Sergeev and Gvozdevsky [12] have defined the IB position using NOAA data and Newell et al. [10] defined a comparable boundary (the b2i boundary) based on Defense Meteorological Satellite Program (DMSP) data. From the ground, Donovan et al. [3] used Meridian Scanning Photometers (MSP) to determine the "optical b2i" and Jayachandran et al. [6] demonstrated the coincidence of the b2i and the equatorward boundary of the SuperDARN evening sector E-region scatter. To complement these methods, an IB determination on a wide range of Magnetic Local Time (MLT) with a high temporal resolution is useful. To do this, Trondsen et al. [13] use IMAGE-FUV-SI12 imager to monitor IB by simultaneous comparison with MSP data during a 7 day period. Recently, Blockx et al., [1] have shown the potential of SI12 data for monitoring the magnetotail stretching during quiet periods. In this study, we focus our attention on the ability of SI12 to provide information on tail stretching during active periods and more specifically during the substorm expansive phase. Because of the dynamic character of expansive phases and mechanisms acting between the plasma sources and ionosphere during this phase, deducing IB position from auroral optical data is likely impossible. In order to avoid confusion between the physical meaning of IB and its role as a stretching indicator, we validate a stretching determination method using the EL indicator (determined by the Donovan's algorithm applied on SI12 data) instead of IB. For this validation, we use more than 250 isolated substorms observed by IMAGE-SI12 between 2000 and 2002. Simultaneous comparison with GOES-8 and DMSP data allows us to estimate how strong is the relation between the EL position deduced from SI12 and the magnetic field stretching. Time evolutions of the EL position are also presented for different local times during individual events.

*Key words:* IMAGE, SI12, Substorms, Global Scale, Isotropic Boundary, Equatorial Limit.

## 1. Introduction

The ion Isotropy Boundary (IB) is known to correlate well with the magnetic field inclination at geosynchronous orbit around the 00 MLT sector, and therefore provide a way to monitor the magnetotail stretching. The IB is a field-aligned surface which separate the region of the magnetosphere where protons bounce between mirror points (adiabatic behavior) and the region where the pitch angle scattering is effective enough to keep the down-going loss cone full (non-adiabatic behavior) [12]. The latitude of this boundary depends on the energy of the particles, with the lower latitudes associated with the highest energies. Consequently to the definition of IB, the main fraction of ion precipitations occurs poleward of the IB and essentially no precipitation exists equatorward of the IB (corresponding to the adiabatic motion of ions).

Several ways to identify the IB have been developed in the literature. Based on data obtained by the NOAA spacecraft, Sergeev and Gvozdevsky [12] defined it as the location where the ratio of precipitating to trapped flux dropped below 1 when the spacecraft moves equatorward. Using DMSP measurements, Newell et al. [10] defined the b2i boundary as the position of the maximum total ion energy flux recorded by the satellite when it crosses the auroral oval. Newell et al. [11] showed a close association between the IB of 30 keV protons detected with NOAA satellites and the b2i boundary. Based on MSP measurements, Donovan et al. [3] developed an algorithm to infer the b2i from latitudinal  $H_{\beta}$  (486.1 nm) profiles and demonstrated a strong correlation between the b2i boundary and this 'optical b2i'. The ability of the SI12 imager onboard the IMAGE spacecraft to monitor magnetospheric stretching was suggested by Trondsen et al. [13]. Using Donovan's algorithm applied on 916 boundary determinations obtained simultaneously by MSP and the SI12 imager, they find a correlation coefficient of 0.65 suggesting a reasonably well correlated data set. This result opens the possibility of monitoring the b2i across all local times at the cadence of the IMAGE data, i.e. one image every two minutes. The ability of SI12 to monitor the magnetospheric stretching was recently confirmed by Blockx et al. [1] during quiet periods. Instead to propose an IB determination from the SI12 data, Blockx et al. use the MAX-SI12 and MLAT-MAX-SI12 (the maximum intensity of SI12 at each

Received 15 May 2006.

**M. Meurant, E. Spanswick, E.F. Donovan, and T.S. Trondsen.** Institute for Space Research, University of Calgary, 2500 University Drive NW, Calgary, AB T2N 1N4, Canada.

**C. Blockx, B. Hubert, and J.-C. Gérard.** Laboratoire de physique atmosphérique et planétaire, Université de Lige, 17 Alle du six Aot, 4000 Lige, Belgium.

**M. Connors.** Athabasca University, 11560 80 Avenue, Edmonton, T6G 0R9, Canada.

local time and its magnetic latitude respectively) as an indicator of the stretching rate. They present the relation between the IB determined by NOAA and DMSP and the latitude of the maximum proton precipitation observed by SI12. The links between SI12 data (MAX-SI12 and MLAT-MAX-SI12) and the magnetic field distortion was established by comparison GOES-8 data.

These different ways (*in situ* - NOAA and DMSP - ground based - MSP - and remote sensing - SI12 - measurements) to determine the IB have their own positive and negative aspects. *In situ* spacecraft provide a high spatial resolution of the IB identification at each transit across the oval, i.e. usually with a period of roughly one hour. This time scale is relevant to study certain processes such as magnetic storms but too large for monitoring the tail stretching during minutes around substorm onset, even if the oval is crossed around the onset meridian, which may not necessarily happen. The high spatial resolution allows however an understanding of injection mechanisms thanks to spectrometric measurements. The MSP allows a continuous monitoring using multiple magnetic local times but is subject to the variation of the atmospheric optical thickness. Finally, monitoring by a remote sensing camera, as the SI12 imager, provides a global covering of the entire auroral region with an appropriate time resolution and with a spatial resolution of  $\sim 100$  km. All these types of measurements are complementary to combine global view and high spatial and time resolution.

During active periods like substorm expansive phase, different mechanisms at the origin of particle precipitation into the ionosphere play a more important role than during quiet periods. These different mechanisms may be fresh particles with isotropic pitch angle distribution, electric fields diffusing particles into the loss cone or a magnetic reconfiguration [8]. Because of the more important role of these possible mechanisms of precipitation during substorms, we cannot claim that the limit deduced from optical data also separates the region where protons have an adiabatic motion from the region where protons present a non-adiabatic motion due to the pitch angle scattering caused by the field line stretching. In order to avoid confusion about the physical meaning of the limit, we will consider the Equatorial Limit (EL) instead of the IB. In this study, we determine if the time evolution of the EL during the substorm expansive phase may be an indicator of magnetotail stretching and we present the evolution of EL during three substorms to illustrate the possibilities of EL as a stretching indicator.

## 2. Data

### 2.1. IMAGE

The FUV instrument [7] onboard the IMAGE satellite [2] provides three simultaneous snapshot with approximately the same field of view of the auroral region with a 2 min time resolution. The SI12 camera is sensitive to the Doppler-shifted Lyman- $\alpha$  auroral emission and provides images of the entire polar cap. The two other snapshots image the pattern of electron induced emissions in the 140 - 180 nm band (WIC) and in a 5-nm region centered on the OI line at 135.6 nm (SI13). Substorm events used for this study are selected on the basis of the list given by Frey et al.[4]. We only consider "isolated

events" and defined them as an event separate from the previous and the next one by at least two hours. The procedure of data selection is extensively developed in Meurant et al. [9]. Restrictions applied to the initial list decrease the number of events from 2437 to 262 events.

The equatorial limit (EL) is deduced from SI12 data using Donovan's algorithm. The process starts with the subtraction of the small background present in SI12 data [5]. In a second step, Donovan's algorithm is applied and consists of a gaussian fit of the longitudinal profile and a determination of the limit at  $1.4\sigma$  equatorward of the gaussian fit's maximum. More details concerning the method are provided in [9].

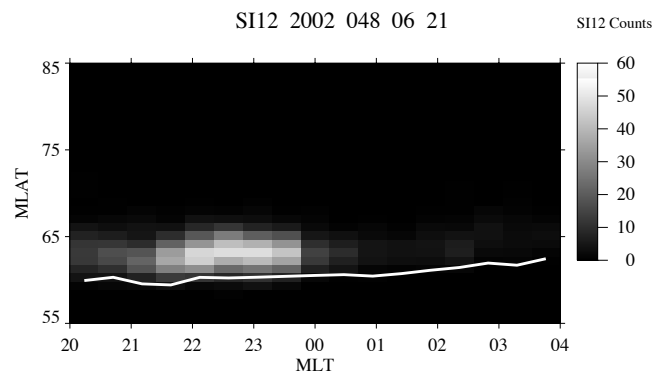


**Fig. 1.** SI12 data displayed in keogram (2002 048 at 0621UT, i.e. 4 minutes after onset). The solid line represents the EL position determined by the Donovan's algorithm. The grey scale represents the intensity recorded by the SI12 instrument for the MLT-MLAT location.

### 2.2. GOES-8

The GOES-8 satellite is a geosynchronous spacecraft. It carries a magnetometer providing continuous measurements of the Earth's magnetic field. These magnetic data are used to monitor the magnetic field stretching via the elevation angle. This elevation angle is deduced from  $B_e$  (the magnetic field parallel to the satellite-Earth center line and points earthward) and  $B_p$  (the magnetic field parallel to the satellite spin axis, perpendicular to the satellite's orbital plane) with the relation  $E_l = \arctan(B_p/B_e)$

### 2.3. DMSP

Spectrograms recorded by the SSJ/4 detectors on board the DMSP spacecraft make it possible to identify several boundaries like the b2i boundary, which is a good proxy of the IB [11]. As developed in [9], in order to evaluate the difference between the EL position determined with SI12 data and b2i positions determined by DMSP crossing, we have selected 304 DMSP crossings in the 20 - 04 MLT sector in the -90 min to +90 min period around onset. Each of these crossings provides the MLAT and MLT of each b2i determination. Because of the DMSP orbit configuration, all these 304 crossing are confined to the 20 - 21.6 MLT sector.

### 3. Validation

In order to evaluate how strong is the relation between the position of EL and the magnetospheric stretching, we present here two comparisons. For the first comparison, we use simultaneous measurements obtained from GOES-8 and SI12. Figure 2a represents the pattern of the 1313 simultaneous measurements. In order to make it easier to read, Figure 2b reproduces the cloud of Figure 2a by squares representing the mean value of each two degree bins and bars indicating a one sigma deviation. The linear regression using the entire sample is represented by the thick solid line and could be compared to results provided by [12] (thin solid line) and the method developed in [1] applied to our sample (dashed line). A shift of one degree between [12] and [1] was already discussed in [1]. However, we observe a larger shift (2 °) due to a larger width of the oval than during quiet periods investigated in [1]. These results are also very close to those obtained by Sergeev and Gvozdevsky [12], both for absolute values and the slope.

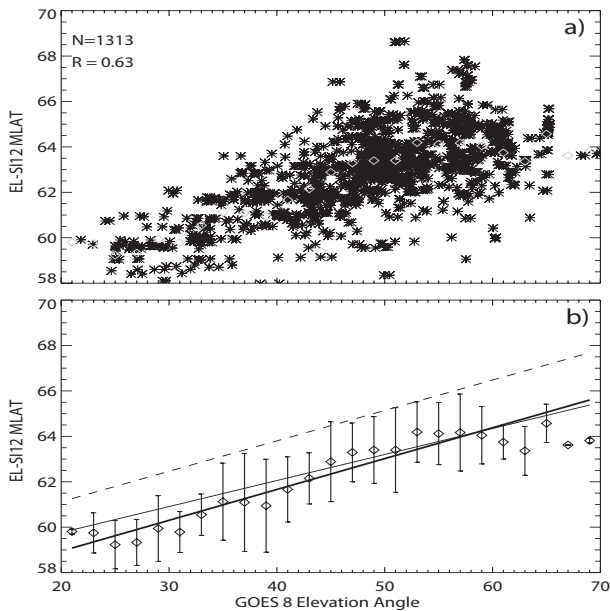


**Fig. 2.** a) Scatter plot of 1313 elevation angles deduced from GOES-8 measurements in the 21-03 MLT sector vs the magnetic latitude of EL deduced from SI12 data at the same MLT. These measurements are recorded by GOES-8 during the 20 minutes following the onset. Squares represent the mean value of the MLAT of EL for bins of an arbitrary width of two degree of the elevation angle. b) The average values obtained with two degree bins are reproduced for the comparison with error bars representing a  $1\sigma$  deviation. The solid line represents the linear regression of the entire sample presented in a). For comparison, the solid-dashed line represents the regression obtained in [12] and the dashed line was obtained by the method developed in [1] and applied to our data set.

In the second comparison, we use b2i boundaries determined by the DMSP spacecraft. This boundary is considered as a good proxy of IB and therefore as a good indicator of the tail stretching. Figure 3 represents the comparison of EL and b2i positions obtained at the same location and the same time.

Typically, the b2i boundary is located  $\sim 1^\circ$  poleward of the EL position and about 72% of the points are within a  $\pm 1.5^\circ$  interval.

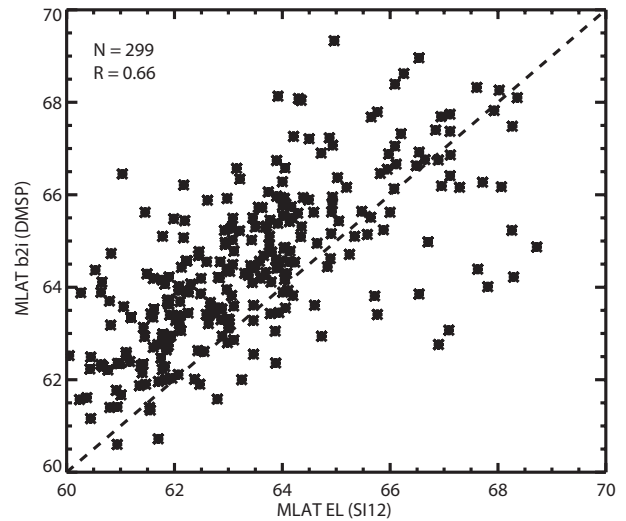


**Fig. 3.** Scatter plot of b2i obtained by DMSP and EL deduced from SI12 data at the DMSP MLT.

These comparisons indicate that the EL position is dependent on the tail stretching and consistent with previous studies [12] [1]. Based on this indicator, Meurant et al. [9] describe the statistical pattern of the time evolution of the EL position during the expansive phase. For this study, we will consider the case study aspect by the description of three individual cases.

### 4. Case Study

#### 4.1. First case

The first substorm studied in this paper occurred on September 29, 2001, and the onset was observed at 0854UT. The position of the EL deduced from SI12 data are plotted in Figure 4a and elevation angles at the same time and at the same MLT deduced from GOES-8 data are plotted in Figure 4b. The onset was observed at 01.05 MLT, i.e. roughly 3 MLT duskward of the GOES-8 position at onset time. The dipolarisation consecutive to onset is observed by GOES-8  $\sim 5$  minutes after the onset identification by IMAGE/FUV. By comparison, the EL position starts a poleward motion  $\sim 8$  minutes after the onset identification. This time delay of three minutes can be interpreted as the reaction time between the modification of the magnetic field topology and the consequences on the ionospheric precipitations.

#### 4.2. Second Case

This second substorm occurred on April 02, 2002 at 05:06 UT (Figure 5). The GOES-8 spacecraft was located  $\sim 2$  hours downward of the onset position. The dipolarisation is observed by GOES-8  $\sim 6$  minutes after the onset identification and presents a sharp increase of the elevation angle. The corresponding poleward motion of the EL position is observed  $\sim 2$  minutes after the magnetic field reconfiguration. The evolution of the EL position doesn't present the sharp variation of the GOES-8 data.

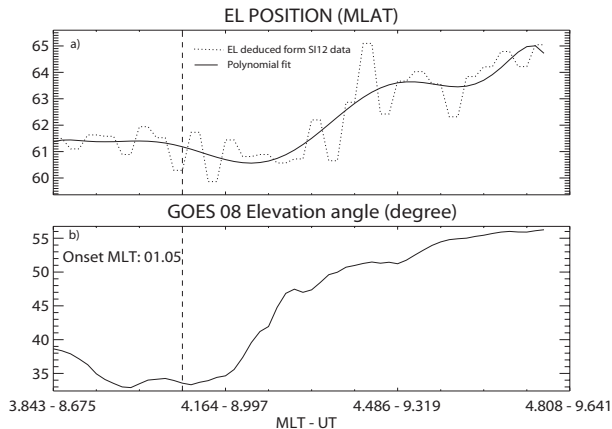


**Fig. 4.** a) EL position deduced from SI12 data at different MLT or UT during the event of Sept. 29, 2001. Dotted line is for real positions of EL and the solid line for a polynomial fit based on the dotted line. The vertical dashed line represent the time of the onset (08:54 UT) observation at the MLT indicated in panel b). b) MLT / time evolution of the elevation angle deduced from GOES-8 measurements.

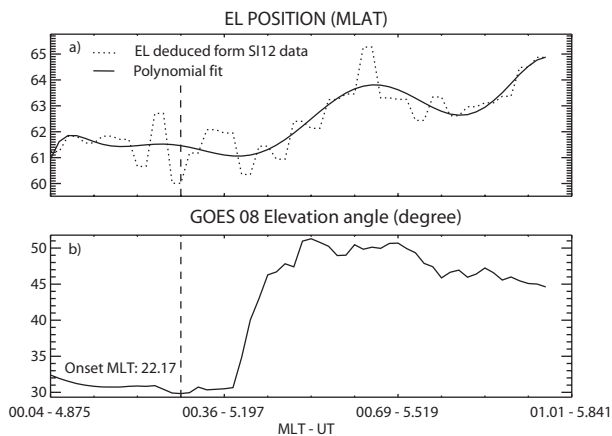


**Fig. 5.** Same caption as Figure 4 for the Apr. 02, 2002 event. Onset is observed at 05:06 UT.

### 4.3. Third case

The third substorm occurred on June 13, 2002 at 03:03 UT (Figure 6). The GOES-8 spacecraft was located less than 1 MLT downward to the onset position (0.82 MLT). A slight stretching is observed in GOES-8 data before the dipolarisation. The dipolarisation is observed 6 minutes after the onset identification and presents a very sharp increase of the elevation angle. By comparison, the evolution of the EL position at the GOES-8 MLT is more smooth than the GOES-8 observations but presents the same trends.

## 5. Discussion and conclusion

The determination of the magnetic field reconfiguration during substorm expansive phase is very challenging because of the large scale of the volume of interest and short periods of time of these mechanisms. Since the direct observation of such

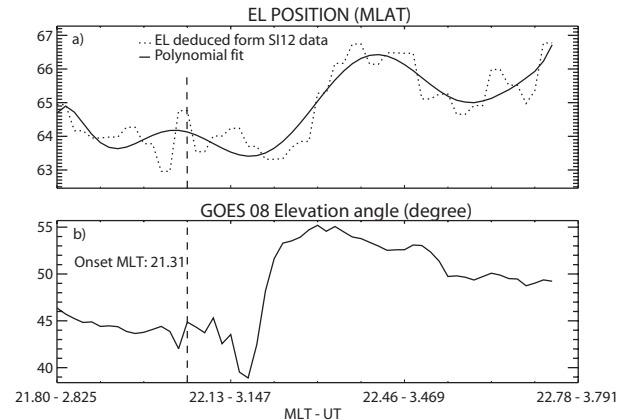


**Fig. 6.** Same caption as Figure 4 for the June 13, 2002 event. Onset is observed at 03:03 UT.

a topology and its observation is impossible, the most convenient ways are modelling and deduction from available data. Data obtained in the auroral region are very interesting to investigate for this purpose since auroral precipitations are the reflect of magnetospheric processes. In this study, we address the question of the monitoring of the magnetospheric stretching by using optical data recorded by IMAGE/FUV/SI12 in which we apply Donovan's algorithm. These data are relevant for this purpose since they cover large regions and they are obtained at the rate of one image each two minutes. Donovan's algorithm was initially developed to infer a proxy of the Isotropic Boundary. However, we have no evidence allowing to say that the boundary provided by this algorithm during active periods is the footprint of the surface separating the magnetospheric region where proton presents an adiabatic motion to the region where their motion is non-adiabatic. For this region and because the IB is typically located close to the oval's equatorward boundary, we consider the Equatorial Limit (EL) in this study.

By comparison with GOES-8 data for 1313 simultaneous measurements during the 20 minutes following onset, the EL position presents a dependence close to those observed in [12] for the isotropic boundary. This relation between the EL position and the magnetic field stretching is confirmed by the comparison with b2i boundaries determined by the DMSP spacecraft. It appears that the EL is located one degree equatorward of the equivalent b2i boundary.

In the second part of this study, we apply Donovan's algorithm to data obtained during three substorms events and compare the results to elevation angles deduced from GOES-8 data. These comparisons show that the trend of GOES-8 observations are reproduced by the time evolution of the EL position. These similarities give us confidence on the ability to monitor magnetotail stretching thanks to Donovan's algorithm applied to optical global scale data such as SI12 data. Pointing problems affecting SI12 data make the polynomial fit necessary. This step affects the time resolution of information provided by the EL position. Beyond this technical problem, EL appears to be an interesting indicator of the magnetospheric stretching, which opens the door to global surveying of the tail stretching during active periods.

## Acknowledgements

M.M is supported by the AIF fellowship, J.C.G. and B.H. are supported by the Belgian National Fund for Scientific Research (FNRS). The IMAGE FUV investigation was supported by NASA through SWRI subcontract 83820 at the University of California, Berkeley, contract NASS-96020. Participation from J.C.G was funded by the PRODEX program of the European Space Agency (ESA) and the Fund for Collective and Fundamental Research (FRFC grant 2.4517.02). We acknowledge data providers to CDAWeb for the GOES data. The DMSP particle detectors were designed by Dave Hardy of AFRL, and data were obtained from JHU/ APL. We thank Dave Hardy, Fred Rich, and Patrick Newell for the use of the particle detector data.

## References

1. Blockx, C., J.-C. Gérard, M. Meurant, B. Hubert, and V. Coumans, Far-Ultraviolet remote sensing of the isotropic boundary and magnetotail stretching, *J. Geophys. Res.*, *110*, A11215, doi:10.1029/2005JA011103., 2005.
2. Burch, J. L., Image Mission Overview, *Space Science Reviews*, *91*, 1-14, 2000.
3. Donovan, E. F., B. J. Jackel, I. Voronkov, T. Sotirelis, F. Creutzberg, and N. A. Nicholson, Ground-based optical determination of the b2i boundary: A basis for an optical MT-index, *J. Geophys. Res.*, *108*, 1115, doi:10.1029/2001JA009198, 2003.
4. Frey, H. U., S. B. Mende, V. Angelopoulos, and E. F. Donovan, Substorm onset observations by IMAGE-FUV, *J. Geophys. Res.*, *109*, A10304, doi:10.1029/2004JA010607, 2004.
5. Hubert B., J.C. Grard, D.S. Evans, M. Meurant, S.B. Mende, H.U. Frey and T.J. Immel, Total electron and proton energy input during auroral substorms: remote sensing with IMAGE-FUV, *J. Geophys. Res.*, *107*, doi:10.1029/2001JA009229, 2002.
6. Jayachandran, P. T., E. F. Donovan, J. W. MacDougall, D. R. Moorcroft, K. Liou, P. T. Newell, and J.-P. St-Maurice, Global and local equatorward expansion of the ion auroral oval before substorm onsets, *J. Geophys. Res.*, *110*, A05204, doi:10.1029/2004JA010837. , 2005.
7. Mende, S. B., H. Heeterds, H.U. Frey, M Lampton, S.P. Geller, S. Habraken, E. Renotte, C. Jamar, P. Rochus, J. Spann, S.A. Fuselier, J.-C Grard, G.R. Gladstone, S. Murphree, and L. Cogger, Far Ultraviolet Imaging from the IMAGE spacecraft : 1 System Design, *Space Science Reviews*, *91*, 243, 2000.
8. Mende, S. B., H. U. Frey, T. J. Immel, D. G. Mitchell, P. Brandt and J.-C. Gérard, Global comparison of magnetospheric ion fluxes and auroral precipitation during a substorm, *Geophys. Res. Lett.*, *29*, 12,1609, doi:10.1029/2001GL014143, 2002.
9. Meurant, M., C. Blockx, E. Spanswick, E.F. Donovan, B. Hubert, J.-C. Gérard, V. Coumans, and M. Connors, EL - a possible indicator to monitor the magnetic field stretching at global scale during substorm expansive phase: statistical study, *J. Geophys. Res.*, *to be submitted*.
10. Newell, P. T., Y. I. Feldstein, Y. I. Galperin, C. I. Meng, Morphology of nightside precipitation, *J. Geophys. Res.*, *101*, 10,737, 1996.
11. Newell, P. T., V. A. Sergeev, G. R. Bikkuzina, and S. Wing, Characterizing the state of the magnetosphere : Testing the ion precipitation maxima latitude (b2i) and the ion isotropy boundary, *J. Geophys. Res.*, *103*, 4739, 1998.
12. Sergeev, V.A. and Gvozdevsky, B. B., MT-index - a possible new index to characterize the magnetic configuration of magnetotail, *Ann. Geophys.*, *13*, 1093, 1995.
13. T. S. Trondsen, E. F. Donovan, N. A. Nicholson, B. J. Jackel, L. L. Cogger, D. Lummerzheim, H. Frey, and M. Meurant, Multipoint Observations of the Ion Isotropy/b2i Boundary, *Annales Geophysicae*, *to be submitted*.



# Magnetic flux transport in the Dungey cycle: the role of substorms in flux closure

S. E. Milan, G. Provan, and B. Hubert

**Abstract:** We investigate the dayside and nightside magnetic reconnection rates that drive the Dungey convection cycle in the magnetosphere, focusing on the contribution of substorms to the flux closure process. We find a good correspondence between substorms and episodes of nightside reconnection; the average amount of open flux closed is 0.3 GWb, which represents almost 50% of the 0.65 GWb that is typically present at substorm onset. Although conventional wisdom suggests that magnetospheric convection is in the main driven by tail reconnection occurring at a distant X-line independently of substorms, we find no clear signatures of reconnection during non-substorm intervals. This suggests that (almost) all of flux closure in the Dungey cycle occurs at a near-Earth X-line during substorms.

*Key words:* Substorms, Magnetic reconnection, Dungey cycle, Flux transport.

## 1. Introduction

The last few years have seen an increasing use of the technique of measuring changes in the size of the polar cap to estimate dayside and nightside reconnection rates (e.g. [15, 9, 10, 13, 11, 12, 7]). These reconnection rates control the rate of flux transport within the Dungey cycle ([2] and [3]), the driver for the majority of magnetospheric dynamic phenomena. When the day- and nightside reconnection rates are unbalanced the open flux content of the magnetosphere waxes and wanes as described by the expanding/contracting polar cap paradigm (ECPC), as proposed by e.g. [16] and [1]. This paper examines the role of substorms in the closure of open flux within the Dungey cycle.

A summary of nightside reconnection rates observed during substorms was recently presented by [14]. These results indicated that while the duration and rate of reconnection was highly variable between substorms, often 0.3 GWb of open flux was closed, representing approximately a half of the open flux in the magnetosphere at onset. Substorms, then, play an extremely important role in flux closure in the Dungey cycle, as predicted by [8]. This brief report presents an extended set of results, and comments on changes in the open flux content of the magnetosphere during substorms.

## 2. Observations and discussion

Changes in the open flux contained within the polar cap are found from auroral images taken from space, SuperDARN radar [5] observations, and measurements of precipitating particles by low-Earth polar orbiting spacecraft, as described in detail by [13]. Results of a 12-hour observing period on 26 August 1998 are shown in Figure 1 (also investigated in detail by [11]). Panel (a) shows the variation in open flux,  $F_{PC}$ , determined using these techniques (thick grey curve) between 00 and 12 UT, the period that auroral images were available.  $F_{PC}$

varies between 0.2 and 0.9 GWb in this interval, increases being due to the opening of flux at the magnetopause by low latitude reconnection when the interplanetary magnetic field (IMF) is directed southwards, and decreases due to reconnection in the tail mainly during substorm activity. Thus, the change in  $F_{PC}$  can be described as a competition between the dayside and nightside rates of reconnection,  $\Phi_D$  and  $\Phi_N$ :

$$\frac{dF_{PC}}{dt} = \Phi_D - \Phi_N. \quad (1)$$

Changes in  $F_{PC}$  do not allow unambiguous measurements of  $\Phi_D$  and  $\Phi_N$ , but only the difference between them. To remove this ambiguity, measurements of the ionospheric convection flow are necessary, as described by [13] and [7]. However, an approximate disentanglement of the contributions of  $\Phi_D$  and  $\Phi_N$  to  $dF_{PC}/dt$  can be found if  $\Phi_D$  is assumed to be proportional to the Y-component of the solar wind motional electric field  $V_{SW}B_S$ , where  $V_{SW}$  is the solar wind speed and  $B_S$  is the southward component of the IMF, as described by e.g. [9]. For reference, IMF  $B_z$  measured by ACE and lagged to the magnetopause is presented in panel (d). Assuming an effective dayside X-line length  $L_{eff} \approx 5R_E$  allows the dayside reconnection rate to be written

$$\Phi_D = L_{eff}V_{SW}B_S \quad (2)$$

which is indicated by the solid curve in panel (e). This time series of  $\Phi_D$  has been used in conjunction with Eq. 1 to find the expected variation in  $F_{PC}$  with time, assuming in the first instance that no nightside reconnection takes place, that is  $\Phi_N = 0$ , and this is shown by the dotted line in panel (a). Although the observed and predicted curves do not match, the rate of increase of  $F_{PC}$  is well-captured by the predictions during periods of southward IMF. Discrepancies between the predicted and observed curves is then due to the occurrence of nightside reconnection. We consider this nightside reconnection to occur in specific episodes (4 in the present interval) which are each associated with uniform  $\Phi_N$  for the duration of the event. We have chosen the start and end of each reconnection burst, and the rate of reconnection during the burst, to achieve as good a fit as possible between predicted  $F_{PC}$  (Eq. 1), shown by the

Received 15 May 2005.

S. E. Milan and G. Provan. University of Leicester, U.K.

B. Hubert. University of Liege, Belgium.

black curve in panel (a), and the observations. The occurrence of these bursts and their associated  $\Phi_N$  is shown by grey rectangles in panel (e).

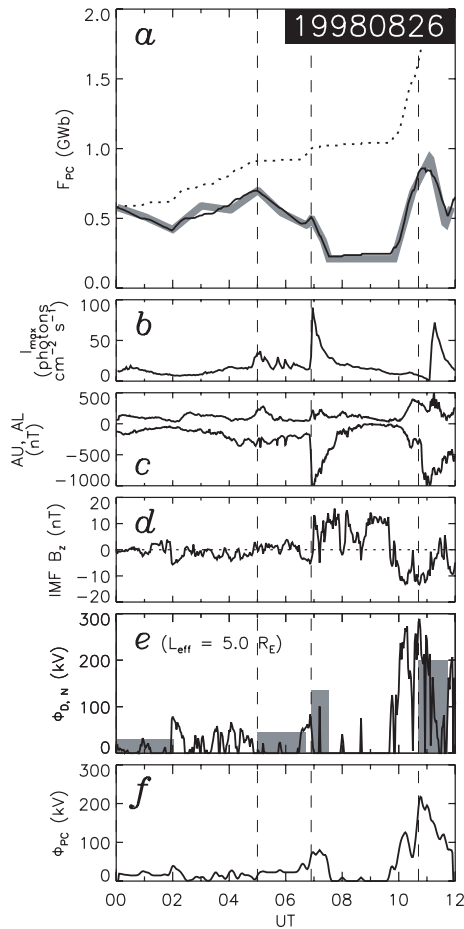


**Fig. 1.** (a) The observed open flux in the northern polar cap (grey curve) for a 12-hour period on 26 August 1998, along with modelled variations (dotted and solid curves, see text for details). (b) Maximum auroral brightness in the nightside sector. (c)  $AL$  and  $AU$  auroral indices. (d) IMF  $B_z$  measured by the ACE spacecraft and lagged to the magnetopause. (e) Estimated dayside (solid curve) and nightside (grey rectangles) reconnection rates. (f) Estimated transpolar voltage,  $\Phi_{PC}$ .

We can assess the association between the reconnection bursts so-determined and substorm activity by comparing with panels (b) and (c) which show the maximum auroral brightness observed in the night sector by the auroral imager and the  $AU$  and  $AL$  indices, respectively. The auroral brightness shows a sharp increase at substorm onset due to the formation of the substorm auroral bulge, e.g. 04:55, 06:55, and 11:00 UT, which then fades over a period of an hour or so. The  $AL$  index exhibits sharp bays at substorm onset due to the formation of the substorm current wedge (SCW), most clear at 06:55, and 10:45 UT. (The delay between the  $AL$  bay and auroral luminosity enhancement at 10:45 is found to be due to incomplete coverage of the nightside auroral oval by the imager of this time.) In some cases the  $AU$  and  $AL$  evidence for substorm activity is not overwhelming, for instance 04:55 UT, though

a clear dipolarization of the tail field is seen at GOES-10 at this time [11], indicative of substorm onset. On the other hand, smaller and more symmetrical increases in  $AU$  and decreases in  $AL$  are associated with enhancements in convection, driven mainly after southward turnings of the IMF, e.g. 02:10 and (most clearly) 10:00 UT. These convection-driven perturbations in  $AU$  and  $AL$  are, as expected from the ECPC model, associated with periods of growth of  $F_{PC}$ .

We find an excellent agreement between the onset of tail reconnection signatures (periods of  $\Phi_N > 0$  and contractions of the polar cap) with auroral and magnetometer signatures of substorms, cementing the relationship between substorms and the Dungey cycle (e.g. [8]). The close association between reconnection onset and  $AL$  bays indicates that the formation of the SCW and the activation of the tail X-line are closely related (at least at our time-resolution of  $\sim 10$  minutes). Due to the link between substorms and reconnection, we assume that the onset of flux closure is associated with the formation of a near-Earth X-line (NEXL). Interestingly, we see no evidence for nightside reconnection during obvious non-substorm intervals, which would be expected to occur at a distant tail X-line (DXL). If reconnection does take place at a DXL, then we conclude that the flux through-put associated with this process is small in comparison to the reconnection at the NEXL during substorms. Magnetospheric convection is often thought of as being driven by reconnection at the dayside and at a DXL, with the formation of a NEXL being necessary only following a large accumulation of open flux during substorm growth phase, which must be rapidly disconnected. Our present observations suggest that a DXL is unnecessary in the convection cycle, and most (or all) accumulated open flux is disconnected during substorms by a NEXL.

Assuming that convection is driven solely by the dayside and nightside reconnection identified in panel (e) we can estimate the transpolar voltage  $\Phi_{PC}$ , the rate of antisunward flux transport in the Dungey cycle, from

$$\Phi_{PC} = \frac{1}{2}(\Phi_D + \Phi_N) \quad (3)$$

([8] and [14]). Estimates of  $\Phi_{PC}$  from Eq. 3 are shown in panel (f), and it would be interesting to compare these with measurements of the transpolar voltage from, for instance, SuperDARN. This will be the subject of a forth-coming study.

The data presented for the 26 August 1998 interval are typical of 9 intervals, totalling 73 hours of observations, that we have analyzed (see forth-coming article in *J. Geophys. Res.*). During the 73 hours of observations we identified 25 nightside reconnection events. The characteristics of these events are indicated in Figure 2 which show, in the form of histograms, (a) the open flux at the onset of each event, (b) the flux remaining at the end of each event, (c) the reconnection rate, (d) the duration, and (e) the total flux closed during each event. The main finding we take from these is that the reconnection events begin in the main once  $F_{PC} > 0.5$  GWb and stop once  $F_{PC} < 0.5$  GWb. The most common value of flux closed is 0.25 GWb. The average flux closed is 0.3 GWb, which compared with the average open flux at onset, 0.65 GWb, indicates that on average almost 50% of the flux present in the polar cap prior to onset is subsequently closed during the event.

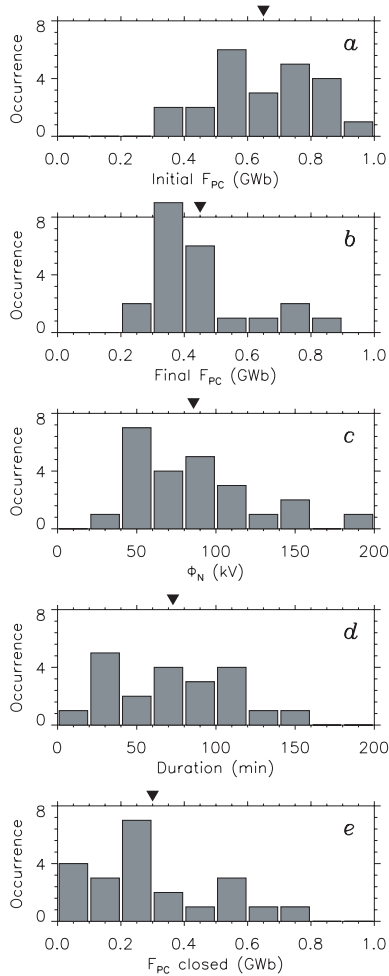


**Fig. 2.** The characteristics of 25 nightside reconnection bursts identified during 73 hours of observations. (a) The open flux  $F_{PC}$  at onset of each event; (b)  $F_{PC}$  at the end of each event; (c) the reconnection rate and (d) duration of each event; (e) the amount of flux closed during each event. Arrows indicate the average of each distribution.

In Figure 3 we investigate the relationship between  $F_{PC}$  and IMF  $B_z$  for the 73 hours of observations. Statistical models suggest that the auroral oval is located at lower latitudes during periods of strong dayside coupling or enhanced geomagnetic activity. An example is the model of [6], based on the observations of [4], which provides a functional representation of the poleward and equatorward boundaries of the auroral oval, parameterized by disturbance level (represented by the  $Q$  index in the model of [6]). However, at any one moment the latitude of the auroral oval is dictated by the open flux content of the magnetosphere, so that when  $F_{PC}$  is large the oval is located at low latitudes and vice versa, and we do not expect a direct relationship between geomagnetic activity and  $F_{PC}$ . Despite this, Fig. 3 indicates that on average  $F_{PC}$  is indeed elevated during periods of southward IMF, though the spread in the data is very large. In actuality, the data show that during periods of southward IMF the polar cap enters a cycle of polar cap expansions and contractions, giving rise to the large spread in  $F_{PC}$  values; when the IMF is directed northward  $F_{PC}$  remains more

uniform and has on average a smaller value. Hence, it is not possible to determine the latitude at which the auroral oval will be located for a given disturbance level, except in a statistical sense. Our results show rather that during disturbed periods the auroral oval will change constantly in latitude.

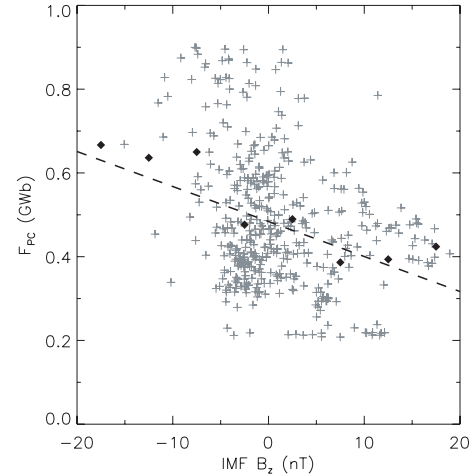


**Fig. 3.** The relationship between  $F_{PC}$  and IMF  $B_z$  for the 73 hours of observations. The diamonds indicate the average  $F_{PC}$  in 5 nT-wide bins of IMF  $B_z$ . The dashed curve indicates a least-squares fit to the distribution.

Finally, we compare the histogram of the open flux at the onset of each reconnection burst (Fig. 2a) with the occurrence distribution of  $F_{PC}$  itself. Figure 4 shows the  $F_{PC}$  occurrence distribution for the 73 hours of observation;  $F_{PC}$  varied between about 0.2 and 0.9 GWb during our observing intervals. The mean value of  $F_{PC}$  is 0.46 GWb, so we notice immediately that substorm onset occurs most frequently when the magnetosphere has accumulated a greater than average open flux content. We take the histogram in Fig. 2a and normalize it with respect to the  $F_{PC}$  occurrence distribution, shown as the black curve in Fig. 4. This represents the number of substorms that occur per hour at different values of  $F_{PC}$ . This shows a dramatic increase in the probability of substorm onset as  $F_{PC}$  rises above 0.6 GWb. This suggests that the tail flaring associated with large amounts of accumulated open flux are partly responsible for triggering substorm onset.

### 3. Conclusions

Determining the open flux content of the magnetosphere from auroral, radar, and LEO particle observations of the size of the polar cap is a powerful technique for the investigation of large-scale solar wind-magnetosphere coupling. This brief investigation of changes in the size of the polar cap allows us to conclude that substorms play a fundamental role in the closure of flux within the Dungey cycle. Substorms on average close 0.3 GWb of open flux, the average flux contained in the magnetosphere at onset being 0.65 GWb. The probability of onset of tail reconnection (or, equivalently, substorm onset) increases dramatically once the open flux accumulated through dayside reconnection grows above 0.6 GWb. Flux closure during substorms appears to be able to account for the full magnetic flux

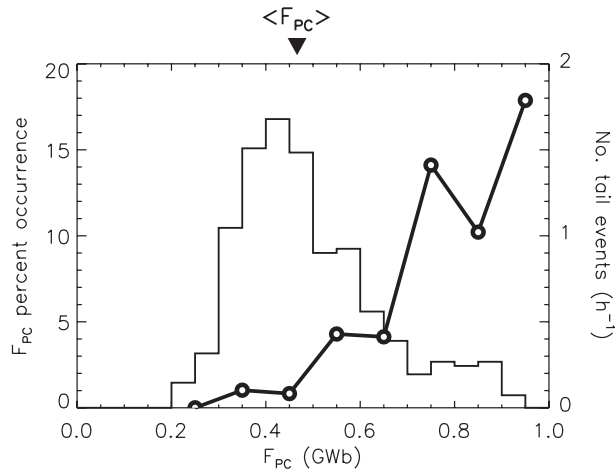


**Fig. 4.** The overall occurrence distribution of  $F_{PC}$  during the 73 hours of observations. Superimposed is the distribution of  $F_{PC}$  at the onset of the 25 reconnection events (Fig. 2a) normalized with respect to occurrence distribution of  $F_{PC}$  (curve).

throughput of the Dungey cycle. This reconnection presumably takes place at a near-Earth X-line, formed at substorm onset. We find no evidence for closure of flux during non-substorm periods, which would take place at a distant X-line. If a DXL does exist, we conclude that it plays only a minor role in flux closure and the Dungey cycle.

**Acknowledgements:** GP was supported by PPARC grant no. PPA/G/O/2003/00013. The ACE data used in this study were accessed through CDAWeb. The authors would like to thank N. F. Ness at the Bartol Research Institute for use of the MAG data. We also thank G. K. Parks for use of auroral images from the Polar UVI instrument; this data was obtained through the UVI Online Search Tool (<http://csds.uah.edu/uvi-ost/>).

## References

1. Cowley, S. W. H., and Lockwood, M., Excitation and decay of solar wind-driven flows in the magnetosphere-ionosphere system, *Ann. Geophysicae*, *10*, 103–115, 1992.
2. Dungey, J. W., Interplanetary magnetic fields and the auroral zones, *Phys. Rev. Letters*, *6*, 47–48, 1961.
3. Dungey, J. W., The structure of the exosphere or adventures in velocity space, in *Geophysics, The Earth's Environment*, eds. C. De Witt, J. Hieblot, and L. Le Beau, Gordon and Breach, New York, p. 503–550, 1963.
4. Feldstein, Y. I., and Starkov, G. V., Dynamics of auroral belt and geomagnetic disturbances, *Planet. Space Sci.*, *15*, 209, 1967.
5. Greenwald, R. A., et al., DARN/SuperDARN: A global view of the dynamics of high-latitude convection, *Space Sci. Rev.*, *71*, 761–796, 1995.
6. Holzworth, R. H., and Meng, C.-I., Mathematical representation of the auroral oval, *Geophys. Res. Lett.*, *2*, 377–380, 1975.
7. Hubert, B., Milan, S. E., Grocott, A., Blockx, C., Cowley, S. W. H., and Grard, J.-C., Dayside and nightside reconnection rates inferred from IMAGE FUV and Super Dual Auroral Radar Network data, *J. Geophys. Res.*, *111*, A03217, doi: 10.1029/2005JA011140, 2006.
8. Lockwood, M., and Cowley, S. W. H., Ionospheric convection and the substorm cycle, in *Proceedings of the International Conference on Substorms (ICS-1)*, 99–109, 1992.
9. Milan, S. E., A simple model of the flux content of the distant magnetotail, *J. Geophys. Res.*, *109*, A07210, doi: 10.1029/2004JA010397, 2004a.
10. Milan, S. E., Dayside and nightside contributions to the cross polar cap potential: placing an upper limit on a viscous-like interaction, *Ann. Geophysicae*, *22*, 3771–3777, 2004b.
11. Milan, S. E., Cowley, S. W. H., Lester, M., Wright, D. M., Slavin, J. A., Fillingim, M., Carlson, C. W., and Singer, H. J., Response of the magnetotail to changes in open flux content of the magnetosphere, *J. Geophys. Res.*, *109*, A04220, doi: 10.1029/2003JA010350, 2004.
12. Milan, S. E., Hubert, B., and Grocott, A., Formation and motion of a transpolar arc in response to dayside and nightside reconnection, *J. Geophys. Res.*, *110*, A01212, doi: 10.1029/2004JA010835, 2005.
13. Milan, S. E., Lester, M., Cowley, S. W. H., Oksavik, K., Brittnacher, M., Greenwald, R. A., Sofko, G., and Villain, J.-P., Variations in polar cap area during two substorm cycles, *Ann. Geophysicae*, *21*, 1121–1140, 2003.
14. Milan, S. E., Wild, J. A., Grocott, A., and Draper, N. C., Space- and ground-based investigations of solar wind-magnetosphere-ionosphere coupling, *Adv. Space. Res.*, in press, 2006.
15. Provan, G., Yeoman, T. K., Lester, M., and Milan, S. E., A multi-instrument approach to mapping the global dayside merging rate, *Ann. Geophysicae*, *20*, 1905–1920, 2002.
16. Siscoe, G. L., and Huang, T. S., Polar cap inflation and deflation, *J. Geophys. Res.*, *90*, 543–547, 1985.

# Pi2 pulsation periodicity and variations in magnetotail flows

K. R. Murphy, A. Kale, I. J. Rae, I. R. Mann, and Z. C. Dent

**Abstract:** Pi2 pulsations are a category of ULF waves with periods between 40–150 seconds frequently observed by ground-based magnetometers predominantly during substorm onset. The origin of these pulsations has been attributed to the coupling of Alfvénic oscillations associated with the generation of the substorm current wedge, and fast-mode compressional waves moving radially inward from the tail, including plasmaspheric cavity modes at low-latitudes. It has recently been suggested that the frequencies of observed night-side auroral zone and low-latitude Pi2 pulsations, or Pi2 waveforms on the flanks, may be due to periodic variations in the sunward plasma flow from the tail such as during multiple bursty bulk flows (BBFs). Using a favourable conjunction of the Geotail satellite with the CARISMA ground-based magnetometers on 23rd December 2000, the relationship between the frequency of Pi2 pulsations observed on the ground and periodicity in Earthward plasma flows has been investigated. Enhanced Earthward flows were seen during periods of substorm activity; however, using time-series analysis a direct link was not observed between the periodicity in the flow-bursts and the periodicity of pulsations within the Pi2 waveband.

*Key words:* Pi2, Bursty Bulk Flows, Flow Bursts, ULF waves.

## 1. Introduction

### 1.1. Pi2 pulsations

Pi2 pulsations are a category of impulsive, irregular Ultra Low Frequency (ULF) pulsations with periods of about 40–150 seconds (6–25 mHz). They often occur during periods of substorm activity, and are associated with impulsive magnetic field dipolarisations. The origin of Pi2s is thought to be disturbances in the near-Earth plasma sheet, including the generation of field-aligned currents in the substorm current wedge.

At higher latitudes, the ground-based magnetic signature of Pi2 pulsations is thought to be dominated by the transient, transverse Alfvén wave carrying the initial field aligned current. If a full substorm onset occurs, then the cross tail current can become diverted through the ionosphere, leading to the formation of the substorm current wedge [9]. If there is an impedance mismatch between the incident wave and the ionosphere, then partial reflection can occur [3, 12]. It is often thought that the Alfvén wave bounces between the plasma sheet and the ionosphere, giving rise to the periodic structure of the Pi2 [3, 12].

The plasmashet disturbance also causes compressional fast-mode waves to move radially inward towards the Earth. These fast mode waves can couple to transverse waves and excite local field line resonances, or can impact the plasmopause and lead to plasmaspheric cavity mode oscillations. These effects are generally responsible for the dominant signal seen at lower latitudes [12].

The exact mechanism by which the near-Earth plasma sheet is disturbed is not fully understood. Recent work suggests that Earthward high-speed magnetotail plasma flows may rapidly brake as they approach the dipolar inner magnetosphere and

may be responsible for the initial plasmashet disturbance [7].

### 1.2. Magnetotail plasma flows

Plasma flows in the central plasma sheet typically have velocities of approximately  $30 \text{ km s}^{-1}$ ; however high-speed Earthward flows with velocities 1 or 2 orders of magnitude higher have been observed at distances as far as  $\sim 30 R_E$  [1]. They are rarely seen closer than  $10 R_E$ , which is thought to be evidence for braking of the flows due to an increased magnetic pressure at the inner magnetosphere. The high-speed flows often exhibit a temporal fine structure—with characteristic timescales of the order of minutes—called flow bursts (FBs). These FBs are often encapsulated in bursty bulk flows (BBFs); envelopes of FB activity with durations of 10's of minutes often occurring within the BBF during which the plasma velocity is greater than  $\sim 400 \text{ km s}^{-1}$ .

### 1.3. Pi2 pulsations and flow bursts

Recently it has been suggested that BBFs may provide a mechanism for the generation of Pi2 pulsations, with reported correlations between the periodicity of FBs seen in the magnetotail and the periodicity of the Pi2 pulsations suggesting the possibility of direct driving [6]. It has been suggested that the braking of the flows generates fast-mode waves that directly drive low-latitude Alfvénic field line oscillations on the flanks, and possibly perturbations on the night-side. The braking of flows is also thought to generate a current contribution to the substorm current wedge, with a larger contribution driven by pressure gradients and flow shears [14, 4]. We investigate these hypotheses below.

## 2. Observations: 23rd December 2000

### 2.1. Instrumentation

To investigate the relationship between the periodic structure of flow bursts seen in the magnetotail and Pi2 periodicity, plasma dynamics, as measured by instruments onboard

Received 6 June 2005.

K. R. Murphy, A. Kale, I. J. Rae, I. R. Mann, and Z. C. Dent.  
Department of Physics, University of Alberta, Edmonton, Alberta,  
Canada.

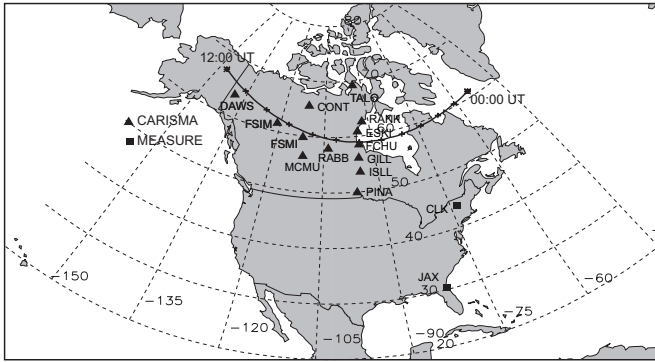


**Fig. 1.** Ground magnetic field trace (north) of the conjunction between Geotail and the CARISMA magnetometer array for 23rd December 2000, 0000–1200 UT, mapped onto the ground using the Tsyganenko 89c model [15]. The overlaid grid shows contours of geographic latitude and longitude.

the Geotail satellite, were compared to ground-based magnetometer data obtained from the Magnetometers Along the Eastern Atlantic Seaboard for Undergraduate Research and Education (MEASURE)[10] and Canadian Array for Real-time Investigations of Magnetic Activity (CARISMA) arrays (<http://www.carisma.ca>; formerly known as the CANOPUS (Canadian Auroral Network for the OPEN Program Unified Study) array [13]).

The Geotail satellite carries a suite of instruments to study the structure and dynamics of the tail region of the magnetosphere. The orbit on the 23rd December 2000 was approximately  $9 \times 30 R_E$ , with an inclination of  $-7^\circ$  to the ecliptic plane. The Low-Energy Particle (LEP) instrument on board measures 3-D ion velocity distributions with energies between 7 eV–42 keV at 12 s resolution, enabling the resolution of structures occurring on P2 time-scales [11]. The Comprehensive Plasma Instrument (CPI) data provides information on plasma densities and temperatures in the 50 eV–48 keV range at 64 s resolution, enabling the calculation of plasma parameters characteristic of specific magnetospheric regions discussed below [5]. The Magnetic Field Instrument (MGF) on board Geotail enabled the determination of the 3-D magnetic field vector at 3 s resolution [8].

Plasma flows occurring in the plasma sheet boundary layer (PSBL) are typically field-aligned and are therefore not subject to the braking in the near-Earth region experienced by BBFs in the central plasma sheet (CPS). The CPS represents a more dipolar region than that of the PSBL, and has a characteristic magnetic-field topology defined by [1] which typically satisfies:

$$\frac{B_z}{(B_x^2 + B_y^2)^{1/2}} > 0.5. \quad (1)$$

The CPS has also been defined as the region with an ion plasma-beta ( $\beta_i$ )—the ratio of ion thermal to magnetic pressures—greater than 0.5 ([1, 2] and references within). Both of these relations are used together to determine whether Geotail resides in the PSBL or CPS.

Site Code	Site	CGM Lat. ( $^\circ$ N)	CGM Lon. ( $^\circ$ E)	L value
TALO	Taloyoak	78.54	330.01	NA
CONT	Contwoyto	72.97	303.87	11.84
RANK	Rankin Inlet	72.47	335.36	11.20
ESKI	Eskimo Point	70.78	332.51	9.37
FCHU	Fort Churchill	68.57	332.92	7.61
FSMI	Fort Smith	67.45	306.16	6.90
FSIM	Fort Simpson	67.33	293.50	6.84
RABB	Rabbit Lake	67.05	318.42	6.68
GILL	Gillam	66.28	332.46	6.27
DAWS	Dawson	65.92	273.16	6.10
MCMU	Fort McMurray	64.31	308.52	5.40
ISLL	Island Lake	63.86	332.80	5.23
PINA	Pinawa	60.19	331.20	4.11
CLK	Clarkson University	55.39	2.14	3.10
JAX	Jacksonville University	41.82	351.41	1.80

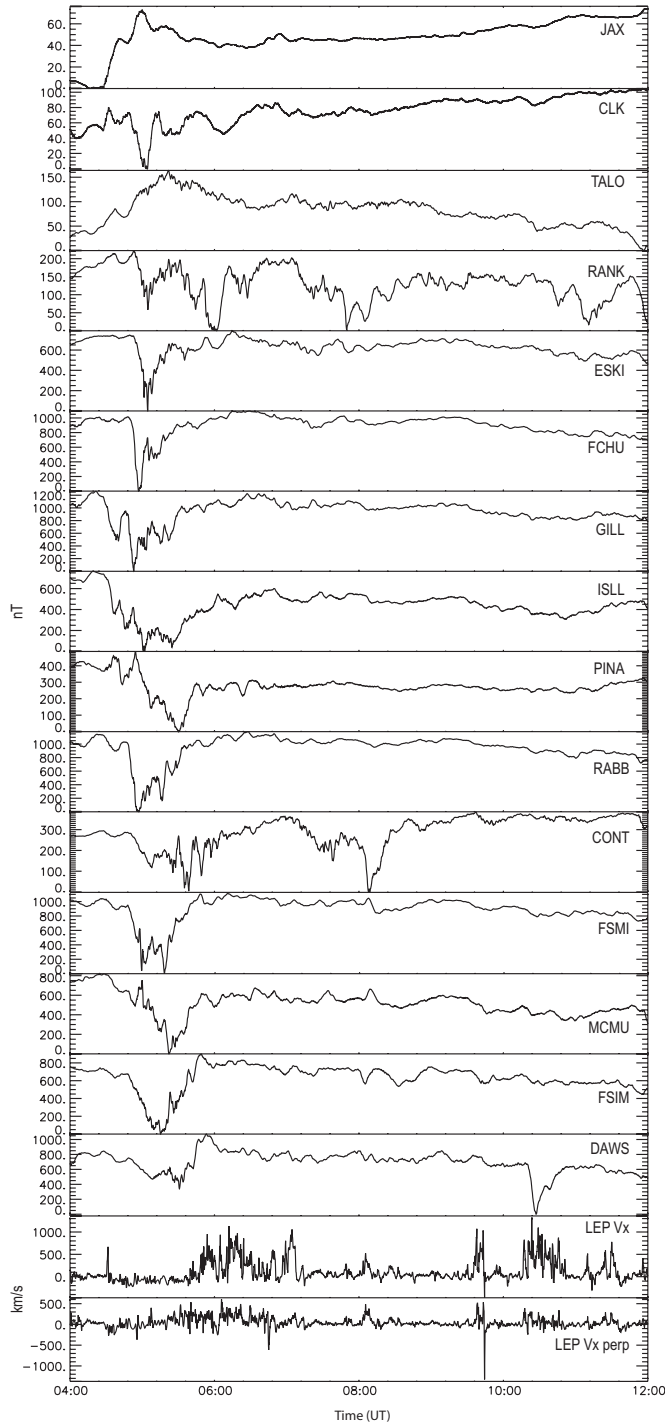
**Table 1.** Ground-based magnetometer stations used during this study. L-shell and CGM position calculated using the NSSDC MODELWeb facility (<http://nssdc.gsfc.nasa.gov/space/cgm/cgm.html>).

## 2.2. Observations

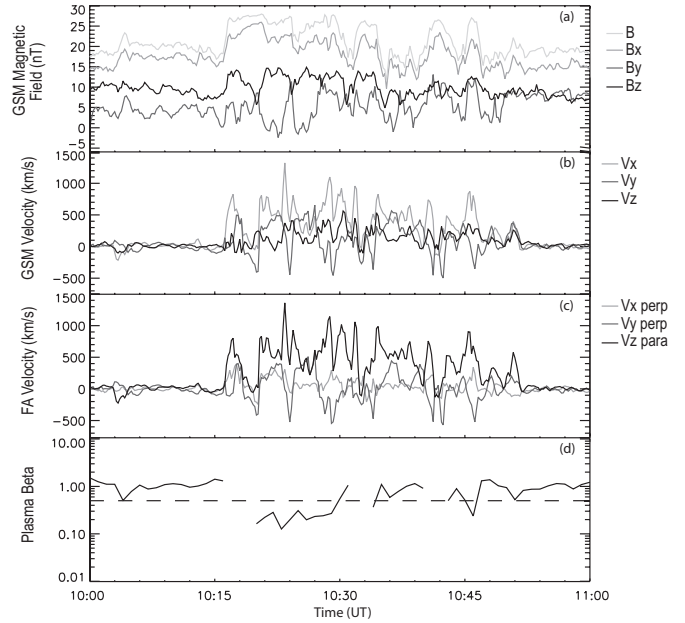
Favourable night-side conjunctions between the Geotail spacecraft and CARISMA during an interval of substorm activity were sought; one such conjunction occurred during a substorm on 23 December 2000 with Geotail situated in the mid-tail at  $X_{GSM} -15$ – $-17 R_E$ . The north ground magnetic field trace (obtained assuming Tsyganenko 89c external and IGRF internal geomagnetic fields [15]) can be seen in Figure 1, along with the positions of the ground-based magnetometers (see also Table 1).

Figure 2 shows the unfiltered ground-based H-component magnetograms for the period 0400–1200 UT on 23rd December 2000. The sites cover a wide range of latitudes, from  $\sim 30^\circ$ – $\sim 70^\circ$  N, with longitudes from  $\sim 220^\circ$ – $\sim 285^\circ$ . Several substorm bay signatures are seen over this period, from  $\sim 0430$  UT at all stations, further activity at  $\sim 0805$  UT being most noticeable at Contwoyto Lake (CONT), and additional activity at  $\sim 1012$  UT, primarily located near Dawson City (DAWS). The bottom two panels are data from the Geotail LEP instrument, the upper panel being  $V_{X_{GSM}}$ , the lower panel being the earthward component of  $V_{X_{GSM}}$  perpendicular to the field vector, B, and is described below.

During the magnetic conjunction, the magnetic field vector direction measured by Geotail has a large  $X_{GSM}$  component, suggesting that Geotail is close to the edge of the CPS in a region of stretched tail-like magnetic field. In this region, a high proportion of the plasma flow is field-aligned and therefore plasma flow velocities perpendicular to the magnetic field direction are considered. To calculate the direction of the measured fields in a coordinate system aligned with the ambient magnetic field, the data was transformed from  $[X_{GSM}, Y_{GSM}, Z_{GSM}]$  to  $[X_{FA}, Y_{FA}, Z_{FA}]$  where  $Z_{FA}$  is field-aligned,  $X_{FA}$  lies in a plane defined by  $Z_{FA}$  and the geocentric radius vector to the spacecraft and is perpendicular to  $Z_{FA}$ , and  $Y_{FA}$  completes this right-handed orthogonal set. This orthogonal co-



**Fig. 2.** Stack plot showing (top down) unfiltered H-component magnetometer data for the period 0400–1200 UT on 23rd December 2000 from two MEASURE magnetometers and the CARISMA magnetometer array. The Earthward velocity component of the plasma flow as measured by the LEP instrument onboard Geotail is shown as both  $V_{X_{GSM}}$  and in terms of field perpendicular velocity,  $V_{perpx}$  (see text for details).



**Fig. 3.** In-situ measurements recorded by Geotail for the period 1000–1100 UT. The panels show (top down) the magnetic field, the plasma velocity in the GSM coordinate system and the flow in field-aligned coordinate system (FA) measured by LEP, and  $\beta_i$  from the CPI instrument.

ordinate system was derived using a running mean of the ambient magnetic field of 20 minutes duration. In this field-aligned co-ordinate system,  $V_{perpx}$  represents the  $V_{X_{GSM}}$  component perpendicular to the field vector,  $B$ .

Two extended BBF events are seen during the conjunction, occurring at times similar to that of the substorms, being approximately 0930–0945 UT, and 1015–1100 UT. There is also smaller flow enhancements at 0755–0812 UT and 0930–0945 UT, though neither fit the criteria of a BBF [1]. Unfortunately, there were periodic data gaps in the Geotail LEP data from 0430–0530 UT, which corresponded with the onset of the largest substorm event measured during the interval, however there is no evidence of strong flows occurring during this substorm onset, hence this event is not studied.

### 2.3. BBF event between 1000–1100 UT

During this event the Geotail satellite was located at  $(-17.5, -2.9, -1.9) R_E$  in GSM coordinates. During this interval, Geotail was not directly conjugate to any CARISMA magnetometer; rather the spacecraft track was located magnetically between the DAWS and FSIM stations (shown in Figure 1). Therefore in this interval, the DAWS and FSIM are situated closest to local midnight and the onset region, and the Churchill Line meridian is  $\sim 3$  hours of local time towards the dawn flank. Geotail was located in the CPS as evidenced by  $\beta_i > 0.5$ , shown in Figure 3d, for the periods preceding and following the flow event. The data gaps in  $\beta_i$  are due to data gaps in the CPI instrument data. During the flow event,  $\beta_i$  decreases below 0.5, due to the increase in the total magnetic field (Figure 3a). Over this period, the CPI-determined ion temperature remains constant, suggesting that Geotail is monitoring the passing of the flow, rather than drifting between the PSBL and CPS.

A small substorm bay occurs around 1012 UT, recorded first at Fort Smith (FSMI). This signature is then recorded at the lower latitude Churchill line magnetometers ( $\sim 265$  degrees geographic longitude) and westwards at DAWS at 1017 UT—the latter having the largest H-component bay of  $\sim 600$  nT. As previously mentioned, DAWS and FSIM are close to local midnight, with the Churchill line of magnetometers being closer to the dawn flank. The first large plasma flow occurs at  $\sim 1016$  UT and continues through successive flow bursts until just after 1050 UT.

A fundamental aspect of the BBF:Pi2 relationship proposed by [6] is that there will be a one-to-one correlation between the FBs and individual oscillations in the waveform of the Pi2 pulsations; both the waveform and the frequency content should therefore be similar between the two data sets. Figure 4 shows ground magnetometer data and Geotail flow burst velocity data (a) band-pass filtered between 40–200 s, and (b) their power spectra in this frequency band. It can be seen from Figure 4(a) that there is no visual temporal correlation evident between the H-component Pi2 signals and the LEP  $V_{\text{perpx}}$  signals. There are, at times, similar Pi2 periodicities coincident in both data, most notably 1040–1050 UT at ESKI, however it must be noted that even this wavepacket connection appears to be acausal with respect to the BBF, the ground oscillations preceding the initial flow onset. It should also be noted that the Geotail flow velocity measurements have not been time-shifted in the manner of [6] to allow for propagation effects. Figure 4(b), in contrast to the time-series data, shows that, at times, similar frequencies are observed on the ground and in space. For example, there are clear peaks in  $V_{\text{perpx}}$  in the  $\sim 7$ –8 mHz,  $\sim 11$ –13 mHz and  $\sim 15$ –16 mHz frequency ranges. There is evidence that there are similar frequencies in the H-component magnetometer data in DAWS-FSMI-RABB-PINA-GILL in the  $\sim 7$ –8 mHz frequency band, at JAX-CLK in the  $\sim 11$ –13 mHz, and in MCMU-PINA-FSMI-RABB in the  $\sim 15$ –16 mHz band, though at much lower amplitudes in several cases. It must be noted that FSIM and DAWS show relatively large amplitude waveforms, compared to those of the other stations, since these two stations were closest to the substorm onset region. Both FSIM and DAWS show evidence of a  $\sim 7$ –8 mHz frequency, however the further peaks in the FSIM and DAWS power spectra appear to be in the troughs of the  $V_{\text{perpx}}$  power spectra in frequency space.

Whilst it is evident that there were similar frequencies observed in some of the ground and spacecraft measurements, inspection of Figures 4(a) and (b) together reveals that these frequencies are not contemporaneously observed throughout the 1 hour window; neither do the waveforms on the ground and in space show any coherency (i.e., the waveforms are dissimilar at similar times).

#### 2.4. BBF event between 0600–0730 UT

During this event, Geotail was both magnetically conjugate to the Churchill Line meridian, and located around 24 MLT, in contrast to the event detailed in Section 2.3. Consequently, the conjugacy at this time is optimal for diagnosing the characteristics of any substorm onsets that occur near local midnight. From Figure 2 it can be seen that there were further FBs and associated Pi2 signatures observed on the ground between 0600–0730 UT. Figure 5 shows the filtered time series

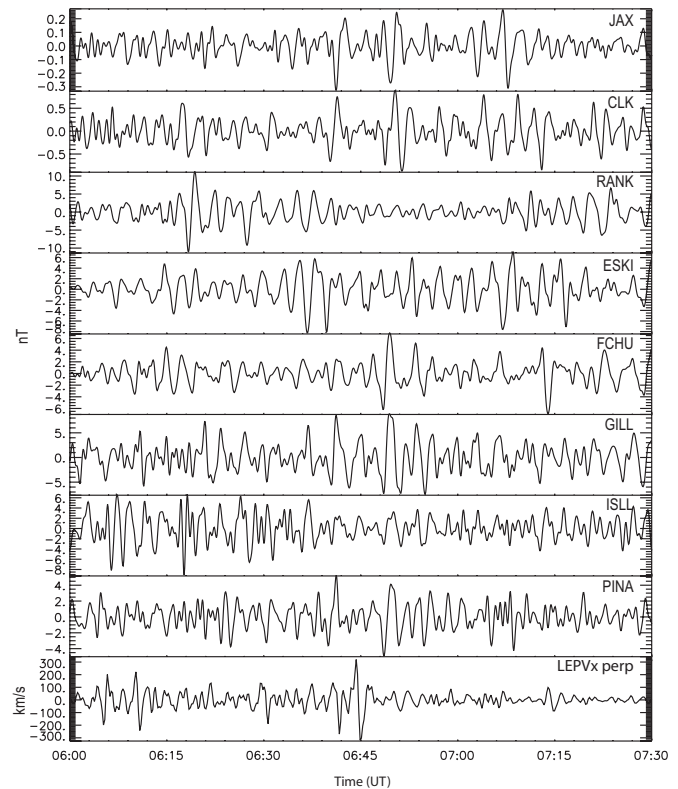


**Fig. 5.** Stack plot showing the H-component oscillations present in the Pi2 waveband during the BBF event occurring between 0600–0730 UT, from the ground-based magnetometers shown in Table 1 (and analogous to Figure 4(a)).

in the Pi2 frequency range for this interval (and is analogous to Figure 4(a)). Again, there are similar frequencies in the Pi2 band in both magnetic perturbations and  $V_{\text{perpx}}$  during this interval (for brevity, a power spectra is not shown), but little one-to-one correlation between the waveforms and certainly no coherent wavepacket activity is observed in  $V_{\text{perpx}}$  concurrent with Pi2 wavepacket observations on the ground.

### 3. Discussion and Conclusions

In this paper we studied a night-side conjunction between the Geotail spacecraft and the CARISMA and MEASURE ground-based magnetometer arrays in the North American sector and investigate the possible relationship between the periodicity present in flow enhancements comprising a BBF and the frequency content of ground-based magnetometer measurements in the Pi2 wave band, first proposed by Kepko and co-workers [6, 7]. In their model, individual flow bursts drive a transient Pi2 pulsation response via induced currents due to flow braking. At lower-latitudes on the flanks, Pi2 signatures are proposed to be directly-driven by compressional fast-mode pulses associated with periodicity in the braking of Earthward flows. The implications of these statements is that as a result of the proposed Pi2 generation mechanisms, both the frequency content of the flow bursts and the waveform should be similar to frequency content and waveform of the magnetic Pi2 measurements on the ground.

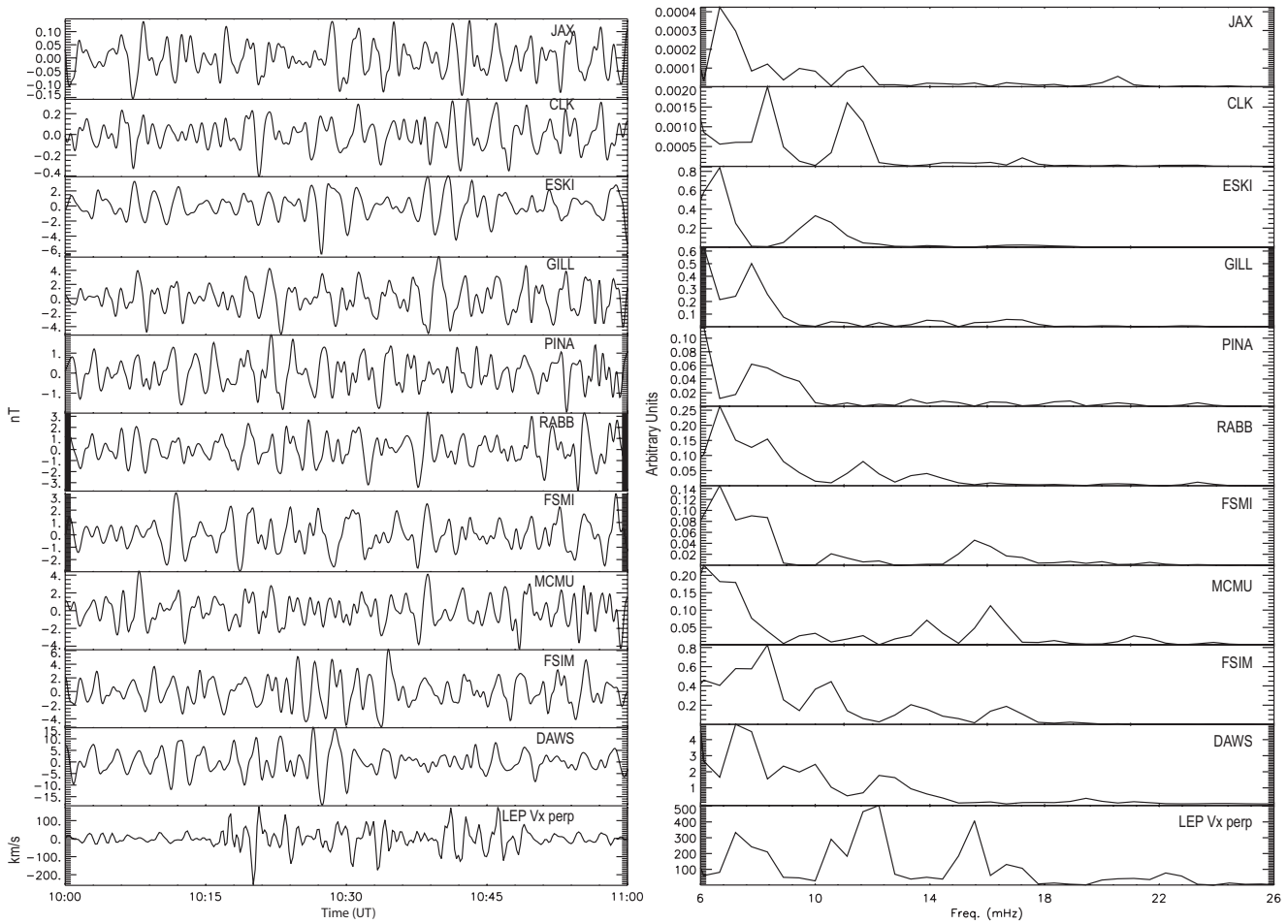


**Fig. 4.** Stack plots of (a) Band-pass filtered Pi2 (40–200 s) time series between 1000–1100 UT (b) their associated power spectra, filtered in the 5–25 mHz band for the period 1010–1040 UT, for the ground H-component magnetometer data and Geotail  $V_{\text{perpx}}$  flow data. Power is expressed in arbitrary units. The stations represent several areas of interest noted in [7] namely, stations between midnight and the dawn flank covering a range of latitudes (JAX-CLK-ESKI-GILL-PINA-RABB-FSMI-MCMU) and stations located radially inward of the magnetotail (DAWS-FSIM).

We analysed three separate events from the 23rd December 2000 interval, whereby Geotail was in an extended conjunction with the CARISMA and MEASURE magnetometer arrays. Due to brevity, we discuss two of these events in this paper, but concentrate on one in order to present the data in its entirety. For the event occurring between 1000–1100 UT, the power is dominant in the FBs (in the Pi2 frequency band) at  $\sim 7\text{--}8$  mHz,  $\sim 11\text{--}13$  mHz and  $\sim 15\text{--}16$  mHz. Nearly all magnetometer sites show the majority of power, within the Pi2 frequency band of the H-component, to be between 5–7 mHz—lower than that of the dominant frequencies seen in the FBs. At higher frequencies, the features in the FB power spectrum do not reflect those measured on the ground for DAWS and FSMI, the two sites closest to the substorm event. There is power present at a single common frequency for some Churchill line sites, such as RABB ( $\sim 11\text{--}13$  mHz) and FSMI ( $\sim 15\text{--}16$  mHz). These features are isolated and, in general, not common between several magnetometer stations, as might be indicative of a common driver. In summary, between 1000–1100 UT, both the Geotail  $V_{\text{perpx}}$  and H-component magnetometer data showed some evidence of similar frequency content in predominantly the

$\sim 7\text{--}8$  mHz and  $\sim 11\text{--}13$  mHz ranges, though not consistently throughout the magnetometer array. However, comparison of the waveforms reveals that these frequencies are not coherent in the ground and spacecraft measurements, and therefore the waveforms do not show any clear evidence for a directly-driven relationship.

In the results obtained by Kepko et al. [7], the authors show visual correlation between the periodic variation in the  $V_{\text{perpx}}$  component of the plasma flow velocity and the unfiltered magnetometer data. In the two events studied in this paper, we see no evidence of this behaviour. This could be due to the nature of the incident flow burst being different in this study, than those used by Kepko et al. In their investigations, the flow bursts had a large amplitude and were distinct, with periods of 1–2 minutes. In our study, the dominant frequencies are less monochromatic, with components outside the Pi2 range of frequencies. Also, the time of increased Pi2 activity is less optimal with respect to the inferred substorm onset meridian, with the dominant ground-based activity measured at  $\sim 10$  UT ( $\sim 4$  MLT) and therefore away from local midnight and discussed in Section 2.3, which may also be a contributing factor.

However, the event discussed in Section 2.4 is both magnetically conjugate and the ground-magnetometers and spacecraft location are in the local midnight region, and this event shows the same result; there is no evidence of a directly-driven Pi2 signature by the FBs within a BBF.

There is evidence for flow enhancements occurring at times similar to that of substorm onset and therefore increased Pi2 wave activity, for 2 of the 3 events, as seen in Figure 2. However, it does not appear that the flow enhancements always occur prior to the periods of increased Pi2 activity, but seem to be acausal in relation. This is illustrated in the interval 1000 UT–1100 UT by the substorm bay observed at FSMI beginning to form at 1012 UT, prior to the enhanced Earthward flow observed by Geotail, located some  $-17.5 R_E$  downtail, at 1016 UT. At DAWs however, the substorm bay begins forming at 1017 UT—after the FB. Similar behaviour is also noted during the 0930–1000 UT BBF event. Therefore it seems apparent that the BBF may not be responsible for the increase Pi2 activity seen in this case.

In summary, there is little evidence for the action of the proposed model outlined [7] in the intervals presented in this paper. Low frequency power ( $\sim 7$ – $8$  mHz) is seen in both the ground H-component and  $V_{\text{perpx}}$ , and sporadic evidence for  $\sim 11$ – $13$  mHz frequencies in some of the ground magnetograms in conjunction with the Geotail  $V_{\text{perpx}}$ , with the location of the ground magnetometer (at midnight or toward the dawn flank) not affecting this observation. However, there is no evidence for coherent wavepackets in the ground and spacecraft measurements at the same time during the studied interval. Thus, we conclude that during the BBF events between 0400 UT–1200 UT on 23rd December 2000, BBFs occur at times similar to periods of increased Pi2 activity, but there is no evidence supporting a causal directly-driven connection between Pi2s and flow burst waveforms, whereby a burst in flow may be responsible for an individual Pi2 pulsation.

## Acknowledgements

This work was partially funded by an NSERC Discovery Grant to IRM and the Canadian Space Agency (CSA). The operation of CARISMA, part of the Canadian Geospace Monitoring Program, is funded by the CSA via a contract to the University of Alberta. Data regarding the position and magnetic mapping of the Geotail satellite, Geotail magnetic field (MGF) data and low energy particle (LEP) data, Geotail comprehensive plasma instrument (CPI) data, were obtained from NASA via, Satellite Situation Center (SSC Web) System and Services, at <http://sscweb.gsfc.nasa.gov/>, T. Nagai and T. Mukai through DARTS at the Institute of Space and Astronautical Science (ISAS) in Japan and B. Patterson through ISTP, International Solar-Terrestrial Physics, at <http://erebus.physics.uiowa.edu/cpi-data/survey/hp/>, respectively. CARISMA data and MEASURE data were obtained from the Space Science Data Portal at <http://www.ssdp.ca> and M. Moldwin and <http://measure.igpp.ucla.edu/measure/team.html>, respectively.

## References

1. Angelopoulos, V., Baumjohann, W., Kennel C. F., Coroniti F. V., Kivelson M. G., Pellat R., Walker R. J., Lühr H. and Paschmann G., Bursty bulk flows in the inner central plasma sheet, *Journal of Geophysical Research*, *97*, 4027–4039, 13321, 1992.
2. Angelopoulos V., Kennel C. F., Coroniti F. V., Pellat R., Kivelson M. G., Walker R. J., Russel C. T., Baumjohann W., Feldman W. C., and Gosling J. T., Statistical characteristics of bursty bulk flow events, *Journal of Geophysical Research*, *99*, 21257, 1994.
3. Baumjohann, W. and Glaßmeier, K. H., The transient response mechanism and Pi2 pulsations at substorm onset—Review and outlook, *Planetary and Space Science*, *32*, 1361–1370, 1984.
4. Birn, J. Hesse, M. Haerendel, G., Baumjohann, W. and Shiokawa, K., Flow braking and the substorm current wedge, *Journal of Geophysical Research*, *104*, 19895, 1999.
5. Frank, L. A., K. L. Ackerson, W. R. Paterson, J. A. Lee, M. R. English, and G. L. Pickett, The Comprehensive Plasma Instrumentation (CPI) for the Geotail spacecraft, *Journal of Geomagnetism and Geoelectricity*, *46*, 23–37, 1994.
6. Kepko, L. E., and Kivelson M. G., Generation of Pi2 pulsations by bursty bulk flows, *Journal of Geophysical Research*, *104*, 25021, 1999.
7. Kepko, L. E., Kivelson M. G. and Yumoto K., Flow bursts, braking, and Pi2 pulsations, *Journal of Geophysical Research*, *106*, 1903, 2001.
8. Kokubun, S., T. Yamamoto, M. H. Acuna, K. Hayashi, K. Shiokawa, and H. Kawano, The Geotail Magnetic Field Experiment, *Journal of Geomagnetism and Geoelectricity*, *46*, 7–21, 1994.
9. Lester, M., Hughes, W. J., and Singer H. J., Longitudinal structure in Pi2 pulsations and the substorm current wedge, *Journal of Geophysical Research*, *89*, 5489–5494, 1984.
10. Moldwin, M. B., and Berube, D., ULF resonance monitoring of diurnal plasmaspheric refilling: Results from the MEASURE magnetometer array, *Eos Trans. AGU*, *85(17)* Jt. Assem. Suppl., Abstract, SM31A-09, 2004.
11. Mukai, T., S. Machida, Y. Saito, M. Hirahara, T. Terasawa, N. Kaya, T. Obara, M. Ejiri, and A. Nishida, The low energy particle (LEP) experiment onboard the Geotail satellite, *Journal of Geomagnetism and Geoelectricity*, *46*, 669–692, 1994.
12. Olsen, J., Pi2 pulsations and substorm onsets: A review, *Journal of Geophysical Research*, *104*, 17499, 1999.
13. Rostoker, G., J. C. Samson, F. Creutzberg, T. J. Hughes, D. R. McDiarmid, A. G. McNamara, A. Vallance Jones, D. D. Wallis and L. L. Cogger, CANOPUS - A ground based instrument array for remote sensing the high latitude ionosphere during the ISTP/GGS program, *Space Science Reviews*, *71*, 743–760, 1995.
14. Shiokawa, K., Baumjohann, W. and Haerendel G., Braking of high-speed flows in the near-Earth tail, *Geophysical Research Letters*, *24*, 1179, 1997.
15. Tsyganenko N. A., A magnetospheric magnetic field model with a warped tail current sheet, *Planetary and Space Science*, *37*, 5–20, 1989.

# Fast flow, dipolarization, and substorm evolution: Cluster/Double Star multipoint observations

R. Nakamura, T. Takada, W. Baumjohann, M. Volwerk, T. L. Zhang, Y. Asano, A. Runov, Z. Vörös, E. Lucek, C. Carr, B. Klecker, H. Rème, and O. Amm

**Abstract:** Fast flow and associated magnetic field disturbances are keys to understand the link between the near-Earth tail and the inner magnetosphere, where the essential energy conversion processes take place during substorms. The four-point Cluster observation allows to investigate spatial structure and associated signature of dipolarization disturbances. With the launch of Double Star, simultaneous observations of the inner magnetosphere and the midtail took place in summer 2004 and 2005. Such a constellation of spacecraft allows us further to study the flow and dipolarization disturbance both in the local and the larger context. That is, by applying multi-point analysis techniques, the direction and speed of the propagation is determined within the Cluster tetrahedron and can then be compared with the global propagation of the disturbances using Double Star as well as relevant ionospheric disturbances. We discuss plasma sheet fast flow and dipolarization characteristics obtained from local as well as global multi-point observations during substorms.

*Key words:* fast flows, dipolarization, substorms, Cluster, Double Star.

## 1. Introduction

High-speed plasma flows in the near-Earth plasma sheet are considered to play a key role in flux and energy transport in the magnetotail and substorm dynamics. Cluster traversed the magnetotail covering regions Earthward of  $19 R_E$  since summer 2001. The four spacecraft observations enabled us to differentiate spatial from temporal disturbances and provided a chance to obtain essential parameters, such as current density or spatial scale of the flow and field disturbances. Since the launch of the two satellites of the Double Star Program (DSP), Cluster and DSP allow large-scale multi-point observations along the same local time sector. Such simultaneous observations of the inner magnetosphere and the near-Earth tail are essential in substorm studies because of the initial local onset and the subsequent global expansion of the disturbance. Particularly, how these two key regions are linked in terms of fast flow and magnetic field dipolarization is yet to be determined to understand the mechanism of the substorm development.

The two satellites of DSP, TC1 and TC2, were launched in December 2003 and TC2 in July 2004, respectively, providing another opportunity to study fast flows in a more global

context. Particularly, TC1, which has an equatorial orbit with an apogee of 13 Earth radii, and Cluster, which has an orbital plane in the same local time sector, can have interesting configurations to study the large scale propagation of the disturbances. Figure 1 shows the Cluster and TC1 location when TC1 observed a dipolarization defined as:  $\Delta\theta_B > 10$  within 5 min, where  $\Delta\theta_B$  is the latitude angle of the magnetic field, and TC1 and Cluster were at the night side,  $X < -6 R_E$  and  $|Y| < 10 R_E$ , between July and October 2004. There are mainly two types of Cluster-TC1 configuration which are useful to study: (1) Changes across the current sheet when Cluster observes dipolarization-associated signatures at the boundary of the plasma sheet or lobe, and (2) Radial propagation of the disturbances when Cluster was near the equatorial plane. In this paper, we will discuss events with the latter type of orbit configuration.

In the following, we first highlight an event study by [1] which shows two examples when Cluster observed dipolarizations and TC1 was located close to its apogee at the same local time. We then survey the relationship between fast flows observed at Cluster and the dipolarization observed at TC1 in a more statistical way. In this study we mainly use data obtained by the fluxgate magnetometer (FGM) experiment on Cluster [2] and on TC1 [3] and also refer to the ion flow data from the Composition and Distribution Function Analyser (CODIF) of the Cluster Ion Spectrometry (CIS) experiment [4] onboard Cluster and from the Hot Ion Analyser (HIA) instrument [5] onboard TC1.

## 2. Local and global propagation of substorm disturbances

In this section, we discuss two events when Cluster observed clear fast flows and TC1 was located near the same local time sector Earthward of Cluster. Both events were observed in the post-midnight sector but during quite different solar wind conditions: disturbed IMF and steady northward IMF. By performing a timing analysis the direction and the propagation speed

Received 18 May 2006.

**R. Nakamura, T. Takada, W. Baumjohann, M. Volwerk, T. L. Zhang, Y. Asano,<sup>1</sup> A. Runov, and Z. Vörös.** Space Research Institute, Austrian Academy of Sciences, Schmiedlstr. 6, A-8042, Graz, Austria.

**E. Lucek and C. Carr.** Imperial College, London, SW7 2BZ, UK  
**B. Klecker.** Max-Planck-Institut für extraterrestrische Physik, Postf. 1312, Garching, D-85741, Germany

**H. Rème.** CESR/CNRS, 9 Ave. du Colonel Roche, B.P. 4346, F-31028 Toulouse Cedex 4, France

**O. Amm.** Finnish Meteorological Institute, P.O. Box 503, FIN - 00101, Helsinki, Finland

<sup>1</sup>Present Address: Tokyo Institute of Technology, Meguro, Japan. (from April, 2006)

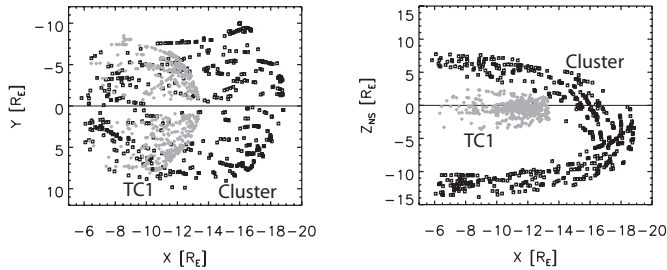


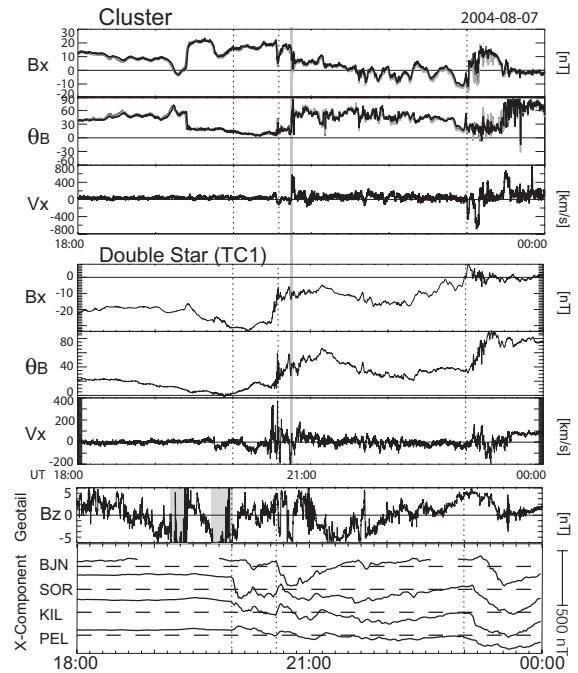
**Fig. 1.** Cluster and TC1 location plotted in the  $X$ - $Y$  plane (left) and in the  $X$ - $Z_{NS}$  plane (right), for those events when TC1 observed dipolarization and both spacecraft were at the night side,  $X < -6 R_E$ , between July and October 2004.  $Z_{NS}$  is  $Z$  distances from the neutral sheet [6].

of the disturbance at Cluster were obtained and compared with the TC1 observations, which enabled to determine further constraints on the spatial and temporal profile of the sources based on these multi-distance multi-point observations with Cluster and TC1.

### 2.1. 20040807 event

Magnetotail data from Cluster and TC1, solar wind data from Geotail and ground magnetograms from selected MIRACLE stations ordered with increasing latitude are shown in Figure 2 adapted from [1]. Geotail was at  $X = 15 \sim 17, Y = 1 \sim 7$ , and  $Z = 3R_E$  mainly in the solar wind except for short periods between 1915 and 2000 UT, indicated as shaded area in the figure, when the spacecraft entered into the magnetosheath. There were two intervals when IMF  $B_Z$  was mainly negative with a minimum of  $-5$  nT: 1845-2010 UT and 2105-2210 UT followed by a period of weak  $B_Z$  with occasional short negative excursions until around 2245 UT when positive IMF  $B_Z$  increased up to  $+5$  nT and stayed northward for the following 45 min. Associated with the first negative IMF  $B_Z$  interval, MIRACLE/IMAGE magnetograms detected an enhancement in westward electrojet activity starting at 2000, 2035 UT, and associated with the following negative IMF  $B_Z$  interval, another onset at 2300 UT as indicated in the figure as vertical dotted lines. Corresponding to these westward electrojet activities, dispersionless injections were observed by LANL satellites at 1955-2000, 2032, 2247 and 2313 UT (not shown). These observations suggest that there were mainly two substorm intervals with multiple intensifications.

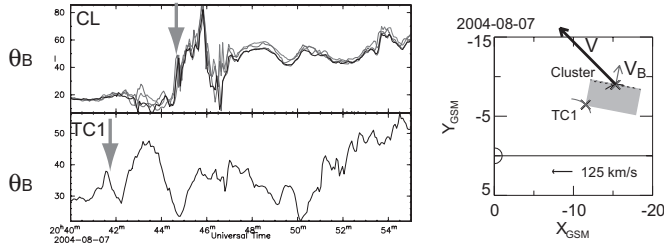
Associated with the first westward electrojet onset at 2000 UT little effects were seen at both spacecraft except for a gradual enhancement in the elevation angle in TC1. IMF  $B_Z$  was still southward and  $B_X$  at Cluster continued to increase ( $\theta_B$  keeps decreasing) indicating further stretching of the field. On the other hand, the second westward electrojet at 2035 UT was accompanied by a clear change in the magnetic field configuration both at Cluster and TC1. Clear enhancement in  $\theta_B$  was observed by Cluster, accompanied by a decrease in  $B_X$ , took place at 2033 and 2044 UT, which indicate a change from a tail-like to a dipolar configuration. TC1 was located in southern hemisphere as can be seen from the negative value of  $B_X$  and also observed enhancements in  $\theta_B$  accompanied by a decrease in the absolute value of  $B_X$  starting at 2030 UT, and followed



**Fig. 2.** Magnetotail data from Cluster and TC1, solar wind data from Geotail and ground magnetograms from selected MIRACLE stations (Adapted from [1]). Shown are  $X$  components and latitude angle of the magnetic field and  $X$  component of the proton flow from Cluster,  $X$  component and latitude angle of the magnetic field and  $X$  component of the ion flow from Double Star TC1,  $X$  component of the magnetic field at Geotail in the solar wind and in the magnetosheath (shaded intervals), and  $X$  component of the ground magnetogram from selected MIRACLE stations: BJN (CGM lat.71.45, CGM long. 108.07), SOR (67.34, 106.17), KIL (65.88, 103.79), PEL (63.55, 104.92) from the top to the bottom. The vertical dotted lines show the onset time of the enhanced westward electrojet, whereas the grey line indicates the dipolarization event discussed in the text in detail.

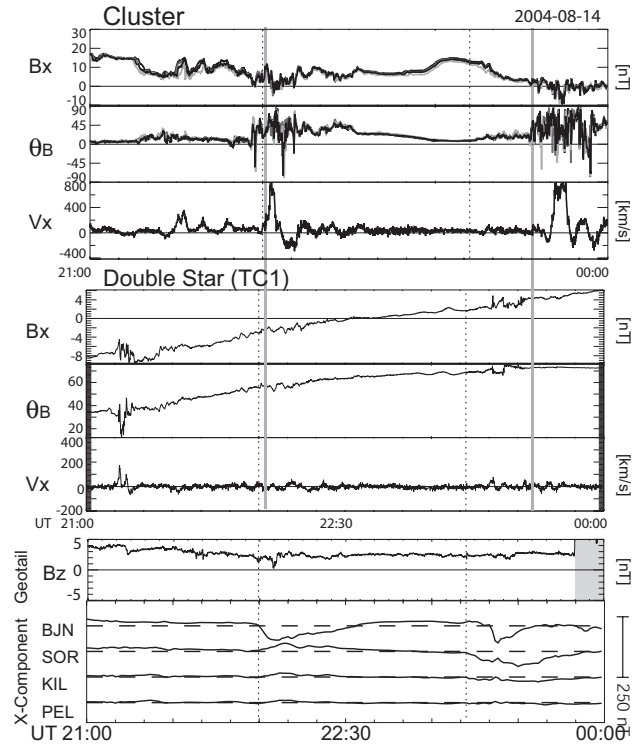
by a sharp increase in  $\theta_B$  at 2034 UT and 2042 UT. Fast Earthward ion bulk flows were detected at TC1 and Cluster starting at 2034 UT and 2044 UT, respectively. The reversal of the flow from tailward to Earthward was observed associated with 2300 UT onset by Cluster, while a clear dipolarization was observed at TC1. In the following we examine the temporal and spatial evolution of the dipolarization and flows at Cluster and TC1 in more detail for the dipolarization event at 2042-2044 UT marked with a grey line in the figure.

Figure 3 shows the  $\theta_B$  profiles during the second dipolarization interval between 2040 and 2050 UT (left panel). To characterize the propagation of the dipolarization more quantitatively, we compared the local propagation properties of the  $B_Z$  or  $\theta_B$  disturbance among the four Cluster spacecraft with the larger scale propagation between Cluster and Double Star. We first determine the motion of the dipolarization signature from the timing analysis of Cluster, assuming the dipolarization front to be a planar structure. For the analysis we use the time difference of  $\theta_B$  among the spacecraft for the events when clear enhancements were observed in  $B_Z$  and  $\theta_B$  and when all the Cluster spacecraft had similar profiles so that a



**Fig. 3.** Left:  $\theta_B$  profiles during the second dipolarization interval between 2040 and 2050 UT observed by Cluster and TC1. The onset of Cluster dipolarization and the estimated onset of the TC1 from propagation speed at Cluster are indicated with arrows. Right: Location of Cluster and TC1 and direction of the fast flow (thick arrow) and propagation vector (thin arrow) of the dipolarization projected in the  $X$ - $Y$  plane.

timing analysis should be valid. Timing, propagation direction, and speed of dipolarization at Cluster are then compared with observed signatures at TC1. The propagation vector,  $\mathbf{V}_B$ , for this events is plotted in the right panel in Figure 3 with thin arrow. The propagation of the disturbances were mainly dawnward with a tailward component. This suggests that the initial source of the disturbance is located duskward and Earthward of Cluster toward the TC1 location. This procedure further allows to determine the arrival time of the disturbance at TC1, which can be expressed as  $t_{TC1} = t_{CL} - ((\mathbf{R}_{CL} - \mathbf{R}_{TC1}) \cdot \mathbf{V}_B) / (\mathbf{V}_B \cdot \mathbf{V}_B)$  assuming the spacecraft motion is negligible. Also we can determine the projected distance between Cluster and TC1 along this plane such as  $|\mathbf{D}| = |\mathbf{R}_{CL} - \mathbf{R}_{TC1} - (t_{CL} - t_{TC1})\mathbf{V}_B|$ . The dashed line perpendicular to the arrow in Figure 3 shows the projected components of displacement vector  $\mathbf{D}$ . Using this simple assumption, i.e., that the dipolarization is a planar front moving with a constant speed, we estimated that at TC1 the disturbance should take place at 2041 UT. For the 2041 UT event, this estimated timing is indicated with the thin arrow in the TC1 panel (bottom left) in Figure 3. TC1 in fact observed some enhancements in  $\theta_B$  around 2042 UT. For this event, therefore, both spacecraft could likely have detected the same disturbances propagated from TC1 to Cluster and they were possibly related to the dipolarization front associated with Earthward flows. The propagation speed,  $\sim 130$  km/s, was within the value of the previously obtained tailward propagation speed of 35-300 km/s [7, 8, 9]. Yet, the major direction was downward such as the case of dawnward expansion of the dipolarization observed in the post-midnight in the geosynchronous region [10]. The minimum required scale-size of the dipolarization disturbance then would have a width of  $3.4 R_E$ , covering both TC1 and Cluster as shown with the hatched area in the right panel in Figure 3. Interesting to note that the propagation direction of the dipolarization is almost perpendicular to the main flow direction at Cluster, as indicated by the thicker arrow. It is therefore not the main flow direction in which the dipolarization front was observed to propagate. Such propagation of the dipolarization front predominantly perpendicular to the main fast flow direction was also reported by [11].



**Fig. 4.** Same as Figure 2 except for time interval between 21 and 24 UT, August 14, 2004 (Adapted from [1]).

**2.2. 20040814 event**

Figure 4 shows data from Cluster and Double Star TC1 together with the Geotail and MIRACLE magnetograms between 21 and 24 UT on August 14, 2004, in the same format as Figure 2. Geotail was located at  $X = 8 \sim 9, Y = 29$ , and  $Z = -1 \sim -2R_E$ , again mainly in the solar wind except for the magnetosheath encounter after 2350 UT. IMF  $B_Z$  was all the time northward with a typical value of  $\sim 3$  nT. Although weak, two westward electrojet disturbances can be identified in the MIRACLE magnetograms at 2157 UT and around 2312 UT, both centered at higher latitude than the previous event. No energetic particle injection was detected by LANL satellites (not shown). These signatures suggest a feature quite different from a usual “substorm”, with disturbances mainly at high latitudes and equatorward propagation but not involving the inner magnetosphere. Cluster detected a sharp enhancement in  $\theta_B$  followed by fast Earthward ion flow at 2156 UT and 2334 UT. The latter flow is almost 15 min delayed from the activation on the ground, although weak magnetic fluctuations started already after 2312 UT. On the other hand, TC1 showed no signature of clear dipolarization, but some magnetic disturbances after 2200 UT onset and after 2320 UT with no ion flow signature.

Similar to the previous event we examine the propagation of the Cluster disturbance and the flow disturbance. This will give us a hint of the maximum scale of the disturbance, not to be observed at TC1. The direction of the propagation of the dipolarization front was mainly Earthward/dawnward for the August 14 event as shown in Figure 5, deviating from the main

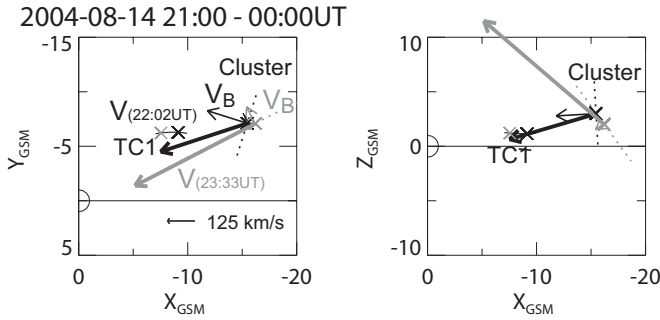


**Fig. 5.** Cluster and TC1 location in the  $X$ - $Y$  plane (left) and in the  $X$ - $Z$  (right) during the 2202 UT and 2333 UT events. The thick arrows show the flow direction while the thin arrows show the motion of the dipolarization front. The dashed lines show the possible spatial scale if it is assumed that the front also will encounter (or had encountered) TC1.

flow direction. Similar Earthward/dawnward motion has been reported by Cluster in the postmidnight region associated with a BBF [11]. If we estimate the arrival time of the  $B_Z$  enhancement at TC1, the 2202 UT and 2333 UT disturbances at Cluster are expected to be observed 3 min and 4 min later at TC1, when the scale size of the disturbance is larger than 3 and 8  $R_E$ , respectively. The lack of such observations at TC1 suggests that the disturbance was either localized or decayed within a shorter time scale than these values. Either the BBF associated dipolarization was a transient phenomena and quenched between Cluster and TC1 or the localized BBF/dipolarization front could not be observed at TC1 resulting in only small magnetic field fluctuation. The lack of any injection signature at LANL as well as the location of the westward electrojet suggests that in fact the energy transported by the BBF is very likely dissipated mostly before reaching the TC1 region. On the other hand, the observation can be also due to the finite width of the flow channel, which was obtained to be 2-3  $R_E$  from a statistical study using Cluster multi-point dataset [12].

### 3. Survey of Cluster BBF and Double Star dipolarization

As shown in the previous sections, the evolution of a BBF can be quite different even though Cluster and TC1 were aligned in similar local time sectors. To determine the general condition of the fast flow evolution, we surveyed the dipolarization events in a more statistical manner. Here, we first created data base of Cluster bursty bulk flow events using data from Cluster 4 and TC1 dipolarization events. Bursty bulk flow events are defined when the spacecraft was in the plasma sheet (ion  $\beta > 2$ ) and observed high speed flow ( $V_{xy} > 300$  km/s) in the component perpendicular to the ambient field using 8 sec data. We take data points fulfilling the BBF condition separated less than 5 minutes as the same event. As for the dipolarization event, we used 5 minutes-long sliding windows of the spin-averaged data and identified a dipolarization when the difference between the minimum and maximum  $\theta_B$  exceeds  $10^\circ$ . The event interval consists of consecutive intervals fulfilling this condition and its start time is defined as the time of min-

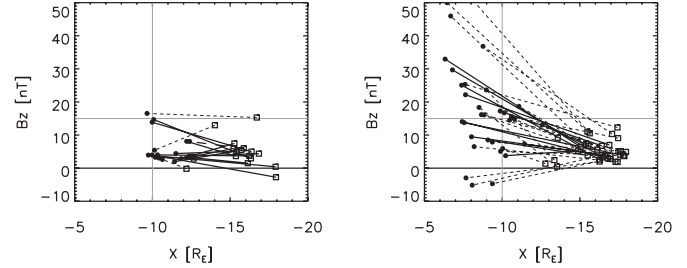


**Fig. 6.**  $B_Z$  of Cluster and TC1 for the Cluster BBF events associated with TC1 dipolarization (left panel) and those without clear TC1 dipolarization (right panel) plotted against  $X$  location of the two satellites. For  $B_Z$  value at TC1, a 5-min average value before the dipolarization (left panel) or before Cluster BBF (right panel) are shown. The dashed (solid) lines indicate events when the two spacecraft were separated in  $Y$  more (less) than 3  $R_E$ .

imum  $\theta_B$  during the first interval and the end time is defined as the maximum  $\theta_B$  during the last interval. We then examined whether such a dipolarization event is observed at TC1 associated with a Cluster BBF or not. That is, we divided the Cluster BBF dataset into two groups: those BBF events when there is TC1 dipolarization event within 5 min before or after the flow, which we call BBF event associated with dipolarization, and those BBF events when no corresponding TC1 dipolarization events can be found.

Figure 6 shows  $B_Z$  of Cluster and TC1 for the Cluster BBF events associated with TC1 dipolarization (left) and those without clear TC1 dipolarization (right) plotted against the  $X$  location of the two satellites during these events. For the  $B_Z$  value at TC1, a 5-min average value before the dipolarization (left panel) or before the Cluster BBF (right panel) is shown. (Taking into account the near-Earth tail configuration, we actually used  $H$  instead of  $B_Z$  when TC1 is Earthward of 10  $R_E$ ). The dashed (solid) lines indicate events when the two spacecraft were separated in  $Y$  more (less) than 3  $R_E$ . It can be seen that when TC1 is located Earthward of 8  $R_E$  there is no clear dipolarization obtained by TC1 associated with a BBF at Cluster, even if the two spacecraft were close in  $Y$ . Another interesting difference between these two events are the  $B_Z$  values at TC1, which is particular clear when we compare only those closely aligned in  $Y$  (solid line) and if one compares TC1 values around  $X = -10 \sim -12 R_E$  where events from both groups exist. It can be seen that  $B_Z$  at TC1 is larger for those events when a dipolarization is not observed at TC1. Note that such difference were also seen between the two events shown in the previous section. Namely,  $\theta_B$  was larger for the 2004-08-14 event, when no clear dipolarization was observed associated with the BBF, compared to the 2004-08-07 event, when a dipolarization was observed both at Cluster and TC1.

One plausible interpretation for these two types is illustrated in Figure 7. That is, a thin current sheet is developed reaching toward the inner magnetosphere when both flows in the near-Earth (Cluster) and dipolarization at  $\sim 10 R_E$  region (TC1) are observed (upper panel in Figure 7). On the other hand, for the cases shown in the right panel in Figure 6 and the August 14 event, the  $\sim 10 R_E$  region (TC1) is in a more dipolar configuration when the flow brakes beyond this region so that dipolar-

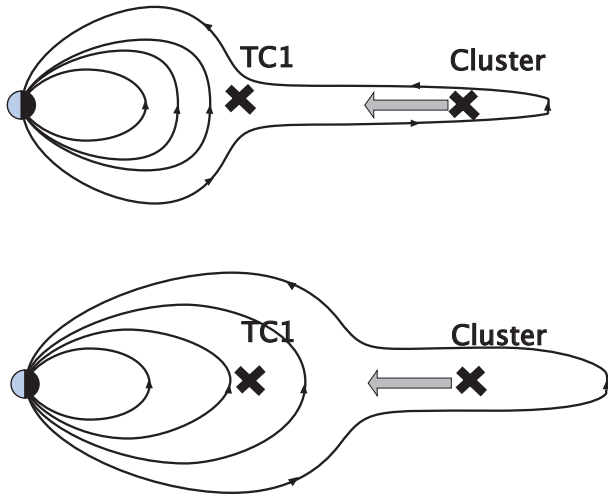


**Fig. 7.** Illustration of plausible tail configuration for events when TC1 observed dipolarization associated with Cluster BBF (upper panel) and those when TC1 observed no clear dipolarization (lower panel).

ization or flux pileup region cannot reach TC 1 region (bottom panel in Figure 7). More complete results of this statistical study will be published elsewhere (Takada et al., manuscript in preparation, 2006).

Note that we could not find any fast flow events associated with clear dipolarization signature in the geosynchronous region. This suggests that the fast flows most likely brakes radially outward than the geosynchronous region, which is also expected from the radial profile of the flux transport rate [13]. On the other hand, since there were no Cluster plasma sheet events when TC1 observed dipolarization in the geosynchronous distance, we have no supporting evidence that dipolarization at geosynchronous region can take place without flows in the near Earth region. Yet, the fact that there were no events with clear TC1 dipolarization at geosynchronous distance associated with Cluster fast flow in our dataset suggests that either a different process than flow braking or flux pile is needed for dipolarization near geosynchronous region or when a dipolarization takes place at geosynchronous region, the near-tail current sheet/plasma sheet is so thin that the chance of detecting plasma sheet flows with Cluster becomes almost zero. It is therefore essential to monitor the current sheet profile along an extended region in radial direction in order to determine the causal relationships between the fast flows and dipolarization. The THEMIS mission with spacecraft aligned in radial direction combined with geosynchronous satellites will be an ideal constellation to obtain a more conclusive answer.

#### 4. Summary

Evolution of the fast flows and dipolarization is studied based on Cluster and Double Star TC1 satellite observations, which enabled large-scale multi-point observations along the same local time sector.

Two types of BBF events were introduced with different IMF conditions when Cluster and Double Star (TC1) were located in the same local time sector: August 7, 2004, 18–24

UT, during a disturbed southward/northward IMF interval, and August 14, 2004, 21–24 UT, when the IMF was stably northward. Cluster observed dipolarization as well as fast flows during both intervals, but this was not the case for TC1. By using multi-point analysis techniques, the direction/speed of the propagation is determined using Cluster and is then compared with the disturbances at TC1 to discuss its spatial/temporal scale. The propagation direction of the  $B_Z$  disturbance at Cluster was mainly downward with a tailward component for August 7 and with a significant Earthward component for August 14 associated with fast flows. These differences suggest that the role of the BBF can be quite different for different IMF condition and resultant tail configurations.

By surveying Cluster BBF events when TC1 was in the tail, we could statistically confirm that there seems to be some difference in the tail configuration between these two types of BBF events. That is, a thin current sheet is most likely developed reaching toward the inner magnetosphere when both flows in the near-Earth tail (Cluster) and dipolarization in the  $\sim 10 R_E$  region (TC1) are observed. On the other hand, the  $\sim 10 R_E$  region (TC1) has likely a more dipolar configuration when there were no dipolarization observed by TC1 at this region associated with the fast flows in the near-Earth tail (Cluster). It should be also noted that we could not find any fast flow events associated with dipolarization when TC1 was near the geosynchronous region. That is, the observed flows most likely brake radially outward than the geosynchronous region. This suggests that either a different process than flow braking or flux pile is needed to explain a clear dipolarization at geosynchronous region or when a dipolarization takes place at geosynchronous region, the near-tail current sheet/plasma sheet is so thin that the chance of detecting plasma sheet flows with Cluster becomes almost zero.

These results show the complicated nature of the propagation of the disturbance in the tail and a new possibility of combining local and global multi-point analysis to further quantify the characteristics of the source regions.

#### Acknowledgements

We acknowledge Z.-X. Liu and C. P. Escoubet for the successful Double Star program. We thank G. Laky for helping in the Cluster/Double Star data analysis, and T. Nagai for providing Geotail data. We acknowledge CDAWeb, WDC-C2, CSDS, GDCD, ACDC, CSSR, and EDDS for making available data used in this study. The work by M. Volwerk is financially supported by the German Bundesministerium für Bildung und Forschung and the Zentrum für Luft- und Raumfahrt under contract 50 OC 0104. A part of the work at IWF is supported by INTAS 03-51-3738 grant.

#### References

1. Nakamura R., et al., Cluster and Double Star observations of dipolarization, *Ann. Geophys.*, 23, 2915–2920, 2005.
2. Balogh, A., et al., The Cluster magnetic field investigation: overview of in-flight performance and initial results, *Ann. Geophys.*, 19, 1207–1217, 2001.

3. Carr, C., et al., The Double Star Magnetic Field Investigation: instrument design, performance and highlights of the first years observations, *Ann. Geophys.*, *23*, 2713-2732, 2005.
4. Rème, H., et al., First multispacecraft ion measurements in and near the Earth's magnetosphere with the identical Cluster ion spectrometry (CIS) experiment, *Ann. Geophys.*, *19*, 1303-1354, 2001.
5. Rème, H., et al., The HIA instrument onboard the Tan Ce 1 Double Star near-equatorial spacecraft and its first results, *Ann. Geophys.*, *23*, 2757-2732, 2005.
6. Nakai, H., et al., Statistical nature of the magnetotail current in the near-Earth region, *J. Geophys. Res.*, *102*, 9573-9586, 1997.
7. Ohtani, S., et al., Radial expansion of the tail current disruption during substorms: a new approach to the substorm onset region, *J. Geophys. Res.*, *97*, 3129-3136, 1992.
8. Jacquy, C., et al., Tailward propagating cross-tail current disruption and dynamics of near-Earth tail: A multi-point measurement analysis, *Geophys. Res. Lett.*, *20*, 983-986, 1993.
9. Baumjohann, et al., Substorm dipolarization and recovery, *J. Geophys. Res.*, *104*, 24995-25000, 1999.
10. Nagai, T., Observed magnetic substorm signatures at synchronous altitude, *J. Geophys. Res.*, *87*, 4405-4417, 1982.
11. Nakamura, R., et al., Motion of the dipolarization front during a flow burst event observed by Cluster, *Geophys. Res. Lett.*, *29*, 1942, doi:10.1029/2002GL015763, 2002.
12. Nakamura, R., et al., Spatial scale of high-speed flows in the plasma sheet observed by Cluster, *Geophys. Res. Lett.*, *31*, L09804, doi:10.1029/2004GL019558, 2004.
13. Schödel, R., et al., Rapid flux transport in the central plasma sheet, *J. Geophys. Res.*, *106*, 301, 2001.

# Simultaneous observations of ions of ionospheric origin over the ionosphere and in the plasma sheet at storm-time substorms

M. Nosé, T. Kunori, Y. Ono, S. Taguchi, K. Hosokawa, T. E. Moore, M. R. Collier, S. P. Christon, and R. W. McEntire

**Abstract:** We investigate variations of ion flux over the ionosphere and in the plasma sheet when storm-time substorms are initiated, using simultaneous observations of neutral atoms in the energy range of up to a few keV measured by the low-energy neutral atom (LENA) imager on board the Imager for Magnetopause-to-Aurora Global Exploration (IMAGE) satellite and energetic (9-210 keV/e) ion flux measured by the energetic particle and ion composition (EPIC) instrument on board the Geotail satellite. We examined three storm intervals during which the IMAGE satellite was located near its apogee and the Geotail satellite was in the plasma sheet on the nightside. Low-energy neutral atoms traveling from the direction of the Earth can be created by outflowing ionospheric ions through charge exchange processes. The observed neutral atom flux enhancement at storm-time substorms indicates that substorms can cause an immediate increase of low-energy ion flux over the ionosphere by a factor of 3-10. In the plasma sheet, the flux ratio of  $O^+/H^+$  is rapidly enhanced at storm-time substorms and then increased gradually or stayed at a constant level in a timescale of  $\sim 60$  minutes, suggesting a mass-dependent acceleration of ions at local dipolarization and a subsequent additional supply of  $O^+$  ions to the plasma sheet which have been extracted from the ionosphere at the substorms.

*Key words:* Ions of Ionospheric Origin, Substorms, Plasma Sheet, Ion Acceleration.

## 1. Introduction

Recent studies revealed the ionosphere as an important source of plasma to the plasma sheet and the magnetosphere. From multi-fluid MHD simulation Winglee [16] has shown that a boundary called “the density geopause,” within which the ionospheric source is the dominant contributor to the plasma, is extended down the tail to  $10\text{-}65 R_E$  during the southward IMF ( $B_Z=0$  to  $-5$  nT). A large number of numerical simulations were performed to trace ions of ionospheric origin after they escaped from the ionosphere [e.g., 2, 4, 6]. They found that most of such ions preferentially move into the plasma sheet through the geomagnetic lobe. Thus it is important to identify how much ions of ionospheric origin are outflowing from the ionosphere and how it depends on the geomagnetic disturbances. Using the Dynamic Explorer -1 observation of low-energy (0.01-17 keV) ions, Yau et al. [17] found a good correlation between the ion outflow rate and the Kp index. As the Kp index increased from 0 to 6, the  $O^+$  flux increased drastically by an

order (from  $1\text{-}3 \times 10^{25} \text{ s}^{-1}$  to  $1\text{-}3 \times 10^{26} \text{ s}^{-1}$ ), while the  $H^+$  flux changed by a factor of  $\sim 3$  (from  $3 \times 10^{25} \text{ s}^{-1}$  to  $1 \times 10^{26} \text{ s}^{-1}$ ). From observations by the EXOS-D satellite of ion outflow in the energy range from  $<1$  to 70 eV, Cully et al. [5] showed that ion outflow rate is correlated with the Kp index and some solar wind parameters. The Kp dependence of  $H^+$  and  $O^+$  flux was almost similar to that by [17]. They also found that the solar wind parameters exhibiting a strong correlation with the outflow flux were the kinetic pressure, the electric field, and the variation in the IMF. In these studies the 3-hour Kp index or the hourly averaged solar wind data (OMNI data) have been used, suggesting that the reported good correlation is correct only in a statistical or average sense. It is not clear yet how outflowing ion flux responds to geomagnetic disturbances with a shorter timescale ( $<1$  hour) such as substorms.

In this study we intended to investigate how ion outflow rate changes at individual substorms, using data obtained by the low-energy neutral atom (LENA) imager on board the Imager for Magnetopause-to-Aurora Global Exploration (IMAGE) satellite. Since IMAGE/LENA is a remote sensing instrument, it provides a global image of outflowing ion flux over the polar region with a time resolution of  $\sim 2$  minutes. We can monitor temporal changes of outflowing ion flux when a substorm occurs. Moreover, in order to investigate how the plasma sheet ion composition responds to the identical substorm, we examined simultaneous observations of energetic (9-210 keV/e) ion flux in the plasma sheet made by the energetic particle and ion composition (EPIC) instrument on board the Geotail satellite. The rest of this paper is organized as follows. Section 2 introduces the data set. In section 3 we describe the event selection procedure. We found 3 time intervals during which the IMAGE and Geotail satellites simultaneously observed ions of ionospheric origin. In section 4 satellite ob-

Received 21 May 2006.

**M. Nosé,<sup>1</sup> T. Kunori, and Y. Ono.** Graduate School of Science, Kyoto University, Kyoto, Japan

**S. Taguchi and K. Hosokawa.** Department of Information and Communication Engineering, University of Electro-Communications, Tokyo, Japan

**T. E. Moore and M. R. Collier.** NASA Goddard Space Flight Center, Greenbelt, Maryland, USA

**S. P. Christon.** Focused Analysis and Research, Columbia, Maryland, USA

**R. W. McEntire.** Applied Physics Laboratory, Johns Hopkins University, Laurel, Maryland, USA

<sup>1</sup>Corresponding author (e-mail: nose@kugi.kyoto-u.ac.jp).

servations will be displayed for the intervals 1 and 3. It was found that substorms caused rapid increases of both the energetic neutral atom (ENA) flux around the Earth and the  $O^+/H^+$  energy density ratio in the plasma sheet. The  $O^+/H^+$  ratio subsequently increased or stayed at a constant level with a time-scale of 60 minutes. We will discuss these observational results in section 5.

## 2. Data Set

The IMAGE satellite is a polar orbiting satellite with a perigee of 1000 km altitude, an apogee of  $8.2 R_E$ , and an orbital period of 14.2 hours [1]. The satellite spins at a rate of  $\sim 0.5$  revolution per minute and its spin vector is anti-parallel to the orbital angular momentum vector. The LENA imager carried by the IMAGE satellite is designed to detect neutral atoms in the energy range of  $\sim 10$  eV to a few keV and has a field of view of  $\pm 45^\circ$  against a satellite spin plane which is divided by 12 polar sectors [12]. Because of the spin, the LENA imager sweeps out  $360^\circ$  in azimuthal direction, which is divided by 45 azimuthal sectors, resulting in one complete image of neutral atom flux covering an area of  $90^\circ$  (polar)  $\times 360^\circ$  (azimuth) at every 2 minutes. Since low-energy neutral atoms traveling from the direction of the Earth are created by outflowing ionospheric ions through charge exchange processes, we can investigate temporal change of the low-energy ion flux over the ionosphere from the LENA data.

The Geotail satellite was placed in the near-Earth orbit of  $\sim 9 \times 30 R_E$  in the fall of 1994 [13] and surveys the near-Earth and midtail plasma sheet frequently. Geotail is equipped with the EPIC instrument which provides mass and charge state information about ions with an energy/charge range of 9 keV/e to 210 keV/e in eight spectral points [15]. The instrument has a spatial coverage of almost  $4\pi$  sr. It takes  $\sim 24$  s to get one complete energy spectrum for  $H^+$  ions, and  $\sim 48$  s for  $O^+$  ions. From each energy spectrum we calculated energy densities of  $H^+$  and  $O^+$ , and then averaged over 5 min to increase statistical significance. We also used the magnetic field data obtained by the magnetic field (MGF) instrument [10] onboard the Geotail satellite.

## 3. Event Selection

From the period of August 2003 through July 2004, we selected time intervals during which IMAGE/LENA and Geotail/EPIC made a simultaneous observation of ions of ionospheric origin, according to the following criteria. During the time interval, (1) geomagnetic storms took place, (2) the Geotail satellite mostly stayed in the nightside plasma sheet, (3) the IMAGE satellite was near its apogee, and (4) clear substorm signatures can be identified by ground stations and geosynchronous satellites. This selection procedure yielded 3 time intervals, that is, 1900-2300 UT on 30 October 2003 (interval 1), 0130-0600 UT on 27 July 2004 (interval 2), and 0400-0730 UT on 10 March 2004 (interval 3). Figure 1 shows orbits of the satellites in the  $X_{GSM}-Y_{GSM}$  and  $X_{GSM}-Z_{GSM}$  planes for these 3 intervals. Thin lines indicate the IMAGE orbits and thick lines indicate the Geotail orbits. Geotail flew at  $X_{GSM} \sim -8, -16,$  and  $-24 R_E$  in the interval 1, 2, and 3, respectively. In the next section we will show simultaneous observations for the interval 1

and 3; data of the interval 2 will be omitted because of limit of paper length.

## 4. Observation and Analysis

### 4.1. Interval 1 (1900-2300 UT on 30 October 2003)

During this interval the SYM-H index decreased from  $-150$  nT to  $-400$  nT, indicating the main phase of the very intense magnetic storm. Substorms were identified at 1947 UT and 2115 UT by energetic electron enhancement at geosynchronous satellites, negative bays at high-latitude ground stations, and positive bays at mid-latitude ground stations (not shown here). Figures 2a and 2b show the ENA images around the Earth obtained by the IMAGE/LENA imager before and after the first substorm onset (1947 UT), respectively. We found that ENA flux coming from the direction of the Earth was enhanced. ENA images before and after the second substorm onset (2115 UT) are shown in Figures 2c and 2d. We also found strong ENA flux enhancement after the substorm onset. In order to see temporal changes of the ENA flux in more detail, we averaged the ENA flux around the Earth over the azimuthal angle of  $\pm 28^\circ$  ( $y$ -direction of the ENA image) and the polar

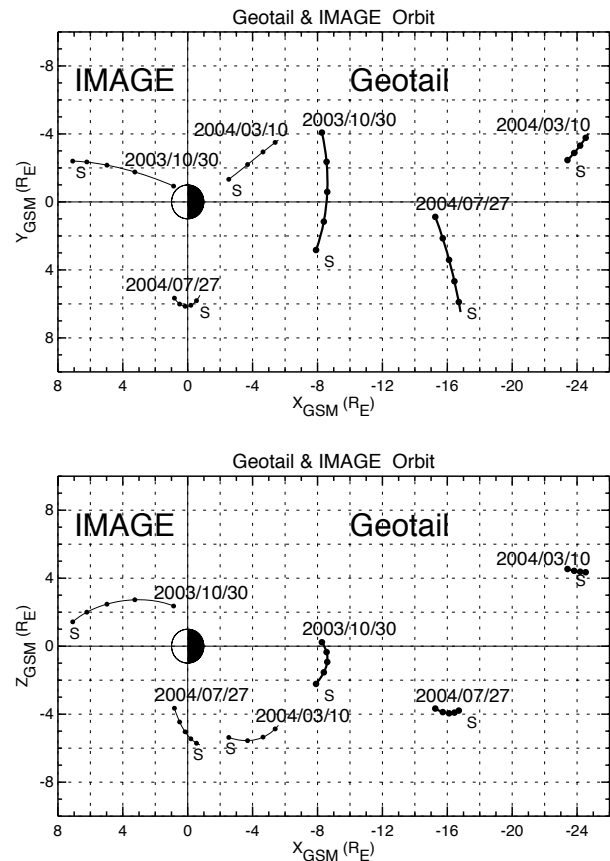


**Fig. 1.** Orbits of the IMAGE and Geotail satellites in the  $X_{GSM}-Y_{GSM}$  (top) and  $X_{GSM}-Z_{GSM}$  (bottom) planes for the 3 selected intervals. Thin and thick lines are for the IMAGE and Geotail orbits, respectively. Dots indicate the satellite locations at integer hour. "S" denotes the start location of the satellite in the interval.

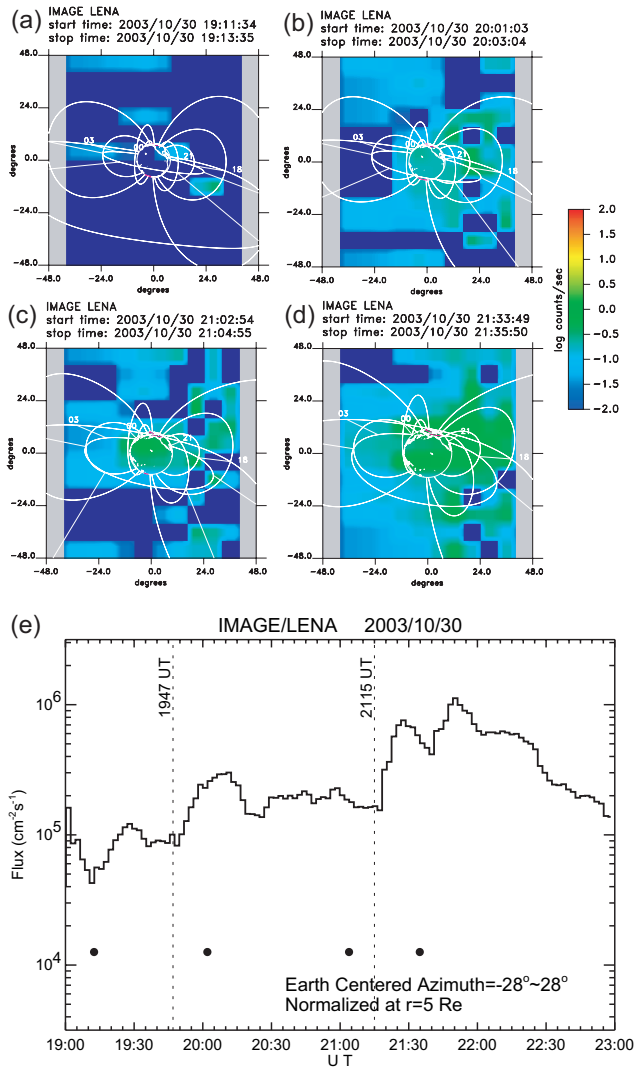


**Fig. 2.** (a, b) ENA images around the Earth obtained by the IMAGE/LENA imager before and after the first substorm onset. (c, d) The same as Figure 2a and 2b, except for the second substorm onset. (e) Temporal variations of the ENA flux around the Earth. Onset times of the substorms were indicated by vertical dashed lines. Four black circles indicate times of Figures 2a-2d.

angle of  $\pm 44^\circ$  (x-direction of the image). Then we computed the normalized ENA flux ( $J_{\text{normalized}}$ ) from the average ENA flux derived above ( $J_{\text{averaged}}$ ) as it is measured at radial distance of  $5 R_E$ , by

$$J_{\text{normalized}} = J_{\text{averaged}} \times \left( \frac{r - 1.5}{5 - 1.5} \right)^2,$$

where  $r$  is the radial distance of the satellite position in  $R_E$ . Here the ENA source was assumed to be at geocentric altitude of  $1.5 R_E$  [8]. This generates time series data of ENA flux around the Earth with a time resolution of 2 minutes. We calculated a running average of  $J_{\text{normalized}}$  with a time window of 8 minutes, which is displayed in Figure 2e. Vertical dashed lines indicate onset time of the substorms. Black circles corresponds to times in which the LENA images of Figures 2a-2d

were taken. At the first substorm the ENA flux was clearly enhanced from  $1 \times 10^5 \text{ cm}^{-2}\text{s}^{-1}$  to  $3 \times 10^5 \text{ cm}^{-2}\text{s}^{-1}$  within 20 minutes. The second substorm was accompanied by a sudden increase of the ENA flux from  $2 \times 10^5 \text{ cm}^{-2}\text{s}^{-1}$  to  $1 \times 10^6 \text{ cm}^{-2}\text{s}^{-1}$ . This indicates that the substorms caused an enhancement of outflowing ion flux by a factor of 3-5.

Figure 3 showed the magnetic field in the  $X_{GSM}$  and  $Z_{GSM}$  components and the  $\text{O}^+/\text{H}^+$  energy density ratio measured by the Geotail which was located at  $X_{GSM} \sim -8 R_E$  (Figure 1). Two vertical lines indicate onset time of the substorms (1947 UT and 2115 UT). At the first substorm onset, the absolute value of  $B_x$  decreased and  $B_z$  increased, indicating that dipolarization took place. At the same time the  $\text{O}^+/\text{H}^+$  energy density ratio increased suddenly from  $\sim 1$  to 3, and then it showed a gradual increase during 2000-2030 UT, even though the substorm expansion phase has already ended at 2000-2010 UT as can be seen in  $B_z$  changes. For the second substorm onset, signatures of the magnetic field and the  $\text{O}^+/\text{H}^+$  energy density ratio were similar to those of the first substorm; that is, the magnetic field was dipolarized and the energy density ratio increased rapidly at substorm onset, followed by a gradual increase with a timescale of 60 minutes (2130-2230 UT).

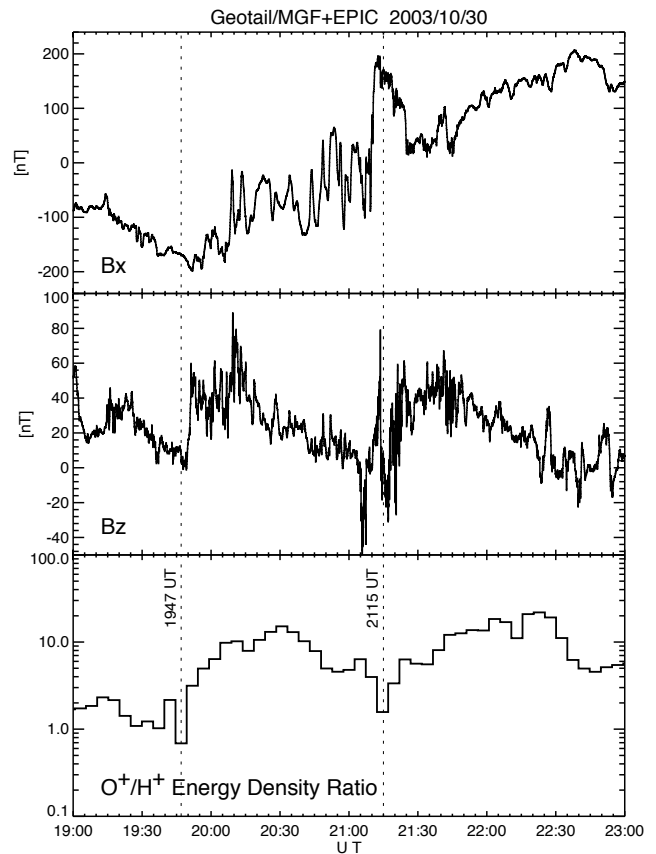


**Fig. 3.** From top to bottom: The magnetic field in the  $X_{GSM}$  and  $Z_{GSM}$  components, and the  $\text{O}^+/\text{H}^+$  energy density ratio measured by the Geotail satellite.

#### 4.2. Interval 3 (0400-0730 UT on 10 March 2004)

This interval was found in the recovery phase of a moderate magnetic storm and the SYM-H index was between  $-100$  nT and  $-60$  nT. We identified occurrence of a substorm at 0528 UT by dipolarization and energetic proton enhancement at geosynchronous satellites, a negative bay at high-latitude ground station, and a positive bay at low-latitude ground station (not shown here). Figures 4a and 4b display the IMAGE/LENA image around the Earth before and after the substorm. It was revealed that the ENA flux traveling from the direction of the Earth was enhanced after the substorm. Figure 4c shows ENA flux variations derived in the same way as Figure 2e. A vertical line and two black circles indicate times when substorm occurred and the LENA images of Figures 4a and 4b were taken. The ENA flux before the substorm stayed around  $1 \times 10^4$   $\text{cm}^{-2}\text{s}^{-1}$ , while it increased up to  $1 \times 10^5$   $\text{cm}^{-2}\text{s}^{-1}$  within 10-20 minutes after the substorm, indicating an enhancement of outflowing ion flux by a factor of 10.

Figure 5 demonstrates the Geotail data at  $X \sim -24 R_E$  in the same format as Figure 3. At the substorm, which is indicated by a vertical line, the absolute value of  $B_X$  decreased and  $B_Z$  increased, being a dipolarization signature. For about 1 hour prior to the substorm onset (i.e., 0430-0528 UT), Geotail was in the magnetic lobe and we could not calculate the energy density ratio in the plasma sheet. However, before 0430 UT the satellite made a measurement of energetic ion flux in the plasma sheet, which indicates the  $\text{O}^+/\text{H}^+$  ratio of 0.02-0.05. Assuming that the  $\text{O}^+/\text{H}^+$  energy density ratio did not change significantly before the substorm onset, we can expect that the

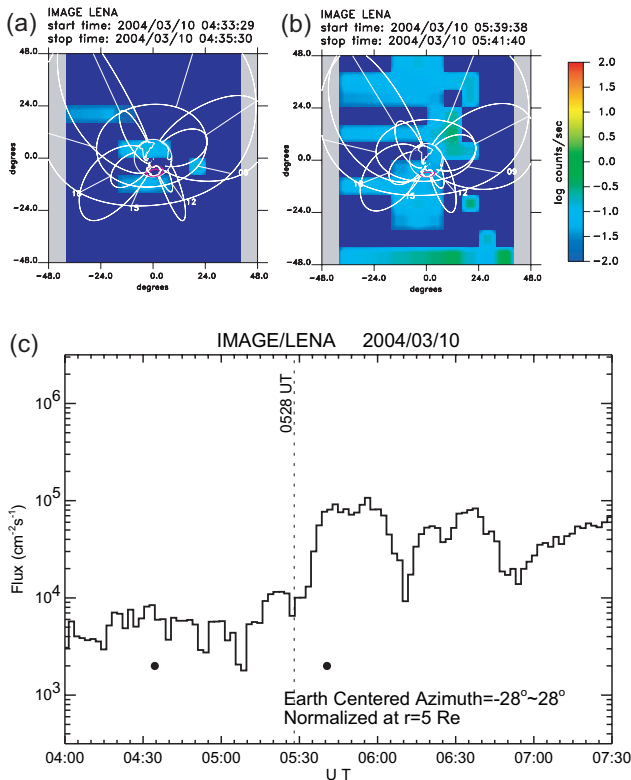


Fig. 4. The same as Figure 2, except for the interval 3.

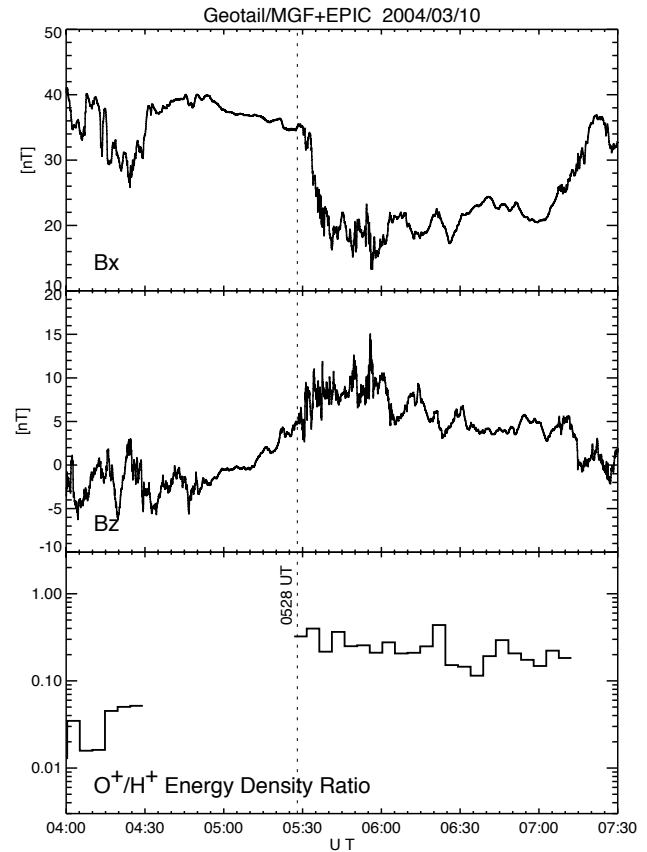


Fig. 5. The same as Figure 3, except for the interval 3.

energy density ratio was strongly enhanced at dipolarization. Even though the substorm expansion phase has ended around 0550-0600 UT as can be noted from the magnetic field data, the  $\text{O}^+/\text{H}^+$  energy density ratio stayed at almost constant level of 0.2-0.3 for about 1 hour.

## 5. Discussion

We examined variations of ions of ionospheric origin over the ionosphere and in the plasma sheet when storm-time substorms were initiated. From the IMAGE/LENA observation we found that the ENA flux around the Earth was enhanced rapidly (within 10-20 minutes) by a factor of 3-10 at substorms. (Substorms in the interval 2 were also accompanied by the ENA flux enhancement in the similar way to those in the interval 1 and 3.) The Geotail/EPIC observation showed that the  $\text{O}^+/\text{H}^+$  energy density ratio in the plasma sheet was immediately enhanced when local dipolarization signatures appeared, and then increased gradually or stayed at nearly constant level in a timescale of 60 minutes. These Geotail observations were similar among three different locations of  $X_{GSM} \sim -8, -16$ , and  $-24 R_E$ , though data at  $X_{GSM} \sim -16 R_E$  were not shown here because of page limit.

### 5.1. Response of outflowing ion flux to substorms

From the IMAGE/LENA observations we suppose that substorms can cause sudden and drastic changes of the ion flux

outflowing from the Earth. Since this flux change caused by substorms is nearly comparable to that during Kp increase from 0 to 6 (i.e., threefold to tenfold) which was statistically revealed by [17] and [5] (see section 1), it is important to take substorm occurrence into consideration when we study outflowing ion flux. We can expect that such drastic change of outflowing ion flux at substorms possibly affect ion composition in the plasma sheet; this issue will be discussed in section 5.2.

It is noteworthy to mention prompt response of outflowing ion flux to the solar wind dynamic pressure, which has been described by [11], [7], and [8]. They reported that enhancements of solar wind dynamic pressure (or standard deviation of dynamic pressure) led to bursts of ion outflow. Their results might be explained by that enhancement of the solar wind dynamic pressure preferentially triggers substorms [9]. In actual fact, the two substorms in the interval 1 appeared to be associated with strong compression of the magnetosphere during high solar wind dynamic pressure, as discussed by [14]. At the substorm onset in the interval 3 there was a weak dynamic

pressure enhancement (from 6 nPa to 7 nPa) which is due to slight solar wind velocity enhancement (from 650 km/s to 700 km/s). On the other hand, we found that there were no clear pressure changes at substorms in the interval 2, but rather there were northward turnings of the IMF with an amplitude of 10-20 nT. It is left for future study to examine which solar wind dynamic pressure enhancement or substorm is more essential to the immediate increases of the ionospheric plasma outflow.

### 5.2. Ion composition change in plasma sheet

We consider that the first sudden enhancement of the  $O^+/H^+$  energy density ratio in the plasma sheet is caused by mass-dependent acceleration of ions at dipolarization and the subsequent gradual increase of the energy density ratio is due to an additional supply of  $O^+$  ions which are extracted from the ionosphere at the substorm onset. This idea is supported by energy spectral changes observed by the Geotail/EPIC instrument. Top two panels of Figure 6 display  $H^+$  and  $O^+$  energy spectra in the plasma sheet for the substorm onset at 1947 UT on 30 October 2003 (the first onset in the interval 1), and bottom two panels, for the substorm onset at 0528 UT on 10 March 2004 (the onset in the interval 3). Different line width means different time intervals; that is, light, medium, and heavy lines represent energy spectra before onset, 10-15 minutes after onset, and 30-60 minutes after onset, respectively. It was found that the  $H^+$  energy spectra did not show significant changes in both substorm onsets. However, the  $O^+$  energy spectra changed drastically at the energy range of a few tens of keV to 100 keV after dipolarization (medium line), implying that acceleration of ions was more effective to  $O^+$  ions than  $H^+$  ions. At 30-60 minutes after the onset, we found that  $O^+$  flux in lower energy range from 9 keV to a few tens of keV showed a further increase (heavy line). The  $O^+$  increase in the lower energy range can be explained by that extra  $O^+$  ions are transported into the plasma sheet within 60 minutes after they are extracted from the ionosphere at substorm onset as confirmed from the LENA observations (Figures 2 and 4). This timescale is consistent with previous studies showing that transit time of ions from the ionosphere to the plasma sheet via the magnetic lobe is  $\leq 1-2$  hours [2, 3, 6].

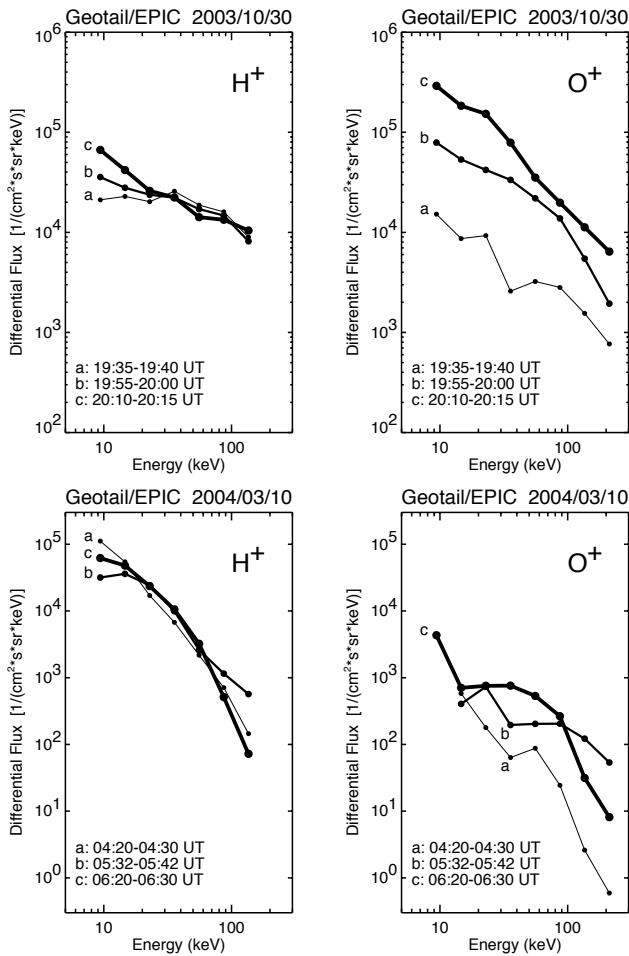


**Fig. 6.** Energy spectra of  $H^+$  and  $O^+$  observed by Geotail/EPIC during the first substorm in the interval 1 (top) and the substorm in the interval 3 (bottom). Light line is for the spectra before the onset; medium line, 10-15 minutes after the onset; and heavy line, 30-60 minutes after the onset.

### Acknowledgements

We thank D. J. Williams and S. R. Nylund for their help in processing the Geotail/EPIC data. We also thank T. Nagai for providing the Geotail/MGF data. This work was supported by the Sumitomo Foundation (grant 030677) and the Ministry of Education, Science, Sports and Culture, Grant-in-Aid for Young Scientists (B) (grant 17740327).

### References

1. Burch, J. L., IMAGE mission overview, *Space Sci. Rev.*, 91, 1-14, 2000.
2. Chappell, C. R., B. L. Giles, T. E. Moore, D. C. Delcourt, P. D. Craven, and M. O. Chandler, The adequacy of the ionospheric source in supplying magnetospheric plasma, *J. Atmos. Sol. Terr. Phys.*, 62, 421-436, 2000.

3. Cladis, J. B., Parallel acceleration and transport of ions from polar ionosphere to plasma sheet, *Geophys. Res. Lett.*, *13*, 893-896, 1986.
4. Cully, C. M., E. F. Donovan, A. W. Yau, and H. J. Opgenoorth, Supply of thermal ionospheric ions to the central plasma sheet, *J. Geophys. Res.*, *108*, 1092, doi:10.1029/2001JA009457, 2003a.
5. Cully, C. M., E. F. Donovan, A. W. Yau, and G. G. Arkos, Akebono/Suprathermal Mass Spectrometer observations of low-energy ion outflow: Dependence on magnetic activity and solar wind conditions, *J. Geophys. Res.*, *108*, 1093, doi:10.1029/2001JA009200, 2003b.
6. Delcourt, D. C., N. Dubouloz, J.-A. Sauvard, and M. Malin- gre, On the origin of sporadic keV ion injections observed by Interball-Auroral during the expansion phase of a substorm, *J. Geophys. Res.*, *104*, 24,929-24,937, 1999.
7. Fuselier, S. A., H. L. Collin, A. G. Ghielmetti, E. S. Clafin, T. E. Moore, M. R. Collier, H. Frey, and S. B. Mende, Localized ion outflow in response to a solar wind pressure pulse, *J. Geophys. Res.*, *107*, doi:10.1029/2001JA000297, 2002.
8. Khan, H., M. R. Collier, and T. E. Moore, Case study of solar wind pressure variations and neutral atom emissions observed by IMAGE/LENA, *J. Geophys. Res.*, *108*, 1093, doi:10.1029/2003JA009977, 2003.
9. Kokubun, S., R. L. McPherron, and C. T. Russell, Triggering of substorms by solar wind discontinuities, *J. Geophys. Res.*, *82*, 74-86, 1977.
10. Kokubun, S., T. Yamamoto, M. H. Acuna, K. Hayashi, K. Shiokawa, and H. Kawano, The GEOTAIL magnetic field experiment, *J. Geomagn. Geoelectr.*, *46*, 7-21, 1994.
11. Moore, T. E., et al., Ionospheric mass ejection in response to a CME, *Geophys. Res. Lett.*, *26*, 2339-2342, 1999.
12. Moore, T. E., et al., The low energy neutral atom imager for IM- AGE, *Space Sci Rev.*, *91*, 155-195, 2000.
13. Nishida, A., The GEOTAIL mission, *Geophys. Res. Lett.*, *21*, 2871-2874, 1994.
14. Nosé, M., S. Taguchi, K. Hosokawa, S. P. Christon, R. W. McEntire, T. E. Moore, and M. R. Collier, Overwhelming O<sup>+</sup> contribution to the plasma sheet energy density during the October 2003 superstorm: Geotail/EPIC and IM- AGE/LENA observations, *J. Geophys. Res.*, *110*, A09S24, doi:10.1029/2004JA010930, 2005.
15. Williams, D. J., R. W. McEntire, C. Schlemm II, A. T. Y. Lui, G. Gloeckler, S. P. Christon, and F. Gliem, Geotail energetic particles and ion composition instrument, *J. Geomagn. Geo- electr.*, *46*, 39-57, 1994.
16. Winglee, Multi-fluid simulations of the magnetosphere: The identification of the geopause and its variation with IMF, *Geo- phys. Res. Lett.*, *25*, 4441-4444, 1998.
17. Yau, A. W., W. K. Peterson, and E. G. Shelley, Quantitative para- meterization of energetic ionospheric ion outflow, in *Modeling Magnetospheric Plasma*, *Geophys. Monogr. Ser.*, vol. 44, edited by T. E. Moore, and J. H. Waite, Jr., pp. 211-217, AGU, Wash- ington, D. C., 1988.

# Automated detection of Pi2 pulsations to monitor substorm signatures: its application to real-time data and archived data

M. Nosé, T. Iyemori, M. Takeda, T. Kamei, F. Honary, S. R. Marple, J. Matzka, T. Ookawa, K. Takahashi, and G. Cifuentes-Nava

**Abstract:** Pi2 pulsations are defined as geomagnetic field variations with a period range of 40-150 s and an irregular waveform. It is generally accepted that Pi2 pulsations appear clearly at mid- or low-latitude ground station on the nightside in a close connection with substorm onsets. Thus nowcasting of substorm onset becomes possible, if we monitor geomagnetic field variations and detect Pi2 pulsations in real-time. We have developed an algorithm to detect Pi2 pulsations with wavelet analysis, which is suitable for investigating waves that are limited in both time and frequency, such as Pi2 pulsations. Using the geomagnetic field data from the Kakioka observatory, we have tested the algorithm and found that detection results by the algorithm on the nightside are fairly consistent with those by visual inspection. Based on this successful test result the algorithm has been applied to real-time geomagnetic field data obtained at the Mineyama and Kakioka observatories in Japan, as well as the York SAMNET station in the U. K. since 1997. We started the Pi2 detection at Fürstentfeldbruck in Germany in July 2005, at APL (Applied Physics Laboratory) in the United States and Teoloyucan in Mexico in September 2005. Detection results are transferred to Kyoto University via the Internet and are available at our WWW site (<http://swdcli40.kugi.kyoto-u.ac.jp/pi2/>). The network of these 6 observatories will result in more reliable detection of Pi2 pulsations, because at least one observatory is located on the nightside at any given time. We plan to analyze archived data with this algorithm and create Pi2 database. Such database will be useful for substorm studies.

*Key words:* Pi2 Pulsation, Space Weather Nowcast, Real-time Geomagnetic Field Data, Substorm Database.

## 1. Introduction

“Pi2” designates a type of geomagnetic field oscillations which have an irregular waveform and a period in the range of 40-150 seconds. There have been a large number of studies on Pi2 pulsations since 1960s [14]. Early studies have noticed that Pi2 pulsations can be observed clearly at mid- or low-latitude ground station on the nightside when substorms were initiated [e.g., 16, 17, 18]. Since Pi2 is thought to be a good indicator of substorm onset, it has been widely used in substorm studies [e.g., 8, 9, 10]. Pi2 pulsations provide information about not only substorm occurrence but also possible longitude of substorm onset. From a longitudinal chain of ground-based magnetometers at mid-latitude, Lester et al. [4, 5, 6] found that the major axis of Pi2 polarization in the horizontal plane is ori-

ented towards the center of the substorm current wedge. This was confirmed by Gelpi et al. [2] who investigated auroral images of the DMSP satellite and the magnetic field data from the longitudinal chain at mid-latitude. Pi2 pulsations might be even related to the magnitude of substorms (i.e., substorm energy), though it is still a controversial issue. Saito and Matsushita [15] showed that the Pi2 period is correlated with the amplitude of mid-latitude positive bays. Takahashi et al. [21] demonstrated a good correlation between the Pi2 amplitude and the auroral power deduced from the ultraviolet luminosity.

Recent progress in computers and instruments for geomagnetic field measurements allows us to obtain real-time geomagnetic field data with a high time resolution less than 5 seconds (typically 1 second). If we detect Pi2 pulsations from the real-time magnetic field records, it is highly possible to obtain real-time information about substorms such as their occurrence, longitudinal location of onset, and magnitude. Thus the real-time detection of Pi2 pulsations can contribute to the space weather nowcasts.

We have developed an algorithm to detect Pi2 pulsations automatically by wavelet analysis [11] and applied it to real-time data at 6 geomagnetic observatories which are distributed in 3 different longitudinal sectors (i.e., the Far East, Europe, and North/Middle America sectors). Since the data analysis system in these observatories are on-line, detection results of Pi2 pulsations can be reported by e-mail to Kyoto University, where the results are processed immediately and become browsable from WWW. The organization of the paper is as follows. Section 2 describes brief introduction of wavelet analysis. In section 3 we show how wavelet analysis works for

Received 12 June 2006.

**M. Nosé,<sup>1</sup> T. Iyemori, M. Takeda, and T. Kamei.** Graduate School of Science, Kyoto University, Kyoto, Japan

**F. Honary and S. R. Marple.** Department of Communication Systems, Lancaster University, Lancaster, U. K.

**J. Matzka.** Department of Earth and Environmental Sciences, Ludwig-Maximilians-Universität, München, Germany

**T. Ookawa.** Kakioka Magnetic Observatory, Japan Meteorological Agency, Ibaraki, Japan

**K. Takahashi.** Applied Physics Laboratory, Johns Hopkins University, Laurel, Maryland, USA

**G. Cifuentes-Nava.** Instituto de Geofísica, Universidad Nacional Autónoma de México, México, D. F., Mexico

<sup>1</sup>Corresponding author (e-mail: [nose@kugi.kyoto-u.ac.jp](mailto:nose@kugi.kyoto-u.ac.jp)).

geomagnetic field data. An algorithm to detect Pi2 pulsations with wavelet analysis was programmed. We show test results of the algorithm. Section 4 introduces the real-time Pi2 detection system.

## 2. Wavelet Analysis

Wavelet analysis is similar to Fourier analysis in that a time series is decomposed into orthonormal basis functions. Easier way to understand wavelet analysis is to describe it in comparison with Fourier analysis. Below is a brief introduction of wavelet analysis which was also described by Nosé et al. [11].

### 2.1. Wavelet analysis in comparison with Fourier analysis

In Fourier analysis, harmonic functions ( $e^{i2\pi ft}$ , where  $f$  is frequency and  $t$  is time) are adopted as orthonormal basis functions. Let  $h(t)$  and  $H(f)$  be a given function in the time domain and its Fourier transform in the frequency domain. The Fourier transform equations can be expressed by

$$h(t) = \int_{-\infty}^{\infty} H(f) \cdot e^{i2\pi ft} df,$$

$$H(f) = \int_{-\infty}^{\infty} h(t) \cdot (e^{i2\pi ft})^* dt,$$

where the asterisk denotes the complex conjugate. The Fourier transform is very popular in analysis of time series data, in particular, periodic signals; but it has a limitation which comes from the characteristics of the harmonic functions. Since the harmonic functions have finite values for  $t \rightarrow \pm\infty$ , Fourier analysis is sometimes not appropriate to analyze phenomena localized in time.

In wavelet analysis, a time series is decomposed into the orthonormal basis functions which are localized in time and limited in a specific frequency range (wavelets). Thus wavelet analysis is a suitable method for investigating the wave power of phenomena which are limited in both time and frequency, such as Pi 2 pulsations. The time series is mapped to the time-frequency domain, so the wavelet transform has two parameters which correspond to time and frequency. For a time series  $x(t)$ , the wavelet transform is expressed as

$$x(t) = \sum_j \sum_k \alpha_{j,k} \cdot \psi_{j,k}(t),$$

$$\alpha_{j,k} = \int_{-\infty}^{\infty} x(t) \cdot \psi_{j,k}^*(t) dt,$$

where  $\alpha_{j,k}$  is the wavelet coefficient and  $\psi_{j,k}(t)$  is the discrete wavelet set.  $\psi_{j,k}(t)$  is constructed from an analyzing wavelet  $\phi(t)$ , which generates the orthonormal wavelet set, by

$$\psi_{j,k}(t) = 2^{\frac{j}{2}} \phi(2^j t - k),$$

where  $j$  and  $k$  are integers. This equation indicates that  $j$  is related to the dilation or contraction of  $\phi(t)$  and  $k$  is related to the shift of  $\phi(t)$  in the time domain. Thus  $j$  and  $k$  can be considered as parameters of frequency and time, respectively.

### 2.2. Meyer Wavelet

A number of analyzing wavelets to generate the orthonormal wavelet set have been found. For example, the Haar wavelet, the Daubechies wavelet [1], and the Meyer wavelet [7] are known. In this study we used the Meyer wavelet, because the Meyer wavelet is band-limited in frequency. The Meyer wavelet is expressed as follows [19, 20, 22, 23, 24]:

$$\phi(t) = \frac{1}{2\pi} \int_{-\infty}^{\infty} \Phi(\omega) e^{i\omega t} d\omega,$$

where  $\omega$  is angular frequency and

$$\Phi(\omega) = \begin{cases} 0 & (|\omega| \geq \frac{8}{3}\pi) \\ e^{-i\frac{\omega}{2}} \left[ 1 + \exp \left\{ \frac{32}{3}\pi \frac{|\omega| - 2\pi}{(|\omega| - \frac{8}{3}\pi)^2 (|\omega| - \frac{4}{3}\pi)^2} \right\} \right]^{-\frac{1}{2}} & (\frac{4}{3}\pi < |\omega| < \frac{8}{3}\pi) \\ e^{-i\frac{\omega}{2}} & (|\omega| = \frac{4}{3}\pi) \\ e^{-i\frac{\omega}{2}} \left[ 1 + \exp \left\{ -\frac{4}{3}\pi \frac{|\omega| - \pi}{(|\omega| - \frac{4}{3}\pi)^2 (|\omega| - \frac{2}{3}\pi)^2} \right\} \right]^{-\frac{1}{2}} & (\frac{2}{3}\pi < |\omega| < \frac{4}{3}\pi) \\ 0 & (0 \leq |\omega| \leq \frac{2}{3}\pi) \end{cases}.$$

For actual analysis we use a discrete time series and take a finite data segment. Assuming a time series which has a sampling rate  $dt$  and a number of data points  $N$  ( $N=2^n$ ,  $n$  is integer), we will obtain wavelet coefficients  $\alpha_{j,k}$  confined in  $0 \leq j \leq n-1$  and  $0 \leq k \leq 2^j - 1$ . The frequency band for each  $j$  is  $2^j/3T \leq f \leq 2^{j+2}/3T$ , where  $T$  is the data length ( $T=Ndt$ ). Note that the widths of time window and frequency window covered by  $\alpha_{j,k}$  are  $T/2^j$  and  $2^j/T$ , respectively. This indicates that the wavelet coefficient with a large value of  $j$  has high resolution in time and low resolution in frequency, and vice versa. The Nyquist frequency is included in the frequency range supported by the maximum value of  $j$ . Figure 1 shows

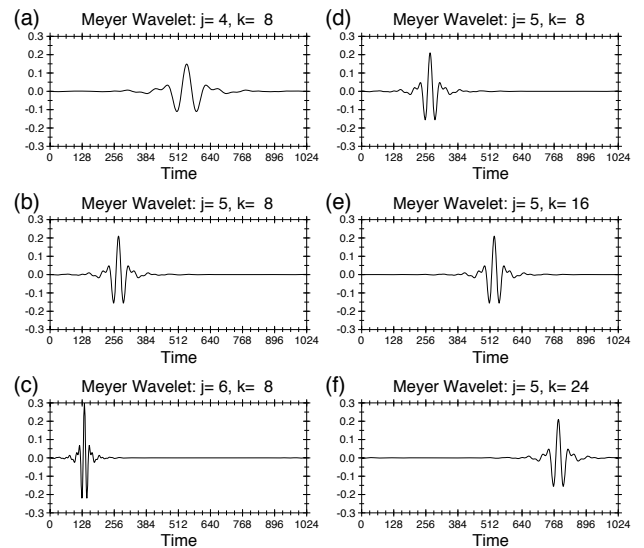


**Fig. 1.** Wavelet functions  $\psi_{j,k}(t)$  which are generated from the Meyer wavelet with  $N=1024$  and  $(j, k)$  of (a) (4,8), (b) (5,8), (c) (6,8), (d) (5,8), (e) (5,16), and (f) (5,24).

waveforms of the wavelet functions  $\psi_{j,k}(t)$  which are generated from the Meyer wavelet with  $N=1024=2^{10}$ . Note that the Meyer wavelet has a symmetric waveform. From Figures 1a-1c which give examples of wavelet functions with different values of  $j$  (i.e.,  $j=4-6$ ), we see that the wavelet function with a smaller value of  $j$  is more dilated than that with a larger value of  $j$ . Figures 1d-1f display examples of wavelet functions with different values of  $k$  (i.e.,  $k=8, 16, 24$ ). For a smaller value of  $k$ , the non-zero part of the wavelet function appears earlier in time. Therefore we can discuss phenomena from the viewpoint of both frequency ( $j$ ) and time ( $k$ ) at once. Even if more than one wave packets having an identical frequency appear at different times, these phenomena are identified by wavelet coefficients with different values of  $k$ .

### 3. Wavelet Analysis of Geomagnetic Field Data

#### 3.1. Pi2 pulsation at 1620 UT on 29 March 2006

We applied the wavelet analysis to geomagnetic field data obtained at Kakioka ( $27.37^\circ$  geomagnetic latitude (GMLAT),  $208.71^\circ$  geomagnetic longitude (GMLON)) with a sampling rate of 1 second. Figure 2 shows an example of the wavelet analysis for data around 1620 UT on March 29, 2006, when the Eighth International Conference on Substorms was held at Banff, Canada. The left panels of Figures 2a-2e display the geomagnetic field variations in the H-component for 512 seconds before the time indicated on the top of each panel. Note that time proceeds forward in 1-minute steps from Figure 2a to Figure 2c, while in 2-minute time steps from Figure 2c to Figure 2e. We found that a Pi2 pulsation with the period of  $\sim 100$  seconds ( $f \sim 10$  mHz) appeared at 1620-1621 UT.

The right panels show the absolute values of normalized wavelet coefficients  $\sqrt{2^j/T}|\alpha_{j,k}|$  with  $j=4-6$  corresponding to the geomagnetic field data in the left panels. The frequency ranges of wavelet functions with  $j=4-6$  are 5.2-20.8 mHz, 10.4-41.7 mHz, and 20.8-83.3 mHz, respectively. Pi2 pulsations which have a frequency range of 6.67-25.0 mHz are mainly represented by wavelet coefficients with  $j=4$  and 5. (Careful readers may notice that the aforementioned frequency ranges are derived in the case of  $N=1024$ . This is because we added 256 data points artificially to both ends of the 512-second data segment before wavelet analysis; the additional data are given to be equal to each end of the data segment. This data processing is necessary to obtain appropriate wavelet coefficients, in particular, when the geomagnetic field data at both ends are largely different.) In the right panels of Figures 2b-2e we find some wavelet coefficients having values larger than 0.5, which are indicated by shading. These wavelet coefficients appeared only in the time intervals when the Pi2 pulsation was initiated and only at  $j=4$  which covers the frequency of the Pi2 pulsation ( $\sim 10$  mHz). Therefore we can identify Pi2 pulsations by detecting large wavelet coefficients for  $j=4$  and 5 (or possibly  $j=6$ ). The detection criteria (i.e., magnitude of wavelet coefficients, etc.) will be determined empirically and depend on geomagnetic observatories.

#### 3.2. Pi2 detection algorithm

We have developed an algorithm to detect Pi2 pulsations automatically. The algorithm basically consists of procedures

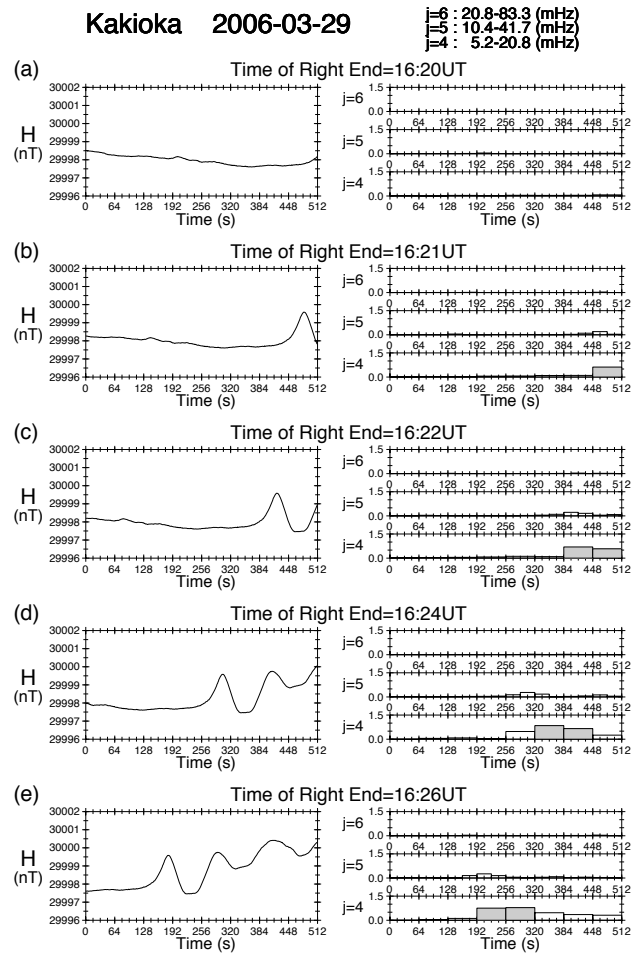


**Fig. 2.** Examples of wavelet analysis for the geomagnetic field data. (a) The left panel indicates the geomagnetic field variations in the H-component at Kakioka for 512 seconds before 1620 UT. The right panel shows the absolute values of normalized wavelet coefficients  $\sqrt{2^j/T}|\alpha_{j,k}|$  with  $j=4-6$  corresponding to the geomagnetic field data in the left panel. (b)-(e) Same as Figure 2a except for time of the right end of 1621 UT, 1622 UT, 1624 UT, and 1626 UT, respectively. Wavelet coefficients with values of  $\geq 0.5$  are indicated by shading.

to analyze the H- and D-components of the geomagnetic field data with the Meyer wavelet and to detect wavelet coefficients with  $j=4$  and 5 which exceed the detection criterion. From the wavelet coefficients we can estimate the amplitude of events. Thus the detection criterion was chosen as events having a peak-to-peak amplitude larger than 0.6 nT are identified. We tested the algorithm using the geomagnetic field data from Kakioka on the nightside (from 1800 magnetic local time (MLT) through midnight to 0400 MLT) in the period of January 2001. The data segment was taken to be 512-second long and was shifted forward by 60 seconds at every analysis, such as Figures 2a-2c. Events detected by the algorithm were visually inspected if they are real Pi2 pulsations.

A test result of the algorithm is summarized in Table 1. The detection algorithm found 90 possible Pi2 pulsations. We classified these events into 4 categories according to the estimated

Kakioka January 2001 1800-0400 MLT		Program Detection [Wavelet Analysis]				
		0.6-1.2 nT	1.2-1.8 nT	1.8-3.0 nT	3.0 nT-	Total
		64	13	9	4	90
Visual Inspection	Pi2	52	13	9	4	78
	Non Pi2	12	0	0	0	12
Rate of Successful Detection		81.3%	100%	100%	100%	86.7%

**Table 1.** Test result of the Pi2 detection algorithm for the Kakioka data in the nighttime (1800-0400 MLT) in January 2001.

peak-to-peak amplitudes, that is, 0.6-1.2 nT, 1.2-1.8 nT, 1.8 nT-3.0 nT, and larger than 3.0 nT. From the table we found that all of events with amplitude larger than 1.2 nT (i.e., 26 events) were Pi2 pulsations. However, 12 out of 64 events with amplitude of 0.6-1.2 nT were not real Pi2 pulsations. Thus the rate of successful detection is calculated to be 86.7% ((90-12)/90). We consider that the Pi2 detection algorithm gives fairly good results on the nightside (1800-0400 MLT). It is worth mentioning here that geomagnetic condition during January 2001 was quiet (monthly averages of Kp and Dst indices were 2– and –8.7 nT, respectively). During more disturbed period the rate of successful detection might become lower, because the geomagnetic field variations in such period often involve a lot of disturbances in the Pi2 frequency band.

#### 4. Automated Detection of Pi2 Pulsations

##### 4.1. Real-time Pi2 detection system

We have applied the Pi2 detection algorithm to real-time geomagnetic field data obtained at low- and mid-latitude observatories. The algorithm has been implemented in the on-site computers at the Mineyama observatory in Japan since February 1996 and at the York SAMNET station in the U. K. since May 1997 [11]. Real-time Pi2 detection was started also at the Fürstenfeldbruck observatory in Germany in July 2005 as well as at APL (Applied Physics Laboratory) in the United States and the Teoloyucan observatory in Mexico in September 2005. The coordinates and locations of these 6 observatories were

Station	(degree)			
	GGLAT	GGLON	GMLAT <sup>1</sup>	GMLON <sup>1</sup>
Mineyama	35.57	135.05	26.31	204.14
Kakioka	36.23	140.19	27.37	208.71
York	53.95	358.95	56.12	85.09
Fürstenfeldbruck	48.17	11.28	48.39	94.56
APL	39.17	283.12	49.37	353.87
Teoloyucan	19.75	260.82	28.76	330.34

<sup>1</sup> Values in January 2005

**Table 2.** Coordinates of observatories where the Pi2 detection algorithm is applied to real-time geomagnetic field data. GGLAT and GGLON denotes geographic latitude and longitude. GMLAT and GMLON means geomagnetic latitude and longitude.

shown in Table 2 and Figure 3. All observatories are located in low- and mid-latitude of the northern hemisphere (26°-56° GMLAT). It is noted that the observatories form a pair in 3 different longitudinal sectors (i.e., the Far East, Europe, and North/Middle America sectors) which were separated by about 120° in geomagnetic longitude. Thus at a given time at least one pair of observatories is located on the nightside where Pi2 pulsations are predominantly observed. A pair of observatories provides a more robust detection of Pi2 pulsations, because occurrence probability of entire data loss in a given sector becomes lower in the case of two observatories than a single observatory.

When Pi2 pulsations were detected by the algorithm, results of detection (i.e., onset time, estimated amplitude, and waveform) are immediately transferred by e-mail to Kyoto University, Japan. The results of real-time Pi2 detection are available from the WWW site (<http://swdcli40.kugi.kyoto-u.ac.jp/pi2/>).

Location of observatories in geomagnetic coordinates

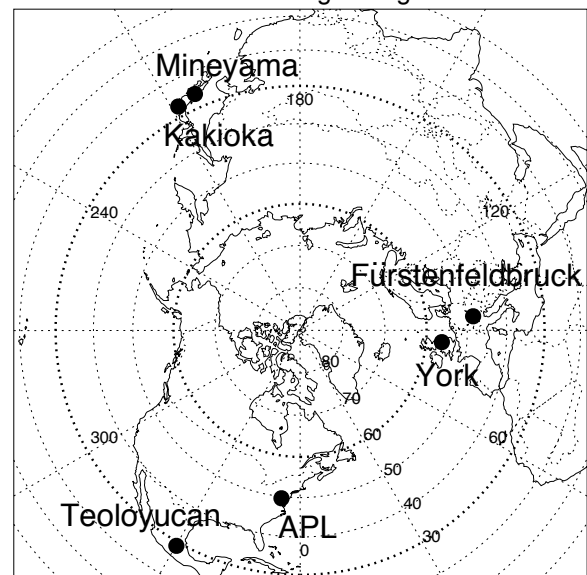


**Fig. 3.** Location of observatories in geomagnetic coordinates where the Pi2 detection algorithm is applied to real-time geomagnetic field data. Latitudinal circles of GMLAT=30° and 60° are shown with thick-dotted lines.

**4.2. Examples of Pi2 detection**

Figures 4a-4c show examples of Pi2 pulsations which were identified by the real-time Pi2 detection system. In each panel we plotted the H-component of the geomagnetic field data from two observatories which were at different magnetic local time (MLT); that is, the nightside (21-23 MLT) for the top and the dayside (12-13 MLT) or the dawn side (~06 MLT) for the bottom. A triangle indicates the onset time which was reported by the detection algorithm in each observatory. A Pi2 pulsation occurrence was reported from Fürstenfeldbruck and Teoloyucan at 1907 UT on May 21, 2006, which is consistent with the visual detection (Figure 4a). Note that time resolution at

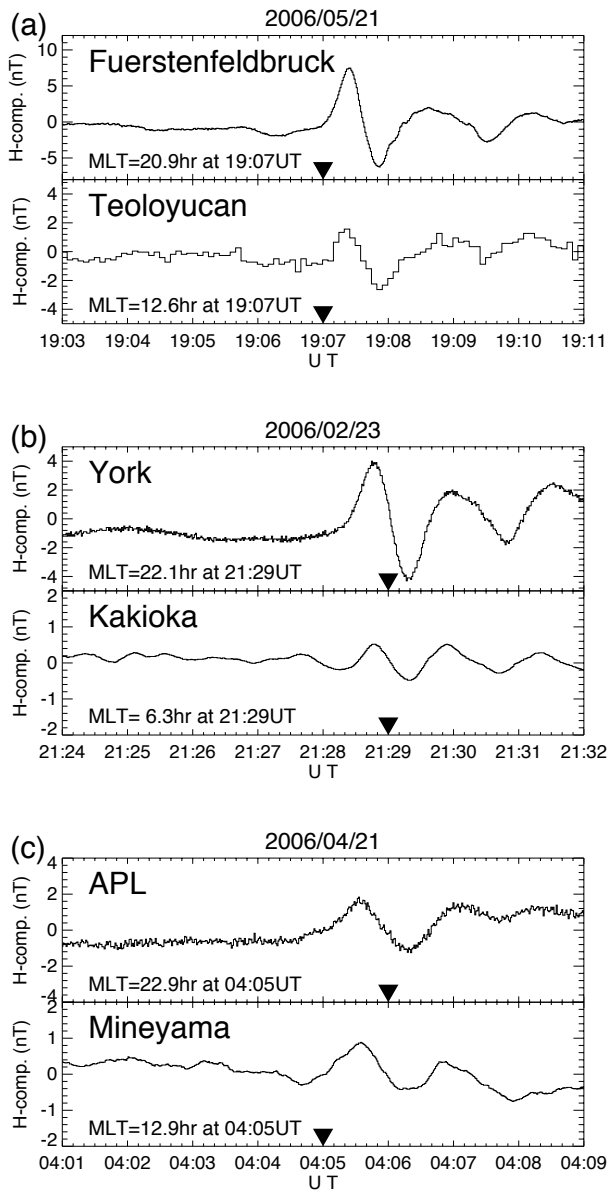


**Fig. 4.** Examples of Pi2 pulsations identified by the real-time Pi2 detection system in two different longitude; (a) Fürstenfeldbruck and Teoloyucan, (b) York and Kakioka, and (c) APL and Mineyama.

Fürstenfeldbruck is 1 second, while that at Teoloyucan is 5 seconds. Figure 4b shows that the detection system identified a Pi2 pulsation at 2129 UT on February 23, 2006 at both York and Kakioka. In Figure 4c there was a 1 minute difference in the reported onset time between APL and Mineyama, though we visually identify onset time of the Pi2 pulsation at 0405 UT on April 21, 2006.

These events reveal that Pi2 pulsations can be observed in two different longitudinal sectors, even if observatories are separated by 8-10 hours of MLT. It is also found that the Pi2 pulsations in Figure 4 have no clear phase difference between the observatories, implying that the longitudinal wave number of the pulsation is ~0. These results are consistent with those by Kitamura et al. [3] and Nosé et al. [12, 13].

**4.3. Pi2 database**

As can be seen in Table 1 or Figure 4, the algorithm developed in this study provides a rather good result of Pi2 detection. Thus we plan to analyze archived geomagnetic field data with this algorithm and create database of Pi2 pulsations. The database will be useful for substorm studies and will become available from our WWW server in future.

**Acknowledgements**

We thank Sven Egdorf, Martin Feller, Bruce Toth, Simon Wing, Linda Burke, and Mark Moldwin for their help in maintaining the Pi2 detection system. This work was supported by the Ministry of Education, Science, Sports and Culture, Grant-in-Aid for Young Scientists (B) (grant 17740327) and the Kurata Memorial Hitachi Science and Technology Foundation (grant 844). Work at JHU/APL was supported by NASA under grant NAG5-13119.

**References**

1. Daubechies, I., Orthonormal bases of compactly supported wavelets, *Comm. Pure Appl. Math.*, 41, 909-996, 1988.
2. Gelpi, C., H. J. Singer, and W. J. Hughes, A comparison of magnetic signatures and DMSP auroral images at substorm onset: Three case studies, *J. Geophys. Res.*, 92, 2447-2460, 1987.
3. Kitamura, T., O. Saka, M. Shimoizumi, H. Tachihara, T. Oguti, T. Araki, N. Sato, M. Ishitsuka, O. Veliz, and J. B. Nyobe, Global mode of Pi2 waves in the equatorial region: Difference of Pi2 mode between high and equatorial latitudes, *J. Geomagn. Geoelectr.*, 40, 621-634, 1988.
4. Lester, M., W. J. Hughes, and H. J. Singer, Polarization patterns of Pi2 magnetic pulsations and the substorm current wedge, *J. Geophys. Res.*, 88, 7958-7966, 1983.
5. Lester, M., W. J. Hughes, and H. J. Singer, Longitudinal structure in Pi2 pulsations and the substorm current wedge, *J. Geophys. Res.*, 89, 5489-5494, 1984.
6. Lester, M., H. J. Singer, D. P. Smith, and W. J. Hughes, Pi2 pulsations and the substorm current wedge: Low-latitude polarization, *J. Geophys. Res.*, 94, 17,133-17,141, 1989.
7. Meyer, Y., Orthonormal wavelets, in *Wavelets*, edited by J. M. Combes, A. Grossmann, and Ph. Tchamitchian, pp. 21-37, Springer-Verlag, Berlin, 1989.

8. Miyashita, Y., S. Machida, A. Nishida, T. Mukai, Y. Saito, and S. Kokubun, Geotail observations of total pressure and electric field variations in the near and mid-distant tail associated with substorm onsets, *J. Geophys. Res.*, *26*, 639-642, 1999.
9. Miyashita, Y., S. Machida, T. Mukai, Y. Saito, K. Tsuruda, H. Hayakawa, and P. R. Sutcliffe, A statistical study of variations in the near and middistant magnetotail associated with substorm onsets: GEOTAIL observations, *J. Geophys. Res.*, *105*, 15,913-15,930, 2000.
10. Nagai, T., M. Fujimoto, Y. Saito, S. Machida, T. Terasawa, R. Nakamura, T. Yamamoto, T. Mukai, A. Nishida, and S. Kokubun, *J. Geophys. Res.*, *103*, 4419-4440, 1998.
11. Nosé, M., T. Iyemori, M. Takeda, T. Kamei, D. K. Milling, D. Orr, H. J. Singer, E. W. Worthington, and N. Sumitomo, Automated detection of Pi 2 pulsations using wavelet analysis: 1. Method and an application for substorm monitoring, *Earth Planet. Space*, *50*, 773-783, 1998.
12. Nosé, M., K. Takahashi, T. Uozumi, K. Yumoto, Y. Miyoshi, A. Morioka, D. K. Milling, P. R. Sutcliffe, H. Matsumoto, T. Goka, and H. Nakata, Multipoint observations of a Pi2 pulsation on morning side: The 20 September 1995 event, *J. Geophys. Res.*, *108*, 1219, doi:10.1029/2002JA009747, 2003.
13. Nosé, M., K. Liou, P. R. Sutcliffe, Longitudinal dependence of characteristics of low-latitude Pi2 pulsations observed at Kakioka and Hermanus, *Earth Planet. Space*, *58*, 775-783, 2006.
14. Saito, T., Geomagnetic pulsations, *Space Sci. Rev.*, *10*, 319-412, 1969.
15. Saito, T. and S. Matsushita, Solar cycle effects on geomagnetic Pi2 pulsations, *J. Geophys. Res.*, *73*, 267-286, 1968.
16. Saito, T., T. Sakurai, and Y. Koyama, Mechanism of association between Pi 2 pulsation and magnetospheric substorm, *J. Atmos. Terr. Phys.*, *38*, 1265-1277, 1976a.
17. Saito, T., K. Yumoto, and Y. Koyama, Magnetic pulsation Pi 2 as a sensitive indicator of magnetospheric substorm, *Planet. Space Sci.*, *24*, 1025-1029, 1976b.
18. Sakurai, T. and T. Saito, Magnetic pulsation Pi 2 and substorm onset, *Planet. Space Sci.*, *24*, 573-575, 1976.
19. Sasaki, F., T. Maeda, and M. Yamada, Study of time history data using wavelet transform, *J. Struc. Eng. Architec. Inst. Japan*, *38B*, 9-20, 1992 (in Japanese with English abstract).
20. Sato, K. and M. Yamada, Vertical structure of atmospheric gravity waves revealed by the wavelet analysis, *J. Geophys. Res.*, *99*, 20,623-20,631, 1994.
21. Takahashi, K., K. Liou, and K. Yumoto, Correlative study of ultraviolet aurora and low-latitude Pi2 pulsations, *J. Geophys. Res.*, *107*, 1417, doi:10.1029/2002JA009455, 2002.
22. Yamada, M. and K. Ohkitani, Orthonormal wavelet analysis of turbulence, *Fluid Dyn. Res.*, *8*, 101-115, 1991.
23. Yamanaka, M. D., T. Shimomai, and S. Fukao, A model of quasi-monochromatic field of middle-atmospheric internal gravity waves, *Proc. of the 1992 STEP Symposium/5th COSPAR Colloquium*, 511-518, 1994.
24. Yomogida, K., Detection of anomalous seismic phases by the wavelet transform, *Geophys. J. Int.*, *116*, 119-130, 1994.

# Conjugate imaging of substorms

N. Østgaard, S. B. Mende, H. U. Frey, J. B. Sigwarth, A. Aasnes, and J. M. Weygand

**Abstract:** Simultaneous imaging in the ultraviolet wavelengths by IMAGE and Polar of substorm onset location in the conjugate hemispheres has shown that there exists a systematic displacement of substorm onset location in one hemisphere compared to the other. The relative displacement of onset locations in the conjugate hemispheres was found to be controlled primarily by the IMF clock-angle, with the dipole tilt angle as a possible second order effect. Compared with some of the existing magnetic field models, the observed asymmetries were found to be an order of magnitude larger than the model predictions. Statistical distribution of substorm onset locations in the southern and northern hemispheres for different clock angles enables us to validate the IMF clock angle control. Based on  $\sim 3000$  substorm onsets in the northern hemisphere and  $\sim 1000$  in the southern hemisphere observed by IMAGE we find a remarkable support for our previous findings.

*Key words:* Substorms, IMF control, aurora, imaging.

## 1. Introduction

In the open magnetospheric model the IMF is assumed to be an important controlling factor of solar wind-magnetosphere coupling. Theoretical considerations have suggested [17, 3] and observations have indeed shown that the IMF penetrates the outer [15] as well as the inner [22] magnetotail. The partial magnetospheric penetration [17] of the IMF has consequently been implemented in the empirical magnetic field models of Tsyganenko; T96 [18] and T02 [19, 20]. It is also well documented that the IMF orientation affects the location of the night-side aurora [2, 4, 16, 13, 7, 5]. However, to determine how auroral phenomena in the northern and southern hemispheres can be of different intensities, asymmetric or even non-conjugate, we need simultaneous conjugate measurements. In-situ conjugate measurements from space are very hard to obtain, because you do not know if you really are on conjugate field lines. Conjugate imaging from ground is difficult because you need clear sky and asymmetries that are less than the field of view of the all-sky cameras [12]. For these reasons, conjugate simultaneous global imaging from space is really what can resolve the degree of conjugacy and non-conjugacy of auroral phenomena. With an imaging cadence of 2 min and 1 min for IMAGE-FUV and Polar VIS Earth camera, respectively, these two missions have made it possible to address some of these questions more quantitatively.

In this paper we report how simultaneous imaging from the conjugate hemispheres has revealed that there exists a systematic displacement of substorm onset location in one hemisphere compared to the other [9, 10]. Furthermore, we show

how this asymmetry is confirmed by a huge dataset of substorm locations from the IMAGE mission [6]. Finally, we identify some questions that naturally arise from these findings.

## 2. Substorm onset location in the conjugate hemispheres

In our first study [9] we investigated thirteen events where we had conjugate simultaneous images of substorm onsets and auroral features that could be easily identified. One of these events are shown in Figure 1. To identify the IMF orientation we used 10-min-average of the IMF data from Wind and ACE time-shifted to  $X = -10R_E$  assuming planar propagation of the solar wind. In agreement with predictions [3] we found that, for southward IMF, there exists a systematic hemispherical asymmetry of substorm onset locations. This asymmetry is strongly correlated with the IMF clock angle (the clockwise angle with respect to the northward direction see Figure 2A) and that the relative displacement ( $\Delta MLT$ ) can be expressed as a linear function of IMF clock angle ranging from  $90^\circ$  to  $270^\circ$  (i.e., for southward IMF). We interpreted these findings as the magnetic tensions force acting on open magnetic field lines before reconnecting in the magnetotail or simply the IMF penetration of the magnetosphere. Based on a slightly larger data set [10] we found that the dipole tilt angle may act as a secondary controlling factor (next to the IMF) of the auroral asymmetries in the conjugate hemispheres. This would be consistent with the field aligned currents (FACs) being stronger in the winter than in the summer hemispheres. Such stronger night-side winter FACs were indeed found by [8] but not in the statistical distribution of FACs based on Iridium measurements [1]. We want to emphasize that the correlation coefficient for a possible dipole tilt angle effect was relatively poor (0.56) and further studies are needed to see if this effect is real. Another result reported in that paper [10] was that the two empirical magnetic field models T96 [18] and T02 [19, 20] field models replicate qualitatively the IMF induced asymmetries, but underestimate this effect by an order of magnitude. This is an important result with implications for field-line mapping, either to find conjugate points in the two ionospheres or at different locations in the magnetosphere. In a recent paper [14] it was re-

Received 29 May 2006.

**N. Østgaard.** Department of Physics and Technology, University of Bergen, Norway

**S. B. Mende and H. U. Frey.** Space Sciences Laboratory, University of California, Berkeley, California, USA

**J. B. Sigwarth.** Goddard Space Flight Center, Greenbelt, Maryland, USA

**A. Aasnes.** Los Alamos National Laboratory, Los Alamos, New Mexico, USA

**J. M. Weygand.** Inst. of Geophys. and Plan. Physics, U.C., Los Angeles, California, USA

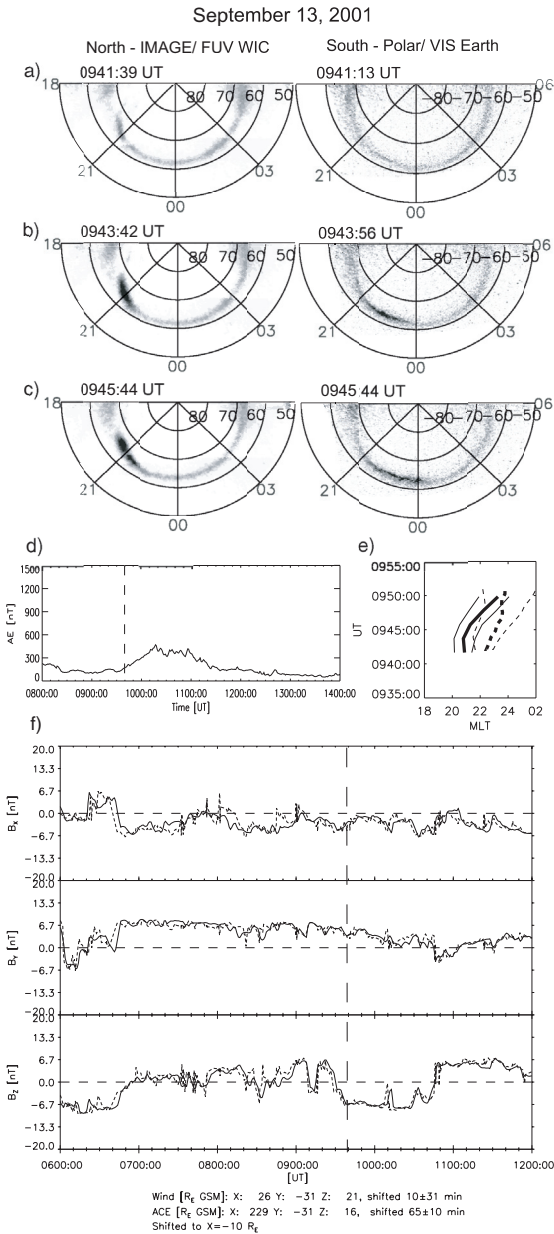


**Fig. 1.** September 13, 2001. (a)-(c) IMAGE WIC images from the northern hemisphere and VIS Earth images from the southern hemisphere mapped onto apex magnetic coordinates. (d) The Quick-look AE index from Kyoto, Japan. (e) The peak (thick) and the 50% intensity contour (thin) local time location for the substorm onset in the southern (dashed) and the northern (solid) hemisphere. (f) The IMF in GSM coordinates measured by Wind (solid) and ACE (dashed) time-shifted to X=-10 R<sub>E</sub>. This figure is from [9].

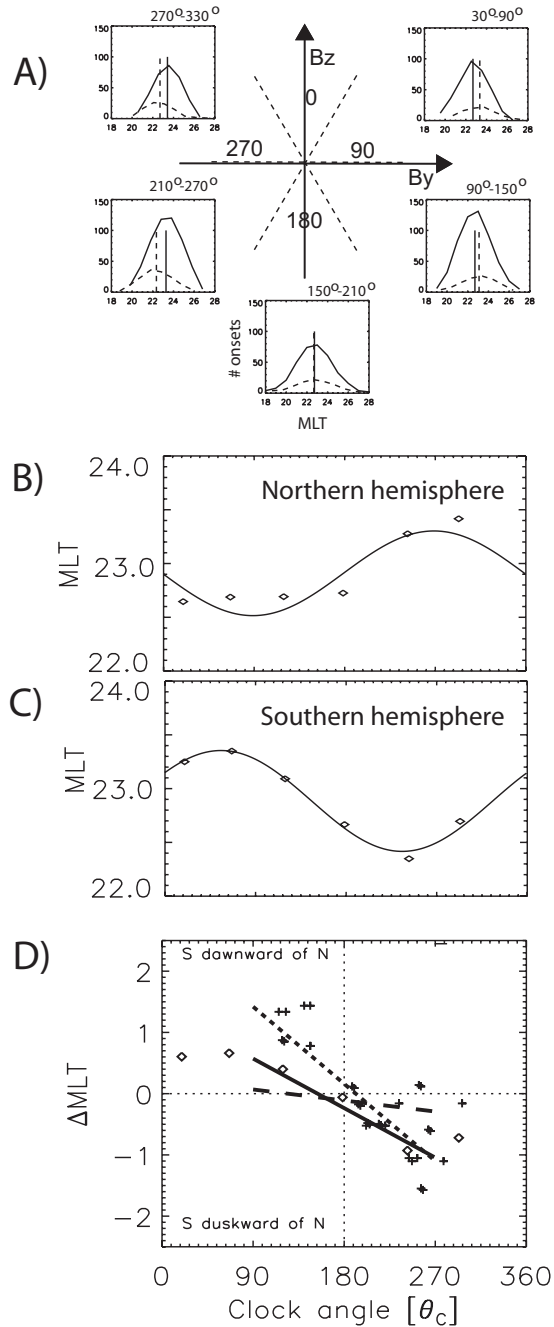


**Fig. 2.** (A) Statistical distributions and average of substorm onset locations in the northern (black) and southern (dashed) hemispheres for 5 different clock angle intervals of 60° using both Wind and ACE data. IMF coordinates are shown in the middle and clock angle is positive in the clockwise direction. (B) Average location of substorm onset as a function of IMF clock angle in the northern hemisphere. (C) Same for the southern hemisphere. (D)  $\Delta$ MLT versus clock angle. Dotted line and crosses: Simultaneous imaging [10], black dashed line: Predicted by T02, black diamonds: points derived from (B and C), i.e., difference between average southern and northern locations, black line: regression line for black diamonds. Panel A and D were also shown by [11].

ported north-south asymmetries of the aurora that partly support and partly contradict this simple linear function ( $\Delta\text{MLT}$  versus clock angle). It should be noticed, however, that the asymmetries were small,  $\Delta\text{MLT}=0.02\text{--}0.2$  and such small fluctuations might have other causes (e.g., FAC) than IMF.

To further investigate this asymmetry we have analyzed the substorm onset locations determined from IMAGE-FUV images from year 2000 to 2004 [6]. This dataset comprises 2760 and 978 substorm onset locations from the northern and southern hemisphere, respectively. For each of these substorms we have determined the 10-min-average IMF clock angle from ACE and Wind data time shifted to  $-10R_E$  using a slightly more sophisticated propagation method [21]. Cases where the clock angle varied more than  $40^\circ$  within the 10-min averaging interval have been excluded. In order to get sufficient statistics we binned the onset locations (MLT) in  $60^\circ$  intervals of IMF clock angles determined from both Wind and ACE data and calculated the average location for substorm onset in each bin for northern and southern hemisphere separately. The number of substorm locations ranges from 92 (southern hemisphere  $30^\circ\text{--}90^\circ$ ) to 547 (northern hemisphere  $90^\circ\text{--}150^\circ$ ). Figure 2A shows the distribution and average onset location in the northern (black) and southern (dashed) hemispheres for 5 of the 6 clock angle intervals. Figure 2B and C show the average substorm locations as a function of IMF clock angle (black diamonds) for northern and southern hemisphere, with a fitted cosine function overlaid (solid line). In Figure 2B you can see the relative asymmetry (southern minus northern average onset location) of the average onset locations. Even if the slope of the regression line (black line) is not as steep as derived from our simultaneous imaging data (dotted line), which one should expect from the averaging, these statistical results demonstrate that the asymmetries are still a factor 5 larger than T02 predicts (dashed line).

As mentioned a time-shift of the IMF orientation to  $-10R_E$  has been used. Considering that there is a response time for the IMF orientation to affect the inner magnetosphere, this may imply that a near-Earth neutral line has to form prior to the onset. On the other hand, if the IMF control on the inner magnetosphere is the effect of magnetic field lines reconnected at the far neutral line convected earthward a much larger time-shift is needed. To address this, we will (in the near future) check if other time-shifts, e.g., to  $-50R_E$ ,  $-100R_E$  or even  $-100R_E$  plus 60 min, will give a similar systematic IMF control.

### 3. Conclusions

In this paper we have reviewed and discussed our main results from analyzing global imaging data by IMAGE and Polar.

(1) There exists a systematical asymmetry of substorm onset locations in the conjugate hemispheres, which is found to be controlled primarily by the IMF clock angle.

(2) Compared with some of the existing magnetic field models, the observed asymmetries are an order of magnitude larger than the model predictions.

(3) These results have been compared with the statistical distribution of substorm onsets observed by IMAGE for different clock angles. Based on  $\sim 3000$  substorm onsets in the northern hemisphere and  $\sim 1000$  in the southern hemisphere we find a

remarkable support for our previous findings. The asymmetries are at least 5 times larger than model predictions.

### Acknowledgements

This study was supported by the Norwegian Research Council, project 165487 and by the ICESTAR program.

### References

1. B. J. Anderson, North-south asymmetries in magnetosphere-ionosphere coupling: Simultaneous observations of Birkeland current signatures in both hemispheres, *J. Geophys. Res.* April (2005) submitted.
2. G. B. Burns, D. J. McEwen, R. A. Eather, F. T. Berkey, J. S. Murphree, Optical auroral conjugacy: Viking UV imager - South Pole station ground data, *J. Geophys. Res.* 95 (1990) 5781–5790.
3. S. W. H. Cowley, J. P. Morelli, M. Lockwood, Dependence of convective flows and particle precipitation in the high-latitude dayside ionosphere and the X and Y components of the interplanetary magnetic field, *J. Geophys. Res.* 96 (1991) 5557–5564.
4. R. D. Elphinstone, K. Jankowska, J. Murphree, L. Cogger, The configuration of the auroral distribution for interplanetary magnetic field -  $B_z$  northward. 1. IMF  $B_x$  and  $B_y$  dependencies as observed by the VIKING satellite, *J. Geophys. Res.* 95 (1990) 5791.
5. L. A. Frank, J. B. Sigwarth, Simultaneous images of the northern and southern auroras from the Polar spacecraft: An auroral substorm, *J. Geophys. Res.* 108 (2003) 8015.
6. H. U. Frey, S. B. Mende, V. Angelopoulos, E. F. Donovan, Substorm onset observations by IMAGE-FUV, *J. Geophys. Res.* 109 (A10) (2004) A10304.
7. K. Liou, P. T. Newell, D. G. Sibeck, C. I. Meng, M. Brittnacher, G. Parks, Observation of IMF and seasonal effects in the location of auroral substorm onset, *J. Geophys. Res.* 106 (2001) 5799.
8. S.-I. Ohtani, G. Ueno, T. Higuchi, H. Kawano, Annual and semiannual variations of the location and intensity of large-scale field-aligned currents, *J. Geophys. Res.* 110 (A1) (2005) A01216.
9. N. Østgaard, S. B. Mende, H. U. Frey, T. J. Immel, L. A. Frank, J. B. Sigwarth, T. J. Stubbs, Interplanetary magnetic field control of the location of substorm onset and auroral features in the conjugate hemispheres, *J. Geophys. Res.* 109 (A7) (2004) A07204.
10. N. Østgaard, N. A. Tsyganenko, S. B. Mende, H. U. Frey, T. J. Immel, M. Fillingim, L. A. Frank, J. B. Sigwarth, Observations and model predictions of auroral substorm asymmetries in the conjugate hemispheres, *Geophys. Res. Lett.* 32 (5) (2005) L05111.
11. N. Østgaard, S. B. Mende, H. U. Frey, J. B. Sigwarth, A. Aasnes, J. M. Weygand, Auroral conjugacy studies based on global imaging, *J. Atmos. Terr. Phys.* - (-) (2006) in press.
12. N. Sato, R. Fujii, T. Ono, H. Fukunishi, T. Hirasawa, T. Araki, S. Kokubun, K. Makita, T. Saemundsson, Conjugacy of proton and electron auroras observed near  $l=6.1$ , *Geophys. Res. Lett.* 13 (1986) 1368–1371.
13. N. Sato, T. Nagaoka, K. Hashimoto, T. Saemundsson, Conjugacy of isolated auroral arcs and non-conjugate auroral break-ups, *J. Geophys. Res.* 103 (1998) 11,641–11,652.

14. N. Sato, A. Kadokura, Y. Ebihara, H. Deguchi, T. Saemundsson, Tracing geomagnetic conjugate points using exceptionally similar synchronous auroras, *Geophys. Res. Lett.* 32 (9) (2005) L17109.
15. D. G. Sibeck, The distant magnetotail's response to a strong interplanetary magnetic field  $B_y$ : twisting, flattening, and field line bending, *J. Geophys. Res.* 90 (1985) 4011.
16. H. C. Stenbaek-Nielsen, A. Otto, Conjugate auroras and the interplanetary magnetic field, *J. Geophys. Res.* 102 (1997) 2223–2232.
17. F. R. Toffoletto, T. W. Hill, Mapping of the solar wind electric field to the Earth's polar cap, *J. Geophys. Res.* 94 (1989) 329–347.
18. N. A. Tsyganenko, Modelling the Earth's magnetospheric magnetic field confined within a realistic magnetopause, *J. Geophys. Res.* 100 (1995) 5599–5612.
19. N. A. Tsyganenko, A model of the near magnetosphere with a dawn-dusk asymmetry 1. mathematical structure, *J. Geophys. Res.* 107 (A8) (2002) 1179.
20. N. A. Tsyganenko, A model of the near magnetosphere with a dawn-dusk asymmetry 2. parametrization and fitting to observations, *J. Geophys. Res.* 107 (A8) (2002) 1179.
21. D. R. Weimer, Correction to Predicting interplanetary magnetic field (IMF) propagation delay times using minimum variance techniques, *J. Geophys. Res.* 109 (A12) (2004) A12104.
22. S. Wing, P. T. Newell, D. G. Sibeck, K. B. Baker, A large statistical study of the entry of interplanetary magnetic field component into the magnetosphere, *Geophys. Res. Lett.* 22 (1995) 2083–2086.

# Time history effects at the magnetopause: hysteresis in power input and its implications to substorm processes

M. Palmroth, T. I. Pulkkinen, T. V. Laitinen, H. E. J. Koskinen, and P. Janhunen

**Abstract:** The energy input processes through the magnetopause are examined in the GUMICS-4 global MHD simulation. We demonstrate that the energy input through magnetopause is strongly controlled by the IMF clock angle, but also on the previous level of magnetic activity. This hysteresis appears in a variety of model runs, and seems to originate from the nature of magnetopause reconnection. These results are shown to imply that the substorm energetics is directly driven by the incoming energy. Based on these results, the differences between the substorm dynamics and substorm energetics are discussed.

*Key words:* Global MHD simulations, Reconnection, Substorm energy budget.

## 1. Introduction

The traditional view of the energy input from the solar wind into the magnetosphere is that it is modulated by the solar wind and interplanetary magnetic field (IMF), which control the rate of dayside reconnection [6]. However, a global MHD simulation GUMICS-4 [7] has recently shown indications that the energy transfer through the magnetopause may not only be a function of the present, but also of the past solar wind and IMF conditions [12]. In other words, the energy input through the magnetopause shows hysteretic behavior with respect to the driving solar wind and IMF parameters so that more intense driving implies large energy input even after the driving has already weakened. This result has important implications to the substorm process [13]: The simulation results indicate that if the energy input is evaluated from a quantitative analysis at the magnetopause, energy dissipation in the tail and in the ionosphere are quite directly proportional to it, not showing the characteristic time delays one gets when comparing observational proxies for the driver and the ionospheric dissipation.

In this paper we examine the energy transfer through the magnetopause. Based on series of simulation runs performed using artificial solar wind and IMF driver conditions we discuss the processes at the magnetopause contributing to the hysteresis and the associated time delays. A particular substorm event is used to discuss the implications of the hysteresis on the global energetics and its possible interpretation in substorm processes. In comparisons with observational data, ionospheric dissipation is assumed to be proportional to the *AE* index [1], while the energy input is parametrized by the often used  $\epsilon = (4\pi/\mu_0)vB^2l_0^2 \sin^4(\theta/2)$ , where  $\mu_0$  is the vacuum permeability,  $v$  solar wind speed,  $l_0 = 7R_E$  a scaling parameter,  $B$

the IMF magnitude, and  $\theta = \tan^{-1}(B_Y/B_Z)$  the IMF clock angle [2].

## 2. GUMICS-4 global MHD simulation

The GUMICS-4 global MHD simulation [7] solves the ideal MHD equations in the solar wind and in the magnetosphere, and is coupled to an electrostatic ionosphere at the inner boundary at  $3.7 R_E$ . The upstream boundary conditions (either measured or idealized) are given by solar wind and IMF conditions at the sunward boundary of the simulation. The ionospheric simulation takes the field-aligned currents and electron precipitation at the inner boundary of the simulation mapped along dipole magnetic field lines, and feeds the MHD part with new solution of the electric potential. For more details of the code structure and setup see e.g. [10]. Quantitative methods have been developed to extract the amount of energy entering through the magnetopause surface sunward of  $X = -30R_E$  [10], reconnection behavior [9], and energy dissipation in the ionosphere (including contributions from both Joule heating and particle precipitation) [11].

## 3. Event study

A moderate substorm (AE maximum of about 500 nT) on August 15, 2001, was simulated with GUMICS-4 to examine the energy transfer and dissipation during actually observed solar wind conditions. Fig. 1 shows the observed  $\epsilon$  parameter giving a proxy for the driver conditions and the AE-index giving a proxy for the ionospheric energy dissipation [1]. Overplotted in a different scale, we show the power transfer through the magnetopause and the ionospheric dissipation evaluated from the simulation. While there is a clear time shift between the observed  $\epsilon$  and energy input through the simulation magnetopause, the dissipation time sequences have quite similar temporal evolution (with the exception that the simulation does not see the rapid rise in dissipation at substorm onset).

The bottom parts of Fig. 1 show the time differences even more clearly. The four hodograms show the various input and dissipation parameters plotted against each other. It is clear that

Received 10 May 2006.

**M. Palmroth and H. E. J. Koskinen.** Finnish Meteorological Institute, Helsinki, Finland.

**T. I. Pulkkinen.** Los Alamos National Laboratory, Los Alamos, NM, USA.

**T. V. Laitinen and P. Janhunen.** Department of Physical Sciences, University of Helsinki, Finland.

using the observational proxies, the system shows increasing input leading to a later dissipation of energy (top left hodogram). The same is true if the  $\epsilon$  is computed from the simulation at the magnetopause and compared with the dissipation in the simulation ionosphere (top right). However, the plot showing the hodogram between  $\epsilon$  and the energy input through the magnetopause (bottom left) demonstrates that the time delay associated with the varying solar wind and dissipation in the ionosphere is associated with processes occurring already at the magnetopause; the hodogram between  $\epsilon$  and magnetopause energy input is identical in shape to those comparing  $\epsilon$  and ionospheric dissipation. On the contrary, if one examines the energy input through the magnetopause as computed from the simulation and compares that with the energy dissipation in the ionosphere, there is almost no time delay associated with the ionospheric dissipation (bottom right). Hence, the energy transferred through the magnetopause is quite directly processed by the system.

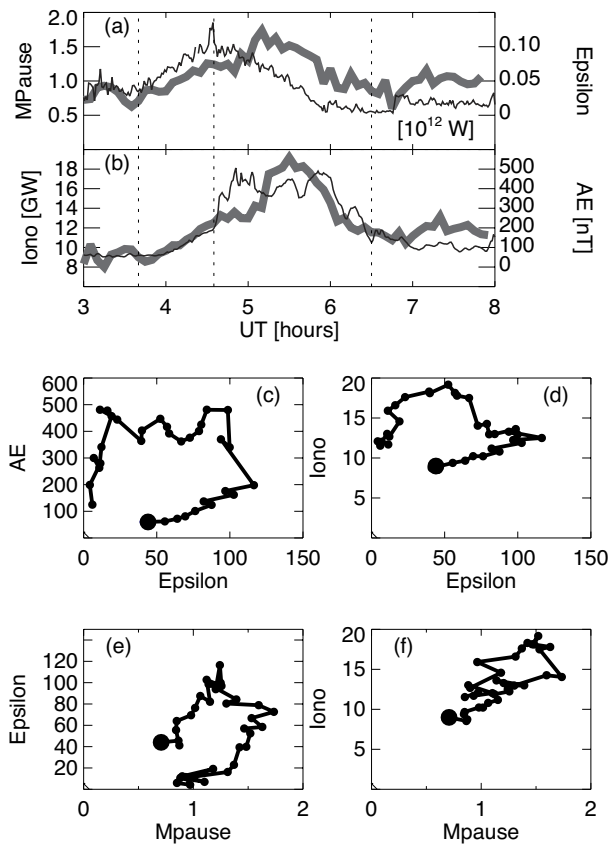


**Fig. 1.** Substorm on Aug 15, 2001. (a) Energy transfer rate through the magnetopause from GUMICS-4 in  $10^{12}$  W (gray, thick line) and measured  $\epsilon$  transferred to the magnetopause (black, thin line, scale on the right). (b) Ionospheric dissipation from GUMICS-4 in GW (gray, thick line) and measured AE-index (black, thin line, scale on the right). (c) Hodogram of the observed  $\epsilon$  vs. AE index. (d)  $\epsilon$  vs. ionospheric dissipation, (e) magnetopause energy transfer vs.  $\epsilon$ , and (f) magnetopause energy transfer vs. ionospheric dissipation all from GUMICS-4. The start points are marked by the large filled circle [13].

#### 4. Energy transfer processes at the magnetopause

To systematically investigate the energy transfer at the magnetopause, we ran four simulations with controlled solar wind data. In the four runs, the solar wind dynamic pressure  $p_{dyn}$  and magnetic field intensity were kept constant, while the IMF was rotated in the  $YZ$  plane from clock angle  $\theta = 0^\circ$  to  $360^\circ$  with  $10^\circ$  steps such that each clock angle value was kept constant for 10 minutes. The full rotation thus lasted for 6 hours. The simulation was initialized by running a steady northward IMF for one hour before the rotation started at the sunward wall of the simulation box. Table 1 summarizes the input parameters.

Fig. 2a-d presents the instantaneous distributions of energy transfer for Run #1, integrated from the nose of the magnetopause to  $-30 R_E$  in the tail. Each sector shows the sum of energy transfer taking place in the angular direction shown in the outer circle, viewing from the Sun looking tailward. The IMF clock angle at the time for which the distribution is plotted is indicated with the black arrow. Fig. 2e shows the total integrated energy across the entire magnetopause as a function of the clock angle (solid line). The vertical dashed lines indicate the times for which the instantaneous energy transfer distributions are shown above. The dashed line in Fig. 2e shows the function  $\sin^2(\theta/2)$  scaled to same minimum and maximum intensity. We use the second power of  $\theta/2$  instead of the fourth (which would give a functional form similar to that of the  $\epsilon$  parameter), as it is a better representative of the simulation results. Thus, the simulation indicates that the energy transfer through the magnetopause scales rather more like the electric field ( $\sin^2(\theta/2)$ ) than  $\epsilon$  ( $\sin^4(\theta/2)$ ).

The gray area, normalized to 800 GW at the outer circle, and negative values in the line plot indicate energy input from the solar wind into the magnetosphere. For the energy transfer there is no information on the distance at which the energy transfer occurs; however, we have previously shown that the energy transfer occurs predominantly Sunward of the  $X = -10 R_E$  [10]. The black circles plotted over the energy transfer sectors highlight the locations where reconnection is likely to occur (for a characterization of magnetopause reconnection, see [9]) ranging from the nose of the magnetopause (center of the panel) to the dawn-dusk terminator.

In Fig. 2a, the IMF has rotated for over an hour to  $\theta = 60^\circ$ . The energy transfer occurs at dawn (dusk) high-latitudes in the northern (southern) hemisphere. Although reconnection does not yet reach the very nose of the magnetopause, it already has a low-latitude component. Hence, the open field lines travel to nightside through dawn (dusk) high latitudes in the northern (southern) hemispheres [4]. As demonstrated in [10], the geometry between the magnetosheath bulk flow and the tailward moving open field line demands that Poynting vector points towards the magnetopause. This implies that electromagnetic energy, which forms the largest component of the transferring energy in all runs at all times, is focused toward the magnetopause at locations where field lines convect to the nightside. This also explains why the energy is mainly transferred sunward of  $X = -10 R_E$  [10]: Tailward of that distance the field lines are already more aligned with the magnetosheath bulk flow, making the Poynting vector component perpendicular to the magnetopause small.

In Fig. 2b the energy is still being transferred in the dawn (dusk) sectors in the northern (southern) high latitudes, perpendicular to the reconnection line. As the low latitude reconnection has now fully started, the high latitude convection and consequently the amount of energy over dawn (dusk) sectors in the northern (southern) hemisphere has been enhanced. In Fig. 2c, the clock angle has rotated to  $240^\circ$ . During the negative IMF  $y$  component, the open field lines convect through the dusk (dawn) sector on the northern (southern) hemisphere [4], which is also where the largest energy transfer is taking place, again due to Poynting flux focussing.

Curiously, in Fig. 2c, the dawn (dusk) high latitude sectors in the northern (southern) hemisphere show more enhanced energy transfer than dusk (dawn) sectors in Fig. 2b, although the driving conditions in the solar wind and IMF are identical during these two time instants (except for the sign reversal of IMF  $y$  component). Furthermore, the reconnection line is more aligned to low latitudes than in Fig. 2b. Both facts imply that (1) convection has not altogether ceased from dawn (dusk) sectors in the northern (southern) hemisphere, and that (2) there is stronger convection taking place in dusk (dawn) high latitudes in Fig. 2c than in Fig. 2b. Consequently, more energy is being transferred during  $\theta = 240^\circ$  than during  $\theta = 120^\circ$ , which shows also in Fig. 2e. As speculated in [12], this may be due to hysteretic behavior of magnetopause reconnection.

In Fig. 2d, the energy transfer is still larger than during  $\theta = 60^\circ$  (Fig. 2a), although the driving conditions during these two time instants are similar (except for the sign reversal of IMF  $y$  component). The larger energy input in Fig. 2d is due to more enhanced convection in the primary energy transfer sectors perpendicular to the reconnection line. The more enhanced convection in these sectors may be explained by the orientation of the reconnection line, which is located at slightly lower latitudes (about from  $320^\circ$  to  $140^\circ$ , whereas in Fig. 2a it is aligned from  $30^\circ$  to  $210^\circ$ ). Furthermore, the low latitude reconnection has not ceased and the reconnection is still taking place at the nose of the magnetopause (unlike in Fig. 2a). Hence, the comparison of Figs. 2a and 2d suggests that the reconnection line rotation follows the IMF rotation with a delay, explaining the larger energy input in Fig. 2d.

The time delay between the scaled  $\sin^2(\theta/2)$  and the total energy transfer is 30 minutes after the due southward IMF in Fig. 2e. For other runs specified in Table 1 the temporal evolution of the total energy transfer is similar as in Fig. 2e [12]. However, the time lag, computed by finding the best correlation for the energy transfer with the  $\sin^2(\theta/2)$  after due south IMF, is different in the other runs (Table 1): For larger IMF the time lag increases, while for larger pressures the time lag decreases. The IMF dependence of the time lags support the hypothesis that reconnection processes may be involved in the hysteretic behavior of energy transfer. The pressure dependence may be caused by the smaller size of the magnetopause when the pressure is large that reduces time scales associated with propagation through the system.

## 5. Summary and discussion

In this paper, we have presented evidence that in GUMICS-4 global MHD simulation the energy transfer through the magnetopause does not directly follow the solar wind driver. Based

**Table 1.** Synthetic run parameters.

Run #	IMF  [nT]	$p_{dyn}$ [nPa]	time lag [min]
1	5	2	30
2	10	2	40
3	5	8	20
4	10	8	30

on the simulation results, it appears that after the reconnection has fully begun, it remains active although the driver conditions in the solar wind subside. This is observed in the following aspects in the simulation results:

- (1) The reconnection line reaches over the subsolar position after due south IMF, although before the due south the line is discontinuous over the subsolar position (compare Figs. 2a and 2d);
- (2) The reconnection line follows the IMF rotation with a delay, and thus stays more aligned to low latitudes after due south IMF (compare Figs. 2a and 2d, 2b and 2c); and
- (3) The tailward convecting field lines remain open until the tail reconnection closes them, and during the convection the Poynting flux continues to focus toward the magnetopause (compare Figs. 2b and 2c).

These observations from the simulations suggest that the magnetopause reconnection is not only a function of the solar wind driver, but also depends on whether reconnection has previously been active.

In order to test these results, a series of other test runs were performed. The results (not shown) indicate that the hysteresis is a general property of the simulation, not dependent on the run or driver details: The dawn-dusk asymmetry effects of the corotation electric field and Hall conductivity in the ionosphere were tested by a run where the IMF rotation occurred in a counter-clockwise direction. The results were identical to those with clockwise rotation. Possible asymmetry effects related to rotation of the clock angle rather than changing IMF  $z$  component was tested by rotating the IMF back from due southward through positive  $B_y$  (clockwise rotation from  $0$  to  $180^\circ$  and counter-clockwise rotation from  $180$  to  $0^\circ$ ). Again, the hysteretic behavior was observed, but this time with a shorter time delay. The speed of the IMF rotation does not eradicate the hysteresis: runs with twice as fast and twice as slow rotation also show hysteretic behavior, but again with a different time delay. An interesting question is what happens if the IMF is rotated clockwise a second time: In this case, after IMF being northward, the energy input followed the IMF rotation as the clock angle increased, identically to what was found during the first rotation. After due southward IMF, the energy input again showed hysteretic behavior with a time delay similar to that in the first rotation. Thus, the northward IMF situation erases the magnetopause memory of past driving.

The  $\epsilon$  parameter is frequently used to parametrize energy transfer processes at the magnetopause. Our simulation results indicate that

- (1) The  $\epsilon$  parameter does not accurately account for the energy input after the IMF has been negative, i.e., after periods of strong driving. During such conditions, the reconnection line remains at low latitudes and energy input remains large;

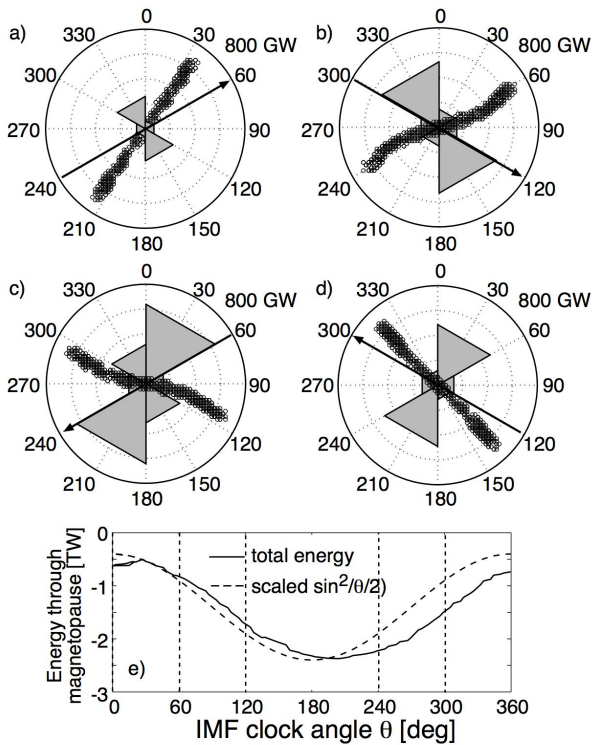


**Fig. 2.** in Run #: a-d) Instantaneous distributions of azimuthal magnetopause energy transfer at angles indicated by dashed vertical lines in panel (e). Grey areas indicate inward (towards magnetosphere) energy to sectors shown outside the outer circle. The sectors scale from 0 GW at the center to 800 GW at the outer circle. The IMF clock angle direction is indicated by a black arrow, while the black circles show the locations where reconnection is likely to occur [9]. e) Total transferred energy as function of clock angle (and time); the dashed line is  $\sin^2(\theta/2)$  scaled to maximum and minimum of the energy transfer curve.

(2) The energy transfer through the magnetopause is best represented by a function proportional to  $\sin^2(\theta/2)$ , indicating that the energy transfer is better correlated with the solar wind electric field scaling as  $\sin^2(\theta/2)$  than the  $\epsilon$  parameter or Poynting flux scaling as  $\sin^4(\theta/2)$ .

These results would imply that the energy input after the substorm onset (when IMF turns northward or becomes less negative) is not accurately accounted for by using either  $\epsilon$  or  $E_Y$  as a proxy for the energy input. The simulation results also hint for a stronger dependence of the energy transfer processes on the dynamic pressure than has been assumed before [12].

Recently, [8] criticize the dynamics in the global MHD simulations for being too directly driven by the solar wind and IMF driver. They assert that the "substorm in the magnetotail is hysteretic: Magnetic flux is added to the tail until the threshold of a still-undetermined instability in the tail is reached at which point unloading begins with the onset of a substorm". They suggest that the tail stability properties are asymmetric: An instability is triggered when a critical current density in the tail

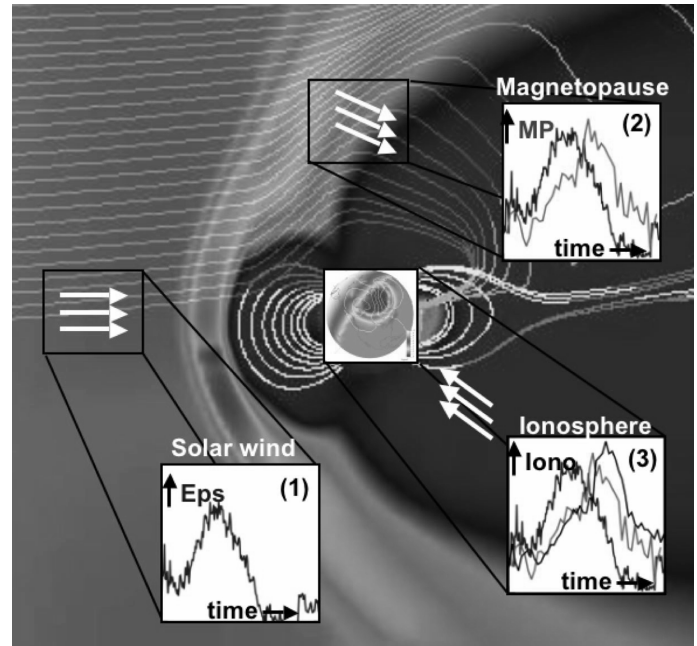


**Fig. 3.** Schematic of energy transfer process: (1) Epsilon in the solar wind; (2) Energy transferred through the magnetopause shows delay with respect to epsilon; (3) ionospheric energy dissipation shows delay with respect to epsilon, but only a small delay with respect to energy input through magnetopause.

is reached. Quenching of the instability occurs when the current density decreases to below another critical current density, smaller than what was required for the instability triggering. Using such formulation leads to a loading-unloading cycle in a driven current sheet even under continuous, steady driving. However, it is interesting to note that no such implementation of critical current density thresholds is needed at the global GUMICS-4 MHD simulation magnetopause to get the hysteretic behavior of the dayside reconnection line location and energy transfer efficiency.

The results presented here have possible implications in substorm dynamics and global energetics that follow. The substorm dynamic cycle can be described in the framework of a loading-unloading process: Growth-phase-associated enhanced energy input leads to a slow change of the magnetospheric state that at a later time allows for a global reconfiguration during the substorm expansion phase [3]. Because of this, and because of the time delays between the solar wind driver parameters such as  $\epsilon$  and dissipation proxies such as AE, the energetics has been interpreted to also show signatures of loading and unloading. However, several studies indicate that this may not be the case: As demonstrated by [15], the energy input *during* the expansion phase, not prior to it, controls the substorm size as determined by ionospheric dissipation. Furthermore, [5] and [14] show respectively that only about a third of substorms show prior tail flux loading, and that there is no critical threshold of lobe magnetic flux that would lead to the substorm onset; these results also would indicate that the energy input prior to the onset is necessary for the configuration change to occur, but not to powering the substorm [13]. Lastly, the GUMICS-4 results

shown here and in [13] indicate that the time delays between the system input and output are nonexistent if one compares the actual energy input through the magnetopause to the ionospheric dissipation, while they do arise if one uses  $\epsilon$  as a proxy for the energy input (see Fig. 3). Hence, if reconnection proves to be hysteretic in nature as the simulation suggests here and in [12], some of the time delays associated with the system input and output that have been interpreted as loading-unloading signatures, may already arise from processes taking place at the magnetopause.

## Acknowledgements

The simulation run for Aug 15, 2001, was carried out using Level 2 data from the ACE MAG and SWEPAM instruments. We thank the instrument PI's N. Ness and D. J. McComas for the inspection of the data as well as their liberal data distribution policy. The work of MP is supported by the Academy of Finland. The stay of T.P. at LANL is sponsored by the IGPP. The work of TVL is supported by the Magnus Ehrnrooth Foundation.

## References

1. Ahn, B.-H., S.-I. Akasofu, and Y. Kamide, The Joule heat production rate and the particle energy injection rate as a function of the geomagnetic indices AE and AL., *J. Geophys. Res.*, *88*, 6275, 1983.
2. Akasofu, S.-I., Energy coupling between the solar wind and the magnetosphere, *Space Sci. Rev.*, *28*, 121, 1981.
3. Baker, D. N., T. I. Pulkkinen, V. Angelopoulos, W. Baumjohann, and R. L. McPherron, The neutral line model of substorms: Past results and present view, *J. Geophys. Res.*, *101*, 12,975, 1996.
4. Cowley, S. W. H., Morelli, J. P., and Lockwood, M., Dependence of convective flows and particle precipitation in the high-latitude dayside ionosphere on the X and Y components of the interplanetary magnetic field, *J. Geophys. Res.*, *96*, 5557-5564, 1991.
5. Dmitreva, N. P., V. A. Sergeev, and M. A. Shukhtina, Average characteristics of the midtail plasma sheet in different dynamic regimes of the magnetosphere, *Ann. Geophys.*, *22*, 2107, SREF-ID: 1432-0576/ag/2004-22-2107, 2004.
6. Dungey, J. R., Interplanetary magnetic field and the auroral zones, *Phys. Rev. Lett.*, *6*, 47, 1961.
7. Janhunen, P., GUMICS-3: A global ionosphere-magnetosphere coupling simulation with high ionospheric resolution, in *Proceedings of Environmental Modelling for Space-based Applications*, ESA-SP 392, p. 205, 1996.
8. Klimas, A. J., V. M. Uritsky, D. Vassiliadis, and D. N. Baker, A mechanism for the loading-unloading substorm cycle missing in MHD global magnetospheric simulation models, *Geophys. Res. Lett.*, *32* (14), L14108, doi:10.1029/2005GL022916, 2005.
9. Laitinen, T. V., Janhunen, P., Pulkkinen, T. I., Palmroth, M., and Koskinen, H. E. J., On the characterization of magnetic reconnection in global MHD simulations, submitted to *Ann. Geophys.*, 2006.
10. Palmroth, M., T. I. Pulkkinen, P. Janhunen, C.-C. Wu, Stormtime energy transfer in global MHD simulation, *J. Geophys. Res.*, *108*(A1), 1048, doi: 101029/2002JA009446, 2003.
11. Palmroth, M., P. Janhunen, T. I. Pulkkinen, and H. E. J. Koskinen, Ionospheric energy input as a function of solar wind parameters: global MHD simulation results, *Ann. Geophys.*, *22*, 549, 2004.
12. Palmroth, M., P. Janhunen, and T. I. Pulkkinen, Hysteresis in the solar wind power input into the magnetosphere, *Geophys. Res. Lett.*, *33*, L03107, doi:10.1029/2005GL025188), 2006.
13. Pulkkinen, T. I., M. Palmroth, E. I. Tanskanen, P. Janhunen, H. E. J. Koskinen, and T. V. Laitinen, New interpretation of magnetospheric energy circulation, *Geophys. Res. Lett.*, *33*, L07101, doi:10.1029/2005GL025457, 2006.
14. Shukhtina, M. A., N. P. Dmitreva, N. G. Popova, V. A. Sergeev, A. G. Yahnin, and I. V. Despirak, Observational evidence of the loading-unloading substorm scheme, *Geophys. Res. Lett.*, *32*, L17107, doi:10.1029/2005GL023779, 2005.
15. Tanskanen, E. I., T. I. Pulkkinen, H. E. J. Koskinen, Substorm energy budget near solar minimum and maximum: 1997 and 1999 compared, *J. Geophys. Res.*, *107*, A6, 10.1029/2001JA900153, 2002.



# Observing the MLT and L-shell dependence of ground magnetic signatures of the ionospheric Alfvén resonator

A. Parent, I. R. Mann, and K. Shiokawa

**Abstract:** The ionospheric Alfvén resonator (IAR) is a natural resonant cavity in the upper ionosphere that can effectively trap shear Alfvén waves within its boundaries, causing them to form a vertical standing wave pattern. The effects of the IAR are observable as discrete spectral features in ground magnetometer data in the 0.1 to 10 Hz range. To date, many studies of ground magnetic signatures of the IAR have focused on observations over time at a single site. In an attempt to understand the global extent of the resonator, we present results of a preliminary study in which we characterize IAR features across a network of stations, mostly within the Canadian sector. We quantify the evolution of IAR eigenfrequencies at each site by analyzing the variation of harmonic frequency values and discrete harmonic frequency spacing over time, and we present the dependence of these properties on magnetic local time (MLT) and L-shell. From our results it can be seen that IAR signatures observed at sites across a wide range of longitudes have characteristics which are ordered by magnetic local time. The IAR eigenfrequencies typically become apparent between 16 and 18 MLT, in the late afternoon/early evening hours, and then increase in frequency, with discrete harmonics becoming spaced further apart, with increasing MLT. Towards midnight, the rate of frequency increase with MLT/UT is observed to slow, with harmonic frequencies reaching a plateau before in some cases decreasing between midnight and 05 MLT. A potential L-shell effect can also be observed by lining up IAR signature onset times and comparing the average frequency spacing between discrete IAR harmonics. The lowest L-value station exhibits the smallest average harmonic frequency spacing and the lowest and most linear rate of increase in harmonic frequency spacing with time. Plans for future work involve further observational studies of IAR magnetic signatures, which will be important in improving our understanding of the physics of the ionospheric Alfvén resonator and its effect upon magnetosphere-ionosphere interactions.

*Key words:* ionosphere, magnetosphere-ionosphere coupling, ULF waves.

## 1. Introduction

The ionospheric Alfvén resonator (IAR) is a resonant cavity that is believed to form in the upper ionosphere between two regions of large Alfvén velocity gradients [e.g., 1, 3, 6]. It is thought to be stimulated by the generation of shear Alfvén waves in the E-layer, which may be triggered by electromagnetic emissions due to thunderstorm activity [1, 8], or possibly by fluctuations in the E-region neutral wind [7]. The Alfvén waves, traveling along geomagnetic field lines, can undergo partial reflection at velocity gradients, leading to a vertical standing wave pattern in the upper ionosphere within the resonant cavity (see e.g., papers in a special IAR-related issue of the *Journal of Atmospheric and Solar-Terrestrial Physics*, Vol.62, No.4, March 2000).

The excitation of the IAR can be observed as distinct spectral features in ground magnetometer data in the 0.1 to 10 Hz range. This frequency range includes Pc1-2 geomagnetic pulsations (0.1 to 5 Hz) within the ULF band [5], and extends into lower frequencies of the ELF band. We characterize IAR features occurring over one day, September 25, 2005, across a

collection of magnetometer stations predominantly in the Canadian sector. We quantify the evolution of IAR eigenfrequencies by determining discrete harmonic frequency values and the average frequency spacing between adjacent harmonics as a function of time at each site. This preliminary study allows us to investigate procedures that can be used to quantify IAR resonance features in ground magnetic data. These are the first steps towards performing more in-depth observational studies of the resonator. Ultimately, by characterizing the variation of IAR features with L-shell and magnetic local time, we hope to better understand how the observed IAR features might be used to monitor in real-time the local structure of the topside ionosphere above a point of observation (i.e., a ground magnetometer site).

## 2. Data Analysis

### 2.1. Search Coil Magnetometer Network

The network of search coil magnetometer instruments used in the September 25, 2005, study is shown in Figure 1. Four of the stations used are located in Canada, while a fifth (UZR) is located near Lake Baikal in Russia. Station details, including coordinate locations, L-values and instrument information, are summarized in Table 1. The 10 Hz instruments at PKS, HRP, LCL and UZR are remnants of the Solar-Terrestrial Energy Program (STEP) Polar Network that operated between 1991 and 1997. For more information, refer to the website:

Received 28 May 2005.

**A. Parent and I. R. Mann.** Department of Physics, University of Alberta, Edmonton, AB, T6G2J1, Canada. (aparent@phys.ualberta.ca)

**K. Shiokawa.** Solar-Terrestrial Environment Laboratory, Nagoya University, Toyokawa 442-8507, Japan.

<http://www-space.eps.s.u-tokyo.ac.jp/hayashi/>. The 64 Hz instrument at ATH is operated by the Solar-Terrestrial Environment Laboratory (STELAB) and is housed by Athabasca University Geophysical Observatory. ATH station information can be found on the website:  
<http://stdb2.stelab.nagoya-u.ac.jp/index/canada.html>.

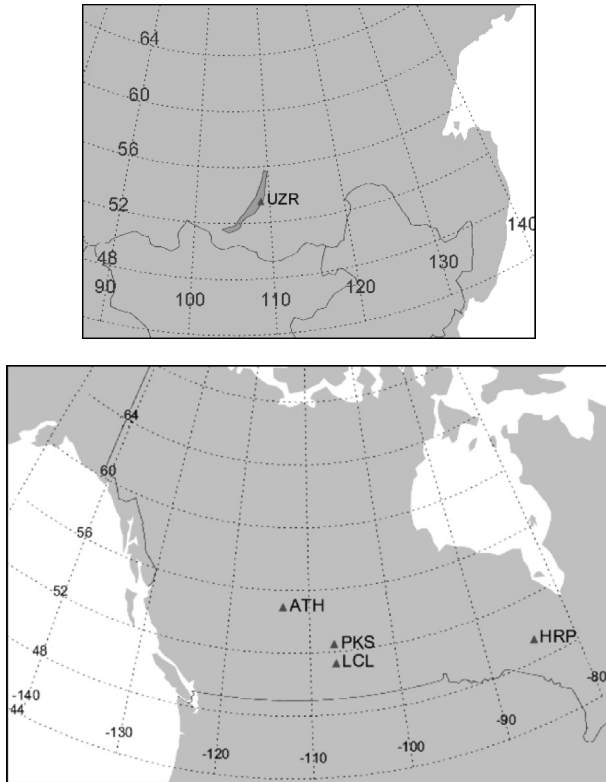


**Fig. 1.** Search coil magnetometer locations in Russia (top) and Canada (bottom). The grid shows lines of geographic latitude and longitude.

Station	CGM		L-value	Magnetometer Info. Cadence, Available Axes
	Lat	Long		
ATH, Athabasca	62.0	306.6	4.61	64 Hz, H and D
PKS, Parksite	60.7	315.3	4.23	10 Hz, D only
HRP, Hornepayne	59.7	348.1	4.00	10 Hz, D only
LCL, Lucky Lake	59.5	315.7	3.94	10 Hz, H and D
UZR, Uzur, Russia	48.37	181.94	2.30	10 Hz, H and D

**Table 1.** Summary of search coil magnetometer station locations and relevant instrument details.

## 2.2. Dynamic Spectra Visualizations of the IAR

Signatures of the IAR, observed in the dynamic power of the D-component (magnetic east-west direction) at each site on September 25, 2005, are shown in Figures 2 and 3 as a function of Universal Time (UT) and magnetic local time (MLT), respectively. The plots from each station listed in Table 1 are shown from top to bottom with decreasing L-value. Data from

the 10 Hz induction magnetometer stations (PKS, HRP, LCL, UZR) was processed using a sliding FFT Hanning window, with a length of 2000 points and a 250 point time step. The 64 Hz induction data from ATH station was processed with a Hanning window length of 12800 points and a 1600 point time step. For all stations, a uniform frequency resolution of 5 mHz and time resolution of 25 seconds were hence obtained.

The IAR signatures are easily identified as the upward sloping, stripe-like structures in the dynamic power spectrograms of Figures 2 and 3. The signatures shown are quite typical of magnetic observations of the resonator [e.g., 2, 3, 9]. Multiple resonance bands (discrete harmonics) generally become visible in the early evening (local time) and increase in frequency, with harmonics becoming spaced further apart, towards local midnight. In some observations of the IAR, harmonics can be seen to decrease in frequency and become spaced closer together as local time progresses from midnight into early morning [9]. Some evidence of this tendency can be seen in the signatures of ATH, PKS and LCL stations, between 00 and 05 MLT in Figure 3.

In Figure 2, in which dynamic power has been plotted as a function of UT, IAR signatures in the ATH, PKS and LCL plots are the most distinctive. Exact onset times are difficult to determine since the discrete banded structure emerges only gradually from the background noise. However, the signatures at these three sites appear to become visible at roughly the same time, around 01 UT, on September 25. This is not surprising, as these stations are located within a small range of longitude (about 10 degrees), and would be rotating into local evening hours at roughly the same UT. It is also interesting to note that in the case of these stations, the power in the discrete frequency signatures of the IAR as compared to background noise (the modulation depth), is observed to increase significantly around 02 UT. IAR features at HRP station are quite diffuse in comparison, with eigenfrequencies difficult to distinguish from the noise, representing a low modulation depth. We would expect IAR signatures at HRP to become visible at an earlier UT, since the station is located about 30 degrees east of the ATH, PKS and LCL stations. However, this is not the case, and the IAR signatures at HRP actually seem to appear at a later UT than they do for the other three stations. Finally, in Figure 2, the UZR station signatures are seen to occur at a much later UT than at any of the other stations. This makes sense since the longitudinal location of the site is very different from the Canadian sector stations. In the course of Universal Time, the Canadian stations rotate into evening first, and the IAR signatures seen during the nighttime at these sites are, in this study, being compared to the IAR signatures seen at the Russian site as UZR rotates hours later into the evening sector. The UZR signatures appear for a much smaller time interval than those seen at the other stations in the Canadian sector.

In Figure 3 essentially the same signatures are displayed, however, their evolution has been plotted as a function of magnetic local time. Most importantly, the signatures for all stations shift in time (from Figure 2 to Figure 3) and become distinct in the late afternoon/early evening hours of MLT, between 16 and 18 MLT. The biggest movement of IAR signatures occurs for UZR station, which shifts from an onset at about 11 UT in Figure 2 to 18 MLT in Figure 3. It is evident then, that for this day at least, as the stations rotate into the evening sec-

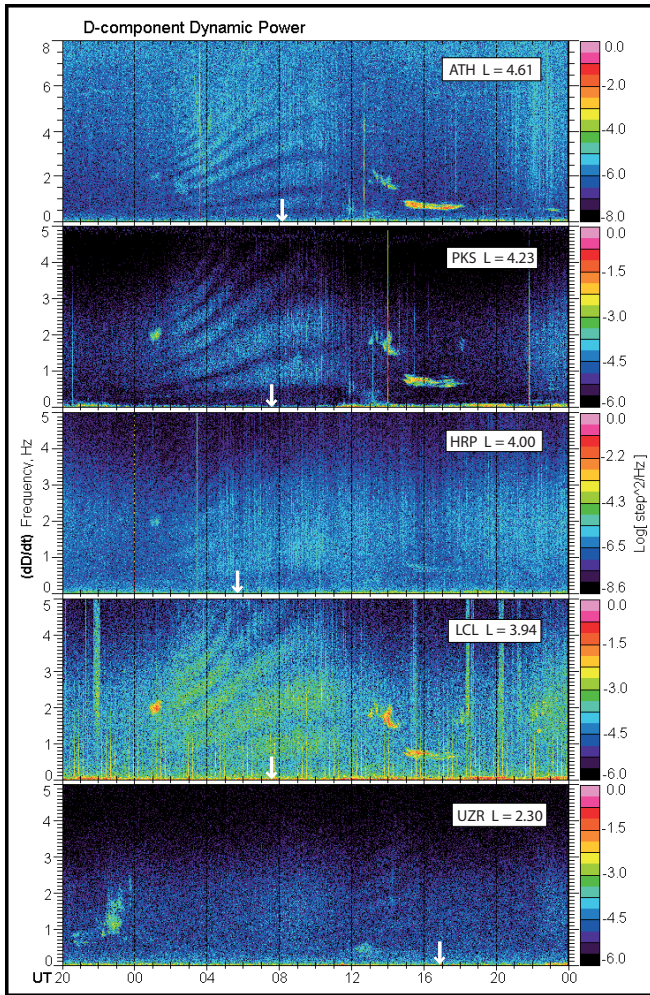


**Fig. 2.** Dynamic power spectrograms of  $dD/dt$  as measured by the magnetometer stations listed in Table 1, in order of decreasing L-shell, as a function of UT. Frequency in Hz is displayed along the ordinate axes, while the abscissa indicates hours of Universal Time, starting at 20 UT on September 24 and running until 00 UT on September 26, 2005. The color-scale represents logarithmic power in arbitrary units. White arrows indicate UT points of local midnight (00MLT). For data processing details, see the text.

tor, the IAR signatures appear in ground magnetic data. This represents a significant MLT effect, indicating that IAR characteristics can be organized by MLT over an extended range of longitudes.

In examining the plots of Figure 3, there appears to be evidence for an L-shell effect as well. The higher L-shell stations (ATH, PKS, HRP and LCL) are perhaps too close in L to exhibit an observable difference when the dynamic power plots are compared by eye. However, the signatures at UZR station, occurring at a significantly lower L-value, appear to exhibit visible differences. The harmonic frequency bands are narrower in frequency and more closely spaced together. Furthermore, the signatures exhibit a less steep slope and evolve in a more linear fashion as time progresses. A more quantitative analysis is presented below and will serve to better measure the differences and similarities of the IAR features at these sites.

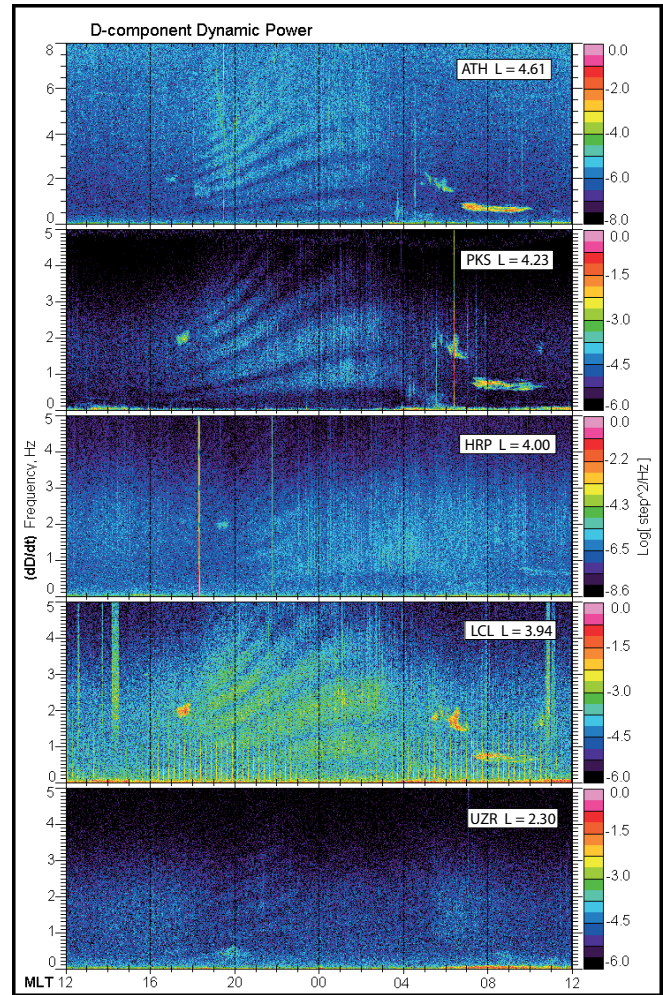


**Fig. 3.** IAR resonance features in the dynamic power spectrograms of  $dD/dt$  as a function of MLT. Frequency in Hz is shown along the ordinate axes. In the top four panels, the 24 hours of MLT (displayed along the abscissa) were formed using data from the UT days: September 24 and 25, 2005. The bottom panel was formed from the UT days: September 25 and 26, 2005. Magnetic data was processed in the same way as in Figure 2; see text for details.

### 2.3. Quantifying IAR Signatures

A technique based upon the ‘interactive on-screen cursor click’ technique of [4] was used to quantify IAR signatures in this study. IAR harmonics were identified by clicking on the magnified dynamic spectra. An illustration of the technique applied to ATH station data is shown in Figure 4. The identified frequency values for each harmonic were then plotted as a function of time, as in Figure 5. This method exploits the fact that the human eye is an excellent natural filter. It yielded harmonics which were very consistent with dynamic spectra visualizations.

## 3. Results: IAR Eigenfrequency Evolution

The variation of discrete harmonic frequency values with magnetic local time is shown in Figure 6. In each panel, frequency values for a specific harmonic number,  $N$ , are plot-

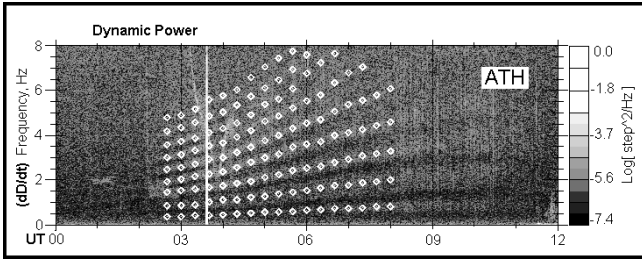


**Fig. 4.** Harmonic frequency values were determined by clicking on the displayed dynamic power plot. White diamonds indicate where eigenfrequency values were identified with a cursor click. This example shows dD/dt dynamic power spectra for ATH station on 25 September, 2005.

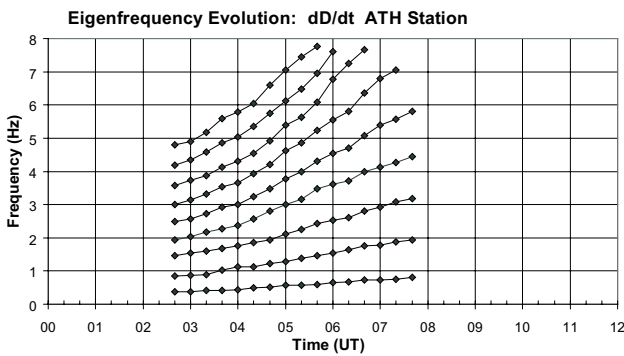


**Fig. 5.** The evolution of resonance features is thus quantified by plotting eigenfrequency values as a function of time. The plot shows results for ATH station on 25 September, 2005. The time resolution is 20 minutes.

ted for all stations that exhibited the harmonic. The plots are ordered by increasing harmonic number from bottom to top. The precise pinpointing of IAR signature onset times is a delicate task involving the local signal to noise response of the instrument, and the comparison of relative power at discrete IAR eigenfrequencies as compared to power at adjacent frequencies. In this preliminary study, it is important to note that the onset times as shown in Figure 6 are only roughly estimated by eye. In future studies, a more systematic determination of IAR signature onsets may allow onset times to be compared with, for example, ionospheric sunrise/sunset times (at different ionospheric layer heights) to determine if a relationship can be observed.

Consider first the fundamental frequency values plotted in the bottom panel of Figure 6. For all stations, the approximate onset times occur between 16 and 18 MLT, confirming the MLT effect observed and discussed in Section 2.2. In addition, the turning points, where the upward-sloping discrete harmonics are seen to flatten out and begin to slope downward, occur for all sites between 00 and 03 MLT. The observations at these sites on this particular day suggest that IAR signatures can be organized according to magnetic local time regardless of longitudinal location, as their onset times tend to become aligned in the late afternoon/early evening MLT hours, and their turning points tend to become aligned around midnight/early morning MLT.

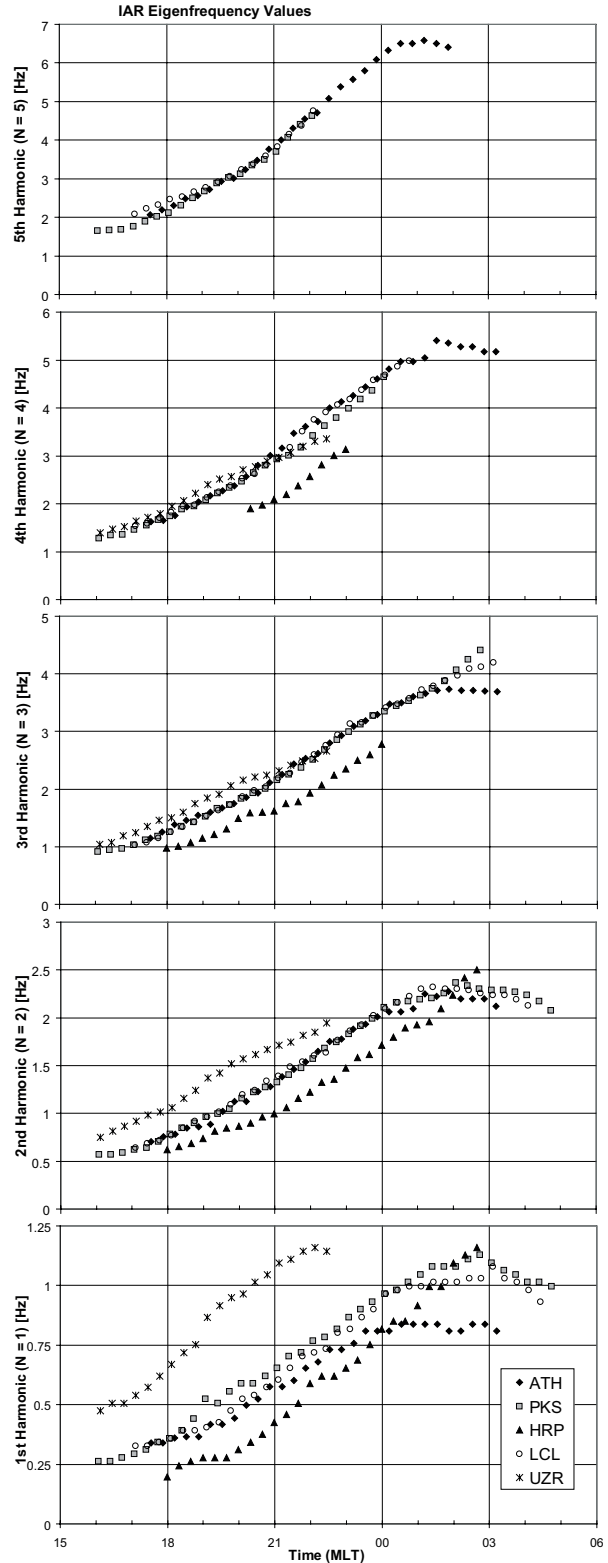


**Fig. 6.** Variation of harmonic frequency values with magnetic local time, as determined from analysis of dD/dt dynamic power spectra. In each panel, frequency values of a specific harmonic number, N, are plotted for each station. Stations and corresponding symbols are indicated in the legend.

In Figure 6, the lowest harmonic ( $N = 1$ ) eigenfrequencies at PKS and LCL behave very similarly, as might be expected since these sites are located close to each other and their local ionospheres may share comparable characteristics. The fundamental harmonic at ATH starts off like that of PKS and LCL, however the positive gradient signature flattens out at a lower frequency value. The stations at HRP and UZR exhibit more unique IAR behavior with respect to the fundamental frequency. The fundamental mode harmonic at HRP shows the lowest frequency values of all the stations, while at UZR, the first harmonic consists of the highest frequency values. It should be noted that the identification of this harmonic as the fundamental one, in the case of UZR station, was very difficult, owing to the large amount of magnetic activity in the Pc1 range occurring around 18 – 21 MLT.

Regarding the higher order harmonics displayed in Figure 6, the discrete IAR eigenfrequencies at each site behave, in relation to one another, very much as they did in the fundamental frequency case. For  $N > 1$ , IAR signatures at ATH follow more closely the behavior of signatures at PKS and LCL. As  $N$  increases, HRP continues to exhibit the lowest harmonic frequency values. At  $N = 3$  and 4, the eigenfrequencies at UZR decrease, approaching those of ATH, PKS and LCL stations, however it can also be seen that the UZR signatures display a slightly less steep slope as frequency values increase with MLT. Finally, in the  $N = 5$  plot, it becomes too difficult to quantify higher harmonic frequency values for UZR and HRP stations. The fifth harmonics at PKS, ATH and LCL behave in a similar manner.

In addition to considering absolute frequency values of IAR harmonics at each site, it is also of interest to calculate the average frequency spacing between adjacent harmonics as a function of time. This quantity, sometimes referred to as frequency scale, effectively describes how spread apart, on average, the discrete eigenfrequencies are, and its time dependence indicates how the spreading evolves (e.g., linearly or non-linearly) and at what rate. In Figure 7, the evolution of harmonic frequency spacing is presented as a function of MLT. The general IAR trend involving an increase in frequency scale over time towards midnight, and then a decrease into the early morning hours is observed here. The frequency spacing of the ATH, PKS and LCL signatures initially evolve in a similar manner, from 17 - 22 MLT. After this time, the frequency scales deviate. The harmonic spacing at ATH increases quickly between 22 and 23 MLT, and then its positive gradient lessens gradually until, from 02 - 03 MLT, a decrease in spacing occurs. Beyond 22 MLT, the frequency spacing at PKS and LCL increase fairly linearly until abrupt drop-offs at about 03 MLT. The discontinuous drop-offs in frequency scale are artifacts of the disappearance of quantifiable upper harmonics that are significantly spread out in frequency. The subsequent decrease in frequency scale at PKS and LCL indicates that the eigenfrequencies become more closely spaced together as they decrease in frequency into the early morning hours of MLT.

The average frequency spacing between IAR harmonics is at all times the lowest at HRP and UZR. In comparing these two stations at each MLT in Figure 7, it is clear that on average the discrete IAR harmonics are closer together at HRP than they are at UZR. Consider now another plot of the average harmonic frequency spacing at each station, shown in Figure 8. In

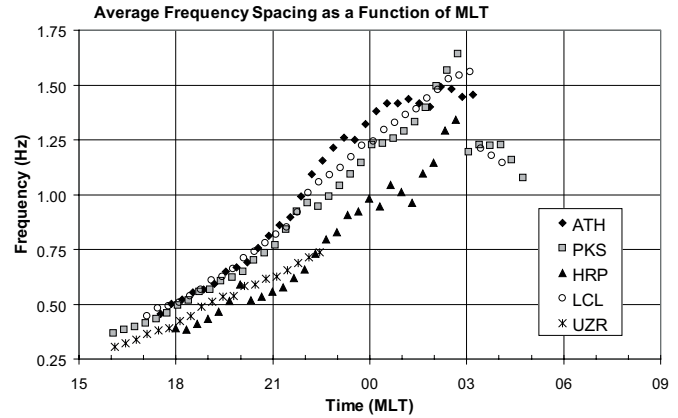


**Fig. 7.** Average frequency spacing between adjacent IAR harmonics at each station, as a function of MLT. The legend indicates stations and corresponding symbols.

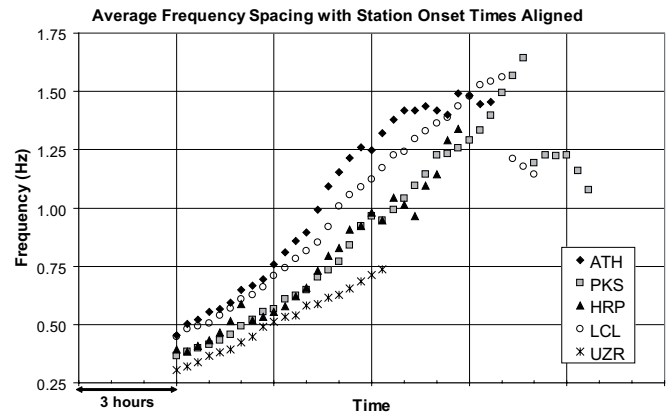


**Fig. 8.** Average frequency spacing between adjacent IAR harmonics with signature onset times at all stations lined up. The data series shown in Figure 7 have essentially been shifted in time so their first data points coincide. The abscissa indicates time intervals during the evolution of eigenfrequencies and does not indicate specific MLT or UT instances. See text for more details.

this figure, the onset times of the IAR signatures at each site have been lined up to coincide with each other. This allows the evolution of frequency scales to be compared from a common starting point (onset time), regardless of when, in MLT, the signatures at each site actually occurred. Hence, the frequency scales plotted in Figure 7 have been shifted in time in Figure 8, so that their first data points occur simultaneously at an arbitrary time. Note that as a result the abscissa in Figure 8 indicates general time intervals only, essentially measuring the evolution of IAR signatures from the moment they become apparent in magnetic data (exhibit onset). The time axis does not indicate specific MLT or UT instances. In Figure 8, it can be seen that UZR station exhibits the lowest average frequency spacing as harmonics evolve. Compared to the other stations in Figure 8, UZR also demonstrates the lowest increase in frequency scale from onset time until its IAR signatures disappear, as well as the most linear increase in frequency scale during this time

period. UZR is the lowest L-shell station, with an L-value of 2.30, and it may be possible that Figure 8 is revealing the L-shell effect that was more qualitatively observed in Section 2.2. The harmonic frequency spacing at ATH, which is the highest L-shell station with  $L = 4.61$ , exhibits the highest frequency values, the sharpest increase over time and the most non-linear trend. The frequency scales of the intermediate L-value stations, PKS, HRP and LCL, do not show a clear ordering of behavior according to L-value in Figure 8. But the differences on average between the higher L stations, in particular, ATH, and the lowest L station, UZR, are marked. This L-shell effect has been reported in previous studies of the IAR, in which high and low L observations have been compared [e.g., 3]. It has typically been found that at lower L-shell stations, as compared to higher L stations, the average frequency spacing between adjacent harmonics is lower and does not exhibit as much of a dependence on local time from the early evening into the night hours.

#### 4. Summary

A preliminary investigation of ground magnetic signatures of the ionospheric Alfvén resonator has been conducted on September 25, 2005, across a network of five search coil magnetometer sites. This preliminary study has allowed us to explore and evaluate methods that can be used to quantify IAR resonance features in ground magnetic data. We have determined that a visual on-screen determination of eigenfrequencies is a reasonable and promising quantification technique. General observations of IAR features are consistent with the results of previous studies. In particular, we have found that when IAR signatures, observed at sites spread across a range of longitudes, are organized by MLT, their onsets tend to become aligned, occurring within a few hours of each other in MLT. The IAR eigenfrequencies emerge from the background noise between 16 and 18 MLT, in the late afternoon/early evening hours, and initially increase in frequency, with harmonics becoming spaced further apart, over time. At some sites, the harmonic frequencies are observed to plateau and then subsequently decrease in frequency between midnight and 05 MLT. There is also evidence for an L-shell effect when the average frequency spacing between discrete IAR harmonics is displayed, this being especially clear when IAR signature onset times at different stations are made to coincide. The lowest L-value station exhibits the smallest average frequency spacing and the lowest and most linear rate of increase in harmonic frequency spacing over time.

Future work involving the IAR will consist of the analysis of magnetic signatures over a longer time interval and a larger network of stations. This will allow us to quantify the occurrence rates of IAR excitation and better analyze the dependence of the properties of IAR features on MLT, L-shell, sunrise/sunset times and geomagnetic activity level. We are also interested in examining the relationship between structured Pc1-2 pulsations and resonant IAR eigenfrequencies. Overall, this research effort has provided a solid foundation for future studies to build upon. Expanded studies will ultimately enable us to explore the global character of the spectral features of the ionospheric Alfvén resonator, and the extent to which

observed IAR characteristics can be used as a real-time monitor of the structure of the topside ionosphere.

**Acknowledgments:** PKS, LCL, HRP and UZR station magnetometer data were provided by Kanji Hayashi. The ATH search coil magnetometer is housed at the Athabasca University Geophysical Observatory. This work was supported by a Canadian NSERC Discovery Grant to I.R.M.

#### References

1. Belyaev, P. P., Polyakov, S. V., Rapoport, V. O. and Trakhtengerts, V. Yu., The ionospheric Alfvén resonator, *Journal of Atmospheric and Terrestrial Physics*, 52, 781, 1990.
2. Belyaev, P. P., Bosinger, T., Isaev, S. V. and Kangas, J., First evidence at high latitudes for the ionospheric Alfvén resonator, *Journal of Geophysical Research*, 104, 4305, 1999.
3. Bosinger, T., Haldoupis, C., Belyaev, P. P., Yakunin, M. N., Semenova, N. V., Demekhov, A. G. and Angelopoulos, V., Spectral properties of the ionospheric Alfvén resonator observed at a low-latitude station ( $L=1.3$ ), *Journal of Geophysical Research*, 107, 1281, 2002.
4. Hebden S. R., Robinson T. R., Wright D. M., Yeoman T., Raita T. and Bosinger T., A quantitative analysis of the diurnal evolution of ionospheric Alfvén resonator magnetic resonance features and calculation of changing IAR parameters, *Annales Geophysicae*, 23, 1711, 2005.
5. Jacobs, J. A., Kato, Y., Matsushita, S. And Troitskaya, V. A., Classification of geomagnetic micropulsations, *Journal of Geophysical Research*, 69, 180, 1964.
6. Lysak, R. L., Generalized model of the ionospheric Alfvén resonator, in: Auroral Plasma Dynamics, Geophysical Monograph 80, American Geophysical Union, 121, 1993.
7. Surkov, V. V., Pokhotelov, O. A., Parrot, M., Fedorov, E. N. and Hayakawa, M., Excitation of the ionospheric resonance cavity by neutral winds at middle latitudes, *Annales Geophysicae*, 22, 2877, 2004.
8. Surkov, V. V., Molchanov, O. A., Hayakawa, M. and Fedorov, E. N. Excitation of the ionospheric resonance cavity by thunderstorms, *Journal of Geophysical Research*, 110, A04308, 2005.
9. Yahnin, A. G., Semenova, N. V., Ostapenko, A. A., Kangas, J., Manninen, J. and Turnunen, T. Morphology of the spectral resonance structure of the electromagnetic background noise in the range of 0.1-4 Hz at  $L = 5.2$ , *Annales Geophysicae*, 21, 779, 2003.

# Strong stretching in dusk sector: stormtime activations and sawtooth events compared

N. Partamies, T. I. Pulkkinen, E. F. Donovan, H. J. Singer, E. I. Tanskanen, R. L. McPherron, M. G. Henderson, and G. D. Reeves

**Abstract:** Using superposed epoch analysis methods, we analyze two sets of events: one of stormtime activations having some characteristics of sawtooth events, and another set of events defined as sawtooth events. We compare and contrast these data sets and show that the sawtooth events are associated with slightly lower than average solar wind driving but the differences are small. While the both sets of events are associated with a positive excursion of the SYM-H index, the stormtime activations show a clearer signal in the ASY-H index highlighting the role of the partial ring current in such events. In the inner magnetotail, both sets of events show qualitatively similar injection and field dipolarization characteristics. We conclude that the repetition period of the sawtooth events is an internal property of the magnetosphere not related to the particular driving conditions that prevail during the sawtooth events.

*Key words:* stormtime substorms, sawtooth events.

## 1. Introduction

Sawtooth events are large-amplitude quasi-periodic oscillations of energetic particle fluxes and the magnetic field at geosynchronous orbit recurring with a period of about 2–4 hours [2, 4]. It is often reported that the particle injection is virtually simultaneous across several local time sectors (up to 12 hours). The events frequently occur embedded in magnetic storms when the solar wind driving is relatively strong and the interplanetary magnetic field (IMF) is continuously southward for a longer period of time. A distinct characteristic of these events is that the geosynchronous magnetic field can become highly stretched not only in the midnight sector but also in the evening sector reaching all the way to the dusk meridian and very close to the Earth [10]. An active debate is presently going on as to whether or not sawtooth events are recurring substorms [12] or a distinct class of activity.

Magnetospheric activity during storms is highly complex with strong fluctuations seen in a wide range of local time sectors. While some features (such as electrojet enhancements, geostationary orbit injections or tail field dipolarizations) sometimes resemble those found during non-storm substorms, at other times they do not: Not all stormtime activations identified from ground magnetometer data correspond to tail signatures typically associated with substorm; there are several types of stormtime activations of which only some resemble non-storm substorms [9].

In this paper, we analyze stormtime activations during the

year 2004. To address the question about whether sawtooth events form a special class of events, we also analyze a set of sawtooth events. We compare and contrast superposed epoch analysis results of both sets of events using measurements in the solar wind, in the geostationary orbit magnetosphere, and in the auroral and mid-latitude ionosphere.

## 2. Data set

A statistical analysis was performed for all storms with Dst less than  $-75$  nT during the year 2004. For each storm, ground magnetic recordings from the IMAGE network in the Scandinavian sector [18] and the CARISMA network in the Canadian sector [13] were visually examined to identify rapid electrojet enhancements exceeding about 200 nT. The activation onset was defined to be an electrojet enhancement on the ground. This analysis produced a list of 150 activations. For each of these events, the geosynchronous energetic electron fluxes and the geosynchronous magnetic field from the LANL and GOES satellites, the symmetric and asymmetric ring current indices (SYM-H, ASY-H) and the auroral electrojet (AL) index, as well as the solar wind parameters and the interplanetary magnetic field (IMF) from the ACE satellite [7, 15] were examined. In combining the results in the form of a superposed epoch analysis, an epoch time of three hours before and after the onset was used.

The geosynchronous magnetic field inclination is defined as the angle between the Earth's magnetic field vector and the equatorial plane in solar magnetic (SM) coordinates to best account for the differences in the dipole tilt angles for the different activations. In the SM coordinates, the Z axis is aligned with the dipole axis, X axis is in the plane defined by the dipole axis and the Sun–Earth line, and the Y axis completes the right-handed triad. The magnetometers onboard the GOES satellites provide a direct measurement of the magnetic field [14]; in addition, the electron anisotropy properties measured by the LANL magnetospheric plasma analyzers (MPA) were used to infer the field direction [17]. If the half-hour mean value of the inclination before and after the onset changed by more than

Received 14 May 2005.

**N. Partamies and E. F. Donovan.** Institute for Space Research, University of Calgary, Calgary, Alberta, Canada

**T. I. Pulkkinen, M. G. Henderson, and G. D. Reeves.** Los Alamos National Laboratory, Los Alamos, NM, USA

**H. J. Singer.** NOAA Space Environment Center, Boulder, CO, USA

**E. I. Tanskanen.** Finnish Meteorological Institute, Space Research, Helsinki, Finland

**R. L. McPherron.** Institute of Geophysics and Planetary Physics, UCLA, Los Angeles, CA, USA

four degrees, the event was categorized as having a magnetic field dipolarization associated with the electrojet enhancement. Similarly, if the half-hour average of the geosynchronous electron fluxes increased by a factor of two from before to after the onset, the event was categorized as having an injection. Note that this definition does not necessarily guarantee that the flux levels increase above the levels observed prior to the substorm growth phase.

Because of the rapidly recurring onsets, the time delays allowed for these to occur were limited to  $\pm 30$  minutes. Thus, a few events may have been misidentified as not having an injection or dipolarization due to the errors caused by the delays associated with particle drift times and/or substorm current wedge expansion times in the tail. For the same reason, the energetic particle injection study was limited to the rapidly drifting electrons. However, it is interesting to note that the injections and dipolarizations did not necessarily occur in the same local time sector. About a third of the stormtime activations did not show an injection or a dipolarisation at geosynchronous orbit simultaneously with the ground onset.

Our objective is to assess whether sawtooth events are in some identifiable way different from stormtime activations. Thus, we selected a subset of the stormtime activations that have characteristics most like the individual sawtooth onsets. Perhaps the most prominent characterizing property of the sawtooth events is strong field stretching at geosynchronous orbit extending to local times far duskward of the midnight sector. On this basis, we restricted our attention to the subset that consists of those stormtime activations (24 events) that showed extreme stretching in the dusk side magnetosphere. Our criterion was that the minimum inclination in the evening sector was less than  $30^\circ$ . We remind the reader that this subset is not comprised of sawtooth events, but rather events that resemble the individual activations during sawtooth events.

A similar superposed epoch analysis was performed for the same solar wind, geosynchronous, and ionospheric parameters for a set of 138 sawtooth events selected from the period 1999–2002.

### 3. Statistical results

#### 3.1. Solar wind parameters

A selection of the solar wind parameters for both data sets is shown in Fig. 1, where the superposed epoch analysis results of the stormtime activations (solid lines) are compared with the superposed epoch analysis results of the sawtooth events (dotted lines). The data measured by instruments onboard the ACE satellite located in the L1 point upstream of the Earth have been propagated to the magnetopause (to the distance of  $10 R_E$  upstream of the Earth) using the upstream distance of the satellite from the magnetopause and the average solar wind speed during that period.

The Z-component of the IMF (top panel) is more negative (by about 5 nT) during the stormtime activations. There is a clear minimum in  $B_Z$  around the onset time for the stormtime activations. For the sawtooth events a less pronounced minimum occurs about half an hour prior to the onset time, which indicates that these sawtooth events are not, for the most part, triggered by IMF northward turnings.

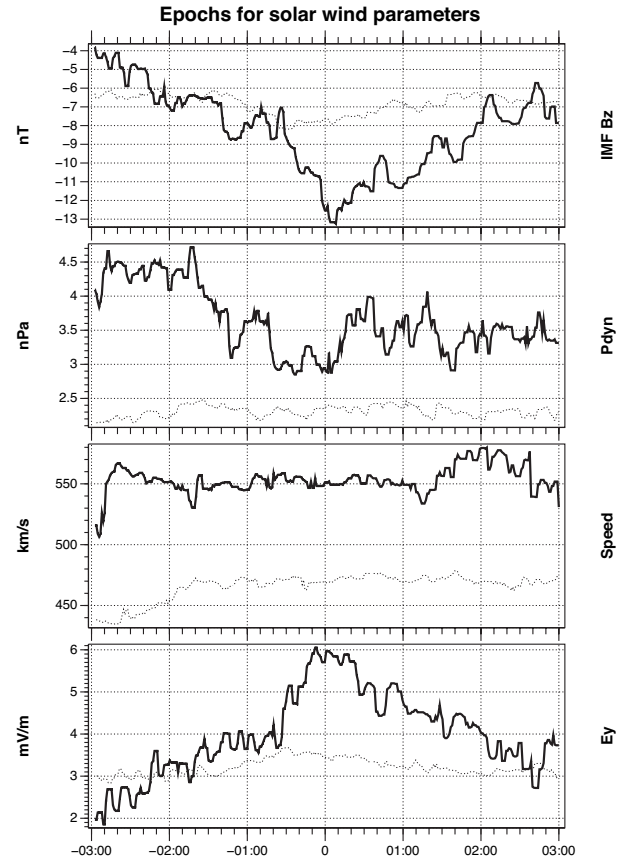


**Fig. 1.** Superposed epoch analysis of the IMF  $B_Z$  (top), the solar wind dynamic pressure (second panel), velocity (third panel) and the Y component of the solar wind electric field (bottom). The stormtime activations are shown with solid lines and the sawtooth events are shown with dotted lines. All parameters are median filtered.

The solar wind dynamic pressure (second panel) changes are very small for both event sets varying between 2.0 and 4.5 nPa throughout the whole epoch. The solar wind velocities (third panel) are relatively steady, but the average speed for the stormtime activations is almost 100 km/s higher than for the sawtooth events.

The solar wind electric field (bottom panel) is stronger and more variable for the stormtime activations than for the sawtooth events. The typical behaviour of the electric field shows a maximum at the onset time for the stormtime activations, while the sawtooth related electric field is more steady showing a broad, slight, maximum during the hour before the event onset.

#### 3.2. Ionospheric activity

To study the ionospheric activity during the stormtime activations and the sawtooth events we analysed the asymmetric and symmetric ring current indices, ASY-H and SYM-H, as well as the local auroral electrojet (AL) index calculated from the CARISMA and IMAGE magnetometer networks. We call this the pseudo-AL index. These indices are plotted in Fig. 2.

ASY-H (top panel) shows only small fluctuations for the sawtooth events, but it is enhanced by about 20 nT around

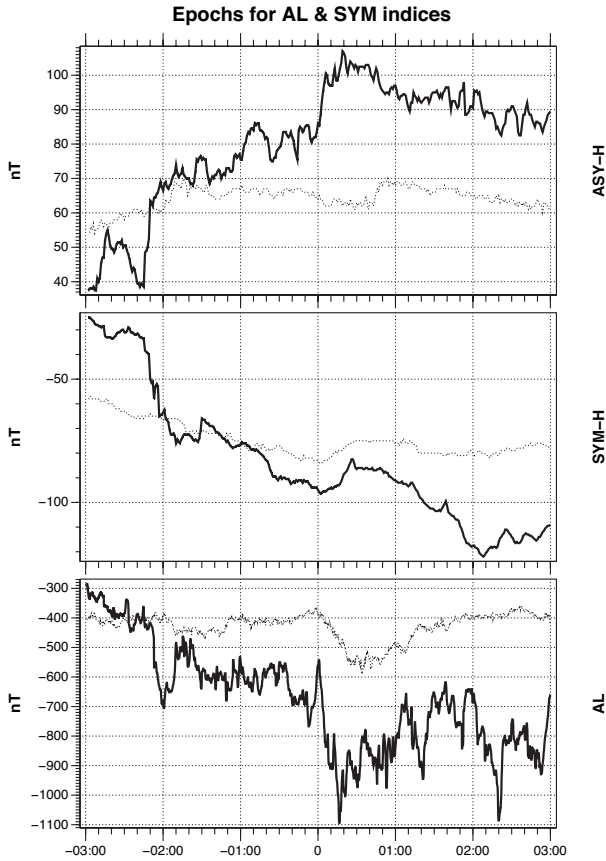


**Fig. 2.** Superposed epoch analysis of the asymmetric ring current index ASY-H (top), the symmetric ring current index SYM-H (middle), and the auroral electrojet index, the pseudo-AL (bottom). The stormtime activations are shown with solid lines and the sawtooth events are shown with dotted lines.

the onset of the stormtime activations. This indicates that the stormtime activations are more clearly associated with a strong partial ring current. SYM-H (middle panel) has a decreasing trend for the whole epoch of the stormtime activations. There is a similar increase in the index value at the onset time of both the sawtooth events (about 10 nT) and the stormtime activations (about 15 nT). Even though the partial ring current has been shown to be strongly enhanced during sawtooth events [10, 11], the superposed epoch result highlights the large-scale nature of both the sawtooth events and the stormtime activations with all local times showing injection and field dipolarization producing a positive effect at the mid-latitude ground magnetograms. The pseudo-AL index (bottom panel) shows a substorm-like decrease at onset for both data sets, but the negative deflection is several 100 nT deeper for the stormtime activations than it is for the sawtooth events. The onset-related decrease is also steeper for the stormtime activations than for the sawtooth events. For the stormtime activations the decrease is consistent with our selection criteria.

### 3.3. Geosynchronous observations

The magnetic field inclination changes and energetic particle injections were recorded by multiple spacecraft at geostationary orbit, in most cases giving a good local time coverage

around the Earth. For each event, each of the measuring satellites was binned into one of the five local time sectors: 12–18, 18–22, 22–02, 02–06 and 06–12 MLT. This allows us to examine the superposed epoch results in the different local time sectors separately. The results for the field inclination are shown in Fig. 3 and the electron data are shown in Fig. 4. As the satellites at different local times are also at different magnetic latitudes, the field inclination changes are not similar everywhere: a satellite at the equator would measure only a decrease in  $B_z$  but no change in field inclination, while a satellite off the equator would measure strong stretching and dipolarization of the field. Here we have made no attempt to correct for these differences; field inclinations are averaged as they were measured. For the electron data, the averages were computed using the logarithms of the fluxes to avoid domination of one or a few strong events.

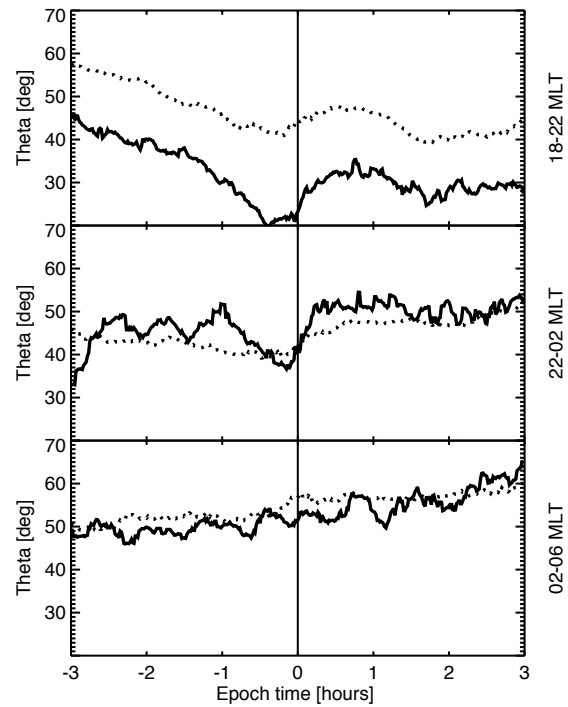


**Fig. 3.** Superposed epoch analysis of the field inclination angle at 18–22 MLT (top), 22–02 MLT (middle) and 02–06 MLT (bottom). The stormtime activations are shown with solid lines and the sawtooth events are shown with dotted lines.

By the selection process, the stormtime activations show a very stretched field in the evening sector prior to the onset. The average field dipolarizes rapidly at substorm onset returning to the average value preceding the growth phase. The dipolarization signature is clear also in the midnight sector. The morning-sector field inclination increases as well, although in that local time sector there is hardly any stretching of the field prior to the onset. The sawtooth events are characterized by strongest field stretching near midnight sector; the stretching–dipolarization cycle is clearly visible in the evening and midnight sectors. In

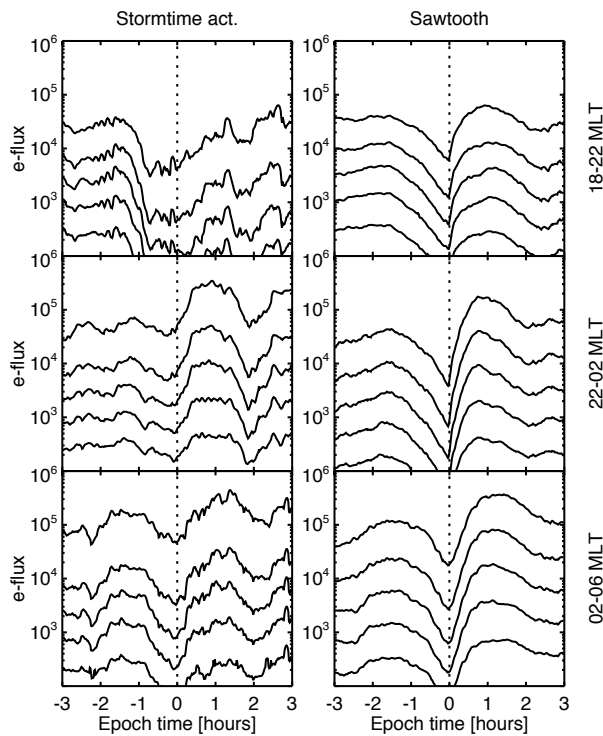


**Fig. 4.** Superposed epoch analysis of the energetic electron injections for the energies of 50–75, 75–105, 105–150, 150–225, 225–315 keV. The stormtime activations are shown in the left panels and the sawtooth events are shown in the right panels.

the morning sector, the field inclination shows a small jump beginning slightly before the onset time.

The injection characteristics for both stormtime activations and sawtooth events show very similar behaviour: There is a clear flux dropout observed at all local times in the hour preceding the onset, and almost simultaneous injections at all local times. Even the flux values are quite similar for both data sets indicating similarity in the overall field configuration (spacecraft mapping to similar radial distances in the equatorial plane). Interestingly, both data sets show a periodic signature with a prior injection about 2.5 hours prior to the selected onset time. This would indicate that the 2.5-hour periodicity reported in association with the sawtooth events is a more general feature of the magnetospheric activity (see also [3]).

#### 4. Discussion

We have analysed the typical behaviour of the solar wind parameters, IMF, geosynchronous magnetic field and injections as well as the ionospheric activity for a set of stormtime activations and sawtooth events. The sawtooth events were compared to the stormtime activations that most resemble observations during individual sawtooth injections: highly stretched dusk sector field followed by field dipolarization and injection over a wide local time sector (a subset of 24 events). The solar wind electric field and IMF  $B_Z$  are on average somewhat stronger for the dusk sector stormtime activations than for the sawtooth

events. The solar wind speed is also clearly higher during the stormtime activations than during the sawtooth events. In the ionosphere, the stormtime activations are related to stronger activity as described by the pseudo-AL index. These events are also associated with more intense partial ring current than the sawtooth events. While by the selection criterion, the stormtime activation data set had stronger stretching in the evening sector, the geostationary orbit observations in general were very similar for both data sets.

The geostationary injection data show a periodicity with a prior activation about 2.5 hours earlier than the selected onset time. The signature is visible as well in the sawtooth event data as in the stormtime activation data. The latter indicates that the periodicity is perhaps related to an internal magnetospheric time scale. Interestingly, Borovsky et al. [3] find that averaged over all activity conditions, so-called periodic substorms recur at a rate of every 2.75 hours, very close to the values seen in both data sets studied here. The period is also similar to the recovery time of the substorm electrojets in the auroral ionosphere, while it is clearly longer than substorm recovery times in the midtail plasma sheet ( $\sim 20$  min) or at the geostationary orbit ( $\sim 90$  min) [8]. In the magnetotail, the key configuration change that is required before the onset is the formation of a thin current sheet in the inner part of the magnetotail [11]. During non-storm conditions, the growth phase time scale during which the current sheet intensifies sufficiently to allow the breakup instability to grow is about 30–60 min, i.e., much shorter than the recurrence period [6]. Thus, while the parameters controlling recurrence of magnetospheric activity remain unresolved, it seems that the recurrence period associated with sawtooth events is not a characteristic of this special class of events but a more general property of the Earth's magnetosphere.

The similarity of the driving conditions during stormtime activations and sawtooth events also points to a common origin of these events. The larger solar wind speed during the stormtime activations may either be a true effect or be due to the fact that the stormtime activations were selected during 2004, during the declining phase of the sunspot cycle. During the declining phase, there is a higher occurrence frequency of coronal high speed streams driving geomagnetic activity [5, 16]. However, it is the solar wind electric field rather than the solar wind speed itself that controls the level of geomagnetic activity [1]. As the driving electric field was quite similar for both cases, it would seem that the sawtooth events occur preferentially during slower speed and steadier  $B_Z$ ; confirming this would require a larger dataset of both event types covering similar solar wind conditions.

Both sets of events tend to occur during decreasing SYM-H, i.e., storm main phases under strong driving. The sawtooth events and the stormtime activations show a similar positive deflection of the SYM-H, while the signature in ASY-H is strong during the stormtime activations and negligible during the sawtooth events. This indicates that the both sets of events have a wide local time range of the injection/dipolarization front. Even though case studies have shown the strong concentration of stretching in the evening sector [10], the sawtooth events seem to be better characterized by their large local time extent than by a concentration of activity in the evening sector. As the auroral electrojet activity is almost at a normal (non-

storm) substorm level [4], the resemblance of these activations to large substorms occurring close to the Earth is further emphasized.

In summary, the examination of stormtime magnetic activations shows that it is possible to select a subset of substorm-like activations in the ionosphere that have the characteristics in the driving solar wind, in geosynchronous field and particle measurements and auroral ionospheric currents that are very close to those observed during sawtooth events. Furthermore, the periodicity of the sawtooth events is repeated both in recurrent substorms and in stormtime activations, indicating that it is not a defining property of sawtooth events. We thus conclude that the sawtooth events are substorm-like activations that occur in sequence when the solar wind conditions are sufficiently constant to allow for the intrinsic magnetospheric time scales to control the activity repetition rate.

## Acknowledgments

The work of NP is supported by the Alberta Ingenuity Fund. TP thanks the IGPP for hosting her visit at Los Alamos. We thank the ACE MAG and SWEPAM instrument teams and the ACE Science Center for providing the ACE data. We also thank the LANL MPA team for the geosynchronous magnetic field data. ASY-H and SYM-H data were obtained from the World Data Center C2 in Kyoto.

## References

- Bargatze, L. F., Baker, D. N., McPherron, R. L., and Hones, E. W., Jr., Magnetospheric impulse response for many levels of geomagnetic activity, *J. Geophys. Res.*, *90*, 6387–6394, 1985.
- Belian, R. D., Cayton, T. E., and Reeves, G. D., Quasi-periodic global substorm-generated variations observed at geosynchronous orbit, in: *Space plasmas: Coupling between small and medium scale processes*, Geophys. Monogr., *86*, AGU, Washington DC 20009, 143, 1995.
- Borovsky, J. E., Nemzek, R. J., and Belian, R. D., The occurrence rate of magnetospheric-substorm onsets: random and periodic substorms, *J. Geophys. Res.*, *98*, 3807–3813, 1993.
- Henderson, M. G., Reeves, G. D., Skoug, R., Thomsen, M. F., Denton, M. H., Mende, S. B., Immel, T. J., Brandt, P. C., and Singer, H. J., Magnetospheric and auroral activity during the 18 April 2002 sawtooth event, *J. Geophys. Res.*, *111*, A01S90, doi:10.1029/2005JA011111, 2006.
- Mavromichalaki, H., Vassilaki, A., and Marmatsouri, E., A catalogue of high-speed solar wind streams: further evidence of their relationship to Ap-index, *Solar Phys.*, *115*, 345–365, 1988.
- McPherron, R. L., Growth phase of magnetospheric substorms, *J. Geophys. Res.*, *75*, 5592–5599, 1970.
- Ogilvie, K. W., Chorney, D. J., Fitzenreiter, R. J., Hunsaker, F., Keller, J., Lobell, J., Miller, G., Scudder, J. D., Sittler, E. C., Jr., Torbert, R. B., Bodet, D., Needell, G., Lazarus, A. J., Steinberg, J. T., Tappan, J. H., Mavretic, A., and Gergin, E., SWE, a comprehensive plasma instrument for the Wind spacecraft, *Space Sci. Rev.*, *71*, 55–77, 1995.
- Pulkkinen, T. I., Baker, D. N., Toivanen, P. K., Pellinen, R. J., Friedel, R. H. W., and Korth, A., Magnetospheric field and current distributions during the substorm recovery phase, *J. Geophys. Res.*, *99*, 10955–10966, 1994.
- Pulkkinen, T. I., Koskinen, H. E. J., Kauristie, K., Palmroth, M., Reeves, G. D., Donovan, E., Singer, H. J., Slavin, J. A., Russell, C. T., and Yumoto, K., Storm-substorm coupling: Signatures of stormtime substorms, Proceedings of the Conference in Memory of Yuri Galperin, CAUSES Handbook-1, edited by L. M. Zelenyi, M. A. Geller and J. H. Allen, Boulder, 309–316, 2004.
- Pulkkinen, T. I., Ganushkina, N. Yu., Tanskanen, E. I., Kubyskhina, M., Reeves, G. D., Russell, C. T., Singer, H. J., and Slavin, J. A., Magnetospheric current systems during stormtime sawtooth events, *J. Geophys. Res.*, *in press*, 2006.
- Pulkkinen, T. I., Goodrich, C. C., and Lyon, J. G., Thin current sheets as part of the substorm process, *this issue*, 2006.
- Reeves, G. D., Henderson, M. G., Skoug, R. M., Thomsen, M. F., Borovsky, J. E., Funsten, H. O., Brandt, P. C., Mitchell, D. J., Jahn, J.-M., Pollock, C. J., McComas, D. J., and Mende, S. B., IMAGE, POLAR, and geosynchronous observations of substorms and ring current ion injection, in *Disturbances in Geospace: The Storm-Substorm Relationship*, Geophys., Monogr. Ser., vol. 142, edited by A. S. Sharma et al., 89–100, AGU, 2004.
- Rostoker, G., Samson, J. C., Creutzberg, F., Hughes, T. J., McDiarmid, D. R., McNamara, A. G., Vallance Jones, A., Wallis, D. D., and Cogger, L. L., CANOPUS - a ground-based instrument array for remote sensing the high latitude ionosphere during the ISTP/GGS program, *Space Sci. Rev.*, *71*, 743–760, 1995.
- Singer, H. J., Matheson, L., Grubb, R., Newman, A., and Bouwer, S. D., Monitoring space weather with the GEOS magnetometers, SPIE conference proceedings, vol. 2812, 299–308, *GEOS-8 and Beyond*, edited by R. Edward, Washwell, 1996.
- Smith, C. W., Heures, J. L., Ness, N. F., Acuna, M. H., Burlaga, L. F., and Scheifele, J., The ACE magnetic fields experiment, *Space Sci. Revs.*, *86*, 613–632, 1998.
- Tanskanen, E. I., Slavin, J. A., Tanskanen, A. J., Viljanen, A., Pulkkinen, T. I., Koskinen, H. E. J., Pulkkinen, A., and Eastwood, J., Magnetospheric substorms are strongly modulated by interplanetary high-speed streams, *Geophys. Res. Lett.*, *32*, L16104, doi:10.1029/2005GL023318, 2005.
- Thomsen, M. F., McComas, D. J., Reeves, G. D., and Weiss, L. A., An observational test of the Tsyganenko (T89a) model of the magnetospheric field, *J. Geophys. Res.*, *101*, 24827–24836, 1996.
- Viljanen, A. and Häkkinen, L., IMAGE magnetometer network. In: *Satellite-Ground Based Coordination Sourcebook* (editors: M. Lockwood, M. N. Wild and H. J. Opgenoorth). ESA publications SP-1198, 111–117, 1997.



# An attempt to locate substorm onsets using Pi1 signatures

V.A. Pilipenko, I.I. Tchebotareva, M.J. Engebretson, J.L. Posch, and A. Rodger

**Abstract:** Pi1 observations, because of their higher frequency, hold the promise of providing better temporal resolution for accurate timing of substorm onsets, thus continuing to be a matter of considerable importance for evaluation of competing substorm mechanisms. In this presentation we show that the same Pi1 signatures detected by the ground magnetometer array can be used also for the spatial location of substorm onsets. We have used data from Antarctic search-coil magnetometers. To locate an ionospheric source of Pi1 signatures we have applied a method of emission tomography that was previously used in seismology. The source image reconstruction algorithm uses scanning of the volume under investigation; for each of the grid points a coherency measure for multi-channel data is calculated. For the source image reconstruction we have introduced a coherency measure, that may be coined the nonlinear semblance. Though the Antarctic stations are elongated in one direction, that is not favorable for tomography methods, the results obtained seems to be very promising for locating substorm onsets with ground magnetometer data.

*Key words:* substorm onset, ULF pulsations, auroral activation, tomography.

## 1. Introduction

Accurate timing and locating of substorm onsets continues to be a matter of considerable importance as the space physics community tries to evaluate competing onset mechanisms. Although UV satellite imagers provide onset location of unparalleled quality, the paucity of satellites and their limited imaging cadence underscore the need for complementary, ground-based monitoring techniques. The long-period nature of Pi2 signals provides only approximate timing ( $\sim$ few min). A spatial pattern of Pi2 signatures in the auroral region is rather complicated, which hampers a straightforward backward ray tracing. Pi1 observations, because of their higher frequency, hold the promise of providing better temporal resolution ( $\sim$ few sec) [1]. In contrast to longer-period Pi2 signals, part of Pi1 wave burst can be trapped in the ionospheric waveguide and propagate along the ionosphere nearly isotropically.

## 2. Current understanding of Pc1/Pi1 signal propagation from an ionospheric source

The ULF waves in the Pc1/Pi1 band are expected to be produced through field-aligned injection of the localized Alfvén wave into the ionosphere. MHD waves in the frequency range around 1 Hz are regarded to propagate in the horizontal direction after being trapped in the upper ionosphere. Thus, a horizontal profile of Pc1/Pi1 magnetic signals is determined by both the mode conversion from incident Alfvén waves into horizontally propagating fast magnetosonic waves owing to anisotropic Hall conductance and trapping of the fast wave in the ionospheric F-layer [4]. The spatial and frequency dependences of the ground magnetic signal are to be different in two

separate regions: in the injection center and in a region with distance much larger than the scale of the incident wave. In the center ( $r < r_0$ , where  $r_0$  is the scale of localization of the incident wave), ground magnetic field disturbances have the same spatial properties of intensity and polarization as those of an incident Alfvén wave. In the far-off region ( $r \gg D$ , where  $D$  is the scale of the waveguide), the electromagnetic field of the fast wave is dominant. In the intermediate transition region between those two regions a numerical approach is necessary to describe the wave pattern.

In a two-layer model (1-magnetosphere, 2-ducting F-layer), a fast wave with  $k_n V_A^{(2)} < \omega < k_n V_A^{(1)}$  is trapped: it is vertically evanescent in the magnetosphere and simultaneously is propagating along the ducting layer. The horizontal wave number  $k_n$  increases in association with an increase of frequency: at the lower cutoff it is  $\omega/V_A^{(1)}$  and tends to be  $\omega/V_A^{(2)}$  in the higher frequency limit. Both phase and group velocities tend to  $V_A^{(1)}$  at the lower cutoff frequency and to  $V_A^{(2)}$  at higher frequency. Each harmonic wave has a minimum group velocity less than the ionospheric Alfvén velocity  $V_A^{(2)}$ . However, the effective average damping rate and apparent propagation velocity are expected to be substantially lower, because in the central and intermediate regions the signal is dominated by Alfvén waves and horizontal propagation does not play a significant role. The important results of analytical and numerical models of MHD wave excitation and propagation in the ionosphere [3] are summarized as follows:

The observed damping rate is about 10dB/100km as a maximum in the injection region and about 2.5dB/100km in the region beyond 500 km. Spatial attenuation is larger in the daytime than in the nighttime;

The ducted wave has a lower cutoff frequency. Attenuation of the ducted wave is generally minimized at the lower cutoff frequency. The attenuation of ducted waves propagating off the geomagnetic meridian is larger than in the meridian plane.

It would be fair to say that we are not aware of any observational study that has unambiguously shown that Pi1 propagation along the Earth's surface is due to ionospheric waveguide

Received 7 June 2006.

V.A. Pilipenko and I.I. Tchebotareva. Institute of the Physics of the Earth, Moscow

M.J. Engebretson and J.L. Posch . Augsburg College, MN

A. Rodger . British Antarctic Survey, Cambridge, UK

propagation. However, the approach used here does not in fact depend on the actual propagation mode, but just assumes isotropic horizontal propagation from a source with some averaged velocity.

### 3. Observational data

We analyze Pi 1 signatures detected by an array of Antarctic search-coil magnetometers. The locations of these stations are shown in Figure 1. Pi1 were observed predominantly when the ground stations were near local midnight (within several hours of MLT). The coordinates and codes of Antarctic stations can be found elsewhere.

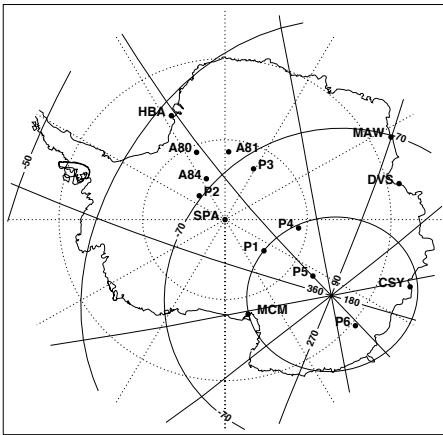


**Fig. 1.** Map of search-coil magnetometers in Antarctica. Solid lines denote geomagnetic coordinates, and dotted lines denote geographic coordinates.

### 4. Algorithm of the source location

To locate an ionospheric source of Pi 1 signatures we have applied the method of emission tomography that was previously used in seismology [5]. This method does not require a picking of onset arrival time in contrast to many other methods of a signal source location. Therefore, it makes it possible to locate simultaneously a few interference events, events with illegible onsets, and events with very weak signals that are nearly obscured by noise. The method permits the processing of both one component data and three component data with polarization focusing. In seismology, emission tomography can provide three-dimensional seismic source distribution, i.e., estimation of their azimuths, apparent distances, and depths.

The idea of the method is as follows. Suppose that a small volume radiates a weak signal with a simple structure, e.g., a spherical wave in a homogeneous medium. In a realistic medium, the signal trajectory may be distorted due to velocity inhomogeneity, but a spatial signal coherence remains. This fact is used for source detection. The source image reconstruction algorithm uses scanning of the volume under investigation over the points of a grid. For each of the grid points a coherency measure for multi-channel data is calculated. One derives

the spatial distribution of the coherency measure that characterizes the emission properties of a medium by scanning the structure over a multi-dimensional rectangular grid.

For the source image reconstruction a different coherency measure may be used, traditionally the semblance  $S$  [7]. If there is no coherent component in recorded data and only independent evenly distributed Gaussian noise is present on each channel, the semblance has a  $\beta$ -distribution with expected mean and variance [5]. That is, when no signal is present, semblance maps provide a uniform distribution of brightness. When coherent signals from an emission source occur in the noise-like wave field, a bright spot appears in the reconstructed image. Semblance sharply increases for those grid points which are closer to the source. Semblance is a function of the signal-to-noise ratio and for a weak signal equals to the product of the signal to noise ratio and the number of channels.

The scale of the bright spot around the probable source location in the image is proportional to the dominant signal wave length. We had intended going to process signal with large wave length, but preliminary analyses of real data resulted in poor spatial resolution. That is why in this work we decided to use another coherent measure. Numerical simulation and analysis of real data has shown that the use of this new coherent measure greatly improves the quality of source images and results in a considerably better spatial resolution. The conventional semblance  $S$  is described by the formula

$$S = \frac{\sum_{j=1}^T \left( \sum_{i=1}^K f_{ij}(\tau_i) \right)^2}{\sum_{j=1}^T \sum_{i=1}^K f_{ij}^2(\tau_i)} \quad (1)$$

where  $f_{ij}$  is the instantaneous amplitude of the  $j$ -th sample at the  $i$ -th recording site,  $K$  is the number of channels, and  $T$  is the time window length in samples. The parameter  $\tau_i$  is the time shift in the  $i$ -th channel appropriate to the path of a hypothetical signal from a focused grid point, and determined by the propagation with velocity  $V$ . In this version of the algorithm isotropic propagation is assumed, but it could be extended to the case of non-isotropic propagation. The term in parenthesis in the  $S$  numerator is coined linear or conventional beamforming. Instead, we use  $N$ -th root beamforming that is known to have a better directivity [6]. Our new measure, which may be coined a nonlinear semblance, is described by the formula

$$S = \frac{K^2 \sum_{j=1}^T B_j^2}{\sum_{j=1}^T \sum_{i=1}^K f_{ij}^2(\tau_i)} - 1 \quad (2)$$

where

$$B_j = |b_j|^N \quad b_j = \frac{1}{K} \sum_{i=1}^K |f_{ij}(\tau_i)|^{1/N} \text{sign}\{f_{ij}(\tau_i)\}$$

Here  $K$ ,  $T$ ,  $f_{ij}$ , and  $\tau$  are the same parameters as for the conventional semblance (1),  $B_j$  is the  $N$ -th root beamforming, and  $N$  is the parameter of nonlinearity. Here we use  $N = 4$  and one-component data. We have added -1 in the formula (2) because in this case in absence of signal the semblance is close to zero,  $S \rightarrow 0$ .

#### 4.1. Pre-processing: The choice of frequency band and an apparent propagation velocity

Spectra of raw data show that Pi1 burst are broadband signals with spectral enhancement around 0.1 Hz (Figure 2). Therefore, raw search coil magnetometer data (H-component) have been preliminary band-pass filtered in the frequency band 0.05-0.3 Hz. The focusing process, that is the search of optimal

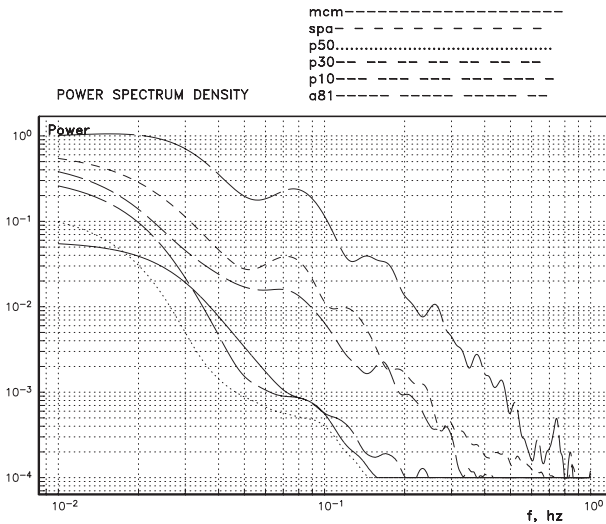


**Fig. 2.** Power spectral density of raw data from various Antarctic stations (indicated by different line patterns) for the event of January 03, 2001.

parameters for the brightest image of  $S$ , has been performed as follows. The start time is chosen in such a way to include the Pi1 burst onset from all stations into an interval to be analyzed. The length of the interval, or time window  $T$ , is to be larger than duration of signal burst.

The additional complications for the source location method is caused by the fact that the actual propagation velocity of a signal along the ionosphere is unknown. The idea of the optimal choice of an apparent average velocity is as follows. Test-and-try modeling provides the brightest (as characterized by the brightness rate  $S$ ) and most focused image of a source when the selected apparent velocity of a signal matches the actual velocity.

### 5. Examples of the Pi1 source location with the nonlinear semblance algorithm

For each of the events below we show stacked line plots of raw search coil data with Pi1 signals. Two examples of Pi1 indicators of substorm onset will be analyzed and presented.

#### 5.1. February 26, 2001 (day 057)

An intense Pi1 burst is evident at US (SPA, MCM) and British sites (A80, A81, A84) and Australian stations (MAW, DAV, CSY) around 0121 UT (Figure 3). The start time chosen is 0121 UT, and the time window is  $T=450$ s. The best-fit velocity was determined to be  $V = 120$  km/s.

The distribution of nonlinear semblance  $S$  constructed for this event is shown in Figure 4 as color-coded brightness. The

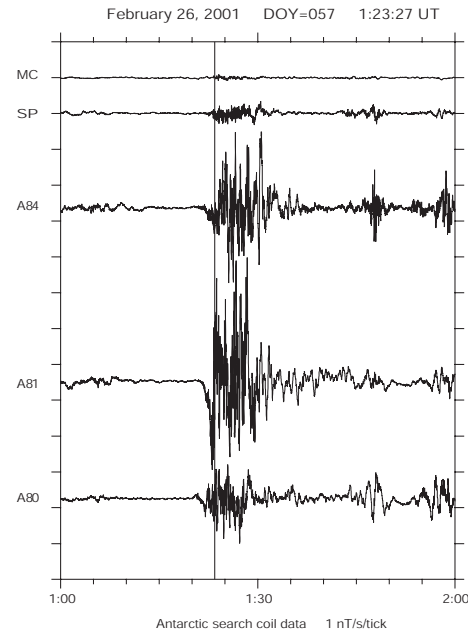


**Fig. 3.** The stacked raw magnetograms of Antarctic search-coil magnetometers for the event of February 26, 2001 (day 057).

semblance algorithm has found the epicenter of the Pi1 signal in an extended area equatorward from station A81.

#### 5.2. January 3, 2001 (day 003)

A relatively weak substorm onset occurred at 0234 UT. Pi1 activity on raw records is evident at the two lowest latitude sites (A80, A81), and much weaker traces are at P3 and SPA (Figure 5), but on filtered records onset becomes evident at sites A80, A81, P1, P3, P5, SPA, and MCM. The start time is 0229 UT, and the time window is  $T = 200$  s. The best-fit velocity was determined to be  $V = 75$  km/s. The Pi1 source location as determined by the algorithm is westward from SPA-P2 stations (Figure 6). This event shows that the algorithm is able to determine the source location even when a source is distant from the station array.

### 6. Conclusion

The location of available stations was very unfavorable for the emission tomography algorithm: practically all stations formed 1D array extended in North-South direction. However, even under these unfavorable conditions the nonlinear semblance algorithm has provided rather reasonable and consistent results. We suppose that this algorithm would be much more efficient for an actual 2D array. Hence, a dense spatial array of magnetometers sensitive to 0.1-1 Hz activity (both search coil instruments and low-noise fluxgate instruments) may provide both improved localization and timing information. The limited spatial range of Pi1 may prove to be an advantage in localizing onsets, and the range over which onsets stimulate Pi1 activity is limited in both local time and latitude.

It would be very interesting to compare the location of Pi1 source identified from ground-based magnetometers with UVI satellite images. Unfortunately, there were no satellite imager

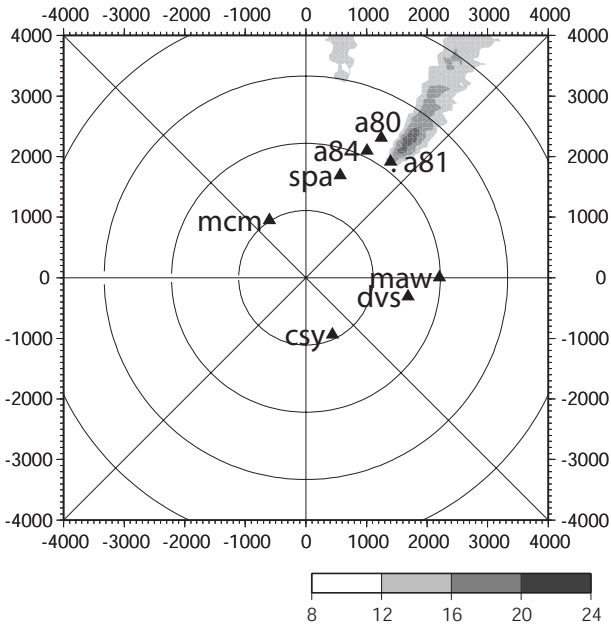


**Fig. 4.** Reconstruction of the Pi1 source location by the semblance method for the event February 26, 2001 (day 057).

observations over Antarctica during the period analyzed. Monitoring of Pi 1 activity can thus contribute to substorm studies in the absence of satellite imager data.

**Acknowledgements.** This study is supported by grant 03-51-5359 from INTAS (VAP, IIT, AR) and by National Science Foundation grant ATM-0305483 to Augsburg College (MJE, JLP). We acknowledge the data of Australian stations provided by P. Ponomarenko.

**References**

1. Bosinger, T., and A.G. Yahnin, Pi1B type magnetic pulsations as a high time resolution monitor of substorm development, *Ann. Geophysicae*, 5A, 231–238, 1987.
2. Douze, E.J., and S.J. Laster, Statistics of semblance, *Geophysics*, 44, 1999–2003, 1979.
3. Fujita S., and T. Tamao, Duct propagation of hydromagnetic waves in the upper ionosphere. 1. Electromagnetic field disturbances in high latitudes associated with localized incidence of a shear Alfvén wave, *J. Geophys. Res.*, 93, 14665–14673, 1988.
4. Greifinger, C., and P.S. Greifinger, Theory of hydromagnetic propagation in the ionospheric wave guide, *J. Geophys. Res.*, 73, 7473–7490, 1968.
5. Tchebotareva, I.I., A.V. Nikolaev, and H. Sato, Seismic emission activity of Earth’s crust in Northern Kanto, Japan, *Phys. Earth Planet. Interiors*, 120, 167–182, 2000.
6. Muirhead, K.J., and R. Datt, The N-th root process applied to seismic array data, *Geophys. J. R. Astr. Soc.*, 47, 197–210, 1976.
7. Taner, F., and N.S. Neidell, Semblance and other coherency measures for multichannel data, *Geophysica*, 36, 482–497, 1971.

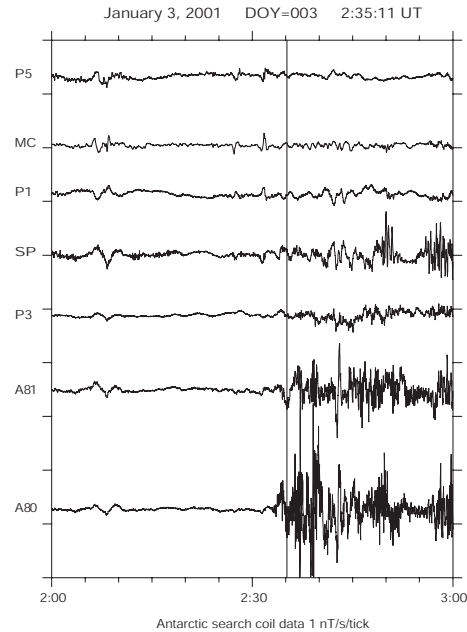


**Fig. 5.** The raw magnetograms of Antarctic search-coil magnetometers for the event of January 03, 2001 (day 003).

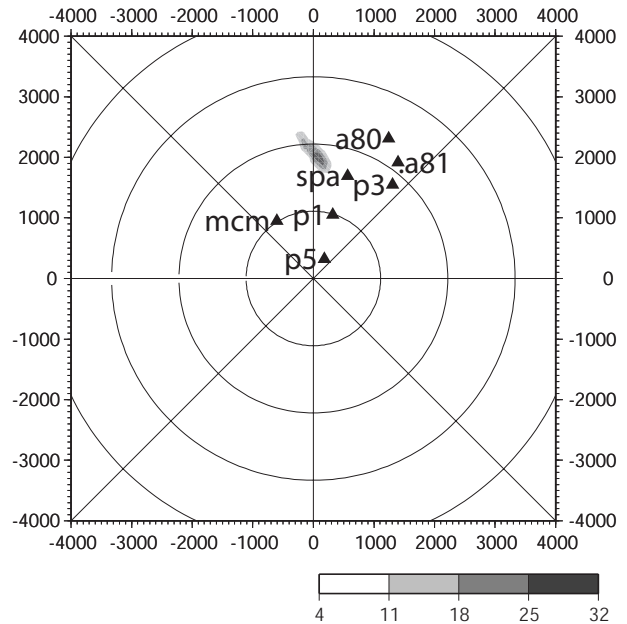


**Fig. 6.** Reconstruction of the Pi1 source location by the semblance method for the event of January 3, 2001 (day 003).

# Effects of pressure gradients and convection on the inner plasma sheet stability

V. Prosolin, I. Voronkov, and E. Donovan

**Abstract:** We present a computer model that solves the system of nonlinear MHD equations in dipolar coordinates and is designed specifically to simulate the near-Earth plasma sheet region which has a near-dipolar field line topology. The objective of this work is a detailed study of the inner plasma sheet as a region of particular importance for auroral processes including the proton aurora and near-Earth breakup. Such factors affecting the stability of the inner plasma sheet as Earthward plasma pressure gradients and different patterns of bulk plasma motion are considered. Modeling results show that pressure gradients lead to magnetic field line stretching and increased values of the ballooning instability growth rate. Both Earthward and tailward convection bursts form a local min-B region. However, effects of tailward bursts are stronger. Earthward convection forms a potentially unstable min-B region at about  $9 R_E$ , whereas tailward convection does not have a destabilizing effect.

*Key words:* Substorm, Ballooning Instability, Modeling, Plasma Dynamics.

## 1. Introduction

It is generally recognized that the primary mechanism for energy and plasma transport through the magnetosphere is magnetospheric convection. In the magnetotail, plasma travels from the nightside reconnection region towards the Earth until it reaches the region of strong near-dipolar magnetic field - near-Earth plasma sheet.

There is no consensus on some particular details of plasma propagation through the plasma sheet, but it is known that flows can be highly variable – for example, periods of steady convection (e.g., [25]), bursty bulk flows (e.g., [1]), and flow reversals [15], have been observed. The complex dynamics of the plasma sheet have been shown to be closely related to many auroral processes. These include, for example, the proton aurora band at the radial boundary of the auroral region ([21], [22]), which maps to the so-called b2i boundary [6]. Also, the most pronounced field line resonances are observed in this region, owing to sharp radial gradients of magnetic field ([20], [8], [23], [17]). The substorm onset auroral arc intensifies and breaks up in this region ([16], [28], [29]). Therefore, there is substantial evidence that energy transport in the inner plasma sheet plays a crucial role in auroral dynamics.

The main idea of how plasma sheet dynamics can be coupled with auroral features involves the transformation of potential energy stored in the near-Earth magnetosphere into kinetic energy of field-aligned plasma flows affecting the ionosphere ([9], [10]). In order to provide this ionosphere-magnetosphere coupling, a quite fast (of the order of tens of seconds) mechanism of energy transformation is required, so a number of authors have proposed that plasma instabilities takes place. These include the current disruption model ([12], [13], [18]), convection reversal model [15], kinetic ballooning instability [4], shear flow ballooning instability ([24], [27]), and non-linear ballooning instability [5]. Another group of models suggests that a distant

magnetotail disruption may trigger the near-Earth energy release and consequent auroral activity when disturbances from the more distant magnetotail reach the inner plasma sheet ([2], [26], [3]). Currently, there is no general public acceptance of either model. However, a common point in all proposed mechanisms is that the sufficient amount of energy must be stored in the inner plasma sheet and one way or another this region should be destabilized (e.g., [29] and references therein). Some aspects of this problem are addressed in this paper.

This study aims to discuss the influence of several factors on the inner plasma sheet stability from the modeling point of view. We use a three dimensional MHD model to simulate the dynamics of the inner plasma sheet for different configurations. In the first part, we perform the stability analysis of plasma sheet configurations with an Earthward pressure gradient present. Different magnitudes of the pressure gradient are tested for the ballooning instability. In the second part, we examine different plasma bulk flow patterns – bursty flows and steady convection. Both tailward and Earthward velocity directions are considered to examine possible destabilization by the convection.

## 2. Ballooning Instability in the Inner Plasma Sheet

It has been observed that active electron arcs, including the pre-onset arc, are often seen within the region of strong  $H\beta$  proton emissions and energetic (tens of keV) proton precipitation at the equatorial edge of the evening sector of the auroral region ([21], [27], [16]). Quite often, Earthward pressure gradients are observed by the satellites crossing or entering the inner plasma sheet at  $8-12 R_E$  ([14], [19]).

A dipolar magnetic field with uniform pressure distribution is an equilibrium configuration. The ballooning instability can occur in a system where the magnetic field is stretched beyond the dipolar shape such that a pressure gradient force is balanced by the Ampere magnetic force (Figure 1).

Under certain conditions, the inner plasma sheet can become ballooning unstable. The following relation for the ballooning

Received 6 June 2006.

V. Prosolin, I. Voronkov, and E. Donovan. Department of Physics and Astronomy, University of Calgary.

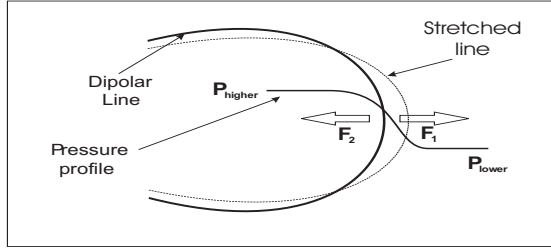


**Fig. 1.** Two forces in balance - Curvature ( $F_1$ ) and pressure gradient ( $F_2$ ).

instability growth rate is derived in [27]:

$$\omega^2 = -\frac{P'_{tot}}{\rho} \left( 2(\ln B)' - \frac{2P'_{tot}}{\rho V_f^2} \right) \quad (1)$$

where  $B$  is the magnetic field,  $P_{tot}$  is the total (magnetic plus thermal) pressure,  $\rho$  is the plasma density,  $V_f$  is the speed of the fast mode, and prime denotes the radial (anti-earthward) derivative. We applied the above formula to data from [11] and identified a potentially unstable region in the vicinity of the strong pressure gradient (Figure 2).

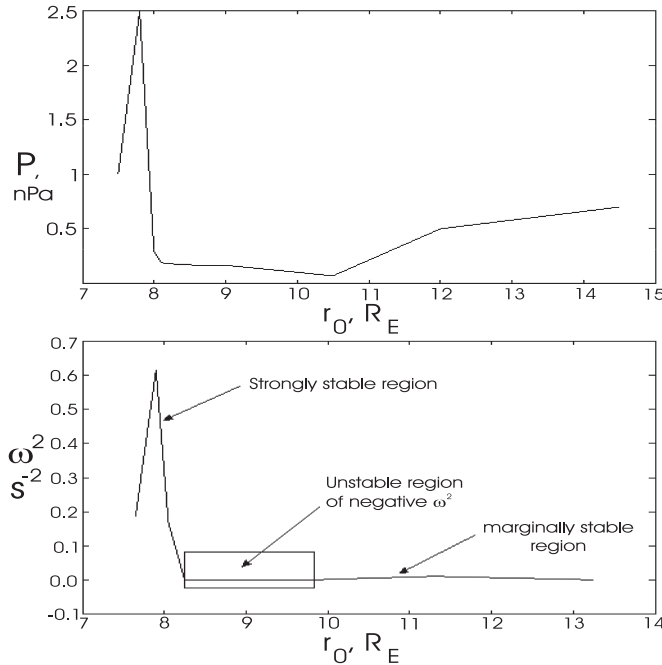


**Fig. 2.** An observed pressure profile (from [11]) and corresponding ballooning instability growth rate ( $\omega^2$ ) in the equatorial plane.

### 3. Effects of Earthward Pressure Gradients

As we have shown that a strong earthward pressure gradient can lead to an unstable region, the following question arises – How strong does the gradient need to be in order to lead to a local instability?

Using the abovementioned computer code we have studied evolution of the system with an initially given pressure profile

in order to find a possible relation between the magnitude of the gradient and the instability growth rate.

The initial configuration for all the runs discussed in this paper is set as follows, unless otherwise specified:

- Dipolar magnetic field
- Uniform plasma pressure and density distribution:  $\rho = 1.67 \cdot 10^{-24} g/cm^3$  ( $n = 1 cm^{-3}$ ),  $P_{max} = 1 nPa$
- Zero velocity

For the purpose of studying effects of pressure gradients we set the initial pressure profile in the following form:

$$P|_{equator} = P_{max} \left( 1 - \frac{\arctan a(r_0 - r_{mid})}{b} \right)$$

where  $P_{max}$  is the maximum value of pressure corresponding to the inner boundary,  $r_0$  is a radial distance along the equator,  $r_{mid}$  is the center of the pressure gradient, and  $a$  and  $b$  are coefficients defining the magnitude and width of the gradient.

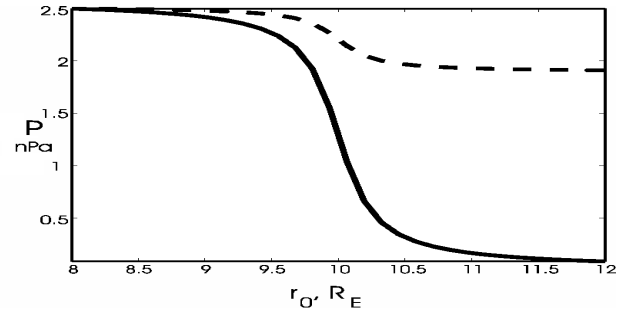


**Fig. 3.** Initial pressure profiles in the equatorial plane

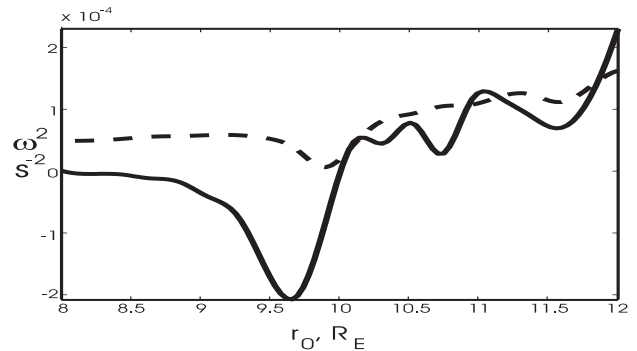


**Fig. 4.**  $\omega^2$  equatorial profile at  $t = 50$  seconds

Two sample initial pressure profiles are shown in Figure 3. Since at  $t = 0$  the system is not in the equilibrium, a reconfiguration process begins. Modeling shows that in the vicinity of the strongest gradient a region of minimum magnetic field is formed (Figure 5) which corresponds to stretching of the field lines. The stretching increases field line curvature thereby creating the curvature force opposing the pressure gradient force to re-establish plasma equilibrium.

By applying Eq. 1, we obtain equatorial profiles of  $\omega^2$  shown in Figure 4. Similarly to the analysis performed with observed

data, we find that the minimum-B region and maximum of the pressure gradient correspond to the minimum in  $\omega^2$  marking an unstable region ( $\omega^2 < 0$ ).

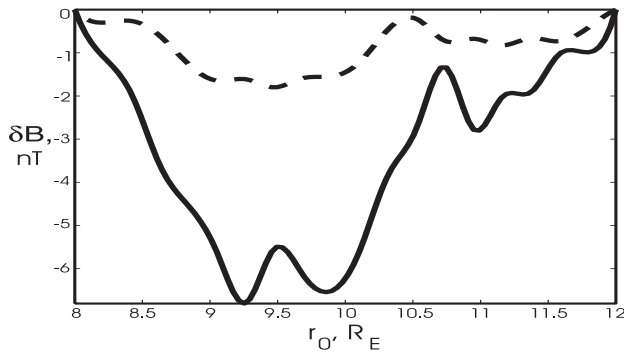


**Fig. 5.** Magnetic field perturbation profile at the equator at  $t = 50$  seconds

As seen in Figures 3 and 4, the maximum magnetic field perturbation and most negative value of  $\omega^2$  correspond to the larger gradient. However, it is obvious that the instability can occur only when the pressure gradient overcomes some threshold. In order to verify that, we have performed computer simulations for several different magnitudes of pressure gradients in the range from  $0.25 \text{ nPa}/R_E$  to  $4.4 \text{ nPa}/R_E$ .

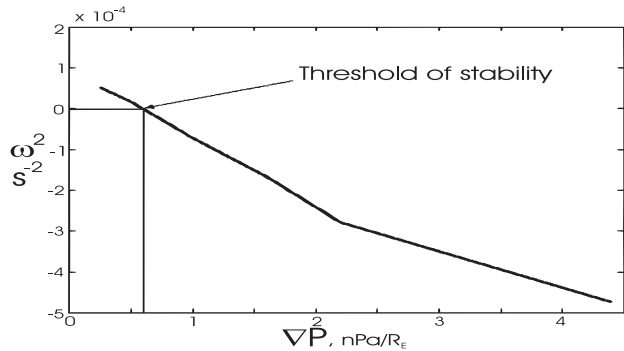


**Fig. 6.** Ballooning instability growth rate  $\omega^2$  vs. plasma pressure gradient  $\nabla P$

By plotting the minimum value of  $\omega^2$  vs. the magnitude of the initial pressure gradient, we have found the point at which  $\omega^2 = 0$  which corresponds to a threshold of the instability. As one can see in Figure 6 the threshold lies at  $0.6 \text{ nPa}/R_E$ .

#### 4. Bulk Plasma Motion

As noted earlier, convection in the magnetotail occurs in different forms, such as steady convection and “discrete bursts of high-velocity flow of limited spatial extent” [7]. In this section we describe four different patterns of plasma bulk motion (i.e., convection): flow bursts and steady convection for both Earthward and tailward velocity directions.

#### 4.1. Bursty Flows

In order to model an Earthward moving pulse we set a gaussian profile of radial velocity with the amplitude of  $1000 \text{ km/sec}$  as shown in Figure 7.

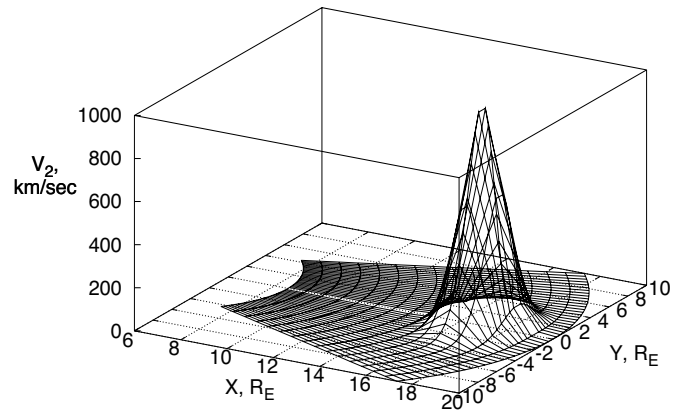


**Fig. 7.** Earthward pulse: radial velocity equatorial profile at  $t = 0$

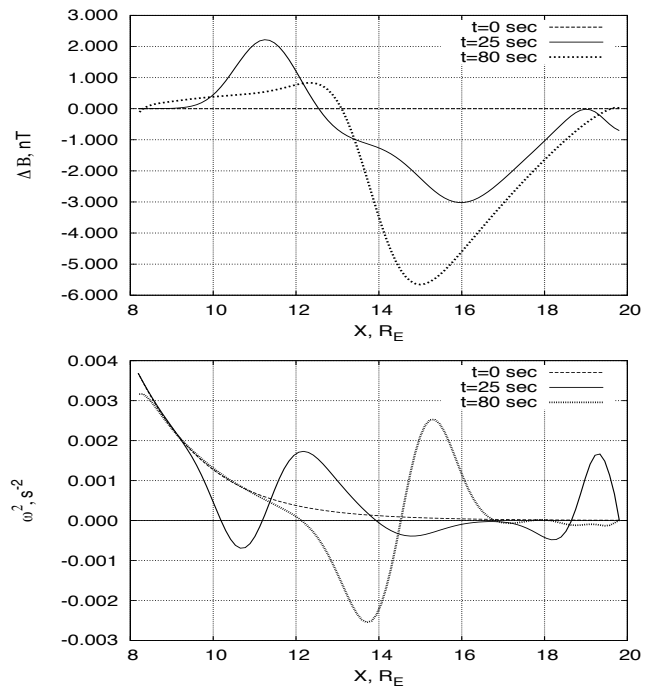


**Fig. 8.** Earthward pulse: magnetic field perturbation and instability growth rate profiles at different times

We take snapshots of the resulting magnetic field perturbation and ballooning instability growth rate at several moments of time. Figure 8 shows that an Earthward pulse modifies the field configuration so that a min-B region is formed along with a potentially unstable ( $\omega^2 < 0$ ) region in the vicinity of magnetic field gradient.

The effects of a tailward pulse (Figure 9) are almost negligible in comparison with the previous case, as seen in Figure 10. No clear change in magnetic field topology is observed, although at times the system may get into a marginal state -  $\omega^2$

is just below 0.

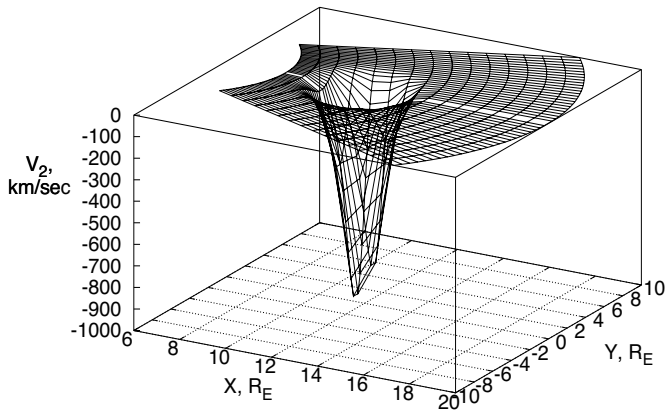


Fig. 9. Tailward pulse: radial velocity equatorial profile at  $t = 0$

$$E_2(x, y, z) = \frac{E_2^{equator} h_2^{equator}}{h_2(x, y, z)}$$

$$E_3(x, y, z) = \frac{E_3^{equator} h_3^{equator}}{h_3(x, y, z)}$$

where  $E_2(x, y, z)$  and  $E_3(x, y, z)$  are two perpendicular to the magnetic field components of the electric field at a point defined by Cartesian coordinates  $(x, y, z)$ ,  $E_2^{equator}$  and  $E_3^{equator}$  are the electric field components in the equatorial plane that lie on the same magnetic field line,  $h_2^{equator}$ ,  $h_3^{equator}$  and  $h_2(x, y, z)$ ,  $h_3(x, y, z)$  are corresponding metrics.

One can notice that for a uniform (in the equatorial plane) electric field, as the dipolar magnetic field increases Earthward, the  $E \times B$  drift velocity descends.

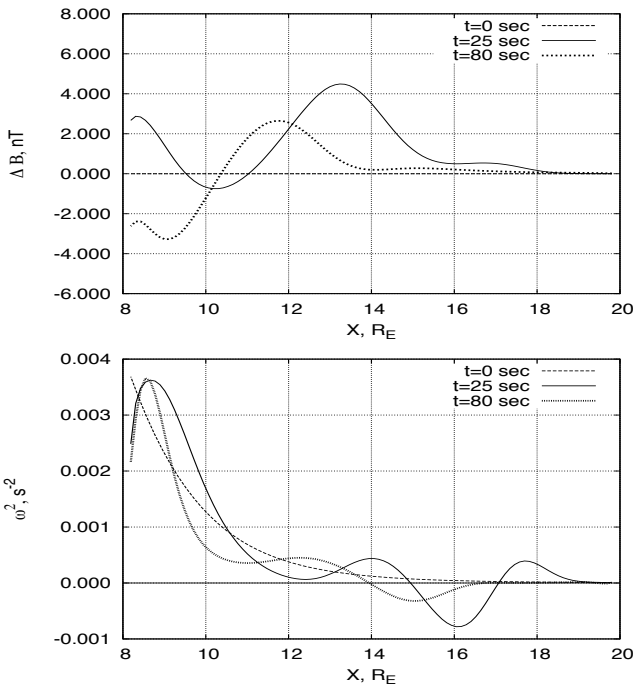


Fig. 10. Tailward pulse: magnetic field perturbation and instability growth rate profiles at different times

#### 4.2. Steady Convection

In an ideal case, the steady convection can be considered an  $E \times B$  drift, so for a dawn-to-dusk (dusk-to-dawn) electric field plasma will drift Earthward (tailward). Here we consider both directions of electric field.

We start by setting the velocity configuration using  $\mathbf{V} = \mathbf{E} \times \mathbf{B} / B^2$  which for dawn-to-dusk electric field gives an equatorial velocity field shown on Figure 11. Since the magnetic field lines are equipotential lines in this case, we can propagate the equatorial profile over the entire three-dimensional computation domain by using the following relations:

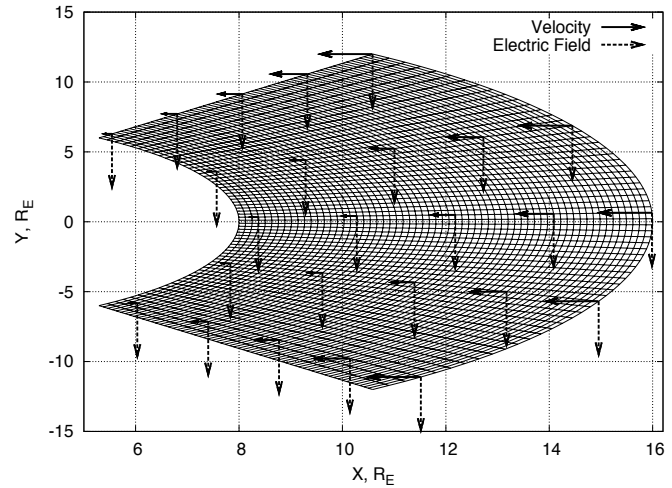
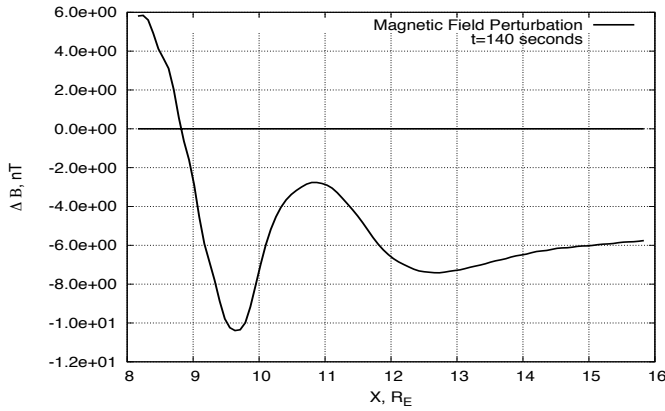


Fig. 11. Electric field and corresponding  $E \times B$  drift velocity distribution in the equatorial plane shown on the computational grid

In order to study the effect of steady convection, the electric field, and therefore velocity derived from it, at the outer domain boundary is sustained at the initial level to represent a constant plasma inflow from outside. The other boundaries are kept open, i.e. zero gradient boundary conditions are imposed.

Since the initial configuration is not an equilibrium state, the first stage of system evolution includes generation of different compressional wave modes that propagate out of the region through the open boundaries and do not play a role in the subsequent dynamics.

After the first stage, a slow evolution stage - not wave-like, takes place. Figure 12 shows that the magnetic field is carried towards the Earth building up an increased magnetic field at the close radial boundary. We find that under the influence of plasma input, the magnetic field configuration changes in such a way that a local minimum forms between 9 and 10  $R_E$  (see Figure 12) by  $t = 140$  seconds of physical time and remains at this level with minor changes until the end of simulation ( $t = 250$  seconds). The region of minimum field strength is then found to be potentially unstable with respect to the ballooning mode (Figure 13).



**Fig. 12.** Magnetic field perturbation at  $t = 140$  seconds for the case of dawn-to-dusk electric field

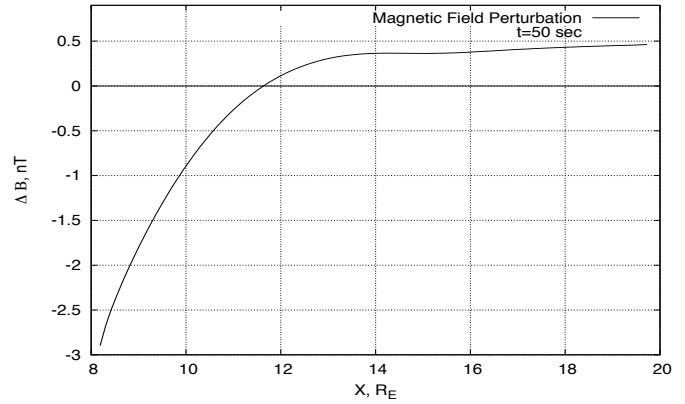


**Fig. 14.** Magnetic field perturbation at  $t = 50$  seconds for the case of dusk-to-dawn electric field

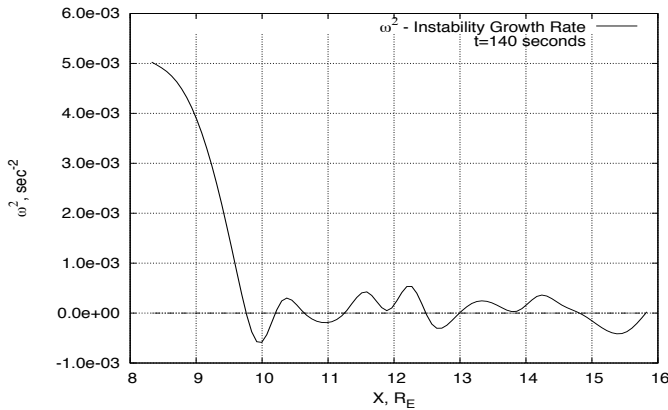


**Fig. 13.** Instability growth rate at  $t = 140$  seconds for the case of dawn-to-dusk electric field

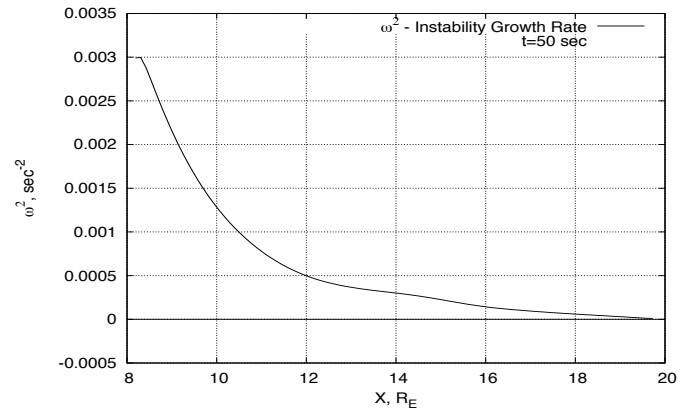


**Fig. 15.** Instability growth rate at  $t = 50$  seconds for the case of dusk-to-dawn electric field

As mentioned above, convection reversals can occur in the near-Earth magnetotail which points to the electric field reversal [15]. As a demonstration of what the inner plasma sheet dynamics may be like in that case, we ran a simulation for a uniform dusk-to-dawn electric field.

Figure 14 illustrates how the magnetic field is driven tailward so that it gradually increases tailward with no destabilizing effect since  $\omega^2 > 0$  in the region. (Figure 15).

### 5. Conclusion

In this paper we have performed a study of different factors that may affect the stability in the inner plasma sheet. We have simulated plasma dynamics in different configurations which include Earthward plasma pressure gradients, Earthward and tailward flow bursts, and convection under the influence of dawn-to-dusk and dusk-to-dawn electric fields.

It has been obtained that Earthward pressure gradients in the inner plasma sheet comparable to observed values lead to magnetic field line stretching and values of the ballooning instability growth rate above the stability threshold. A dependence between the magnitude of the pressure gradient and values of the instability growth rate has been observed and a threshold of stability found from simulations -  $0.6 \text{ nPa}/R_E$ .

The analysis of different bursty flow patterns shows that the ballooning instability can be expected for both Earthward and tailward velocity directions. We have considered two bulk flow types - bursty motion and steady convection. The Earthward flow burst forms a local min-B region where the ballooning instability is possible. The effect of the tailward burst is less significant as it does not lead to a dramatic magnetic field re-configuration, although the system may reach a marginal stability state.

In the last part, both directions of the cross-tail electric field have been modeled. Earthward convection has been found to form a localized min-B region and provide favorable conditions for development of the ballooning instability. On the other hand, tailward convection does not bring the system to an unstable state.

### References

1. Angelopoulos, V., W. Baumjohann., C. F. Kennel, F. V. Coroniti, M. G. Kivelson, R. Pellat, R. J. Walker, H. Luhr, and G. Paschmann, Bursty bulk flows in the inner center plasma sheet, *Journal of Geophysical Research*, 97, 4027, 1996.
2. Baker, D. N., T. I. Pulkkinen, V. Angelopoulos, W. Baumjohann, and R. L. McPherron, Neutral line model of substorms:

- Past results and present view. *Journal of Geophysical Research*, 101:12,975, 1996.
3. Birn, J., M. Hesse, G. Haerendel, W. Baumjohann, and K. Shiokawa, Flow braking and substorm current wedge. *Journal of Geophysical Research*, 104:19,895, 1999.
  4. Cheng, C. Z., and A. T. Y. Lui (1998), Kinetic ballooning instability for substorm onset and current disruption observed by AMPTE/CCE, *Geophys. Res. Lett.*, 25(21), 4091–4094.
  5. Dobias, P., I. O. Voronkov, and J. C. Samson, On nonlinear plasma instabilities during the substorm expansive phase onset. *Physics of Plasmas*, 11:2046, 2004.
  6. Donovan, E. F., B. J. Jackel, I. Voronkov, T. Sotirelis, F. Creutzberg, and N. A. Nicholson, Ground-based optical determination of the b2i boundary: a basis for an optical mt-index. *Journal of Geophysical Research*, 108:1115, 2003.
  7. Fairfield, D. H., T. Mukai, M. Brittnacher, G. D. Reeves, S. Kokobun, G. K. Parks, T. Nagai, H. Matsumoto, K. Hashimoto, D. A. Gurnett, and T. Yamamoto, Earthward flow bursts in the inner magnetotail and their relation to auroral brightenings, AKR intensifications, geosynchronous particle injections and magnetic activity, *Journal of Geophysical Research*, 104, 355–370, 1999.
  8. Fenrich, F. R., J. C. Samson, G. Sofko, and R. A. Greenwald, Ulf high- and low-*m* field line resonances observed with the super dual auroral radar network. *Journal of Geophysical Research*, 100:21,535, 1995.
  9. Galperin, Yu. I., A. V. Volosevich, and L. M. Zeleny, Pressure gradient structures in the tail neutral sheet as "roots of the arcs" with some effects of stochasticity, *Geophys. Res. Lett.*, 19(21), 2163–2166, 1992.
  10. Galperin, Yu. I., An onset development according to the "minimum-B" concept: further analysis, In *Substorms-5, Proceedings of the 5th International Conference on Substorms (ICS-5)*, page 291, Eur. Space Agency Spec. Publ., SP-443, 2000.
  11. Kistler, L. M., E. Möbius, W. Baumjohann, and G. Paschmann, Pressure changes in the plasma sheet during substorm injections. *Journal of Geophysical Research*, 97:2993, 1992.
  12. Lui, A. T. Y., R. E. Lopez, S. M. Krimigis, R. W. McEntire, L. J. Zanetti, and T. A. Potemra, A case study of magnetotail current sheet disruption and diversion, *Geophys. Res. Lett.*, 15(7), 721–724, 1988.
  13. Lui, A. T. Y., A synthesis of magnetospheric substorm models, *Journal of Geophysical Research*, 96(A2), 1849–1856, 1991.
  14. Lui, A. T. Y., R. E. Lopez, B. J. Anderson, K. Takahashi, L. J. Zanetti, R. W. McEntire, T. A. Potemra, D. M. Klumpar, E. M. Greene, and R. Strangeway, Current disruptions in the near-earth neutral sheet region. *Journal of Geophysical Research*, 97:1461, 1992.
  15. Lyons, L. R., A new theory for magnetospheric substorms, *Journal of Geophysical Research*, 100(A10), 19,069–19,082, 1995.
  16. Lyons, L. R., I. O. Voronkov, E. F. Donovan, and E. Zesta, Relation of substorm breakup arc to other growth-phase auroral arcs. *Journal of Geophysical Research*, 107:1390, 2002.
  17. Mann, I. R., I. Voronkov, M. Dunlop, E. Donovan, T. K. Yeoman, D. K. Milling, J. Wild, K. Kauristie, O. Amm, S. D. Bale, A. Balogh, A. Viljanen, and H. J. Opgenoorth, Coordinated ground-based and cluster observations of large amplitude global magnetospheric oscillations during a fast solar wind speed interval. *Ann. Geophys.*, 20:1, 2002.
  18. Ohtani, S., F. Creutzberg, T. Mukai, H. Singer, A. T. Y. Lui, M. Nakamura, P. Prikryl, K. Yumoto, and G. Rostoker, Substorm onset timing: The December 31, 1995, event, *J. Geophys. Res.*, 104(A10), 22,713–22,728, 1999.
  19. Ohtani, S., K. Takahashi, L. J. Zanetti, T. A. Potemra, R. W. McEntire, and T. Iijima, Initial signatures of magnetic field and energetic particle fluxes at tail reconfiguration: Explosive growth phase. *Journal of Geophysical Research*, 97:19,311, 1992.
  20. Ruohoniemi, J. M., R. A. Greenwald, and K. B. Baker. Hf radar observations of pc 5 field line resonances in the mid-night/early morning mlt sector. *Journal of Geophysical Research*, 96:15,697, 1991.
  21. Samson, J. C., L. R. Lyons, P. T. Newell, F. Creutzberg, and B. Xu, Proton aurora and substorm intensifications. *Geophys. Res. Lett.*, 19:2167, 1992.
  22. Samson, J. C. Mapping substorm intensifications from the ionosphere to the magnetosphere. In J. R. Kan, J.D. Craven, and S.-I. Akasofu, editors, *SUBSTORM-2, International Conference on Substorms-2*. Univ. of Alaska, Fairbanks, 1994.
  23. Samson, J. C., L. L. Cogger, and Q. Pao, Observations of field line resonances, auroral arcs and auroral vortex structures. *Journal of Geophysical Research*, 101:17,793, 1996.
  24. Samson, J. C., R. Rankin, and I. Voronkov, Field line resonances, auroral arcs, and substorm intensifications. In J.L. Horwitz, editor, *Geospace Mass and Energy Flow: Results from the International Solar-Terrestrial Physics Program*, *Geophys. Monogr. Ser.*, volume 104, page 161. AGU, Washington, D.C., 1998.
  25. Sergeev, V. A., R. J. Pellinen, and T. I. Pulkkinen, Steady magnetospheric convection: Review of recent results, *Space Sci. Rev.*, 75, 551, 1996.
  26. Shiokawa, K., W. Baumjohann, and G. Haerendel, Braking of high-speed flows in the near-earth tail. *Geophys. Res. Lett.*, 10:1179, 1997.
  27. Voronkov, I. O., E. F. Donovan, B. J. Jackel, and J. C. Samson, Large-scale vortex dynamics in the evening and midnight auroral zone: Observations and simulations. *Journal of Geophysical Research*, 105:18,505, 2000.
  28. Voronkov, I. O., E. F. Donovan, and J. C. Samson, Observations of the phases of the substorm. *Journal of Geophysical Research*, 108:1073, 2003.
  29. Voronkov, I. O., E. F. Donovan, P. Dobias, V. I. Prosolin, M. Jankowska, and J.C. Samson, Late growth phase and breakup in the near-earth plasma sheet. In *Proceedings of the 7th International Conference on Substorms (ICS-7)*. 140, 2004.

# Thin current sheets as part of the substorm process

T. I. Pulkkinen, C. C. Goodrich, J. G. Lyon, and H. J. Singer

**Abstract:** This paper reviews properties of thin current sheets and their association with a variety of magnetospheric activations. It is demonstrated that thin current sheets are a major part of substorm growth phases as well as of sawtooth events and steady convection intervals. Observations, empirical models, and MHD simulations suggest that thin current sheets have thickness of the order of ion gyroradius, cross-tail width about 15–25  $R_E$  and along-tail dimension of about 20  $R_E$ . The current sheet inner edge is typically at or slightly tailward of geostationary orbit; during storms it can extend around the Earth in the duskward direction. As global simulations suggest that the magnetotail flow is diverted around the thin current sheet to the flanks in the inner part of the tail, the temporal scale associated with the current sheet intensification and thinning may play a role in determining the type of activity developing in the magnetotail.

*Key words:* Substorms, Thin current sheets, MHD simulations.

## 1. Introduction

Formation of an intense and thin current sheet in the inner part of the magnetotail is a well-documented feature of the substorm growth phase. This process is an indication of flux loading in the magnetotail as a consequence of enhanced dayside reconnection following southward turning of the interplanetary magnetic field (IMF) [1]. However, it has been shown that the thinning is stronger than that obtained by compression by the enhanced lobe pressure. Theoretically, it has been argued that thin current sheets are formed as a response to changing boundary conditions at the magnetopause [18].

It has been suggested that thin current sheets play an important role in the substorm onset process by thinning the tail sufficiently to demagnetize the ions and thereby destabilizing the ion tearing instability and initiating reconnection in the mid-magnetotail [3]. While the current sheet has been demonstrated to reach such small thickness values [14, 19, 17], the tearing instability growth conditions are still under debate [12].

During isolated substorms, thin current sheet formation is a slow process with gradual thinning over the duration of the growth phase (typically 30–60 min). At onset, this current is disrupted, which leads to rapid reconfiguration of the tail field to a more dipolar state. During the recovery phase, gradual tail current buildup brings the tail to its nominal state. On the other hand, the role of thin current sheets during storms, storm-time substorms, sawtooth events, or steady convection periods (SMC) has not been systematically examined.

We review properties of thin current sheets during a variety of activity conditions. The results are derived from observations, empirical models, and global magnetohydrodynamic (MHD) simulations. Section 2 briefly reviews the methodology while sections 3, 4, and 5 present results for isolated substorms, sawtooth events, and SMC periods, respectively.

Received 15 May 2006.

**T. I. Pulkkinen.** Los Alamos National Laboratory, Los Alamos, NM

**C. C. Goodrich.** Boston University, Center for Space Physics, Boston, MA

**J. G. Lyon.** Dartmouth College, Dept. of Physics and Astronomy, Hanover, NH

**H. J. Singer.** Space Environment Center, Boulder, CO

## 2. Methodology

Empirical magnetic field models [22, 23] give an average representation of the magnetospheric field configuration based on statistical fitting of parametrized current systems to a large number of spacecraft observations. While these models provide a good general understanding of the magnetic environment, they do not necessarily give an accurate representation of the field for individual events, especially during complex magnetic activity. However, these models have been used as starting points for event-specific models created by fitting the field model to data from individual substorms [14]. The fitting procedure includes current systems in the statistical model together with added current systems representing the (growth-phase-associated) thin current sheet at the tail center [14] and storm-time symmetric and partial ring currents in the inner magnetosphere [5]. The resulting time-evolving models have been shown to provide quite an accurate representation of magnetospheric magnetic field when sufficient data are available for the fitting procedure.

Global MHD simulations are presently the only means to model the large-scale dynamic evolution of the coupled solar wind – magnetosphere – ionosphere system in a self-consistent way. The Lyon-Fedder-Mobarry (LFM) global MHD simulation solves the ideal MHD equations in the solar wind and the magnetosphere, and is coupled to an electrostatic, height-integrated ionosphere via field-aligned currents at the inner boundary [4]. The simulation is driven by measured solar wind and IMF values at the external boundaries as well as the F10.7 flux that controls the level of ionization in the ionosphere. The spatial resolution in the code is variable, with highest resolution within the inner magnetosphere, plasma sheet, and boundaries where the gradients can be expected to be largest. Comparisons of simulation results with high-altitude satellite data as well as with ionospheric parameters show that these simulations can quite realistically represent a variety of dynamic conditions in the magnetotail [24].

## 3. Isolated substorm

During isolated substorms, when the tail is in a relatively low-energy state at the beginning of the growth phase, the formation of the thin current sheet is clearly seen as an enhancement

of  $B_X$  and a decrease in  $B_Z$  both in the inner and midtail. Figure 1 shows an example of a substorm during which the magnetotail field was monitored by GOES-8 and GOES-9 at geostationary orbit, Geotail in the plasma sheet, and Interball Tail probe in the tail lobe (all in GSM coordinates) [13]. As Geotail was relatively close to the current sheet center, it was possible to deduce that the current sheet became thinner than it would only following from compression caused by the lobe flux increase (which would be about a factor of 2 for a lobe flux increase from 20 to 30 nT). Thus, the thin current sheet was embedded within the (pre-existing) thicker plasma sheet.

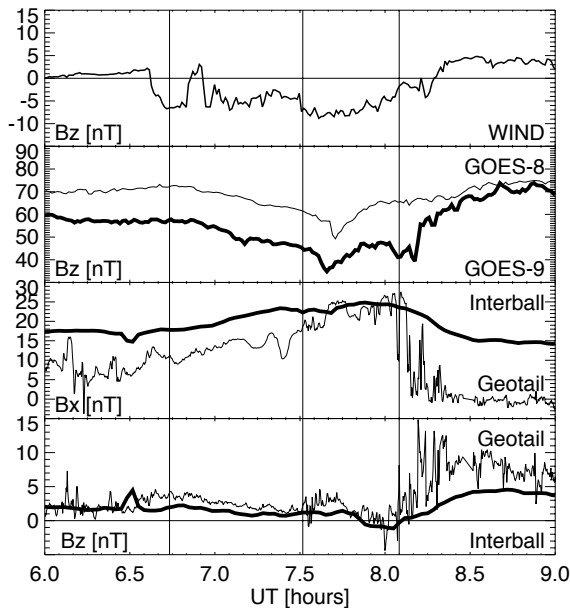


**Fig. 1.** Substorm on Dec 10, 1996: From top to bottom: IMF  $B_Z$  from Wind,  $B_Z$  from GOES-8 (thin line) and GOES-9 (thick line),  $B_X$  and  $B_Z$  from Geotail (thin line) and Interball (thick line). The vertical lines mark the beginning of substorm growth phase and two following onsets determined from the Geotail measurements and ground magnetic data, respectively [13].

Empirical magnetic field modeling for the growth phase of this substorm using methods developed in [14] show that a thin and intense current sheet was formed with its earthward edge slightly tailward of geostationary orbit. In the tailward and cross-tail directions, the current sheet extended at least to the satellite locations, but from this technique it is difficult to limit the extent of the current sheet. However, the model gave lower limits of  $-20R_E$  in the tailward and  $15R_E$  in the cross-tail direction [13].

The LFM simulation was run for this event at high resolution with smallest gridsize of  $0.3 R_E$ . Figure 2 shows a cut near the equatorial plane of the plasma sheet with the cross-tail current intensity color-coded and velocity vectors shown with white arrows. The thin current sheet in the simulation is the region of highest current density shown with the warmer colors, roughly extending from  $-8R_E$  to  $-20R_E$  along the tail and from  $-5R_E$  to  $5R_E$  in the cross-tail direction. The thin cur-

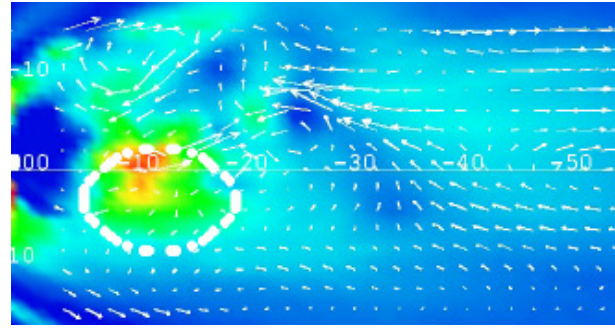


**Fig. 2.** Substorm on Dec 10, 1996: LFM simulation results at  $Z = \text{const}$  plane near the current sheet center. The color coding shows the cross-tail current intensity with warmer colors showing larger intensity. The arrows show the flow velocity and the dotted circle marks the thin current sheet location in the empirical magnetic field model (see text, after [13]).

rent sheet identified from the empirical magnetic field model described above is shown with the white dotted circle. In this case, the empirical model and the MHD simulation were in excellent agreement. Similar values obtained for other events suggest that a typical location of thin current sheets extends from slightly beyond geosynchronous orbit out to  $20\text{--}30 R_E$  in the tail, i.e., to the typical location of the near-Earth reconnection site [9].

#### 4. Sawtooth event

Sawtooth events are strong, quasiperiodic injections observed most clearly in geosynchronous orbit ion measurements [2, 7]. These events resemble large substorms in many ways, but have received special attention due to their large azimuthal extent and quasi-periodicity. Sawtooth events are almost always associated with magnetic storms during which the enhanced ring current allows for activity development close to the Earth.

Figure 3 shows a sample sawtooth event that occurred during a magnetic cloud passage. The main phase of the storm was driven by the sheath region of the cloud, while the cloud proper had  $B_Z$  northward at the leading edge and southward at the trailing edge [15]. The sawtooth event commenced as soon as the IMF turned southward within the cloud; during the following 10 hours, four clear sawtooth-like injections were recorded at multiple locations around the geostationary orbit.

During the sawtooth oscillations, two LANL geostationary satellites, LANL-97A and 1994-084 were passing through the evening-midnight sector magnetosphere. These satellites carry magnetospheric plasma analyzers (MPA) that measure electrons and protons in the energy range from below 1 keV up to 40 keV. The magnetic field inclination can be deduced from the electron or ion pitch-angle symmetry properties [21]. Both satellites recorded extremely strong stretching of the night and dusk sector field, with very low field inclination values even several hours away from midnight. Figure 3 shows the field inclination measurements together with the energetic electron data from the synchronous orbit particle analyzer (SOPA) onboard 1994-084.

The empirical magnetic field model for this event revealed a very strong modulation of the cross-tail current by the sawtooth

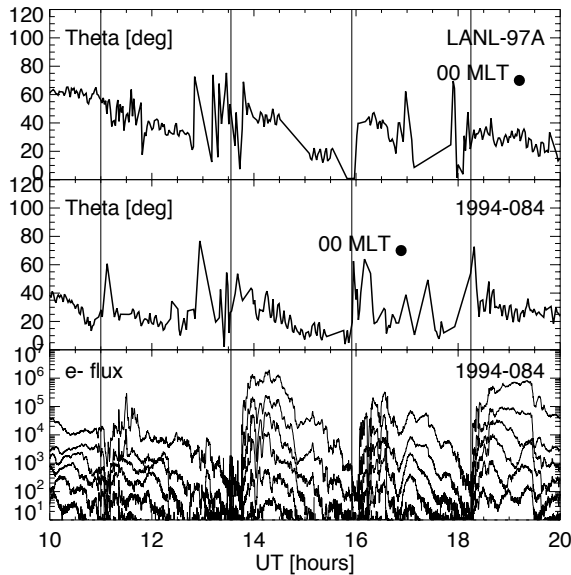


**Fig. 3.** Sawtooth event on Oct 22, 2001: Magnetic field inclination from geostationary satellites LANL-97A and 1994-084. Bottom panel shows electron flux in the energy range from 50 keV to 300 keV from s/c 1994-084 (after [15]).

injections. The current increased strongly between the sawteeth, while the injections were followed by abrupt decreases in the current intensity [15]. As shown in Figure 4, the event was characterized by a strongly asymmetric partial ring current in the dusk sector that varied in phase with the cross-tail current. The strong activity brought the thin current sheet inside geostationary orbit and drifting particles extended the current sheet to the dusk sector. The sawtooth injections periodically disrupted part of this current, but the field never fully dipolarized to values exceeding the quiet-time inclination value. This behavior is characteristic of sawtooth events, but is also often found during other stormtime activations [11].

Thus, in this case the activity was strong enough to bring the cross-tail current to the synchronous orbit, and the thin current sheet had a larger than typical cross-tail size extending around the Earth to the dusk sector. The sawtooth injections disrupted this current in a manner quite similar to current disruptions observed in association with substorm onsets.

## 5. Steady convection event

The steady convection event on Feb 3–4, 1998, was driven by an interplanetary magnetic cloud that had a steadily southward  $B_Z$ , a slowly rotating  $B_Y$ , and positive  $B_X$ . The solar wind velocity had a large component away from the Sun-Earth line, which led to rotation of the entire magnetotail in the direction of the solar wind flow. The  $V_Z$  component varied but reached values close to  $-100$  km/s, while  $V_Y$  rotated from about  $50$  km/s to  $-50$  km/s (Figure 5). The cloud caused only moderate activity with Kp between 2 and 4 during the event

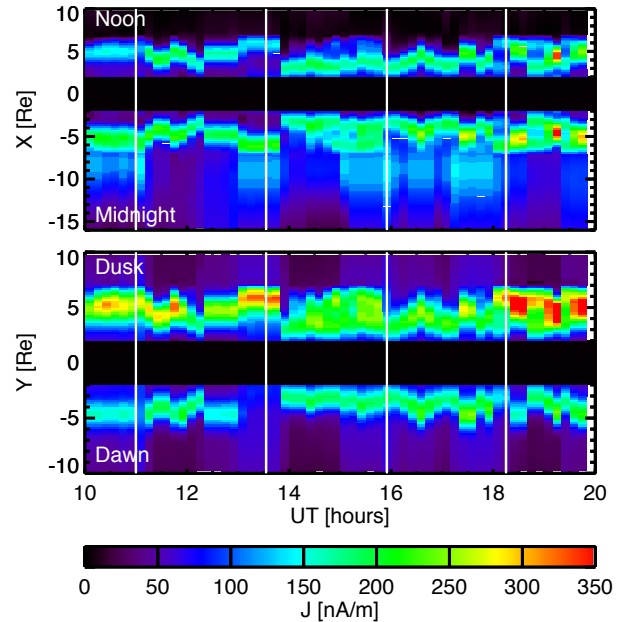


**Fig. 4.** Sawtooth event on Oct 22, 2001: Empirical magnetic field model results of  $Z$ -integrated current intensity through the noon-midnight (top panel) and dawn-dusk (bottom panel) meridians (after [15]).

and Dst minimum at about  $-40$  nT.

While the dayside geostationary field was close to quiet-time values as measured by GOES-8 and GOES-9, the nightside field inclination inferred from the MPA data from spacecraft 1994-084 and LANL-97A indicate that the inner tail field was stable and continuously more stretched than during quiet times. Geotail was at  $\sim X = -30R_E$  slightly below the GSM  $Z = 0$  plane. Immediately following the event onset, the magnetic field increased and temperature and density showed very small values (data not shown). These data indicate that Geotail moved to the northern tail lobe where it stayed throughout the SMC interval. Because the large solar wind velocity tilted the tail away from the Sun-Earth line, Figure 5 shows the Geotail magnetic field measurements rotated to a coordinate system aligned with the flow velocity vector. In this coordinate system it is clear that the magnetic field was very close to radial and that the field component normal to the current sheet at Geotail location was almost zero.

The LFM simulation was run for this event at a resolution which gives smallest cell size at the current sheet of about  $1R_E$ , which naturally limits the model capability to reproduce current sheet features below this scale. However, the simulation shows excellent agreement with both geosynchronous orbit and tail field measurements indicating that the large-scale properties of the current sheet are consistent with those observed. Figure 6 shows a comparison of both the geostationary orbit field inclination and Geotail (all in GSM coordinates) with the model results.

The LFM results show that immediately following the event onset, the tail organized into a very stable configuration where the plasma sheet was relatively thick, but had an embedded

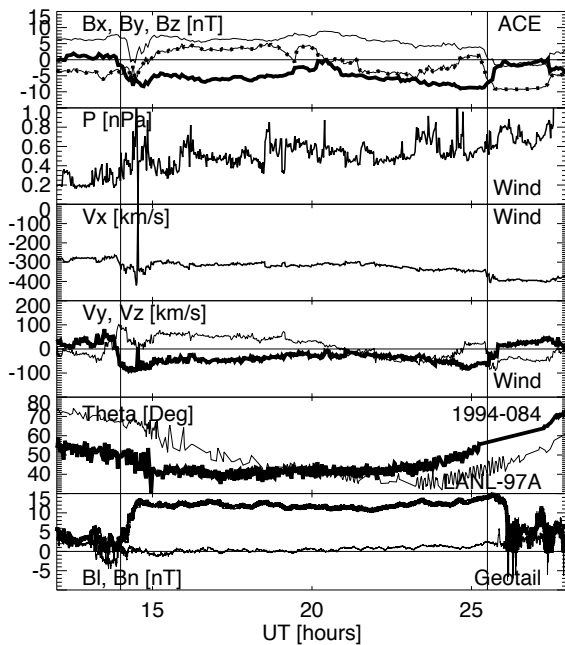


**Fig. 5.** SMC event on Feb 3–4, 1998: From top to bottom: IMF  $B_X$  (thin line),  $B_Y$  (dotted) and  $B_Z$  (Thick line) from ACE, propagated to subsolar point by 75 min. Solar wind dynamic pressure,  $V_X$ ,  $V_Y$  (thin line), and  $V_Z$  (thick line) from Wind, propagated to the subsolar point by 75 min. Geosynchronous orbit field inclination from LANL-97A (thin line) and from 1994-084 (thick line). Geotail magnetic field measurements rotated to coordinates along the solar wind flow velocity vector,  $B_{lobe}$  (thick line) and  $B_{normal}$  (thin line).

current sheet that had a scale size of about  $1R_E$ , i.e., thickness of the order of the grid spacing. The current sheet inside of  $X = -30R_E$  was remarkably stable throughout the event. There was a quasi-steady-state large-scale reconnection site at about  $X = -30R_E$  [6], but instead of disrupting the current sheet, flows from the reconnection region were diverted to the flanks around the thin current sheet. Thus, the persistent thin current sheet was a key factor in maintaining tail stability over the extended period of enhanced driving.

Figure 7 shows a side view and Figure 8 a top view of a rendering of  $B/|\nabla \times \mathbf{B}|$ , which is a proxy for the scale length in the direction perpendicular to the current sheet. As the rendering looks through all  $Y$  or  $Z$ -values, it is not sensitive to the correct choice of the cut-plane, but reflects the properties of the current sheet at all values perpendicular to the plane shown. The side view illustrates the steady thickness scale of the order of an Earth radius of the current sheet throughout the central part of the tail as well as the southward tilting of the current sheet in response to the nonradial component of the solar wind flow. The top view shows the flows originating from the reconnection region and how the flows are diverted around the current sheet without disrupting the current. It is clear that smaller-scale activity is created by the reconnection flows, but that the activity does not reach the inner part of the tail and does not cause global reconfigurations such as those observed during substorms.

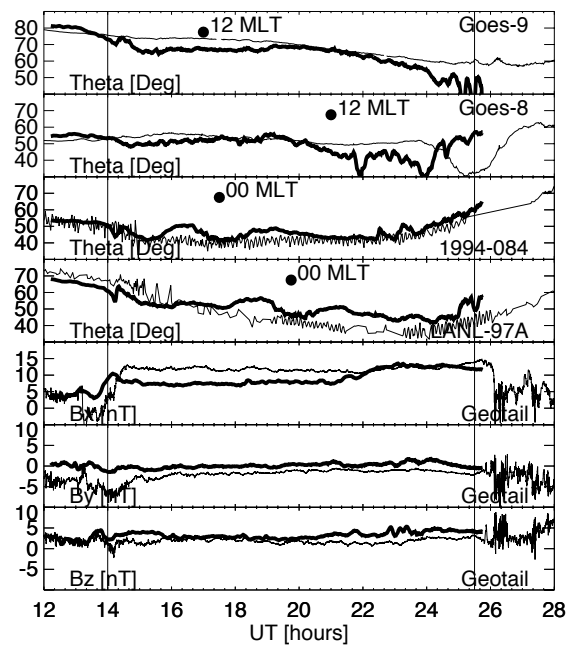


**Fig. 6.** SMC event on Feb 3–4, 1998: From top to bottom: Field inclination from GOES 9, GOES-8, 1994-084, and LANL-97A and 1984-084, and Geotail  $B_X$ ,  $B_Y$ , and  $B_Z$ . Data (in GSM coordinates) are shown with thin lines and LFM simulation results with thick lines.

## 6. Discussion

In response to solar wind driving, the magnetosphere can enter a variety of dynamic cycles to process the energy entering through enhanced dayside reconnection. In the large scale, tail reconnection in some form is required to maintain flux balance between the open tail lobes and the closed plasma sheet region. However, flow bursts, pseudobreakups, substorms, steady convection events, and sawtooth events can all accomplish the flux balance while their dynamics in the magnetosphere – ionosphere system is very different. Magnetic storms can host a variety of these activations in addition to a strong enhancement of the inner magnetosphere ring current, which allows activity to develop much closer to the Earth than during non-storm conditions.

Global MHD simulations are excellent tools to monitor the large-scale evolution of the tail plasma sheet during a variety of driving conditions. The LFM simulations consistently show that as the IMF turns southward, the inner part of the tail becomes thinner and the current intensity increases at the tail center in a region Earthward of about  $X = -20 \dots -30R_E$ . The concentration of the current and changes in the inner part of the magnetosphere are easily explained by following Poynting flux flow lines from the solar wind to the magnetosphere [10]: Poynting flux ( $S = E \times B/\mu_0$ ) entering through the magnetopause into the tail lobe is directed toward the tail center, and as the field tilts northward closer to the current sheet, the Poynting flux is directed Earthward. Thus, it is natural that the largest changes are associated with the region where the dipole field still gives a contribution to the total field.

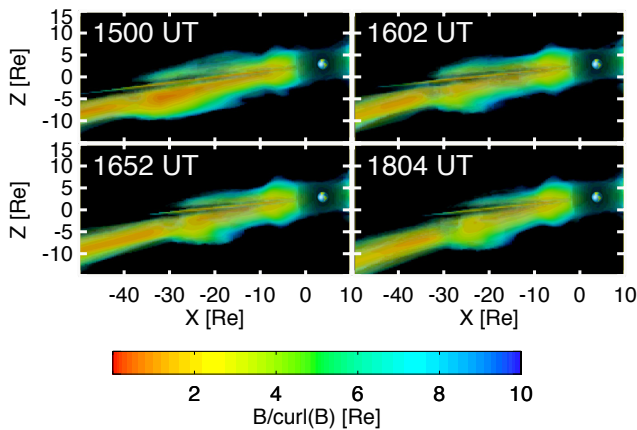


**Fig. 7.** SMC event on Feb 3–4, 1998: Side view of the current sheet at four time instants, at 1500, 1602, 1652, and 1804 UT. The color coding shows a perpendicular scale length ( $B/|\nabla \times \mathbf{B}|$ ) in units of  $R_E$ . The fine line across the current sheet is an artefact arising from the grid structure.

As the driving continues, reconnection starts near the tailward end of the current sheet and fast flows begin to enter the inner magnetosphere. In the LFM simulation, the dynamics and consequences of these flows are different for substorms, sawtooth events, and steady convection periods. During substorms, fast but relatively narrow flow channels are formed already during the growth phase (one example can be seen in Figure 2). These flow channels may disrupt part of the current sheet, but most of the time get diverted back tailward before affecting the current sheet very much [24]. At substorm onset, the flow channels merge to form a large-scale reconnection region and fast flows that disrupt the cross-tail current in the inner tail. Steady convection periods have a relatively large-scale reconnection region from early on, but the flows are mostly diverted toward the flanks leaving the current sheet intact (see Figures 7 and 8). The flows fed by a large-scale reconnection region associated with sawtooth events are much more complicated with flow channels occasionally gaining access to the inner parts of the tail partially disrupting the inner tail current [6]. The simulations seem to indicate that the type of magnetospheric activity is determined by the interplay of the reconnection flows and the thin current sheet in the inner tail.

Observations and empirical models suggest that the thin current sheet has a scale thickness of a fraction of  $R_E$ , comparable to the local thermal ion gyroradius. The MHD simulations tend to give current sheet thicknesses of the order of the simulation gridsize; increasing resolution leads to thinner current sheets. As the current sheet reaches such small thickness, the ions within the current sheet become non-magnetized and the electron and ion motions are decoupled. While the reconnection region is typically found to be around  $25 - 30R_E$  distance, the nonadiabatic regime can extend to  $8 - 10R_E$  or during stronger activity even close to geostationary orbit. It thus seems that rather than triggering reconnection onset, the role of the nonadiabatic motion is to allow the flows initiated by bursts of reconnection to enter the inner parts of the tail and disrupt the intense current. This still leaves open the question why or

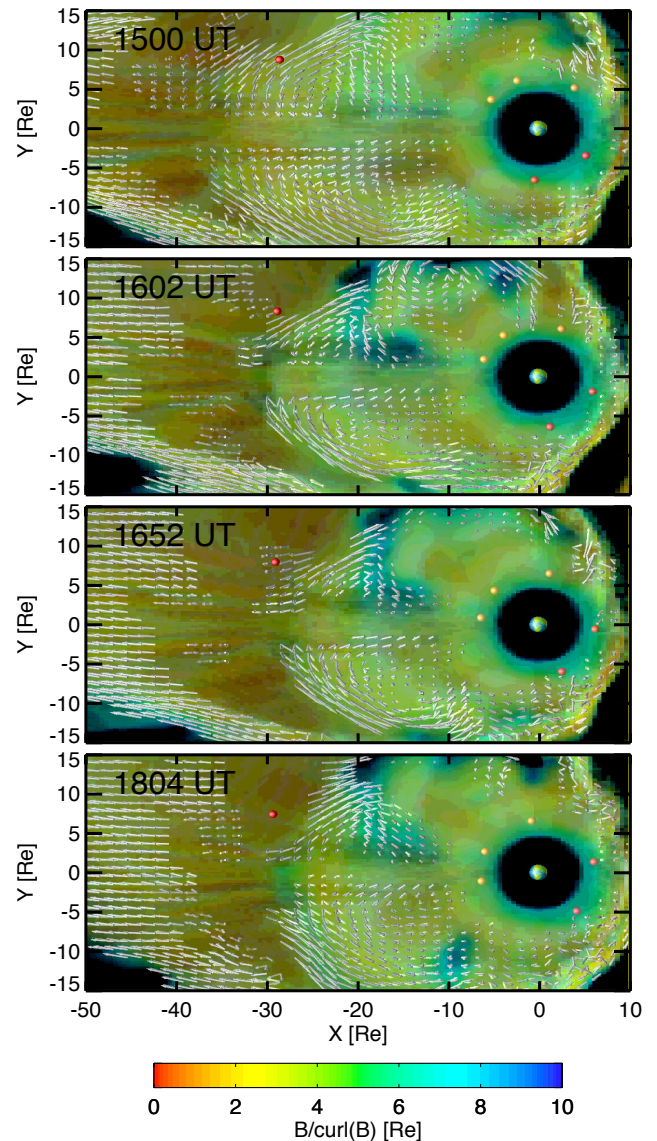


**Fig. 8.** SMC event on Feb 3–4, 1998: Top view of the current sheet at four time instants, at 1500, 1602, 1652, and 1804 UT. The color coding shows a perpendicular scale length ( $B/|\nabla \times \mathbf{B}|$ ) in units of  $R_E$  and the flow velocity is shown by arrows.

how reconnection is initiated in the midtail; in the MHD simulations tail reconnection seems to be quite directly driven by the external conditions and the amount of energy entering the magnetosphere [8, 16].

An interesting feature observed during storms is the extension of the thin current sheet duskward (or sometimes dawnward) such that the geostationary field can become highly stretched even several hours away from midnight. Especially, during sawtooth events, the combination of the partial ring current and cross-tail current is very strong such that even the intense sawtooth injections can only partially disrupt this current (see Figures 3 and 4). Such a current configuration also leads to the geostationary orbit being in the region of open drift paths,

which limits the number of particles that can obtain trapped orbits and leads to the typically relatively constant values of the Dst index throughout sawtooth events [15]. However, despite the different geometry of the current sheet, the dynamics seems to be quite similar to those limited to the tail region.

In summary, thin current sheets play a major role in controlling the magnetospheric dynamics. Flows entering the inner part of the tail are diverted by the intense current; this occurs during substorm growth phases as well as during SMCs and between sawtooth injections. Global reconfigurations such as substorm onsets or sawtooth injections occur when the flows finally enter the current sheet leading to its disruption and consequent field dipolarization. Future work is needed to address how much the current sheet dynamics is controlled by internal magnetospheric (or ionospheric) processes and to which extent the dynamics is driven by the driving solar wind and IMF characteristics.

### Acknowledgements

Dr. K. Ogilvie (PI for Wind SWE) and Dr. C. Smith (PI for ACE MFI) are acknowledged for providing the solar wind observations obtained through the CDAWeb data facility operated and maintained by the NSSDC. We thank T. Nagai and the DARTS system at ISAS for making the Geotail LEP and MFI data available.

### References

- Baker, D. N., T. I. Pulkkinen, V. Angelopoulos, W. Baumjohann, and R. L. McPherron, The neutral line model of substorms: Past results and present view, *J. Geophys. Res.*, *101*, 12,975, 1996.
- Belian, R. D., T. E. Cayton, and G. D. Reeves, Quasi-periodic global substorm-generated variations observed at geosynchronous orbit, in: *Space plasmas: Coupling between small and medium scale processes*, Geophys. Monogr., 86, AGU, Washington DC 2009, p. 143, 1995.
- Büchner, J., and L. M. Zelenyi, Chaotization of the electron motion as the cause of an internal magnetotail instability and substorm onset, *J. Geophys. Res.*, *92*, 13456, 1987.
- Fedder, J. A., S. P. Slinker, J. G. Lyon, and R. D. Elphinstone, Global numerical simulation of the growth phase and expansion onset for a substorm observed by Viking, *J. Geophys. Res.*, *100*, 19,083, 1995.
- Ganushkina, N. Yu., T. I. Pulkkinen, M. V. Kubyshkina, H. J. Singer, and C. T. Russell, Long-term evolution of magnetospheric current systems during storm periods, *Ann. Geophys.*, *22*, 1317, 2004.
- Goodrich, C. C., et al., this issue.
- Henderson, M. G., G. D. Reeves, R. Skoug, M. F. Thomsen, M. H. Denton, S. B. Mende, T. J. Immel, P. C. Brandt, and H. J. Singer, Magnetospheric and auroral activity during the 18 April 2002 sawtooth event, *J. Geophys. Res.*, *111*, A01S90, doi:10.1029/2005JA011111, 2006.
- T. V. Laitinen, T. I. Pulkkinen, M. Palmroth, P. Janhunen, and H. E. J. Koskinen, The magnetotail reconnection region in a global MHD simulation, *Ann. Geophys.*, *23*, 3753, 2005.
- Nagai, T., M. Fujimoto, Y. Saito, S. Machida, T. Terasawa, R. Nakamura, T. Yamamoto, T. Mukai, A. Nishida, and S. Kokubun, Structure and dynamics of magnetic reconnection for substorm onsets with Geotail observations, *J. Geophys. Res.*, *103*, 4419, 1998.
- Papadopoulos, K., C. Goodrich, M. Wiltberger, R. Lopez, and J. G. Lyon, The physics of substorms as revealed by the ISTP, *Phys. Chem. Earth (c)*, *24*, 189, 1999.
- Partamies, N., T. I. Pulkkinen, E. I. Tanskanen, G. D. Reeves, E. F. Donovan, H. J. Singer, J. A. Slavin, R. L. McPherron, and M. Henderson, Strong stretching in dusk sector: storm-time substorms and sawtooth events compared, *this issue*, 2006.
- Pellat, R., F. Coroniti, and P. L. Pritchett, Does iontearing exist? *Geophys. Res. Lett.*, *18*, 143, 1991.
- Pulkkinen, T. I., and M. Wiltberger, Thin Current Sheet Evolution as seen in Observations, Empirical Models and MHD Simulations, *Geophys. Res. Lett.*, *27*, 1363, 2000.
- Pulkkinen, T. I., D. N. Baker, R. J. Pellinen, J. Büchner, H. E. J. Koskinen, R. E. Lopez, R. L. Dyson, and L. A. Frank, Particle scattering and current sheet stability in the geomagnetic tail during the substorm growth phase, *J. Geophys. Res.*, *97*, 19,283, 1992.
- Pulkkinen, T. I., N. Yu. Ganushkina, E. I. Tanskanen M. Kubyshkina, G. D. Reeves, C. T. Russell, H. J. Singer, J. A. Slavin, Magnetospheric current systems during stormtime sawtooth events, *J. Geophys. Res.*, submitted, 2006.
- Pulkkinen, T. I., M. Palmroth, E. I. Tanskanen, P. Janhunen, H. E. J. Koskinen, and T. V. Laitinen, New interpretation of magnetospheric energy circulation, *Geophys. Res. Lett.*, *33*, L07101, doi:10.1029/2005GL025457, 2006.
- Runov, A., R. Nakamura, W. Baumjohann, R. A. Treumann, T. L. Zhang, M. Wolwerk, Z. Voros, A. Balogh, K.-H. Glassmeier, B. Klecker, H. Reme, and L. Kistler, Current sheet structure near magnetic X-line observed by Cluster, *Geophys. Res. Lett.*, *30*, 11, 1579, doi: 10.1029/2002GL016730, 2003.
- Schindler, K., and J. Birn, On the cause of thin current sheets in the near-Earth magnetotail and their possible significance for magnetospheric substorms, *J. Geophys. Res.*, *98*, 15477, 1993.
- Sergeev, V. A., D. G. Mitchell, C. T. Russell, D. J. Williams, Structure of the tail plasma/current sheet at 11 Re and its changes in the course of a substorm, *J. Geophys. Res.*, *98*, 17345, 1993.
- Thomsen, M. F., S. J. Bame, D. J. McComas, M. B. Moldwin, K. R. Moore, The magnetospheric lobe at geosynchronous orbit, *J. Geophys. Res.*, *99*, 17,283, 1994.
- Thomsen, M. F., D. J. McComas, G. D. Reeves, and L. A. Weiss, An observational test of the Tsyganenko (T89a) model of the magnetospheric field, *J. Geophys. Res.*, *101*, 24827, 1996.
- Tsyganenko, N. A., Magnetospheric magnetic field model with a warped tail current sheet, *Planet. Space Sci.*, *37*, 5, 1989.
- Tsyganenko, N. A., Modeling the Earth's magnetospheric magnetic field confined within a realistic magnetopause, *J. Geophys. Res.*, *100*, 5599, 1995.
- Wiltberger, M., T. I. Pulkkinen, J. G. Lyon, and C. C. Goodrich, MHD simulation of the magnetotail during the December 10, 1996 substorm, *J. Geophys. Res.*, *105*, 27649, 2000.

# Pi2 pulsations: field line resonances or a driven response?

I. J. Rae, I. R. Mann, D. K. Milling, Z. C. Dent, and A. Kale

**Abstract:** We present an interval on 7<sup>th</sup> March 2004 whereby clear quasi-periodic Pi2 pulsations are observed following the onset of an isolated magnetospheric substorm. During this interval, we successfully employ cross-phase analysis techniques to recreate discrete points along the Alfvén continuum for the first time following the substorm expansion phase onset. Using the complex demodulation analysis technique, we study the latitudinal and longitudinal properties of the Pi2 pulsations in terms of amplitude, phase, ellipticity and polarisation and demonstrate that the Pi2 pulsations have the characteristics of a driven field line resonance. These results allow us to answer a long-standing question in substorm physics; whether the frequency of the high-latitude Pi2 pulsation results from a directly-driven response to a magnetotail driver, or from the properties of the magnetospheric field lines. We find that, at least in this event study, that the Pi2 structure is most likely determined from inherent frequencies of the nightside magnetosphere including the natural frequencies of the standing Alfvén waves, specifically resulting in a monochromatic field line resonance (FLR), rather than any variation in the temporal dynamics of the magnetotail driver.

*Key words:* ULF waves, Field Line Resonance, Pi2, substorm.

## 1. Introduction

Ultra Low Frequency (ULF) wave activity has been associated with the auroral substorm for nearly 40 years [1]. More specifically, the time of substorm onset has been shown to be concurrent with the excitation of impulsive pulsations in the Pi2 (40–200s or 6–25 mHz) frequency range [7]. The origin of Pi2s is thought to be disturbances in the near-Earth plasma sheet, resulting in the generation of field aligned currents in the substorm current wedge. The field-aligned currents are carried by the transient, transverse Alfvén wave generated during substorm onset. If there is an impedance mismatch between the incident Alfvén wave and the ionosphere, then the wave may be partially reflected. The Alfvén wave can thus bounce between the Central Plasma Sheet (CPS) and ionosphere, giving rise to the decaying periodic Pi2 waveform [3, 13]. In ground-based magnetograms, this creates the well-known observation of Pi2 pulsations “riding on” the magnetic bays associated with the substorm current wedge (SCW).

In addition to the auroral zone Pi2 pulsations related to establishing the substorm current wedge, Pi2 pulsations may also be observed over a wider range of latitude and longitude away from the onset region. A range of authors have proposed that CPS disturbances at substorm onset may excite compressional fast mode waves. These fast mode waves may impact the plasmasphere, generating compressional plasmaspheric cavity mode Pi2 signatures [15], or propagate towards the flanks where they may excite a field line resonant Pi2 signature. In some cases, substorm onset has been linked to the Earthward propagation of Bursty Bulk Flows (BBFs) [2]. Braking of these BBFs may generate inertial field-aligned currents, which may also be established by Alfvén waves with a Pi2 signature, in ad-

dition to possibly directly-driving Pi2 waveforms identical to the flow burst structure within the BBF [8, 9, 10]. An extensive review of Pi2 pulsations is provided in [13] and references therein.

Presumably the frequency content of bursts of Pi2 pulsations is governed by either the natural frequencies within the near-Earth CPS, or by the frequency content of the CPS disturbances at substorm onset, or in fact a combination of the two. It is often suggested that the dominant periodicity in a Pi2 packet is determined by the bounce time of the Alfvén waves as they propagate along the magnetic field and set up the field aligned currents in the substorm current wedge. Indeed, studies of the Pi2 polarisation ellipse [11] have shown that the upward and downward field aligned current elements of the SCW can be determined from the properties of Pi2s. In this model, the Pi2 periodicity should be determined either by the bounce time (there and back) between the ionosphere and the CPS or between conjugate ionospheres.

In this study we identify and analyse clear quasi-periodic frequencies in the Pi2 frequency band associated with substorm onset on 7th March 2004. Through the application of the cross-phase technique [16], we are able, for the first time, to identify a snapshot of part of the structure of the Alfvén continuum in the nightside magnetosphere for a short period of time following expansion phase onset. By comparing the properties of the wave with the structure of the continuum, we examine the hypothesis that the Pi2 pulsations observed on this day were a field line resonant enhancement within the Alfvén continuum.

## 2. Instrumentation

In this paper we utilise the Canadian Array for Realtime Investigations of Magnetic Activity (CARISMA) magnetometer network, formerly the Canadian Auroral Network for the OPEN Program Unified Study [14] – CANOPUS. In its present incarnation, the CARISMA magnetometer array is able to re-

Received 6 June 2005.

I. J. Rae, I. R. Mann, D. K. Milling, Z. C. Dent, and A. Kale.  
Dept of Physics, University of Alberta, Edmonton, Alberta, Canada.  
T6G 2J1

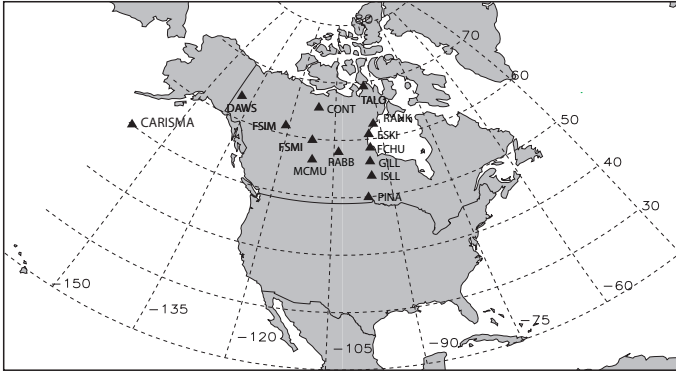


**Fig. 1.** The locations of the magnetometers comprising the current CARISMA magnetometer array. The overlaid grid shows contours of geographic latitude and longitude.

Site Code	Site	CGM Lat. ( $^{\circ}$ N)	CGM Lon. ( $^{\circ}$ E)	L value
TAL	Taloyoak	78.54	330.01	NA
CON	Contwoyto	72.97	303.87	11.84
RAN	Rankin Inlet	72.47	335.36	11.20
ESK	Eskimo Point	70.78	332.51	9.37
FCH	Fort Churchill	68.57	332.92	7.61
FSM	Fort Smith	67.45	306.16	6.90
FSI	Fort Simpson	67.33	293.50	6.84
RAB	Rabbit Lake	67.05	318.42	6.68
GIL	Gillam	66.28	332.46	6.27
DAW	Dawson	65.92	273.16	6.10
MCM	Fort McMurray	64.31	308.52	5.40
ISL	Island Lake	63.86	332.80	5.23
PIN	Pinawa	60.19	331.20	4.11

**Table 1.** Locations of the CARISMA magnetometers used during this study. Dipole-L and CGM latitudes and longitudes are calculated using the NSSDC MODELWeb facility (<http://nssdc.gsfc.nasa.gov/space/cgm/cgm.html>).

solve both latitudinal and longitudinal current structures associated with a substorm when in the correct local time sector; with the forthcoming upgrade and deployment of 15 further fluxgate magnetometers, CARISMA will be able to measure these current systems in extended regions of latitude, longitude and local times, including to mid-latitude regions.

Figure 1 shows the location of the relevant magnetometer stations used in this study, and Table 1 lists their station ID, CGM (Corrected Geomagnetic) coordinates and dipole L-value. We concentrate on the latitudinal “Churchill line” magnetometers in this paper, though information is required on the azimuthal characteristics on the Pi2 pulsations, obtained from measurements along a line of approximately constant latitude.

### 3. Observations: 7<sup>th</sup> March 2004

The CARISMA magnetometer database (<http://www.ssdpc.ca>) was surveyed in order to find an interval which contained an isolated substorm within two hours of local midnight, and which contained quasi-periodic and clear Pi2 signatures in order to test the hypotheses outlined in

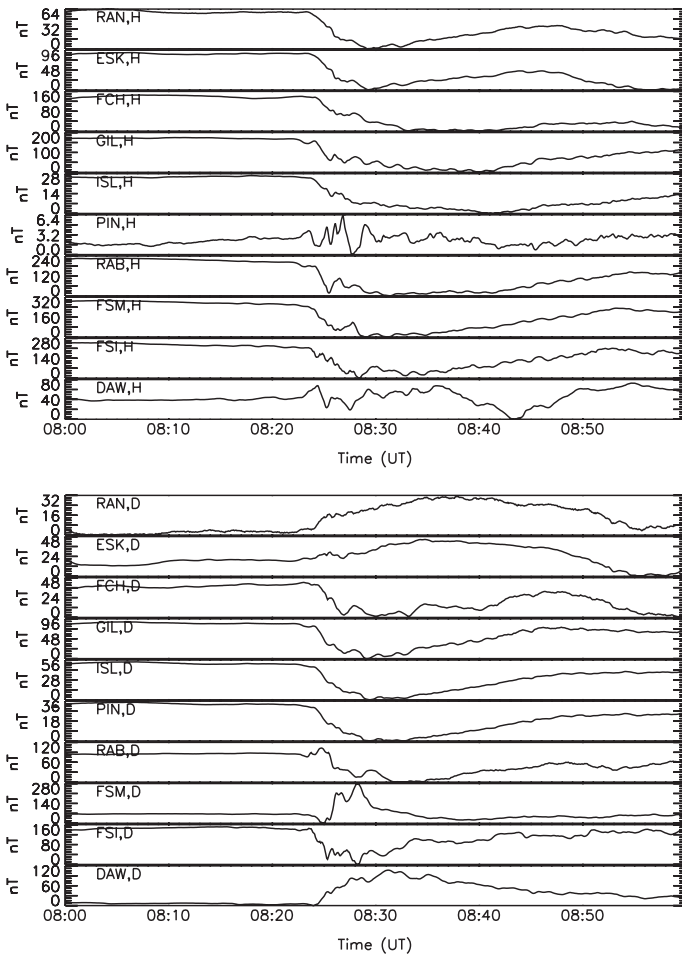
Section 1. Figure 2 shows one such event and the corresponding (a) H- and (b) D-component magnetic field measurements between 0800-0900 UT on the 7<sup>th</sup> March 2004. A clear substorm bay can be seen in both components around 0825 UT, maximising at the 66–68° latitudes (GIL-RAB-FSM-FSI), and having a local maxima at FSM where the substorm bay is -320 nT in the H- and -280nT in the D-component. Since the largest bays are located at FSM evidence this is a strong indication that FSM was close to the centre of the substorm current wedge [6]. Following this time, clear, quasi-periodic pulsations were observed, again clearest between 66–68°.

Figure 3 shows the filtered (20–200s) H- and D-component magnetometer data for the same interval, 0800–0900 UT on the 7<sup>th</sup> March 2004. Large-amplitude Pi2 pulsations are observed between 0825–0900 UT, following substorm onset. The amplitudes maximise around 66–68°, and interestingly are maximised in the D-component (160 nT peak-to-peak) at FSM, but at RAB (96 nT peak-to-peak) in the H-component. The filtered wavetrain observed at GIL is surprisingly periodic. A Pi2 wavetrain following expansion phase onset is rarely monochromatic and the pulsations in both the H- and D-components at GIL are both remarkably quasi-periodic in the 0825–0900 UT interval.

Figure 4 shows the H- and D-component power spectra between 0800–0900 UT. Data were subjected to high-pass filtering at 300s and Hanning windowed. Clear in both H- and D-components are two discrete peaks in the power spectra: one between 5–6 mHz and one between 8–9 mHz. The 5–6 mHz peak tends to be prevalent in one particular meridian, that of the “Churchill Line”, whereas the 8–9 mHz peak is pervasive over the entire dataset. We concentrate on the clear 8–9 mHz frequency peak prevalent at all latitudes and longitudes.

From top to bottom, Figure 5 shows complex demodulation [4] analysis of high-pass filtered (at 300s) H and D signals, as well as the amplitude and phase of the 8.8 mHz component, along with the ellipticity, and the polarisation angle of the wave for the 8.8 mHz demodulate from GIL. For a dominantly Alfvénic field line resonance, it has been shown that the perturbations in the magnetosphere are rotated through 90° upon transmission through a uniformly conducting ionosphere to the ground [5]. Therefore a toroidally (azimuthal magnetic field perturbation) polarised wave in the magnetosphere is expected to be dominated by the H-component when measured by a ground-based magnetometer. Evident from Figure 5 is that the 8.8 mHz component peaks shortly after substorm onset, that the phase of both the H- and D-components is approximately constant through the period of maximum amplitude, and the ellipticity is approximately zero, indicative of linear polarisation. These characteristics all suggest that the GIL station lies under the 8.8 mHz resonant field line.

Figure 6 shows the amplitude and phase characteristics of the 8.8 mHz component from complex demodulation of the “Churchill Line” magnetometers at 0828 UT; just after expansion phase onset. Immediately obvious is the amplitude maxima at GIL and the 180° phase change across the amplitude peak in the H-component, as well as a smaller amplitude peak and phase change in the D-component. These characteristics support the conclusion that the 8.8 mHz waves represent a driven field line resonance, the resonant field line lying close to GIL.



**Fig. 2.** The raw (a) H- and (b) D-component magnetograms from 0800-0900 UT from the 7<sup>th</sup> March 2004.

Figure 7 shows the variation in amplitude and phase of the 8.8 mHz component from complex demodulation as a function of longitude. The H-component amplitude peaks around RAB, but there is a D-component maxima at FSM. However, the H-component phase reveals the central location of the westward electrojet as being close to both the RAB and FSM stations, as the phase peaks at these stations, and decreases to both the east and west. This means that the phase propagation of the 8.8 mHz component is westward to the west of FSM and eastward of RAB, which is consistent with the entral location of the westward electrojet being located between RAB and FSM.

The ellipticity of the wave is the ratio of the minor axis to the major axis of the ellipse formed by the two wave components. The polarization angle is the azimuth of the ellipse measured positive clockwise from H. If the two components are the same size, the wave is circularly polarized and the ellipticity is unity. If the ellipticity is +(-) 1, then H (D) leads D (H) and the wave is clockwise (anticlockwise) polarized. Figure 8 shows the ellipticity and polarisation characteristics of the 8.8 mHz component magnetic field as a function of longitude. These characteristics are well-known for mid-latitude Pi2s (see [11] Figure 1), but are somewhat more complicated at high-latitudes (see [11] Figure 5). Mid-latitude Pi2s exhibit solely anti-clockwise polarisation, and the polarisation angle determines the location

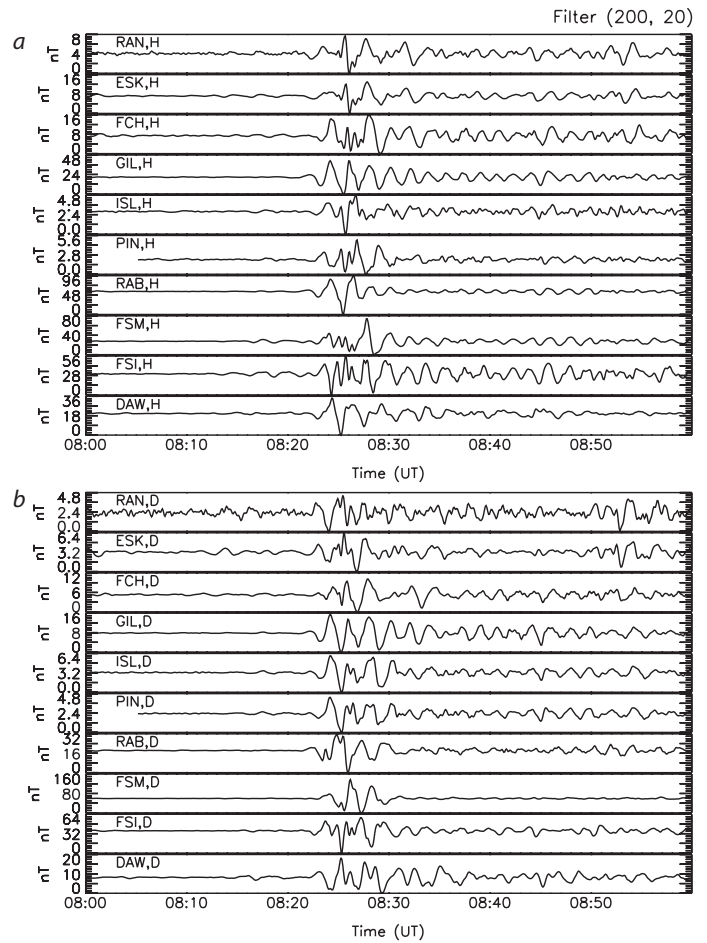


**Fig. 3.** Band-pass (20-200s) filtered (a) H- and (b) D-component magnetograms from 0800-0900 UT from the 7<sup>th</sup> March 2004.

of the magnetometer within the SCW. Figure 8 shows broadly the same features as [11] Figure 1: zero polarisation between RAB-GIL (318-332°) indicating the central meridian between the upward and downward field-aligned current regions, anti-clockwise polarisation to the west of this meridian, but interestingly clockwise polarisation eastward of the GIL-RAB meridian (c.f.,[11] Figure 5). Future work will include a comparison between the mid-latitude ellipticities and polarisations of Pi2 signatures, and those at high latitudes.

The cross-phase technique [16] allows the determination of the fundamental resonant toroidal eigenfrequency of a field line that lies at the mid-point of two latitudinally separated magnetometers. It is generally assumed that this technique does not work in the nightside magnetosphere/ionosphere perhaps due to the lack of ionospheric conductivity. Figure 9 shows the cross-phase between the ISL:PIN magnetometers for the entire day of the 7<sup>th</sup> March 2004 as a function of frequency. From Figure 9, it can be seen that there is a clear 8-9 mHz negative cross-phase peak between 0800-0930 UT, confirming that the eigenfrequency of the field lines increases with decreasing L (the peak is negative as the ISL:PIN magnetometer pair shown is poleward:equatorward respectively).

Figure 10 shows the fundamental toroidal mode eigenfrequency as a function of latitude for the interval 0825-0900 UT

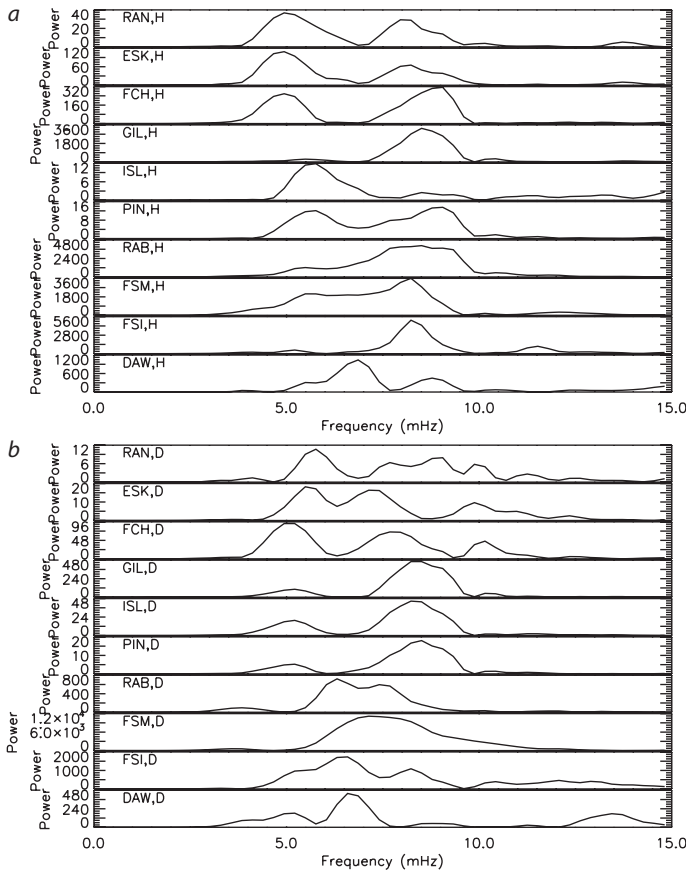


**Fig. 4.** High-pass (at 200s) filtered power spectra of the (a) H- and (b) D-component magnetograms from 0800-0900 UT from the 7<sup>th</sup> March 2004. The power scale is in arbitrary units.

for the magnetometer pairs that could be extracted from the data. The bore sites are marked by arrows, and the discrete 8.8 mHz frequency peak is marked by the dashed line. Remarkably, the 8.8 mHz resonant peak observed at GIL lies within errors close to the resonant local toroidal field line eigenfrequency as obtained from the cross-phase technique. This is indeed strong evidence that frequency of the 8.8 mHz observed frequency Pi2 perturbations is clearly determined by the night-side field line geometry.

**4. Discussion and Conclusions**

As seen clearly in Figures 2 and 3, the isolated substorm on this day is, as expected, clearly associated with the onset of a burst of Pi2 pulsation activity. Data, for example GIL, shows the classic substorm response of a Pi2 wavetrain “riding on” the substorm bay. The largest amplitude Pi2 response is seen on the latitudes of 66-68°. Interestingly, at these latitudes the Pi2 is extremely monochromatic; at other latitudes, the Pi2 waveform appears to be more broad-band and irregular, in keeping with the Pi2 classification. Of the pulsation classifications introduced by [7], only the Pi2 category has become synonymous with a single physical process. Even though the wavepacket observed, for example, at GIL, cannot be described as irregular, we continue to label the waves observed

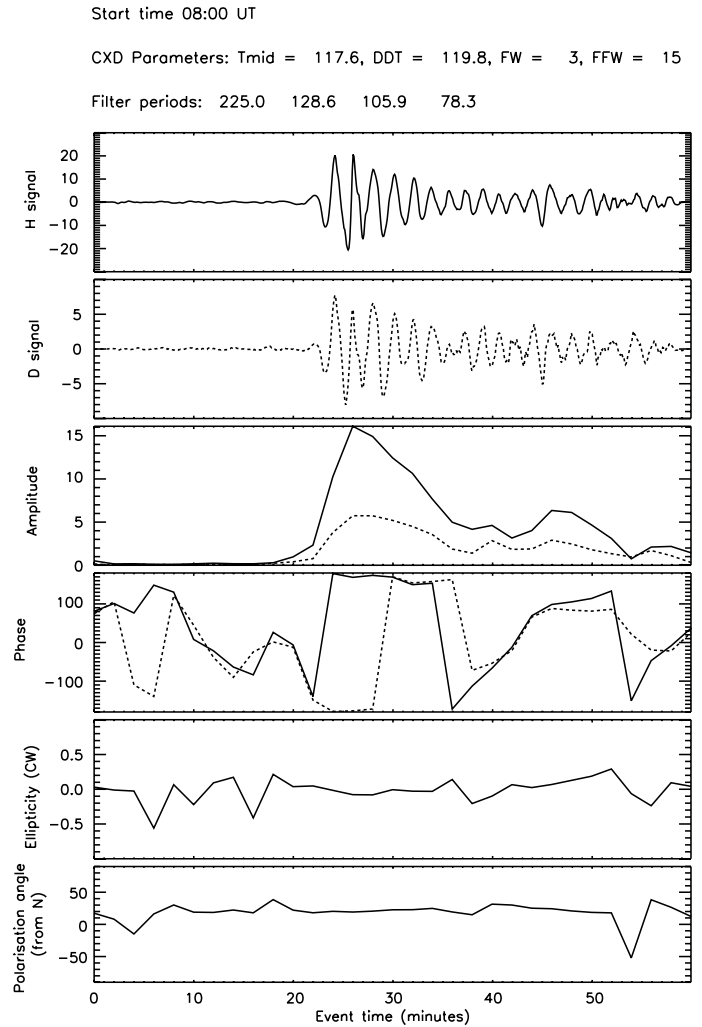


**Fig. 5.** Complex Demodulation[4] results of the 8.8 mHz frequency peak at GIL. From top to bottom Figure 5 shows the H and D amplitudes (high-pass filtered at 200s), the amplitude and phase of the 8.8mHz component of the signals, and the ellipticity and polarisation of the magnetic perturbations.

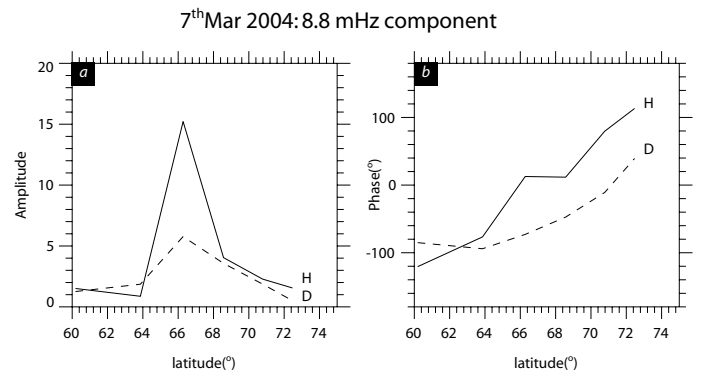


**Fig. 6.** Complex Demodulation of the latitudinal variation of the 8.8mHz H- and D-component (a) amplitude peaks and (b) relative phase at 0828 UT on the 7<sup>th</sup> March 2004.

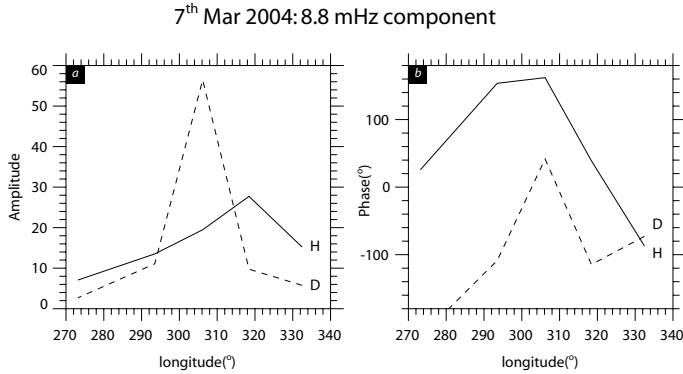


**Fig. 7.** Complex Demodulation of the longitudinal variation of the 8.8mHz H- and D-component (a) amplitude peaks and (b) relative phase at 0828 UT on the 7<sup>th</sup> March 2004.

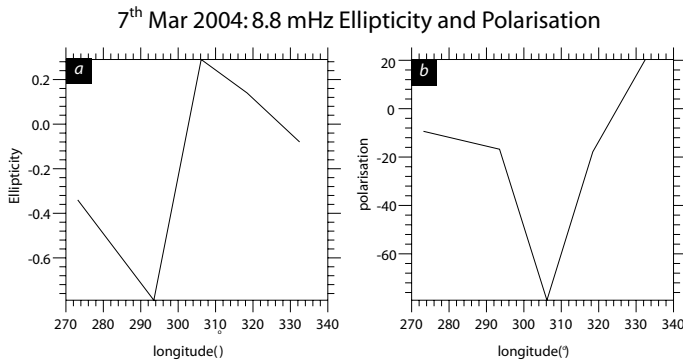


**Fig. 8.** Ellipticity and Polarisation characteristics of the 8.8mHz H- and D-component magnetograms on the 7<sup>th</sup> March 2004.

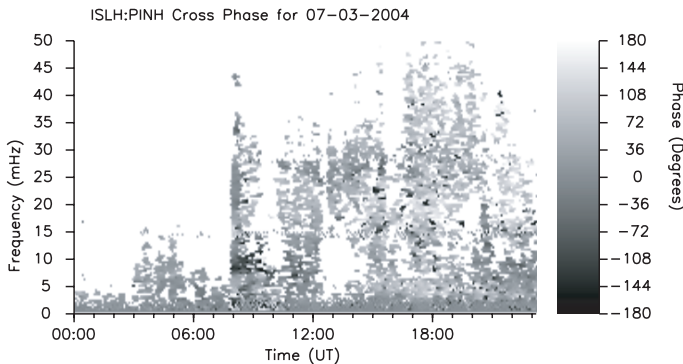


**Fig. 9.** Cross-phase results from the ISL and PIN H-component magnetometer data for the period 0-24 UT on the 7<sup>th</sup> March 2004.

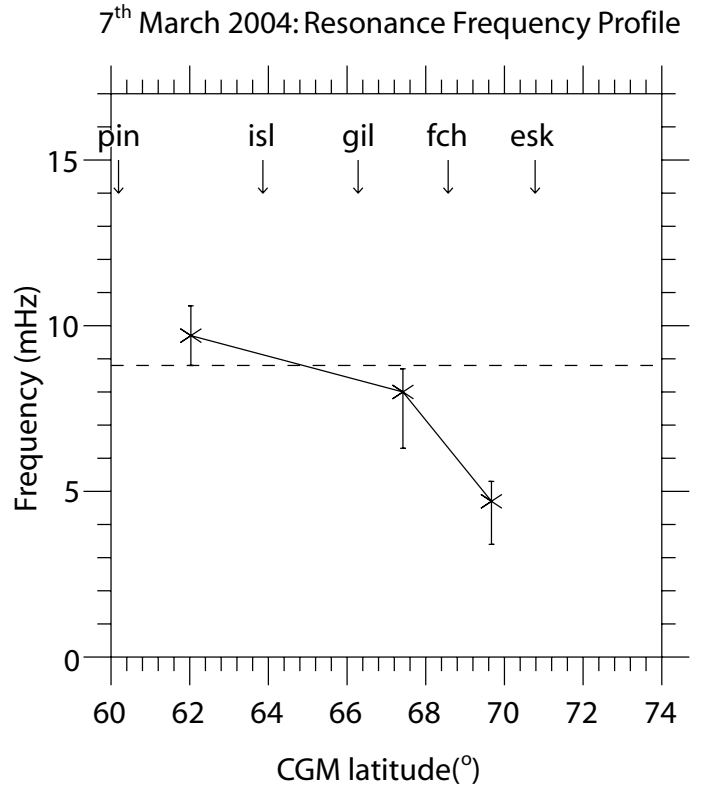


**Fig. 10.** Resonance Frequency Profile for the interval 0825-0900 UT for the available magnetometer pairs (the boresites of which are denoted by the vertical arrows) derived from the cross-phase technique (see text for details).

during this event as Pi2s because of their global characteristics and their association with the onset of a substorm.

The monochromatic nature of this pulsation provides the opportunity to investigate the relationship between Pi2 periodicity and the Alfvén continuum. Figure 6 shows clearly that the dominant Pi2 pulsation power has the characteristics of a toroidal mode 8.8 mHz FLR. The amplitude peaks at latitudes where the Pi2 is most monochromatic, consistent with a bouncing Alfvén wave source generating a field-aligned current around 66-68° CGM. The wave polarisation characteristics at GIL (Figure 5) demonstrate linear polarisation, also consistent with an FLR at this latitude. Most significantly, Figures 9 and 10 demonstrate that the cross-phase technique can work for a limited period of time following substorm onset. Usually cross-phase does not work on the nightside, which is usually attributed to rapid and perhaps critical damping by the nightside ionosphere. However, perhaps as a result of additional ionospheric conductivity arising from auroral precipitation following substorm onset, sufficient coherency enabled three pairs of stations to be used to recreate three discrete points along the Alfvén continuum. Remarkably, within the margins of error, these results showed that the 8.8 mHz frequency would be expected to resonate around the latitude of Gillam, at exactly the same location as the observed maximum. This demonstrates very clearly, at least for this event, that the dominant Pi2 frequency is indeed determined by the bounce time of Alfvén waves. Moreover, this also points to the relev-

ant bounce path of the Alfvén waves being between conjugate ionospheres. Given that these waves are excited by disturbances in the near-equatorial CPS, one might expect an antinodal velocity perturbation in the equatorial plane for these standing Alfvén waves. This is entirely consistent with the conclusions drawn from the cross-phase results.

The longitude dependence of the Pi2 amplitudes shown in Figure 7 appears to be approximately consistent with the longitude dependence of the bay amplitudes seen in Figure 2. Further analysis, and data from additional mid-latitude magnetometers, may allow a closer correspondence between the Pi2 waveforms and the magnetic bays to be established. This will be considered in future publications. In conclusion, we believe that this is the first time that the cross-phase technique has been applied successfully to the determination of the Alfvén continuum in the nightside magnetosphere. In combination with the characteristics of the Pi2 waveforms, this has enabled us to show for the first time that the dominant element in the Pi2 pulsation response can be characterised as a field line resonant enhancement in the Alfvén continuum. This suggests that a significant contribution to determining Pi2 structure may come from a natural frequency resonant response of the nightside magnetosphere, including the subsequent excitation of a classical field line resonance, rather than being determined by driver periodicities such as the flow burst structure within BBFs.

## Acknowledgements

This work was partially funded by an NSERC Discovery Grant to IRM and the Canadian Space Agency (CSA). The operation of CARISMA, part of the Canadian Geospace Monitoring Program, is funded by the CSA via a contract to the University of Alberta.

## References

1. Akasofu, S.-I., Polar and Magnetospheric Substorms, D. Reidel, Norwell, Mass., 1968.
2. Angelopoulos, V., Baumjohann, W., Kennel C. F., Coroniti F. V., Kivelson M. G., Pellat R., Walker R. J., Lühr H., and Paschmann G., Bursty bulk flows in the inner central plasma sheet, *Journal of Geophysical Research*, 97, 4027-4039, 1992.
3. Baumjohann, W. and Glaßmeier, K. H., The transient response mechanism and Pi2 pulsations at substorm onset—Review and outlook, *Planetary and Space Science*, 32, 1361-1370, 1984
4. Beamish, D., Hanson, H. W. and Webb, D. C., Complex demodulation applied to Pi2 geomagnetic pulsations. *Geophysical Journal of the Royal Astronomical Society* 58: 471-493, 1979.
5. Hughes, W. J., and Southwood, D. J., The screening of micropulsation signals by the atmosphere and ionosphere, *Journal of Geophysical Research*, 81, 3234, 1976.
6. Cramoisan, M., Bunting, R., and Orr, D., The use of a model current wedge in the determination of the position of substorm current systems, *Ann. Geophys.*, 13, 583, 1995.
7. Jacobs, J. A., Kato, Y., Matsushita, S. and Troitskaya, V. A. Classification of geomagnetic micropulsations, *Journal of Geophysical Research*, 69, 180, 1964.
8. Kepko, L. E., and Kivelson M. G., Generation of Pi2 pulsations by bursty bulk flows, *Journal of Geophysical Research*, 104, 25021, 1999.
9. Kepko, L. E., Kivelson M. G. and Yumoto K., Flow bursts, braking, and Pi2 pulsations, *Journal of Geophysical Research*, 106, 1903, 2001.
10. Kepko, L., Kivelson M. G. McPherron, R. L. and Spence, H. E., Relative timing of substorm onset phenomena, *Journal of Geophysical Research*, 106, doi: 10.1029/2003JA010285, 2004.
11. Lester, M., Hughes, W. J., and Singer, H. J., Polarisation patterns of Pi2 magnetic pulsations at the substorm current wedge, *Journal of Geophysical Research*, 88, 7958, 1983.
12. Lester, M., Hughes, W. J., and Singer, H. J., Longitudinal Structure in Pi2 Pulsations and the Substorm Current Wedge, *Journal of Geophysical Research*, 89, 5489, 1984.
13. Olsen, J., Pi2 pulsations and substorm onsets: A review, *Journal of Geophysical Research*, 104, 17499, 1999.
14. Rostoker, G., J. C. Samson, F. Creutzberg, T. J. Hughes, D. R. McDiarmid, A. G. McNamara, A. Vallance Jones, D. D. Wallis and L. L. Cogger, CANOPUS - A ground based instrument array for remote sensing the high latitude ionosphere during the ISTEP/GGS program, *Space Sci. Rev.*, 71, 743-760, 1995.
15. Takahashi, K. and Lee, D.-H. and Nosé, M., Anderson, R. R. and Hughes, W. J., CRRES electric field study of the radial mode structure of Pi2 pulsations, *Journal of Geophysical Research*, 106, 108, doi: 10.1029/2002JA009761, 2003
16. Waters, C. L., F. W. Menk, and B. J. Fraser, The Resonance Structure of Low Latitude Pc3 Geomagnetic Pulsations, *Geophys. Res. Lett.*, 18, 2293, 1991.

# Auroral oval boundary observations by Meteor 3M satellite

M. O. Riazantseva, E. E. Antonova, B. V. Marjin, V. V. Hoteenkov, I. L. Ovchinnikov, M. A. Saveliev, V. M. Feigin, and M. V. Stepanova

**Abstract:** The results of the observations of auroral oval boundaries by satellite METEOR 3M are presented. The satellite was launched December 10, 2002 to the polar heliosynchronous orbit with the altitude of 1018 km and the inclination of  $99.63^\circ$ . The satellite mission includes the observations of the Earth's resources, the control of the conditions in the near the Earth environment, meteorological and heliogeophysical parameters. The main goals of the mission are the forecast of the solar flare activity, control and prediction of the Earth's radiation and the state of the Earth's magnetic field, prediction of the conditions for the radio wave propagation, diagnostic and the control of the conditions in the magnetosphere and ionosphere. The electrostatic analyser MSGI-5EI is used for the analysis of the variations of the fluxes of auroral protons and electrons. It measures the electron and proton fluxes within the energy range from 0.1 to 10 keV in 50 energetic channels and the integral flux of electrons with energies  $> 40$  keV. Determined by MSGI-5EI positions of the auroral oval boundaries are compared with the predictions of OVATION model. It is shown that due to auroral substorm activity the difference between observed and predicted by OVATION positions can exceed 5 degrees in latitude.

*Key words:* auroral oval, auroral satellite, OVATION model.

## 1. Introduction

Study of the main features of auroral substorm development requires constant monitoring of radiation and plasma near the Earth, determination of the position of the auroral oval and variations of fluxes of auroral particles, what is one of the main goals of the Meteor-3M No 1 satellite mission. Auroral oval boundaries move to the equator during substorm growth phase. Polar boundary move to the pole after substorm expansion phase onset forming the auroral bulge. OVATION model based on DMSP, POLAR and radar observations gives the position of auroral oval for concrete time intervals.

In this paper we describe the main features of satellite operation, present examples of particle measurements and results of the comparison of the predictions of OVATION model with the Meteor-3M No 1 measurements.

## 2. The features of the operation of the satellite METEOR 3M No 1

The satellite Meteor-3M No 1 mission includes study of the natural resources, the control of the environment conditions, the hydrometeorological and heliospherical testing. The satellite was launched December 10, 2002 to the heliosynchronous orbit with the altitude 1018 km and the inclination  $99.63^\circ$  by the rocket "Zenit" from the Baikonur cosmodrom. Table 1 summarizes the main technical characteristics of the satellite.

Received 15 May 2006.

**M. O. Riazantseva, E. E. Antonova, B. V. Marjin, V. V. Hoteenkov, and I. L. Ovchinnikov.** Skobeltsyn Institute of Nuclear Physics Moscow State University, Moscow, 119992, Russia

**M. A. Saveliev and V. M. Feigin.** Russian Space Agency, Russia  
**M. V. Stepanova.** Departamento de Fisica, Universidad de Santiago de Chile, Casilla 347, Correo2, Santiago, Chile

Satellite Meteor-3M No 1 is designed by the Electromechanical Institute in Istra town having as a prototype the satellite Meteor-3M. However, significant changes have been introduced including the modification of attitude system, installation of new radio transmission system and modification of the information devices and measurement instruments. According to the main goals of the mission, the complete set of instruments includes three main subsets:

1. Visual informative nature-resources complex (BIK-M1);
2. Complex of scientific measuring instruments (BKNA);
3. Complex of meteorological instruments (MP-700M).

Heliophysical instruments realize measurements of solar flare particles and radiation in the inner magnetosphere that allows forecasting of radiation conditions and conditions of radio wave propagation. One of the applied aspects of the mission is to guarantee more reliable and effective work of satellites due to developing of more confident forecast of near-Earth radiation environment, and also due to improvement of the satellite design.

## 3. Spectrometer MSGI-5EI

Measurements of auroral particle fluxes are made using the MSGI-5EI spectrometer [1]. The instrument includes the following sub-systems: high sensitive spectrometric module for low energy ion and proton measurements; high sensitive spectrometric module of low energy electron measurements; low sensitive spectrometric module for low energy electron measurements, and module for the measurements of integral flux of charged particles with the energies  $> 40$  keV.

The detection of low energy particles, energy-charge separation is realized by two kinds of spectrometric modules representing the cylindrical electrostatic analyzers, secondary electron multipliers of the type VEU-6 (low sensitive module) or VEU-7 (high sensitive module), charge-sensitive amplifier and

Orbital parameters, technical characteristics	Value
Local solar time of rising knot	9 h 15 min $\pm$ 15 min
Altitude	1018.63 $\pm$ 10.71 km
Inclination	99.63°
Orbital period	105.33 $\pm$ 0.06 min
Eccentricity	0.000806
The angle distance between turns	-26.334°
Daily change of the longitude of rising knot	-8.670°
Period of izorote	3 days (41 turn)
Total mass	2600 kg
Mass of the paying load	800 – 1000 kg
Time of operation, year	greater than 3
Parameters of three axial orientation: accuracy	10'
accuracy of the stabilization	0.005°/s

**Table 1.** Orbital parameters and the main technical characteristics of the Meteor-3M No 1 satellite

the device for the formation of normalized pulses. The spectrometric modules measure differential energy spectra of low energy ions (protons) and electrons in the energy range from 0.1 to 20 keV. Dynamical range of the measurements of the ion channel is  $10^3$ – $10^8$  particles/( $\text{cm}^2 \cdot \text{s} \cdot \text{ster} \cdot \text{keV}$ ). Dynamical range of the measurements of low energy electrons for the spectrometer MSGI-5EI is  $10^3$ – $2 \cdot 10^9$  particles/( $\text{cm}^2 \cdot \text{s} \cdot \text{ster} \cdot \text{keV}$ ). Measurements of energy spectra of electrons and ions (protons) have two modes, controlled by external commands. The fast one is used for the study of space-time variations during the periods of geomagnetic disturbances. The time of measurements of energy spectra is 2 s, the number of energy channels is equal 10. The second mode (the slow one) has the time of measurements of energy spectra of 10 s, but the number of energy channels is substantially higher and equal to 50. Batten gas discharge detectors realize measurements of charged particles of medium energy. Dynamical range of the integral channel constitute  $1$ – $10^3$  pulses per second. Measurements are realized in monitor regime independent on the regime of the work of spectrometer. Figure 1 demonstrates the example of auroral oval crossing.

The data base of the satellite Meteor-3M No 1 contains the values of particle fluxes with energy 0.1–10 keV and particle spectra. Every flight gives four auroral oval boundary crossing for each hemisphere to determine the auroral oval position. The determination of inner auroral oval boundary becomes difficult in cases of overlapping of auroral oval and external electron radiation belt.

#### 4. Comparison of results of Meteor-3M No 1 observations with OVATION model

OVATION model [<http://sd-www.jhuapl.edu/Aurora/>] (see [3, 4]) uses multiple data sets cross-calibrated to a single standard. The model gives and predicts the position of auroral oval in real time. Data from the DMSP satellites, from NASA's Polar UVI imager, from the University of Alaska, Fairbanks

Meridian Scanning Photometer and SuperDARN are used for model fitting. The DMSP particle precipitation data provides the “core” of OVATION. But DMSP temporal resolution is poor (about 50 minutes per updated position). The time resolution of Polar UVI (in the LBH-L filter used for this work) is typically one image every 1 min 30 s, but auroral images are available only for the northern hemisphere. Large data gaps occur daily, whenever Polar is not in position to observe the northern hemisphere polar regions. The Super Dual Auroral Radar Network consists of a collection of HF radars located in the Northern and Southern hemispheres, but its data are used not in all cases. University of Alaska, Fairbanks MSP (Meridian Scanning Photometer) data is high time resolution, but only works (1) in darkness, (2) under fair skies, (3) when the auroral oval is within a few degrees of Fairbanks. The verification of OVATION model requires using of data of auroral satellite which was not used in OVATION model.

In this study we compare the predictions of OVATION model with the results of Meteor-3M No 1 observations. This includes the determination of the geomagnetic coordinates and time of the oval boundary crossings by Meteor-3M No 1 satellite and simultaneously the position of auroral boundaries according to the OVATION model. After that we determine a difference in degrees between both geomagnetic latitudes. Fig. 1 shows precipitating electron fluxes observed by the METEOR-3M satellite January 1, 2003. Fig. 2 shows the auroral oval position provided by the OVATION model for the event January 9, 2003. The Meteor-3M crossings of auroral oval boundaries are shown by black squares, and the closest in time DSMP satellite trajectories are shown by white squares. “R” are the results of radar measurements used in the OVATION model. As it can be seen from Fig. 2, the auroral oval position provided by the OVATION model coincides very well with the Meteor-3M No 1 measurements for the event January 9, 2003. Nevertheless this coincidence is not observed for all events analyzed. Fig. 3 shows precipitating electron fluxes observed by the METEOR-3M satellite January 8, 2003 and Fig. 4 shows the auroral oval position provided by the OVATION model for this event. The discrepancy larger than  $4^\circ$  is observed.

To make a statistical analysis of discrepancies observed we separated all events analyzed in 6 sets according to the absolute value of the difference: from 0 to 1 degrees, from 1 to 2 degrees, from 2 to 3 degrees, from 3 to 4 degrees, from 4 to 5 degrees and larger than 5 degrees. Fig. 5 shows the results of produced analysis. Values on the ordinate axes show the number of analyzed events (in %). Upper part of the figure corresponds to the equatorial boundary of the oval; lower part corresponds to the polar boundary. It is possible to see that the model gives quite good predictions of auroral oval location in half of cases. Events with large discrepancy correspond to substorm periods or to cases when the angular difference of DMSP and Meteor-3M trajectories is larger than  $20^\circ$  (in longitudes). Medium value of the discrepancy is  $1.8^\circ \pm 1.3^\circ$  for the equatorial boundary and  $2.8^\circ \pm 2.5^\circ$  for the polar boundary.

The average positions of polar and equatorial auroral boundaries are also determined. Equatorial boundary is located at  $68^\circ \pm 4^\circ$  near noon and  $62^\circ \pm 6^\circ$  near midnight. Polar boundary is located  $77^\circ \pm 3^\circ$  near noon and  $70^\circ \pm 10^\circ$  near midnight. These values are in agreement with existing models of auroral oval position [2, 5–9].

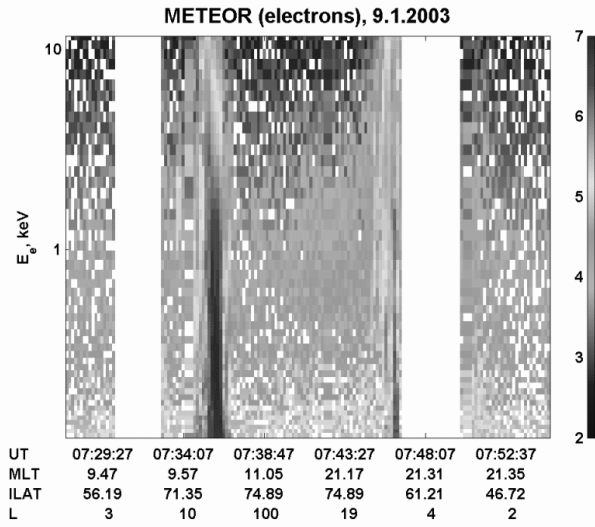


Fig. 1. Precipitating electron fluxes observed by the METEOR-3M satellite January 9, 2003

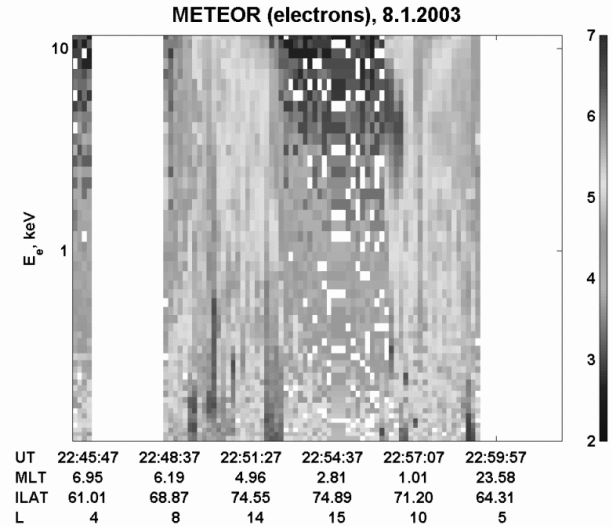


Fig. 3. Precipitating electron fluxes observed by the METEOR-3M satellite January 8, 2003

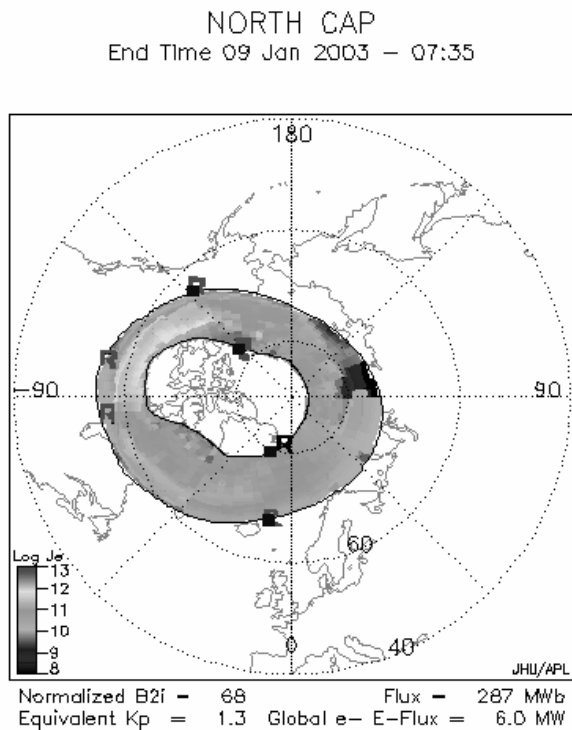


Fig. 2. Visualization of the results of the comparison of the OVATION model with Meteor-3M No 1 data for the January 9, 2003 event. Crossings of the Meteor-3M No 1 trajectories of the auroral oval are shown by black squares, white squares show nearly simultaneous crossings by one of the DMSP satellites, *R* are the results of radar measurements used in OVATION model

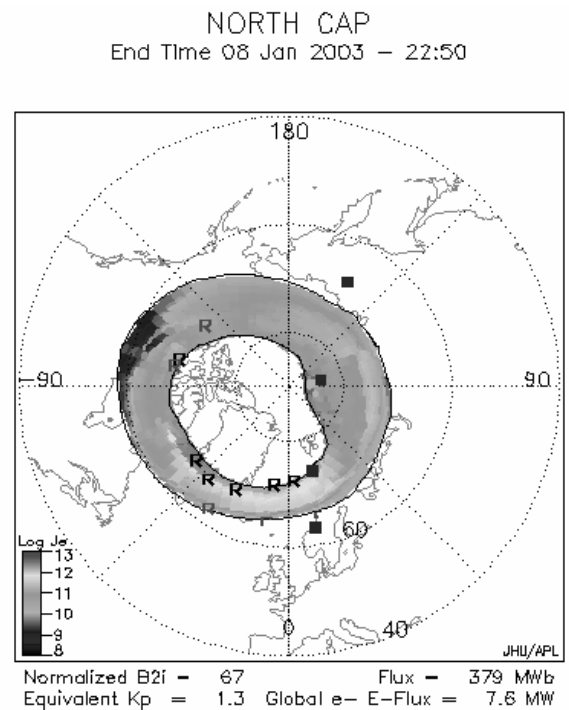
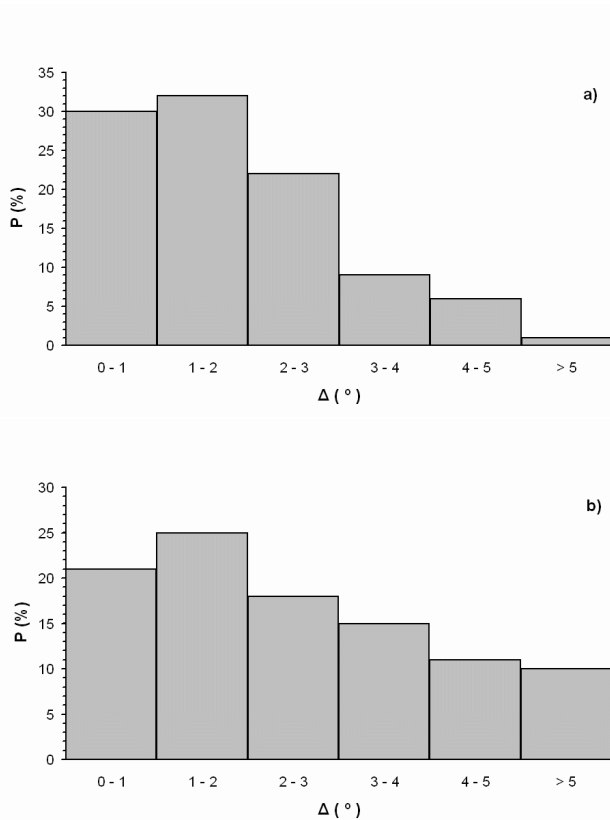


Fig. 4. Visualization of the results of the comparison of the OVATION model with Meteor-3M No 1 data for the January 8, 2003 event



**Fig. 5.** Results of statistical analysis of coincidence of OVATION model predictions with Meteor-3M No 1 observations: a) for the equatorial boundary, b) for the polar boundary

## 5. Discussion and conclusions

The preliminary results presented here show the capability of the Meteor-3M No 1 satellite to verify and precise the auroral oval positions given by the OVATION model. We have found that the positions of the auroral oval boundaries, observed using the Meteor-3M precipitating particle flux measurements, generally coincide with these provided by the OVATION model. Nevertheless, for some events observed and modeled boundaries differ in a few degrees in geomagnetic latitude. It was found that this discrepancy increases with the angular distance between Meteor-3M No 1 and DMSP satellite used by the OVATION model as an input. We consider that the main reason of observed noncoincidence when the angular distance of DMSP and Meteor-3M No 1 satellite is small is the auroral boundary motions during magnetospheric substorms.

## Acknowledgments

The research was supported by RFBR 05-05-64394-a and FONDECYT 1020293 grants.

## References

1. Marjin B. V., M. V. Teltsov, M. O. Riazantseva, E. E. Antonova, V. V. Khotenkov, M. A. Saveliev, V. M. Feigin. Meteor-3M No 1

- particle observations: Initial results, *Proceedings of the 5th International Conference Problems of Geocosmos St. Petersburg, Petrodvorets, May 24–28, 92–95, 2004.*
2. McDiarmid I. B., Burrows J. R., Budzinski E. E. Average characteristics of magnetospheric electrons /150 eV to 200 keV/ at 1400 km, *J. Geophys. Res.*, 80, 73–79, 1975.
3. Newell P. T., Sotfrelfs T., Ruohonfemf J. M., *Ovation: Oval variation, assessment, tracking intensity, and online nowcasting, Annales Geophysicae*, 20, 1039–1047, 2002
4. Sotirelis T., Newell P. T., Boundary-oriented electron precipitation model, *J. Geophys. Res.*, 105, 18655, 2000.
5. Spiro D. J., Reiff P. Y., Maher L. J. Precipitating electron energy flux and auroral one conductances an empirical model, *J. Geophys. Res.*, 87, 8215, 1982.
6. Hardy D. A., Gussenhoven M. S., Holeman E. A statistical model of auroral electron precipitation, *J. Geophys. Res.*, 90, 4229, 1985.
7. Vorobjev V. G., O. I. Yagodkina, G. V. Starkov, Ya. I. Feldstein, A substorm in midnight auroral precipitation, *Annales Geophysicae*, 21(12), 2271–2280, 2003.
8. Vorobjev V. G., Yagodkina O. I. Midnight electron precipitation pattern for substorm development. *Proceedings of the conference in memory of Yuri Galperin "Auroral Phenomena and Solar-Terrestrial Relations"*, eds: L. M. Zelenyi, M. A. Geller, J. H. Allen, *CAWSES Handbook-001*, 341–349, 2004.
9. Yagodkina O. I. Vorobjev V. G., Daytime auroral precipitation during substorm development. *Proceedings of the 26th Annual Seminar Physics of auroral phenomena. Apatity, 2003.* 49–52, 2003

# Substorm theories and Cluster multi-point measurements

A. Roux, O. Le Contel, D. Fontaine, P. Robert, P. Louarn, J.A. Sauvaud, and A.N. Fazakerley

**Abstract:** The development of the collisionless tearing instability is often considered as the trigger for substorms and magnetic reconnection in the tail current sheet (CS). Yet published results show that unless the number of particles in a flux tube drastically changes via strong spatial diffusion across B, tearing modes are stable. We review this long lasting controversy and conclude that the collisionless ion and electron tearings are stable, or weakly unstable, at least at low frequencies and therefore at the large scale where neutral lines are expected to form. As well, tearing modes have  $K_x \gg K_y$ , but Cluster observations show large amplitude perturbations have  $K_y \gg K_x$  (mostly azimuthal propagation). To identify the signature of the breakup instability we analyze Cluster data from a substorm that occurred while Cluster was in the CS. At the end of the growth phase, enhanced fluxes of field aligned electrons ( $\sim 1\text{keV}$ ) are observed together with a  $\sim 1\text{keV}$  decrease in the energy of the original plasma sheet population. This field aligned component corresponds to ionospheric electrons accelerated by an (induced) parallel electric field. Both azimuthally propagating fluctuations with quasi periods of  $\sim 60$  sec, and higher frequency wide band electromagnetic fluctuations are observed. As the active phase starts, the waves intensify, reaching 2nT and 20mV/m for HF, and 10nT for LF. The CS gets even thinner leaving only one satellite inside it, which observes that electrons are heated and have variable fluxes. We suggest that electron heating is due to bounce resonance with HF waves. This is followed by a series of short lasting ( $\sim 60$  sec) magnetic structures in  $B_y$  and  $B_z$ . These correspond to field aligned currents and partial dipolarizations and are observed to move azimuthally. They are associated with fast ion flows (1000km/sec), and with bursts in the amplitude of HF waves. This data analysis suggests that HF waves produced by bouncing electrons, in an increasingly thin current sheet, interrupt the current, thereby producing a local dipolarization and the corresponding ion flow bursts. This is consistent with the CD model.

## 1. Introduction

During substorm growth phase, the tail current sheet (CS) becomes thin. The contrast between a slow ( $\sim 30\text{mn}$ ) growth phase and a sudden breakup ( $\sim 1\text{mn}$ ) suggests that a plasma instability plays the major role of a trigger in substorm dynamics. The two primary and competing paradigms are the Near-Earth Neutral Line (NENL) and Current Disruption (CD) models. In the NENL model the filamentation of the CS is associated with the development of the tearing instability, leading to the formation of neutral line(s) in the mid-tail (20-30 Re) and to subsequent fast flows. Earthward of the reconnection site (X-line) the flow is directed earthward. Braking of these fast flows as they approach the dipolar region can result in a dipolarization, in the near Earth plasmasheet. This dipolarization in turn propagates tailward. In the CD (also called diffusion) model(s), the dipolarization results directly from the development of an instability that reduces/diffuses spatially the tail current (Jy). Later the dipolarization may expand radially, thereby causing the reduction/spatial diffusion of the current in a broad region. In this type of model the formation of X-line/point can be the consequence of the dipolarization instead of being its cause.

In sections 2 and 3 we review theory and observations rel-

evant to the two kinds of instabilities. The two models have similarities. For instance field aligned currents are expected to develop in both cases. Yet their characteristics also differ. For instance, the tearing instability has to produce a spatial modulation in the radial direction ( $K_x$ ), while instabilities involved in CD/diffusion should produce an azimuthal modulation ( $K_y$ ). As well, the instability mechanism must develop on a time scale consistent with that of breakup. In section 4 we present Cluster data from a substorm that occurred while Cluster spacecraft (s/c) were located in the CS, and try to determine what model fits best with the data.

## 2. Can tearing instability produce spontaneous reconnection in collisionless plasmas?

In most recent literature, it is assumed that the X-line(s) structure(s) can be formed, either via tearing instability, or by suitably controlling external conditions (forced reconnection). A particular emphasis has been put on the potential role of Hall currents in a situation where the current sheet is very thin, so that ions are demagnetized. Yet in a real situation, how external constraints could lead to the formation of an X-line remains unclear and we do not know how this X-line could remain quasi-stable for quite a long time. On the other hand the tearing instability is known to be a viable mechanism to form X-line(s). A reversed magnetic field configuration is indeed a source of free energy. Tearing modes have a negative energy and can therefore be destabilized via a dissipative process. In collision dominated plasmas, collisions ensure this dissipation: the tearing modes are therefore unstable, and their development leads to the formation of X-lines and O-type islands. In

Received 24 May 2006.

A. Roux, O. Le Contel, D. Fontaine, and P. Robert. CETP-IPSL-CNRS, 10-12 avenue de l'Europe, 78140 VÉLIZY-VILCOUBLAY, FRANCE

P. Louarn and J.A. Sauvaud. CESR, 9 avenue du Colonel Roche, BP 4346, 31028 TOULOUSE CEDEX 4, FRANCE

A.N. Fazakerley. MSSL, UNITED KINGDOM

the Earth's plasmasheet, some form of collisionless dissipation must play the role of collisions. [4] suggested that electron Landau damping for this, which can work provided there is no normal component. It was soon realized that even a small Bz stabilizes the electron tearings. Indeed the presence of a finite Bz modifies electron motion (they are magnetized) which removes the Landau resonance and the corresponding collisionless dissipation (e.g. [6], [9]).

Schindler [18] suggested that ion Landau damping (associated with unmagnetized non-adiabatic ions) could provide the dissipation required for tearing instability to develop. However, he assumed that electrons were cold ( $T_e=0$ ). [10] have shown that with finite  $T_e$ , the energy associated with electron compressibility is larger than the free energy available from the reversed magnetic field configuration. Hence ion tearing cannot develop over realistic distances. [10] showed that  $L_T < (\pi^2 B_o H / 2 B_n)$  is a sufficient condition for stability. Here  $L_T$  is the wave length of the tearing mode, H the CS thickness, and  $B_o$  and  $B_n$  the lobe and normal magnetic fields. For an already thin CS ( $L \sim 2000 \text{ km}$ ), and  $B_o/B_n \sim 20$  we get  $L_T > 30 R_e$ , which is still much too large. Furthermore the WKB domain is limited by  $k > (B_n / H B_o)$ , and hence  $L_T < (2\pi B_o H / B_n)$ . Combining the two inequalities we find that there is no parameter space for ion tearing instability to develop. This stabilizing effect, called the electron compressibility, is linked to the strong magnetization of CS electrons. In order to preserve charge neutrality ions should follow electrons, which requires more energy than available in the reversed field configuration. Hence ion tearing instability is unlikely to develop.

Pitch angle diffusion or electron stochasticity could replace the role normally played by collisions. It was thus suggested that electron scattering could restore the ion tearing by removing the stabilization due to electron compressibility [5, 2]. This idea was incorrect: it was found that what really matters is the conservation of the number of electrons on a flux tube [14]. Neither pitch angle diffusion nor electron stochasticity change significantly the number of electrons in the flux tube.

More recently [19] suggested that an untrapped electron population could reduce the stabilizing effect associated with trapped electrons. [19] showed that transient/untrapped electrons do modify the stability condition (above). They showed that inclusion of untrapped electrons introduces a factor  $(3T_e/T_i)^2$  in the Lembege and Pellat sufficient condition for stability. Thus it seems there is still a window where ion tearings could develop  $((\pi^2 B_o L / 2 B_n) (3T_e/T_i)^2 < L_T < \pi B_o L / B_n)$ . For  $T_i/T_e \sim 7$ , and the same parameters as above, we get  $L_T > 6 R_e$ , implying that the CS should be homogeneous over at least  $6 R_e$ , which is still large. Marginal stability threshold analysis showed that collisionless tearing instability is much less sensitive to the ratio  $T_i/T_e$  than expected from the criterion quoted above [20]. That study also evaluated the growth rate and found that when tearing modes are unstable they grow over a typical time scale of  $\sim 5 \text{ mn}$ , which is too long for breakup.

Thus, in a collision-free plasma, spontaneous reconnection via tearing modes leading to X-line(s) formation does not seem to be a viable mechanism to trigger substorms. Of course the formation of X-line(s) can be forced via external conditions as it is often the case in numerical simulations.

Artificially applied or numerical resistivity determines the formation of X-line(s) in MHD simulations, which therefore

cannot be used to investigate spontaneous tearing modes. Most recent simulations take into account Hall effects, which can provide collisionless dissipation, in the Ohm's law. Fully kinetic 2.5 and 3D simulations are now used to explore the nature of collisionless dissipation process (e.g. see [7]). Computing time constraints, however, introduce serious limitations. The formation of X-lines is forced by external conditions, or simulations start with a Harris sheet (with  $B_z=0$  and thus no electron bounces). Even in the cases where the modes are allowed to grow spontaneously, constraints on computing time and the dimensions of the 2 or 3D simulation boxes are such that electron bounce motion cannot properly be described for realistic ion to electron mass ratios. Thus, different simulation parameter domain and boundary conditions lead to differences in the predicted development of the tearing instability. For instance while [22] concluded, from kinetic simulations, that ion tearings are unstable, [16] concluded to stability irrespective of  $T_i/T_e$ .

Inclusion of Hall terms is an important improvement, but they are not sufficient to describe important kinetic effects. Furthermore it is not clear that kinetic effects are limited to a small diffusion region at the electron scale ( $L_e \sim \text{few km}$ ). In this paper, we discuss the possible role of electron bounce resonance, which has associated dissipation that occurs at the larger scale of the CS. The electron bounce period ( $T_{be}$ ) is comparable to the proton gyroperiod in the lobes ( $T_{H+}$ ).

In order to identify the dissipation mechanism, simulations runs with initially closed field lines, where electrons can undergo several bounces, and carried out in a parameter regime such that  $T_{be} \sim T_{H+}$ , are needed. Note that the ratio  $T_{be}/T_{H+}$  depends on the mass ratio  $M/m$  which is used in the simulation. Thus it is still unclear that X-lines can develop in a realistic collision-free plasma and remain stable for a long time.

### 3. Current disruption model(s)

The CD models are much less developed than reconnection models. Unlike tearing, the modes that disrupt  $J_y$  lead to azimuthal modulation. The premise is that once the CS gets very thin,  $J_y$  can exceed the instability threshold [12]. The enhanced  $J_y$  can be produced by a strong ion pressure gradient, as required for the ballooning instability (e.g. [17]). Current driven instabilities can interrupt or spatially diffuse the tail current. In the latter case the total current remains the same, but  $J_y$  decreases in the equatorial region. This decrease in  $J_y$  leads to a local dipolarization. For a full substorm the current disruption/diffusion expands, leading to a more dipolar configuration over the whole plasma sheet. The dynamics of this expansion depends on the non-linear evolution of the instability and on the distribution of the currents. For a large substorm the instability is likely to develop in the near Earth plasma sheet, magnetically conjugate to the equatorward most (breakup) arcs, and then expand azimuthally and radially outward.

An earthward expansion is not ruled out in weak and/or pseudo substorms with onset arcs at higher latitudes. Although the instability mechanism is essentially the same, whatever the radial distance, the non linear evolution does produce different effects at small and large distances. Indeed at large distances ( $\sim 20 R_e$  and beyond), B is in general small enough that the instability can reverse the sign of Bz, and thus the sense of the

flow. Similarly changes in the currents can produce a negative  $B_z$  and lead to a magnetic null. Therefore an X-line/X-point can be the consequence of current disruption. In the current disruption models the ion flow is produced by an inductive electric field:  $E_y = -\partial A_y/\partial t$ , where the characteristic time is given by the time variation of the magnetic field associated with the dipolarization. Then the ion flow is simply given by the corresponding  $\vec{E} \times \vec{B}/B^2$ .

As alluded to above, CD/diffusion can be produced by different instabilities. *T. Lui* proposed that CD is achieved via lower hybrid drift or ion Weibel instability. The ballooning instability proposed by *Roux et al.* was investigated in a series of papers, based upon MHD, multi-fluid, and kinetic approach. [13] concluded that ballooning modes are generally stable, while [11] concluded that ballooning modes are unstable for  $\beta \sim 1$ . From a kinetic description carried out in a regime where both ions and electrons are non-adiabatic, [8] concluded that ballooning modes are weakly unstable.

Given the short time scale of CD (and substorm breakup), [15] suggested that the “high frequency” ( $\geq 1$  Hz) waves they observe together with lower frequency ( $T \sim 60$ s) ballooning modes can disrupt the parallel current associated with the modulation of the perpendicular current ( $J_y$ ) by the ballooning modes. If the current sheet becomes very thin  $J_y$  has to be carried by electrons (see next section). Then high frequency waves can act directly, disrupting  $J_y$ , as will be discussed later.

#### 4. Comparisons with observations

It is not easy to find tests that could be applied to determine which model fits best observations. For example, the existence of a quadrupolar  $B_y$  is a candidate signature of a nearby diffusion region associated with an X-line. In fact this kind of signature can also be produced by the field aligned current associated with the development of the ballooning instability. Here we discuss tests that can be applied to Cluster data to discriminate the two types of theories. In particular, the direction of the spatial perturbation. Tearing like perturbations correspond to radial modulation and therefore are characterized by  $k_x$  ( $k_x \gg k_y$ ). On the other hand ballooning modes and current driven instabilities are characterized by large  $k_y$  ( $k_y \gg k_x$ ). Thus a Hall structure should be essentially invariant by translation along the Y, and its magnetic signature should be observed on  $B_y$ . On the other hand an azimuthally moving perturbation ( $k_y$ ) should lead to an azimuthal modulation of  $J_y$  and hence, via  $\text{div}J=0$ , to localized filamentary field aligned current structures. The passage of a filamentary structure should produce simultaneous perturbations on the  $B_y$  and  $B_z$ . We investigate a substorm that developed on September 12, 2001, while the 4 Cluster s/c were inside a relatively thick current sheet (CS) for  $\sim 45$ mn. A negative bay was observed at Tixi at 13:10, followed by a positive bay at 13:15. Weak  $\text{Pi}2$ , observed at Kakioka, intensify after 13:10.

**Fields:** Figure 1 shows relevant Cluster data. The s/c were located near midnight LT, at  $\sim 19$ Re. The distance between the s/c was of order 2000km, with s/c3 at a lower Z than the others. Estimates of CS thickness (H) and the location of CS center ( $Z_0$ ) based on fits to a Harris sheet are also included. The fits are good when the magnetic components are different at the 4s/c, and  $B_x$  different from  $B_{\text{lobe}}$  (the s/c are inside the CS). As well, between 13:09 and 13:15, only one s/c is inside the

CS and the fit overestimates the CS thickness and underestimates the current. With these restrictions in mind we can try to investigate a possible relation between CS dynamics and CS thickness.

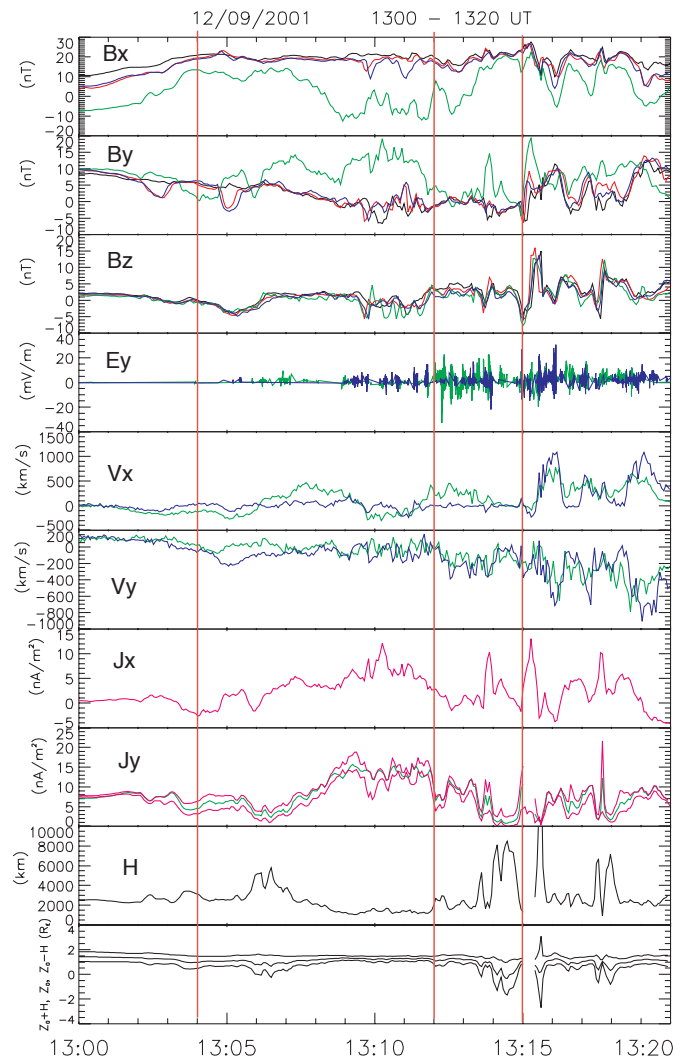


**Fig. 1.** Cluster filed parameters for this event. H and  $Z_0$  are the CS thickness and center, respectively. The two vertical lines bracket the filamentary magnetic structure at  $\sim 13:15$  and the associated local dipolarization (see end of section 4).

Before 13:04 (not shown) the CS thickness decreases from  $\sim 10000$ km to  $\sim 3000$ km. Low frequency ( $T \sim 5$ mn.) oscillations are observed in the CS, but  $E_y$  and  $V_x$  remain steady and very small.  $J_x$  is negligible while  $J_y$  increases from 3 to  $8 \text{ nA/m}^2$ . The ion velocity,  $V_{yi} \sim 100$ km/sec, is sufficient to carry the westward current. In Figure 1, between 13:04 and 13:15 the CS gets very thin  $H \sim 2000$ km or less, since only s/c3 remains inside it. Hence  $H \sim \rho_i$ , the ion Larmor radius in the lobes. Larger amplitude, shorter period ( $T \sim 100$ sec) fluctuations, together with HF fluctuations (on  $\delta E$  and  $\delta B$ ), are observed. Panel 4 shows electric fluctuations. During this period  $V_{xi}$  (panel 5) seems to increase, but this enhancement can be due to the finite radii effects in a very thin CS, as pointed out by [21]. In any case the estimated  $V_{xi}$  remains relatively small.

$V_{yi}$  (panel 6) becomes negative, thus the  $J_y$  current, which is positive and enhanced during this period, has to be carried by electrons. The large negative values of  $V_{yi}$  can be due to an electric field  $E_z$ , pointing towards CS center (e.g. [1]), or to a finite radius effect (e.g. [21]), or both. During this period, the interspacecraft distance is at least the CS thickness so  $J$  is likely underestimated, hence  $J_x > 10 nA/m^2$  (panel 7) and  $J_y > 20 nA/m^2$  (panels 8). The increase in the current density  $J_y$  and the decrease in the CS thickness are approximately consistent with conservation of total current.

Between 13:15 and 13:20 large amplitude fluctuations ( $\sim 100$  sec) continue to modulate  $B_x$ , but the amplitudes at the 4 s/c are similar and  $B_x$  decreases, indicating the CS is thick. These structures correspond to fast ion flow bursts ( $\sim 1000 km/sec$ ) around 13:15:30. Examination of the ion distributions indicates that we are observing ion flow bursts (see below). Large amplitude high frequency (HF) fluctuations ( $B \sim 0.5-2 nT$ ,  $E \sim 5-20 mV/m$ ) are simultaneously observed (see panel 4).

During the thinning of the CS (13:04-13:12) the s/c3  $B_z$  component is weak and often changes sign. The s/c3  $B_y$  component increases and becomes very different from  $B_y$  at the other three s/c. Thus  $B_y$  depends on how deep the s/c is in the CS and so does not correspond to a uniformly applied guide field. During this early period the variations of  $B_z$  are smaller than the variations of the other components. Thus the current density is essentially invariant along Y. Between 13:12 and 13:15  $|B|$  is very small around 13:12:25, 13:13:00, and 13:14:15. This near cancellation does not correspond to a particular ion acceleration. Indeed the electric component  $E_y$  changes sign simultaneously, which indicates that electric and magnetic fluctuations correspond to low frequency fluctuations propagating essentially eastward (they are seen first at C2 which is located to the west of the other s/c). After 13:13 (in particular  $\sim 13:15:30$ ) the variations of  $B_z$  and  $B_y$  are comparable in amplitude and simultaneous; they correspond to filamentary currents. Full resolution data from EFW (Figure 1, panel 4) and STAFF (not shown) give evidence for large amplitude (5-20 mV/m, 0.5-2 nT) "HF" fluctuations ( $< 10 Hz$ ). These fluctuations are confined in the CS, but they are not localized near the quasi-nulls in the magnetic field.

**Electron Dynamics:** Figure 2 displays PEACE parallel electron fluxes over a longer time period. Before 13:04, the energetic electron (few keV) flux is about the same at the 4 s/c, consistent with the CS thickness being larger than the interspacecraft distance. Low energy, quasi-monoenergetic electrons (up to a few 100eV) are sporadically observed along with the quasi steady energetic ( $\sim$  few keV) plasma sheet component. This low energy component is only observed in parallel and anti-parallel fluxes and the variations in the energies of these two components are in antiphase. After 13:04 the energy of plasma sheet electrons decreases at all s/c, but a component with a very low initial energy is observed on s/c3. Its energy increases up to 1keV as it merges with plasma sheet electrons.

Figure 3 shows s/c3 antiparallel, perpendicular, and parallel electron fluxes from 13:00 to 13:20. Around 13:04 (first vertical red line) we observe an accelerated electron component. The energy increases from  $< 100 eV$  to  $\sim 1 keV$ , when this component merges with the pre-existing plasma sheet population. This electron structure is observed only on s/c3. The enhanced flux around 1keV lasts  $\sim 7$ mn, but its energy and its

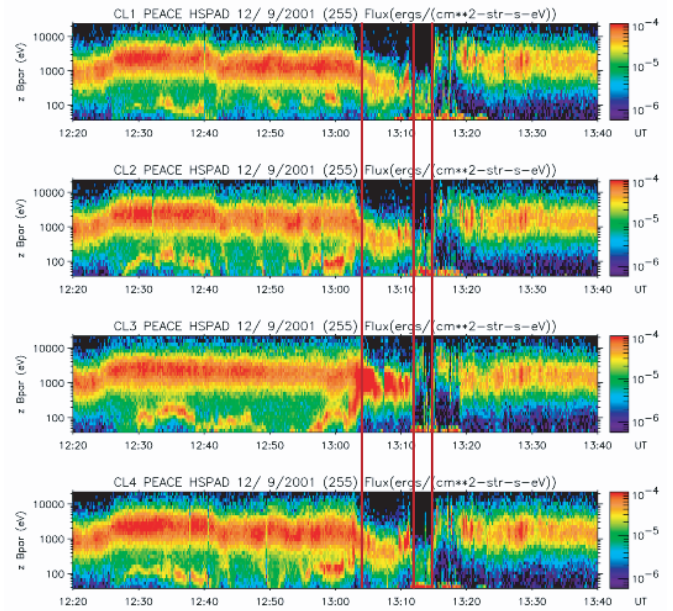


Fig. 2. PEACE parallel electron energy fluxes from the four s/c

intensity fluctuate. This initially very low energy population of (presumably) ionospheric electrons gains about 1keV. Between  $\sim 13:12$  and 13:15 the electron energy suddenly increases at s/c3, but the flux is highly sporadic. Simultaneously, the energy and flux decrease at s/c 1, 2, and 4, suggesting they are in the BL. Hence, the CS is likely even thinner than during the previous period.

The energetic electrons observed on s/c3 correspond to a bursty electron population accelerated in the near equatorial region. Between 13:15 and 13:19 the bursty electron acceleration continues, but now on all 4 s/c, suggesting that the CS has expanded irregularly. This is confirmed by an increase in  $H$  just after 13:20 (not shown in Figure 1). After 13:19 the electron flux on the 4 s/c is more steady, less energetic, and isotropic, again indicating a typical electron plasma sheet. In summary, as the CS thins, we observe first an accelerated ionospheric electron population merged with a decelerated plasma sheet population, and then, as the CS gets even thinner, bursty accelerated electrons.

## 5. Discussion

On September 12, 2001, Cluster monitored the thinning of the CS. From 13:04 to 13:12, as the CS thickness decreases and  $H \sim \rho_i$ , an initially low energy electron population shows up. These electrons are accelerated up to 1 keV and their flux is very large, at least at s/c3, which is closer to the equator. The lack of significant signature at s/c 1, 2, and 4 indicates that this accelerated electron population is highly confined near the magnetic equator. Electrons are, however, field aligned. If they were accelerated in a diffusion region near a neutral line, the  $B_y$  signature should change sign as  $B_x$  changes sign (at least as long as  $B_z$  does not change sign). A large  $B_y$  component is indeed observed at s/c3 until 13:12 (Figure 1, panel 2), but  $B_y$  remains positive as  $B_x$  changes sign around 13:08:30, and  $B_z$  remains small but positive. Another interpretation should be sought. We suggest that this initially low energy component

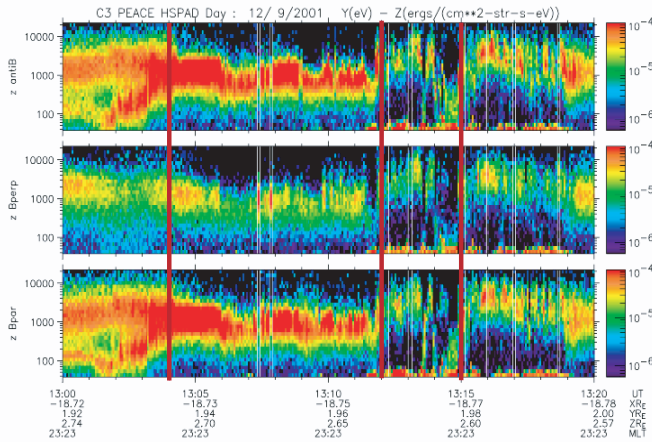


**Fig. 3.** s/c3 PEACE Electron energy fluxes in 3 directions: opposite (top), perpendicular (middle), and parallel (bottom) to  $B$ .

is low energy electrons coming from the ionosphere or from adjacent regions, and which are accelerated by a parallel electric field directed towards the equator (on both sides of the equator), and confined in the near equatorial region. This could also account for the arch-shaped structures observed before 13:04. The arch-shaped acceleration structures observed before 13:04, however, have much smaller fluxes and reach lower energies (few 100eV). They should therefore correspond with much smaller parallel electric fields. In both cases trapped electrons (plasma sheet) loose energy while passing ionospheric electrons gain energy in the near equatorial region. This is consistent with the conservation of the total energy and of the first and second invariant for electrons. Data displayed in Figures 1 and 2 indicate that the energy reached by accelerated electrons is controlled by two factors: the distance from the equator, normalized to the CS thickness, and the modulation by LF waves. Hence the parallel electric field is induced (not static) and is associated with the CS fluctuations. A mechanism for the formation of parallel electric fields, via fluctuations in the current density, is discussed by [3].

Between 13:12 and 13:14 the amplitude of HF fluctuations increases at s/c3 (see Figure 1, panel 4), while it decreases at the other s/c. When the s/c leave the CS, as is the case when all do between 13:14:30 and 13:15, the fluctuation level decreases significantly. This indicates the waves are confined to the CS, and that their intensities are maximum near the equator. Figure 4 illustrates the relation between HF fluctuations and electron acceleration. It shows the electron flux, integrated over all pitch angles, versus time and energy. The electric component of the ( $<10$ Hz) HF fluctuations ( $\delta E_y$ ) is also plotted. Bursts of energetic electrons (typically above 1keV) correspond to bursts in the amplitude of electric and magnetic HF fluctuations. During these bursts the amplitude of the waves is very large (typically 0.5- 2nT, 5-20 mV/m). The largest bursts occur between 13:12 and 13:14:30, for s/c3, and around 13:15 and 13:16, for all s/c. The good correspondence between electron and wave bursts suggests that the waves heat the electrons. Given the frequency range we expect that acceleration occurs via bounce resonance. Indeed  $T_{be} \sim 2$ sec, for 4keV, which is comparable to the period of the waves. It is suggested that HF/small scale fluctuations accelerate and isotropize electrons.

During the early period (13:04-13:12)  $B_y > 0$  and large at

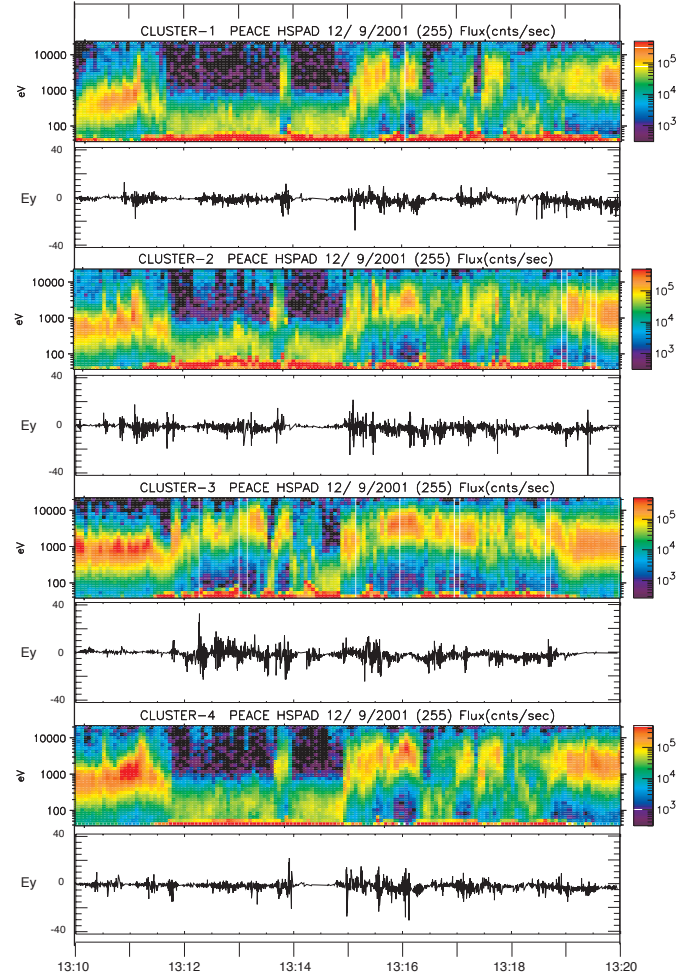


**Fig. 4.** Figure 5 shows the electron flux, integrated over pitch angle, together with the electric field  $E_y$ . Largest  $E_y$  fluctuations generally correspond to bursts of energetic electrons.

s/c3, while  $B_z$  is small. Hence the  $J_x$  current corresponds to a plane sheet more or less invariant along  $Y$ . Yet, as pointed out above, the  $B_y$  signature does not correspond to that of a Hall current structure. At  $\sim 13:15:40$ , and  $13:17:40$ , large amplitude fluctuations are observed simultaneously on  $B_y$  and  $B_z$ ; their signatures correspond to filamentary currents. The most prominent structure is at  $\sim 13:15:40$ . It corresponds to a filament with the current along the  $X$  direction, not to a flux rope extended along  $Y$ . As the structure is observed first at s/c2, it is moving eastward. The same is true for the other structure which is also propagating eastward. As pointed out in section 4, a simultaneous  $B_y$  and  $B_z$  signature, and azimuthal propagation are expected for an instability which develops in the azimuthal direction and leads to a cancelation of the tail current. In line with this, we observe that the CS thickens after the passage of each structure, as evidenced by large decreases in the  $B_x$  components. For instance, the large amplitude structure observed in  $B_y$  and  $B_z$  between 13:15 and 13:16 precedes a decrease in the  $B_x$  component at all s/c, and hence a decrease in the current density  $J_y$ . Current density perturbations move azimuthally eastward as expected from current disruption model.

The flow velocity remains small until 13:15. Between 13:15

and 13:16 a fast ion flow burst takes place ( $\sim 1000\text{km/sec}$ ) while the CS thickness increases. This suggests the filamentary field aligned current structures produce a local reduction of  $J_y$  via  $\nabla \cdot \mathbf{J} = 0$ , which leads to enhanced  $E_y$ , and earthward ion acceleration. The induced electric field  $E_y$  and ion flow  $V_x$  are linked to the variation of  $J_y$ :  $\partial J_y / \partial t \approx \partial^2 E_y / \partial z^2$ , which is valid as long as  $\partial / \partial z \gg \partial / \partial y, \partial / \partial x$ , and  $\nabla \cdot \mathbf{E} = 0$ . These conditions are fulfilled for a thin CS, in the low frequency limit. For  $J_y 25nA/m^2$ ,  $H 2000\text{km}$ , and a rise time (for  $E_y$  or  $V_x$ )  $t \sim 25\text{sec}$ , we get  $E_y \sim 4\text{mV/m}$ , consistent with that measured by EFW. For  $E_y \sim 4\text{mV/m}$ , and  $B_z \sim 5\text{nT}$  we get  $V_x \sim 800\text{km/sec.}$ , also in agreement with observations. Thus the short lasting fast flow bursts during the thickening of the CS can be interpreted as a consequence of the reduction in  $J_y$ .

## 6. Conclusions

In a collisionless plasma, spontaneous reconnection via tearing instability does not seem to be a viable mechanism to form X-lines. In order to initiate magnetic reconnection the key question is to produce a large  $\partial A_y / \partial t$  (an inductive  $E_y$ ). Since the tearing instability is unlikely to develop in a collisionless plasma,  $\partial A_y / \partial t$  has to be achieved by (fast) changes in external conditions, or by local interruption of  $J_y$  over a short time scale via an instability. We have shown here an example of how a large electric field  $E_y$  can be induced by a fast reduction in the  $J_y$  current. This reduction is associated with the development of filamentary current structures that can result from the development of an azimuthally propagating (ky) modulation (such as a ballooning mode), or from a smaller scale instability that reduces the currents. Large amplitude (0.5-2nT, 5-20 mV/m) high frequency fluctuations are indeed observed in association with the eastward travelling low frequency current structures. These HF electromagnetic fluctuations are confined in the thin active CS. Their close association with bursts of energetic electrons suggest that HF fluctuations accelerate and isotropize the electrons. When the  $J_y$  current is carried by bouncing electrons, as it is the case for the event discussed here, HF fluctuations can directly reduce  $J_y$  by scattering field aligned electrons, and/or reducing field aligned currents  $J_x$ .

In summary we suggest that the reduction in the tail current is achieved via a series of local "dipolarization" events, such as the ones described here. Then the dipolarization in the whole plasma sheet would result from the overall summation of local events corresponding to interruption/diffusion of  $J_y$ . This resembles a "chain reaction".

## References

- Asano, Y., Mukai, T., Hoshino, M., Saito, Y., Hayakawa, H., and Nagai, T., Current sheet structure around the near-Earth neutral line observed by geotail, *J. Geophys. Res.*, 109, 1029, 2004.
- Büchner, J. and Zelenyi, L. M., reconnection instability in collisionless plasma, in *Proceedings of an international Workshop on Reconnection in Space Plasma*, volume 2, edited by C. I. Meng, M. J. Rycroft, and L. A. Frank, 21, European Space Agency, Paris, 1989 b.
- Contel, O. L., Pellat, R., and Roux, A., Plasma transport associated with low frequency perturbations; application to the substorm growth phase, *J. Geophys. Res.*, 105, 12929–12944, 2000.
- Coppi, B., Laval, G., and Pellat, R., Dynamics of the geomagnetic tail, *Phys. Rev. Lett.*, 16, 1207, 1966.
- Coroniti, F. V., On the tearing mode in quasi-neutral sheets, *J. Geophys. Res.*, 85, 6719, 1980.
- Galeev, A. A. and Zelenyi, L. M., Tearing instability in plasma configuration, *Sov. Phys. JETP*, 43, 1113, 1976.
- Hesse, M., Schindler, K., Birn, J., and Kuznetsova, M., the diffusion region in collisionless magnetic reconnection, *Phys. Plasmas*, 6, 1781–1795, 1999.
- Hurricane, O. A., Pellat, R., and Coroniti, F. V., The stability of a stochastic plasma with respect to low frequency perturbations, *Phys. Plasmas*, 2, 289, 1995.
- Lembège, B., *Stabilité d'un modèle bidimensionnel de la couche quasi-neutre de la queue magnétosphérique terrestre, vis à vis du mode de "cisaillement" (tearing mode) linéaire*, Ph.D. thesis, Paris, XI, 1976.
- Lembège, B. and Pellat, R., Stability of a thick two-dimensional quasineutral sheet, *Phys. Fluids*, 25, 1995, 1982.
- Liu, W., Physics of explosive growth phase: ballooning instability revisited, *J. Geophys. Res.*, 102, 4927, 1997.
- Lui, A. T. Y., Chang, C.-L., Mankofsky, A., Wong, H.-K., and Winske, D., A cross-field current instability for substorm expansions, *J. Geophys. Res.*, 96, 11,389–11,401, 1991.
- Ohtani, S.-I. and Tamao, T., Does the ballooning instability trigger substorms in the near-Earth magnetotail, *J. Geophys. Res.*, 98, 19369, 1993.
- Pellat, R., Coroniti, F. V., and Pritchett, P. L., Does ion tearing exist?, *Geophys. res. Lett.*, 18, 143, 1991.
- Perraut, S., Le Contel, O., Roux, A., Pellat, R., Korth, A., Holter, Ø., and Pedersen, A., Disruption of parallel current at substorm breakup, *J. Geophys. Res.*, 2000, in preparation.
- Pritchett, P., F.V. Coroniti, and V.K. Decyk, Three-dimensional stability of thin quasi-neutral current sheets, *J. Geophys. Res.*, 101, 27,413, 1994.
- Roux, A., Perraut, S., Robert, P., Morane, A., Pedersen, A., Korth, A., Kremser, G., Aparicio, B., Rodgers, D., and Pellinen, R., Plasma sheet instability related to the westward traveling surge, *J. Geophys. Res.*, 96, 17697, 1991.
- Schindler, K., A theory of the substorm mechanism, *J. Geophys. Res.*, 79, 2803, 1974.
- Sitnov, M., Malova, H., and Sharma, A., Role of temperature ratio in the linear stability of the quasi-neutral sheet tearing mode, *J. Geophys. Res.*, 25, 269–272, 1998.
- Sitnov, M., Sharma, A., Guzdard, P., and Yoon, P., Reconnection onset in the tail of earth's magnetosphere, *J. Geophys. Res.*, 107, 1256, 2002.
- Wilber, M. *et al.*, Cluster observations of velocity space-restricted ion distributions near the plasma sheet, *Geophys. Res. Lett.*, 31, 2004.
- Zwingmann, W., J. Wallace, Schindler, K., and J. Birn, particle simulations of magnetic reconnection in the magnetotail configuration, *J. Geophys. Res.*, 95, 20,877, 1990.

# Cluster observations during pseudo-breakups and substorms

A. Runov, I. O. Voronkov, Y. Asano, R. Nakamura, W. Baumjohann, M. Volwerk, T. Takada, Z. Voros, T. L. Zhang, A. Vaivads, S. Haaland, H. Rème, and A. Balogh

**Abstract:** We discuss Cluster observations of the magnetotail plasma sheet during a set of successive auroral activations between 0300 and 0600 UT on September 15, 2001. Cluster was located near the midnight meridian at about  $19 R_E$  downtail, with foot points on the CANOPUS network, staying in the plasma sheet. Analyzing Cluster magnetometer and ion spectrometer data, we found that the activity in the plasma sheet starts after a 2.5 hours long interval of  $B_z$  decrease; the pseudo-breakups and small substorms, detected by CANOPUS, are associated with enhancements of tailward ion flow. The substorm, following the pseudo-breakups, corresponds to a high-speed ion flow reversal from tailward to Earthward, with a quadrupolar magnetic field structure and intensive ion heating. Thus, the substorm is associated with magnetic reconnection in the near-Earth ( $X > -19 R_E$ ) plasma sheet. The current sheet half-thickness, estimated using four-point magnetic field measurements, gradually decreased prior to the flow reversal, achieving a minimum (less than 1000 km) at expansion phase onset. Finally, the excitation of quasi-harmonic waves with periods of 150 - 200 s, propagating duskward with velocities of 50 - 100 km/s, was detected by the Cluster magnetometers during and after the flow enhancements. Since the IMF was mostly northward, the plasma sheet disturbances during this interval were most likely internally triggered.

*Key words:* Substorms, Pseudo-breakups, Current sheet, Reconnection.

## 1. Introduction

In situ observations in the mid tail plasma sheet are important for understanding physical mechanisms of energy conversion during magnetospheric substorms and substorm-like activations. Key issues are the evolution of the magnetotail current sheet structure and the spatial localization of instabilities, responsible for burst-like energy release. Numerous previous studies with single spacecraft or occasional spacecraft constellations gave the basic information to construct physical models of a substorm. For example, ISEE-1/2 observations show temporal changes of the magnetotail current sheet thickness and structure [1] and formation of a thin current sheet prior to expansion phase [2]; observations by the Geotail spacecraft allowed to place the most probable location of a reconnection region associated with substorm onset between  $X = -20 - -30 R_E$  and  $0 < Y < 8 R_E$  [3, 4, 5].

The four Cluster spacecraft have polar orbits with apogee at  $\sim -19 R_E$ . Forming a quasi-regular tetrahedron in the magnetotail, Cluster enable to identify moving spatial structures like boundary layers, current sheets, wave and flow burst fronts. Four-point timing analysis [6] allows to determine the direction of the spatial structures motion. Therefore, Cluster ob-

servations may provide information about meso-scale (with scales in between several hundreds and several thousands km) transient structures, their internal structure and motion during substorm-like events.

This paper presents a detailed analysis of four-point Cluster observations during a set of successive pseudo-breakups and substorms between 0300 and 0600 UT on September 15, 2001. We will focus on the detection of spatial structures and characterization of their motion. A description and analysis of ground-based observations, IMAGE and GOES spacecraft measurements are contained in the accompanied paper by Voronkov et al., this issue.

## 2. Overview

The overview plot for interval 0000 - 0600 UT on September 15, 2001 is presented in Fig. 1. The IMF  $B_z$  (Wind and Geotail data, Fig. 1, a,  $X$  and  $Y_{GSM}$  positions are specified on the plot) was southward during 0000 - 0045 UT, turned northward at 0045 - 0050 and stays mainly northward except for short excursions at about 0400 and 0530 UT. The substorm with the  $AL$  peak of -700 nT (Fig. 1, b) was observed between 0000 - 0050 UT. After the northward turning of the IMF, the  $AL$  index decreases to zero. The activity starts again apparently without external triggering at  $\sim 0340$  UT, with a drop of  $H_e$  and a local increase of  $H_p$  detected by GOES-8 at geostationary orbit (the vertical dashed line in Fig. 1).

During 0000 - 0600 UT the Cluster quartet traveled between  $[-18.9, 3.5, 1.1]$  and  $[-18.5, 3.3, -3.4] R_E$  (barycenter, GSM coordinates), forming a nearly regular tetrahedron with the largest inter-spacecraft distance of 1700 km (Fig. 1, uppermost panel). The  $X_-$  and  $Z_-$  (GSM coordinates are used overall the paper) components of the magnetic field from the Cluster Fluxgate Magnetometer (FGM, [7]) at the most northern (C4, thick line)

Received 17 May 2006.

**A. Runov, R. Nakamura, W. Baumjohann, M. Volwerk, T. Takada, Z. Voros, and T. L. Zhang.** Space Research Institute Austrian Academy of Sciences, Schmiedlstrasse 6, A-8042 Graz, Austria  
**I. O. Voronkov.** University of Calgary, Calgary, Canada  
**Y. Asano.** Tokyo Institute of Technology, Tokyo, Japan  
**A. Vaivads.** Swedish Institute of Space Physics, Uppsala, Sweden  
**S. Haaland.** MPE, Garching, Germany  
**H. Rème.** CESR/CNRS, Toulouse, France  
**A. Balogh.** Imperial College, London, UK

and most southern (C3, thin line) spacecraft are plotted in Fig. 1, (panels e and f). The ion time-energy spectrogram and proton bulk velocity from Cluster Ion Spectrometry experiment (CIS, [8]) are presented in Fig. 1 g and h. Fig. 1 d shows the magnetic field strength in the lobe, estimated from the FGM and CIS data assuming pressure balance. During the substorm between 0000 - 0050 UT Cluster observed a set of Earthward high speed bulk flow bursts followed by strong dipolarization in the mid-tail plasma sheet ( $B_z \sim 15$  nT). Between 0100 - 0340 UT Cluster observed a gradual decrease of  $B_z$  down to zero and increase of the magnetic field gradient (difference between  $B_x$  at C3 and C4). The ion flow is near zero level and ion temperature gradually decreases.

After  $\sim 0340$  UT the activity in the plasma sheet arises again: Cluster detects a sequence of three successive tailward high-speed ion flow bursts followed by high-speed flow reversal. During approximately 0300 - 0600 UT Cluster foot points were conjuncted to the CANOPUS network. The observations on CANOPUS (see Voronkov et al., this issue) show the set of successive small local substorms and pseudo-breakups associated with the tailward ion flow bursts between 0340 - 0445 UT and a moderate full developed substorm during the ion flow reversal at 0455 - 0535 UT.

Further we discuss Cluster observations during small substorms and pseudo-breakups (0340 - 0445 UT) and during the substorm interval (0455 - 0535 UT) separately.

### 3. Cluster Observations During Small Substorms and Pseudo-Breakups

Fig. 2 presents the Cluster observations in the magnetotail plasma sheet during 0315 - 0445 UT on September 15, 2001. Before the activity starts at 0340 UT, the magnetotail current sheet at the Cluster orbit was stable and quasi-1D, with the gradient directed dominantly along  $Z$ . The half-thickness of the current sheet, estimated using the Harris function ( $HL$ ) varies between 1 - 2  $R_E$ , showing a breathing of the sheet. Ion flows in the plasma sheet are at the near-zero level and the lobe field is stable at a level of 36 nT, indicating rather quiet plasma sheet prior to the activation.

The situation changes dramatically at 0341 UT (vertical dashed line), when the 370 s. long tailward flow burst with velocity of -400 km/s at 0345 UT and large-amplitude variations of the magnetic field were detected by Cluster. The tailward flow burst was followed by the negative variation of  $B_z$  with minimum of -10 nT, bipolar variations of  $B_y$  (mainly negative during the tailward flow).  $B_x$  first slightly increases then abruptly drops to zero. The quasi-1D current sheet structure changes abruptly to a complex 3D one with all three components of the electric current density vary between -5 - 5 nA/m<sup>2</sup>. The current sheet half-thickness estimation using the Harris function can not be meaningfully made during this interval. The energy of ions increases, some exceeding the CIS energy range (40 keV). The estimated lobe field first increases, has a local minimum, increases again up to 38 nT and then decreases down to 32 nT. The  $Y$ -component of the convection electric field, estimated as  $-\mathbf{V} \times \mathbf{B}$  increases up to 3.5 mV/m (Fig 1, i), indicating that the tailward flow carries a significant amount of the magnetic flux.

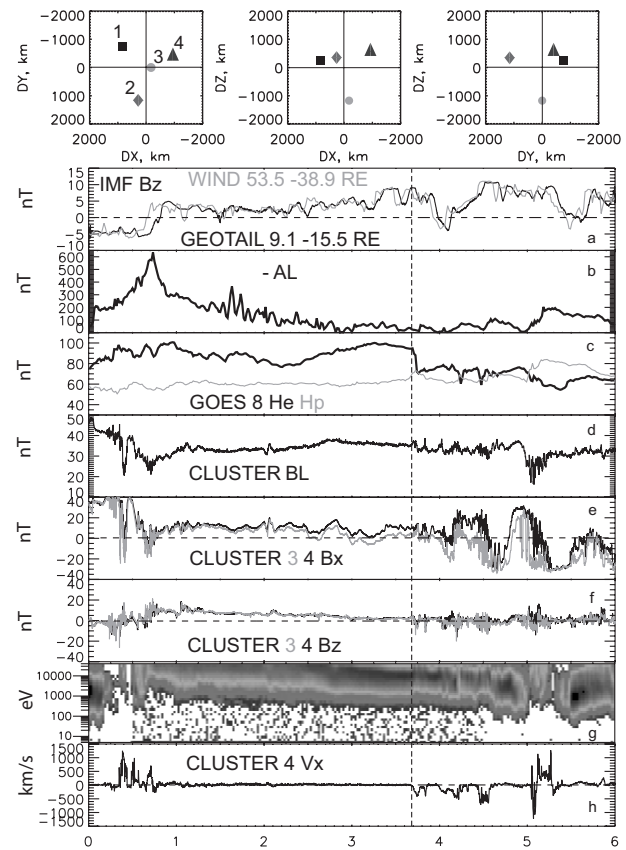


**Fig. 1.** September 15, 2001: The Cluster tetrahedron configuration in respect for the tetrahedron barycenter and event overview plot: IMF  $B_z$  at Wind and Geotail (a), abs. values of  $AL$ -index from Kyoto monitor (b),  $p$ - and  $e$ - components of the magnetic field at geostationary orbit (c), the magnetic field strength in the lobe estimated from the Cluster CIS and FGM data (d),  $B_x$  and  $B_z$  (GSM) at Cluster 3 (thin) and 4 (thick) (e and f, respectively), ion energy-time spectrogram from Cluster 1 (g),  $X$ -component of the ion bulk velocity at Cluster 4 (h).

At  $\sim 0350$  UT Cluster detected the next tailward ion flow burst with duration of 150 s and velocity of -400 km/s.  $B_x$  at Cluster 1, 2 and 4 increases up to 17 nT, while  $B_x$  at Cluster 3 stays around zero.  $B_y$  at Cluster 1,2 and 4 shows a negative excursion down to -16 nT, while  $B_y$  at Cluster 3 varies in the range of  $\pm 3$  nT.  $B_z$  at all four spacecraft shows bipolar variation, associated with minimum of  $B_y$ . The corresponding current density increases up to 10 nA/m<sup>2</sup>, with positive peaks of  $j_y$  and  $j_x$  and bipolar variation of  $j_z$ . The lobe magnetic field strength locally increases up to 39 nT. These signatures allow interpreting this structure as the tailward propagating flux rope [9]. The Harris estimate of the half-thickness of this structure locally decreases down to 3000 km.

During 0359 - 0417 UT Cluster observed the tailward ion flow with velocity varying between -600 and -200 km/s with two distinct velocity enhancements, corresponding to two different auroral activations (see Voronkov et al., this issue). The first flow enhancement was detected at about 100 s earlier than the magnetic field variations. At the very beginning of the flow interval  $B_x$  at Cluster 3 was around zero and the other three

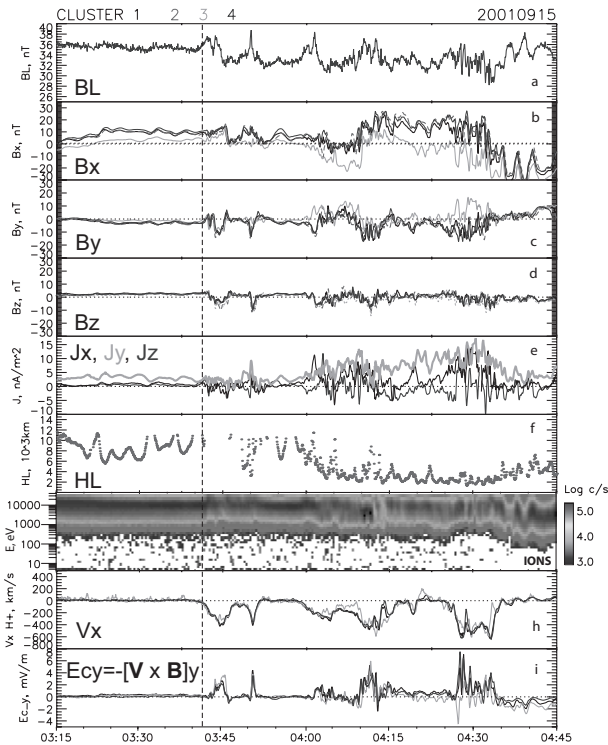


**Fig. 2.** Estimated lobe magnetic field (a),  $X$ -,  $Y$ - and  $Z$ -components of the magnetic field (GSM) (b,c,d) from Cluster 1 (solid black), 2 (dashed), 3 (gray) and 4 (thin black),  $X$ -,  $Y$ - and  $Z$ -components of the calculated current density (e), estimated half-thickness of the current sheet in  $10^3$  km (f), time-energy spectrogram, Cluster 1 (g),  $X$ -component of the ion bulk velocity (h), and calculated convective electric field (i) versus UT.

spacecraft detect  $B_x \sim 5$  nT. At the same time,  $B_y$  at Cluster 3 locally increases up to  $\sim 10$  nT, and  $B_y$  at Cluster 1, 2 and 4 locally decreases down to  $\sim -10$  nT;  $B_z$  at all four spacecraft exhibits a bipolar variation from positive to negative. The lobe field strength has a local peak of 38 nT. The magnetic field data are consistent with a downward ( $-Y$ ) motion of the  $X$ -directed current. About 1.5 min later on, at 0403 UT, Cluster 2 shows a negative excursion of  $B_x$  down to  $-10$  nT and positive excursion of  $B_y$  up to 10 nT, Cluster 4, a positive variation of  $B_x$  up to 10 nT and a negative one of  $B_y$  down to  $-10$  nT, while  $B_x$  and  $B_y$  at Cluster 1 vary between  $-2$  and 5 nT,  $B_x$  and  $B_y$  at Cluster 3 stay at about  $-10$  nT and  $\sim 10$  nT, respectively.  $B_z$  at all four probes reverses from negative to positive. These observations can be interpreted as signatures of tailward propagation of the  $Z$ -directed current filament. The estimated thickness of the current sheet decreases down to  $\sim 2000$  km. At 0405 UT,  $B_x$  and  $B_y$  at all four spacecraft are close to zero, while  $B_z$  trace from Cluster 2 differs from the others, indicating a presence of the current, directed tailward ( $-X$ ). At  $\sim 0410$  UT Cluster crossed a relatively thin current sheet with current density increasing up to  $14$  nA/m $^2$ . Assuming that this current sheet is a planar boundary, four-point timing gives an estimate of the boundary normal velocity  $[0.0, 0.53, -0.85] \times 83$  km/s: The current sheet moves south- and dusk-ward. Estimated half-thickness of the sheet is about

2500 km. The tailward flow velocity increases to 500 km/s, and Cluster/CIS detects a short increase of plasma density with decrease of ion energy. The convection electric field increases up to 6 mV/m.

During 0425 - 0435 UT, Cluster observed tailward ion flow with velocity of  $-600$  km/s. The magnetic field is strongly fluctuating, with amplitude of fluctuations of 15 - 20 nT.  $B_x$  is mainly negative at Cluster 3 and positive at the three others.  $B_y > 0$  at Cluster 3 and  $B_y < 0$  at the three others.  $B_z$  is mainly negative at the all four. The electric current directed mainly along  $Y$  with significant positive  $X$ .  $j_z$  experiences bipolar variation, indicating the current sheet corrugation in  $YZ$  plane. The current density reaches 18 nA/m $^2$ , and the estimated half-thickness of the current sheet decreases down to 1500 - 2000 km. Energy of ions increases to  $\sim 8$  keV during this interval.

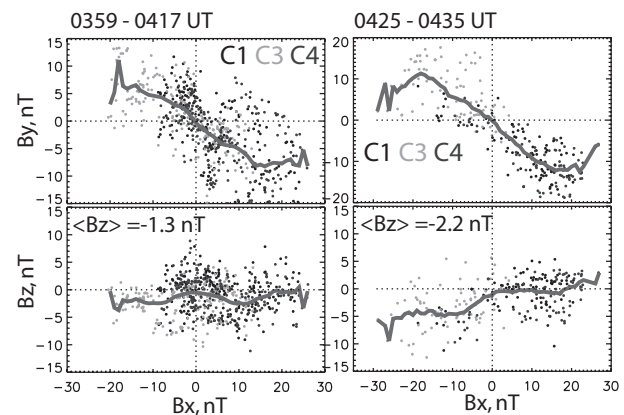


**Fig. 3.**  $Y$ - (upper row) and  $Z$ - (bottom row) components of the magnetic field at Cluster 1, 3, and 4 versus  $B_x$  for 0359 - 0417 and 0425 - 0435 UT. Samples with  $V_x < -100$  km/s are used only. The thick lines show the average values in each 2 nT bin.

During the tailward fast flows intervals 0359 - 0417 UT and 0425 - 0435 UT the magnetic field at the most southern spacecraft (Cluster 3) was smaller and at the most northern one (Cluster 4) was larger than at the others, which is consistent with their GSM location (Fig., 1, uppermost panel). Thus, the GSM system is an appropriate proxy for the current sheet normal coordinate system. Fig. 3 shows  $Y$  and  $Z$  components of the magnetic field from Cluster 1, 3 and 4 corresponding to  $V_x < -100$  km/s versus  $B_x$ . For both intervals  $B_z$  is positive in the southern half and negative in the northern half of the sheet, while  $B_y$  is predominantly negative, which is consistent with the quadrupolar out-of-plane field pattern at tailward side of reconnection site [3]. The same analysis applied to the first two flow bursts (0341 and 0350 UT) does not show any regular behavior of  $B_y$  and  $B_z$  in respect to  $B_x$ .

Fig. 4 presents low-pass filtered  $B_x$  and  $B_z$  time series from all four Cluster spacecraft and  $V_x$  time series from Cluster 1, 3 and 4. Note, that time (in seconds after 0340:00 UT) increases from right to left in this plot. It is visible from the presented data that the ion bulk flow enhances instantaneously with  $B_z$  reversals from some positive value to a negative one. Considering the  $B_z$  reversals as a signatures of a spatial boundary, separating accelerated plasma flow carrying the southward

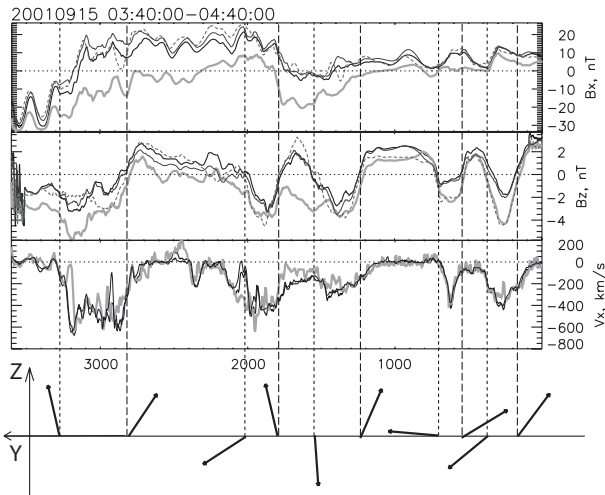


**Fig. 4.** Low-pass filtered  $B_x$  and  $B_z$  reverse time series from all Cluster spacecraft,  $V_x$  from Cluster 1, 3 and 4, and  $YZ_{GSM}$  projections of normal vector resulting from  $B_z$  timing analysis.

magnetic field and a quiet plasma with predominantly northward  $B_z$ , we performed four-point timing analysis to determine directions of these boundaries motion. The analysis shows that the boundaries moves mainly in  $YZ$  plane (Fig. 4, bottom panel), indicating up-down and dawn-dusk motion. The inward boundary crossings with  $B_z > 0 \rightarrow B_z < 0$  variations are associated with upward ( $+Z$ ) and mainly downward motion of the boundaries while the outward crossings - with duskward and downward, except for the last (most left-hand-side) reversal. Thus Cluster was situated above and downward of the flow channel, expanding during the flow enhancements. Cluster crossed the flow channel during the tailward flow between 0425-0435 UT.

Quasi-periodic oscillations with period of 2-3 min were observed by Cluster/FGM during  $\sim 0400 - 0445$  UT. They become more pronounced during and after the the boundary crossing at  $\sim 0410$  UT. Timing of the magnetic field traces show that the oscillations are slowly propagating duskward with velocity of several tens km/s. The nice looking train of the oscillations with  $T \sim 180$  s during 0435 - 0445 UT allows to perform more precise timing analysis which gives the duskward propagating velocity of 60-70 km/s.

#### 4. Cluster Observations During the Substorm

Fig. 5 shows an hour of Cluster data during the substorm interval 0445 - 0545 UT. The vertical dashed line at  $\sim 0454$  UT indicates the substorm onset, observed at PBQ (see Voronkov et al., this issue).

Before the substorm onset, during 0445 - 0454 UT, all four Cluster spacecraft cross the quiet current sheet (from  $B_x = 20$  nT to  $B_x \sim 25$  nT).  $B_y$  anti-correlates with  $B_x$ , changing from positive to negative values during the sheet crossing.  $B_z$  also changes from a small negative value in southern half to a positive one in the northern half of the sheet. Timing analysis of the magnetic field time series shows the current sheet normal direction  $\mathbf{N} = [0.20, -0.05, -0.98]$  (the  $N_z < 0$  indicates southward motion of the current sheet during the crossing). The nor-

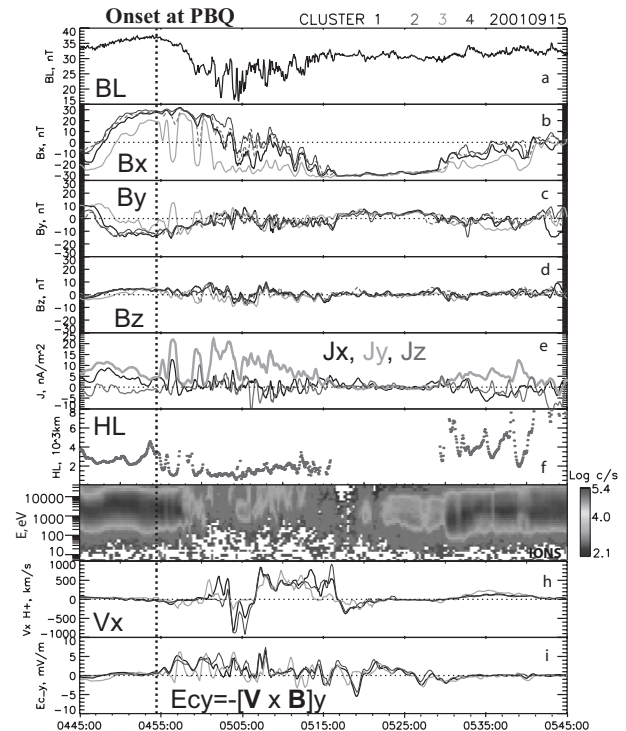


**Fig. 5.** The same as in Fig. 2 for the substorm interval 0445 - 0545 UT.

mal velocity of the sheet motion, estimated by timing, is very small, about 10 - 15 km/s. Minimum Variance Analysis (MVA, [10]), being applied for the magnetic field time series of all four spacecraft, gives essentially the same results with the normal directed basically along  $Z$  and the main field (the maximum variance eigenvector) along  $\mathbf{L} = [0.9, -0.5, 0.1]$ , indicating the significant shear component of the magnetic field at  $\sim 3.4 R_E$  from midnight. The current density reaches  $13 \text{ nA/m}^2$  with current directed in  $Y$  and  $X$  and a local minimum of the current density at  $B_x = 0$  at the Cluster barycenter. The estimated current sheet half-thickness is about 3000 km. The lobe field slightly increases from 34 to 38 nT. The count rate locally increases at ion energies between 2 and 5 keV during 0446 - 0453 UT.

Immediately after substorm onset, during 0454 - 0502 UT, Cluster observed a train of magnetic field variations with a quasi-period of 180 s and amplitude up to 25 nT. The largest variations with change of the magnetic field polarity were observed by the most southern spacecraft (Cluster 3). Assuming that these variations are due to the current sheet kinking and that the current sheet is a plane boundary during the kinking, application of timing analysis shows that the kinks propagate duskward with the normal velocity about 60 km/s. The large shear of the magnetic field persists during the kinking: Cluster 3 detects  $B_y > 0$  during excursions to the southern half of the sheet while the others, staying in the northern half, show  $B_y < 0$ .  $B_z$  varies between -12 and 10 nT, displaying bipolar variations, coinciding with the  $B_x$  variations. Current density increases up to  $22 \text{ nA/m}^2$ , and the corresponding current sheet half-thickness drops down to about 1000 km. The estimated lobe field strength decreases from 38 to 18 nT. The electric

field  $E_{cy} = -(V_z B_x - V_x B_z)$  increases up to 5 mV/m, indicating a considerable vertical flux transfer.

During 0501 - 0504 UT Cluster observed a thin current sheet:  $B_x$  at Cluster 3 varies around -23 nT, while Cluster 4, located in 1739 km northern, detected  $15 \leq B_x \leq 20$  nT. Cluster 1 and 2, located almost at the same  $Z$ , show similar magnetic field behavior crossing the neutral sheet. The current density, estimated using the Linear Gradient Estimator technique [11] varies in the range 15 - 22 nA/m<sup>2</sup>. Using the differences between  $B_x$  at Cluster 1 and 2 as a proxy of the inner sheet current density and Cluster 3 and 4 as one of the entire sheet, we have found 85 nA/m<sup>2</sup> and  $\sim 18$  nA/m<sup>2</sup>, respectively. The CIS/HIA count rate at Cluster 1 decreases dramatically, showing an absence of low-energy ions in the thin sheet. Calculated moments, however questionable because of low density, show Earthward flow enhancements at Cluster 1 and 3.

Between 0504 and  $\sim 0517$  UT, the ion bulk flow reversal from tailward ( $V_x \sim -900$  km/s) to Earthward ( $V_x \sim 800$  km/s) was observed by Cluster 1, 3 and 4. The ion time-energy spectrogram shows a presence of mixed low- (1 - 3 keV) and high-energy ( $\geq 10$  keV) population.  $B_x$  at Cluster 1, 2 and 4 first varied between -20 and 10 nT, then decreased down to -30 nT at the end of the flow reversal interval.  $B_x$  at Cluster 3 varied in the range -20 - -30 nT.  $B_y$  and  $B_z$  were fluctuating during this interval,  $B_z$  was mainly negative during the tailward flow and mainly positive at the beginning of the Earthward flow.

Fig. 6 shows the scatter plots of  $V_x$  at Cluster 1 and 4 versus  $X$ -component of the magnetic field curvature vector  $\mathbf{C} = (\mathbf{b} \cdot \nabla)\mathbf{b}$  and  $X$ -component of the Lorentz force  $\mathbf{F}_L = \mathbf{j} \times \mathbf{B}$ . Points are clearly concentrated in bottom left ( $V_x < 0$ ,  $C_x < 0$ ,  $F_{Lx} < 0$ ) and upper right quadrants ( $V_x > 0$ ,  $C_x > 0$  and  $F_{Lx} > F_0$ ), showing signatures typical for magnetic  $X$ -line configuration (e.g., [12]).

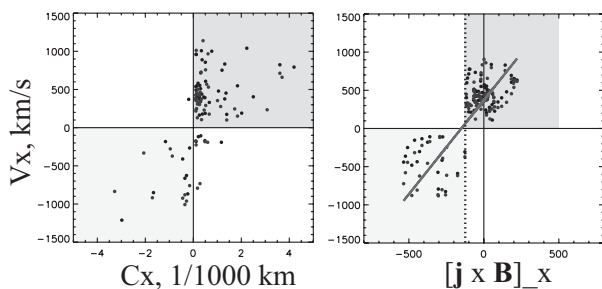


**Fig. 6.** Left-hand panel:  $X$ -component of the ion bulk velocity versus  $X$ -component of the magnetic field curvature vector; right-hand panel:  $X$ -component of the ion bulk velocity versus  $X$ -component of the Lorentz force during the flow-reversal interval 0504 - 0517 UT.

Fig. 7 shows  $B_y$  and  $B_z$  at Cluster 1, 3, and 4 versus  $B_x$  for the tailward flow ( $V_x < -100$  km/s) and for the Earthward flow ( $V_x > 100$  km/s) intervals. During the tailward flow  $B_y > 0$  at  $B_x < 0$  and  $B_y < 0$  at  $B_x > 0$ , while  $B_z < 0$ . This behavior is consistent with the Hall quadrupolar field pattern tailward of  $X$ -line. During the Earthward flow, contrary,  $B_y > 0$  at  $B_x < 0$  in agreement with the Hall pattern Earthward of the  $X$ -line [3].

It is interesting to note that after a stay in the southern lobe and/or PSBL during 0517 - 0529 UT Cluster entered into re-

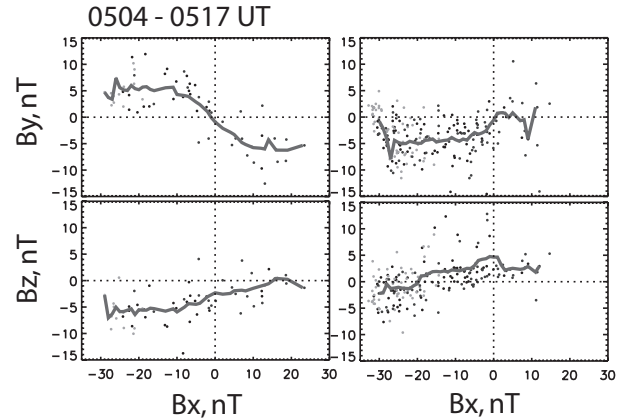


**Fig. 7.**  $Y$ - (upper row) and  $Z$ - (bottom row) components of the magnetic field at Cluster 1, 3 and 4, samples with corresponding  $V_x < -100$  km/s (left column)  $V_x > 100$  km/s (right column) versus corresponding  $B_x$  during the flow reversal interval 0504 - 0517 UT. The thick lines show the average values in each 2 nT bin.

latively cold and dense plasma sheet. The ion energy spectrum after 0529 UT is similar to one observed during 0445 - 0459 UT before the substorm onset. Therefore during the substorm, Cluster crossed the spatially localized rarefied volume of the plasma sheet populated by hot accelerated rarefied plasma embedded into colder and denser plasma sheet. Fig. 8 shows  $B_x$ , low-pass filtered normalized spacecraft potential  $U$  from Cluster/EFW [13], which may be used as a proxy of the particle density [14] (applications of this technique to the magnetopause are discussed in [15]) and ion number density from Cluster/CIS during 0450 - 0540 UT. Although Active Spacecraft Potential Control (ASPOC, [16]) was on at Cluster 3 and 4 the normalized time series of the double probe  $U$  at four spacecraft may be used for approximate timing. Applying this, we found that the front of the rarefaction at 0459 UT was propagating tailward and downward with approximate normal velocity  $[-0.9, -0.5, 0.1] * 50$  km/s.

## 5. Summary

Analyzing the Cluster observations at  $X \simeq -19 R_E$  during the set of substorm-like activations, we found that five successive small local substorms (pseudo-breakups) were associated with tailward ion bulk flow bursts with duration varying from 3 to 15 min. The flow enhancement in the near-Earth magnetotail started without external triggering (IMF was northward, except for the short negative excursion at  $\sim 0400$ , which may cause the fourth activation) and was likely caused by internal instability in the near-Earth plasma sheet which may be resulted from the mid tail magnetic field stretching after the strong dipolarization during preceding substorm. The magnetic field transported by first two short flow bursts and by the first part of the third longer flow shows signatures of flux ropes, while the magnetic field during the second part of the third and during the fourth tailward flow intervals displays the quadrupolar Hall field pattern, which may be interpreted as signatures of magnetic reconnection occurred in the near-Earth plasma sheet (Earthward

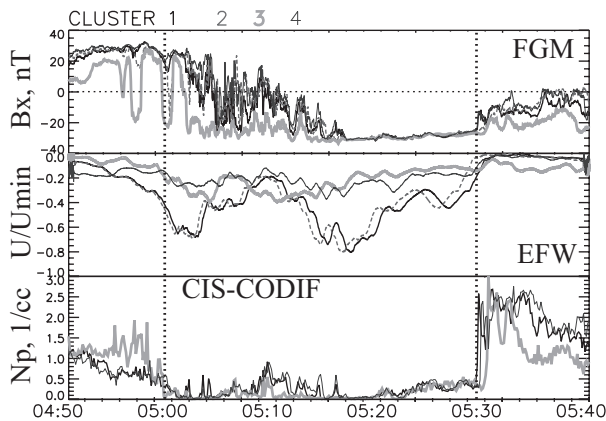


**Fig. 8.**  $X$ - component of the magnetic field (upper panel), low-pass filtered spacecraft potential (double probe), normalized by its minimum unfiltered value (mid panel) from all four Cluster spacecraft and proton number density from Cluster 1, 3 and 4 versus UT during the substorm interval.

of the Cluster position). Analysis shows that Cluster was situated upper and dawn-aside of the bulk flow channel, coming in the channel during flow enhancements.

The fully developed substorm following the set of pseudo-breakups was associated with high-speed flow reversal from tailward to Earthward, preceded by the magnetotail current sheet thinning. Analysis of the magnetic field and ion flow shows that plasma is accelerated by tailward and Earthward directed magnetic tensions. The signatures of the Hall current structure were found during tailward and Earthward parts of flow reversal. Therefore, tailward moving magnetic  $X$ -line was observed by Cluster during the substorm.

During the substorm, Cluster crossed a region in the mid tail plasma sheet populated by hot ions with much smaller number density, than in the surrounding relatively cold plasma sheet. This region of rarefied accelerated hot plasma moved tailward from the near-Earth plasma sheet.

Cluster four-point observations show that spatial structures (boundaries of flow channel, wave fronts, boundaries of the rarefaction region) move in cross-tail direction along with tail-Earthward motion. Therefore, simple 2-D cartoons, often used to describe the magnetotail dynamics during substorm-like events, are incomplete. Motions in third, cross-tail dimension seem to play an important role in the magnetotail plasma sheet dynamics.

#### Acknowledgements

We wish to thank H.-U. Eichelberger, G. Laky, M. Andre, C. Mouikis, L. Kistler, E. Georgescu and E. Penou for help with data and software, the ISSI Team 91 for fruitful discussion. The WIND and Geotail data are available on CDAWeb. We thank WDC for Geomagnetism, Kyoto providing AL indices. This work is supported by INTAS 03-51-3738.

#### References

1. Sergeev, V. A., Mitchell, D. G., Russell, C. T., and Williams, D. J., Structure of the tail plasma/current sheet at  $\sim 11 R_E$

and its changes in the course of a substorm, *J. Geophys. Res.*, **98**, 17345–17365, 1993.

2. Sanny, J., McPherron, R. L., Russel, C. T., Baker, D. N., Pulkkinen, T. I., and Nishida, A.: Growth-phase thinning of the near-Earth current sheet during CDAW 6 substorm, *J. Geophys. Res.*, **99**, 5805–5816, 1994.
3. Nagai, T., Fujimoto, M., Saito, Y., Machida, S., Terasawa, T., Nakamura, R., Yamamoto, T., Mukai, T., Nishida, A., and Kokubun, S.: Structure and dynamics of magnetic reconnection for substorm onsets with Geotail observations, *J. Geophys. Res.*, **103**, 4419–4440, 1998.
4. Baumjohann, W., Hesse, M., Kokubun, S., Mukai, T., Nagai, T., and Petrukovich, A. A., Substorm dipolarization and recovery, *J. Geophys. Res.*, **104**, 24995 – 25000, 1999.
5. Nagai, T., Fujimoto, M., Nakamura, R., Baumjohann, W., Ieda, A., Shinohara, I., Machida, S., Saito, Y., and Mukai, Y. (2005), Solar wind control of the radial distance of the magnetic reconnection site in the magnetotail, *J. Geophys. Res.*, **110**, A09208, doi:10.1029/2005JA011207.
6. Harvey, C. C.: Spatial gradients and volumetric tensor, in: Analysis Methods for Multi-Spacecraft Data, edited by Paschmann, G. and Daly, P., pp. 307–322, ESA, Noordwijk, 1998.
7. Balogh, A., Carr, C. M., Acuña, M. H., et al., The Cluster magnetic field investigation: Overview of in-flight performance and initial results, *Ann. Geophys.*, **19**, 1207–1217, 2001.
8. Rème, H., Aostin, C., Bosqued, J. M., et al., First multispacecraft ion measurements in and near the Earth's magnetosphere with the identical Cluster ion spectrometry (CIS) experiment, *Ann. Geophys.*, **19**, 1303–1354, 2001.
9. Slavin, J. A., Lepping, R. P., Gjerloev, J., et al., Cluster electric current density measurements within a magnetic flux rope in the plasma sheet, *Geophys. Res. Lett.* **30**(7), 1362, doi:10.1029/2002GL016411, 2003.
10. Sonnerup, B. U. Ö. and Schneible, M., Minimum and maximum variance analysis, in: Analysis Methods for Multi-Spacecraft Data, edited by Paschmann, G. and Daly, P., pp. 185–220, ESA, Noordwijk, 1998.
11. Chanteur, G., Spatial interpolation for four spacecraft: Theory, in Analysis Methods for Multi-Spacecraft Data, edited by Paschmann, G. and Daly, P., pp. 349–369, ESA, Noordwijk, 1998.
12. Runov, A., Nakamura, R., Baumjohann, W., et al., Current sheet structure near magnetic  $X$ -line observed by Cluster, *Geophys. Res. Lett.*, **30**, 1579, doi:10.1029/2002GL016730, 2003.
13. Gustafsson, G., André, M., Carozzi, T., et al., First results of electric field and density observations by Cluster EFW based on initial months of operation, *Ann. Geophys.*, **19**, 1219–1240, 2001
14. Pedersen, A., Décréau, P., Escoubet, C.-P. et al., Four-point high time resolution information on electron densities by the electric field experiments (EFW) on Cluster, *Ann. Geophys.*, **19**, 1483–1489, 2001
15. Paschmann, G., Haaland, S., Sonnerup, B. U. Ö., Hasegawa, H., Georgescu, E., Klecker, B., Phan, T. D., Rème, H., and Vaivads, A., Characteristics of the near-tail dawn magnetopause and boundary layer, *Ann. Geophys.*, **23**, 1481–1497, 2005
16. Torkar, K., Riedler, W., Escoubet, C. P. et al., Active spacecraft potential control for Cluster - implementation and first results, *Ann. Geophys.*, **19**, 1289–1302, 2001.

# Magnetic reconnection and current disruption in the inner magnetosphere — a case study

V. Sergeev, M. Kubyshkina, W. Baumjohann, R. Nakamura, A. Runov, Z. Voros, T. Zhang, K. Glassmeier, J.-A. Sauvaud, P. Daly, V. Angelopoulos, H. Frey, and H. Singer

**Abstract:** Three consecutive turbulent magnetic dipolarizations accompanied by auroral brightenings near the equatorward boundary of wide auroral oval were observed with fortuitous spacecraft constellation on September 26, 2005. All were associated with strong near-Earth reconnection pulses (at  $r \leq 14\text{Re}$  with Cluster probed the tailward reconnection outflow region) with separatrix mapped to  $\sim 64^\circ\text{CGLat}$  in the ionosphere where a narrow energy-dispersed ion injection was observed. Onset of magnetic reconnection was nearly simultaneous or lead as compared to the turbulent dipolarization and energetic particle injection onsets. The reconnection tailward outflow contained intense turbulence with the properties similar to that in the turbulent dipolarization regions and with intensity correlating with the outflow amplitude. We conclude that the reconnection process and the growth of strong turbulence in the near tail are strongly coupled together, at least in near-Earth reconnection events, and that near-Earth location of the reconnection site may be more frequent phenomenon than typically thought. In that case it assumed to be possible due to enhanced SW flow pressure which kept the magnetic configuration very stretched in the absence of strong energy loading into the magnetosphere; the ground magnetic perturbations ranged between 50 and 300nT in these intense reconnection events.

*Key words:* Substorms, reconnection, current disruption.

## 1. Introduction

Turbulent current disruption (CD) in the inner magnetosphere or the explosive growth of magnetic reconnection (MR) in the midtail current sheet were considered as alternative substorm onset mechanisms, whose distinction is a one of main targets of the forthcoming THEMIS project. Most controversy comes from ample but indirect evidence of near-Earth location of the substorm onset (deep on closed field lines, around 10 Re, near the transition between the current sheet and dipole-like region, see e.g. a summary by [5, 11], as contrasted to the statistics of reconnection flows from Geotail observations showing that most probable location of the X-line was at 20-30Re [7]. Because of that MR and CD are often treated as spatially far separated and, therefore, different processes. However a large separation may not necessarily be the case: recent indirect evidence of near-Earth onsets were emphasized by [11], a small number of direct observations of near-Earth ( $r \leq 15\text{Re}$ ) reconnection events have also been published [1, 12, 6]. The scarcity of direct observations could in fact be due to the little chance to observe in the very thin reconnection-related current sheet, due to difficulty to diagnose the reconnection with one (or few occasionally located) spacecraft, and due to a number of other important variables (azimuthal and meridional separations between spacecraft and onset locations, magnetic config-

uration etc) which are rarely under the control.

Here we show a unique event in which we look simultaneously at signatures of both (MR and CD) processes in the rare case of near-Earth reconnection where all main variables were under the control. This possibility have occurred largely due to fortuitous spacecraft configuration, with the Cluster and Double Star (Tc2) spacecraft bracketed the near-Earth neutral line near the central meridian of tail activity in the course of 3 subsequent events. (See *Annales Geophysicae* 2001 (N10-12) and 2005 (N11) for the description of instruments). This provides us with reliable observations of very intense reconnection reappearing on closed field lines in the near-Earth tail region.

## 2. Observations

Between 08 and 10 UT on September 26, 2005 (when Cluster spacecraft approached and crossed the current sheet at 14–15 Re distance) 3 plasma injections and dipolarization events (*a*, *b*, *c*) were detected in the inner magnetosphere at 0843, 0931 and 0941 UT - Figure 1(bottom), accompanied by corresponding localized auroral brightenings centered at the 23 h MLT meridian and at  $\sim 64^\circ\text{CGLat}$  (from IMAGE WIC observations, not shown here). Between the activations (*a*) and (*c*) the Cluster baricenter moved from  $[-15.3; 3.7; -0.1]\text{Re}$  to  $[-15.8; 3.8, -0.9]\text{Re}$  GSM, and TC2 was moving upward in Z (from  $-1.4\text{Re}$  to  $-0.5\text{Re}$ ) in the plasma sheet with  $X=-6.5\text{Re}$  and  $Y=+1.9\text{Re}$ , therefore they all stay near 23 h MLT meridional plane, near the central longitude of activation. Other spacecraft (LANL084, Goes10) were within 1-2h MLT from this meridian. At this time Cluster C1,C2 and C3 formed a triangle in XY plane with separations about 9000km whereas C3/C4 (closest to the Earth) had the same X,Y but were separated by 900km in Zgsm allowing to distinguish the thin and thick current sheets.

Received 7 June 2006.

V. Sergeev and M. Kubyshkina. St.Petersburg State University, St.Petersburg, Russia.

W. Baumjohann, R. Nakamura, A. Runov, Z. Voros, and T. Zhang. Space Research Institute, Graz, Austria

K. Glassmeier. IGEP, Braunschweig, Germany

J.-A. Sauvaud. CESR, Toulouse, France

P. Daly. MPAAE, Lindau, Germany

V. Angelopoulos and H. Frey. UCB, Berkeley, USA

H. Singer. NOAA, Boulder, USA

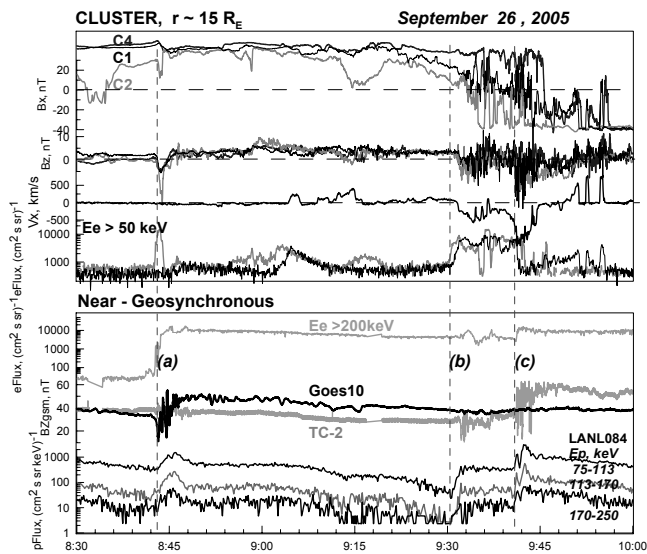


**Fig. 1.** Survey of observations at Cluster spacecraft (top) and in the geosynchronous region (at TC2, Goes10 and LANL084, bottom).

In this favourable configuration Cluster provided decisive evidence of tailward reconnection-related outflow, as specified below. During activations *b*, *c* the spacecraft crossed the current sheet (Figure 1, top), detecting strong ion and convection tailward outflows (up to 500km/s and 1000km/s, correspondingly) synchronous with southward  $B_z$  variation and energetic (isotropic) electron beam (during the activation *b*). Of particular notice is the large difference between  $B_x$  components at C3, C4, suggesting a proximity of very thin current sheet (expected near the reconnection region) with current density up to 30-40 nA/m<sup>2</sup>. Systematic large ( $\sim 0.5B_{LOBE}$ , sign  $(B_y \cdot B_x) < 0$ , not shown here) Hall quadrupole  $B_y$  magnetic field was also observed suggesting the more Earthward position of nearby reconnection region. All main predictions of active reconnection operated at  $X > -15 R_e$  (thin CS, quadrupole Hall  $B_y$ , fast tailward outflow of plasma carrying southward  $B_z$ , particle acceleration) were reliably observed in these events, rejecting any doubts in near-Earth location of magnetic reconnection.

During the activation *a* strong southward  $B_z$  (down to -15nT), intense Eygse up to  $> 10$  mV/m (resulting in tailward outflows ( $(\mathbf{E} \times \mathbf{B})_x / B^2 \sim -400$ km/s in cross-B flow component), and strong energetic electron beam were observed but only by one spacecraft C2, closest to the neutral sheet. A strong evidence in favor of near-Earth reconnection source was also a strong tailward field-aligned anisotropy of electron beam measured by RAPID instrument (by a factor of 5-10 flux increase of electrons in tailward direction during  $\sim 10$  spins, not shown here), this energetic electron beam was observed up to the energy as high as  $\sim 300$  keV.

In contrast to the later events, here other Cluster spacecraft (at larger  $Z$  coordinates) did not register neither the energetic electron beam nor the fast flows, so although they stayed in-

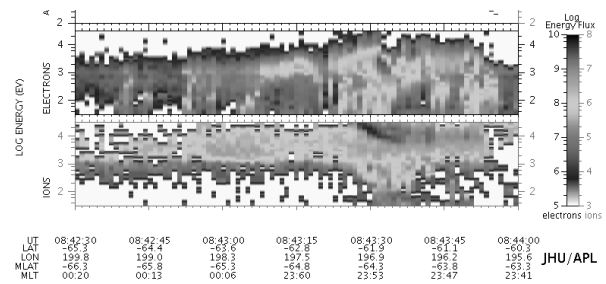


**Fig. 2.** Spectrograms of precipitated auroral electrons and proton fluxes measured by DMSP F15.

side the plasma sheet (and within 0.5Re from both each other and from the neutral sheet), they apparently did not cross the reconnection separatrix staying in the reconnection inflow region. However the obvious tailward progression of magnetic perturbations was observed between C3/C4 and C1 (time delay about 10 sec over  $\sim 9000$ km separation distance), suggesting their  $\sim 900$ km/s tailward propagation velocity, also consistent with reconnection.

A new observation is of low-altitude particle signatures of the near-Earth reconnection region. Tuning the T96 magnetospheric model to fit the magnetic fields observed by Cluster, Tc2 and Goes10 spacecraft at 0842 UT, just prior to the activation *a* (see [4] for the method description), indicated that Cluster C2 spacecraft should map to very low latitude,  $\leq 64^\circ$  CGLat. (With this best possible model the model field at Cluster was still less than observed, the full agreement could not be obtained since further intensification of the tail current quickly brought to the growth of unphysical structure, a large magnetic island). This equatorial part of the auroral zone was crossed by DMSP F15 spacecraft between 084320 and 084350 UT, i.e. just 1 min after the onset of energetic electron burst at C2 and Tc2 (a first indication of strong reconnection-related acceleration). Most spectacular feature in this region is the very intense and energetic energy-dispersed ion beam observed between  $64^\circ$  and  $64.5^\circ$ . The dispersion was very well fitted by the time-of-flight equation  $t_2 - t_1 = (L/k)(1/v_2 - 1/v_1)$  (where indices 1, 2 correspond to different energies  $W_1$  and  $W_2$ ) confirming its TOF nature. The apparent distance was however too short,  $(L/k) = 2.4 R_e$ , to be a pure TOF ( $k=1$ ) effect. (It may be consistent with the reconnection at 12 Re taking into account the fast poleward progression of the ionospheric footpoints of magnetic separatrix which increases  $k$ ; not shown here). The facts (narrow source of very energetic ions with unusual steep slope near the expected separatrix footpoint when the reconnection is going on) support that this narrow energetic ion beam provides the mapping of near-Earth reconnection region, similarly to the well-known VDIS structures existing at the poleward edge of the auroral oval which are the mappings of distant reconnection lines, e.g. [2]. But here the energetic energy-dispersed ion beam is located near the equatorward boundary of otherwise very wide auroral oval (from  $63^\circ$  to  $70^\circ$  CGLAT according to the measurements at DMSP F15).

### 3. Discussion

#### 3.1. Occurrence of near-Earth reconnection

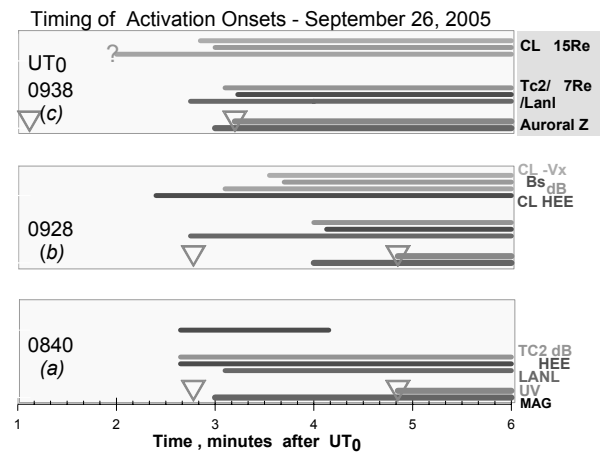
All (three) consecutive turbulent dipolarization and HE particle injection events in our case were observed with excellent spacecraft coverage allowing all major activity parameters to be controlled. Cluster-TC2 constellation bracketed the near-Earth reconnection region, being at the central meridian of corresponding auroral activation. Presence of near-Earth reconnection was established undoubtedly by registering all major reconnection signatures, such as (1) tailward fast flows and southward Bs on the tailward side of reconnection line, (2) Hall By perturbations in this region, (3) acceleration of energetic electrons with occasional tailward beam feature (in the event *a*), (4) thin current sheet signature. In addition, narrow energy-dispersed intense beam of energetic ions was observed in the ionosphere in the expected ionospheric projection of the reconnection separatrix (event *a*), this time near the equatorward edge of the wide auroral oval. The fact, that neither of Cluster spacecraft left the plasma sheet during the whole period 0830-1000 UT, together with a large width of auroral oval in DMSP observations indicate that these intense reconnection pulses occurred deep in the closed flux tubes. The fact of intense reconnection going on on closed field lines at  $r < 14$  Re during events with typical CD signatures in the inner magnetosphere seems to be firmly established in our case.

Generally the probability of such near-Earth location of reconnection is considered as very small one (e.g. recent work [8]). However this also could partly be explained by very small probability to encounter very thin reconnection region, as argued in [11, 12]. Our direct observation of the reconnection systematically reappearing at so small distance require to re-evaluate this possibility. One should not also ignore a possibility of another X-line forming further downtail with a possibility of nearly-simultaneous multiple active reconnection sites, as suggested by some observations (e.g. [10]). These (why/when near-Earth events occur? and, could there be multiple active centers?) could be the interesting questions to address in the forthcoming THEMIS project.

The reason of repeating X-lines appearance at so close location is not quite obvious to us. The tail configuration was very stretched as indicated by the lobe field values exceeding 50 nT and by the low geosynchronous H-(Bz)-component field values of 30-40 nT existing at that time. However the IMF during the period of interest was slightly northward which is reflected in weak auroral zone currents. The SW flow pressure during that time approached  $P_d \sim 8$  nPa (due to the SW density exceeding  $20 \text{ cm}^{-3}$ ) according to WIND and ACE measurements, so we may assume that it is enhanced flow pressure which kept the tail in a stressed state favored the near-Earth onset. This has some indirect support in statistical data [3] which showed that a decrease of substorm onset latitude correlates best with the  $P_d$  parameter. However a direct study of X-line positions depending on solar wind parameters did not reveal any role of flow pressure whereas the dependence on IMF Bz was quite obvious [8]. So the question is open, it should be addressed again, possibly with trying different criteria to define the crossing of reconnection region (high electron temperature criterion used in [8] seems too restrictive, at least it rejects our events if applied).

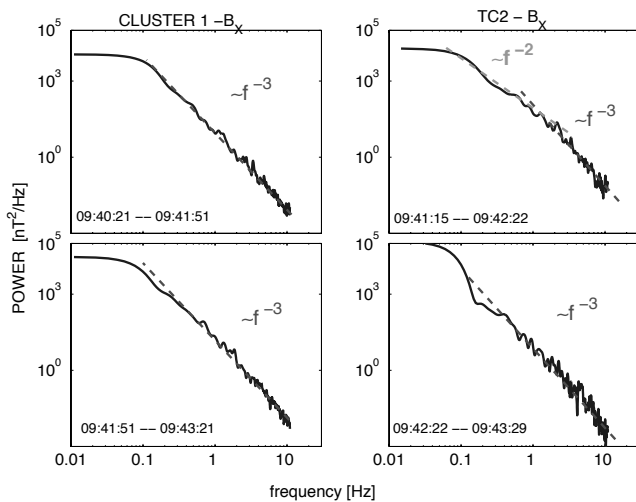
#### 3.2. Reconnection versus current disruption?

Figure 3 shows our attempt to compare the onset times of different activity characteristics during three activations (*a*, *b*, *c*). These characteristics include the energetic electron bursts, southward Bz, tailward flows and turbulence in the tail, energetic electron flux increase, particle injection and turbulent dipolarization in near-Earth region, as well as auroral brightening (from IMAGE WIC camera, at 2 min time resolution) and ground magnetic bay (at 1 min resolution) in the ionosphere. Although onset determination could be questioned in some cases (e.g. onset of plasma sheet turbulence in non-isolated event *c*), the earliest onsets in both regions (near-geosynchronous and plasma sheet on the tailward side of the X-line) are nearly simultaneous (to within 10-20s). During isolated onsets *a*, *b* the earliest signature was that of energetic electron beam at Cluster location. The durations of activations in both regions are also comparable.



**Fig. 3.** Timing of different signatures in the ionospheric, geosynchronous and current sheet regions during three activations.

One weak point in the discussion of the reconnection (MR) and current disruption (CD) as the alternative mechanisms of substorm onsets seems to be the observational characterization of the current disruption, that is a number of signatures allowing to establish its presence and distinguish from another disruptive process, like the reconnection. In fact, the list of predictions provided by CD proponents (e.g. [5]) mostly include those related to the localized nature and near-Earth appearance of the activation in the intense current sheet region (which are suitable for near-Earth reconnection as well), rather than the properties intimately related to the basic physics of current disruption. Its main physical distinction is the high-amplitude turbulence which is able to destruct temporarily the frozen-in plasma behavior. However the strong turbulence is also a feature of the plasma sheet, particularly during high-speed flows (e.g. [13]). Strong turbulence was also observed by Cluster in the tailward reconnection outflows in our events *b*, *c*, see e.g. Fig.1, at the same time when it was probed on



**Fig. 4.** Power spectra of Bx magnetic component at Cluster1 and TC2 spacecraft for two brief episodes of the event c.

the Earthward side by Tc2 spacecraft. Detailed comparison of turbulence properties observed with similar instruments operating on both sides from the reconnection is possible in this event (here we show the first results, more detailed investigation will be published elsewhere).

Figure 4 illustrates an interesting detail: Whereas the peak low-frequency wave activity seem to be stronger in the Earthward region that is in stronger mean magnetic field (e.g. at 094222UT), the power spectra of magnetic field variations during this most powerful turbulence event have similar power law in the high-frequency part (above 0.2-0.3 Hz, that is above the proton gyrofrequency) at both Cluster1 and Tc2. Its slope  $\alpha \approx 3$  is not far from those previously reported either in the plasma sheet BBFs ( $\alpha \approx 2.6$  [13]) or in the near-Earth current disruption events ( $\alpha \approx 2.4$  [9]).

Whereas the more detailed intercomparisons and a study of the turbulence character are the subjects of special study which will be published elsewhere, these initial comparisons show, that not only the CD-like turbulence in near-geosynchronous region on dipole-like field lines appears simultaneously with the turbulence in the plasma sheet tailward of the X-line, the high-frequency turbulence in both regions may be of the same character and origin. This suggests another view of MR/CD, being the close partners (rather than opponents) in the initiation of the localized explosive reconfiguration. This may be realized either if (a) the MR-produced fast outflows generate and transport intense turbulence, or (b), the turbulence created by some current instability (CFCI or others, [5]) plays an important role in the initiation of reconnection.

As the concluding remark we may point out three questions which would be important to address in the THEMIS project. (1) We need to develop the better operational criteria to identify/distinguish the CD process from magnetic reconnection; (2) To study the turbulence in strong Bz-field as compared to the turbulence in BBFs and near the X-line; (3) A comparative study of dynamics in the plasma sheet and near-Earth region for the events with mid-tail reconnection onset as compared to the near-Earth MR events.

**Acknowledgements.** The data of CARISMA and GIMA magnetometer networks were used in this study, the solar wind observations from ACE and WIND were made available at CDAWeb website, and DMSP particle spectrograms were made available at JHU/APL website. The work by V.S. and M.K. was supported by INTAS grant 03-51-3738, RFFI grant 04-05-64932 as well as Russian Ministry of science grant 15392. V.S. also thanks Ics8 LOC for the financial support.

## References

- Baker, D.N., T.I.Pulkkinen, V.Angelopoulos, W.Baumjohann, R.L.McPherron, The neutral line model of substorms: past results and present view, *Journal of Geophysical Research*, *101*, 12975, 1996
- Elphic, R.C., T.Onsager, M.F.Thomsen and J.T.Gosling, Nature and location of the source of plasma sheet boundary layer ion beams, *Journal of Geophysical Research*, *100*, 1857-1869,1995
- Gerard, J.-C., B.Hubert, A.Grad, M.Meurant, Solar wind control of auroral substorm onset locations observed with IMAGE-FUV imagers, *Journal of Geophysical Research*, *109*, A03208, doi:10.1029/2003JA010129, 2004
- Kubyskhina, M. V., Sergeev, V. A., Pulkkinen, T. I., Hybrid Input Algorithm: An event-oriented magnetospheric model, *Journal of Geophysical Research*, *104*, 24,977, 1999
- Lui, A.T.Y., Current disruption in the Earth's magnetosphere : Observations and models, *Journal of Geophysical Research*, *101*, 13067,1996
- Miyashita, Y., A.Ieda, Y.Kamide, S.Machida, T.Mukai et al., Plasmoids observed in the near-Earth magnetotail at  $X \sim -7$  Re, *Journal of Geophysical Research*, *110*,doi:10.1029/2005JA011263, 2005
- Nagai, T., M.Fujimoto, Y.Saito, S.Machida, T.Terasawa et al., Structure and dynamics of magnetic reconnection for substorm onsets with Geotail observations, *Journal of Geophysical Research*, *103*, 4419-4440, 1998.
- Nagai, T., M. Fujimoto , R. Nakamura et al., Solar wind control of the radial distance of the magnetic reconnection site in the magnetotail, *Journal of Geophysical Research*, *110*, doi:10.1029/2005JA011207, 2005
- Ohtani, S., K.Takahashi, T.Higuchi et al., AMPTE/CCE-SCATHA simultaneous observations of substorm-associated magnetic fluctuations, *Journal of Geophysical Research*, *103*, 4671-4682, 1998
- Owen, C.J., J.A.Slavin, A.N.Fazakerley, M.W.Dunlop, A.Balogh, Cluster electron observations of the separatrix layer during traveling compression regions, *Geophysical Research Letters*, *32*, L03104, doi:10.1029/2004GL021767, 2005
- Petrakovich, A.A., A.G.Yahnin, The substorm onset location controversy, *Space Sci.Rev.*, , in press, 2006.
- Sergeev, V.A., V.Angelopoulos, D.G.Mitchell and C.T.Russell, In situ observations of magnetotail reconnection prior to the onset of small substorm, *Journal of Geophysical Research*, *100*, 19121-19133, 1995
- Voros, Z., W.Baumjohann, R.Nakamura et al., Magnetic turbulence in the plasma sheet, *Journal of Geophysical Research*, *109*, A11215, doi:10.1029/2004JA010404, 2004

# Multilayered structure of thin current sheets: multiscale "Matreshka" model

A. S. Sharma, L. M. Zelenyi, H. V. Malova, V. Yu. Popov, and D. C. Delcourt

**Abstract:** Current sheets in the Earth's magnetosphere are the sites where the plasma processes leading to magnetic energy storage and subsequent fast release are initiated. Analytical self-consistent model of multicomponent thin current sheets has been developed in which the tension due to the magnetic field lines is balanced by particle inertia, and the plasma consists of ions of both solar wind and ionospheric origin. The influence of electron population is taken into account assuming Boltzman-like quasi-equilibrium distribution in the ambipolar field, and can lead to a sharp peak in the electron current density in the center. The inclusion of non-adiabatic  $O^+$  ions in the model leads to a new source of current in the Grad-Shafranov-like system of equations describing the quasi-equilibrium configuration. The  $O^+$  current dominates in the outer parts of the current sheet, yielding a multilayered or "Matreshka"-like structure. Thus the magnetotail itself exhibits multiscale behavior evident in the magnetosphere.

*Key words:* Multilayered thin current sheet, Multiscale phenomena, Reconnection onset, CLUSTER, MMS.

## 1. Introduction

The magnetosphere is a strongly coupled system due to the cross-scale coupling among the many phenomena in the different regions, viz. magnetosheath, tail lobes, plasma sheet, ring current and ionosphere. The thin current sheet in the magnetotail is a key boundary region where the processes responsible for the onset of explosive release of energy takes place during substorms. Although these processes are kinetic in nature with scale sizes as short as the electron gyro radius, the strong cross-scale coupling leads to the global magnetospheric features such as plasmoid formation and release.

The basic plasma processes that transport, accelerate, and energize plasmas in the thin boundary and current layers are crucial to the understanding of geospace and this has motivated the recent multi-spacecraft missions. The CLUSTER mission has provided unprecedented measurements of the plasma parameters to spatial scales corresponding to the ion gyro radius and has led to a new understanding of the plasma boundaries and sheets, e. g., the magnetopause and magnetotail. The Magnetospheric Multiscale (MMS) mission will explore the whole range of microscale processes associated with magnetic reconnection on scales that have been inaccessible so far [18].

The coupling of the solar wind mass, momentum and energy leads to the thinning of the magnetotail current sheet and eventually to magnetic reconnection. A key to the understanding of the current sheet, and hence of magnetic reconnection, is its equilibrium. The plasma equilibria underlying the magnetotail current sheet have been studied extensively since its discovery. Recent in-situ measurements by CLUSTER space-

craft [17, 13, 1] demonstrated that current sheets in the Earth's magnetotail can be as thin as to 1 – 2 ion Larmor radii and have complicated internal structures with a hierarchy of spatial scales [16]. The cross-tail current profiles are observed to be substantially different from the well-known Harris model [6] and a schematic of the magnetotail current sheet is shown in Fig. 1 where the magnetic field has a finite  $B_z$  or  $B_n$  component.

The plasma mantle is usually considered to be a primary source for populating the Earth's magnetotail [12]. However measurements of the magnetospheric plasma composition [10] have shown the important role of particles of ionospheric origin. The spacecraft measurements of ion composition in the lobes at distances  $10R_E > X > 22R_E$  have shown the presence of relatively low energy ( $\sim 10eV - 1keV$ ) heavy ions streaming anti-sunward [4, 21, 15]. It was demonstrated that  $O^+$  ions dominate both the pressure and density of the plasma sheet before the substorm onset and their contribution increases even more after substorm expansion begins. In modeling the current sheet of the Earth's magnetotail it is therefore important to take into account its multicomponent composition including solar wind ( $H^+$ ,  $He^{++}$ ) and ionospheric ( $O^+$ ,  $He^+$ ) ions. The effects of such complicated compositions both on the structure of kinetic quasi-equilibria and dynamical processes are not well understood till recently [27]. Recent estimates [8] of the upper limit for the contribution of oxygen ions to the total cross-tail current has shown it to be as much as 10%. This is already a considerable effect and the presence of oxygen ions is found to have important consequences, viz. it dominates the cross-tail current outside the rather narrow tail midplane [27].

The contribution of  $O^+$  ions to the magnetotail plasma equilibrium has been modeled on the lines of the thin current sheet models developed earlier [9, 20, 23, 26]. In the first attempt [27] to model the effect of ions other than  $H^+$ , the other relatively minor ions such as  $He^+$ ,  $He^{++}$  were neglected. Using the semi-analytical Vlasov model of magnetotail quasi-equilibria the dependence of the shape of the cross-tail current profile on a number of parameters, viz.  $B_n/B_0$ ,  $n_{O^+}/n_{H^+}$ ,  $T_{O^+}/T_{H^+}$ , and  $T_{e\perp}/T_i$ ,  $T_{e\parallel}/T_{e\perp}$  were obtained. Here  $B_n$  is

Received 26 June 2005.

**A. S. Sharma.** Department of Astronomy, University of Maryland, College Park, Maryland, U. S. A.

**L. M. Zelenyi and H. V. Malova.** Institute for Space Research, Moscow, Russia

**V. Yu. Popov.** Physics Department, Moscow State University, Moscow, Russia

**D. C. Delcourt.** Centre d'études des Environnements Terrestres et Planétaires-CNRS, Saint-Maur des Fausses, France

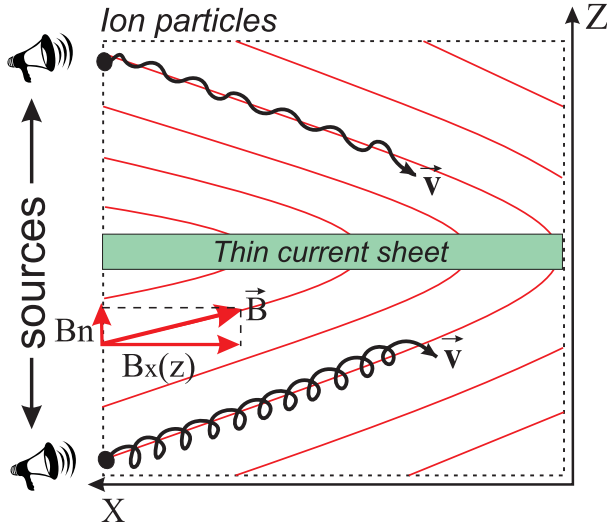


**Fig. 1.** The schematic diagram of the 1D model of the magnetotail current sheet. The particles entering the region on the left execute different orbits depending on their energy and location in the inhomogeneous magnetic field. The different types of particle trajectories are shown in Fig.2.

the normal component of the magnetic field and  $B_0$  is the total magnetic field,  $n$  and  $T$  are the density and temperature (with parallel and perpendicular components), respectively.

## 2. Multi-component model of the magnetotail current sheet

A self-consistent equilibrium model of 1D anisotropic current sheet with a small normal component of the magnetic field ( $B_z$  in GSM system of reference) has been developed considering the particle orbits to be quasi-adiabatic [9, 20]. The tension of the curved magnetic field lines is balanced by the centrifugal force acting on ions crossing the sheet midplane, leading to a 1D equilibria with  $\partial/\partial x = 0$  (e.g. without pressure gradient along tail axis). The plasma in the source region enters the central region (as shown on the outer regions on the left) in Fig. 1) where they carry a cross-tail current ( $J_y$  in our geometry) consistent with the magnetic field reversal in the vicinity of the  $z = 0$  plane. The electric field component  $E_y$  can be neglected without any loss of generality by selecting a suitable deHoffmann-Teller frame of reference. The dynamics of ions and electrons are different inside the thin current sheet (TCS), so a hybrid approach can be used to describe the behavior of the different particle species. The non-adiabatic hydrogen ( $H^+$ ) and oxygen ( $O^+$ ) ions moving across the sheet with Speiser orbits will be described in the so called quasi-adiabatic approximation [20, 22]. The electrons are considered magnetized with finite inertia across the field lines and negligible inertia for field-aligned motion. The resulting charge separation generates an ambipolar electric field  $E_z$  supporting the quasi-neutrality of the plasma. The problem is then reduced to the solution of a Grad-Shafranov type equation, where currents from all particles species are self-consistently calculated from the equations of motion in the electric and magnetic fields generated by these currents.

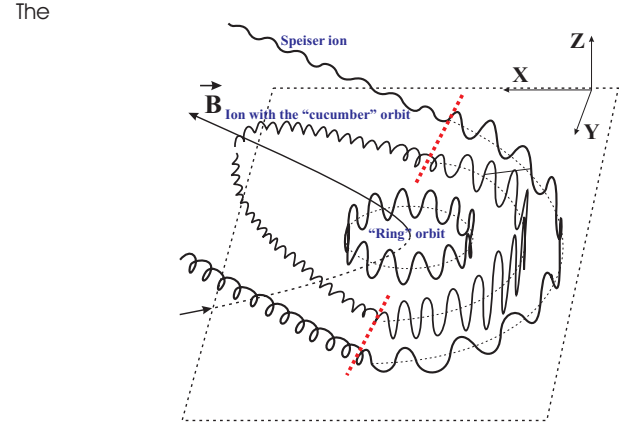


**Fig. 2.** The three different types of particle trajectories in the current sheet with finite  $B_z$ , viz. trapped, quasi-trapped and transient particles.

When the ions cross the current sheet (CS) region, their motion is characterized by three integrals of motion: the total energy  $W_0 = m(v_x^2 + v_y^2 + v_z^2)/2 + e\phi$ , the canonical momentum  $P_y = mv_y - (e/c)A_y(z)$  and the approximate integral of motion or adiabatic invariant  $I_z = \frac{1}{2\pi} \oint mv_z dz$  (here  $\vec{v}$  is the particle velocity,  $A_y(z)$  is the vector-potential, and  $\phi$  is the electrostatic potential).  $I_z$ , the so called Speiser CS invariant, is approximately conserved in a TCS where particle oscillations along the  $z$  and  $x$  coordinates are decoupled because of the widely separated oscillation frequencies:  $\omega_x/\omega_z \ll 1$  [2, 3]. In the quasi-adiabatic approximation, the invariant  $I_z \approx const.$  is used to render the equations of motion integrable and to determine the ion distribution at any position using the Liouville theorem. The value of  $B_n$ , the small normal component of the magnetic field is a parameter with a specified value, and the only assumption is that it is strong enough to keep the electrons magnetized. In these studies it is set to the value of  $B_n = 0.1B_0$ , and the electron motion along the field lines is assumed to be fast enough to support a quasi-equilibrium Boltzmann distribution in the presence of an electrostatic potential and mirror forces.

## 3. Magnetotail equilibrium with oxygen ions

The current sheet model in the presence of  $O^+$  is derived following the theoretical model developed earlier [24, 25]. In the previous models only two plasma components, protons and electrons, were taken into account. The Ampere's equation in the 1D case acquires the simple form:

$$\frac{dB_x}{dz} = \frac{4\pi}{c} (j_H + j_O + j_e) \quad (1)$$

The total magnetic field  $B_x$  arises from the contributions from the currents carried by  $H^+$ ,  $O^+$  and electrons  $e^-$ . The boundary condition is  $B_x(\infty) = B_0$  and the current densities  $j_H$  and  $j_O$  are given by

$$j_{H,O}(z) = e \int_0^\infty dv_x \int_0^\infty dv_z \int_0^\infty v_y f_{H,O}(\vec{v}, z) dv_y \quad (2)$$

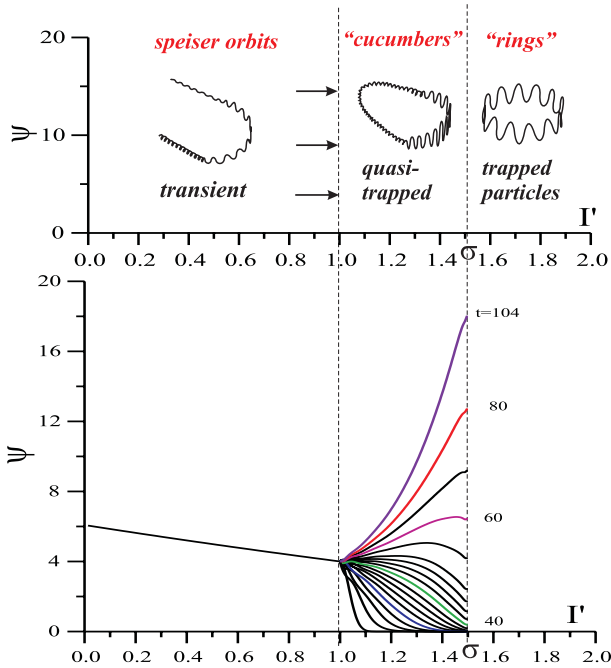


**Fig. 3.** The distribution functions of the different types of particles for an initially maxwellian distribution [23]. The different lines for the quasi-trapped particles correspond to different stages of evolution, starting with the left most.

with the distribution function  $f_{H,O}$  to be taken in the form of a shifted Maxwellian function at the location of the plasma source, i.e., at the boundary of the system  $z = \pm L$  (Fig. 1):

$f_{H,O} \sim \exp \left\{ -\left( v_{\parallel} - v_{D_{H,O}} \right)^2 + v_{\perp}^2 / v_{T_{H,O}}^2 \right\}$  where  $v_{T_{H,O}}$  are the thermal velocities, and  $v_{D_{H,O}}$  are the drift velocities of the  $H^+/O^+$  ions. The electron motion is described by fluid-like equation, but with the pressure anisotropy ( $p_{\parallel} \neq p_{\perp}$ ) taken into account:

$$m d\vec{r}/dt = -e \left( \vec{E} + \frac{1}{c} [\vec{v} \times \vec{B}] \right) - \frac{\hat{\nabla} p_e}{n_e} - \mu \vec{\nabla} B \quad (3)$$

A semi-hydrodynamic approach has been developed for obtaining the electron current  $j_e$ , the ambipolar electric field  $E_z(z)$  and its influence on electrons and protons [24]. Finally the full system of equations for  $B_x$ ,  $j_y$ ,  $\phi$  and  $n$  (plasma density) is solved using the integrals of motion  $W_0$ ,  $P_y$  and  $I_z$  for the particle orbits shown in Fig. 2. The distribution function corresponding to these different types of orbits is shown in Fig. 3. The evolution of the distribution of quasi-trapped particles due to the scattering is shown by the different lines in the middle panel, with the lowest curve corresponding to the earliest instant.

#### 4. Multilayered structure of thin current sheets

The self-consistent system of equations for the magnetic and electric fields, the total and partial current densities as well as the electrostatic potential and the plasma densities are solved numerically using a two-step iteration procedure for the ions and electrons [24, 25]. The results of this model are

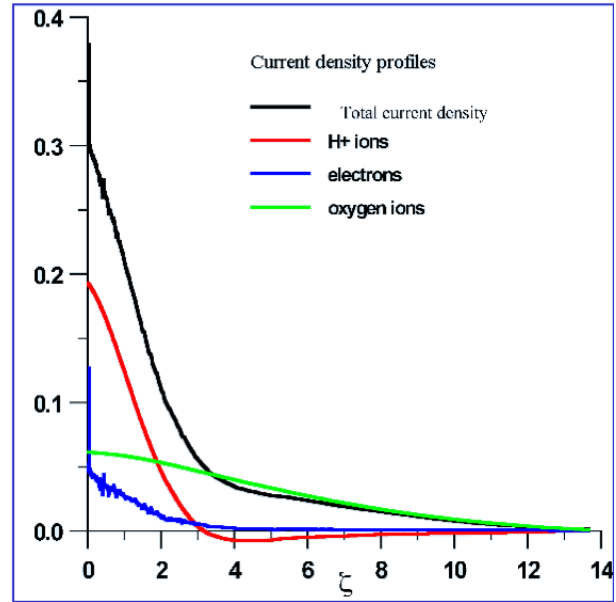


**Fig. 4.** The current densities of the different plasma species. The contributions of the different species have different characteristic lengths, with the oxygen having the broadest and the electrons the narrowest profile [27].

shown in Fig. 4, where the partial profiles of current densities and the corresponding magnetic fields of different plasma constituents, and the total profiles are plotted. The plasma parameters were chosen to be close to the observed values, e.g., the oxygen to hydrogen temperature ratio outside the sheet is  $T_0/T_H = 1, 0.5, 0.25, 0.1$ , and  $0.0$ . The values of the initial density of oxygen is chosen to be  $(0, 0.1, 0.25, 0.5, 1.0) n_H$  outside the sheet. The case of  $n_{O^+}/n_{H^+} = 1$  is shown Fig. 4 for reference. The role of electrons is the most substantial in the center of the current sheet, where the electrons dominate and support a very narrow and peaked current embedded in the proton current, which in turn is embedded in the oxygen current. The currents of the  $O^+$  ions are comparable with that of the  $H^+$  ions, but the half- thickness of the oxygen current density ( $\sim 6\rho_L$ ) is three times larger than that of the protons ( $\sim 2\rho_L$ ). It is clear from this figure that both the ion populations contribute approximately equally to the total cross-tail current, although the total CS thickness is determined generally by the oxygen ion current. Also the net contribution of  $O^+$  is seen to be about 30% of the total current density.

The role of  $O^+$  shown in Fig. 4 could be somewhat exaggerated, and additional studies are shown in Fig. 5. The observations [21, 4, 15] show that the relative fraction of oxygen in the magnetotail may vary widely during different phases of magnetospheric activity (but very rarely exceed the density of hydrogen ions) and accordingly the dependence of  $I_O/I_{total}$  (where  $I_O$  and  $I_{total}$  are the  $O^+$  and total currents, respectively) are investigated as a function of the ratio of densities  $n_O$  and  $n_H$  (Fig. 5). A similar variation is found for different values of the temperature ratio  $T_O/T_H$  [27]. An increase of oxygen ion content in the magnetotail plasma from 25% to 100% leads to an enhancement of its the relative contribution to cross-tail current from 18% to  $\sim 30\%$ . Similar results were

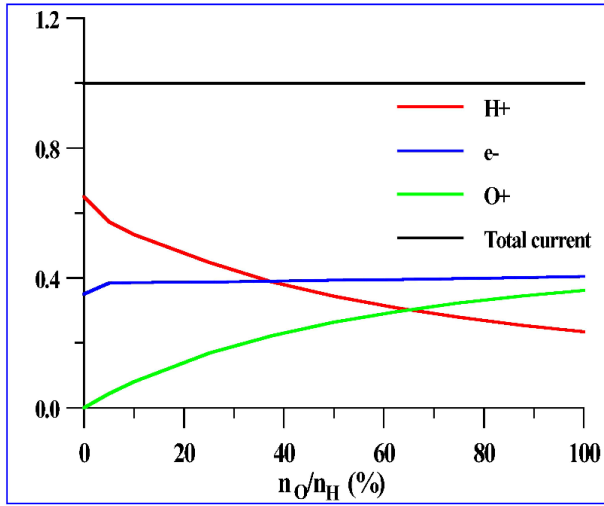


**Fig. 5.** The cross-tail currents carried by the different species as a function of the relative densities of the oxygen to hydrogen ions [27].

achieved if one decreases  $O^+$  temperature in comparison with that of  $H^+$ . The oxygen current contribution, although being sensitive to  $O^+$  temperature, still remain in the (20 – 30)% range.

The contributions of oxygen ions to the magnetotail current, shown in Fig. 5, can be compared with the estimates from the spacecraft observations. Estimates using CLUSTER measurements [8] yield the relative density of oxygen ions to be of the order of 15%. It should be noted that the estimate of 30% is the upper limit, and it depends strongly on the oxygen flux at the source and on the oxygen temperature. In general these results provide estimates of the same order as the observations. The main conclusion concerning the role of oxygen in the structure of thin current sheets in the Earth’s magnetotail is that the current of the  $O^+$  ions leads to an effective thickening of the total current profile and is dominant at the outer regions of the sheet.

A combination of the contributions of the oxygen ions, as shown in Fig. 4, and the earlier results of thin current sheets [24, 25], yields an interesting multilayer structure of the current sheet resembling a “matreshka”, a popular Russian nesting doll. A very thin electron layer  $L \sim 0.05 - 0.1\rho_i$  is embedded in a thin proton sheet with ( $L \sim \rho_i$ ), which in turn is embedded in a thick oxygen sheet ( $L \sim 7 - 10\rho_i$ ). Further, the CS as a whole is embedded inside the thicker plasma sheet, i.e., generally there are four levels of embedding (Fig. 4).

**5. Bifurcated thin current sheet**

The profile of the magnetotail current sheet is generally found to be peaked on the axis, in agreement with the plasma equilibrium conditions. However some observations have shown the current density to be depleted in the center [7, 14, 17] resulting into double humped profiles. Such cases are widely referred to as bifurcated current sheets and can be a consequence of the nature of particle trajectories in the vicinity of the center of the current sheet. A simplified picture of the particle trajectory corresponding to the Harris sheet is shown in Fig. 6 to illustrate this. The particles with meandering or Speiser orbits can

carry a current which is opposed to that carried by the bulk of the plasma away from the center. The population of such particles can increase due to the unavoidable quasi-adiabatic scattering of transient particles near the neutral plane due to the jumps in their adiabatic invariants. Consequently there can be a net reduction in the current locally when the scatterings are significant, e.g., when the current sheet is highly stretched during late growth phase of substorms. The model of thin current sheets for such conditions leads to the bifurcated current profiles, as shown in Fig. 7 [26].

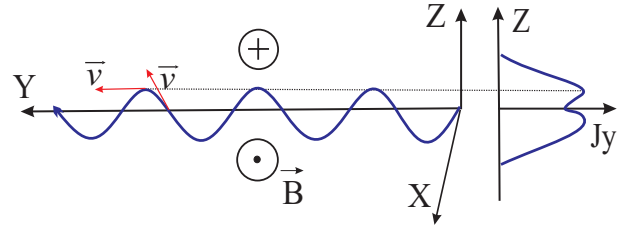


**Fig. 6.** The simplified particle trajectories in the case of a Harris-like current sheet. The meandering or Speiser orbit particles are confined to the central region of the current sheet and carries a current whose direction is opposite to the current carried by the particles located away from the axis. This can lead to a depletion in the current density in the center of the current sheet, as shown by the right panel.

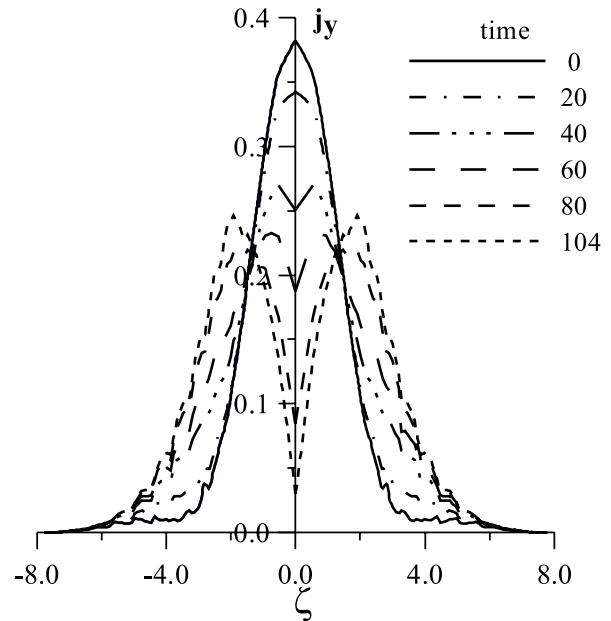


**Fig. 7.** The bifurcated current density inside a thin current sheet at different instants in its evolution, starting with an initial current density peaked on the axis [26].

The bifurcated current sheets can lead to further deterioration of the current sheet and “aging” [23]. The scenario of current sheet evolution that emerges from these considerations is that the initially peaked current profile leads to a bifurcated profile due to an increase in the quasi-adiabatic scattering dur-

ing the growth phase of substorms. As the magnetotail is driven further and becomes more stretched the scattering increases till the current sheet disrupts [23]. The GEOTAIL observation of bifurcated current sheets has been associated with the electron dynamics during magnetic reconnection [7]. It should be noted that CLUSTER observations associate the bifurcated current sheet with finite  $B_z$  and thus may not be associated with magnetic reconnection. This implies that the bifurcated current sheets observed by CLUSTER are more likely a feature of the quiet time or stable magnetotail, rather than those associated with reconnection during the expansion phase of substorms. The model of the bifurcated current sheet developed from the plasma equilibrium, presented above, is in agreement with the observations in this aspect also.

## 6. Multiscale phenomena in the magnetosphere

The two features of the current sheet discussed above, viz. the multilayered structure and bifurcated profile, leads to a picture of the magnetotail in which many scales are involved. This recognition is closely tied with the multiscale characteristics of the magnetosphere [19]. The magnetospheric multiscale phenomena has three main origins, viz. the driving by the turbulent solar wind, nonlinearity and cross-scale coupling among the plasma processes. Due to the wide range of space and time scales underlying the plasma processes in the magnetosphere, the multiscale phenomena are not described by a single first principles model at present. The extensive observational data, especially the long time series data from ground-based and spacecraft-borne measurements, have been used fruitfully to model the global and multiscale phenomena of the magnetosphere [19]. These models are enabled by recent developments in the theory of nonlinear dynamics and complexity, and represent the features inherent in the data, independent of modeling assumptions. The reconstruction of the dynamics of the solar wind - magnetosphere coupling from observational data has led to models which have been used to develop reliable space weather forecasting tools.

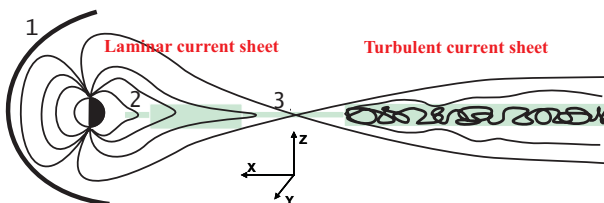


**Fig. 8.** The different types of current sheets in the magnetosphere. The near-Earth tail current sheet is mostly laminar, while the current sheet beyond the neutral sheet can be turbulent. The multiscale nature of the magnetosphere is influenced by the turbulent solar wind, the internal dynamics of the magnetosphere and the turbulent current sheet.

The multiscale features of the magnetosphere is often expressed in terms of power law distributions of the scale sizes. Such power law distributions have been obtained from the extensive data of auroral electrojet indices and solar wind variables. The burst life time distribution of the solar wind variables show scale-free behavior but the magnetosphere exhib-

its a significant deviation with preferred lifetimes of 2-5 h, showing the co-existence of global and multiscale features [5]. These results [5], [19] show that the magnetotail processes play an important role in the global as well as multiscale phenomena in the magnetosphere, as shown schematically in Fig. 8.

## 7. Summary

The magnetotail plays an important role in the understanding of geospace in general and the magnetosphere in particular. The global processes such as plasmoid formation and ejection are initiated in the magnetotail current sheet and thus the plasma processes span from the microphysics at kinetic scales to the macroscale physics at MHD scales though cross-scale coupling. This also points to the importance of the magnetotail in the global and multiscale phenomena in the magnetosphere.

The theory of thin current sheets based on the complicated particle trajectories in the strongly inhomogeneous magnetic field of the magnetotail has been successful in describing some of its observed features, such as its embedded structure, bifurcated profile, multilayered nature, etc. It should however be noted that in order to understand the dynamical behavior of the magnetotail, such as plasmoid formation and dipolarization, it is essential to consider its multidimensional nature. For example, the well known Harris sheet is unstable to tearing instability and thus lead to island formation but these islands are stationary due to the one dimensionality of the equilibrium. An equilibrium with dependence on the Sun-Earth axis will naturally lead to the dynamics of the islands or plasmoids and dipolarization of the magnetic field [11]. Also multi-dimensional equilibria are appropriate for modeling the interaction of the magnetotail processes with the inner magnetosphere.

**Acknowledgements.** The work was supported by NSF grants ATM - 0318629 and DMS - 0417800, NASA grant 04GE37G, RFBR grants 05-02-17003, 04-02-17371, 05-05-64993, RFBR GFEN 04-02-39021, and INTAS grant 03-51-3738.

## References

- Asano, Y., R. Nakamura, W. Baumjohann, A. Runov, Z. Voros, M. Volwerk, T.L. Zhang, A. Balogh, B. Klecker, H. Reme, How typical are atypical current sheets? *Geophysical Research Letters*, 32, L03108, 2005.
- Buchner, J., and L.M.Zelenyi, Regular and chaotic charged particle motion in magnetotail-like field reversals: 1. basic theory of trapped Motion, *Journal of Geophysical Research*, 94, 11821, 1989.
- Chen, J., Nonlinear dynamics of charged particles in the magnetotail, *Journal of Geophysical Research*, 97, 15011, 1992.
- Delcourt, D. C., J.-A. Sauvaud, O.L. Vaisberg, L.A. Avakov, J.L. Burch, J. H. White, Signatures of impulsive convection in the magnetospheric lobes, *Geophysical Research Letters*, 23, 129, 1996.
- Freeman, M. P., Watkins, N. W., Riley, D. J., Evidence for a solar wind origin of the power law burst lifetime distribution of the AE indices, *Geophysical Research Letters*, 27, 1087, 2000.
- Harris, E. G., On a plasma sheath separating regions of oppositely directed magnetic fields, *Nuovo Chimento*, 23, 115, 1962.

7. Hoshino, M., A. Nishida, T. Mukai, Y. Saito, and T. Yamamoto, Structure of plasma sheet in the magnetotail: Double-peaked electric current sheet, *Journal of Geophysical Research*, *101*, 24,775, 1996.
8. Kistler, M., C. Mouikis, E. Mobius, B. Klecker, J.-A. Sauvaud, H. Reme, A. Korth, M. F. Marcucci, R. Lundin, G. K. Parks, and A. Balogh, Contribution of nonadiabatic ions to the cross-tail current in an  $O^+$  dominated thin current sheet, *Journal of Geophysical Research*, *110*, A06213, doi:10.1029/2004JA010653, 2005.
9. Kropotkin, A. P., Domrin, V. I., Theory of a thin one-dimensional current sheet in collisionless space plasma, *Journal of Geophysical Research*, *101*, 19,893, 1996.
10. Lennartsson, W., and E.G. Shelley, Survey of 0.1- to 16-keV/e plasma sheet ion composition, *Journal of Geophysical Research*, *91*, 3061, 1986. *Journal of Geophysical Research*, *83*, 5670, 1978.
11. Otto, A., Schindler, K., Birn, J., Quantitative study on the nonlinear formation and acceleration of plasmoids in the Earth's magnetotail, *Journal of Geophysical Research*, *95*, 15,023, 1990.
12. Pilipp, W. G., and G. Morfill, The formation of the plasma sheet resulting from plasma mantle dynamics, *Journal of Geophysical Research*, *83*, 5670, 1978.
13. Runov, A., R. Nakamura, W. Baumjohann, R.A. Treumann, T.L. Zhang, M. Volwerk, Z. Voros, A. Balogh, K.-H. Glassmeier, B. Klecker, H. Reme, L. Kistler, Current sheet structure near magnetic X-line observed by Cluster, *Geophysical Research Letters*, *30* 33-1, doi:10.1029/2002GL016730, 2003.
14. Runov, A., R. Nakamura, W. Baumjohann, T.L. Zhang, M. Volwerk, Cluster observation of a bifurcated current sheet, *Geophysical Research Letters*, *30* 1036, doi:10.1029/2002GL016136, 2003.
15. Sauvaud, J.-A., and R.A. Kovrazhkin, Two types of energy-dispersed ion structures at the plasma sheet boundary, *Journal of Geophysical Research*, *109*, 12,213, 2004.
16. Sergeev, V. A., D. G. Mitchell, C. T. Russell, D. J. Williams, Structure of the tail plasma/current sheet at 11 Re and its changes in the course of a Substorm, *Journal of Geophysical Research*, *98* 17345, 1993.
17. Sergeev, V., A. Runov, W. Baumjohann, R. Nakamura, T.L. Zhang, M. Volwerk, A. Balogh, H. Reme, J.-A. Sauvaud, M. Andre, B. Klecker, Current sheet flapping motion and structure observed by Cluster, *Geophysical Research Letters*, *30*, 60-1, CiteID 1327, DOI 10.1029/2002GL016500, 2003.
18. Sharma, A. S., Curtis, S. A., Magnetospheric Multiscale Mission: Cross-scale exploration of complexity in the magnetosphere, in *Nonequilibrium Phenomena in Plasmas*, edited by A. S. Sharma, P. K. Kaw, pp. 179-198, Springer, 2005.
19. Sharma, A. S., A. Y. Ukhorskiy, and M. I. Sitnov, Global and multiscale phenomena of the magnetosphere, in *Nonequilibrium Phenomena in Plasmas*, edited by A. S. Sharma, P. K. Kaw, pp. 117-144, Springer, 2005.
20. Sitnov, M.I., L.M. Zelenyi, H.V. Malova, and A. S. Sharma, Thin current sheet embedded within a thicker plasma sheet: self-consistent kinetic theory, *Journal of Geophysical Research*, *105*, 13029, 2000.
21. Vaisberg, O.L., L.A. Avakov, J.L. Burch, and J.H. Waite, Jr., Measurements of plasma in the magnetospheric tail lobes, *Advances in Space Research*, *8*, (8)63, 1996.
22. Zelenyi, L., M.I. Sitnov, H.V. Malova, and A.S. Sharma, Thin and superthin ion current sheets, quasiadiabatic and nonadiabatic models, *Nonlinear Processes in Geophysics*, *7*, 127, 2000.
23. Zelenyi, L.M., D. C. Delcourt, H. V. Malova, and A. S. Sharma, "Aging" of the magnetotail thin current sheets, *Geophysical Research Letters*, *29*, 49, doi : 10.1029/2001GL013789, 2002.
24. Zelenyi, L. M., H. V. Malova, V. Yu. Popov, D.C. Delcourt, and A.S. Sharma, Nonlinear equilibrium structure of thin currents sheets: influence of electron pressure anisotropy, *Nonlinear Processes in Geophysics*, *11*, 1, 2004.
25. Zelenyi, L.M., H. V. Malova, V. Yu. Popov, D. C. Delcourt, A. S. Sharma, Role of electrostatic effects in thin current sheets, *NATO science series, Multiscale processes in the Earth's magnetosphere: from Interball to Cluster*, edited by J.-A. Sauvaud and Z. Nemecek, Kluwer Academic Publishers, 275-288, 2004.
26. Zelenyi, L.M., H. V. Malova, V. Yu. Popov, D. C. Delcourt, A. S. Sharma, Bifurcated thin current sheets in the Earth's magnetosphere: Comparison of model and *in situ* observations, *Frontiers in Magnetospheric Plasma Physics, COSPAR Colloquia Series, Vol. 16*, edited by M. Hoshino, Y. Omura and L. J. Lanzerotti, Elsevier, Amsterdam, pp. 100-107, 2005.
27. Zelenyi, L.M., H. V. Malova, V. Yu. Popov, D. C. Delcourt, A. S. Sharma, "Matreshka" model of multilayered current sheet, *Geophysical Research Letters*, *33*, L05105, doi:10.1029/2005GL025117, 2006.

# Decrease in $B_z$ prior to the dipolarization in the near-Earth plasma sheet

K. Shiokawa, Y. Miyashita, I. Shinohara, and A. Matsuoka

**Abstract:** We examine in detail the rapid decrease in  $B_z$  just before dipolarizations observed by the GEOTAIL satellite in the near-Earth plasma sheet at  $(X_{GSM}, Y_{GSM}) = (-8.3 R_E, -5.1 R_E)$ . The observations were made using high-time-resolution data from a fluxgate magnetometer (16-Hz sample), a search-coil magnetometer (128 Hz), and an electric field antenna (64 Hz). Two dipolarizations were observed during a short time interval of 2 min. The magnetic  $B_z$  component suddenly decreased 2–4 s prior to the dipolarization. Characteristic waves with frequencies of 5–20 Hz and amplitudes of 1–3 mV/m and 5–15 nT/s were observed in the electric and magnetic field data at the time of the sudden decreases in  $B_z$ . We discuss two possible causes of the sudden decreases in  $B_z$  prior to the dipolarizations: (1) passage of a field-aligned line current associated with the substorm current wedge, and (2) explosive growth phase and subsequent disruption of the tail current caused by the observed characteristic field oscillations.

*Key words:* dipolarization, explosive growth phase, substorm, current disruption.

## 1. Introduction

Dipolarization of the tail magnetic field is an important feature at the onset of magnetospheric substorms. The dipolarization indicates a sudden decrease of the duskward tail current that prevailed during the substorm growth phase. [7] explained dipolarizations as tail current disruption due to wave turbulence in the thin current sheet. [16] and [1] explained dipolarizations as Earthward flow braking (dawnward inertia current) and subsequent pileup of northward magnetic flux transported from tail reconnection.

On the basis of magnetic field measurements made by the AMPTE/CCE satellite inside  $10 R_E$ , [11] found the explosive growth phase, which is characterized by a rapid decrease of magnetic field elevation angles prior to the dipolarization. [21] reported similar “bipolar” structure (a decrease and then an increase) of  $B_z$  during the magnetic flux ropes associated with Earthward convective flow in the tail plasma sheet at  $|X| > 14 R_E$ . They explained these flux ropes as coming from the multiple reconnection  $X$ -lines in the near tail. [14] have also reported flux rope structures during nightside magnetic flux transfer events, which are probably caused by impulsive reconnection in the near-Earth plasma sheet. A statistical analysis of GEOTAIL data at  $\sim 10$ – $30 R_E$  by [13] shows that sharp dipolarizations tend to be preceded by a transient decrease in  $B_z$ , indicating that this is a common feature during the dipolarizations. [18] noted that about half of the 21 dipolarization events they studied show decrease in  $B_z$  prior to the dipolarization at  $X \sim 10 R_E$ . [4] and N. Shirataka et al. (private communication, 2004) found that by introducing a guide field  $B_y$  in their three-dimensional reconnection model, a decrease in  $B_z$  occurs prior to the dipolarization due to a pileup of the  $B_y$  field at the leading edge of Earthward flow.

In the ICS-8 presentation, we reported a detailed analysis of a sequence of rapid decreases in  $B_z$  prior to the dipolarizations, using high-time-resolution data from GEOTAIL measurements of magnetic and electric fields. We found intense 5–20 Hz waves during the events. The observed feature seems not to be the flux ropes or  $B_y$  pileups. We discuss alternative causes of these characteristic field variations in light of the substorm current wedge and tail current disruption. The full version of this work has already been published by [19].

## 2. Observation

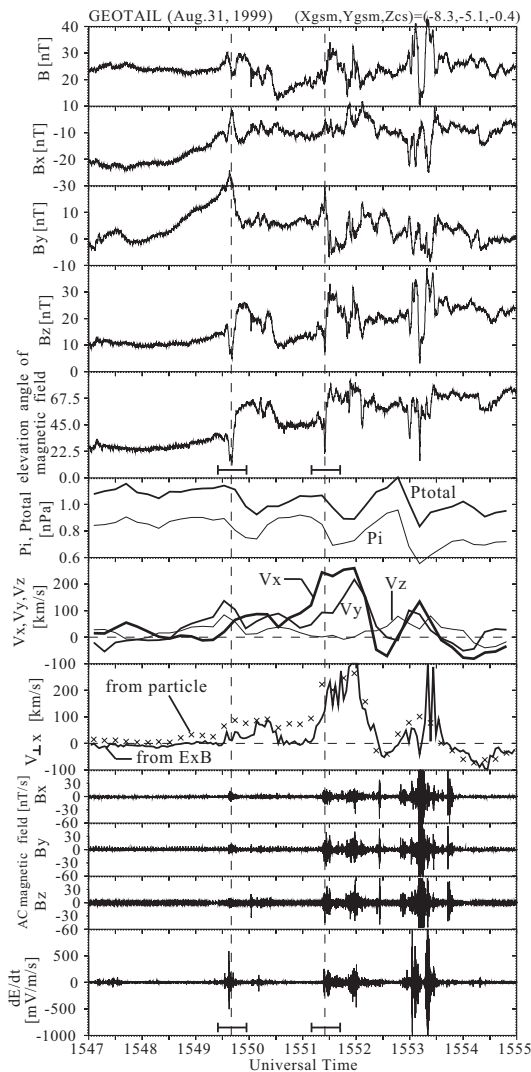
GEOTAIL satellite data with high time resolution are used in this work. They consist of 16-Hz sampled magnetic field data obtained by a fluxgate magnetometer, 128-Hz sampled magnetic field fluctuations obtained by a search coil magnetometer, and 64-Hz sampled electric field data obtained by a 100-m tip-to-tip probe antenna. Plasma velocities were obtained by an electrostatic analyzer with a time resolution of 12 s and from DC electric field measurements with a time resolution of 3 s. Details of these instruments are given by [5], [22], and [10].

Figure 1 shows an 8-min interval of the dipolarization events observed by the GEOTAIL satellite, using the high time resolution data (16 Hz sampling in the DC magnetic field, 128 Hz in the AC magnetic field, and 64 Hz in the electric field). Two sequential dipolarizations can be clearly identified at 1549:40 UT and 1551:25 UT, as indicated by the vertical dashed lines. The elevation angle and  $B_z$  of the magnetic field rapidly decrease prior to these dipolarizations.  $B_y$  increases and then decreases at these events. The magnetic field intensity  $B$  does not significantly change at the first event, while it slightly increases at the dipolarization of the second event.

These dipolarizations are observed at the beginning of Earthward plasma velocity enhancements, as shown in the  $V_{x,y,z}$  and  $V_{\perp,x}$  panels. The thermal ( $P_i$ ) and total ( $P_{total}$ ) pressures decrease at or after these dipolarizations. The AC magnetic field obtained by a search coil magnetometer and the time derivative of the electric field ( $dE/dt$ ) in the bottom panels show bursts of waves at the time of these dipolarization events. There

Received 18 May 2006.

**K. Shiokawa and Y. Miyashita.** Solar-Terrestrial Environment Laboratory, Nagoya University, Toyokawa 442-8507, Japan  
**I. Shinohara and A. Matsuoka.** Institute of Space and Astronautical Sciences, Japan Aerospace Exploration Agency, Sagamihara 229-8510, Japan



**Fig. 1.** From top to bottom: 16-Hz sampled  $B$ ,  $B_x$ ,  $B_y$ ,  $B_z$ , and elevation angle ( $0^\circ = \text{tail-like}$ ,  $90^\circ = \text{dipolar}$ ) of the magnetic field obtained by a fluxgate magnetometer, thermal pressure ( $P_i$ ) and total pressure ( $P_{total} = P_i + P_b$ , where  $P_b$  is the magnetic pressure),  $V_x$ ,  $V_y$ , and  $V_z$  obtained by the particle detector,  $V_{\perp,x}$  obtained by a particle detector (crosses, 12-s resolution) and calculated from  $E_y B_z / B^2$  (solid curves, 3-s resolution), 128-Hz sampled magnetic field fluctuations of  $B_x$ ,  $B_y$ , and  $B_z$ , obtained by a search coil magnetometer, and the time derivative of 64-Hz sampled electric field data, obtained by GEOTAIL for an 8-min interval at 1547–1555 UT on August 31, 1999. The data are in GSM coordinates. The GEOTAIL location  $Z_{cs}$  at the top is the Z-distance from the model current sheet determined by [23]. For the  $v_{\perp,x}$  calculation from the electric field data, only the  $E_y$  component is used, because GEOTAIL does not measure the  $E_z$  component. The two horizontal bars indicate the time intervals shown in Figure 2.

may be a third event at  $\sim 1553:30$  UT. Here, we focus on the first two events.

At the time in Figure 1, GEOTAIL was at  $(X_{GSM}, Y_{GSM}, Z_{cs}) = (-8.3, -5.1, -0.4) R_E$ , where  $Z_{cs}$  is the distance from the

model neutral sheet as determined by [23]. Two low-latitude Pi 2 pulsations with onset times at 1526 UT and 1544 UT were observed at three Japanese ground stations in the midnight local time sector (00:26 and 00:44 LT, respectively). An auroral initial brightening was observed by the POLAR UVI imager associated with the second Pi 2 onset at 1544 UT in the dusk sector at  $\sim 22$  magnetic local time (MLT). The auroral brightening expanded toward the dawn sector, where GEOTAIL was located at 02:04 MLT at 1550 UT. The ion density, temperature, and plasma  $\beta$  (ratio of thermal pressure to magnetic pressure) were  $\sim 0.5\text{--}1.0 \text{ cm}^{-3}$ , 5–8 keV, and 2–5, respectively, at 1540–1610 UT, indicating that GEOTAIL was well within the central plasma sheet (see Figures 1 and 2 of [19]).

Figures 2a and 2b are expanded plots of the GEOTAIL data for 32-s intervals (indicated by the two horizontal bars in Figure 1) around the two dipolarizations at (a) 1549:25–1549:57 UT and (b) 1551:10–1551:42 UT. Since the electric field in the bottom panels consists of raw data from the 100-m probe antenna, 3-s spin modulation is clearly seen with some distortions due to photoelectrons ([22]).

In both Figures 2a and 2b,  $B_z$  decreases 2–4 s before the dipolarizations.  $B_y$  has peaks near the local minimum of  $B_z$  in both cases.  $B_x$  tends to decrease at the same time as  $B_z$  in Figure 2a. The total field intensity  $B$  does not significantly change in Figure 2a, while it increases coincident with the  $B_z$  increase in Figure 2b.

Intense waves are seen in both magnetic and electric field data from the beginning of the  $B_z$  decrease in Figure 2a and from  $\sim 1$  s before the  $B_z$  decrease in Figure 2b. Although the time resolution of plasma velocity is low, the Earthward convective plasma velocities in Figure 2a are rather small, less than 100 km/s, while those in Figure 2b are 100–200 km/s during the  $B_z$  decrease.

The plots in Figure 3 are a further expansion of the GEOTAIL data for 4-s intervals (indicated by the horizontal bars in Figure 2) at the beginning of the intense waves. The waves in the electric field data seem to have characteristic frequencies of 5–20 Hz and amplitudes of  $\sim 3$  mV/m in Figure 3a and  $\sim 1\text{--}3$  mV/m in Figure 3b. Waves with a similar frequency range are seen in the search-coil magnetic field data with amplitudes of  $\sim 5$  nT/s in Figure 3a and  $\sim 15$  nT/s in Figure 3b. Waves with a higher frequency range can also be seen in the search coil data, because of the higher sampling rate of 128 Hz.

### 3. Discussion

We observed rapid decreases in  $B_z$  2–4 s before the dipolarizations. The event was observed two times within the 2-min interval. Convective plasma velocity was small ( $< 100$  km/s) for the first event, while it was 100–200 km/s for the second event. Characteristic waves were observed from the beginning of the decrease in  $B_z$  in both the electric and the magnetic field data. The high-time-resolution data shows that the waves have frequencies of 5–20 Hz, and large amplitudes of 1–3 mV/m in the electric field data and 5–15 nT/s in the search coil magnetic field data. The frequency of 5–20 Hz is in the range of the lower hybrid waves.

As cited in the introduction, several authors explained the decrease in  $B_z$  prior to the dipolarization as flux ropes due

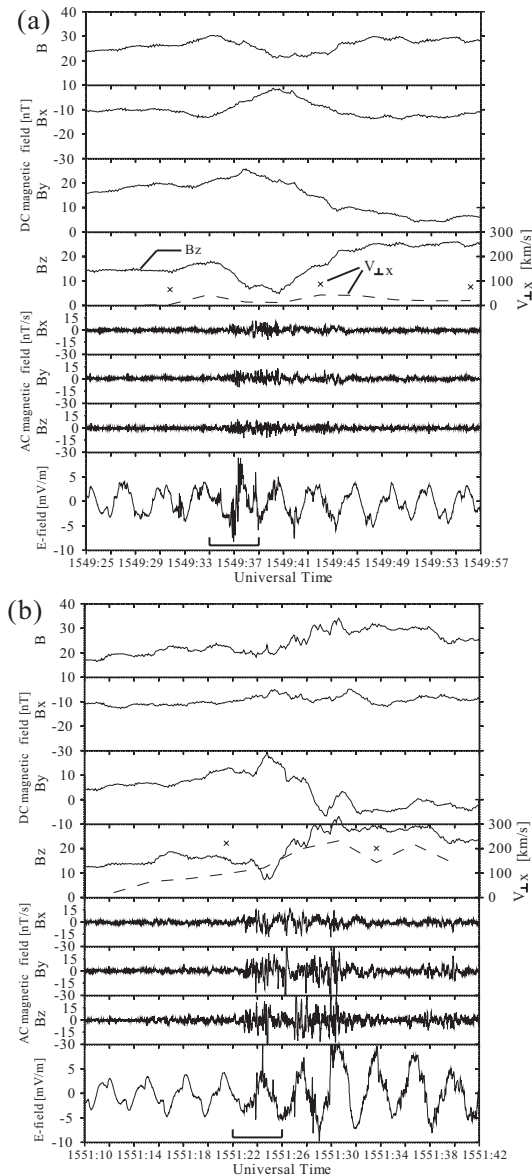


**Fig. 2.** From top to bottom:  $B$ ,  $B_x$ ,  $B_y$ , and  $B_z$  (solid curves), obtained by a fluxgate magnetometer,  $v_{\perp,x}$  (crosses: from a particle detector, 12-s resolution, and dashed curves: from  $E_y B_z / B^2$ , 3-s resolution), AC magnetic field fluctuations of  $B_x$ ,  $B_y$ , and  $B_z$ , obtained by a search coil magnetometer, and 64-Hz sampled electric field data, for 32-s intervals at (a) 1549:25–1549:57 UT and (b) 1551:10–1551:42 UT obtained by GEOTAIL on August 31, 1999. The two horizontal bars indicate the time intervals shown in Figure 3.

to multiple/impulsive reconnection and pileup of the  $B_y$  field. The present event seems to be different from the flux ropes or pileup, because the peak in  $B_y$  is almost coincident with the local minimum of  $B_z$  and  $B_z > 0$  everywhere. For flux ropes and  $B_y$  pileups, there would be a bipolar  $B_z$  with a peak in  $B_y$  near the inflection point of the  $B_z$  signature. Moreover, intense waves were observed in the lower hybrid frequency range. In this work, we would like to consider two alternative explanations for the observed decrease in  $B_z$  prior to the dipolariza-

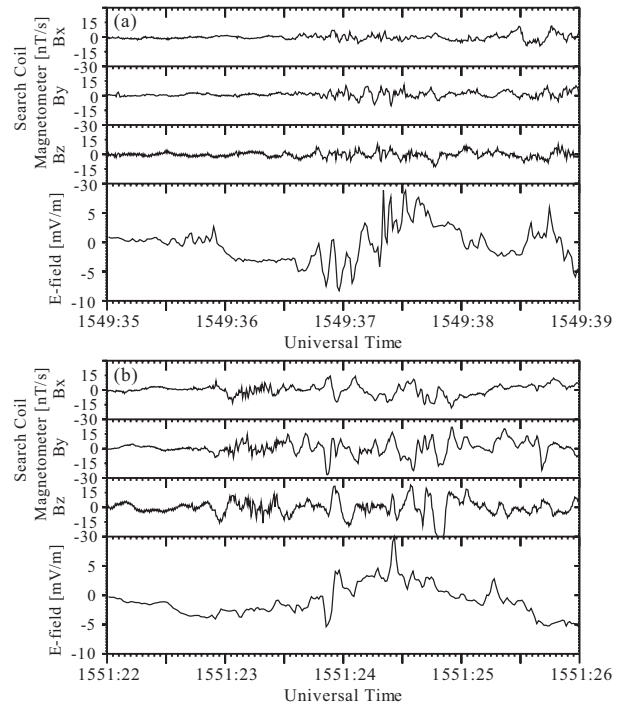


**Fig. 3.** 128-Hz sampled magnetic field variations obtained by a search coil magnetometer, and 64-Hz sampled electric field data, for 4-s intervals at (a) 1549:35–1549:39 UT and (b) 1551:22–1551:26 UT obtained by GEOTAIL on August 31, 1999.

tion.

One explanation is the passage of field-aligned line current associated with the substorm current wedge, as shown schematically in Figure 4. Because  $B_x$  was continuously negative, GEOTAIL was in the south of the tail current sheet. If GEOTAIL was above (north of) the upward field-aligned current (b) or below (south of) the downward field-aligned current (c), it would observe a decrease and then an increase in  $B_z$ , as shown in Figure 4d.  $B_y$  would have a peak when the line current is closest to the satellite. This configuration may explain the observed  $B_z$  and  $B_y$  changes in Figure 1. The model in Figure 4 predicts that the  $B_y$  peak will coincide with zero crossing of  $B_z$ . The  $B_y$  peak, however, coincides with the negative peak of  $B_z$  in Figure 2. If the field-aligned current not only aligns with GSM- $X$  but has some component in the GSM- $Y$  and - $Z$  directions or if the current has some sheet structures, it may be possible to reproduce the observed  $B_z$  and  $B_y$  variations by a crossing of field-aligned currents. However, this model requires that for the present case, the field-aligned current expands quickly in longitude two times during the 2-min interval. This model also does not explain why the intense 5–20 Hz waves were observed at the start of the decrease in  $B_z$ .

The idea of field-aligned line current was first considered by [11] for the events of the explosive growth phase. They excluded this idea because the observed variation in the geomagnetically outward component of the magnetic field was opposite to that of the model in the VDH coordinate system. It is not clear whether the same logic using the VDH coordinates is applicable to the present case, since the radial distance of 10

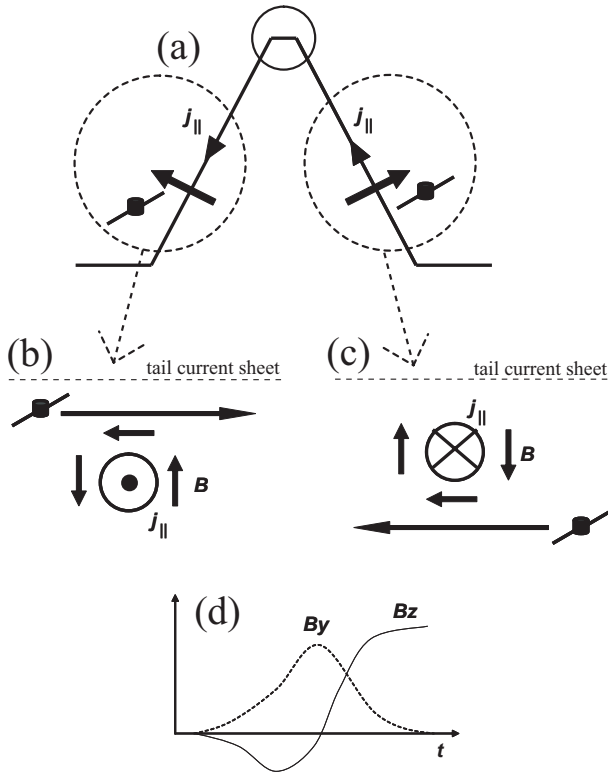


**Fig. 4.** Schematics of (a) the substorm current wedge, (b) and (c) two possible motions of GEOTAIL relative to the field-aligned line current (looking from the tail to Earth), which explain the observed decrease in  $B_z$  and increase in  $B_y$  prior to the dipolarization (d). Because  $B_x$  was negative throughout the event, GEOTAIL was southward of the tail current sheet.

$R_E$  is just at the geomagnetic hinging distance, where dipole configuration changes to the tail configuration ([3]).

The other explanation for the rapid decrease in  $B_z$  prior to the dipolarization is an explosive growth phase and a localized tail current disruption, as schematically shown in Figure 5. Because  $B_x$  was continuously negative during the present event, GEOTAIL was in the south of the tail current sheet (Figure 5a). At the late growth phase, the tail current sheet can be suddenly intensified by some processes discussed below (explosive growth phase, Figure 5b). The magnetic field becomes tail-like Earthward of the current intensification region and dipolar tailward of the intensification region. This explains the sudden decrease in  $B_z$ , if the satellite was located Earthward of the current intensification region.

Then in Figure 5c, a localized current disruption occurs, as expressed by an equivalent downward current, possibly because of an anomalous resistivity due to the observed intense waves with frequencies of 5–20 Hz. The intense waves may be generated by the cross-tail current instability due to the sudden intensification of the tail current in Figure 5b. The magnetic field configuration just tailward of the current disruption region becomes more tail-like due to this localized current disruption. This again explains the observed decrease in  $B_z$  on a short time scale, if the satellite is located tailward of the disruption region. The disrupted current will be closed to the field-aligned current, forming a substorm current wedge.

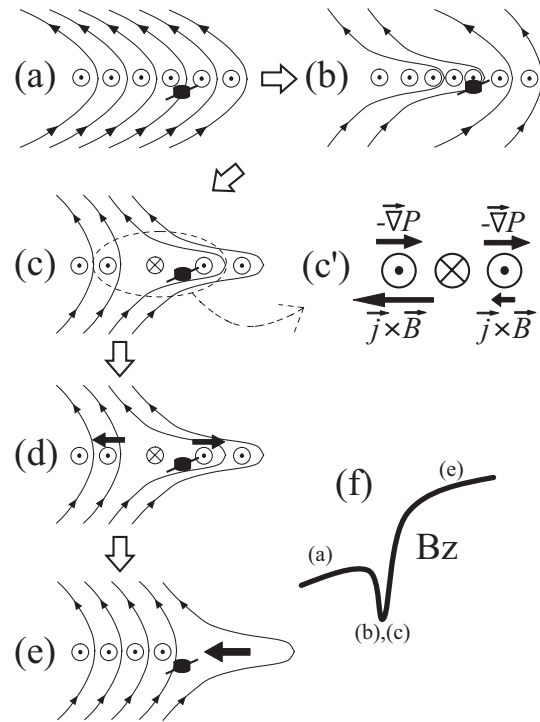


**Fig. 5.** Schematics (X-Z plane looking from dusk to dawn) of a sequence of explosive growth and disruption of the tail current, explaining the observed decrease in  $B_z$  prior to the dipolarization (indicated in (f)). (a) Before the event, (b) intensification of tail current (explosive growth phase), (c) localized tail current disruption (indicated as a downward tail current), (c') enhanced (reduced) magnetic field inside (outside) the current disruption region increases (decreases) the Earthward  $\mathbf{j} \times \mathbf{B}$  force, (d) plasma tries to move Earthward (tailward) inside (outside) the current disruption region, and (e) the whole plasma moves Earthward due to a reduction in pressure gradient force, causing dipolarization (increase in  $B_z$ ) on the MHD time scale. The accumulation of plasma and magnetic field may then increase the tailward pressure gradient force to stop the flow (back to (a)). Satellite location was just tailward of the current disruption region in the southern hemisphere.

The field configuration in Figure 5c is, however, unstable on an MHD time scale, which is longer than a few seconds. The current disruption (equivalent downward current) produces additional northward  $B_z$  Earthward of the disruption region and southward  $B_z$  tailward of the disruption region. Thus, as shown in Figure 5c', the Earthward  $\mathbf{j} \times \mathbf{B}$  force becomes larger than the prevailing tailward pressure gradient force Earthward of the current disruption region, while it becomes smaller tailward of the current disruption region. As a result, plasma tends to move Earthward/tailward at Earthward/tailward of the current disruption region (Figure 5d). Since the Earthward plasma motion reduces the pressure gradient force tailward of the moving region, the whole plasma finally moves Earthward (Figure 5e). This unbalance of  $\mathbf{j} \times \mathbf{B}$  force has been discussed by [8] (Section 6.6).

Because the Earthward plasma motion causes accumulation of the plasma and magnetic field inside the disruption region, the tailward pressure gradient force may increase again and the

whole plasma may stop moving (back to Figure 5a). This may explain the sequence of the present event, where dipolarizations took place twice within 2 min. The  $B_x$  and  $B_y$  changes observed at the time of the decrease in  $B_z$  may be explained if the duskward sheet current at the explosive growth phase and/or the dawnward disruption current are tilted in the  $X - Y$  plane.

In the above discussion, two processes, i.e., explosive growth phase (Figure 5b) and subsequent localized current disruption (Figure 5c), are considered for the cause of the sudden decrease in  $B_z$ . For the explosive growth phase, [11] and [12] proposed that sudden intensification of the cross-tail current sheet with a time scale of  $\sim 1$  min can be caused by a positive feedback process between the unmagnetization of ions and the thinning of the current sheet. [2] proposed that the kinetic ballooning instability can cause explosive growth phase with a time scale (period) of 50–75 s. [6] proposed that the entropy antidiffusion by lower-hybrid drift instability can cause sudden intensification of cross-tail current sheet with a time scale of  $\sim 1$  min. All these possible processes of explosive growth phase predict the time scale of  $\sim 1$  min, which is longer than that of the present events (2–4 s). The decrease in  $B_z$  by a localized current disruption can be a time scale of a few seconds, since the current disruption is a non-MHD process, which should be relaxed on MHD time scale as shown in Figures 5c–5e. As shown in Figure 2, the intense 5–20 Hz waves were observed from the beginning of the  $B_z$  decrease. This fact also supports the idea that the waves are responsible for the current disruption that causes decrease in  $B_z$ . Anyhow, if explosive growth phase occurs prior to the current disruption to drive the thinning and intensification of the cross-tail current sheet, it would be difficult to distinguish which (explosive growth phase or current disruption) is the cause of the observed decrease in  $B_z$ .

The intense lower hybrid waves with frequencies of 5–20 Hz and amplitudes of 1–3 mV/m observed at the decrease in  $B_z$  may be responsible for the tail current disruption. Model calculations would be necessary to check whether these waves are sufficient to disrupt the tail current. Recently [20] reported similar waves at a lower hybrid frequency range ( $\sim 5$ –16 Hz) based on the GEOTAIL observation in the tail plasma sheet at 10–13  $R_E$ . They concluded that these waves are not likely to be the cause of the tail current disruption, because their maximum amplitude was not observed until after the start of magnetic field dipolarization and Earthward flow. They suggest that these waves are a consequence of the dynamics of the magnetotail, since they are associated with plasma flow. In the present case, the amplitude of the waves is already very high at the start of the decrease in  $B_z$ , as shown in Figures 1 and 2. Thus, the waves may be responsible for substorm initiation through cross-tail current instability. If the waves in the lower hybrid frequency range are also generated by plasma dynamics, it would be very difficult to distinguish the cause and the result based on a single satellite measurement.

The relation between the observed field variations and the Earthward plasma flow is important for verifying these models. For the first event in Figure 2a, the plasma velocity increases slightly to  $\sim 100$  km/s, while the second event in Figure 2b occurs when the plasma velocity increases to a few hundred km/s. This flow enhancement would be consistent with the longitudinal expansion of field-aligned line current model in Figure 4,

if, for example, the substorm current wedge is driven by the braking of Earthward flow ([16] and [17]).

The decrease of the total pressure at or after the dipolarization in Figure 1 may not be consistent to the flow braking view for the present cases. We should note that for the present events the ion energy tends to exceed the upper limit of the ion detector (40 keV), so that the pressure measurements may become ambiguous. However, this pressure reduction at the dipolarization has been reported in several literatures. [15] called the reduction of the plasma pressure associated with dipolarization and earthward bursty flow as plasma bubbles. [9] reported similar reduction of the plasma pressure in the equatorial inner plasma sheet at substorm onset, and concluded that this reduction leads to the expansion-phase reduction of cross-tail current.

The model of explosive growth and disruption of tail current (Figure 5) also predicts Earthward flow enhancement at the time of dipolarization. For the second event in Figure 2b, the flow was enhanced prior to the decrease in  $B_z$ . This may contradict the current disruption model. However, if the tail current disruption and subsequent Earthward flow occur on a different spatial scale, one could expect an overlap of Earthward flow and a decrease in  $B_z$  on a non-MHD short time scale.

In any case, the time resolutions of the plasma velocities (3 s in  $\mathbf{E} \times \mathbf{B}$  and 12 s in plasma moment) are not sufficient to allow a discussion of timing in relation to field variation. Both methods have problems in the determination of plasma velocities, i.e., the electric field is reliable only for the  $E_y$  direction, and ion energy exceeds the upper limit (40 keV) of the plasma detectors for the present event. High-time-resolution measurement over a broad energy range (up to 100 keV) would be essential for plasma velocity determination in the near-Earth tail.

#### 4. Conclusion

We have investigated a sequential dipolarization event observed by the GEOTAIL satellite in the near-Earth plasma sheet at  $(X_{GSM}, Y_{GSM}) = (-8.3, -5.1)R_E$ , using high-time-resolution data from a fluxgate magnetometer (16-Hz), a search-coil magnetometer (128 Hz), and an electric field antenna (64 Hz). The dipolarization event took place 5–7 min after ground Pi 2 onset and a POLAR UVI auroral brightening, and was observed dawnside (02 MLT) of the main onset region (22 MLT). The observed characteristics of the dipolarization are summarized as follows:

1. Two dipolarizations were observed within a 2 min interval. The magnetic field  $B_z$  suddenly decreased 2–4 s before the dipolarization in both cases.
2. Characteristic electric and magnetic field oscillations with frequencies of 5–20 Hz (lower hybrid frequency range) and amplitudes of 1–3 mV/m and 5–15 nT/s were observed coincident with the sudden decrease in  $B_z$ .

We discuss two possible causes of the sudden decrease in  $B_z$  prior to dipolarization: (1) passage of field-aligned line current associated with the substorm current wedge, and (2) explosive growth and disruption of the cross-tail current sheet. From the present observation it is difficult to distinguish which process caused the observed magnetic field features. In the former case, the observed intense waves may be a consequence

of plasma dynamics (plasma flow) during dipolarization. In the latter case, the observed waves may cause the tail current disruption. Plasma measurements with a high time resolution (higher than 1 s) would be key to differentiating between these two models.

**Acknowledgments:** GEOTAIL data were provided through DARTS at the Institute of Space and Astronautical Science (ISAS), Japan Aerospace Exploration Agency, Japan. K. S. is grateful to A. T. Y. Lui and T. Nagai for their helpful comments. The Principal Investigator of the Polar UVI experiment is G. K. Parks. The POLAR UVI images were supplied through the NASA MSFC home page. This work was supported by a Grant-in-Aid for Scientific Research of the Ministry of Education, Culture, Sports, Science and Technology of Japan (13640449).

## References

- Baumjohann, W., M. Hesse, S. Kokubun, T. Mukai, T. Nagai, and A. Petrukovich, Substorm dipolarization and recovery, *J. Geophys. Res.*, *104(A11)*, 24,995–25,000, 1999.
- Cheng, C. Z., and A. T. Y. Lui, Kinetic ballooning instability for substorm onset and current disruption observed by AMPTE/CCE, *Geophys. Res. Lett.*, *25(21)*, 4091–4094, 1998.
- Fairfield, D. H., A statistical determination of the shape and position of the geomagnetic neutral sheet, *J. Geophys. Res.*, *85*, 775–780, 1980.
- Hashimoto, C., R. TanDokoro, and M. Fujimoto, Effects of guide field in three-dimensional magnetic reconnection, in *Frontiers in magnetospheric plasma physics*, edited by M. Hoshino, Y. Omura, and L. J. Lanzerotti, pp. 130–134, 2005.
- Kokubun, S., T. Yamamoto, M. H. Acuña, K. Hayashi, K. Shiokawa, and H. Kawano, The GEOTAIL magnetic field experiment, *J. Geomag. Geoelectr.*, *46*, 7–21, 1994.
- Lee, L. C., L. Zhang, A. Otto, G. S. Choe, H. J. Cai, Entropy antidiffusion instability and formation of a thin current sheet during geomagnetic substorms, *J. Geophys. Res.*, *103(A12)*, 29,419–29,428, 1998.
- Lui, A. T. Y., R. E. Lopez, B. J. Anderson, K. Takahashi, L. J. Zanetti, R. W. McEntire, T. A. Potemra, D. M. Klumpar, E. M. Greene, and R. Strangeway, Current disruptions in the near-Earth neutral sheet region, *J. Geophys. Res.*, *97*, 1461–1480, 1992.
- Lui, A. T. Y., P. H. Yoon, and C.-L. Chang, Quasi-linear analysis of ion Weibel instability in the Earth's neutral sheet, *J. Geophys. Res.*, *98*, 153–163, 1993.
- Lyons, L. R., C.-P. Wang, T. Nagai, T. Mukai, Y. Saito, and J. C. Samson, Substorm inner plasma sheet particle reduction, *J. Geophys. Res.*, *108(A12)*, 1426, doi:10.1029/2003JA010177, 2003.
- Mukai, T., S. Machida, Y. Saito, M. Hirahara, T. Terasawa, N. Kaya, T. Obara, M. Ejiri, and A. Nishida, The low energy particle (LEP) experiment onboard the GEOTAIL satellite, *J. Geomag. Geoelectr.*, *46*, 669–692, 1994.
- Ohtani, S., K. Takahashi, L. J. Zanetti, T. A. Potemra, and R. W. McEntire, Initial signatures of magnetic field and energetic particle fluxes at tail reconfiguration: Explosive growth phase, *J. Geophys. Res.*, *97*, 19,311–19,324, 1992.
- Ohtani, S., A. T. Y. Lui, K. Takahashi, D. G. Mitchell, and T. Sarris, Ion dynamics and tail current intensification prior to dipolarization: The June 1, 1985, event, *J. Geophys. Res.*, *105(A11)*, 25,233–25,246, 2000.
- Ohtani, S., M. A. Shay, and T. Mukai, Temporal structure of the fast convective flow in the plasma sheet: Comparison between observations and two-fluid simulations, *J. Geophys. Res.*, *109*, A03210, doi:10.1029/2003JA010002, 2004.
- Sergeev, V. A., R. C. Elphic, F. S. Mozer, A. Saint-Marc, and J. A. Sauvaud, A two-satellite study of nightside flux transfer events in the plasma sheet, *Planet. Space Sci.*, *40*, 1551–1572, 1992.
- Sergeev, V. A., V. Angelopoulos, J. T. Gosling, C. A. Cattell, and C. T. Russell, Detection of localized, plasma-depleted flux tubes or bubbles in the midtail plasma sheet, *J. Geophys. Res.*, *101(A5)*, 10,817–10,826, 1996.
- Shiokawa, K., W. Baumjohann, and G. Haerendel, Braking of high-speed flows in the near-Earth tail, *Geophys. Res. Lett.*, *24*, 1179–1182, 1997.
- Shiokawa, K., et al., High-speed ion flow, substorm current wedge, and multiple Pi 2 pulsations, *J. Geophys. Res.*, *103*, 4491–4507, 1998.
- Shiokawa, K., I. Shinohara, T. Mukai, H. Hayakawa, and C. Z. Cheng, Magnetic field fluctuations during substorm-associated dipolarizations in the nightside plasma sheet around  $X = -10 R_E$ , *J. Geophys. Res.*, *110*, A05212, doi:10.1029/2004JA010378, 2005a.
- Shiokawa, K., Y. Miyashita, I. Shinohara, and A. Matsuoka, Decrease in Bz prior to the dipolarization in the near-Earth plasma sheet, *J. Geophys. Res.*, *110*, A09219, doi:10.1029/2005JA011144, 2005b.
- Sigsbee, K., C. A. Cattell, D. Fairfield, K. Tsuruda, and S. Kokubun, Geotail observations of low-frequency waves and high-speed earthward flows during substorm onsets in the near magnetotail from 10 to 13 RE, *J. Geophys. Res.*, *107(A7)*, 1141, doi:10.1029/2001JA000166, 2002.
- Slavin, J. A., R. P. Lepping, J. Gjerloev, D. H. Fairfield, M. Hesse, C. J. Owen, M. B. Moldwin, T. Nagai, A. Ieda, and T. Mukai, Geotail observations of magnetic flux ropes in the plasma sheet, *J. Geophys. Res.*, *108(A1)*, 1015, doi:10.1029/2002JA009557, 2003.
- Tsuruda, K., H. Hayakawa, M. Nakamura, T. Okada, A. Matsuoka, F. S. Mozer, and R. Schmidt, Electric field measurements on the GEOTAIL satellite, *J. Geomag. Geoelectr.*, *46*, 693–711, 1994.
- Tsyganenko, N. A., Modeling the Earth's magnetospheric magnetic field confined within a realistic magnetopause, *J. Geophys. Res.*, *100*, 5599–5612, 1995.

# Ground and satellite observations of substorm onset arcs

K. Shiokawa, K. Yago, K. Yumoto, K. Hayashi, D. G. Baishev, S. I. Solovyev, F. J. Rich, and S. B. Mende

**Abstract:** Auroral features and associated particles and fields are investigated for three auroral substorms (pseudo-breakups) observed at 19-20 MLT on December 30, 1994 and October 24 and 31, 2000. We identified the substorms using Pi 2 wave packets, positive/negative H variations at mid-/high-latitudes, and auroral brightenings in auroral images obtained by a ground all-sky camera and by the IMAGE FUV imager. The DMSP satellites crossed brightening arcs during the Pi 2 pulsations in the field-of-view of the ground camera at Fort Smith (67 MLAT), Canada, and Tixie (66 MLAT), Russia. The crossings were 1-2 hours duskside of the main onset local time. The brightening arcs were located at the equatorward boundary of the region 1 current and in the sunward convection region. The arcs corresponded to inverted-V accelerated electrons. From these observations, we suggest that the arc brightening occurs in the inner plasma sheet at the inner edge of the region 1 current source in the sunward convection region.

*Key words:* auroral initial brightening, precipitating particles, region 1 current, sunward convection.

## 1. Introduction

An auroral substorm is a manifestation of a magnetospheric substorm, which is a fundamental disturbance that releases the energy stored in the magnetosphere to the ionosphere. The onset mechanism of magnetospheric substorms is still controversial (see *Space Science Reviews*, vol. 113, No. 1-2, March 2004, for a review). Substorm onset is commonly described using the following two models.

The first is the near-Earth onset model, in which some instability in the nightside near-Earth plasma sheet inside  $10 R_E$  causes a substorm (e.g., [17], [18], [12], and [5]). The fact that the auroral substorm starts from the most equatorward arc (e.g., [1] and [19]) supports this idea. [21] showed that the location of the auroral initial brightening was mapped inside  $15 R_E$  in the magnetosphere. However, field-line mapping of the auroral brightening region to the magnetosphere is always ambiguous because of the tailward-stretched magnetic field configuration that is present during the substorm growth phase.

The other model of substorm onset is the near-Earth neutral line (NENL) model, in which the magnetic reconnection at  $20-30 R_E$  in the tail causes the substorm (e.g., [14] and [3]). The NENL formation at radial distances of  $20-30 R_E$  is supported by observations of the statistical flow-reversal location (e.g.,

[2], [23], and [20]) and of the detailed structure of the reconnection region (e.g., [24] and [27]). The mismatch between the auroral initial brightening (inside  $10-15 R_E$ ) and the reconnection region ( $20-30 R_E$ ) may be explained by considering the braking of Earthward flow launched from the reconnection region as a generator of auroral brightening ([31]). [26] suggested that the two mechanisms (near-Earth instability and reconnection) may operate simultaneously in a coordinated way.

Particle and field signatures of the auroral initial brightening may be a key to identifying the source location of the brightening in the magnetosphere, and may help to verify the different models. For that purpose, several authors have compared auroral images and satellite particles and fields ([28]: meridian-scanning photometers and DMSP, [8]: ground auroral images and FAST, and [22]: satellite auroral images and FAST). These studies indicate that the onset arc is located in the middle part or the equatorward edge of the electron precipitation region, and in the intense ion precipitation region, suggesting that the source is located in the inner part of the plasma sheet.

Despite these previous studies, simultaneous observation of auroral images and in situ plasma data at substorm onset is still very limited. In the ICS-8, we reported simultaneous measurements of substorm brightening arcs for three ground-satellite conjunction events, using auroral images and in situ particle, field-aligned current, and plasma convection data. Due to the limit of the total pages of this proceedings, we show only some parts of the measurements. The full descriptions of these three events were reported by [36], [34] and [37].

## 2. Observations

In this work, we use auroral images obtained by panchromatic all-sky TV cameras with image intensifier at Tixie (TIK,  $71.6^\circ\text{N}$ ,  $128.8^\circ\text{E}$ , magnetic latitude (MLAT) =  $66.0^\circ$ ) and at Fort Smith (FSM,  $60.0^\circ\text{N}$ ,  $248^\circ\text{E}$ ,  $67.0^\circ\text{MLAT}$ ). The cameras take auroral images in visible wavelengths with a time resolution of 1-4 s. Details of the cameras are given by [29]. [35] and

Received 18 May 2006.

**K. Shiokawa.** Solar-Terrestrial Environment Laboratory, Nagoya University, Toyokawa 442-8507, Japan

**K. Yago.** Konica Minolta, Japan

**K. Yumoto.** Space Environment Research Center, Kyushu University, Fukuoka, Japan

**K. Hayashi.** Department of Earth and Planetary Science, The University of Tokyo, Tokyo, Japan

**D. G. Baishev and S. I. Solovyev.** Yu. G. Shafer Institute of Cosmophysical Research and Aeronomy, Yakutsk, Russia

**F. J. Rich.** Air Force Research Laboratory, Hanscom Air Force Base, MA, USA

**S. B. Mende.** Space Science Laboratory, University of California, Berkeley, CA, USA

[33] used the cameras for a detailed comparison of substorm arcs with Pi 2 pulsations.

Using auroral images over 4 years (1997-2000) at TIK and one month (December 1994 - January 1995) at FSM, we searched simultaneous observations of substorm-associated auroral arcs detected by the ground all-sky camera and auroral particle and field data obtained by the DMSP satellites in the field-of-view of the cameras. Only three events were available during which DMSP crossed the brightening arc within 10 min of the brightenings. This fact indicates the difficulty of obtaining simultaneous ground and satellite observations of substorm brightening arcs.

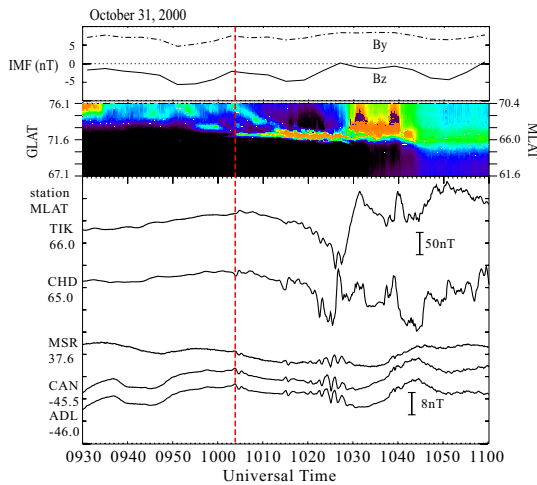


**Fig. 1.** Interplanetary magnetic field (IMF) variations obtained by the ACE spacecraft, time variations of auroral intensity in a north-south meridian obtained by the all-sky camera at Tixie (TIK), and H-component magnetic field variations at TIK, Chokurdakh (CHD), Moshiri (MSR), Canberra (CAN), and Adelaide (ADL) in the magnetic meridian of TIK, for the substorm brightening event of October 31, 2000. The magnetic field data are shown as 50 nT/division for TIK and CHD, and 8 nT/division for MSR, CAN, and ADL. The vertical red-dashed line indicates the time when the DMSP F12 satellite crossed the brightening arc, as shown in Figure 2.

Figure 1 is an example of IMF and ground auroral and magnetic field data during the ground-satellite conjunction event. It shows interplanetary magnetic field (IMF) variations obtained by the ACE spacecraft, auroral intensity variations in a north-south meridian (keogram) obtained by the all-sky camera at TIK, and H-component magnetic field variations at the CPMN stations at TIK, Chokurdakh (CHD), Moshiri (MSR), Canberra (CAN), and Adelaide (ADL) ([38]), for the substorm event on October 31, 2000, which was reported by [37]. IMF data is shifted 63 min by taking into account the travel time from the ACE spacecraft to the magnetopause. The all-sky images are converted to geographical coordinates, assuming an auroral altitude of 120 km. The keogram shows auroral intensity variations at a geographical longitude of TIK (128.8°E).

In Figure 1, IMF  $B_z$  measured by the ACE spacecraft at  $X = 219 R_E$  was almost continuously southward ( $\sim 0$  to  $-5$  nT), and  $B_y$  was duskward ( $> 5$  nT) for 0930 – 1100 UT. In the keogram, the equatorward boundary of the auroral zone

gradually shifts equatorward during the plotted interval. As indicated by the vertical dashed line, an auroral intensification took place at  $\sim 1004$  UT (18.5 MLT at TIK) at the equatorial boundary of the auroral zone at  $\sim 66^\circ$  MLAT ( $\sim 72^\circ$  GLAT). The DMSP F12 satellite crossed the arc at this time, as shown later. An equatorward-drifting aurora was observed simultaneously poleward of the brightening arc. However, auroral expansion was not observed in the keogram. Small magnetic field variations were seen in the high-latitude magnetograms at TIK and CHD at this time. Pi 2 pulsations with a coherent phase structure were identified in the midlatitude magnetic field data at MSR, CAN, and ADL. These features indicate that this auroral brightening is categorized as a pseudo-breakup. A major substorm took place at  $\sim 1020$ – $1040$  UT, as characterized by an auroral expansion at TIK, high-latitude magnetic field variations and midlatitude Pi 2 pulsations.

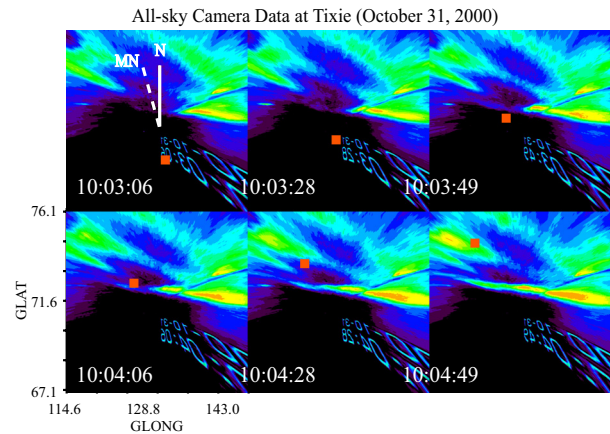


**Fig. 2.** Auroral images obtained at Tixie. Geographic north (N) and geomagnetic north (MN) are indicated in the 1003:06 UT image. Geographic latitude and longitude are indicated in the 1004:06 UT image. The orange squares indicate the footprint of the DMSP F12 spacecraft at an altitude of 120 km.

Figure 2 shows ground auroral images ( $1000 \text{ km} \times 1000 \text{ km}$ ) obtained at TIK from 1003:06 to 1004:49 UT. The images have been converted from the original all-sky coordinates to geographical coordinates by assuming an auroral altitude of 120 km. Geomagnetic north (MN) is  $17^\circ$  westward from geographic north (N). The image center is the zenith of TIK. The orange squares indicate the footprints of the DMSP F12 spacecraft at an altitude of 120 km.

In Figure 2, an auroral arc extends from east to west at 1003:49–1004:49 UT at a latitude of  $72^\circ$ N, which is the equatorward boundary of the auroral region. The arc completely expands to the west at 1004:49 UT. The arc width is less than 1 degree in latitude. The DMSP footprint crosses the western edge of the brightening arc from low to high latitudes at 1004:06 UT. Two auroral arcs in the NW-SE direction can be seen poleward of this brightening arc. They show continuous equatorward motion, as shown in Figure 1.

The DMSP spacecraft is in circular polar orbit, and it observes precipitating electrons and ions, ion drift velocities, and magnetic field variations at an altitude of 840 km. These data from 1003:00 to 1006:29 UT on October 31, 2000, are shown

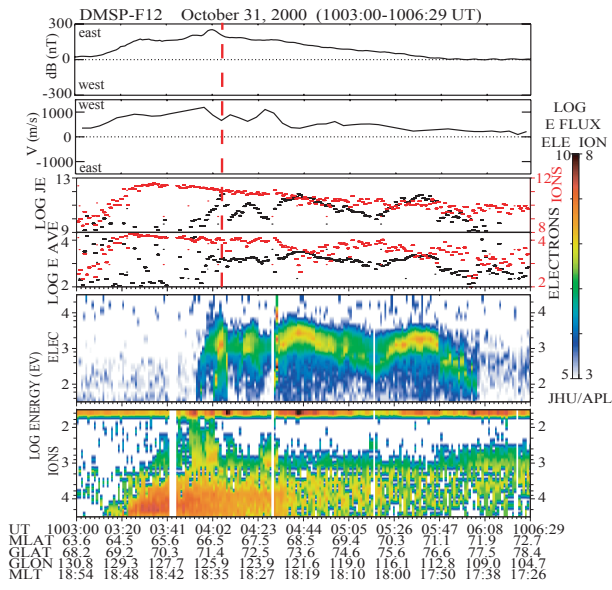


**Fig. 3.** Magnetic field, plasma speed, and precipitating particle data obtained by the DMSP F12 spacecraft at an altitude of 840 km at 1003:00–1006:29 UT on October 31, 2000. From top to bottom, magnetic field, plasma speed, electron (black) and ion (red) energy flux ( $\text{eV}/\text{cm}^2 \text{ s sr}$ ), average energy (eV), and electron and ion energy spectrograms. The dashed red line indicates the time (1004:06 UT) when the DMSP footprint crossed the brightening arc, as shown in Figure 2 (after [37]).

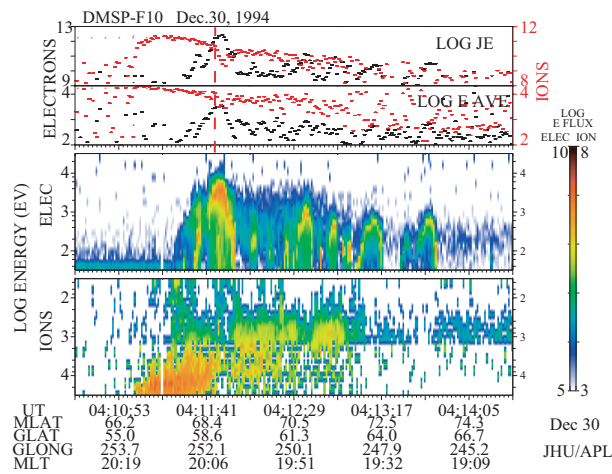


**Fig. 4.** Precipitating particle data obtained by the DMSP F10 spacecraft at an altitude of 840 km at 0410:30 UT – 0414:29 UT on December 30, 1994. From top to bottom, electron (black) and ion (red) energy flux ( $\text{eV}/\text{cm}^2 \text{ s sr}$ ), average energy (eV), and electron and ion energy spectrograms are shown. The vertical red-dashed line indicates the time (0411:48 UT) when the DMSP footprint crossed the brightening arc (after [36]).

in Figure 3. As shown by the vertical dashed line, the brightening arc corresponds to an electron inverted-V structure with a peak energy of  $\sim 1 \text{ keV}$  at the equatorward edge of the electron precipitation region. The latitudinal width of the inverted-V structure is less than 1 degree, which is consistent with the

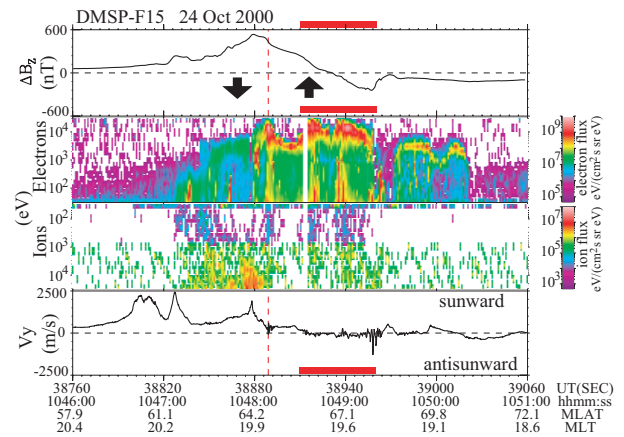


**Fig. 5.** Magnetic field, ion drift, and precipitating ion and electron data obtained by the DMSP F15 satellite at 1046:00–1051:00 UT on October 24, 2000. The vertical red-dashed line and horizontal red lines indicate satellite crossings of brightening arcs. The upward and downward arrows in the top panel indicate directions of the large-scale field-aligned currents inferred from the magnetic field data (after [34]).

observed arc width at Tixie. It is located  $\sim 3^\circ$  (in latitude) poleward of the equatorward boundary of the ion precipitation region and  $\sim 6^\circ$  equatorward of the poleward boundary of the electron precipitation region. The inverted-V structure is also located at the middle part of the energetic ( $> 1 \text{ keV}$ ) ion precipitation region.

In the top and second panels of Figure 3, we show magnetic field and ion drift velocities for the component perpendicular to the DMSP spacecraft’s trajectory in the horizontal plane. The component can approximately be regarded as east-west component. For the magnetic field data, eastward magnetic field intensity increases (downward field-aligned current) from lower latitudes up to  $66.5^\circ \text{ MLAT}$ , and then decreases (upward field-aligned current) to  $72^\circ \text{ MLAT}$ . This feature is a typical pair of region 1 and 2 currents in the dusk sector ([15]). The auroral particles associated with the brightening arc (indicated by the vertical dashed line) are located at the equatorward edge of the upward region 1 field-aligned current, with a local enhancement of the current intensity.

The plasma velocity data obtained by the ion drift meter indicates that the whole region plotted in Figure 3 corresponds to the westward (sunward in this local time) convection region. The brightening arc at  $66.6^\circ \text{ MLAT}$  is located in the middle of this sunward convection region. The arc corresponds to a local enhancement of velocity shear from west to east, which is a typical feature of auroral arcs (e.g., [4]).

Figure 4 shows the particle data for another ground-satellite conjunction event obtained by the DMSP F10 spacecraft from 0410:30 UT to 0414:29 UT on December 30, 1994. This event was reported in detail by [36] as the conjugate ground-satellite observation of a substorm brightening arc during a pseudo onset observed at FSM. As shown by the vertical red-dashed line, the brightening arc corresponds to a clear electron inverted-V structure with a peak energy of  $\sim 3 \text{ keV}$  near the equatorward edge of the electron precipitation region. The inverted-V structure has a latitudinal width of  $\sim 1$  degree and is located about 2

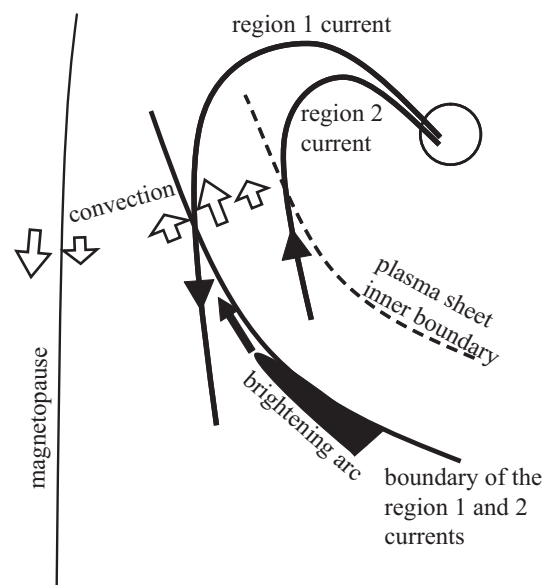
degrees poleward of the equatorward boundary of the ion precipitation region and  $\sim 5$  degrees equatorward of the poleward boundary of the electron precipitation region. It is also located at the poleward boundary of the energetic ( $> 1$  keV) ion precipitation region. The greatest ion energy flux region is located about 1 degree equatorward of the inverted-V structure. For this event, magnetic field and plasma drift data were not available.

Figure 5 shows the particle and field data for the third ground-satellite conjunction event obtained by the DMSP F15 spacecraft from 1046:00 UT to 1051:00 UT on October 24, 2000. This event was reported in detail by [34] as the conjugate ground-satellite observation of a sequence of substorm brightening arcs. During a 30-min interval at 1020–1050 UT, three Pi 2 wave packets and associated auroral brightenings are observed. The DMSP F15 satellite crossed the brightening arc just after the third brightening in the field of view of TIK. The DMSP F15 satellite crosses the most equatorward arc at  $\sim 1048:15$  UT, which brightened at the second Pi 2 onset. Intense accelerated electrons are observed around this time (1048:06–1048:12 UT), as indicated by the vertical dashed line. Then at  $\sim 1048:40$ –1049:20 UT the satellite enters the region of westward-expanding auroras, which is brightened at the third Pi 2 onset. Two inverted-V type accelerated electrons are observed around this time (1048:30–1049:20 UT), as indicated by the horizontal red bars in Figure 5. The energy of these accelerated electrons reaches 10 keV. These accelerated electrons are located in the region of high-energy ion precipitation, which can be recognized at 61–68° MLAT (1047:00–1049:30 UT).

In the top panel of Figure 5, large-scale upward and downward field-aligned currents are observed, as shown by the black arrows. They are probably the region 1 (upward) and region 2 (downward) field-aligned currents in the evening sector ([15]). The brightening auroras indicated by the dashed line and horizontal bars are located in the region 1 upward field-aligned current. The ion drift data indicates that the plotted interval is mostly in the westward (sunward) convection region except for the latitudes higher than the electron precipitation region ( $> 70$  MLAT). The ion drift velocities in the onset arcs (indicated by the vertical red-dashed line and horizontal bars) show intense turbulences with peak-to-peak amplitudes up to  $\sim 1000$  m/s, while the background convection velocity is rather weak. It is noteworthy that the most equatorward arc (dashed line), which brightened after the second Pi 2 pulsation, is located at the equatorward edge of the region 1 current. This arc is located in the sunward convection region, where the convection velocity suddenly decreases from lower latitudes to higher latitudes. This decrease in convection velocity corresponds to converging poleward-directed Pedersen currents, which would give rise to the upward field-aligned currents of the arc. This decrease in convection velocity may also correspond to the duskward extension of the Harang discontinuity, though the velocity does not turn to negative. The intense westward drift at 59–62 MLAT (1046:30–1047:20 UT) is probably the Subauroral Ion Drift (SAID) associated with the high geomagnetic activity (e.g., [10] and [9]).

### 3. Summary and Discussion

We have shown particle and field features associated with auroral initial brightenings for three auroral substorms (pseudo-breakups) observed at 19–20 MLT on December 30, 1994 and October 24 and 31, 2000. The DMSP satellites crossed brightening arcs in the field-of-view of the ground all-sky cameras. All the crossings were 1–2 hours duskside of the main onset local time. The brightening arcs correspond to the inverted-V accelerated electrons at or near the equatorward edge of the electron precipitation region. They were located just poleward of the main ion precipitation region. They were located near the equatorward boundary of the region 1 current, in the sunward convection region, and in the localized turbulence region of ion drift velocity.



**Fig. 6.** Schematic picture of the observed features of the substorm brightening arc mapped to the equatorial plane of the magnetosphere. The observation was made at 1–2 hours duskside of the main onset local time. The brightening arc is located at the equatorward edge of the region 1 upward field-aligned current in the sunward convection region.

Figure 6 illustrates the observed features of the brightening arc mapped to the equatorial plane of the magnetosphere. For all the three events, the observations were made 1–2 hours duskside of the main onset local time. The brightening arc extended from the nightside just after the ground Pi 2 pulsation. The arc was located at the equatorward edge of the region 1 upward field-aligned current in the sunward convection region. This fact suggests that the onset occurs at the boundary of the region 1 and 2 current drivers in the magnetosphere.

According to MHD theory, the major field-aligned current drivers in the magnetosphere are particle inertia, pressure gradient, and temporal variation of flow shear (e.g., [13] and [11]). The pressure gradient force in the longitudinal direction from midnight to both evening and morning sectors possibly generates both the region 1 and 2 current systems ([32]), but mainly drives the region 2 current due to the inward gradient of the magnetic field. The partial ring current due to the gradient and

curvature of the magnetic field also drives the region 2 current system (e.g., [16] and [7]). These considerations suggest that the region 2 current drivers mainly act in the dipolar field region. The temporal development of the flow shear of the increase in westward flow with increasing latitude (inner part of the sunward convection belt) can also cause the region 2 downward current system in the evening sector. On the other hand, the temporal development of the flow shear of the decrease in westward flow with increasing latitude can drive the region 1 upward field-aligned current in the evening sector. This region 1 type flow shear is expected in the plasma sheet from the outer part of the sunward convection region to the antisunward convection region near the tail flank, as shown in Figure 6. The magnetospheric source of the most equatorward brightening arc is located at the boundary of these two current drivers.

[34] discussed the implication of the above observed facts in relation to the substorm models. The brightening arc is probably not connected directly to the lobe reconnection. However, these observations cannot differentiate between near-Earth onset models, i.e., flow braking ([30] and [31]), IMF northward turning and associated convection inhomogeneity ([18]), and near-Earth plasma sheet instability ([17], [6], and [25]). However, we would like to draw attention to the fact that the most equatorward arc that brightens at the substorm onset is not at the equatorward edge of the auroral oval and associated field-aligned current systems, but that the region 2 current system exists equatorward of the brightening arc.

It should be noted that our measurements were made 1–2 hours duskside of the main onset longitudes. For all the three events, the auroral arcs come from the east (nightside) in the field-of-view of the ground cameras. This motion is different from that in the onset region, where aurora simply brightens at the equatorward-most arc and expands poleward (e.g., [1] and [19]). [22] have shown, using the FAST particle data, that the auroral brightening at the onset longitude is caused by suprathermal electron precipitation. This fact suggests that at the exact onset longitude the brightening arc may not be the inverted-V accelerated electrons.

**Acknowledgments:** The IMF data of the ACE satellite was provided by the CDAWweb. The magnetic field data at TIK, CHD, RIK, CAN, and ADL were provided by the 210MM and CPMN projects. The IMAGE FUV data were provided by the IMAGE FUV group at the Space Science Laboratory of the University of California, Berkeley. We thank D. A. Hardy and P. T. Newell for their efforts to make the DMSP particle data available. We gratefully acknowledge the Center for Space Sciences at the University of Texas at Dallas and the US Air Force for providing the DMSP thermal plasma and magnetic field data. This work was supported by the Ministry of Education, Culture, Sports, Science and Technology, Japan (Dynamics of the Sun-Earth-Life Interactive System, No. G-4, the 21st Century COE Program, Grant-in-Aid for Scientific Research No. 16403007, and the International STEP project) and by the Russian Foundation of Basic Research (Project No. 03-05-39011-GFEN).

## References

1. Akasofu, S. I., The development of the auroral substorm, *Planet Space Sci.*, *12*, 273, 1964.
2. Angelopoulos, V., et al., Statistical characteristics of bursty bulk flow events, *J. Geophys. Res.*, *99*, 21257, 1994.
3. Baker, D., N., T. I. Pulkkinen, V. Angelopoulos, W. Baumjohann, and R. L. McPherron, Neutral line model of substorms: past results and present view, *J. Geophys. Res.*, *101*, 12,975–13,010, 1996.
4. Burke, W. J., M. S. Gussenhoven, M. C. Kelly, D. A. Hardy, and F. J. Rich, Electric and magnetic field characteristics of discrete arcs in the polar cap, *J. Geophys. Res.*, *87*, 2431, 1982.
5. Cheng, C. Z., and A. T. Y. Lui, Kinetic ballooning instability for substorm onset and current disruption observed by AMPTE/CCE, *Geophys. Res. Lett.*, *25*, 4091–4094, 1998.
6. Cheng, C. Z., and S. Zaharia, MHD ballooning instability in the plasma sheet, *Geophys. Res. Lett.*, *31*, L06809, doi:10.1029/2003GL018823, 2004.
7. Crooker, N. U., and R. L. McPherron, On the distinction between the auroral electrojet and partial ring current systems, *J. Geophys. Res.*, *77*, 6886–6889, 1972.
8. Dubyagin, S. V., V. A. Sergeev, C. W. Carlson, S. R. Marple, T. I. Pulkkinen, and A. G. Yahnin, Evidence of near-Earth breakup location, *Geophys. Res. Lett.*, *30*, 10.1029/2002GL016569, 2003.
9. Foster, J. C., and H. B. Vo, Average characteristics and activity dependence of the subauroral polarization stream, *J. Geophys. Res.*, *107*(A12), 1475, doi:10.1029/2002JA009409, 2002.
10. Galperin, Y., V. N. Ponomarev, and A. G. Zosimova, Plasma convection in the polar ionosphere, *Ann. Geophys.*, *30*, 1, 1974.
11. Haerendel, G., Field-aligned currents in the Earth's magnetosphere, in *Physics of Magnetic Flux Ropes*, *Geophys. Monogr. Ser.*, vol. 58, edited by C. T. Russell, E. R. Priest, and L. C. Lee, pp. 539–553, AGU, Washington, D. C., 1990.
12. Haerendel, G., Disruption, Ballooning or auroral avalanche – on the cause of substorms, *Proc. of the First International Conference on Substorms (ICS-1)*, Kiruna, Sweden, pp.417–420, ESA, 1992.
13. Hasegawa, A., Generation of field aligned current during substorm, in *Dynamics of the Magnetosphere*, edited by S.-I. Akasofu, 529, D. Reidel, Norwell, Mass., 1979.
14. Hones, E. W., D. N. Baker, S. J. Bame, W. C. Feldman, J. T. Gosling, D. J. McComas, R. D. Zwickl, J. A. Slavin, E. J. Smith, and B. T. Tsurutani, Structure of the magnetotail at 220  $R_E$  and its response to geomagnetic activity, *Geophys. Res. Lett.*, *11*, 5–8, 1984.
15. Iijima, T., and T. A. Potemura, Large-scale characteristics of field-aligned currents associated with substorm, *J. Geophys. Res.*, *83*, 599, 1978.
16. Kamide, Y., and N. Fukushima, Positive geomagnetic bays in evening high-latitudes and their possible connection with partial ring current, *Rep. Ionosph. Space Res. Jpn.*, *26*, 79–101, 1972.
17. Lui, A. T. Y., R. E. Lopez, B. J. Anderson, K. Takahashi, L. J. Zanetti, R. W. McEntire, T. A. Potemra, D. M. Klumppar, E. M. Greene, and R. Strangeway, Current disruptions in the near-Earth neutral sheet region, *J. Geophys. Res.*, *97*, 1461–1480, 1992.
18. Lyons, L. R., A new theory for magnetospheric substorms, *J. Geophys. Res.*, *100*, 19,069–19,081, 1995.

19. Lyons, L. R., I. O. Voronkov, E. F. Donovan, and E. Zesta, Relation of substorm breakup arc to other growth-phase auroral arcs, *J. Geophys. Res.*, *107*, 10.1029/2002JA009317, 2002.
20. Machida, S., Y. Miyashita, A. Ieda, A. Nishida, T. Mukai, Y. Saito, and S. Kokubun, GEOTAIL observations of flow velocity and north-south magnetic field variations in the near and mid-distant tail associated with substorm onsets, *Geophys. Res. Lett.*, *26(6)*, 635–638, 1999.
21. Murphree, J. S., R. D. Elphinstone, L. L. Cogger, and D. Hearn, Viking optical substorm signatures, in *Magnetospheric Substorms*, edited by J. R. Kan, T. A. Potemra, S. Kokubun, and T. Iijima, AGU Mono. 64, pp.241, 1991.
22. Mende, S. B., C. W. Carlson, H. U. Frey, L. M. Peticolas, and N. Østgaard, FAST and IMAGE-FUV observations of a substorm onset, *J. Geophys. Res.*, *108*, 10.1029/2002JA009787, 2003.
23. Nagai, T., M. Fujimoto, Y. Saito, S. Machida, T. Terasawa, R. Nakamura, T. Yamamoto, T. Mukai, A. Nishida, and S. Kokubun, Structure and dynamics of magnetic reconnection for substorm onsets with Geotail observations, *J. Geophys. Res.*, *103(A3)*, 4419–4440, 1998.
24. Nagai, T., I. Shinohara, M. Fujimoto, M. Hoshino, Y. Saito, S. Machida, and T. Mukai, Geotail observations of the Hall current system: Evidence of magnetic reconnection in the magnetotail, *J. Geophys. Res.*, *106(A11)*, 25,929–25,950, 2001.
25. Ohtani, S., A. T. Y. Lui, K. Takahashi, D. G. Mitchell, and T. Sarris, Ion dynamics and tail current intensification prior to dipolarization: The June 1, 1985, event, *J. Geophys. Res.*, *105(A11)*, 25,233–25,246, 2000.
26. Ohtani, S.-I., Substorm trigger processes in the magnetotail: Recent observations and outstanding issues, *Space Sci. Rev.*, *95*, 347, 2001.
27. Runov, A., et al., Current sheet structure near magnetic X-line observed by Cluster, *Geophys. Res. Lett.*, *30(11)*, 1579, doi:10.1029/2002GL016730, 2003.
28. Samson, J. C., L. R. Lyons, P. T. Newell, F. Creutzberg, and B. Xu, Proton aurora and substorm intensifications, *Geophys. Res. Lett.*, *19*, 2167, 1992.
29. Shiokawa, K., et al., Auroral observations using automatic instruments: Relations with multiple Pi 2 magnetic pulsations, *J. Geomag. Geoelectr.*, *48*, 1407, 1996.
30. Shiokawa, K., W. Baumjohann, and G. Haerendel, Braking of high-speed flows in the near-Earth tail, *Geophys. Res. Lett.*, *24*, 1179–1182, 1997.
31. Shiokawa, K., et al., High-speed ion flow, substorm current wedge, and multiple Pi 2 pulsations, *J. Geophys. Res.*, *103*, 4491–4508, 1998a.
32. Shiokawa, K., G. Haerendel, and W. Baumjohann, Azimuthal pressure gradient as driving force of substorm currents, *Geophys. Res. Lett.*, *25(7)*, 959–962, 1998b.
33. Shiokawa, K., K. Yumoto, and J. V. Olson, Multiple auroral brightenings and associated Pi 2 pulsations, *Geophys. Res. Lett.*, *29(11)*, 10.1029/2001GL014583, 2002.
34. Shiokawa, K., K. Yago, K. Yumoto, D. G. Baishev, S. I. Solov'ev, F. J. Rich, and S. B. Mende, Ground and satellite observations of substorm onset arcs, *J. Geophys. Res.*, *110*, A12225, doi:10.1029/2005JA011281, 2005.
35. Solov'ev, S. I., D. G. Baishev, E. S. Barkova, N. E. Molochushkin, and K. Yumoto, Pi2 magnetic pulsations as response on spatio-temporal oscillations of auroral arc current system, *Geophys. Res. Lett.*, *27(13)*, 1839–1842, 2000.
36. Yago, K., K. Shiokawa, K. Hayashi, and K. Yumoto, Auroral particles associated with a substorm brightening arc, *Geophys. Res. Lett.*, *32*, L06104, doi:10.1029/2004GL021894, 2005.
37. Yago, K., K. Shiokawa, K. Yumoto, D. G. Baishev, S. I. Solov'ev, and F. J. Rich, Simultaneous DMSP, all-sky camera, and IMAGE FUV observations of a substorm onset arc, *submitted to Earth Planets Space*, 2006.
38. Yumoto, K., and the CPMN group, Characteristics of Pi 2 magnetic pulsations observed at the CPMN stations: A review of the STEP results, *Earth. Planets. Space.*, *53*, 981, 2001.

# Auroral secondary ions in the inner magnetosphere

G. Sofko, M. Watanabe, R. Schwab, and C. Huang

**Abstract:** Radar measurements of the global convection pattern and satellite observations of nightside low-energy ion populations are presented for magnetically disturbed conditions. The results form a consistent picture, namely that the ions are secondary ions (mostly  $O^+$ ) produced in the auroral zone ionospheric F-region during bombardment by primary auroral electrons, and that these ions subsequently undergo TAI (transverse acceleration of ions) which raises their energy from the ionospheric value of about 0.1 eV to suprathermal and sub-auroral energies from a few tens of eV to a few hundred eV. The ions subsequently undergo a combination of bounce motion and ExB drift along the streamlines of the convection pattern, which has recently been shown to include some new features. We can classify three populations of these low-energy ions, namely DAPS (Dusk Auroral Positive Stream) ions, SAPS (Sub-Auroral Polarization (or Positive) Stream) ions and MAPS (Morning Auroral Positive Stream) ions. When conditions are not too disturbed, these ions show some characteristic features such as energy bands with integer energy ratios and a dispersive signature (decreasing energy with decreasing latitude). It is proposed that these low-energy ions, particularly the MAPS ions on the dawnside, may alter the shielding conditions in the inner magnetosphere.

*Key words:* Auroral secondary ions, Radar convection, Shielding, Satellite particle observations.

## 1. Introduction

As the dayside ionosphere rotates around to the nightside, the photoionization in the E-region disappears and the F-region survives only because the loss rate is low. During magnetically disturbed conditions when the electric field increases, the loss rates increase and the photoionization can decrease to very low levels, or even disappear. However, during disturbed conditions, a strong new source of ionization appears, namely bombardment of the ionosphere by auroral primary particles, mainly precipitating electrons in the 1–10 keV range which flow from the central plasma sheet to the ionosphere and are associated with upward field-aligned currents (FACs). These FACs carry substantial energy, as evidenced by the optical aurora they produce. Every kiloRayleigh (kR) of optical emission requires a primary energy flux of about  $1 \text{ erg cm}^{-2} \text{ s}^{-1}$ . Typically, optical auroras are at least about 10 kR during moderately disturbed conditions, but they can attain intensities of more than 100 kR during intense events. Thus, substantial energy fluxes from 10–100  $\text{ergs cm}^{-2} \text{ s}^{-1}$  are carried by the primary electrons, resulting in a large production of secondary ion-electron pairs.

In a sense, the ionosphere acts as a “particle amplifier” since an average energy of only about 35 eV from a primary precipitating particle is required to produce a secondary ion-electron pair. Thus, a 1 keV auroral primary electron can produce about 30 low-energy secondary ions and electrons. Furthermore, the number of secondary pairs produced is large, since an energy flux of  $1 \text{ erg cm}^{-2} \text{ s}^{-1}$  produces  $1.79 \times 10^{10}$  secondary pairs  $\text{cm}^{-2} \text{ s}^{-1}$ . The observed auroral optical intensities of 10–100 kR require that the actual secondary production rate

would be 10–100 times the above figure. As shown in Figs. 3.3.4. of [17], the secondary electrons will have energies up to a few tens of eV (some of them will have enough energy to produce another secondary pair) but the secondary ions will remain near their ionospheric energy ( $\sim 0.1 \text{ eV}$ ). In the present paper, we focus on the ion production in the F-region, particularly above about 160 km where the loss rates are low and the lifetimes are long. Figure 3.3.3 of [17] shows that, particularly for the primary electrons in the 1–5 keV range, a non-negligible fraction of the secondary ions would be produced above 160 km, these being predominantly  $O^+$  ions. The contribution of ionospheric  $O^+$  to the magnetosphere has been noted in many satellite papers (e.g., [1, 3, 8, 11, 22]). As a result, there will be a reasonable supply of low-energy secondary  $O^+$  ions from the upper E-region and lower F-region, even if only a percent or two of the original primary bombardment energy goes into secondary production above 160 km.

It is well known that magnetic storms and substorms are accompanied by turbulence that is both electrostatic and electromagnetic. One example of the electromagnetic turbulence is the presence of ion cyclotron waves, whose effects have been invoked (e.g., [4, 15]) to explain the transverse acceleration of ions (TAI) (see the extensive list of references in [16] and the review by [2]) that leads to the many observations of ion conics. Such transverse energization of the secondary ions above 160 km leads to a strengthening of their magnetic moment, and hence of the mirror force  $\vec{F} = -\mu \nabla B$ . As a result, F-region secondary ions above 160 km that undergo TAI will travel up the magnetic field lines, executing bounce motion. (There also is ample evidence of parallel acceleration above auroras, presumably due to the upward polarization field caused when the secondary electrons move up the field line away from the secondary ions.)

Satellite observations of TAI and ion conics show that most of these secondary ions, even after some TAI and parallel acceleration, remain at energies below 1 keV, most being in the range from a few tens to a few hundreds of eV. Because of their low energies, they participate only in ExB drift, not curvature-gradient drift. These bouncing and drifting low-energy sec-

Received 16 May 2006.

**G. Sofko, M. Watanabe, and R. Schwab.** Institute of Space and Atmospheric Studies, University of Saskatchewan, 116 Science Place, Saskatoon, Saskatchewan, Canada

**C. Huang.** Atmospheric Sciences Group, Haystack Observatory, Massachusetts Institute of Technology, Westford, Massachusetts, USA

ondary ions thus will act as tracers of the streamlines (equipotentials) of the convective flow patterns in the ionosphere and magnetosphere. New pictures of the convection streamlines have been obtained using recent Millstone Hill and Wallops Island SuperDARN results. A cartoon summarizing the convection pattern results is presented in the next Section.

We shall present satellite evidence showing that there are three distinct populations of the low-energy secondary ions that have bounced and drifted away from their production sites in the auroral zone. Indeed, many satellites have shown the presence of these ions, such as DE1 and 2 [21], AKEBONO (EXOS-D) [9, 10], DMSP and CRRES. A recent statistical study of DMSP and CRRES data [14] has revealed the frequent presence of these low-energy ions on the morning side. We will show only a small sample of the extensive satellite results.

Because the ions are positive particles that flow along the equipotential streamlines, we will refer to them as “Auroral Positive Stream (APS)” ions. Two of the three ion populations will remain at auroral latitudes on auroral streamlines, namely the population that drifts to the west in the afternoon convection cell (the **Dusk Auroral Positive Stream**, or **DAPS**, ions) and the one that drifts to the east in the morning convection cell (the **Morning Auroral Positive Stream**, or **MAPS**, ions). The third stream flows westward in the **SAPS** (Sub-Auroral Polarization Stream) region defined by [5]. These westward-drifting ions in the plasmatrough region will be referred to as **SAPS** (Sub-Auroral Positive Stream) ions. Their ExB motion is an ideal tracer of the equipotentials in the Sub-Auroral Polarization Stream.

## 2. The Ionospheric Convection Pattern

Figure 1 shows a pictorial representation of the convection pattern during disturbed conditions with a  $B_y+$  IMF. This is basically the two-cell convection pattern, but with the recent radar observations relevant to the SAPS region. The SAPS flows result from an arm of the afternoon cell that protrudes into the morning sector at low latitudes. There is a convection reversal associated with this arm, and the heavy dashed line in the figure divides the eastward flows in the auroral zone portion of the arm from the westward streaming flows in the equatorward SAPS region of the arm.

SAPS has been defined [5] as a relatively broad ( $\sim 5^\circ$  latitude) region of poleward (ionosphere) or radially outward (magnetosphere) electric field in the region equatorward of the inner auroral-energy electron boundary of the plasma sheet. At ionospheric heights, the SAPS region is one of low density and conductivity, particularly during disturbed periods when the electric field and the resulting ion convective speed are higher so that the cross-section for recombination of ionospheric ions and electrons is elevated, with the result that the electron density in the plasmatrough is further decreased [18, 20]. As a result, the electric field must strengthen in order to increase the Pedersen closure currents to the level required for Region 2 current closure in this subauroral region. The resulting strong convective flows, first seen as latitudinally confined (about  $1^\circ$ ) regions, were referred to as Polarization Jets (PJ) [7] and SAIDs (Sub-Auroral Ion Drifts) [19]. It was observed that the flows could be broader, spanning about  $5^\circ$  [23]. The acronym SAPS

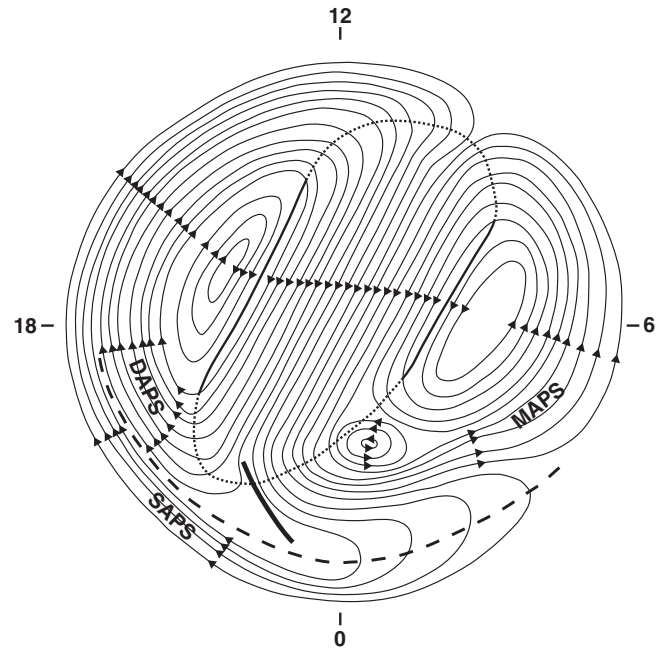


**Fig. 1.** Pictorial representation of convection including trends indicated by recent SuperDARN and Millstone Hill convection results. The pattern indicates the locations of the DAPS, MAPS and SAPS populations. The heavy line near midnight marks a very rough approximation to the location of the Harang discontinuity. The dotted lines are the mappings of the dayside and nightside reconnection lines to the ionosphere and the solid lines that join the dotted lines represent the OCFLB (open-closed field line boundary). The heavy dashed line spanning the midnight sector represents the convection reversal boundary which separates the SAPS region from the auroral zone. The small counterclockwise cell is not discussed here.

was defined in part to describe the broadened electric field region associated with the latter broader flows [23], which presumably incorporate the narrower PJ and SAID flows seen earlier. Millstone radar results [12] showed that the westward flows of the Polarization Jet (they used this term because the definition of SAPS occurred a year later) could be seen well into the postmidnight sector, as late as 04 or 05 LT. Although not specifically stated in the original SAPS definition by Foster and Burke [2002], the region of the SAPS poleward electric field is within the nightside low-latitude portion of the afternoon convection cell, which develops the arm shown in Fig. 1 that can extend well into the post-midnight sector during disturbed conditions. In addition to the [12] study, the postmidnight SAPS occurrence was revealed in a statistical study by [6] who, for the relatively large KP value of  $6^-$ , showed that the penetration of SAPS into low latitudes in the postmidnight sector could extend almost as far eastward as dawn.

In Figure 1, the auroral zone includes the streamlines that, starting from the dayside, cross the polar cap and then flow through the “merging line” (dashed) on the nightside. Many streamlines then turn westward into the afternoon cell. Since these streamlines turn clockwise, the flow is characterized by downward vorticity, which is associated with upward FACs, particularly near the late evening convection reversal region.

It is there that the auroral secondaries will be produced, after which they flow westward on auroral zone streamlines, leading to the observations of DAPS ions in the post-evening sector.

However, some of the afternoon (PM) cell streamlines emerging from the polar cap first turn eastward on the poleward portion of a morning-side low latitude “extension arm” of the PM cell, and then they undergo a convection reversal so that the flow on the equatorward side of the reversal is westward in the poleward electric field of the SAPS region, where the SAPS ions are found. It should be noted that the downward flow vorticity across that convection reversal is again consistent with the presence of upward field-aligned currents; the SAPS ions are the secondary ions that result from the primary electron bombardment associated with those upward FACs. Consistent with this scenario are observations of strong optical aurora in the vicinity of that low-latitude early morning convection reversal, and even onsets of substorm expansive phases in that region.

Finally, the origin of the MAPS particles should be addressed. At first sight, it would seem that the morning auroral streamlines emerging from the polar cap undergo a counterclockwise rotation, which implies downward, rather than upward, FAC. However, if the streamlines in Fig. 1 are examined just equatorward of the small counterclockwise cell, it will be noticed that their separation increases in the equatorward direction. This shows that there is a shear which is characterized by downward vorticity. Further along these streamlines, there is more downward vorticity as the streamlines curve clockwise to lower latitudes around the eastward end of the PM cell “extension arm” where the SAPS ions are produced. Overall, then, there are indeed several regions of downward vorticity (upward FACs) in the morningside auroral zone too, and these regions are where the MAPS ions will be produced. After production, they simply undergo drift eastward toward dawn, where we will show in the following section some AKEBONO measurements [9, 10] and discuss the DMSP statistical study by [14] which shows that dawnside low-energy ions are a persistent feature during disturbed conditions.

### 3. Satellite Observations Of Low-Energy Ions

Some of the earliest low-energy SAPS ion observations were made by the Dynamics Explorer satellites DE-1 (~10,000 km latitude) and DE-2 (~925 km). Two fine examples of pitch angle observations near  $0^\circ$  in the evening sector on October 22, 1981, are shown by [21], in their Plate 1 which shows LAPI (Low Altitude Particle Instrument) data.

Figure 2 shows DMSP evening sector results at about 20 MLT from both the SSJ/4 and ion drift meter instruments. The figure clearly reveals two of the three low-energy ion populations, namely the SAPS ions, found equatorward of the auroral particles, and the DAPS ions, seen within the auroral zone in the latitude range from about  $-53.7^\circ$  to  $-56.5^\circ$  MLAT. Of course, the DAPS ions are coincident with the more energetic (~1 keV) auroral ions and electrons. The electron and ion spectra in the top panels of Fig. 2 show that the inner edge of both the electron and ion auroral energy precipitation on this very disturbed day is located at about  $-53.6^\circ$  in the southern hemisphere. The SAPS ions (~1 keV) extend into the plasmatrough region well equatorward of the auroral electron bound-

ary, which would be conjugate to the inner edge of the electron plasma sheet. The low-energy SAPS ions have the following features: (a) they are bursty in space and time; (b) their energies range from the detector low-limit energy (30 eV) up to ~1 keV; (c) they have a banded structure in energy, with several bands of energy occurring at any given latitude; (d) they show a signature of dispersion, namely a slope that reflects a decrease in energy with decreasing latitude; (e) the lowest energy band (< 100 eV) is usually the strongest in flux, as seen clearly in Fig. 2 at the lower latitude end ( $-50^\circ$  to  $-52^\circ$ ).

The DAPS ions have similar features except that the dispersion slope (property d) is smaller than that of the SAPS ions. The ion drift meter convective motion results seen in the bottom panel show that both the auroral zone DAPS ions and the plasmatrough SAPS ions are drifting westward, although there is a latitudinal region (from about  $-53^\circ$  to  $-52^\circ$ ) of weaker drift separating these two low-energy populations. Most of the SAPS secondary ions produced in the zone of primary electron precipitation initially move eastward just poleward of the convection reversal before turning equatorward and then traveling westward in the plasmatrough, as shown in Figure 1. The DAPS secondary ions are produced at slightly higher latitudes nearer to dusk and subsequently drift directly westward toward dusk on evening cell streamlines. It should be noted that the DAPS ions all travel directly along streamlines from the auroral production region toward dusk, and these paths do not differ much in length. On the other hand, the SAPS ions travel on longer routes because they may first travel eastward at auroral latitudes before crossing the convection reversal to travel westward in the plasmatrough. As a result, there can be a considerable difference in length between adjacent paths of the SAPS ions. This accounts for the different slopes in the dispersion signatures of the DAPS and SAPS ions.

Because of their shorter paths, DAPS ions are not subject to as much loss as the SAPS ions, and would be expected to show higher energy fluxes. This is revealed rather clearly in the middle panel of Figure 2, where the DAPS population has fluxes well in excess of  $10^7$  eV cm<sup>-2</sup> s<sup>-1</sup> sr<sup>-1</sup> eV<sup>-1</sup> whereas the SAPS population values are close to  $10^7$ . In Figure 2, the important boundary between the DAPS and SAPS ion populations is the equatorward auroral boundary at  $-53.7^\circ$ , which is roughly the low-latitude boundary for both auroral energy ions and electrons. (Although ring current ions are normally too high in energy to be seen by the SSJ/4 detector, Fig. 2 shows a ring current ion population - the whitish-pink high flux region - seen both in the auroral zone in the plasmatrough from  $\sim -53.7^\circ$  to  $\sim -52.1^\circ$  at the highest SSJ/4 energies (> 10 keV)).

The SAPS and DAPS energy bands, which are shown even more clearly in upcoming Figure 3, have been explained in detail by [9, 10]. They result from differences in lengths of the streamline paths between the secondary production region and the satellite. When DMSP is traveling poleward through the plasmatrough, as in Fig. 2, the streamline path lengths are shorter at the higher latitudes, longer at the lower latitudes. If we assume for simplicity that the electric field is roughly constant in the plasmatrough, the ExB drift time will be directly proportional to the path length. For the longer path lengths, the time must be longer. That time must be equal to the time for the half-bounce along the field line from the northern hemi-

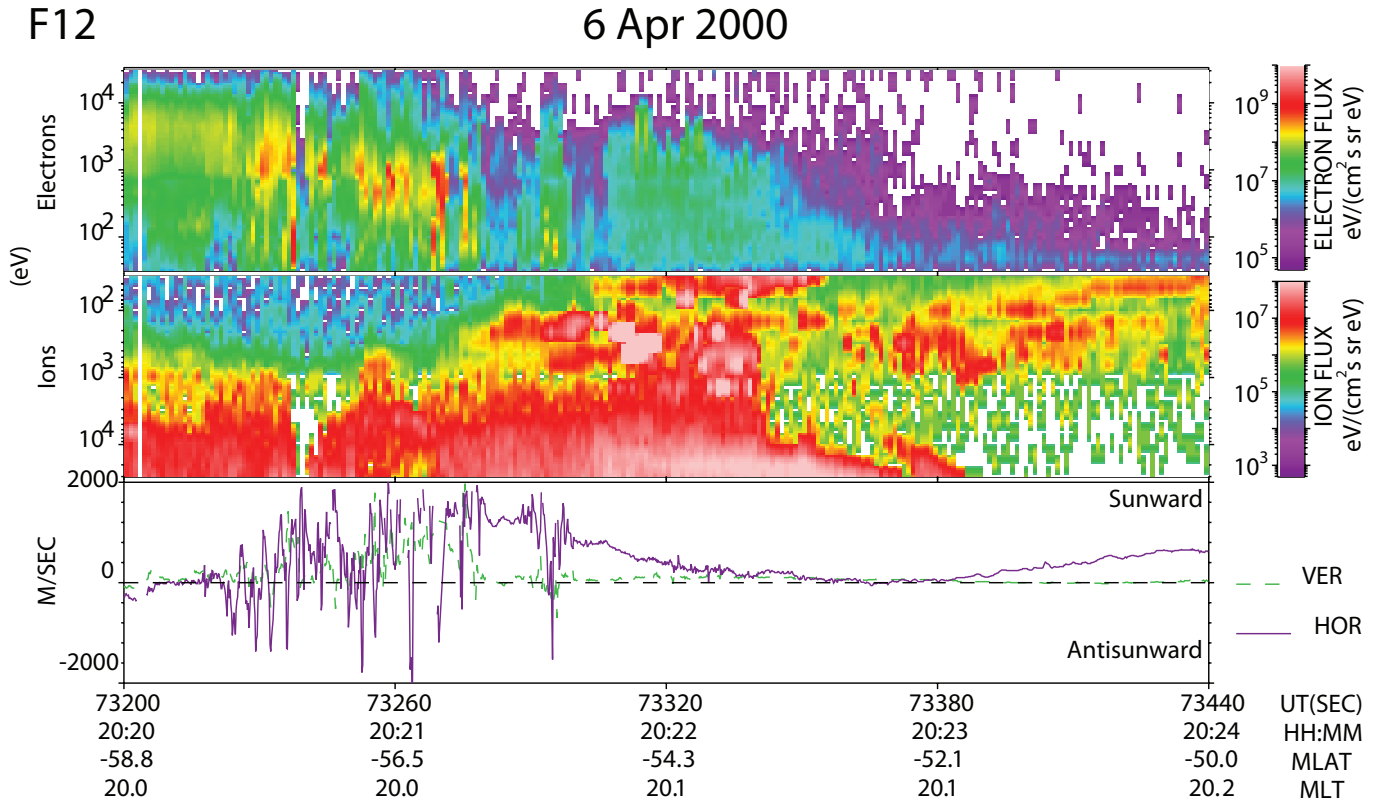


**Fig. 2.** DMSP evening sector SSJ/4 particle spectra (electrons in the top panel, ions in the middle panel) and ion drifts (bottom panel), in the evening sector. Low-energy ions in the SAPS region are clearly seen in the low latitude portion of the ion spectrum.

sphere production site to the southern hemisphere observation site. Therefore, the lower-latitude bouncing particles must have lower energy so that their half-bounce time matches the long drift time. On the other hand, the shorter drift times on the shorter paths at higher latitudes require that the half-bounce be made in a shorter time, which can only be done if the energy of the bouncing particles is higher. Thus, higher energies are seen at higher latitudes.

Actually, in travelling from the initial northern hemisphere production site to the southern hemisphere satellite, the ions can make either one half-bounce, three-half-bounces, five half-bounces, etc. This is the reason for the observed energy-banding. Since the field-aligned bounce path lengths have ratios of 1:3:5:7, the parallel speed ratios must be 1:3:5:7 and therefore the energy ratios must be 1:9:25:49. Our analysis of the bands in Figure 2 showed that the ratios are close to the values 1:9:25:49, so we assume the ionization source for the southern hemisphere observations of Figure 2 was indeed in the northern hemisphere. If the particles had originated in the same (southern) hemisphere that they were observed, then they would have had to make one, two, three, etc. complete bounces between production and observation, in which case their velocities would have been in the ratios 1:2:3:4... and their energies in the ratios 1:4:9:16.

We now turn our attention to the third low-energy population, namely the MAPS ions near dawn. Figure 3 shows EXOS/D (AKEBONO) ion spectra in the dawn sector at about 4.5 MLT (taken from Plate 3 of [9]). This time, however, the ions were

detected in four sets of pitch angles in  $20^\circ$  intervals, starting with the  $0 - 20^\circ$  range of nearly field-aligned ions. In the upper panel, we see characteristics similar to those of the pre-midnight DAPS and SAPS ions observations by DMSP in Figure 2, namely the bursty nature, several energy bands, the dispersion signature of decreasing energy with decreasing latitude, and the prominence of the lowest-energy band of particles. The AKEBONO mass spectrometers (IMS, SMS) showed that this band is composed primarily of  $O^+$  ions. The drift meter showed that these particles convect eastward, as expected for ions on streamlines in the morning convection cell. The banded energy structure is much clearer at the higher pitch angles, such as  $40 - 60^\circ$ , where the bands are characterized by energy ratios of 1:9:25:49, or  $1^2:3^2:5^2:7^2$ . As mentioned above, this is a direct result of the fact that these particles were produced in the opposite hemisphere to that of the AKEBONO observations.

#### 4. Discussion

The satellite results shown in Figures 2 and 3 reveal three classes of low-energy ions, namely SAPS, DAPS and MAPS ions, all with similar characteristics - multiple energy bands, bursty appearance in space and time (particularly those in the loss cone), and often an energy dispersion signature. We note that the latter is not always seen, particularly during fairly disturbed conditions when the secondary source region is extended and the energy banding is "smeared out" as a consequence.

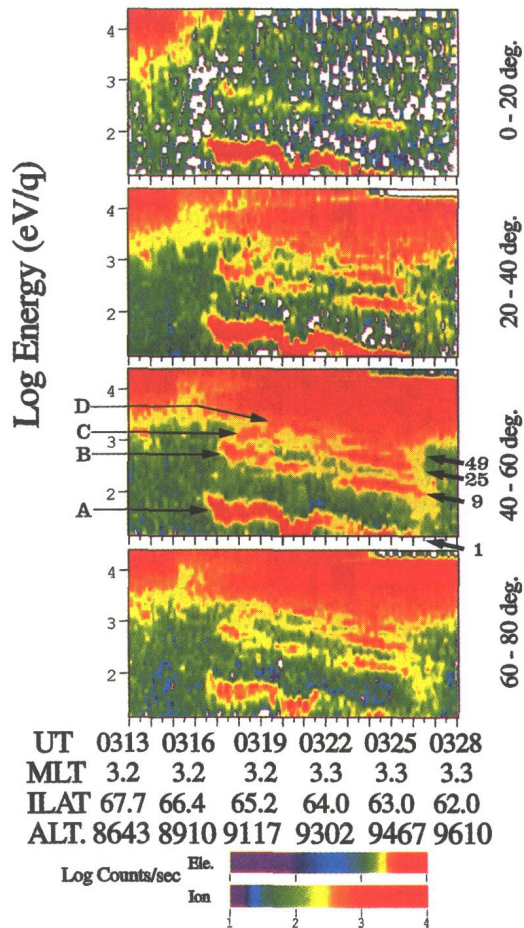


**Fig. 3.** AKEBONO Ion spectra in four pitch-angle ranges (permission granted by Dr. Hirahara) in the postmidnight sector. Note the banding of the low-energy ions, best seen in the  $40^\circ - 60^\circ$  pitch angle panel, and the presence of the auroral ions which show a flat top at an energy of just under 10 keV. These measurements were made in the auroral zone, which is seen to extend at these times to latitudes lower than  $63.8^\circ$  ILAT.

During any major storm, the primary auroral bombardment would result in a large production of the secondary ions (principally  $O^+$ ) because  $O^+$  ions dominate in the upper E- and lower F-regions of the auroral ionosphere, where the SAPS, DAPS and MAPS ions are produced.

The MAPS secondary ions could play an important role in reducing the shielding in the morning sector. Normally, that shielding would be attributed to the effect of the curvature-gradient (CG) drift of the high-energy particles, leading to a separation between the high-energy ions and electrons, with the electrons drifting toward dawn while the ions drift toward the evening sector. The eastward CG drift of the high-energy electrons to the dawnside leads to a negative charge layer which shields the morning plasmasphere from the dawn-dusk field. Sometimes this is stated in a different manner, because the dawnside at low latitudes outside the plasmasphere is also where the Region 2 upward FACs occur, and the precipitation of dawnside high-energy electrons in the associated upward FACs is said to cause the shielding. Here, we prefer the Gauss' law ap-

proach in which electric fields start and stop on charge distributions. It is not difficult to show from a kinetic approach that the higher energy particles produce a total drift (the sum of three drifts, namely the gradient, curvature and magnetization drifts) given by

$$\vec{v}_D = \frac{\vec{B} \times \nabla p_\perp}{qnB^2} + \frac{p_\parallel - p_\perp}{qnB^2} \cdot \frac{\vec{B}}{B^2} \times [(\vec{B} \cdot \nabla)\vec{B}]. \quad (1)$$

This shows that, when the pressure is isotropic, the drift arises from the first term on the right, namely the pressure gradient drift, to which the shielding has sometimes been attributed. By undergoing eastward ExB drift along the streamlines that pass through the auroral zone, the low-energy MAPS ions can arrive at the same position as the high energy electrons. The overall net effect would be the cancellation of the shielding negative charge of the high-energy electrons by the positive charge of the low-energy ions. This might explain the loss of shielding discussed by [13].

Confirmation of the low-energy ions in the morning sector is well-documented by [14], who undertook a statistical study of DMSP results and also looked at CRRES data. They modeled the particle trajectories using a Volland-Stern model, making allowances for time-varying electric fields and azimuthal magnetic field gradients. Another possible explanation for their observations is that adopted here, namely that these ions were originally secondaries from the auroral zone F-region.

## 5. Conclusions

(a) Satellite observations in the evening sector (DMSP results in Fig. 2), and the morning sector (such as the AKEBONO results in Fig. 3 and an extensive DMSP study by [14]), reveal the presence of three low-energy ion populations during disturbed conditions. We propose that these ions (mainly  $O^+$ ) are the secondary ions that result from primary auroral electron bombardment of the auroral zone ionosphere.

(b) The secondary ions populations undergo ExB drift along the streamlines of the global convection pattern, sketched in Figure 1. Two of these populations flow on afternoon convection cell streamlines, namely the westward-flowing SAPS (SubAuroral Plasma Stream) ions in the plasmatrough (which can flow westward from postmidnight locations), and the DAPS (Dusk Auroral Positive Stream) ions which are produced mainly in the evening sector at auroral latitudes and which subsequently flow almost directly westward on auroral streamlines that are poleward of those on which the SAPS ions are seen. There is evidence in Figure 2 of a small observable latitudinal gap between these two ion populations in the evening sector. The third population consists of ions which have flowed eastward from the auroral zone on morning-cell streamlines. They are MAPS (Morning Auroral Positive Stream) ions seen clearly in the dawn sector.

(c) The observations of bright visual aurora in the auroral zone reveal that primary particle energy fluxes of tens of  $\text{ergs cm}^{-2} \text{s}^{-1}$  are common during disturbed periods. Making conservative estimates of the resulting secondary particle production, it is not unreasonable to expect that the low-energy ion populations, particularly the MAPS ions, could be strong

enough to add enough positive charge in the region of the negative shielding charge provided by high-energy electrons on the dawnside to reduce the shielding effect of the electrons.

(d) The low-energy secondary ions clearly undergo some initial acceleration that raises their energies to the range 0.1 eV to energies from a few tens to a few hundred eV. There has been ample evidence of TAI (transverse acceleration of ions) leading to ion conics, and of parallel acceleration, causing beams. As a result of such energization, the DAPS, SAPS and MAPS populations consist of suprathermal to sub-auroral energy ions that undergo bounce and convective drift motions in traveling along the streamlines (equipotential contours) from the source region in the auroral ionosphere to the observation regions in the evening or morning sectors. The combination of these motions leads to the energy banding and dispersive signature of decreasing energy with decreasing latitude. The observed satellite locations of these ions are in good agreement with the predictions of the convection patterns.

## References

1. Abe, T., Whalen, B. A., Yau, A. W., Horita, R. E., Wanatabe, S., and Sagawa, E., Exos D (Akebono) suprathermal mass spectrometer observations of the polar wind, *Journal of Geophysical Research*, 98, 11,191–11,203, 1993.
2. André, M., and Yau, A., Theories and observations of ion outflow in the high latitude magnetosphere, *Space Science Reviews*, 80, 27–48, 1997.
3. Chandler, M. O., Waite, J. H., Jr., and Moore, T. E., Observations of polar ion outflows, *Journal of Geophysical Research*, 96, 1421–1428, 1991.
4. Chang, T., Crew, G. B., Hershkowitz, N., Jasperse, J. R., Retterer, J. M., and Winningham, J. D., Transverse acceleration of oxygen ions by electromagnetic ion cyclotron resonance with broad band left-hand polarized waves, *Geophysical Research Letters*, 13, 636, 1986.
5. Foster, J. C., and Burke, W. J., SAPS: A new characterization for subauroral electric fields, *EOS AGU Transcripts*, 83, 393–394, 2002.
6. Foster, J. C. and Vo, H. B., Average characteristics and activity dependence of the subauroral polarization stream, *Journal of Geophysical Research*, 107, A12, 1475, doi:10.1029/2002JA009409, 2002.
7. Galperin, Y., Ponomarev, V. N., and Zosimova, A. G., Plasma convection in the polar ionosphere, *Annales Geophysicae*, 30, 1, 1974.
8. Heelis, R. A., Winningham, J. D., Suguira, M., and Maynard, N. C., Particle acceleration parallel and perpendicular to the magnetic field observed by DE-2, *Journal of Geophysical Research*, 89, 3893–3902, 1984.
9. Hirahara, M., Mukai, T., Sagawa, E., Kaya, N., and Hayakawa, H., Multiple energy-dispersed ion precipitations in the low-latitude auroral oval: Evidence of ExB drift effect and upward flowing ion contribution, *Journal of Geophysical Research*, 102, 2513, 1997 (February).
10. Hirahara, M., Mukai, T., Sagawa, E., Kaya, N., and Hayakawa, H., Characteristics of downward flowing in energy dispersions observed in the low-altitude central plasma sheet by Akebono and DMSP, *Journal of Geophysical Research*, 102, 4821, 1997 (March).
11. Ho, C. W., Horwitz, J. L., and Moore, T. E., Observations and simulations of centrifugally-accelerated polar O<sup>+</sup> outflows, in *Proceedings of International Conference on Substorms 2*, Fairbanks, U.S.A., March 7–11, edited by J. R. Kan, J. D. Craven and S.-I. Akasofu, pp. 577–581, Univ. of Alaska, Fairbanks, 1994.
12. Huang, C.-S., Foster, J. C., and Holt, J. M., Westward plasma drift in the midlatitude ionospheric F region in the midnight-dawn sector, *Journal of Geophysical Research*, 106, 30,349–30,362, 2001.
13. Huang, C.-S., Foster, J. C., and Kelley, M. C., Long-duration penetration of the interplanetary electric field to the low-latitude ionosphere during the main phase of magnetic storms, *Journal of Geophysical Research*, 110, A11309, doi:10.1029/1005JA011020, 2005.
14. Huang, C. Y., Burke, W. J., and Lin, C. S., Ion precipitation in the dawn sector during geomagnetic storms, *Journal of Geophysical Research*, 110, A11213, doi:1029/2005JA011116, 2005.
15. Kintner, P., Kelly, M. C., Sharp, R. D., Ghielmetti, A. G., Temerin, M., Cattell, C., Mizera, P. R., and Fennell, J. F., Simultaneous observations of energetic (keV) upstreaming ions and electrostatic hydrogen cyclotron waves, *Journal of Geophysical Research*, 84, 7201–7212, 1979.
16. Klumpp, K. M., A digest and comprehensive bibliography on transverse auroral ion acceleration, in *Ion Acceleration in the Magnetosphere and Ionosphere*, *Geophysical Monograph Series, Volume 39*, edited by T. Chang, p. 389, AGU, Washington, D.C., 1986.
17. Rees, M. H., *Physics and chemistry of the upper atmosphere*, Cambridge University Press, Cambridge, England, 1989
18. Schunk, R. W., Raitt, W. J., and Banks, P. M., Effect of electric fields on the daytime high-latitude E and F regions, *Journal of Geophysical Research*, 80, 321, 1975.
19. Spiro, R. W., Heelis, R. H., and Hanson, W. B., Rapid subauroral ion drifts observed by Atmospheric Explorer C, *Geophysical Research Letters*, 6, 657, 1979.
20. St.Maurice, J.-P., and Hanson, W. B., Ion frictional heating at high latitudes and its possible use for an in-situ determination of neutral thermospheric winds and temperatures, *Geophysical Research Letters*, 87, 7580, 1982.
21. Winningham, J. D., Burch, J. L., and Frahm, R. A., Bands of Ions and Angular V's: A Conjugate Manifestation of Ionospheric Ion Acceleration, *Journal of Geophysical Research*, 89, 1749, 1984.
22. Yau, A. W., Beckwith, P. H., Peterson, W. K., and Shelly, E. G., Distribution of upflowing ionospheric ions in the high-altitude polar cap and auroral ionosphere, *Journal of Geophysical Research*, 89, 5507–5522, 1984.
23. Yeh, H.-C., Foster, J. C., Rich, F. J., and Swider, W., Storm time electric field penetration observed at mid-latitude, *Journal of Geophysical Research*, 96, 5707–5721, 1991.

# The macroscale evolution of the substorm injection

E. Spanswick, E. Donovan, R. Friedel, and D. Danskin

**Abstract:** Particle injections occur during most, if not all, substorm expansive phases. Although it has yet to be worked out, there is clearly a relationship between the various macroscale expansive phase features which include not only the injection, but also the current disruption, fast flows, formation of the near-Earth neutral line, the dipolarization, auroral brightenings, Pi2s and PiBs, and more. In recent work, Spanswick et al. [13] have demonstrated that it is possible to identify a dispersionless injection using ground-based riometers, regardless of the fact that *in situ* identifications of these events are based on information from multiple particle flux energies. This work opens up the possibility, for the first time, of tracking the spatio-temporal evolution of the injection region (alternately the evolution of the injection boundary), at least as projected along magnetic field lines into the ionosphere. In this paper, we present initial results of a statistical survey of data from the CANOPUS (now NORSTAR) riometers. Based on these initial results, we argue that the dispersionless injection begins as a radially localized, azimuthally extended region that is, on average, beyond 8 Re in radial distance from the Earth. Once begun, the injection region as inferred from the riometer data expands both poleward (tailward) and equatorward (Earthward), although the equatorward expansion of the process appears to be limited to roughly 2° degrees latitude. Further, we carry out a superposed epoch analysis on a subset of our dispersionless injection events and fast flows as observed by Geotail when it is in the Central Plasma Sheet (CPS). Our results indicate that when a field line is engulfed by dispersionless injection (ie., by either moving across the injection boundary or as a consequence of the field line threading the initial injection region), instruments on a satellite on that field line in the CPS would detect fast flow starting at that same time. These initial results, though preliminary, point towards the expansive phase onset being on field lines that thread the inner CPS. Finally, we discuss the implications of this work for the upcoming NASA Time History of Events and Macroscale Interactions in Substorms MIDEX mission.

## 1. Introduction

The dramatic changes in the magnetospheric magnetic field, convection, and particle populations that occur during the substorm expansive phase give us significant clues about the macro- and micro-scale processes that are at work. These changes start with expansive phase onset, and include the dipolarization, formation of the substorm current wedge, injection, electron and proton auroral brightening, current disruption, fast flows, Pi2s and PiBs, and formation of the near-Earth neutral line. Although it is obvious that there interrelationships between these phenomena, attempts to elucidate a complete picture of these dynamics, including an understanding of cause and effect, have been frustrated by limitations in observation. It is widely held that sorting out these interrelationships would answer the long-standing question of what macroscale instability causes (or is) substorm expansive phase onset. Over the years, this has driven a multitude of event studies using extensive combinations of satellites and ground-based instrumentation. It is also the primary scientific objective of the upcoming NASA Time History of Events and Macroscale Interactions in Substorms (THEMIS) mission.

The desire to understand the macroscale substorm dynamics has been a motivation not only for event studies, but also for work aimed at developing observational tools for better characterizing the ionospheric and magnetospheric substorm

dynamics. Work that would fall under this category includes the development of methods to infer the open-closed field line boundary from auroral redline emissions and the magnetic field stretching in the inner Central Plasma Sheet (CPS) from *in situ* ion precipitation measurements [3, 11]. These two studies in particular led to techniques for tracking changes in the magnetosphere using ground-based instruments. Although information so obtained is always *compromised* in some way, at the very least because it is a projection of information along magnetic field lines into the ionosphere, it is tremendously valuable because it provides us with the possibility of tracking the substorm dynamics on a global scale. Recent work has shown that the injected electron population can be seen in riometers as an azimuthally drifting signature, and that the proton aurora is enhanced by injected protons [6, 4]. In recent work (see below), [13] have shown that riometers can be used to unambiguously identify dispersionless injections. This adds the injection to the growing list of magnetospheric processes that can be investigated using remote sensing of their ionospheric projection. In this paper, we discuss why riometers are an important tool for studying the injection, some specific new results, and how riometers will play an important role in the upcoming THEMIS mission.

Injections are dramatic increases in the fluxes of high energy electrons and protons in the CPS that occur during substorm expansive phase. These enhanced fluxes are a consequence of some combination of transport and energization. When the enhancements occur simultaneously (for practical purposes across several channels separated by at least tens of keV in less than two minutes) across a number energy channels, the injection is said to be *dispersionless* [2]. A dispersionless injection indicates that the satellite is in the region where the energization and/or transport is taking place. Significant dispersion indic-

Received 22 June 2006.

**E. Spanswick and E. Donovan.** Department of Physics and Astronomy, University of Calgary

**R. Friedel.** Los Alamos National Laboratory

**D. Danskin.** Natural Resources Canada Geomagnetic Laboratories

ates that the satellite is outside of that region (herein the “injection region”). The dispersion results from energy dependent primarily azimuthal drifts. Until recently, the injection has been exclusively studied by *in situ* observations, most often with the Synchronous Orbit Particle Analyzers (SOPA) on the Los Alamos National Laboratory (LANL) geosynchronous satellites.

Based on statistical studies using the SOPA data, it is now understood that dispersionless injections occur most often within a region centred about midnight but with ion injections displaced a half hour in local time to the west and electron injections displaced the same amount to the east [14]. [7] traced both ions and electrons observed in a dispersed injection with energies characteristic of relevant energy channels back to the point at which they would have been dispersionless to establish the azimuthal extent of the dispersionless injection on the drift paths that pass through the LANL satellites. Given that the LANL satellites are at geosynchronous orbit, the particle drift paths did not allow for exploration of the radial evolution of the injection region. For example, if the injection region formed outside of geosynchronous then the *Reeves et al.* analysis of the SOPA data provides a picture of the injection front as it passes through the geosynchronous region. [5] used Combined Release and Radiation Effects Satellite (CRRES) Medium Energy B (MEB) electron data to explore the distribution in radial distance of dispersionless injection (CRRES sampled a much broader range of L-shells than do the geosynchronous satellites). Their results indicated that the injection region forms at a range of L-shells, and in some events they managed to demonstrate an outer limit to the initial injection region. In another study, [10] used data from the LANL SOPA and CRRES MEB detectors, when the satellites were relatively close in space, to explore the radial motion and location of the injection region as it formed. Although their study was limited to the relatively few events where CRRES was near to a LANL satellite when both detected a dispersionless injection, they were able to infer that the injection region typically moves earthward inside of geosynchronous and forms within a few  $R_E$  of geosynchronous orbit. The picture that has evolved from this and other work is that the injection forms in the pre-midnight sector, and is often, if not always, initially radially localized.

In a recent study, [13] have demonstrated that it is possible to use riometer data to identify a dispersionless injection in the magnetically conjugate CPS. Their work was motivated by an earlier study by [1] who showed that riometer absorption is very correlated with the integrated high energy electron flux measured at a satellite magnetically conjugate to that riometer, provided the conditions in the magnetosphere support strong pitch angle scattering of the electrons in that energy range. [13] reasoned that if one could develop a criterion for identifying a dispersionless injection from the integrated electron flux as measured at the satellite, then subject to the pitch angle scattering criterion being met, we should be able to accomplish the same thing using riometer data. If this is possible, then networks of riometers could be used to track the spatio-temporal evolution of the injection region with even one second time resolution. Of course, the results would be subject to the normal constraints on mapping that apply to all ionospheric observations that serve as a proxy for magnetospheric processes and boundaries; however, the riometer data can be placed in

an appropriate context by comparing it directly with the other ionospheric data. For example, we could investigate the relationship between dipolarization, current disruption, and injection by using ground-based magnetometer, photometer, and riometer data.

Spanswick et al. [13] did find that there was a simple criterion that could apply to integrated MEB electron flux that *unambiguously* identified dispersionless injections as determined from the energy resolved data. Their criterion was that the electron flux rose to its peak value in less than 3 minutes, stayed elevated for at least 15 minutes, and was associated temporally with a substorm onset as identified by other observations. While every event identified with this criterion was a dispersionless injection, the criterion does not allow us to identify every such event. That is, this criterion misses some dispersionless injections that are clearly evident in the energy resolved data. [13] went on to find 15 events where CRRES was magnetically conjugate to the Canadian Auroral Network for the OPEN Unified Study (CANOPUS) network of single beam riometers. In each of these cases, the riometer data satisfied the criterion that was used to identify the dispersionless injection in the MEB integrated electron flux. As well, [13] went on to present the results of an extensive survey of the CANOPUS Gillam (ostensibly at or near geosynchronous) riometer data, and demonstrated that events that have this signature identified in the riometer data have essentially the same MLT distribution as do dispersionless electron injections identified by LANL SOPA. Given these results, [13] asserted that they are able to identify the dispersionless electron injection using the riometers, thus opening the door for more extensive studies of the spatio-temporal evolution of the injection region.

In this paper we present some additional results from the CANOPUS riometer data. In section 2, we explore the radial location of the initial injection region as projected along magnetic field lines in the ionosphere. In section 3, we use GEOTAIL INSTRUMENT data to study the relationship between the dispersionless electron injection and expansive phase fast flow in the CPS. Finally, in section 4 we summarize our results and point towards the future, with a particular eye on an upcoming and significant enhancement of the Canadian riometer network, and what that means for the upcoming THEMIS satellite mission.

## 2. The Radial Extent and Location of the Injection Region as it Forms

As discussed above, [5] showed that the injection at least sometimes forms on L-shells probed by CRRES with a clear tailward boundary. This result is consistent with an initial disturbance in the inner plasma sheet; however more work needs to be done. Even if the injection forms in the inner CPS region typically associated with current disruption, that does not mean it was not caused by something that happened further downtail. As well, the [5] study did not find this radial localization in all events, just a subset of those examined. Clearly, more work needs to be done to explore the radial extent of the initial injection region and its relationship to other substorm macroscale phenomena.

In this section, we use data from the CANOPUS “Churchill-line” riometers, which is aligned roughly along a geomagnetic

meridian, and spans latitudes ranging from  $L=4.3$  (Pinawa) up to well inside the typical polar cap. In particular, we use data from Pinawa ( $L=4.3$ ), Island Lake ( $L=5.5$ ), Gillam ( $L=6.7$ ), Fort Churchill ( $L=8.2$ ), Eskimo Point ( $L=10.2$ ), and Rankin Inlet ( $L=12.4$ ). Gillam would map to very near geosynchronous in the absence of magnetotail stretching, and Rankin Inlet would typically be inside the polar cap at expansive phase onset. These data provide an opportunity to explore the radial extent and location of the injection region as it forms.

## 2.1. Radial Extent

We surveyed 2 years of data from the Churchill line and manually identified all dispersionless injections according to the criteria of [13]. We are unable to find a single event in which a dispersionless injection was seen simultaneously at two riometers separated in latitude. There is always an unambiguous “start” of the injection at one station, flowed by an expansion on the timescale of 10’s of seconds which can engulf as many as 4-5 riometers along the Churchill line. The spacing between the stations combined with a  $\sim 60^\circ$  beam width gives a separation between the instruments of approximately 1-2 $R_E$  in the equatorial plane (obviously dependant on the magnetic configuration). This requires that the initial injection region form in a radially thin region such that the absorption would never be seen in two beams simultaneously. That puts an upper bound on the width of the injection region (when it forms) of about 1 Earth Radii.

## 2.2. Radial Location

From the same survey of the Churchill line we are able to compile statistics of the onset location (in latitude) and radial propagation characteristics. The majority of injection “onsets” along the Churchill line occur at Gillam ( $L=6.7$ ) while the bulk of the injections are seen at Churchill ( $L=8.2$ ). This is an artifact of propagation seen on the ground. We tend to see poleward motion of the injection region for most substorm injections, but equatorward motion is not guaranteed. For example, the vast majority of injection onsets observed at Gillam will also propagate poleward to Churchill. Those onsets that occur at Churchill will not necessarily propagate equatorward to Gillam. This preferential poleward motion for the ground-based mapping of the injection region skews the occurrence statistics, placing more injections at Churchill while the onset typically happens at Gillam. This implies that the radial location for the formation of the injection region is outside of geosynchronous, probably at distances of 8-10 Earth Radii down tail (again, depending on the magnetic configuration). This also implies that a fair number of injection will likely not reach geosynchronous orbit. They occur at higher latitudes and are not able to reach  $L=6.6$ .

## 3. The Relationship Between Fast Flows and Dispersionless Injections

Fast flows in the CPS are commonly observed during substorm expansive phase. They are related to the expansive phase change from stretched to dipolar, however the cause and effect issues have not been resolved. In other words, these flows can be either launched from a forming neutral line in the mid-tail or

represent material being drawn in by a collapsing current sheet in the inner CPS. This problem plagues our field, and will be a central issue in the upcoming THEMIS mission. Furthermore, the fast flow is crucial mode of transport between the current disruption and near Earth neutral line regions, and so sorting out the relationship between, for example, the fast flow and the dispersionless electron injection can be expected to be an important contribution to the overall resolution key substorm questions.

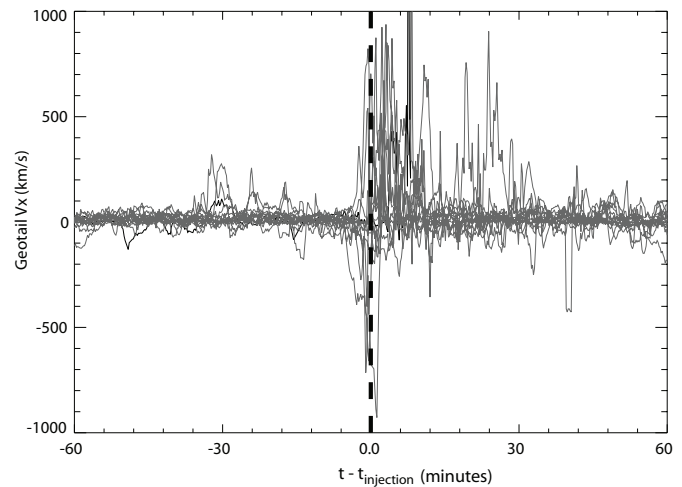


**Fig. 1.** Geotail flow ( $V_x$ ) for the 14 events used in this study.  $t_{injection}$  corresponds to onset of a dispersionless injection seen in the riometer closest to the footprint of Geotail.

In this section we use data from the CANOPUS riometer network and the Geotail Low Energy Particle experiment (LEP) to investigate the relationship between fast flows in the CPS and the dispersionless electron injection. There are 14 events in the CANOPUS riometer data set for which: (1) Geotail is in the near Earth plasma sheet, (2) Geotail maps to the Canadian sector, (3) there is a dispersionless injection as identified by the CANOPUS riometers, and (4) Geotail does not enter the lobe during the growth phase. These events offer the best chance of simultaneously observing plasma sheet flows and the onset of the injection.

For all events, there was an associated plasma sheet flow and the time delay between the flow seen at Geotail and the injection was smallest for the riometer located the closest to the approximate footprint of the Geotail satellite. The injection could be seen prior to the flow, but this always corresponds to a riometer not in the meridian of Geotail. In those cases, as the injection region expanded to the riometer closest to the footprint, the flow would be seen at Geotail.

Figure 1 shows the timing between injection onset and earthward flow seen at Geotail. Again, this is for the riometer closest to the approximate footprint of the Geotail satellite. The onset of the flow is within 1-2 minutes of the onset of injection seen in the riometers. The majority of the flow is earthward (positive) and occurs after the onset of injection. Within our set of events there are also 4 events over the Churchill line, where we have radial coverage with the riometers. For those events the onset of flow was still observed at the same time of injection

onset and there was no evidence of activity in the riometers poleward of the onset station.

#### 4. Discussion

We have used data from the CANOPUS riometer network to study the radial extent and location of the dispersionless electron injection. We found that with the resolution of riometers in the Churchill line (which maps to approximately 1-2 $R_E$  resolution in the equatorial plane) we cannot simultaneously observe an injection in two stations separated in latitude. This puts an upper bound on the radial extent of the injection region as it forms. We also found that the injection region forms typically at latitudes of 67° invariant (Gillam), and then expands with a ground-based projection that is preferentially poleward.

In addition, we have used CANOPUS riometer and Geotail LEP data to study the relationship between the dispersionless electron injection and fast flows in the CPS during the expansive phase. We found 14 events for which Geotail maps to the Canadian sector, was the CPS, and a substorm associated dispersionless injection was observed in the CANOPUS riometers. For all of these events we found that the timing between earthward flow observed at Geotail and the injection seen on the ground was smallest ( $\pm 1-2$  minutes) for the riometer closest to the footpoint of Geotail. An injection can occur prior to the onset of high speed flow at Geotail, but as the injection region expanded to the riometer near the footpoint, earthward flow was observed. There are also 4 events for which the location of Geotail maps to the Churchill line. For those events there is no evidence of activity in the riometers poleward of the injection onset location prior to onset.

We summarize our results as follows. The dispersionless electron injection always forms as a radially localized region, strengthening the earlier results of [10]. The injection region typically forms on field lines that map to outside of geosynchronous, and that are most likely in the transition region between dipolar and tail-like fields in the CPS (ie., 8-10  $R_E$ ). The injection expands both tailward and Earthward. The Earthward expansion usually but does not always reach stations that are ostensibly at or near being magnetically conjugate to the geosynchronous region. Whenever Geotail was in the CPS during the expansive phase, and its instruments first detected a fast flow, the riometer that is closest to being magnetically conjugate to the satellite detected the signature of a dispersionless injection. Moreover, the riometer and geotail results indicate that at least in our subset of 14 events, we saw no evidence of flow preceding observations of dispersionless injection. Given the radial location of the initial injection region, and the flow results, we assert that the fast flows are initiated by the same process that initiates dispersionless injection, and that they begin in the same region.

The upcoming THEMIS satellite mission will involve 5 satellites on equatorial orbits with periods of integer numbers of sidereal days (3, 1, and 1 satellites with 1, 2, and 4 sidereal day orbits, respectively). These satellites will be relatively phased on those orbits so that all 5 come together in apogee conjunctions every 4 days. As well, the conjunction meridian will be locked over central Canada throughout the mission. Of particular relevance to this study, and future work that will follow

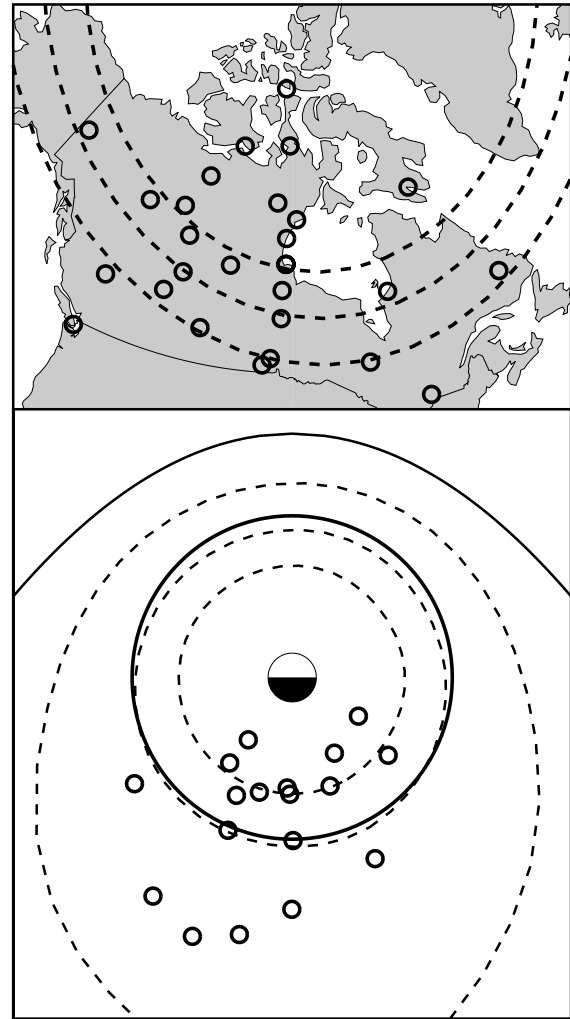


**Fig. 2.** The map at top shows the locations of the 13 existing NORSTAR riometers, as well as the riometers that Natural Resources Canada (NRCan) is planning to deploy in the summer of 2006. The three dashed contours on the map indicate 61°, 64° and 69° invariant magnetic latitude. The bottom plot shows the locations of the NORSTAR and planned NRCan riometers, as mapped to the equatorial plane using the T87 magnetic field model. The solid circle centered on the Earth indicates geosynchronous orbit.

from it, are the three THEMIS satellites that have one day orbits (and hence a mini conjunction every day), and that have apogees in the transition region between dipolar and tail like within which we think the injection starts. These satellites will provide observations of flows, dipolarizations, and injections in the region conjugate to the Canadian riometer network. This network will continue to operate during the THEMIS project as part of the Canadian GeoSpace Monitoring program (see <http://cgsm.ca>). In fact CGSM will boast a significantly enhanced riometer network during the THEMIS era (see Figure 2), operated by two separate CGSM program elements. NORSTAR (see <http://cgsm.ca/norstar>) will continue operation of the former CANOPUS riometers, and the Canadian Geological Survey will be deploying identical riometers at its

13 CANadian Magnetic Observatory System (CANMOS) sites and the four SuperDARN sites that are in Canada.

In summary, the work presented here provides important insights into the nature of the dispersionless electron injection, and the substorm expansive phase. Furthermore, it lays the foundation for an exciting future in our ability to track the substorm dispersionless electron injection. During the THEMIS era, our community will have at its fingertips data from three satellites in the region where the dispersionless injection typically forms. Furthermore, for all of those events, those satellites will be magnetically conjugate to a region within which 30 riometers will be operating. We will thus be able to follow the spatio-temporal evolution of the dispersionless injection from its very beginnings, with contemporaneous *in situ* observations of the dipolarization, fast flows, and the injection itself.

## Acknowledgements

Operational support for the CANOPUS (now NORSTAR) riometers has and continues to be provided by the Canadian Space Agency. Don Wallis was principally responsible for the scientific management of the riometer network during the CANOPUS era, and has provided the authors with valuable input during many discussions. Field support for the riometers has been provided by SED systems (Saskatoon). GEOTAIL LEP plasma data were provided by T. Mukai through DARTS at the Institute of Space and Astronautical Science (ISAS) in Japan. We also acknowledge Axel Korth, who is the PI of the CRRES MEB instrument.

## References

1. Baker, D., P. Stauning, E. Higbie, and R. Belian, Near equatorial high-resolution measurements of electron precipitation at  $L \sim 6.6$ , *J. Geophys. Res.*, *86*, 2295, 1981.
2. Birn, J., M.F. Thomsen, J.E. Borovsky, G.D. Reeves, D.J. McComas, and R.D. Belian, Characteristic plasma properties during dispersionless substorm injections at geosynchronous orbit, *J. Geophys. Res.*, *102*, 2309, 1997.
3. Blanchard, G., L. Lyons, J. Samson, and F. Rich, Locating the polar cap boundary from observations of 6300 Å auroral emission, *J. Geophys. Res.*, *100*, 7855, 1995.
4. Chi, E., S. Mende, M.-C. Fok, and G. Reeves, Proton auroral intensifications and injections at synchronous altitude, *Geophys. Res. Lett.*, *33*, doi:10.1029/2005GL024656, 2006.
5. Friedel, R., A. Korth, and G. Kremser, Substorm onsets observed by CRRES: Determination of energetic particle source regions, *J. Geophys. Res.*, *101*, 13137, 1996.
6. Kavanagh, A., F. Honary, I. W. McCrea, E. Donovan, E. Woodfield, J. Manninen, and P. Anderson, Substorm related changes in precipitation in the dayside auroral zone a multi instrument case study, *Annales Geophysicae*, *20*, 1321, 2002.
7. Reeves, G., T. Fritz, T. Clayton, and D. Belian, Multi-satellite measurements of the substorm injection region, *Geophys. Res. Lett.*, *11*, 2015, 1990.
8. Reeves, G., D. Belian, and T. Fritz, Numerical tracing of energetic particle drifts in a model magnetosphere, *J. Geophys. Res.*, *106*, 13997, 1991.
9. Reeves, G., G. Kettmann, T. A. Fritz, R. D. Belian, Further investigation of the CDAW 7 Substorm Using Geosynchronous Particle Data: Multiple Injections and Their Implications, *J. Geophys. Res.*, *107*, 6147, 1992.
10. Reeves, G., M. G. Henderson, P.S. McLachlan, R.D. Belian, R. Friedel, and A. Korth, Radial propagation of substorm injections, in *International Conference on Substorms - 3, ESA SP-339*, 576, 1996.
11. Sergeev, V., and B. Gvozdevsky, MT-index - a possible new index to characterize the magnetic configuration of the magnetotail, *Annales. Geophys.*, *13*, 1093, 1995.
12. Shiokawa, K., W. Baumjohann, G. Harendel, G. Paschmann, J. F. Fennel, E. Friis-Christensen, H. Luhr, G. D. Reeves, C. T. Russell, P. R. Sutcliffe, and K. Takahashi, High-speed ion flow, substorm current wedge, and multiple Pi 2 pulsations, *J. Geophys. Res.*, *103*, 4491, 1998.
13. Spanswick, E., E. Donovan, R. Friedel, and A. Korth, Ground-based identification of dispersionless electron injections, submitted to *Geophys. Res. Lett.*, 2006.
14. Thomsen, M.F., J. Birn, J.E. Borovsky, K. Morzinski, D.J. McComas, and G.D. Reeves, Two-satellite observations of substorm injection at geosynchronous orbit, *J. Geophys. Res.*, *106*, 8405, 2001.



# Automatic classification of auroral images in substorm studies

M. T. Syrjäsuo, E. F. Donovan, X. Qin, and Y.-H. Yang

**Abstract:** Millions of auroral images are captured every year by ground-based imagers. Even though the auroral appearance or “type” yields relevant information about the physical processes in the ionosphere and the magnetosphere, qualitative descriptions of auroras are typically used. Modern methods including those widely used in computer vision research can, however, make it possible to use objective and quantitative measures in analysing auroral appearance. We are currently developing techniques for automated auroral image analysis. In order to numerically compare auroral objects, we can either describe individual auroral shapes — such as arcs — or use statistical appearance models (texture). We demonstrate how one can use Fourier Descriptors to compare shapes extracted from auroral images. Also, using a recently developed texture analysis technique, we show how texture measurements can be used in classifying auroral type in a timeseries.

*Key words:* Aurora, pattern recognition, computer vision.

## 1. Introduction

Imaging the aurora by using ground-based optical instruments has long traditions in substorm research. The spectral, temporal and spatial resolution have been increasing, and now we are facing a problem of data: large imaging networks such as MIRACLE [10] and NORSTAR [3] produce millions of all-sky images annually. The situation will become worse with the launch of Time History of Events and Macroscale Interactions during Substorms (THEMIS) programme, which will produce over 100 million images every year.

The traditional data analysis in substorm studies uses actual measurements of physical properties (e.g. solar wind speed, electron density). Also, derived quantities are commonly used in order to understand the plasma processes in the magnetosphere and the ionosphere. Regardless of this quantitative information, the auroral image data are studied by using qualitative descriptors such as “bright auroral arcs” or “patchy aurora”. Undoubtedly the “type” of the aurora yields relevant information about the physics. More importantly, a self-consistent global model should be able to predict this auroral type: otherwise our understanding, upon which the model is based, is not accurate.

Computer vision is a branch of computer science in which techniques for automated image analysis and processing are studied and developed. Automating the analysis makes it possible to browse through vast image sets, extract information and learn and recognise patterns. In [11], we used automated processing to obtain diurnal auroral occurrence statistics. While the actual results were not new, the analysis was: the statistics were based on 350,000 auroral images, from which an automated routine extracted information about whether an image contained aurora and if so what was its type. The type of au-

roras was learned from 258 manually labelled example images, after which the computer could provide a classification to all remaining images.

While we chose to use a three distinct auroral types (arcs, patchy aurora and Omega-bands) in [11], there is, of course, more variation in auroral types. In fact, the automatic classifier could only provide a clear category for 12% of the images that contained auroras. Also, the detection of Omega-bands was quite inaccurate, possibly because contrary to arcs and patchy auroras, we had a small number of examples for training the classifier.

There clearly is a need for more accurate mathematical treatment of auroral image contents. We can use example images for training a classifier to recognise certain types of auroras, but obviously learning the type categories from actual data would provide more objective type definitions. In the rest of this paper, we concentrate on describing the shape of an auroral object by using mathematical methods and demonstrate the use of texture measures for classification of auroral images.

## 2. Shape analysis

Extracting shapes is one of the most intensively studied problems in computer vision. Of course, there is no algorithm that works well for all applications. For our purposes, we have used a modified version of the isolabel-contour map algorithm from medical imaging [9]. The algorithm consists of four steps: 1) extract contours; 2) detect strongest edges; 3) score individual contours based on their overlap on edges; 4) choose non-overlapping contours with the highest scores. An example of detected auroral shapes can be seen in Fig. 1 and selection of extracted shapes is shown in Fig. 2. Details and practical applications of this algorithm can be found in [12, 13].

Once an auroral object is outlined, we can form a mathematical expression for the shape. Let  $x_i$  and  $y_i$  be the pixel coordinates  $i = 1, \dots, N$  on the outline. Now, we can define a centroid shape signature

$$r_i = \sqrt{(x_i - x_c)^2 + (y_i - y_c)^2}, \quad (1)$$

Received 11 May 2006.

**M. T. Syrjäsuo and E. F. Donovan.** Institute for Space Research, University of Calgary, Alberta, Canada.

**X. Qin and Y.-H. Yang.** Department of Computing Science, University of Alberta, Alberta, Canada.

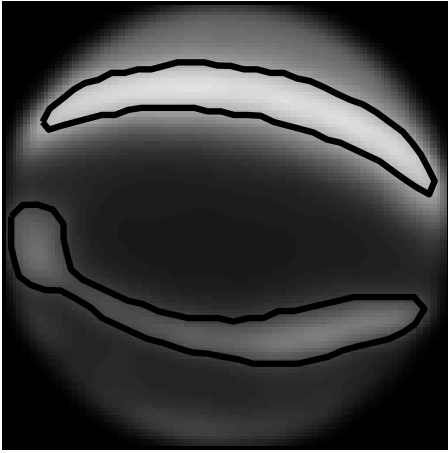


**Fig. 1.** Two salient auroral objects detected and outlined by the shape extraction algorithm.

where  $(x_c, y_c)$  is the centroid of the shape. The Fourier coefficients of the signature are then

$$a(k) = \sum_{i=0}^{N-1} r_i e^{-j2\pi(k-1)(i-1)/N}, \quad k = 0 \dots N-1, \quad (2)$$

where  $j$  is the imaginary unit. The use of centroid provides a translation invariant representation. We can represent the shape by first defining the Fourier Descriptors (FD) of the shape

$$\text{FD}(k) = \left| \frac{a(k)}{a(0)} \right|, \quad k = 0 \dots N-1, \quad (3)$$

and then using a subset of these FDs to provide a more compact approximation of the shape:

$$\mathbf{f} = [\text{FD}(2) \text{FD}(3) \dots \text{FD}(M+1)], \quad (4)$$

where  $M = 16$  has experimentally been found to provide a good approximation of the shape for comparison purposes.

Given two auroral shapes and their FD-representation, we can measure their similarity by using the Euclidian distance:

$$d_{\text{FD}}(\mathbf{f}_1, \mathbf{f}_2) = \|\mathbf{f}_1 - \mathbf{f}_2\|_2, \quad (5)$$

where  $\mathbf{f}_1$  and  $\mathbf{f}_2$  correspond to the two different shapes being compared and  $\|\cdot\|_2$  denotes an  $L_2$ -norm. We further assert that small distances correspond to more similar shapes. Similarity, of course, is a complex human concept, but for practical purposes, this definition works surprisingly well. A selection of shapes was organised by their mathematical representation in Fig. 3 illustrating how well this approach captures the apparent similarity.

We have implemented a content-based image retrieval system based on the Fourier Descriptors. The system lets the user choose an initial search shape, after which images which contain similar shapes are returned. The system currently contains 20,000 extracted shapes and can be experimented with at <http://aurora.phys.ucalgary.ca/cbir/>.

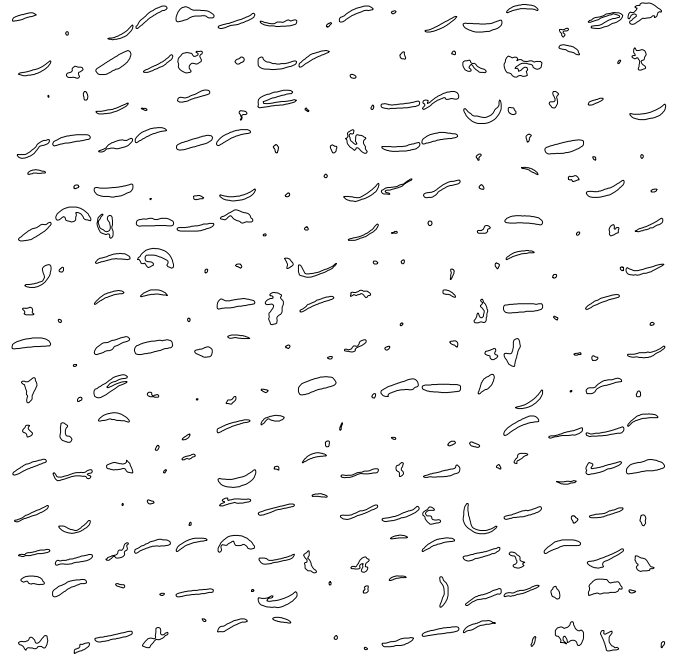


**Fig. 2.** A selection of extracted auroral shapes [13]. While the arcs are most obvious shapes, there are many other irregular shapes in different orientations and sizes.

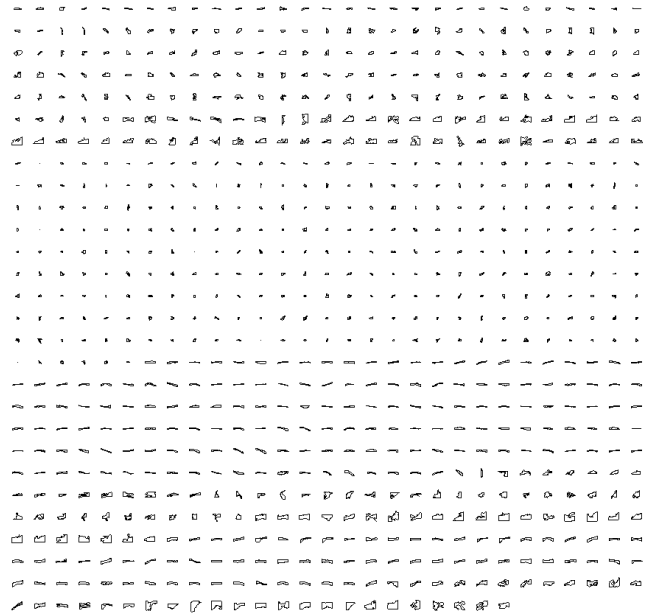


**Fig. 3.** Extracted shapes sorted by using their numerical representation.

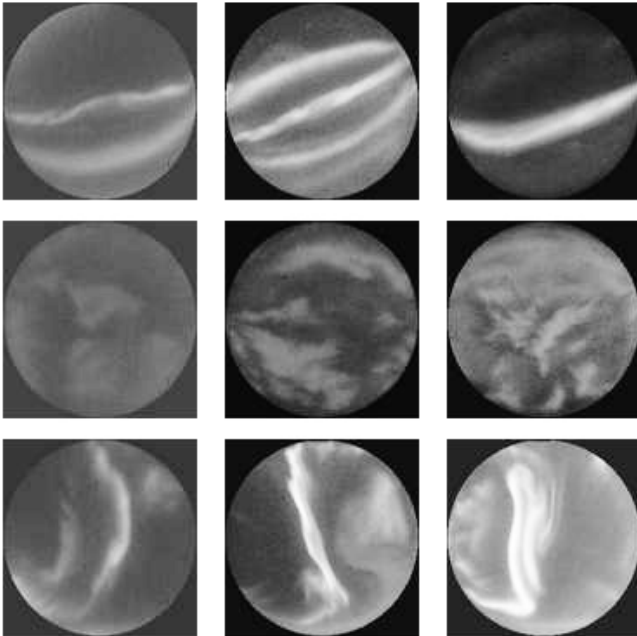


**Fig. 4.** Top row to bottom row: auroral arcs, patchy auroras and north-south structures. These all-sky images show north at the top and east on the right; the circular field-of-view captures the whole sky.

### 3. Aurora content as a texture

#### 3.1. Gray level aura matrices

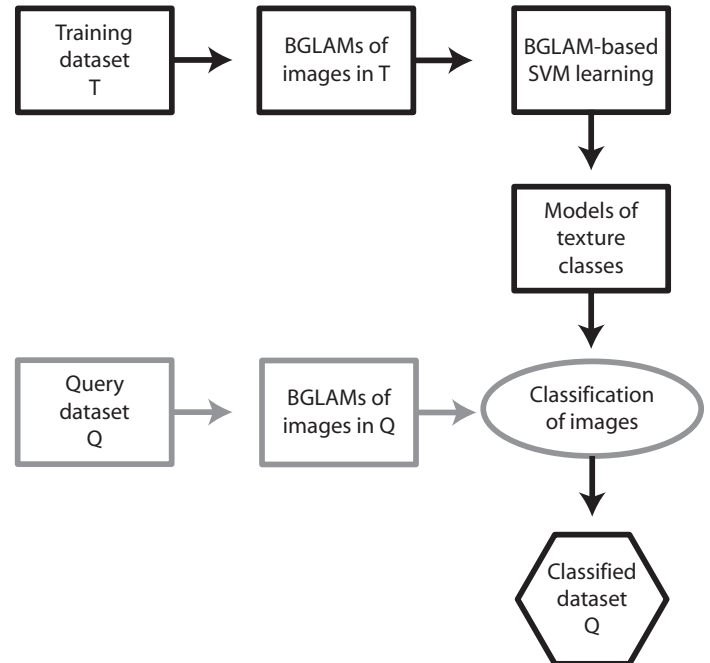
Texture can be defined as a characteristic property of any object or image. In the case of aurora, the patterns that appear in images share perceived similarities even if the individual shapes are not the same. Some of the commonly used terminology relies on texture: for example, patchy aurora usually refers to irregular auroral “blobs” whose characteristic sizes and blob distributions create a patchy appearance.

Fig. 4 shows three auroral categories — arcs, patchy aurora and north-south aligned auroral features. While the elements of arcs and north-south structures are similar, their orientation is different. Also their pattern is significantly different from patchy auroras.

There are mathematical methods which can be used to extract information about the texture. As with shapes, a texture distance measure can be utilised to classify auroras based on their general appearance in the images. One of these methods is based on gray level aurora matrices (GLAM).

As a generalisation of gray level co-occurrence matrix [2, 15], gray level aura matrix [4] has been used as a powerful tool for texture analysis, synthesis, segmentation and classification [5, 6, 7]. Among all the GLAMs, basic GLAMs (BGLAMs) are particularly important. In fact, BGLAMs are a basis of GLAMs and two images are the same if and only if their corresponding BGLAMs are the same — for the proof, see [8]. In other words, an image can be uniquely represented by and then faithfully reconstructed from its BGLAMs.

Based on the above BGLAM theory, we can use a BGLAM-based distance function for quantitatively measuring the simil-



**Fig. 5.** An overview of the BGLAM-based algorithm for texture classification.

arity between texture images. The new distance function satisfies the important properties of non-negativity, symmetry, and triangle inequality, and thus is metric. Furthermore, one unique property of the BGLAM-based distance function is that it is one-to-one. Namely, a zero value of the distance measure will guarantee that the two images are identical. Since the distance function is continuous, the one-to-one property implies that if the distance of image Y from image X gradually changes (i.e. converges) to zero, image Y will gradually get close (i.e. converge) to X. For texture images, this one-to-one property guarantees that the smaller the distance value, the more similar the two texture images are. A distance measure without the one-to-one property cannot guarantee this.

#### 3.2. Auroral textures

Texture classification can be done using a BGLAM-based approach (Fig. 5). Given an unseen texture image, the approach classifies it into one of the pre-learned classes. There are two states in the algorithm: a learning stage and a classification stage. In the first stage, models of texture classes are learned from the BGLAMs of training examples using the Support Vector Machine [14], and in the second stage, a given texture image is classified into one of the pre-learned classes, to which the image has the largest signed distance.

We used a small number of sample all-sky images with varying contents: 401 arcs, 355 patchy auroras, 52 north-south structures, 76 Omega-bands and 113 cloudy skies. These images were used in training a classifier to recognise the image contents. The accuracy of the classifier in the training set was very good (over 90% correct classification).

The classifier was then used in determining the class for all auroral images acquired during one night. In order to compare the classifications of these previously unseen images, we also

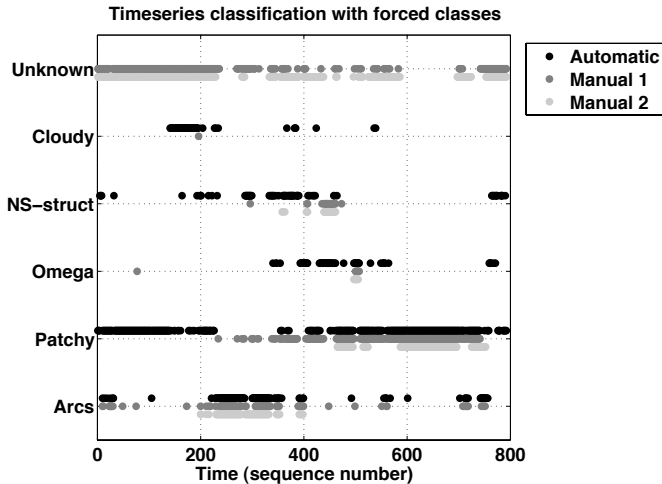


**Fig. 6.** One night of images as classified by the automatic method. For comparison, two manual classifications performed by two auroral image experts are provided. The auroral images were classified into “Cloudy”, “North-south structures”, “Omega-bands”, “Patchy auroras” and “Arcs”. The automatic classifier had no option to choose the “Unknown” auroral class.

provided manual classification for each image. The manual classification was performed by two auroral experts (Syrjäsuo and Donovan) who examined each of the images in random order to guarantee an independent auroral type for each image. Because the complexity of the image contents, the experts utilised a special category (“unknown”) for images whose contents could not be classified unambiguously.

We performed two automatic classification runs. In the first run, the classifier was forced to choose one auroral category, whereas the second run included an “unknown” category also in the automated classification.

The first run results are shown in Fig. 6. The overall agreements with the two experts were 42% (“Manual 1”) and 34% (“Manual 2”). Not surprisingly, when including the unknown class in the automated classification, the results (Fig. 7) are noticeably better with 53% and 50% agreement.

While there are differences between the classifier’s and experts’ classes, there are two important observations: (1) the experts agreed on the class in about 70% of the images and (2) the experts chose the unknown class in almost 50% of all images. With those images that the experts did not classify as unknown, the automatic method is much more accurate with 72% and 81% correct classification.

#### 4. Discussion

In this paper, we have presented some recent results from our efforts to develop automatic classification algorithms for auroral images. The essence of our approach is a common feature of all computer vision techniques: we use a training set and algorithms that map unclassified images into a hyperspace. The automatic algorithms classify images as similar if they are close together. The effectiveness of the algorithm is assessed by whether or not images that are close together in that space

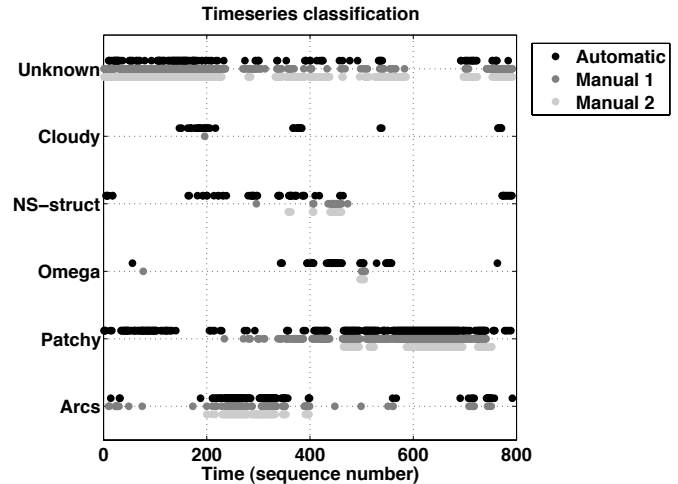


**Fig. 7.** The same time-series of auroral images as in Fig. 6. This time, however, the automatic classifier could use the “Unknown” auroral class.

are actually similar in a meaningful way. This is not as subjective as it sounds: the idea is that a truly successful auroral image classification technique would group images of aurora caused by some common underlying physical process close together in the appropriate space. So, ideally, inverted-V arcs would be near other inverted-V arcs, polar cap patches near other polar cap patches, etc.

In particular, we have very strong motivations for carrying out this work. On the practical side, we are creating hundreds of millions of auroral images and are in the very beginnings of developing an auroral virtual observatory. We want to be able to attach content descriptors to every image in our data set, likely including that information in the overarching data base and meta data structures. This would greatly facilitate studies of auroral physics with these large cumbersome data sets. That being said, however, we have a much more important motivation, namely to use these classification algorithms to help us better understand the physics of the aurora and geospace dynamics.

For example, in this paper we have presented what is to our knowledge the first creation of time series of such classifications. This was done using texture analysis, applied to one night of data. If one examines Figs. 6 and 7, we see that there is an evolution through the night as the aurora evolves from patchy, to arcs, then NS-structures and Omega-bands, and then to patchy again. Qualitatively this evolution is well known in the literature as a common diurnal variation, as evidenced as far back as in Akasofu’s early work (see eg., Fig. 1 of [11] which is a modified version of an earlier figure from [1]). What is new here is capturing this variation over the course of a typical night quantitatively. Further, we can see hints that the automatic algorithm is responding to transition between types in some meaningful way. In particular, the experts classified only a few images as Omega bands around image number 500. The automatic method classified images leading to that time also as Omega bands. Our idea is that the classifier is seeing some Omega-like features in the preceding images and responding to those.

The hope is that we will be able to create time series of quantitative and — more importantly — physically meaningful classifications of auroral images. In reality, the transition from arc, to NS-structures and Omega-bands, and ultimately patchy aurora is a repeatable consequence of the typical substorm looked at through one all-sky imager. This transition, then, reflects physics that we as a community are struggling to understand. These time series of auroral classification should prove to be an excellent tool when used in an assimilative way with global geospace models. For example, the above mentioned evolution reflects both the magnetospheric evolution in the substorm and the changing magnetosphere-ionosphere coupling. These changes in the system, if properly understood, should allow us to predict the changes in the aurora. These quantitative time series of image classification will be an essential ingredient in testing the output of global models.

## References

1. Akasofu, S.-I., The auroral oval, the auroral substorm, and their relations with the internal structure of the magnetosphere, —em Planet. Space Sci., *14*, 587?-595, 1966.
2. Davis, L. S., Johns, S. A. and Aggarwal, J.K., Texture analysis using generalized cooccurrence matrices, *IEEE Transactions on Pattern Analysis and Machine Intelligence*, *1*(3), 251–259, 1979.
3. Donovan, E. F., Trondsen, T. S., Cogger, L. L. and Jackel, B. J., Auroral imaging in Canadian CANOPUS and NORSTAR programs, *Proc. of Atmospheric Studies by Optical Methods*, 109–112, 2003.
4. Elfadel, I. M. and Picard, R. W., Gibbs random fields, cooccurrences, and texture modeling, *IEEE Transactions on Pattern Analysis and Machine Intelligence*, *16*(1), 24–37, 1994.
5. , Elfadel, I. M. and Picard, R. W., Miscibility matrices explain the behavior of grayscale textures generated by Gibbs random fields, *SPIE Conference on Intelligent Robots and Computer Vision IX*, 524–535, 1990
6. Picard, R. W. and Elfadel, I. M., Structure of aura and co-occurrence matrices for the Gibbs texture model, *Journal of Mathematical Imaging & Vision*, *2*, 5–25, 1992.
7. Qin, X. and Yang, Y.-H., Similarity measure and learning with gray level aura matrices (GLAM) for texture image retrieval, *Proc. IEEE Conf. Computer Vision and Pattern Recognition, CVPR-04*, 326-333, 2004.
8. Qin, X. and Yang, Y.-H., Basic gray level aura matrices: theory and its application to texture synthesis, *IEEE Int. Conf. Computer Vision*, 128–135, 2005.
9. Shiffman, S., Rubin, G. D. and Napel, S., Medical image segmentation using analysis of isolabel-contour maps, *IEEE Transactions on Medical Imaging*, *19*(11), 1064–1074, 2000.
10. Syrjäsuo, M. T., Pulkkinen, T. I., Janhunen, P., Viljanen, A., Pellinen, R. J., Kauristie, K., Opgenoorth, H. J., Wallman, S., Eglitis, P., Karlsson, P., Amm, O., Nielsen, E. and Thomas, C., Observations of substorm electrodynamics by using the MIRACLE network, *Proc. the Fourth Int. Conf. Substorms, ICS-4*, 111–114, 1998
11. Syrjäsuo, M. T. and Donovan, E. F., Diurnal auroral occurrence statistics obtained via machine vision, *Annales Geophysicae*, *22*(4), 1103–1113, 2004.
12. Syrjäsuo, M. T. and Donovan, E. F., Content-based retrieval of auroral images — thousands of irregular shapes, *Proc. IAS-TED Int. Conf. Visualization, Imaging, and Image Processing, VIIP 2004*, 224–228, 2004.
13. Syrjäsuo, M. T. and Donovan, E. F., Using relevance feedback in retrieving auroral images, *Proc. IASTED Computational Intelligence, CI 2005*, 420– 425, 2005.
14. Vapnik, V. N., Statistical learning theory, John Wiley & Sons, New York, 1998.
15. Zucker, S. W., Finding structure in co-occurrence matrices for texture analysis, *Proc. Computer Vision and Graphic Image Processing*, *12*, 286–308, 1980



# Impossibility of calculating magnetic field change from current disruption

V. M. Vasyliūnas

**Abstract:** The picture of the substorm current wedge, formed by visualizing the cross-tail current as reduced or disrupted and thus diverted through the ionosphere, provides a compact summary of the magnetic field changes observed during substorms. There has long been a tendency, however, to view current disruption as an actual explanation, not just a convenient representation, of the magnetic field changes — to search for some model by which first to predict the current disruption and then, as a consequence, to calculate the magnetic field dipolarization from the Biot-Savart integral over the reduced current. Formally, the time derivative of the magnetic field can be expressed as the Biot-Savart integral over the time derivative of the current density, which in turn can be calculated in principle by summing all the forces (weighted by charge/mass) on all the charged particles. In the resulting expression, the integrand includes an electric field term which can be transformed (by means of an integration by parts) into curl  $\mathbf{E}$ . Thus, the time derivative of  $\mathbf{B}$  cannot be calculated directly from the Biot-Savart integral because one term in the integrand contains the time derivative itself, and the contribution of that term is very large when the electron inertial length is small in comparison to the spatial scale of the system; instead, the time derivative of  $\mathbf{B}$  must be calculated by solving what is now an integral equation. In the limit of small electron inertial length, the solution reduces to the curl of all the terms other than  $\mathbf{E}$ ; this is identical to the method described by Vasyliūnas [9, 10] for obtaining the time evolution of  $\mathbf{B}$  — determined directly by plasma dynamics through the generalized Ohm's law and not by the changing current (which cannot be calculated except as the time derivative of curl  $\mathbf{B}$ ).

*Key words:* current disruption, dipolarization, magnetic field change, substorm expansion.

## 1. Introduction

The notion that magnetic fields and their changes are to be understood by reference to electric currents is deeply ingrained in the thinking of many researchers on the magnetosphere. In particular, the striking phenomenon known as dipolarization of the magnetic field in the nightside magnetosphere, observed in association with the substorm expansion, is widely interpreted as the formation and evolution of an (inferred) substorm current wedge (e.g. [5]): the cross-tail current is reduced over a limited local time sector by having part of the current flow down along magnetic field lines to the ionosphere, westward across the ionosphere, and back up along the field lines. The process is often referred to as an example of “current disruption,” and much of the modeling under that label would seem to be aimed at predicting the formation and subsequent evolution of the current wedge, from which the dipolarization of the magnetic field could then be deduced.

A basic presumption of such an approach is that Ampère's law

$$\mathbf{J} = \frac{c}{4\pi} \nabla \times \mathbf{B} \quad (1)$$

(I use Gaussian units throughout) determines the magnetic field  $\mathbf{B}$  given the current density  $\mathbf{J}$ , with the further implicit understanding that this holds for time variations as well: to determine the time evolution of  $\mathbf{B}$ , one seeks first to specify the time evolution of  $\mathbf{J}$ . The contrary view, that Ampère's law determines  $\mathbf{J}$  given  $\nabla \times \mathbf{B}$ , has long been a familiar concept

within magnetohydrodynamics [1, 2, 6, 8], where the time evolution of  $\mathbf{B}$  is taken as determined by Faraday's law

$$\frac{\partial \mathbf{B}}{\partial t} = -c \nabla \times \mathbf{E} \quad (2)$$

with  $\mathbf{E}$  given, in the simplest case, by the MHD (frozen-flux) approximation in terms of the plasma bulk flow. The undeniable importance of non-MHD effects in some aspects of the substorm process, however, has been invoked as an argument for ignoring any MHD constraints.

In two recent papers [9, 10], I have examined the time evolution and interrelationships of  $\mathbf{E}$ ,  $\mathbf{J}$ , and  $\mathbf{B}$  on the basis of the exact fundamental equations and have shown that, provided  $\mathbf{E}$  is calculated from the full generalized Ohm's law rather than just the MHD approximation, the time evolution of  $\mathbf{B}$  is determined by Faraday's law (2), not by the time derivative of Ampère's law (1) (which serves instead to determine the time evolution of  $\mathbf{J}$  from that of  $\mathbf{B}$ ), and that this (nominally large-scale) approach remains valid on space and time scales down to those of electron plasma oscillations, thus extending well beyond the range of MHD (generally considered no longer applicable once scales as small as ion gyroperiod or ion inertial length are approached); it is limited ultimately by the breakdown of charge quasineutrality, not of the frozen-flux approximation. Concerning current disruption, I summarized the conclusion of [9] as follows: “The results in the present paper imply that any such theoretical model of dipolarization, in terms of the current as the primary quantity, is not possible: *on time scales appropriate to substorm expansion, there is no equation from which the time evolution of the current could be calculated, prior to and independently of  $\nabla \times \mathbf{B}$ .* ... These limitations apply to any attempts at accounting for changing magnetic fields by invoking changing currents — current disruption, diversion, wedge

Received 24 May 2006.

V. M. Vasyliūnas. Max-Planck-Institut für Sonnensystemforschung, Katlenburg-Lindau, Germany

formation, etc. Over the wide range of time scales from electron plasma period to Alfvén wave travel time, there simply is no way to calculate the changing currents except by taking the curl of the changing magnetic fields; statements about changes of current are not explanations but merely descriptions of changes in the magnetic field.”

## 2. Evolution of electric current

Note that the above conclusion is a very specific one: within the stated range of length and time scales, there is no usable equation from which one could calculate the time evolution of the current independently, i.e., other than from  $(\partial/\partial t)\nabla \times \mathbf{B}$ . It is thus absolutely pointless, for anyone who wants to question the conclusion, to talk about approaches or paradigms and to invoke general arguments such as those in the controversy [6, 7, 8, 3, 4] on whether the magnetic field and the plasma flow or the electric current and the electric field are to be treated as the primary variables; rather, the only effective counterargument is to write down what one claims to be the usable independent equation for  $\partial\mathbf{J}/\partial t$ .

An independent equation for  $\partial\mathbf{J}/\partial t$  always exists, of course, in principle: with the current density obtained by summing the motions of all the charged particles, its time rate of change can be determined by summing the accelerations of all the charged particles. In terms of velocity distribution functions,  $\mathbf{J}$  is defined by

$$\mathbf{J} = \sum_a q_a \int d^3v \mathbf{v} f_a(\mathbf{v}) \quad (3)$$

where  $f_a(\mathbf{v})$  is the velocity distribution function of charged particles of species  $a$ . The equation for time evolution of  $\mathbf{J}$  can then be calculated from the appropriate sum of velocity-moment equations (see, e.g., [9] and references therein)

$$\frac{\partial\mathbf{J}}{\partial t} = \sum_a \left\{ \frac{q_a^2 n_a}{m_a} \left( \mathbf{E} + \frac{\mathbf{V}_a}{c} \times \mathbf{B} \right) - \frac{q_a}{m_a} (\nabla \cdot \kappa_a) + q_a n_a \mathbf{g} \right\} + \left( \frac{\delta\mathbf{J}}{\delta t} \right)_{coll} \quad (4)$$

where  $q_a$ ,  $m_a$ ,  $n_a$ ,  $\mathbf{V}_a$ , and  $\kappa_a$  are the charge, mass, concentration, bulk velocity, and kinetic tensor, respectively, of species  $a$ ,  $\mathbf{g}$  is the gravitational acceleration (included here for exactness but, as far as phenomena in the terrestrial magnetosphere are concerned, mostly not important in practice), and  $(\delta\mathbf{J}/\delta t)_{coll}$  represents the sum of all collision effects. Except for being non-relativistic, equation (4) is exact, with no approximations.

The essential point demonstrated in [9] is that while equation (4) always holds *in principle*, its left-hand side becomes negligibly small in comparison to the individual terms on the right-hand side, except when variations on space and time scales at and below those of electron plasma oscillations are involved; on all larger scales the equation is thus *in practice* not usable for determining  $\partial\mathbf{J}/\partial t$ . When small-scale variations are important, they can be averaged over, and equation (4) can be

transformed into the corresponding equation for the time evolution of the averaged  $\mathbf{J}$  (expressed in terms of average quantities and fluctuation correlations):

$$\begin{aligned} \frac{\partial\langle\mathbf{J}\rangle}{\partial t} = & \sum_a \left\{ \frac{q_a^2 \langle n_a \rangle}{m_a} \left( \langle \mathbf{E} \rangle + \frac{\langle \mathbf{V}_a \rangle}{c} \times \langle \mathbf{B} \rangle \right) \right. \\ & + \frac{q_a^2}{m_a} \left( \langle \delta n_a \delta \mathbf{E} \rangle + \left\langle \frac{\delta(n_a \mathbf{V}_a)}{c} \times \delta \mathbf{B} \right\rangle \right) \\ & \left. - \frac{q_a}{m_a} \nabla \cdot \langle \kappa_a \rangle + q_a \langle n_a \rangle \mathbf{g} \right\} + \left\langle \left( \frac{\delta\mathbf{J}}{\delta t} \right)_{coll} \right\rangle. \end{aligned} \quad (5)$$

Equation (5) is still exact (except for being non-relativistic) and in particular does *not* presuppose any small-amplitude or quasilinear approximation (as long as the average moments are properly defined as moments of the averaged distribution function [9]).

It is convenient to rewrite (5) in a simplified notation as

$$\frac{\partial\langle\mathbf{J}\rangle}{\partial t} = \frac{\omega_p^2}{4\pi} (\langle \mathbf{E} \rangle - \langle \mathbf{E}^* \rangle) \quad (6)$$

where the effective electron plasma frequency  $\omega_p$  is defined by

$$\omega_p^2 \equiv 4\pi \sum_a \frac{q_a^2 \langle n_a \rangle}{m_a} \approx \frac{4\pi n_e e^2}{m_e} \quad (7)$$

and  $-\langle \mathbf{E}^* \rangle$  represents the sum of all the terms on the right-hand side other than  $\langle \mathbf{E} \rangle$ ; this is purely a matter of notation and does not presuppose any restrictions.

## 3. Evolution of magnetic field

The following argument can be (and has been) made: regardless of any conclusions in [9] about orders of magnitude and small-scale fluctuations, equations (4) and (5) do represent, formally at least, the time evolution of the current density, so why can they not be used to calculate the time evolution of the magnetic field? Equation (4) includes all space and time scales (including those that may be considered too small to be of interest) and describes, strictly speaking, every individual plasma oscillation, but if that is perceived as a problem, then the averaged equation (5) can always be used instead. I consider now the consequences of applying this seemingly straightforward procedure.

### 3.1. Application of Biot-Savart law

Solved for  $\mathbf{B}$  in terms of  $\mathbf{J}$ , Ampère's law (1) yields the Biot-Savart integral

$$\mathbf{B}(\mathbf{r}, t) = \frac{1}{c} \int d^3r' \mathbf{J}(\mathbf{r}', t) \times \frac{\mathbf{r} - \mathbf{r}'}{|\mathbf{r} - \mathbf{r}'|^3} \quad (8)$$

which, by a simple integration by parts, can be rewritten in the form

$$\mathbf{B}(\mathbf{r}, t) = \frac{1}{c} \int d^3r' \frac{\nabla' \times \mathbf{J}(\mathbf{r}', t)}{|\mathbf{r} - \mathbf{r}'|} \quad (9)$$

( $\nabla'$  = gradient with respect to the coordinate vector  $\mathbf{r}'$ ). Differentiating with respect to time gives

$$\frac{\partial\mathbf{B}(\mathbf{r}, t)}{\partial t} = \frac{1}{c} \int d^3r' \frac{\partial\mathbf{J}(\mathbf{r}', t)}{\partial t} \times \frac{\mathbf{r} - \mathbf{r}'}{|\mathbf{r} - \mathbf{r}'|^3} \quad (10)$$

or equivalently

$$\frac{\partial \mathbf{B}(\mathbf{r}, t)}{\partial t} = \frac{1}{c} \int d^3 r' \frac{\nabla' \times \partial \mathbf{J}(\mathbf{r}', t) / \partial t}{|\mathbf{r} - \mathbf{r}'|} \quad (11)$$

and the idea is to calculate  $\partial \mathbf{B} / \partial t$  by using (5) for  $\partial \mathbf{J} / \partial t$  within the integrals. (It is taken for granted that the time variations of interest here occur on scales long compared to light travel times; hence the neglect of the displacement current term in Ampère's law and consequently of time retardation in the integrals.)

Substituting  $\partial \mathbf{J} / \partial t$  from (5) and invoking Faraday's law (2) to evaluate  $\nabla \times \mathbf{E}$  transforms the Biot-Savart integral (11) for  $\partial \mathbf{B} / \partial t$  into

$$\frac{\partial \mathbf{B}(\mathbf{r}, t)}{\partial t} = - \int d^3 r' \frac{\partial \mathbf{B}(\mathbf{r}', t) / \partial t + \nabla' \times c \mathbf{E}^*(\mathbf{r}', t) - \Delta}{4\pi \lambda_e^2 |\mathbf{r} - \mathbf{r}'|} \quad (12)$$

$$\Delta \equiv (\nabla' n_e / n_e) \times c(\mathbf{E} - \mathbf{E}^*)$$

where

$$\lambda_e \equiv c / \omega_p = 5 \text{ km} (1 \text{ cm}^{-3} / n_e)^{1/2} \quad (13)$$

is the electron inertial length (also known as the collisionless skin depth). The difficulty is now apparent:  $\partial \mathbf{B} / \partial t$  cannot be calculated simply by evaluating the integral in (12) because the integrand contains  $\partial \mathbf{B} / \partial t$  itself as one of the terms. Nor can this term be considered as a small correction: the order of magnitude of the integral over  $\partial \mathbf{B} / \partial t$  on the right-hand side, compared to the term  $\partial \mathbf{B} / \partial t$  on the left-hand side, is  $O(\mathcal{L} / \lambda_e)^2$ , where  $\mathcal{L}$  is the spatial scale of the system. Equation (12) must in fact be viewed as an integral equation for  $\partial \mathbf{B} / \partial t$ , not just a plain integral.

### 3.2. Large-scale limit

The integral equation (12) can be solved explicitly for  $\partial \mathbf{B} / \partial t$  if  $\lambda_e$  varies only on a spatial scale large compared to itself ( $\lambda_e \ll \mathcal{L}$ ); to lowest order in  $\lambda_e / \mathcal{L}$ ,

$$\frac{\partial \mathbf{B}(\mathbf{r}, t)}{\partial t} = - \int d^3 r' \exp \left\{ \frac{-|\mathbf{r} - \mathbf{r}'|}{\lambda_e} \right\} \frac{\nabla' \times c \mathbf{E}^*(\mathbf{r}', t)}{4\pi \lambda_e^2 |\mathbf{r} - \mathbf{r}'|} \quad (14)$$

(the term  $\Delta$  in (12) has been neglected, as it can be shown to be of order  $(\lambda_e / \mathcal{L})^2$  in comparison to the others). The solution (14) is most readily derived by transforming the integral equation (12) back into a differential form by making use of the fact that the Green's function  $\psi = 1 / |\mathbf{r} - \mathbf{r}'|$  is a solution of

$$\nabla^2 \psi = -4\pi \delta(\mathbf{r} - \mathbf{r}') \quad (15)$$

and then placing all the  $\partial \mathbf{B} / \partial t$  terms in the consequent differential equation on its left-hand side, with the result that the Green's function is now a solution of

$$\nabla^2 \psi - \frac{\psi}{\lambda_e^2} = -4\pi \delta(\mathbf{r} - \mathbf{r}') \quad (16)$$

instead of (15); if  $\lambda_e$  can be treated (locally at least) as a constant, the solution of (16) is the well-known Debye or Yukawa potential. Alternatively, the differential form of the equation

for  $\partial \mathbf{B} / \partial t$  can be obtained directly from the curl of the time derivative of Ampère's law (1), with the use of (5) and (2).

Equation (14) expresses  $\partial \mathbf{B} / \partial t$  as a straightforward integral (one that no longer contains  $\partial \mathbf{B} / \partial t$  itself in the integrand). It differs from (12) also in the form of the kernel (Green's function): the Coulomb potential in (12) has been replaced in (14) by a potential of the Debye form (but note that the shielding distance here is the electron inertial length  $\lambda_e$ , not the Debye length).

Changing the variable of integration from  $\mathbf{r}'$  to  $\mathbf{s}$  with  $\mathbf{r}' \equiv \mathbf{r} + \lambda_e \mathbf{s}$  and writing the integral over  $\mathbf{s}$  in spherical coordinates finally gives

$$\frac{\partial \mathbf{B}(\mathbf{r}, t)}{\partial t} = - \int \frac{d\Omega}{4\pi} \int_0^\infty s ds e^{-s} \nabla \times c \mathbf{E}^*(\mathbf{r} + \lambda_e \mathbf{s}, t). \quad (17)$$

In the limit  $\lambda_e \ll \mathcal{L}$  this reduces to

$$\frac{\partial \mathbf{B}(\mathbf{r}, t)}{\partial t} \approx -\nabla \times c \mathbf{E}^*(\mathbf{r}, t) \quad (18)$$

which is equivalent to

$$\frac{\partial \mathbf{B}}{\partial t} = -c \nabla \times \mathbf{E} \quad \text{with} \quad \mathbf{0} = \mathbf{E} - \mathbf{E}^* \quad (19)$$

But this is precisely the method of calculating the time evolution of  $\mathbf{B}$  arrived at in [9, 10]: on length scales  $\gg \lambda_e$  and time scales  $\gg 1 / \omega_p$ , the electric field is determined by plasma dynamics via the generalized Ohm's law (neglecting the  $\partial \mathbf{J} / \partial t$  term), and the evolution of the magnetic field is then determined, via Faraday's law, directly by the curl of the electric field. There is no longer any direct reference to the electric current density, which is determined — and this is now the only role of Ampère's law — by the curl of the magnetic field.

## 4. Conclusion

The presence of a large concentration of free charged particles (particularly electrons) in a plasma means that an electric field can, by accelerating positive and negative charges in opposite directions, very quickly and efficiently change the electric current density — unless other forces (e.g. magnetic forces or pressure gradients) counteract this differential acceleration. What constitutes a "large" concentration in this context is defined precisely by the value of  $n_e$  implied by the condition  $\lambda_e \ll \mathcal{L}$ : when this condition is satisfied, a very large current density can result from even a small differential acceleration of positive and negative particles, with the result that the electric field must be determined largely by the requirement that the differential acceleration remain sufficiently close to zero. This is the basic reason why the time evolution of the current cannot be specified independently of and logically prior to the time evolution of the magnetic field: if the change of current is assumed to be specified somehow, then Ampère's law implies a change of the magnetic field, which by Faraday's law must be accompanied by a (non-curl-free) electric field, which implies in turn a change of current, much larger than (and hence inconsistent with) that assumed initially.

Here I have demonstrated this inconsistency by an explicit calculation: in order to obtain the time derivative of the magnetic field, insert the changing current density, deduced from

the forces acting on all the charged particles, into the time derivative of the Biot-Savart integral. Depending on how one handles the mathematics, there are two possible results. Either, if the integral is simply evaluated as given, one finds that the time evolution of the magnetic field cannot be calculated at all unless it is known already (and known indeed to a much higher precision,  $\ll O(\lambda_e/L)^2$ , than that of the result to be calculated). Or else, if the appropriate mathematical manipulations are carried out, one *can* obtain the time evolution of the magnetic field, but (one finds) it is actually being calculated from the changes in the balance (described by the generalized Ohm's law) between the electric field and the plasma flows and stresses: even though the Biot-Savart integral was taken as the starting point, the final formula arrived at for the time derivative of the magnetic field gives it directly as minus the curl of the electric field derived from the generalized Ohm's law, *not* as the integrated magnetic effect of any specified varying currents.

## References

1. Cowling, T. G., *Magnetohydrodynamics*, Section 1.3, Interscience Publishers, Inc., New York, 1957.
2. Dungey, J. W., *Cosmic Electrodynamics*, p.10, Cambridge University Press, London, 1958.
3. Heikkila, W. J., Comment on "The alternative paradigm for magnetospheric physics" by E. N. Parker, *J. Geophys. Res.*, *102*, 9651–9656, 1997.
4. Lui, A. T. Y., Electric current approach to magnetospheric physics and the distinction between current disruption and magnetic reconnection, in *Magnetospheric Current Systems*, edited by S.-I. Ohtani, R. Fujii, M. Hesse, and R. L. Lysak, pp. 31–40, AGU Geophysical Monograph 118, Washington, D.C., 2000.
5. McPherron, R. L., Russell, C. T., and Aubry, M. P., Satellite studies of magnetospheric substorms on August 15, 1968, 9. Phenomenological model for substorms, *J. Geophys. Res.*, *78*, 3131–3149, 1973.
6. Parker, E. N., The alternative paradigm for magnetospheric physics, *J. Geophys. Res.*, *101*, 10587–10625, 1996.
7. Parker, E. N., Reply, *J. Geophys. Res.*, *102*, 9657–9658, 1997.
8. Parker, E. N., Newton, Maxwell, and magnetospheric physics, in *Magnetospheric Current Systems*, edited by S.-I. Ohtani, R. Fujii, M. Hesse, and R. L. Lysak, pp. 1–10, AGU Geophysical Monograph 118, Washington, D.C., 2000.
9. Vasyliūnas, V. M., Time evolution of electric fields and currents and the generalized Ohm's law, *Ann. Geophys.*, *23*, 1347–1354, 2005a.
10. Vasyliūnas, V. M., Relation between magnetic fields and electric currents in plasmas, *Ann. Geophys.*, *23*, 2589–2597, 2005b.

# Features of magnetosphere-ionosphere coupling during breakups and substorm onsets inferred from multi-instrument alignment

I. Voronkov, A. Runov, A. Koustov, K. Kabin, M. Meurant, E. Donovan, C. Bryant, and E. Spanswick

**Abstract:** We consider a sequence of activations which include pseudo-breakups, small local substorms, and a full substorm using a fortunate multi-instrument coverage between 0300 and 0700 UT on September 15, 2001. For this period of time, there was a radial alignment of GOES, and Cluster ( $\sim 19 R_E$ ) in the near-midnight magnetotail mapped to the Canadian sector covered by the IMAGE field of view along with fully functional hi-resolution photometers, and magnetometers. This allows reasonable featuring of auroral breakup and substorm onset components as they are observed both in the magnetosphere and ionosphere. In this paper, we concentrate on general description and relative timing of the auroral breakup signatures, dipolarization and onset of Pi pulsations at geostationary orbit, and large (up to 1000 km/s) tailward flows and strong bipolar variations in the central plasma sheet. This paper is meant to complement the accompanying paper [10].

*Key words:* Breakup, Onset, Substorm.

## 1. Introduction

In a substorm onset problem, one of the central issues is the inter-scale interactions of various regions. These include processes in the near-Earth plasma sheet (NEPS) and the auroral intensification and current formation in the ionosphere, processes in the near-Earth breakup region and in the mid-tail reconnection region, and coupling of the central plasma sheet (CPS) and ionosphere at onset.

In studying the essential relations between the substorm onset components, significant successes have been recently achieved in both micro-scale analysis of plasma sheet processes and global picturing of the magnetosphere-ionosphere coupling using multi-instrument alignments. Some observations indicate that onset is an interactive process involving the near-Earth breakup and mid-tail reconnection. It has been suggested that the near-Earth breakup is associated with some sort of the interchange instability, most probably a drift ballooning mode, leading to a current disruption at roughly  $6-10 R_E$ , whereas reconnection is presumably a result of the Hall effect in the very thin, and sometimes bifurcated, current sheet at larger radial distances. The most disputed mechanisms of interaction between these two processes, or triggering one another, are rarefaction or compressional waves propagating from the NEPS to the CPS and earthward bursty flows from the reconnection region to the NEPS. For reference purposes, we overview sev-

eral recent observation-based studies which also provide more complete list of literature on the subject.

A drift ballooning instability in the NEPS was observed by Wind [3] and CRRES [5] and the spatial and temporal characteristics of unstable modes are in agreement with nonlinear auroral vortex formation at breakups [13]. In the more distant plasma sheet, thin and bifurcated current sheet was detected by Cluster [2], [9]. The Hall current structure at the reconnection region was observed by Geotail [6] and Cluster [1] providing support for the Hall reconnection model being a likely mechanism for the mid-tail reconnection.

Perhaps the most challenging problem is to detect a mechanism which provides an interaction between these regions. Presumably, this interaction can proceed in both ways, earthward and tailward, and even as a simultaneous collapse of the entire plasma sheet (PS). Roux et al. [8] identified azimuthally propagating waves seen by Cluster in a mid-tail region as a result of a ballooning or another local instability which is able to reduce or interrupt a cross tail current. They suggested that in series, these local processes can result in a global CPS current reduction and dipolarization. In contrast, using a radial alignment of Cluster and ISTP, Sergeev et al. [11] interpreted onset as earthward-contracting reconnected tube produced by impulsive reconnection in the mid-tail PS. On the other hand, some substorms are initiated by bursty bulk flows, presumably launched from the reconnection regions and propagating earthward (see, e.g., [7] and references therein). The near-Earth breakup triggering by bursty flows is the subject of discussions but some recent observations and modeling suggest that compressional waves may provide an energy transport channel from the flow braking region to the NEPS (e.g., [4], [12], [14]).

In this study, we attempt to use a fortunate alignment of Cluster, GOES, IMAGE, and Canadian ground based instruments to investigate sequences of substorm onset signatures in the system of NEPS, mid-tail PS, and auroral ionosphere. The detailed local Cluster observations and their analysis for

Received 14 June 2006.

**I. Voronkov, M. Meurant, E. Donovan, C. Bryant, and E. Spanswick.** Dpt. of Physics and Astronomy, University of Calgary, Calgary, AB, T2N 1N4, Canada

**A. Runov.** Space Research Institute, Austrian Academy of Sciences, Schmiedlstrasse 6, A-8042, Graz, Austria

**A. Koustov.** Dpt. of Physics and Engineering, University of Saskatchewan, 116, Science Place Saskatoon, SK, S7N 5E2, Canada

**K. Kabin.** Dpt. of Physics, University of Alberta, Edmonton, AB, T6G 2J1, Canada

this event are described in the accompanying paper [10]. Here, we concentrate on the temporal and spatial description of onsets in a more global context of the ionosphere-magnetosphere system.

## 2. Observations on September 15, 2001

During the time interval from 0100 through 0630 UT on September 15, 2001, Cluster was, for the most part, in the night-side central plasma sheet. During the interval of 0330-0630 UT, several auroral activations (from small PSBs to a full substorm) were registered over the Canadian sector bracketed by two geostationary satellites, GOES 8 and GOES 10. The Cluster barycenter position was  $(-18.9, 3.7, -1.9) R_E$  at 0400 UT and  $(-18.5, 3.3, -3.4) R_E$  at 0600 UT. The IMAGE satellite observed auroral emissions for the entire interval over the Canadian sector. This provides a unique opportunity to use this conjunction of Cluster, IMAGE, GOES, CANOPUS, and NR-Can facilities for studying substorm processes, namely to collocate mid-tail and ground-based signatures of different substorm stages. Mapping of Cluster, IMAGE, and GOES with respect to ground-based stations is illustrated by Figure 1.

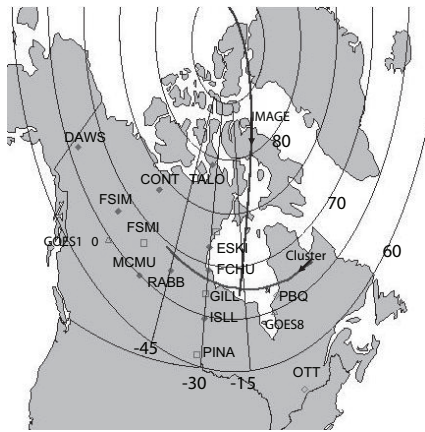


**Fig. 1.** Locations of NORSTAR, CANOPUS, and NRCan observatories along with ionospheric footprints of the Cluster, IMAGE, and GOES 8 and 10 satellites.

Good quality meridian scanning photometer (MSP) data obtained at Forth Smith and Gillam, including high-resolution data at Gillam, position of IMAGE capturing the Canadian sector, available data from Cluster, and high resolution GOES data bring events during this interval of time to a great spot of interest.

The entire data set used for this study can be outlined as follows. WIND and Geotail were used to monitor solar wind (SW) parameters. IMAGE provided global auroral imaging of the Canadian sector. This was used to identify the position of onset and its further temporal and spatial dynamics (e.g., vortex and surge formation and propagation). With the global framework provided by IMAGE, the fine structure of auroral dynamics can be revealed using higher-resolution optical data from MSPs. Cluster observations showed the dynamics of the near-midnight plasma sheet at roughly  $19 R_E$  down the tail.

GOES spacecraft provided timing for dipolarization and onset of Pi2. Finally, the overall picture of disturbances was monitored by the CANOPUS and NRCan magnetometers.

## 3. Pre-history and the growth phase

Prior to the period of the immediate interest for this study, there was a large substorm which started after 2330 UT on September 14, 2001 and ended at roughly 0145 UT on September 15, 2001. This was the latest noticeable perturbation prior to activations between 0340 and 0630 UT, which are focused in this study. After 0100 UT, the IMF  $B_z$  was dominantly northward until  $\sim 0335$  UT when the sharp negative turning started. Other SW parameters ( $B_y$ ,  $N$ ,  $P$ ,  $V$ ) also showed rather smooth variations during that time as illustrated in Figure 2 showing  $B_y$ ,  $B_z$ , and  $V_x$  measured by Geotail traveling approximately at  $(10, 15, 1.5) R_E$ . Geotail and WIND data closely followed each other suggesting that the SW parameters were homogeneous on the scale size of the Earth magnetosphere.

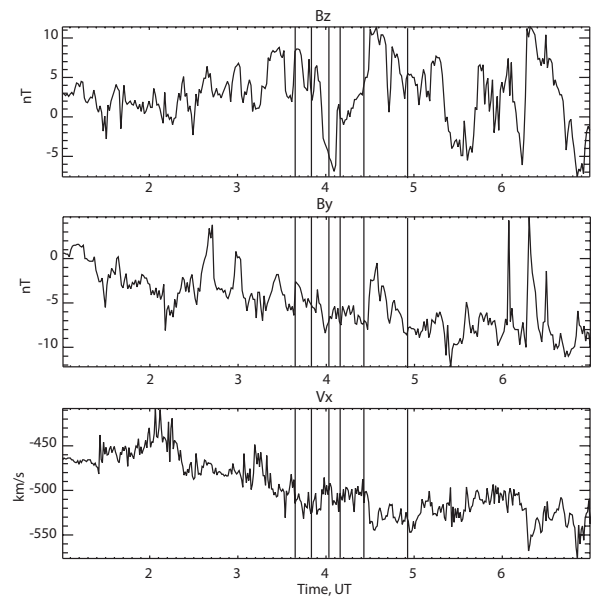


**Fig. 2.** IMF  $B_z$  and  $B_y$  and solar wind  $V_x$  components as measured by the Geotail. Vertical lines indicate times of onsets.

After 2350 UT, GOES 8 registered very strong stretching of field lines with the maximum of  $H_e/H_p \sim 2$ . It gradually reduced to  $\sim 1.5$  after 0200 UT and stayed at this level until the first dipolarization occurred at 0339 UT. During this interval, GOES 10 was in the near-dipolar field region and magnetic field variations at the satellite location were very smooth.

After  $\sim 0100$  UT, Cluster was in the central PS and observed no significant disturbances until the first intensification at 0338-0340 UT. During this interval,  $B_z$  gradually decreased, indicating stretching. Also, the post-substorm (after 0100 UT) PS can be characterized as rather "hot" with the proton temperature around 10 keV (which is high but not anomalous). The Cluster summary plot is shown in Figure 3. For more data plots and detailed discussion, see [10] in this issue.

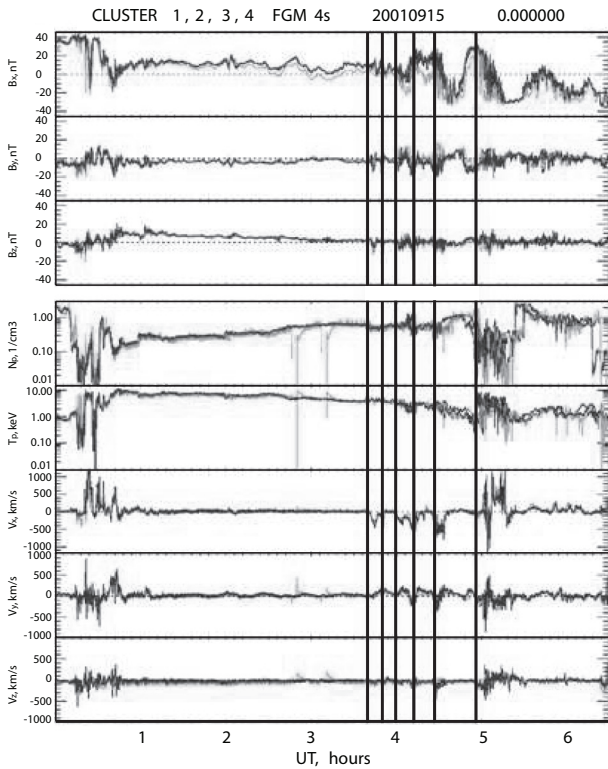


**Fig. 3.** The Cluster summary plot. Vertical lines indicate times of onsets.

The magnetic field perturbation in the Canadian sector recovered after 0100 UT and remained quiet until the first onset at 0338-0340 UT. Also according to IMAGE, the auroral zone was also very quiet and dim after 0100 until onset at 0338 UT.

The growth phase timing is quite uncertain for this event, mostly due to the lack of any pronounced signatures in the solar wind. One could even argue whether there was a growth phase at all. We will simply describe variations, which can be considered as growth phase signatures. Cluster showed continuous field line stretching. According to the Gillam MSP, equatorward motion of auroras started after roughly 0220-0230 UT and continued until 0340 UT. At the late growth phase, IMAGE registered dimming and virtually disappearance of the oval in both electron and proton auroras which also can be attributed to significant stretching of the magnetotail. No any other significant variations were registered until onset at 0339 UT.

All these observations for the post-substorm period of time (~0100-0335 UT) suggest that the magnetosphere-ionosphere system was in a stationary state free of any noticeable disturbances. At the same time, the plasma sheet was at a fairly high energy level, quite stretched and hot. Presumably, this was the main background condition for the active period discussed below. The growth phase was not too pronounced for this event. The main signatures can be interpreted as continuous stretching of the entire plasma sheet.

#### 4. Onset positions and timing

Large scale optical onset positions and timing were defined using the IMAGE WIC data with temporal resolution of 2 min. According to IMAGE (Figure 4), the first five onsets prior the main substorm (at 0455 UT) occurred in a longitudinal sector monitored by the Canadian MSPs and magnetometers. High resolution ground-based measurements allowed us to study dynamics of disturbances in greater details. Sample data from magnetometers encountering the activation region and GILL MSP are shown in Figure 5 (CANOPUS) and Figure 6 (NR-Can). In this section, only these five activations are targeted whereas the last more eastward substorm onset will be considered separately. Because all five onsets occurred close to the GILL MSP, we used high-resolution MSP data to find times and longitudinal positions of auroral breakups (Figure 7). GOES 8 (Figure 8) provided the timing of dipolarization.

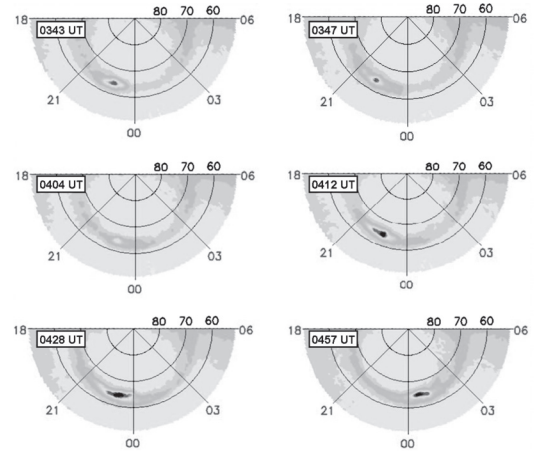


**Fig. 4.** IMAGE WIC snapshots at onsets.

##### 4.1. Timing

From analysis of GOES 8 data for these activations, we concluded that dipolarization and  $Pi2$  at geostationary orbit represent the most reliable signatures of onset. Analyzing all other data described above, the following timing of observed features with respect to the moment of dipolarization (taken as  $t = 0$  min) has been revealed. Time is given in minutes with respect to dipolarization at  $t = 0$  (e.g., -6 means 6 min prior to dipolarization, or : 1 stands for 1 min after dipolarization)

###### #1 (0339 UT):

- 6: Equatorward auroral precursor;
- 0: Dipolarization and  $Pi2$  at GOES, GBO breakup;
- 1: GBO  $Pi2$  and magnetic bay;
- 2: Onset seen by IMAGE, tailward flow and bipolar variation of the magnetic field at Cluster;
- 5: The maximum tailward flow seen at Cluster.

###### #2 (0350 UT):

- 3: GBO and IMAGE auroral breakup.
- 0:  $Pi2$  and dipolarization at GOES, magnetic bay at PBQ, fast tailward flow and bipolar magnetic fluctuations at Cluster.

###### #3 (0402 UT):

- 3: Tailward flow and bipolar variations at Cluster;

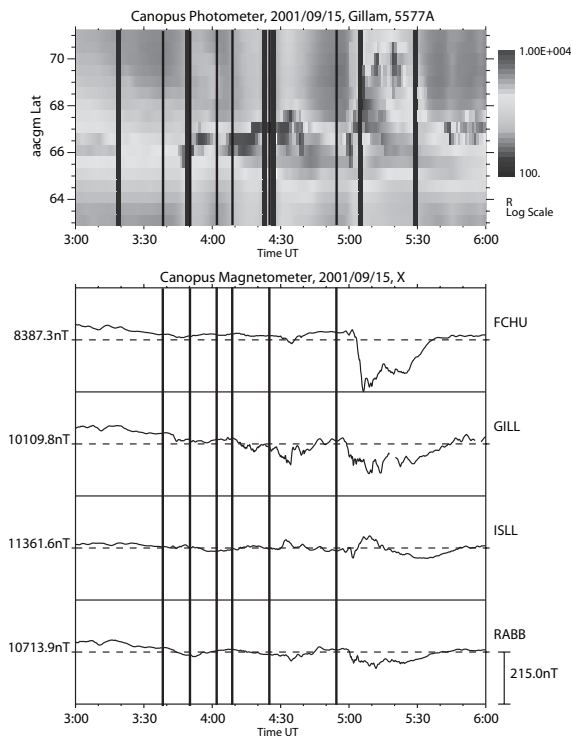


**Fig. 5.** Summary plot of Gillam MSP observations (sampling data are used) and magnetic field X-component variations at a number of CANOPUS sites. Black vertical lines indicate times of onsets.

0: Pis and dipolarization at GOES, GBO and IMAGE breakup, GBO magnetic bay, very strong magnetic field oscillations at Cluster.

**#4 (0409 UT):**

-2: Northward turning of the  $B_Z$  IMF, start of bipolar variations at Cluster;

0: Pi and dipolarization at GOES, tailward flow at Cluster;

2-3: GBO and IMAGE optical breakup, GBO magnetic bay;

3-4: westward travelling surge (WTS), maximum of the tailward flow at Cluster.

**#5 (0425 UT):**

-1: auroral breakup;

0: Pis and dipolarization at GOES, GBO magnetic onset;

1: Onset detected by IMAGE, Cluster registered a tailward flow, growth of the proton temperature, and bipolar variations;

3: Fully developed WTS and electrojet;

#### 4.2. Position of auroral onset

As seen from IMAGE data (Figure 4), all five onsets occurred at longitudes close to the Churchill line. This allows us to use the Gillam MSP data in order to identify the latitudinal positions of the activations. For this purpose, we analyzed the high-resolution data (Figure 7).

The first two intensifications could have been treated as one local substorm with double onset (or pseudo-breakup and onset) from the point of view of the GBO, IMAGE, and geostationary observations. However, Cluster registered two distinct tailward flow bursts accompanied by the  $B_Z$  reversals (see [10] for details).

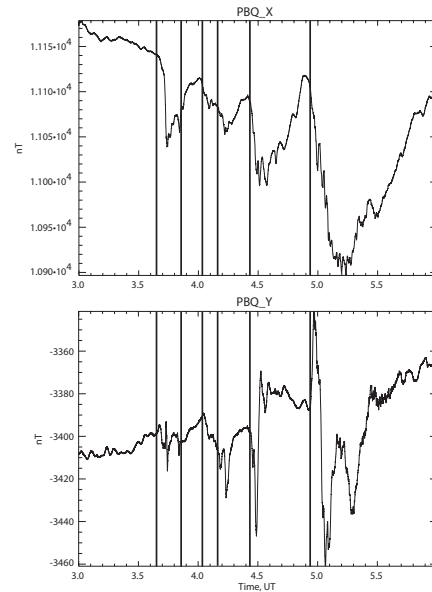


**Fig. 6.** PBQ magnetic data used for the electrojet and Pi2 onset timing. Black vertical lines indicate times of onsets.

The first activation started in a rather typical way (Figure 9): equatorward auroral precursor intensified  $\sim 6$  min prior to onset (0333 UT) and led to auroral breakup (PSB) at the poleward edge of the proton aurora band (0339 UT), with some latitudinal expansion at onset.

This first PSB at the equatorward boundary developed into full onset (activation #2) with much stronger brightening and noticeable poleward expansion after 0347 UT roughly 3 min prior to other onset signatures. This brightening was also seen in IMAGE data. Since the previous activity did not move too far northward from the origin, this activation still started at the equator-most aurora.

Activation #3 commenced in a similar way to the first one with aurora intensification at the equatorward edge at 0402 UT. In this case, it happened virtually at the same time as onset was registered by GOES, PBQ, and IMAGE. However, the further dynamics was quite different. When the auroral activation began saturating (0408-0410 UT), a sharp northward gradient of the IMF  $B_Z$  close to magnetopause was detected by Geotail. Perhaps, this caused activation #4 which can be considered as triggered continuation of the previous one and developed into a quite pronounced, though still rather local, substorm. Unlike previous three activations, it started from the most active region (remaining from activation #3) quite poleward from the equator-ward boundary of the auroral zone marked by the proton aurora band. This optical onset was simultaneously observed by the GILL MSP and IMAGE with a delay of 2-3 minutes of onset at geostationary orbit.

Activation #5 started in the same way as #4: at the time of onset at geostationary orbit (slightly preceding it), the most active region from the previous substorm intensified and resulted in a fully developed WTS 3-4 minutes later. Again, this onset occurred poleward from the equatorial boundary and proton aurora band.

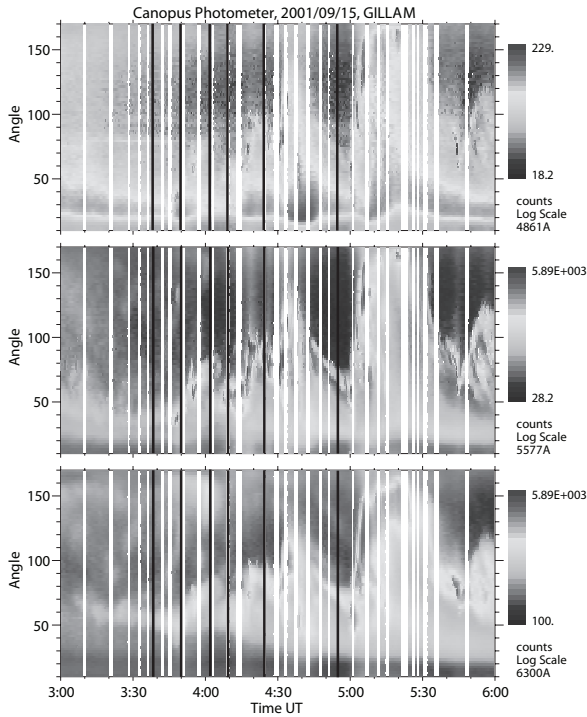


**Fig. 7.** Summary plots of GILL high resolution MSP. Black vertical lines indicate times of onsets.

### 5. Full substorm onset features

The first signatures of onset were detected as the magnetic bay and Pi commencement at PBQ (0454 UT) and the Pi onset at OTT (pulsations lasted until 0525 UT). Lower frequency (2 min) pulsations and strong variations in Z also started at PBQ and lasted until 0515 UT. The magnetic signatures were delayed at the Churchill line owing to the westward propagation of the disturbances from their more eastbound origin. Preceding the onset, Cluster measurements showed a thin (half thickness on the order of 3000 km) and bifurcated plasma sheet. At the time of 0455-0502 UT, Cluster registered very strong (up to 25 nT) oscillations (which can be interpreted as a kinking mode [10]) of the magnetic field on the background of the large B-gradient and azimuthal duskward motion of the current sheet [10].

Optical onset was registered by IMAGE at 0457 UT in the post-midnight sector. Figure 10 provides key snapshots of WIC during the entire event.

Due to the position of onset, the optical signatures of the surge reached Gillam only at 0459 UT, as seen in high resolution MSP (Figure 8). After that, the surge showed significant poleward expansion (at 0459-0506 UT) in a "jump-like" manner. Also owing to the eastward location of onset, the dipolarization at GOES 8 did not start until 0500 UT.

After 0500 UT, the current sheet became very dynamic. At 0459-0501 UT, Cluster registered a pulse of tailward and duskward bulk flow (roughly up to 200 km/s). Following this at 0501-0502 UT, Cluster showed a sharp growth in the proton energy roughly from 1 to 10 keV where it stayed for a long while. This growth was accompanied by the earthward bulk of high energy (more than 10 keV) protons. At that time (0501-

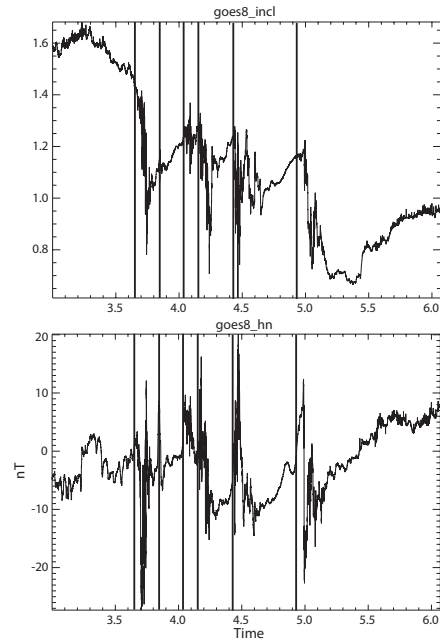


**Fig. 8.** Magnetic field inclination (representing dipolarizations) and  $H_n$  component (illustrating onsets of Pi) as detected by GOES 8. Black vertical lines indicate times of onsets.

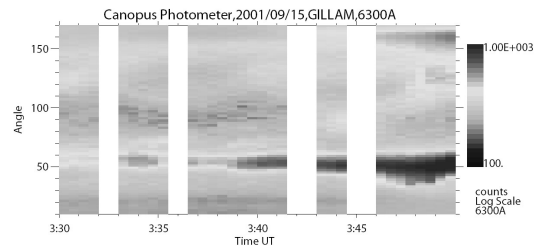


**Fig. 9.** 630 nm high resolution MSP data for activation 1 (white lines indicate periods with no data).

0504 UT) a very thin (half-thickness less than 1000 km) current sheet was detected.

During this period of time, the ground-based instruments registered further expansion of the activation. At 0501 UT, brightening and poleward expansion began at FSMI, which is in agreement with the IMAGE data. At 0502 UT, the main substorm bay started at FCHU and a current loop formed above GILL indicating large expansion of the electrojet.

Following this, at 0503-0505 UT, the surge reached its greatest magnitude and poleward expansion. As seen from IMAGE and MSP data, the high latitude portion of the surge brightens dramatically at this time (whereas the equatorward activity recovered). This was the time when Cluster detected a sharp reversal of the bulk flow from tailward to Earthward of the magnitude up to 800 km/s. Analysis of Cluster data indicates that variations of plasma parameters are consistent with signatures of the Hall reconnection in the CPS. After 0506-0507 UT, a double oval was seen by the GILL MSP and IMAGE (Figure 10), and the largest magnitude in the magnetic bay was registered above FCHU.

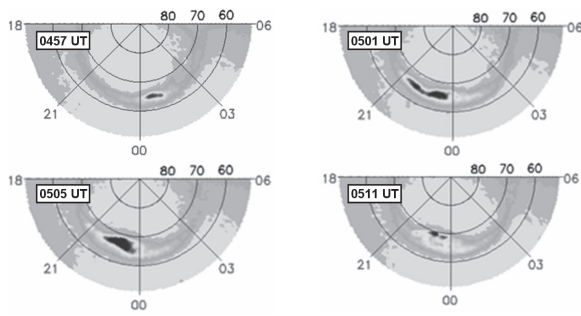


**Fig. 10.** IMAGE snapshots of the auroral breakup (0457 UT), surge formation (0501 UT), full substorm onset vortex (0505 UT), and double oval at the beginning of the recovery phase (0511 UT).

After roughly 0511 UT, the recovery phase signatures were observed in all main substorm components.

## 6. Conclusions and assertions

Owing to good longitudinal alignment of ground based and satellite observations, five activations, including local substorms and pseudo-breakups, on September 15, 2001 were used to infer onset features and their relative timing in the plasma sheet and ionosphere. The main results can be summarized as follows.

1. The most robust and repeatable features of onsets were dipolarization and onset of Pis in the near-Earth plasma sheet. We used this time-point as "the time of onset".

2. Auroral breakup can start from the precursor at the equatorial boundary of the auroral zone (which is more typical for isolated activations) as well as from most active regions which remain from the previous substorm quite poleward of the equatorial auroral boundary matching the proton aurora band.

3. Near-Earth breakups (including pseudo-breakups) were associated with strong tailward bursty flows (up to 1200 km/s) and large bipolar variations of the magnetic field.

4. For these activations, all signatures of onsets, from the NEPS to CPS and from the magnetosphere to the ionosphere, were seen within the time frame of 2-3 minutes.

Full substorm can be interpreted as a double onset event. The first one occurred in a similar way as the near-Earth breakups discussed above. The second led to a much larger substorm with fully developed WTS and electrojet. This onset was observed by Cluster at  $19 R_E$  as a sharp reversal of the flow and other signatures which allow us to interpret it as the Hall-type reconnection. In the ionosphere, the large-scale vortex on the spatial scale of the auroral oval width was observed. These features followed by the formation of a double oval.

## Acknowledgements

The CANOPUS and NORSTAR arrays are ground-based facilities funded by the Canadian Space Agency. We acknowledge NASA/GSFC, CDAWeb, and DARTS/Geotail data providers. We thank H. Singer for providing high resolution GOES 8 and GOES 10 data. The IMAGE FUV investigations were supported by NASA through SWRI subcontract. Poste-de-la-Baleine and Ottawa magnetic stations are funded and operated by The Geological Survey of Canada (National Resources of Canada). We thank A. Balogh for providing

Cluster FGM data and H. Reme for providing Cluster CIS data. This research was supported by the Natural Sciences and Engineering Research Council of Canada (NSERC) and the Canadian Space Agency.

## References

1. Alexeev, I. V., C. J. Owen, A. N. Fazakerley, A. Runov, J. P. Dewhurst, A. Balogh, H. Rème, B. Klecker, and L. Kistler, Cluster observation of currents in the plasma sheet during reconnection, *Geophys. Res. Lett.*, **32**, L03101, 2005.
2. Asano, Y., R. Nakamura, W. Baumjohann, A. Runov, Z. Vörös, M. Volwerk, T. L. Zhang, A. Balogh, B. Klecker, and H. Rème, How typical are atypical current sheets? *Geophys. Res. Lett.*, **32**, L03108, 2005.
3. Chen, L.-J., A. Bhattacharjee, K. Sigsbee, G. Parks, M. Fillingim, and R. Lin, Wind observations pertaining to current disruption and ballooning instability during substorms, *Geophys. Res. Lett.*, **30**, 1335, 2003.
4. Kepko, L., M. G. Kivelson, and K. Yumoto, Flow bursts, breaking, and Pi2 pulsations, *J. Geophys. Res.*, **106**, 1903, 2001.
5. Kozelova, T. V., L. L. Lazutin, B. V. Kozelov, N. Meredith, and M. A. Danielides, Alternating bursts of low energy ions and electrons near the substorm onset, *Ann. Geophys.*, 2006, accepted.
6. Nagai, T., I. Shinohara, M. Fujimoto, S. Machida, R. Nakamura, Y. Saito, and T. Mukai, Structure of the Hall current system in the vicinity of the magnetic reconnection site, *J. Geophys. Res.*, **108**, 1357, 2003.
7. Nakamura, R., W. Baumjohann, R. Schödel, M. Brittnacher, V. A. Sergeev, M. Kubyshkina, T. Mukai, and K. Liou, Earthward flow bursts, auroral streamers, and small expansions, *J. Geophys. Res.*, **106**, 10,791, 2001.
8. Roux, A., O. Le Contel, D. Fontaine, P. Robert, P. Louarn, J.A. Sauvaud, and A.N. Fazakerley, Substorm theories and Cluster multi-point measurements, *ICS8 proceedings*, this issue, 2006.
9. Runov, A., R. Nakamura, W. Baumjohann, T. L. Zhang, M. Volwerk, H.-U. Eichelberger, and A. Balogh, Cluster observation of a bifurcated current sheet, *Geophys. Res. Lett.*, **30**, 1036, 2003.
10. Runov, A., I. O. Voronkov, Y. Asano, W. Baumjohann, R. Nakamura, M. Volwerk, A. Balogh and H. Reme, Cluster observations during pseudo-breakups and substorms, *ICS8 proceedings*, this issue, 2006.
11. Sergeev, V. A., M. V. Kubyshkina, W. Baumjohann, R. Nakamura, O. Amm, T. Pulkkinen, V. Angelopoulos, S. B. Mende, B. Klecker, T. Nagai, J.-A. Sauvaud, J. A. Slavin, and M. F. Thomsen, Transition from substorm growth to substorm expansion phase as observed with a radial configuration of ISTP and Cluster spacecraft, *Ann. Geophys.*, **23**, 1, 2005.
12. Shiokawa, K., I. Shinohara, T. Mukai, H. Hayakawa, and C. Z. Cheng, Magnetic field fluctuations during substorm-associated dipolarizations in the nightside plasma sheet around  $X=-10 R_E$ , *J. Geophys. Res.*, **110**, A05212, doi:10.1029/2004JA010378, 2005.
13. Voronkov, I., E. F. Donovan, B. J. Jackel, and J. C. Samson, Large-scale vortex dynamics in the evening and midnight auroral zone: Observations and simulations, *J. Geophys. Res.*, **105**, 18,505, 2000.
14. Voronkov, I. O., Near-Earth breakup triggered by the earthward traveling burst flow, *Geophys. Res. Lett.*, **32**, L13107, doi:10.1029/2005GL022983, 2005.

# Scaling properties of high latitude magnetic field data during different magnetospheric conditions

J. A. Wanliss and D. O. Cersosimo

**Abstract:** We investigate the statistical properties of high-latitude magnetometer data for differing geomagnetic activity. This is achieved by characterizing changes in the nonlinear statistics of the Earth's magnetic field, by means of the Hurst exponent, measured from a single ground-based magnetometer station. The long-range statistical nature of the geomagnetic field at a local observation site can be described as a particular statistical process, viz. a multifractional Brownian motion, thus suggesting the required statistical structure of the mathematical models of magnetospheric activity. We also find that, in general, the average Hurst exponent for quiet magnetospheric intervals is smaller than that for more active intervals.

*Key words:* Substorms, Storms.

## 1. Introduction

Ground-based geomagnetic indices [27, 32] and individual magnetometer stations [29, 34, 33] have been used to provide excellent indicators of space weather conditions. Part of the reason for this is the property of the Earth's magnetic field lines to focus and converge as they approach the Earth. These field lines extend far into space and since they are connected to the Earth, nonlinear plasma processes that occur far away are mapped all the way down to the Earth. Observation of ground-based magnetometer stations can thus serve as a remote sensing tool of distant magnetospheric processes.

Over the years, several indices were developed to monitor geomagnetic activity. The most used are the disturbance storm time index (Dst), the planetary index ( $Kp$ ) and the auroral electrojet index with its variations (AE, AU and AL). These indices provide global information about current magnetospheric activity based on different inputs at different locations around the globe.

If we are interested in the local aspects of geomagnetic activity, i.e. to forecast the geomagnetic conditions for Hydro-Quebec or other power utilities, we need to develop ways to understand the geomagnetic activity in a more localized way. This is especially important since temporal fluctuations of the geomagnetic field depend on geographic location and time [34].

In this paper we extend previous analyses that used global statistics to study the differences between quiet and active magnetospheric times [32, 31], and which were used to suggest the possibility of a first-order like phase transition at space storm onset [30]. But global studies only give average behavior rather than local information. Our goal then is to learn about local behavior of the magnetic field, for differing geomagnetic activity. We will characterize changes in the nonlinear statistics of the Earth's magnetic field, by means of the Hurst exponent, measured from a single ground-based magnetometer station. The changes in statistics can be used as a local indicator of the magnetospheric conditions, which may be useful to develop re-

liable warning and forecasting systems using information not available in geomagnetic indices.

A second objective is to determine the long-range statistical nature of the geomagnetic field at a local observation site. If the time series can be described as a particular statistical process Brownian motion for example then this knowledge can be used for future space weather modeling purposes. The statistical structure of the magnetometer time series will provide key clues for the development of mathematical models.

## 2. Data

We chose the three hour  $Kp$  index to discriminate between different levels of magnetospheric activity. We could have used other indices, for example DST or AE, but we chose  $Kp$  since we considered that it, as a mid-latitude index, would best reflect the mean magnetospheric activity. Several methods for the classification of geomagnetic activity using the  $Kp$  index have been proposed and used by different authors. [2] used the criteria for selecting quiet and active events based on  $Kp \leq 1$  as an indicator of quiet periods, and  $Kp \geq 4$  indicates disturbed periods [2, 23]. [11] used  $Kp$  to classify several levels of geomagnetic activity in more detailed fashion ranging from small storms to major storms. In this work our interest focuses on two averaged geomagnetic states: active and quiet.

Data selected for quiet times (QT) were based on those periods between 1991 and 2001 where  $Kp \leq 1$  for no less than two days. The average length of the quiet events selected was 2.6 days. On the other hand, active events were selected from those periods of time having a  $Kp \geq 4$  for no less than a day. Twenty active events matching these criteria were selected with an average length of 2.2 days. The length of each event is determined only by continuous intervals where the  $Kp$  matches the criterion. Once the  $Kp$  value moves outside the criterion, it sets the boundaries to that particular event. Fig. 1 shows the mean  $Kp$  values of all the selected events, active and quiet, chronologically from 1991 to 2001. Most of the active events are close to solar maxima while the majority of the quiet events occur near solar minimum (1997).

We selected 40 events with the given criteria using the CAN-OPUS Fort Churchill magnetometer station (FCHU) as the primary data source. These data have a cadence of 5 (five) seconds. The

Received 12 May 2005.

J. A. Wanliss. ERAU, Daytona Beach 32114, USA.

D. O. Cersosimo. University of Missouri, Mechanical and Aerospace Engineering

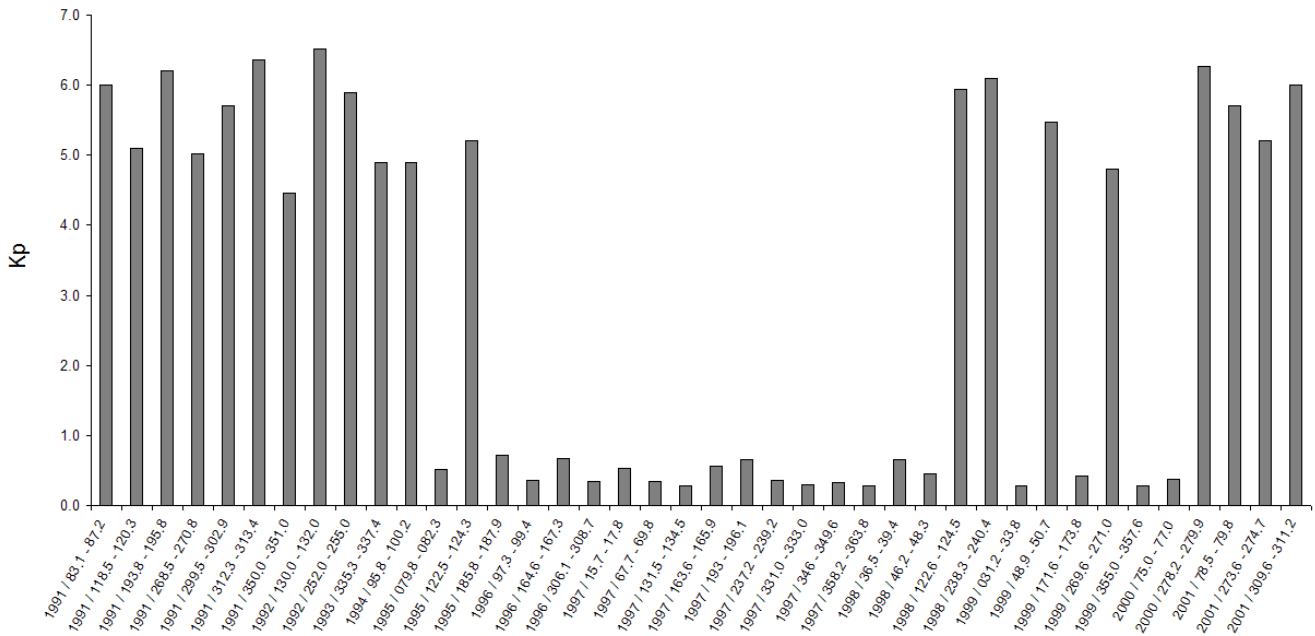


**Fig. 1.** Mean  $Kp$  values for the events analyzed from 1991 to 2001 are shown chronologically. The labels on the horizontal axis indicate the year and the start day through the end day using day of year notation.

reason behind the selection of this source is its geographic location (58.76N and 265.91W), which is frequently in the auroral oval. This location has the particular advantage that the data for the selected events are consistent with the location of stations used to make the  $Kp$  index, thus the selection criteria would be more likely to accurately discriminate activity levels.

The distribution functions of the magnetic field for QTs and ATs are presented in Fig. 2. In this plot the wider curve characterizes the magnetic field behavior during AT, while the thin curve represents the selected time series during QT.

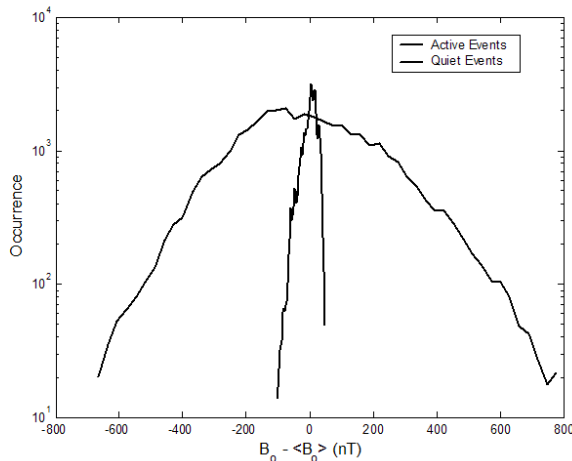


**Fig. 2.** Distribution functions for the active and quiet events analyzed. The solid line represents the averaged distributions for the 20 quiet events and the dash-dot line represents the averaged distributions for the 20 active events.

### 3. Analysis

We employ a detrended fluctuation analysis [22] to determine the statistical nature of the signal. If the signal is fractional Brownian motion (fBm), it exhibits power-law scaling with slope in the frequency domain between 1 and 3. In this case the signal is nonstationary but has stationary increments over a range of scales. For fBm a power spectrum slope  $b = 2H + 1$ , where  $H$  is the scaling exponent also known as the Hurst exponent. The special case where  $H=0.5$  indicates Brownian motion. Fig. 3 displays the PSD vs. frequency for a QT (a) and AT (b) for which the average  $Kp$  was 0.3 and 5.2 respectively.

To determine the self similarity parameter  $H$  we implement detrended fluctuation analysis (DFA) developed by [22] and recently implemented in space physics research by [32] and [31]. The technique is designed to determine the scaling exponent of nonstationary signal and provides better precision than the power spectral analysis and other classical techniques.

In DFA the time average of the time series is subtracted from the original series and then it is integrated. Once the series is integrated, it is divided into boxes of equal size  $n$ . In each box a linear least squares line is fit to the data, representing the trend of the series in that particular box. The next step is to remove the local trend in each box. The characteristic size of the fluctuations  $F(n)$ , is then calculated as the root mean squared deviation between the signal and its trend in each box. The process is repeated over all time scales (box sizes). The presence of scaling is indicated by a power-law relationship between  $F(n)$  and  $n$ .

We analyzed the QT and AT time series from two different approaches. The first approach measures long term correlation for the event, and a single value of the scaling exponent  $H$  is obtained for the entire series; this is a time-independent

monofractal approach. Next, we extend this approach to the time-dependent case where the scaling exponent is calculated in patches along the series. Rather than simply probe the existence of correlated behaviour over the entire time series, what we do is find a "local measurement" of the degree of long-range correlations described by the time variations of the scaling exponent. The probe used is the observation box of length 10000 data points; this box is placed at the beginning of the data, and then the scaling exponent is calculated for the data contained in the box. Next, the box is shifted in time one point along the series, and the scaling exponent for the new box is calculated. This procedure is iterated for the entire sequence. This time-dependent approach allows one to consider a the time series dominated by multi-scale processes or multifractional Brownian motion (mfBm). Multifractional Brownian motion is a generalised version of fBm in which the scaling exponent is no longer a constant, but a function of the time index [22]. In this case the increments of mfBm are nonstationary and the process is no longer self-similar.

### 4. Results

Fig. 4 summarizes the values obtained for  $H$  from the monofractal analysis. For this case DFA is applied for the whole event, and no sliding windows are used. Here we can clearly observe that the majority of the events have a value of  $H \sim 0.5$ , indicating the presence of similar statistical processes in both type of events (QT and AT). We found average  $H$  values to be  $\langle H_{QT} \rangle = 0.52 \pm 0.06$  and  $\langle H_{AT} \rangle = 0.51 \pm 0.05$ , implying the presence of a Brownian motion process dominating for the scale length of a particular event. To determine whether these QT and AT average Hurst exponents are significantly different from the null hypothesis that the difference is due purely to randomness we applied the students-t test to the distributions of the Hurst exponent. The important output of the t test is the value of  $p$ , which is the probability that the difference in the means of the two distributions being compared is due to random variation. We found  $p = 0.78$ . This suggests that the statistical differences between the sets are insignificant; although their fluctuations are very different, the overall nonlinear statistics across QT and AT are indistinguishable.

In Fig. 4, results are presented as a function of the event duration showing that intervals of different length have similar scaling exponents ranging from weak antipersistent to weakly

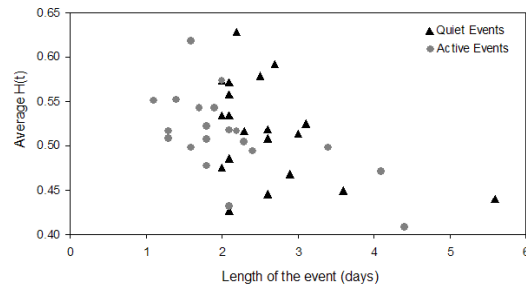


**Fig. 4.** Distributions of the Hurst exponent for quiet and active events vs. the event length. No direct evidence was found to suggest that the Hurst exponent is affected by the events length. The average Hurst exponent for quiet times is  $\langle H_{QT} \rangle = 0.52 \pm 0.06$  and for active times  $\langle H_{AT} \rangle = 0.51 \pm 0.05$ . The difference is statistically insignificant.

persistent fBm. The fact that most of the events fall near a random walk process is an indicative that long range correlations are not preserved along the time span of any particular event studied and thus become a random walk. These results were unexpected since as shown on Fig. 2, the distributions for quiet and active events encompasses marked differences as the result of different processes dominating the dynamics of the magnetosphere, i.e. during quiet times energy is stored and slowly burned keeping the magnetosphere in a relative low energy state, but during active times higher energy influx from the solar wind causes the magnetosphere to move to higher energy states where stronger nonlinear processes dominate the dynamical release of energy.

In order to find short term correlations we implement DFA using a smaller window size of 10000 data points that slides along the entire event and returns a single value of  $H$  for each window view. Tests on artificial data indicate that this method allows one to find correlations that span short periods of time within the event length. The results found now are quite different from the time-independent analysis; on average, we found that ATs have higher mean  $H$  values than QTs. The mean self similarity index for QTs was found to be  $\langle H(t)_{QT} \rangle = 0.73 \pm 0.05$  and for ATs,  $\langle H(t)_{AT} \rangle = 0.87 \pm 0.06$ . Indicating that, on average, higher correlation of the magnetic field fluctuations is expected during active magnetospheric periods. Fig. 5 shows the time-dependent distributions of the mean  $H$  for QTs and ATs as a function of the event length. In this case the student-t test applied to the time dependent analysis for QT and AT found  $p = 2.79e - 9$ , implying that the differences in the statistics of the averaged  $H(t)$  for the computed quiet and active events are significant.

### 5. Conclusions

We have presented an attempt to characterize the fractal behavior of the bulk magnetic field time series obtained from a single ground based observatory. Previous works reported the existence of multiscale statistics in a variety of geomagnetic indices [29, 13, 33, 32, 31] and in the interplanetary magnetic field [4, 5], [20] and [7] previously reported changes in stat-

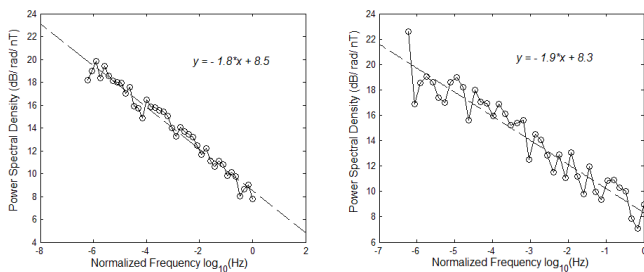


**Fig. 3.** Power spectral density for the quiet event of 1999, day of year 31 with slope  $b = 1.8$  (left) and active event of 1995, day of year 122 with slope  $b = 1.9$  (right). The mean  $Kp$  values for these QT and AT were 0.3 and 5.2 respectively.

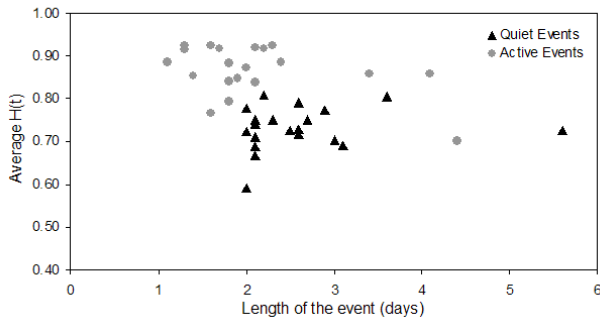


**Fig. 5.** Distributions of the time average Hurst coefficients for quiet and active events vs. the event length. No direct dependences were found that the average Hurst exponent is affected by the duration of the event. The average Hurst exponent for quiet times is  $\langle H_{QT} \rangle = 0.73 \pm 0.05$  and for active times  $\langle H_{AT} \rangle = 0.87 \pm 0.06$ .

istics of the earth's magnetic field in association with different levels of magnetospheric activity. They examined the scaling properties of the magnetic field fluctuations in the magnetotail and found evidence of multifractality with a Hurst coefficient of  $H \sim 0.5$  before current disruption and  $H \sim 0.7$  after current disruption.

In this study we classified the data into quiet and active periods using the  $Kp$  index as the discriminator. DFA was the technique selected due to its performance in dealing with non-stationary data. In terms of the time-dependent monofractal approach the differences presented between QT and AT are less clear, suggesting that the fingerprints of local magnetic activity are not conserved during the time scale of a particular quiet or active event as determined by our selection criteria. On average, we found  $\langle H_{QT} \rangle = 0.52 \pm 0.06$  and  $\langle H_{AT} \rangle = 0.51 \pm 0.05$  for quiet and active times respectively. This is indicative that on relatively long timescales both QT and AT are uncorrelated Brownian noise. This led us to consider the prospect that these data are multifractal, i.e. the scaling exponent changes as a function of time.

The possibility of correlated patches led us to investigate shorter window sizes. By sliding this window along the time series we were able to determine the temporal fluctuations in the Hurst exponent for each data set. Averaging all the  $H$  values found in each particular event we were able to distinguish clear differences in the statistical processes for both types of events. Results from this approach showed that both QTs and ATs have stronger correlations far from a random walk as was suggested by the previous monofractal approach. The mean Hurst exponent  $H(t)$  for quiet events was  $\langle H(t)_{QT} \rangle = 0.73 \pm 0.05$  and for active events  $\langle H(t)_{AT} \rangle = 0.87 \pm 0.06$ . As these results show, the correlation is high while the error in the determination of  $H(t)$  is about 6%, and overlap exists between the values of the temporal  $H$  for both types of event. The Students-t test returned results consistent with our expectations (i.e., quiet and active event data come from different populations). The time-dependent, or multifractal approach, showed that the statistics of the local magnetic field are not steady and changes through different levels of correlation, indicating that

this correlation increases as the level of geomagnetic activity increases. It appears that the magnetic field at a single high latitude location is best described as a mfBm rather than as a fBm process. This can serve as a guide suggesting the required statistical structure for mathematical models of magnetospheric activity. We also offer a possible explanation relating the physics of QT and AT with their different Hurst exponents. Our results are consistent with [8] who examined scaling properties of magnetic fluctuations in the magnetotail. They consistently found a lower scaling exponent before current disruption, followed by higher values afterward. They interpreted the change in scaling exponent as a reorganization during current disruption.

Further research will focus on the time where a transition from quiet to active event occurs. We do not distinguish between global and local-time effects so future studies will consider how the variability of Hurst exponent is affected by different local time selections. Whether or not local-time effects result in Hurst exponent variability does not affect our major conclusions.

## 6. Acknowledgments

This material is based on work supported by the National Science Foundation under Grants No. 0449403/0417690. The CANOPUS instrument array was constructed and is maintained and operated by the Canadian Space Agency. We are grateful to them for making high-quality data readily available via the CANOPUS website. SDG.

## References

- Allen, J., Frank, L., Sauer, H., Reif, P., Effects of the March 1989 solar activity, *EOS Trans. AGU*, 70, 1479, 1989.
- Bartels J., Discussion of time variations of geomagnetic indices  $Kp$  and  $Ap$ , *Ann Geophysicae*, 19, 1, 19323-19361, 1963.
- Boteler, D. H., Pirjola R. J., and Nevanlinna H., The effects of geomagnetic disturbances on electrical systems at the earth's surface, *Advances in Space Research*, 22, 17-27, 1998.
- Burlaga L. F. and Mish W. H., Large-Scale fluctuation in the interplanetary medium, *J. Geophys. Res.*, v 92, A2, 1261-1266, 1987.
- Burlaga L. F., Multifractal structure of the interplanetary magnetic field, Voyager 2 observations near 25 AU, 1987-1988, *Geophys. Res. Lett.*, 18(1), 69, 1991.
- Burton, R. K., McPherron R. L. and Russell, C. T., An empirical relationship between interplanetary conditions and Dst, *J. Geophys. Res.*, 80, 4204, 1975.
- Consolini G., De Michelis P., and Meloni, A., Multifractality and punctuated equilibrium in the Earth's magnetic field polarity reversals, *Geophys. Res. Lett.*, 27, 293-296, 2000.
- Consolini, G., and A. T. Y. Lui (2000), Symmetry breaking and nonlinear wave-wave interaction in current disruption: Possible evidence for a phase transition, in *Magnetospheric Current Systems*, *Geophys. Monogr. Ser.*, vol. 118, edited by S.-I. Ohtani et al., p. 395, AGU, Washington, D. C.
- Daglis I. A., Kozyra J. U., Kamide Y., Vassiliadis D., Sharma A. S., Liemohn M. W., Gonzalez W. D., Tsurutani B. T., Lu G., Intense space storms: Critical issues and open disputes, *J. Geophys. Res.*, v 108, A5 1208, 2003.

10. Gonzalez, W. D., Joselyn, J. A., Kamide, Y., Kroehl, H. W., Rostoker, G., Tsurutani B. T., and Vasyliunas V. M., What is a geomagnetic storm?, *J. Geophys. Res.*, v 99, A4, 5771-5792, 1994.
11. Gosling J. T., McComas, D. J. Phillips, J. L. and Bame S. J., Geomagnetic activity associated with Earth passage of interplanetary shock disturbances and coronal mass ejections, *J. Geophys. Res.*, 96, 7831, 1991.
12. Hergarten, S., Self-organized criticality in earth systems, *Springer Academic Press*, 49, 2002.
13. Hnat B., Chapman S. C., Rowlands G., Watkins N. W., and Freeman M. P., Scaling in long term data set of geomagnetic indices and solar wind ? as seen by WIND spacecraft, *Geophys. Res. Lett.*, v30, 22, 2174-2178, 2003.
14. Huttunen, K. E. J., Koskinen, H. E. J., Pulkkinen, T. I., Pulkkinen A., Palmroth M., Reeves, E. G. D., and Singer H. J., April 2000 magnetic storm: Solar wind driver and magnetospheric response, *J. Geophys. Res.*, v 107, A12, 1440-1461, 2003.
15. Iyemori T. and Hiroshi M., Impulse response of geomagnetic indices to interplanetary magnetic field, *J. Geomag. Geoelectr.*, 31, 1-9, 1979.
16. Kamide Y., Baumjohann W., Daglis I. A., Gonzalez W. D., Grande M., Joselyn J. A. McPherron R. L., Phillips J. L., Reeves E. G. D., Rostoker G., Sharma A. S., Singer H. J., Tsurutani B. T. and Vasyliunas V. M., Current understanding of magnetic storms: Storm-substorm relationships, *J. Geophys. Res.*, v 103, A8, 17705-17728, 1998.
17. Kantelhardt J. W., Zschiegner S. A., Koscielny-Bunde E., Bunde A., Havlin S., and Stanley, H. E., Multifractal detrended fluctuation analysis of nonstationary time series, *Physica A*, 316, 87, 2002.
18. Kivelson, M. and C. T. Russell, *Introduction to Space Physics*, Cambridge University Press, Cambridge, 1995.
19. Kugblenu S., Taguchi S. and Okuzawa T., Prediction of the geomagnetic storm associated Dst index using an artificial neural network algorithm, *Earth planets Space*, 51, 307-313, 1999.
20. Ohtani, S., Higuchi T., Lui, A. T. Y., and Takahashi, K., Magnetic fluctuations associated with tail current disruption: Fractal analysis, *J. of Geophysical Research*, 100, A10, 19135-19145, 1995.
21. Peltier, R. and J. Levy Vehel, Multifractional Brownian motion: Definition and preliminary results, *Technical report INRIA 2645*, 1995.
22. Peng, C.-K., S. Havlin, H. E. Stanley, A. L. Goldberger, Quantification of scaling exponents and crossover phenomena in non-stationary heartbeat timeseries, *Chaos*, 5(1), 8287, 1995.
23. Rangarajan, G. K. and Iyemori T, Time variations of geomagnetic activity indices Kp and Ap: an update, *Ann. Geophysicae*, 15, 1271-1290, 1997.
24. Richardson, I. G., Cliver, E. W., Cane, H. V., Sources of geomagnetic storms for solar minimum and maximum conditions during 1972-2000, *Geophys. Res. Lett.*, 28, 2569, 2001.
25. Russell, C. T., McPherron R. L. and Burton P. K., On the cause of geomagnetic storms, *J. Geophys. Res.*, 79, 1105, 1974.
26. Stanley, H. E., Amaral, L. A. N., Goldberger, A. L., Havlin, S., Ivanov, P. Ch., and Peng, C. K., Statistical physics and physiology: monofractal and multifractal approaches, *Physica A*, 270 309-324, 1999.
27. Takalo J., Timonen J., Klimas A., J Valdivia and Vassiliadis D., Nonlinear energy dissipation in a cellular automaton magnetotail field model, *Geophys. Res. Lett.*, 26, 13, 1813-1816, 1999.
28. Tsurutani, B. T., Gonzalez, W. D., Tang, F., and Lee Y. T., Great magnetic storms, *Geophys. Res. Lett.*, 19, 1, 73-76, 1992.
29. Vrs Z., On multifractality of high-latitude geomagnetic fluctuations, *Ann. Geophysicae*, 18, 1273-1282, 2000.
30. Wanliss, J. A. and P. Dobias, Space Storm as a Phase Transition, in review *J. Of Physics A*, 2006.
31. Wanliss, J., Fractal properties of SYM-H during quiet and active times, *J. of Geophysical Research*, 110, A03202, doi:10.1029/2004JA010544, 2005.
32. Wanliss, J. A., Nonlinear variability of SYM-H over two solar cycles, *Earth Planets Space*, 56, e13-e16, 2004.
33. Wanliss and Reynolds, Measurement of the stochasticity of low-latitude geomagnetic temporal variations, *Ann. Geophysicae*, 21, 1-6, 2003.
34. Weigel R. S., Vassiliadis D., Klimas A. J., Coupling of the solar wind to temporal fluctuations in ground magnetic fields, *Geophys. Res. Lett.*, 29, 19, 1915, 2002.



# IMAGE analysis and modelling of substorm onsets

J. A. Wanliss and G. Rostoker

**Abstract:** We consider the list of substorm 'onsets' from the IMAGE satellite and use the recent Tsyganenko models (T96, T01) to map these ionospheric locations into the magnetotail. We investigate, in a statistical fashion, the source region of the auroral arc that brightens at the onset of expansive phase. This arc is usually identified as the ionospheric signature of the expansive phase onset that occurs in the magnetotail. The arc that brightens maps to a most likely downtail position of  $X_{GSM} = -6.6 \pm 0.2R_E$ . Mappings during space storms are even closer to the earth;  $X_{GSM} = -4.7 \pm 0.1R_E$ . These results can be interpreted in two ways. First, onsets are initiated in the near-earth magnetotail, typically within geostationary orbit. Second, the mappings are too close to the earth, so the Tsyganenko models are insufficiently stretched in these regions. Finally, we used CANOPUS data to demonstrate that the IMAGE onset list contains auroral brightenings that are not classical substorm onsets, but are actually poleward border intensifications.

*Key words:* Substorms, modelling, PBI.

## 1. Introduction

Many event studies have considered the location in the magnetotail of the substorm expansive phase ignition site or zone [14, 9, 10, 7, 3, 4, 2]. Several of these studies used satellite data and the Tsyganenko models to study various aspects related to substorms, for example to map ionospheric auroral brightenings to the distant location in the magnetotail. The statistical samples were very small; so for example, in their work Pulkkinen et al. [10] found it difficult to paint a coherent picture in mapping of individual substorm auroral arcs.

The magnetospheric location of the expansive phase onset is important since mechanisms that may be responsible for the onset of instability, for example the Kelvin-Helmholtz instability [?] or the kinetic ballooning instability [1], to name only two possible candidates, are strongly dependent upon spatially variable parameters such as plasma density and magnetic field strength. Frank and Sigwarth [4] and Erickson et al. [3] used the Polar and CRRES satellites, respectively, to present evidence that expansive phase is triggered as close as 4 to 7  $R_E$  from the Earth. This was consistent with earlier evidence from ground-based data presented by Samson et al. [14], which suggested expansive phase onset occurs between 6 to 10  $R_E$ . Recently, Dubyagin et al. [2] used data from the FAST satellite and ground-based instruments, along with a mapping via the Tsyganenko magnetic field model [18] to provide evidence of a near-earth breakup location. Wanliss [25] recently used data from many isolated substorms compiled over the most recent solar cycle to map onsets to about 14  $R_E$  downtail. All indications are that the onset location is usually very close to the Earth.

In this paper we extend these studies through the use of the recently available list of substorm onsets [5] estimated from the IMAGE FUV instrument. Rather than considering detailed event studies, this paper describes the extension of mapping efforts that include multiple substorms from an ionospheric perspective. As was the case for previous small sample event

studies (e.g. [14, 9, 10, 8, 3, 4, 2]), we trace back from the ionosphere along the magnetic field lines to pinpoint the magnetospheric location of the ignition site. Although it is difficult to accurately map the onset location to the magnetotail, we believe that the statistical nature of the investigation will provide an average onset location consistent with reality. In addition, mapping of the onset arcs from the ionosphere to the plasma sheet was performed with several different models than those used in the studies mentioned above. We employed the empirical magnetospheric magnetic field models of Tsyganenko [15, 16, 18, 20, 21, 22], and make comparisons between mappings produced by the various models (hereinafter referred to as T87, T89, T96, T01).

## 2. Models

The models of N. A. Tsyganenko and his collaborators are widely used [15, 16, 18, 20, 21, 17]. Since substorm time scales are so short, and the Tsyganenko models are averages, it is not strictly appropriate to use them to study substorms, even though they have been commonly used in this manner, as noted above by many references. During the expansive phase of substorms it is almost certainly inappropriate to use the Tsyganenko models, since this is when dramatic and highly dynamic processes such as dipolarization and particle injections occur. But the growth phase is quite different. Steady equatorward motion of the auroral oval during growth phase is associated with slow stretching of the inner magnetotail field [23]. We assume that during the growth phase stretching of the tail and plasma sheet thinning take place without a major reconfiguration of magnetic field lines. This is not an unreasonable assumption, and several studies have shown how this is consistent with observations [6, 24]. Wanliss [25] exploited this loophole to map onset locations for several hundred substorms. The important thing to note is that mapping was done during substorm growth phase when slow changes ensure that the models are most likely to provide results that are within reason. Since the IMAGE list [5] gives the location of the centre of the arc that brightens the real location of the onset, i.e. the location of the most equatorward arc that brightens, is always equatorward of the location given in the IMAGE list. We are nevertheless

Received 15 May 2005.

J. A. Wanliss, ERAU, Daytona Beach.

G. Rostoker, University of Alberta, Department of Physics

able to obtain an *upper limit* to the downtail location of the mapped IMAGE ionospheric brightening.

For the purposes of this work we have used T96 and T01 models. T01 is supposed to be the most realistic model, especially in mapping the inner magnetotail. We used T96 since T01 is only strictly valid earthward of 15 RE, and onset sites could be further downtail where the other models are valid. Secondly, even though T01 is ostensibly the best model, it is also the least used. It was not used in any of the event studies listed above, so the results found here could cast a cautionary or different light on previous work.

Whereas the models prior to T96 did not have a pre-defined magnetopause and were calibrated exclusively by the magnetic dipole tilt and Kp index, the T96 and T01 models explicitly include (i) the solar-wind controlled magnetopause, (ii) region 1 and 2 Birkeland currents, and (iii) the interconnection of the magnetospheric and solar wind fields at the boundary. They include further parameterization with the solar wind dynamic pressure, DST-index, and interplanetary magnetic field By and Bz.

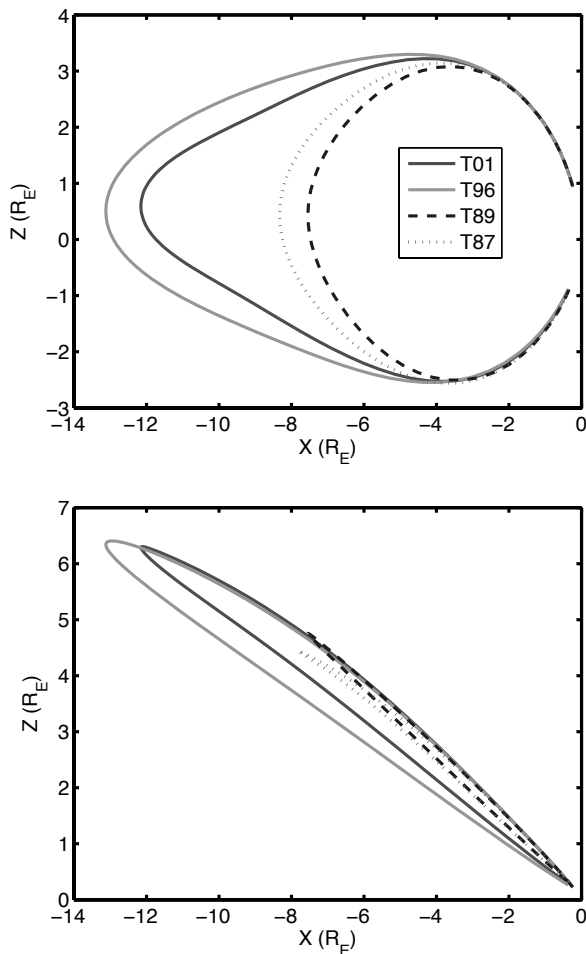


**Fig. 1.** Meridian plots of the model magnetic field lines mapped from the ionospheric onset location to the magnetotail for the April 30, 2002 brightening at 05:50:52 UT.

The earlier models appear to be too stretched in the inner

magnetosphere as compared to in-situ observations, particularly during active times. The most recent model, namely T01, is probably the best suited to determine onset locations, since previous observations suggest that substorm onset occurs in the inner magnetotail. In fact, T01 was intended primarily to improve the description of the inner magnetospheric field ( $X \geq -15R_E$ ), and unlike the previous models, includes in the modeling database measurements from within geostationary orbit. T01 follows the same approach as in T96, but uses an improved approximation for the ring current field [20].

Figure 1 shows two different cross-sectional views of model magnetic field lines that map from the ionospheric onset position for the April 30, 2002 image brightening that occurred at 05:50:58 UT. The magnetospheric source of the auroral precipitation is understood to map along the corresponding magnetic field line to its greatest radial distance from the Earth. The T87 and T89 model results are also shown, and these map much closer than do the T96 and T01 models. The latter two models include field-aligned currents which may be responsible for the mapping differences. Furthermore, when mappings are so close to the Earth, it has been shown that T87 and T89 require modifications to take into account the behavior of the inner magnetotail and plasma sheet, which call into question the validity of these earlier models unless suitably modified during late growth phase [9, 10, 12]. Note that the models also predict quite different flankward (Y) positions.

### 3. Results

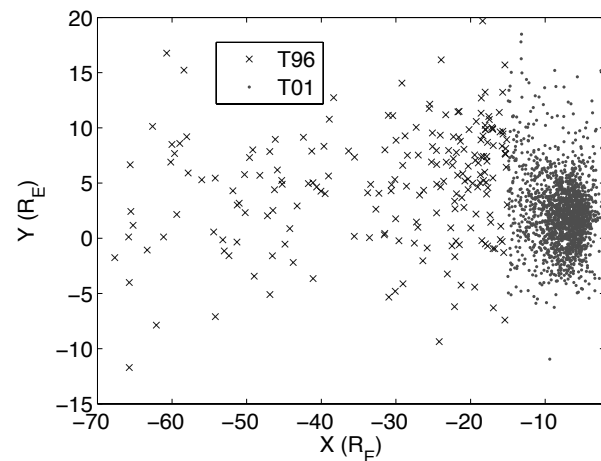


**Fig. 2.** Location of the model mapped brightenings in X-Y plane. T96 mappings are indicated with crosses and T01 mappings with dots.

Because the differences in the field configuration during quiet and disturbed times are large, it is essential that the effects of varying geomagnetic activity be taken into account in the mapping studies. However, the T87 and T89 models are parameterized by the Kp index which is a three-hour average. Thus the veracity of these two models is expected to be inferior to results from T96 and T01. We were able to perform mappings for 2588 events between May 2000 and April 2003.

In Figure 2 the model onset locations are projected onto the  $X - Y$  plane. T01 mappings are shown by the dots. The T96 mappings (crosses) were selected for the cases where the mapping was tailward of T01 applicability (i.e.  $-15 R_E$ ). As found by Wanliss [25] there is a clear preference for the auroral brightenings to map to the dusk side of the magnetotail, and each of the pre-midnight brightenings map to the dusk side.

Figure 3 shows the relationship between the mapped locations of the IMAGE brightenings as a function of Dst. The light curve (bottom) shows the results when sorted for their dates between October-March. The darker curve is the result for brightening between April-September. Since all the brightenings mapped were from the geographic northern hemisphere this plot seems to indicate a difference between the 'summer' (April to September) and 'winter' brightenings. The summer brightening occur at consistently less negative Dst values; i.e. the same value of the downtail mapped distance ( $X_{GSM}$ ) is achieved for smaller Dst values during summer. There is also a clear change of the curves for brightenings that occur during space storms ( $Dst \leq -30 nT$ ). In this case the onset or brightening locations map much closer to the earth, within geostationary orbit.

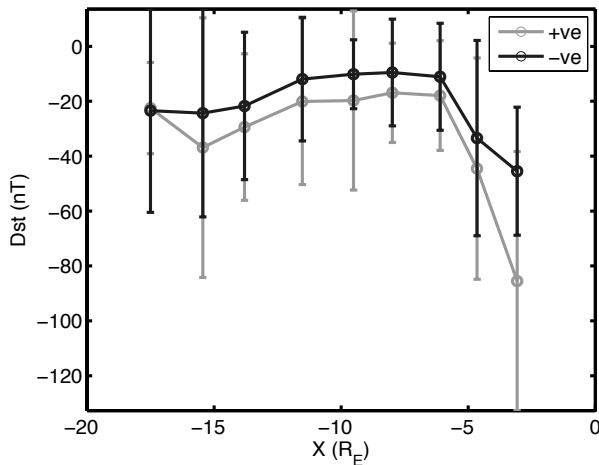


**Fig. 3.** Mapped locations of the IMAGE brightenings as a function of Dst. The light curve (bottom) shows the results when sorted for their dates between October-March. The darker curve is the result for brightening between April-September.

Finally, Figure 4 shows the most probable location of the downtail mapping. The dark curve shows the normalized result for all 2588 mappings, and the light curve shows the normalized result for space storm time mappings only. The most probable location of the mapped auroral brightening tends to be slightly closer to the earth during storms. For all data  $X_{GSM} = -6.6 \pm 0.2 R_E$  and for storms (480 events)  $X_{GSM} = -4.7 \pm 0.1 R_E$ .

#### 4. Conclusions

Taken at face value, these results suggest that enormous stretching of the magnetotail is possible during substorms. The most

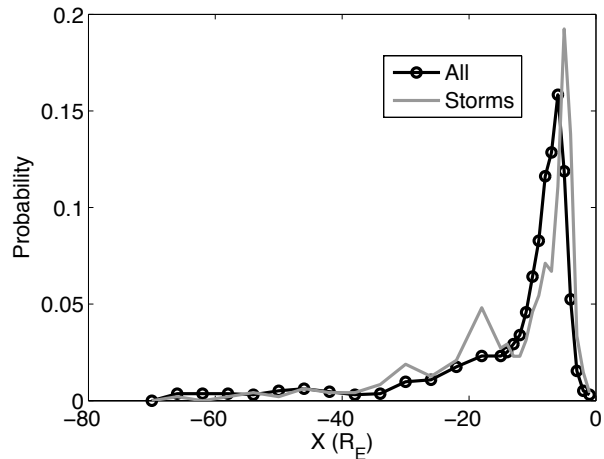


**Fig. 4.** Most probable mapped downtail location of the auroral brightenings. The dark curve shows the normalized result for all 2588 mappings, and the light curve shows the normalized result for space storm time mappings only.

probable mapped downtail distances are consistent with results of Frank and Sigwarth [4] that place the onset location near the ring current. They are also consistent with the results of Tsyganenko [22] "that during storms with  $DST < -250$  nT the tail-like deformation of the nightside field penetrates so close to Earth that the quasidipolar approximation breaks down at distances as small as  $3-4 R_E$ ." In fact, if these results are realistic, then the tail is potentially even more stretched, since the IMAGE list gives the location of the centre of the arc that brightens [5]. If the brightening corresponds to a substorm, the real location of the onset will always be equatorward of the location given in the IMAGE list. Thus magnetic field stretching at the end of the growth phase will be even more severe than our results indicate.

Additional caveats are also in order. Figure 5a shows an auroral brightening listed as a substorm in the Frey list [5], for 30 April 2002 at 05:50:58 UT. The brightening occurs at geographic latitude and longitude of 59.53 and 251.44 degrees. The Tsyganenko model topologies for this event are shown in Figure 1. Figure 5b shows the IMAGE FUV data 6 minutes later. The original brightening is still visible, but there is an additional brightening that occurs at higher latitude and westward of the initial one. We examined CANOPUS magnetometer latitude and longitude profiles (not shown) which indicate a substorm onset just after 05:00 UT, long before the image brightening. The signal for the westward electrojet is very clear prior to the image brightening, as shown in the latitude profile at 05:49 UT in Figure 6a. It is most obvious in the  $X$ -component trace with a deep minimum near 64 degrees AACGM latitude, which remained stable at that latitude since at least 05:44 UT. A smaller minimum is observed near 70 degrees, which is a possible signature of the beginnings of a poleward border intensification (PBI). The profile at 05:53 UT shows the same two minima, but the poleward minimum has increased five-fold. The auroral brightening associated with this higher latitude current system, near the poleward edge of the oval, appears indicative of a PBI rather than an expansion phase onset.

These data clearly indicate the danger in relying on only one

data source and automated techniques of substorm onset identification. Rostoker [13] previously illustrated this danger by giving several examples of PBIs that might erroneously be interpreted as substorm onsets on the basis of their auroral signatures.

## 5. Acknowledgments

The CANOPUS instrument array was constructed and operated by the Canadian Space Agency. IMAGE FUV data are courtesy of CDAWeb and S. Mende at UC Berkeley.

## References

- Cheng, C.Z., and A.T.Y. Lui, Kinetic ballooning instability for substorm onset and current disruption observed by AMPTE/CCE, *Geophys. Res. Lett.*, 25, 4091–4094, 1998.
- Dubyagin, S. V., V. A. Sergeev, C. W. Carlson, et al., Evidence of near-Earth breakup location, *Geophys. Res. Lett.*, 30, 1282, doi:10.1029/2002GL016569, 2003.
- Erickson, G.M., N. C. Maynard, W. J. Burke, et al., Electromagnetics of substorm onsets in the near-geosynchronous plasma sheet, *J. Geophys. Res.*, 105, 25265–25290, 2000.
- Frank, L. A. and J. B. Sigwarth, Findings concerning the positions of substorm onsets with auroral images from the Polar spacecraft, *J. Geophys. Res.*, 105, 12747–12762, 2000.
- H.U. Frey, S.B. Mende, V. Angelopoulos, E.F. Donovan, Substorm onset observations by IMAGE-FUV, *J. Geophys. Res.*, 109, A10304, doi:10.1029/2004JA010607, 2004.
- Kaufmann, R.L., Substorm currents: growth phase and onset, *J. Geophys. Res.*, 92, 7471–7486, 1987.
- Kubyschkina, M. V., V. A. Sergeev, T. I. Pulkkinen, Hybrid Input Algorithm: An event-oriented magnetospheric model, *J. Geophys. Res.*, 104(A11), 24977–24994, 10.1029/1999JA900222, 1999.
- Lu, G., N. A. Tsyganenko, A. T. Y. Lui, et al., Modeling of time-evolving magnetic fields during substorms, *J. Geophys. Res.*, 104(A6), 12,327–12,338, 1999.
- Pulkkinen, T. I., A study of magnetic field and current configurations in the magnetotail at the time of a substorm onset, *Planet. Space. Sci.*, 39, 833–845, 1991.
- Pulkkinen, T. I., D. N. Baker, R. J. Pellinen, et al., Mapping of the auroral oval and individual arcs during substorms, *J. Geophys. Res.*, 100, 21987–21994, 1995.
- Pulkkinen, T. I., D. N. Baker, M. Wiltberger et al., Pseudobreakup and substorm onset, Observations and MHD simulations compared, *J. Geophys. Res.*, 103,14847–14854, 1998.
- Pulkkinen, T. I., D. N. Baker, L. L. Cogger, et al., Spatial extent and dynamics of a thin current sheet during the substorm growth phase on December 10, 1996, *J. Geophys. Res.*, 104, 28475–28490, 1999.
- Rostoker, G, Identification of substorm expansive phase onsets, *J. Geophys. Res.*, 107, doi:10.1029/2001JA003504, 2002.
- Samson, J.C., et al., Proton aurora and substorm intensifications, *Geophys. Res. Lett.*, 19, 2167–2170, 1992.
- Tsyganenko, N. A., Global Quantitative Models of the Geomagnetic Field in a Cislunar Magnetosphere for Different Disturbance Levels, *Planet. Space. Sci.*, 35, 1347–1358, 1987.
- Tsyganenko, N. A., A magnetospheric magnetic field model with a warped tail current sheet, *Planet. Space. Sci.*, 37, 5–20, 1989.
- Tsyganenko, N.A., M. Peredo, Analytical Models of the magnetic field of disk-shaped current sheets, *J. Geophys. Res.*, 99, 199, 1994.
- Tsyganenko, N. A., Modelling the Earth's magnetospheric magnetic field confined within a realistic magnetopause, *J. Geophys. Res.*, 100, 5599–5612, 1995.
- Tsyganenko, N. A., Effects of the solar wind conditions on the global magnetospheric configuration as deduced from data-based models, in Proceedings: *Third International Conference on Substorms (ICS-3)*, ed. E. J. Rolfe and B. Kaldeich, European Space Agency Spec. Publ., ESA SP-399, 181–185, 1996.
- Tsyganenko, N.A., A model of the near magnetosphere with a dawn-dusk asymmetry 1. Mathematical structure, *J. Geophys. Res.*, 107, 10.1029/2001JA000219, 2002a.
- Tsyganenko, N.A., A model of the near magnetosphere with a dawn-dusk asymmetry 2. Parameterization and fitting to observations, *J. Geophys. Res.*, 107, 10.1029/2001JA000220, 2002b.
- Tsyganenko, N.A., H.J. Singer, J.C. Kasper, Storm-time distortion of the inner magnetosphere; How severe can it get?, *J. Geophys. Res.*, 108, 10.1029/2002JA009808, 2003.
- Voronkov, I., E. Friedrich, and J.C. Samson, Dynamics of the Substorm Growth Phase as Observed using CANOPUS and SuperDARN Instruments, *J. Geophys. Res.*, 104, 28491–28505, 1999.
- Wanliss, J.A., J.C. Samson, and E. Friedrich, On the use of photometer data to map dynamics of the magnetotail current sheet during substorm growth phase, *J. Geophys. Res.*, 105, 27673–27684. 2000.
- Wanliss, J. A., Substorm onset location and dipole tilt angle, *Annales Geophysicae*, 24: 577–588, 2006.
- Yoon, P. H., J. F. Drake, A. T. Y. Lui, Theory and simulation of Kelvin-Helmholtz instability in the geomagnetic tail, *J. Geophys. Res.*, 101, 27327–27339, 1996.

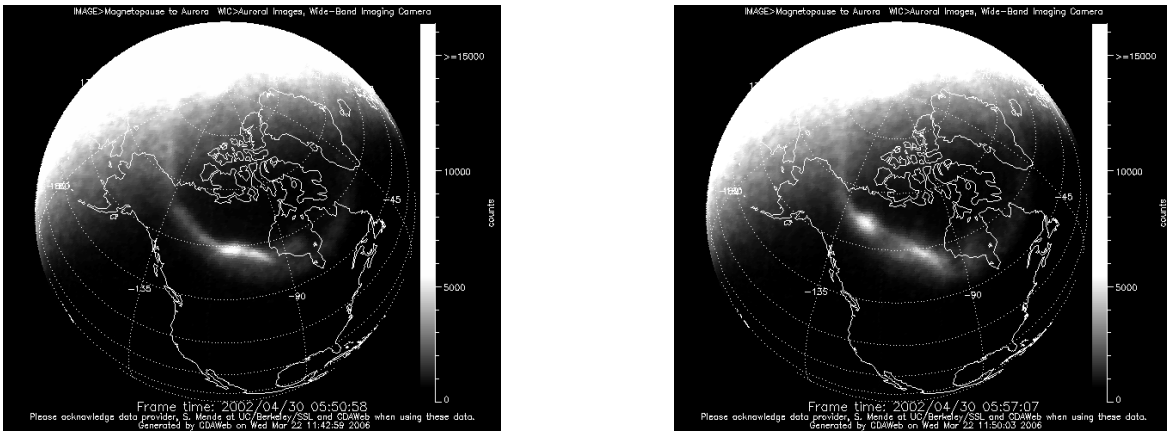


Fig. 5. IMAGE FUV observations of the auroral oval at (a.) 05:50:58 UT and (b.) 05:57:07 UT.

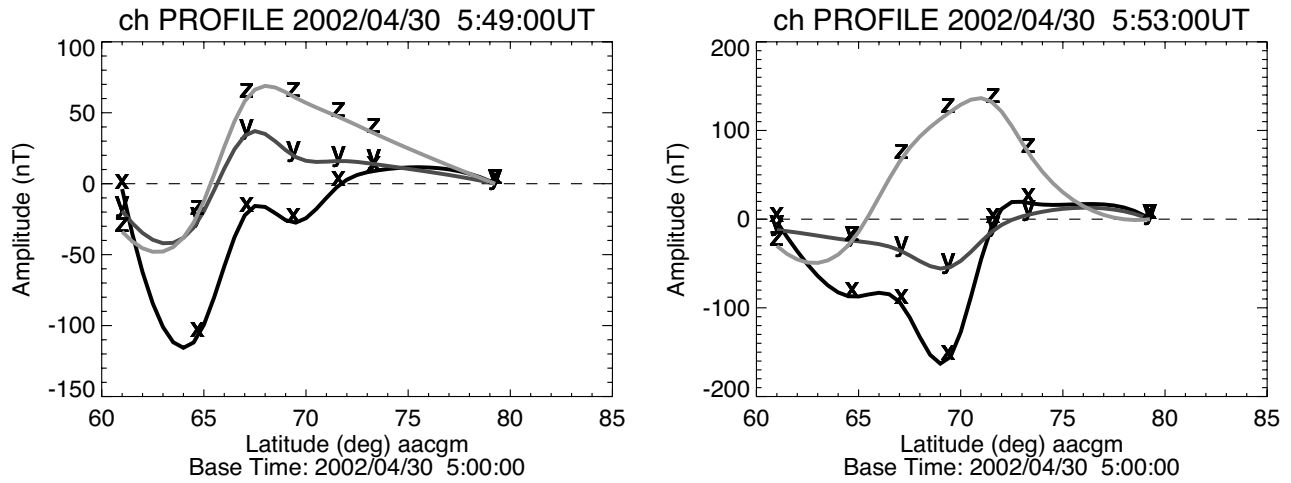


Fig. 6. CANOPUS magnetometer latitude profiles from the Churchill line at (a.) 05:49 UT and (b.) 05:53 UT.



# Five plus four equals nine: combining the THEMIS and Cluster missions

J. A. Wild and M. A. Hapgood

**Abstract:** THEMIS represents the most ambitious coordinated multi-spacecraft and ground-based programme ever attempted. It is expected that this mission will dramatically increase our understanding of the substorm process. In the years leading up to the launch of the five THEMIS probes, the four-spacecraft Cluster mission has defined the state of the art in the field of multi-spacecraft/ground-based investigations of the geospace environment. Hitherto unprecedented coordination of space- and ground-based experiments have yielded multi-point (in situ and remotely sensed) measurements of magnetospheric structure and dynamics. The overlap of the Cluster and THEMIS missions presents an excellent opportunity to move the multi-point measurement technique to the next stage. Since the apogees of the Cluster and THEMIS satellites orbits are separated by nearly 12 hour of local time, the synergy of these two missions and ground-based experiments will allow the detailed observation of solar wind-magnetosphere-ionosphere on both the day and nightside of the Earth. Several experimental scenarios will be presented.

*Key words:* Cluster, THEMIS.

## 1. Introduction

Cluster is the first multi-spacecraft magnetospheric satellite mission [2, 3] to yield three-dimensional measurements of the geospace environment and allow the resolution of spatial/temporal ambiguities inherent in single-spacecraft observations. It is now operating in the extended phases of its mission and is scheduled to continue until 2010. The four identical Cluster satellites orbit the Earth in highly elliptical ( $4\text{--}20 R_E$ ) polar orbits with periods  $\sim 57$  hours that precess through twenty four hours of local time every twelve months. Cluster is also unusual in that it was one of the first missions to include planning for coordinated ground-based measurements from an early stage in the mission's design [8, 9]. This coordination has resulted in a plethora of Cluster/ground-based studies [1].

Following launch in October 2006, the five THEMIS (Time History of Events and Macroscale Interaction during Substorms) spacecraft will be manoeuvred into equatorial orbits with apogees of  $\sim 30 R_E$  (one spacecraft),  $\sim 20 R_E$  (one spacecraft) and  $\sim 10 R_E$  (three spacecraft) with orbital periods of  $\sim 4$  days,  $\sim 2$  days and  $\sim 1$  day, respectively.

The orbits of the THEMIS spacecraft (or "probes") have been selected such that at least three of the THEMIS probes become meridionally aligned every four days. In this arrangement, the spacecraft are in the optimum configuration to distinguish between competing substorm theories and it is estimated that over 180 hours of such alignments will occur each year [5]. Meanwhile, a network of ground-based auroral all-sky imagers (ASIs) and magnetometers in Canada and Alaska [4] will ensure that the probe alignments (at the substorm onset meridian)

can be scrutinized in detail using both in situ (satellite) and remotely-sensed (ground-based) observations.

The orbits of these ground-breaking missions are such that the apogees of the THEMIS probes and the Cluster spacecraft are separated by  $\sim 11$  hours of magnetic local time, as indicated in Figure 1. Consequently, the space- and ground-based conjunctions arising during the coming years present unprecedented opportunities for multi-scale and multi-point measurements of solar wind-magnetosphere-ionosphere coupling. These are explored below.

## 2. Methodology

### 2.1. Predicted satellite positions

For the purposes of this investigation, predicted THEMIS orbital information (courtesy of S. Frey, UC Berkeley) has been compared to Cluster Predicted Geometric Position (PGP) data. In advance of the launch, the THEMIS orbital information must be considered as provisional. Similarly, the Cluster orbital information is also subject to change due to spacecraft manoeuvring. Nevertheless, these data allow a preliminary investigation to be carried out looking into the various configurations of multiple satellites and ground-based instruments. Therefore, while we shall present scenarios drawn from the preliminary orbital information, we shall consider them examples of generic conjunction configurations rather than an attempt to plan for specific dates and times.

### 2.2. Magnetic field mapping

The Tsyganenko 1996 (T96) model [12, 13] has been employed in order to estimate the magnetic conjugacy of the Cluster and THEMIS spacecraft with ground-based experiments. In each case, fixed input parameters corresponding to "average" solar wind and interplanetary magnetic field conditions have been used (specifically  $P_{SW}=2$  nPa,  $Dst=0$  nT, IMF  $B_Y=0$  nT, and IMF  $B_Z=0$  nT). The approximate fields-of-view of the THEMIS ASIs and the international network of SuperDARN coherent-scatter radars have also been considered.

Received 15 May 2006.

**J. A. Wild.** Space Plasma Environment and Radio Science Group, Department of Communication Systems, Infolab21, Lancaster University, Lancaster, LA1 4WA, UK.

*Corresponding author:* j.wild@lancaster.ac.uk

**M. A. Hapgood.** Rutherford Appleton Laboratory, Didcot, Oxfordshire, OX11 0QX, UK.

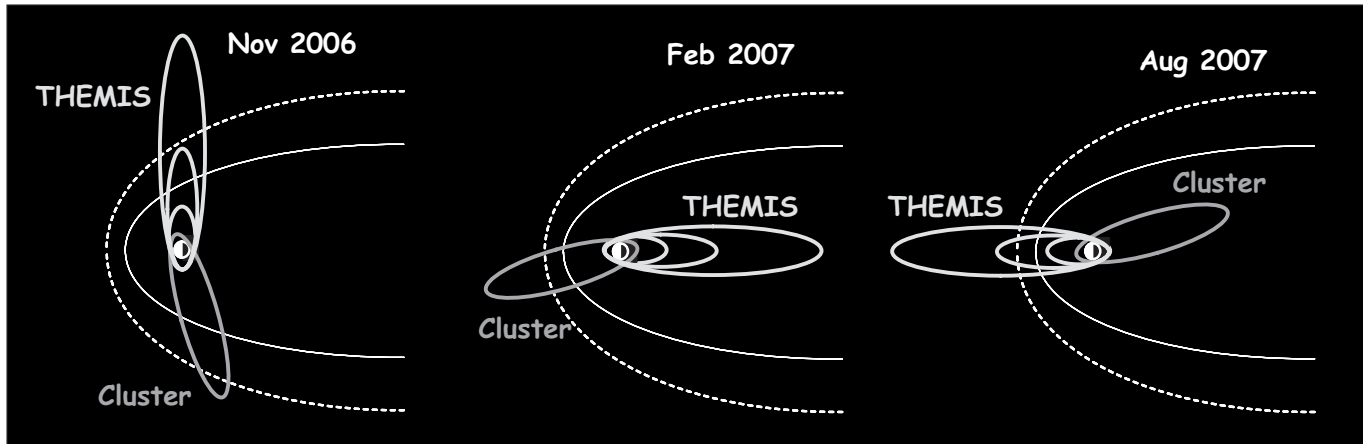


**Fig. 1.** The approximate configuration of the Cluster and THEMIS satellite orbits in the GSE X–Y plane during Nov 2006 (shortly after launch), Feb 2007 (during the first planned THEMIS tail observations season) and August 2007 (during the first planned THEMIS dayside observation season).

### 3. THEMIS conjunctions in the magnetotail

As indicated above, when the apogees of the THEMIS spacecraft are in the terrestrial magnetotail, the four Cluster spacecraft pass through apogee in the solar wind (some 11 hours earlier in magnetic local time). Figure 2 shows the location of the THEMIS and Cluster spacecraft on 6 January (left) and 3 February (right) 2007, when the THEMIS spacecraft align meridionally in the post-midnight and midnight regions.

The format of Figure 2, used throughout this paper, is as follows. For each date/time included, four sub-panels are shown. These present the location of the THEMIS probes (square symbols) and the Cluster spacecraft (circular symbols) in the GSM X–Z and X–Y planes. For comparison, field lines of the T96 model magnetic field model (in the GSM  $Y=0$  and  $Z=0$  planes) are also shown. The magnetic footprint of each spacecraft (square symbols for THEMIS and circular symbols for Cluster) at an altitude of 100 km are indicated in both the northern and southern hemispheres. The footprint panels are presented in magnetic latitude/magnetic local time coordinates centred upon the geomagnetic poles with midnight located at the bottom, dawn to the right, noon at the top and dusk at the left of each panel. This applies to both the northern and southern hemispheres such that the Antarctic coastline appears as if viewed from above the northern magnetic pole in order to preserved the midnight-dawn-noon-dusk position in each plot. Overlaid on the footprint panels are the approximate fields-of-view of the THEMIS ASIs (white circles) and the fields-of-view of the 10 northern hemisphere and 7 southern hemisphere SuperDARN radars [6] currently in operation (shaded grey). We note that, in general, the inter-spacecraft separation of the Cluster satellites is sufficiently small ( $\sim 1 R_E$ ) that the individual spacecraft cannot be resolved on the scale of the figures used in this paper. Furthermore, the preliminary THEMIS orbital data places probes 3 and 4 in close orbits such that they cannot be resolved in the figures presented here.

During both of the meridional alignments presented in Figure 2, the THEMIS probes are magnetically conjugate to the Canadian sector such that the probes' magnetic footprints lie within the fields-of-view of the THEMIS ASI array. Such con-

figurations are the primary goal of the mission and occur approximately every four days. In the two examples shown, separated by about 1 month, the probes are aligned in the pre-midnight (6 January) and midnight (3 February) sectors. On both occasions, the four Cluster spacecraft are located upstream of the dayside magnetopause and can therefore provide detailed three-dimensional measurements of the field and plasma environment in the magnetosheath/solar wind. Such observations will remove the timing ambiguities inherent in applying propagation delays to single-point solar wind/IMF measurements traditionally made in the vicinity of the L1 position some  $225 R_E$  upstream of the Earth and will allow the detailed investigation of the solar wind/IMF drivers and possible triggers of magnetospheric substorms.

Note also the coverage of the SuperDARN radar network during such conjunctions. In addition to the obvious (and invaluable) overlap of the THEMIS ASI array and the SuperDARN radars in the Canadian and Alaskan sectors, the CUTLASS [7] and Kurguelan SuperDARN radars provide coverage of the dayside cusp region in the northern and southern hemispheres, respectively. As such it will be possible to monitor the ionospheric signatures of dayside reconnection - the driving force behind magnetospheric substorms - while simultaneously observing the ionospheric flows within the fields-of-view of the THEMIS ASIs. Furthermore, global estimates of ionospheric convection pattern in both hemispheres derived from SuperDARN data [10, 11] will provide global context to the remotely-sensed and in situ observations of the magnetotail.

Figure 3 presents a pair of THEMIS tail conjunctions similar to those shown in Figure 2. However, in these cases, the Cluster spacecraft are passing through perigee at relatively low altitude ( $\sim 2-3 R_E$ ) on the nightside of the Earth. In the 14 January example (left hand side of Figure 3) the THEMIS and Cluster spacecraft come into close conjunction some 6 hours after the optimum THEMIS probe/ASI array alignment. Consequently, the THEMIS ASI array spans magnetic local times from midnight to noon across the dawn sector. Such conjunctions could be exploited to study morning sector auroral dynamics such as auroral  $\Omega$  bands by comparing magnetotail dy-

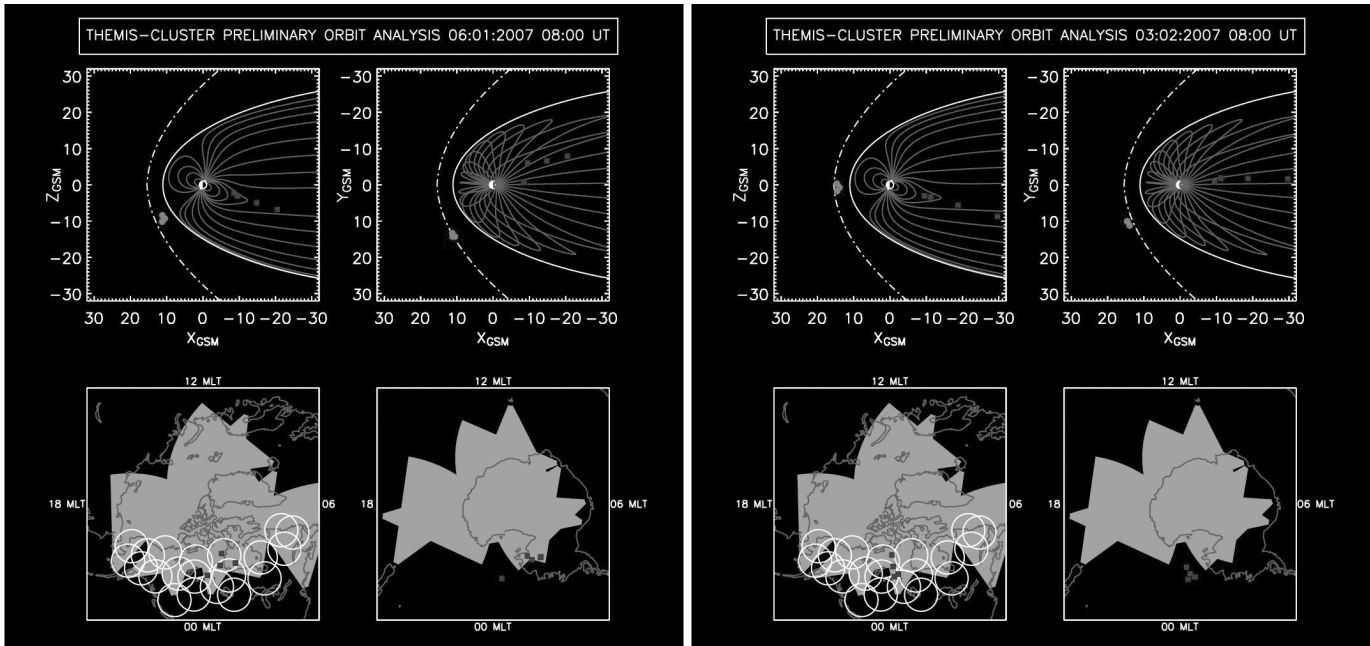


**Fig. 2.** THEMIS and Cluster locations and footprints on 6 January 2007 (left) and 3 February 2007 (right). In each case, the position of the THEMIS and Cluster spacecraft in the X–Z and X–Y GSM planes are indicated by square and circular plot symbols respectively. The T96 magnetospheric magnetic field configuration, is also shown in each case. The magnetic footprints of the spacecraft shown in the orbit panels are shown in both the northern and southern hemispheres. The footprint panels are presented in magnetic latitude/magnetic local time coordinates as described in the text. Overlaid on the footprint panels are the approximate fields-of-view of the THEMIS ASIs (white circles) and the fields-of-view SuperDARN radars.

namics (THEMIS), plasma dynamics in the auroral acceleration region (Cluster) and the auroral and ionospheric dynamics (THEMIS ASIs, magnetometers and SuperDARN).

The 7 February 2007 conjunction (right hand side of Figure 3) presents a similar arrangement of the THEMIS and Cluster spacecraft, save that in this example, the Cluster perigee pass has occurred during the primary midnight meridian THEMIS probe and ASI configuration. Given suitable substorm conditions, such a conjunction would result in multi-spacecraft measurements of the auroral acceleration region by Cluster at a similar magnetic local time as the radial distribution of THEMIS probes.

## 4. Dayside THEMIS conjunctions

### 4.1. Cluster in the nightside magnetosphere

Clearly, the THEMIS mission has been driven by a desire to understand the time-history of events in the magnetotail during magnetospheric substorms. However, for several months of each year, the apogees of two of the five probes will be located in the solar wind or magnetosheath. At these times, the azimuthal separation between the THEMIS and Cluster orbits is such that the Cluster spacecraft pass through apogee in the magnetic tail. In effect, when compared to the configuration presented in Figure 2, the roles of THEMIS and Cluster have been reversed; THEMIS now acts as an upstream solar wind monitor while Cluster observes the field and plasma processes and dynamics in the magnetotail.

Figure 4 shows two configurations of the THEMIS and Cluster spacecraft during the THEMIS dayside exploration season: 5

September 2007 (left) and 12 September 2007 (right). In each case, the Cluster spacecraft are passing through the plasma sheet region of the magnetotail in the vicinity of magnetic midnight. On the dayside, the THEMIS probes are distributed throughout the dayside magnetosphere, low-latitude boundary layer, magnetosheath and solar wind (depending upon the exact time selected). Once again, this will enable multi-spacecraft observations of the upstream solar wind, IMF and magnetosheath conditions that ultimately drive the substorm process without having to rely upon upstream measurements lagged to the dayside magnetopause.

While the orbits of the THEMIS probes will be arranged such that ground-based ASI array in the Canadian sector will straddle the midnight sector when the spacecraft are at apogee in the midnight sector (achieving multi-spacecraft conjunctions with various combinations of probes every 1, 2 and 4 days), the same is not true for the Cluster spacecraft. Indeed, with their 57 hour orbits, the location of the THEMIS ASI array when the Cluster satellites pass through apogee will vary from orbit to orbit. Nevertheless, interesting and potentially useful conjunctions between Cluster (in the plasma sheet) and the THEMIS ASI array occur in a significant fraction of Cluster orbits (at least half). The left hand side of Figure 4 presents an example of a “best case scenario” conjunction (which will occur 5 times per month) whereas the right hand side shows an example of partial conjunction with the THEMIS ASI array (which occur at a comparable frequency).

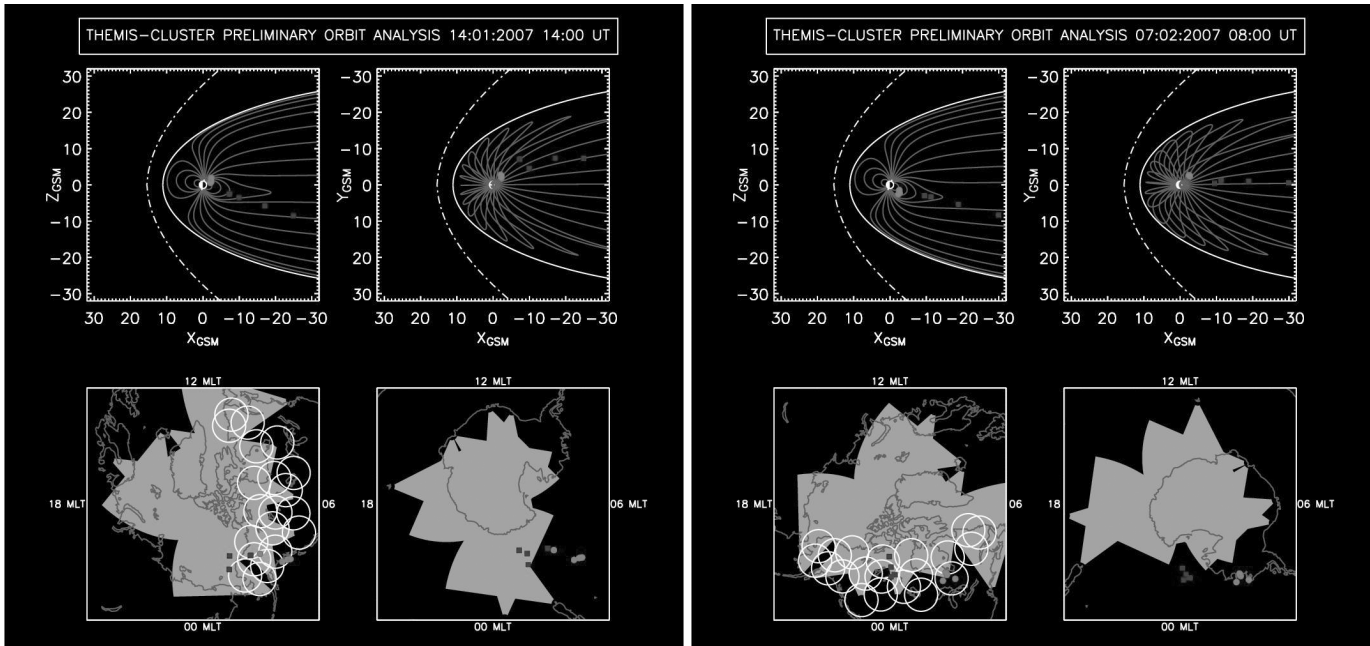


Fig. 3. Estimated THEMIS and Cluster locations and footprints on 14 January 2007 (left) and 7 February 2007 (right).

#### 4.2. Cluster in the dayside magnetosphere

Since the Cluster and THEMIS apogees are separated by  $\sim 11$  hours of magnetic local time, the separation between the THEMIS apogee and the Cluster *perigee* is  $\sim 1$  hour. Therefore, when the THEMIS orbit takes the probes into the dayside magnetosphere, magnetosheath and solar wind, the Cluster orbits take the spacecraft through the mid-altitude magnetospheric cusps in both hemispheres as they pass through perigee. This class of Cluster-THEMIS conjunction is perfectly suited to the investigation of dayside solar wind-magnetosphere-ionosphere coupling with spacecraft ideally placed to monitor the upstream/magnetosheath magnetic field, the low-latitude boundary layer, the low-latitude dayside magnetopause and the mid-altitude magnetospheric cusps.

Two examples are presented in Figure 5. During the conjunction on 16 September 2007 (left hand side of Figure 5), two of the THEMIS probes are located in the solar wind while their companions are sampling the low-latitude boundary layer and dayside magnetopause. Meanwhile, the four Cluster spacecraft are moving from low-to-high latitudes at mid-altitudes ( $\sim 2 R_E$ ) through the northern hemisphere cusp (having traversed the southern hemisphere cusp as the spacecraft move inbound to perigee  $\sim 1$  hour earlier). At perigee, the orbital motion of the four Cluster spacecraft causes the inter-spacecraft configuration to distort from the often-cited tetrahedral geometry and adopt a “string of pearls” arrangement. While this linear distribution of spacecraft compromises the capability to perform truly three-dimensional measurements, it does result in four traversals of very nearly the same region of space over a period of time slightly shorter than one hour. As such, the mid-altitude cusp crossings by the Cluster spacecraft are spread out in time, increasing the likelihood of a Cluster spacecraft being located in the cusp when one of the innermost THEMIS probes traverse or skim the low-latitude magnetopause.

The 23 September 2007 conjunction, presented on the right

hand side of Figure 5, demonstrates a further configuration of the THEMIS probes that might be exploited to investigate solar wind-magnetosphere-ionosphere coupling processes at the dayside magnetopause. In this case, the THEMIS probes make outbound traversals of the pre-noon sector low-latitude magnetopause in a “line abreast” formation. In the history of magnetospheric exploration, no other mission has offered the capability of sampling the dayside magnetopause at several local times within over a short time interval. In this case, the magnetopause crossings occur as the Cluster spacecraft traverse the southern hemisphere magnetospheric cusp.

This underlines the point that although the THEMIS mission is primarily optimized for space-ground coordination with instruments in the northern hemisphere (and the Canadian and the Alaskan sectors in particular), excellent conjunction will arise between the THEMIS probes, the Cluster spacecraft and ground-based experiments in the southern hemisphere. Clearly, since the THEMIS spacecraft probe the dayside magnetosphere, magnetosheath and solar wind during the northern hemisphere summer month, optical measurements of the cusp aurora will be not be possible using the THEMIS ASI array. However, optical instruments in the southern (winter) hemisphere will be able to make daytime measurements of the cusp aurora. Ionospheric radar observations (using both the coherent- and incoherent-scatter technique) and ground magnetometer measurements made in both hemispheres will also prove to be invaluable.

#### 5. Summary and conclusions

Above, we have presented several examples of favorable conjunctions between Cluster, THEMIS and ground-based experiments. While the THEMIS mission is primarily intended to study the timing of substorm dynamics in the magnetotail, it

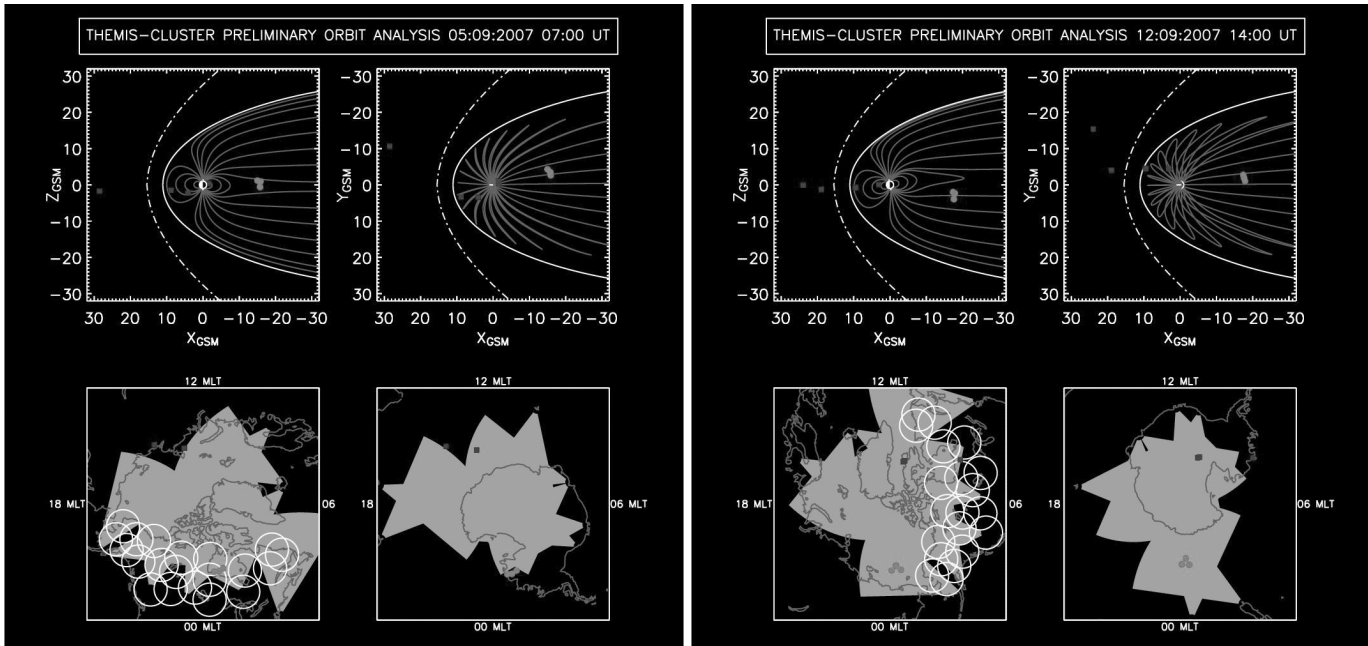


**Fig. 4.** Estimated THEMIS and Cluster locations and footprints on 5 September 2007 (left) and 12 September 2007 (right).

also presents a unique opportunity to investigate dayside coupling processes and the dynamics of the flank magnetopause (not shown). When combined with the multi-spacecraft Cluster mission and ground-based experiments with extended field-of-view, such as the international network of SuperDARN radars, the capabilities of this unique mission are enhanced greatly. In particular, the separation of the Cluster and THEMIS orbital apogees will allow the simultaneous observation of both dayside coupling and substorm dynamics. We note that uncertainties regarding the final orbits of the various spacecraft at the time of writing mean that specific examples may not occur at the exact dates/times indicated. However, the general arrangement of the various space- and ground-based instruments presented here will occur regularly and present unrivaled opportunities to investigate the dynamics of the terrestrial magnetosphere.

## 6. Acknowledgements

The authors would like to thank Sabine Frey (Space Physics Group, University of California, Berkeley), David Sibeck (Applied Physics Laboratory, Johns Hopkins University), and the THEMIS PI, Vassilis Angelopoulos (Space Physics Group, University of California, Berkeley) for their input. J. A. Wild gratefully acknowledges the support provided by the Royal Astronomical Society and the ICS8 Organising Committee in order to attend the ICS8 meeting.

## References

1. Amm, O., Donovan, E. F., Frey, H., Lester, M., Nakamura, R., Wild, J. A., Aikio, A., Dunlop, M., Kauristie, K., Marchaudon, M., McCrea, I. W., Opgenoorth, H. J. and Strømme, A., Coordinated studies of the Geospace environment using Cluster, satellite and ground-based data: An interim review, *Annales Geophysicae*, 23, 2129–2170, 2005.
2. Escoubet, C. P., Schmidt, R., and Goldstein, M. L., Cluster – science and mission overview, *Space Science Reviews*, 79, 391–391, 1997.
3. Escoubet, C. P., Fehringer, M., and Goldstein, M. L., The Cluster mission, *Annales Geophysicae*, 19, 1197–1200, 2001.
4. <http://aurora.phys.ucalgary.ca/themis/>
5. <http://sprg.ssl.berkeley.edu/themis/>
6. Greenwald, R. A., Baker, K. B., Dudeney, J. R., Pinnock, M., Jones, T. B., Thomas, E. C., Villain, J. P., Cerisier, J. C., Senior, C., Hanuise, C., Hunsucker, R. D., Sofko, G., Koehler, J., Nielsen, E., Pellinen, R., Walker, A. D. M., Sato, N., and Yamagishi, H., Darn/SuperDARN: a global view of the dynamics of high-latitude convection, *Space Science Reviews*, 71, 761–796, 1995.
7. Lester, M., Chapman, P., Cowley, S., Crooks, S., Davies, J., Hamadyk, P., McWilliams, K., Milan, S., Parsons, M., Payner, D., Thomas, E., Thornhill, J., Wade, N., Yeoman, T., and Barnes, R., Stereo CUTLASS - A new capability for the SuperDARN HF radars, *Annales Geophysicae*, 22, 459–473, 2004.
8. Lockwood M., and Opgenoorth H. J., Opportunities for magnetospheric research using EISCAT/ESR and Cluster, *Journal of Geomagnetism and Geoelectricity*, 47, 699–719, 1995.
9. Opgenoorth H. J., and Lockwood M., Opportunities for magnetospheric research with coordinated Cluster and ground-based observations, *Space Science Reviews*, 79, 599–637, 1997.
10. Ruohoniemi, J. M., and Greenwald, R. A., Statistical patterns of high-latitude convection obtained from Goose Bay HF radar observations, *Journal of Geophysical Research*, 101, 21746–21763, 1996.
11. Ruohoniemi, J. M., and Baker, K. B., Large-scale imaging of high-latitude convection with Super Dual Auroral Radar Network HF radar observations, *Journal of Geophysical Research*, 103, 20797–20811, 1998.

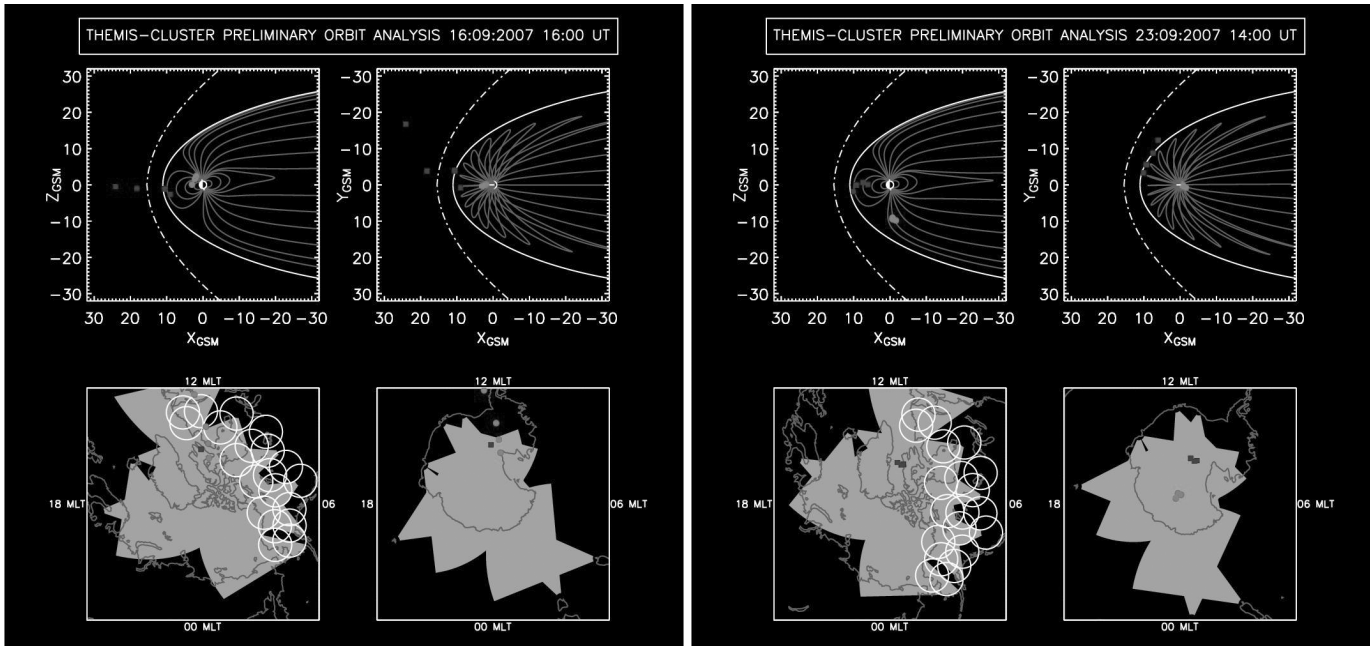


**Fig. 5.** Estimated THEMIS and Cluster locations and footprints on 16 September 2007 (left) and 23 September 2007 (right).

12. Tsyganenko, N. A., Modeling the Earth's magnetospheric magnetic field within a realistic magnetopause, *Journal of Geophysical Research*, *100*, 5599–5612, 1995.
13. Tsyganenko, N. A., Effects of the solar wind conditions on the global magnetospheric configuration as deduced from data-based field, *Proceedings of the Third International Conference on Substorms (ICS-3)*, ESA SP-389, 181–185, 1996.